Bioactive Glasses and Glass-Ceramics

Fundamentals and Applications

Edited by:
Francesco Baino
Saeid Kargozar

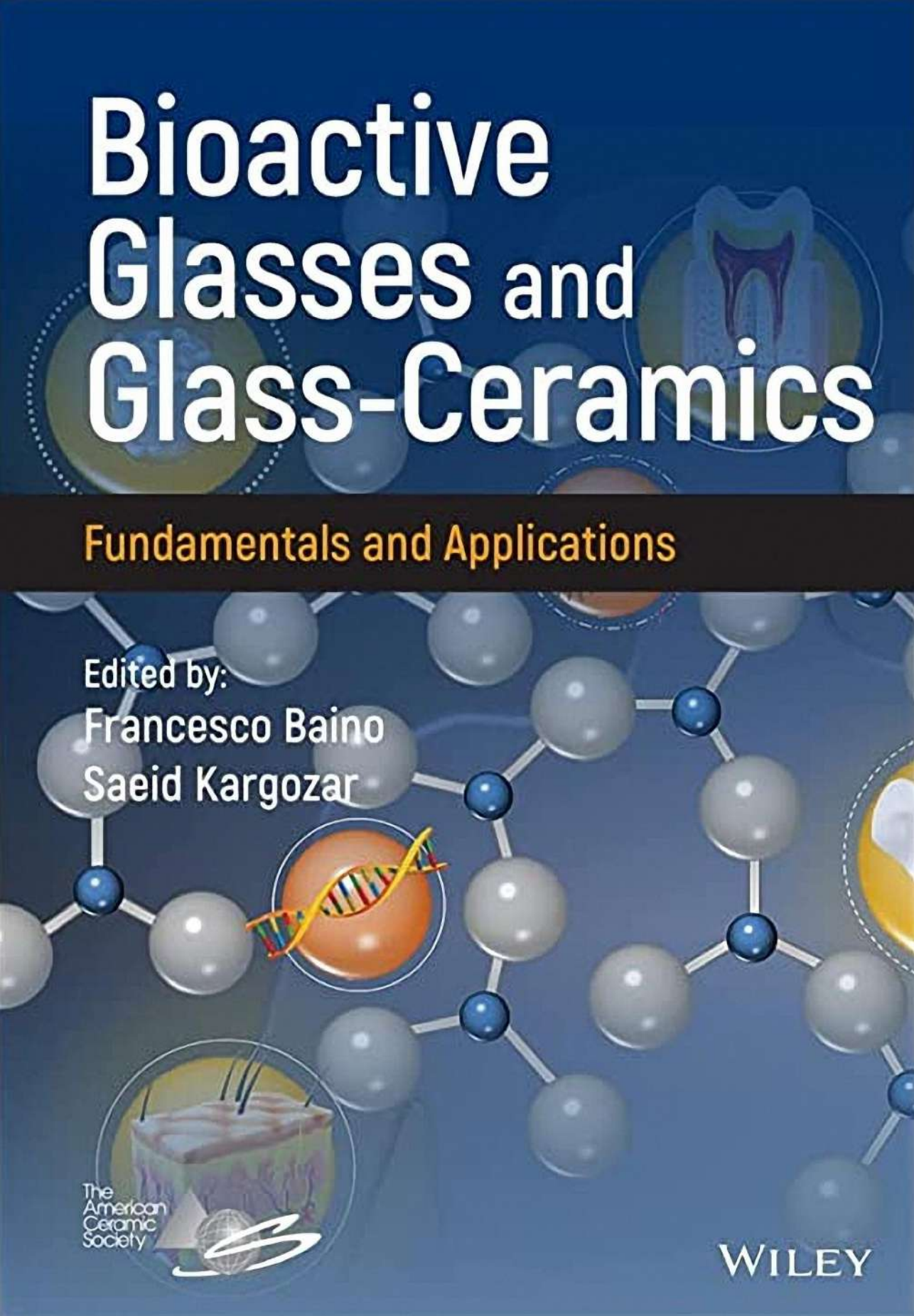

The American Ceramic Society

WILEY

Bioactive Glasses and Glass-Ceramics

Bioactive Glasses and Glass-Ceramics

Fundamentals and Applications

Edited by

Francesco Baino and Saeid Kargozar

The American Ceramic Society

WILEY

Published by John Wiley & Sons, Inc., Hoboken, New Jersey.

Published simultaneously in Canada.

Registered Office
John Wiley & Sons, Inc., 111 River Street, Hoboken, NJ 07030, USA

Editorial Office
111 River Street, Hoboken, NJ 07030, USA

For details of our global editorial offices, customer services, and more information about Wiley products visit us at www.wiley.com.

Wiley also publishes its books in a variety of electronic formats and by print-on-demand. Some content that appears in standard print versions of this book may not be available in other formats.

Library of Congress Cataloging-in-Publication Data

Names: Baino, Francesco, editor. | Kargozar, Saeid, editor.
Title: Bioactive glasses and glass-ceramics : fundamentals and applications / edited by Francesco Baino, Saeid Kargozar.
Description: Hoboken, New Jersey : Wiley-American Ceramic Society, [2022] | Includes bibliographical references and index.
Identifiers: LCCN 2022009994 (print) | LCCN 2022009995 (ebook) | ISBN 9781119724513 (cloth) | ISBN 9781119724889 (adobe pdf) | ISBN 9781119724667 (epub)
Subjects: LCSH: Bioactive glasses. | Glass-ceramics. | Glass in medicine. | Bioactive glasses–Therapeutic use. | Glass-ceramics–Therapeutic use.
Classification: LCC R857.G55 B544 2022 (print) | LCC R857.G55 (ebook) | DDC 610.28/4–dc23/eng/20220329
LC record available at https://lccn.loc.gov/2022009994
LC ebook record available at https://lccn.loc.gov/2022009995

Cover image: Courtesy Francesco Baino and Elisa Fiume
Cover design by Wiley

Set in 9.5/12.5pt STIXTwoText by Straive, Chennai, India

Contents

Preface

Bioactive glasses and glass-ceramics are a versatile class of biocompatible materials that have an astonishing impact in biomedicine. There is a long successful history in the synthesis, characterization, and utilization of these man-made materials. Generally, the expertise of researchers and scientists working in materials science, tissue engineering, biology, and medicine are required for producing the "best" glass and glass-ceramic formulations with optimized properties in favor of tissue repair and regeneration.

The first and foremost application of such biomaterials is addressed to treat hard tissue damages and injuries because of their inherent characteristics such as stiffness and bone-bonding ability. Bioactive glasses were first invented by Professor Larry L. Hench at the University of Florida more than half a century ago in 1969. The original bioactive glass, designed in a silicate system with a composition of $45SiO_2$–$24.5Na_2O$–$24.5CaO$–$6P_2O_5$ (wt%), was initially developed to meet the need for bone replacement of injured soldiers returned from the Vietnam War. Since then, a huge number of other compositions and bioactive glass-based products have been proposed and introduced into the market for managing hard tissue diseases and disorders. PerioGlas® and BonAlive® are two well-known synthetic bone grafts based on bioactive glasses with admirable success in the clinic. Over the last couple of decades, other types of bioactive glasses, including phosphate- and borate-based glasses, have been developed and applied for treating a wide range of tissue damages, including soft tissue injuries. In this regard, RediHeal™, a borate-based bioactive glass, is currently being used for managing wounds in animals and is awaiting for getting Food and Drug Administration (FDA) approval for practicing in humans suffering from slow-healing wounds (e.g. diabetic foot ulcers).

The main advantages of bioactive glasses are associated with their exceptional versatility in terms of composition–property relationships, controlled crystallized that can dictate the physicochemical and mechanical characteristics, and inherent ability to attach to both hard and soft tissues. Specifically, the ability to bond to living bone is related to the formation of a nano-crystalline hydroxyapatite layer, similar to bio-apatites, on the surface of bioactive glasses after exposure to body fluids. From a biological point of view, bioactive glasses cause no short- and long-term adverse effects on human cells, tissues, and organs; therefore, they are generally identified as biocompatible substances in biomedicine. Bioactive glasses are considered the osteoconductive and osteoinductive materials as they can provide a suitable substrate for adhesion and growth of bone-forming cells as well as induce osteoprogenitor cells to differentiate toward osteogenic lineages. In addition, bioactive glasses exhibit antibacterial, anti-inflammatory, and pro-angiogenic activities *in vitro* and *in vivo*. On this matter, a broad range of therapeutic ions (e.g. silver [Ag^+] and copper [Cu^{2+}]) are incorporated into the basic compositions of bioactive glasses to improve their biological performances imparting extra-functionalities, like antibacterial and pro-angiogenic properties. Indeed,

the release of therapeutic ions from bioactive glasses allows their usage as drug delivery vehicles for biomedical strategies. Recently published scientific reports emphasize the therapeutic capacity of bioactive glasses in battling against different types of cancers, especially those associated with hard tissues. On this point, mesoporous bioactive glasses possess an added value since their inherently nano-textured structure also provides a suitable platform for the incorporation and controlled delivery of a wide range of anti-cancer drugs to desired sites. With the advent of three-dimensional (3D) printing or additive manufacturing, the fabrication of 3D constructs based on or containing bioactive glasses and glass-ceramics offers a plethora of advantages, including improved mechanical strength and biological performance.

The present book aims to provide an updated understanding of biocompatible glasses and glass-ceramics based on current evidence in the literature and draw their future in the fields of biomaterials and tissue engineering. Basic aspects of bioactive glasses and glass-ceramics along with their fabrication routes and the latest processing strategies (e.g. additive manufacturing, laser treatments) are well-discussed from a materials science point of view. Besides, the biological effects of glasses and glass-ceramics have been considered on the living systems (*in vitro* and *in vivo*) as well as the current market needs and clinical challenges. The pros and cons of mesoporous bioactive glasses are argued in terms of drug delivery systems in relevant chapters. From a tissue engineering point of view, the regenerative capacity of different types of bioactive glasses and glass-ceramics has been reviewed in connection with hard (e.g. bone and teeth) and soft (e.g. skin) tissue healing. Moreover, hopes raised by these synthetic biomaterials in the treatment of malignancies have been well explored to shed light on their possible roles in the next-generation therapies. We hope that the present book is beneficial for the potential readership working in a broad community, who has a scientific background ranging from materials science and bioengineering to medicine and tissue engineering.

Politecnico di Torino, Turin, Italy — *Francesco Baino*
Mashhad University of Medical Sciences, Mashhad, Iran — *Saeid Kargozar*
March 26, 2022

List of Contributors

Simeon Agathopoulos
Department of Materials Science and Engineering
University of Ioannina
Ioannina
Greece

William Alles
Kazuo Inamori School of Engineering
Alfred University
Alfred, NY
USA

Felipe Arias-González
LaserON Laser Applications Research Group
Research Center in Technologies, Energy and Industrial Processes
CINTECX
University of Vigo
Vigo
Spain

and

Applied Physics Department
EEI, University of Vigo
Vigo
Spain

Mostafa Awaid
Department of Engineering
University of Rome "Niccolò Cusano", INSTM RU
Rome
Italy

Francesco Baino
Institute of Materials Physics and Engineering
Department of Applied Science and Technology (DISAT)
Politecnico di Torino
Torino
Italy

Sadaf Batool
School of Chemical and Materials Engineering (SCME)
National University of Sciences and Technology (NUST)
Islamabad
Pakistan

Stefano Berrettini
Laboratory of Temporal Bone Dissection and Otologic Tissue Engineering (OtoLab)
Department of Surgical, Medical, Molecular Pathology and Emergency Medicine
University of Pisa
Pisa
Italy

Aldo R. Boccaccini
Department of Materials Science and Engineering
Institute of Biomaterials
University of Erlangen-Nuremberg
Erlangen
Germany

Roger Borges
Centro de Ciências Naturais e Humanas
Universidade Federal do ABC
Santo André
Brazil

Mohamed Boutinguiza
LaserON Laser Applications Research Group
Research Center in Technologies, Energy and Industrial Processes
CINTECX
University of Vigo
Vigo
Spain

and

Applied Physics Department
EEI, University of Vigo
Vigo
Spain

Delia S. Brauer
Otto Schott Institute of Materials Research
Faculty of Chemistry and Earth Sciences
Friedrich Schiller University
Jena
Germany

Ilaria Cacciotti
Department of Engineering
University of Rome "Niccolò Cusano"
INSTM RU
Rome
Italy

Rafael Comesaña
LaserON Laser Applications Research Group
Research Center in Technologies, Energy and Industrial Processes
CINTECX
University of Vigo
Vigo
Spain

and

Department of Materials Engineering
Applied Mechanics and Construction
EEI, University of Vigo
Vigo
Spain

Glauco Cristofaro
Division of Otorhinolaryngology (ORL)
Arcispedale di "Santa Maria Nuova"
Florence
Italy

and

Laboratory of Temporal Bone Dissection and Otologic Tissue Engineering (OtoLab)
Department of Surgical, Medical, Molecular Pathology and Emergency Medicine
University of Pisa
Pisa
Italy

Serena Danti
Laboratory for Atomistic and Molecular Mechanics (LAMM)
Massachusetts Institute of Technology
Cambridge, MA
USA

and

University of Pisa Research Unit
National Interuniversity Consortium of Materials Science and Technology (INSTM)
Florence
Italy

and

Laboratory of Temporal Bone Dissection and Otologic Tissue Engineering (OtoLab)
Department of Surgical, Medical, Molecular Pathology and Emergency Medicine
University of Pisa
Pisa
Italy

and

Department of Civil and Industrial Engineering
University of Pisa
Pisa
Italy

Durgalakshmi Dhinasekaran
Department of Medical Physics
Anna University
Chennai
India

Konstantinos Dimitriadis
Department of Materials Science and Engineering
University of Ioannina
Ioannina
Greece

and

Division of Dental Technology
Department of Biomedical Sciences
University of West Attica
Athens
Greece

Ahmed El-Fiqi
Glass Research Department
Advanced Materials Technology and Mineral Resources Research Institute
National Research Centre
Cairo 12622
Egypt

Elisa Fiume
Institute of Materials Physics and Engineering
Department of Applied Science and Technology (DISAT)
Politecnico di Torino
Torino
Italy

Jessica Fletcher
Kazuo Inamori School of Engineering
Alfred University
Alfred, NY
USA

Qiang Fu
Science and Technology Division
Corning Inc.
Corning, NY
USA

Luis A. Genova
Centro de Ciência e Tecnologia dos Materiais
Instituto de Pesquisas Energéticas e Nucleares
São Paulo
Brazil

Smriti Gupta
Neurotherapeutics Laboratory
Department of Pharmaceutical Engineering and Technology
Indian Institute of Technology (Banaras Hindu University)
Varanasi
India

Leena Hupa
Johan Gadolin Process Chemistry Centre
Faculty of Science and Technology
Åbo Akademi University
Turku
Finland

Zakir Hussain
School of Chemical and Materials Engineering (SCME)
National University of Sciences and Technology (NUST)
Islamabad
Pakistan

Kanwal Ilyas
Department of Materials Science and Engineering
Institute of Biomaterials
University of Erlangen-Nuremberg
Erlangen
Germany

Giselle Z. Justo
Departamento de Bioquímica
Universidade Federal de São Paulo
São Paulo
Brazil

Saeid Kargozar
Tissue Engineering Research Group (TERG)
Department of Anatomy and Cell Biology,
School of Medicine
Mashhad University of Medical Sciences
Mashhad
Iran

Timothy James Keenan
Kazuo Inamori School of Engineering
Alfred University
Alfred, NY
USA

Sairam Krishnamurthy
Neurotherapeutics Laboratory
Department of Pharmaceutical Engineering and Technology
Indian Institute of Technology (Banaras Hindu University)
Varanasi
India

Anuj Kumar
School of Chemical Engineering
Yeungnam University
Gyeongsan
Republic of Korea

Usman Liaqat
School of Chemical and Materials Engineering (SCME)
National University of Sciences and Technology (NUST)
Islamabad
Pakistan

Nina C. Lindfors
Department of Hand Surgery
Helsinki University Hospital
Helsinki
Finland

and

Department of Surgery
Helsinki University
Helsinki
Finland

Fernando Lusquiños
LaserON Laser Applications Research Group
Research Center in Technologies
Energy and Industrial Processes
CINTECX
University of Vigo
Vigo
Spain

and

Applied Physics Department
EEI, University of Vigo
Vigo
Spain

Joel Machado Jr.
Departamento de Ciências Biológicas
Universidade Federal de São Paulo
Diadema
Brazil

Shreyasi Majumdar
Neurotherapeutics Laboratory
Department of Pharmaceutical Engineering and Technology
Indian Institute of Technology (Banaras Hindu University)
Varanasi
India

Juliana Marchi
Centro de Ciências Naturais e Humanas
Universidade Federal do ABC
Santo André
Brazil

Jonathan Massera
Faculty of Medicine and Health Technology
Tampere University
Tampere
Finland

John C. Mauro
Department of Materials Science and Engineering
The Pennsylvania State University
University Park, PA
USA

Tina Mehrabi
Biomaterials Laboratory, Division of Biomedical Engineering
Department of Life Science Engineering
Faculty of New Sciences and Technologies
University of Tehran
Tehran
Iran

Abdorreza S. Mesgar
Biomaterials Laboratory, Division of Biomedical Engineering
Department of Life Science Engineering
Faculty of New Sciences and Technologies
University of Tehran
Tehran
Iran

Carla Migneco
Institute of Materials Physics and Engineering
Department of Applied Science and Technology (DISAT)
Politecnico di Torino
Torino
Italy

Mario Milazzo
Laboratory for Atomistic and Molecular Mechanics (LAMM)
Massachusetts Institute of Technology
Cambridge, MA
USA

University of Pisa Research Unit
National Interuniversity Consortium of Materials Science and Technology (INSTM)
Florence
Italy

and

Department of Civil and Industrial Engineering University of Pisa
Pisa
Italy

Zahra Mohammadi
Biomaterials Laboratory, Division of Biomedical Engineering
Department of Life Science Engineering
Faculty of New Sciences and Technologies
University of Tehran
Tehran
Iran

Maziar Montazerian
Department of Materials Engineering
Northeastern Laboratory for Evaluation and Development of Biomaterials (CERTBIO)
Federal University of Campina Grande
Campina Grande
Brazil

Araceli de Pablos Martín
Otto Schott Institute of Materials Research
Faculty of Chemistry and Earth Sciences
Friedrich Schiller University
Jena
Germany

Juan Pou
LaserON Laser Applications Research Group
Research Center in Technologies
Energy and Industrial Processes
CINTECX
University of Vigo
Vigo
Spain

and

Applied Physics Department
EEI, University of Vigo
Vigo
Spain

Félix Quintero
LaserON Laser Applications Research Group
Research Center in Technologies
Energy and Industrial Processes
CINTECX
University of Vigo
Vigo
Spain

and

Applied Physics Department
EEI, University of Vigo
Vigo
Spain

Antonio Riveiro
LaserON Laser Applications Research Group
Research Center in Technologies
Energy and Industrial Processes
CINTECX
University of Vigo
Vigo
Spain

and

Department of Materials Engineering
Applied Mechanics and Construction
EEI, University of Vigo
Vigo
Spain

Daniel J. Sola
Laboratorio de Óptica
Centro de Investigación en Óptica y Nanofísica (CIOyN)
Campus Espinardo,
Universidad de Murcia
Murcia
Spain

and

Aragonese Foundation for Research and Development (ARAID)
Government of Aragon
Zaragoza
Spain

Ana Carolina S. Souza
Centro de Ciências Naturais e Humanas
Universidade Federal do ABC
Santo André
Brazil

Dilshat U. Tulyaganov
Department of Natural–Mathematical Sciences
Turin Polytechnic University in Tashkent
Tashkent
Uzbekistan

Jesús del Val
LaserON Laser Applications Research Group
Research Center in Technologies
Energy and Industrial Processes
CINTECX
University of Vigo
Vigo
Spain

and

Applied Physics Department
EEI, University of Vigo
Vigo
Spain

Enrica Verné
Institute of Materials Physics and Engineering
Department of Applied Science and
Technology (DISAT)
Politecnico di Torino
Torino
Italy

Fabian Westhauser
Orthopedic University Hospital
Heidelberg
Germany

Sebastian Wilkesmann
Orthopedic University Hospital
Heidelberg
Germany

Collin Wilkinson
Department of Materials Science and
Engineering
The Pennsylvania State University
University Park, PA
USA

Anthony William Wren
Kazuo Inamori School of Engineering
Alfred University
Alfred, NY
USA

Seiji Yamaguchi
Department of Biomedical Sciences
College of Life and Health Sciences
Chubu University
Kasugai
Aichi
Japan

Min Zhu
School of Materials and Chemistry
University of Shanghai for Science and
Technology
Shanghai
PR China

Yufang Zhu
State Key Laboratory of High Performance
Ceramics and Superfine Microstructure
Shanghai Institute of Ceramics
Chinese Academy of Sciences
Shanghai
PR China

1

Glass Crystallization and Glass-Ceramics – An Overview

Araceli de Pablos Martín and Delia S. Brauer

Otto Schott Institute of Materials Research, Faculty of Chemistry and Earth Sciences, Friedrich Schiller University, Jena, Germany

1.1 Introduction

Glass-ceramics were first developed in 1952 by Stanley Donald Stookey, a glass researcher at Corning Glass Works. He realized that by controlled thermal treatment of the parent glass, it would be possible to transform a glass into a partially or fully crystalline material with new properties, which depend on the nature of the crystals formed [1–5] (and refs. therein).

Applications of glass-ceramics [6, 7] include technical applications, e.g. as photosensitive [8–10] or machinable glass-ceramics [11–13] (including magnesia aluminosilicate glass-ceramics [14]) or for radioactive waste immobilization [15–17]. Fresnoite glass-ceramics [18] have been shown to be very versatile in the technical field owing to their pyroelectric, piezoelectric as well as nonlinear optical properties. Glass-ceramics are also used in many consumer products. The heat resistance and very low coefficient of thermal expansion of lithium aluminosilicate (LAS) glass-ceramics make them ideal for use as cooker top panels, doors for fireplaces, and opaque and transparent cookware [19]. Transparent glass-ceramics based on nanocrystallization are employed as passive optical glass-ceramics, like telescope mirrors based on the LAS system, as well as active optical glass-ceramics, like oxyfluoride glass-ceramics, which are doped with lanthanide ions to achieve interesting optical properties [4, 20], e.g. up-conversion emission. Energy applications include ion-conducting glass-ceramics as components for lithium batteries and sealants for solid oxide fuel cells [21]. For architectural applications, the wollastonite glass-ceramic Neopariés® [3], used in construction, is a good example. In the biomedical field, glass-ceramics are used for bone replacement materials or as dental restoration [22–28].

Important glass-ceramics for biomedical applications, their crystalline phases, properties, and application are listed in Table 1.1. These glass-ceramics exhibit better mechanical properties than bioactive glasses, but their bioactivity is lower. Thus, a research aim in the 1990s was to develop a new glass-ceramic, combing the high bioactivity of Bioglass 45S5 with the good mechanical properties of the glass-ceramic Cerabone. The glass-ceramic Biosilicate, developed in 2007, fulfilled these requirements, highlighting the role of crystallization in both, bioactivity and mechanical properties [30, 33, 49].

Bioactive Glasses and Glass-Ceramics: Fundamentals and Applications, First Edition.
Edited by Francesco Baino and Saeid Kargozar.

Table 1.1 Selection of commercial bioactive glass-ceramics: composition, crystalline phases, crystallization mechanism and applications.

Composition (wt%)	Crystalline phases	Crystallization mechanism	Application	References
		Dicor		
56–64SiO_2 15–20MgO 12–18K_2O 4–9F 0.5ZrO_2	Mica ($K_2Mg_5Si_8O_{20}F_4$)	Internal crystallization from phase separation	Dentistry	[29]
		Ceravital		
40–50SiO_2 5–10Na_2O 30–35CaO 10–50P_2O_5 2.5–5MgO 0.5–3K_2O	Devitrite ($Na_2Ca_3Si_6O_{16}$) Ap	Internal crystallization	Replacing the ossicular chain (middle ear)	[30, 31]
		A/W Cerabone		
34.0SiO_2 4.6MgO 44.7CaO 16.2P_2O_5 0.5CaF_2	Ap Wollastonite ($CaSiO_3$)	Surface crystallization (from the surfaces of glass particles)	Bone replacement (e.g. iliac crest)	[25, 32]
		Biosilicate		
48.5SiO_2 23.75Na_2O 23.75CaO 4P_2O_5	$Na_2CaSi_2O_6$ or $Na_2CaSi_2O_6$ and $NaCaPO_4$ (depending on the thermal conditions)	Internal crystallization	Orthopedics, dentistry, treatment of dental hypersensitivity	[30, 33–38]
		Bioverit I		
5.5–9.5Na_2O/K_2O 13–28CaO 6–28MgO 0–19.5Al_2O_3 29.5–50SiO_2 8–18P_2O_5 2.5–7F some TiO_2	Fluorophlogopite mica ($Na/KMg_3(AlSi_3O_{10}F_2)$) Ap	Internal crystallization from phase separation droplets	Orthopedics, head and neck surgery	[32, 39]
		Bioverit II		
7–10.5Na_2O/K_2O 0.1–3CaO 11–15MgO 26–30Al_2O_3 43–50SiO_2 0.1–5P_2O_5 3.3–4.8F	Fluorophlogopite mica ($Na/KMg_3(AlSi_3O_{10}F_2)$) Cordierite ($Mg_2Si_5Al_4O_{18}$)	Internal crystallization from phase separation droplets	Orthopedics, head and neck surgery	[32, 39–43]

(Continued)

Table 1.1 (Continued)

Composition (wt%)	Crystalline phases	Crystallization mechanism	Application	References
		Lithium silicate glass-ceramics		
Li_2O–K_2O–Al_2O_3–SiO_2–(ZnO)	Li_2SiO_3 $Li_2Si_2O_5$ Li_3PO_4 Depending on the composition	Internal crystallization	Dentistry	[44–47]
		Bioverit III		
45–44P_2O_5 6–18Al_2O_3 3–19CaO 11–18Na_2O 1.5–10 Additional agents	Ap Berlinite ($AlPO_4$) Varulite-like type (Na–Ca–Fe phosphate)	Internal crystallization	Orthopedics	[39, 40]
		IPS d.SIGN®		
50–65SiO_2 8–20Al_2O_3 7–13K_2O 4–12Na_2O 0.1–6CaO 0–5P_2O_5 0.1–3F 0–3 Additional agents	Leucite ($KAlSi_2O_6$) Ap $NaCaPO_4$	Surface crystallization of Leucite. Internal crystallization of Ap and $NaCaPO_4$ from phase separation	Dentistry	[48]

Ap: (Fluor)Apatite.

1.2 Controlled Crystallization of Glasses

Glass-ceramics are prepared by controlled heat treatment of glasses. When discussing crystallization of glasses, two different sequences must be distinguished: (i) spontaneous and uncontrolled crystallization occurring during cooling of the melt, which is an undesired event and typically leads to poor mechanical properties of the final material, and (ii) controlled crystallization by performing a single or successive heat treatments on a glass by following a well-defined time–temperature protocol, obtaining the desired crystalline fractions, crystal sizes, and morphologies. The process is described in several reviews [6, 50–53]. Controlled heat treatment allows us to obtain *glass-ceramics*. In 2017, technical committee TC07 of the International Commission on Glass (ICG), dedicated to crystallization and glass-ceramics, published an updated definition of glass-ceramics, considering current advanced preparation routes, new compositional families, a broader range of crystalline fractions, and including both surface and bulk crystallization [54]. Thus, a more complete definition was proposed: "Glass-ceramics are inorganic, non-metallic materials prepared by controlled crystallisation of glasses via different processing methods. They contain at least one type of functional crystalline phase and a residual glass. The volume fraction crystallised may vary from ppm to almost 100%." (Bioactive) Glass-ceramics are typically

prepared by (i) conventional melting and thermal treatment of the parent glass; (ii) sintering and crystallization of glass powders, or (iii) by sol–gel technology, which is an interesting example for the development of new coatings of orthopedic metallic implants (such as Ti-based alloys) to improve their integration with the host tissue and facilitate bone induction and cell proliferation [55–57]. It is also possible to prepare glass-ceramics by simultaneous sintering and crystallization of glass powder compacts with or without dopants to stimulate local tissue repair [25, 58].

Crystallization is an exothermic process and occurs in two stages: first, at temperatures slightly above the glass transition, *nucleation* takes place. The second stage, *crystal growth*, takes place at higher temperatures to promote the growth of those nuclei. The time necessary to develop the desired crystal fraction, including crystal size, depends on well-defined nucleation (I) and crystal growth (U) rates at a given temperature. The crystallization process is framed in the classical nucleation theory (CNT) [50, 52, 53, 59, 60], which is still being updated [6, 61–65].

1.3 Nucleation

The atoms in a glass constantly vibrate owing to their inherent thermal energy. Given the right circumstances of compositional fluctuations, temperature (below *liquidus* T_L), and time, individual structural units can join to form a nucleus of critical size, with radius r^*. This will be the precursor of a crystal with further heat treatment. Below the critical size r^* the nuclei are not stable and dissolve in the glassy matrix. In order to cover the whole r range, from nonstable embryos to stable nuclei above the critical size, we will refer to *clusters*.

Nucleation can be *homogeneous* (HOM) or *heterogeneous* (HET), depending on the existence of nucleation sites [63, 66]. Table 1.2 summarizes the most important features of both mechanisms [63, 66, 67].

The equations needed to calculate the thermodynamic and kinetic parameters of nucleation and crystallization are very usefully summarized in some publications [62, 68–71]. Assuming a spherical cluster, the variation of the free energy associated to the cluster formation can be expressed as a

Table 1.2 Differences between homogeneous (HOM) and heterogeneous (HET) nucleation.

HOM	HET
Main characteristics	
Nucleation without nucleation sites	Presence of nucleation sites
Nucleation starts in the volume of the glass and the probability of nucleation is equal everywhere	Nucleation can start in the volume (through the addition of nucleating agents) or at the surface (through foreign species). It can enable epitaxial growth
Variables	
Temperature, time, pressure	Temperature, time, pressure, specific energy, chemical gradients, stresses
Free energy for the formation of a critical size nucleus, ΔG^*	
$\Delta G^*(\mathrm{HOM}) = \frac{16\pi\sigma^3}{3\Delta G_V^2}$	$\Delta G^*(\mathrm{HET}) = \Delta G^*(\mathrm{HOM}) \cdot \left[\frac{(1-\cos\theta)^2 \cdot (2+\cos\theta)}{4}\right]$

θ is the contact angle of the nuclei species at the surface of the active sites ($\theta = 180°$ for HOM, $\theta < 180°$ for HET), σ is the free energy per unit area of crystal/glass interface, and ΔG_V is the free energy change per unit volume of crystals.

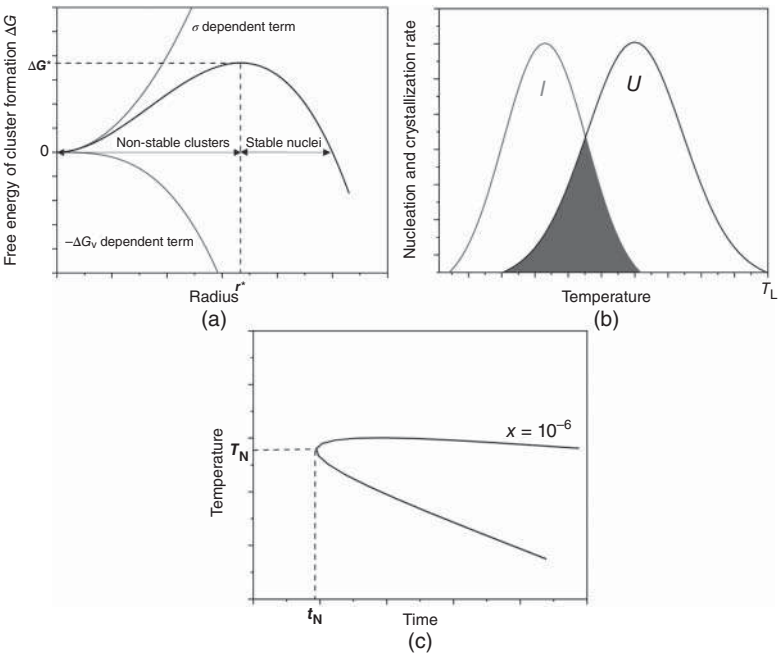

Figure 1.1 (a) Schematic representation of the free energy for cluster formation, ΔG, as a function of cluster size r. ΔG^* and r^* are the thermodynamic barrier for nucleation and critical cluster size, respectively. (b) Schematic illustration of Tammann's curves, showing nucleation and crystallization rates, I and U. The overlapping area of both curves (shaded in grey) usually gives the interval of crystallization. (c) Sketch of a TTT curve for a crystallized volume fraction of $x = 10^{-6}$. Nose temperature and the corresponding time are indicated as T_N and t_N, respectively.

function of its radius r. This variation of free energy is represented as the sum of two contributions (Eq. (1.1)):

$$\Delta G = \frac{4}{3}\pi r^3 \Delta G_V + 4\pi r^2 \sigma \tag{1.1}$$

which contains a volume-dependent term (cubed dependence with radius, r^3) and a surface-dependent term (squared dependence with radius, r^2) (Figure 1.1a). The former represents the energy decrease on ordering an amorphous region to form a crystalline lattice, and it is given by the volume $V = 4\pi r^3/3$ (for a spherical cluster) multiplied by the free energy of crystallization per unit volume, ΔG_V. The second term is surface-dependent, and it is associated with the energy involved to form a new spherical surface of solid/liquid interfacial area $4\pi r^2$, i.e. the crystal/liquid interfacial free energy, σ, which can be estimated [68]. The free energy of crystallization, ΔG_V, depends on the undercooling, $\Delta T = T - T_L$, according to $\Delta G_V = \Delta T\, L/T_L$, where T_L is the liquidus temperature, T is a given nucleation temperature and L is the latent heat of fusion per unit volume. ΔG_V is negative ($\Delta G_V = G_{V(crystal)} - G_{V(amorphous)}$), since the forming nucleus has a lower Gibbs free energy than the undercooled liquid for $T < T_L$. The actual *driving force for nucleation* is ΔG_V. Figure 1.1a shows schematically the plot of ΔG as a function of r (Eq. (1.1)). For low values of r, the square term dominates over the cubic term, so that ΔG initially increases until a maximum and then decreases, when the volume-dependent term dominates. The maximum of the curve of ΔG vs. r corresponds to the critical radius r^*, where $d\Delta G = 0$. Deriving Eq. (1.1) and equaling zero, the

critical radius r^* is given by

$$r^* = \frac{-2\sigma}{\Delta G_V} \tag{1.2}$$

Note that ΔG_V is negative and, thus, r is a positive value. Substituting in the volume term of Eq. (1.1),

$$\Delta G^* = \frac{16\pi\sigma^3}{3(\Delta G_V)^2} \tag{1.3}$$

where ΔG^* (or W^* in some publications) represents the energy to overcome the nucleation barrier, i.e. the *free energy for the formation of a critical size nucleus* (Figure 1.1a). From Eq. (1.3), the strong (square) dependence of ΔG^* on the temperature is clear (since $\Delta G_V = \Delta T\, L/T_L$). Thus, the ΔG curve (Figure 1.1a) will vary depending on the nucleation temperature [62]. Considering that $\Delta G = \Delta G_V \cdot V_m$ and $\Delta G = (\Delta H_m \cdot \Delta T)/T_m$ (V_m is the molar volume of the crystalline phase, ΔH_m is the melting enthalpy per mole, ΔT is the undercooling, and T_m is the melting temperature), and substituting ΔG_V in Eq. (1.3), a more practical expression of ΔG^* is given [68]:

$$\Delta G^* = \frac{16\pi\sigma^3 V_m^2 T_m^2}{3\Delta H_m^2 \Delta T^2} \tag{1.4}$$

It is worth noting that r^* (Eq. (1.2)) and ΔG^* (Eq. (1.3)) decrease with increasing the degree of undercooling, ΔT, i.e. with decreasing temperature. At very high temperatures (small undercooling ΔT) r^* would be so large that it would not be possible to form a stable nucleus (note that for the extreme case of $\Delta T = 0$ the values of r^* and ΔG^* become infinite, Eqs. (1.2) and (1.4)). Moreover, this would imply that all glasses should be able to nucleate at temperatures well below T_L (because of the very low thermodynamic barrier ΔG^*), which does not agree with the experimental results. Thereof, kinetic considerations must be taken into account.

Considering the kinetic aspect of the nucleation, the rate at which the nuclei will appear in the glass at a given temperature is given by the steady-state nucleation rate, I (nuclei/m^3 s):

$$I = A \exp\left(-\frac{\Delta G^* + \Delta G_D}{kT}\right) \tag{1.5}$$

where A is a preexponential factor, $A = n_v \cdot kT/h$, h is the Planck constant and n_v is the number of atoms per unit volume, $n_v = N_A/V_m$ [68], and represents the probability of formation of a nucleus of critical size ($<10^{13}$ s^{-1} m^{-3} for HOM nucleation of silicate glasses [62]). $\Delta G^*/kT$ (or W^*/kT) and $\Delta G_D/kT$ (k is the Boltzmann constant) in Eq. (1.5) represent the thermodynamic and the diffusion barriers for the formation of a critical size nucleus and for diffusion (of atoms toward the nucleus interface), respectively.

The kinetic barrier, $\Delta G_D/kT$, can be expressed considering the atomic jump distance, λ, and the diffusion coefficient, $D = kT/\lambda\eta$, [62] as follows:

$$\frac{\Delta G_D}{kT} = \ln\left(\frac{kT\lambda^2}{hD}\right) \tag{1.6}$$

ΔG^* increases with increasing (nucleation) temperature (Eq. (1.4)), and thus, I increases until a maximum, which is close to the glass transition temperature, T_g, of the glass (Figure 1.1b). A detailed study of the relationship between the temperature of maximum nucleation rate and the T_g is reported in [72]. At temperatures lower than the temperature of maximum nucleation rate, ΔG_D dominates in Eq. (1.5), and nucleation becomes slower (I decreases), owing to an increase of viscosity (diffusion coefficient D decreases) and the associated limited atomic mobility with decreasing temperature from T_g (Figure 1.1b).

A very useful example of how the thermodynamic parameters of the nucleation process are calculated is found in the paper by Cabral et al. [68], where I, ΔG^*, ΔG_V, and σ are represented as a function of temperature for fresnoite glass. In practice, I can be also determined from the plot of the nucleus number density (N_v, nuclei/m^3) as a function of time of treatment at a fixed nucleation temperature. N_v is determined from optical or scanning microscopy experiments using image analysis software, by counting the number of nuclei per unit of area [73], or even through thermal analysis [74]. At the beginning of a nucleation treatment N_v increases quasi exponentially with time, then a linear increase of N_v takes place, which is the stationary nucleation regime. The nucleation rate, I (nuclei/m^3 s), corresponds to the slope of that straight segment. An interesting example for a high value of nucleation rate is that of fresnoite glass, which exhibits one of the highest nucleation rates (10^{17} m^{-3} s^{-1}) measured in inorganic glasses [68, 75]. Nucleation rates of $Li_2O{\cdot}SiO_2$ and $Na_2O{\cdot}2CaO{\cdot}3SiO_2$ glasses have been also determined [70, 73].

Experimentally, an estimation of the temperature of maximum nucleation can be obtained from thermal analysis [74]. Plotting the crystallization temperatures of differential scanning calorimetry (DSC) curves (crystallization peak, T_c) as a function of different nucleation temperatures, a curve will be obtained, whose minimum is the most effective nucleation temperature.

For the two mechanisms of nucleation (Table 1.2), the energy for critical cluster formation is usually lower in HET than in HOM, since nucleation is facilitated (catalyzed) in the presence of a crystalline primary nucleus in the former. Moreover, in HET, the interfacial energy (Eq. (1.1)) is reduced. These active nucleation sites can be nucleating agents intentionally added to the composition for this purpose (typical examples are TiO_2, ZrO_2, Fe_2O_3, Au, Ag, Pt, or Pd), or it may happen in an undesired/uncontrolled way through impurities, bubbles, foreign species on the container walls or in the atmosphere, etc. The main condition for HET to take place is proper wettability of the primary nucleus with the nucleating sites, which is given by the contact angle Θ. HET is particularly effective if the lattice parameters of crystal and nucleating site (in at least two directions) do not differ by more than 15%, which is called *epitaxial growth*. Table 1.2 displays the thermodynamic barrier for formation of a critical size (r^*) nucleus (ΔG^*) for both mechanisms. Nucleation rates of both mechanisms can be determined experimentally [71].

As part of the nucleation stage, *phase separation* (PS) phenomena in glasses must be considered. Although PS phenomena are inevitably associated with a source of defects in industrial glass production (mainly loss of transparency), for the preparation of glass-ceramics by controlled crystallization may be considered as an advantage. PS can have two different mechanisms: *nucleated* and *spinodal*. For the purpose of this chapter, only nucleated PS will be discussed. Usually, PS droplets are enriched in network modifiers, while the glassy matrix becomes enriched in SiO_2 or other network formers [19]. In a phase-separated base glass, nucleating agents may accumulate in one of the microphases [66]. These compositional fluctuations inevitably affect the kinetic of nucleation. Recently, Zanotto reviewed the aspects of PS influence in crystallization [76]. As reported, PS leads to a higher thermodynamic driving force, an increase in the diffusion of atoms, also increasing the nucleation rate, and lowering the interfacial energy, σ. Various N_v vs. time curves of phase-separated glasses were reviewed. For many years, it was believed that PS droplets act as active sites for nucleation in the volume of the glass, favoring internal crystallization. However, according to Zanotto [76], PS acts in a different way, in which PS shifts the composition of the glass matrix toward that of the stoichiometric crystal phase, increasing the crystal nucleation rate, which is actually the real effect rather than the presence of nucleation sites. New insight into the role and development of PS droplets in glass-ceramics has been obtained in the last years thanks to the availability of latest generation transmission electron microscopes. The work by Höche and coauthors is worth mentioning here [19, 77–82].

1.4 Crystal Growth

Once the nuclei have reached the critical size (r^*), they are able to grow to form crystals through deposition of atomic layers. Similar to the nucleation process, this stage is characterized by the crystal growth nucleation rate, U, which also contains a thermodynamic and a kinetic barrier. The kinetic term is governed by the diffusion of atoms, which are joined with the growing crystal (proportional to the activation energy for diffusion ΔG_D), but also those which are detached and return to the liquid (proportional to $\Delta G_D + \Delta G_V$). Considering these two contributions, the net crystal growth rate is expressed by:

$$U = f\lambda\frac{kT}{h}\exp\left(\frac{-\Delta G_D}{kT}\right)\left(1-\exp\left(\frac{\Delta G_V}{kT}\right)\right) \tag{1.7}$$

where f is the fraction of sites on the interface where the atoms are preferentially attached or removed, and can be determined experimentally [83], λ is the diffusion distance or distance advanced by the interface (usually taken as a molecular diameter) [83], and η is the shear viscosity. The diffusion coefficient of the Stokes–Einstein/Eyring equation: $D = kT/\lambda\eta$ is implicit in Eq. (1.7) through Eq. (1.6). Note that the diffusion in the crystal growth stage is not necessarily the same as for the nucleation stage, since the diffusion of the atoms during nucleation is more local (over smaller distances) than during the crystal growth stage. A very useful description of the role of the diffusion coefficient in the crystal growth has been published [84]. Note that at T_L (undercooling $\Delta T = 0$), $\Delta G_V = 0$ and $U = 0$ (Figure 1.1b). Lowering the temperature from T_L (increasing undercooling) leads to an increase in the crystal growth rate U until a maximum is reached. Similarly to the nucleation rate I, when the diffusion term governs at low temperatures and approaches zero, the crystal growth rate U decreases (Figure 1.1b).

In practice, and similar to I, U can be also determined from plots of size (or radius) of crystals (determined by microscopy or from X-ray diffraction analyses using the Scherrer equation) as a function of treatment time at a fixed temperature. The slope of the straight line is the crystallization rate U (μm/min) [75].

Moreover, the time dependence of the crystal size (r) can be fitted according to $r = U \cdot t^p$, where r is the average crystal radius, U is the growth rate, t is the dwell time of the heat treatment, and p is the growth exponent [85].

When preparing (bioactive) glass-ceramics, controlled heat treatment is usually performed below liquidus temperature. U usually increases with temperature until a maximum (Figure 1.1b). At higher temperatures than that of the maximum, the crystal growth rate decreases, owing to the difficulty of dissipating the heat from the crystallization process. At lower temperatures, high viscosity hinders crystal growth. Thus, the role of viscosity (and thus, diffusion) is key to improve and update nucleation and crystal growth equations [61, 83, 86–88].

If nucleation and crystal growth rates (I and U) are plotted together as a function of temperature (Tammann's curves [51, 62]), it is obvious that the maximum of I occurs at lower temperatures than that of U. The overlapping of both curves usually gives the interval of crystallization, in the way that the larger the overlap, the higher the crystallization tendency [89] (Figure 1.1b).

In a typical double-stage heat treatment, where nucleation treatment is carried out first and then crystal growth treatment follows at higher temperature (this is carried out when the I and U curves overlap only minimally or not at all), the kinetics of both processes are key for the development of glass-ceramics. The kinetic dependence [71, 90, 91] can be described through the following time parameters: an initial time, t_0, which is the time at which the first structural units are experimentally detected, and which corresponds to the first experimental point of the N_v vs. time curve; the

induction time, t_{ind}, which in the N_v vs. time curve comprises the time between $t = 0$ and the interception of the straight line with the time axis [70, 73]. The induction time, t_{ind}, is in fact the sum of three contributions [91]: *time lag*, τ, which is the period of time in which the size of the nuclei grows until r^* ($r \leq r^*$ regime), the average time of formation of the first supercritical nucleus in the steady-state nucleation regime, t_{ss} [91], and *incubation time*, t_i, which is the time required by the nuclei/crystals to grow to a detectable size and, of course, depends on the temperatures of the nucleation and crystal growth processes [91]. Moreover, the heating rate of the heat treatment plays a significant role in the kinetics of nucleation and crystal growth, as discussed by Deubener et al. [91], since the induction time, t_{ind}, increases with increasing heating rates with a cubic root dependence.

From a practical point of view, thermal characterization techniques, like DSC [74, 92], heating microscopy, or viscometry [93], also in combination with optical and electron microscopy nucleation studies, are widely employed to determine the thermodynamics and kinetics of crystallization in glasses. Good examples are the studies by the groups of Zanotto and Deubener, among others [62, 63, 74, 83, 84, 86–88, 91].

Time–temperature–transformation curves (TTT curves) are a very useful representation of the crystallization process [54, 71] (Figure 1.1c). A very illustrative use of TTT curves is for the determination of the minimum cooling rate necessary to form a glass (without crystallization occurring), which is the *critical cooling rate*, q_c. Uncontrolled crystallization upon cooling of the glass melt can be avoided if cooling is rapid enough (there is no time for reorganization of atoms to form ordered structures). The critical cooling rate can be determined from the TTT curve for transformation (crystals concentration) $x = 10^{-6}$ (1 ppm), which is assumed to be the detection limit by conventional experimental techniques. The critical cooling rate is then $q_c = (T_L - T_N)/t_N$, where T_N is the "nose temperature" of the TTT curve, which corresponds to the temperature at which the time to achieve a crystal fraction of 10^{-6} is the shortest (shortest time, t_N) [54, 71] (Figure 1.1c).

Related to the HOM and HET classification, crystallization can be also classified as *internal* (also called volume or bulk crystallization) or *surface crystallization* [94], depending on where the nuclei formation starts. Although most glasses undergo internal crystallization (HOM or HET) [22, 30], some well-known glass-ceramics which crystallize following a surface crystallization mechanism are cordierite ($2MgO{\cdot}2Al_2O_3{\cdot}5SiO_2$), diopside ($MgO{\cdot}CaO{\cdot}2SiO_2$), and devitrite ($Na_2O{\cdot}3CaO{\cdot}6SiO_2$) glass-ceramics, which are obtained from stoichiometric or near-stoichiometric glass compositions [95] (and refs. therein). Moreover, a third possibility exists, since surface and bulk crystallization may occur simultaneously (even competing) (Figure 1.2) [64, 97]. Table 1.1 displays some of the bioactive glass-ceramic systems showing internal or surface crystallization, or a combination of both.

Although it can occur in bulk pieces, surface crystallization is the predominant mechanism in powders, owing to the larger relative surface area. Thus, its study is particularly important when the bioactive glass-ceramics are intended to be used as powders, particulates, or slurries [98] or as scaffolds obtained by sintering of glass powders. By contrast, internal crystallization of bioactive glass-ceramics must be investigated when bulk pieces are used for application as monoliths. Unlike glass powders, bulk pieces can be machined to specific geometries. As a combination of both, powder compacts can be prepared by sintering of glass powders as well. Here, surface crystallization takes place at the surface of the powder grains, while internal nucleation may occur in the interior of the grains. Whether powder or bulk material are used depends on the final application.

The influence of the heat treatment on glass-ceramic microstructure is illustrated in Figure 1.2, using leucite-apatite glass-ceramics as an example [48, 64, 96, 99]. Leucite crystals form at the surface and grow dendritically into the bulk, as shown in a cross-section micrograph in [48]. Apatite crystals are formed in the bulk of the glass-ceramic, and their morphology can be tuned from droplets to needles, depending on the heat treatment (Figure 1.2) [64].

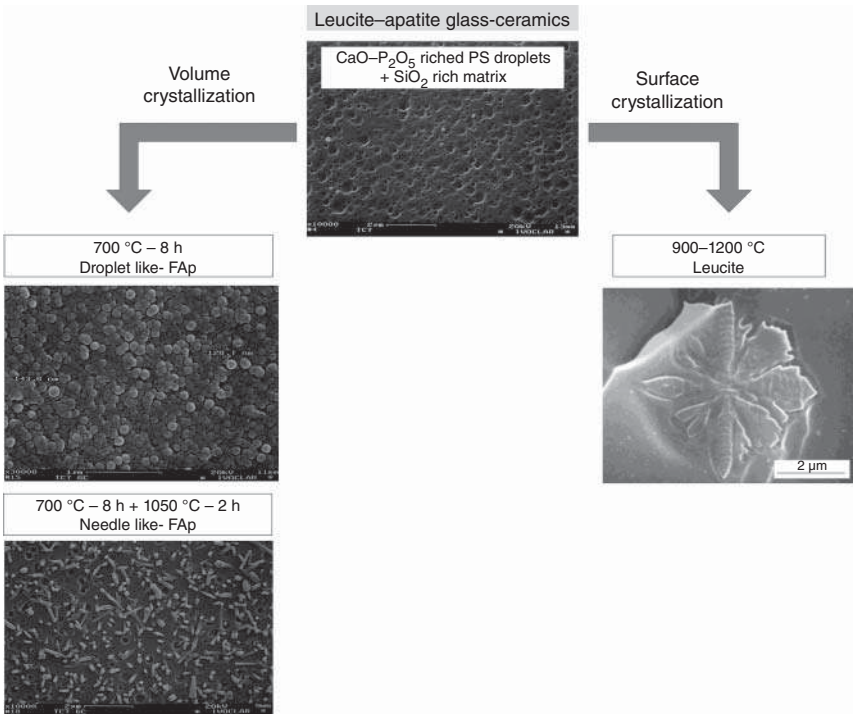

Figure 1.2 Scheme of leucite-apatite glass-ceramics, showing the crystallization of leucite at the surface (right) and that of fluorapatite (FAp) in two different morphologies in the volume (left). Source: Micrographs of the phase separated glass, droplet like- and needle like-FAp are from Höland et al. [64], with permission of Elsevier. Micrograph of the surface crystallization of leucite is from Höland et al. [96], Figure 03, p. 03/with permission of John Wiley & Sons, Inc.

1.5 Conclusion

Glass-ceramics offer the possibility to fine-tune crystal phase, size and fraction, and, ultimately, the bioactivity of a material via heat treatment. This illustrates the relevance and possible impact of crystallization for bioactive glass-ceramics, but it also shows that for these materials a broader range of applications may be possible than for the precursor parent glasses. If we know the main parameters governing nucleation and crystallization processes in glasses and understand the influence of temperature, diffusion, viscosity, phase separation or nucleating agents, a successful temperature–time protocol can be established to obtain the desired microstructure. This makes it possible to prepare (bioactive) glass-ceramics which meet the requirements for a particular clinical application.

References

1 Beall, G.H. and Pinckney, L.R. (1999). Nanophase glass-ceramics. *Journal of the American Ceramic Society* 82: 5–16.

2 Stookey, S.D. (2000). *Explorations in Glass: An Autobiography*. Wiley.

3 Zanotto, E.D. (2010). A bright future for glass-ceramics. *American Ceramic Society Bulletin* 89: 19–27.

4 De Pablos-Martin, A., Ferrari, M., Pascual, M.J., and Righini, G.C. (2015). Glass-ceramics: a class of nanostructured materials for photonics. *La Rivista del Nuovo Cimento* 38: 311–369.

5 Hench, L.L. (2011). Glass and glass-ceramic technologies to transform the world. *International Journal of Applied Glass Science* 2: 162–176.

6 Höland, W. and Beall, G.H. (2012). *Glass-Ceramic Technology*. Wiley.

7 Davis, M.J. and Zanotto, E.D. (2017). Glass-ceramics and realization of the unobtainable: property combinations that push the envelope. *MRS Bulletin* 42: 195–199.

8 Borrelli, N.F. (2016). *Photosensitive Glass and Glass-Ceramics*. CRC Press.

9 Stoica, M., Patzig, C., Bocker, C. et al. (2017). Structural evolution of CaF_2 nanoparticles during the photoinduced crystallization of a Na_2O–K_2O–CaO–CaF_2–Al_2O_3–ZnO–SiO_2 glass. *Journal of Materials Science* 52: 13390–13401.

10 Nascimento, M.L.F. (2016). Centenary of a serendipitous inventor: Stookey and a short statistical overview of photosensitive glass & glass-ceramics science and technology. *Recent Patents on Materials Science* 9: 33–44.

11 Henry, J., Chen, X., Law, R.V., and Hill, R.G. (2018). The investigation of the crystalline phases development in Macor® glass-ceramic. *Journal of the European Ceramic Society* 38: 245–251.

12 Guedes, A., Pinto, A.M.P., Vieira, M., and Viana, F. (2001). Multilayered interface in Ti/Macor® machinable glass-ceramic joints. *Materials Science and Engineering A* 301: 118–124.

13 Höland, W. and Vogel, W. (2013). Machinable and phosphate glass-ceramics. In: *An Introduction to Bioceramics*, 2e (ed. L.L. Hench), 215–228. World Scientific Publishing Company.

14 Benitez, T., Veber, A., Pagnan Furlan, K. et al. (2020). Development of magnesium-aluminum-silicate glass-ceramics nucleated with Nb_2O_5. *International Journal of Applied Glass Science* 11: 155–169.

15 Cao, C. and Goel, A. (2016). Apatite based ceramic waste forms for immobilization of radioactive iodine, an overview – 16155. *WM2016 Conference, March 6 – 10, 2016, Phoenix, Arizona, USA*, WM Symposia.

16 Ojovan, M.I. and Batyukhnova, O.G. (2007). Glasses for nuclear waste immobilization. In: *WM '07 Conference, Tucson, AZ, USA*, 15. WM Symposia.

17 Donald, I.W., Metcalfe, B.L., and Taylor, R.N.J. (1997). The immobilization of high level radioactive wastes using ceramics and glasses. *Journal of Materials Science* 32: 5851–5887.

18 Wisniewski, W., Thieme, K., and Rüssel, C. (2018). Fresnoite glass-ceramics – a review. *Progress in Materials Science* 98: 68–107.

19 Kleebusch, E., Patzig, C., Höche, T., and Rüssel, C. (2018). The evidence of phase separation droplets in the crystallization process of a Li_2O–Al_2O_3–SiO_2 glass with TiO_2 as nucleating agent – an X-ray diffraction and (S)TEM-study supported by EDX-analysis. *Ceramics International* 44: 2919–2926.

20 Berneschi, S., Soria, S., Righini, G.C. et al. (2010). Rare-earth-activated glass-ceramic waveguides. *Optical Materials* 32: 1644–1647.

21 de Pablos-Martin, A., Rodriguez-Lopez, S., and Pascual, M.J. (2020). Processing technologies for sealing glasses and glass-ceramics. *International Journal of Applied Glass Science* 11: 552–568.

22 Fu, L., Engqvist, H., and Xia, W. (2020). Glass-ceramics in dentistry: a review. *Materials* 13: 1049.

23 Pollington, S. (2011). Novel glass-ceramics for dental restorations. *Journal of Contemporary Dentistry* 12: 60–67.

24 Kasuga, T. (2007). Development of phosphate glass-ceramics for biomedical applications. *Journal of the Ceramic Society of Japan* 115: 455–459.

25 Kokubo, T. (1991). Bioactive glass ceramics: properties and applications. *Biomaterials* 12: 155–163.

26 Fernandes, H.R., Gaddam, A., Rebelo, A. et al. (2018). Bioactive glasses and glass-ceramics for healthcare applications in bone regeneration and tissue engineering. *Materials* 11: 2530.

27 Jones, J.R., Brauer, D.S., Hupa, L., and Greenspan, D.C. (2016). Bioglass and bioactive glasses and their impact on healthcare. *International Journal of Applied Glass Science* 7: 423–434.

28 Jones, J.R. (2013). Review of bioactive glass: from hench to hybrids. *Acta Biomaterialia* 9: 4457–4486.

29 Bapna, M.S. and Mueller, H.J. (1996). Study of devitrification of Dicor® glass. *Biomaterials* 17: 2045–2052.

30 Crovace, M.C., Souza, M.T., Chinaglia, C.R. et al. (2016). Biosilicate® – a multipurpose, highly bioactive glass-ceramic. In vitro, in vivo and clinical trials. *Journal of Non-Crystalline Solids* 432: 90–110.

31 Ohtsuki, C., Kushitani, H., Kokubo, T. et al. (1991). Apatite formation on the surface of Ceravital-type glass-ceramic in the body. *Journal of Biomedical Materials Research* 25: 1363–1370.

32 Montazerian, M. and Dutra Zanotto, E. (2016). History and trends of bioactive glass-ceramics. *Journal of Biomedical Materials Research Part A* 104: 1231–1249.

33 Moura, J., Teixeira, L.N., Ravagnani, C. et al. (2007). In vitro osteogenesis on a highly bioactive glass-ceramic (Biosilicate®). *Journal of Biomedical Materials Research Part A* 82: 545–557.

34 Azenha, M.R., Peitl, O., and Barros, V.M.R. (2010). Bone response to biosilicates® with different crystal phases. *Brazilian Dental Journal* 21: 383–389.

35 Peitl, O., Dutra Zanotto, E., and Hench, L.L. (2001). Highly bioactive P_2O_5–Na_2O–CaO–SiO_2 glass-ceramics. *Journal of Non-Crystalline Solids* 292: 115–126.

36 Peitl, O., La Torre, G.P., and Hench, L.L. (1996). Effect of crystallization on apatite-layer formation of bioactive glass 45S5. *Journal of Biomedical Materials Research* 30: 509–514.

37 Peitl, O., Zanotto, E.D., Serbena, F.C., and Hench, L.L. (2012). Compositional and microstructural design of highly bioactive P_2O_5–Na_2O–CaO–SiO_2 glass-ceramics. *Acta Biomaterialia* 8: 321–332.

38 Daguano, J.K.M.F., Rogero, S.O., Crovace, M.C. et al. (2013). Bioactivity and cytotoxicity of glass and glass-ceramics based on the 3CaO–P_2O_5–SiO_2–MgO system. *Journal of Materials Science: Materials in Medicine* 24: 2171–2180.

39 Vogel, W. and Höland, W. (1987). The development of bioglass ceramics for medical applications. *Angewandte Chemie International Edition in English* 26: 527–544.

40 Vogel, W. and Höland, W. (1990). Development, structure, properties and application of glass-ceramics for medicine. *Journal of Non-Crystalline Solids* 123: 349–353.

41 Höland, W., Wange, P., Naumann, K. et al. (1991). Control of phase formation processes in glass-ceramics for medicine and technology. *Journal of Non-Crystalline Solids* 129: 152–162.

42 Li, H., You, D.Q., Zhou, C.R., and Ran, J.G. (2006). Study on machinable glass-ceramic containing fluorophlogopite for dental CAD/CAM system. *Journal of Materials Science: Materials in Medicine* 17: 1133–1137.

43 Gali, S. (2019). Mica glass ceramics for dental restorations. *Materials and Technology* 34: 2–11.

44 Krüger, S., Deubener, J., Ritzberger, C., and Höland, W. (2013). Nucleation kinetics of lithium metasilicate in ZrO_2-bearing lithium disilicate glasses for dental application. *International Journal of Applied Glass Science* 4: 9–19.

45 Liao, W.-C., Rampf, M., Dittmer, M. et al. (2019). Nucleation and crystal formation in lithium disilicate-apatite glass-ceramic from a combined use of X-ray diffraction, solid-state NMR, and microscopy. *Helvetica Chimica Acta* 102: e1800210.

46 Höland, W., Rheinberger, V., Apel, E., and van't Hoen, C. (2007). Principles and phenomena of bioengineering with glass-ceramics for dental restoration. *Journal of the European Ceramic Society* 27: 1521–1526.

47 Soares, V.O., Serbena, F.C., Mathias, I. et al. (2021). New, tough and strong lithium metasilicate dental glass-ceramic. *Ceramics International* 47: 2793–2801.

48 Höland, W., Rheinberger, V., Wegner, S., and Frank, M. (2000). Needle-like apatite-leucite glass-ceramic as a base material for the veneering of metal restorations in dentistry. *Journal of Materials Science: Materials in Medicine* 11: 11–17.

49 Massera, J. (2020). Bioactive glass-ceramics: from macro to nano. In: *Nanostructured Biomaterials for Regenerative Medicine* (ed. V. Guarino, M. Iafisco and S. Spriano), 275–292. Woodhead Publishing.

50 Gutzow, I., Kashchiev, D., and Avramov, I. (1985). Nucleation and crystallization in glass-forming melts – old problems and new questions. *Journal of Non-Crystalline Solids* 73: 477–499.

51 Schmelzer, J.W.P. (2004). A new approach to nucleation theory and its application to phase formation processes in glass-forming melts. *Physics and Chemistry of Glasses* 45: 116–120.

52 Weinberg, M.C. (1995). Nucleation and crystallization in glass. *Abstracts of Papers of the American Chemical Society* 209: 1–14.

53 Weinberg, M.C. (1999). A few topics concerning nucleation and crystallization in glasses. *Journal of Non-Crystalline Solids* 255: 1–14.

54 Deubener, J., Allix, M., Davis, M.J. et al. (2018). Updated definition of glass-ceramics. *Journal of Non-Crystalline Solids* 501: 3–10.

55 Samuneva, B., Kalimanova, S., Kashchieva, E. et al. (2003). Composite glass-ceramics in the systems $MgO–SiO_2$, $MgO–Al_2O_3–SiO_2$ and fluorapatite obtained by sol–gel technology. *Journal of Sol-Gel Science and Technology* 26: 273–278.

56 Nawaz, Q., de Pablos-Martín, A., e Silva, J.M.S. et al. (2021). Crystallization study of sol–gel derived 13-93 bioactive glass powder. *Journal of the European Ceramic Society* 41 (2): 1695–1706.

57 Nawaz, Q., de Pablos-Martín, A., e Silva, J.M.S. et al. (2020). New insights into the crystallization process of sol–gel-derived 45S5 bioactive glass. *Journal of the American Ceramic Society* 103: 4234–4247.

58 Blaeß, C., Müller, R., Poologasundarampillai, G., and Brauer, D.S. (2019). Sintering and concomitant crystallization of bioactive glasses. *International Journal of Applied Glass Science* 10: 449–462.

59 Yinnon, H. and Uhlmann, D.R. (1982). A kinetic treatment of glass-formation. Transient nucleation in non-isothermal crystallization during cooling. *Journal of Non-Crystalline Solids* 50: 189–202.

60 McMillan, P.W. (1964). *Glass-ceramics*. London/New York: Academic Press.

61 Bocker, C. and Russel, C. (2017). Percolation, phase separation and crystallisation. *Physics and Chemistry of Glasses – European Journal of Glass Science and Technology Part B* 58: 133–141.

62 Deubener, J. (2018). Controlled crystallization of glasses – from transformation kinetics to glass-ceramics. In: *Teaching Glass Better: Tenth Anniversary of the ICG Summer School* (Chapter 11) (ed. A. Takada, J. Parker, A. Duran and K. Bange), 213–231. International Commission on Glass (ICG).

63 Fokin, V.M., Zanotto, E.D., Yuritsyn, N.S., and Schmelzer, J.W.P. (2006). Homogeneous crystal nucleation in silicate glasses: a 40 years perspective. *Journal of Non-Crystalline Solids* 352: 2681–2714.

64 Höland, W., Rheinberger, V., and Frank, M. (1999). Mechanisms of nucleation and controlled crystallization of needle-like apatite in glass-ceramics of the SiO_2–Al_2O_3–K_2O–CaO–P_2O_5 system. *Journal of Non-Crystalline Solids* 253: 170–177.

65 Karpukhina, N., Hill, R.G., and Law, R.V. (2014). Crystallisation in oxide glasses – a tutorial review. *Chemical Society Reviews* 43: 2174–2186.

66 Holand, W., Rheinberger, V., and Schweiger, M. (2003). Control of nucleation in glass ceramics. *Philosophical Transactions of the Royal Society of London, Series A: Mathematical, Physical and Engineering Sciences* 361: 575–588.

67 Krüger, S. and Deubener, J. (2015). Heterogeneous surface nucleation of lithium disilicate glass: an isothermal DSC study. *Journal of Non-Crystalline Solids* 417: 45–51.

68 Cabral, A.A., Fokin, V.M., and Zanotto, E.D. (2004). Nanocrystallization of fresnoite glass. II. Analysis of homogeneous nucleation kinetics. *Journal of Non-Crystalline Solids* 343: 85–90.

69 J.M. Fernández Navarro (2003). *El vidrio, Consejo Superior de Investigaciones Cientificas (CSIC), Madrid*.

70 Fokin, V.M., Yuritsyn, N.S., and Zanotto, E.D. (2005). Nucleation and crystallization kinetics in silicate glasses: theory and experiment. In: *Nucleation Theory and Applications* (ed. J.W.P. Schmelzer), 74–125. Berlin-Weinheim: Wiley-VCH.

71 Krüger, S. and Deubener, J. (2016). The TTT curves of the heterogeneous and homogeneous crystallization of lithium disilicate – a stochastic approach to crystal nucleation. *Frontiers in Materials* 3: 42.

72 Fokin, V.M., Zanotto, E.D., and Schmelzer, J.W.P. (2003). Homogeneous nucleation versus glass transition temperature of silicate glasses. *Journal of Non-Crystalline Solids* 321: 52–65.

73 Macena, G.S., Abyzov, A.S., Fokin, V.M. et al. (2020). Off-stoichiometry effects on crystal nucleation and growth kinetics in soda-lime-silicate glasses. The combeite ($Na_2O{\cdot}2CaO{\cdot}3SiO_2$) – devitrite ($Na_2O{\cdot}3CaO{\cdot}6SiO_2$) joint. *Acta Materialia* 196: 191–199.

74 Zheng, Q.J., Zhang, Y.F., Montazerian, M. et al. (2019). Understanding glass through differential scanning calorimetry. *Chemical Reviews* 119: 7848–7939.

75 Cabral, A.A., Fokin, V.M., Zanotto, E.D., and Chinaglia, C.R. (2003). Nanocrystallization of fresnoite glass. I. Nucleation and growth kinetics. *Journal of Non-Crystalline Solids* 330: 174–186.

76 Zanotto, E.D. (2020). Effect of liquid phase separation on crystal nucleation in glass-formers. Case closed. *Ceramics International* 46: 24779–24791.

77 De Pablos-Martin, A., Patzig, C., Höche, T. et al. (2013). Distribution of thulium in Tm^{3+}-doped oxyfluoride glasses and glass-ceramics. *CrystEngComm* 15: 6979–6985.

78 Höche, T., Patzig, C., Gemming, T. et al. (2012). Temporal evolution of diffusion barriers surrounding $ZrTiO_4$ nuclei in lithia aluminosilicate glass-ceramics. *Crystal Growth and Design* 12: 1556–1563.

79 Kleebusch, E., Rüssel, C., Patzig, C., and Höche, T. (2018). Evidence of epitaxial growth of high-quartz solid solution on $ZrTiO_4$ nuclei in a Li_2O–Al_2O_3–SiO_2 glass. *Journal of Alloys and Compounds* 748: 73–79.

80 Patzig, C., Dittmer, M., Gawronski, A. et al. (2014). Crystallization of ZrO_2-nucleated $MgO/Al_2O_3/SiO_2$ glasses – a TEM study. *CrystEngComm* 16: 6578–6587.

81 Patzig, C., Höche, T., Dittmer, M., and Rüssel, C. (2012). Temporal evolution of crystallization in MgO–Al_2O_3–SiO_2–ZrO_2 glass ceramics. *Crystal Growth and Design* 12: 2059–2067.

82 Vladislavova, L., Thieme, C., Zscheckel, T. et al. (2018). $BaO/SrO/ZnO/SiO_2$ glass system: influence of different nucleation agents: bulk versus surface crystallisation. In: *NATO Science for Peace and Security Series B: Physics and Biophysics*, 361–366. Dordrecht: Springer.

83 Nascimento, M.L.F. and Zanotto, E.D. (2010). Does viscosity describe the kinetic barrier for crystal growth from the liquidus to the glass transition? *Journal of Chemical Physics* 133: 174701.

84 Cassar, D.R., Rodrigues, A.M., Nascimento, M.L.F., and Zanotto, E.D. (2018). The diffusion coefficient controlling crystal growth in a silicate glass-former. *International Journal of Applied Glass Science* 9: 373–382.

85 de Pablos-Martin, A., Hemono, N., Mather, G.C. et al. (2011). Crystallization kinetics of LaF_3 nanocrystals in an oxyfluoride glass. *Journal of the American Ceramic Society* 94: 2420–2428.

86 Nascimento, M.L.F. and Zanotto, E.D. (2006). Mechanisms and dynamics of crystal growth, viscous flow, and self-diffusion in silica glass. *Physical Review B: Condensed Matter* 73: 024209.

87 Zanotto, E.D. and Cassar, D.R. (2017). The microscopic origin of the extreme glass-forming ability of albite and B_2O_3. *Scientific Reports* 7: 43022.

88 Nascimento, M.L.F., Fokin, V.M., Zanotto, E.D., and Abyzov, A.S. (2011). Dynamic processes in a silicate liquid from above melting to below the glass transition. *Journal of Chemical Physics* 135: 194703.

89 Rodrigues, A.M., Costa, A.M.C., and Cabral, A.A. (2012). Effect of simultaneous nucleation and crystal growth on DSC crystallization peaks of glasses. *Journal of the American Ceramic Society* 95: 2885–2890.

90 Schmelzer, J.W.P., Abyzov, A.S., and Baidakov, V.G. (2017). Time of formation of the first supercritical nucleus, time-lag, and the steady-state nucleation rate. *International Journal of Applied Glass Science* 8: 48–60.

91 Deubener, J., Montazerian, M., Kruger, S. et al. (2017). Heating rate effects in time-dependent homogeneous nucleation in glasses. *Journal of Non-Crystalline Solids* 474: 1–8.

92 Pascual, M., Perez Lara, C., and Duran, A. (2006). Non-isothermal crystallisation kinetics of devitrifying $RO–BaO–SiO_2$ (R = Mg, Zn) glasses. *Physics and Chemistry of Glasses* 47: 572–581.

93 Pascual, M.J., Durán, A., and Prado, M.O. (2005). A new method for determining fixed viscosity points of glasses. *Physics and Chemistry of Glasses* 46: 512–520.

94 Müller, R., Zanotto, E.D., and Fokin, V.M. (2000). Surface crystallization of silicate glasses: nucleation sites and kinetics. *Journal of Non-Crystalline Solids* 274: 208–231.

95 Höland, W., Rheinberger, V.M., Ritzberger, C., and Apel, E. (2013). Surface or internal nucleation and crystallization of glass-ceramics. *Optical Materials* 35: 1756–1758.

96 Höland, W., Rheinberger, V., and Schweiger, M. (2001). Nucleation and crystallization phenomena in glass-ceramics. *Advanced Engineering Materials* 3: 768–774.

97 Casasola, R., Pérez, J.M., and Romero, M. (2015). Devitrification behavior and preferred crystallization mechanism of glasses based on fluorrichterite ($Na_2CaMg_5Si_8O_{22}F_2$) composition. *Thermochimica Acta* 619: 32–40.

98 Tezvergil-Mutluay, A., Seseogullari-Dirihan, R., Feitosa, V.P. et al. (2017). Effects of composites containing bioactive glasses on demineralized dentin. *Journal of Dental Research* 96: 999–1005.

99 Höland, W., Ritzberger, C., Apel, E. et al. (2008). Formation and crystal growth of needle-like fluoroapatite in functional glass-ceramics. *Journal of Materials Chemistry* 18: 1318–1332.

2

Crystallization of Glasses and Its Impact on Bioactivity and Other Properties

Araceli de Pablos Martín and Delia S. Brauer

Otto Schott Institute of Materials Research, Faculty of Chemistry and Earth Sciences, Friedrich Schiller University, Jena, Germany

2.1 Bioactive Glasses

Bioactive glasses present two main advantages compared to other materials used as clinical bone-grafts [1]: it is possible to tune their physical, chemical, and biological properties via their composition as they do not depend on a specific stoichiometry, and they allow for shaping at elevated temperatures, to obtain fibers, coatings, or complex sintered structures such as three-dimensional porous scaffolds [2]. There are, however, still several open questions, which prevent us from exploiting these materials to their full extent. Many of these questions are related to the crystallization behavior of these glasses and how it affects key properties such as sintering, mechanical stability, and bioactivity. Some researchers claim that this crystallization impedes bioactivity and thus needs to be avoided at all cost [3, 4], while others state that bioactivity is not affected significantly or even improves bioactivity [5–8].

Bioactive glasses contain large amounts of modifier ions (Na^+, K^+, Mg^{2+}, Ca^{2+}), and as a result, their silicate network is highly disrupted, with large concentrations of non-bridging oxygens [9]. This disrupted silicate network is critical for degradation and ion release [10]. However, such a highly disrupted silicate network also means that these glasses crystallize easily during heat treatment, such as sintering [11–13]. This pronounced tendency to crystallize means that a lot of available data on bioactive "glass" scaffolds in the literature actually represent data on glass-ceramics or crystallized glasses [14].

The design of bioactive glasses is often based on the network connectivity (NC) model. NC is the average number of bridging oxygens per network forming element (here silicon) in the glass structure [9, 15]. Considering a maximum of four bridging oxygen atoms per silicon atom, and phosphorus only present as orthophosphate species (PO_4^{3-}) [9], NC of a glass is calculated according to Eq. (2.1), where $M^I{}_2O$ and $M^{II}O$ are typical modifier oxides [16, 17]:

$$NC_{Si} = \frac{4\left[SiO_2\right] - 2\left[M^I{}_2O + M^{II}O\right] + 6\left[P_2O_5\right]}{\left[SiO_2\right]} \tag{2.1}$$

NC must be adjusted to fulfill the ion release requirements and thus, the bioactivity, while maintaining the desired thermal behavior and stability, e.g. tendency to crystallize. An NC between 2.0 and 2.6 has been suggested optimum for bioactive glasses [18], and while NC = 2.4 has been put forward as the cutoff value for bioactivity [19], glasses with higher NC have been shown to degrade and surface mineralize in aqueous environments and perform well during *in vitro* cell culture studies [20].

Bioactive Glasses and Glass-Ceramics: Fundamentals and Applications, First Edition.
Edited by Francesco Baino and Saeid Kargozar.

2.2 Bioactive Glass-Ceramics

Glass-ceramics are prepared by controlled crystallization of glasses. Initially, the motivation to study bioactive glass-ceramics originated from the mechanical limitations of bioactive glasses [21]. Results indicated, though, that additional improvements can be obtained by crystallization. In 1982, Kokubo et al. [22] developed the bioactive glass-ceramic Cerabone-AW® (Nippon Electric Glass Co, Japan), obtained from the crystallization of a glass in the system SiO_2–P_2O_5–CaO–MgO–CaF_2, containing oxyfluorapatite and wollastonite crystal phases. This glass-ceramic not only exhibits much better mechanical properties than bioactive glasses, it also forms a tight bond to bone *in vivo*. Moreover, it can be machined into various shapes, which is an important benefit for clinical applications [22–24]. Since then, glass-ceramics have been used clinically as structural materials in load-bearing applications such as vertebral spacers or iliac crest prostheses [25].

Beside the possibility to tune properties via composition, glass-ceramics provide an additional variable with the type of crystalline phase(s) present. The presence of certain crystalline phases can be tuned via glass composition and subsequent heat treatment. As shown below, the nature of the crystals embedded in the glassy matrix as well as their morphology, size, and quantity has tremendous influence on the thermal, mechanical, and biological properties of a glass-ceramic. On the one hand, the mechanical properties of glass-ceramics are superior than those of glasses [26, 27]; on the other hand, crystallization may compromise bioactivity in some cases. Thus, to achieve an ideal biomaterial, a balance between bioactivity and mechanical strength must be achieved.

2.3 Influence of Crystallization on Processing

The thermal properties of a glass determine the processing regime for bioactive glasses and glass-ceramics, while thermal properties in turn are governed by glass composition and structure. Controlled crystallization is key for tailoring the properties of glass-ceramics. Spontaneous crystallization, by contrast, caused by a pronounced tendency to devitrify during cooling of the melt, is undesirable because it prevents us from obtaining a bioactive glass in an amorphous state and makes it challenging if not impossible to control crystal phases, number, and size via heat treatment.

There are two main network formers in bioactive glasses: SiO_2 and P_2O_5. In general, it can be said that SiO_2 provides a low-solubility matrix that compensates the excess of solubility of the phosphate part. The role of network formers in the structure of bioactive glasses and glass-ceramics, their crystallization and bioactivity have been discussed previously [9, 15, 28, 29]. In general, while SiO_2 increases glass stability against crystallization, P_2O_5 can favor crystallization through phase separation, or strongly reduce the nucleation rate above a threshold content [28].

Bioactive glasses tend to crystallize easily during both cooling of the melt and heat treatment of a glass, and one main reason is their low NC compared to conventional silicate glasses. This low degree of polymerization of the silicate network causes a high mobility of network fragments at high temperatures, thus facilitating nucleation and subsequent crystallization. While many bioactive glasses show surface crystallization (Figure 2.1), one of the most well-known compositions, Bioglass 45S5, shows both surface and internal crystallization [33], which seems to impede viscous flow for both bulk (Figure 2.1a,b) and powder samples (Figure 2.1c,f) [31, 34, 35], thereby impeding full densification [21]. Only when physical load is applied during sintering, densely sintered

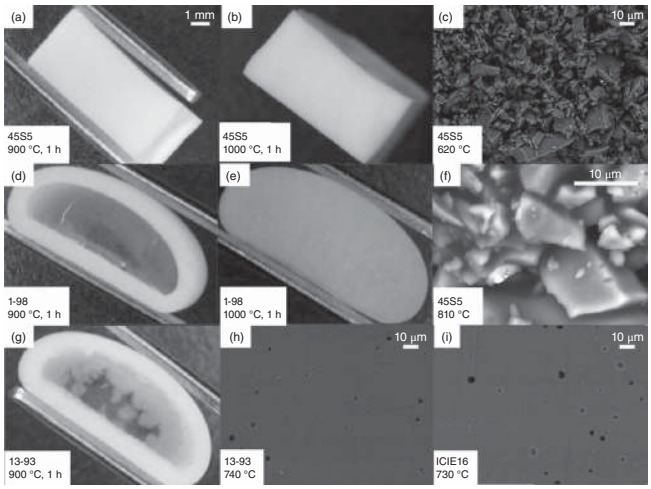

Figure 2.1 Cross sections of heat-treated bioactive glass bulk pieces (a, b) 45S5, (d, e) 1-98, and (g) 13-93 and of heat-treated powder compacts (c, f) 45S5, (h) 13-93, and (i) ICIE16. Compositions (d, e) 1-98 and (g) 13-93 started to flow during heat treatment, causing their shape to become rounded. By contrast (a, b) 45S5 kept the cubic shape. In addition, during sintering of (c, f) 45S5 powder at temperatures up to 300 K above glass transition, no dense sintering occurred and individual grains can still be distinguished, while during the sintering of powders of (h) 13-93 or (i) ICIE16 only small round pores remained behind. Source: (a, b, d, e) Arstila et al. [30], Figure 01, p. 03/with permission of Elsevier; (c, f, h, i) Blaeß et al. [31], Figure 02, p. 05/John Wiley & Sons, Inc./CC BY 4.0; (g) Fagerlund et al. [32], Figure 03, p. 04/with permission of Elsevier.

Bioglass 45S5 powder compacts can be obtained [34]. To facilitate the sintering of porous scaffolds without crystallization occurring, several bioactive glasses with a reduced crystallization tendency have been developed, e.g. 13-93 (Figure 2.1g,h [36]) or ICIE1 (Figure 2.1i [37]). Crystallization does not always negatively affect sintering; however, key is that the crystal phases forming do not impede viscous flow sintering [31].

In order to obtain glass-ceramics of a desired shape, processing is necessary. Systems which crystallize by a volume nucleation process, i.e. showing internal crystallization, can be cast to shape from the melt. The resulting glass is then exposed to an additional heat-treatment procedure where crystallization is achieved. Apatite-mullite glass-ceramics are a good example for such a system [24]. By contrast, in Kokubo's apatite-wollastonite glass-ceramic [22], both crystal phases formed by surface crystallization, and heat treatment of the bulk glass is not a viable option to obtain mechanically stable bulk glass-ceramic pieces. Implants are therefore prepared by heat treating powder compacts to allow for shaping while still having a homogeneous distribution of crystals distributed in the bulk and obtaining good mechanical stability.

2.4 Influence of Crystallization on Mechanical Properties

The mechanical properties of implants need to be suited to the application of the material. First, the morphology of the bioactive glass-ceramics must be considered. Whether the final product is intended to be used as powder, granules, slurries or scaffolds, or as monoliths, to be machined to specific geometries, is crucial to determine the mechanical properties needed. Second, an estimate of the mechanical stresses, to which the material is exposed, is also needed, as the load impact of a knee or a tooth prothesis is not the same as that of a middle-ear implant. For this reason, Bioglass 45S5 bulk pieces were used successfully as implants to replace the ossicular chain in the middle ear [3] as mechanical load here is negligible and the mechanical properties of Bioglass were acceptable. Another example is the glass-ceramic Ceravital, which was also used as middle-ear implants [27], despite its mechanical properties being below the 160 MPa of the human cortical bone. (It later turned out, however, that fast degradation of Ceravital prevented its successful use as ossicular prostheses [38].)

It is well known that the mechanical properties of glass-ceramics are superior of those of glasses [26, 27]. The presence of crystals embedded in a glassy matrix is responsible for crack deflections and, thus, for improving the resistance to crack propagation. If crystallization of glass powders (e.g. during the preparation of scaffolds) occurs at lower temperatures than the end of the sintering, however, full densification is not achieved (Figure 2.1c,f) and the mechanical properties may be compromised [31, 34, 35]. As a result, mechanical stability of sintered constructs such as porous scaffolds tends to be lower for 45S5 than for bioactive glasses with improved sintering such as 13-93 [22]. By contrast, if crystallization takes place in a controlled manner, not only the mechanical properties but also the bioactivity can be improved with respect to those of the parent glasses. Thus, where crystallization originally seemed to be a disadvantage, it has become a possibility to improve these materials, by turning glasses into glass-ceramics.

Studies on Biosilicate [39] showed that the glass-ceramic with 34% of crystalline volume showed much better mechanical properties than the parent glass, while the crystal size seemed to have a lower influence on mechanical performance. The type of crystal phases present can also have direct influence on the mechanical properties of a glass-ceramic. This is particularly noticeable in apatite-containing glass-ceramics such as the apatite-wollastonie, apatite-mica, or apatite-mullite systems [24], where the function of the apatite phase was to provide bioactivity (as

discussed below), while the additional phase provided mechanical strength. The glass-ceramic Cerabone-AW possesses excellent mechanical properties [24, 27, 40]. Of the crystalline phases present, wollastonite ($CaSiO_3$) strongly improves the mechanical properties of glass-ceramics. Especially compressive strength (up to 1080 MPa), flexural strength (up to 215 MPa), Young's modulus (118 GPa), and fracture toughness (up to 2 $MPa/m^{1/2}$) are much higher than those of bioactive glass-ceramics without wollastonite crystal phase [24]. Machinability of glass-ceramics is important in orthopedics and dentistry. In the Bioverit glass-ceramics, machinability originates from the presence of mica crystals. While both Bioverit I and Bioverit II contain a mica crystal phase, the mica crystals present in Bioverit I show the typical morphology of flat flakes, while those present in Bioverit II are curved, arranging themselves in spherical lamellae, giving the crystals a cabbage-like appearance [41, 42]. As a result, Bioverit II is easier to machine than Bioverit I. The influence of variation in composition or heat treatment on glass-ceramic microstructure is illustrated in Figure 2.2, using Bioverit as an example [41, 43, 44, 47].

2.5 Influence of Crystallization on Bioactivity

In the literature, the term "bioactivity" of glasses or glass-ceramics may refer to one of several aspects of behavior. Strictly speaking, bioactivity can only be tested *in vivo*, showing the integration of an implant material into the living tissue, such as the bonding of bioactive glasses to bone [48]. Many people, however, refer to *in vitro* apatite formation as "bioactivity," even if no living system, not even cells *in vitro*, are present. Others talk about bioactivity if compositions have shown good results during *in vitro* cell culture studies, e.g. with osteoblasts or other relevant cell lines. In this chapter, to avoid confusion, we will refer to "*in vitro* apatite formation" when talking about the precipitation of apatite-like crystal phases on the surface of a bioactive glass or glass-ceramic when immersed in acellular simulated physiological solutions (such as simulated body fluid, SBF). When referring to results from cell culture studies, we will talk about "*in vitro* bioactivity."

Bioactivity *in vitro* or *in vivo* is often related to solubility or ion release rate from a material. In addition, for many bioactive glasses or glass-ceramics, the subsequent process of surface mineralization, e.g. by apatite precipitation, plays a significant role. Both differ for glasses and glass-ceramics, and for the latter, they also vary with composition of the crystalline phase, as shown in Table 2.1.

We will first look at the effect of **solubility** or ion release. It has long been known that bioactive glasses not only bond to living tissue when implanted but they also degrade over time [53, 54], allowing for bone to be regenerated and, eventually, replaced by the body's own bone tissue [55]. Degradation rate here needs to match the rate of tissue formation. If the implant degrades too fast, not only will this prevent cells from attaching and proliferating on the implant surface but also high ionic concentrations owing to fast dissolution may compromise cell viability and result in cytotoxicity [56]. While the pronounced pH increase caused by fast ion release from Bioglass 45S5 makes preconditioning necessary for *in vitro* cell culture studies [57], this has not prevented its successful clinical application [58], showing that *in vivo* fluid exchange may overcome some issues related to degradation and solubility. The inherent release of ions from bioactive glasses is also related to their bioactivity *in vitro* and *in vivo*. The controlled release of ions in therapeutic concentrations, e.g. the release of specific amounts of soluble silica species, has been shown to stimulate cells *in vitro* [59], making bioactive glasses of interest for the controlled release of therapeutic ions directly at the implant site [60]. In addition, the release of ions such as calcium or phosphate is a key step during the formation of mineralized surface layers, as discussed further below.

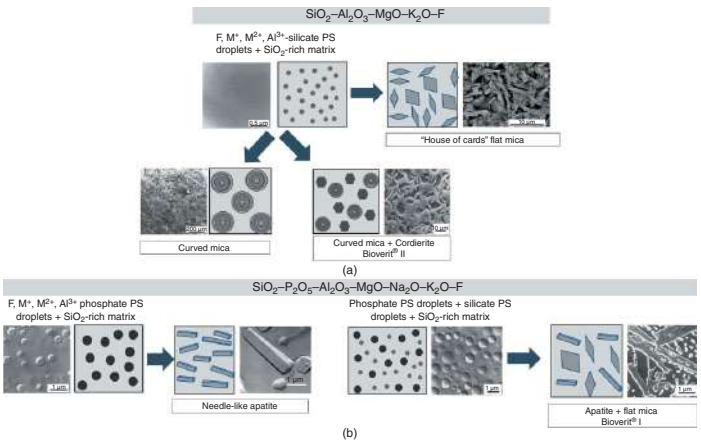

Figure 2.2 Influence of changes in composition or heat treatment regime on crystal type (phlogopite mica, apatite) and microstructures of Bioverit glass-ceramics [41, 43, 44]. Arrows indicate heat treatment. (a) $SiO_2–Al_2O_3–MgO–K_2O–F$ system. The base glass shows silicate phase separation (PS) droplets. Controlled crystallization resulted in flat, flake-shaped ("house of cards") phlogopite mica $Na/KMg_3AlSi_3O_{10}F_2$. After increasing the Al_2O_3 and MgO content, curved phlogopite mica crystallized. As the glassy matrix becomes depleted in F and alkali during mica crystallization, additional crystallization of cordierite, $Mg_2(Si_5Al_4O_{18})$, takes place (the same thing happens if the concentrations of MgO and Al_2O_3 increase further with respect to SiO_2), which is the final microstructure of Bioverit II. By controlling both crystallizations, it is possible to tune the degree of transparency of the final glass-ceramic. (b) An increase in CaO and P_2O_5 content can lead to the separation in two or three phases (left and right, respectively). (b, left) In the P_2O_5-enriched mica-based glass-ceramic-controlled heat treatment leads to crystallization of needle-like apatite. (b, right) For high MgO and Al_2O_3 content in addition to P_2O_5 enrichment, three phases are formed in the glass. From the small droplet phase rich in Si, M^+, and F, flat mica crystals form, while the large droplet phase rich in M^{2+}, P_2O_5, and F leads to homogeneous nucleation of apatite, resulting in the typical microstructure of Bioverit I. Source: Micrographs of silicate PS droplets, curved mica, and phosphate PS droplets adapted with permission from Vogel et al. [44], Figure 03, 07, 08, p 04, 07, 08 / With permission of Elsevier. Micrograph of the house-of-cards flat mica reprinted with permission from Rashwan et al. [45], Figure 05, p 06 / With permission of Elsevier. Micrographs of curved mica and cordierite, phosphate and silicate PS droplets and apatite-flat mica reprinted with permission from Vogel and Höland [43], Figure 01, 02, 03, p 02, 03 / With permission of Elsevier. Micrograph of apatite needles reprinted with permission from Höche et al. [46], Figure 03, p 05 / With permission of American Chemical Society.

A crystalline phase is more thermodynamically stable than an amorphous phase of the same composition, providing bioactive glasses with a higher solubility than the respective crystalline materials. Controlled crystallization thus reduces and can even tune the dissolution rate, enabling a better control of cytotoxicity [51]. For some phosphate glass compositions, an increased solubility of the glass-ceramic compared to the parent glass has been reported [61], showing that it is not the presence or absence of crystalline phases *per se* but the type of crystal phase which needs to be considered. Some studies pointed out that volume crystallization leads to a lower cytotoxicity than surface crystallization [52]. Silicon ion release was reported not to vary significantly with crystallization [23], which may be related more to the low solubility of silica species in aqueous solutions [62]. In each case, however, solubility of the final glass-ceramics not only depends on the type and relative amount of crystal phases present but also on the composition and structure of the glassy matrix. If the NC of the glassy matrix in a glass-ceramic is higher than that of the parent glass, it can be expected to have a lower solubility. Should the NC of the glassy matrix remain constant, however, solubility can be expected not to change.

The mechanism of interaction between a 45S5-based glass-ceramic surface and SBF was shown to comprise the following stages [35]: (i) preferential dissolution at glass/crystal interfaces, (ii) preferential dissolution at crystal structural defects causing break-down of crystalline particles into finer grains, and (iii) amorphization through introduction of point defects produced during ion exchange, leading to an optimum ion release in the studied glass-ceramics. Therefore, the assumption that ion release decreases with decreasing residual glassy matrix must be considered carefully.

The second factor affecting bioactivity is surface **apatite formation** in contact with physiological solutions. It is typically lower for crystalline solids than for amorphous glasses [63], likely owing to lower ion release from crystalline phases. Li et al. [4] suggested that apatite deposition on the surface of a bioactive glass is caused by the formation of a negatively charged surface, which attracts cations (Ca^{2+}) from the solution. Such a negatively charged surface is formed when cationic species, i.e. modifier ions, are released from the glass. According to them, the existence of a residual glassy matrix is key for the deposition of an apatite layer on the surface of the glass-ceramics.

However, other studies reported on crystallization not inhibiting the development of an apatite surface layer, even in fully crystallized glass-ceramics, although the kinetics differed for glasses and glass-ceramics. Peitl et al. [49] studied apatite formation on 45S5 glass-ceramics during immersion in SBF. They reported that while all glass-ceramics, with crystallinity ranging from 8% to 100%, formed an apatite surface layer during immersion, the onset of apatite formation shifted from 10 hours for the amorphous glass to 22–25 hours for the 60–100% crystalline material.

The formation of a crystalline apatite layer depends on several variables, including the rate of ion exchange, hydroxylation of the glass surface, and pH and ion concentration of the solution. The effect of crystallinity on apatite formation appears to be related to the connectivity of the residual glassy phase, which controls the rate of ion exchange and silanol formation. The generally observed trend is that the crystallization of silicate phases delays but not inhibits the formation of the apatite layer [64–66] with respect to the parent glasses (Table 2.1). Many bioactive glass-ceramics contain a phosphate crystal phase, typically an apatite phase either on its own or together with silicate crystal phases. Duminis et al. [24] and Chen et al. [29] postulate that apatite crystals within a glass-ceramic may act as nuclei for apatite surface precipitation, by reducing the apatite nucleation energy, which is typically the limiting factor of apatite crystallization. It further has been reported that apatite surface precipitation was five times faster in a whitlockite (calcium phosphate phase) glass-ceramic than in the precursor glass [51]. The authors explained this with two characteristics of the crystalline phase whitlockite: it is a soluble phase, and it accelerates the crystallization of hydroxycarbonate apatite (HCA) by acting as a preferential site for nucleation and crystal growth.

Table 2.1 Selection of bioactive glass-ceramics reported in literature and comparison of the ***in vitro* bioactivity** between glasses and glass-ceramics.

Glass composition (wt%)	Crystalline phase (heat treatment)	Crystallinity	Test solution	*In vitro* bioactive properties of the glass(es)	*In vitro* bioactive properties of the GCs	References
48SiO_2 9.5P_2O_5 20Na_2O 22.5CaO	$Na_2CaSi_3O_8$ $Ca_{10}(PO_4)_6(O(OH)_2)$ (nucleation at 670 °C – 15–180 min; crystallization at 750 °C – 15–180 min)	62–100%	Tris buffer	HCA formation within 5 h	HCA layer formed in GC with 62% and 89% crystalline fraction after >100 h immersion No HCA formation in GCs from 95% crystal phase	Li et al. [4]
Bioglass 45S5 45SiO_2 6P_2O_5 24.5Na_2O 24.5CaO	$Na_2Ca_2Si_3O_9$ (nucleation at 550 °C – 150 h; crystallization at 680 °C – 113–66 min)	8–100 vol%	SBF	HCA formation after 8 h	No inhibition of HCA formation even with a fully crystallized GC Onset of HCA crystallization increases with crystallinity up to 22–25 h for the 60–100% crystalline material	Peitl et al. [49]
47.5–50.3SiO_2 23.2–18.5Na_2O 23.2–31.3CaO 0–6P_2O_5	$Na_2Ca_2Si_3O_9$ (nucleation at 520–590 °C – 3 min to 150 h; crystallization at 620–700 °C – 5–80 min)	5–100%	SBF	Onset of HCA formation increases with decreasing P content between 8 h (6% P_2O_5) and 31 h (0% P_2O_5)	Onset of HCA crystallization increases with crystallinity between 12 h (10% crystallinity) and 25 h (100% crystallinity), and decreases with the addition of P_2O_5	Peitl et al. [7]

Table 2.1 (Continued)

Glass composition (wt%)	Crystalline phase (heat treatment)	Crystallinity	Test solution	*In vitro* bioactive properties of the glass(es)	*In vitro* bioactive properties of the GCs	References
Bioglass 45S5 47.3SiO_2 22.1Na_2O 24.2CaO (after chemical analysis) 6.2P_2O_5	$Na_2Ca_2Si_3O_9$ (1000 °C – 1 h)	100%	SBF (large SBF volume/glass surface ratio)	Ca_2SiO_4 layer formed on the surface after 7 d, $CaCO_3$ layer after 14 d immersion No apatite formation (aggressive corrosion under the SBF test conditions)	Apatite formation after 7 and 14 d immersion	Plewinski et al. [50]
(mol%) 28.4–38.1SiO_2 41.4–55.5CaO/SrO 4.7–6.3P_2O_5 0–25.5CaF_2/SrF_2	Compositions with high CaF_2/SrF_2 content: uncontrolled crystallization of FAp and CaF_2/SrF_2 upon cooling of the melt	n.m.	SBF, Tris buffer	FAp formation within 3 h in Tris and within 24 h in SBF P release: very small percentages (less than 2%)	FAp formation between 3 and 6 h in both, Tris and SBF Precrystallization favors further FAp formation during immersion P release: higher concentrations (up to 11%)	Chen et al. [29]
52.75$Ca_3(PO_4)_2$ 30SiO_2 17.25MgO	3(Ca,Mg)O·P_2O_5 (775 °C–4h) 3(Ca,Mg)O·P_2O_5 + not cataloged silicate (775 and 975 °C–4h)	27% 63%	SBF	Formation of an amorphous Ca–P layer after 48 h Onset of HCA formation after 5 d	GC-27% crystallinity: onset for HCA formation after 24 h and complete formation after 7 d Data nonconclusive for the GC-63% crystallinity	Daguano et al. [51]
(in mol%) 75$NaPO_3$–(25 − x) CaO–xCaF_2 (x = 0, 5, 10, 15, 20)	$Ca_2P_2O_7$ CaF_2 for x = 20	n.m.	Tris buffer	An increase in CaF_2 content leads to an increase in glass solubility	The high dissolution rate of the CaF_2-free (x = 0) GC leads to the loss of bioactivity and increased cytotoxicity. The GC with x = 20 shows bioactivity and a faster dissolution compared to the glass when immersed for up to 6 h in Tris buffer, but it shows slower dissolution than the glass at longer immersion times	Nommeots-Nomm et al. [52]

GC, glass-ceramic; SBF, simulated body fluid; HCA, hydroxycarbonate apatite; FAp, fluorapatite; TCP, $Ca_3(PO_4)_2$; W, $CaSiO_3$; T, 3MgO·4SiO_2; n.m., not mentioned.

Glass-ceramics in which phosphate phases or both silicate and phosphate phases crystallize have been studied extensively [24, 67–71]. Besides apatite, crystalline phases include rhenanite [72] and various calcium phosphates [52, 73].

Factors mentioned above may also to some extent affect bioactivity *in vitro* and *in vivo*. Azenha et al. [74] report on two similar glass-ceramics in the system SiO_2–CaO–MgO–P_2O_5–Al_2O_3–F, both containing apatite and wollastonite crystal phases in similar weight percentages but showing completely different bioactivity. While the glass-ceramic with higher Al_2O_3 content (19.04 mol%) in the residual glassy matrix was bioinert, the glass with much lower content (1.19 mol%) showed bioactivity *in vitro* and *in vivo*. Thus, not only the NC of the parent glass should be considered, but in the case of glass-ceramics also that of the residual glassy matrix.

Unlike glasses, glass-ceramics present a nonhomogeneous elemental distribution, owing to elemental depletions and enrichments caused by the formation of crystalline phases [74]. Living cells are pH sensitive, and *in vitro* cell culture experiments have shown cells reacting positively to the presence of Na-enriched areas in a glass-ceramic, which produced a slightly alkaline pH favorable to osteoblast differentiation and function. This means that this nonhomogenous microstructure facilitated a beneficial release of ions here in a way more effective than in an amorphous material with homogeneous elemental distribution [75].

Kokubo's apatite-wollastonite (Cerabone) glass-ceramics show a high bioactivity *in vivo*, with bonding to bone apparently occurring via the formation of a calcium phosphate surface layer bearing pronounced similarity to apatite [76]. This bond to bone has been shown to be so strong that tensile fracture never occurs at the glass-ceramic/bone interface, but rather in the bone [23]. Interestingly, apatite-wollastonite glass-ceramics did not form such an apatite-like surface layer during immersion experiments in Tris buffer solution *in vitro*, inspiring Kokubo to develop his SBF [77].

In vivo studies [78] have suggested that the presence of an apatite crystal phase within a glass-ceramic induces bone bonding in an otherwise bioinert material. Here, a glass of the composition $4.5SiO_2$–$3Al_2O_3$–$3.2P_2O_5$–3CaO–$1.51CaF_2$ (mol%) was either implanted into rat femurs as-cast, i.e. in a glassy state, or heat-treated before implantation to obtain a glass-ceramic containing principally fluorapatite or both fluorapatite and mullite as crystal phases. While the amorphous glass showed no integration with bone at four weeks, both glass-ceramics showed good integration with intimate bone contact.

We take this as an indication that the presence of apatite crystals, whether by crystallization following heat treatment or by surface mineralization creates a biomimetic environment, which bone cells adhere to, proliferate and differentiate on to form bone. Depending on the nature and extent of additional processes such as ion release or degradation, this bone integration may be further enhanced or slowed down.

2.6 Conclusions and Perspectives

Spontaneous, i.e. uncontrolled, crystallization of bioactive glasses is well known to negatively affect performance. This is particularly noticeable for Bioglass 45S5, where crystallization impedes viscous flow sintering and thereby drastically lowers the mechanical properties of scaffolds. Crystallization of the silicate network slows down degradation, ion release, and apatite surface precipitation, but several materials containing such phases, e.g. Biosilicate or Cerabone (apatite-wollastonite) glass-ceramics, have shown that this does not necessarily translate to lower *in vivo* bioactivity. Controlled crystallization is an excellent tool for fine-tuning of various materials properties. Especially the crystallization of apatite-type phases may induce bioactivity

to otherwise inert materials. But controlled crystallization is particularly useful to improve mechanical properties, with glass-ceramics currently used in dental restorations (see Chapter 18) showing excellent strength. While bioactive glasses, e.g. compositions Bioglass 45S5 or BonAlive S53P4, have been used successfully as bone regeneration materials, their glassy nature limits their use to nonload bearing applications. Nevertheless, one focus in bioactive glass research has long been to avoid crystallization during sintering. Depending on the effect of crystallization on type, size, and morphology of crystals forming as well as on the properties of the glassy matrix; however, changes in properties may actually be favorable rather than destructive.

We hope that reading this chapter encourages researchers in the field of bioactive glasses to embrace controlled crystallization as a valuable tool for tailoring the properties of bioactive glasses in order to broaden their application range and pave the way toward new clinical implant materials.

References

1 Gong, T., Xie, J., Liao, J. et al. (2015). Nanomaterials and bone regeneration. *Bone Research* 3: 15029.

2 Jones, J. (2009). New trends in bioactive scaffolds: the importance of nanostructure. *Journal of the European Ceramic Society* 29: 1275–1281.

3 Jones, J.R. (2013). Review of bioactive glass: from Hench to hybrids. *Acta Biomaterialia* 9: 4457–4486.

4 Li, P., Yang, Q., Zhang, F., and Kokubo, T. (1992). The effect of residual glassy phase in a bioactive glass-ceramic on the formation of its surface apatite layer in vitro. *Journal of Materials Science – Materials in Medicine* 3: 452–456.

5 Al-Noaman, A., Rawlinson, S.C.F., and Hill, R.G. (2012). The role of MgO on thermal properties, structure and bioactivity of bioactive glass coating for dental implants. *Journal of Non-Crystalline Solids* 358: 3019–3027.

6 Magallanes-Perdomo, M., Luklinska, Z.B., De Aza, A.H. et al. (2011). Bone-like forming ability of apatite–wollastonite glass ceramic. *Journal of the European Ceramic Society* 31: 1549–1561.

7 Peitl, O., Dutra Zanotto, E., and Hench, L.L. (2001). Highly bioactive P_2O_5–Na_2O–CaO–SiO_2 glass-ceramics. *Journal of Non-Crystalline Solids* 292: 115–126.

8 Peitl, O., Zanotto, E.D., Serbena, F.C., and Hench, L.L. (2013). Bioactive glass-ceramics for load-bearing applications. In: *An Introduction to Bioceramics*, Default Book Series, 2e (ed. L.L. Hench), 495–503.

9 Brauer, D.S. (2015). Bioactive glasses – structure and properties. *Angewandte Chemie International Edition* 54: 4160–4181.

10 Tilocca, A. and Cormack, A.N. (2008). Exploring the surface of bioactive glasses: water adsorption and reactivity. *Journal of Physical Chemistry C* 112: 11936–11945.

11 Cengiz, I.F., Oliveira, J.M., and Reis, R.L. (2018). Micro-CT – a digital 3D microstructural voyage into scaffolds: a systematic review of the reported methods and results. *Biomaterials Research* 22: 26.

12 Negut, I., Dorcioman, G., and Grumezescu, V. (2020). Scaffolds for wound healing applications. *Polymers* 12: 1–19.

13 Qu, H., Han, Z., Zhuo, Y., and Fu, H. (2019). Review of the design of porous bio-scaffolds for bone tissue engineering. *Journal of Mechanical Engineering* 55: 71–80.

14 Chen, Q.Z., Thompson, I.D., and Boccaccini, A.R. (2006). 45S5 Bioglass®-derived glass-ceramic scaffolds for bone tissue engineering. *Biomaterials* 27: 2414–2425.

15 Hill, R.G. and Brauer, D.S. (2011). Predicting the bioactivity of glasses using the network connectivity or split network models. *Journal of Non-Crystalline Solids* 357: 3884–3887.

16 Dietzel, A. (1941). Strukturchemie des Glases. *Naturwissenschaften* 29: 537–547.

17 Dietzel, A. (1942). Die Kationenfeldstärken und ihre Beziehungen zu Entglasungsvorgängen, zur Verbindungsbildung und zu den Schmelzpunkten von Silicaten. *Zeitschrift für Elektrochemie* 48: 9–23.

18 Eden, M., Sundberg, P., and Stalhandske, C. (2011). The split network analysis for exploring composition–structure correlations in multi-component glasses: II. Multinuclear NMR studies of alumino-borosilicates and glass-wool fibers. *Journal of Non-Crystalline Solids* 357: 1587–1594.

19 Hill, R. (1996). An alternative view of the degradation of bioglass. *Journal of Materials Science Letters* 15: 1122–1125.

20 Hoppe, A., Jokic, B., Janackovic, D. et al. (2014). Cobalt-releasing 1393 bioactive glass-derived scaffolds for bone tissue engineering applications. *ACS Applied Materials & Interfaces* 6: 2865–2877.

21 Montazerian, M. and Zanotto, E.D. (2016). History and trends of bioactive glass-ceramics. *Journal of Biomedical Materials Research Part A* 104: 1231–1249.

22 Kokubo, T., Shigematsu, M., Nagashima, Y. et al. (1982). Apatite- and wollastonite-containing glass-ceramics for prosthetic application. *Bulletin of the Institute for Chemical Research, Kyoto University* 60: 260–268.

23 Kokubo, T. (1991). Bioactive glass ceramics: properties and applications. *Biomaterials* 12: 155–163.

24 Duminis, T., Shahid, S., and Hill, R.G. (2017). Apatite glass-ceramics: a review. *Frontiers in Materials Research* 3: 1–15.

25 Hench, L.L. (1998). Bioceramics. *Journal of the American Ceramic Society* 81: 1705–1728.

26 Höland, W. and Beall, G.H. (2012). *Glass-Ceramic Technology*. Wiley.

27 de Aza Moya, A.H., de Aza Pendas, S., De Aza, P.N., and Pena, P. (2007). Bioactive glasses and glass-ceramics. *Boletín de la Sociedad Española de Cerámica y Vidrio* 46: 45–55.

28 Brauer, D.S. and Möncke, D. (2017). Introduction to the structure of silicate, phosphate and borate glasses. In: *Bioactive Glasses: Fundamentals, Technology and Applications, RSC Smart Materials* (Chapter 3) (ed. A.R. Boccaccini, D.S. Brauer and L. Hupa), 61–88. RSC.

29 Chen, X., Chen, X., Brauer, D.S. et al. (2014). Bioactivity of sodium free fluoride containing glasses and glass-ceramics. *Materials* 7: 5470–5487.

30 Arstila, H., Hupa, L., Karlsson, K.H., and Hupa, M. (2008). Influence of heat treatment on crystallization of bioactive glasses. *Journal of Non-Crystalline Solids* 354: 722–728.

31 Blaeß, C., Müller, R., Poologasundarampillai, G., and Brauer, D.S. (2019). Sintering and concomitant crystallization of bioactive glasses. *International Journal of Applied Glass Science* 10: 449–462.

32 Fagerlund, S., Massera, J., Hupa, M., and Hupa, L. (2012). T-T-T behaviour of bioactive glasses 1-98 and 13-93. *Journal of the European Ceramic Society* 32: 2731–2738.

33 Massera, J., Fagerlund, S., Hupa, L., and Hupa, M. (2012). Crystallization mechanism of the bioactive glasses, 45S5 and S53P4. *Journal of the American Ceramic Society* 95: 607–613.

34 Guillon, O., Cao, S., Chang, J. et al. (2011). Effect of uniaxial load on the sintering behaviour of 45S5 Bioglass® powder compacts. *Journal of the European Ceramic Society* 31: 999–1007.

35 Boccaccini, A.R., Chen, Q., Lefebvre, L. et al. (2007). Sintering, crystallisation and biodegradation behaviour of Bioglass®-derived glass-ceramics. *Faraday Discussions* 136: 27–44.

36 Brink, M. (1997). The influence of alkali and alkaline earths on the working range for bioactive glasses. *Journal of Biomedical Materials Research* 36: 109–117.

37 Elgayar, I., Aliev, A.E., Boccaccini, A.R., and Hill, R.G. (2005). Structural analysis of bioactive glasses. *Journal of Non-Crystalline Solids* 351: 173–183.

38 Brewis, C., Orrell, J., and Yung, M.W. (2003). Ceravital revisited: lessons to be learned. *Otology & Neurotology* 24: 20–23.

39 Peitl, O., Zanotto, E.D., Serbena, F.C., and Hench, L.L. (2012). Compositional and microstructural design of highly bioactive P_2O_5–Na_2O–CaO–SiO_2 glass-ceramics. *Acta Biomaterialia* 8: 321–332.

40 Crovace, M.C., Souza, M.T., Chinaglia, C.R. et al. (2016). Biosilicate® – a multipurpose, highly bioactive glass-ceramic. In vitro, in vivo and clinical trials. *Journal of Non-Crystalline Solids* 432: 90–110.

41 Vogel, W. and Höland, W. (1987). The development of bioglass ceramics for medical applications. *Angewandte Chemie International Edition in English* 26: 527–544.

42 Gebhardt, A., Höche, T., Carl, G., and Khodos, I.I. (1999). TEM study on the origin of cabbage-shaped mica crystal aggregates in machinable glass-ceramics. *Acta Materialia* 47: 4427–4434.

43 Vogel, W. and Höland, W. (1990). Development, structure, properties and application of glass-ceramics for medicine. *Journal of Non-Crystalline Solids* 123: 349–353.

44 Vogel, W., Höland, W., Naumann, K., and Gummel, J. (1986). Development of machineable bioactive glass ceramics for medical uses. *Journal of Non-Crystalline Solids* 80: 34–51.

45 Rashwan, M., Cattell, M., and Hill, R. (2019). The effect of barium content on the crystallization and microhardness of barium fluormica glass-ceramics. *Journal of the European Ceramic Society* 39: 2559–2565.

46 Höche, T., Moisescu, C., Avramov, I. et al. (2001). Microstructure of SiO_2–Al_2O_3–CaO–P_2O_5–K_2O–F^- glass ceramics. 1. Needle like versus isometric morphology of apatite crystals. *Chemistry of Materials* 13: 1312–1319.

47 Höland, W., Wange, P., Naumann, K. et al. (1991). Control of phase formation processes in glass-ceramics for medicine and technology. *Journal of Non-Crystalline Solids* 129: 152–162.

48 Bohner, M. and Lemaitre, J. (2009). Can bioactivity be tested in vitro with SBF solution? *Biomaterials* 30: 2175–2179.

49 Peitl, O., La Torre, G.P., and Hench, L.L. (1996). Effect of crystallization on apatite-layer formation of bioactive glass 45S5. *Journal of Biomedical Materials Research* 30: 509–514.

50 Plewinski, M., Schickle, K., Lindner, M. et al. (2013). The effect of crystallization of bioactive bioglass 45S5 on apatite formation and degradation. *Dental Materials* 29: 1256–1264.

51 Daguano, J.K.M.F., Rogero, S.O., Crovace, M.C. et al. (2013). Bioactivity and cytotoxicity of glass and glass-ceramics based on the 3CaO–P_2O_5–SiO_2–MgO system. *Journal of Materials Science – Materials in Medicine* 24: 2171–2180.

52 Nommeots-Nomm, A., Houaoui, A., Pradeepan Packiyanathar, A. et al. (2020). Phosphate/oxyfluorophosphate glass crystallization and its impact on dissolution and cytotoxicity. *Materials Science and Engineering C* 117: 111269.

53 Wheeler, D.L., Stokes, K.E., Hoellrich, R.G. et al. (1998). Effect of bioactive glass particle size on osseous regeneration of cancellous defects. *Journal of Biomedical Materials Research* 41: 527–533.

54 Fujibayashi, S., Neo, M., Kim, H.M. et al. (2003). A comparative study between in vivo bone ingrowth and in vitro apatite formation on Na_2O–CaO–SiO_2 glasses. *Biomaterials* 24: 1349–1356.

55 Lindfors, N.C., Koski, I., Heikkilä, J.T. et al. (2010). A prospective randomized 14-year follow-up study of bioactive glass and autogenous bone as bone graft substitutes in benign bone tumors. *Journal of Biomedical Materials Research Part B Applied Biomaterials* 94B: 157–164.

56 Fernandes, H.R., Gaddam, A., Rebelo, A. et al. (2018). Bioactive glasses and glass-ceramics for healthcare applications in bone regeneration and tissue engineering. *Materials* 11: 2530.

57 Gentleman, E., Fredholm, Y.C., Jell, G. et al. (2010). The effects of strontium-substituted bioactive glasses on osteoblasts and osteoclasts in vitro. *Biomaterials* 31: 3949–3956.

58 Jones, J.R., Brauer, D.S., Hupa, L., and Greenspan, D.C. (2016). Bioglass and bioactive glasses and their impact on healthcare. *International Journal of Applied Glass Science* 7: 423–434.

59 Xynos, I.D., Edgar, A.J., Buttery, L.D.K. et al. (2000). Ionic products of bioactive glass dissolution increase proliferation of human osteoblasts and induce insulin-like growth factor II mRNA expression and protein synthesis. *Biochemical and Biophysical Research Communications* 276: 461–465.

60 Hoppe, A., Güldal, N.S., and Boccaccini, A.R. (2011). A review of the biological response to ionic dissolution products from bioactive glasses and glass-ceramics. *Biomaterials* 32: 2757–2774.

61 Massera, J., Mayran, M., Rocherullé, J., and Hupa, L. (2015). Crystallization behavior of phosphate glasses and its impact on the glasses' bioactivity. *Journal of Materials Science* 50: 3091–3102.

62 Iler, R.K. (1979). *The Chemistry of Silica: Solubility, Polymerization, Colloid and Surface Properties and Biochemistry of Silica*. Wiley.

63 Kim, H.-M., Himeno, T., Kokubo, T., and Nakamura, T. (2005). Process and kinetics of bone-like apatite formation on sintered hydroxyapatite in a simulated body fluid. *Biomaterials* 26: 4366–4373.

64 Kansal, I., Goel, A., Tulyaganov, D.U. et al. (2011). Diopside ($CaO{\cdot}MgO{\cdot}2SiO_2$)–fluorapatite ($9CaO{\cdot}3P_2O_5{\cdot}CaF_2$) glass-ceramics: potential materials for bone tissue engineering. *Journal of Materials Chemistry* 21: 16247–16256.

65 Motealleh, A., Eqtesadi, S., Civantos, A. et al. (2017). Robocast 45S5 bioglass scaffolds: in vitro behavior. *Journal of Materials Science* 52: 9179–9191.

66 Sainz, M.A., Pena, P., Serena, S., and Caballero, A. (2010). Influence of design on bioactivity of novel $CaSiO_3$–$CaMg(SiO_3)_2$ bioceramics: in vitro simulated body fluid test and thermodynamic simulation. *Acta Biomaterialia* 6: 2797–2807.

67 Höland, W., Rheinberger, V., Wegner, S., and Frank, M. (2000). Needle-like apatite-leucite glass-ceramic as a base material for the veneering of metal restorations in dentistry. *Journal of Materials Science – Materials in Medicine* 11: 11–17.

68 Höland, W., Ritzberger, C., Apel, E. et al. (2008). Formation and crystal growth of needle-like fluoroapatite in functional glass-ceramics. *Journal of Materials Chemistry* 18: 1318–1332.

69 Müller, R., Abu-Hilal, L.A., Reinsch, S., and Höland, W. (1999). Coarsening of needle-shaped apatite crystals in $SiO_2{\cdot}Al_2O_3{\cdot}Na_2O{\cdot}K_2O{\cdot}CaO{\cdot}P_2O_5{\cdot}F$ glass. *Journal of Materials Science* 34: 65–69.

70 Ritzberger, C., Schweiger, M., and Höland, W. (2016). Principles of crystal phase formation in Ivoclar Vivadent glass-ceramics for dental restorations. *Journal of Non-Crystalline Solids* 432: 137–142.

71 Höland, W., Rheinberger, V., and Frank, M. (1999). Mechanisms of nucleation and controlled crystallization of needle-like apatite in glass-ceramics of the SiO_2–Al_2O_3–K_2O–CaO–P_2O_5 system. *Journal of Non-Crystalline Solids* 253: 170–177.

72 Höland, M., Dommann, A., Höland, W. et al. (2005). Microstructure formation and surface properties of a rhenanite-type glass-ceramic containing 6.0 wt% P_2O_5. *Glass Science and Technology* 78: 153–158.

73 Kasuga, T. (2007). Development of phosphate glass-ceramics for biomedical applications. *Journal of the Ceramic Society of Japan* 115: 455–459.

74 Azenha, M.R., Peitl, O., and Barros, V.M.d.R. (2010). Bone response to biosilicates® with different crystal phases. *Brazilian Dental Journal* 21: 383–389.

75 Moura, J., Teixeira, L.N., Ravagnani, C. et al. (2007). In vitro osteogenesis on a highly bioactive glass-ceramic (Biosilicate®). *Journal of Biomedical Materials Research Part A* 82: 545–557.

76 Kitsugi, T., Yamamuro, T., and Kokubo, T. (1990). Analysis of A·W glass-ceramic surface by micro-beam X-ray diffraction. *Journal of Biomedical Materials Research* 24: 259–273.

77 Kokubo, T., Kushitani, H., Sakka, S. et al. (1990). Solutions able to reproduce in vivo surface-structure changes in bioactive glass-ceramic A-W. *Journal of Biomedical Materials Research* 24: 721–734.

78 Freeman, C.O., Brook, I.M., Johnson, A. et al. (2003). Crystallization modifies osteoconductivity in an apatite–mullite glass-ceramic. *Journal of Materials Science – Materials in Medicine* 14: 985–990.

3

Bioactive Glass S53P4 – From a Statistically Suggested Composition to Clinical Success

Leena Hupa[1] *and Nina C. Lindfors*[2,3]

[1] *Johan Gadolin Process Chemistry Centre, Faculty of Science and Technology, Åbo Akademi University, Turku, Finland*
[2] *Department of Hand Surgery, Helsinki University Hospital, Helsinki, Finland*
[3] *Department of Surgery, Helsinki University, Helsinki, Finland*

3.1 Background

About 50 years after the first scientific publications of bioactive glasses, two compositions dominate the market of clinical products: bioactive glass Bioglass 45S5® discovered by Professor Larry Hench in Florida, USA, and bioactive glass S53P4 developed and widely tested in Finland. This chapter summarizes the road to the clinical applications of S53P4, commercial products based on it, and the current activities for new clinical applications.

3.1.1 Discovery of the Concept of Bioactive Glass and 45S5 Composition

The concept of bioactive glass was introduced in 1971 based on the ability of the glass to chemically bond with the bone after implantation [1]. The bonding developed between the bone apatite and the hydroxyapatite (HAp) crystals that nucleated and grew at the glass surface due to a sequence of dissolution and precipitation reactions *in vivo*. Accordingly, the compositions showing HAp surface layer formation were classified as bioactive glasses. Ideally, the bioactive glasses were thought to react and gradually dissolve in a controlled manner while new bone grows. The subsequent glass dissolution reactions were closely characterized and used to understand tissue-bonding ability [2].

In the beginning, the main focus was on the development of glass compositions that would be suitable prosthesis or graft materials to restore diseased or damaged bone. The first bioactive glasses were composed of four oxides only: SiO_2 as the glass network former, Na_2O and CaO in relatively high contents to provide a composition that would dissolve in aqueous solutions, i.e. extracellular fluid, and some P_2O_5 for the formation of the calcium phosphate compound, HAp [3]. When the bone-bonding and new bone formation mechanisms in the presence of bioactive glasses were explored in more detail, the ion dissolution products of the glass, mainly soluble Ca and Si species, were found to activate and stimulate cellular processes in bone regeneration [3, 4]. The increasing molecular biology knowledge of inorganic ions as activators in the cellular processes turned a new page in developing and understanding bioactive glasses in soft and bone tissue regeneration. Today, bioactive glasses are classified as materials that bond to bone and stimulate bone and soft tissue growth while dissolving over time.

Successful inventions and research outcomes often have a good history behind them. In the well-known review article "The story of Bioglass 45S5®," Professor Larry L. Hench describes how

Bioactive Glasses and Glass-Ceramics: Fundamentals and Applications, First Edition.
Edited by Francesco Baino and Saeid Kargozar.

he discovered the first bioactive glass [3]. Before initiating the search of glasses for prosthetic materials, Professor Hench explored other types of materials, such as radiation-resistant semiconducting glass-ceramics, to be used in satellites. However, a conversation with an Army Medical Corps officer changed his future research efforts to glasses and glass-ceramics for medical applications. The rest is history, and Professor Hench is today recognized as the man behind the new generations of ceramic implant materials, i.e. the bioactive glasses and glass-ceramic for tissue regeneration.

3.1.2 Development of Bioactive Glasses in Finland

The story behind bioactive glass S53P4 is partly similar to 45S5: a meeting with two professors in two different science fields, chemical engineering and medicine, at the two universities in Turku, Finland, in the early 1980s. Professor in Prosthetic Dentistry Antti Yli-Urpo at the University of Turku explored the interactions of metallic restoration materials with porcelain and mucosa [5, 6]. Inspired by the new ideas of bioactive glasses, he asked professor in Inorganic Chemistry Kaj H. Karlsson, a glass scientist at Åbo Akademi University, whether they could together develop glass or glaze coatings suitable on metal prostheses to enhance the tissue adherences (Karlsson, K.H. Personal communication, spring 2021). At that time, Professor Karlsson's research areas included the relationships between glass structure, properties, and oxide composition [7–9]. After this discussion, the interdisciplinary collaboration in bioactive glasses started between the two neighboring universities.

After some preliminary trials, *in vitro* and physical properties of several glass series were tested at Åbo Akademi University. The *in vivo* studies were carried out at the University of Turku and Turku University Hospital. These collaboration projects were financed by the Finnish Technology Agency and the Academy of Finland. The material research goal was to understand the physical and biological properties as functions of the glass oxide composition. These functions would then be used to tailor the most suitable compositions to various clinical needs. The first properties studied included the glass transition temperature, thermal expansion, and water durability [10]. As brittleness of glasses was considered a critical property, the aim was to develop novel compositions for coatings on metals. The glass or glass-ceramic coating should then protect the metal from corrosion and enhance the prosthesis's attachment to bone. Glass transition temperature and thermal expansion described the suitability of the glass to coating processes. Correspondingly, water durability was correlated with the corrosion protection properties. The glasses were directly tested *in vivo* as cylinders drilled in rabbit tibia for eight weeks without any prior *in vitro* testing in buffered solutions. At that time, the protocols and procedures were not as strictly controlled as today, thus, partly explaining the large numbers of rabbit and rat tests done during the early years of bioactive glass research. In total, nine compositions were studied and used as the basis for property modeling. The compositions were statistically chosen in the oxide range (all in wt%) 47.5–68.0SiO_2, 15.2–27.3Na_2O, 8.9–20.6CaO, 2.3–8.9P_2O_5, 0–3.2Al_2O_3, and 0–3.3B_2O_3 to provide a wide range of soluble glasses. The results were then used to express all the properties as functions of the glass composition. An additional goal was to embed the models in a computerized routine for optimizing glass batch compositions to satisfy a selected set of desired properties [11].

3.1.3 Bioactive Glass S53P4 Today

The early studies provided the basis for intensive bioactive glass research in Finland. Research methods and protocols for preclinical and clinical tests were developed and applied for assessing

the suitability of bioactive glasses for the treatment of craniomaxillofacial, dental and orthopedic trauma, tumors, and diseases. Eventually, glass S53P4 became a clinically tested composition in several indications, especially in Finland.

This chapter describes some milestones of Bioactive glass S53P4 on its route to commercial products. Thirty years after the composition was published for the first time, several research efforts are still paid to better understand the physical, *in vitro*, and *in vivo* properties and clinical outcomes of bioactive glass S53P4. Why is this motivated? Dr. Fredrik Ollila, executive chairman and founder of Bonalive Biomaterials Ltd. replied to this question as follows: "Bioactive glass S53P4 performs very well clinically in the currently approved indication areas. However, to be able to solve new clinical challenges, it is helpful to acquire a complete understanding of its properties. All new results enhance our understanding and ensure safe and effective clinical utilization of the bioactive glass S53P4 in current and future applications."

In total, more than 200 scientific papers have been published on the *in vitro*, *in vivo*, preclinical, and clinical studies of bioactive glass S53P4. Also, the glass composition has been discussed in several more papers as a reference composition to new glass formulations. More than 50 papers discuss the *in vitro* properties and physical properties of S53P4. These studies include physical properties of interest for the manufacture of melt-derived products. Noteworthy, the *in vivo* and preclinical studies have been reported in more than 50 papers. The number of clinical case reports and review papers is almost 100, thus indicating the large spectrum of applications tested. This chapter reviews some of the highlights that paved the road to the clinical applications of Bioactive glass S53P4.

3.2 Bioactive Glass S53P4 – From a Concept to First Clinical Trials

3.2.1 The First Series of Glasses, Including S53P4

Among the nine first glasses for bone applications studied in Turku, some showed good bonding to bone, while the bonding was very poor or negligible for some compositions [10]. Based on the results, a new statistical series of 16 compositions was developed within a slightly different range (in wt%): 46–65.5SiO_2, 15–30Na_2O, 11–25CaO, 0–8P_2O_5, 0–3Al_2O_3, and 0–3B_2O_3 [12]. Glass nr. 9 in this series has the composition of 53SiO_2, 23Na_2O, 20CaO, and 4P_2O_5, all in wt%. Today, we know this composition as S53P4, or as Bonalive®, i.e. a commercial product available in different product forms [13].

Unfortunately, no SEM (scanning-electron microscopy)-images have been published of S53P4 in the first *in vivo* study. The desired response, bone bonding, was measured not only for S53P4 but also four other compositions. Two of the compositions did not bind to bone at all, and four had poor contact while five had contact with bone. When examining the history of S53P4, two questions have to be answered: How was the bone bonding defined? Why did the composition S53P4 become the only composition that is used today commercially?

3.2.2 Phenomenological Model of Bone Bonding

The 16 compositions in the glass series were statistically chosen within a wide range to ensure apparent differences in the properties. This approach enabled establishing the limits of bioactivity and gave the basis for numerical modeling of properties as composition functions [12]. The *in vitro* properties, specified as weight loss for grains immersed in Tris-buffer for 6 and 24 hours at 36.5 °C,

varied considerably with the glass composition. The variation was assumed to lead to large differences in the tissue response as well. Then, six cones of each composition were implanted in the rat tibia for eight weeks. The tissue response and the glass surface reactions were evaluated from the cone and surrounding bone cross-sections using SEM imaging and energy-dispersive X-ray spectroscopy (EDS). The EDS line analyses were used to verify whether silica-rich and calcium phosphate-rich (Ca,P) surface layers had formed at the cone surfaces. The glasses showed a wide range of interactions with the bone, ranging from inert compositions to glasses that had bonded to the bone. Poor bone contact was characterized as low *in vitro* solubility combined with a thin or no silica-rich layer at the glass. Three compositions with a high silica content (63.5–65.5 wt%) showed poor bone contact and were thus classified as inert *in vivo*. Five glasses showed bone bonding with distinct silica-rich and Ca,P surface layers. These glasses had high *in vitro* dissolution and were classified as bioactive compositions. The rest of the compositions showed varying bone contact degrees, silica-rich layer and Ca,P-layer thicknesses.

The results were used to establish a phenomenological model of *in vivo* bone bonding, expressed as the reaction number, RN. The weight loss *in vitro*, *in vivo* formation of silica-rich and Ca,P-layers, and bone contact type were evaluated for each composition. Based on these characteristics, the glasses were divided into groups with numerical values from 1 to 6. Group 1 glasses had low weight loss, no or negligible layers and no bone contact, while group 6 glasses showed high weight loss, distinct silica-rich and Ca,P-layers, and chemical bonding to bone [12]. The other behavior combinations gave the numbering for the other glass groups. The developed RN-model expresses the bioactivity as a function of the composition of the glass in wt%. For a glass to be bioactive, the RN value should be higher than 5:

$$\begin{aligned} RN = {} & 88.3875 - 0.011\,627\,2[SiO_2]^2 - 0.980\,188[Na_2O] - 1.123\,06[CaO] \\ & - 1.205\,56[P_2O_5] - 0.056\,052\,7[B_2O_3]^2 - 2.086\,89[Al_2O_3] \end{aligned}$$

The model was not verified with other compositions and not used to computerize new compositions. The calculated RN value for the original bioactive glass 45S5 by Professor Hench well satisfies the bioactivity criterion. Later, the model has been shown to work with some other compositions. However, the lack of other alkali or alkaline earth oxides than Na_2O and CaO limits the RN model's usability range [14].

3.2.3 *In Vivo* Bone Bonding vs. Glasses with Al_2O_3 and P_2O_5

Alumina's role on the bone bonding was studied in more detail with a few compositions selected from the series of 16 glasses. As the glasses with the highest alumina contents had not shown bone bonding, six compositions containing 0–3 wt% Al_2O_3 and one reference titanium cone were implanted in rabbit tibia, and the push-out strength of the implants was measured after six weeks. All three cones with 2.5 or 3 wt% Al_2O_3 showed low push-out strengths, also, if the cones had a Ca,P surface layer [15]. Thus, the formation of Ca,P surface layer *in vivo* was not a sufficient bone-bonding criterion. Earlier *in vitro* studies of alumina-containing glasses in Tris-buffer had shown that aluminum was enriched in the silica-rich layer and interfered with the formation of calcium phosphate surface layer [16]. Alumina in the Ca,P layer was thus assumed to prevent the implant's proper chemical bonding to bone.

In an another early *in vivo* study, two other bone bonding compositions than S53P4 from the same glass series were selected to study the impact of P_2O_5 in the glass on the initial stage of calcium phosphate formation on the glass surface. After eight weeks in rat tibia, both the composition without

and with 4 wt% P_2O_5 showed good bone bonding [17]. The results showed that the migration of phosphate from the glass is not a prerequirement for bonding to bone. The hydrated silica gel's flexible structure at the surface provides nucleation sites for phosphate ions from the physiological solution.

Alumina-free, bone-bonding compositions were selected for further *in vivo* studies and clinical tests. Two of the glasses in the series of 16 glasses fulfilled these criteria: S53P4 and S46P7. The latter contains 46 wt% SiO_2 and 7 wt% P_2O_5 and is thus close to 45S5 composition. Based on the first trials' clinical outcome [18, 19], S53P4 became the composition that was tested using several animal models for various potential clinical applications.

3.2.4 Soft and Hard Tissue Bonding *In Vivo*

The first *in vivo* studies of S53P4 in soft tissue of rabbits and hard tissue in sheep were reported in 1994 [20]. Granules of the glass were implanted in muscle and connective tissue of rabbit and mandibular bone of sheep. Similar reactions were reported after two to three months in all three implantation sites: silica-rich layer with calcium phosphate precipitates. In soft tissues, large precipitates with a composition close to apatite were analyzed. The molar ratio Ca:P suggested that the Ca,P precipitation in the silica-rich layer originated from the ions released from the glass. Correspondingly, the Ca:P-ratio in the surface apatite implied phosphate incorporation from the physiological environment. Figure 3.1 shows an SEM image of an S53P4 granule surrounded by new bone after the implantation in the sheep jaw. The EDS analyses of the points shown in the SEM image are listed in Table 3.1. A silica-rich layer with increasing P_2O_5 content (Pts 3–5) surrounds the granule core with a composition close to the original glass (Pt 1). The Ca/P molar ratios are almost similar in the outermost granule layer (Ca/P = 1.4 in Pt 6) and the new bone (Ca/P = 1.3 in Pt 7), thus verifying chemical bonding between them [20].

3.2.5 *In Vivo* Evidence of S53P4 in Bone Healing

In one early *in vivo* study, bioactive glass S53P4 granules were compared with polytetrafluoroethylene (PTFE) membrane to repair cortical bone defects in rabbit tibia [21]. After 6 and 12 weeks, a markedly better bone repair was obtained when using the bioactive glass than PTFE or empty control defects. The new bone that grew along the bioactive glass granules formed a continuous bridge over most defects, as shown in Figure 3.2.

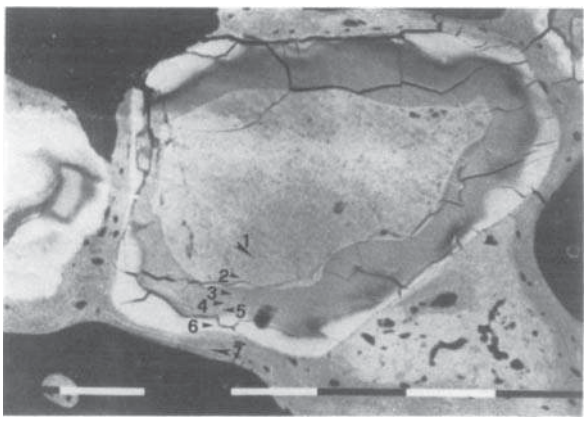

Figure 3.1 SEM micrograph of an S53P4 granule implanted in a sheep's mandibular bone. The numbers indicate the points of the EDS analyses in Table 3.1. The bar equals 100 µm. Source: Gatti et al. [20]/with permission from Elsevier.

Table 3.1 EDS analyses of the degrading S53P4 granule (Pt 1–6) and the surrounding bone in Figure 3.1 (Pt 1 and 2 glass, Pt 3–4 silica rich layer, Pt 6 Ca,P layer, Pt 7 bone).

	Pt 1	Pt 2	Pt 3	Pt 4	Pt 5	Pt 6	Pt 7
SiO_2	49.2	50.2	76	70.5	64.7	2	0.9
Na_2O	20.1	20	0.3	0	0	0.5	0.5
CaO	19.5	10.5	7.9	9.5	9.9	45.5	39.9
P_2O_5	4.2	4.2	5.5	7.2	7.8	32.2	30.5
Total	93	94	89.9	87.5	82.8	81	72.9

Source: Gatti et al. [20]/with permission of Elsevier.

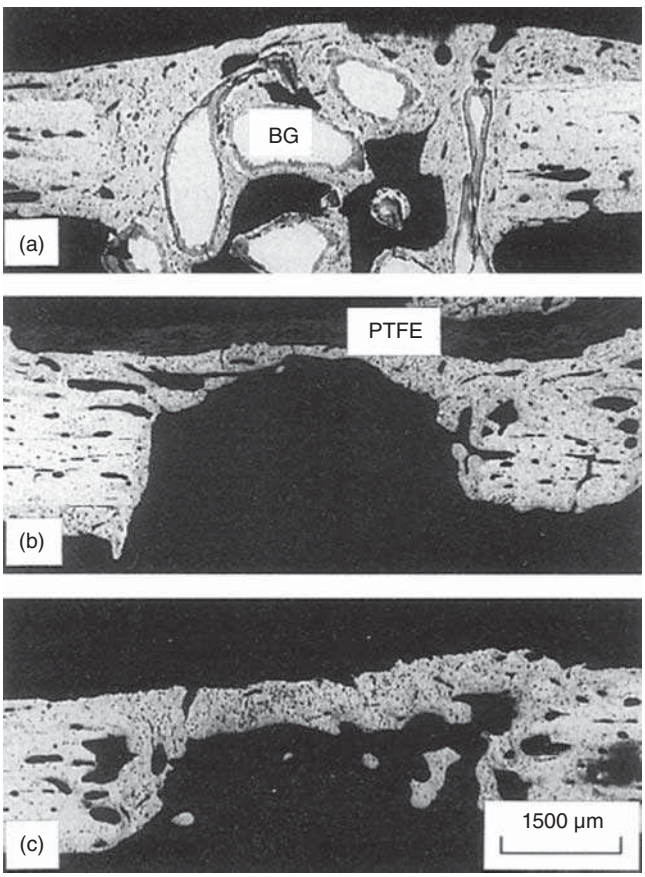

Figure 3.2 SEM images showing defect closure in rabbit tibia after six weeks for (a) defect filled with S53P4 granules, (b) defect covered with polytetrafluoroethylene membrane, and (c) empty control defect. Source: Turunen et al. [21]/with permission from Springer Nature.

3.2.6 Stimulatory Effect of S53P4 on Bone Healing

The first indications of the stimulatory effect of S53P4 on new bone growth were received from histologic, histomorphometric, and molecular biologic healing pattern comparisons of the glass granules with autografts and empty controls in defects drilled in rat tibia [22]. The analyses showed reaction layers on the glass granules already after three days. The layer thickness significantly increased with implantation time, reaching a mean thickness of 40 ± 4 μm at 56 days. At the same time point, 70 ± 14% of the granular surfaces had direct bone contact. The healing patterns showed that new bone growth was faster in autografted defects, but no adverse cell reactions were observed for the defects filled with S53P4 granules. The results confirmed that the S53P4 glass surface was not only osteoconductive but also osteoproductive. The glass promoted migration, replication, and differentiation of osteogenic cells and their matrix production.

3.2.7 Antibacterial Effect of S53P4 *In Vitro*

The first studies of the antibacterial effect of S53P4 were carried out in glass powder suspension containing the oral microorganisms *Actinobacillus actinomycetemcomitans*, *Porphyromonas gingivalis*, *Actinomyces naeslundii*, *Streptococcus mutans*, and *Streptococcus sanguis* [23]. Powdered S53P4 was found to have a broad antimicrobial effect on these microorganisms typical for supra- and subgingival plaque. This powdered glass was suggested as an ingredient in tooth-care products.

The therapeutic value of granules and plates of S53P4 were tested against the growth and colonization of *Klebsiella ozaenae*, a microorganism frequently isolated from patients with atrophic rhinitis [24]. In these tests, S53P4 did not favor adhesion and colonization of the microorganism. The *in vitro* study was completed with five atrophic rhinitis patients surgically treated with plates and granules of S53P4 at the Turku University Hospital. After 19–74 months' follow-up periods, no reinfections or extrusion of the glass implants were found. The patients' symptoms were eliminated or markedly reduced, suggesting S53P4 glass to be a potential filling material of nasal cavities in patients suffering from ozena [24].

In later studies, fine powders ($\leq$45 μm) of six different glasses, including S53P4, were tested against 29 aerobic [25] and 17 anaerobic bacteria species [26]. In both studies, glass S53P4 inhibited the growth of all bacteria tested. In many cases, the antibacterial effect was measured at lower concentrations for S53P4 than the other glasses. The mechanisms behind the observed antimicrobial effects of the bioactive glasses are not fully understood. The ion release from the glasses into simulated body fluid (SBF) and the changes in the pH of the solution were measured for 48 hours [27]. The antibacterial effect did not correlate with the ion concentrations released. However, the high and rapid pH-increase inside the glass powder bed during the first 24 hours of incubation was assumed to explain the bacteria growth-inhibiting effect of S53P4.

The antibacterial effect of S53P4 *in vivo* is thought to be mediated by changes in the local physiological surroundings that occur after implantation, including an increase in pH and an osmotic pressure, which can stress the bacteria and lead to subsequent changes in the bacterial morphology and ultrastructure. The cell membrane-bound proton transport system is critical for pH resistance. The bacteria attempt to maintain cytoplasmic pH by secreting protons from the cell, which cannot occur via H^+-ATPase activity at >pH 8 [28]. Granules (<45 μm) and putty based on microspheres (<45 μm) of S53P4 tested on multidrug-resistant (MDR) bacteria *in vitro* showed bactericidal activity of the two different sample types without selection for resistance [29]. SEM analysis revealed changes in morphology and cell shrinkage of bacteria such as *Staphylococcus epidermidis*, *Klebsiella pneumoniae*, and *Acinetobacter baumannii*.

Colonizing bacteria can also produce biofilms, which are considerably more resistant to antibiotic treatment than the same bacteria in a planktonic phase. Bioactive glass S53P4 showed antibacterial properties on MDR species of *S. epidermidis*, *A. baumannii*, and *K. pneumoniae* on titanium disks [30], indicating that the S53P4 is effective not only against planktonic bacteria but also against bacteria in biofilms. This is in concordance with the reported effect of S53P4 granules (500–800 μm), powder (<45 μm), and putty (500–800 μm granules and <45 μm powder embedded in a blend of polyethylene glycols and glycerol) on methicillin-resistant *Staphylococcus aureus* and MDR *Pseudomonas* biofilms, showing a significant reduction in biomass and cell volume on a prosthetic material [31].

3.3 Clinical Trials for the Development of Commercial Products

Clinical trials of using bioactive glass S53P4 in the oral and maxillofacial area started shortly after the first *in vivo* studies. Also, cavity filling of trauma, tumors, and infections in orthopedics with S53P4 granules started in the 1990s. Preliminary observations were reported in conference proceedings [18, 19]. These results are included also in later publications reporting the clinical outcome after extended follow-up studies.

3.3.1 Glass Granules and Plates in the Oral and Maxillofacial Area

Bioactive glass S53P4 granules and blocks were used in the obliteration of osteoblastic frontal sinus operation at the Department of Otorhinolaryngology – Head and Neck Surgery, Turku University Hospital (ENT-HNS-Tyks) during 1990–1993 [32]. Clinical examinations and symptoms of the five patients were recorded every month postoperatively for six months and then every third month up to an average follow-up time of five years. The results were promising as all the patients had obtained relief of their main symptom, chronic frontal pain, after 12 months. Complete obliteration of all sinusal recesses and excavations was achieved. Although available only as experimental samples, the bioactive glass plates and granules were considered easy-to-handle materials.

The utilization of S53P4 granules in mastoid obliteration surgery was evaluated for 25 patients with chronic otitis media and one with cerebrospinal fluid leakage at ENT-HNS-Tyks between the years 1996 and 2011 [33]. The follow-up periods varied between 1 and 182 months. No adverse effects were seen in any patient. S53P4 granules were considered a noteworthy material in mastoid obliteration surgery in patients with previous failed efforts in achieving a dry, safe ear.

Granules or plates of S53P4 were utilized in the treatment of 150 patients suffering from chronic frontal sinus inflammations (62), fronto-orbital and skull-base traumas (65), and fronto-orbital tumors (23) at ENT-HNS-Tyks during the years 1991 and 2004 [34]. In all cases, S53P4 was well tolerated and had good functional and aesthetic outcomes. The overall success rate five or three years after the reconstructions are summarized in Table 3.2.

S53P4 granules and plates were also used to treat 11 patients suffering from septal perforations at ENT-HNS-Tyks [35]. At the end of the follow-up periods, 2–37 months, none of the 10 successfully treated patients complained of any symptoms. The plates and granules did not favor the adhesion and growth of two typical respiratory pathogens, *Haemophilus influenzae* and *Streptococcus pneumoniae* [35]. In a later study, 23 patients with septal perforations were surgically treated with S53P4 plates combined with mucoperiosteal flaps [36]. In 16 patients, the surgery was performed with mucoperiosteal flaps only. Twenty-two patients were followed up for 12–68 months. At the end of the follow-up, none of the patients complained of any adverse symptoms. The results

Table 3.2 The number of patients treated with bioactive glass S53P4 in different fronto-orbital defects, follow-up time, and success rate (%).

Defect	Number of patients	Follow-up time (years)	Success rate (%)
Frontal sinus obliteration with glass granules	62	5	95
Fronto-orbital trauma reconstruction with glass plate	65	5	89
Fronto-orbital tumor reconstruction with glass plates and granules			
Benign tumor	12	3	91
Malignant tumor	11	3	55

Source: Aitasalo and Peltola [34].

suggested that the plates of S53P4 are good grafts in the repair of medium and large nasal septal perforations.

Granules and plates of S53P4 were also tested in facial reconstructions at 36 sites in 13 patients with autologous bone as a reference at the Department of Plastic Surgery, Helsinki University Hospital, Finland [37]. Nineteen glass plates were used in orbital wall reconstruction and one plate in maxillary augmentation. The glass granules were used as on lay augmentation in sub-periosteal pockets over frontal, temporal, zygomatic, and maxillary bones. In two cases, the granules were used to the obliteration of the frontal sinus. The follow-up period was 6–24 months. No adverse effects were reported, and the glass implants were resistant to infections. During the period that followed, the glass plates did not resorb but were osteoconductive and better incorporated into bone than bone grafts and glass granules.

3.3.2 S53P4 Granules in Orthopedics

Granules of S53P4 were compared with autologous bone as bone graft materials in the operative treatments of benign bone tumors in randomized control trials [38, 39]. The surgeries were conducted during 1993–1997 at the Department of Surgery, Turku University Hospital (DS-Tyks). In total, 21 of the 25 patients continued with the total postoperative follow-up of 14 years. Eleven of them had been treated with bioactive glass and ten with autologous bone harvested from the iliac crest. The tumor size varied from small tumors in fingers to large ones in the proximal humerus and distal tibia. After the follow-up period, X-ray analyses revealed some undefined glass granules embedded in new bone in six of the eight treated large tumors. In small bone tumors, no granules were identified. Interestingly, the cortex appeared thicker than normal in all small and four large cavities filled with the glass granules (Figure 3.3). This cortical thickening had been observed already eight months after the operation.

The treatment of a recurrent aneurysmal bone cyst in the index finger of a three-year-old child with granules of S53P4 showed that the bone had remodeled to a normal shape after 24 months postoperatively [40]. The long-term results of utilizing S53P4 granules as a bone substitute in hand were later summarized to show the desired properties: the glass bonded to the bone, the glass was osteostimulating and also had angiogenic stimulating properties [41]. Noteworthy, granules of S53P4 did not disturb the growth of bone in the hand in children. Thus, the glass was regarded as a safe material in treating bone tumors of children and adults. The suitability of S53P4 granules in treating aneurysmal bone cysts in the femur or pelvis in children was verified in a clinical study with 18 patients between the ages of 4 and 16 years at three university central hospitals in Finland [42].

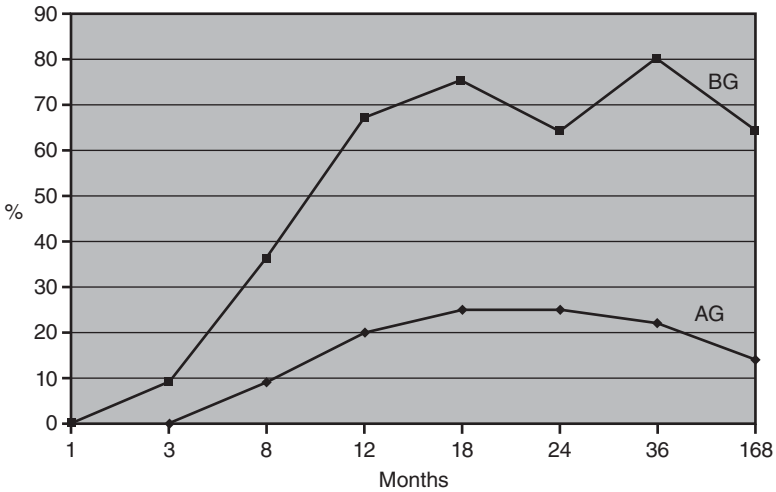

Figure 3.3 Evolution of cortical thickness in the treatment of benign bone tumors with bioactive glass S53P4 granules and autologous bone as functions of follow-up time. Source: Lindfors et al. [39]/with permission from John Wiley & Sons, Inc.

Clinical trials of using bioactive glass S53P4 granules in treating depressed tibial plateau fracture were conducted at DS-Tyks, in 1995–1998 [43]. These were the first clinical trial in which S53P4 was utilized under load-bearing conditions. In the randomized study, autologous bone harvested from the iliac crest was used as a reference. The subchondral cavity caused by the fracture was filled with glass granules or autologous bone and then supported with an anatomical condylar plate. In total, 5 patients with bioactive glass and 10 with autologous bone completed the long-term follow-up of 10–14 years, with a mean of 11 years. The volume of large bone cavities filled with the glass granules started to diminish after 12 months, indicating that the glass dissolved slowly. The desired bone formation and structural integrity of the fractures treated with the glass granules were also achieved. Figure 3.4 shows the radiological outcomes of the fracture before the

Figure 3.4 X-ray images of a lateral tibial plateau fracture: (a) before the treatment with granules of S53P4; (b) postoperative; and (c) after 11 years. Source: Pernaa et al. [43]/with permission from Begell House, Inc.

operation (Figure 3.4a), after the treatment with S53P4 granules (Figure 3.4b), and after 11 years (Figure 3.4c).

Clinical trials of spinal surgeries using S53P4 at DS-Tyks were carried out in 1996–1997 [44]. The 11-year follow-up study compared S53P4 granules with autologous bone in the posterolateral spinal fusion of 17 patients. Glass granules were implanted on one side and autologous on the other side of the posterolateral fusion bed. Overall opinion after the follow-up period was good: 15 patients reported better subjective satisfaction than before the operation. Computer tomography showed a 100% fusion rate for the autologous bone side. Correspondingly, solid fusion was seen in 12 patients and partial fusion in 5 patients for the bioactive glass side, giving a total fusion rate of 80.5%.

A similar approach to implanting S53P4 granules on the one side and autologous bone on the other sides was used to treat unstable lumbar spine burst fractures in 16 patients at Turku and Helsinki University Hospitals during 1996–1998 [45]. The computer tomography scans showed solid bone fusion on the autologous bone side. In contrast, the total fusion rate was 71% of all fused segments in the bioactive glass side for the 10 patients that participated in the 10-year follow-up.

3.3.3 Clinical Use of S53P4 in the Treatment of Bone Infections

Osteomyelitis is a destructive infection of the bone structure that eventually leads to bone necrosis. The infection may be caused by trauma, surgical procedures, or the bacteria spread in the blood. Bone infection can be caused by many pathogens, including MDR bacteria, with a subsequent need for antibiotic treatment. However, antibacterial resistance to frequently used antibiotics is a serious global threat and an increasing problem worldwide. To eradicate the bone infection, the bone tissue has to be removed, often resulting in a large bone defect, which needs to be restored. The antibacterial effects observed on bioactive glass S53P4 have contributed to the growing interest in using bioactive glasses in infection treatment.

The proven antibacterial and osteoconductive properties of the bioactive glass S53P4 encouraged to utilizing it as a bone graft substitute in treating osteomyelitis [46]. The clinical trials were done on 11 patients with chronic infection and verified osteomyelitis in four central hospitals in Finland during 2007–2009. The mean follow-up time after the surgery was 24 months. The clinical outcome was good or excellent in nine of the patients. Figure 3.5 shows X-ray images of the distal tibia before (Figure 3.5a) and after treatment with S53P4 granules (Figure 3.5b). At five months, no signs of osteomyelitis were seen (Figure 3.5c).

This study was followed by a cohort study in Italy on 27 patients with clinically and radiologically diagnosed osteomyelitis treated with bioactive glass S53P4. An excellent recovery was observed in 24 patients [47]. To use bioactive glasses without local antibiotics in the treatment of osteomyelitis was strengthened by a comparative study on S53P4 and an antibiotic-loaded HAp sulfate-based bone substitute, and a mixture of tricalcium phosphate combined with an antibiotic-loaded demineralized bone matrix bone [48]. The success rate for S53P4 was 92.6% compared to 88.9% and 86.3% for the antibiotic-containing bone substitutes. Less wound drainage was also observed for the bioactive glass S53P4. An equally effective treatment outcome has been reported from a retrospective study on 25 patients comparing S53P4 and calcium-sulfate antibiotic beads as a bone substitute [49].

In the Netherlands, the first series of osteomyelitis treatments using bioactive glass S53P4 in 15 patients started in 2011. The infection was eradicated in all patients [50]. In a subsequent study, the one-stage treatment with S53P4 was compared with the two-stage treatment using gentamicin-loaded polymethyl methacrylate (PMMA) beads. The results revealed lower costs and better clinical outcomes for the S53P4 group, thus changing the institutional protocol for

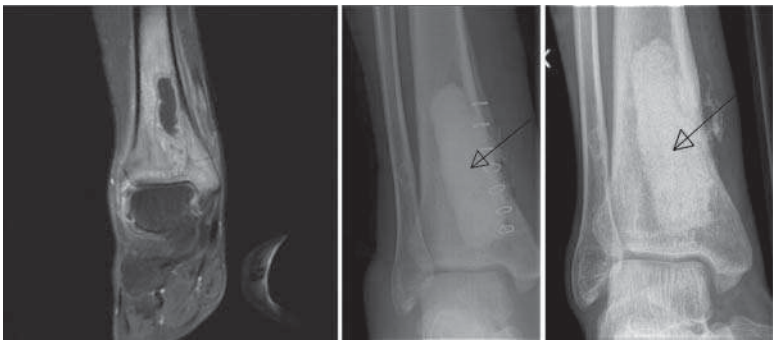

Figure 3.5 Treatment of osteomyelitis caused by *Staphylococcus aureus* in the distal tibia: (a) preoperative magnetic resonance images showing osteomyelitis, (b) postoperative X-ray showing S53P4 in the treated cavity (arrow), and (c) X-ray at five months showing the treated region (arrow). Source: Lindfors et al. [46]/with permission from Elsevier.

treating chronic osteomyelitis from a two-stage procedure to a one-stage procedure by Geurts et al. [51].

The outcome of using glass S53P4 in the treatment of osteomyelitis was further evaluated in a multinational cohort study in 6 countries (Finland, Italy, the Netherlands, Germany, Azerbaijan, and Poland) in 11 centers. The study was performed on 116 patients. Most of the patients had suffered from the infection for years and had been treated with numerous procedures without success. The success rate of the treatment was 90%, and most of the patients showed a rapid recovery even after having suffered from osteomyelitis for decades [52]. These results are in concordance with several other reports on using bioactive glass S53P4 in the treatment of osteomyelitis [53–56].

Bioactive glass S53P4 has also been used in specific demanding indications such as the diabetic foot, with equally promising results [57–59].

Excellent results have also been reported when using S53P4 to treat infected nonunions [60–62]. In 2018, a randomized controlled clinical study of using bioactive glass S53P4 in treating nonunions of the tibia and femur was initiated at the Department of Orthopedics and Traumatology, Heidelberg University in Germany. The randomized trial was planned to reveal the potential benefits and limitations of using bioactive glass in S53P4 in segmental bone defects [63]. The assessments of the clinical, radiological, and subjective outcomes are planned to continue to 2022.

The use of bioactive glass S53P4 in treating infected vertebral osteomyelitis has been reported in three patients with severe spondylodiscitis caused by *Mycobacterium tuberculosis*, *Candida tropicalis*, and *S. aureus*. Fusion was observed for all patients, and they recovered well without relapses or complications [64].

Systematic reviews have revealed that bioactive glass S53P4 is a useful bone substitute for long bone infections. Due to its antimicrobial action [65, 66] it enables treatments to be performed as single-stage procedures [67], thus providing attractive alternatives for bone void filling after debridement in the treatment of chronic osteomyelitis.

3.3.4 S53P4 in Fiber-Reinforced Calvarial Implants

Composites containing granules of S53P4 have been developed for calvarial implants [68]. The first clinical trials were conducted using implants of a PMMA bone cement and bioactive glass

S53P4 composite on four patients at ENT-HNS-Tyks in 2005–2006. PMMA bone cement enabled additive manufacturing of the custom-made implant before the operation. The glass granules were used due to their osteoconductive and antibacterial properties in the composite. After five years, no complications were reported.

The following clinical studies were carried out using composite implants consisting of two parts: inert glass fiber-reinforced polymer acting as a laminated supporting framework and a lamellar porous scaffold filled with S53P4 granules [69]. The glass granules provided osteoconductive and antibacterial properties also for this composite. The overall implant structure was designed to allow for patient-specific dimensions and easy fixation. The results after the follow-up times between six months and four years of the 12 patients were promising.

The fiber-reinforced calvarial implants containing S53P4 particles were also tested in seven children with large skull bone defects [70]. The average follow-up time was 35 months. Three patients needed revision surgery. After treatment of complications, the functional and cosmetic outcomes were good.

However, a clinical case study reported infection for one patient with the prototype fiber-reinforced implant after two years [71]. The implant was removed and analyzed in detail. In the areas near the implant margin, osteoblasts, collagenous fibers with osteoid formation, and small clusters of more mature tissue were identified. In contrast, only fibrous tissue was found in the implant center. The partly reacted residual glass particles in the composite middle parts suggested poor contact with blood.

The clinical findings with the composite implants have led to a new implant design perforated throughout the inner and outer layers to allow rapid penetration of blood with osteogenic cells for interaction with the glass particles [72, 73]. Figure 3.6 shows a schematic drawing of calvarial implant design: a sandwich structure of inert E-glass fiber reinforced polymer laminates with a space for free glass granules in between the laminates [73]. As the laminates are perforated, the implant rapidly absorbs blood and cells for interactions with the bioactive glass particles.

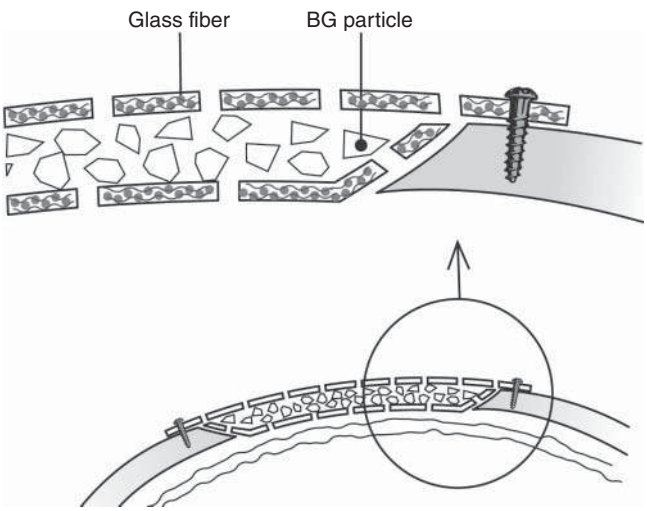

Figure 3.6 Schematic drawing of a calvarial implant with bioactive glass particles between the fiber-reinforced laminates. Source: Vallittu et al. [73]. © Elsevier.

Based on the preclinical tests and clinical trials, the fiber-reinforced composite implants containing bioactive glass granules have been developed into a commercial product by Skulle Implants Ltd., Turku Finland [74]. The custom-made GLACE™ cranial implants are light-weight, strong, and easily installed in the surgery. The bioactive glass granules provide the implant osteoconductive and antibacterial properties. As the implant is fully nonmetallic, it does not prevent magnetic imaging or radiotherapy. GLACE cranial implants have been used to reconstruct cranial and maxillofacial bone defects in more than 1700 surgeries in Europe, especially Finland, Germany, and France [74]. However, the composition of the GLACE implant components and the glass used in it have not been published.

3.4 Commercial Products

The first *in vivo* and clinical trials were carried out using granules melted at Åbo Akademi. Later, the samples were synthesized at Abmin Technologies Ltd. and Vivoxid Ltd. in Turku, Finland. Today, S53P4 glass is commercially known as Bonalive and produced by Bonalive Biomaterials Ltd. in Turku. As described in Section 3.3, S53P4 was tested for clinical applications shortly after the first *in vivo* results. These clinical trials paved the road to approval for the first clinical products. The first approval of BonAlive granules and plates was received for craniomaxillofacial indications in Europe (CE-mark, European Conformity) in 2004. The CE mark for Bonalive granules for orthopedic indications was received in 2006. In 2008, Bonalive granules received the US Food and Drug Administration 510k clearance for orthopedic, craniomaxillofacial, and dental indications [13]. To date, more than 50 000 patients worldwide have received Bonalive Biomaterials' S53P4 glass granules, and the Bonalive products are distributed in 40+ countries.

Bonalive granules are available today for bone infection surgery, trauma surgery, benign bone tumor surgery, spine fusion surgery, and mastoid surgery [13]. Thus, most of the clinical trials have led to clinical practices. In some early clinical trials, the glass granules were reported as an easy-to-handle material [32]. Noteworthy, the product packages, technologies, and surgical techniques have been markedly improved since the first trials to sterilized granules to be applied with a sterile instrument in the reconstruction of chronically infected and discharging mastoid cavities, Figure 3.7a. A highly moldable putty is designed for easy filling of bone voids and gaps, Figure 3.7b. The prefilled cartridge with dispenser ensures a stable positioning and controlled access for minimally invasive bone surgery, Figure 3.7c.

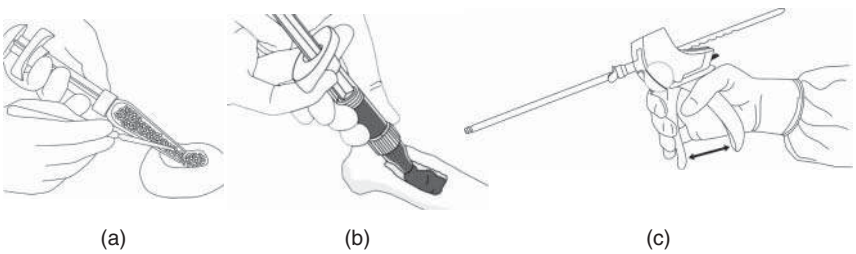

Figure 3.7 Bonalive® products for filling S53P4 granules in (a) infected cavities, (b) filling bone voids and gaps as a putty, and (c) filling bone cavities as putty in hard-to-reach bone defects using minimally invasive surgery. Source: Figure courtesy of Bonalive Ltd.

3.5 Research for New Compositions and Applications

3.5.1 Compositions Derived from S53P4

After 50 years of the first bioactive glasses, new glass compositions and manufacturing techniques are actively developed to meet new clinical needs and challenges. The search for new compositions can partly be explained by the increasing knowledge of the impact of inorganic ions on the cellular processes in soft and hard tissue regeneration. Glasses possess unique properties: they are excellent solvents of almost all elements, and within certain limits, the release of these elements to the surrounding solution can be controlled by proper tailoring of the overall glass composition [75]. Calcium, phosphorus, and silicate species dissolving from the first commercial bioactive glasses, 45S5 and S53P4, stimulate the expression of osteogenetic genes and, thus, enhance bone formation [4]. However, several other elements have also been reported to affect osteogenesis and angiogenesis, i.e. bone formation [76]. These so-called "bio-inorganics" include, e.g. the ions of Cu, Co, Zn, Mg, Sr, Li, and Ce. The antibacterial effect also depends on the dissolution reactions of the bioactive glass in the extracellular solution.

Glass composition tailoring has also aimed at adjusting the physical properties to easier manufacturing processes into devices with desired structure and morphology. The first composition adjustments of S53P4 arose from the need to manufacture the glass in other product forms than granules or small monoliths. Due to their low silica content, the bioactive glasses 45S5 and S53P4 easily crystallize during thermal treatments [77]. The crystallization challenges the hot working of porous amorphous 3D scaffolds of these compositions for tissue engineering or wound-healing applications. Several studies report on the impact of partial substitution of some components in the original S53P4 composition on the thermal properties and *in vitro* properties.

A series of 26 compositions in the Na_2O–K_2O–MgO–CaO–B_2O_3–P_2O_5–SiO_2 system was designed at Åbo Akademi University to allow for easier hot-working of the bioactive glasses into continuous fibers, flame-sprayed microspheres, and sintered porous scaffolds [78, 79]. Similarly to the earlier glass series [12], the statistically chosen compositions were utilized to develop composition models for the properties. In this new series, glass 13-93 turned out to have *in vivo* behavior similar to S53P4 but did not crystallize in hot-working of the glass melt. Both glasses contain equal amounts of SiO_2, P_2O_5, and CaO, but in addition to Na_2O, 13-93 also contains MgO and K_2O:

	SiO_2	P_2O_5	CaO	Na_2O	K_2O	MgO
S53P4 (in wt%)	53	4	20	23		
13-93 (in wt%)	53	4	20	6	12	5

Glass 13-93 has later been well known for its suitability in porous tissue engineering scaffolds manufactured through various techniques.

Substituting MgO and SrO for CaO impacts the hot-working properties and bioactivity of S53P4. The introduction of up to 4 mol% of MgO in S53P4 slightly slowed down the *in vitro* reactivity and increased the hot-working window, i.e. decreased the crystallization tendency [80]. Substituting SrO for CaO retarded the bioactivity and did not markedly impact the hot-working window for drawing of continuous fibers or sintering of porous scaffolds [81]. S53P4-derived compositions in which Na_2O was gradually replaced with K_2O or CaO with MgO and SrO indicated marked differences in the initial release of ions into a continuous flow of Tris-buffer [82]. Gradual substitution of

K_2O for Na_2O led to higher total concentrations of alkali ions released into the solution. The concentration of potassium ions was high, which might have a deleterious cellular effect *in vivo*. While partial substitution of MgO for CaO did not markedly affect the ion release, the gradual substitution of SrO for CaO led to increased release of all ions.

3.5.2 *In Vitro* Ion Release and Cell Culture Studies

Bioactive glasses bond to bone and dissolve in a controlled manner while releasing ionic species in the surrounding solution. Most *in vitro* studies of S53P4 have been carried out with glass granules, powder, or plates in static solutions of 2-amino-2-hydroxymethyl-propane-1,3-diol (Tris) buffer or the so-called "simulated body fluid" (SBF) buffered with Tris. Composites of biodegradable polymers and S53P4 have also been studied in sodium phosphate-buffered saline [83, 84]. All these studies nicely show the expected formation of silica- and Ca,P-rich layers at the glass surface. While static *in vitro* experiments are useful in comparing the *in vitro* behavior of different glass compositions, they do not give the ion concentrations releasing from the bioactive glass in the dynamic body environment. Recent *in vitro* studies of S53P4 have discussed the initial release of ions in conditions mimicking the human body's solution flow [14, 82]. The initial ion release patterns correlated with the *in vivo* bioactivity of S53P4 cones in rat femur [14]. The dynamic *in vitro* ion release patterns have also provided additional information on the clinical behavior of S53P4 [71].

The release of vascular endothelial growth factors (VEGF) to cultivation solutions of human fibroblasts in contact with S53P4 granules showed that the smaller size fractions (0.5–0.8 and 1.0–2.0 mm) enhanced the VEGF release, while the largest particles (2.0–3.15 mm) inhibited the VEGF release [85]. As the VEGF stimulate neovascularization of the tissue, the results implied that the size and the concentration of the S53P4 granules affect VEGF expression. Consequently, the ion release from S53P4 is essential in controlling the growth factor expression and tissue neovascularization stimulation.

S53P4 discs stimulated the early osteogenic differentiation of human adipose stem cells (hASCs) [86]. However, when the glass disks were placed into cell culture inserts in the absence of direct cell contact, the ions released from S53P4 did not stimulate the osteogenic differentiation. Thus, the cell attachment on the bioactive glass had an essential role in the early osteogenetic differentiation. This result was in line with an earlier study of using a basic medium prepared of ions dissolved from S53P4 to induce osteogenic differentiation of hASCs [87]. The basic medium could not stimulate differentiation. When osteogenesis-inducing chemical supplements were added to the basic medium, excessive Ca,P mineral formation with an exceptionally early onset was observed.

Recently, porous scaffolds sintered of S53P4 were found to stimulate osteogenesis [88]. The scaffolds with and without poly(D,L-lactide-*co*-glycolide) (PLGA) coating were cultured with rabbit mesenchymal cells. Higher mineralization was observed for the uncoated scaffolds. Also, the inflammatory response of the uncoated and PLGA-coated S53P4 scaffolds was measured using human primary macrophages. The thin PLGA coating on the scaffold did not induce a stronger inflammatory response than the scaffold without the coating. The release of the ions from the scaffolds to the cell culture medium was assessed to understand the underlying cellular biological mechanisms. The results suggested that the PLGA coating served as a biodegradable physical barrier that slowed the ion release. Thus, the coating could be utilized to tailor the immunomodulatory and osteogenic effects of the S53P4 scaffold. The *in vitro* cell culture partly supported the *in vivo* observations of the same scaffolds in rabbit tibia as described in Section 3.5.3.

Ideally, bioactive glasses gradually dissolve and are replaced by new tissue. However, some studies have shown glass remnants of S53P4 still after long clinical follow-up times [39, 44, 45]. The impact of osteoclasts on the dissolution of S53P4 discs was studied using rat bone-marrow-derived cells containing osteoclasts and osteoblasts [89]. The culture conditions promoted the differentiation of the marrow cells to osteoblasts. Both osteoblasts and osteoclasts grew well on the disks. However, the intact glass matrix did not degrade to any significant degree. Recently, the resorption of the calcium phosphate layer on S53P4 granules by osteoclasts was studied *in vitro* [90]. The osteoclasts actively resorbed pits in the calcium phosphate on the glass surface. Whether the osteoclast activity resulted in a local decrease of pH similarly to bone resorption was not verified. Such a pH decrease leads to faster formation of a silica-rich layer due to dissolution of sodium, calcium, and phosphate ions from S53P4 than in solutions adjusted to the physiological solution's pH of 7.4 [90, 91]. However, the osteoclasts seem not to degrade the silica-rich layer [89, 90].

3.5.3 Porous S53P4 Scaffolds in Weight-Bearing Applications

Bioactive glasses are extensively studied as materials for tissue-engineering scaffolds providing temporary support for tissue regeneration. Fabrication of porous scaffolds based on melt-derived bioactive glasses requires close control of the hot-working properties to meet the requirements of the desired porous structure, mechanical strength, biodegradability, and cellular interactions. Interestingly, the slightly wider sintering window compared to 45S5 enabled the manufacture of amorphous porous S53P4 scaffolds at 635–650 °C [77, 92]. Amorphous and partly crystalline S53P4 scaffolds were sintered of irregular particles (500–800 µm) in graphite forms at 600–1000 °C for one hour [92]. The mechanical strength varied from 0.7 MPa for the amorphous implants sintered at 635 °C to 10 MPa for the partly crystalline implants sintered at 1000 °C. All implants showed HAp formation *in vitro*, but the layer thickness varied with the phase composition.

Although the scaffold strength was low or moderate, the porous structure was considered feasible for *in vivo* testing as such or after coating with biodegradable polymers in load-bearing applications for the healing of critical-sized defects [93]. For the *in vivo* tests, the scaffolds were sintered from 300 to 500 µm S53P4 granules at 720 °C for 90 minutes. This thermal processing resulted in porous structures with a thin crystallized surface layer consisting of $Na_2O{\cdot}CaO{\cdot}2SiO_2$ crystals and residual glass, but the bulk consisted of amorphous S53P4. One end of the partly crystallized S53P4 scaffolds was coated with PLGA to induce a strong initial inflammatory reaction to enhance induced membrane formation around the implant according to the so-called "Masquelet" technique [93].

Critical-sized defects in weight-bearing bones are traditionally treated with the two-stage Masquelet technique, which requires two operations [94]. However, when using the first experimental S53P4 scaffold, the goal was to use a single-staged induced membrane technique [93]. The bioactive glass scaffold surface was hypothesized to induce a foreign body membrane, supporting bone formation in large defects. After the membrane has formed, the porous bioactive glass scaffold would act as a bone graft and vascularize the new bone.

The partly crystallized S53P4 scaffolds with and without PLGA-coating were implanted in the distal metaphyseal region of rabbit femurs for two, four, and eight weeks to evaluate the vascular expression in the induced membranes. Both coated and uncoated scaffolds positively affected the expression of the VEGF and tumor necrosis factor-α (TNF) in the induced membranes [93]. Bone growth into the PLGA-coated and uncoated S53P4 scaffolds is shown in Figure 3.8 [95]. The bone growth increased over time, and new bone and reaction layers were similar in both scaffolds.

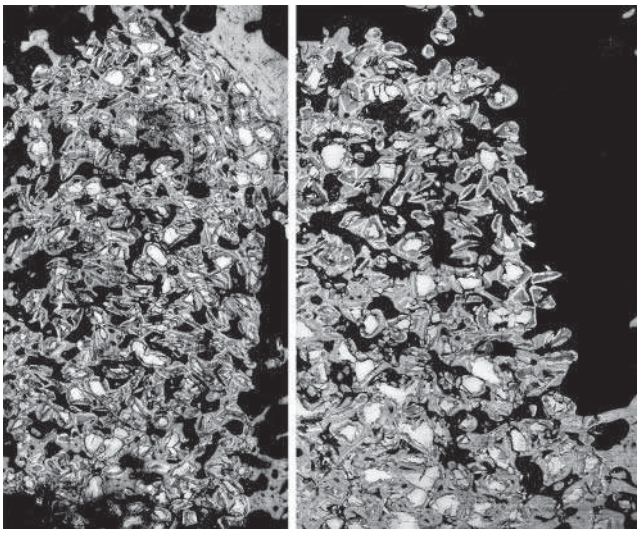

Figure 3.8 SEM micrographs of partly crystallized S53P4 scaffold cross-sections after eight weeks in rabbit femur: (a) uncoated scaffold, (b) PLGA-coated scaffold. The white areas show unreacted scaffold parts (BAG) and the gray areas are for new bone (NB). Source: Björkenheim et al. [95]/with permission from John Wiley & Sons, Inc.

However, the bone formation was more rapid in the coated scaffolds. *In vitro* cell culture studies with human primary macrophages and rabbit mesenchymal stem cells verified that the S53P4 scaffolds had anti-inflammatory and osteogenic properties [88].

After optimizing the sintering conditions, amorphous S53P4 scaffolds with a mechanical strength of 4.8 MPa were successfully manufactured [96]. The amorphous scaffolds were assumed to have similar osteostimulative properties as S53P4 granules and strength high enough for surgery without scaffold failure. The scaffolds were implanted in critical-sized segmental weight-bearing diaphysis defects in rabbit femurs. After eight weeks, the S53P4 scaffolds had induced osteostimulative defect-enclosing membranes and achieved stable osseointegration (Figure 3.9). These results suggest that the porous amorphous S53P4 scaffolds are suitable bone substitutes in a single-staged induced membrane treatment of defects in long bones [96].

3.5.4 Putty-Like S53P4 Bone Filler

Putty-like products have been introduced to the market during the past years [97]. The putty consistency resembles a mixture of blood and bioactive glass particles in conditions when the blood begins to clot. The Bonalive S53P4 glass granules are also available as a putty consisting of S53P4 granules, S53P4-based microspheres, and a polymeric matrix (Figure 3.7b,c). Clinical trials of the utilization of the novel S53P4 putty are sparse. Spinal fusions using the Bonalive putty were carried out on 20 patients at the Department of Neurosurgery, Tyks, in 2014–2016 [98]. The putty consisted of 48 wt% S53P4 granules (0.5–0.8 mm) mixed with 12 wt% of S53P4-based spheres (0.09–0.425 mm), the rest being a mixture of glycerol and polyethene glycols. The putty was used together with the autologous bone to fill the fusion beds. The minimum follow-up time was 12 months. According to the clinical trial outcome, the bioactive glass S53P4 putty gave at least comparable results with previously tested bone graft expanders and fusion enhancers.

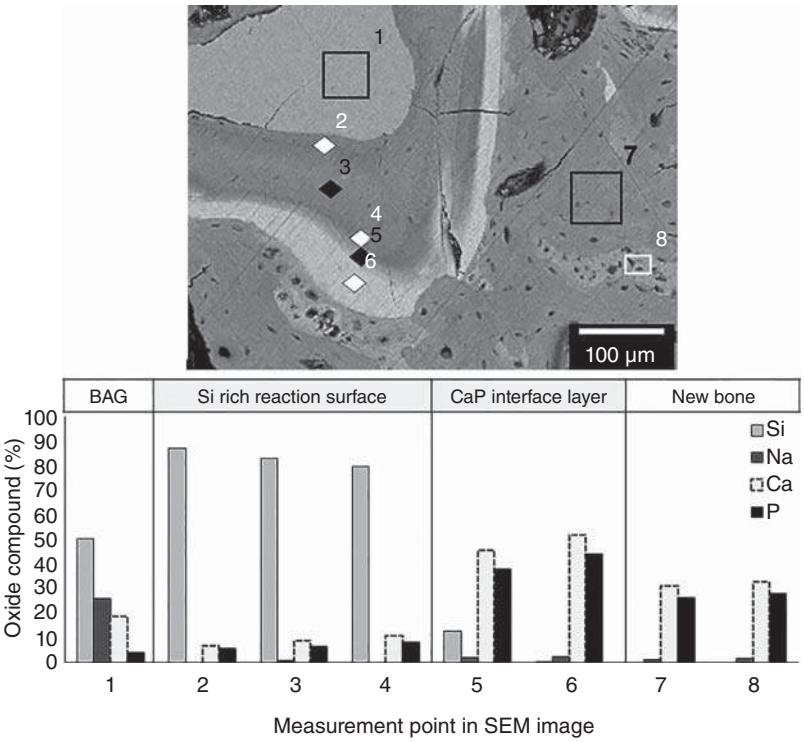

Figure 3.9 Bone growth into S53P4 scaffold after eight weeks in rabbit tibia. The EDS analysis of the points shown in the SEM images show the typical layer Si-rich layer formation (2–4) directly on the surface of remaining S53P4 (1), mixed Si-rich + HAp (5), Ca,P layer (6) and new woven bone in the porous scaffold spaces. Source: Eriksson et al. [96]/with permission from Elsevier.

In a recent *in vitro* dissolution study, the microspheres used in the S53P4 putty were characterized. The composition of the spheres markedly varied with the sphere size fraction [99]. The smaller the spheres, the more their composition deviated from the largest spheres and the original S53P4 composition. In the smallest fractions, the contents of Na_2O and P_2O_5 were very low. Thus, the smallest SiO_2-rich spheres dissolved only slowly *in vitro*. Consequently, these smallest spheres might alter the putty's *in vivo* behavior compared to the nominal S53P4 glass.

3.5.5 Recent Clinical Outcomes

In recent years, increasing clinical case reports and case reviews of bioactive glass S53P4-based products have been published. Clinical outcomes of larger group treatments not discussed in the preceding paragraphs are summarized below.

Large, infected bone defects in the maxilla and mandible were successfully treated with S53P4 granules [100]. After the average follow-up time of 34 months, the treated defects in 20 patients were infection-free, and the bone had regenerated. The radiologic analyses suggested that the glass had remodeled to the bone after two years.

Mastoid obliteration for tegmen bony defect treatment was carried out with S53P4 granules in 17 patients in 2013–2018 [101]. After the mean follow-up time of 22 months, the tegmen bony defect's repair with the glass granules was assessed as a safe and effective method. In a review paper of mastoid obliteration follow-up studies using synthetic materials, the number of

reported cases using S53P4 granules was as high as 199 [102]. In only one case, the material was rejected. In general, bioactive glasses were regarded as the most reliable materials in mastoid obliteration.

3.6 Summary and Future Trends

Bioactive glass S53P4 has actively been studied for different clinical applications during the past 30 years. The increasing number of clinical applications and reports suggests that clinicians around the world have well-accepted the glass. Much of the increasing clinical utilization is due to the development of surgery-friendly products. The road to clinical success was paved by the scientists' and medical doctors' enthusiasm for this material that showed rapid positive results in the tested applications. The combination of bacteriostatic and osteostimulative properties has enabled the utilization of S53P4 to treat various diseases and trauma of bone. The development of porous tissue engineering scaffolds based on S53P4 bioactive glass to challenging bone surgery applications is a topical research area. Also, S53P4 composites are likely to support new clinical applications. The recent cell culture studies provide a firm basis for further studies and a detailed understanding of the behavior and fate of the bioactive glass S53P4 upon implantation.

References

1 Hench, L.L., Splinter, R.J., Allen, W.C., and Greenlee, T.K. (1971). Bonding mechanisms at the interface of ceramic prosthesis materials. *Journal of Biomedical Materials Research* 2 (1): 117–141. https://doi.org/10.1002/jbm.820050611.

2 Hench, L. (1998). Bioceramics. *Journal of the American Ceramic Society* 81 (7): 1705–1728. https://doi.org/10.1111/j.1151-2916.1998.tb02540.x.

3 Hench, L. (2008). The story of Bioglass. *Journal of Materials Science – Materials in Medicine* 17 (11): 967–978. https://doi.org/10.1007/s10856-006-0432-z.

4 Xynos, I., Edgar, A.J., Buttery, L.D.K. et al. (2000). Ionic products of bioactive glass dissolution increase proliferation of human osteoblasts and induce insulin-like growth of factor II mRNA expression and protein synthesis. *Biochemical and Biophysical Research Communications* 276: 461–465. https://doi.org/10.1006/bbrc.2000.3503.

5 Syrjänen, S., Syrjänen, K., and Yli-Urpo, A. (1985). Assessment of oral mucosal changes in patients treated with different metallic restorations and prostheses. *Journal of Dentistry* 13 (3): 244–254. https://doi.org/10.1016/0300-5712(85)90006-5.

6 Yli-Urpo, A. and Uusitalo, E. (1982). Microhardness of alloys for porcelain veneering. *Journal of Prosthetic Dentistry* 47 (4): 396–398. https://doi.org/10.1016/S0022-3913(82)80089-6.

7 Hatakka, L. and Karlsson, K.H. (1986). Optimization of batch costs for an industrial furnace. *Glass Technology* 27 (1): 17–20.

8 Karlsson, K., Fröberg, K., and Perander, M. (1986). On the structure of silicate glass melts. *Journal of Non-Crystalline Solids* 1–3: 184–185. https://doi.org/10.1016/0022-3093(86)9077-3.

9 Karlsson, K., Fröberg, K., and Skrifvars, B. (1990). Chemical approach to medium-range order in glass. *Glastechnische Berichte* 63 (2): 37–47.

10 Andersson, Ö.H., Karlsson, K.H., and Yli-Urpo, A. (1988). Models for physical properties and bioactivity of phosphate opal glasses. *Glastechnische Berichte* 61 (10): 300–305.

11 Westerlund, T., Hatakka, L., and Karlsson, K.H. (1983). A model for optimizing glass batch compositions. *Journal of the American Ceramic Society* 66 (8): 574–579. https://doi.org/10.1111/j.1151-2916.1983.tb10094.x.

12 Andersson, Ö.H., Liu, G., Karlsson, K.H. et al. (1990). In vivo behaviour of glasses in the SiO_2–Na_2O–CaO–P_2O_5–Al_2O_3 system. *Journal of Materials Science – Materials in Medicine* 1 (4): 219–227. https://doi.org/10.1007/BF00701080.

13 Bonalive (2021). Bonalive products. www.bonalive.com/en/products (accessed 17 February 2021).

14 Fagerlund, S., Hupa, L., and Hupa, M. (2013). Dissolution patterns of biocompatible glasses in 2-amino-2-hydrocymethyl-propane-1,3-diol (Tris) buffer. *Acta Biomaterialia* 9: 5400–5410. https://doi.org/10.1016/j.actbio.2012.08.051.

15 Andersson, Ö.H., Liu, G., Kangasniemi, K., and Juhanoja, J. (1992). Evaluation of acceptance of glass in bone. *Journal of Materials Science – Materials in Medicine* 3: 145–150. https://doi.org/10.1007/BF00705283.

16 Andersson, Ö.H., Rosenqvist, J., and Karlsson, K.H. (1990). Dissolution, leaching and Al_2O_3 enrichment at the surface of bioactive glasses studied by solution analysis. *Journal of Biomedical Materials Research* 22 (7): 941–948. https://doi.org/10.1002/jbm.820270713.

17 Andersson, Ö.H., Karlsson, K.H., and Kangasniemi, K. (1990). Calcium phosphate formation at the surface of bioactive glass in vivo. *Journal of Non-Crystalline Solids* 119 (3): 290–296. https://doi.org/10.106/0022-3093(90)90301-2.

18 Aitasalo, K., Peltola, M., Suonpää, J. et al. (1994). Obliteration of frontal sinuses with bioactive glass after chronic sinusitis. One year follow-up. In: *Bioceramics*, vol. 7 (ed. Ö.H. Andersson, R.P. Happonen and A. Yli-Urpo), 409–414. Oxford: Butterworth-Heinemann Ltd.

19 Heikkilä, J.T., Mattila, K.T., Andersson, Ö.H. et al. (1995). Behavior of bioactive glass in human bone. In: *Bioceramics*, vol. 8 (ed. J. Wilson, L.L. Hench and D. Greenspan), 35–40. Oxford: Pergamon/Elsevier Science Ltd.

20 Gatti, A.M., Valdrè, G., and Andersson, Ö.H. (1994). Analysis of the in vivo reactions of bioactive glass in soft and hard tissue. *Biomaterials* 15 (3): 208–212. https://doi.org/10.1016/0142-9612(94)90069-8.

21 Turunen, T., Peltola, J., Happonen, R.P., and Yli-Urpo, A. (1995). Effect of bioactive glass granules and polytetrafluoroethylene membrane on repair of cortical bone defect. *Journal of Materials Science – Materials in Medicine* 6: 639–641. https://doi.org/10.1007/BF00123444.

22 Virolainen, P., Heikkilä, J., Yli-Urpo, A. et al. (1997). Histomorphometric and molecular biological comparison of bioactive glass granules and autogenous bone graft in augmentation of bone defect healing. *Journal of Biomedical Materials Research* 35 (1): 9–17. https://doi.org/10.1002/(sici)1097-4636(199704)35:1<9::aid-jbm2>3.0.co;2-s.

23 Stoor, P., Söderling, E., and Salonen, J.I. (1998). Antibacterial effects of a bioactive glass paste on oral microorganisms. *Acta Odontologica Scandinavica* 56 (3): 161–165. https://doi.org/10.1080/000163598422901.

24 Stoor, P., Söderling, E., and Grénman, R. (1999). Interactions between the bioactive glass S53P4 and the atrophic rhinitis-associated mircroorganism *Klebsiella ozaenae*. *Journal of Biomedical Materials Research* 48 (6): 8690–8874. https://doi.org/10.1002/(SICI)1097-4636(1999)48:6<869::AID-JBM16>3.0.CO;2-6.

25 Munukka, E., Leppäranta, O., Korkeamäki, M. et al. (2008). Bactericidal effects of bioactive glasses on clinically important bacteria. *Journal of Materials Science – Materials in Medicine* 19: 27–32. https://doi.org/10.1007/s10856-007-3143-1.

26 Leppäranta, O., Vaahtio, M., Peltola, T. et al. (2008). Antibacterial effect of bioactive glasses on clinically important anaerobic bacteria in vitro. *Journal of Materials Science – Materials in Medicine* 19: 547–551. https://doi.org/10.1007/s10856-007-3018-5.

27 Zhang, D., Leppäranta, O., Munukka, E. et al. (2009). Antibacterial effects and dissolution behavior of six bioactive glasses. *Journal of Biomedical Materials Research Part A* 93A (2): 475–483. https://doi.org/10.1002/jbm.a.32564.

28 Ran, S., He, Z., and Liang, J. (2013). Survival of *Enterococcus faecalis* during alkaline stress: changes in morphology, ultrastructure, physiochemical properties of the cell wall and specific gene transcripts. *Archives of Oral Biology* 58 (11): 1667–1676. https://doi.org/10.1016/j.archoralbio.2013.08.013.

29 Drago, L., De Vecchi, E., Bortolin, M. et al. (2015). Antimicrobial activity and resistance selection of different bioglass S53P4 formulations against multidrug resistant strains. *Future Microbiology* 10 (8): 1293–1299. https://doi.org/10.2217/FMB.15.57.

30 Bortolin, M., De Vecchi, M., Romanò, C.L. et al. (2016). Antibiofilm agents against MDR bacterial strains: is bioactive glass BAG-S53P4 also effective? *Journal of Antimicrobial Chemotherapy* 71: 123–127. https://doi.org/10.1093/jac/dkv327.

31 Drago, L., Vassena, C., Fenu, S. et al. (2014). In vitro antibiofilm activity of bioactive glass S53P4. *Future Microbiology* 95 (5): 593–601. https://doi.org/10.2217/fmb.

32 Peltola, M., Suonpää, J., Aitasalo, K. et al. (1998). Obliteration of the frontal sinus cavity with bioactive glass. *Head & Neck* 20 (4): 315–319. https://doi.org/10.1002/(sici)1097-0347(199807)20:4<315::aid-hed6>3.0.co;2-1.

33 Sarin, J., Grénman, R., Aitasalo, K., and Pulkkinen, J. (2012). Bioactive glass S53P4 in mastoid obliteration surgery for chronic otitis media and cerebrospinal fluid leakage. *Annals of Otology, Rhinology and Laryngology* 121 (9): 536–569. https://doi.org/10.1177/000348941212100901.

34 Aitasalo, K.M.J. and Peltola, M.J. (2007). Bioactive glass hydroxyapatite in fronto-orbital defect reconstruction. *Plastic and Reconstructive Surgery* 120 (7): 1963–1972. https://doi.org/10.1097/01.prs.0000287319.34425.27.

35 Stoor, P., Söderling, E., and Grénman, R. (2001). Bioactive glass S53P4 in repair of septal perforations and its interactions with the respiratory infection-associated microorganisms *Heamophilus influenzae* and *Streptococcus pneumoniae*. *Journal of Biomedical Materials Research* 58 (1): 113–120. https://doi.org/10.1002/1097-4636(2001)58:1<113::aid-jbm170>3.0.co;2-v.

36 Stoor, P. and Grénman, R. (2004). Bioactive glass and turbinate flaps in the repair of nasal septal perforations. *Annals of Otology, Rhinology and Laryngology* 113 (8): 655–661. https://doi.org/10.1177/000348940411300811.

37 Suominen, E.A. and Kinnunen, J. (1996). Bioactive glass granule and plates in the reconstruction of defects of the facial bones. *Scandinavian Journal of Plastic and Reconstructive Surgery and Hand Surgery* 30 (4): 281–289. https://doi.org/10.3109/02844319609056406.

38 Lindfors, N.C., Heikkilä, J.T., Koski, I. et al. (2008). Bioactive glass and autogenous bone as bone graft substitutes in benign bone tumors. *Journal of Biomedical Materials Research Part B Applied Biomaterials* 90B: 131–136. https://doi.org/10.1002/jbm.b.31263.

39 Lindfors, N.C., Koski, I., Heikkilä, J.T. et al. (2010). A prospective randomized 14-year follow-up study of bioactive glass and autogenous bone as bone graft substitutes in benign bone tumors. *Journal of Biomedical Materials Research Part B Applied Biomaterials* 94B (1): 157–164. https://doi.org/10.1002/jbm.b.31636.

40 Lindfors, N.C. (2009). Treatment of a recurrent aneurysmal bone cyst with bioactive glass in a child allows for good bone remodelling and growth. *Bone* 45: 398–400. https://doi.org/10.1016/j.bone.2009.04.195.

41 Lindfors, N.C. (2011). Clinical experience of bioactive glass S53P4 in reconstructive surgery of the upper extremity showing bone remodelling, vascularization, cartilage repair and antibacterial properties of S53P4. *Journal of Biotechnology and Biomaterials* 1 (5): 111. https://doi.org/10.4172/2155-952X.1000111.

42 Syvänen, J., Nietosvaara, Y., Korhonen, I. et al. (2018). Treatment of aneurysmal bone cysts with bioactive glass in children. *Scandinavian Journal of Surgery* 107 (1): 76–81. https://doi.org/10.1177/1457496917731185.

43 Pernaa, K., Koski, I., Mattila, K. et al. (2011). Bioactive glass S53P4 and autograft bone in treatment of depressed tibial plateau. *Journal of Long-Term Effects of Medical Implants* 21 (2): 139–148. https://doi.org/10.1615/jlongtermeffmedimplants.v21.i2.40.

44 Frantzén, J., Rantakokko, J., Aro, H.T. et al. (2011). Instrumented spondylodesis in degenerative spondylolisthesis with bioactive glass and autologous bone: a prospective 11-year follow-up. *Journal of Spinal Disorders & Techniques* 24 (7): 455–461. https://doi.org/10.1097/BSD.0b013e31822a20c6.

45 Rantakokko, J., Frantzén, J., Heinänen, J. et al. (2012). Posterolateral spondylodesis using bioactive glass S53P4 and autogenous bone in instrumented unstable lumbar spine burst fractures. A prospective 10-year follow-up study. *Scandinavian Journal of Surgery* 101 (1): 66–71. https://doi.org/10.1177/145749691210100113.

46 Lindfors, N.C., Hyvönen, P., Nyyssönen, M. et al. (2010). Bioactive glass S53P4 as bone graft substitute in treatment of osteomyelitis. *Bone* 47 (2): 212–218. https://doi.org/10.1016/j.bone.2010.05.030.

47 Drago, L., Romanò, D., De Vecchi, E., et al. (2013). Bioactive glass BAG-S53P4 for the adjunctive treatment of chronic osteomyelitis of the long bones: an in vitro and prospective clinical study. *BMC Infectious Diseases* 13:584, https://doi.org/10.1186/1471-2334-13-584.

48 Romanò, C.L., Logoluso, N., Meani, E. et al. (2014). A comparative study of the use of bioactive glass S53P4 and antibiotic-loaded calcium-based bone substitutes in the treatment of chronic osteomyelitis – a retrospective comparative study. *The Bone & Joint Journal* 96B (6): https://doi.org/10.1302/0301-620X.96B6.33014.

49 Ferrando, A., Part, J., and Baeza, J. (2017). Treatment of cavitary bone defects in chronic osteomyelitis: bioactive glass S53P4 vs. calcium sulphate antibiotic beads. *The Journal of Bone and Joint Infection* 2 (4): 194–201. https://doi.org/10.7150/jbji.20404.

50 Geurts, J., Vranken, T., and Arts, C.J.J. (2016). Treatment of osteomyelitis by means of bioactive glass – initial experience in the Netherlands. *Nederlands Tijdschrift voor Orthopaedie* 23 (2): 37–41.

51 Geurts, J., van Vugt, T., Thijssen, E., and Arts, J.J. (2019). Cost-effectiveness study of one-stage treatment of chronic osteomyelitis with bioactive glass S53P4. *Materials* 12: 3209. https://doi.org/10.3390/ma12193209.

52 Lindfors, N.C., Geurts, J., Drago, L. et al. (2017). Antibacterial bioactive glass, S53P4, for chronic bone infections – a multinational study. *Advances in Experimental Medicine and Biology* 971: 81–92. https://doi.org/10.1007/5584_2016_156.

53 Al Malat, T.A., Glombitza, M., Dahmen, J., and Hax, P.-M. (2018). The use of bioactive glass S53P4 as bone graft substitute in the treatment of chronic osteomyelitis and infected non-unions – a retrospective study of 50 patients. *Zeitschrift für Orthopädie und Unfallchirurgie* 156 (2): 152–159. https://doi.org/10.1055/s-0043-124377.

54 Lupescu, O., Nagea, M., and Antoniac, V.J. (2017). Bioactive glasses in treating bone infections. *Key Engineering Materials* 758: 245–249. https://doi.org/10.4028/www.scientific.net/KEM.758.245.

55 McAndrew, J., Efrimescu, C., Sheehan, E., and Niall, D. (2013). Through the looking glass; bioactive glass S53P4 (BonAlive®) in the treatment of chronic osteomyelitis. *Irish Journal of Medical Science* 182: 509–511. https://doi.org/10.1007/s11845-012-0895-5.

56 Oosthuysen, W., Venter, R., Tanwar, Y., and Ferreira, N. (2020). Bioactive glass as dead space management following debridement of type 3 chronic osteomyelitis. *International Orthopaedics* 44: 421–428. https://doi.org/10.1007/s00264-019-04442-7.

57 De Giglio, R., Di Vieste, G., Mondello, T. et al. (2020). Efficacy and safety of bioactive glass S53P4 as a treatment for diabetic foot osteomyelitis. *The Journal of Foot and Ankle Surgery* 60 (2): 292–296. https://doi.org/10.1053/j.jfas.2020.06.029.

58 Godoy-Santos, A.L., Rosemberg, L.A., de Cesar-Netto, C., and Armstrong, D.G. (2019). The use of bioactive glass S53P4 in the treatment of an infected Charcot foot: a case report. *Journal of Wound Care* 28 (1): S14–S17. https://doi.org/10.12968/jowc.2019.28.Sup1.S14.

59 Iacopi, E., Pieruzzi, L., Goretti, C., and Piaggesi, A. (2020). Pilot experience on the use of S53P4 bioactive glass in the surgical management of diabetic foot osteomyelitis. *The International Journal of Lower Extremity Wounds* https://doi.org/10.1177/1534734620926003.

60 Gaiarsa, G., Dos Reis, P., Kodi, K.E. et al. (2019). A retrospective case-series on the use of S53P4 bioactive glass for the adjunctive treatment of septic diaphyseal non-union. *Acta Ortopédica Brasileira* 27 (5): 273–275. https://doi.org/10.1590/1413-785220192705220540.

61 Pagliarello, C., Testa, G., Lombardini, A.A. et al. (2016, 2017). Two-stage treatment for infected nonunion of the humerus: a case report. *Infectious Diseases & Tropical Medicine* 3 (2): e390.

62 Testa, G., Vescio, A., Aloj, D.C. et al. (2020). Treatment of infected tibial nonunions with Ilizarov technique: a case series. *Journal of Clinical Medicine* 9 (5): 1352. https://doi.org/10.3390/jcm9051352.

63 Tanner, M.C., Heller, R., Westhauser, F. et al. (2018). Evaluation of the clinical effectiveness of bioactive glass (S53P4) in the treatment of non-unions of the tibia and femur: study protocol of a randomized controlled noninferiority trial. *Trials* 19: 299. https://doi.org/10.1186/s13063-018-2681-9.

64 Kankare, J. and Lindfors, N.C. (2016). Reconstruction of vertebral bone defects using an expandable replacement device and bioactive glass S53P4 in the treatment of vertebral osteomyelitis: three patients and three pathogens. *Scandinavian Journal of Surgery* 105 (4): 248–253. https://doi.org/10.1177/1457496915626834.

65 Aurégan, J.C. and Bégué, T. (2015). Bioactive glass for long bone infection: a systematic review. *Injury* 46 (S8): S3–S7. https://doi.org/10.1016/S0020-1383(15)30048-6.

66 Bigoni, M., Turati, M., Zanchi, N. et al. (2019). Clinical applications of bioactive glass S53P4 in bone infections: a systematic review. *European Review for Medical and Pharmacological Sciences* 23 (2 Suppl): 240–251. https://doi.org/10.26355/eurrev_201904_17498.

67 Tanwar, Y. and Ferreira, N. (2020). The role of bioactive glass in the management of chronic osteomyelitis: a systematic review of literature and current evidence. *Infectious Diseases* 52 (4): 219–226. https://doi.org/10.1080/23744235.2019.1695059.

68 Peltola, M.J., Vallittu, P.K., Vuorinen, V. et al. (2012). Novel composite implant in craniofacial bone reconstruction. *European Archives of Oto-Rhino-Laryngology* 269 (2): 623–628. https://doi.org/10.1007/s00405-011-1607-x.

69 Aitasalo, K.M.J., Piitulainen, J.M., Rekola, J., and Vallittu, P.K. (2014). Craniofacial bone reconstruction with bioactive fiber-reinforced composite implant. *Head & Neck* 36: 722–728. https://doi.org/10.1002/hed.23370.

70 Piitulainen, J.M., Posti, J.P., Aitasalo, K.M.J. et al. (2015). Paediatric cranial defect reconstruction using bioactive fibre-reinforced composite implant: early outcomes. *Acta Neurochirurgica* 157: 681–687. https://doi.org/10.1007/s00701-015-2363-2.

71 Posti, J.P., Piitulainen, J.M., Hupa, L. et al. (2015). A glass fibre-reinforced composite – bioactive glass cranioplasty implant: a case study of an early development stage implant moved due to a late infection. *Journal of the Mechanical Behavior of Biomedical Materials* 55: 191–200. https://doi.org/10.1016/j.jmbbm.2015.10.030.

72 Moritz, N. and Vallittu, P.K. (2017). Bioactive silicate glass in implantable medical devices: from research to clinical applications. In: *Bioactive Glasses, Fundamentals, Technology and Applications* (ed. A.R. Boccaccini, D.S. Brauer and L. Hupa), 442–470. Cambridge: The Royal Society of Chemistry https://doi.org/10.1039/9781782622017-00442.

73 Vallittu, P.K., Närhi, T.O., and Hupa, L. (2015). Fiber glass – bioactive glass composite for bone replacing and bone anchoring implants. *Dental Materials* 31 (4): 371–381. https://doi.org/10.1016/j.dental.2015.01.003.

74 Skulle Implants (2021). https://skulleimplants.com/ (accessed 25 February 2021).

75 Hupa, L. and Karlsson, K.H. (2017). Tailoring of bioactive glasses. In: *Bioactive Glasses, Fundamentals, Technology and Applications* (ed. A.R. Boccaccini, D.S. Brauer and L. Hupa), 136–160. Cambridge: The Royal Society of Chemistry https://doi.org/10.1039/9781782622017-00136.

76 Hoppe, A., Güldal, N.S., and Boccaccini, A.R. (2011). A review of the biological response to ionic dissolution products from bioactive glasses and glass-ceramics. *Biomaterials* 32 (11): 2757–2774. https://doi.org/10.1016/j.biomaterials.2011.01.004.

77 Massera, J., Fagerlund, S., and Hupa, L. (2012). Crystallization mechanisms of the bioactive glasses 45S5 and S53P4. *Journal of the American Ceramic Society* 95 (2): 607–613. https://doi.org/10.1111/j.1551-2916.2011.05012.x.

78 Brink, M. (1997). The influence of alkali and alkaline earths on the working range for bioactive glasses. *Journal of Biomedical Materials Research* 36 (1): 109–117. https://doi.org/10.1002/(SICI)1097-4636(199707)36:1<109::AID-JBM13>3.0.CO;2-D.

79 Brink, M., Turunen, T., Happonen, R.-P., and Yli-Urpo, A. (1997). Compositional dependence of bioactivity of glasses in the system Na_2O–K_2O–MgO–CaO–B_2O_3–P_2O_5–SiO_2. *Journal of Biomedical Materials Research* 37 (1): 114–121. https://doi.org/10.1002/(sici)1097-4636(199710)37:1<114::aid-jbm14>3.0.co;2-g.

80 Massera, J., Hupa, L., and Hupa, M. (2012). Influence of partial substitution of CaO with MgO on the thermal properties and in vitro reactivity of the bioactive glass S53P4. *Journal of Non-Crystalline Solids* 358 (18–19): 2701–2707. https://doi.org/10.1016/j.jnoncrysol.2012.06.032.

81 Massera, J. and Hupa, L. (2014). Influence of SrO substitution for CaO on the properties of bioactive glass S53P4. *Journal of Materials Science – Materials in Medicine* 25 (3): 657–668. https://doi.org/10.1007/s10856-013-5120-1.

82 Hupa, L., Fagerlund, S., Massera, J., and Björkvik, L. (2016). Dissolution behaviour of the bioactive glass S53P4 when sodium is replaced by potassium, and calcium with magnesium or strontium. *Journal of Non-Crystalline Solids* 432: 41–46. https://doi.org/10.1016/j.jnoncrysol.2015.03.026.

83 Fagerlund, S., Hupa, M., and Hupa, L. (2010). Comparison of reactions of bioactive glasses in different aqueous solutions. *Ceramic Transactions* 218: 101–113, Advances in Bioceramics and Biotechnologies (eds. Roger Narayan, Joanna McKittrick, Mrityunjay Singh), Wiley.

84 Varila, L., Fagerlund, S., Lehtonen, T. et al. (2012). Surface reactions of bioactive glasses in buffered solutions. *Journal of the European Ceramic Society* 32: 2757–2763. https://doi.org/10.1016/jeurceramsoc.2012.01.025.

85 Detsch, R., Stoor, P., Grünewald, A. et al. (2014). Increase in VEGF secretion from human fibroblast cells by bioactive glass S53P4 to stimulate angiogenesis in bone. *Journal of Biomedical Materials Research Part A* 102A (11): 4055–4061. https://doi.org/10.1002/jbm.a.35069.

86 Ojansivu, M., Wang, X., Hyväri, L. et al. (2018). Bioactive glass induced osteogenic differentiation of human adipose stem cells is dependent on cell attachment mechanisms and mitogen-activated protein kinases. *European Cells & Materials* 35: 53–71. https://doi.org/10.22203/eCM.v035a05.

87 Ojansivu, M., Vanhatupa, S., Björkvik, L. et al. (2015). Bioactive glass ions as strong enhancers of osteogenic differentiation in human adipose stem cells. *Acta Biomaterialia* 21: 190–203. https://doi.org/10.1016/j.actbio.2015.04.017.

88 Björkenheim, R., Jämsen, E., Eriksson, E. et al. (2021). Sintered S53P4 bioactive glass scaffolds have anti-inflammatory properties and stimulate osteogenesis in vitro. *European Cells & Materials* 41: 15–30. https://doi.org/10.22203/eCM.v041a02.

89 Wilson, T., Parikka, V., Holmbom, J. et al. (2006). Intact surface of bioactive glass S53P4 is resistant to osteoclastic activity. *Journal of Biomedical Materials Research Part A* 77A (1): 67–74. https://doi.org/10.1002/jbm.a.30600.

90 Van Gestel, N.A.P., Schuiringa, G.H., Hennissen, J.H.P.H. et al. (2019). Resorption of the calcium phosphate layer on S53P4 bioactive glass by osteoclasts. *Journal of Materials Science – Materials in Medicine* 30 (8): 1–13. https://doi.org/10.1007/s10856-019-6295-x.

91 Björkvik, L., Wang, X., and Hupa, L. (2016). Dissolution of bioactive glasses in acidic solutions with the focus on lactic acid. *International Journal of Applied Glass Science* 7 (2): 154–163. https://doi.org/10.1111/ijag.12198.

92 Fagerlund, S., Massera, J., Moritz, N. et al. (2012). Phase composition and in vitro bioactivity of porous implants made of bioactive glass S53P4. *Acta Biomaterialia* 8 (6): 2331–2339. https://doi.org/10.1016/j.actbio.2012.03.011.

93 Björkenheim, R., Strömberg, G., Pajarinen, J. et al. (2017). Polymer-coated bioactive glass S53P4 increases VEGF and TNF expression in an induced membrane model in vivo. *Journal of Materials Science* 52 (15): 9055–9065. https://doi.org/10.1007/s10853-017-0839-6.

94 Masquelet, A.C., Fitoussi, F., Beque, T., and Muller, G.P. (2000). Reconstruction of the long bones by the induced membrane and spongy autograft (article in French). *Annales de Chirurgie Plastique Esthétique* 45 (3): 346–353.

95 Björkenheim, R., Strömberg, G., Ainola, M. et al. (2019). Bone morphogenic protein expression and bone formation are induced by bioactive glass S53P4 scaffolds in vivo. *Journal of Biomedical Materials Research Part B Applied Biomaterials* 107 (3): 847–857. https://doi.org/10.1002/jbm.b.34181.

96 Eriksson, E.K.E., Björkenheim, R., Strömberg, G. et al. (2021). S53P4 bioactive glass scaffolds induce BMP expressions and integrative bone formation in a critical-sized diaphysis defect treated with a single-staged induced membrane technique. *Acta Biomaterialia* 126: 463–476. https://doi.org/10.1016/j.actbio.2021.03.035.

97 Jones, J.R., Brauer, D., Hupa, L., and Greenspan, D.C. (2016). Bioglass and bioactive glasses and their impact on healthcare. *International Journal of Applied Glass Science* 7 (4): 423–434. https://doi.org/10.1111/ijag.12252.

98 Saarenpää, I., Hirvonen, J., Rinne, J., and Frantzén, J. (2018). Novel bioactive glass putty (S53P4) as bone graft expander in minimally invasive lumbosacral interbody fusion. *Journal of Minimally Invasive Spine Surgery and Technique* 3 (2): 52–58. https://doi.org/10.21182/jmisst.2018.00332.

99 Sinitsyna, P., Karlström, O., and Hupa, L. (2022). In vitro dissolution of bioactive glass S53P4 microspheres. *Journal of the American Ceramic Society* 105 (3): 1658–1670. https://doi.org/10.1111/jace.18014.

100 Stoor, P., Apajalahti, S., and Kontio, R. (2017). Regeneration of cystic bone cavities and bone defects with bioactive glass S53P4 in the upper and lower jaws. *Journal of Craniofacial Surgery* https://doi.org/10.1097/SCS.0000000000003649.

101 Remangeon, R., Lahlou, G., Alciato, L. et al. (2020). Management of tegmen defects with mastoid and epitympanic obliteration using S53P4 bioactive glass. *Laryngoscope Investigative Otolaryngology* 1–8. https://doi.org/10.1002/lio2.374.

102 Skoulakis, C., Koltsidopoulous, P., Iyer, A., and Kontorinis, G. (2019). Mastoid obliteration with synthetic materials: a review of the literature. *The Journal of International Advanced Otology* 15 (3): 400–404. https://doi.org/10.5152/iao.2019.7038.

4

Melt-Derived Bioactive Glasses: Beyond Silicate Glasses

Jonathan Massera

Faculty of Medicine and Health Technology, Tampere University, Tampere, Finland

4.1 Introduction

Glass is a highly versatile material which is commonly known for its technological or decorative use. Common application of glass are windows, tableware, labware, or photonics, just to cite a few. The main advantage of melt-derived glass lies in the ability to control the oxide composition to tailor the physical and chemical properties of the obtained material. In general, such unique aptitude to incorporate ions in the glass structure, was mainly directed to confer the material additional properties such as, but not limited, color (Au, Ag, Fe, Mn, etc.) [1], resistance to hydrolysis (Al, B, etc.) [2], or photonic properties (rare earth ions) [3, 4]. While the main body of work is focused on silica-based glasses, technological needs have driven glass scientists to develop new glass compositions based on phosphate or borate. Phosphate glasses have attracted interests based on their ability to accommodate larger amount of metallic or rare-earth ions [5–7] and their generally lower processing temperatures [8]. Therefore, the main applications for phosphate glasses have been glass-to-metal seal, containments of radioactive wastes or laser host materials [9]. Another class of glass that has attracted significant interest are the borate glasses. While their high affinity for water and subsequent low chemical resistance has limited their technological applications, their low processing temperature (melting and softening) when compared to traditional silicate glasses, has led to their use as sealant and passivation of electronics components [10].

It is only since 1969, with the work by Prof. Larry Hench that glass found applications in the medical field [11]. Since the discovery of the first silicate bioactive glass, these materials have found significant space in clinics: from dental (toothpaste) to bone fillers. Silicate bioactive glasses have the ability to not only promote osteoprogenitor cells adhesion and proliferation but also to favor the differentiation of stem cells into an osteoblast's lineage. As such bioactive glass was categorized as class A bioactive material, i.e. a biomaterial with an index of bioactivity >8, where the index of bioactivity is calculated as $I_b = \frac{100}{t_{0.5}}$ with $t_{0.5}$ the time necessary for 50% of the implant surface to be covered with the new formed bone [12, 13]. Such bioactive materials are expected to not only bond to bone but also to soft tissue. Furthermore, class A biomaterials are at best osteoinductive (promote the formation of bone in place where no osteoprogenitor cells are present) but at least osteostimulative (favor the differentiation of stem cells and stimulate neobone formation) [13].

However, glasses have intrinsic properties that have limited their use in clinics. For example, the brittle nature of glasses prevents their use in load-bearing applications [14]. Furthermore, the typical surface-driven corrosion process driving the dissolution of bioceramics limit their use, in

Bioactive Glasses and Glass-Ceramics: Fundamentals and Applications, First Edition.
Edited by Francesco Baino and Saeid Kargozar.

the bulk form, in applications where bioresorption is a prerequisite. Finally, in bone regeneration it is well accepted that the optimum shape for the medical device would be a porous scaffold. Among other properties, the scaffold should be biocompatible, osteoconductive (ultimately osteoinductive), have mechanical properties at least similar to the cancellous bone and tailored porosity (overall porosity, pore size, and interconnection) to enable cell and nutrient migration within the construct and favor a 3D reconstruction of the tissue [15]. The challenge in processing such porous construct, is that, alike all ceramics, sintering should be used to fuse the particles together into the foreseen construct [16–18]. Keeping in mind that glass is a metastable material, hot-working processes can lead to uncontrolled crystallization [19, 20]. Uncontrolled crystallization not only reduces the material bioactivity but also prevents a key aspect of biomedical devices that is to be reproducible [19, 21].

To overcome the limitations of bioactive glasses, while maintaining their unique properties in bone regeneration, they have been combined with natural and synthetic polymers, into composites or hybrids. When considering natural polymer, collagen is the material of choice. Collagen is a protein that constitutes the extracellular matrix [22]. Also, Collagen I is, in the body, combined with the hydroxycarbonated apatite (HCA) to create a biocomposite, highly organized at the nano and macroscopic length [23]. Apart from the osteoconductive/osteoinductive properties of bioactive glasses, research has demonstrated that, adding the glass as a secondary phase in collagen also, decrease the degradation rate, that is often considered too fast for clinical applications, as well as their mechanical properties [24]. Combination of bioactive glasses to collagen produces a biomimetic material with high potential in replacing autografts, often associated with donor-site morbidity. Recently, following the hybrid strategy developed by Jones and coauthors [25, 26], using sol–gel bioactive glasses, hybrid biomaterials based on gelatin/bioactive glass, crossed link with 3-glycidoxypropyltrimethoxysilane (GPTMS) were developed [27]. The large variety of synthetic polymer/bioactive glass and their production method have been reviewed extensively [28]. As, previously, the aim of combining a synthetic polymer with a osteopromotive materials lies in using the advantages of both materials while reducing/suppressing their disadvantages. The main advantage of the polymer is its ability to be shaped easily along with its biodegradability. Polymers can also be used as a reservoir for growth factor or drugs. The bioactive glass will enable to promote bone regeneration while reducing the excessively slow degradation rate of polymers such as polycaprolactone PCL, poly(glycolic acid) (PGA), or polylactic acid (PLA). The challenge in producing the composites lies in maintaining the integrity of the polymer structure postprocessing. For instance, it was reported that the coextrusion of PLA, bioactive glass 45S5 led to significant degradation of the polymer [29]. Later on, it was shown that the high versatility of glasses allowed to developed glasses that interacted less with the polymer during processing [30]. The bioactive glass, despite being embedded into the polymer matrix, maintain its ability to release ions, that will confer the composite bioactivity (in this case assessed by the precipitation of an hydroxyapatite (HA) layer at the polymer surface) and osteostimulation [29, 30].

The properties of the bioactive glasses are connected to their structure. Their structure will dictate their dissolution rate, their ability to release therapeutic ions in a control manner as well as their interaction with tissues.

4.2 Silicate Bioactive Glasses

Silica and silicate glasses are the most widely known glasses and also the most widely used commercially. Their properties can be tailored by controlling the amount of oxides in the structure.

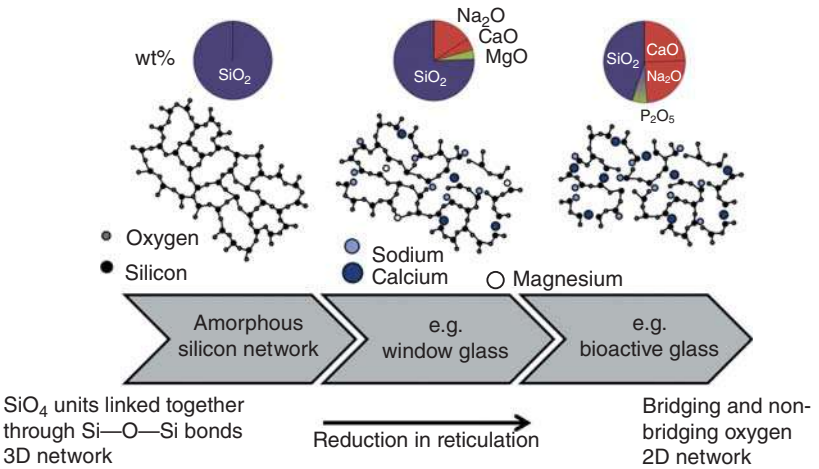

Figure 4.1 Structure/composition of silica and silicate glasses.

As shown in Figure 4.1, amorphous silica is made of highly connected Si–O–Si forming a 3D network. Such glasses are generally used in optics and telecommunication. The high Si—O—Si bond strength confer to the glass an extremely high resistance to hydrolysis, thereby the glass does not degrade when immersed in aqueous solution. One major challenge with amorphous SiO_2 lies in the high melting temperature and fast cooling rate necessary to process the glass. To decrease, the melting temperature, one can add, to the glass composition, alkaline and alkaline earth ions, such as, but not limited to, Na, Ca, K, Mg. The addition of such ions, listed as modifiers in textbook leads to the creation of nonbridging oxygens (NBO), which in turns reduces their thermal processing as well as their stability in aqueous solutions [31]. The NBOs (negatively charged) are charge balanced by the positively charge cations. In applications, where the thermal processing should be decreased while maintaining a high hydrolytic resistance, elements such Zn, Al, or B, can be incorporated into the structure. Those elements that are considered as either glass formers or intermediates will lead to a denser structure and to the decrease in the number of NBOs, while maintaining a thermal processing window lower than for the pure SiO_2 glass [31]. It is only in 1969 that L.L. Hench had the brilliant idea to decrease even further the SiO_2 content and increased the content of the alkaline and alkaline earth, in order to design a glass, soluble in aqueous solution, able to release substantial amount of Ca ions. As it was well known that the inorganic part of the bone was hydroxyapatite (mainly Ca and P), L.L. Hench also incorporated low concentration of P, in order to favor the supersaturation of the solutions with Ca and P to induce the precipitation of an hydroxyapatite, similar to the natural phase of the bone. The first bioactive glass developed was 45S5 with composition in (wt%) $45SiO_2$–$24.5CaO$–$24.5Na_2O$–$6P_2O_5$.

The mechanism of dissolution and reaction in aqueous solution (in static and dynamic) has been widely discussed, reported, and modeled [32–36]. In short, the first event is the ionic exchange between Na^+ from the glass and H^+ from the solution. This step is diffusion-controlled and as such exhibit a dependence with $\sqrt{t}$. Later, the soluble silica from the structure is released in the solution in the form of $Si(OH)_4$. This results in the breaking of Si—O—Si bonds which in turn leads to the formation of silanol (SiOH) groups. This reaction is surface-driven and therefore shows a dependence with t. The unsoluble silica, left in the glass network, forms a SiO_2-rich layer through a condensation and repolymerization process. This layer is depleted in alkaline and alkaline earth ions. Finally, the solution becomes supersaturated with calcium and phosphorus. Given the high

affinity between those two elements, in solution, a CaP reactive layer (initially amorphous) will form onto the SiO_2-rich surface, where silanols act as nucleation points. Later the reactive layer will crystallize and incorporate CO_3^{2-} and OH^- to form a crystalline HCA. Figure 4.2 presents a scanning electron microscopy (SEM) image of a bioactive glass particle, postimmersion in simulated body fluid, showing the remnant glass, the SiO_2-rich layer and the HCA at the surface.

Later on, researchers strived to understand the relationship between the glass composition and its ability to promote the precipitation of hydroxyapatite. The SiO_2 structure is widely discussed based on the Q_n annotation (Figure 4.3).

In such annotation, the "*n*" stands for the number of Si bridged to two O. Based on these structures one can calculate and anticipate the network connectivity of relatively simple glass system.

The first bioactive glass developed contained not only SiO_2, Na_2O, CaO but also P_2O_5. However, research showed that the phosphate did not form Si—O—P bonds, but rather remained as orthophosphate in the network. While this holds true for the traditional 45S5, it is also the case of the glass S53P4 (another bioactive glass commonly used clinically).

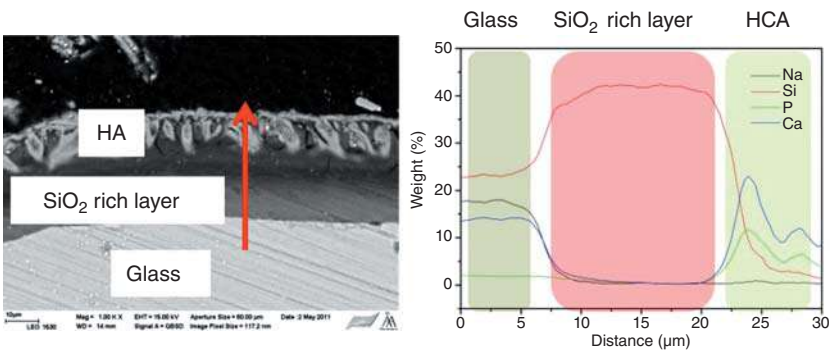

Figure 4.2 SEM image of a bioactive glass immersed for 72 hours in simulated body fluid (a) and the composition analysis across the red line (b). EDX analysis clearly exhibit the remnant glass, the SiO_2-rich layer, and the HCA layer.

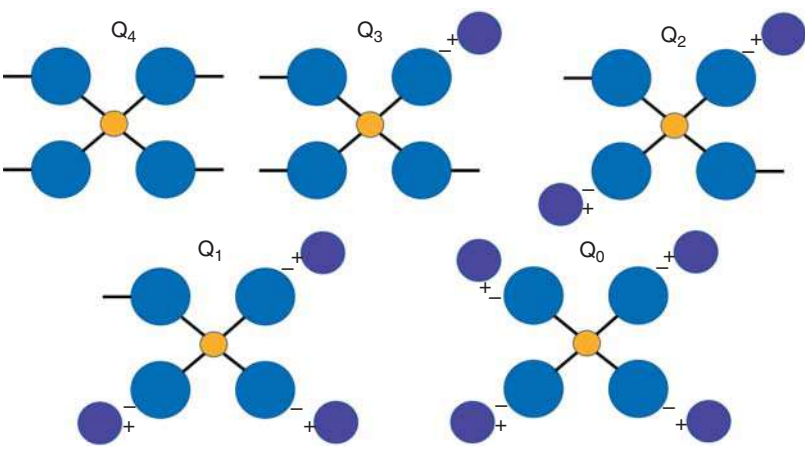

Figure 4.3 Q_n structure in silica and silicate (yellow sphere = silicon; blue sphere = oxygen, purple sphere = cations).

Using the following equation [37], Hill and Brauer demonstrated that the bioactivity (assumed to be the speed of precipitation of HA) is directly correlated to the network connectivity:

$$NC = \frac{4[SiO_2] - 2\left[M^{I}_{2}O + M^{II}O\right] + 6[P_2O_5]}{[SiO_2]} \tag{4.1}$$

where NC is the calculated network connectivity and $M^{I}_{2}O$ and $M^{II}O$ are the mono- and divalent modifier oxide in the glass. All concentrations are expressed in mol%.

Indeed, the authors demonstrated that for connectivity higher than 2.4 the glasses lost their ability to precipitate HA and therefore where not deemed to be employed in places where bioactivity is of paramount importance.

4.2.1 Silicate Glass for Bone Tissue Engineering

The majority of the research, aiming at demonstrating the osteoconductivity and osteoinductivity of bioactive glasses have been performed on the Food and Drug Administration (FDA)-approved 45S5 and S53P4. For instance, *in vitro*, Xynos et al. studied the impact of bioglass® 45S5 on the behavior of osteoblasts isolated from human trabecular bone of femoral heads [38]. The 45S5-induced osteoblasts during the DNA synthesis (S) and mitosis (G2/M) phase. It was also revealed that the glass augmented osteoblasts commitment as well as mature osteoblastic phenotype. Other glasses, such as BonAlive S53P4, have also been found to favor the differentiation of stem cells (adipose stem cells or bone marrow stromal cells) toward osteoblast lineages [39, 40].

Since the discovery of the first bioactive glass and the development of new compositions, approved by the FDA (in the USA) or European Medicines Agency (EMA) (in EU), these materials have found substantial space in clinics. The first reported clinical application aimed at the reconstruction of the ossicular chain of the middle ear [41]. Since bioactive glasses have been used in clinics as bone graft (for the reconstruction of bone critical defects) [42], in toothpaste (to battle hypersensitivity) [43] or even as ocular implant [11]. Finally, bioactive glasses have been used as coatings on metal implant in order to favor the tissue/implant interactions.

However, despite the tremendous clinical results in those applications, bioactive glasses still suffer from limitations. Indeed, it is well accepted, that in view of designing an optimum bone scaffold, the graft should be highly porous, while demonstrating mechanical properties at least in line with cancellous bone. As mentioned earlier, the difficulty in designing bioactive glass grafts lies in their 2D metastable structure that often leads to crystallization over the course of the sintering process. Peitl et al. have shown that during crystallization upon crystallization the bioactivity of bioglass 45S5 decreases drastically [21]. Furthermore, it is generally accepted that the crystallization of the traditional, FDA-approved silicate bioactive glass is surface initiated [19]. It was also demonstrated that the kinetics of crystallization is too fast and the hot working domain to narrow to allow for proper sintering without any adverse crystallization [19].

To overcome such limitations, researchers have studied the impact of glass structure on the thermal properties. However, most studies revolve toward adding ions to the glass composition. As mentioned earlier, the benefit of bioactive glass is its ability to include any ions into its structure. Therefore, B (in small amount), Mg, Al, Zn among other ions have been introduced in the glass network in view of improving their thermal resistance to crystallization [16, 44–46].

In addition to benefit the thermal properties of the glass, adding such ions can have therapeutic interest. Indeed, Mg is known to promote new bone formation [47] and favor bone cell adhesion [47, 48]. Zn demonstrates anti-inflammatory effect and activate protein synthesis in osteoblast [49]. Zn also helps in regulating the transcription of osteoblastic differentiation genes [50]. However,

while Al is an efficient element to stabilize the glass network and prevent crystallization, it is not often used in medical graft as it is known to be toxic to the skeleton, thus leading to fractures accompanying a painful osteomalacia and renal failure [51]. Al is also considered a potent inhibitor of calcium phosphate precipitation [52]. Aside from those elements, Sr, Cu, Ag, Ti, among others have been found to be of therapeutic interest. Strontium is routinely used for treatment of osteoporosis in the form of strontium ranelate [53]. Sr is also known to enter the HCA layer to form a Sr-substituted HCA layer as shown in Figure 4.4 [54]. This layer is denser than the traditional HCA and therefore provides higher mechanical properties to the neo-bone. Cu and Ag have been

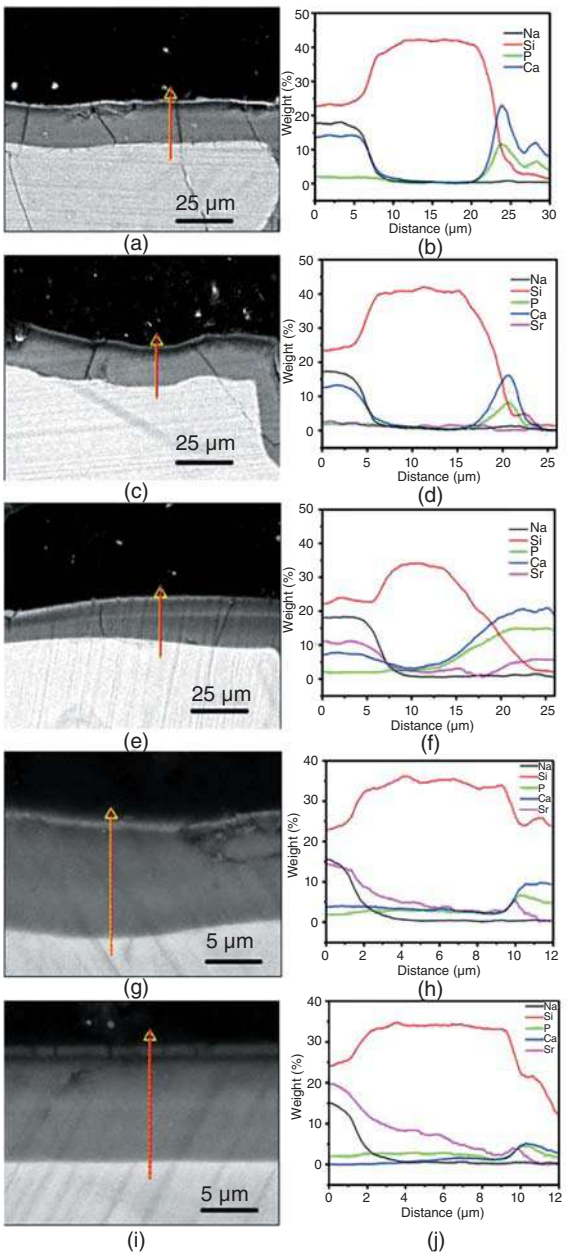

Figure 4.4 SEM images and line scans across the reaction layer formed at the surface of S53P4 (a, b), Sr5 (c, d), Sr10 (e, f), Sr15 (g, h), and Sr21.77 (i, j) after immersion in simulated body fluid (SBF) for 72 hours. Source: Massera and Hupa [54], Figure 09, p. 09/with permission of Springer Nature.

both used to confer to the glass-enhanced antimicrobial properties [55, 56]. Cu has also been found to promote angiogenesis [57] and to induce differentiation of mesenchymal stem cells toward an osteogenic lineage [58]. Titanium, as an ion, has been associated with stimulation of the expression of alkaline phosphatase (ALP), osteopontin (OPN), and osteonectin [59], therefore, demonstrating the Ti role as promoter of the differentiation. Laio et al. also tested the impact of Ti concentration from 0.1 to 5.0 ppm and reported, within such range, an increased osteoblasts proliferation [60]. Mine et al. also tested the impact of Ti ions concentration (1–20 ppm) on osteoblastic MC3T3-E1, osteoclastic RAW264.7, and epithelial cells-like GE-1. For concentrations between 1 and 9 ppm no statistically significant effect was reported on either cell lines. However, a significant drop in cell viability was reported at a concentration of 20 ppm [61].

While silicate bioactive glasses have had a tremendous impact in clinics some drawbacks remain to be overcome: For instance, while it is possible to increase the resistance to crystallization and process scaffolds with structural and mechanical properties encouraging for application in bone reconstruction, generally the dissolution rate is drastically reduced [44]. Furthermore, the typical noncongruent dissolution of silicate bioactive glasses (i) does not allow for a control release of therapeutic ions and (ii), as reported by N.C. Lindfors et al. [62], even 14 years postsurgery remnants of the bioactive glass can still be detected at the surgical site. While the latter did not alter the bone remodeling functions nor its mechanical functions, this still lead to question if there is a need for materials that would degrade more completely into the body.

4.3 Phosphate Bioactive Glasses

When dealing with biomaterials for bone regeneration, the most used bioceramics in clinics remain, to date, synthetic hydroxyapatite and tri-calcium phosphate. Both materials are based on calcium phosphate and their use is directly correlated to their chemical similarity with the natural bone. It was, therefore, somehow logical that glass scientist started to develop calcium-phosphate glasses for use in the biomedical field.

4.3.1 Structure/Dissolution

As for the silicate, the phosphate structure is typically discussed based on the Q_n structure as shown in Figure 4.5.

The phosphate structure can be made from solely Q_3 units (pure P_2O_5), from a polymer-like structure composed of metaphosphate (Q_2) chains, or even from pyro- and ortho-phosphate (Q_1 and Q_0, respectively) called invert glass. A thorough review of the structure of simple phosphate glasses has been published by Richard K. Brow [9]. The network connectivity of the phosphate network can be calculated in a similar manner than for silicate, using the following equation:

$$NC = \frac{3[P_2O_5] - [M_2O] - [M'O]}{[P_2O_5]} \tag{4.2}$$

where $[P_2O_5]$, $[M_2O]$, and $[M'O]$ are the molar concentration in phosphate, the mono- and divalent modifier oxide. Alike in silicate glasses the addition of modifiers breaks the P—O—P bonds and create NBO charged balanced by the cations. However, as opposed to silica and silicate glasses, the pure P_2O_5 glass is highly hygroscopic and degrade readily in any aqueous solution. This can be assigned to the double bond that forms, between the phosphorus and oxygen ions which prevent the formation of a stiff 3D network. Also, as opposed to the silicate counterpart, adding alkaline or

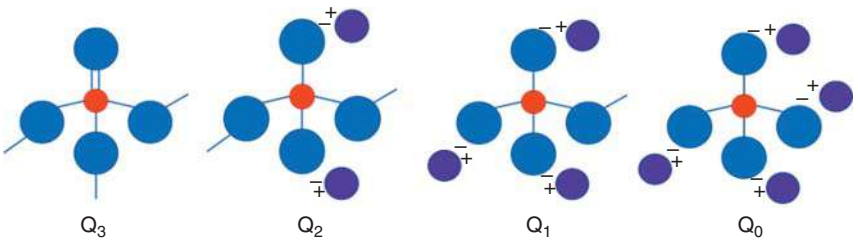

Figure 4.5 Q_n structure in phosphate glasses (red sphere = silicon; blue sphere = oxygen, purple sphere = cations).

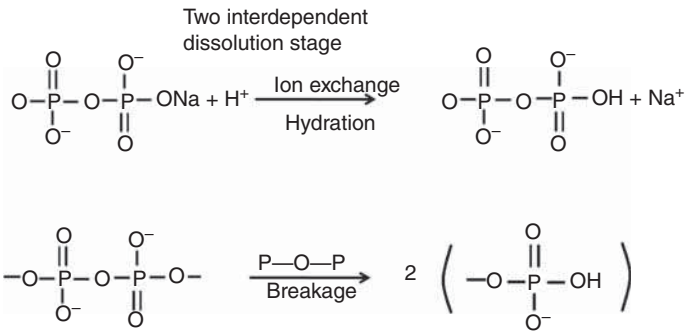

Figure 4.6 Dissolution mechanism of phosphate glasses.

alkaline earth ions stabilize the structure, instead of decreasing its stability. Finally, as opposed to the incongruent dissolution of silicate glasses, phosphates are, generally, dissolving in a congruent manner, i.e. the composition of the parent glass is maintained throughout the dissolution process (Figure 4.6).

As proposed Bunker et al. [63], phosphate dissolves due to acid- or base-catalyzed hydration of the polymeric phosphate chains. It was then further demonstrated that the dissolution of the phosphate network involves both the hydration of the phosphate chains and hydrolysis of the P—O—P bonds.

The phosphate glasses dissolution mechanism resembles more closely the dissolution of polymer chain thereby the longer chains are primarily dissolved. Figure 4.7 showing the infrared spectra of

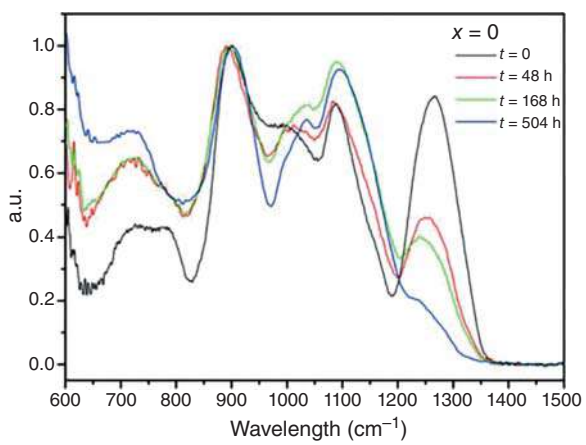

Figure 4.7 Fourier-transform infrared (FTIR) spectra of metaphosphate glass ($50P_2O_5-40CaO-10Na_2O$) at various immersion times in simulated body fluid [64].

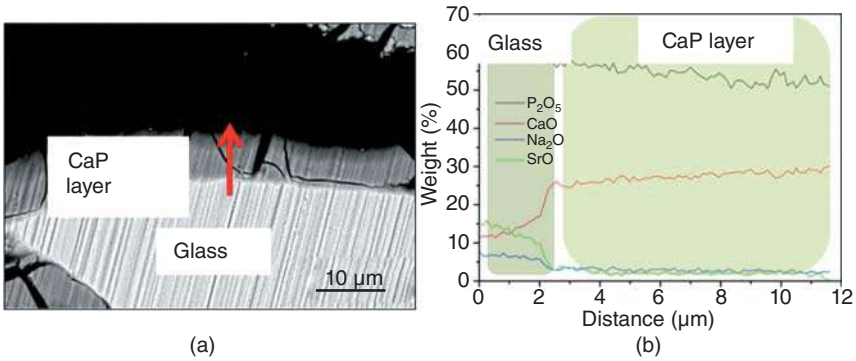

Figure 4.8 SEM images of metaphosphate glass immersed for two weeks in SBF (a) and the corresponding EDX line scan analysis (b).

a metaphosphate glass immersed for up to two weeks in simulated body fluid clearly shows that (i) initially the glass is mainly formed of Q_2 and Q_1 units, (ii) upon dissolution the Q_2 units are predominantly dissolved, and (iii) new vibrations related to the precipitation of a reactive layer appears [64].

As compared with silicate bioactive glasses, the dissolution mechanism does not lead to the formation of phosphate-rich layer. Therefore, the reactive layer deposit directly at the surface of the parent glass as shown in the SEM image and energy-dispersive X-ray (EDX) analysis presented in Figure 4.8.

It is important to note that in this particular case the Ca/P ratio released in the solution was thermodynamically favoring the precipitation of a dicalcium dihydrate phosphate layer rather than a HA layer [64].

4.3.2 Phosphate Glass for Bone Tissue Engineering

Significant work was conducted to assess the impact of the glass degradation rate on the survival of cells of interests for bone applications. In 1998, Uo et al. and Salih et al. study the impact of CaO on content in phosphate glasses on human pulp cells and osteosarcoma MG63 cells [65, 66]. In both case, it was revealed that the faster the degradation, the lower the cell survival, most likely due to excessive phosphate release and acidic interfacial pH. Later, Massera et al. study the impact of SrO substitution for CaO ($50P_2O_5$–$(40-x)$CaO–xSrO–$10Na_2O$ with $0<x<40$) in human gingival fibroblasts survival [67]. It was found that the substitution led to a mix-alkali effect when considering the dissolution rate, with the faster dissolution rate for SrO-free glass and the slowest dissolution rate for the glass containing 20 mol% of CaO and 20 mol% of SrO. While all glasses demonstrated poor cell adhesion at their surface for the first three days, due to the congruent dissolution which inhibits cells from attaching to the glass surface, once a firm reactive layer was formed, cells grew exponentially at the surface of all SrO-containing glasses. Only the SrO-free glass was found to lead to cell death. Based on such results, researcher mainly focused their attention on invert-phosphate glasses that exhibit slower dissolution rate than metaphosphate glasses and enhanced cell attachment and proliferation.

The advantage of phosphate glasses in bone regeneration, lies in the congruent dissolution, that enables control release of ions of therapeutic interest. Taken as an example Se-, Cu-, and Co-doped COSECURE glass boluses were tested on animal to overcome acute as well as marginal

deficiencies [68]. The main conclusion was in regard to Se-doped boluses. It was found that this material can efficiently prevent selenium deficiency for over a year and give protection to the fetus as well as the young lamb in its early life [68].

Following this breakthrough, studies, like for silicate was directed in understanding the positive outcome of releasing, in a control manner, ions of therapeutic interest. In the literature, it appears that doping the phosphate glasses with Ag or Cu, in view of conferring the bioactive glass superior antimicrobial properties, is predominant. Ag- and Cu-doped phosphate glasses were found to demonstrate superior antimicrobial activity than silicate bioactive glasses. Loading glasses with as little as 3 mol% of Ag led to eradication of a large variety of bacteria, such as *Staphylococcus aureus, Escherichia coli,* and *Candida albicans* [69] or *Staphylococcus epidermidis* [70]. Another doping element that is attracting great interest is fluorine. While fluorine has been heavily studied in silicate bioactive glasses, in view of promoting the precipitation of fluorapatite, it became apparent that addition of fluorine in the silicate network was not straightforward. Indeed, significant decrease in bioactivity were reported [71]. Interestingly, addition of fluorine in phosphate glasses was found to form P—O—F bonds, leading to enhanced bioactivity. Furthermore, the addition of F in phosphate glasses was also found to promote bulk crystallization, opening the path to new bioactive glass-ceramics [72]. However, the most abundant body of work lies in developing thermally processed structure such as fibers [73–75] and scaffolds [17, 76], given their superior resistance to crystallization when compared to silicate bioactive glasses.

4.4 Phosphate Glass Fibers

Lapa et al. provided a thorough review of the phosphate glass fiber processing and their high potential in hard, but also, soft tissue engineering [73]. The main body of works lies in utilizing the phosphate fibers in combination with a bioresorbable to obtain bone fixation devices possessing mechanical properties similar to the natural bone [77–79]. Those fiber-reinforced composites have been found to be promising in substitution of metal fixation implants known to cause stress-shielding.

While the congruent dissolution and ability to draw fibers with high mechanical properties and high mechanical properties retention during *in vitro* dissolution has led to significant amount of work being done for orthopedics application, a field that has emerged is the use of such fibers for biosensing.

For instance, single core [80], core-clad [81], or structured fibers [82] have been drawn out of bioresorbable phosphate glasses to be used as biosensors. The most up-to-date work relies in combining the unique optical properties, thermal properties, and bioresorbable properties of phosphate glasses to design new biosensors. Initially, researches have demonstrated that the ability of the fiber to guide efficiently light was directly link to the various events occurring at the fiber/liquid interface, as shown in Figure 4.9 [80]. Initially (Stage I), no change in the light guidance efficiency was recorded. This is due to the congruent dissolution of the glass that does not interfere with the light propagation. In a second time (Stage II), the sporadic precipitation of a CaP layer can be seen. The light will interact with the CaP layer at the fiber interface, leading to scattering. In Stage III, the loss in light transmission becomes more drastic due to the surface of the fiber being fully covered by the CaP layer, while the diameter of the fiber decrease drastically. Finally, in Stage IV, the loss in light propagation decreases. This is assumed to be due to the thick reactive layer forming, acting as a dissolution barrier to the glass.

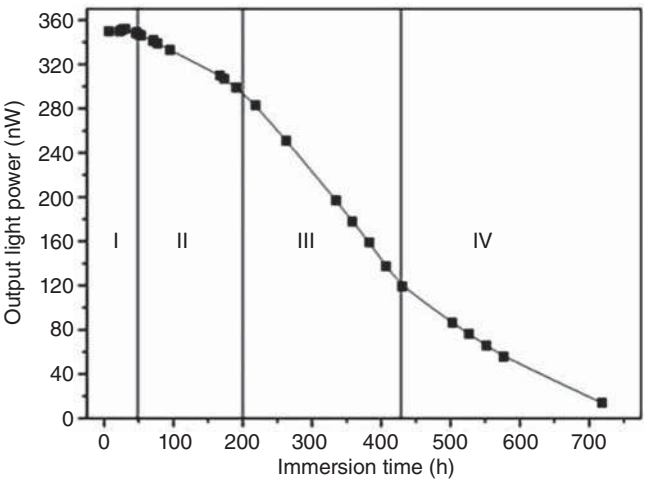

Figure 4.9 Output light power through the phosphate bioactive glass (PBG) fiber as a function of immersion time in SBF [80].

This works demonstrated that the dissolution of bioresorbable fibers could be tracked optically. This study also shows the potential of bioresorbable fibers to be used as biosensors for a significant amount of time. It is commonly accepted that to efficiently guide light, core-clad fibers are more efficient [81]. Therefore, later, it was shown that one could develop fully bioresorbable core-clad fibers, demonstrating total internal reflectance. A sensing region was revealed by etching the cladding using H_3PO_4. This study demonstrated that not only resorbable core-clad fibers could be developed, but also their mechanical properties (postetching of the clad to reveal the sensing region) remain high enough to support their use as *in vivo* biosensors. Finally, using an extrusion process a group at Politecnico di Torino developed microstructured bioresorbable phosphate glass optical fibers [83]. Such an approach opens the path to manufacturing complex bioresorbable glass fibers for optical, gas, and fluidic sensors and therapies

4.5 Borate, Borosilicate, and Borophosphate Bioactive Glasses

The use of boron in place of silicate or phosphate has been widely study in the past. Typically, the rational for adding boron was to improve the thermal properties of silicate [16, 84] or control the *in vitro* dissolution of phosphate glasses/fibers [85]. It is only recently that borate and borosilicate glasses truly find space as biomaterials.

4.5.1 Structure/Dissolution

The structure of borate glasses is significantly more complex than silicate and phosphate. Pure B_2O_3 is usually composed of a majority of boroxol rings and trigonal BO_3 [86]. However, unlike for silicate and phosphate where the change in structure is monotone with addition of modifiers, the borate structure changes differently depending on the MO and M_2O content. Initially, the addition of cations will result in neutral trigonal BO_3 forming negatively charged BO_4^- units, thus leading to an initial increase in the network coordination. The BO_4 units can arrange into borate rings or even diborate [86]. When increasing further the concentration in cations in the borate structure,

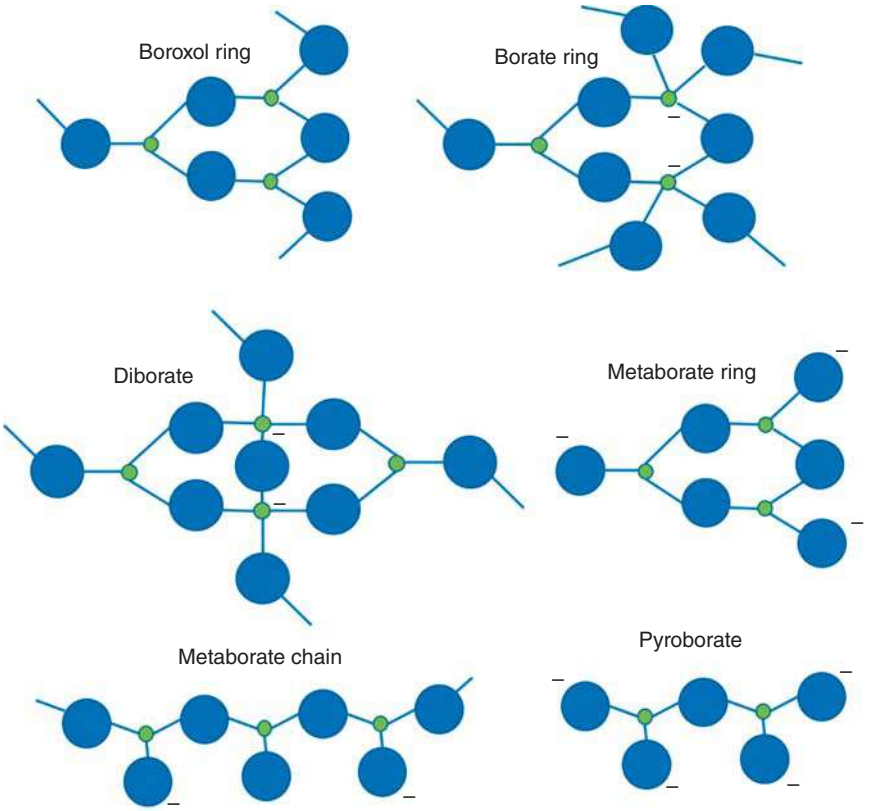

Figure 4.10 Borate structure (green sphere = boron; blue sphere = oxygen).

the borate tetrahedra convert back to trigonal units, thus decreasing the network connectivity. In such a case, pyro-borate and orthoborate can form. However, the formation of either structure is dependent on the cation introduced into the glass network. Figure 4.10 presents the various borate structure.

It is interesting to note that the binary B_2O_3–LiO_2 glass dissolution in water and buffer solution, as opposed to silicate glasses, exhibit a decrease in the dissolution rate with an increase in pH. This is consistent with Zapol's calculation, i.e. protonated attack of the borate units has a lower activation energy than neutral or deprotonated attack [87]. This is most likely due to the inability of the borate network to form a hydrated layer, unlike silicate bioactive glasses.

Figure 4.11 shows S53P4 ($53.8SiO_2$–$21.8CaO$–$22.7Na_2O$–$1.7P_2O_5$ [in mol%]) after 168 hours of immersion in simulated body fluid and B53P4 ($53.8B_2O_3$–$21.8CaO$–$22.7Na_2O$–$1.7P_2O_5$ [in mol%]) after 48 hours of immersion in simulated body fluid. One can see that the borate glass dissolved drastically faster than its silicate counterpart.

Borate bioactive glasses started to find space in the clinics with the development of Mirragen™. Mirragen is a borate bioactive glass nanofibers looking like cotton-candy. The agglomeration of the nanofibers forms the scaffolds, similarly than natural fibrin scaffolds. Mirragen is now FDA-approved, following a clinical trial that shined light on the benefit of using borate nanofibers, to treat diabetic ulcer patient at high risk of amputation [88].

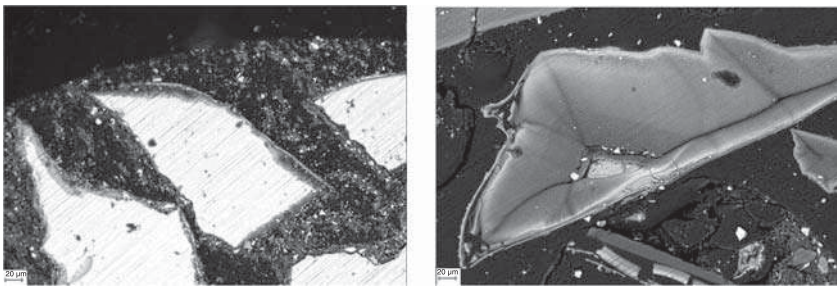

(a) (b)

Figure 4.11 SEM images of S53P4 (a) and B53P4 (b) particles, immersed for 168 and 48 hours, respectively.

4.5.2 Borate Glass for Tissue Engineering

With the development of new borate glasses, increasing interest has arised in the development of borosilicate glasses. Huang et al. studied the kinetics of hydroxyapatite formation on 45S5 and its borate/borosilicate analogs [89]. They demonstrated that increasing the boron substitution for SiO_2 led to an increase in the rate of conversion of the glass to HA. Such a study was later confirmed with repeating the study with S53P4 and borosilicate analogs [90]. When studying the osteogenic commitment of human adipose stem cells in direct contact with glasses and with the extract from the borosilicate glasses, it was found that the borosilicate glasses outperformed the FDA-approved S53P4. However, some questions arise as regard to some inhibitory effect of the borosilicate glasses on the cell proliferation. Such results are in favor of a more dynamic testing of the cell viability *in vitro*. Modglin et al. studied the cytotoxicity of 13-93 (silicate) and its borosilicate and borate analogs in a dynamic cell culture [91]. While in a static condition cytotoxicity was reported, a dynamic *in vitro* cell culture showed promising results toward cytocompatibility of MLO-A5 osteogenic cells. Aside from the ability of the bioactive glass to promote osteogenesis. A significant impact on angiogenic factors was reported [90]. Indeed, Ojansivu et al. reported that the S53P4- borosilicate analogs upregulated von Willebrand factor (vWF) and PECAM-1, two endothelial markers, thus making the borosilicate glass attractive from an angiogenic point of view.

4.6 Conclusion

Bioactive glass is a unique class of bioceramics able to favor osteogenesis. It is a highly versatile material as one can tailor not only the dissolution rate but also the release of therapeutic ions to the need of the patient. Such materials are one step further in the development of patient-centric tissue graft.

While the "traditional" silicate bioactive glasses have demonstrated unique ability to regenerate hard tissue and have found a significant space in clinics, limitations intrinsic to their network structure has limited their use. These limitations have been partly overcome by developing new bioactive glass amenable to be drawn into fibers or sintered into porous scaffolds. Furthermore, the development of phosphate and borate fiber, along with the borosilicate and borophosphate, has extended significantly the range of application where bioactive glass can be of interest. Indeed, new clinical material have been developed for control ion release or even for wood healing. Furthermore, the newly developed materials open the path to the development of new composites, thereby the unique biological properties of the glasses can be exploited. In recent

years, much work has focused on reinforcing polymer matrices with bioactive glass particles or fibers, made from silicate, phosphate, or borate glasses. It was shown that not only the bioactive glass can reduce the biodegradation time of relatively stable polymers but also the control release of ions also confers the composites with bioactivity and osteogenic properties [29, 30].

References

1 Möncke, D., Papageorgiou, M., Winterstein-Beckmann, A., and Zacharias, N. (2014). *Journal of Archaeological Science* 46: 23–36.
2 Kramer, D., Schaut, R., Bakowska, E., et al. (2018). Extractables testing of aluminosilicate and borosilicate glass containers. *2018 PDA Annual Meeting*, Taipei Taiwan (08–09 November). https://www.pda.org/pda-letter-portal/home/full-article/extractables-testing-of-aluminosilicate-and-borosilicate-glass-containers.
3 Righini, G.C., Armellini, C., Berneschi, S. et al. (2007). *Journal of Non-Crystalline Solids* 353: 753–756.
4 Auzel, F. and Goldner, P. (2001). *Optical Materials* 16: 93–103.
5 Mogus-Milankovic, A., Santic, A., Reis, S.T., and Day, D.E. (2009). *IOP Conference Series: Materials Science and Engineering* 2: 012004.
6 Galleani, G., Santagneli, S.H., Messaddeq, Y. et al. (2017). *Physical Chemistry Chemical Physics* 19: 21612–21624.
7 Lopez-Iscoa, P., Ojha, N., Aryal, U. et al. (2019). *Materials* 12: 129.
8 Kim, C.W. and Day, D.E. (2003). *Journal of Non-Crystalline Solids* 331: 20–31.
9 Brow, R.K. (2000). *Journal of Non-Crystalline Solids* 263 & 264: 1.
10 Bengisu, M. (2016). *Journal of Materials Science* 51: 2199–2242.
11 Greenspan, D.C. (2016). *International Journal of Applied Glass Science* 7: 134–138.
12 Strnad, Z. and Sestak, J. Bio-compatible ceramics as mimetic material for bone tissue substitution. In: *Proceedings of the Second International Conference on Intelligent Processing and Manufacturing of Materials (PMM '99)*, Honolulu, HI, USA (10–15 July 1999), vol. 1, 431–436. IEEE https://ieeexplore.ieee.org/document/792518.
13 Hench, L.L. (1994). Bioceramics: theory and clinical applications. In: *Proceedings of the 7th International Symposium on Ceramics in Medicine*, Turku, vol. 7 (ed. O.H. Andersson and A. Yli-Urpo), 3. Elsevier https://www.sciencedirect.com/science/article/pii/B9780080421445500054.
14 Fu, Q., Saiz, E., Rahaman, M.N., and Tomsia, A.P. (2011). *Materials Science and Engineering C* 31: 1245–1256.
15 Gerhardt, L.-C. and Boccaccini, A.R. (2010). *Materials* 3: 3867–3910.
16 Fabert, M., Ojha, N., Erasmus, E. et al. (2017). *Journal of Materials Chemistry B* 5: 4514–4525.
17 Erasmus, E.P., Johnson, O.T., Sigalas, I., and Massera, J. (2017). *Scientific Reports* 7: 6046.
18 Blaeß, C., Müller, R., Poologasundarampillai, G., and Brauer, D.S. (2019). *International Journal of Applied Glass Science* 10: 449–462.
19 Massera, J., Fagerlund, S., Hupa, L., and Hupa, M. (2012). *Journal of the American Ceramic Society* 95: 607–613.
20 Fagerlund, S., Massera, J., Hupa, M., and Hupa, L. (2012). *Journal of the European Ceramic Society* 32: 2731–2738.
21 Peitl Filho, O., LaTorre, G.P., and Hench, L.L. (1996). *Journal of Biomedical Materials Research* 30: 509–514.
22 Sergi, R., Bellucci, D., and Cannillo, V. (2020). *Materials* 6: 5560.

23 Weiner, S. and Wagner, H.D. (1998). *Annual Review of Materials Science* 28: 271–298.
24 Sarker, B., Hum, J., Nazhat, S.N., and Boccaccini, A.R. (2015). *Advanced Healthcare Materials* 4: 176–194.
25 Mahony, O., Tsigkou, O., Ionescu, C. et al. (2010). *Advanced Functional Materials* 20: 3835–3845.
26 Jones, J.R. (2013). *Acta Biomaterialia* 9: 4457–4486.
27 Houaoui, A., Szczodra, A., Lallukka, M. et al. (2021). *Biomolecules* 11: –444.
28 Redenti, S., Neeley, W.L., Rompani, S. et al. (2012). *Progress in Biomaterials* 1: 2.
29 Vergnol, G., Ginsac, N., Rivory, P. et al. (2016). *Journal of Biomedical Materials Research Part B* 104: 180–191.
30 Houaoui, A., Lyyra, I., Agniel, R. et al. (2020). *Materials Science and Engineering C* 107: 110340.
31 Shelby, J.E. (2005). *Introduction to Glass Science and Technology*. RSC.
32 Greenspan, D.C. (1999). *Tandläkartidningen Årg* 91 (8).
33 Välimäki, V.-V. and Aro, H.T. (2006). *Scandinavian Journal of Surgery* 95: 95–102.
34 Fagerlund, S., Ek, P., Hupa, L., and Hupa, M. (2012). *Journal of the American Ceramic Society* 95: 3130–3137.
35 Tilocca, A. (2009). *Proceedings of the Royal Society of London Series A* 465: 1003–1027.
36 Sanz-Herrera, J.A. and Boccaccini, A.R. (2011). *International Journal of Solids and Structures* 48: 257–268.
37 Hill, R.G. and Brauer, D.S. (2011). *Journal of Non-Crystalline Solids* 357: 3884–3887.
38 Xynos, I.D., Hukkanen, M.V.J., Batten, J.J. et al. (2000). *Calcified Tissue International* 67: 321–329.
39 Dieudonné, S.C., van den Dolder, J., de Ruijter, J.E. et al. (2002). *Biomaterials* 23: 3041–3051.
40 Waselau, M., Patrikoski, M., Mannerström, B. et al. (2012). *Journal of Stem Cell Research & Therapy* 2: 1000125.
41 Greenspan, D.C. (1999). Developments in biocompatible glass compositions. *Medical Device and Diagnostics Industry* (An MD&DI March 1999 Column), p. 150.
42 Towler, M.R., Crowley, C.M., Murphy, D., and O'Callaghan, A. (2002). *Journal of Materials Science Letters* 21: 1123.
43 Tai, B.J., Bian, Z., Jiang, H. et al. (2006). *Journal of Clinical Periodontology* 33: 86–91.
44 Brink, M., Turunen, T., Happonen, R.-P., and Yli-Urpo, A. (1997). *Journal of Biomedical Materials Research* 37: 114.
45 Massera, J., Hupa, L., and Hupa, M. (2012). *Journal of Non-Crystalline Solids* 358: 2701–2707.
46 Tainio, J.M., Avila Salazar, D.A., Nommeots-Nomm, A. et al. (2020). *Journal of Non-Crystalline Solids* 533: 119893.
47 Zreiqat, H., Howlett, C.R., Zannettino, A. et al. (2002). *Journal of Biomedical Materials Research* 62: 175–184.
48 Yamasaki, Y., Yoshida, Y., Okazaki, M. et al. (2002). *Journal of Biomedical Materials Research* 62: 99–105.
49 Yamaguchi, M. (1998). *Journal of Trace Elements in Experimental Medicine* 11: 119–135.
50 Kwun, I.-S., Cho, Y.-E., Lomeda, R.-A.R. et al. (2010). *Bone* 46: 732–741.
51 Klein, G.L. (2019). *Osteoporosis and Sarcopenia* 5: 2–5.
52 Talwar, H.S., Reddi, A.H., Menczel, J. et al. (1986). *Kidney International* 29: 1038–1042.
53 Cianferotti, L., D'Asta, F., and Brandi, M.L. (2013). *Therapeutic Advances in Musculoskeletal Disease* 5: 127–139.
54 Massera, J. and Hupa, L. (2014). *Journal of Materials Science – Materials in Medicine* 25: 657–668.

55 Bellantone, M., Williams, H.D., and Hench, L.L. (2002). *Antimicrobial Agents and Chemotherapy* 46: 1940–1945.

56 Rivadeneira, J. and Gorustovich, A. (2017). *Journal of Applied Microbiology* 122: 1424–1437.

57 Finney, L., Vogt, S., Fukai, T., and Glesne, D. (2009). *Clinical and Experimental Pharmacology and Physiology* 36: 88–94.

58 Rodríguez, J.P., Ríos, S., and González, M. (2002). *Journal of Cellular Biochemistry* 85: 92–100.

59 Sun, Z.L., Wataha, J.C., and Hanks, C.T. (1997). *Journal of Biomedical Materials Research* 34: 29–37.

60 Liao, H.H., Wurtz, T., and Li, J.G. (1999). *Journal of Biomedical Materials Research* 47: 220–227.

61 Mine, Y., Makihira, S., Nikawa, H. et al. (2010). *Journal of Prosthodontic Research* 54: 1–6.

62 Lindfors, N.C., Koski, I., Heikkilä, J.T. et al. (2010). *Journal of Biomedical Materials Research Part B Applied Biomaterials* 94: 157–164.

63 Bunker, B.C., Arnold, G.W., and Wilder, J.A. (1984). *Journal of Non-Crystalline Solids* 64: 291–316.

64 Massera, J., Petit, L., Cardinal, T. et al. (2013). *Journal of Materials Science – Materials in Medicine* 24: 1407–1416.

65 Uo, M., Mizuno, M., Kuboki, Y. et al. (1998). *Biomaterials* 19: 2277–2284.

66 Salih, V., Patel, A., Knowles, J.C., and Olsen, I. (2001). *Biomaterials* 22: 2817–2824.

67 Massera, J., Kokkari, A., Nähri, T., and Hupa, L. (2015). *Journal of Materials Science – Materials in Medicine* 26: 196.

68 Zervas, G., Telfer, S.B., Carlos, G., and Anderson, P. (1988). *Animal Feed Science and Technology* 21: 23–39.

69 Ahmed, I., Ready, D., Wilson, M., and Knowles, J.C. (2006). *Journal of Biomedical Materials Research Part A* 79: 618–626.

70 Mishra, A., Petit, L., Pihl, M. et al. (2017). *Journal of Materials Science* 52: 8957–8972.

71 Brauer, D.S., Karpukhina, N., Law, R.V., and Hill, R.G. (2009). *Journal of Materials Chemistry* 19: 5629–5636.

72 Nommeots-Nomm, A., Houaoui, A., Pradeepan Packiyanathar, A. et al. (2020). *Materials Science and Engineering C* 117: 111269.

73 Lapa, A., Cresswell, M., Jackson, P., and Boccaccini, A.R. (2020). *Advances in Applied Ceramics* 119: 1–14.

74 Muñoz-Senovilla, L., Muñoz, F., Tricot, G. et al. (2017). *Journal of Materials Science* 52: 9166–9178.

75 Colquhoun, R. and Tanner, K.E. (2016). *Biomedical Materials* 11: 014105.

76 Bose, S., Bhattacharjee, A., Banerjee, D. et al. (2021). *Additive Manufacturing* 40: 101895.

77 Ahmed, I., Cronin, P.S., Abou Neel, E.A. et al. (2009). *Journal of Biomedical Materials Research Part B Applied Biomaterials* 89: 18–27.

78 Felfel, R.M., Ahmed, I., Parsons, A.J. et al. (2013). *Materials Science and Engineering C* 33: 1914–1924.

79 Brauer, D.S., Rüssel, C., Vogt, S. et al. (2008). *Journal of Materials Science – Materials in Medicine* 19: 121.

80 Massera, J., Ahmed, I., Petit, L. et al. (2014). *Materials Science and Engineering C* 37: 251–257.

81 Mishra, A., Désévédavy, F., Petit, L. et al. (2019). *Materials Science and Engineering C* 96: 458–465.

82 Pugliese, D., Gallichi-Nottiani, D., Boetti, N.G. et al. (2020). Bioresorbable phosphate glass microstructured optical fiber for simultaneous light and drug delivery (Conference Presentation). In: *Proceedings Micro-Structured and Specialty Optical Fibres VI*, vol. 11355, 113550J. International Society for Optics and Photonics.

83 Gallichi-Nottiani, D., Pugliese, D., Boetti, N.G. et al. (2020). *International Journal of Applied Glass Science* 11: 632–640.

84 Massera, J., Claireaux, C., Lehtonen, T. et al. (2011). *Journal of Non-Crystalline Solids* 357: 3623–3630.

85 Mishra, A., Noppari, P., Boussard-Plédel, C. et al. (2020). *International Journal of Applied Glass Science* 11: 622–631.

86 Youngman, R.E. and Zwanziger, J.W. (1996). *Journal of Physical Chemistry* 100: 16720–16728.

87 Zapol, P., He, H., Kwon, K.D., and Criscenti, L.J. (2013). *International Journal of Applied Glass Science* 4: 395–407.

88 Krista Grayson (2017). https://mo-sci.com/borate-bioactive-glass-wound-healing/ (accessed 25 May 2021).

89 Huang, W., Day, D.E., Kittiratanapiboon, K., and Rahaman, M.N. (2006). *Journal of Materials Science – Materials in Medicine* 17: 583–596.

90 Ojansivu, M., Mishra, A., Vanhatupa, S. et al. (2018). *PLoS One* 13: e0202740.

91 Modglin, V.C., Brown, R.F., Jung, S.B., and Day, D.E. (2013). *Journal of Materials Science – Materials in Medicine* 24: 1191–1199.

5

Borate Bioactive Glass

Seiji Yamaguchi

Department of Biomedical Sciences, College of Life and Health Sciences, Chubu University, Kasugai, Aichi, Japan

5.1 Introduction

Certain compositions other than silica-based bioactive glasses, such as borate-based bioactive glasses, including borate bioactive glasses and borosilicate glasses, also exhibit a bioactive response. Borate bioactive glasses usually degrade faster than silica-based bioactive glasses because they have a threefold coordinate [BO_3] site that forms trihedrals or chains in the glass network, and thus it is easier to match the degradation rate of the borate bioactive glasses with that of the target tissue. On the other hand, there are some concerns regarding the cytotoxity of borate bioactive glasses as they tend to release large amounts of borate ions.

In this chapter, the biological reaction of boron and the capacity of the borate bioactive glass for both hard and soft tissue regeneration are described.

5.2 Composition and Fabrication Process

Various types of borate bioactive glasses such as 45S5B1 and 13-93B1 have been developed by a partial or full replacement of SiO_2 in silica-based glasses like 45S5 and 13-93 with B_2O_3 [1–4]. The typical compositions of the borate bioactive glasses are listed in Table 5.1 [1–4]. In most cases, melt-derived borate bioactive glasses particles are prepared and then cast into various shapes, including trabecular [5], oriented pore, and fibrous [6], while the grid-like structure is prepared by a robocasting technique [7], as shown in Figure 5.1. Borate bioactive glasses' fine fibers several micrometers in diameter are fabricated by a melt-blow process in which the molten glass is blown by a high-speed, high-temperature airflow onto a net screen for collection. The degradation rate and mechanical strength mainly depend upon the glass composition and the microstructure [9–12]. It was shown by Fu et al. [12] that the compressive strength of trabecular glass scaffolds of approximately 80% porosity and 100–500 μm pore size decreased along with an increasing B_2O_3 content of the glass, from 11 MPa for silicate 13-93 glass to 5 MPa for borate 13-93B3, which values are in the range of human trabecular bone (2–12 MPa) [13].

They also showed that the weight loss of the same trabecular glass scaffolds in a simulated body fluid (SBF) that has ion concentrations nearly equal to those of human blood plasma [14] increased markedly with B_2O_3 content of the glass, and its limiting value was 8% for 13-93 and 67% for 13-93B3 (Figure 5.2a).

Bioactive Glasses and Glass-Ceramics: Fundamentals and Applications, First Edition.
Edited by Francesco Baino and Saeid Kargozar.

Table 5.1 Nominal composition of borate bioactive glasses.

	Composition (mol%)						
Sample	**Na_2O**	**K_2O**	**MgO**	**CaO**	**SiO_2**	**B_2O_3**	**P_2O_5**
45S5B1	24.4	0	0	26.9	30.7	15.4	2.6
45S5B2	24.4	0	0	26.9	15.4	30.7	2.6
45S5B3	24.4	0	0	26.9	0	46.1	2.6
13-93B1	6.0	7.9	7.7	22.1	36.4	18.2	1.7
13-93B2	6.0	7.9	7.7	22.1	18.2	36.4	1.7
13-93B3	6.0	7.9	7.7	22.1	0	54.6	1.7

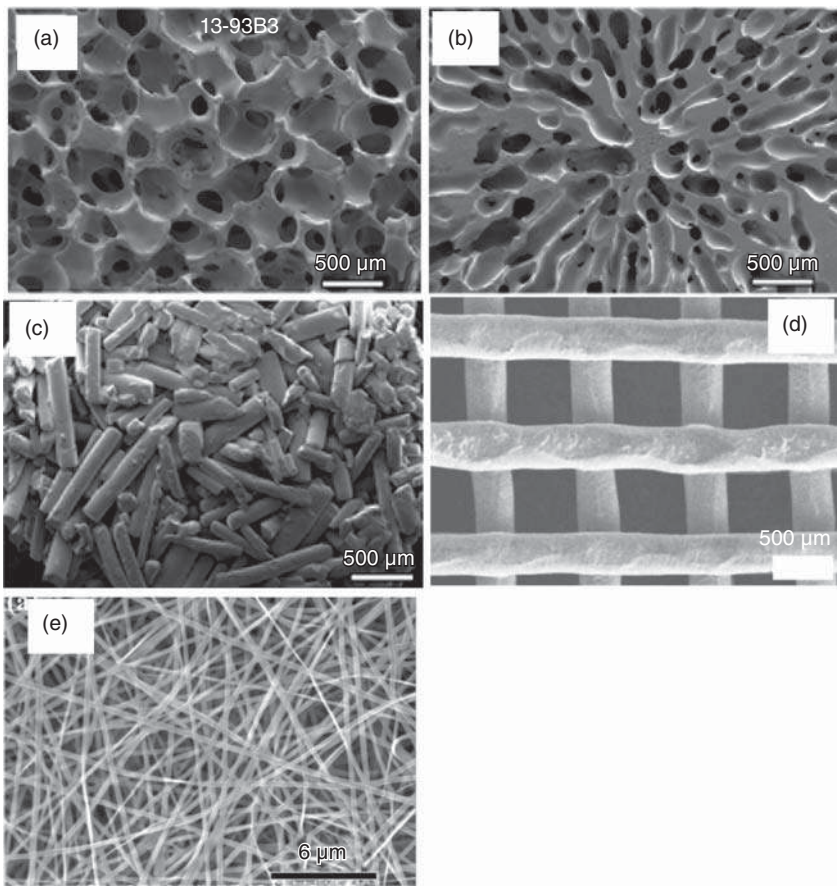

Figure 5.1 SEM photographs of borate bioactive glasses with various microstructures of (a) trabecular, (b) oriented pores, (c) fibrous, (d) grid prepared by robocasting, (e) microfibers prepared by melt-blow. Source: (a–c) Bi et al. [6], Figure 01, p. 04/with permission of Elsevier; (d) Deliormanlı [7], Figure 02, p. 04/with permission of Elsevier; (e) Rahaman et al. [8], Figure 03, p. 06/with permission of Elsevier.

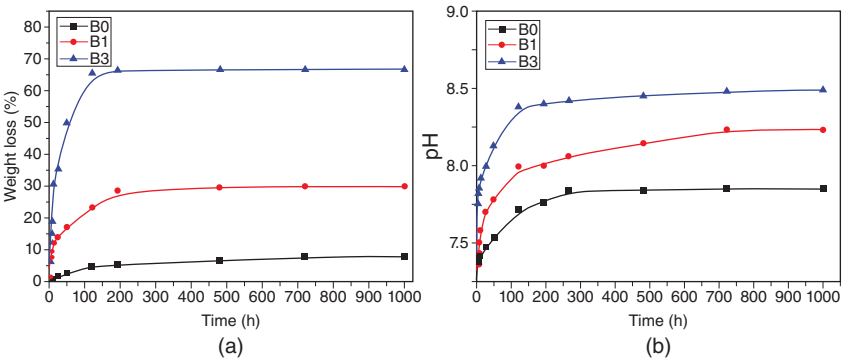

Figure 5.2 (a) Weight loss of scaffold and (b) pH of a simulated body fluid (SBF) as a function of immersion time of silicate 13-93 (B0), borosilicate 13-93B1, and borate13-93B3 bioactive glass scaffolds in the SBF. Source: Reproduced from Fu et al. [12].

The rapid increase of pH of the SBF was also observed with increasing the B_2O_3 content of the glass (Figure 5.2b), resulted from the rapid reaction between the glasses and the SBF accompanied by a conversion of the glasses into apatite or apatite-like phase. The mechanism of degradation and conversion of the borate bioglasses to apatite in the SBF was reported by Haung et al. [4] as follows: when the borate glasses are soaked in the SBF, the glass components such as Na_2O, K_2O, B_2O_3, and SiO_2 are dissolved into the solution to form Na^+, K^+, BO_3^{3-}, and SiO_4^{4-} ions, coupled with the reaction of Ca^{2+} ions from the glass with PO_3^{4-} ions from the solution to form a apatite/apatite-like layer on the glass. They also showed that no silica-rich layer is present in the conversion of 13-93B3 glass while a thin silica-rich layer initially forms on 13-93B1 glass.

5.3 Biological Reaction of Boron

It has been argued that one concern for the borate bioactive glasses is the borate ions released into the surrounding solution in the course of the biological reaction. Boron is taken into the human body through the daily food consumption [15] and is present in the body as boric acid [16]. It has roles in steroid hormone metabolism, healthy bone development, and cell membrane maintenance [17, 18]. It has been shown that boron affects the activities of certain enzymes such as elastase, the trypsin-like enzymes and collagenase so as to regulate the extracellular matrix, and it also induces the release of tumor necrosis factor α (TNF-α) in fibroblasts [19]. The gene expression levels of some of the bone tissue related extracellular matrix proteins such as collagen type I, osteopontin, osteocalcin, and bone sialoprotein are increased by boron treatment [20, 21]. It has been also suggested that boron may also improve wound healing by the action of boron on the extracellular matrix [22]. In contrast to these beneficial effects, high amounts of boron are cytotoxic [23, 24] and reported to interfere with the development of certain organs and the immune system [25]. It has been reported that cell viability of human tooth germ stem cells (hTGSCs) is significantly decreased by exposure to sodium pentaborate pentahydrate (NaB) at doses of more than 200 μg/ml [23]. It has also been shown that boron nitride nanotubes exhibit a more toxic effect on RAW 264.7 macrophages and 3T3-L1 fibroblast cells than carbon nanotubes [24]. The cytotoxicity of borate bioactive glasses prepared by a partial or complete replacement of SiO_2 in 45S5 glass with B_2O_3 was evaluated by Brown et al. [26]. They showed that the borate bioactive glasses with the higher B_2O_3 content resulted in greater inhibition of MC3T3-E1 cell proliferation under a static cell culture condition, while no

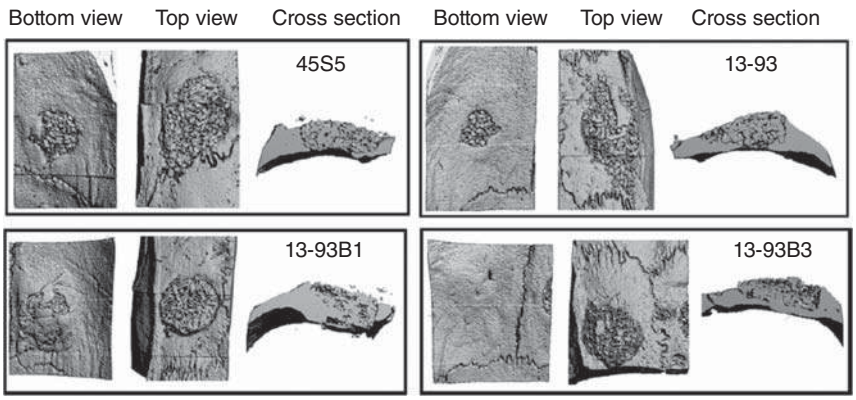

Figure 5.3 Micro CT images of critical-sized rat calvarial defects implanted with the bioactive glass 45S5, 1393, 1393B1, and 1393B3 at 12-weeks postsurgery. Complete bridging of the dural side is observed with the 1393B3 scaffolds. Source: Bi et al. [28], Figure 02, p. 04/with permission of John Wiley & Sons, Inc.

cytotoxicity was observed under dynamic culture conditions mimicking the body environment [26]. Fu et al. reported that the cell proliferation and alkaline phosphate activity of MLO-A5 on a trabecular scaffold composed of silicate or borate bioactive glasses decreased with the increasing borate content in the glasses [27]. Bi et al. reported that 13-93B3 glass induced greater new bone formation than a conventional 45S5 glass [28]. Rahaman et al. have reported that borate bioactive glasses, including 13-93B3, exhibit no observable toxic effects *in vivo* [8]. It has been shown that the incorporation of strontium into borate bioactive glasses minimizes the cytotoxicity of borate bioactive glasses by suppressing borate ions [3].

5.4 Hard Tissue Regeneration

When the borate bioactive glasses are used as a scaffold in bone tissue, they react with the surrounding biological solution so as to convert to apatite and/or an apatite-like phase [11, 12] and directly bond to bone [28], as in the case of silica-based bioactive glasses. Bi et al. [28] prepared various compositions of 13-93, 13-93B1, and 13-93B3 trabecular scaffold, with 50% porosity and a pore size of 50–500 μm by fusing randomly oriented short fibers of 100–300 μm diameter and implanted them into rat calvaria bone defects. They reported that a greater amount of new bone formation was observed for 13-93B3 after 12 weeks than the 13-93 glass scaffold due to the complete conversion of 13-93B3 to hydroxyapatite, as shown in Figure 5.3. Jia et al. implanted 13-93B3 glass particles loaded with teicoplanin (TEC) into methicillin-resistant *Staphylococcus aureus* (MRSA)-induced osteomyelitis in a rabbit model [29]. They reported that the TEC-loaded 13-93B3 reduced the number of bacterial cells and promoted bone regeneration compared with TEC-loaded calcium sulfate and the untreated defect.

5.5 Soft Tissue Regeneration

The efficacy of borate bioactive glasses on soft tissue regeneration has been investigated over the past decade. The remarkable progress in soft tissue regeneration reported by Jung and Day in 2011 and shows that a cotton-like glass fiber pad of 13-93B3 glass exerts a tremendous wound healing

effect [30, 31]. Borate glass fibers of micrometer diameter scale easily dissolve in the body environment due to their large surface area and release borate, calcium, and potassium ions while forming an apatite layer on its surface [2]. Such ion release capacity resulted in the promotion of angiogenesis in a rat subcutaneous model and broad-spectrum antibacterial activity [32, 33] as shown in Figures 5.4 and 5.5. These glass fibers received USA Food and Drug Administration (FDA) approval for the management of acute and chronic wounds in 2016.

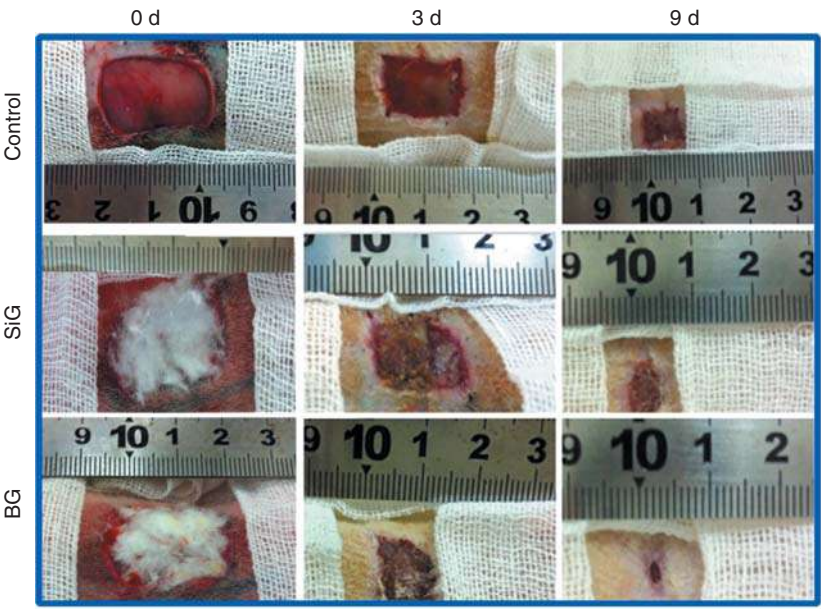

Figure 5.4 Images of skin wounds treated with borate bioactive glasses (BG) and silicate bioactive glasses (SiG) microfiber wound dressings for zero, three, and nine days, and the untreated wound surfaces as control. Source: Zhou et al. [32], Figure 08, p. 05/with permission of Elsevier.

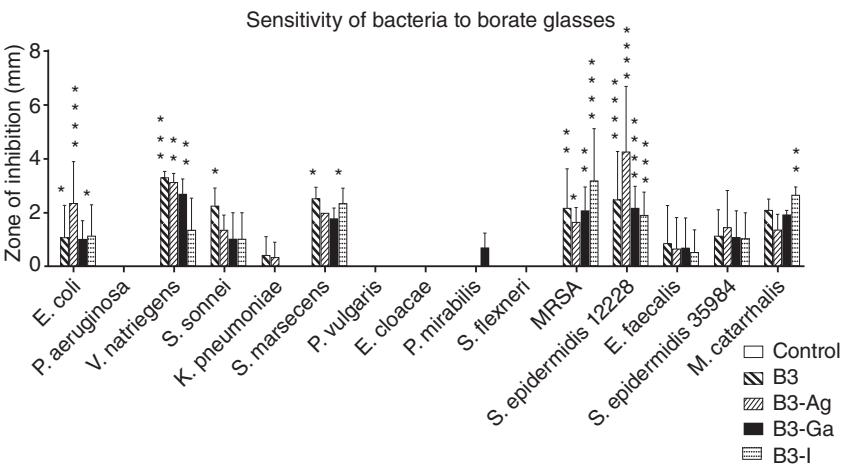

Figure 5.5 Sensitivity of bacteria to borate glasses of 13-93B3 with or without additive of silver (Ag), gallium (Ga), or iodine (I). * = $p \leq 0.05$; ** = $p \leq 0.01$; *** = $p \leq 0.001$; **** = $p \leq 0.0001$. Source: Reproduced from Ottomeyer et al. [33].

Recent studies have attempted to elucidate the mechanism of wound healing by the borate microfibers, but the details remain unclear [34]. Zhou et al. reported that the borate 13-93B3 glass fibers achieve faster wound healing than the conventional silicate Bioglass 45S5 glass fibers and attributed this result to the boron component in the borate glass [32]. On the other hand, Liu et al. attributed the faster healing by the borate glass to a faster release of calcium ions from [2]. Lin et al. [35], Zhao et al. [36], and Chen et al. [37] showed that the addition of copper and/or zinc ions to the borate glass promotes the healing effect. Recently, Thyparambil et al. reported that 13-93B3 glass can trigger phenotypic change in adipose stem cells [38]. Further study is required to fully understand the mechanism of the wound healing process induced by the borate microfibers.

5.6 Summary

Since the original development of borate bioactive glasses, cytotoxicity has been the main concern. Recent studies have accumulated results that little or no cytotoxicity *in vivo* and enhancement of hard and soft tissue regeneration. The application of borate bioactive glasses to wound healing was remarkably advanced by the introduction of the cotton-like glass pad into the 13-93B3 glass, although further study is still required to fully understand the mechanism of wound healing process induced by the borate microfibers.

References

1 Day, D.E., White, J.E., Brown, R.F., and McMenamin, K.D. (2003). Transformation of borate glasses into biologically useful materials. *Glass Technology: European Journal of Glass Science and Technology, Part A* 44: 75–81.

2 Liu, X., Rahman, M.N., and Day, E.D. (2013). Conversion of melt-derived microfibrous borate (13-93B3) and silicate (45S5) bioactive glass in a simulated body fluid. *Journal of Materials Science – Materials in Medicine* 24: 583–595.

3 Pan, H., Zhao, X., Zhang, X. et al. (2010). Strontium borate glass: potential biomaterial for bone regeneration. *Journal of the Royal Society, Interface* 7: 1025–1031.

4 Huang, W., Day, D.E., Kittiratanapiboon, K. et al. (2006). Kinetics and mechanisms of the conversion of silicate (45S5), borate, and borosilicate glasses to hydroxyapatite in dilute phosphate solutions. *Journal of Materials Science – Materials in Medicine* 17: 583–596.

5 Gu, Y., Wang, G., Zhang, X. et al. (2014). Biodegradable borosilicate bioactive glass scaffolds with a trabecular microstructure for bone repair. *Materials Science and Engineering C* 36: 294–300.

6 Bi, L., Rahaman, M.N., Day, D.E. et al. (2013). Effect of bioactive borate glass microstructure on bone regeneration, angiogenesis, and hydroxyapatite conversion in a rat calvarial defect model. *Acta Biomaterialia* 9: 8015–8026.

7 Deliormanlı, A.M. (2012). In vitro assessment of degradation and bioactivity of robocast bioactive glass scaffolds in simulated body fluid. *Ceramics International* 38: 6435–6444.

8 Rahaman, M.N., Day, D.E., Bal, B.S. et al. (2011). Bioactive glass in tissue engineering. *Acta Biomaterialia* 7: 2355–2373.

9 Kotani, S., Fujita, Y., Kitsugi, T. et al. (1991). Bone bonding mechanisms of β-tricalcium phosphate. *Journal of Biomedical Materials Research* 25: 1303–1315.

10 Hench, L.L., Splinter, R.J., Allen, W.C., and Greenlee, T.K. Jr., (1971). Bonding mechanisms at the interface of ceramic prosthetic materials. *Journal of Biomedical Materials Research* 5: 117–141.

11 Yao, A., Wang, D.P., Huang, W. et al. (2007). In vitro bioactive characteristics of borate-based glasses with controllable degradation behavior. *Journal of the American Ceramic Society* 90: 303–306.

12 Fu, Q., Rahaman, M.N., Fu, H., and Liu, X. (2010). Silicate, borosilicate, and borate bioactive glass scaffolds with controllable degradation rate for bone tissue engineering applications. I. Preparation and in vitro degradation. *Journal of Biomedical Materials Research* 95A: 164–171.

13 Fung, Y.C. (1993). *Biomechanics: Mechanical Properties of Living Tissues*. New York: Springer.

14 Kokubo, T. and Takadama, H. (2006). How useful is SBF in predicting in vivo bone bioactivity? *Biomaterials* 27: 2907–2915.

15 Baker, S.J., Tomsho, J.W., and Benkovic, S.J. (2011). Boron-containing inhibitors of synthetases. *Chemical Society Reviews* 40 (8): 4279–4285.

16 Hunt, C.D. (1998). Regulation of enzymatic activity – one possible role of dietary boron in higher animals and humans. *Biological Trace Element Research* 66 (1–3): 205–225.

17 Tanaka, M. and Fujiwara, T. (2008). Physiological roles and transport mechanisms of boron: perspectives from plants. *Pflügers Archiv: European Journal of Physiology* 456 (4): 671–677.

18 Cui, Y., Winton, M.I., Zhang, Z.F. et al. (2004). Dietary boron intake and prostate cancer risk. *Oncology Reports* 11 (4): 887–892.

19 Benderdour, M., Bui, T.V., Hess, K. et al. (2000). Effects of boron derivatives on extracellular matrix formation. *Journal of Trace Elements in Medicine and Biology* 14 (3): 168–173.

20 Dzondo-Gadet, M., Mayap-Nzietchueng, R., Hess, K. et al. (2002). Action of boron at the molecular level – effects on transcription and translation in an acellular system. *Biological Trace Element Research* 85 (1): 23–33.

21 Hakki, S.S., Bozkurt, B.S., and Hakki, E.E. (2010). Boron regulates mineralized tissue-associated proteins in osteoblasts (MC3T3-E1). *Journal of Trace Elements in Medicine and Biology* 24 (4): 243–250.

22 Nzietchueng, R.M., Dousset, B., Franck, P. et al. (2000). Mechanisms implicated in the effects of boron on wound healing. *Journal of Trace Elements in Medicine and Biology* 16 (4): 239–244.

23 Demirci, S., Doğan, A., Şişli, B., and Sahin, F. (2014). Boron increases the cell viability of mesenchymal stem cells after long-term cryopreservation. *Cryobiology* 68: 139–146.

24 Horváth, L., Magrez, A., Golberg, D. et al. (2011). In vitro investigation of the cellular toxicity of boron nitride nanotubes. *ACS Nano* 5 (5): 3800–3810.

25 Hu, Q., Li, S., Qiao, E. et al. (2014). Effects of boron on structure and antioxidative activities of spleen in rats. *Biological Trace Element Research* 158 (1): 73–80.

26 Brown, R.F., Rahaman, M.N., Dwilewicz, A.B. et al. (2009). Effect of borate glass composition on its conversion to hydroxyapatite and on the proliferation of MC3T3-E1 cells. *Journal of Biomedical Materials Research* 88A: 392–400.

27 Fu, Q., Rahaman, M.N., Bal, B.S. et al. (2010). Silicate, borosilicate, and borate bioactive glass scaffolds with controllable degradation rate for bone tissue engineering applications. II. In vitro and in vivo biological evaluation. *Journal of Biomedical Materials Research* 95A: 172–179.

28 Bi, L., Jung, S., Day, D. et al. (2012, 2012). Evaluation of bone regeneration, angiogenesis, and hydroxyapatite conversion in critical-sized rat calvarial defects implanted with bioactive glass scaffolds. *Journal of Biomedical Materials Research Part A* 100A: 3267–3275.

29 Jia, W.-T., Fu, Q., Huang, W.-H. et al. (2015). Comparison of borate bioactive glass and calcium sulfate as implants for the local delivery of teicoplanin in the treatment of methicillin-resistant

Staphylococcus aureus induced osteomyelitis in a rabbit model. *Antimicrobial Agents and Chemotherapy* 59: 7571–7580.

30 Wray, P. (2011). Cotton candy' that heals? Borate glass nanofiber look promising. *American Ceramic Society Bulletin* 90 (4): 25–29.

31 Wray, P. (2013). Wound healing: an update on Mo-Sci's novel borate glass fibers. *American Ceramic Society Bulletin* 92 (4): 30–35.

32 Zhou, J., Wang, H., Zhao, S. et al. (2016). In vivo and in vitro studies of borate based glass micro-fibers for dermal repairing. *Materials Science and Engineering C* 60: 437–445.

33 Ottomeyer, M., Mohammadkah, A., Day, E.D., and Westenberg, D. (2016). Broad-spectrum antibacterial characteristics of four novel borate-based bioactive glasses. *Advances in Microbiology* 6: 776–787.

34 Naseri, S., Lepry, W.C., and Nazhat, S.N. (2017). Bioactive glasses in wound healing: hope or hype? *Journal of Materials Chemistry B* 5: 6167–6174.

35 Lin, Y., Brown, R.F., Jung, S.B., and Day, D.E. (2014). Angiogenic effects of borate glass micor-fibers in a rodent model. *Journal of Biomedical Materials Research Part A* 102A: 4491–4499.

36 Zhao, S., Li, L., Wang, H. et al. (2015). Wound dressing composed of copper-doped bioactive microfibers stimulate angiogenesis and heal full-thickness skin defects in a rodent model. *Biomaterials* 53: 379–391.

37 Chen, S.S., Yang, O., Brown, R.K. et al. (2017). In vitro stimulation of vascular endothelial growth factor by borate-based glass fibers under dynamic flow conditions. *Materials Science and Engineering C* 73: 447–455.

38 Thyparambil, N.J., Gutgesell, L.C., Bromet, B.A. et al. (2020). Bioactive borate glass triggers phenotypic changes in adipose stem cells. *Journal of Materials Science – Materials in Medicine* 31: 35.

6

Fabrication of Bioactive Structures from Sol–Gel Derived Bioactive Glass

Durgalakshmi Dhinasekaran[1] *and Anuj Kumar*[2]

[1] *Department of Medical Physics, Anna University, Chennai, India*
[2] *School of Chemical Engineering, Yeungnam University, Gyeongsan, Republic of Korea*

List of Abbreviations

ADA-GEL	Alginate dialdehyde-gelatin
AM	Additive manufacturing
ASTM	American Society for Testing and Materials
BG/BAG	Bioactive glass
C-ES	Cell-electrospinning
CNF	Cellulose nanofibril
CS/CH	Chitosan
DBB	Droplet-based bioprinting
Dex	Dextran
EBB	Extrusion-based bioprinting
EPD	Electrophoretic deposition method
FDA	Food and Drug Administration
GelMA	Gelatin methacryloyl
GP	Glycerophosphate composites
HA/HAp/apatite	Hydroxy apatite
HCA	Hydroxycarbonate apatite
HF	Hydrofluoric acid
LASER	Light amplification by stimulated emission of radiation
LBB	Laser-based bioprinting
mBGNP	Mesoporous bioactive glass nanoparticles
NMR	Nuclear magnetic resonance spectroscopy
OAL	Oxidized alginate
OCS	Oxidized chondroitin sulfate
PCL	Polycaprolactone
PDLLA	Poly(D,L-lactic acid)
PEGDMA	Poly(ethylene glycol) dimethacrylate
PEGSH	Poly(ethylene glycol) self healing
pHEMA	Poly-hydroxyethyl methacrylate
PLGA	Poly(lactic-*co*-glycolic acid)

Bioactive Glasses and Glass-Ceramics: Fundamentals and Applications, First Edition.
Edited by Francesco Baino and Saeid Kargozar.

PLLA	Poly-L-lactic acid
PU	Polyurethane
SA	Sodium alginate
SAg	*Spongia agaricina*
SCS	Succinyl chitosan
SF	Silk fibroin
SL	*Spongia lamella*
SPI	Soy protein isolate
TEOS	Tetraethylorthosilicate
ZBG	Zinc-doped bioactive glass

6.1 Regenerative Glasses – An Introduction

Synthetic materials mimicking nature in terms of physical, chemical, and structural characteristics to help diseased parts or assist the defective organs of the body give the necessity for the development of biomaterials. The usage of biomaterials is not new; the earlier Romans, Chinese, and Aztec used gold in dentistry more than 2000 years ago. Through much of recorded history, evidences of using glass eyes and wooden teeth have been found in common use. Based on the interaction of the synthetic materials to the physiological environment, the biomaterials community has referred it as four generation of biomaterials [1]. The first-generation biomaterials (1950s–1970s) are bioinert materials; it was neither recognized nor rejected by the physiological medium. The second-generation biomaterials (1970s–1990s) are bioactive materials that have minimal reactivity to the physiological medium and some have biodegradable properties that help for the stable performance of the biomaterials for a long time. The third-generation biomaterials (1990s–2010) are bioresorbable materials that can be completely resorbed by the physiological medium. The fourth generation biomaterials (2010 to present) are the period of regeneration materials that deals with biomimetic tissue engineering scaffolds.

The concept of regeneration dates back to Greek mythology of Titan Prometheus punishments followed by the ability of the liver to regenerate itself, overnight. This story also opens the way for the scientific community to study hepatic diseases. The recent studies also on the biochemical evidences show that the damaged liver cells have the potential of repairing and restoring themselves through the signal pathway and can return to the postnatal organ. However, as of now, the regeneration possibility and its research are only limited to liver since the Greek mythological time [2]. In the present generation of tissue engineering, the achievement of hard tissue replacement is most needed. The bone and dental structures are very complex with the combination of systematic hierarchical arrangement of organic and inorganic matrix [3]. This dense matrix consisting of bundles of collagenous fibers interwoven within the amorphous ground substance (cement) impregnated with calcium phosphate complexes. Unfortunately, during defects or diseased conditions these three separate elements, viz, fibers, cement, and calcium salts, disappear together. And hence a suitable biomaterial needs to be engineered to mimetic the structural and functional properties of these hard tissues. Most often, calcium salts have been used as biomaterials for hard tissue application including hydroxyapatite, tricalcium phosphate, and bioactive glass (BG).

In these materials, hydroxyapatite is bioactive material and tricalcium phosphate is a bioresorbable materials. The bioactive glass is in between the bioactive and bioresorbable property with higher surface reactivity. Hench in 1969, discovered bioactive glass as second-generation bioactive glass that can bond with the host tissue. The story of bioactive glass starts with the necessity for

discovering new material by the US army to cure several amputation due to Vietnam war, and a material which cannot be rejected by body. This necessity gives birth for Bioglass®, which has the capability to bond the bone and living tissue, discovered by L. Hench. This bioactive glass has the composition of SiO, CaO, Na_2O, and P_2O_5 in their system. The later advances on gene activation properties extends the bioactive glass potentialities toward tissue regenerative biomaterial. Even though the first invented bioactive glass systems were melt-derived, the alternative approach on the synthesis of these bioactive glass systems were first reported by Li et al. along with Hench for tertiary systems SiO, CaO, and P_2O_5. They also termed this system of glasses as alkaline free gel glass powders and concluded these gel powders, with lower SiO_2 content and higher CaO and P_2O_5 content, exhibit higher rates of apatite formation [4]. The notable result on comparison with melt-derived bioglass is in case of sol–gel bioactive glass the maximum silica percentage for apatite formation is from 40 to 90 mol%, whereas for melt-derived glasses, it is narrowed down from 40 to 60 mol%. Later, Saravanapavan, Hench, et al. [5] reported that binary bioactive glass system (SiO_2 and CaO) by a sol–gel method could be bioactive with SiO_2 content up to 90 mol%. The advantages of the sol–gel bioactive glass start with the enhanced surface area and higher surface reactivity. This opens the possibility of developing various composition of bioactive glass by sol–gel method from 1991. Notably, some of the classes of these bioactive glasses have the capability to bond both with hard tissue and soft tissue.

6.2 Glass Network and Bioactivity

The domestic usage of glasses was known since the early times. Some of the archeological evidences and monuments of Thebes and Beni Hassan give us the proof for this glass making known for the human for a long time. There were also some evidences that show exporting of glasses to Greece and Rome from Egypt. The ancients greet scripts by Aristophanes, has mentioned glasses as *hyalos*, a transparent stone for kindling fire. The Romans and Egyptians probably used sand (Silica source) mixed with ground seashells (lime source) as raw materials and hardwood ash as the source of soda. They also used various metallic oxides to make color glass. Cuprous oxide was used to make red glasses, and these glasses were called as *haematinon* of Pliny. Whereas the green glasses were made by using cupric oxide and the famous blue glasses were found to have cobalt in the glass structure.

This history is more suitable for melt-derived glasses, and the methodology also holds a major portion same for bioactive melt-derived glasses. However, for melt-derived bioactive glasses an additional care needs to be taken in choice of crucible and addition of metal oxides, which may greatly affect the bioactivity of the materials. In case of melt-derived bioactive glass methodology, it involves both melting and annealing steps. Whereas for sol–gel bioactive glass, it involved sol–gel drying followed by annealing, and the operating temperature was maintained below the melting point of the glass ceramic. And hence, the later method involves more of room temperature reaction for network/gel formation, and this makes the choice of silica often too organic for precursors, i.e. tetraethylorthosilicate (TEOS).

The bioactive glass system prepared by both the methods follows the same rule for network formation. This involves the combination of network formers and network modifiers. Silica is the network former, and the network modifiers are calcium and sodium. The network modifiers play a major role in altering the silica network flexibility, transparency, hardness, and bioactivity. The schematic representation of two-dimensional bioactive glass molecular structure is given in Figure 6.1, where the structure has both the bridging oxygen with the nearby silica and nonbridging oxygen. SiO_2 and P_2O_5 are the network formers. The network modifier (Na^+, Ca^{2+}, K^+, Zn^{2+}, Sr^{2+},

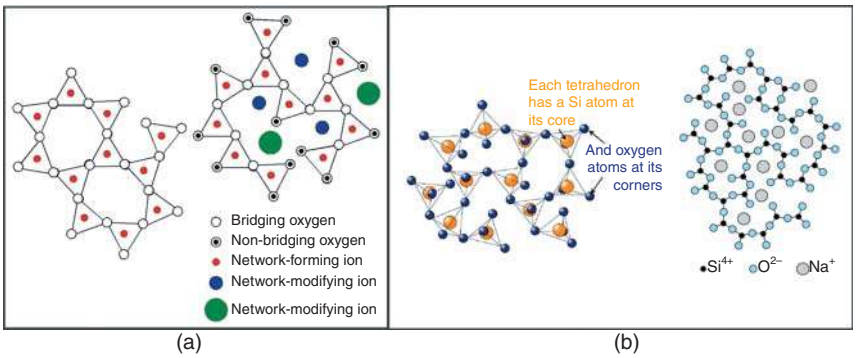

Figure 6.1 Network structure of bioactive glass with arrangements of network formers and network modifiers. (a) 2D diagram of glass networks, (b) arrangements of silica in bioactive glass networks.

Ag^+, Mg^{2+}) does not create a covalent/ionic bonding with the network structure and often has electrostatic interactions. The intermediate network former/modifier compounds ($A1_2O_3$, TiO_2) will also use and enhance the mechanical property of the glass. The sol–gel glasses based on the choice of network modifiers and operating temperature resulted in glass ceramics with polycrystalline structures embedded in the glass network. These types of polycrystalline glasses by melt-quenching method were first discovered accidently by S.D. Stookey in the early 1960s [6]. However, the crystal size within the glass network was expected to be less than 1 μm for an uniform structure. The sol–gel chemistry helps us to develop amorphous homogenous glass network and can also make nanostructure polycrystalline material based on the requirements.

The major portion of the bioactive glass is silica and depends on the addition of network modifier, and there results in different phase formation. The bioactive glass phase diagram for phase structure formation with respect to temperature and bioactivity is often discussed. For the widely suggested bioactive glass composition with SiO_2–CaO–Na_2O–P_2O_5 systems, phosphate wt% is kept as constant for 6% and the different composition with respect to bioactivity gives division in bioactive glass system as class A and class B (Figure 6.2a). Class A bioactive glasses have both osteoconductive and osteoproductive properties; in these glasses, surface apatite formation will occur within hours. The Bioglass with $45SiO_2$–24.5CaO–$24.5Na_2O$–$6P_2O_5$ (wt%) comes under this class A bioactive glass. Class B has only osteoconductive property and hence bonding only to hard tissues. Also, in the class B systems, the surface apatite formation duration occurs from one to several days. The glass systems such as ceravital and Bioglass 8625 are some of the examples of class B system.

The same principle is followed for tertiary bioactive glass system (SiO_2–CaO–P_2O_5), highly suitable for preparing sol–gel bioactive glasses (Figure 6.2b). It could be observed that higher percentage of CaO leads to crystallization and higher amount of P_2O_5 results in non-gelation. An appropriate percentage of the glass composition needs to be chosen with higher SiO_2 and lesser CaO source and very lesser P_2O_5 source to achieve proper gelling and bioactivity by means of apatite formation on the surface. In addition to silica and calcium sources, the significant role on the presence of P_2O_5 is not yet understood well. And the broad hypothesis is the network formation of P_2O_5 similar to silica and may contribute to hydroxycarbonate apatite: HCA (apatite) crystallization. Earlier results show that amounts higher than 12% in weight inhibit the bioactivity of bioactive glasses [8].

The binary SiO_2–CaO is often discussed with phase diagram with respect to temperature and composition variations (Figure 6.3) [9]. As for bioactive glass synthesized by sol–gel method, the optimum temperature is between 600 and 700 °C, and as with higher temperature, there occurs

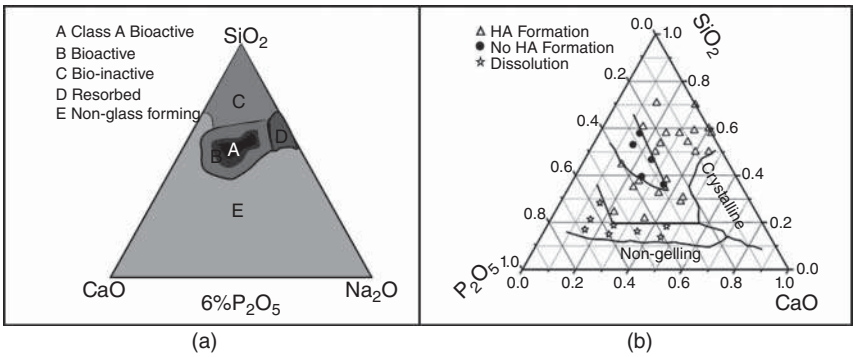

Figure 6.2 Phase diagram of bioactive glasses with (a) tertiary diagram of SiO_2–CaO–Na_2O glass system with constant 6% P_2O_5 and (b) tertiary diagram of SiO_2–CaO–P_2O_5 glass system [7].

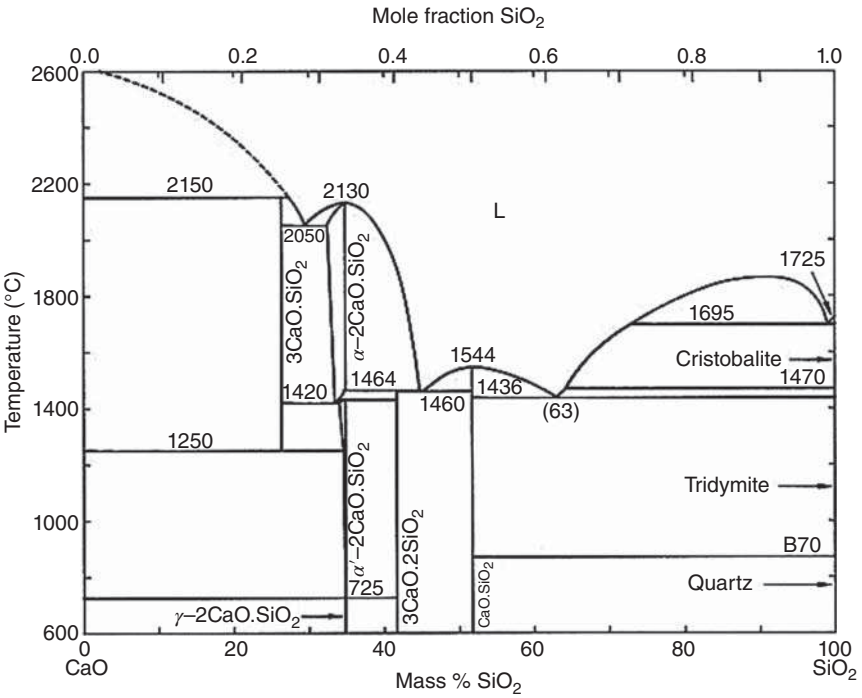

Figure 6.3 Phase diagram of binary bioactive glass system with respect to temperature. Source: Based on Sasaki et al. [9].

multiple crystallization and retards the bioactivity. In the binary system of bioactive glass, a higher percentage of SiO_2 will lead to stable quartz structuring with operating temperature, a mixture of quartz with $CaSiO_3$ peak is often expected from this glass system for higher apatite formation.

The formation of silica network in the bioactive glasses and its possible bioactivity, i.e. surface apatite formation, can be correlated from its spectral vibration signature of bridging and non-bridging oxygens of silica with other silica subunits. These structures can be studied from ^{29}Si nuclear magnetic resonance spectroscopy (NMR) and Raman spectral signatures. The Si–O–Si tetrahedra interaction with the silica subunits is represented by Q^n, where n is the number of

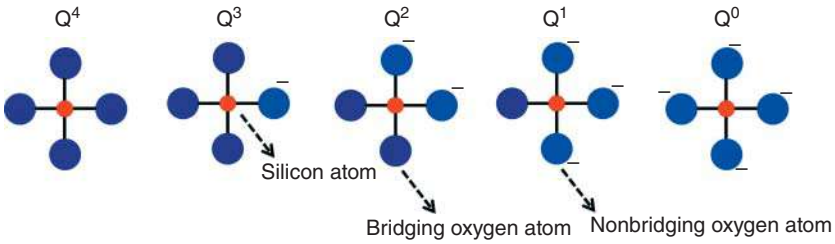

Figure 6.4 Possible ways of Si–O–Si tetrahedra interaction in bioactive glass.

bridging oxygen atoms per SiO_4 tetrahedron and it varies from 0 to 4 (i.e. Q^0, Q^1, Q^2, Q^3, and Q^4). Q^n units form a continuous random network of glasses or silicate anions through the Si–O–Si bridging linkages. The mode of silica interaction with the subunits is represented as Q^0, Q^1, Q^2, Q^3, and Q^4. In this, Q^0 type refers to a silicon atom with zero connections to another silicon species and the maximum Q^4 is the condition of fully occupied silicon atom with four oxygen bonding resulted in SiO_4 tetrahedra. The breaking of the Si–O–Si linkages and the formation of terminal oxygen atoms is due to the addition of alkali oxides (i.e. network modifiers) to silica network and the formation of Q^n species with $n < 4$ in the glass structure (Figure 6.4). The bioactive glass with higher Q^2 units represents chains of metasilicates and higher abundance of this structure in the glass structure is characteristic of higher bioactivity [10].

The mechanism for dissolution and bone bonding of a bioactive glass (Figure 6.5) proposed by Larry Hench is a multistage process involving the following steps [11, 12]:

Step 1 Rapid ion exchange of alkali-metal cations (e.g. Na^+, Ca^{2+}) with H^+ from body fluid.
Step 2 Loss of soluble silica, leaving behind —Si—OH bonds.

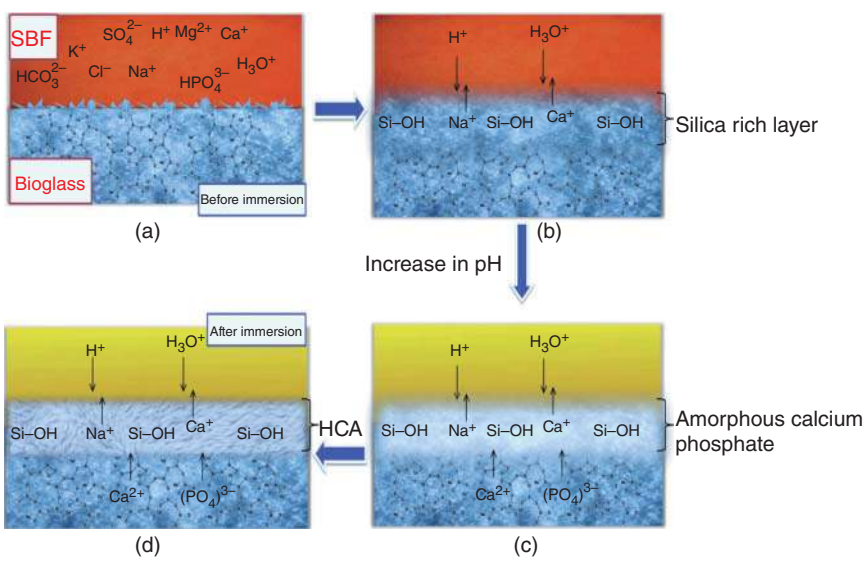

Figure 6.5 HCA formation mechanism of bioglass when immersed in simulated body fluid is as follows. (a) Bioactive glass immersed in simulated body fluid; (b) silica rich layer formed on the surface of bioactive glass (step 1 to 3); (c) transformation of silica rich layer to amorphous calcium phosphate layer (step 4); (d)crystallization of HCA layer (step 5).

Step 3 Condensation and repolymerization of the Si—OH bonds to create a silica-rich (cations-depleted) layer.

Step 4 Migration of Ca^{2+} and $[PO_4]^{3-}$ groups from inside the glass and from the body fluid, forming an amorphous calcium phosphate layer that grows on the silica-rich layer surface.

Step 5 Crystallization of the amorphous layer by incorporation of OH^- and $[CO_3]^{2-}$ from solution to form HCA.

Step 6 After the formation of crystalline HCA, the following steps were proposed by Hench to occur:

Step 6a Biological moieties absorbed in HCA layer.

Step 6b Macrophage actions.

Step 6c Attachment of stem cells.

Step 6d Differentiation of stem cells.

Step 6e Generation of matrix.

Step 6f Crystallization of matrix.

6.3 Sol–Gel Process of Synthesizing Bioactive Glass Structures

Preparation of silica gels was old as mentioned in the first report in 1746 by Pott. These silica gels were often reported with inorganic silica precursor (i.e. TEOS). Some notable works were also reported with sodium silica and potassium silicate precursors [13]. The same protocol has been followed for soda lime silica-based bioactive glasses obtained by sol–gel method. Similar to silica precursor, the choice of sodium, calcium, and phosphorous sources also shows the influence of crystal phase determination in the bioactive glasses. Bobo Yu et al. [14] and Ben-Arfa et al. [15, 16] studied the influence of choice based on calcium sources in the crystal structure formation of the bioactive glass system. Szu et al. reported the effect of the phosphorous precursor on the synthesis of phosphosilicate gels [17]. Other than the choice of precursors either by organic or inorganic, the parameters such as pH, reaction temperature, and choice of acid catalyst were important for synthesis of sol–gel bioactive glass.

Briefly, after the choice of precursors, the dilution of the precursors in the solvent condition is estimated. The solvent will be H_2O, ethanol, or the combination of both. Ethanol will be used for hydrolysis of silica organic precursor. The presence of H_2O helps the reaction during homogenous dissolution, hydrolysis, and condensation. The bioactive glass structures can be formed from this step of complete dissolving of the precursors and homogenization of metal alkoxide solution. This solution can be used for spray coating and spin coating followed by allowing it for xerogel formation and the resultant will be dense bioactive glass gel coating on the desired substrates. With an addition of acid catalyst to the solution for hydrolysis and condensation, there occurs an initiation of silica network formation that results in sol formation. This sol can also be used for thin film coating by dip coating and spin coating methods. The sol upon polymerization of silica network results in dense gel formation (Figure 6.6). This gel contains lot of water accumulation due to hydrolysis. The wet gel upon controlled heat treatment condition evaporates to the aqueous solution and results in xerogel and aerogel, a 3D networking arrangement. Upon heat treatment, the xerogels resulted in dense ceramic powders that can be used for casting of small implants, electrophoretic deposition (EPD) on substrates, and as fillers. The homogenous sol can be used to obtain homogenous structure of nano- to micron-sized particles by precipitation methods. The addition of sol with higher molecular weight polymers opens the possibility of the developing 1D fibers that can be made as 3D tissue engineering scaffolds. For this both synthetic and natural polymers such as chitosan,

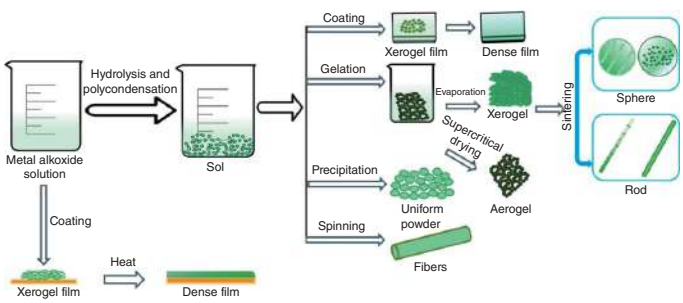

Figure 6.6 Sol–gel synthesis process of various forms of bioactive glass structures.

poly-L-lactic acid (PLLA) will be used to alter the degradability and regenerative property of the 3D scaffolds.

The first generation of bioactive glass was much about melt-derived bioactive glasses. This method of preparing bioactive glasses had some limitations in using it for treatments for urinary incontinence and periodontal lesions. This is due to its larger particle size, higher alkaline percentage compared to silica due to its higher sintering temperature synthesis conditions. And hence it paves the way for second generation of bioactive glasses that involve its synthesis by sol–gel method. In 1991, Li et al. was the first to synthesize bioactive glass by sol–gel process [4]. Sodium is often used for network modification in melt-derived glasses, and it causes higher alkalinity in sol–gel method; hence, the first achieved sol–gel method of glasses is for ternary system (SiO_2–CaO–P_2O_5) [4]. The additional advantages of the sol–gel bioactive glasses were low sintering temperatures (600–700 °C), higher purity, higher surface area, and higher bioactivity. The sol–gel bioactive glasses were involving the same process of sol–gel process as discussed above. Where the initial steps involve hydrolysis and condensation of silica. To this, the additional precursors required for specific bioactive glass composition were added and stirred to get homogenous gelation. The gel is dried and sintered to get bioglass powder [18]. The sol–gel bioactive glasses were initially often synthesized under acid conditions (e.g. HNO_3, HCl, citric acid). Later, to enhance the surface area and to develop controlled microstructure bioactive glass particles, Stöber method was adopted [19]. This method greatly helped to synthesize bioactive glass nanoparticles (BGNPs)[20]. As achieving higher surface area was one of the important factors in synthesizing bioactive glass by sol–gel methods, the surface area of greater than 150 m^2/g was only achieved by conventional sol–gel methods. Zhong et al. was the first to report on the crack-free homogenous sol–gel bioactive glass with higher surface area by sol–gel method [21]. From the sol-gel to monolith formation there occur volume variation, as shown in Figure 6.7 [23]. However, when adopting Stöber method, large specific surface area of ~1040 m^2/g was achieved [23]. Also, this method with suitable modifications opens the possibility of developing mesoporous bioactive glass nanoparticles (mBGNPs). Owing to its smaller particle size and higher surface area, it exhibits higher bioactivity, quick adsorption, and advantageous for drug delivery applications. The limitation in synthesizing BGNP is that it is prone to agglomeration very quickly due to the presence of alkaline precursors. This might be due to the synthesis in base condition in Stöber method that induce quick precipitation. It also depends on the order of adding the precursor and humidity of the temperature conditions. The first report on monodispersed BGNP with binary (SiO_2–CaO) system with size ~400 nm was first achieved by Zheng et al. [24]. In their work, they

Figure 6.7 Photographic representation of first reported homogenous sol–gel bioactive glass [22].

observed that the time of the addition of calcium precursor could also affect the morphology, composition, and dispersity of the resulting BGNP. It was also observed in earlier works that the addition of calcium precursors after the formation of homogenous spherical silica nanoparticles does not interfere in the formation of initial silica sphere nucleation. By optimizing the suitable synthesis parameters, particle size as low as 40–50 nm can also be achievable by this method [22]. Recently, more work is also contributed for mBGNP, and it is considered as third general bioactive glasses, as it accelerates the bioactive response mechanisms [25]. The possibility of surface functionalization and incorporation of structure directing agents has opened the possibility of designing it as multifunctional material, including systematic delivery systems to implantable local-delivery devices [26].

6.4 Scaffold Structuring from Bioactive Glass

The opportunities of developing tissue engineering scaffolds started with the first experiment by W.T. Green, by his development of new cartilage using chondrocytes seeded onto the spicules of bone and implanted at the back of nude mice [27]. Although the outcome results are not as successful as expected, it shows the way for lot of research avenue and developments in the field of tissue engineering. The term "tissue engineering" was officially coined at a National Science Foundation workshop in 1988 to mean "the application of principles and methods of engineering and life sciences toward the fundamental understanding of structure-function relationships in normal and pathological mammalian tissues and the development of biological substitutes to restore, maintain or improve tissue function" [28]. The tissue engineering scaffold development involves both resorbable and nonresorbable material and designed based on the need of the operative condition. The future will be on these types of personalized 3D tissue engineering scaffolds that will be more adaptive as a native tissue. As for hard tissue replacement, it is often narrowed down toward developing monolithic bone grafts. The first successful case study on Bioglass 45S5 monolith is for the treatment toward air-bone gap closures done on 37 patients between April 1984 and November 1987 by University of Florida. Their follow-up results after 10 years for four patients demonstrated that Bioglass middle-ear prostheses have excellent long-term tissue compatibility. However, there occurs fractures in the implant that may be due to lesser mechanical property and noncustomized design of the implants.

The development of tissue engineering scaffold aims to regenerate defective or damaged tissues by combining cells from the autonomous body with biomimetic scaffolds, which act as templates for tissue regeneration. During the designing of monolith scaffolds for bone tissue engineering applications, the following properties have been defined as essential [29]: biocompatibility, porosity, pore size, surface properties, mechanical properties, and biodegradability. The specificity of the individual properties of the scaffolds are given as follows:

Biocompatibility: It should be well integrated in the host's tissue without eliciting an immune response.

Porosity: It must possess an open pore, fully interconnected geometry in a highly porous structure with a large surface area to volume ratios and this will facilitate the neovascularization of the construct from the surrounding tissue.

Pore size: It is well accepted that for bone tissue engineering purposes, pore size should be within the range of 200–900 μm.

Surface properties: Both chemical and topographical properties can control and affect cellular adhesion and proliferation. It must be developed to mimic the structure of the bone.

Mechanical properties: *In vitro*, it should have sufficient mechanical strength to withstand the hydrostatic pressures and to maintain the spaces required for cell in-growth and matrix production. *In vivo*, since the bone is always under continuous stress, the mechanical properties of the implant constructed should ideally match those of living bone so that an early mobilization of the injured site can be made possible.

Biodegradability: The degradation rate of the scaffold must be tuned appropriately with the growth rate of the new tissue formation in such a way that by the time the injury site is totally regenerated, the scaffold is totally degraded.

In addition to the monoliths, the biologically functional tissue engineering scaffolds play a critical role in providing a 3D structure for cellular functions such as attachment, migration proliferation, and differentiation. These surfaces also serve as a vehicle for delivery of cells to the implant site. The success of this process is determined by the biological and functional similarity of engineered scaffolds with the native tissue [30]. Herein we focus on some of the methodologies on fabricating 3D tissue engineering scaffolds using bioactive glasses.

6.4.1 Foam Replication Method

The first report on polymeric foam replication method was patented in 1963 for the development of ceramic foams. The polymeric foams act as a 3D sacrificial template for the preparation of open porous ceramic foam, which has wide applications as adsorbent, catalytic converters, and biomedical applications. As for tissue engineering applications to have higher cell penetration and to have open porous structure for new tissue formation, this method has been adopted for developing biomaterial scaffolds for monolithic bone grafts. The American Society for Testing and Materials (ASTM) standard such as ASTM C271-94, ASTM C1161-94, and C773-88 were, respectively, used to study the porosity, bending, and mechanical properties of the ceramic foams. Micro-computed tomography (μCT) method was also used to find the interconnected porous structure. Bioactive glass of various glass systems based on scaffolds was developed by polymer foam replication method. The polymers used for the template will be chosen based on the porous structure, evaporating point, and the toxicity residues left over after heat treatment conditions. As the porosity greatly affects the mechanical property of the resultant bioceramic scaffolds, care will be taken in the choice of porosity and open porous structure of the sacrificial polymers. Earlier reports show a good comparison of the scaffolds prepared by this method with similar properties of trabecular bone in terms of mechanical and interconnected porosity (PMC3169803). Often, for the preparation of ceramic slurries, melt-derived bioactive glass in polymer (binder) solution is used. The size of the bioactive glass particles for the preparation of the slurries and viscosity of the slurries also plays a vital role in resultant scaffold geometry. And a very limited work is reported on sol–gel derived bioactive glass gels/powders for foam replication method. The advantage of 3D scaffold by sol–gel foam replication method is achieving porous template with higher surface area and bioactivity. The sol–gel foam replication method involves the method similar to conventional melt-derived bioactive glass prepared slurry formation followed by dipping in polymer foams, drying, and sintering at optimal temperature to get 3D bioactive glass scaffolds (Figure 6.8). The difference in the sol–gel foaming method is that the polymeric foam will be immersed in sol–gel of bioactive glass after hydrolysis and condensation reaction. And hence the 3D scaffold obtained from sol–gel method will be of controlled shape, homogenous crystallization, lower sintering temperature, and thus of higher purity [31]. The widely used polymers are polyurethane (PU) foams, PLLA, and natural marine sponges.

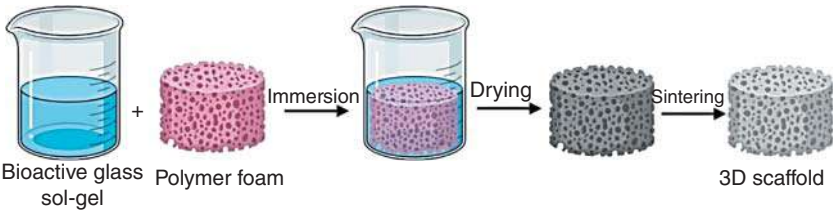

Figure 6.8 Synthesis procedure for preparing bioactive glass scaffolds by foam replication method.

The procedure for the scaffolds prepared by polymer foam replication method starts cleaning the sacrificial polymer scaffold and dipped into the ceramic slurry by slurry infiltration method. The resultant will be polymer scaffold homogenously coated ceramic 3D structure green body. The green body is allowed to slow dry at temperature range between 60 and 80 °C. After drying, the polymer template has been removed by heat treatment condition above 450 °C, the heating rate needs to optimize to minimize the microcracking on the bioactive glass surfaces (Patent No: WO 2007/017756 A2).

The sol–gel bioactive glasses were coated on PU foams by EPD method, resulted in higher interconnected porosity [32]. A notable work on two-step fabrication method including development of hydroxy apatite (HAp) scaffolds foam replication method and coated with poly(lactic-*co*-glycolic acid) PLGA/BG shows good osteogenic property. Bioactive glass scaffolds by mixture of borosilicate glass (S53B50), borophosphate glass (P40B10), and a phosphate glass (PSr40) was also developed using 60 and 70 vol% $NH_4(HCO_3)$ as foaming agent (Figure 6.9) [34]. Porosity formation by vigorous agitation of sol–gel bioactive glass in presence of 0.5 ml Teepol and 1.5 ml 5 vol% hydrofluoric acid (HF) also shows promising enhancement in mechanical properties [35]. Earlier reports on melt-derived particulate prepared Bioglass scaffolds by this method with biodegradable polymers opens the possibility for drug-released bone tissue engineering applications [36, 37]. Similar work was also done in the presence of silver doping in bioactive glass scaffold which has been explored [38, 39]. These procedures can also be adopted for sol–gel bioactive glass scaffolds. Some of the earlier reports on bioactive glass scaffolds prepared by foam replication method and its essential properties are listed in Table 6.1.

6.4.2 Hydrogel Method

Hydrogel-based tissue engineering scaffolds are widely explored due to its quick regenerative properties and adaptability to *in vivo* conditions [44]. The uniqueness of hydrogel scaffolds is to mimic the structural and functional properties of various tissues of the body [45]. Most of the hydrogels were made by polymeric substances into 3D structure, which can swell in presence of biological fluids. Hence, the hydrogels were often categories based on swelling ratio of the scaffolds. The swelling mechanism involves osmotic driving force followed by cohesive force of extension in the hydrophilic hydrogel matrix that allows surrounding aqueous medium to absorb until it reaches equilibrium state [46]. As most of the hydrogels are highly biocompatible for cell growth and proliferation, the hydrogels were incorporated with suitable cells in their structure. It also permits oxygen and nutrient transport in the tissue environment and mimic the native physical and biological property of the soft tissue [47]. Careful designing of cell-seeded hydrogel scaffolds in the physiological condition with degradation acts as a platform to form healthy tissue. Some of the hydrogels can also act as drug carriers for epidermic tissue engineering applications [48]. Yet another important

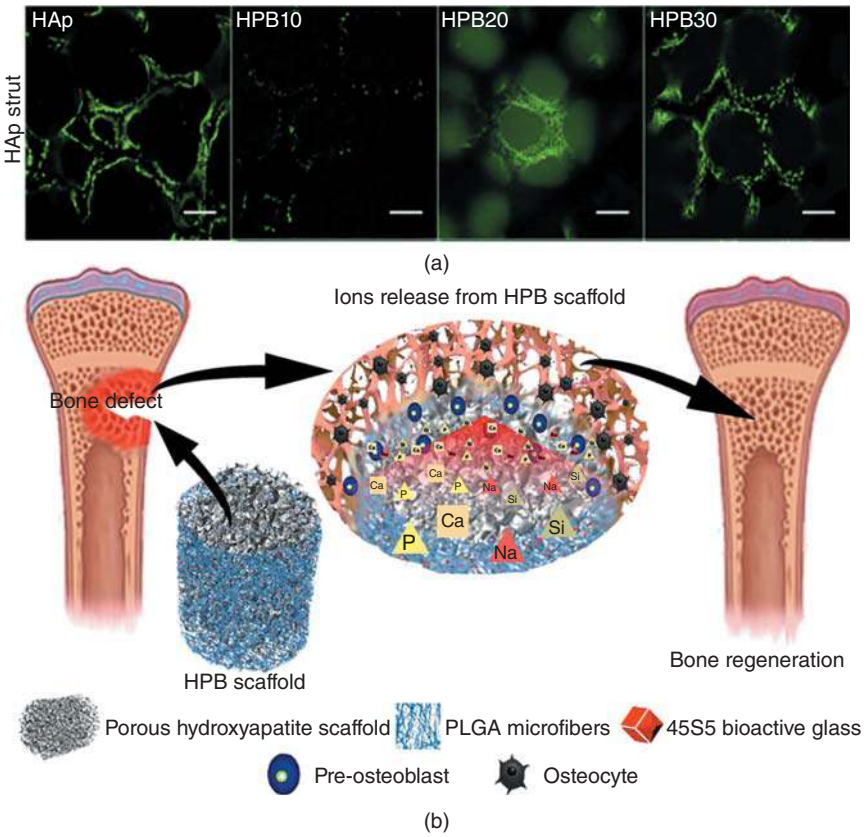

Figure 6.9 (a) Schematic representation of porous HA scaffolds prepared by foam replication method are selectively covered with a BG-containing PLGA microfiber layer toward potential bone substitute for tissue engineering (scale bar = 200 μm). (b) The schematic representation of the apatite formation of the scaffolds. Source: Jeong-Hyun et al. [33], Figure 04, p. 04/with permission of American Chemical Society.

property of the scaffold is their porosity, where through their porous structure, it promotes influx of cell metabolites and the cell wastes will be disposed.

The first report on the use of polymers for biomedical application dates back to 1960s [49]. The widely used materials in early days were only of crosslinked homopolymers in which methacrylate compound-based hydrogels with a swelling ratio less than 30% were experimented toward making contact lens and arteries applications. For tissue engineering applications, biodegradable polymers were of wide choice also for injectable scaffolding. These include cellulose, chitosan, alginate, poly lactic acid, etc. A detailed review on this biodegradable polymers for tissue engineering application is documented by Sivashanmugam et al. [50] The synthesis procedure of hydrogels involves both physical and chemical methods [51]. In chemical method, the reaction starts with covalent bond formation, followed by crosslinking of polymerization. Whereas, in physical method, there often occurs polymer entanglement by means of Van der Waals/electrostatic/hydrogen bonding. In composite hydrogel, any one or the combination of the abovementioned methods will be adopted. Stimulation-based hydrogel formation involves external stimulation such as temperature, pH, light ration, electric field, magnetic field, and solvent-mediated reaction kinetics (Figure 6.10) [52].

Bioactive glass-based hydrogels were extensively used both for orthopedic and dental applications [53]. Especially for the treatment of dental caries, the choice of material requirements needs

Table 6.1 Earlier works of bioactive glass scaffolds prepared by foam replication method.

Glass composition	Porosity/porous%	Mechanical property	Tissue engineering applications	Cell culture studies	References
(mol%)60.8% SiO_2, 30.9% CaO, 2.4% P_2O_5, and 5.8% Na_2O (PU foam)	High level of interconnective porous (99.99%)	—	Bone regeneration	—	[32]
13-93 bioactive glass (PU foam)	Porosity: $85 \pm 2\%$ and pore size: 100–500 µm	Compressive strength of 11 ± 1 MPa, and elastic modulus of 3.0 ± 0.5 GPa	Bone repair and regeneration	MC3T3-E1 preosteoblastic cells	[40]
45S5 Bioglass powder (particle size 5 mm). *Spongia agaricina* (SAg) and *Spongia lamella* (SL), as template materials	0–200 µm highly interconnective porous (99.99%)	Compressive strength up to 4 MPa	Bone regeneration	—	[41]
70S30C	300–600 µm at 82% porosity	Compressive strength of 2.26 MPa	—	—	[42]
70S30C 70 mol% SiO_2, 30 mol% CaO	78%	Compressive strength 6.0 MPa	—	—	[35]
45S5 bioactive glass	200–500 µm and 80–90%	—	—	MC3T3-E1	[33]
(wt%): 50SiO_2, 22.6CaO, 5.9Na_2O, 4P_2O_5, 12K_2O, 5.3MgO, and 0.2B_2O_3 (poly(D,L-lactic acid) [PDLLA])	68–73%	Compressive strength of 0.4 MPa for uncoated and 0.6 MPa for coated scaffolds	—	—	[43]

to satisfy regenerative and antibacterial properties. Also, for a successful endodontic regeneration, the biomaterial has the potentiality of controlling inflammation. A combination of graphene and chitosan with the presence of bioactive glass shows enhanced *in vitro* odontogenic differentiation in presence of dental pulp cells. This combination of this hydrogel also shows good antibacterial and anti-inflammatory properties [54]. The reinforcement of bioactive glass particles has proven to improve the mechanical property of the hydrogels. And hence, it was also suggested for soft bone tissue engineering applications, as it promotes efficient osteogenic differentiation. The bioactive glass ions in the presence of gellan gum and collagen type I hydrogels induce efficient osteogenic differentiation of human adipose stem cells [55, 56]. The gelling can also be achieved by theromogelling method, in presence of combining bioactive glass with chitosan and collagen

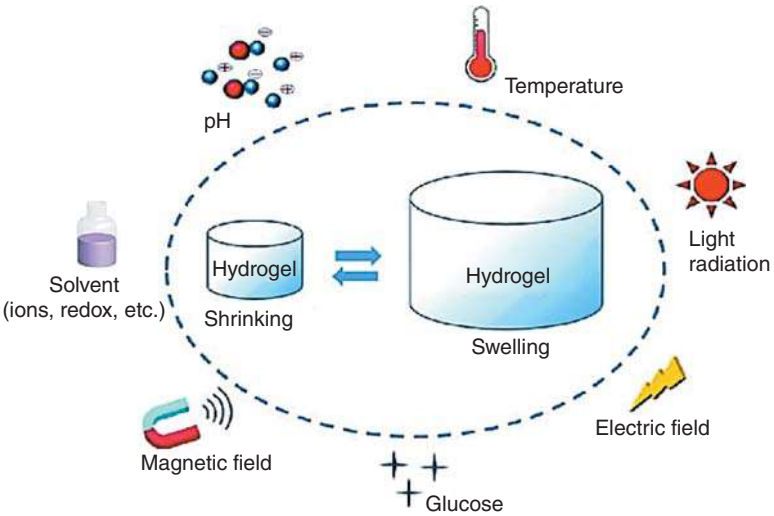

Figure 6.10 Stimuli–responsive hydrogel swelling in presence of various external stimuli [51].

for tissue engineering applications [57, 58]. The bioactive glass used as hybrid material shows higher potential when it is of nanosized and hence a lot of work has been reported on bioactive glass nanoparticle incorporated gels for wound dressing and tissue engineering applications. The combination of alginate dialdehyde, gelatin, and nano-bioactive glass (45S5) has shown the efficacy of combined excellent cellular adhesion, proliferation and differentiation properties, good biocompatibility, and predictable degradation rates [59]. Compared to pure hydrogels, when incorporated with BGNP, the loss of hydrogel mass *in vitro* was decreased by 4.3% [60]. The development of bioactive and biodegradable chitosan-based injectable systems containing bioactive glass nanoparticles strategies to deliver cells and bioactive agents encapsulated in a biodegradable matrix through minimally invasive procedures with results indicates that the stimuli-responsive hydrogels could potentially be used as temporary injectable scaffolds in bone tissue engineering applications [61]. Self-healing property of the hydrogels is enhanced in the presence of hydrogel nanocomposites [Au-$(PEGSH)_4$–BAG] in which 100 nm bioactive glass nanoparticles produced via a particulate sol–gel method used in the formation of hydrogels [62]. In addition to pure bioactive glass, zinc-doped bioactive glass (ZBG)/succinyl chitosan (SCS)/oxidized alginate (OAL) composite hydrogels gelatin-zinc-doped bioactive glass (Gel-ZBG) were also proven to accelerate the wound closure by formation of granulation tissue, deposition of collagen and myofibril, the release of anti-inflammatory factors, and angiogenesis (Figure 6.11). Due to these potentialities in enhanced healing property of this composite hydrogels, it has been addressed as a superior material for wound dressings [63]. Hydrogel system consisting of copper-containing bioactive glass nanoparticles and chitosan/silk fibroin (CH/SF) composite showed injectability and thermally triggered *in situ* gelation properties and were able to administer the release of ions at safe but effective doses in a controlled manner while inducing the seeded cells toward osteogenesis and angiogenesis (Figure 6.12).

A grid-like highly hydrated composite constructs were prepared using alginate dialdehyde-gelatin (ADA-GEL) incorporated strontium-doped bioactive glass nanoparticles [64, 65]. The effects of BG/sodium alginate (SA) hydrogel (BG/SA hydrogel) on the behaviors of macrophages as well as on the interactions between macrophages and repairing cells were investigated by Zhu

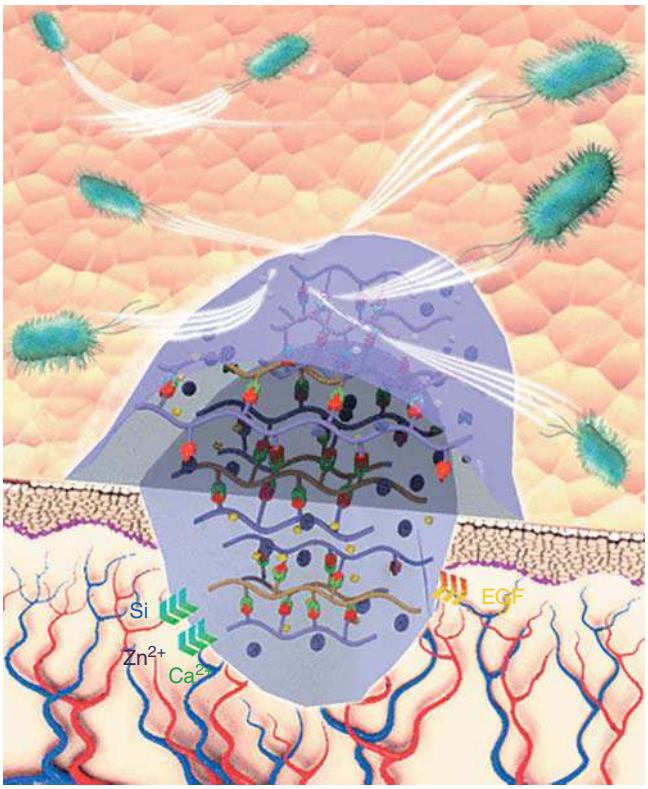

Figure 6.11 Schematic representation of new tissue formation with angiogenesis and antibacterial efficacy of zinc bioactive glass composite hydrogels [63].

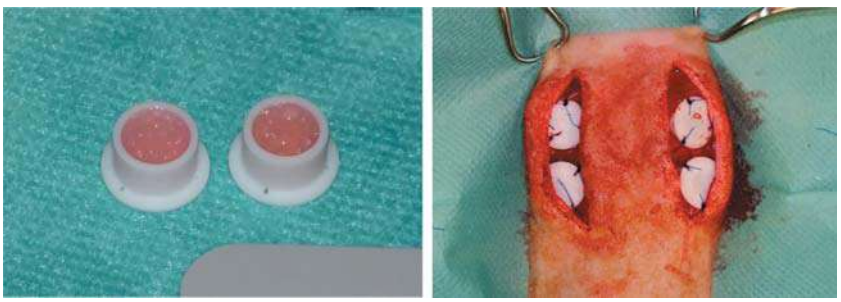

(a) (b)

Figure 6.12 Pictures of bioactive glass-based hydrogels. (a) Teflon chambers filled with nano bioactive glass composite hydrogels. (b) Subcutaneous implantation of hydrogels on Lewis rats and after results evidences good *in vitro* compatibility. Source: Rottensteiner et al. [59], Figure 01, p. 06/with permission of MDPI.

et al. [66]. Their results provide an insight into the biomaterial–immune system interactions and demonstrate that modulation of macrophages by BG/SA hydrogel in the inflammatory response is crucial in skin regeneration enhanced by the hydrogel [66]. Some of the earlier reports on bioactive glass scaffolds prepared by hydrogel method and its essential properties are listed in Table 6.2.

Table 6.2 Earlier works of bioactive glass scaffolds prepared by the hydrogel method.

Glass composition	Swelling ratio	Mechanical property	Tissue engineering applications	Cell culture studies	References
Silver-doped bioactive glass (BG) in a chitosan (CS) hydrogel at a 1 : 1 wt ratio (Ag-BG/CS)	—	—	Endodontic regeneration	Dental pulp cells	[54]
Bioactive-glass-reinforced gellan-gum spongy-like hydrogels $70SiO_2$–30CaO (% n/n) $66SiO_2$–22CaO–$10Na_2O$–$2P_2O_5$ (% n/n)	—	Young's modulus (225 MPa)	Osteogenic differentiation	Human adipose stem cells	[55]
$0.2SrO/0.2Na_2O/0.1CaO/0.1ZnO/0.4SiO_2$ (mol. fraction) PEGDMA-photopoly-merization	50%	Young's modulus (2–8 MPa)	Bone graft substitutes in cancellous bone defects	—	[45]
BG/gelatin methacryloyl (GelMA) molar ratio of SiO_2:CaO:P_2O_5 = 40 : 45 : 15	75%	Compressive modulus of 237.9 kPa	Bone regeneration		[65]
Dextran (Dex) and sol–gel derived bioactive glass ceramic nanoparticles (nBGC: 0–16 (wt%))	Pore size of 240 µm. Swelling capacity up to 1200%	Compressive modulus, 33.42 and 76.61 kPa	Bone tissue engineering	Human osteoblasts	[67]
Copper-containing bioactive glass nanoparticles (Cu-BG NPs)/chitosan (CH)/silk fibroin (SF)/glycerophos-phate (GP) composites	—	—	Cell-free bone repair	MC3T3-E1 and human umbilical vein endothelial cells	[68]

(*continued*)

Table 6.2 (Continued)

Glass composition	Swelling ratio	Mechanical property	Tissue engineering applications	Cell culture studies	References
Alginate dialdehyde-gelatin (ADA-GEL) constructs incorporating bioactive glass nanoparticles (BGNPs) with the composition SiO_2–CaO–P_2O_5 (mol%) = 55 : 40 : 5	—	—	Bone tissue engineering	MG-63 cells	[64]
Zinc-doped bioactive glass (ZBG) nanoparticles (60 mol% SiO_2, 30 mol% CaO, 5 mol% ZnO, 5 mol% P_2O_5)	Swelling ratio of gel is close to 560%	—	Wound dressing	Epidermal growth factor (EGFs)	[63]
Gelatin collagen bioactive glass nanocomposite (Gel/Col/BG). BG consisting of 45% SiO_2, 24.5% Cao, 24.5% Na_2O, and 6% P_2O_5 mol%	Porosity 85%	—	**Myocardial tissue engineering**	Endometrial stromal stem cells (EnScs)	[69]

6.4.3 Electrospinning Method

Scaffolds prepared by electrospinning method give us engineered 3D fibrous structures that can act as functional tissues. The electrospun fiber mats have the ability to mimic extracellular matrix (ECM), and hence provide the room for oxygen and nutrient circulation to the nearby tissues and enhance the ability for tissue regeneration. The era of electrospinning started from the year 1930s, and during those time, it was named as electrostatic spinning; later in 1990s, it is termed as electrospinning as it involved the combination of two techniques viz electrospray and spinning. The solution used for electrospinning has higher molecular weight polymers, that has been feed through a syringe nozzle and the droplet outlet is applied with high electric field difference. The resulting fibers at the counter side of the potential, often called as collector will collect the linear fibers as mats [70]. The fiber size can be altered from nano- to micron-size and also as hollow fiber based on the choice of solvent used for preparing the sol for electrospinning. These wide adjustable fabrication methodology opens the possibility of developing it as therapeutic scaffolding [71–74].

The electrospun fiber mats are in the form of loosely networked 3D porous mats with higher porosity and hence also has higher surface area. Due to this advantageous structure and

functionalization potentiality of the scaffold material, it can mimic the ECM with good biocompatibility and optimal biodegradability. Earlier works show that the scaffold 3D architecture also has prominent role in affecting cell attachment and proliferation [71, 75, 76]. For tissue engineering applications, compared to micron fibers, nanostructure fibers with microporous arrangement have greater cell binding affinity and also have higher rate of protein adsorption. Both synthetic and natural polymers will be used for electrospinning process. Polymer composited with bioceramics shows higher potentialities for bone tissue engineering applications. Multilayered assemblies of fibers including nonwoven fiber mesh, patterned fiber mesh, and random structures were arranged for the need of the end applications [77]. Some of the electrospun fibers show limited toxicity, poor cell infiltration, and differentiation due to the choice of solvent for electrospinning process. To overcome this limitation, cell-electrospinning (C-ES) method gives greater possibilities for higher compatible scaffold fabrication. Even though this process is new from 2006, lot of works were explored in this field as cells were loaded inside the fibers and have higher infiltration and compatibility during soft tissue engineering applications [78, 79].

As this process mostly depends on the polymer chemistry, an interface between the composited bioactive glass with polymers needs to be understood for sol preparation for electrospinning process. Most of the electrospinning sol were prepared by mixing sintered bioactive glass powders at different ratio to the polymer sol. Compared to micron-sized nanopowders nano-bioactive glass powders mixed polymer sol shows higher rate of apatite formation. The polymers can be of natural soy protein isolate (SPI), silk fiber, or synthetic polymers such as polycaprolactone (PCL) and chitosan macromolecules [80, 81]. In addition to pure bioactive glass incorporation in polymer matrix, some of the works on cerium-doped bioactive glass and strontium–copper doped bioactive glass were also a promising result for tissue engineering applications [82, 83]. Especially strontium–copper bioactive glass fibers have shown potential for bone regeneration and angiogenesis properties [83]. Bioactive glass nanofibers with B and Co also show enhancement in the vascular endothelial growth factor and there by promoting angiogenesis for soft tissue engineering application [84]. When bioactive glass particles in the form of mesoporous structuring have excellent drug loading efficacy, they also had therapeutic potentialities [85]. In addition to the bioactive glass particle incorporated into polymer fiber mats, some literatures were also focused on bioactive glass sol mixed polymer solution and heat treatment after obtaining the fiber mats. For 45S5, bioactive glass fibers obtained from its sol-based electrospinning, after heat treatment there occurs crystalline phase formation. And thus, the bioactivity of the crystal structures formed in the fibers needs to be evaluated and based on this calcination temperature need to be optimized [86]. In sol-based bioactive glass fiber preparation, 70S bioactive glass systems show good cell compatibility in both osteoblast and chondrocytes [87]. Some of the polymer/bioactive glass fibers with nanostructured morphology also suggested for the treatment for oral lesion. The procedure for that poly/bioactive glass fibers is shown in Figure 6.13 [88]. There is also an increase in the mechanical property in the presence of bioactive sol-prepared fiber mats [89]. Some of the electrospun bioglass fibers can also be composited/layered with silk yarn [87]. Coaxial or hollow fiber mats were also achievable by the electrospinning method. One of the methods shows obtaining sub-micron bioactive glass tubes by modifying the nozzle by injecting mineral oil to the core and bioactive glass as shell, with the resultant as homogenous hollow fiber mats, used for drug delivery applications [90]. Some of the earlier reports on bioactive glass scaffolds prepared by the electrospinning method and its essential properties are listed in Table 6.3.

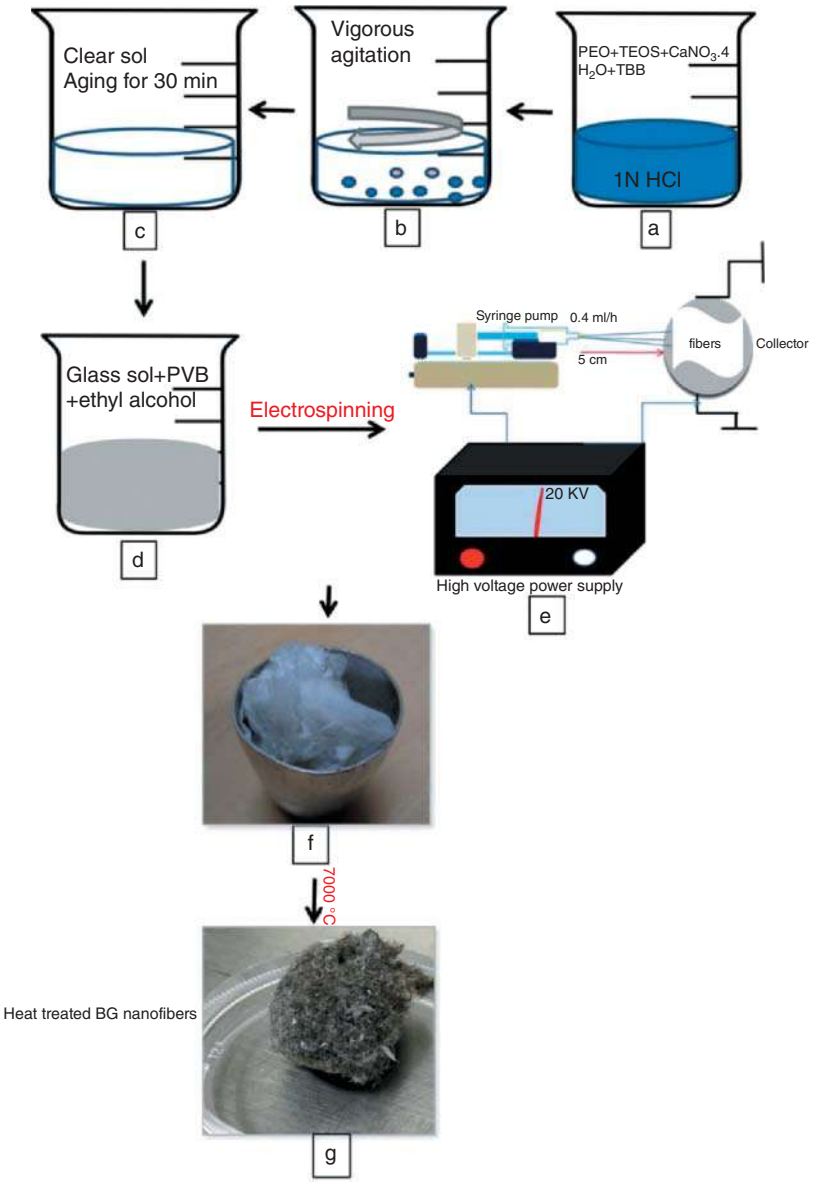

Figure 6.13 Schematic representation of fabrication of bioactive glass fibers by electrospinning method. Where (a–d) represent the procedure for the preparation of composited polymer/bioactive glass sol. (e) Pictorial representation of electrospun fiber. (f–g) Before and after heat-treatment of electrospun bioglass fibers. Source: Based on Reardon et al. [87], Abstract Figure, p. 49/with permission of American Chemical Society.

6.4.4 3D Printing Method

Each human system is complex and has its own individuality in physiological structuring and its dependent functioning. During diseased or defective conditions, the biomaterial supports developed in the structure of the defect will be of much compatible fixing, and this opens the era of customized implantation by 3D printing method. This method was first widely explored by additive

Table 6.3 Earlier works of bioactive glass scaffolds prepared by the electrospinning method.

Glass composition	Porosity/porous%	Mechanical property	Tissue engineering applications	Cell culture studies	References
Silk fibroin/polyvinyl alcohol/sol–gel bioactive glass (58S) composite	—	UTS was 9.2 ± 0.6 MPa	Bone tissue grafts	Cord blood derived mesenchymal stem cells	[91]
Soy protein isolate (SPI)/nano- and micron-sized 45S5 bioactive glass (BG) powders	0.01–4.2 μm	UTS 1.04 N/mm^2	Tissue engineering	MEF cells	[80]
PCL/chitosan	—	Ultimate tensile strength (UTS) 17 ± 11 MPa	Bone tissue engineering		[81]
Polycaprolactone (PCL) fiber mats embedded with B and Co codoped bioactive glass nanoparticles (BCo.BGNs)	—	Young's modulus 11 ± 3	Soft tissue engineering	ST-2 cells	[84]
70S bioactive glass/silk layer	Pore diameter 0.97 ± 0.34 μm	Elastic modulus (MPa) 86.66 ± 4.32	Bone tissue engineering	MG63–osteoblast	[88]
Gelatin and bioactive glass (BG-70S)	—	Tensile strength of 4.3 ± 1.2 MPa	Bone regeneration	MC3T3-E1 cells	[92]
PLA and bioactive glass (BG-70S)	—	—	Regeneration of hard tissues	MC3T3-E1	[93]
Polycaprolactone-gelatin incorporating mesoporous bioactive glass nanoparticles (mBGn)	—	—	Novel osteogenic matrices	Stem cells derived from periodontal ligament	[85]
Polyhydroxybutyrate/ Poly(ε-caprolactone)/ 58S Sol–gel bioactive glass	—	Young's modulus 85–101 MPa	Biodegradable fibrous scaffolds for bone regeneration applications	MG-63	[94]

manufacturing (AM) technique that was quickly adopted in the field of biofabrication of scaffolds. The term "biofabrication" is also applied to the area of "organ-printing." The combinatory printing with microfluid channels inside the structures is also termed as "Organ-on-a-chip engineering," that has defined microscale fluid channels, intended to mimic the constructs that closely mimic the human organs. The works of developing cancer models by means of 3D printing methods give an opportunity to understand the drug response in the controlled environmental condition. With the advent of 3D printing, we predict that single-step fabrication of these devices will enable rapid design and cost-effective iterations in the development stage, facilitating rapid innovation in this field. AM technique has an advantage of creating specific shapes of 3D structures with high

precision, that is difficult in earlier methods. When adopting this technique in developing tissue engineering, we can fabricate scaffolds with defined geometry and at required pore structures [95]. Even though, it may be considered as similar to hydrogel scaffold, it has numerous advantages in precise control of inner pore structure that was limited in hydrogel method. The porous structuring helps for cell growth, proliferation, and organization of multiple cell types in the multilayer 3D structures of the scaffolds. Notable among the various *in vitro* systems of tissue engineering scaffolding is 3D bioprinting methodology for co-culturing of cells with low risk of cross-contamination [96]. This variability in porous structures in these scaffolds can also be utilized as drug-loaded scaffold with controlled degradation rate, which is one of the essential parameters for tissue regeneration. A detailed review on 3D bioprinting is contributed by Jose et al. [97]. Yet another important review on bioprinting of biomaterials is by Xinda Li et al. that clearly demonstrates from basic methodologies to future perspectives [98].

In the biofabrication method, a much higher percentage of importance is given for "bio-ink" preparation followed by the processing conditions. The basic concept of bio-ink preparation is developed by understanding the concepts of AM methods with added knowledge of cell compatibility and scaffold requirements. The bioprinting modalities are broadly classified under three types (Figure 6.14): (i) extrusion-based bioprinting (EBB), (ii) droplet-based bioprinting (DBB), and (iii) laser-based bioprinting (LBB). In EBB method, a small amount of bio-ink suspension is dispensed on the flat platform by means of shear force. The force at the nozzle output is controlled to get the optimal diameter of the cylindrical filaments that was moved in programmable manner to obtain desired 3D structure [99]. Particularly, when the bio-ink having a biomaterial solution containing living cells is subject to bioprinting, the stress induced to the cells due to extension and shear is also needed to be considered [100]. EBB method is the widely used method for bioprinting due to its distinct advantages by means of its outcome of high-density structures and also a cost-effective process. The DBB method of printing scaffold includes inkjet printing and acoustic-droplet-ejection. The bio-ink droplet formation and its size can be controlled by mechanical actuation, thermal, and piezoelectric mechanism [101]. DBB also offers several advantages including deposition of multiple types of different cells with higher free flow and at desired location. The LBB involves light amplification by stimulated emission of radiation (LASER) as an absorbing material, which causes solidification of the bio-ink during processing conditions [102]. Even though LBB has numerous

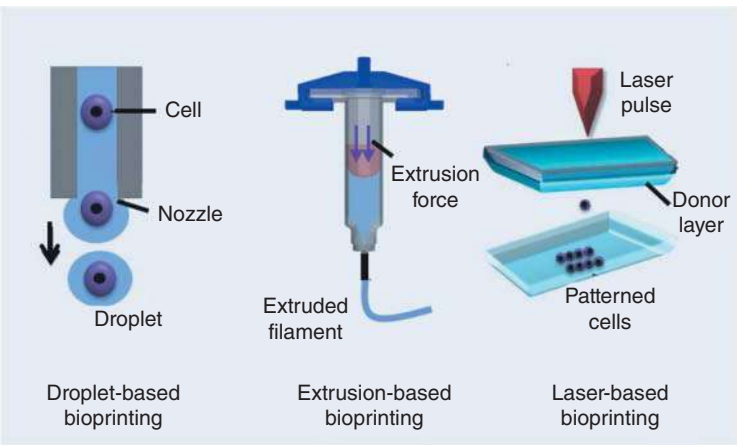

Figure 6.14 Modalities of bioprinting process for the fabrication of bioactive glass scaffolds [95].

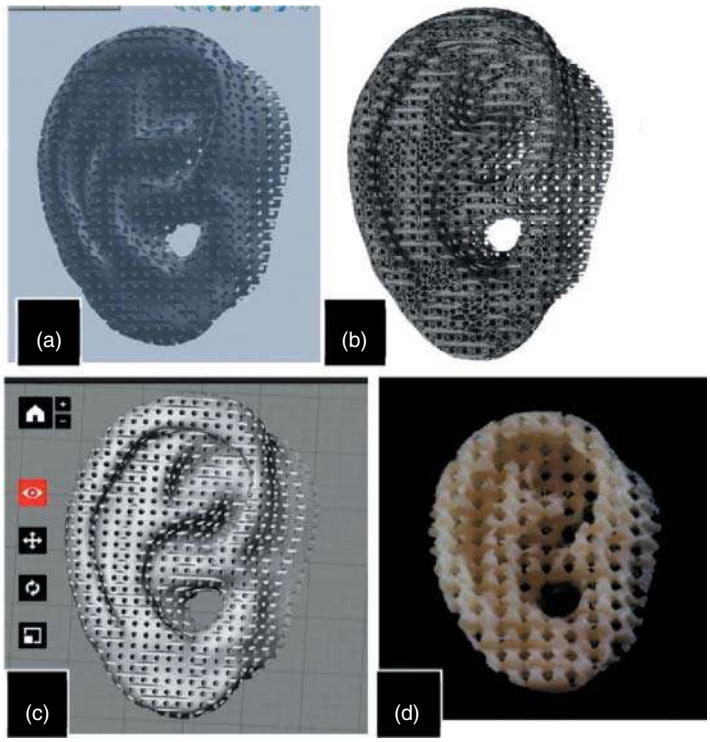

Figure 6.15 Steps involved in the 3D printing of scaffolds for biomedical applications. (a–c) 3D computer modeling, aligning, and slicing of various layers, (d) final 3D printed scaffold. Source: Tappa and Jammalamadaka [104].

advantages by means of developing precise fine structuring of scaffolds, it has its limitation in loading cells in the bio-ink. With a parallel development in the field of AM industrial revolution, 3D bioprinting is also adopted to new technologies and had the stable growth in fabricating medical devices with aesthetic geometries and tissue scaffolds. This method gives us a promising future toward patient-specific tissue modeling as a reality [103].

The scaffolds prepared by bioprinting method are often done with polymers that comprises both natural and synthetic polymers (Figure 6.15) [104]. These polymers act as a basic matrix in which bioceramics, drugs, and sometimes growth factors will be loaded for desired applications [105]. Bioactive glass in the form of powder will be loaded in the polymer bio-ink at a suitable proportion to alter the mechanical and enhance the mechanical property of the end products. ADA-GEL constructs incorporating strontium-doped bioactive glass nanoparticles (BGNPs) show good results with higher apatite formation, cell distribution, and has high efficiency in ibuprofen drug delivery studies [59, 64]. Adeptly, in the presence of mesoporous bioactive glass incorporated bio-inks, in addition to apatite formation, it also opens the possibility of drug-incorporated 3D printable gel with sustained drug release performances. One notable work is mesoporous bioactive glass, sodium alginate and gelatin composited scaffold co-printed with Naringin, and calcitonin gene-related peptide that shows a steady release for two days with good biocompatible properties [106]. In this similar type of composited scaffold instead of sodium alginate oxidized chondroitin sulfate (OCS) was also shown similar properties [107]. Chondroitin sulfate (CS) is a glycosaminoglycan found in the non-collagenous ECM of human bone and incorporation of this compound in hydrogels

shows potential toward improving bone regeneration. However, in both these cases, mesoporous bioactive glass plays a major role in enhancing the mechanical property and biomineralization for bone tissue engineering applications. The bio-ink prepared by wood-based cellulose nanofibrils (CNF) and bioactive glass (BG) incorporated gelatin–alginate shows optimal biological and physicochemical properties. This work elucidates that the rheological properties of the bio-ink can be adjustable with the ratio of bioactive glass and it greatly helps the structural property of the resultant hydrogel scaffolds [108]. The 50 : 50 PCL/13-93B3 glass with bioactive borate glass (13-93B3) shows higher degradation percentage during *in vitro* condition and recently proposed for both hard and soft tissue engineering applications [109, 110]. This glass is also a Food and Drug Administration (FDA)-approved material currently widely used for soft tissue regeneration and vascularization, wound repair. For these types of borate glasses, melt-based 3D printing can also be achieved due to high temperature glass phase stability [111]. Some of the earlier reports on bioactive glass scaffolds prepared by the 3D printing method and its essential properties are listed in Table 6.4.

Table 6.4 Earlier works of bioactive glass scaffolds prepared by the 3D printing method.

Glass composition	Porosity/porous%	Mechanical property	Tissue engineering applications	Cell culture studies	References
PCL + 13-93B3	Pore size of ~400 μm	—	—	—	[109]
ADA-GEL incorporated Sr-BGNPs		—	Bone tissue engineering	MG 63	[64]
Wood-based cellulose nanofibrils (CNF) and bioactive glass (BaG) incorporated gelatin–alginate bio-inks	Pore size of ~400 μm	—	Bone tissue engineering applications	Saos-2 and human bone marrow-derived mesenchymal stem cells (hBMSCs)	[108]
Mesoporous bioactive glass/sodium alginate/gelatin	80% porosity	—	Bone tissue engineering	MG-63 cell	[106]
Mesoporous bioactive glass/oxidized chondroitin sulfate (OCS)/gelatin	Pore size of the stent is 200–350 μm	Compression modulus ~58 kPa	Bone regeneration/repair applications	Rat bone marrow mesenchymal stem cells *in vitro* and rat cranial defect restoration *in vivo*	[107]
MBG/silk fiber	Porosity 70%	Compressive strength 19.9 ± 0.6 MPa	Bone tissue engineering	hBMSCs	[112]

6.5 Conclusion

Understanding the evolution, chemical, physical, and morphological nature of human system is still an unresolved area of research. However, treating human needs for diseased, damaged, and restoration requires new biocompatible materials for treatment conditions. The fourth-generation tissue engineering scaffolds have a lot of regenerative potentialities and also have flexibility to modify their various structures. This advantage opens the futuristic era of customized implantation and 3D bioprinting. This also makes promises for the development of 4D scaffolds which involve combination of 3D patterning with microtubule structuring and dynamic shape changing scaffolds [113, 114]. All these developments are aimed to make biomaterial scaffolds as near as the performance of biological tissues, attaining the ability to self-heal and remodel with response to external stimuli with good mechanical properties. As for now, the bioactive glasses are very promising for bone tissue engineering applications, whereas for 3D scaffolding and flexibility of it toward structuring and controlled degradability with higher tissue compatibility hybrid scaffolds are one best option. As some of the works mentioned in this chapter, altering the glass system without compromising the basic potentiality of bioglass of its apatite formation, in future it can also be optimized for both soft and hard tissue regeneration.

Acknowledgment

One of the authors D. Durgalakshmi gratefully acknowledges DST-INSPIRE Faculty Fellowship under the sanction DST/INSPIRE/04/2016/000845.

References

1 Ratner, B.D., Hoffman, A.S., Schoen, F. et al. (2013). *Introduction – Biomaterials Science: An Evolving, Multidisciplinary Endeavor*. Cambridge, MA: Elsevier, Academic Press.

2 Bangru, S., Arif, W., Seimetz, J. et al. (2018). Alternative splicing rewires Hippo signaling pathway in hepatocytes to promote liver regeneration. *Nature Structural & Molecular Biology* 25 (10): 928–939.

3 Goldberg, M., Kulkarni, A.B., Young, M., and Boskey, A. (2011). Dentin: structure, composition and mineralization: the role of dentin ECM in dentin formation and mineralization. *Frontiers in Bioscience* 3: 711.

4 Li, R., Clark, A., and Hench, L. (1991). An investigation of bioactive glass powders by sol–gel processing. *Journal of Applied Biomaterials* 2 (4): 231–239.

5 Saravanapavan, P., Jones, J.R., Verrier, S. et al. (2004). Binary $CaO–SiO_2$ gel-glasses for biomedical applications. *Bio-Medical Materials and Engineering* 14 (4): 467–486.

6 Beall, G.H. (2016). Dr. S. Donald (Don) Stookey (1915–2014): Pioneering researcher and adventurer. *Frontiers in Materials* 3: 37.

7 Li, A. and Qiu, D. (2011). Phytic acid derived bioactive $CaO–P_2O_5–SiO_2$ gel-glasses. *Journal of Materials Science – Materials in Medicine* 22 (12): 2685–2691.

8 Vallet-Regí, M. and Arcos, D. (2008). *Biomimetic Nanoceramics in Clinical Use: From Materials to Applications*. Royal Society of Chemistry.

9 Sasaki, Y., Ishii, K., Arahata, D., and Iguchi, M. (2000). Rupture phenomena of molten alkali silicate thin films. *ISIJ International* 40 (10): 949–953.

10 Kwiatkowska, J., Suchanek, K., and Rajchel, B. (2012). Bioactive glass coatings synthesized by pulsed laser deposition technique. *Acta Physica Polonica A* 121 (2): 502–505.

11 Best, S.M., Porter, A.E., Thian, E.S., and Huang, J. (2008). Bioceramics: past, present and for the future. *Journal of the European Ceramic Society* 28 (7): 1319–1327.

12 O'Donnell, M.D. (2012). Melt-derived bioactive glass. In: *Bio-glasses* (ed. J.R. Jones and A.G. Clare), 13–28. Chichester: Wiley.

13 Katoueizadeh, E., Rasouli, M., and Zebarjad, S.M. (2020). A comprehensive study on the gelation process of silica gels from sodium silicate. *Journal of Materials Research and Technology* 9 (5): 10157–10165.

14 Yu, B., Turdean-Ionescu, C.A., Martin, R.A. et al. (2012). Effect of calcium source on structure and properties of sol–gel derived bioactive glasses. *Langmuir* 28 (50): 17465–17476.

15 Ben-Arfa, B.A., Fernandes, H.R., Miranda Salvado, I.M. et al. (2018). Synthesis and bioactivity assessment of high silica content quaternary glasses with Ca:P ratios of 1.5 and 1.67, made by a rapid sol–gel process. *Journal of Biomedical Materials Research Part A* 106 (2): 510–520.

16 Ben-Arfa, B.A., Palamá, I.E., Salvado, I.M.M. et al. (2020). The role of calcium (source & content) on the in vitro behaviour of sol–gel quaternary glass series. *Ceramics International* 46 (1): 1065–1075.

17 Szu, S.P., Klein, L., and Greenblatt, M. (1992). Effect of precursors on the structure of phosphosilicate gels: 29Si and 31P MAS-NMR study. *Journal of Non-Crystalline Solids* 143: 21–30.

18 Izquierdo-Barba, I., Salinas, A.J., and Vallet-Regí, M. (2013). Bioactive glasses: from macro to nano. *International Journal of Applied Glass Science* 4 (2): 149–161.

19 Brinker, C.J. and Scherer, G.W. (2013). *Sol–Gel Science: The Physics and Chemistry of Sol–Gel Processing*. Academic Press.

20 Zheng, K. and Boccaccini, A.R. (2017). Sol–gel processing of bioactive glass nanoparticles: a review. *Advances in Colloid and Interface Science* 249: 363–373.

21 Zhong, J. and Greenspan, D.C. (2000). Processing and properties of sol–gel bioactive glasses. *Journal of Biomedical Materials Research* 53 (6): 694–701.

22 Naruphontjirakul, P., Greasley, S.L., Chen, S. et al. (2016). Monodispersed strontium containing bioactive glass nanoparticles and MC3T3-E1 cellular response. *Biomedical Glasses* 2 (1): 72–81.

23 Yun, H.-s., Kim, S.-h., Lee, S., and Song, I.-h. (2010). Synthesis of high surface area mesoporous bioactive glass nanospheres. *Materials Letters* 64 (16): 1850–1853.

24 Zheng, K., Taccardi, N., Beltrán, A.M. et al. (2016). Timing of calcium nitrate addition affects morphology, dispersity and composition of bioactive glass nanoparticles. *RSC Advances* 6 (97): 95101–95111.

25 Hench, L.L. and Polak, J.M. (2002). Third-generation biomedical materials. *Science* 295 (5557): 1014–1017.

26 Tabia, Z., El Mabrouk, K., Bricha, M., and Nouneh, K. (2019). Mesoporous bioactive glass nanoparticles doped with magnesium: drug delivery and acellular in vitro bioactivity. *RSC Advances* 9 (22): 12232–12246.

27 Vacanti, C.A. (2006). The history of tissue engineering. *Journal of Cellular and Molecular Medicine* 10 (3): 569–576.

28 O'brien, F.J. (2011). Biomaterials & scaffolds for tissue engineering. *Materials Today* 14 (3): 88–95.

29 Durgalakshmi, D. and Balakumar, S. (2015). Analysis of solvent induced porous PMMA–Bioglass monoliths by the phase separation method – mechanical and in vitro biocompatible studies. *Physical Chemistry Chemical Physics* 17 (2): 1247–1256.

30 Guilak, F., Butler, D.L., Goldstein, S.A., and Baaijens, F. (2014). Biomechanics and mechanobiology in functional tissue engineering. *Journal of Biomechanics* 47: 1933–1940.

31 Ros-Tárraga, P., Murciano, A., Mazón, P. et al. (2017). New 3D stratified Si–Ca–P porous scaffolds obtained by sol–gel and polymer replica method: microstructural, mineralogical and chemical characterization. *Ceramics International* 43 (8): 6548–6553.

32 Cabanas-Polo, S., Philippart, A., Boccardi, E. et al. (2016). Facile production of porous bioactive glass scaffolds by the foam replica technique combined with sol–gel/electrophoretic deposition. *Ceramics International* 42 (5): 5772–5777.

33 Ryu, J.-H., Kwon, J.-S., Kim, K.-M. et al. (2019). Synergistic effect of porous hydroxyapatite scaffolds combined with bioactive glass/poly(lactic-*co*-glycolic acid) composite fibers promotes osteogenic activity and bioactivity. *ACS Omega* 4 (1): 2302–2310.

34 Erasmus, E., Sule, R., Johnson, O. et al. (2018). In vitro evaluation of porous borosilicate, borophosphate and phosphate bioactive glasses scaffolds fabricated using foaming agent for bone regeneration. *Scientific Reports* 8 (1): 1–13.

35 Poologasundarampillai, G., Lee, P.D., Lam, C. et al. (2016). Compressive strength of bioactive sol–gel glass foam scaffolds. *International Journal of Applied Glass Science* 7 (2): 229–237.

36 Li, W., Ding, Y., Rai, R. et al. (2014). Preparation and characterization of PHBV microsphere/45S5 bioactive glass composite scaffolds with vancomycin releasing function. *Materials Science and Engineering C* 41: 320–328.

37 Nooeaid, P., Li, W., Roether, J.A. et al. (2014). Development of bioactive glass based scaffolds for controlled antibiotic release in bone tissue engineering via biodegradable polymer layered coating. *Biointerphases* 9 (4): 041001.

38 Li, W., Wang, H., Ding, Y. et al. (2015). Antibacterial 45S5 Bioglass®-based scaffolds reinforced with genipin cross-linked gelatin for bone tissue engineering. *Journal of Materials Chemistry B* 3 (16): 3367–3378.

39 Vitale-Brovarone, C., Miola, M., Balagna, C., and Verné, E. (2008). 3D-glass–ceramic scaffolds with antibacterial properties for bone grafting. *Chemical Engineering Journal* 137 (1): 129–136.

40 Fu, Q., Rahaman, M.N., Bal, B.S. et al. (2008). Mechanical and in vitro performance of 13-93 bioactive glass scaffolds prepared by a polymer foam replication technique. *Acta Biomaterialia* 4 (6): 1854–1864.

41 Boccardi, E., Philippart, A., Juhasz-Bortuzzo, J. et al. (2015). Characterisation of Bioglass based foams developed via replication of natural marine sponges. *Advances in Applied Ceramics* 114 (sup1): S56–S62.

42 Jones, J.R., Ehrenfried, L.M., and Hench, L.L. (2006). Optimising bioactive glass scaffolds for bone tissue engineering. *Biomaterials* 27 (7): 964–973.

43 Mantsos, T., Chatzistavrou, X., Roether, J. et al. (2009). Non-crystalline composite tissue engineering scaffolds using boron-containing bioactive glass and poly(D,L-lactic acid) coatings. *Biomedical Materials* 4 (5): 055002.

44 Kumar, A. and Han, S.S. (2017). PVA-based hydrogels for tissue engineering: a review. *International Journal of Polymeric Materials and Polymeric Biomaterials* 66 (4): 159–182.

45 Killion, J.A., Kehoe, S., Geever, L.M. et al. (2013). Hydrogel/bioactive glass composites for bone regeneration applications: synthesis and characterisation. *Materials Science and Engineering C* 33 (7): 4203–4212.

46 El-Sherbiny, I.M. and Yacoub, M.H. (2013). Hydrogel scaffolds for tissue engineering: progress and challenges. *Global Cardiology Science & Practice* 2013 (3): 38.

47 Spicer, C.D. (2020). Hydrogel scaffolds for tissue engineering: the importance of polymer choice. *Polymer Chemistry* 11 (2): 184–219.

48 Hunt, J.A., Chen, R., van Veen, T., and Bryan, N. (2014). Hydrogels for tissue engineering and regenerative medicine. *Journal of Materials Chemistry B* 2 (33): 5319–5338.

49 Lee, S.C., Kwon, I.K., and Park, K. (2013). Hydrogels for delivery of bioactive agents: a historical perspective. *Advanced Drug Delivery Reviews* 65 (1): 17–20.

50 Sivashanmugam, A., Kumar, R.A., Priya, M.V. et al. (2015). An overview of injectable polymeric hydrogels for tissue engineering. *European Polymer Journal* 72: 543–565.

51 Fu, L.-H., Qi, C., Ma, M.-G., and Wan, P. (2019). Multifunctional cellulose-based hydrogels for biomedical applications. *Journal of Materials Chemistry B* 7 (10): 1541–1562.

52 Rao, K.M., Kumar, A., and Han, S.S. (2018). Polysaccharide-based magnetically responsive polyelectrolyte hydrogels for tissue engineering applications. *Journal of Materials Science and Technology* 34 (8): 1371–1377.

53 Bargavi, P., Ramya, R., Chitra, S. et al. (2020). Bioactive, degradable and multi-functional three-dimensional membranous scaffolds of bioglass and alginate composites for tissue regenerative applications. *Biomaterials Science* 8 (14): 4003–4025.

54 Zhu, N., Chatzistavrou, X., Ge, L. et al. (2019). Biological properties of modified bioactive glass on dental pulp cells. *Journal of Dentistry* 83: 18–26.

55 Gantar, A., da Silva, L.P., Oliveira, J.M. et al. (2014). Nanoparticulate bioactive-glass-reinforced gellan-gum hydrogels for bone-tissue engineering. *Materials Science and Engineering C* 43: 27–36.

56 Vuornos, K., Ojansivu, M., Koivisto, J.T. et al. (2019). Bioactive glass ions induce efficient osteogenic differentiation of human adipose stem cells encapsulated in gellan gum and collagen type I hydrogels. *Materials Science and Engineering C* 99: 905–918.

57 Moreira, C.D., Carvalho, S.M., Mansur, H.S., and Pereira, M.M. (2016). Thermogelling chitosan–collagen–bioactive glass nanoparticle hybrids as potential injectable systems for tissue engineering. *Materials Science and Engineering C* 58: 1207–1216.

58 Moreira, C.D., Carvalho, S.M., Sousa, R.G. et al. (2018). Nanostructured chitosan/gelatin/bioactive glass in situ forming hydrogel composites as a potential injectable matrix for bone tissue engineering. *Materials Chemistry and Physics* 218: 304–316.

59 Rottensteiner, U., Sarker, B., Heusinger, D. et al. (2014). In vitro and in vivo biocompatibility of alginate dialdehyde/gelatin hydrogels with and without nanoscaled bioactive glass for bone tissue engineering applications. *Materials* 7 (3): 1957–1974.

60 Moreira, C.D., Carvalho, S.M., Florentino, R.M. et al. (2019). Injectable chitosan/gelatin/bioactive glass nanocomposite hydrogels for potential bone regeneration: in vitro and in vivo analyses. *International Journal of Biological Macromolecules* 132: 811–821.

61 Couto, D.S., Hong, Z., and Mano, J.F. (2009). Development of bioactive and biodegradable chitosan-based injectable systems containing bioactive glass nanoparticles. *Acta Biomaterialia* 5 (1): 115–123.

62 Gantar, A., Drnovšek, N., Casuso, P. et al. (2016). Injectable and self-healing dynamic hydrogel containing bioactive glass nanoparticles as a potential biomaterial for bone regeneration. *RSC Advances* 6 (73): 69156–69166.

63 Zhu, J., Jiang, G., Song, G. et al. (2019). Incorporation of ZnO/bioactive glass nanoparticles into alginate/chitosan composite hydrogels for wound closure. *ACS Applied Bio Materials* 2 (11): 5042–5052.

64 Leite, Á.J., Sarker, B., Zehnder, T. et al. (2016). Bioplotting of a bioactive alginate dialdehyde-gelatin composite hydrogel containing bioactive glass nanoparticles. *Biofabrication* 8 (3): 035005.

65 Zheng, J., Zhao, F., Zhang, W. et al. (2018). Sequentially-crosslinked biomimetic bioactive glass/gelatin methacryloyl composites hydrogels for bone regeneration. *Materials Science and Engineering C* 89: 119–127.

66 Zhu, Y., Ma, Z., Kong, L. et al. (2020). Modulation of macrophages by bioactive glass/sodium alginate hydrogel is crucial in skin regeneration enhancement. *Biomaterials* 256: 120216.

67 Nikpour, P., Salimi-Kenari, H., Fahimipour, F. et al. (2018). Dextran hydrogels incorporated with bioactive glass-ceramic: nanocomposite scaffolds for bone tissue engineering. *Carbohydrate Polymers* 190: 281–294.

68 Wu, J., Zheng, K., Huang, X. et al. (2019). Thermally triggered injectable chitosan/silk fibroin/bioactive glass nanoparticle hydrogels for in-situ bone formation in rat calvarial bone defects. *Acta Biomaterialia* 91: 60–71.

69 Barabadi, Z., Azami, M., Sharifi, E. et al. (2016). Fabrication of hydrogel based nanocomposite scaffold containing bioactive glass nanoparticles for myocardial tissue engineering. *Materials Science and Engineering C* 69: 1137–1146.

70 Dhinasekaran, D., Selvaraj, V., Rajendran, A.R. et al. (2021: 111856). Bio-inspired multifunctional collagen/electrospun bioactive glass membranes for bone tissue engineering applications. *Materials Science and Engineering C* 126.

71 Agarwal, S., Wendorff, J.H., and Greiner, A. (2008). Use of electrospinning technique for biomedical applications. *Polymer* 49 (26): 5603–5621.

72 Robb, B. and Lennox, B. (2011). The electrospinning process, conditions and control. In: *Electrospinning for Tissue Regeneration* (ed. L.A. Bosworth and S. Downes), 51–66. Elsevier.

73 Wang, L. and Ryan, A. (2011). Introduction to electrospinning. In: *Electrospinning for Tissue Regeneration* (ed. L.A. Bosworth and S. Downes), 3–33. Elsevier.

74 Durgalakshmi, D. and Balakumar, S. (2015). Phase separation induced shell thickness variations in electrospun hollow Bioglass 45S5 fiber mats for drug delivery applications. *Physical Chemistry Chemical Physics* 17 (23): 15316–15323.

75 Braghirolli, D.I., Steffens, D., and Pranke, P. (2014). Electrospinning for regenerative medicine: a review of the main topics. *Drug Discovery Today* 19 (6): 743–753.

76 Barker, T.H. (2011). The role of ECM proteins and protein fragments in guiding cell behavior in regenerative medicine. *Biomaterials* 32 (18): 4211–4214.

77 Teo, W.E. and Ramakrishna, S. (2006). A review on electrospinning design and nanofibre assemblies. *Nanotechnology* 17 (14): R89.

78 Townsend-Nicholson, A. and Jayasinghe, S.N. (2006). Cell electrospinning: a unique biotechnique for encapsulating living organisms for generating active biological microthreads/scaffolds. *Biomacromolecules* 7 (12): 3364–3369.

79 Lim, S., Jatakanon, A., Meah, S. et al. (2000). Relationship between exhaled nitric oxide and mucosal eosinophilic inflammation in mild to moderately severe asthma. *Thorax* 55 (3): 184–188.

80 Tansaz, S., Liverani, L., Vester, L., and Boccaccini, A.R. (2017). Soy protein meets bioactive glass: electrospun composite fibers for tissue engineering applications. *Materials Letters* 199: 143–146.

81 Liverani, L., Lacina, J., Roether, J.A. et al. (2018). Incorporation of bioactive glass nanoparticles in electrospun PCL/chitosan fibers by using benign solvents. *Bioactive Materials* 3 (1): 55–63.

82 Saatchi, A., Arani, A.R., Moghanian, A., and Mozafari, M. (2021). Synthesis and characterization of electrospun cerium-doped bioactive glass/chitosan/polyethylene oxide composite scaffolds for tissue engineering applications. *Ceramics International* 47 (1): 260–271.

83 Weng, L., Boda, S.K., Teusink, M.J. et al. (2017). Binary doping of strontium and copper enhancing osteogenesis and angiogenesis of bioactive glass nanofibers while suppressing osteoclast activity. *ACS Applied Materials & Interfaces* 9 (29): 24484–24496.

84 Chen, S., Galusková, D., Kaňková, H. et al. (2020). Electrospun PCL fiber mats incorporating multi-targeted B and Co co-doped bioactive glass nanoparticles for angiogenesis. *Materials* 13 (18): 4010.

85 El-Fiqi, A., Kim, J.-H., and Kim, H.-W. (2015). Osteoinductive fibrous scaffolds of biopolymer/mesoporous bioactive glass nanocarriers with excellent bioactivity and long-term delivery of osteogenic drug. *ACS Applied Materials & Interfaces* 7 (2): 1140–1152.

86 Deliormanlı, A.M. (2015). Preparation and in vitro characterization of electrospun 45S5 bioactive glass nanofibers. *Ceramics International* 41 (1): 417–425.

87 Reardon, P., Konwarh, R., Knowles, J.C., and Mandal, B.B. (2017). Mimicking hierarchical complexity of the osteochondral interface using electrospun silk-bioactive glass composites. *ACS applied materials interfaces* 9 (9): 8000–8013.

88 Elshazly, N., Khalil, A., Saad, M. et al. (2020). Efficacy of bioactive glass nanofibers tested for oral mucosal regeneration in rabbits with induced diabetes. *Materials* 13 (11): 2603.

89 Gao, C., Gao, Q., Li, Y. et al. (2012). Preparation and in vitro characterization of electrospun PVA scaffolds coated with bioactive glass for bone regeneration. *Journal of Biomedical Materials Research Part A* 100 (5): 1324–1334.

90 Xie, J., Blough, E.R., and Wang, C.-H. (2012). Submicron bioactive glass tubes for bone tissue engineering. *Acta Biomaterialia* 8 (2): 811–819.

91 Singh, B. and Pramanik, K. (2017). Development of novel silk fibroin/polyvinyl alcohol/sol–gel bioactive glass composite matrix by modified layer by layer electrospinning method for bone tissue construct generation. *Biofabrication* 9 (1): 015028.

92 Gao, C., Gao, Q., Li, Y. et al. (2013). In vitro evaluation of electrospun gelatin-bioactive glass hybrid scaffolds for bone regeneration. *Journal of Applied Polymer Science* 127 (4): 2588–2599.

93 Noh, K.-T., Lee, H.-Y., Shin, U.-S., and Kim, H.-W. (2010). Composite nanofiber of bioactive glass nanofiller incorporated poly(lactic acid) for bone regeneration. *Materials Letters* 64 (7): 802–805.

94 Ding, Y., Li, W., Müller, T. et al. (2016). Electrospun polyhydroxybutyrate/poly(ε-caprolactone)/58S sol–gel bioactive glass hybrid scaffolds with highly improved osteogenic potential for bone tissue engineering. *ACS Applied Materials & Interfaces* 8 (27): 17098–17108.

95 Kang, Y., Datta, P., Shanmughapriya, S., and Ozbolat, I.T. (2020). 3D bioprinting of tumor models for cancer research. *ACS Applied Bio Materials* 3 (9): 5552–5573.

96 Peng, W., Unutmaz, D., and Ozbolat, I.T. (2016). Bioprinting towards physiologically relevant tissue models for pharmaceutics. *Trends in Biotechnology* 34 (9): 722–732.

97 Jose, R.R., Rodriguez, M.J., Dixon, T.A. et al. (2016). Evolution of bioinks and additive manufacturing technologies for 3D bioprinting. *ACS Biomaterials Science & Engineering* 2 (10): 1662–1678.

98 Li, X., Liu, B., Pei, B. et al. (2020). Inkjet bioprinting of biomaterials. *Chemical Reviews* 120 (19): 10793–10833.

99 Ozbolat, I.T. and Hospodiuk, M. (2016). Current advances and future perspectives in extrusion-based bioprinting. *Biomaterials* 76: 321–343.

100 Ning, L., Betancourt, N., Schreyer, D.J., and Chen, X. (2018). Characterization of cell damage and proliferative ability during and after bioprinting. *ACS Biomaterials Science & Engineering* 4 (11): 3906–3918.

101 Gudapati, H., Dey, M., and Ozbolat, I. (2016). A comprehensive review on droplet-based bioprinting: past, present and future. *Biomaterials* 102: 20–42.

102 Kingsley, D.M., Roberge, C.L., Rudkouskaya, A. et al. (2019). Laser-based 3D bioprinting for spatial and size control of tumor spheroids and embryoid bodies. *Acta Biomaterialia* 95: 357–370.

103 Wang, X., Molino, B.Z., Pitkänen, S. et al. (2019). 3D scaffolds of polycaprolactone/copper-doped bioactive glass: architecture engineering with additive manufacturing and cellular assessments in a coculture of bone marrow stem cells and endothelial cells. *ACS Biomaterials Science Engineering* 5 (9): 4496–4510.

104 Tappa, K. and Jammalamadaka, U. (2018). Novel biomaterials used in medical 3D printing techniques. *Journal of Functional Biomaterials* 9 (1): 17.

105 Jammalamadaka, U. and Tappa, K. (2018). Recent advances in biomaterials for 3D printing and tissue engineering. *Journal of functional biomaterials* 9 (1): 22.

106 Wu, J., Miao, G., Zheng, Z. et al. (2019). 3D printing mesoporous bioactive glass/sodium alginate/gelatin sustained release scaffolds for bone repair. *Journal of Biomaterials Applications* 33 (6): 755–765.

107 Zhou, L., Fan, L., Zhang, F.-M. et al. (2021). Hybrid gelatin/oxidized chondroitin sulfate hydrogels incorporating bioactive glass nanoparticles with enhanced mechanical properties, mineralization, and osteogenic differentiation. *Bioactive Materials* 6 (3): 890–904.

108 Ojansivu, M., Rashad, A., Ahlinder, A. et al. (2019). Wood-based nanocellulose and bioactive glass modified gelatin–alginate bioinks for 3D bioprinting of bone cells. *Biofabrication* 11 (3): 035010.

109 Kolan, K., Liu, Y., Baldridge, J. et al. (2017). Solvent based 3D printing of biopolymer/bioactive glass composite and hydrogel for tissue engineering applications. *Procedia CIRP* 65: 38–43.

110 Kolan, K.C., Semon, J.A., Bromet, B. et al. (2019). Bioprinting with human stem cell-laden alginate-gelatin bioink and bioactive glass for tissue engineering. *International Journal of Bioprinting* 5 (2.2): 204, 3–215.

111 Kolan, K., Li, W., Althage, R. et al. (2018). Solvent and melt based extrusion 3D printing of polycaprolactone bioactive glass composite for tissue engineering. In: *Proceedings of the 3rd International Conference on Progress in Additive Manufacturing, Singapore*, 14–17.

112 Du, X., Wei, D., Huang, L. et al. (2019). 3D printing of mesoporous bioactive glass/silk fibroin composite scaffolds for bone tissue engineering. *Materials Science and Engineering C* 103: 109731.

113 Zhao, W., Zhang, F., Leng, J., and Liu, Y. (2019). Personalized 4D printing of bioinspired tracheal scaffold concept based on magnetic stimulated shape memory composites. *Composites Science and Technology* 184: 107866.

114 Tamay, D.G., Dursun Usal, T., Alagoz, A.S. et al. (2019). 3D and 4D printing of polymers for tissue engineering applications. *Frontiers in Bioengineering and Biotechnology* 7: 164.

7

Processing of Bioactive Glass Scaffolds for Bone Tissue Engineering

Elisa Fiume[1], Carla Migneco[1], Saeid Kargozar[2], Enrica Verné[1], and Francesco Baino[1]

[1] *Institute of Materials Physics and Engineering, Department of Applied Science and Technology (DISAT), Politecnico di Torino, Torino, Italy*
[2] *Tissue Engineering Research Group (TERG), Department of Anatomy and Cell Biology, School of Medicine, Mashhad University of Medical Sciences, Mashhad, Iran*

7.1 Introduction

Bone grafting for the clinical management of medium-to-critically sized bone defects is currently considered a routine procedure, and more than 2 million surgeries are performed all over the world every year, thus making bone the second most frequently transplanted tissue after blood [1].

In the last decades, the scientific community has been involved in active and fruitful research activity to develop novel bone substitutes addressed to overcoming the limitations of the current therapies, which are still mainly based on the use of autologous and allogenic grafts from transplantation. Despite all the efforts, autologous bone continues to be considered the golden standard in bone grafting surgeries, but drawbacks deriving from its clinical usage are undeniable, thus creating a pressing need for more effective solutions.

From this perspective, synthetic bone substitutes may represent a high-value asset to be used either alone or in combination with cells and growth factor therapy in order to restore the original functionality of the native tissue [2].

The last approach is known by the name of bone tissue engineering (BTE), which was officially defined in 1993 as *an interdisciplinary field that applies the principles of engineering and life science toward the development of biological substitutes that restore, maintain or improve the tissue function* [3].

A schematic representation of a typical BTE cycle is provided in Figure 7.1.

In general, the key elements required for the implementation of a tissue engineering (TE) approach are the following:

(i) *Cells* which are essential for the synthesis of new tissues. The most beneficial approach for the individual to avoid the risk of rejection is the use of autologous cells directly collected by biopsy from the site of interest. Another option is represented by the use of stem cells, which are able to evolve to multiple cell lines by applying proper external stimulation. Currently, multipotent stem cells are used due to their easy availability within the human body; they are often collected from bone marrow and adipose tissue [4].

Bioactive Glasses and Glass-Ceramics: Fundamentals and Applications, First Edition.
Edited by Francesco Baino and Saeid Kargozar.

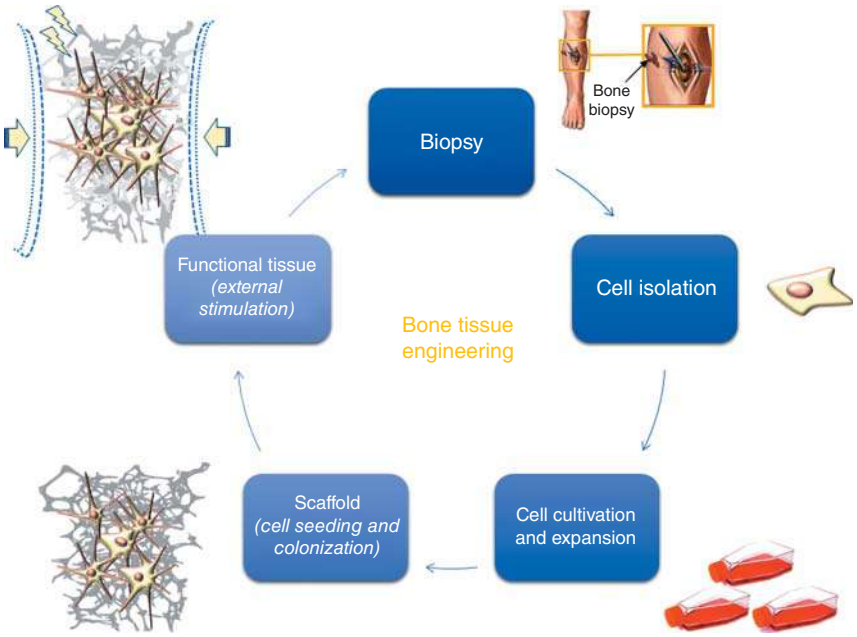

Figure 7.1 Schematic of a typical bone tissue engineering cycle including biopsy of the bone tissue, cell isolation, cell cultivation, and subsequent expansion, seeding on 3D porous scaffolds, and development of functional tissue by providing proper biochemical-physical stimulation (i.e. growth factors, mechanical loading, exposure to electrical fields).

(ii) *Scaffolds*, i.e. three-dimensional (3D) implantable devices, with specific physical, chemical, and biological properties to promote cell infiltration, adhesion, colonization, and differentiation until the formation of mature and functional tissue. Both natural and synthetic scaffolds are currently available. Natural scaffolds often derive from extracellular matrix (ECM) extracted by the patient or by donors, but scaffolds based on biopolymers can also be found, while synthetic scaffolds are made of biocompatible materials that are carefully designed in order to mimic the features of physiological tissue [5].

(iii) *Signals* required for the development of a functional tissue. They can be biological, chemical, or physical–mechanical. Specific stimulation procedures are able to affect cell pathways during the processes of proliferation and differentiation by fostering the evolution toward specific phenotypes. These signals are fundamental because they are able to guarantee cell survival and, therefore, it is required that all the cells in the scaffold are influenced by them likewise [6].

Undoubtedly, the main advantage related to the implementation of BTE strategies lies in the possibility to by-pass organs and tissue transplantation, which apart from the risks of rejection and transmission of pathologies, is usually associated to very long waiting lists due to the shortage of organs available for the transplant [7].

Thus, over the last decades, experimental research focused on bone regenerative strategies has been involved in the development of new-generation engineered synthetic bone grafts in order to meet this growing demand. Scaffold design requires a deep understanding of the overall biological and structural properties of the tissue for the optimization of the biological response after implantation [8]. Table 7.1 summarizes the main requirements which an ideal scaffold should exhibit in order to stimulate bone tissue growth and regeneration.

Table 7.1 List of the minimum requirement that a bone tissue engineering scaffold should exhibit.

Characteristic	Function	References
Biocompatibility	– Promote cell adhesion and proliferation – Promote cell differentiation and migration – Promote ECM synthesis – Induce minimal immune response	[9]
Bioactivity	– Create a stable bonding interface with the host tissue	[10]
Biodegradability	– Match the physiological healing time of the tissue – Do not release toxic degradation products	[11]
Mechanical properties	– Shear mechanical load with the host bone – Maintain mechanical integrity during degradation and tissue remodeling	[10]
3D-structure	– Open-cell architecture – Promote mass transport – Support cell migration, vascularization, and bone ingrowth	[11, 12]
Manufacturing technology	– Cost-effectiveness – Scalability – Repeatability/reliability – Sterilization, delivery, and storage of the final product	[10]

Over the last 30 years, several materials have been proposed for the fabrication of BTE scaffolds, including metals, ceramics, polymers, and composites, processed both by traditional techniques and the latest additive manufacturing (AM) technologies [13, 14]. Among these, bioactive glasses (BGs) indeed deserve a special attention [12, 15, 16]. In this chapter, BGs will be presented as promising biomaterials for the development of 3D porous scaffolds for BTE approaches, providing a brief overview of structural features and manufacturing processes that are currently available for their fabrication. Furthermore, applications of BG scaffolds in interfacial TE and tumor therapy/drug delivery will be briefly discussed as the new frontiers beyond "pure" bone regenerative purposes.

7.2 Critical Issues and Challenges Related to Bioactive Glass Scaffolds

Since the early 2000s, a great potential has been attributed to BGs to be used in TE and regenerative medicine as basic materials for the production of functional 3D scaffolds for the regeneration of both hard and soft tissues. Since their invention in 1969 [17], indeed, BGs have been considered materials of choice for BTE applications because of their ability to react very effectively with the physiological environment by forming a strong bonding interface with the bone through the formation of a nanocrystalline hydroxyapatite (HA) layer, thus inducing a stable fixation of the material to the host tissue while promoting osteointegrative pathways.

According to the production method used, BGs can be characterized by chemical and microstructural features varying over a wide range. In particular, glasses produced by the melt-quenching technique are dense materials, while the sol–gel process allows the production of nanotextured materials exhibiting higher reactivity in contact with body fluids.

BG-based products have been successfully implanted in millions of patients worldwide since the late 1980s, mainly to repair bone and dental defects and, over the years, several bioactive compositions have been proposed for innovative biomedical applications, such as osteochondral tissue engineering, soft tissue repair, and tumor treatment [16].

However, despite these enthusiastic and promising results, BTE based on BG-based scaffolds has not yet achieved a full translation to clinical practice. Probably, the most critical issue about the use of BGs for making porous bone substitutes concerns the possibility of obtaining suitable mechanical performances. In fact, as widely known, glass materials are characterized by an intrinsic brittleness which mostly limits their use to nonload-bearing applications.

In order to regenerate bone, mechanically performant materials are required to provide support during the whole healing process. Stiff and tough materials, like metals, would theoretically be the best choice if their high values of rigidity did not cause bone tissue resorption due to the lack of load transmission at the host tissue/implant interface (stress shielding). In order to avoid this problem, the use of materials with elastic properties comparable to those of human trabecular bone has to be preferred.

Concerning BG-based scaffolds, a linear relation was observed between porosity and elastic modulus, as shown in Figure 7.2. In particular, the value of elastic modulus decreases as the scaffold porosity increases [18].

According to this, improved mechanical properties can be ideally obtained by reducing scaffold porosity; however, a minimum value of 50 vol% must be guaranteed to allow proper cell migration and tissue ingrowth within the 3D volume of the graft [12].

Nevertheless, over the years, several research groups succeeded in producing glass scaffolds showing comparable mechanical properties to those of the human bone [19].

Mechanical properties can be improved by a proper optimization of processing parameters. As an example, highly densified and mechanically performant struts can be obtained by increasing the sintering temperature [12, 20]. The drawback is that the application of high-temperature treatments can lead to the formation of crystalline phases within the amorphous matrix (devitrification) and, consequently, to a lower chemical reactivity of the material. This aspect has to be carefully evaluated when BGs are used as crystallization can significantly decrease the rate of HA formation (i.e. the bioactivity kinetics) on the surface of the glass-ceramic scaffold as compared to the parent glass [21].

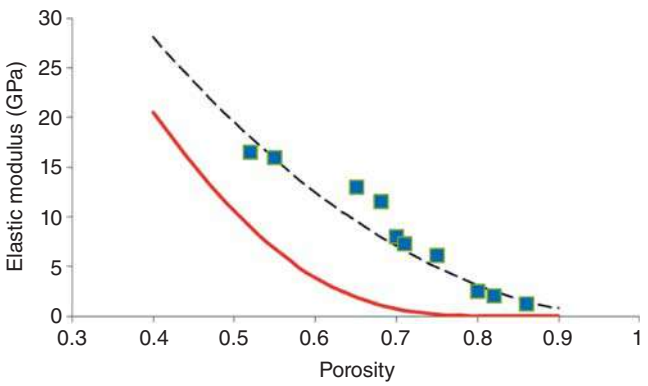

Figure 7.2 Elastic modulus of BG-based scaffolds as a function of the total porosity. Source: Baino et al. [18]/Multidisciplinary Digital Publishing Institute/CCBY 4.0.

Another important aspect to be considered is related to the type of mechanical loading which the scaffolds will undergo in the clinical scenario. Grafts implanted in load-bearing bone defects are normally exposed to cyclic loading; thus, besides elastic modulus and compressive strength, fracture toughness and fatigue resistance are also crucial. Due to its low fracture toughness, glass is extremely sensitive to the presence of small defects (~10 μm), and it can fail under tensile or flexural stresses much lower than its compressive strength. This criticality cannot be totally controlled, but it can be minimized through an optimization of the design and execution phase. A valid solution to mitigate the insidious effect of small defects within the glass structure could be the production of glass/polymer composite scaffolds, in which, however, the presence of two distinct phases could cause a limited interaction between BG particles and cells due to the shielding effect provided by the polymeric phase, as well as a mismatch in the degradation rates of glass and polymer [12, 19].

In recent years, much interest has also been addressed to the development of inorganic/organic hybrid scaffolds with controllable degradation and bioactive properties for bone engineering. In this regard, in fact, hybrid materials exhibit several advantages as compared to traditional composites due to the presence of fine-scale interactions between polymeric and the glassy phases, which make the material behave as if it was made up of a single phase. In this way, a fine control on both the mechanical properties and the degradation rate can be achieved owing to the formation of covalent bonds between the glass network and the polymeric chains [22, 23].

7.3 Fabrication Techniques

BG-based scaffolds were produced for the first time in 2002 by Sepulveda et al., who implemented a sol–gel process combined with *in situ* foaming to produce a macroporous structure [24]. Since then, many research groups have carried out several studies aimed at improving BTE scaffolds properties by developing and optimizing new manufacturing strategies able to meet the minimum requirements discussed above. In this regard, the introduction of AM technologies has represented a big step forward in achieving a high level of reproducibility and standardization of manufacturing processes, with the possibility to obtain patient-specific products as an undisputable added value [25]. Here, a brief overview of scaffold fabrication techniques is provided, with a particular attention on methods, materials, and processing parameters.

7.3.1 Foaming Methods

In foaming methods, the porous macrostructure is generated by the use of proper foaming agents which are added to BGs produced either by melt-quenching or sol–gel process in order to create air bubbles acting as a template for the formation of pores. In particular, the foaming agent can be added either to a glass slurry, obtained by suspending glass particles into a fluid media, or to a sol, i.e. a colloidal suspension of nanometric particles (1–100 nm).

The most commonly used foaming strategies for the production of 3D highly porous BG-based scaffolds include direct injection of gases, vigorous agitation, gas generation through a chemical reaction, or thermal decomposition of hydrogen peroxide [13]. Some of these processes have been adapted from industrial contexts far from the biomedical field, as further proof of the exceptional versatility of glass as a material suitable for a wide variety of different applications.

7.3.1.1 Gel-Cast Foaming

In gel-cast foaming, melt-derived glass particles are added to a solution of organic monomers (usually acrylates) to produce a slurry. Then, the slurry is foamed under vigorous agitation to induce *in situ* polymerization in the presence of a surfactant, which stabilizes the air bubbles, and a catalyst, to lower the energy of activation of the polymerization reaction. As the polymerization progresses, the viscosity increases, and, just prior to gelation, the foams are poured into molds, then dried to remove the solvents, and finally sintered at high temperature to remove the polymeric organic phase and densify the strut [26]. The main steps of gel-cast foaming are summarized in Figure 7.3a.

In order to achieve proper porosity features for BTE applications, the bubbles have to be large enough to touch each other in the solution until the gelation point is achieved, thus allowing the formation of interpore windows upon sintering.

The porosity of the scaffold can be adjusted by acting on the induction period, also known as "idle time," which is the time interval between the addition of the polymerization initiator and the catalyst and the beginning of the polymerization reaction [13].

Identifying the right pouring window is crucial for the final outcome of the process: in fact, if the foam is poured too soon, it will collapse under its own weight.

The sintering temperature has to be defined according to the thermal properties of the glass system considered in order to achieve good mechanical performance. However, sintering parameters are not the only factors affecting the mechanical behavior of the glass foams: the amount of glass powders is likewise crucial to get well-densified struts as it affects the number of contact points between adjacent particles, which will form sintering necks upon heating.

One of the most common solvents is water because it can be easily eliminated by drying processes slightly above 100 °C [13]. However, the exposure of BGs to an aqueous environment during the manufacturing could lead to an early reaction of the material even for very short times, depending on the glass composition.

Wu et al. [27] fabricated gel-cast BG foams with a modal pore size of 379 μm and modal interconnect size of 141 μm, which are suitable values for BTE applications (Figure 7.3d). They were

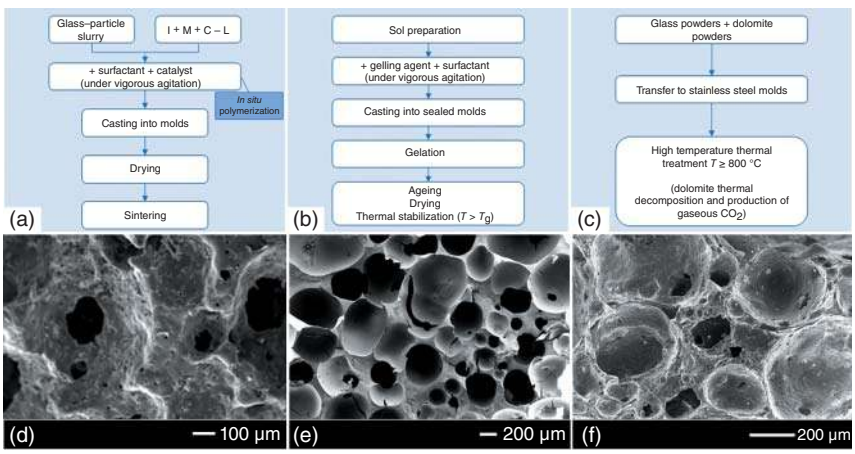

Figure 7.3 Foaming techniques for BG-based scaffold manufacturing: schematic of the gel-cast (a), sol–gel (b), and dolomite (c) foaming methods for producing porous glasses and glass-ceramics and scanning electron microscopy (SEM) micrographs showing the resulting morphologies (d, e, and f, respectively). Source: (d) Wu et al. [27], Figure 04, p. 05/with permission of Elsevier; (e) Courtesy of Elisa Fiume (Author); (f) Fiume et al. [28], Figure 02, p. 06/MDPI/CC BY 4.0.

characterized by a compressive strength close to the lower limit of spongy bone and the ability to form HA *in vitro*.

In general, scaffolds produced by gel casting are characterized by proper features for bone regenerative approaches; however, there is little chance of scalability of the process to an industrial level.

7.3.1.2 Sol–Gel Foaming

Sol–gel foaming was the process implemented by Sepulveda et al. for the development of the first BG-based scaffold in 2002 [24].

In a typical process, once all the reagents are completely dissolved within the sol, a surfactant and a gelation catalyst are added under vigorous agitation. Just prior to gelation, the foam is poured into a sealed mold and undergoes aging and drying processes to remove the liquid by-products (typically alcohols). Finally, the BG-based scaffold is obtained by high-temperature sintering treatment, which is performed to remove the organic residuals and densify the structure [29] (Figure 7.3b,e).

Most sol–gel BG foams are based on simple binary (SiO_2–CaO) or ternary compositions (SiO_2–CaO–P_2O_5) [30, 31].

Scaffolds obtained by sol–gel foaming are characterized by a hierarchical organization of pores, consisting of interconnected macropores (10–500 μm) deriving from the foaming process and mesopores (2–50 nm) that inherently result from the sol–gel process [19].

This hierarchical pore architecture is considered advantageous to stimulate cell–scaffold interactions because it imitates the hierarchical structure of natural bone, thus simulating the physiological environment [29].

Sol–gel-derived scaffolds usually have a high surface area (100–200 m^2/g) due to the presence of mesopores. Consequently, interactions with the physiological environment are favored, leading to a faster conversion to HA and a better bioactive response. Despite this promising aspect, which allows obtaining exceptional bioactivity in a wide compositional range, sol–gel-foamed scaffolds are characterized by a very low compression strength (0.3–2.3 MPa), and therefore, their usage in load-bearing applications is not recommended [19].

7.3.1.3 Thermal Decomposition of Chemical Compounds

All the methods that produce foams by gas generation through the thermal decomposition of chemicals can be included in the present group. Here, just a couple of representative examples will be described in order to provide a general idea.

Hydrogen peroxide (H_2O_2) foaming allows the production of porous scaffolds by heating a peroxide solution to 60 °C; as a result, water vapor and oxygen are released that act as foaming agents producing bubbles during the reaction [13].

Navarro et al. [32] mixed powders of phosphate glass with different amounts of H_2O_2 solution. The resulting slurry was poured into a mold, foamed at 60 °C and subjected to drying and sintering. They found that the amount of H_2O_2 was the principal factor affecting scaffold porosity. In particular, an increase in H_2O_2 content led to an increase in porosity, pore interconnectivity, and pore size.

In a very recent study, Fiume et al. [28] described the production of highly porous scaffolds with high bioactive potential and good mechanical properties (with compressive strength up to 3.9 MPa) by using dolomite ($CaMg(CO_3)_2$) powder as a foaming agent for generating interconnected macropores. The foaming process was based on the thermal decomposition of dolomite associated with CO_2 production, together with small amounts of calcium and magnesium, incorporated in the glass-derived foams [33]. In this regard, the choice of dolomite as a foaming agent was appropriate for the intended purpose as Ca^{2+} and Mg^{2+} ions are physiologically involved in bone

metabolism and, when released from BGs, stimulate osteoblasts toward a path of regeneration and self-repair [34].

The schematic diagram of the dolomite-foaming manufacturing process is schematically depicted in Figure 7.3c. From a morphological point of view, dolomite-foamed scaffolds exhibit a bubble-like architecture (Figure 7.3f), with a strong similarity to that of traditional sol–gel glass scaffolds previously described.

7.3.2 Thermal Consolidation of Particles

This large family of manufacturing strategies is based essentially on particle sintering and may include or not the use of porogen particles in the preparation of the green bodies, which are then thermally removed during the sintering process [13, 19, 26].

BG-based scaffolds in a wide compositional range have been produced by these methods, which are conceptually easy and relatively affordable; however, achieving adequate porosity levels and interpore connectivity, as well as a homogeneous distribution of pores within the whole 3D volume of the scaffold, is still challenging, as shown in Figure 7.4.

7.3.2.1 Scaffold Manufacturing by the Use of Porogen Particles

This technique, also known as the space-holder method, is based on the addition of a pore-forming agent to glass or ceramic particles before molding in order to introduce a certain porosity with controlled shape and size, directly inherited from the sacrificial particles used (Figure 7.5a).

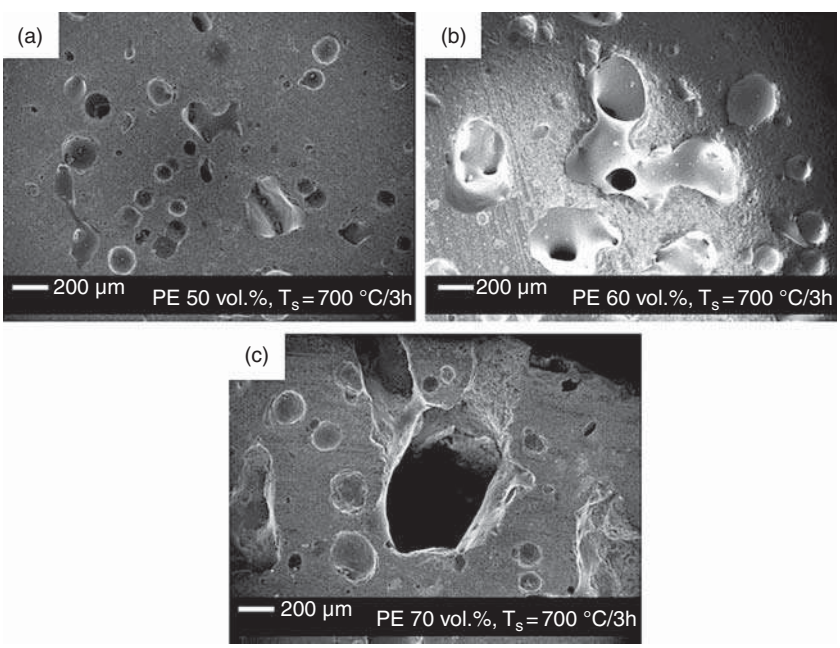

Figure 7.4 BG-based scaffolds obtained by thermal consolidation of particles around a sacrificial template (PE). The figure shows how, despite pore size was in the typical reference range of trabecular bone and the overall porosity of the scaffolds increases by increasing the volumetric content of sacrificial particles (from (a) to (c)), pores remain almost isolated, with few inter-pore windows. Source: Courtesy of Elisa Fiume (Author).

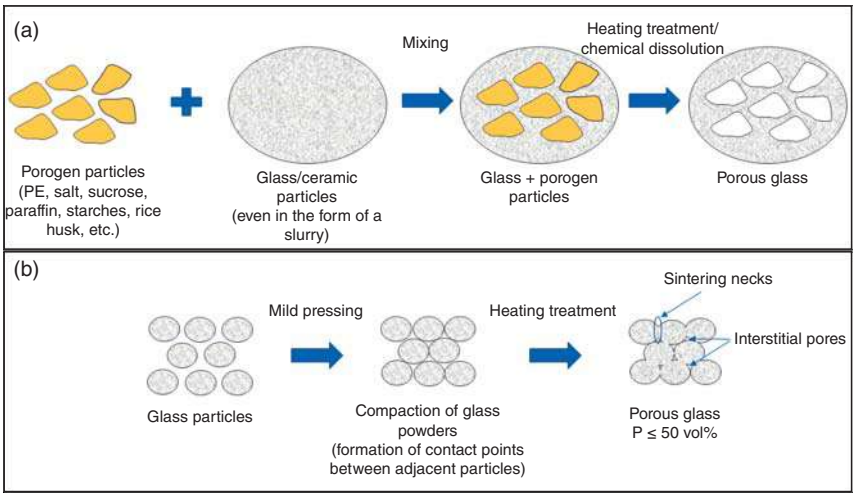

Figure 7.5 Thermal consolidation of particles: scaffold manufacturing with and without the use of sacrificial particles (a and b, respectively).

It is important to induce the thermal degradation of the sacrificial particles before the formation of sintering necks between adjacent glass particles because their presence can lead to the formation of black char (organic combustion residue) on the surface of the green body, thus hindering the sintering process and reducing the overall bioactive properties of the material.

Pore-forming agents are generally polymers of natural (e.g. starch, rice husk) or synthetic origin (e.g. polyethylene particles) [13, 19, 26]. As an example, starches of different plants were used by Vitale-Brovarone et al. [35] to produce BG scaffolds based on the system $50SiO_2$–$25CaO$–$16Na_2O$–$9MgO$ (mol%). The use of corn starch grains led to the production of scaffolds with too small pore size, while potato and rice starches allowed obtaining scaffolds with well-interconnected pores between 50 and 100 μm and compressive strength of 6 MPa, which definitely falls in the range of spongy bone [35].

Wu et al. [36] used rice husk as a space-holder to produce 45S5 Bioglass®-based scaffolds. These scaffolds exhibited low porosity (43–49 vol%) compared to the reference ranges of human trabecular bone, while the compressive strength (5–7 MPa) was suitable for bone substitution [36].

In another study by Vitale-Brovarone et al. [37], polyethylene particles were used as an organic filler for the fabrication of melt-derived BG scaffolds. Varying the size and amount of polyethylene particles, a total porosity from 50 to 70 vol% was obtained with well-interconnected pores within 100–200 μm or above 200 μm. By using small amounts and sizes of polyethylene particles, a maximum compressive strength of 6 MPa was obtained. In addition, these scaffolds exhibited surface micropores smaller than 10 μm, the presence of which was attributed to the nucleation of β-wollastonite crystals upon sintering [37]. The same fabrication method was also used to produce ultrastrong fluoroapatite-containing glass-ceramic scaffolds (compressive strength up to 150 MPa) for the substitution of cortical bone portions [38].

7.3.2.2 Scaffold Manufacturing Without the Use of Porogen Particles

This method requires that no sacrificial components are added to the glass or ceramic particles used to fabricate the green body (Figure 7.5b). The porosity of the scaffolds can be modified by varying the particle size and acting on the sintering process. Indeed, the sintering process must be stopped as soon as enough sintering necks between adjacent particles are formed in order to

ensure the achievement of suitable mechanical properties as well as adequate porosity for BTE applications. This approach is very easy but allows producing only scaffolds with very low porosity levels (usually <50 vol%) [13]. For example, the scaffolds developed by Fu et al. [39] with 13-93 glass showed 40 vol% porosity and high compressive strength (22 MPa).

Borate glass-based scaffolds obtained by Liang et al. [40] also had a porosity of less than 40 vol%, thus confirming the limit of the technique for producing scaffolds with sufficient porosity to induce proper cell migration, tissue ingrowth, and vascularization of the synthetic graft.

7.3.3 Freeze-Drying

In general, freeze-drying techniques take advantage of the formation of ice crystals to create the porous structure of the scaffold.

7.3.3.1 Freeze-Casting of Suspensions

This approach consists of pouring a colloidal suspension of glass particles into a mold and quickly freezing it. Oriented and elongated ice crystals are formed because usually the cooling rate is not homogeneous in all directions. The frozen solvent is removed by sublimation in vacuum conditions at moderately cold temperature (around −20 °C). This step is very critical because, if the solvent is removed uncontrollably, the porous structure of the scaffold could be destroyed. After complete removal of the solvent, the scaffold is thermally treated in order to sinter the inorganic particles.

The scaffolds obtained by this technique have a rather high compressive strength due to the oriented microstructure of the pores. However, the use of water as the only solvent does not allow obtaining scaffolds with appropriate pore dimensions for BTE applications because the typical range of pore sizes that can be obtained is within 10–40 μm, which is too low compared to spongy bone (well above 100 μm). The addition of other solvents such as 1,4-dioxane or camphene in the solution allows a larger pore size to be obtained. In fact, these solvents cause a change in the microstructure from lamellar to columnar and an increase in the pore size [19].

BG scaffolds (13-93 composition) with columnar microstructures and pore diameters of 100–150 μm were produced by Fu et al. [41]. Such scaffolds exhibited high mechanical strength and good ability to promote cell proliferation and differentiation *in vitro*, as well as tissue infiltration *in vivo*.

7.3.3.2 Ice-Segregation-Induced Self-Assembly Combined with the Sol–Gel Method

This technique relies on immersing the sol in liquid nitrogen at a controlled rate. Rapid freezing of the sol is then followed by sublimation of the frozen solvent. The resulting microstructure can be controlled by adjusting the nature and concentration of the solute, the solvent composition, the cooling rate, and the temperature gradient [13].

This method was implemented by Minaberry and Jobbágy [42] to produce porous scaffolds starting from BG sols. At the end of the process, the green body was subjected to annealing in order to remove residuals such as organic phases, acid, and salts and consolidate the structure. This structure showed pores ≤20 μm and low compressive strength (<0.2 MPa), thus, suggesting the unsuitability of this scaffold for BTE approaches.

7.3.4 Foam Replica Method

The foam replica method is recognized to be a valuable technique for the production of highly porous BG scaffolds. In particular, scaffolds of silicate, phosphate, and borate BGs have been successfully obtained by this fabrication strategy. This technique allows producing BG scaffolds with

open and interconnected porosity in the range of 40–95 vol% and microstructural features similar to those of human trabecular bone. However, foam-replicated scaffolds are typically affected by poor mechanical properties, with compressive strength in the lower range of that of trabecular bone, which limits its application to the repair of nonload-bearing bone areas [19].

The foam replica method was originally patented by Schwartzwalder and Somers in 1963 for the manufacturing of ceramic foams in industrial applications [43]. In 2006, Chen et al. [44] and Park et al. [45] were the first to use this technique in BTE for the development of BG scaffolds. Since then, the foam replica method has been widely used by several research groups to obtain porous glass scaffolds for bone regeneration.

The process is based on the replication of the porous structure of a sacrificial organic template in order to obtain its positive replica made of glass or glass-ceramic particles sintered around the sponge struts. In a typical process, the foam is dipped in a slurry consisting of glass powders suspended into a binder solution in order to obtain a consistent coating on the foam struts [19, 46]. The coating thickness is adjustable according to the number of consecutive immersions performed and the glass content (solid load) within the slurry [47]. The excess slurry is removed by squeezing the foams, which are then left to dry in order to obtain the green bodies (in this case, glass-coated sponges). After drying, the foam is burnt out by thermal treatments at high temperature, typically between 300 and 600 °C, and the glass struts are then densified by sintering at 600–1000 °C, depending on the composition and particle size of the glass [19, 46].

Frequently, foam removal and glass sintering are combined in a single treatment, which is carried out by maintaining a very low heating rate in order to burn out the foam while preserving the integrity of the BG structure. Then the treatment involves keeping the sample at the chosen sintering temperature for a few hours in order to sinter the glass struts and properly modulate the porosity [47, 48]. Figure 7.6 provides a schematization of the foam replica process.

Currently, the foam replica method is one of the most popular, affordable, relatively easy, and effective techniques for the development of 3D highly porous bone-like scaffolds [49]. The success of this method is also attributed to its versatility, which relies upon the possibility to use a wide variety of sacrificial templates both of synthetic (e.g. commercial polymeric sponges [44]) and natural origin (e.g. marine sponges [50]), as well as the opportunity of processing both traditional melt-derived glasses and sol–gel materials. As an example, foam replica method was used in combination with the evaporation-induced self-assembly (EISA) [51] to fabricate hierarchical porous bioactive glasses (HPBG) scaffolds, where a polyurethane foam and a surfactant are used as cotemplates for scaffold macropores and mesopores, respectively [52, 53].

Moreover, in the last years, the use of natural biological materials as macroporous templates has been particularly appreciated due to their easy availability and low cost, thus leading to the possibility of obtaining diverse and environment-friendly structures with even improved mechanical properties [54].

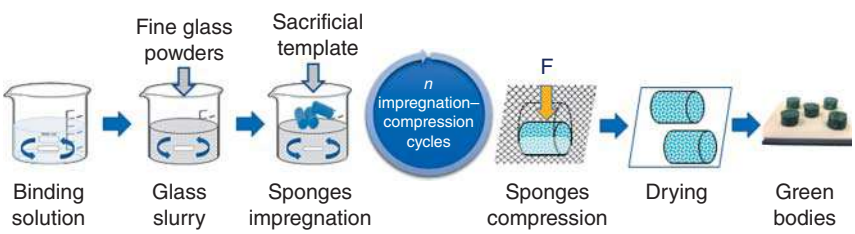

Figure 7.6 Scaffold manufacturing process by foam replica method.

One limitation of the foam replica method is that a good reproducibility of the process can be achieved only for a restricted number of small samples per time characterized by simple geometries, thus making it difficult to scale up the manufacturing process [13]. In addition, although the pore/strut characteristics of final scaffolds can be modulated to some extent by selecting templates with different porosities, this technique does not allow implementing an effective custom-made approach like AM strategies [55].

7.3.5 Solid Freeform Fabrication

Solid freeform fabrication (SFF) techniques, also known as AM, allow the fabrication of design-controlled 3D structures with specific features, optimized according to the desired application by simply acting on processing parameters. SFF techniques rely on layer-wise manufacturing technologies since the final 3D scaffold is obtained by subsequent deposition of material following a bottom-up process.

In the last decades, the extraordinary potential of AM in the biomedical field has been recognized worldwide, especially due to the possibility to obtain patient-specific devices on the basis of anthropomorphic models derived from clinical imaging techniques, e.g. computer tomography (CT) and magnetic resonance (MR) [16].

AM technologies are based on four main steps [56]:

(i) creation of a computer-generated model of the desired geometry by the use of a computer-aided design (CAD) software;
(ii) segmentation of the model into cross sections;
(iii) data implementation and processing;
(iv) creation of the physical model, i.e. the final or semifinal scaffold that may require further treatments (e.g. thermal consolidation).

SFF techniques can be further classified into two different groups: direct SFF, in which the scaffold is directly produced from the biomaterial, and indirect SFF, in which the biomaterial is cast into molds that are later dissolved by using a proper solvent.

The main advantage of using a direct SFF technique is the possibility to achieve high reproducibility of results due to the intrinsic automation of the process, even if the process might be very difficult to implement owing to the compatibility required between apparatus and biomaterials used. As an example, when glass slurries are printed to create a layer-wise scaffold, a typical problem is the risk of nozzle occlusion due to the formation of clots [16].

Sections 7.3.5.1–7.3.5.6 provide a picture of the most common SFF techniques that can be applied to fabricate BG-based scaffolds, including selective laser sintering (SLS), stereolithography (SL), fused deposition modeling (FDM), ink-jet printing (IJP), three-dimensional printing (3DP), and robocasting [57].

Table 7.2 summarizes the main characteristics of currently available AM technologies.

7.3.5.1 Selective Laser Sintering

SLS employs CO_2 or Nd:YAG (neodymium-doped yttrium aluminum garnet; Nd:$Y_3Al_5O_{12}$) lasers to selectively sinter successive layers of powder materials, thus creating a 3D object [57, 58].

A typical SLS setup consists of a laser, a scanning system, and two different chambers. One of the two chambers is intended for the preparation of the powder feedstock. A roller transfers the powders from one chamber to another and, as soon as it finishes preparing the layer, the laser beam sinters the powders. Subsequently, the roller creates another layer, and so on. During the manufacturing process, the structure is surrounded and supported by nonsintered powders. Once

Table 7.2 Overview of AM technologies for the processing of BG-based porous scaffolds: strengths and limits.

Technique	Achievable pore size	Advantages	Limitations	References
SLS	45–100 μm	↑ High porosity ↑ High surface area to volume ratio ↑ Complete pore interconnectivity ↑ Macro shape control ↑ Independent control of porosity and pore size ↑ Wide range of materials ↑ Solvent-free	↑ High processing temperatures ↑ Limited to small pore size	[58]
SL	≥70 μm	↑ Control over the internal and external geometry of the structure ↑ Well-defined pore sizes, pore geometries, and porosities ↑ Good compressive strengths ↑ High resolution ↑ Wide range of materials	↑ Limited number of resins commercially available	[59, 60]
FDM	250–1000 μm	↑ High porosity ↑ High surface area to volume ratio ↑ Complete pore interconnectivity ↑ Macro shape control ↑ Independent control of porosity and pore size ↑ Good compressive strengths ↑ Solvent-free	↑ High processing temperatures ↑ Limited material range ↑ Inconsistent pore opening in x-, y and *z*-directions ↑ Pore occlusion at boundaries ↑ Requires support structures for irregular shapes	[58]
IJP	Customer-based	↑ High resolution ↑ Good surface finish ↑ Good mechanical properties ↑ Controllable porosity and pore geometry. Can integrate with cells and growth factors	↑ Limited to the production of miniaturized structures ↑ Limited material range ↑ Use of solvent ↑ High cost	[61, 62]
3DP	45–100 μm	↑ Easy process ↑ High porosity ↑ High surface area to volume ratio ↑ Complete pore interconnectivity ↑ Macroshape control ↑ Independent control of porosity and pore size ↑ Suitable for many kinds of materials	↑ Use of toxic organic solvents ↑ Lack of mechanical strength ↑ Limited to small pore sizes	[58, 59]
Robocasting	300–500 μm	↑ Simple, flexible, and inexpensive approach ↑ Suitable for many kinds of materials ↑ Low cost ↑ Fast	↑ Need for an ink with appropriate rheological properties	[61, 63]

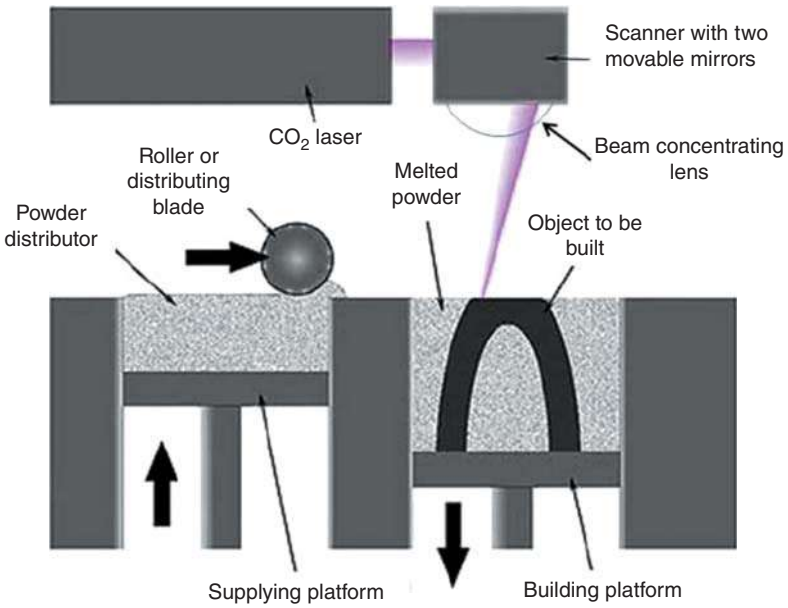

Figure 7.7 Schematic diagram of a SLS system. Source: Legutko [64] available via license: Creative Commons Attribution 3.0 Unported (CC BY 3.0).

the structure is completed, it is extracted from the powders [57, 58]. The schematic representation of a typical setup for SLS is depicted in Figure 7.7.

A material is suitable to be processed by SLS if it absorbs light in the laser wavelength range and if it is formed by flowable powders to form the bed correctly. Ideally, the particles should be between 10 and 150 μm in size.

The porosity of SLS scaffolds can be controlled by adjusting processing parameters, such as laser energy density, scanning speed, and the hatching distance, i.e. the distance between two lines scanned by the laser [13, 58].

In 2012, Liu et al. [65] produced the first Bioglass scaffold via SLS. They optimized the laser power to obtain good sintering and densification and, as a result, potentially suitable porosity and mechanical property for bone repair. They found that the material melts and starts flowing through the layers below, creating holes and voids in the glass layer if a very high laser power is used [65].

Although SLS was developed as a direct technique, it was also used as an indirect method in order to reduce the laser power and to achieve better dimensional accuracy.

In indirect SLS, a binder is added to the powders; then, the laser melts the binder, which holds together the glass particles. After SLS, the de-binding and sintering process are necessary to remove the binder and to sinter the glass, respectively [57]. For example, Kolan et al. [66] produced 13-93 glass scaffolds by indirect SLS using stearic acid as a binder. The surface roughness and the presence of micropores due to SLS increased the surface area of the scaffold, improving bioactivity as well as cell attachment and proliferation. In addition, these scaffolds exhibited total porosity (50–62 vol%) and compressive strength (5.9–20.4 MPa) comparable to those of human spongy bone.

7.3.5.2 Stereolithography

SL is based on spatially controlled solidification of liquid-based resins by photopolymerization to produce a 3D structure. Ultraviolet (UV) light is typically used and irradiated on the photosensitive resin surface in a precise pattern, which is defined by CAD files.

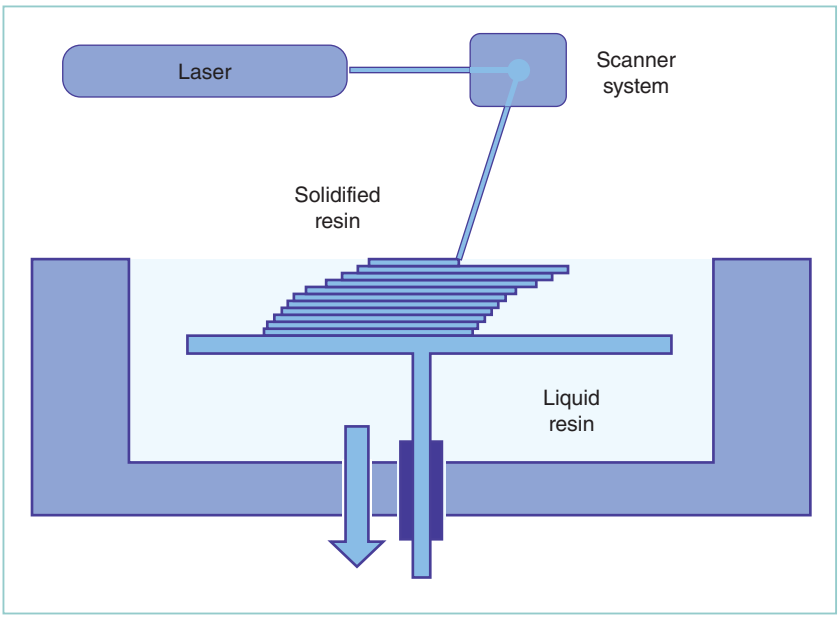

Figure 7.8 Schematic diagram of SL. Source: Kim et al. [67].

Free radicals and other reactive species, which are formed upon excitation of photo-initiator molecules by UV light, cause resin polymerization and formation of a solid phase.

A build platform is used to provide support to the structure during the manufacturing process. Therefore, the first layer of photopolymerized polymer adheres to this platform and, once it is polymerized, the platform is moved a defined distance for the polymerization of the subsequent layer. This procedure is repeated until the whole 3D structure is obtained [60]. Figure 7.8 shows a schematic of the SL process.

In order to apply SL technology to BG-based scaffolds manufacturing, it is necessary to combine the liquid photopolymer with glass or ceramic particles. Once the 3D structure is obtained, a heat treatment is required, aiming at eliminating the organic component and achieving greater densification [61].

In 2012, SL was applied for the first time for the production of Bioglass-based scaffolds, characterized by arbitrary porosity and pore sizes of about 500 µm, similar to that of spongy bone [68]. Subsequently, dense structures of BGs and glass-ceramics were also fabricated by SL [69].

7.3.5.3 Fused Deposition Modeling

FDM employs the melt extrusion process to deposit a series of parallel fibers, thus forming a single layer of material; stacking of layers generates the whole 3D object [58].

A heated liquefier head melts the filament material (generally thermoplastic polymers), which is extruded by a nozzle with a small orifice [58]. The first extruded filament adheres to the support platform and solidifies as it cools. Subsequently, the support platform is lowered a distance equal to the thickness of the new layer, and the extrusion and lowering process is repeated until the structure is completed [70], as depicted in Figure 7.9.

FDM technology allows to obtain scaffolds with highly uniform internal honeycomb-like structures, controllable pore morphology, and complete pore interconnectivity by modifying the material deposition direction for consecutively layers and the space between the material fibers.

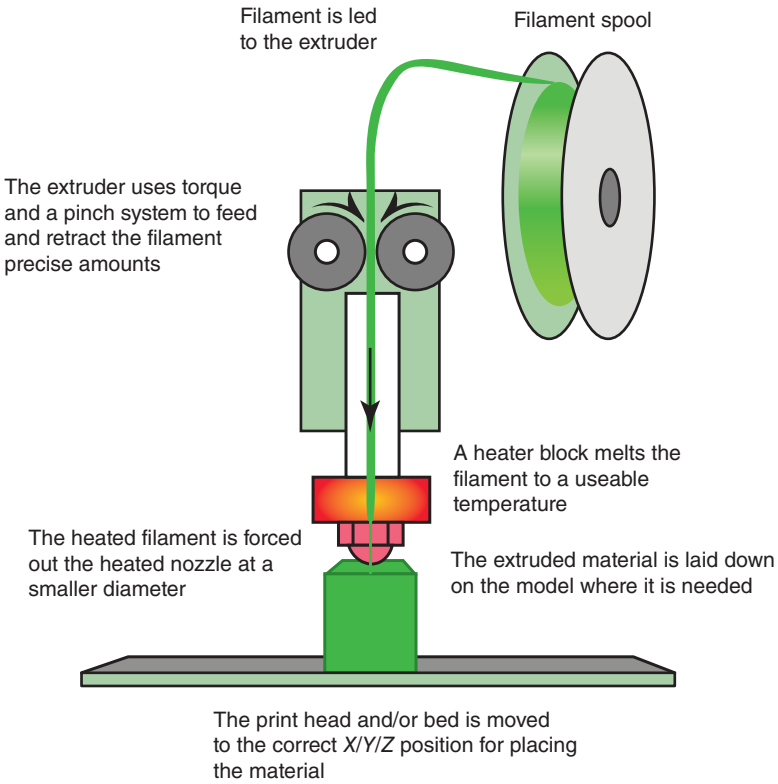

Figure 7.9 Schematic diagram of a typical FDM setup. Source: Ciobota and Gheorghe [71]/Sciendo.

Furthermore, FDM allows developing scaffolds with overhanging features by depositing removable supporting structures alongside the scaffold [58].

FDM can be basically implemented to obtain polymeric products; in order to apply FDM to the fabrication of glass-based porous structures, filaments composed of BG particles and binder thermoplastic polymers have to be prepared. After obtaining the green body by FDM, de-binding and sintering processes are necessary to get a fully ceramic sample [70].

7.3.5.4 Ink-Jet Printing

IJP employs micrometric printhead nozzles to dispense liquid-phase materials in a controlled manner. The liquid-phase material, also known as ink, is dispensed in the form of droplets onto a surface and, as the ink dries, a thin layer of ink residue is created. Subsequently, other layers are placed on top of the previous ones in order to form a multilayer 3D structure [61].

The IJP technique can use two different ink delivery methods: continuous inkjet (CIJ) or drop-on-demand (DOD) printing, as shown in Figure 7.10.

In the CIJ method, a stream of drops is dispensed by a controllable micronozzle. Afterward, an electrostatic field influences the formed droplets and deviates their trajectories to print on a surface or allows them to reach the collector for reuse. Just a few drops are printed on a substrate, and the largest number of drops is recycled. Therefore, CIJ is not very cost-effective [61].

The DOD method is more affordable than CIJ because it produces ink droplets when and where it is required. In addition, it is more suitable for printing 3D structures due to the small size of

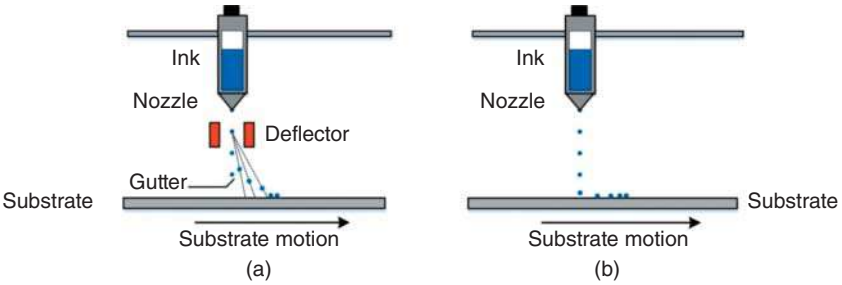

Figure 7.10 IJP delivery methods: (a) continuous and (b) drop-on demand printing modes. Source: Figure reproduced from Solís Pinargote et al. [61] under the Creative Commons Attribution License.

droplets and the high positioning accuracy. In the DOD method, the ink droplets can be formed by the piezoelectric effect or thermal excitation in the printing nozzle head [61].

IJP can be used to print a wide range of materials. To date, this technique was used to produce scaffolds based on natural and synthetic polymers as well as on calcium phosphates [72]. In principle, ceramics cannot be processed in a molten state because of their high melting temperature; therefore, in order to obtain an adequate ink, a binder is added to them. In this case, once the 3D structure is fabricated, a thermal treatment is necessary to eliminate the binder and sinter the ceramic particles [73].

IJP allows multiple nozzles to be used simultaneously to speed up the printing process for each layer and to obtain composite structures by using different inks [73].

No publications about IJP of BGs have been reported so far [57]; however, silica-based sol–gel derived materials were inkjet-printed for biosensor applications [74].

7.3.5.5 Three-Dimensional Printing

The 3DP technique has a setup similar to that of the SLS. In fact, there is a first chamber where a powder bed is created and a printing chamber where the actual printing process takes place. The powders are transferred from one room to another by a set of rollers [13], as displayed in Figure 7.11.

3DP technique incorporates IJP technology for processing powders and, just like a common ink-jet printer, it allows using two different ink delivery modes: CIJ or DOD [58].

A binder is ejected by a jet head, which moves onto thin layers of powder in accordance with the object profile generated by the computer system [58, 76]. The binder dissolves and joins adjacent particles. The piston chamber is lowered and filled with another layer of powder, and the process is repeated [76]. After several cycles, the complete structure of the object is created. The final object is incorporated inside unbound powders and can be extracted by brushing away the powders [58].

Although 3DP has its own technical characteristics and is a well-defined method in the wide family of SFF approaches, generally speaking, this expression is often used in a broader sense as an interchangeable synonym for AM.

Before printing, the parameters of the powder bed and ink delivery system should be optimized in order to achieve a satisfactory final outcome. The powders must have a good packaging capacity and sufficient flowability to be transferred from the feed bed to the printing one. These aspects depend primarily not only on particle shape, size, size distribution, and roughness but also on the wettability of the powders and ink droplets.

The 3D-printed ceramic and glass structures must be heat-treated after the molding process. The heat treatment comprises the de-binding and sintering phases. Crystalline phase(s) may form during the sintering process.

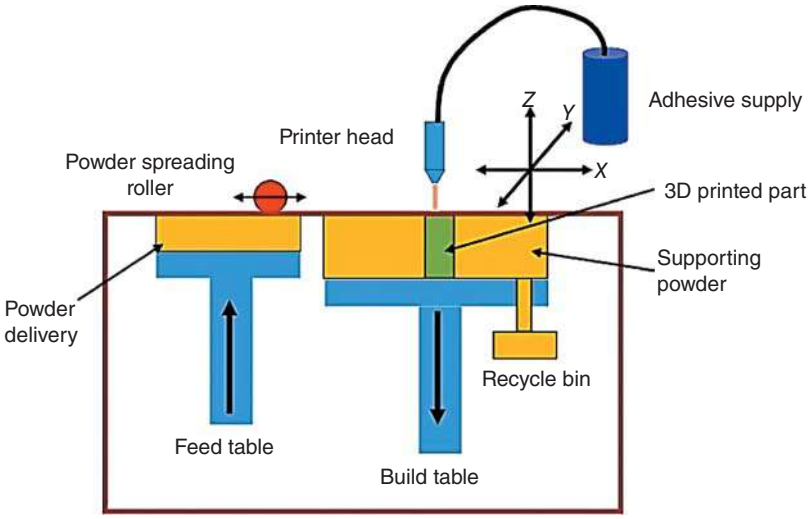

Figure 7.11 Setup for 3DP manufacturing technology. Source: Alaboodi and Sivasankaran [75]/with permission of Elsevier.

HA, several kinds of calcium phosphates, 45S5 Bioglass, 13-93 glass, and mesoporous bioactive glasses (MBGs) were used to produce 3D-printed scaffolds. All of them exhibited low porosity (<50 vol%) and compressive strength up to 70 MPa, thus proving to be suitable for load-bearing applications [57].

Recently, Mancuso et al. [77] produced porous silicate glass-ceramic scaffolds by 3DP having mechanical properties comparable to those of cortical bone and dimensions of several centimeters.

7.3.5.6 Robocasting

Robocasting is an extrusion-based technique. A moving controlled nozzle extrudes the ink in order to form a bidimensional pattern [61]. Once a layer is printed, the support platform is lowered to the same distance as the new-layer thickness and a new layer is deposited on the top of the previous one. Therefore, through a layer-by-layer procedure, the 3D structure is created [61] (Figure 7.12).

If the goal is to obtain a glass or ceramic product, the ink should be composed of inorganic particles and a polymeric binder. In order to be used for robocasting, the ink should

(i) Be pseudoplastic, i.e. it should flow through the nozzle by applying a small pressure.
(ii) Set-up into a nonflowable mass, i.e. it should preserve the rod-like shape of filaments once extruded on the support platform.
(iii) Be strong enough to bear the weight of the overlying layers without undergoing deformation.

Extrusion can occur directly in the air or in a nonwetting oil bath. Extrusion in the air can cause uneven shrinkage due to several air flows in the structure. In addition, the feed rate must be coordinated with the drying kinetics to obtain sufficiently resistant layers. It is possible to bypass these problems by extruding in an oil bath. This approach prevents drying of the structure at first; then, the sample is extracted and dried in a controlled environment. In addition, this type of extrusion prevents clogging of the nozzle [78]. On the other hand, the latter approach is more challenging than the former from a technological viewpoint.

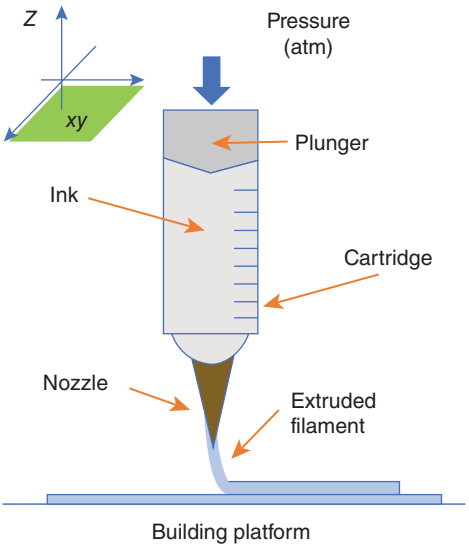

Figure 7.12 Schematic representation of a layer-by-layer deposition process by robocasting technology.

In robocasting, the ink can be delivered in two different ways [79]:

(i) *Constant displacement*: the ink is extruded at a constant flow rate by moving the cartridge plunger in a mechanical way by changing the extrusion pressure as needed.
(ii) *Constant pressure*: pressurized air, which is maintained at a constant pressure, moves the plunger.

In addition to the intrinsic properties of the ink, other factors can influence the final structure of the final scaffold. For example, the nozzle diameter, air pressure, and printing speed determine the final diameter of the extruded rod. Moreover, the space between the various layers is crucial to achieve good adhesion between the layers and good mechanical properties. The initial substrate has to be flat and allow the ink attachment as well as the easily detachment of the final scaffold [13].

Glasses or ceramics were extensively used to fabricate scaffolds by robocasting. De-binding and sintering postprocess are necessary to produce BG or ceramic scaffolds without any organic components [61]. Robocasting was first experimented for the fabrication of bioceramic scaffolds in 2010 by Franco et al. [80], who used an ink containing calcium phosphates (HA and β-tri-calcium phosphate [β-TCP]) and pluronic as a binder. Pluronic was also used as a binder by Fu et al. [81] to fabricate BG (13-93)-based scaffolds for the first time by robocasting technology. Pluronic F-127 is one of the most frequently used binders for robocasting in BTE, along with ethyl cellulose, poly(ethylene glycol), and carboxymethyl cellulose [78].

Eqtesadi et al. [82] produced 45S5 Bioglass scaffolds by robocasting using carboxymethyl cellulose as the binder. All the scaffolds, including those sintered at temperatures below the onset of crystallization (Tx), exhibited interconnected porosities ranging from 60 to 80 vol% and compressive strength comparable to that of spongy bone. Therefore, robocasting was recognized to be the first technique that allows obtaining vitreous 45S5 Bioglass scaffolds (no crystallization) with suitable mechanical properties for clinical applications.

Recently, robocasting was successfully used to produce hierarchical scaffolds based on MBGs. Wu et al. [83] robocast SiO_2–CaO–P_2O_5 MBG powders using poly(vinyl alcohol) as a binder. They obtained hierarchical scaffolds with a compressive strength of 16 MPa and an excellent

mineralization (i.e. HA-forming) capacity as well as sustained drug release property. A comprehensive overview of MBG scaffolds produced by robocasting has been recently reported elsewhere [84].

7.4 Beyond Bone Tissue Engineering Through Using BG-Based Scaffolds

7.4.1 Hierarchical MBG-Based Scaffolds as Drug Release Platforms for *In Situ* Therapy

In recent years, the production of BGs in a mesoporous form has dramatically expanded the versatility of glass systems, opening up new horizons especially in tumor therapy and drug delivery applications. MBGs exhibit ultrafast HA deposition rates as well as an intrinsic attitude to be used as carriers for drugs and molecules owing to the presence of a well-organized mesoporous structure [85].

MBGs are produced using sol–gel synthesis combined with structure directing agents (SDAs) to create the ordered mesostructure. Some of the most commonly used mesopore templates are cetyltrimethylammonium bromide (CTAB) and nonionic surfactants, such as Pluronic 123 (P123) and Pluronic F-127, which are able to self-organize in micelles under specific pH and temperature conditions [86, 87].

Using MBGs in the production of BTE scaffolds can be beneficial from different points of view, the first of which is the possibility to provide multiple therapeutic actions at the defect site by incorporating and synergistically releasing therapeutic ions and molecules [88, 89].

The easiest approach for the production of hierarchical MBG scaffolds is to combine the EISA method – responsible for the formation of ordered mesopores – with the replication of macroporous templates or porogen burn-off techniques [88–92]. However, macro-mesoporous scaffolds produced by such combinations of conventional fabrication methods exhibit either poor mechanical strength or low inter-pore connectivity, thus arousing considerable interest in the application of AM technologies to the processing of MBGs.

Despite promising results have been already obtained by several research groups, further efforts are needed to define standardized protocols for both the printing process and the synthesis of raw materials in order to promote the extensive use of 3D-printed MBG-based scaffolds in clinical practice. For further details concerning the synthesis of MBGs and the production of MBG-based scaffolds, the readers may refer to the dedicated bibliography [86, 93, 94].

7.4.2 Multilayer Scaffolds for Interfacial Tissue Engineering

Interfacial tissue engineering (ITE) deals with the application of basic TE principles at the interface between two or more biological tissues characterized by different structural and biological properties. This approach mainly relies upon the production of functionally graded scaffolds and/or multilayered scaffolds able to mimic the complexity of the physiological environment by exhibiting gradients of densities, morphology, composition, and function [95].

Thinking about the bone tissue, the first interface that comes to mind is indeed the trabecular/cortical one, characterized by a distinct change in microstructural and density features. Pore-graded BG scaffolds mimicking the natural microarchitectural gradients of bone were obtained by preforming the polymeric template in the foam replica method [96] or by combining

foam replication with porogen burn-off and coating techniques [97]. Recently, scaffolds with finely controlled porosity gradients were easily obtained by using AM technologies simply optimizing the initial CAD model or text file. As an example, silica-based grid-like scaffolds with graded porosity have been successfully obtained by Barberi et al. [98] using robocasting technology.

Concerning multi-layered scaffolds, osteochondral and periodontal regeneration certainly are the most active research fields based on the use of BGs at tissue interface. Nevertheless, soft TE and, in particular, dermal repair, should be mentioned.

As an example, bi-layered scaffolds have been produced by Balasubramanian et al. [99] through combining BGs and polymers in order to mimic the interface between bone tissue and cartilage. Specifically, polycaprolactone (PCL)-coated BG scaffolds served as a support for the bone side, while composite collagen-PCL submicrometric fibers were intended for the cartilage side. This study actually represents a successful combination of two of the most versatile strategies available in material processing: on the one side, highly porous (about 95.8 vol%), trabecular like BG-based scaffolds were obtained by foam replication technique, later coated by deep coating with a layer of PCL to improve the compressive strength, and on the other side electrospun polymeric fibers were used.

In another study, foam replication, gelation, and freeze-drying techniques were combined in order to obtain stratified scaffolds mimicking the layered structure of native osteochondral tissue. The 45S5 Bioglass and alginate were used to fabricate porous bioactive scaffolds for the underlying subchondral bone layer, while freeze-dried alginate-based scaffolds were produced for the cartilaginous side. The two layers were finally integrated by a novel alginate/45S5 Bioglass hybrid adhesive interface substituting the cartilage–bone interfacial layer [100].

More recently, a tri-layered, functionally graded chitosan membrane (FGM) with BG gradient (50, 25, and 0 wt%) was developed by lyophilization for potential application in periodontal regeneration. The lower layer was designed to replicate alveolar bone (with 50 wt% of BG), the middle layer contained 25 wt% of BG, and the upper layer was nonporous (without BG) and did not support cell growth. The interaction of the tissue with these tri-layered membranes was also investigated *in vivo*, revealing good biocompatibility and confirming the suitability of these scaffolds for the intended purpose [101].

7.5 Conclusion

After 50 years from their invention, BGs are still considered materials of choice in bone regeneration owing to their capability to be gradually osteointegrate while stimulating osteogenetic pathways.

Their enormous potential as basic materials for the production of synthetic bone grafts has been recognized by many research teams all over the world and, over time, BG-based porous scaffolds with morphological and structural features similar to that of human trabecular bone have been successfully obtained by using both traditional and AM methods.

Despite this, there is still a long road ahead before this technology will be fully fledged in clinical practice.

Most of the techniques currently available for the manufacturing of BG scaffolds, in fact, are operator-dependent, poorly reproducible, and standardized. The only exception is currently represented by AM technologies, but their spread in biomedicine is clearly lagging behind other industrial fields due to the high technological costs required for the processing of high-quality raw materials under strictly controlled environmental conditions.

As a result, the clinical treatment of bone defects still is a quite controversial matter affected by an obstinate lack of consensus around the definitions, robust models, and best practices for surgical management.

Nevertheless, the world of BGs continues to have a huge charm, offering many new possibilities year by year in several research fields, from traditional bone engineering applications to tumor therapy and interfacial TE applications.

Despite this, the main line of research is still focused on the development of mechanically performant 3D structures to be used in load-bearing applications as an alternative to metal implants, most of the times associated to bone resorption resulting from the mismatch in metal-bone elastic modulus.

References

1 Wang, W. and Yeung, K.W.K. (2017). Bone grafts and biomaterials substitutes for bone defect repair: a review. *Bioactive Materials* 2 (4): 224–247.

2 Moore, W.R., Graves, S.E., and Bain, G.I. (2001). Synthetic bone graft substitutes. *ANZ Journal of Surgery* 71 (6): 354–361.

3 Vacanti, J.P. and Langer, R. (1999). Tissue engineering: the design and fabrication of living replacement devices for surgical reconstruction and transplantation. *Lancet* 354 (S1): 32–34.

4 Lanza, R., Langer, R., Vacanti, J.P. et al. (2020). *Principles of Tissue Engineering*. Academic Press.

5 Karp, J.M., Dalton, P.D., and Shoichet, M.S. (2003). Scaffolds for tissue engineering. *Materials Research Society* 28 (4): 301–306.

6 Carthew, J., Shrestha, S., Donderwinkel, I. et al. (2019). Physical stimulation in tissue-engineering. In: *Tissue Engineering in Oral and Maxillofacial Surgery* (ed. R. Seppänen-Kaijansinkko), 33–52. Cham: Springer.

7 Stevens, M.M. (2008). Biomaterials for bone tissue engineering. *Materials Today* 11 (5): 18–25.

8 Fernandez de Grado, G., Keller, L., Idoux-Gillet, Y. et al. (2018). Bone substitutes: a review of their characteristics, clinical use, and perspectives for large bone defects management. *Journal of Tissue Engineering* 9: 1–18.

9 O'Brien, F.J. (2011). Biomaterials & scaffolds for tissue engineering. *Materials Today* 14 (3): 88–95.

10 Jones, J.R. (2013). Review of bioactive glass: from Hench to hybrids. *Acta Biomaterialia* 9 (1): 4457–4486.

11 Rahaman, M.N., Day, D.E., Bal, B.S. et al. (2011). Bioactive glass in tissue engineering. *Acta Biomaterialia* 7 (6): 2355–2373.

12 Gerhardt, L.-C. and Boccaccini, A.R. (2010). Bioactive glass and glass-ceramic scaffolds for bone tissue engineering. *Materials* 3 (7): 3867–3910.

13 Baino, F. and Fiume, E. (2019). Elastic mechanical properties of 45S5-based bioactive glass-ceramic scaffolds. *Materials (Basel)* 12 (19): 3244.

14 Roseti, L., Parisi, V., Petretta, M. et al. (2017). Scaffolds for bone tissue engineering: state of the art and new perspectives. *Materials Science and Engineering C* 78: 1246–1262.

15 Baino, F., Novajra, G., and Vitale-Brovarone, C. (2015). Bioceramics and scaffolds: a winning combination for tissue engineering. *Frontiers in Bioengineering and Biotechnology* 3: 1–17.

16 Fiume, E., Barberi, J., Verné, E. et al. (2018). Bioactive glasses: from parent 45S5 composition to scaffold-assisted tissue-healing therapies. *Journal of Functional Biomaterials* 9 (1): 24.

17 Hench, L.L. (2006). The story of Bioglass®. *Journal of Materials Science – Materials in Medicine* 17: 967–978.

18 Baino, F., Fiume, E., Barberi, J. et al. (2019). Processing methods for making porous bioactive glass-based scaffolds – a state-of-the-art review. *International Journal of Applied Ceramic Technology* 16 (5): 1762–1796.

19 Fu, Q., Saiz, E., Rahaman, M.N. et al. (2011). Bioactive glass scaffolds for bone tissue engineering: state of the art and future perspectives. *Materials Science and Engineering C* 31 (7): 1245–1256.

20 Thompson, I.D. and Hench, L.L. (1998). Mechanical properties of bioactive glasses, glass-ceramics and composites. *Proceedings of the Institution of Mechanical Engineers, Part H: Journal of Engineering in Medicine* 212: 127–137.

21 Plewinsky, M., Schickle, K., Lindner, M. et al. (2013). The effect of crystallization of bioactive bioglass 45S5 on apatite formation and degradation. *Dental Materials* 29 (12): 1256–1264.

22 Baino, F., Fiorilli, S., and Vitale-Brovarone, C. (2017). Composite biomaterials based on sol–gel mesoporous silicate glasses: a review. *Bioengineering* 4: 15.

23 Jones, J.R. (2009). New trends in bioactive scaffolds: the importance of nanostructure. *Journal of the European Ceramic Society* 29 (7): 1275–1281.

24 Sepulveda, P., Jones, J.R., and Hench, L.L. (2002). Bioactive sol–gel foams for tissue repair. *Journal of Biomedical Materials Research* 59 (2): 340–348.

25 Fazlollahi, M., Pooshidani, Y., and Eskandari, M. (2020). Additive manufacturing in bone tissue engineering. In: *3D Printing in Biomedical Engineering* (ed. S. Singh, C. Prakash and R. Singh), 95–125. Singapore: Springer.

26 Jones, J.R. (2012). Bioactive glass as synthetic bone grafts and scaffolds for tissue engineering. In: *Bio-glasses: An Introduction* (ed. J.R. Jones and A.G. Clare), 177–201. Chichester, UK: Wiley.

27 Wu, Z.Y., Hill, R.G., Yue, S. et al. (2011). Melt-derived bioactive glass scaffolds produced by a gel-cast foaming technique. *Acta Biomaterialia* 7 (4): 1807–1816.

28 Fiume, E., Tulyaganov, D., Ubertalli, G. et al. (2020). Dolomite-foamed bioactive silicate scaffolds for bone tissue repair. *Materials* 13 (3): 628.

29 Baino, F., Fiume, E., Miola, M. et al. (2018). Bioactive sol–gel glasses: processing, properties and applications. *International Journal of Applied Ceramic Technology* 15: 841–860.

30 Jones, J.R., Ehrenfried, L.M., and Hench, L.L. (2006). Optimizing bioactive glass scaffolds for bone tissue engineering. *Biomaterials* 27 (7): 964–973.

31 Midha, S., Kim, T.B., Van Den Bergh, W. et al. (2013). Preconditioned 70S30C bioactive glass foams promote osteogenesis in vivo. *Acta Biomaterialia* 9 (11): 9169–9182.

32 Navarro, M., Del Valle, S., Martinez, S. et al. (2004). New macroporous calcium phosphate glass ceramic for guided bone regeneration. *Biomaterials* 25 (18): 4233–4241.

33 Gunasekaran, S. and Anbalagan, G. (2007). Thermal decomposition of natural dolomite. *Bulletin of Materials Science* 30: 339–344.

34 Hoppe, A., Güldal, N.S., and Boccaccini, A.R. (2011). A review of the biological response to ionic dissolution products from bioactive glasses and glass-ceramics. *Biomaterials* 32: 2757–2774.

35 Vitale-Brovarone, C., Vernè, E., Bosetti, M. et al. (2005). Microstructural and in vitro characterization of SiO_2–Na_2O–CaO–MgO glass-ceramic bioactive scaffolds for bone substitutes. *Journal of Materials Science – Materials in Medicine* 16 (10): 909–917.

36 Wu, S.C., Hsu, H.C., Hsiao, S.H. et al. (2009). Preparation of porous 45S5 Bioglass®-derived glass-ceramic scaffolds by using rice husk as a porogen additive. *Journal of Materials Science – Materials in Medicine* 20 (6): 1229–1236.

37 Vitale-Brovarone, C., Verné, E., and Appendino, P. (2006). Macroporous bioactive glass-ceramic scaffolds for tissue engineering. *Journal of Materials Science – Materials in Medicine* 17 (11): 1069–1078.

38 Baino, F., Verné, E., and Vitale-Brovarone, C. (2009). 3-D high strength glass-ceramic scaffolds containing fluoroapatite for load-bearing bone portions replacement. *Materials Science and Engineering C* 29: 2055–2062.

39 Fu, Q., Rahaman, M.N., Bal, B.S. et al. (2007). Preparation and bioactive characteristics of a porous 13-93 glass, and fabrication into the articulating surface of a proximal tibia. *Journal of Biomedical Materials Research Part A* 82 (1): 222–229.

40 Liang, W., Rahaman, M.N., Day, D.E. et al. (2008). Bioactive borate glass scaffold for bone tissue engineering. *Journal of Non-Crystalline Solids* 354 (15–16): 1690–1696.

41 Fu, Q., Rahaman, M.N., Bal, B.S. et al. (2010). Preparation and in vitro evaluation of bioactive glass (13-93) scaffolds with oriented microstructures for repair and regeneration of load-bearing bones. *Journal of Biomedical Materials Research Part A* 93 (4): 1380–1390.

42 Minaberry, Y. and Jobbágy, M. (2011). Macroporous bioglass scaffolds prepared by coupling sol–gel with freeze drying. *Chemistry of Materials* 23 (9): 2327–2332.

43 Schwartzwalder, K. and Somers, A.W. (1963). Method of making ceramic articles. US Patent 3,090,094, filed 21 February 1962 and issued 21 May 1963.

44 Chen, Q.Z., Thompson, I.D., and Boccaccini, A.R. (2006). 45S5 Bioglass®-derived glass-ceramic scaffolds for bone tissue engineering. *Biomaterials* 27 (11): 2414–2425.

45 Park, Y.S., Kim, K.N., Kim, K.M. et al. (2006). Feasibility of three-dimensional macroporous scaffold using calcium phosphate glass and polyurethane sponge. *Journal of Materials Science* 41 (13): 4357–4364.

46 Chen, Q., Roether, J.A., and Boccaccini, A.R. (2008). Tissue engineering scaffolds from bioactive glass and composite materials. In: *Topics in Tissue Engineering*, vol. 4 (ed. N. Ashammakhi, R. Reis and F. Chiellini), 1–27.

47 Vitale-Brovarone, C., Baino, F., Bretcanu, O. et al. (2009). Foam-like scaffolds for bone tissue engineering based on a novel couple of silicate-phosphate specular glasses: synthesis and properties. *Journal of Materials Science – Materials in Medicine* 20 (11): 2197–2205.

48 Fiume, E., Schiavi, A., Orlygsson, G. et al. (2021). Comprehensive assessment of bioactive glass and glass-ceramic scaffold permeability: experimental measurements by pressure wave drop, modelling and computed tomography-based analysis. *Acta Biomaterialia* 119: 405–418.

49 Baino, F., Caddeo, S., Novajra, G. et al. (2016). Using porous bioceramic scaffolds to model healthy and osteoporotic bone. *Journal of the European Ceramic Society* 36 (9): 2175–2182.

50 Cunningham, E., Dunne, N.J., Clarke, S.A. et al. (2011). Comparative characterisation of 3-D hydroxyapatite scaffolds developed via comparative characterisation of 3-D hydroxyapatite scaffolds developed via replication of synthetic polymer foams and natural marine sponges. *Journal of Tissue Science & Engineering* S1: 1.

51 Brinker, C.J., Lu, Y., Sellinger, A. et al. (1999). Evaporation-induced self-assembly: nanostructures made easy. *Advanced Materials* 11 (7): 579–585.

52 Zhu, Y. and Kaskel, S. (2009). Comparison of the in vitro bioactivity and drug release property of mesoporous bioactive glasses (MBGs) and bioactive glasses (BGs) scaffolds. *Microporous and Mesoporous Materials* 118 (1–3): 176–182.

53 Zhu, Y., Wu, C., Ramaswamy, Y. et al. (2008). Preparation, characterization and in vitro bioactivity of mesoporous bioactive glasses (MBGs) scaffolds for bone tissue engineering. *Microporous and Mesoporous Materials* 112 (1–3): 494–503.

54 Jiang, P., Lin, H., Xing, R. et al. (2012). Synthesis of multifunctional macroporous–mesoporous TiO_2-bioglasses for bone tissue engineering. *Journal of Sol-Gel Science and Technology* 61 (2): 421–428.

55 El-Rashidy, A.A., Roether, J.A., Harhaus, L. et al. (2017). Regenerating bone with bioactive glass scaffolds: a review of in vivo studies in bone defect models. *Acta Biomaterialia* 62: 1–28.

56 Sachlos, E. and Czernuszka, J.T. (2003). Making tissue engineering scaffolds work. Review on the application of solid freeform fabrication technology to the production of tissue engineering scaffolds. *European Cells & Materials* 5: 29–39.

57 Gmeiner, R., Deisinger, U., Schönherr, J. et al. (2015). Additive manufacturing of bioactive glasses and silicate bioceramics. *Journal of Ceramic Science and Technology* 6 (2): 75–86.

58 Leong, K.F., Cheah, C.M., and Chua, C.K. (2003). Solid freeform fabrication of three-dimensional scaffolds for engineering replacement tissues and organs. *Biomaterials* 24 (13): 2363–2378.

59 Lee, J.W., Lan, P.X., Kim, G. et al. (2008). Fabrication and characteristic analysis of a poly(propylene fumarate) scaffold using micro-stereolithography technology. *Journal of Biomedical Materials Research Part B Applied Biomaterials* 87 (1): 1–9.

60 Skoog, S.A., Goering, P.L., and Narayan, R.J. (2014). Stereolithography in tissue engineering. *Journal of Materials Sciences – Materials in Medicine* 25 (3): 845–856.

61 Solís Pinargote, N.W., Smirnov, A., Peretyagin, N. et al. (2020). Direct ink writing technology (3D printing) of graphene-based ceramic nanocomposites: a review. *Nanomaterials* 10 (7): 1300.

62 Zhang, Y., Tse, C., Rouholamin, D. et al. (2012). Scaffolds for tissue engineering produced by inkjet printing. *Central European Journal of Engineering* 2 (3): 325–335.

63 Nommeots-Nomm, A., Lee, P.D., and Jones, J.R. (2018). Direct ink writing of highly bioactive glasses. *Journal of the European Ceramic Society* 38 (3): 837–844.

64 Legutko, S. (2018). Additive techniques of manufacturing functional products from metal materials. *IOP Conference Series: Materials Science and Engineering* 393 (1): 012003.

65 Liu, J., Hu, H., Li, P. et al. (2013). Fabrication and characterization of porous 45S5 glass scaffolds via direct selective laser sintering. *Materials and Manufacturing Processes* 28 (6): 610–615.

66 Kolan, K.C.R., Leu, M.C., Hilmas, G.E. et al. (2011). Fabrication of 13-93 bioactive glass scaffolds for bone tissue engineering using indirect selective laser sintering. *Biofabrication* 3 (2): 025004.

67 Kim, G.B., Lee, S., Kim, H. et al. (2016). Three-dimensional printing: basic principles and applications in medicine and radiology. *Korean Journal of Radiology* 17 (2): 182–197.

68 Tesavibul, P., Felzmann, R., Gruber, S. et al. (2012). Processing of 45S5 Bioglass® by lithography-based additive manufacturing. *Materials Letters* 72: 81–84.

69 Gmeiner, R., Mitteramskogler, G., Stampfl, J. et al. (2015). Stereolithographic ceramic manufacturing of high strength bioactive glass. *International Journal of Applied Ceramic Technology* 12 (1): 38–45.

70 Shashi, G.M., Laskar, M.A.R., Biswas, H. et al. (2017). A brief review of additive manufacturing with applications. *Proceedings of 14th Global Engineering and Technology Conference*, Dhaka, Bangladesh (29–30 December). BIAM Foundation, 63 Eskaton.

71 Ciobota, N.-D. and Gheorghe, G. (2018). 3D complex structures through fused deposition modeling as a rapid prototyping technology designed for replacing anatomic parts of human body. *Scientific Bulletin of Valahia University: Materials and Mechanics* 16 (15): 30–33.

72 Preethi Soundarya, S., Haritha Menon, A., Viji Chandran, S. et al. (2018). Bone tissue engineering: scaffold preparation using chitosan and other biomaterials with different design and fabrication techniques. *International Journal of Biological Macromolecules* 119: 1228–1239.

73 Guvendiren, M., Molde, J., Soares, R.M.D. et al. (2016). Designing biomaterials for 3D printing. *ACS Biomaterials Science & Engineering* 2 (10): 1679–1693.

74 Monton, M.R.N., Forsberg, E.M., and Brennan, J.D. (2012). Tailoring sol–gel-derived silica materials for optical biosensing. *Chemistry of Materials* 24 (5): 796–811.

75 Alaboodi, A.S. and Sivasankaran, S. (2018). Experimental design and investigation on the mechanical behavior of novel 3D printed biocompatibility polycarbonate scaffolds for medical applications. *Journal of Manufacturing Processes* 35: 479–491.

76 Sachs, E., Curodeau, A., Fan, T. et al. (1998). Three dimensional printing system. US Patent 5, 807, 437, filed 5 February 1996 and issued 25 April 2000.

77 Mancuso, E., Alharbi, N., Bretcanu, O. et al. (2017). Three-dimensional printing of porous load-bearing bioceramic scaffolds. *Proceedings of the Institution of Mechanical Engineers, Part H: Journal of Engineering in Medicine* 231 (6): 575–585.

78 Fiume, E. and Baino, F. (2021). Robocasting of mesoporous bioactive glasses (MBGs) for bone tissue engineering. In: *Bioceramics: From Macro to Nanoscale* (ed. A. Osaka and R. Narayan), 227–249. Elsevier.

79 Lewis, J.A., Smay, J.E., Stuecker, J. et al. (2006). Direct ink writing of three-dimensional ceramic structures. *Journal of the American Ceramic Society* 89 (12): 3599–3609.

80 Franco, J., Hunger, P., Launey, M.E. et al. (2010, 2010). Direct write assembly of calcium phosphate scaffolds using a water-based hydrogel. *Acta Biomaterialia* 6 (1): 218–228.

81 Fu, Q., Saiz, E., and Tomsia, A.P. (2011, 2011). Direct ink writing of highly porous and strong glass scaffolds for load-bearing bone defects repair and regeneration. *Acta Biomaterialia* 7 (10): 3547–3554.

82 Eqtesadi, S., Motealleh, A., Miranda, P. et al. (2014). Robocasting of 45S5 bioactive glass scaffolds for bone tissue engineering. *Journal of the European Ceramic Society* 34 (1): 107–118.

83 Wu, C., Luo, Y., Cuniberti, G. et al. (2011). Three-dimensional printing of hierarchical and tough mesoporous bioactive glass scaffolds with a controllable pore architecture, excellent mechanical strength and mineralization ability. *Acta Biomaterialia* 7 (6): 2644–2650.

84 Baino, F. and Fiume, E. (2020). 3D printing of hierarchical scaffolds based on mesoporous bioactive glasses (MBGs) – fundamentals and applications. *Materials* 13: 1688.

85 Kargozar, S., Mozafiri, M., Hamzehlou, S. et al. (2019). Mesoporous bioactive glasses (MBGs) in cancer therapy: full of hope and promise. *Materials Letters* 251: 241–246.

86 Arcos, D. and Vallet-Regı, M. (2010). Sol–gel silica-based biomaterials and bone tissue regeneration. *Acta Biomaterialia* 6 (8): 2874–2888.

87 Wu, C., Zhou, Y., Fan, W. et al. (2012). Hypoxia-mimicking mesoporous bioactive glass scaffolds with controllable cobalt ion release for bone tissue engineering. *Biomaterials* 33 (7): 2076–2085.

88 Wu, C., Fan, W., Zhu, Y. et al. (2011). Multifunctional magnetic mesoporous bioactive glass scaffolds with a hierarchical pore structure. *Acta Biomaterialia* 7 (10): 3563–3572.

89 Wu, C., Miron, R., Sculean, A. et al. (2011). Proliferation, differentiation and gene expression of osteoblasts in boron-containing associated with dexamethasone deliver from mesoporous bioactive glass scaffolds. *Biomaterials* 32 (29): 7068–7078.

90 Wu, C., Zhou, Y., Lin, C. et al. (2012). Strontium-containing mesoporous bioactive glass scaffolds with improved osteogenic/cementogenic differentiation of periodontal ligament cells for periodontal tissue engineering. *Acta Biomaterialia* 8 (10): 3805–3815.

91 Wu, C., Zhou, Y., Xu, M. et al. (2013). Copper-containing mesoporous bioactive glass scaffolds with multifunctional properties of angiogenesis capacity, osteostimulation and antibacterial activity. *Biomaterials* 34 (2): 422–433.

92 Yun, H., Kim, S., Hyun, Y. et al. (2008). Hierarchically mesoporous–macroporous bioactive glasses scaffolds for bone tissue regeneration. *Journal of Biomedical Materials Research Part B* 87B (2): 374–380.

93 Migneco, C., Fiume, E., Verné, E. et al. (2020). A guided walk through the world of mesoporous bioactive glasses (MBGs): fundamentals, processing and applications. *Nanomaterials* 10 (12): 2571.

94 Wu, C. and Chang, J. (2012). Mesoporous bioactive glasses: structure characteristics, drug/growth factor delivery and bone regeneration application. *Interface Focus* 2 (3): 292–306.

95 Seidi, A., Ramalingam, M., Elloumi-Hannachi, I. et al. (2011). Gradient biomaterials for soft-to-hard interface tissue engineering. *Acta Biomaterialia* 7 (4): 1441–1451.

96 Bretcanu, O., Samaille, C., and Boccaccini, A.R. (2008). Simple methods to fabricate Bioglass-derived glass-ceramic scaffolds exhibiting porosity gradient. *Journal of Materials Science* 43: 4127–4134.

97 Vitale-Brovarone, C., Baino, F., and Verné, E. (2010). Feasibility and tailoring of bioactive glass-ceramic scaffolds with gradient of porosity for bone grafting. *Journal of Biomaterials Applications* 24: 693–712.

98 Barberi, J., Baino, F., Fiume, E. et al. (2019). Robocasting of SiO_2-based bioactive glass scaffolds with porosity gradient for bone regeneration and potential load-bearing applications. *Materials* 12 (17): 2691.

99 Balasubramanian, P., Roether, J.A., Schubert, D.W. et al. (2015). Bi-layered porous constructs of PCL-coated 45S5 bioactive glass and electrospun collagen-PCL fibers. *Journal of Porous Materials* 22: 1215–1226.

100 Nooeaid, P., Roether, J.A., Weber, E. et al. (2014). Technologies for multilayered scaffolds suitable for interface tissue engineering. *Advanced Engineering Materials* 16 (3): 319–327.

101 Shah, A.T., Zahid, S., Ikram, F. et al. (2019). Tri-layered functionally graded membrane for potential application in periodontal regeneration. *Materials Science and Engineering C* 103: 109812.

8

Strong, Tough Bioactive Glasses and Composite Scaffolds

Qiang Fu

Science and Technology Division, Corning Inc., Corning, NY, USA

8.1 Introduction

Tissue and organ failures resulting from trauma, disease, or aging have been reported to account for half of the annual health care expenditures in the United States [1]. Among them, bone is the second most commonly transplanted tissue with blood being the first [2, 3]. Recent years have seen an increasing demand of bone grafts to treat bone fractures or disease. There are over 6.2 million bone fractures in the United States each year, and among them 10% fail to heal properly due to nonunion or delayed union [4, 5]. Osteoporosis currently affects 10 million people, resulting in healthcare costs of over US $25 billion per year [6]. An estimated 2.2 million bone graft procedures are performed worldwide annually to promote fracture healing, fill defects, or repair spinal lesions [7]. Current treatments such as transplantation of tissues and organs; surgical repair; the use of artificial prostheses or mechanical devices; and drug therapy are effective but suffer from limitations [1]. For the regeneration of bone defects, autograft with optimal osteoconductive, osteoinductive, and osteogenic properties remains the gold standard [8], despite disadvantages of donor site morbidity and limited availability. In the last two decades, tissue engineering has emerged as a promising approach for the repair and regeneration of tissues and organs [5, 9]. Skin [10–13], bone [14–16], and cartilage [17, 18] have been successfully regenerated. The approach has the potential to overcome the problem of a shortage of available living tissues and organs for transplantation. Biomaterials with a well-defined architecture are a critical component in this approach and serve as temporary structures for cells and guide their proliferation and differentiation into the desired tissue or organ while growth factors and other bio-molecules can be incorporated into the scaffold along with the cells.

So far, autografts have been the gold standard for treatment of bone defects despite limited supply and donor site morbidity [8, 19]. Bone allografts as an alternative to autografts are expensive with potential risks such as disease transmission and adverse host immune response. Synthetic biomaterials would be ideal bone substitutes, but the clinical success of procedures performed with available synthetic biomaterials does not currently approach that for autologous bone. Biomaterials used for creating scaffolds are designed to meet a set of stringent requirements that are either essential or desirable for optimizing tissue formation [20]. However, there are no clear definite criteria for the mechanical properties of scaffolds intended for bone repair, particularly for those to be used in load-bearing bone defects.

Bioactive Glasses and Glass-Ceramics: Fundamentals and Applications, First Edition.
Edited by Francesco Baino and Saeid Kargozar.

Table 8.1 Summary of the mechanical properties of human bone [22–30].

	Compressive strength (MPa)	Flexural strength (MPa)	Tensile strength (MPa)	Modulus (GPa)	Fracture toughness (MPa $m^{1/2}$)	Porosity (%)
Cortical bone	100–150	135–193	50–151	10–20	2–12	5–10
Cancellous bone	2–12	10–20	1–5	0.1–5	0.1–0.8	50–90

It is generally recognized that the scaffolds should mimic the morphology, structure, and function of bone in order to optimize integration with surrounding tissues. The variability in the architecture and mechanical properties of bone, coupled with differences in age, nutritional state, activity (mechanical loading), and disease status of individuals, provide a major challenge in the design and fabrication of scaffolds for specific defect sites.

A typical long bone of the limbs is composed of two types of bone, each having a different structural organization: cortical bone, also referred to as compact bone; and trabecular bone, also referred to as cancellous or spongy bone [21] (Figure 8.1). Comprised mostly of an inorganic phase (hydroxyapatite, HA) and an organic phase (collagen), cortical bone has a unique combination of strength and toughness. Cortical bone has a compressive strength of 100–150 MPa in the long direction, and a flexural strength of 135–193 MPa (Table 8.1) [22–30]. The fracture toughness, K_{IC}, of cortical bone (2–12 MPa·$m^{1/2}$) has an upper range that is much higher than the values for most ceramics and inorganic glass (typically K_{IC} = 0.5–5 MPa·$m^{1/2}$ for ceramics and 0.5–1 MPa·$m^{1/2}$ for glass). Extrinsic toughening mechanisms, such as microcracking, crack bridging, and deflection, are the primary factors contributing to the high-fracture toughness of human cortical bone [31]. Although the requisite mechanical properties of scaffolds for bone repair is still the subject of debate, it is accepted that their initial mechanical strength should be adequate to withstand subsequent changes resulting from degradation and tissue ingrowth in the *in vivo* environment.

For synthetic biomaterials, the intrinsic material property determines their potential mechanical performance. Figure 8.2a shows a map of the strength and elastic modulus of natural and synthetic materials (typically with a dense microstructure containing no porosity). It is clear that the mechanical response of bone is not matched by any synthetic materials used in orthopedic applications. However, the properties of some synthetic materials can be made to approach those of bone by incorporating a designed pore architecture into the microstructure of these materials. Despite low fracture toughness (K_{IC}) in inorganic oxide glasses, recent progress in glass-ceramics with toughness close to Al_2O_3 ceramics suggests the feasibility to achieve improved mechanical performance in this material family (Figure 8.2b).

A variety of materials, including polymeric and inorganic, have been investigated to be used as scaffolding materials. Synthetic bone substitutes based on biodegradable polymeric materials and metals are commonly used [34–41]. However, for the regeneration of load-bearing bones, the use of biodegradable polymer scaffolds is challenging because of their low mechanical strength. Metallic implants have well-documented fixation problems, and unlike natural bone, cannot self-repair or adapt to changing physiological conditions [42]. They are stronger and stiffer than bone and promote bone resorption by shielding the surrounding skeleton from its normal stress levels. As a consequence, the implant becomes loose over time [34, 35].

Although brittle, scaffolds fabricated from inorganic materials such as calcium phosphate-based bioceramics and bioactive glass can provide higher mechanical strength than polymeric scaffolds. There is an increasing interest in creating and evaluating scaffolds of these materials. Extensive

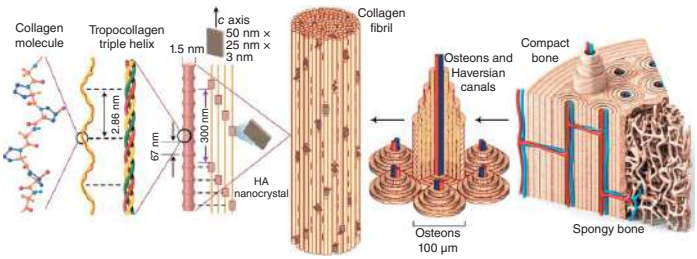

Figure 8.1 Hierarchical structure of bone. In bone, macroscale arrangements involve both compact/cortical bone at the surface and spongy/trabecular bone (foam-like material with ~100-μm-thick struts) in the interior. Cortical bone is composed of osteons and Haversian canals, which surround blood vessels. Osteons have a lamellar structure, with individual lamella consisting of fibers arranged in geometrical patterns. The fibers comprise several mineralized collagen fibrils, composed of collagen protein molecules (tropocollagen) formed from three chains of amino acids and nanocrystals of hydroxyapatite (HA), and linked by an organic phase to form fibril arrays. Source: Reprinted with permission from Wegst et al. [21].

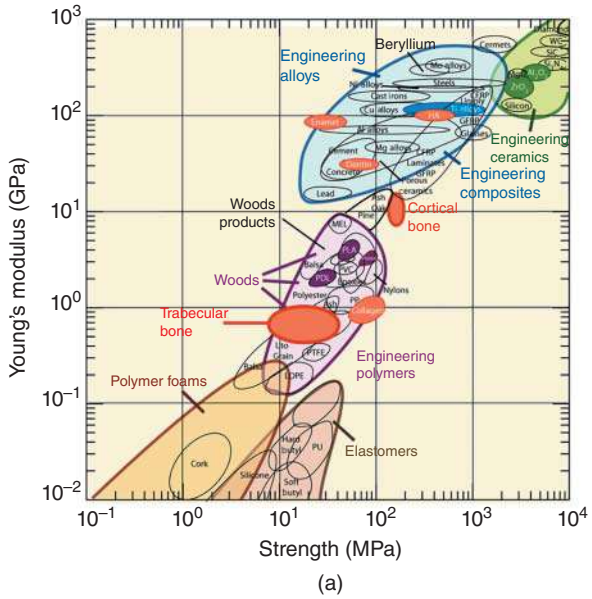

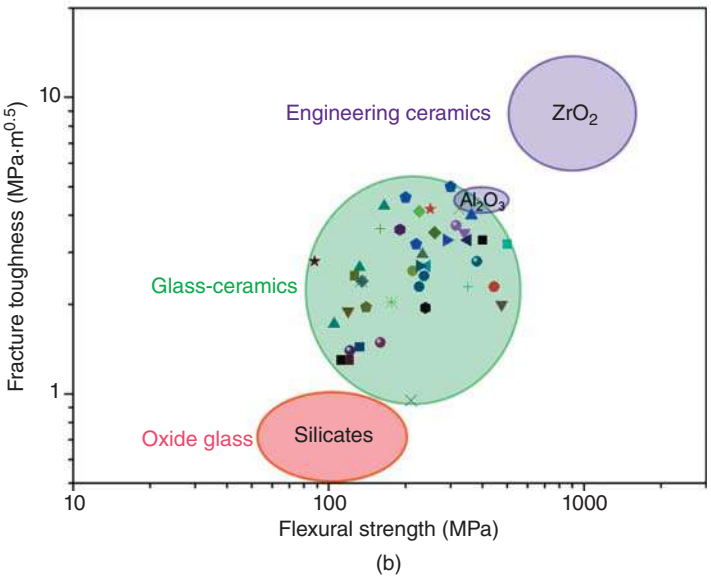

Figure 8.2 (a) Material property chart showing Young's modulus vs. strength. Source: Reprinted with permission from Wegst and Ashby [32]. (b) Materials properties of glass, glass-ceramics, and ceramics. Source: Reprinted with permission from Fu et al. [33].

reviews on the fabrication and properties of the calcium phosphate based bioceramics have been published elsewhere and are not covered here [43–47].

This chapter provides an overview of recent development in the creation of bioactive glass and composite scaffolds with the requisite structure and properties for bone tissue engineering, with a focus on their mechanical properties. It is organized in the following manner: Section 8.2 provides a brief summary of key bioactive glass families; Section 8.3 provides a brief description of typical fabrication technologies that have been commonly used to produce bioactive glass scaffolds, followed

by Section 8.4 that contains a detailed analysis of the strength, fracture toughness, and toughening mechanisms. Finally, a brief conclusion and future trends are included to provide suggestions for future directions on the development of strong, tough, and reliable bioactive glass and composite scaffolds.

8.2 Glass Composition

Certain compositions of glass are known to form a mechanically strong bond to bone [48]. Since the discovery of 45S5 bioactive glasses by Hench et al. [49], they have been frequently used as scaffold materials for bone repair [48–51]. Bioactive glasses have a widely recognized ability to foster the growth of bone cells [52, 53] and to bond strongly with hard and soft tissue [48, 49]. Upon implantation, bioactive glasses undergo specific reactions, leading to the formation of an amorphous calcium phosphate (ACP) or crystalline HA phase on the surface of the glass, which is responsible for their strong bonding with the surrounding tissue [48]. Bioactive glasses are also reported to release ions that activate expression of osteogenic genes [54, 55] and to stimulate angiogenesis [56–58].

Bioactive glass has demonstrated appealing characteristics including ease in controlling the chemical composition and, thus, the rate of degradation, making them attractive for a variety of applications. Several groups of glasses, based on silicate, borate, and phosphate glass compositions, have been shown to be bioactive [48, 59, 60]. Among them, silicate-based glasses are the most widely studied bioactive glass systems. In particular, 45S5 glass, sometimes referred to by its commercial name Bioglass®, remains the *de facto* standard in this material family. Particles of 45S5 glass have been commercialized in several successful medical products including Perioglas (NovaBone Products LLC, Alachua, FL), Novabone (NovaBone Products LLC), and NovaMin (Glaxo-Smith-Kline, UK) [61]. Another silicate glass designated 13-93 has received increasing attention due to its better processing characteristics by viscous flow sintering [62, 63]. Borate glasses such as 13-93B3 have a lower chemical durability than silicate-based bioactive glasses, resulting in faster degradation kinetics [64–66]. The fast ion release resulting from glass degradation is also found to promote angiogenesis and wound healing [67, 68]. Phosphate glasses have the lowest chemical durability and are soluble in body fluid, which makes them a suitable candidate for restorable materials [63]. A summary of major bioactive glass compositions is shown in Table 8.2.

8.3 Fabrication Methods

In general, scaffolds containing interconnected pores with a mean diameter (or width) of 100 μm or greater, and open porosity of >50% are considered to fulfill the minimum requirements to permit tissue ingrowth and function in porous scaffolds [69–71]. A variety of methods have been used to fabricate bioactive glass scaffolds, including sol–gel; thermally bonding of particles, fibers, or spheres; polymer foam replication; freeze casting; and solid freeform fabrication (SFF). Depending on the pore orientation and architecture, bioactive glass scaffolds can be categorized into three groups: isotropic, anisotropic, and periodic types. Representative microstructures of these structures made from bioactive glass 13-93 scaffolds are shown in Figure 8.3. A brief review of these fabrication techniques is presented to give a general idea of the methodology.

Table 8.2 Key bioactive glass compositions published in literature.

Composition (wt%)	45S5	13-93	S53P4	1-98	FL107	6P53B	58S	70S30C	13-93B1	13-93B3	P50C35N5	Apatite-wollastonite (A-W)
Na_2O	24.5	6	23	6	10	10.3	0	0	5.8	5.5	9.3	0
K_2O	0	12	0	11	0	2.8	0	0	11.7	11.1	0	0
MgO	0	5	0	5	6	10.2	0	0	4.9	4.6	0	4.6
CaO	24.5	20	20	22	16	18	32.6	28.6	19.5	18.5	19.7	44.7
CaF_2	0	0	0	0	0	0	0	0	0	0	0	0.5
SiO_2	45	53	53	53	64	52.7	58.2	71.4	34.4	0	0	34.0
P_2O_5	6	4	4	2	2	6	9.2	0	3.8	3.7	71	16.2
B_2O_3	0	0	0	1	2	0	0	0	19.9	56.6	0	0

8.3.1 Sol–Gel Processing

Sol–gel process typically involves the foaming of a sol with the aid of a surfactant, followed by condensation and gelation reactions, as described for the glasses designated 58S and 70S30C [73–77]. The gel is then subjected to aging processes to strengthen it, drying to remove the liquid by-product, and sintering to form porous, three-dimensional scaffolds. The scaffolds have a hierarchical pore architecture, consisting of interconnected macropores (10–500 μm) resulting from the foaming process, and mesopores (2–50 nm) that are inherent to the sol–gel process. The hierarchical pore architecture is considered to be beneficial for stimulating the response of the scaffold to cells because it mimics the hierarchical structure of natural tissues and more closely simulates a physiological environment. High surface area (100–200 m^2/g) is often measured in sol–gel derived scaffolds due to the nanopores in the glass network. As a result, these scaffolds degrade and convert faster to HA than scaffolds of melt-derived glass with the same composition. However, these sol–gel derived scaffolds suffer from low strength (0.3–2.3 MPa) [76], and consequently, they are suitable for substituting defects in low-load sites only.

8.3.2 Thermal Bonding of Particles or Fibers

In this process, the scaffold is formed by thermally bonding a loose and random packing of particles (irregular or spherical in shape) or short fibers in a mold with the desired geometry [78–88]. A wide range of compositions (e.g. 45S5; A-W; 13-93) have been fabricated into porous constructs using this technique. In some studies, a porogen (such as NaCl, starch, or organic polymer particles) is mixed with the bioactive glass particles as a fugitive phase to increase the pore size and porosity of the scaffolds. The porogen is removed by leaching or decomposition after forming the scaffold, but prior to sintering. The technique offers the advantage of ease of fabrication without the need for complex machinery. However, the key disadvantage of the method is the poor pore interconnectivity at low porogen loading.

8.3.3 Polymer Foam Replication

There has been increased interest in using the polymer foam replication method to create porous glass scaffolds although the technique was first used almost 60 years ago to produce macroporous

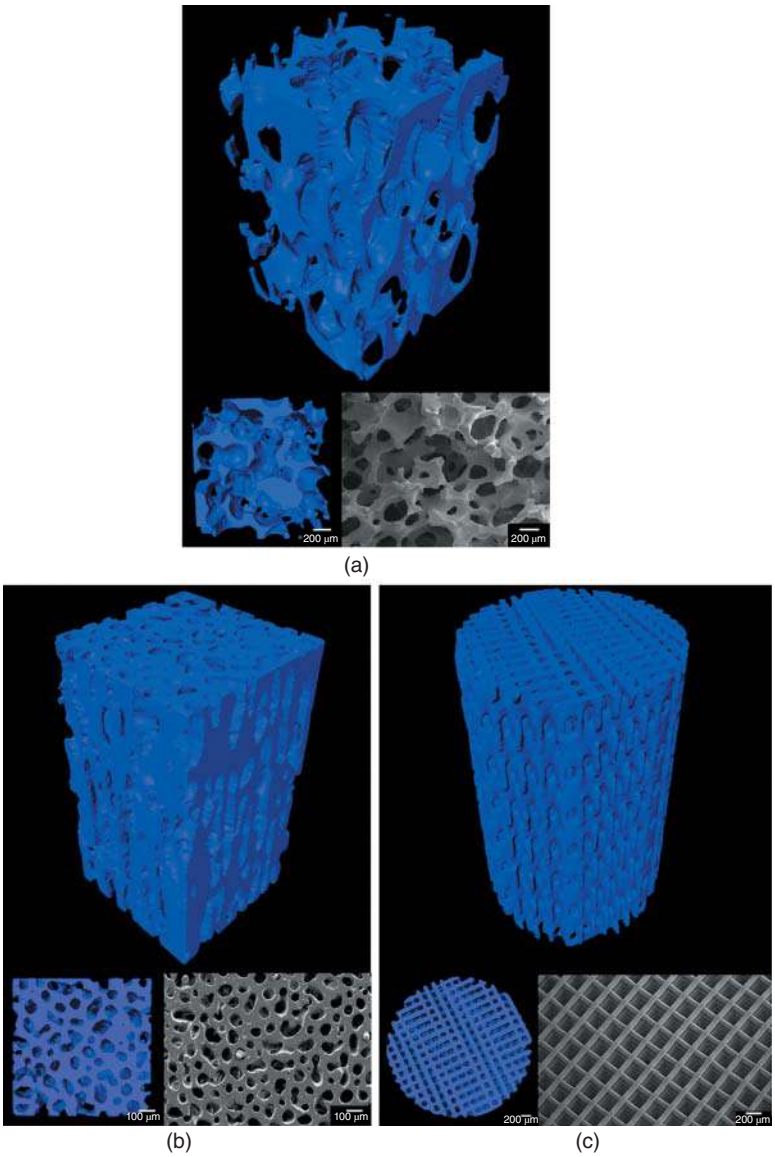

Figure 8.3 Representative microstructure of bioactive glass 13-93 scaffolds prepared by different techniques: (a) isotropic scaffold by a polymer foam replication technique; (b) anisotropic scaffold prepared by a freeze casting technique; (c) periodic scaffold by a direct-ink writing technique. Source: Fu et al. [72], Figure 03, p. 04/with permission of John Wiley & Sons, Inc.

ceramics [89]. A synthetic (e.g. polyurethane, PU) or natural (e.g. coral; wood) foam is initially immersed in a ceramic suspension to obtain a uniform coating on the foam struts. After drying the coated foam, the polymer template and organic binders are burned out through careful heat treatment, typically between 300 and 600 °C, and the glass struts are densified by sintering at 600–1000 °C, depending on the composition and particle size of the glass.

The polymer foam replication technique creates an isotropic microstructure similar to that of dry human trabecular bone (Figure 8.3a). Scaffolds of silicate, borosilicate, and borate bioactive

glass have been prepared using this method [66, 90–102]. This technique produces scaffolds with high porosity, in the range 40–95%, while containing open and interconnected pores. However, the strength of the scaffold is low, typically in the range reported for trabecular bone, which limits its use to the repair of low-load bone sites.

8.3.4 Freeze Casting of Suspensions

The freeze casting route involves rapid freezing of colloidally stable suspension of glass particles in a nonporous mold, and sublimation of the frozen solvent under cold temperatures in a vacuum. After drying, the porous constructs are sintered to remove the fine pores between the particles in the walls of the macropores, which results in an improvement in the mechanical strength. Directional freezing of the suspensions leads to growth of the ice in a preferred direction, resulting in the formation of porous scaffolds with an oriented anisotropic microstructure. The technique has been used to produce porous polymer, glass, and ceramic scaffolds [103–112]. A benefit of the oriented microstructure is higher scaffold strength in the direction of orientation, compared to the strength of a scaffold with a randomly oriented microstructure [113]. Both 45S5 and 13-93 glass scaffolds have been prepared using the technique [106, 109].

It has been shown that the addition of an organic solvent such as 1,4-dioxane to the aqueous solvent [109], or the use of an organic solvent such as camphene [111], results in a change of the lamellar microstructure to a columnar microstructure and an increase in the pore width. Bioactive glass (13-93) scaffolds with columnar microstructures and pore diameters of 100–150 μm have been prepared (Figure 8.3b). In addition to their higher strength, these anisotropic bioactive glass scaffolds have shown the ability to support cell proliferation and differentiation *in vitro*, as well as tissue infiltration *in vivo* [109, 110].

8.3.5 Solid Freeform Fabrication

SFF, also referred to as rapid prototyping or additive manufacturing, is a term to describe a group of techniques that can be used to manufacture objects in a layer-by-layer fashion from a computer-aided design (CAD) file, without the use of traditional tools such as dies or molds. The technique can be used to build scaffolds whose structure follows a predesigned architecture modeled on a computer. In that way, the scaffold architecture can be controlled and optimized to achieve the desired mechanical response, accelerate the bone-regeneration process, and guide the formation of bone with the anatomic cortical-trabecular structure [114]. Several SFF techniques have been used for scaffold fabrication, including three-dimensional printing (3DP), fused deposition modeling (FDM), ink-jet printing, stereolithography (SL), selective laser sintering (SLS), and robocasting [114, 115].

Scaffolds of apatite-mullite glass-ceramics, 13-93, and 6P53B glasses have been manufactured using freeze extrusion, SLS, and robocasting methods [116–118]. The technique enables precise manipulation of the three-dimensional architecture (Figure 8.3c) and printing of lines as thin as 30 μm using micron-sized glass powders. The sintered glass scaffolds, with a periodic structure, show a compressive strength (136 MPa) comparable to human cortical bone, which indicates that these scaffolds have excellent potential for the repair and regeneration of load-bearing bone defects [116].

8.4 Mechanical Properties

Mechanical properties (compressive strength, flexural strength, fracture toughness, fatigue, and reliability) of the bioactive glass and composite scaffolds are reviewed in this section with special reference to their process–structure–property relationships for improved mechanical performance.

Numerous studies have been conducted to evaluate the strength and elastic modulus of porous bioactive glass and ceramic scaffolds in compression. However, during normal physiological activity, bone in load-bearing sites is subjected to multiple loading modes as well as cyclic loading. Consequently, the response of porous scaffolds in multiple loading modes – such as compression, flexure, and torsion – is necessary. Bioactive glass scaffolds are also brittle, so their resistance to fracture, as determined by their fracture toughness, and evaluation of their mechanical reliability using statistical analysis (Weibull statistics) are relevant to brittle materials.

8.4.1 Strength

Compressive strengths of bioactive glass scaffolds prepared from different compositions and using a variety of methods were compiled in Figure 8.4a. A few trends can be observed. First, the compressive strengths span almost 3 orders of magnitude, ranging from 0.2 to 150 MPa for porosities of 30–95%. For the same glass composition and scaffold microstructure (fabrication method), the strength increases with a decrease in porosity, which is also commonly observed for other porous materials. The data show that porous bioactive glass scaffolds can be fabricated with compressive strengths comparable to the values reported for human trabecular and cortical bones (Table 8.1).

Additionally, the data show that the architecture (or microstructure) of the scaffold, which results from the fabrication method, has a strong effect on the strength, regardless of the composition of the glass. For the same porosity, scaffolds with an oriented pore architecture show far higher compressive strength (along the pore orientation direction) than scaffolds with a random or isotropic pore architecture. Among the common fabrication methods, unidirectional freezing of suspensions and SFF provide greater ease for the production of glass scaffolds with oriented pores. For example, 13-93 bioactive glass scaffolds by unidirectional freezing of camphene-based suspensions exhibited a compressive strength along the pore orientation direction two to three times the value in the direction perpendicular to the pore orientation direction [111]. Similar finding was reported in 6P53B bioactive glass scaffolds fabricated using a robocasting technique. The compressive strength along the pore orientation direction was 2.5 times the value in the perpendicular direction [116]. The strength of these scaffolds in the orientation direction (136 MPa) is in the range reported for human cortical bone. These “oriented” bioactive glass scaffolds are likely to provide the requisite strength for the repair of load bearing applications.

The strength–porosity data in Figure 8.4a also suggests that for a given architecture (fabrication method), the glass composition can also have a marked effect on the mechanical strength of the scaffold. As an example, the strength of 13-93 bioactive glass scaffolds (11 MPa) was almost 20 times the value for 45S5-derived glass-ceramic scaffolds (0.5 MPa), each prepared by a polymer foam replication technique and each with greater than 80% porosity. This difference in strength resulted primarily from the difference in sintering characteristics of the two glasses. 45S5 glass is prone to crystallization (devitrification) at sintering temperatures above ~1000 °C, which leads to the formation of a predominantly combeite crystalline phase. This crystallization reduces the

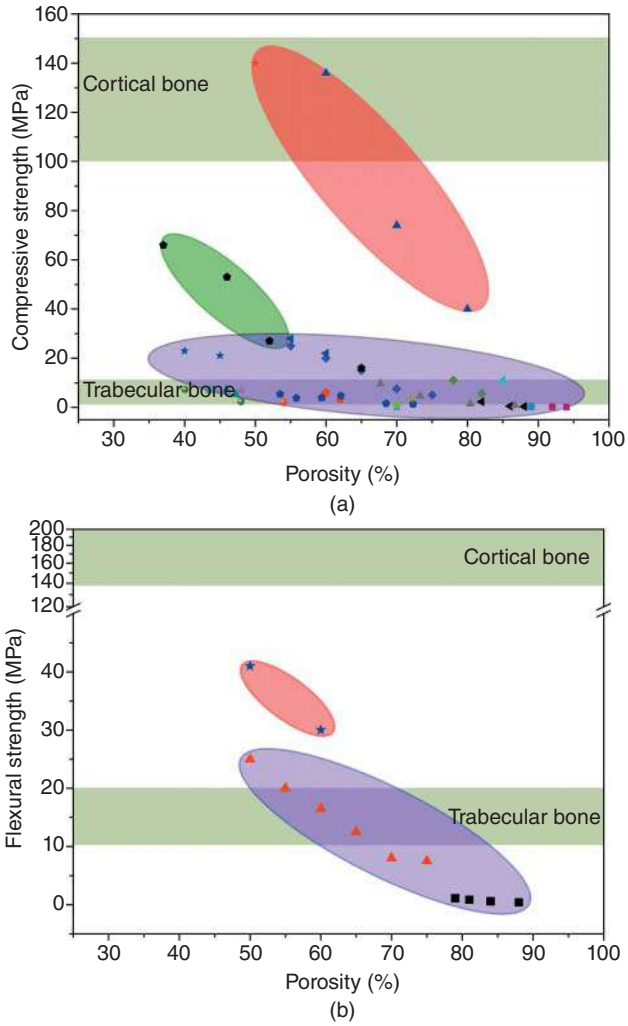

Figure 8.4 (a) Compressive strength of bioactive glass scaffolds compiled from literature and grouped based on their structures. (b) Flexural strength of bioactive glass scaffolds and grouped based on their structures. Each color symbol represents a specific study in literature. Purple: isotropic scaffolds; green: anisotropic scaffolds; pink: periodic scaffolds. Source: Reprinted with permission from Fu et al. [72].

tendency of 45S5 glass to densify by viscous flow sintering. As a result, voids remaining from the burnout of the polymer foam are difficult to fill and may remain as triangular-shaped pores in the struts; these pores within the glass struts lead to a reduction in the strength of the scaffold. In comparison, as the sintering temperature of 13-93 glass is below its crystallization temperature, viscous flow sintering can lead to complete filling of the voids in the glass struts, leading to an improvement in the strength of the scaffold.

Flexural strength data for bioactive glass scaffolds with isotropic and periodic microstructures are shown in Figure 8.4b. The flexural strengths span almost 2 orders of magnitude, in the range 0.4–41 MPa for bioactive glass scaffolds [119, 120], within the range of trabecular bone and much lower than that of cortical bone (Table 8.1). Similar as the trend in Figure 8.4a, both porosity and structure impact the flexural strength in bioactive glass scaffolds. Bioactive glass scaffolds with a

periodic microstructure prepared by a direct ink writing technique show a much higher flexural strength than the scaffolds with an isotropic scaffold (Figure 8.4b). Failure typically occurs in the regions of the scaffold that experience tensile stress during the bending test. Brittle materials such as glass and ceramics are weak in tension, so they typically have flexural strengths that are much lower than their typical compressive strength [47, 121, 122].

There have been limited studies on the testing of tensile strength of bioactive glass scaffolds due to the complexity in machining, usually requiring numerically controlled machining and a large amount of sample material removal from a cylinder, and the brittleness of the scaffolds. And the testing methodology from American Society for Testing and Materials (ASTM) requires dumbbell-shaped specimens placed in the grips of a tensile testing machine [123]. To overcome these limitations, nonstandard setups were used for porous scaffolds by gluing them to the two loading fixtures prior to the test [124–126]. Tensile strength of 0.011 MPa was determined for 45S5 glass scaffolds (porosity >90%) prepared from a polymer foam replication method [125], and 7.4–2.3 MPa for wollastonite glass-ceramic scaffolds with 40–79% porosity prepared using the same foam replication method [124, 126]. These tensile strength values fall within that of trabecular bone and are much lower than that of cortical bone (Table 8.1).

To summarize, the compressive strength of bioactive glass scaffold falls within the range of that for cortical and trabecular bone, indicating their great potential for applications in nonloading and load-bearing sites. Both flexural and tensile strengths of glass scaffolds fall within the range of trabecular bone, suggesting future work is needed to address the failure under tensile loading. Optimization of the glass composition, coupled with improved control of the pore architecture and application of desired polymeric coating are potential approaches for the creation of scaffolds with the requisite combination of strength and porosity.

8.4.2 Fatigue Resistance

One of the primary causes of bone fracture in humans is repetitive and cyclic loading of bone during daily living [127, 128]. Stress fracture, which is caused by prolonged and intense loading; and fragility fracture, caused by a reduction of bone strength due to osteoporosis, are both reported to occur in the trabecular bone region [129, 130]. Therefore, in addition to the investigation of sudden, catastrophic failure, investigation of fatigue resistance in scaffolds for load-bearing applications is essential for a safe design. Fatigue in glass and ceramics is a term used to measure processes that lead to degradation of mechanical properties over time [131]. Two types of fatigue have been observed in glass and ceramic materials: (i) slow crack growth resulting from stress-corrosion cracking; (ii) cyclic fatigue resulting from fatigue-crack propagation [132].

For bioactive glasses, stress corrosion is caused and controlled by a chemical reaction between water and the glasses, i.e. water attack on the Si–O network [133–135]. The presence of open porosity in porous HA reduces fatigue resistance considerably in comparison to that in dense ceramics [136]. There is as yet no systematic understanding of the impact of microstructure and porosity on slow crack growth in bioactive glass and ceramic scaffolds.

Fatigue resistance of bioactive glass scaffold is relevant given that these scaffolds may be applied in load-bearing sites in body fluid. A recent study indicates that bioactive glass 13-93 scaffolds with a periodic structure have an excellent fatigue resistance at stresses far higher than normal physiological stresses [137]. When tested in air at room temperature or in phosphate-buffered saline (PBS) at 37 °C, fatigue life decreased with an increase of maximum cyclic compressive stress from 10 to 30 MPa (Figure 8.5). And a significant decrease was only observed for the samples tested in PBS, suggesting the crack growth mechanism is due to the stress corrosion of Si—O—Si bonds at

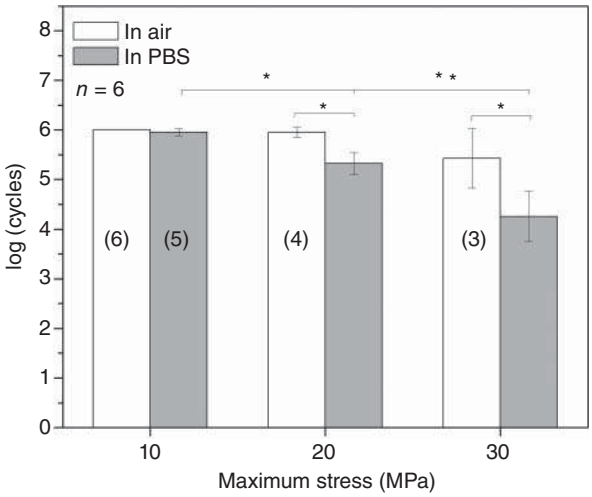

Figure 8.5 Fatigue life (average number of cycles to failure) of 13-93 bioactive glass scaffolds tested in air and PBS under cyclic compressive stresses. The stresses shown are the maximum applied stress in the cyclic loading. *Significant difference between groups, $p < 0.05$. The number in the bar indicates the number of samples (out of six) that survived 106 cycles, when the test was terminated. Source: Reprinted with permission from Liu et al. [137].

the crack tip [134, 138]. By assuming a uniform load distribution, the stress on an implant in a segmental femoral defect was estimated to be <2 MPa [137]. The finding confirms the excellent fatigue resistance of periodic bioactive glass scaffolds at stresses far higher than normal physiological stresses. Fatigue resistance of glass scaffolds with isotropic or anisotropic structure has yet to be tested.

8.4.3 Fracture Toughness and Reliability

Although high compressive strength can be achieved in bioactive glass scaffolds to meet the minimal requirement for the repair of load-bearing bone defects, their use in these applications may be limited by their intrinsic brittleness or low resistance to crack propagation (K_{IC}). The K_{IC} values for ceramics and glass, as shown in Figure 8.2b, are inherently low (typically $K_{IC} = 0.5–5\ MPa{\cdot}m^{1/2}$ for ceramics and $0.5–1\ MPa{\cdot}m^{1/2}$ for glass), making them sensitive to the presence of small defects and flaws (~10 μm). They tend to fail catastrophically when subjected to tensile or flexural stresses far lower than their compressive strength [139, 140]. Therefore, it is necessary to quantify their brittle behavior using one or more of the following parameters: fracture toughness, Weibull modulus, and work of fracture.

Standard test methods for measuring the fracture toughness of brittle materials are specified by ASTM [141]. The relatively low strength and the presence of surface defects in some bioactive glass scaffolds often results in difficulties in sample preparation and a large scattering in the testing results. Using a single edge notched beam (SENB) technique, K_{IC} values of 0.5 and $0.8\ MPa{\cdot}m^{1/2}$, was reported in bioactive glass13-93 scaffolds with a periodic microstructure [122, 137], and $0.2–0.6\ MPa{\cdot}m^{1/2}$ for a $CaO–Al_2O_3–P_2O_5$ glass scaffold with porosities of 50–75% prepared using a polymer foam replication method [120]. Both are far lower than the values reported for cortical bone ($2–12\ MPa{\cdot}m^{1/2}$).

Another way to measure the fracture toughness of porous scaffolds may be the work of fracture, γ_{wof}, i.e. the total energy consumed to produce a unit area of fracture surface during complete fracture [142]. Several groups have used the work of fracture to evaluate the toughness of porous glass and ceramic scaffolds [119, 143–145]. However, the work of fracture can only be used for comparison within a given study because it is not a true material property and it may vary due to the differences in sample dimension, sample geometry, and testing conditions.

In addition to fracture toughness, Weibull distribution serves as another means to quantify the brittle behavior in glass and ceramics [146]. The Weibull distribution is given as a cumulative distribution:

$$P_f(\sigma) = 1 - \exp\left[\frac{-(\sigma - \sigma_t)^m}{\sigma_\varphi^m}\right] \tag{8.1}$$

where $P_f(\sigma)$ is the probability of failure at a stress σ, σ_0 is a scaling constant, σ_t is the threshold stress below which no failure occurs in the material, that practically can be taken as zero for brittle ceramics, and m is the Weibull modulus. The Weibull modulus, m, determines the reliability of the materials, with larger values corresponding to more reliable materials. To get an unbiased estimate of the failure probability, the recommended number of specimens is between 20 and 30 [147, 148].

Despite the use of Weibull distribution in the evaluation of the reliability of porous ceramic scaffolds [121, 149, 150], few studies are focused on porous bioactive glass scaffolds. In one study, Weibull modulus of 6.0 and 5.3 were measured on porous periodic bioactive glass 13-93 scaffolds in compression and three-point bending test, respectively [122]. The finding is consistent with other reported values on porous glass scaffolds [120, 137]. The measured Weibull modulus, in the range 3–8, was comparable to the values reported for porous calcium phosphate scaffolds [121, 149, 150]. The disadvantage of the evaluation is the requirement of many test specimens which may not be practical for some studies.

In summary, while the compressive strength and elastic modulus of bioactive glass scaffolds have been widely studied, more efforts are needed to quantity the brittle behavior and reliability of these scaffolds, especially on those intended for the repair of defects in loaded bone. Based on the discussions of strength, toughness, reliability, and fatigue resistance, it is clear that compressive strength is not a controlling factor limiting application of some types of (anisotropic and periodic) scaffolds in load-bearing sites. However, applications for these scaffolds are still constrained by the intrinsic low-fracture toughness of their constituent materials. Further improvements on the toughness of scaffolds utilizing extrinsic toughening mechanisms are being explored. The properties of strong and tough natural biological materials such as bone and nacre are inspiring new approaches in the design of strong yet tough scaffolds for bone tissue engineering.

8.4.4 Toughening of Bioactive Glass

Biological mineralized composites such as bone, dentin, and nacre are known to have unique structures that enable a high resistance to crack propagation when subjected to applied loads [151–154]. Extrinsic toughening mechanisms, shown in Figure 8.6a, including microcracking, crack bridging, and deflection, are the primary factors contributing to the high fracture toughness of human cortical bone and nacre. The knowledge from these natural minerals and their intriguing mechanisms have provided a fresh stimulus for the design of new synthetic materials with unprecedented properties and performance.

The first approach comes from creation of a stronger and tougher scaffold material through microstructure control and/or the addition of reinforcing phase(s) [156, 157]. Glass-ceramic A-W is an example demonstrating the importance of the microstructure and reinforcing phase on its strength and toughness [158]. The fracture toughness of the materials increased from 0.8 to 1.2 and 2.0 MPa·m$^{1/2}$ when the crystallinity increased from 0% to 72%, which in turn resulted in an increase of bending strength from 70 to 90 and 200 MPa. The increase in its body strength is attributed to the crack deflection mechanisms from the formation of wollastonite phase [159]. A similar finding has been observed in lithium disilicate, leucite, and apatite glass-ceramics, materials used for

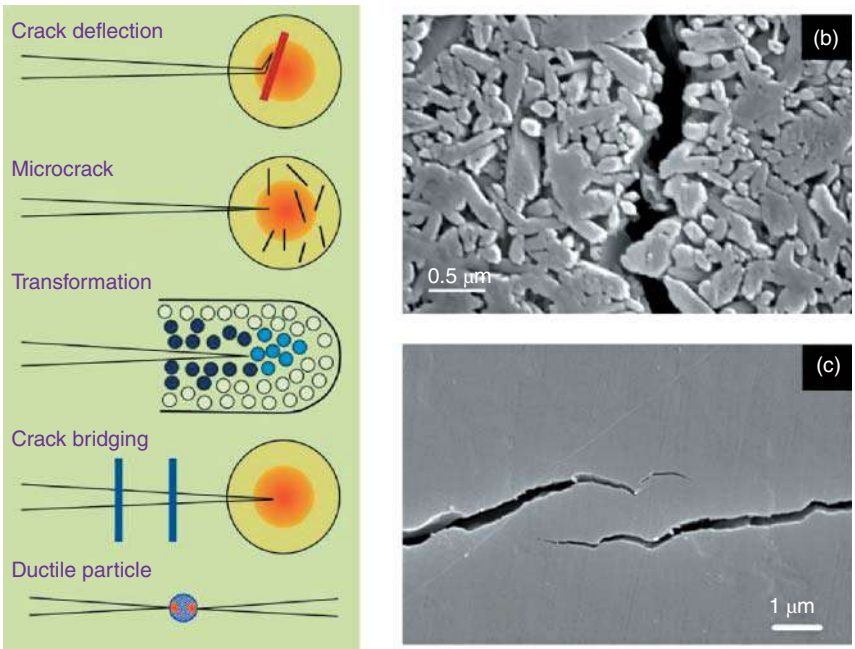

Figure 8.6 (a) Schematic illustration of the primary toughening mechanisms, including crack deflection, microcrack, phase transformation, crack bridging, and presence of a ductile phase, in ceramics and ceramic-matrix composites that enable their exceptional mechanical performance. Source: (a) Reprinted with permission from Fu et al. [33]. (b) Crack deflection observed in lithium disilicate glass-ceramics. (c) Crack bridging observed in leucite glass-ceramics (stoichiometric composition: $K_2O{\cdot}Al_2O_3{\cdot}4SiO_2$). Source: (b, c) Apel et al. [155], Figure 03,05, p. 05,06/with permission of Elsevier.

dental replacement [155]. Crack bridging and crack deflection in these materials were determined to be the most potent toughening mechanisms (Figure 8.6b,c), which were also the key extrinsic toughening mechanisms of bone [31, 160]. Formation of interlocking microstructures and high crystalline content in lithium disilicate glass-ceramics produced a crack deflection toughening mechanism and a high fracture toughness (2.7 $MPa{\cdot}m^{1/2}$) [155]. The combination of high strength and toughness in glass-ceramics has generated wide interest for development of new glass-ceramic materials [33, 48, 161–167]. Although the fracture toughness values (1–3 $MPa{\cdot}m^{1/2}$) of some bioactive glass-ceramics are in the lower range for cortical bone (2–12 $MPa{\cdot}m^{1/2}$), they are definitely much tougher than either bioactive glass or ceramics (K_{IC} in the range of 0.5–1 $MPa{\cdot}m^{1/2}$) [157]. Considering the high strength achieved in both anisotropic and periodic scaffolds, scaffolds made of glass-ceramics may be potent candidates for load-bearing site applications.

The creation of an inorganic/organic composite serves as a second attempt to mimic the structure of bone, which is mainly composed of organic fibrils and inorganic HA. When measured by the work of fracture, significant increases in toughness have been reported for polymer-coated glass scaffolds. A variety of biodegradable polymers including poly(D,L-lactic acid), PDLLA [119, 168]; poly(3-hydroxybutyrate), P(3HB) [145]; alginate [169], and polycaprolactone, PCL [60] have been used to toughen glass scaffolds. Upon compression, polymer-toughened scaffolds exhibit a "plastic" deformation with a gradual failure mode, rather than "brittle" behavior with catastrophic failure [60]. The primary energy dissipation mechanism is believed to be PCL fibril extension and

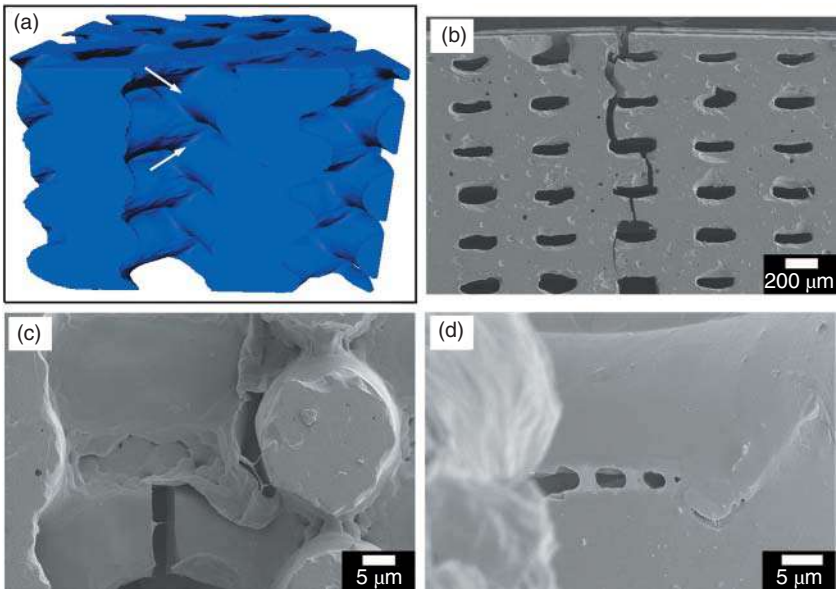

Figure 8.7 (a) A three-dimensional view of the joining of adjacent glass struts using synchrotron X-ray tomography; (b) crack propagation path in a precracked uncoated glass scaffold; (c) crack propagation path in a precracked PCL-coated glass scaffold; (d) PCL fibril elongation in coated glass scaffold after bending test. Source: Fu et al. [122], Figure 09, p. 07/with permission of John Wiley & Sons, Inc.

crack bridging on the strut surface (Figure 8.7). Much success of toughening from polymer coating is observed primarily in isotropic scaffolds, which are generally much weaker than anisotropic and periodic scaffolds. However, it is worth noting that the measurement of work of fracture is not a standard method for testing the true toughness of a material, and the measured value is highly dependent on sample geometry and other experimental factors [47]. A recent work on the PCL-coated periodic glass (13-93) scaffold showed that the polymer coating failed to improve the flexural strength or fracture toughness [122], suggesting the limited capability in providing effective toughening mechanisms to the scaffolds with high strength intended for load-bearing sites.

The third approach focuses on the engineering of polymer/ceramic composites with a "brick and mortar" structure similar to nacre (Figure 8.8a). In nacre, the "bricks" are platelets of the mineral aragonite comprising around 95 vol% of the structure and contributing to its high strength, while the "mortar" is an organic biopolymer filled in-between that provides extrinsic and intrinsic toughening mechanisms [171–174]. Composites made by infiltrating an anisotropic Al_2O_3 scaffold (fabricated using the freeze casting technique) with an organic phase (poly(methyl methacrylate), PMMA) have shown exceptionally high flexural strength of ~200 MPa and high fracture toughness, up to 30 MPa·$m^{1/2}$ (Figure 8.8b–d) [170, 175]. Multiple extrinsic toughening mechanisms including microcracking, crack bridging, and crack deflection accounts for its unique mechanical properties, making it an attractive material for applications in load-bearing bone sites. However, the drawback of the method is the formation of a dense scaffold, which does not have sufficient porosity for the ingrowth of new tissue/bone. This can be potentially mitigated by choosing a biodegradable polymer as an infiltration material to create open porosity upon degradation.

Although brittle than cortical bone, anisotropic and periodic scaffolds have demonstrated high mechanical strength that are approaching that of cortical bone. However, challenges remain in the

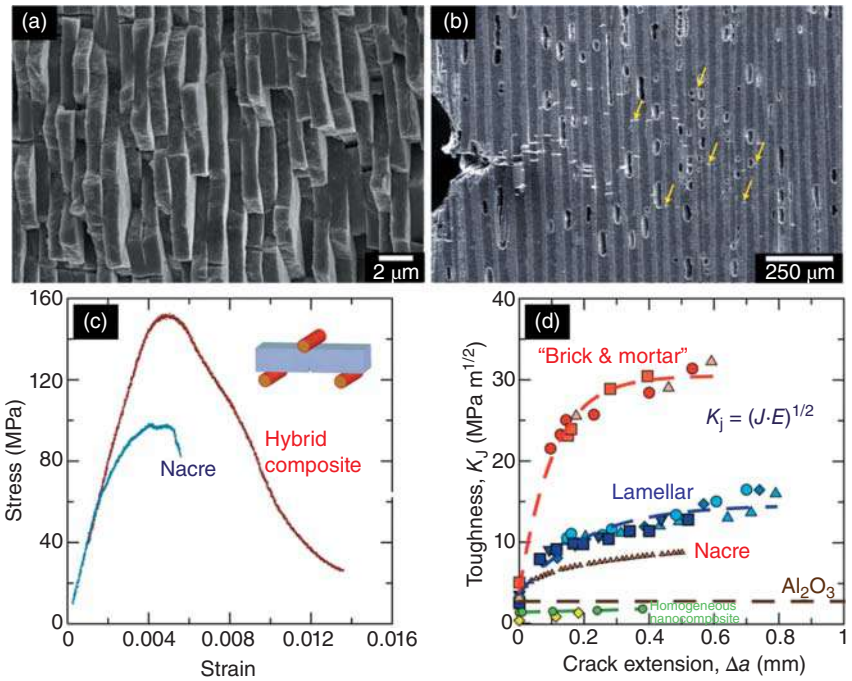

Figure 8.8 Mechanical response and toughening mechanisms in the synthetic hybrid composites. (a) Scanning electron microscopy (SEM) image of the structure of nacre. (b) SEM image taken during an *in situ* R-curve measurement of a lamellar structure. (c) Bending stress–strain curves for the Al_2O_3/PMMA hybrid materials mimic those of nacre and show >1% inelastic deformation before failure. (d) Exceptional toughness for crack growth, similar to that of natural composites, and display significant rising R-curve behavior. Source: Launey et al. [170]/with permission of Elsevier.

development of new materials and methods to toughen the bioactive glass and ceramic scaffolds for applications in load-bearing sites.

8.5 Conclusions and Future Trends

Despite their intrinsically low fracture toughness, bioactive glass scaffolds with compressive strengths comparable to those of trabecular and cortical bone have been prepared using desired fabrication methods. The toughness and mechanical reliability of bioactive glass scaffolds remain limiting factors for their applications in loaded bone repair, which highlights the importance of having additional toughening mechanisms in the materials. The incorporation of a biocompatible polymer phase, as a coating or a secondary phase, provides multiple toughening mechanisms for energy dissipation. A focus of future work should be on the creation of strong and tough bioactive glass scaffolds using advanced fabrication techniques and their evaluation in loaded and nonloaded bone defect sites both *in vitro* and *in vivo*.

References

1 Persidis, A. (1999). Tissue engineering. *Nature Biotechnology* 17 (5): 508–510.
2 Boyce, T., Edwards, J., and Scarborough, N. (1999). Allograft bone – the influence of processing on safety and performance. *Orthopedic Clinics of North America* 30 (4): 571–581.

3 Van Heest, A. and Swiontkowski, M. (1999). Bone-graft substitutes. *Lancet* 353: SI28–SI29.
4 Praemer, A., Furner, S., and Rice, D.P. (1999). *Musculoskeletal Conditions in the United States*, 2e. Park Ridge, IL: American Academy of Orthopaedic Surgeons.
5 Langer, R. and Vacanti, J.P. (1993). Tissue engineering. *Science* 260 (5110): 920–926.
6 Lane, N.E. (2006). Epidemiology, etiology, and diagnosis of osteoporosis. *American Journal of Obstetrics and Gynecology* 194 (2): S3–S11.
7 Giannoudis, P.V., Dinopoulos, H., and Tsiridis, E. (2005). Bone substitutes: an update. *Injury* 36: 20–27.
8 Cypher, T. and Grossman, J. (1996). Biological principles of bone graft healing. *The Journal of Foot & Ankle Surgery* 35: 413–417.
9 Nerem, R.M. (1991). Cellular engineering. *Annals of Biomedical Engineering* 19 (5): 529–545.
10 Cooper, M.L. and Hansbrough, J.F. (1991). Use of a composite skin-graft composed of cultured human keratinocytes and fibroblasts and a collagen-GAG matrix to cover full-thickness wounds on athymic mice. *Surgery* 109 (2): 198–207.
11 Hansbrough, J.F., Morgan, J., Greenleaf, G. et al. (1994). Evaluation of Graftskin composite grafts on full-thickness wounds on athymic mice. *Journal of Burn Care & Rehabilitation* 15 (4): 346–353.
12 Eaglstein, W.H. and Falanga, V. (1997). Tissue engineering and the development of Apligraf®, a human skin equivalent. *Clinical Therapeutics* 19 (5): 894–905.
13 Black, A.F., Berthod, F., L'Heureux, N. et al. (1998). In vitro reconstruction of a human capillary-like network in a tissue-engineered skin equivalent. *FASEB Journal* 12 (13): 1331–1340.
14 Vacanti, C.A., Bonassar, L.J., Vacanti, M.P., and Shufflebarger, J. (2001). Replacement of an avulsed phalanx with tissue-engineered bone. *New England Journal of Medicine* 344 (20): 1511–1514.
15 Kruyt, M.C., van Gaalen, S.M., Oner, F.C. et al. (2004). Bone tissue engineering and spinal fusion: the potential of hybrid constructs by combining osteoprogenitor cells and scaffolds. *Biomaterials* 25 (9): 1463–1473.
16 Marcacci, M., Kon, E., Moukhachev, V. et al. (2007). Stem cells associated with macroporous bioceramics for long bone repair: 6- to 7-year outcome of a pilot clinical study. *Tissue Engineering* 13 (5): 947–955.
17 Cao, Y., Vacanti, J.P., Paige, K.T. et al. (1997). Transplantation of chondrocytes utilizing a polymer-cell construct to produce tissue-engineered cartilage in the shape of a human ear. *Plastic and Reconstructive Surgery* 100 (2): 297–302; Discussion 303–304.
18 Valonen, P.K., Moutos, F.T., Kusanagi, A. et al. (2010). In vitro generation of mechanically functional cartilage grafts based on adult human stem cells and 3D-woven poly(ε-caprolactone) scaffolds. *Biomaterials* 31 (8): 2193–2200.
19 De Long, W.G., Einhorn, T.A., Koval, K. et al. (2007). Bone, grafts and bone graft substitutes in orthopedic trauma surgery – a critical analysis. *Journal of Bone and Joint Surgery American Volume* 89A (3): 649–658.
20 Hutmacher, D.W. (2000). Scaffolds in tissue engineering bone and cartilage. *Biomaterials* 21 (24): 2529–2543.
21 Wegst, U.G.K., Bai, H., Saiz, E. et al. (2015). Bioinspired structural materials. *Nature Materials* 14 (1): 23–36.
22 Martin, R.B., Burr, D.B., and Sharkey, N.A. (1998). *Skeletal Tissue Mechanics*. New York/London: Springer.

23 Reilly, D.T., Burstein, A.H., and Frankel, V.H. (1974). Elastic-modulus for bone. *Journal of Biomechanics* 7 (3): 271–275.

24 Rho, J.Y., Hobatho, M.C., and Ashman, R.B. (1995). Relations of mechanical-properties to density and CT numbers in human bone. *Medical Engineering & Physics* 17 (5): 347–355.

25 Fung, Y.C. (1993). *Biomechanics: Mechanical Properties of Living Tissues*, 2e. New York/London: Springer-Verlag.

26 Keaveny, T.M.H.W. (1993). Mechanical properties of cortical and trabecular bone. In: *Bone. A Treatise* (ed. B.K. Hall), 285–344. Boca Raton, FL: CRC Press.

27 Zioupos, P. and Currey, J.D. (1998). Changes in the stiffness, strength, and toughness of human cortical bone with age. *Bone* 22 (1): 57–66.

28 Goldstein, S.A. (1987). The mechanical-properties of trabecular bone – dependence on anatomic location and function. *Journal of Biomechanics* 20 (11–12): 1055–1061.

29 Rohl, L., Larsen, E., Linde, F. et al. (1991). Tensile and compressive properties of cancellous bone. *Journal of Biomechanics* 24 (12): 1143–1149.

30 Oyen, M.L. (2008). The materials science of bone: lessons from nature for biomimetic materials synthesis. *MRS Bulletin* 33 (1): 49–55.

31 Launey, M.E., Buehler, M.J., and Ritchie, R.O. (2010). On the mechanistic origins of toughness in bone. *Annual Review of Materials Research* 40 (40): 25–53.

32 Wegst, U. and Ashby, M. (2004). The mechanical efficiency of natural materials. *Philosophical Magazine* 84 (21): 2167–2186.

33 Fu, Q., Beall, G.H., and Smith, C.M. (2017). Nature-inspired design of strong, tough glass-ceramics. *MRS Bulletin* 42 (3): 220–225.

34 Huiskes, R., Weinans, H., and Vanrietbergen, B. (1992). The relationship between stress shielding and bone-resorption around total hip stems and the effects of flexible materials. *Clinical Orthopaedics and Related Research* 274: 124–134.

35 Webster, T.J., Siegel, R.W., and Bizios, R. (1999). Design and evaluation of nanophase alumina for orthopaedic/dental applications. *Nanostructured Materials* 12 (5–8): 983–986.

36 Hayashi, T. (1994). Biodegradable polymers for biomedical uses. *Progress in Polymer Science* 19 (4): 663–702.

37 Agrawal, C.M. and Ray, R.B. (2001). Biodegradable polymeric scaffolds for musculoskeletal tissue engineering. *Journal of Biomedical Materials Research* 55 (2): 141–150.

38 Griffith, L.G. (2000). Polymeric biomaterials. *Acta Materialia* 48 (1): 263–277.

39 Lee, K.Y. and Mooney, D.J. (2001). Hydrogels for tissue engineering. *Chemical Reviews* 101 (7): 1869–1879.

40 Varghese, S. and Elisseeff, J.H. (2006). Hydrogels for musculoskeletal tissue engineering. In: *Polymers for Regenerative Medicine* (ed. C. Werner), 95–144. Springer.

41 Reis, R.L. (2008). *Natural-Based Polymers for Biomedical Applications*. Cambridge, UK: Woodhead Publishing Limited.

42 Piehler, H.R. (2000). The future of medicine: biomaterials. *MRS Bulletin* 25 (8): 67–70.

43 de Groot, K. (1993). Clinical applications of calcium phosphate biomaterials: a review. *Ceramics International* 19: 363–366.

44 Daculsi, G., Laboux, O., Malard, O., and Weiss, P. (2003). Current state of the art of biphasic calcium phosphate bioceramics. *Journal of Materials Science – Materials in Medicine* 14 (3): 195–200.

45 Dorozhkin, S.V. (2010). Bioceramics of calcium orthophosphates. *Biomaterials* 31 (7): 1465–1485.

46 Levengood, S.K.L., Polak, S.J., Poellmann, M.J. et al. (2010). The effect of BMP-2 on micro- and macroscale osteointegration of biphasic calcium phosphate scaffolds with multiscale porosity. *Acta Biomaterialia* 6 (8): 3283–3291.

47 Wagoner Johnson, A.J. and Herschler, B.A. (2011). A review of the mechanical behavior of CaP and CaP/polymer composites for applications in bone replacement and repair. *Acta Biomaterialia* 7 (1): 16–30.

48 Hench, L.L. (1998). Bioceramics. *Journal of the American Ceramic Society* 81 (7): 1705–1728.

49 Hench, L.L., Splinter, W.C., Allen, W.C., and Greenlee, T.K. (1971). Bonding mechanisms at the interface of ceramic prosthetic material. *Journal of Biomedical Materials Research Symposium* 2: 117–141.

50 Rahaman, M.N., Brown, R.F., Bal, B.S., and Day, D.E. (2006). Bioactive glasses for nonbearing applications in total joint replacement. *Seminars in Arthroplasty* 17: 102–112.

51 Yunos, D.M., Bretcanu, O., and Boccaccini, A.R. (2008). Polymer-bioceramic composites for tissue engineering scaffolds. *Journal of Materials Science* 43 (13): 4433–4442.

52 Wheeler, D.L., Stokes, K.E., Park, H.M., and Hollinger, J.O. (1997). Evaluation of particulate Bioglass® in a rabbit radius ostectomy model. *Journal of Biomedical Materials Research* 35 (2): 249–254.

53 Wheeler, D.L., Stokes, K.E., Hoellrich, R.G. et al. (1998). Effect of bioactive glass particle size on osseous regeneration of cancellous defects. *Journal of Biomedical Materials Research* 41 (4): 527–533.

54 Xynos, I.D., Edgar, A.J., Buttery, L.D.K. et al. (2000). Ionic products of bioactive glass dissolution increase proliferation of human osteoblasts and induce insulin-like growth factor II mRNA expression and protein synthesis. *Biochemical and Biophysical Research Communications* 276 (2): 461–465.

55 Xynos, I.D., Edgar, A.J., Buttery, L.D.K. et al. (2001). Gene-expression profiling of human osteoblasts following treatment with the ionic products of Bioglass® 45S5 dissolution. *Journal of Biomedical Materials Research* 55 (2): 151–157.

56 Leach, J.K., Kaigler, D., Wang, Z. et al. (2006). Coating of VEGF-releasing scaffolds with bioactive glass for angiogenesis and bone regeneration. *Biomaterials* 27 (17): 3249–3255.

57 Leu, A. and Leach, J.K. (2008). Proangiogenic potential of a collagen/bioactive glass substrate. *Pharmaceutical Research* 25 (5): 1222–1229.

58 Gorustovich, A.A., Roether, J.A., and Boccaccini, A.R. (2010). Effect of bioactive glasses on angiogenesis: a review of in vitro and in vivo evidences. *Tissue Engineering Part B* 16 (2): 199–207.

59 Rahaman, M.N., Day, D.E., Bal, B.S. et al. (2011). Bioactive glass in tissue engineering. *Acta Biomaterialia* 7 (6): 2355–2373.

60 Fu, Q., Saiz, E., Rahaman, M.N., and Tomsia, A.P. (2011). Bioactive glass scaffolds for bone tissue engineering: state of the art and future perspectives. *Materials Science and Engineering C* 31 (7): 1245–1256.

61 Hench, L.L. (2013). Chronology of bioactive glass development and clinical applications. *New Journal of Glass and Ceramics* 03 (02): 67–73.

62 Brink, M. (1997). The influence of alkali and alkaline earths on the working range for bioactive glasses. *Journal of Biomedical Materials Research* 36 (1): 109–117.

63 Brink, M., Turunen, T., Happonen, R.P., and Yli-Urpo, A. (1997). Compositional dependence of bioactivity of glasses in the system Na_2O–K_2O–MgO–CaO–B_2O_3–P_2O_5–SiO_2. *Journal of Biomedical Materials Research* 37 (1): 114–121.

64 Yao, A., Wang, D., Huang, W. et al. (2006). In vitro bioactive characteristics of borate-based glasses with controllable degradation behavior. *Journal of the American Ceramic Society* 90 (1): 303–306.

65 Huang, W., Day, D.E., Kittiratanapiboon, K., and Rahaman, M.N. (2006). Kinetics and mechanisms of the conversion of silicate (45S5), borate, and borosilicate glasses to hydroxyapatite in dilute phosphate solutions. *Journal of Materials Science – Materials in Medicine* 17 (7): 583–596.

66 Fu, Q., Rahaman, M.N., Fu, H.L., and Liu, X. (2010). Silicate, borosilicate, and borate bioactive glass scaffolds with controllable degradation rate for bone tissue engineering applications. I. Preparation and in vitro degradation. *Journal of Biomedical Materials Research Part A* 95A (1): 164–171.

67 Bi, L., Jung, S., Day, D. et al. (2012). Evaluation of bone regeneration, angiogenesis, and hydroxyapatite conversion in critical-sized rat calvarial defects implanted with bioactive glass scaffolds. *Journal of Biomedical Materials Research Part A* 100 (12): 3267–3275.

68 Zhao, S., Li, L., Wang, H. et al. (2015). Wound dressings composed of copper-doped borate bioactive glass microfibers stimulate angiogenesis and heal full-thickness skin defects in a rodent model. *Biomaterials* 53: 379–391.

69 Hulbert, S.F., Young, F.A., Mathews, R.S. et al. (1970). Potential of ceramic materials as permanently implantable skeletal prostheses. *Journal of Biomedical Materials Research* 4: 433–456.

70 Hollinger, J.O., Brekke, J., Gruskin, E., and Lee, D. (1996). Role of bone substitutes. *Clinical Orthopaedics and Related Research* 324: 55–65.

71 Karageorgiou, V. and Kaplan, D. (2005). Porosity of 3D biomaterial scaffolds and osteogenesis. *Biomaterials* 26 (27): 5474–5491.

72 Fu, Q., Saiz, E., Rahaman, M.N., and Tomsia, A.P. (2013). Toward strong and tough glass and ceramic scaffolds for bone repair. *Advanced Functional Materials* 23 (44): 5461–5467.

73 Jones, J.R. and Hench, L.L. (2003). Effect of surfactant concentration and composition on the structure and properties of sol–gel-derived bioactive glass foam scaffolds for tissue engineering. *Journal of Materials Science* 38 (18): 3783–3790.

74 Jones, J.R., Ahir, S., and Hench, L.L. (2004). Large-scale production of 3D bioactive glass macroporous scaffolds for tissue engineering. *Journal of Sol-Gel Science and Technology* 29 (3): 179–188.

75 Gough, J.E., Jones, J.R., and Hench, L.L. (2004). Nodule formation and mineralisation of human primary osteoblasts cultured on a porous bioactive glass scaffold. *Biomaterials* 25 (11): 2039–2046.

76 Jones, J.R., Ehrenfried, L.M., and Hench, L.L. (2006). Optimising bioactive glass scaffolds for bone tissue engineering. *Biomaterials* 27 (7): 964–973.

77 Rainer, A., Giannitelli, S.M., Abbruzzese, F. et al. (2008). Fabrication of bioactive glass-ceramic foams mimicking human bone portions for regenerative medicine. *Acta Biomaterialia* 4 (2): 362–369.

78 Vitale-Brovarone, C., Di Nunzio, S., Bretcanu, O., and Verne, E. (2004). Macroporous glass-ceramic materials with bioactive properties. *Journal of Materials Science – Materials in Medicine* 15 (3): 209–217.

79 Brovarone, C.V., Verne, E., and Appendino, P. (2006). Macroporous bioactive glass-ceramic scaffolds for tissue engineering. *Journal of Materials Science – Materials in Medicine* 17 (11): 1069–1078.

80 Fu, Q., Rahaman, M.N., Bal, B.S. et al. (2007). Preparation and bioactive characteristics of a porous 13-93 glass, and fabrication into the articulating surface of a proximal tibia. *Journal of Biomedical Materials Research Part A* 82A (1): 222–229.

81 Liang, W., Rahaman, M.N., Day, D.E. et al. (2008). Bioactive borate glass scaffold for bone tissue engineering. *Journal of Non-Crystalline Solids* 354 (15–16): 1690–1696.

82 Vitale-Brovarone, C., Verne, E., Robiglio, L. et al. (2008). Biocompatible glass-ceramic materials for bone substitution. *Journal of Materials Science – Materials in Medicine* 19 (1): 471–478.

83 Brown, R.F., Day, D.E., Day, T.E. et al. (2008). Growth and differentiation of osteoblastic cells on 13-93 bioactive glass fibers and scaffolds. *Acta Biomaterialia* 4 (2): 387–396.

84 Zhang, H., Ye, X.J., and Li, J.S. (2009). Preparation and biocompatibility evaluation of apatite/wollastonite-derived porous bioactive glass ceramic scaffolds. *Biomedical Materials* 4 (4): 045007.

85 Haimi, S., Gorianc, G., Moimas, L. et al. (2009). Characterization of zinc-releasing three-dimensional bioactive glass scaffolds and their effect on human adipose stem cell proliferation and osteogenic differentiation. *Acta Biomaterialia* 5 (8): 3122–3131.

86 Baino, F., Verne, E., and Vitale-Brovarone, C. (2009). 3-D high-strength glass-ceramic scaffolds containing fluoroapatite for load-bearing bone portions replacement. *Materials Science and Engineering C* 29 (6): 2055–2062.

87 Wu, S.C., Hsu, H.C., Hsiao, S.H., and Ho, W.F. (2009). Preparation of porous 45S5 Bioglass®-derived glass-ceramic scaffolds by using rice husk as a porogen additive. *Journal of Materials Science – Materials in Medicine* 20 (6): 1229–1236.

88 Bellucci, D., Cannillo, V., Ciardelli, G. et al. (2010). Potassium based bioactive glass for bone tissue engineering. *Ceramics International* 36 (8): 2449–2453.

89 Schwarzwalder, K. and Somers, A.V. (1963). Methods of making porous ceramic articles, US Patent 3, 090, 094A, issued 21 February 1963.

90 Chen, Q.Z.Z., Thompson, I.D., and Boccaccini, A.R. (2006). 45S5 Bioglass®-derived glass-ceramic scaffolds for bone tissue engineering. *Biomaterials* 27 (11): 2414–2425.

91 Vitale-Brovarone, C., Verne, E., Robiglio, L. et al. (2007). Development of glass-ceramic scaffolds for bone tissue engineering: characterisation, proliferation of human osteoblasts and nodule formation. *Acta Biomaterialia* 3 (2): 199–208.

92 Li, Y., Rahaman, M.N., Fu, Q. et al. (2007). Conversion of bioactive borosilicate glass to multilayered hydroxyapatite in dilute phosphate solution. *Journal of the American Ceramic Society* 90 (12): 3804–3810.

93 Chen, Q.Z., Efthymiou, A., Salih, V., and Boccaccini, A.R. (2008). Bioglass®-derived glass-ceramic scaffolds: study of cell proliferation and scaffold degradation in vitro. *Journal of Biomedical Materials Research Part A* 84A (4): 1049–1060.

94 Fu, Q., Rahaman, M.N., Bal, B.S. et al. (2008). Mechanical and in vitro performance of 13-93 bioactive glass scaffolds prepared by a polymer foam replication technique. *Acta Biomaterialia* 4 (6): 1854–1864.

95 Vitale-Brovarone, C., Baino, F., and Verne, E. (2009). High strength bioactive glass-ceramic scaffolds for bone regeneration. *Journal of Materials Science – Materials in Medicine* 20 (2): 643–653.

96 Fu, H.L., Fu, Q., Zhou, N. et al. (2009). In vitro evaluation of borate-based bioactive glass scaffolds prepared by a polymer foam replication method. *Materials Science and Engineering C* 29 (7): 2275–2281.

97 Liu, X., Huang, W., Fu, H. et al. (2009). Bioactive borosilicate glass scaffolds: improvement on the strength of glass-based scaffolds for tissue engineering. *Journal of Materials Science – Materials in Medicine* 20 (1): 365–372.

98 Liu, X., Huang, W., Fu, H. et al. (2009). Bioactive borosilicate glass scaffolds: in vitro degradation and bioactivity behavior. *Journal of Materials Science – Materials in Medicine* 20 (6): 1237–1243.

99 Renghini, C., Komlev, V., Fiori, F. et al. (2009). Micro-CT studies on 3-D bioactive glass-ceramic scaffolds for bone regeneration. *Acta Biomaterialia* 5 (4): 1328–1337.

100 Fu, Q.A., Rahaman, M.N., Bal, B.S. et al. (2010). Silicate, borosilicate, and borate bioactive glass scaffolds with controllable degradation rate for bone tissue engineering applications. II. In vitro and in vivo biological evaluation. *Journal of Biomedical Materials Research Part A* 95A (1): 172–179.

101 Liu, X., Pan, H.B., Fu, H.L. et al. (2010). Conversion of borate-based glass scaffold to hydroxyapatite in a dilute phosphate solution. *Biomedical Materials* 5 (1): 15005.

102 Xia, W. and Chang, J. (2010). Bioactive glass scaffold with similar structure and mechanical properties of cancellous bone. *Journal of Biomedical Materials Research Part B Applied Biomaterials* 95 (2): 449–455.

103 Schoof, H., Apel, J., Heschel, I., and Rau, G. (2001). Control of pore structure and size in freeze-dried collagen sponges. *Journal of Biomedical Materials Research* 58 (4): 352–357.

104 Zhang, H.F., Hussain, I., Brust, M. et al. (2005). Aligned two- and three-dimensional structures by directional freezing of polymers and nanoparticles. *Nature Materials* 4 (10): 787–793.

105 Deville, S., Saiz, E., Nalla, R.K., and Tomsia, A.P. (2006). Freezing as a path to build complex composites. *Science* 311 (5760): 515–518.

106 Song, J.H., Koh, Y.H., Kim, H.E. et al. (2006). Fabrication of a porous bioactive glass-ceramic using room-temperature freeze casting. *Journal of the American Ceramic Society* 89 (8): 2649–2653.

107 Fu, Q., Rahaman, M.N., Dogan, F., and Bal, B.S. (2008). Freeze casting of porous hydroxyapatite scaffolds. I. Processing and general microstructure. *Journal of Biomedical Materials Research Part B Applied Biomaterials* 86B (1): 125–135.

108 Fu, Q., Rahaman, M.N., Dogan, F., and Bal, B.S. (2008). Freeze casting of porous hydroxyapatite scaffolds. II. Sintering, microstructure, and mechanical behavior. *Journal of Biomedical Materials Research Part B Applied Biomaterials* 86B (2): 514–522.

109 Fu, Q., Rahaman, M.N., Bal, B.S., and Brown, R.F. (2010). Preparation and in vitro evaluation of bioactive glass (13-93) scaffolds with oriented microstructures for repair and regeneration of load-bearing bones. *Journal of Biomedical Materials Research Part A* 93A (4): 1380–1390.

110 Fu, Q.A., Rahaman, M.N., Bal, B.S. et al. (2010). In vivo evaluation of 13-93 bioactive glass scaffolds with trabecular and oriented microstructures in a subcutaneous rat implantation model. *Journal of Biomedical Materials Research Part A* 95A (1): 235–244.

111 Liu, X., Rahaman, M.N., and Fu, Q.A. (2011). Oriented bioactive glass (13-93) scaffolds with controllable pore size by unidirectional freezing of camphene-based suspensions: microstructure and mechanical response. *Acta Biomaterialia* 7 (1): 406–416.

112 Wegst, U.G.K., Schecter, M., Donius, A.E., and Hunger, P.M. (2010). Biomaterials by freeze casting. *Philosophical Transactions of the Royal Society of London, Series A: Mathematical, Physical and Engineering Sciences* 368 (1917): 2099–2121.

113 Deville, S., Saiz, E., and Tomsia, A.P. (2006). Freeze casting of hydroxyapatite scaffolds for bone tissue engineering. *Biomaterials* 27 (32): 5480–5489.

114 Hollister, S.J. (2005). Porous scaffold design for tissue engineering. *Nature Materials* 4 (7): 518–524.

115 Chu, T.-M.G. (2005). Solid freeform fabrication of tissue engineering scaffolds. In: *Scaffolding in Tissue Engineering* (ed. X. Ma and J. Eliseeff), 139–154. Marcel Dekker, Inc.

116 Fu, Q., Saiz, E., and Tomsia, A.P. (2011). Bio-inspired highly porous and strong glass scaffolds. *Advanced Functional Materials* 21: 1058–1063.

117 Goodridge, R.D., Wood, D.J., Ohtsuki, C., and Dalgarno, K.W. (2007). Biological evaluation of an apatite-mullite glass-ceramic produced via selective laser sintering. *Acta Biomaterialia* 3 (2): 221–231.

118 Huang, T.S., Rahaman, M.N., Doiphode, N.D. et al. (2011). Porous and strong bioactive glass (13-93) scaffolds prepared by freeze extrusion fabrication. *Materials Science and Engineering C* 31 (7): 1482–1489. (submitted).

119 Chen, Q.Z. and Boccaccini, A.R. (2006). Poly(D,L-lactic acid) coated 45S5 Bioglass®-based scaffolds: processing and characterization. *Journal of Biomedical Materials Research Part A* 77A (3): 445–457.

120 Pernot, F., Etienne, P., Boschet, F., and Datas, L. (1999). Weibull parameters and the tensile strength of porous phosphate glass-ceramics. *Journal of the American Ceramic Society* 82 (3): 641–648.

121 Miranda, P., Pajares, A., Saiz, E. et al. (2008). Mechanical properties of calcium phosphate scaffolds fabricated by robocasting. *Journal of Biomedical Materials Research Part A* 85A (1): 218–227.

122 Fu, Q., Jia, W., Lau, G.Y., and Tomsia, A.P. (2018). Strength, toughness, and reliability of a porous glass/biopolymer composite scaffold. *Journal of Biomedical Materials Research Part B Applied Biomaterials* 106 (3): 1209–1217.

123 ASTM C1161-18 (2008). *Standard test method of flexural strength of advanced ceramics at ambient temperature*. West Conshohocken, PA: ASTM International.

124 Chen, Q., Baino, F., Pugno, N.M., and Vitale-Brovarone, C. (2013). Bonding strength of glass-ceramic trabecular-like coatings to ceramic substrates for prosthetic applications. *Materials Science and Engineering C* 33 (3): 1530–1538.

125 Řehořek, L., Chlup, Z., Meng, D. et al. (2013). Response of 45S5 Bioglass® foams to tensile loading. *Ceramics International* 39 (7): 8015–8020.

126 Baino, F. and Pons, E. (2019). Modelling the relationship between tensile strength and porosity in bioceramic scaffolds. *International Journal of Applied Ceramic Technology* 16 (5): 1823–1829.

127 Freeman, M.A.R., Todd, R.C., and Pirie, C.J. (1974). Role of fatigue in pathogenesis of senile femoral-neck fractures. *Journal of Bone and Joint Surgery British Volume* 56-B (4): 698–702.

128 Riggs, B.L. and Melton, L.J. (1995). The worldwide problem of osteoporosis – insights afforded by epidemiology. *Bone* 17 (5): S505–S511.

129 Daffner, R.H. and Pavlov, H. (1992). Stress-fractures – current concepts. *American Journal of Roentgenology* 159 (2): 245–252.

130 Silva, M.J., Keaveny, T.M., and Hayes, W.C. (1997). Load sharing between the shell and centrum in the lumbar vertebral body. *Spine* 22 (2): 140–150.

131 Evans, A.G. (1980). Fatigue in ceramics. *International Journal of Fracture* 16 (6): 485–498.

132 Ritchie, R.O. and Dauskardt, R.H. (1991). Cyclic fatigue of ceramics – a fracture-mechanics approach to subcritical crack-growth and life prediction. *Nippon Seramikkusu Kyokai Gakujutsu Ronbunshi/Journal of the Ceramic Society of Japan* 99 (10): 1047–1062.

133 Wiederho, S.M. and Bolz, L.H. (1970). Stress corrosion and static fatigue of glass. *Journal of the American Ceramic Society* 53 (10): 543–548.

134 Bloyer, D.R., McNaney, J.M., Cannon, R.M. et al. (2007). Stress-corrosion crack growth of Si–Na–K–Mg–Ca–P–O bioactive glasses in simulated human physiological environment. *Biomaterials* 28 (33): 4901–4911.

135 Pavon, J., Jimenez-Pique, E., Anglada, M. et al. (2006). Stress-corrosion cracking by indentation techniques of a glass coating on Ti6Al4V for biomedical applications. *Journal of the European Ceramic Society* 26 (7): 1159–1169.

136 Barinov, S.M. and Shevchenko, V.Y. (1995). Dynamic fatigue of porous hydroxyapatite bioceramics in air. *Journal of Materials Science Letters* 14 (8): 582–583.

137 Liu, X., Rahaman, M.N., Hilmas, G.E., and Bal, B.S. (2013). Mechanical properties of bioactive glass (13-93) scaffolds fabricated by robotic deposition for structural bone repair. *Acta Biomaterialia* 9 (6): 7025–7034.

138 Michalske, T.A. and Freiman, S.W. (1983). A molecular mechanism for stress corrosion in vitreous silica. *Journal of the American Ceramic Society* 66 (4): 284–288.

139 Davidge, R.W. (1979). *Mechanical Behaviour of Ceramics*. Cambridge/New York: Cambridge University Press.

140 Sakai, M. and Bradt, R.C. (1993). Fracture-toughness testing of brittle materials. *International Materials Reviews* 38 (2): 53–78.

141 ASTM C1421 (2010). *Standard test methods for determination of fracture toughness of advanced ceramics at ambient temperature*, West Conshohocken, PA: ASTM International.

142 Barinov, S.M. and Sakai, M. (1994). The work-of-fracture of brittle materials – principle, determination, and applications. *Journal of Materials Research* 9 (6): 1412–1425.

143 Peroglio, M., Gremillard, L., Gauthier, C. et al. (2010). Mechanical properties and cytocompatibility of poly(ε-caprolactone)-infiltrated biphasic calcium phosphate scaffolds with bimodal pore distribution. *Acta Biomaterialia* 6 (11): 4369–4379.

144 Peroglio, M., Gremillard, L., Chevalier, J. et al. (2007). Toughening of bio-ceramics scaffolds by polymer coating. *Journal of the European Ceramic Society* 27 (7): 2679–2685.

145 Bretcanu, O., Misra, S., Roy, I. et al. (2009). In vitro biocompatibility of 45S5 Bioglass®-derived glass-ceramic scaffolds coated with poly(3-hydroxybutyrate). *Journal of Tissue Engineering and Regenerative Medicine* 3 (2): 139–148.

146 Weibull, W. (1951). A statistical distribution function of wide applicability. *ASME Journal of Applied Mechanics* 18 (3): 293–297.

147 Bergman, B. (1984). On the estimation of the Weibull modulus. *Journal of Materials Science Letters* 3 (8): 689–692.

148 Sullivan, J.D. and Lauzon, P.H. (1986). Experimental probability estimators for Weibull plots. *Journal of Materials Science Letters* 5 (12): 1245–1247.

149 Cordell, J.M., Vogl, M.L., and Wagoner Johnson, A.J. (2009). The influence of micropore size on the mechanical properties of bulk hydroxyapatite and hydroxyapatite scaffolds. *Journal of the Mechanical Behavior of Biomedical Materials* 2 (5): 560–570.

150 Martinez-Vazquez, F.J., Perera, F.H., Miranda, P. et al. (2010). Improving the compressive strength of bioceramic robocast scaffolds by polymer infiltration. *Acta Biomaterialia* 6 (11): 4361–4368.

151 Peterlik, H., Roschger, P., Klaushofer, K., and Fratzl, P. (2006). From brittle to ductile fracture of bone. *Nature Materials* 5 (1): 52–55.

152 Meyers, M.A., Chen, P.Y., Lin, A.Y.M., and Seki, Y. (2008). Biological materials: structure and mechanical properties. *Progress in Materials Science* 53 (1): 1–206.

153 Tang, Z.Y., Kotov, N.A., Magonov, S., and Ozturk, B. (2003). Nanostructured artificial nacre. *Nature Materials* 2 (6): 413–418.

154 Fratzl, P. and Weinkamer, R. (2007). Nature's hierarchical materials. *Progress in Materials Science* 52 (8): 1263–1334.

155 Apel, E., Deubener, J., Bernard, A. et al. (2008). Phenomena and mechanisms of crack propagation in glass-ceramics. *Journal of the Mechanical Behavior of Biomedical Materials* 1 (4): 313–325.

156 Evans, A.G. (1990). Perspective on the development of high-toughness ceramics. *Journal of the American Ceramic Society* 73 (2): 187–206.

157 Becher, P.F. (1991). Microstructural design of toughened ceramics. *Journal of the American Ceramic Society* 74 (2): 255–269.

158 Kokubo, T. (1991). Bioactive glass-ceramics – properties and applications. *Biomaterials* 12 (2): 155–163.

159 Kokubo, T., Ito, S., Shigematsu, M. et al. (1985). Mechanical-properties of a new type of apatite-containing glass ceramic for prosthetic application. *Journal of Materials Science* 20 (6): 2001–2004.

160 Nalla, R.K., Kinney, J.H., and Ritchie, R.O. (2003). Mechanistic fracture criteria for the failure of human cortical bone. *Nature Materials* 2 (3): 164–168.

161 Amaral, M., Lopes, M.A., Silva, R.F., and Santos, J.D. (2002). Densification route and mechanical properties of Si_3N_4-bioglass biocomposites. *Biomaterials* 23 (3): 857–862.

162 Liu, D.M. and Chou, H.M. (1994). Formation of a new bioactive glass-ceramic. *Journal of Materials Science – Materials in Medicine* 5 (1): 7–10.

163 Ryu, H.S., Lee, J.K., Seo, J.H. et al. (2004). Novel bioactive and biodegradable glass ceramics with high mechanical strength in the $CaO–SiO_2–B_2O_3$ system. *Journal of Biomedical Materials Research Part A* 68A (1): 79–89.

164 Marghussian, V.K. and Mesgar, A.S.M. (2000). Effects of composition on crystallization behaviour and mechanical properties of bioactive glass-ceramics in the $MgO–CaO–SiO_2–P_2O_5$ system. *Ceramics International* 26 (4): 415–420.

165 Kanchanarat, N., Bandyopadhyay-Ghosh, S., Reaney, I.M. et al. (2008). Microstructure and mechanical properties of fluorcanasite glass-ceramics for biomedical applications. *Journal of Materials Science* 43 (2): 759–765.

166 Thompson, I.D. and Hench, L.L. (1998). Mechanical properties of bioactive glasses, glass-ceramics and composites. *Proceedings of the Institution of Mechanical Engineers, Part H: Journal of Engineering in Medicine* 212 (H2): 127–136.

167 Rahaman, M.N., Yao, A.H., Bal, B.S. et al. (2007). Ceramics for prosthetic hip and knee joint replacement. *Journal of the American Ceramic Society* 90 (7): 1965–1988.

168 Mantsos, T., Chatzistavrou, X., Roether, J.A. et al. (2009). Non-crystalline composite tissue engineering scaffolds using boron-containing bioactive glass and poly(D,L-lactic acid) coatings. *Biomedical Materials* 4 (5): 055002.

169 Mourino, V., Newby, P., and Boccaccini, A.R. (2010). Preparation and characterization of gallium releasing 3-D alginate coated 45S5 Bioglass® based scaffolds for bone tissue engineering. *Advanced Engineering Materials* 12 (7): B283–B291.

170 Launey, M.E., Munch, E., Alsem, D.H. et al. (2009). Designing highly toughened hybrid composites through nature-inspired hierarchical complexity. *Acta Materialia* 57 (10): 2919–2932.

171 Sanchez, C., Arribart, H., and Guille, M.M.G. (2005). Biomimetism and bioinspiration as tools for the design of innovative materials and systems. *Nature Materials* 4 (4): 277–288.

172 Smith, B.L., Schaffer, T.E., Viani, M. et al. (1999). Molecular mechanistic origin of the toughness of natural adhesives, fibres and composites. *Nature* 399 (6738): 761–763.

173 Mayer, G. (2005). Rigid biological systems as models for synthetic composites. *Science* 310 (5751): 1144–1147.

174 Song, F., Soh, A.K., and Bai, Y.L. (2003). Structural and mechanical properties of the organic matrix layers of nacre. *Biomaterials* 24 (20): 3623–3631.

175 Munch, E., Launey, M.E., Alsem, D.H. et al. (2008). Tough, bio-inspired hybrid materials. *Science* 322 (5907): 1516–1520.

9

Nano-bioactive Glass: Advances and Applications

Ahmed El-Fiqi

Glass Research Department, Advanced Materials Technology and Mineral Resources Research Institute, National Research Centre, Cairo, Egypt

9.1 Introduction

Glass has been known by mankind for more than 10 000 years [1]. Glass is typically an inorganic material which is chemically composed of oxides such as SiO_2, P_2O_5, and B_2O_3 (glass-formers) along with glass-modifiers, e.g. Na_2O, CaO, and MgO. Actually, many organic substances form glass however, inorganic glass is much more common. Accordingly, glass is defined by standards of the American Society for Testing Materials (ASTM) as "glass is an inorganic product of fusion which has been cooled to a rigid condition without crystallizing" [2]. Thus, glass is traditionally prepared by melting together powders of oxides such as SiO_2, P_2O_5, B_2O_3, Na_2O, CaO, MgO, etc., usually in the range of ~850–1550 °C depending on the chemical composition and then molten glass is cooled to room temperature (by annealing or quenching) to form solid glass [3]. However, melting is not the only route to prepare a glass and other methods such as sol–gel is also used for glass preparation [4]. Structurally, the atomic arrangements in glass are random and atoms are not ordered in a well-defined pattern like observed in crystals, i.e. glass lacks long-range ordered atomic structure and it possesses noncrystalline (amorphous) structure [5]. Importantly, glass possesses diverse structural, physical, chemical, optical, and electrical properties. The properties of glass can be tailored through design and control of its chemical composition [6]. The great flexibilities in composition–property designing, manufacturing, and processing allow glass to be considered as an excellent material for many engineering and technological applications that are unmet by other materials [7]. For example, glass can be manufactured into large segments of a 100 m diameter primary telescope mirror [8] and as nanofibers for photonic devices [9].

Interestingly, a special type of melt-derived glass named bioactive glass was discovered by Larry Hench in 1969 [10, 11]. Typically, bioactive glass (later known as Bioglass®) possesses a biologically reactive chemical composition containing 45% SiO_2, 24.5% CaO, 24.5% Na_2O, and 6% P_2O_5 by weight. Bioglass has a reactive and biodegradable surface which releases soluble ionic species, e.g. soluble silicates (SiO_4^{4-}), soluble phosphates (PO_4^{3-}), and calcium ions (Ca^{2+}) when in contact with biological fluids or physiological solutions. Such bioreactive surface of Bioglass can directly and strongly bond to living bone tissue through the formation of hydroxycarbonate apatite (HCA) layer on the interface between the host bone and the surface of the implanted Bioglass [12]. Therefore, various bioactive glass compositions have been developed and widely investigated for bone repair. Bioactive glasses have been mainly produced by the melting method used in glass-making

Bioactive Glasses and Glass-Ceramics: Fundamentals and Applications, First Edition.
Edited by Francesco Baino and Saeid Kargozar.

industry in the form of blocks, micropowders, and microfibers [13, 14]. Conventional processing of bioactive glass into powder is made either by crushing bulk bioactive glass into small pieces and their subsequent grinding into micron-sized powder or by pouring the molten glass into water to obtain bioactive glass frits followed by grinding step into fine powder [14]. Usually powder sieving is necessary to prepare bioactive glass powder with a specific micron-size range. However, there are several limitations and disadvantages of such conventional bioactive glass processing methods in reducing the particle size below the conventional micrometer scale [15]. To this end, this chapter mainly focuses on bioactive glass nanoparticles (BGn) and the impact of nanoscale processing and advances of sol–gel synthesis on the properties of BGn. Furthermore, highlighting the recent progress and advances in the biomedical applications of BGn in bone and skin tissue regeneration.

9.2 Bioactive Glass Nanoparticles

BGn are processed or synthesized with particle sizes in the nanoscale range, typically less than 100 nm [16, 17]. Interestingly, reducing the particle size below the conventional micrometer scale leads to significant improvements in physicochemical properties, bioactivity, biodegradability, and biological properties of BGn [18, 19]. Therefore, BGn were developed in an attempt to increase their specific surface area and enhance their properties. Actually, large specific surface area is a very favored factor for the surface chemistry of BGn, i.e. the surface bioreactivity (which involves surface dissolution, ions release, and calcium phosphate deposition reactions), protein adsorption, and surface functionalization. Such increase in specific area significantly improves surface bioreactivity, ions release kinetics, and biodegradability which would allow BGn to be completely replaced by new bone tissue during bone regeneration process [20]. Indeed, blocks of silicate-based bioactive glass takes long time to be completely resorbed when implanted into a living body [21]. Collectively, large specific surface area, fast biodegradability, rapid release of bioactive ions, excellent bioactivity, injectability, high-protein adsorption and intracellular uptake are among the merits of BGn.

9.2.1 Synthesis Approaches

Generally, BGn can be prepared either by the classical top-down [22–24] or the advanced bottom-up synthesis approaches [18]. Accordingly, BGn can have an irregular or regular shape and broad or narrow particle size distributions depending on the synthesis method. The bioactive glass particles obtained by conventional grinding/sieving processing of bulk bioactive glass, typically exhibit particle sizes of several tens to hundred micrometers [25]. However, it is possible to prepare BGn from bulk bioactive glass by the classical top-down approach which is the extension of mechanical milling used for producing micron sized particles [22–24, 26]. Top-down approach starts with a bulk glass and then breaks it into smaller pieces using some sort of energy, e.g. mechanical energy. Mechanical milling, e.g. grinding, pulverization, and attrition is a traditional processing method for macro- or microscale bioactive glass (m-BG) particles [27]. Grinding mills are mainly ball mills with rotating balls (e.g. a planetary ball mill) to crush the material by impact and attrition into a fine powder. The attrition mill mechanically reduces particle size by intense agitation of a slurry of the material particles and coarse milling media. The nanoparticles produced by such classical top-down approaches are neither uniform in size (broad size particle size distribution from tens to hundreds of nanometers) nor regular in shape. Actually, there are several physical and technical factors that limit the smallest particle size that can be produced by top-down milling of materials, e.g. to obtain 100 nm particles, the ratio of the diameters of the milling balls and the particles should be 1000 : 1, i.e. the milling balls should have a diameter of 100 μm [28]. Generally, top-down

milling of materials is considered to be an energy- and a time-consuming process. Furthermore, no control over the particle size, particle shape, size distribution, particle contamination, and degree of agglomeration which all have significant impact on their biomedical applications.

Top-down processing of commercially available 45S5 Bioglass powder with nominal particle size of 22 μm by wet comminution in a stirred media mill using *n*-pentanol was used to prepare submicron bioactive glass particles [25]. Crushing and grounding in an attrition mill with high-purity Y_2O_3-stabilized ZrO_2 milling media and ethanol as the solvent were used in preparation of 100 nm 1393 melt-derived BGn [24]. Bioactive glass submicron particles with a wide size distribution from ~100 to 800 nm were prepared by milling of bioactive glass frit (obtained by quenching molten glass in distilled water) in a milling machine using zirconia cups [22]. Nanoscale sol–gel derived 58S bioactive glass powder with irregular particles and a size of 30–60 nm were obtained by freeze-drying and grinding process [23].

The bottom-up synthesis approaches of BGn involve wet chemical reactions and self-assembly processes of atomic or molecular species where particles can grow in size or gradually assemble into a desired structure. The bottom-up synthesis approaches are more relevant in synthesis of BGn due to several merits, e.g. better control on homogeneity, particle size distribution, particle shape, surface chemistry, and textural properties. Among bottom-up synthesis approaches, sol–gel [18, 20, 29–39], modified sol–gel [40–65], and modified Stöber [66–78] methods are widely used in preparation of BGn along with other methods, e.g. microemulsion [79–87] and flame spray synthesis [88–93]. However, this chapter focuses only on sol–gel and modified sol–gel methods for production of BGn.

9.2.1.1 Sol–Gel Synthesis

Sol–gel synthesis is a liquid state synthetic route involving hydrolysis, condensation and polycondensation reactions (inorganic polymerization) of alkoxide precursor under acid, base, or acid/base catalysis at room temperature [4, 94–96]. The sol–gel synthesis of bioactive glass powder started beginning of 1990s [15]. Indeed, sol–gel bioactive glass can be prepared with higher silica contents (up to 90% SiO_2) compared to the melt-derived ones (limited to 60% SiO_2). Nowadays, sol–gel synthesis is considered a potential route for preparing bioactive glasses [97], mesoporous bioactive glasses [98–101], and dense or mesoporous BGn [18, 20, 29, 31, 102]. Actually, sol–gel synthesis of BGn can be achieved through acid/base cocatalyzed route [18, 103], base-catalyzed route [104, 105], and modified Stöber method [35, 67, 76]. The acid/base co-catalyzed sol–gel route is a two-step process involving acid hydrolysis of a silicon alkoxide precursor, usually tetraethoxysilane (TEOS) to silicate sol and then base polycondensation to silicate gelled nanoparticles. The base-catalyzed sol–gel route is a single-step one-pot process involving a quick alkali-mediated hydrolysis and polycondensation of silicate precursor with a rapid formation (gelation) of nanoparticles.

9.2.1.2 Modified Sol–Gel Synthesis

High-particle agglomeration, particle shape irregularity, polydispersity, and an uncontrolled mesoporosity were found to be associated with BGn prepared either by the acid/base cocatalyzed [106] or base-catalyzed sol–gel routes [104]. Therefore, modified sol–gel routes were developed by involving soft-templates such as polymers and surfactants (template-assisted sol–gel synthesis) and/or coupling with assisting techniques such as ultrasound irradiation (ultrasonic-assisted sol–gel synthesis) or microemulsion formation (microemulsion-assisted sol–gel synthesis) [18, 40, 41, 47, 50, 59, 61, 79]. Soft templates such as surfactants or polymers can form micelles or self-assemble into polymeric aggregates and thus can act as structure-directing agents by guiding hydrolysis and condensation of silicate precursor [107, 108]. This can provide better control over particle size, particle

shape, particle texture, and reduce particles agglomeration. There are two common examples of widely used soft templates, namely polyethylene glycol (PEG) and cetyltrimethylammonium bromide (CTAB). PEG is widely used as a nonionic polymer template to tailor the particle size, particle shape as well as to improve the dispersibility of BGn [17, 32, 45, 61, 109, 110], whereas CTAB is a cationic surfactant mainly used in synthesis of mesoporous BGn [48, 49, 58, 65, 111–113]. Two representative routes of modified sol–gel synthesis methods, namely ultrasonic-assisted sol–gel synthesis and modified Stöber synthesis are given on Sections 9.2.1.3 and 9.2.1.4.

9.2.1.3 Ultrasonic-Coupled Sol–Gel Synthesis

Ultrasound has been introduced into the synthesis of a variety of novel nanomaterials with unique properties [114–118]. The sonochemical effect is based on acoustic cavitation process (Figure 9.1) which involves formation, growth, and implosive collapse of microbubbles (within 400 μs) in a

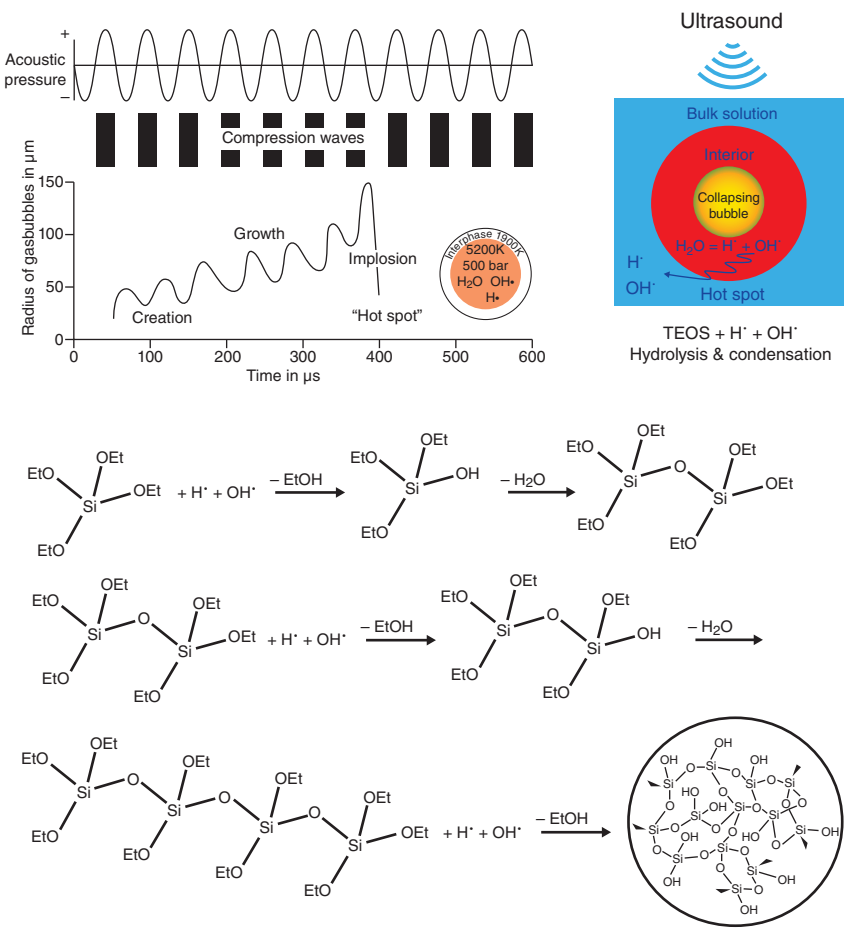

Figure 9.1 Acoustic cavitation process which involves formation, growth, and implosive collapse of microbubbles (within 400 μs) in a liquid medium. The violent collapse of microbubbles produces ultrahot spots with an extremely high temperature (5200 K) and pressure (500 bar). Ultrahot spots rapidly initiate production of $H^{\bullet}$ and $OH^{\bullet}$ free radicals from H_2O molecules ($H_2O = H^{\bullet} + OH^{\bullet}$) in the aqueous sol–gel reaction medium. The produced $H^{\bullet}$ and $OH^{\bullet}$ free radicals diffuse into the bulk solution and initiate hydrolysis, condensation, and polycondensation reactions of TEOS. Source: Rearranged from El-Fiqi and Bakry [119] with permission from Elsevier.

liquid medium [115]. During this process, the violent collapse of microbubbles produces ultrahot spots with an extremely high temperature (5200 K) and pressure (500 bar) [116]. These ultrahot spots can rapidly initiate chemical reactions and product formation. For example, for an aqueous solution, water molecules can be broken into hydrogen ($H^{\cdot}$) and hydroxyl radicals ($OH^{\cdot}$) which can migrate into the bulk solution and participate in further chemical reactions (Figure 9.1). Based on this mechanism, ultrasound has been widely applied to the synthesis of metals [117, 120, 121], oxides [118, 122–125], mesoporous silica nanoparticles (MSN) [119, 126–131]. Of note, compared with the conventional synthesis routes of MSN, the hydrolysis and condensation time of TEOS was greatly shortened under ultrasonic conditions [128, 130]. Sonochemistry is, thus, an efficient method for rapid and facile synthesis of a variety of novel nanomaterials. Interestingly, ultrasound was coupled with sol–gel method for synthesis of BGn [41]. Figure 9.1 shows ultrasonic irradiation during sol–gel processing of BGn. Application of ultrasound to the aqueous sol–gel reaction medium leads to formation of ultrahot spots. These ultrahot spots rapidly initiate primary reactions involving production of $H^{\cdot}$ and $OH^{\cdot}$ free radicals from H_2O molecules ($H_2O = H^{\cdot} + OH^{\cdot}$) in the reaction medium. Then, the produced $H^{\cdot}$ and $OH^{\cdot}$ free radicals diffuse into the bulk solution and initiate hydrolysis, condensation, and polycondensation reactions of TEOS and ultimately lead to the formation of the silicate network.

9.2.1.4 Modified Stöber Synthesis

Modified Stöber method is another sol–gel procedure used to synthesize spherical BGn with controlled particle size under basic conditions [76, 132]. Actually, Stöber synthesis is a well-known sol–gel route for production of uniform, monodispersed silica nanoparticles with highly tailorable size [133]. Stöber synthesis is an ammonia-catalyzed sol–gel reaction where hydrolysis of TEOS occurs in the presence of water and ethanol, that is followed by subsequent condensation and polycondensation reactions. Modified Stöber synthesis of BGn is illustrated in Figure 9.2. A monodispersed silica nanoparticles are first formed through the hydrolysis and polycondensation of TEOS in a highly alkaline media. Next, a calcium precursor such as $Ca(NO_3)_2{\cdot}4H_2O$ is added to the silica nanoparticles. Then, post-treatment processes including washing and calcination (600–700 °C) are performed to remove unbounded Ca and allow diffusion of bounded Ca into the silica network of the nanoparticles, respectively. However, in this method much amount of Ca is lost during the washing step and the maximum amount of Ca that can be incorporated using this method is limited to 10 mol% CaO [76]. Accordingly, the actual composition of BGn prepared by modified Stöber method significantly deviates from the nominal one.

9.3 Compositions of Sol–Gel BGn

Interestingly, sol–gel synthesis allowed production of bioactive glasses with just two components namely, CaO and SiO_2 [134]. Actually, it was reported that the 30% CaO–70% SiO_2 bioactive glass was as bioactive as the melt-derived 45S5 Bioglass [10, 134]. This CaO–SiO_2 system is the basis for many of the third-generation tissue regeneration biomaterials presently under development [10, 47, 135–138]. Therefore, sol–gel BGn compositions basically depend on binary or ternary calcium silicate-based glass systems with fewer components than melt-derived BG. Furthermore, sol–gel BGn can have up to 95 mol% SiO_2, while melt-derived BG cannot exceed 60 mol% of SiO_2. Typical sol–gel BGn compositions based on, e.g. the binary CaO–SiO_2 system or the ternary CaO–P_2O_5–SiO_2 system are summarized in Table 9.1.

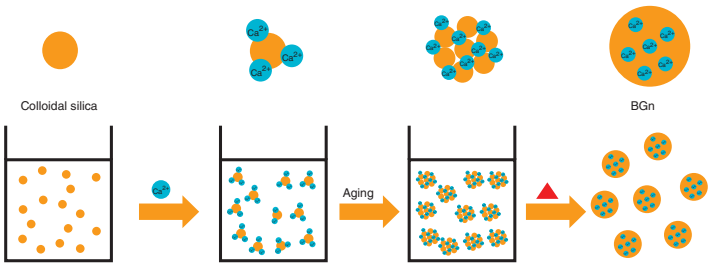

Figure 9.2 Modified Stöber synthesis of spherical BGn with controlled particle size under basic conditions. Monodispersed silica nanoparticles are first formed through the hydrolysis and polycondensation of TEOS in a highly alkaline media. Next, a calcium precursor such as $Ca(NO_3)_2 \cdot 4H_2O$ is added to the silica nanoparticles. Washing of particles is necessary to remove unbounded Ca and calcination (600–700 °C) is performed to allow diffusion of bounded Ca into the silica network of the nanoparticles.

Table 9.1 Chemical compositions, synthesis approach, particle size, Brunauer-Emmett-Teller method (BET)-specific surface area (SSA), and texture of sol–gel BGn.

Particle composition	Synthesis approach	Template type	Particle size (nm)	BET-SSA (m^2/g)	Texture	References
Binary systems						
15% CaO–85% SiO_2	US/sol–gel	PEG	85 ± 15	54	Mesoporous	[41]
15% CaO–85% SiO_2	US/sol–gel	CTAB	95 ± 15	830	Mesoporous	[41]
25% CaO–75% SiO_2	US/sol–gel	PEG	62.7 ± 12.3	47.2	Mesoporous	[139]
15% CaO–85% SiO_2	MS/sol–gel	Boltorn	250 ± 75	28	Nonmesoporous	[59]
30% CaO–70% SiO_2	ME/sol–gel	CTAB	130 ± 10	229	Mesoporous	[50]
40% CaO–60% SiO_2	ME/sol–gel	CTAB	250	424	Mesoporous	[54]
05% CaO–95% SiO_2	MS/sol–gel	Nil	110	31.3	Nonmesoporous	[71]
10% CaO–90% SiO_2	MS/sol–gel	Nil	110	29.7	Nonmesoporous	[71]
30% CaO–70% SiO_2	MS/sol–gel	Nil	110	27.2	Nonmesoporous	[71]
20% CaO–80% SiO_2	ME/sol–gel	CTAB	171 ± 21	677	Mesoporous	[51]
Ternary systems						
10% P_2O_5–40% CaO–50% SiO_2	MS/sol–gel	CTAB	130 ± 10	309	Mesoporous	[68]
9% P_2O_5–33% CaO–58% SiO_2	Sol–gel	Nil	20	63.5	Mesoporous	[103]
10% B_2O_3–40% CaO–50% SiO_2	ME/sol–gel	CTAB	194	346	Mesoporous	[55]
15% CuO–15% CaO–70% SiO_2	MS/sol–gel	Nil	466 ± 31	11.1	Nonmesoporous	[67]
05% Ce_2O_3–35% CaO–60% SiO_2	ME/sol–gel	CTAB	130 ± 24	314	Mesoporous	[51]
05% Ga_2O_3–35% CaO–60% SiO_2	ME/sol–gel	CTAB	146 ± 25	496	Mesoporous	[51]
05% Fe_2O_3–10% CaO–85% SiO_2	US/sol–gel	PEG	19.4 ± 2.9	117.9	Mesoporous	[46]
10% Fe_2O_3–05% CaO–85% SiO_2	US/sol–gel	PEG	13.8 ± 2.2	288.1	Mesoporous	[46]
05% SrO–10% CaO–85% SiO_2	US/sol–gel	PEG	58.3 ± 3.2	66.5	Mesoporous	[43]
05% AgO–10% CaO–85% SiO_2	US/sol–gel	PEG	55.7 ± 6.1	84.4	Mesoporous	[42]
4% P_2O_5–36% CaO–60% SiO_2	Sol–gel	DDA	551 ± 137.8	233.7	Mesoporous	[140]

US, ultrasound-assisted; MS, modified Stöber; ME, microemulsion-assisted; DDA, dodecylamine.

9.4 Nanoscale Properties of Sol–Gel BGn

BGn have been prepared by several methods [17], e.g. modified Stöber method [67, 76, 132, 141], microemulsion method [82, 83] and modified-sol–gel methods including template-assisted [40, 142], microemulsion assisted [55], and ultrasound-assisted sol–gel [41]. Actually, depending on the synthesis method and type of template used, BGn have shown to have wide variations in their properties including particle size, particle morphology, textural properties, bioactivity, ions release kinetics, and biological behavior [17, 65]. Summary of common synthesis approaches, particle size, and textural properties of some sol–gel BGn are given in Table 9.1.

Importantly, bone-like hydroxyapatite (HA) formation in vitro (in vitro bioactivity) is a characteristic property of a bioactive glass [47, 143]. Actually, the bioactivity is greatly influenced by glass composition, particle size, and textural properties (specific surface area and mesoporosity).

The smaller the particle size (the larger the specific surface area), the faster HA formation rate. Thus, decreasing the size of BG particles to nanoscale significantly improves their bioactivity and ions release kinetics [19]. BGn prepared by ultrasound-assisted sol–gel method and PEG as a soft template exhibited excellent *in vitro* bioactivity [143]. BGn showed the generation of HA spheres with a few micrometers in size through a series of intriguing yet unprecedented phenomenon involving aggregation of BGn, mineralization, and HA sphere growth during simulated body fluid (SBF) immersion (Figure 9.3). Interestingly, the nano/micromorphology and HA crystal growth changed dramatically during the SBF immersion period (Figure 9.3, field-emission scanning electron microscopy [FE-SEM] panel).

High resolution transmission electron microscopy (HR-TEM) images along with the corresponding selected area electron diffraction (SAED) patterns (Figure 9.3, HR-TEM and SAED panels) showed the progressive development of HA nanocrystals from the aggregates of BGn during immersion in SBF for different time periods up to 21 days. Of note, focused ion beam-field emission scanning electron microscopy (FIB-SEM) cross-sectional image and energy-dispersive X-ray (EDX) point analysis (right image and its inset on Figure 9.3) at the core of the hydroxyapatite microsphere (HAM) after 14 days of growth in SBF revealed the presence of Si element with approximately 1–1.5 at%. Another illustrative example of the excellent bioactivity of BGn and its nanohybrid with collagen porous scaffold is shown in Figures 9.4 and 9.5.

HR-TEM image and SAED pattern (Figure 9.4a,c) of mesoporous BGn (prepared by ultrasound-assisted sol–gel method and CTAB as a soft template) show spherical nanomorphology, mesoporous texture, and amorphous structure prior to SBF immersion. Immersion of mesoporous BGn in SBF for three days led to significant growth of HA nanocrystals with needle-like morphology as shown in HR-TEM image displayed in Figure 9.4b along with the corresponding electron diffraction pattern (Figure 9.4d) which belongs to HA crystalline phase as indexed on the diffraction rings [47]. Figure 9.5 shows BGn hybridized with fibrillar network of collagen scaffold prior to SBF immersion along with the EDX spectrum (inset of Figure 9.5). The BGn-collagen nanohybrid scaffold demonstrated excellent bioactivity after SBF immersion for 7 and 14 days. Significant growth of needle-like HA nanocrystals along collagen fibrils after 7 days of SBF immersion was observed which then transformed to plate-like HA nanocrystals (flower-like morphology) at 14 days. The HR-TEM images show well integration between the HA nanocrystals and collagen fibrillar network. The TEM-SAED pattern of the scaffold at 7 days exhibited diffused electron diffraction rings, whereas at 14 days, intense dotted electron diffraction rings were observed which indicates to a significant increase in the bioactivity of the nanohybrid thanks to the excellent bioactivity of BGn.

9.5 Biomedical Applications of BGn

The remarkable merits of BGn have attracted a wide interest for fabrication of novel nanomaterials for biomedical applications, e.g. bone regeneration [47, 58, 81, 83, 135–137, 144–156], dental applications [37, 42, 43, 45, 48, 103, 157–165], skin regeneration, wound healing [140, 152, 166–176], and drug delivery [136, 159, 177–181]. Indeed, BGn showed promising outcomes in bone regeneration [136, 138, 147, 150, 182], dental adhesive resins [160, 183–187], dentin remineralization [90, 188, 189], dentine regeneration [103, 161, 190], dentin hypersensitivity [191–193], enamel demineralization prevention [185, 194, 195], cementum regeneration [77], pulp capping [45, 81, 161], periodontal regeneration [196–198], chronic, and diabetic wound healing [140, 152, 166, 168, 169, 173, 199]. Herein, representative examples of biomedical applications of BGn and its nanocomposites will be

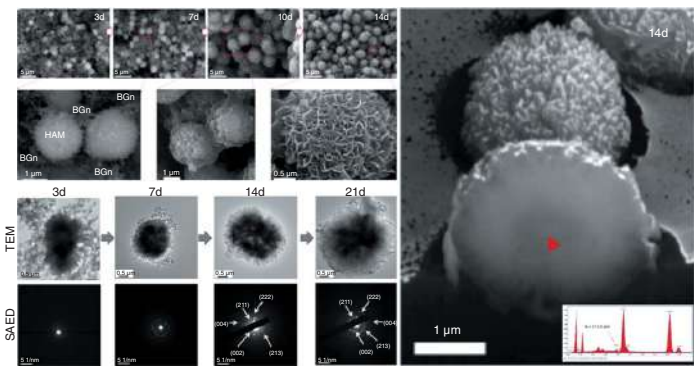

Figure 9.3 FE-SEM images, showing the growth of HA from aggregates of BGn at different periods up to 14 days. High-magnification FE-SEM (red rectangles) reveals the surface nanomorphology of HA crystals. HR-TEM images showing the development of HA from aggregates of BGn during immersion in SBF for different time periods up to 21 days, along with the corresponding SAED patterns. FIB-SEM image and EDX point probing (inset) of the core part of the HA microsphere developed after 14 days in SBF (indicated as an arrowhead in cross-sectional sphere), revealing the presence of Si with approximately 1–1.5 at%. Source: El-Fiqi et al. [143], Figure 01,02,03, p. 26,27,28/with permission of Elsevier.

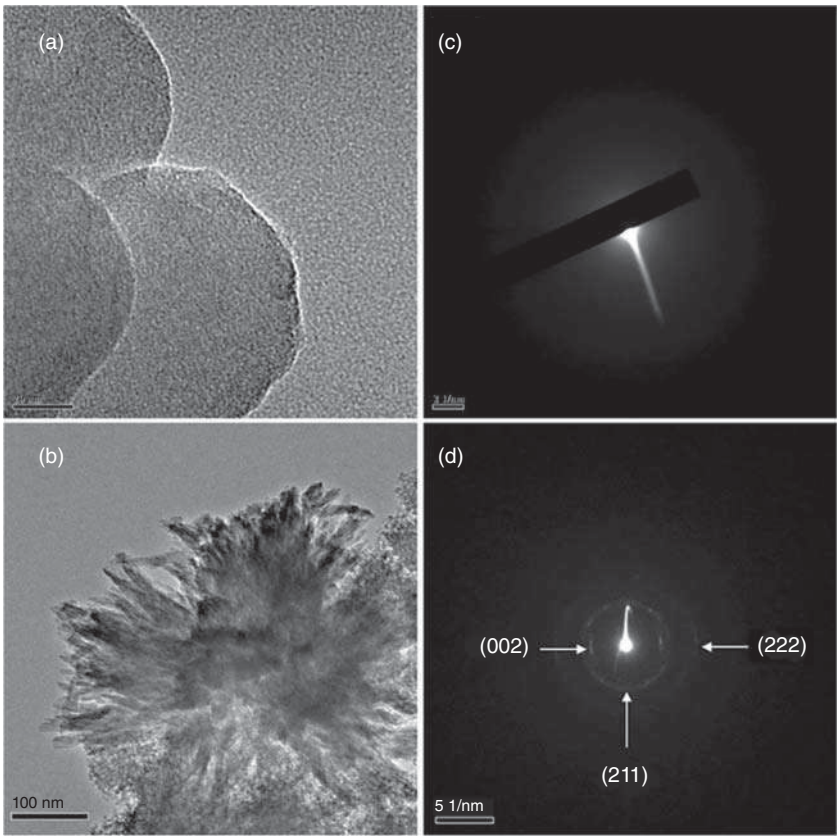

Figure 9.4 HR-TEM images (a, b) and TEM-SAED patterns (c, d) of as-prepared and SBF-immersed mesoporous BGn. Immersion of mesoporous BGn in SBF for three days led to a significant growth of HA nanocrystals with needle-like morphology showing the excellent *in vitro* bone-like hydroxyapatite formation ability of BGn. Source: El-Fiqi et al. [45], Figure 01, p. 02/with permission of Elsevier.

highlighted. Interestingly, BGn were used as precursor for formation of biomimetic Si-containing HAM in SBF [143].

The developed HAMs showed unique physicochemical properties including unique nano-/micro-patterned surface topography, biomimetic composition, high mesoporosity, large specific surface area, high protein adsorption, and release of bioactive ions, e.g. PO_4^{4-}, Ca^{2+}, and SiO_4^{4-}. Furthermore, the HAMs mediated excellent cellular interactions in 3D cultures demonstrating its great potential for engineering of 3D cell spheroids for bone tissue engineering (Figure 9.6). Thanks to BGn from which biomimetic Si-containing HAMs were obtained. On the other hand, BGn are very promising in dental applications. Particularly, the effects of nanoscale bioactive glass (n-BG) on odontogenic differentiation and dentin formation of dental pulp cells were investigated and compared with those of m-BG [103]. Human dental pulp cells (hDPCs) from third molars were cultured directly with m-BG and n-BG *in vitro*. The mineralization capacity and expression of odontogenic-related proteins and genes (dentin sialophosphoprotein, dentin matrix protein 1, and collagen type I) of hDPCs were significantly upregulated under BG induction, and were particularly higher in the n-BG group than in the control group. Moreover, m-BG and n-BG combined with pulp tissues were transplanted into the dorsum of immunodeficient mice to observe their biological effects on dental pulp cells *in vivo* (Figure 9.7). A continuous layer

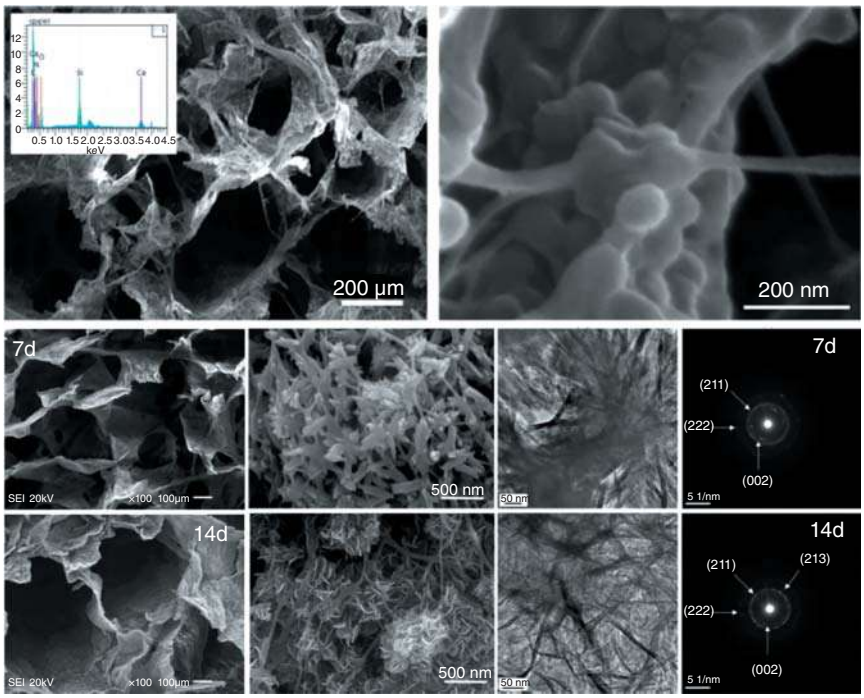

Figure 9.5 Low- and high-magnification FE-SEM images and EDX spectrum (inset) of BGn/collagen nanohybrid porous scaffold. Low- and high-magnification FE-SEM images of BGn/collagen nanohybrid porous scaffold after immersion in SBF for 7 and 14 days along with the corresponding HR-TEM images and SAED patterns. Significant growth of needle-like HA nanocrystals along collagen fibrils after 7 days of SBF immersion were observed which then transformed to plate-like HA nanocrystals (flower-like morphology) at 14 days. Source: El-Fiqi et al. [47], Figure 04,05,06, p. 04,05/with permission of Elsevier.

of dentin-like tissue with uniform thickness, a well-organized dentinal tubule structure, and polarizing odontoblast-like cells aligned along it was generated upon the n-BG layer, whereas some irregular sporadic osteodentin-like mineralized tissues were observed in the control group (Figure 9.7a–j). The study reveals that BG, especially n-BG, induces the odontogenic differentiation and dentin formation of dental pulp cells and may serve as a potential material for pulp repair and dentin regeneration [103].

Lately, there is a rapidly growing interest in application of BGn-based nanomaterials for chronic and diabetic wound healing [140, 151, 152, 166, 168, 169, 173, 199]. The effects of BGn on macrophages and their contribution to healing of diabetic wounds were investigated in rats [140]. Interestingly, BGn affected the proliferation/viability and polarization of macrophages in a dose-dependent manner. A low concentration of BGn stimulated the proliferation/viability of macrophages, promoted the M1-to-M2 phenotype switch of macrophages and facilitated wound closure. Whereas a high concentration of BGn showed significant cytotoxicity to macrophages, prolonged the M1 phenotype of macrophages, and decelerated wound closure. Li et al. [152] developed a bioactive self-healing antibacterial injectable dual-network silica-based nanocomposite hydrogel scaffolds that can significantly enhance the diabetic wound healing/skin tissue formation through promoting early angiogenesis without adding any bioactive factors. The nanocomposite scaffold comprises a main network of polyethylene glycol diacrylate (PEGDA) forming scaffolds, with an auxiliary dynamic network formed between bioactive glass nanoparticles containing

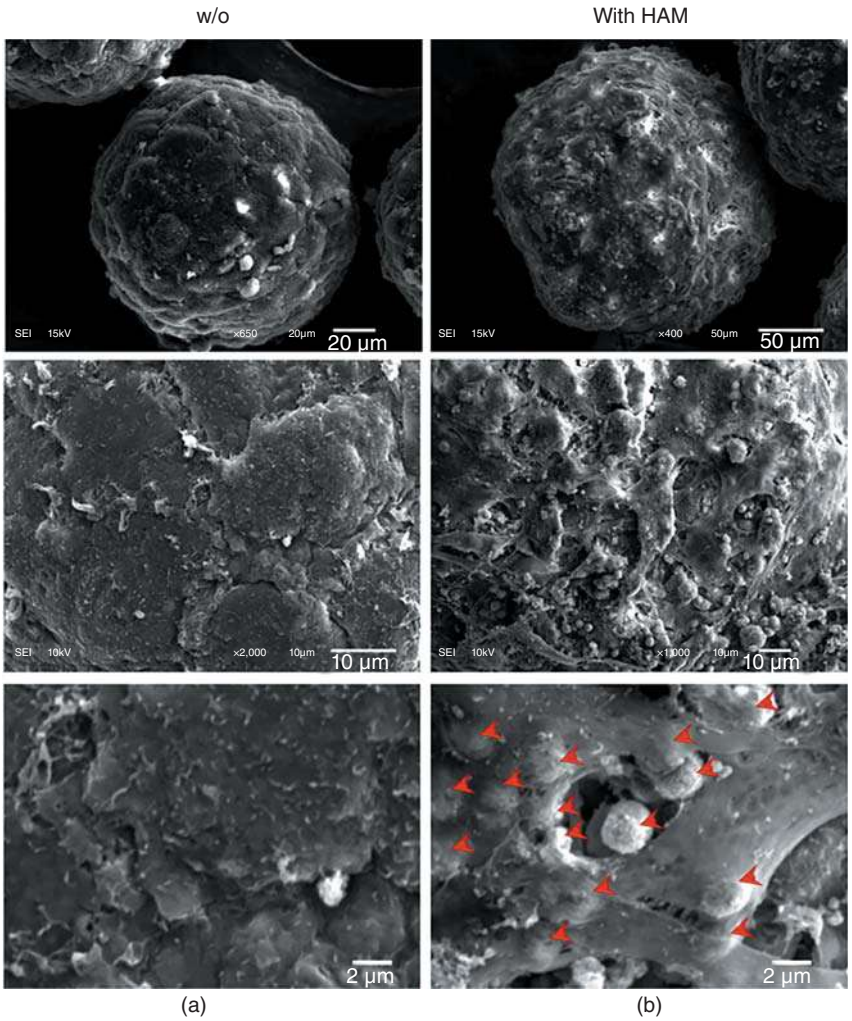

Figure 9.6 Cell spheroid formation (from mesenchymal stem cells derived from rat dental pulp) mediated by biomimetic HA microspheres produced by biomineralization of BGn: low- and high-magnification SEM images (a) of cell spheroids without HAM (W/O) and with HAM (b). HAMs present in cell spheroid are indicated by red arrows. Source: El-Fiqi et al. [143], Figure 08, p. 33/with permission of Elsevier.

copper (BGNC) and sodium alginate (ALG) (PABC scaffolds) [152]. PABC scaffolds exhibited the biomimetic elastomeric mechanical properties, excellent injectabilities, self-healing behavior, as well as the robust broad-spectrum antibacterial activity. Importantly, PABC hydrogel significantly promoted the viability, proliferation, and angiogenic ability of endothelial progenitor cells (EPCs) *in vitro*. *In vivo*, PABC hydrogel could efficiently restore blood vessels networks through enhancing hypoxia-inducible factor 1α (HIF-1α)/vascular endothelial growth factor (VEGF) expression and collagen matrix deposition in the full-thickness diabetic wound, and significantly accelerates wound healing and skin tissue regeneration [152]. A nanocomposite wound dressing with a spatially designed multilayer structure composed of chitosan, polyvinyl alcohol (PVA), and nanobioglass (nBG) was fabricated by sequential electrospinning for accelerating cutaneous wound healing, especially chronic wound healing [166].

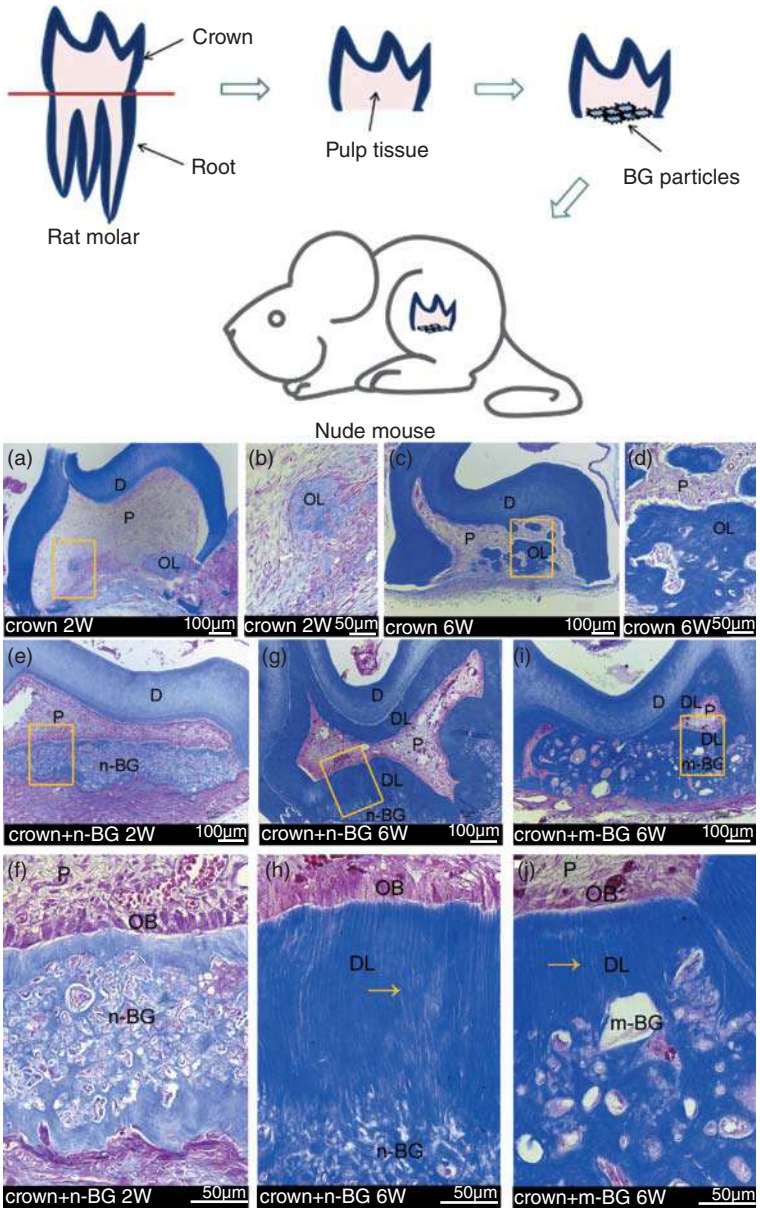

Figure 9.7 *In vivo* model of subcutaneous transplantation in nude mouse. Masson's trichrome staining evaluation of the effects of m-BG and n-BG on dentin formation. (a, b) (b is a magnified image of a) crowns implanted alone for two weeks; (c, d) crowns implanted alone for six weeks; (e, f) crowns covered with n-BG after two weeks of transplantation; (g, h) crowns covered with n-BG after six weeks of transplantation; (i, j) crowns covered with m-BG after six weeks of transplantation. The yellow arrow points to the odontoblastic processes embedded in the newly generated dentin-like matrix. Abbreviations: D, dentin; DL, dentin-like tissues; m-BG, microbioactive glass; n-BG, nanobioactive glass; OB, odontoblast-like cells; OL, osteodentin-like tissues; P, pulp tissue. Source: Wang et al. [103], Figure 08, p. 09/with permission of Elsevier.

In vivo studies on a rat full-thickness skin defects model and mice diabetic wound model demonstrated its significant efficiency in improving healing. As illustrated by histological assessments (Figure 9.8), regenerated skin tissue exhibited complete re-epithelialization, improved collagen alignment, and regeneration of skin appendages. For diabetic chronic wound, nBG-trilayer fibrous membrane (TFM) accelerated wound closure through upregulating growth factors of VEGF, transforming growth factor β (TGF-β) and downregulating inflammatory cytokines of tumor necrosis factor α (TNF-α), interleukin-1β (IL-1β). Therefore, nBG-TFM possesses a great potential in

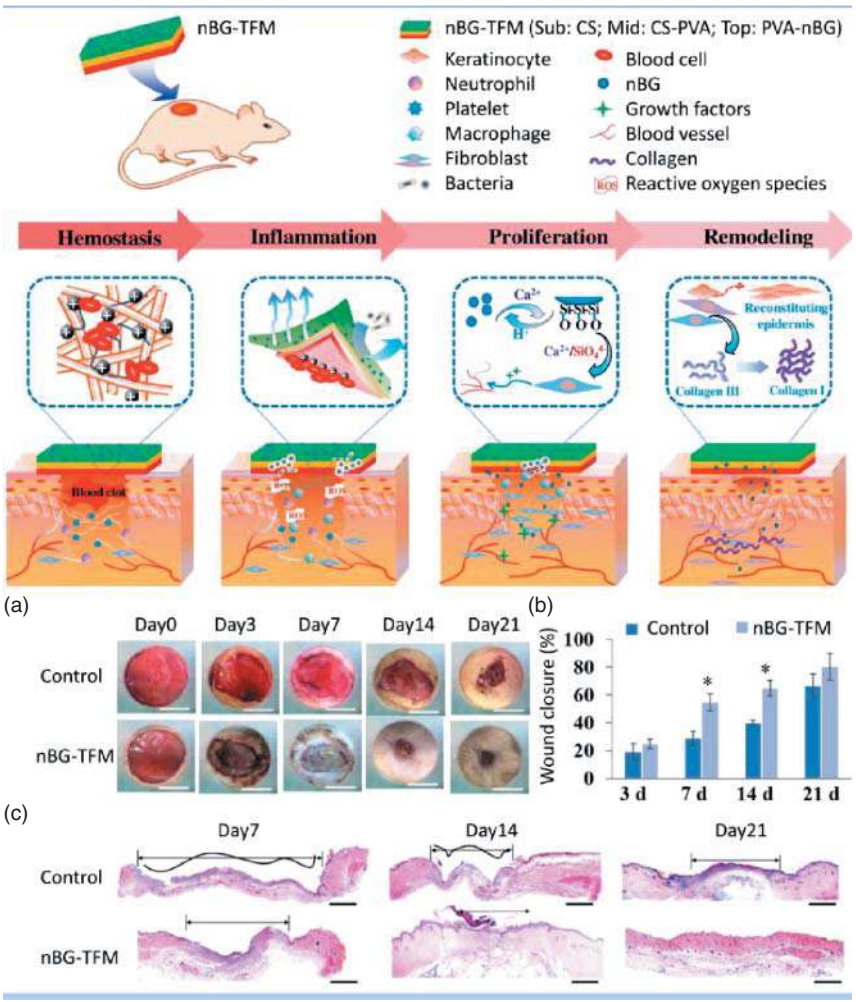

Figure 9.8 The mechanism of synergistic effect of multiple components and the hierarchical structure of nBG-TFM on exerting proper function at different healing stages in accelerating wound healing (upper schematic). Evaluation of nBG-TFM on rat full-thickness cutaneous wound healing: (a) representative images of full-thickness skin defects treated with the petrolatum gauze (control) and nBG-TFM at predetermined time postsurgery (scale bar: 10 mm), and (b) quantified as wound closure percentage, $n = 3$. (c) H&E stained sections for the gross wound revealing similar tendency of healing. Also, the total epithelium was significantly increased in nBG-TFM treated group, and the thickness of regenerated epidermis was almost the same as the healthy skin. The black arrows indicate the width of unhealed site. Blue arrows indicate inflammatory cells and black arrows indicate capillary vessels. Scale bar: 2 mm. Source: (a, c) Chen et al. [166], Figure 05, p. 08/with permission of Elsevier.

cutaneous wound healing and chronic wound healing applications. The synergistic effect of multiple components and the spatially designed multilayer structure were assumed to be the main reason for accelerating chronic wound healing. nBG-TFM exerts proper functions at different healing stages as illustrated in Figure 9.8 (upper schematic). The rapid hemostasis after injury was reached by chitosan in the sublayer with high density of positive charge to electrostatically interact with erythrocytes and activate platelets, leading to blood coagulations formation. Platelets released growth factors to attract neutrophils and macrophages to initiate inflammatory stage. With insufficient perfusion and angiogenesis in diabetic wounds, hypoxia amplified the inflammatory response through augmentation of inflammatory mediators and increasing of reactive oxygen species (ROS) production. The diabetic wounds usually get stuck in the inflammatory phase with continuing influx of neutrophils that cause extensive collateral damage to surrounding tissue. nBG-TMF reduced persistent inflammation by decreasing inflammatory cytokines (e.g. TNF-α and IL-1β) and enhancing angiogenesis. The bioactive ions originated from nBG in the top-layer accelerated wound healing through stimulating the angiogenesis and tissue regeneration, which were especially important for chronic wound healing.

A micropatterned electrospun scaffold, with BGn incorporated inside the core layer of coaxial polylactic acid (PLA) nanofibers with gelatin as the outer layer, was developed to accelerate angiogenesis in diabetic wound sites [172]. Inorganic Si ions and Ca ions could be controllably released from the BGn loaded inside the coaxial fibers in appropriate concentrations, which could upregulate the expression of angiogenesis-related cytokines such as HIF-1α and VEGF. Furthermore, the extracellular matrix (ECM)-like structure of the micropatterned scaffold provided a large number of adhesion sites and sufficient growth space for the cells, and thus played a role in temporarily replacing the defective ECM at the wound site. The results showed that under the synergistic effect of the composition and structure of the scaffold, the angiogenesis rate and collagen deposition of the wound were significantly improved, and the wound-healing period was also significantly shortened, which provides an ideal solution for the healing of chronic diabetic wounds with impaired angiogenesis. The BGn loaded inside the coaxial PLA nanofibers can play a synergistic role in promoting wound healing, which can not only act as a temporary ECM to promote endothelial cell adhesion and growth but also upregulate the expression of proangiogenesis cytokines and effectively promote the angiogenesis in the diabetic wound.

Bone ECM-biomimetic cell-free nanofibrous scaffolds were also developed for enhancing healing in diabetic full-thickness wounds [173]. This bioactive nanofibrous matrix was composed of ECM-componential collagen (Col, mimicking protein), polycaprolactone (PCL), and BGn (mimicking biological apatite) (collagen (Col)- polycaprolactone (PCL)- bioactive glass nanoparticles (BGNs) scaffold [CPB]) [173]. CPB significantly improved attachment and proliferation of endothelial cells and upregulated the expression of the angiogenesis marker (CD31). *In vivo*, CPB also significantly enhanced the angiogenesis, through greatly upregulating the mRNA and protein expressions of HIF-1α, VEGF, Col1, and alpha smooth muscle actin (α-SMA).

Furthermore, due to rapid angiogenesis, granulation tissue formation, collagen matrix remodeling, and epidermis differentiation were accelerated in the CPB group, and as a result efficient diabetic wound healing was observed. These results demonstrated that the cell-free bone-ECM-biomimetic BGn-based nanofibrous matrix could efficiently enhance blood tissue regeneration and diabetic wound healing without additional growth factors. Wang et al. [174] reported efficient local delivery of EPCs using a bioactive nanofibrous scaffold composed of collagen, PCL, and BGns (CPB) for enhancing angiogenesis and wound healing [174]. Under the stimulation of CPB nanofibrous system, the viability and angiogenic ability of EPCs were significantly enhanced through the activation of HIF-1α/VEGF/stromal derived factor 1α (SDF-1α)

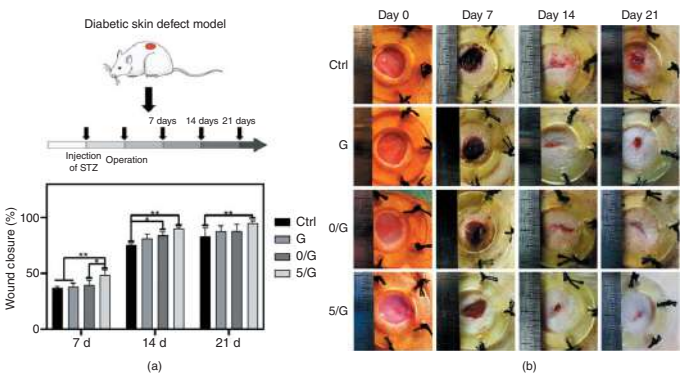

Figure 9.9 *In vivo* wound healing after different treatments with Ce-BGn/GelMA hydrogels. (a) The diabetic skin defect model and flow chart of the *in vivo* experiments. (b) Representative images of the skin wound area after different treatments on days 0, 7, 14, and 21. (c) Quantification of wound closure rate of different treatment groups ($n = 5$). * $p < 0.05$, ** $p < 0.01$. The abbreviations of the hydrogels: GelMA (G), 0 Ce-BGn/GelMA (0/G), and 5 Ce-BGn/GelMA (5/G). Source: (b) Chen et al. [199], Figure 06, p. 11/MDPI/CC BY 4.0.

signaling. Moreover, owing to the increased local delivery of cells and fast neovascularization within the wound site, cell proliferative activity, granulation tissue formation, and collagen synthesis and deposition were greatly promoted by CPB/EPC constructs resulting in a rapid re-epithelialization and regeneration of skin appendages. Therefore, CPB/EPC constructs effectively stimulated the regeneration of diabetic wounds with a satisfactory vascularization and better healing outcomes in a full-thickness wound model. Chen et al. [199] developed a multifunctional injectable composite hydrogel based on cerium-containing bioactive glass nanoparticles (Ce-BGn) and gelatin methacryloyl (GelMA) hydrogel for diabetic wound healing. The Ce-BGn were synthesized by template-assisted sol–gel method using DDA (dodecylamine) as a soft template. The incorporation of Ce-BGn into the GelMA hydrogel endowed the hydrogel with angiogenic effect via releasing Si ions [200]. The Ce-BGn/GelMA hydrogels showed a good cytocompatibility, promoted endothelial cells (HUVECs) migration and tubular formation. *In vitro* antibacterial tests showed that 5 mol% CeO_2-containing bioactive glass/GelMA composite hydrogel (5/G) exhibited excellent antibacterial properties. In *in vivo* study (Figure 9.9), the macroscopic images of diabetic skin wounds with different Ce-BGn/GelMA hydrogels treatments revealed that the wound closure time in groups of 0/G, and 5/G were faster than the G and control groups. The quantitative analysis of skin wound area (Figure 9.9c) confirmed that the wound closure rate of 5/G group was the highest compared to other groups. Therefore, the 5Ce-BGn/GelMA hydrogel could significantly improve wound healing in diabetic rats by accelerating the formation of granulation tissue, collagen deposition, and angiogenesis.

9.6 Conclusion

BGn have demonstrated excellent merits compared with conventional bioactive glass including nanoscale size, uniform spherical shape, large specific surface area, fast biodegradability, rapid release of bioactive ions, superior bioactivity, injectability, and intracellular uptake. Such unique merits made BGn a potential platform for developing novel BGn-based biomaterials for a wide range of biomedical applications such as bone regeneration, dental tissue repair, drug delivery, wound healing, and skin regeneration. Especially, BGn-based biomaterials are currently receiving a rapidly growing interest for chronic and diabetic wound healing. Thanks to the remarkable merits of BGn which allowed development of highly promising biomaterials for hard and soft tissue regeneration. Finally, current biomedical applications of BGn and BGn-based biomaterials are mainly directed to regeneration of normal bone and skin tissues. However, BGn and BGn-based biomaterials are expected to be more potentially explored in treatment and repair of bone and skin cancers.

References

1 Varshneya, A.K. (1994). Introduction. In: *Fundamentals of Inorganic Glasses* (Chapter 1) (ed. A.K. Varshneya), 1–11. San Diego: Academic Press.
2 Varshneya, A.K. (1994). Fundamentals of the glassy state. In: *Fundamentals of Inorganic Glasses* (Chapter 2) (ed. A.K. Varshneya), 13–25. San Diego: Academic Press.
3 Sukenaga, S. and Shibata, H. (2021). High-temperature characterization of glasses and melts. In: *Encyclopedia of Materials: Technical Ceramics and Glasses* (ed. M. Pomeroy), 689–703. Elsevier.

4 Hench, L.L. and West, J.K. (1990). The sol–gel process. *Chemical Reviews* 90: 33–72.
5 Parker, J.M. (2005). Glasses. In: *Encyclopedia of Condensed Matter Physics* (ed. F. Bassani, G.L. Liedl and P. Wyder), 273–280. Oxford: Elsevier.
6 Holand, W. and Beall, G.H. (2019). *Glass-Ceramic Technology*. Wiley.
7 Axinte, E. (2011). Glasses as engineering materials: a review. *Materials and Design* 32: 1717–1732.
8 Martin, H. (2019). *Making Mirrors for Giant Telescopes*. SPIE.
9 Tong, L. and Mazur, E. (2008). Glass nanofibers for micro- and nano-scale photonic devices. *Journal of Non-Crystalline Solids* 354: 1240–1244.
10 Hench, L.L. (2006). The story of Bioglass®. *Journal of Materials Science – Materials in Medicine* 17: 967–978.
11 Hench, L.L. and Jones, J.R. (2015). Bioactive glasses: frontiers and challenges. *Frontiers in Bioengineering and Biotechnology* 3: 194.
12 Hench, L.L. (2013). Chronology of bioactive glass development and clinical applications. *New Journal of Glass and Ceramics* 03 (02): 7.
13 Kaur, G., Pandey, O.P., Singh, K. et al. (2014). A review of bioactive glasses: their structure, properties, fabrication and apatite formation. *Journal of Biomedical Materials Research Part A* 102: 254–274.
14 Schmitz, S.I., Widholz, B., Essers, C. et al. (2020). Superior biocompatibility and comparable osteoinductive properties: sodium-reduced fluoride-containing bioactive glass belonging to the CaO–MgO–SiO_2 system as a promising alternative to 45S5 bioactive glass. *Bioactive Materials* 5: 55–65.
15 Li, R., Clark, A.E., and Hench, L.L. (1991). An investigation of bioactive glass powders by sol–gel processing. *Journal of Applied Biomaterials* 2: 231–239.
16 Mačković, M., Hoppe, A., Detsch, R. et al. (2012). Bioactive glass (type 45S5) nanoparticles: in vitro reactivity on nanoscale and biocompatibility. *Journal of Nanoparticle Research* 14: 966.
17 Vichery, C. and Nedelec, J.-M. (2016). Bioactive glass nanoparticles: from synthesis to materials design for biomedical applications. *Materials (Basel)* 9: 288.
18 Zheng, K. and Boccaccini, A.R. (2017). Sol–gel processing of bioactive glass nanoparticles: a review. *Advances in Colloid and Interface Science* 249: 363–373.
19 Erol Taygun, M. and Boccaccini, A.R. (2018). Nanoscaled bioactive glass particles and nanofibers. In: *Bioactive Glasses* (Chapter 10), 2e (ed. H. Ylänen), 235–283. Woodhead Publishing.
20 Lukowiak, A., Lao, J., Lacroix, J., and Nedelec, J.-M. (2013). Bioactive glass nanoparticles obtained through sol–gel chemistry. *Chemical Communications* 49: 6620–6622.
21 Jones, J.R. (2013). Review of bioactive glass: from Hench to hybrids. *Acta Biomaterialia* 9: 4457–4486.
22 Romeis, S., Hoppe, A., Detsch, R. et al. (2015). Top-down processing of submicron 45S5 Bioglass® for enhanced in vitro bioactivity and biocompatibility. *Procedia Engineering* 102: 534–541.
23 Gao, C., Liu, T., Shuai, C., and Peng, S. (2014). Enhancement mechanisms of graphene in nano-58S bioactive glass scaffold: mechanical and biological performance. *Scientific Reports* 4: 4712.
24 Liu, J., Gao, C., Feng, P. et al. (2015). A bioactive glass nanocomposite scaffold toughed by multi-wall carbon nanotubes for tissue engineering. *Journal of the Ceramic Society of Japan* 123: 485–491.

25 Romeis, S., Hoppe, A., Eisermann, C. et al. (2014). Enhancing in vitro bioactivity of melt-derived 45S5 Bioglass® by comminution in a stirred media mill. *Journal of the American Ceramic Society* 97: 150–156.

26 Shams, M., Karimi, M., Ghollasi, M. et al. (2018). Electrospun poly-L-lactic acid nanofibers decorated with melt-derived S53P4 bioactive glass nanoparticles: the effect of nanoparticles on proliferation and osteogenic differentiation of human bone marrow mesenchymal stem cells in vitro. *Ceramics International* 44: 20211–20219.

27 Olhero, S.M., Fernandes, H.R., Marques, C.F. et al. (2017). Additive manufacturing of 3D porous alkali-free bioactive glass scaffolds for healthcare applications. *Journal of Materials Science* 52: 12079–12088.

28 Jandt, K.D. and Watts, D.C. (2020). Nanotechnology in dentistry: present and future perspectives on dental nanomaterials. *Dental Materials* 36: 1365–1378.

29 Kesse, X., Vichery, C., Jacobs, A. et al. (2020). Unravelling the impact of calcium content on the bioactivity of sol–gel-derived bioactive glass nanoparticles. *ACS Applied Bio Materials* 3: 1312–1320.

30 Barrioni, B.R., Oliveira, A.C., de Fátima Leite, M., and de Magalhães Pereira, M. (2017). Sol–gel-derived manganese-releasing bioactive glass as a therapeutic approach for bone tissue engineering. *Journal of Materials Science* 52: 8904–8927.

31 Pajares-Chamorro, N. and Chatzistavrou, X. (2020). Bioactive glass nanoparticles for tissue regeneration. *ACS Omega* 5: 12716–12726.

32 Luz, G.M. and Mano, J.F. (2011). Preparation and characterization of bioactive glass nanoparticles prepared by sol–gel for biomedical applications. *Nanotechnology* 22: 494014.

33 Kazemian, Z., Varzandeh, M., and Labbaf, S. (2021). A facile synthesis of mono dispersed spherical silver doped bioactive glass nanoparticle. *Journal of Materials Science – Materials in Medicine* 32: 29.

34 Fan, J.P., Kalia, P., Di Silvio, L., and Huang, J. (2014). In vitro response of human osteoblasts to multi-step sol–gel derived bioactive glass nanoparticles for bone tissue engineering. *Materials Science and Engineering C* 36: 206–214.

35 El-Rashidy, A.A., Waly, G., Gad, A. et al. (2018). Preparation and in vitro characterization of silver-doped bioactive glass nanoparticles fabricated using a sol–gel process and modified Stöber method. *Journal of Non-Crystalline Solids* 483: 26–36.

36 de Oliveira, A.A.R., de Souza, D.A., Dias, L.L.S. et al. (2013). Synthesis, characterization and cytocompatibility of spherical bioactive glass nanoparticles for potential hard tissue engineering applications. *Biomedical Materials* 8: 025011.

37 Ajita, J., Saravanan, S., and Selvamurugan, N. (2015). Effect of size of bioactive glass nanoparticles on mesenchymal stem cell proliferation for dental and orthopedic applications. *Materials Science and Engineering C* 53: 142–149.

38 Naruphontjirakul, P., Porter, A.E., and Jones, J.R. (2018). In vitro osteogenesis by intracellular uptake of strontium containing bioactive glass nanoparticles. *Acta Biomaterialia* 66: 67–80.

39 Leite, Á.J., Gonçalves, A.I., Rodrigues, M.T. et al. (2018). Strontium-doped bioactive glass nanoparticles in osteogenic commitment. *ACS Applied Materials & Interfaces* 10: 23311–23320.

40 Mao, Y., Liao, J., Wu, M. et al. (2020). Preparation of nano spherical bioglass by alkali-catalyzed mixed template. *Materials Research Express* 7: 105202.

41 El-Fiqi, A., Kim, T.-H., Kim, M. et al. (2012). Capacity of mesoporous bioactive glass nanoparticles to deliver therapeutic molecules. *Nanoscale* 4: 7475–7488.

42 Lee, J.-H., El-Fiqi, A., Mandakhbayar, N. et al. (2017). Drug/ion co-delivery multi-functional nanocarrier to regenerate infected tissue defect. *Biomaterials* 142: 62–76.

43 Lee, J.-H., Mandakhbayar, N., El-Fiqi, A., and Kim, H.-W. (2017). Intracellular co-delivery of Sr ion and phenamil drug through mesoporous bioglass nanocarriers synergizes BMP signaling and tissue mineralization. *Acta Biomaterialia* 60: 93–108.

44 Kim, T.-H., Kang, M.S., Mandakhbayar, N. et al. (2019). Anti-inflammatory actions of folate-functionalized bioactive ion-releasing nanoparticles imply drug-free nanotherapy of inflamed tissues. *Biomaterials* 207: 23–38.

45 El-Fiqi, A., Mandakhbayar, N., Jo, S.B. et al. (2021). Nanotherapeutics for regeneration of degenerated tissue infected by bacteria through the multiple delivery of bioactive ions and growth factor with antibacterial/angiogenic and osteogenic/odontogenic capacity. *Bioactive Materials* 6: 123–136.

46 El-Fiqi, A. and Kim, H.-W. (2021). Iron ions-releasing mesoporous bioactive glass ultrasmall nanoparticles designed as ferroptosis-based bone cancer nanotherapeutics: ultrasonic-coupled sol–gel synthesis, properties and iron ions release. *Materials Letters* 294: 129759.

47 El-Fiqi, A., Kim, J.-H., and Kim, H.-W. (2020). Novel bone-mimetic nanohydroxyapatite/collagen porous scaffolds biomimetically mineralized from surface silanized mesoporous nanobioglass/collagen hybrid scaffold: physicochemical, mechanical and in vivo evaluations. *Materials Science and Engineering C* 110: 110660.

48 Mandakhbayar, N., El-Fiqi, A., Dashnyam, K., and Kim, H.-W. (2018). Feasibility of defect tunable bone engineering using electroblown bioactive fibrous scaffolds with dental stem cells. *ACS Biomaterials Science & Engineering* 4: 1019–1028.

49 Bari, A., Bloise, N., Fiorilli, S. et al. (2017). Copper-containing mesoporous bioactive glass nanoparticles as multifunctional agent for bone regeneration. *Acta Biomaterialia* 55: 493–504.

50 Neščáková, Z., Zheng, K., Liverani, L. et al. (2019). Multifunctional zinc ion doped sol–gel derived mesoporous bioactive glass nanoparticles for biomedical applications. *Bioactive Materials* 4: 312–321.

51 Kurtuldu, F., Mutlu, N., Michálek, M. et al. (2021). Cerium and gallium containing mesoporous bioactive glass nanoparticles for bone regeneration: bioactivity, biocompatibility and antibacterial activity. *Materials Science and Engineering C* 124: 112050.

52 Deshmukh, K., Kovářík, T., Křenek, T. et al. (2020). Recent advances and future perspectives of sol–gel derived porous bioactive glasses: a review. *RSC Advances* 10: 33782–33835.

53 Zheng, K., Kang, J., Rutkowski, B. et al. (2019). Toward highly dispersed mesoporous bioactive glass nanoparticles with high Cu concentration using Cu/ascorbic acid complex as precursor. *Frontiers in Chemistry* 7: 497.

54 Zheng, K., Fan, Y., Torre, E. et al. (2020). Incorporation of boron in mesoporous bioactive glass nanoparticles reduces inflammatory response and delays osteogenic differentiation. *Particle and Particle Systems Characterization* 37: 2000054.

55 Liang, Q., Hu, Q., Miao, G. et al. (2015). A facile synthesis of novel mesoporous bioactive glass nanoparticles with various morphologies and tunable mesostructure by sacrificial liquid template method. *Materials Letters* 148: 45–49.

56 Souza, I.E.P.e., Carvalho, S.M.d., Martins, T., and Pereira, M.d.M. (2020). Fluorine-containing bioactive glass spherical particles synthesized by sol–gel route assisted by ultrasound energy or mechanical mixing. *Journal of Materials Research* 23 (3): e20200070.

57 Lei, B., Chen, X., Han, X., and Zhou, J. (2012). Versatile fabrication of nanoscale sol–gel bioactive glass particles for efficient bone tissue regeneration. *Journal of Materials Chemistry* 22: 16906–16913.

58 Taghvaei, A.H., Danaeifar, F., Gammer, C. et al. (2020). Synthesis and characterization of novel mesoporous strontium-modified bioactive glass nanospheres for bone tissue engineering applications. *Microporous and Mesoporous Materials* 294: 109889.

59 Labbaf, S., Tsigkou, O., Müller, K.H. et al. (2011). Spherical bioactive glass particles and their interaction with human mesenchymal stem cells in vitro. *Biomaterials* 32: 1010–1018.

60 Lins, C.E.C., Oliveira, A.A.R., Gonzalez, I. et al. (2018). Structural analysis of fluorine-containing bioactive glass nanoparticles synthesized by sol–gel route assisted by ultrasound energy. *Journal of Biomedical Materials Research Part B* 106: 360–366.

61 de Oliveira, A.A.R., de Carvalho, B.B., Sander Mansur, H., and de Magalhães Pereira, M. (2014). Synthesis and characterization of bioactive glass particles using an ultrasound-assisted sol–gel process: engineering the morphology and size of sonogels via a poly(ethylene glycol) dispersing agent. *Materials Letters* 133: 44–48.

62 Hong, Z., Liu, A., Chen, L. et al. (2009). Preparation of bioactive glass ceramic nanoparticles by combination of sol–gel and coprecipitation method. *Journal of Non-Crystalline Solids* 355: 368–372.

63 Min, Z., Huixue, W., Yujie, Z. et al. (2016). Synthesis of monodispersed mesoporous bioactive glass nanospheres for bone repair. *Materials Letters* 171: 259–262.

64 Li, X., Chen, X., Miao, G. et al. (2014). Synthesis of radial mesoporous bioactive glass particles to deliver osteoactivin gene. *Journal of Materials Chemistry B* 2: 7045–7054.

65 Zheng, K., Sui, B., Ilyas, K., and Boccaccini, A.R. (2021). Porous bioactive glass micro- and nanospheres with controlled morphology: developments, properties and emerging biomedical applications. *Materials Horizons* 8: 300–335.

66 Naruphontjirakul, P., Tsigkou, O., Li, S. et al. (2019). Human mesenchymal stem cells differentiate into an osteogenic lineage in presence of strontium containing bioactive glass nanoparticles. *Acta Biomaterialia* 90: 373–392.

67 Zheng, K., Dai, X., Lu, M. et al. (2017). Synthesis of copper-containing bioactive glass nanoparticles using a modified Stöber method for biomedical applications. *Colloids and Surfaces B: Biointerfaces* 150: 159–167.

68 Nawaz, Q., Rehman, M.A.U., Burkovski, A. et al. (2018). Synthesis and characterization of manganese containing mesoporous bioactive glass nanoparticles for biomedical applications. *Journal of Materials Science – Materials in Medicine* 29: 64.

69 Barrioni, B.R., Naruphontjirakul, P., Norris, E. et al. (2019). Effects of manganese incorporation on the morphology, structure and cytotoxicity of spherical bioactive glass nanoparticles. *Journal of Colloid and Interface Science* 547: 382–392.

70 Westhauser, F., Wilkesmann, S., Nawaz, Q. et al. (2020). Osteogenic properties of manganese-doped mesoporous bioactive glass nanoparticles. *Journal of Biomedical Materials Research Part A* 108: 1806–1815.

71 Kapp, M., Li, C., Xu, Z. et al. (2021). Protein adsorption on SiO_2–CaO bioactive glass nanoparticles with controllable Ca content. *Nanomaterials* 11: 561.

72 Kesse, X., Vichery, C., and Nedelec, J.-M. (2019). Deeper insights into a bioactive glass nanoparticle synthesis protocol to control its morphology, dispersibility, and composition. *ACS Omega* 4: 5768–5775.

73 Zheng, K., Taccardi, N., Beltrán, A.M. et al. (2016). Timing of calcium nitrate addition affects morphology, dispersity and composition of bioactive glass nanoparticles. *RSC Advances* 6: 95101–95111.

74 Zheng, K., Lu, M., Liu, Y. et al. (2016). Monodispersed lysozyme-functionalized bioactive glass nanoparticles with antibacterial and anticancer activities. *Biomedical Materials* 11: 035012.

75 Ouyang, S., Zheng, K., Huang, Q. et al. (2020). Synthesis and characterization of rubidium-containing bioactive glass nanoparticles. *Materials Letters* 273: 127920.

76 Greasley, S.L., Page, S.J., Sirovica, S. et al. (2016). Controlling particle size in the Stöber process and incorporation of calcium. *Journal of Colloid and Interface Science* 469: 213–223.

77 Carvalho, S.M., Oliveira, A.A.R., Jardim, C.A. et al. (2012). Characterization and induction of cementoblast cell proliferation by bioactive glass nanoparticles. *Journal of Tissue Engineering and Regenerative Medicine* 6: 813–821.

78 Kozon, D., Zheng, K., Boccardi, E. et al. (2016). Synthesis of monodispersed Ag-doped bioactive glass nanoparticles via surface modification. *Materials (Basel)* 9: 225.

79 Wu, Y., Tang, L., Zhang, Q. et al. (2021). A novel synthesis of monodispersed bioactive glass nanoparticles via ultrasonic-assisted surfactant-free microemulsion approach. *Materials Letters* 285: 129053.

80 Zhao, N.R., Wang, Y.J., Chen, X.F. et al. (2005). Preparation of bioactive nanoparticles in the system $CaO–P_2O_5–SiO_2$ using microemulsions. *Key Engineering Materials* 288–289: 179–182.

81 Kang, M.S., Lee, N.-H., Singh, R.K. et al. (2018). Nanocements produced from mesoporous bioactive glass nanoparticles. *Biomaterials* 162: 183–199.

82 Kim, T.-H., Singh, R.K., Kang, M.S. et al. (2016). Inhibition of osteoclastogenesis through siRNA delivery with tunable mesoporous bioactive nanocarriers. *Acta Biomaterialia* 29: 352–364.

83 Kim, T.-H., Singh, R.K., Kang, M.S. et al. (2016). Gene delivery nanocarriers of bioactive glass with unique potential to load BMP2 plasmid DNA and to internalize into mesenchymal stem cells for osteogenesis and bone regeneration. *Nanoscale* 8: 8300–8311.

84 Seo, J.J., Mandakhbayar, N., Kang, M.S. et al. (2021). Antibacterial, proangiogenic, and osteopromotive nanoglass paste coordinates regenerative process following bacterial infection in hard tissue. *Biomaterials* 268: 120593.

85 Li, X., Liang, Q., Zhang, W. et al. (2017). Bio-inspired bioactive glasses for efficient microRNA and drug delivery. *Journal of Materials Chemistry B* 5: 6376–6384.

86 Deepa, K. and Jaisankar, V. (2019). A facile synthesis and characterisation of novel mesoporous bioactive glass nanoparticles/xylitol based biodegradable polyester composites for in vitro degradation studies and anti-inflammatory activity. *Materials Today: Proceedings* 14: 461–470.

87 Wang, H., Chen, X., Wang, Y., and Cheng, D. (2013). Preparation and characterization of the system $SiO_2–CaO–P_2O_5$ bioactive glasses by microemulsion approach. *Journal of Wuhan University of Technology Materials Science Edition* 28: 1053–1057.

88 Brunner, T.J., Grass, R.N., and Stark, W.J. (2006). Glass and bioglass nanopowders by flame synthesis. *Chemical Communications* 7 (13): 1384–1386.

89 Mohn, D., Zehnder, M., Imfeld, T., and Stark, W.J. (2010). Radio-opaque nanosized bioactive glass for potential root canal application: evaluation of radiopacity, bioactivity and alkaline capacity. *International Endodontic Journal* 43: 210–217.

90 Vollenweider, M., Brunner, T.J., Knecht, S. et al. (2007). Remineralization of human dentin using ultrafine bioactive glass particles. *Acta Biomaterialia* 3: 936–943.

91 Shih, S.-J., Chou, Y.-J., and Chien, I.C. (2012). One-step synthesis of bioactive glass by spray pyrolysis. *Journal of Nanoparticle Research* 14: 1299.

92 Strobel, L.A., Hild, N., Mohn, D. et al. (2013). Novel strontium-doped bioactive glass nanoparticles enhance proliferation and osteogenic differentiation of human bone marrow stromal cells. *Journal of Nanoparticle Research* 15: 1780.

93 Mačković, M., Hoppe, A., Detsch, R. et al. (2012). Bioactive glass (type 45S5) nanoparticles: in vitro reactivity on nanoscale and biocompatibility. *Journal of Nanoparticle Research* 14: 1–22.

94 Ciriminna, R., Fidalgo, A., Pandarus, V. et al. (2013). The sol–gel route to advanced silica-based materials and recent applications. *Chemical Reviews* 113: 6592–6620.

95 Owens, G.J., Singh, R.K., Foroutan, F. et al. (2016). Sol–gel based materials for biomedical applications. *Progress in Materials Science* 77: 1–79.

96 Danks, A.E., Hall, S.R., and Schnepp, Z. (2016). The evolution of 'sol–gel' chemistry as a technique for materials synthesis. *Materials Horizons* 3: 91–112.

97 Baino, F., Fiume, E., Miola, M., and Verné, E. (2018). Bioactive sol–gel glasses: processing, properties, and applications. *International Journal of Applied Ceramic Technology* 15: 841–860.

98 Migneco, C., Fiume, E., Verné, E., and Baino, F. (2020). A guided walk through the world of mesoporous bioactive glasses (MBGs): fundamentals, processing, and applications. *Nanomaterials* 10: 2571.

99 Schumacher, M., Habibovic, P., and van Rijt, S. (2021). Mesoporous bioactive glass composition effects on degradation and bioactivity. *Bioactive Materials* 6: 1921–1931.

100 Kumar, A., Murugavel, S., Aditya, A., and Boccaccini, A.R. (2017). Mesoporous 45S5 bioactive glass: synthesis, in vitro dissolution and biomineralization behavior. *Journal of Materials Chemistry B* 5: 8786–8798.

101 Yan, X.X., Deng, H.X., Huang, X.H. et al. (2005). Mesoporous bioactive glasses. I. Synthesis and structural characterization. *Journal of Non-Crystalline Solids* 351: 3209–3217.

102 Lin, W.W., Fang, W., Chen, I.H. et al. (2018). Fabrication of mesoporous bioactive glass nanoparticles by sol–gel method. *Key Engineering Materials* 765: 136–139.

103 Wang, S., Gao, X., Gong, W. et al. (2014). Odontogenic differentiation and dentin formation of dental pulp cells under nanobioactive glass induction. *Acta Biomaterialia* 10: 2792–2803.

104 Xia, W. and Chang, J. (2007). Preparation and characterization of nano-bioactive-glasses (NBG) by a quick alkali-mediated sol–gel method. *Materials Letters* 61: 3251–3253.

105 Yun, H.-s., Kim, S.-h., Lee, S., and Song, I.-h. (2010). Synthesis of high surface area mesoporous bioactive glass nanospheres. *Materials Letters* 64: 1850–1853.

106 Prabhu, M., Kavitha, K., Manivasakan, P. et al. (2013). Synthesis, characterization and biological response of magnesium-substituted nanobioactive glass particles for biomedical applications. *Ceramics International* 39: 1683–1694.

107 Zhao, T., Elzatahry, A., Li, X., and Zhao, D. (2019). Single-micelle-directed synthesis of mesoporous materials. *Nature Reviews Materials* 4: 775–791.

108 Wan, Y. and Zhao, D. (2007). On the controllable soft-templating approach to mesoporous silicates. *Chemical Reviews* 107: 2821–2860.

109 Peng, T.-Y., Tsai, P.-Y., Chen, M.-S. et al. (2021). Mesoporous properties of bioactive glass synthesized by spray pyrolysis with various polyethylene glycol and acid additions. *Polymers* 13: 618.

110 Luz, G.M. and Mano, J.F. (2013). Nanoengineering of bioactive glasses: hollow and dense nanospheres. *Journal of Nanoparticle Research* 15: 1457.

111 Li, Y., Chen, X., Ning, C. et al. (2015). Facile synthesis of mesoporous bioactive glasses with controlled shapes. *Materials Letters* 161: 605–608.

112 Yoon, J.-Y., Kim, J.-J., El-Fiqi, A. et al. (2017). Ultrahigh protein adsorption capacity and sustained release of nanocomposite scaffolds: implication for growth factor delivery systems. *RSC Advances* 7: 16453–16459.

113 Zheng, K., Torre, E., Bari, A. et al. (2020). Antioxidant mesoporous Ce-doped bioactive glass nanoparticles with anti-inflammatory and pro-osteogenic activities. *Materials Today Bio* 5: 100041.

114 Hinman, J.J. and Suslick, K.S. (2017). Nanostructured materials synthesis using ultrasound. *Topics in Current Chemistry* 375: 12.

115 Xu, H., Zeiger, B.W., and Suslick, K.S. (2013). Sonochemical synthesis of nanomaterials. *Chemical Society Reviews* 42: 2555–2567.

116 Bang, J.H. and Suslick, K.S. (2010). Applications of ultrasound to the synthesis of nanostructured materials. *Advanced Materials* 22: 1039–1059.

117 Hujjatul Islam, M., Paul, M.T.Y., Burheim, O.S., and Pollet, B.G. (2019). Recent developments in the sonoelectrochemical synthesis of nanomaterials. *Ultrasonics Sonochemistry* 59: 104711.

118 Pokhrel, N., Vabbina, P.K., and Pala, N. (2016). Sonochemistry: science and engineering. *Ultrasonics Sonochemistry* 29: 104–128.

119 El-Fiqi, A. and Bakry, M. (2020). Facile and rapid ultrasound-mediated synthesis of spherical mesoporous silica submicron particles with high surface area and worm-like mesoporosity. *Materials Letters* 281: 128620.

120 Shchukin, D., Radziuk, D., and Möhwald, H. (2010). Ultrasonic fabrication of metallic nanomaterials and nanoalloys. *Annual Review of Materials Research* 40: 345–362.

121 Suslick, K.S., Choe, S.-B., Cichowlas, A.A., and Grinstaff, M.W. (1991). Sonochemical synthesis of amorphous iron. *Nature* 353: 414–416.

122 Zhang, X., Zhao, H., Tao, X. et al. (2005). Sonochemical method for the preparation of ZnO nanorods and trigonal-shaped ultrafine particles. *Materials Letters* 59: 1745–1747.

123 Díez-García, M.I., Manzi-Orezzoli, V., Jankulovska, M. et al. (2015). Effects of ultrasound irradiation on the synthesis of metal oxide nanostructures. *Physics Procedia* 63: 85–90.

124 Ohayon, E. and Gedanken, A. (2010). The application of ultrasound radiation to the synthesis of nanocrystalline metal oxide in a non-aqueous solvent. *Ultrasonics Sonochemistry* 17: 173–178.

125 Gedanken, A. and Perelshtein, I. (2015). Power ultrasound for the production of nanomaterials. In: *Power Ultrasonics* (Chapter 18) (ed. J.A. Gallego-Juárez and K.F. Graff), 543–576. Oxford: Woodhead Publishing.

126 Sun, S., Wang, S., Wang, P. et al. (2015). Ultrasound assisted morphological control of mesoporous silica with improved lysozyme adsorption. *Ultrasonics Sonochemistry* 23: 21–25.

127 Run, M., Wu, S., and Wu, G.J.M. (2004). Ultrasonic synthesis of mesoporous molecular sieve. *Microporous and Mesoporous Materials* 74: 37–47.

128 Vetrivel, S., Chen, C.-T., and Kao, H.-M. (2010). The ultrafast sonochemical synthesis of mesoporous silica MCM-41. *New Journal of Chemistry* 34: 2109–2112.

129 Fan, J., Du, P., Wang, X. et al. (2018). Ultrasound-assisted synthesis of ordered mesoporous silica FDU-12 with a hollow structure. *New Journal of Chemistry* 42: 2381–2384.

130 Chareonpanich, M., Nanta-ngern, A., and Limtrakul, J. (2007). Short-period synthesis of ordered mesoporous silica SBA-15 using ultrasonic technique. *Materials Letters* 61: 5153–5156.

131 Jiang, S.-D., Tang, G., Bai, Z., and Pan, Y. (2019). Ultrasonic-assisted synthesis of hollow mesoporous silica as a toxic gases suppressant. *Materials Letters* 247: 139–142.

132 Naruphontjirakul, P., Greasley, S.L., Chen, S. et al. (2016). Monodispersed strontium containing bioactive glass nanoparticles and MC3T3-E1 cellular response. *Biomedical Glasses* 2: 72–81.

133 Ghimire, P.P. and Jaroniec, M. (2021). Renaissance of Stöber method for synthesis of colloidal particles: new developments and opportunities. *Journal of Colloid and Interface Science* 584: 838–865.

134 Saravanapavan, P., Jones, J.R., Pryce, R.S., and Hench, L.L. (2003). Bioactivity of gel–glass powders in the $CaO–SiO_2$ system: a comparison with ternary ($CaO–P_2O_5–SiO_2$) and quaternary glasses ($SiO_2–CaO–P_2O_5–Na_2O$). *Journal of Biomedical Materials Research Part A* 66A: 110–119.

135 El-Fiqi, A., Lee, J.H., Lee, E.-J., and Kim, H.-W. (2013). Collagen hydrogels incorporated with surface-aminated mesoporous nanobioactive glass: improvement of physicochemical stability and mechanical properties is effective for hard tissue engineering. *Acta Biomaterialia* 9: 9508–9521.

136 El-Fiqi, A., Kim, J.-H., and Kim, H.-W. (2015). Osteoinductive fibrous scaffolds of biopolymer/mesoporous bioactive glass nanocarriers with excellent bioactivity and long-term delivery of osteogenic drug. *ACS Applied Materials & Interfaces* 7: 1140–1152.

137 Kim, J.-J., El-Fiqi, A., and Kim, H.-W. (2017). Synergetic cues of bioactive nanoparticles and nanofibrous structure in bone scaffolds to stimulate osteogenesis and angiogenesis. *ACS Applied Materials & Interfaces* 9: 2059–2073.

138 Zhou, L., Fan, L., Zhang, F.-M. et al. (2021). Hybrid gelatin/oxidized chondroitin sulfate hydrogels incorporating bioactive glass nanoparticles with enhanced mechanical properties, mineralization, and osteogenic differentiation. *Bioactive Materials* 6: 890–904.

139 El-Fiqi, A. and Kim, H.-W. (2014). Mesoporous bioactive nanocarriers in electrospun biopolymer fibrous scaffolds designed for sequential drug delivery. *RSC Advances* 4: 4444–4452.

140 Xie, W., Fu, X., Tang, F. et al. (2019). Dose-dependent modulation effects of bioactive glass particles on macrophages and diabetic wound healing. *Journal of Materials Chemistry B* 7: 940–952.

141 Tsigkou, O., Labbaf, S., Stevens, M.M. et al. (2014). Monodispersed bioactive glass submicron particles and their effect on bone marrow and adipose tissue-derived stem cells. *Advanced Healthcare Materials* 3: 115–125.

142 Li, Y., Hu, Q., Miao, G. et al. (2016). Size-dependent mechanism of intracellular localization and cytotoxicity of mono-disperse spherical mesoporous nano- and micron-bioactive glass particles. *Journal of Biomedical Nanotechnology* 12: 863–877.

143 El-Fiqi, A., Buitrago, J.O., Yang, S.H., and Kim, H.-W. (2017). Biomimetically grown apatite spheres from aggregated bioglass nanoparticles with ultrahigh porosity and surface area imply potential drug delivery and cell engineering applications. *Acta Biomaterialia* 60: 38–49.

144 Erol-Taygun, M., Unalan, I., Idris, M.I.B. et al. (2019). Bioactive glass-polymer nanocomposites for bone tissue regeneration applicatıons: a review. *Advanced Engineering Materials* 21: 1900287.

145 Kong, C.H., Steffi, C., Shi, Z., and Wang, W. (2018). Development of mesoporous bioactive glass nanoparticles and its use in bone tissue engineering. *Journal of Biomedical Materials Research Part B* 106: 2878–2887.

146 Gantar, A., Drnovšek, N., Casuso, P. et al. (2016). Injectable and self-healing dynamic hydrogel containing bioactive glass nanoparticles as a potential biomaterial for bone regeneration. *RSC Advances* 6: 69156–69166.

147 El-Fiqi, A., Kim, J.-H., Perez, R.A., and Kim, H.-W. (2015). Novel bioactive nanocomposite cement formulations with potential properties: incorporation of the nanoparticle form of mesoporous bioactive glass into calcium phosphate cements. *Journal of Materials Chemistry B* 3: 1321–1334.

148 Olmos Buitrago, J., Perez, R.A., El-Fiqi, A. et al. (2015). Core–shell fibrous stem cell carriers incorporating osteogenic nanoparticulate cues for bone tissue engineering. *Acta Biomaterialia* 28: 183–192.

149 Lee, J.H., El-Fiqi, A., Han, C.-M., and Kim, H.-W. (2015). Physically-strengthened collagen bioactive nanocomposite gels for bone: a feasibility study. *Tissue Engineering and Regenerative Medicine* 12: 90–97.

150 Park, J.-H., Kim, M.-K., El-Fiqi, A. et al. (2014). Bioactive and porous-structured nanocomposite microspheres effective for cell delivery: a feasibility study for bone tissue engineering. *RSC Advances* 4: 29062–29071.

151 Lin, C., Mao, C., Zhang, J. et al. (2012). Healing effect of bioactive glass ointment on full-thickness skin wounds. *Biomedical Materials* 7 (4): 045017.

152 Li, Y., Xu, T., Tu, Z. et al. (2020). Bioactive antibacterial silica-based nanocomposites hydrogel scaffolds with high angiogenesis for promoting diabetic wound healing and skin repair. *Theranostics* 10: 4929–4943.

153 Hu, M., Fang, J., Zhang, Y. et al. (2020). Design and evaluation a kind of functional biomaterial for bone tissue engineering: selenium/mesoporous bioactive glass nanospheres. *Journal of Colloid and Interface Science* 579: 654–666.

154 Pontremoli, C., Izquierdo-Barba, I., Montalbano, G. et al. (2020). Strontium-releasing mesoporous bioactive glasses with anti-adhesive zwitterionic surface as advanced biomaterials for bone tissue regeneration. *Journal of Colloid and Interface Science* 563: 92–103.

155 Wang, L., Yan, J., Hu, X. et al. (2020). Effect of nanoscale bioactive glass with radial spherical particles on osteogenic differentiation of rat bone marrow mesenchymal stem cells. *Journal of Materials Science – Materials in Medicine* 31: 29.

156 El-Fiqi, A. and Kim, H.-W. (2015). Nano/micro-structured poly(ε-caprolactone)/gelatin nanofibers with biomimetically-grown hydroxyapatite spherules: high protein adsorption, controlled protein delivery and sustained bioactive ions release designed as a multifunctional bone regenerative membrane. *Ceramics International* 29 (7): 954–964.

157 Zhang, J., Park, Y.-D., Bae, W.-J. et al. (2014). Effects of bioactive cements incorporating zinc-bioglass nanoparticles on odontogenic and angiogenic potential of human dental pulp cells. *Journal of Biomaterials Applications* 29: 954–964.

158 Lee, S.I., Lee, E.S., El-Fiqi, A. et al. (2016). Stimulation of odontogenesis and angiogenesis via bioactive nanocomposite calcium phosphate cements through integrin and VEGF signaling pathways. *Journal of Biomedical Nanotechnology* 12: 1048–1062.

159 Lim, H.-C., Nam, O.H., Kim, M.-J. et al. (2016). Delivery of dexamethasone from bioactive nanofiber matrices stimulates odontogenesis of human dental pulp cells through integrin/BMP/mTOR signaling pathways. *International Journal of Nanomedicine* 11: 2557–2567.

160 Jun, S.-K., Yang, S.-A., Kim, Y.-J. et al. (2018). Multi-functional nano-adhesive releasing therapeutic ions for MMP-deactivation and remineralization. *Scientific Reports* 8: 5663.

161 Mandakhbayar, N., El-Fiqi, A., Lee, J.-H., and Kim, H.-W. (2019). Evaluation of strontium-doped nanobioactive glass cement for dentin–pulp complex regeneration therapy. *ACS Biomaterials Science & Engineering* 5: 6117–6126.

162 Lee, J.-H., Kang, M.-S., Mahapatra, C., and Kim, H.-W. (2016). Effect of aminated mesoporous bioactive glass nanoparticles on the differentiation of dental pulp stem cells. *PLoS One* 11: e0150727.

163 Wang, S., Huang, G., and Dong, Y. (2020). Directional migration and odontogenic differentiation of bone marrow stem cells induced by dentin coated with nanobioactive glass. *Journal of Endodontics* 46: 216–223.

164 Moonesi Rad, R., Alshemary, A.Z., Evis, Z. et al. (2018). Structural and biological assessment of boron doped bioactive glass nanoparticles for dental tissue applications. *Ceramics International* 44: 9854–9864.

165 Huang, W., Yang, J., Feng, Q. et al. (2020). Mesoporous bioactive glass nanoparticles promote odontogenesis and neutralize pathophysiological acidic pH. *Frontiers in Materials* 7: 241. https://doi.org/10.3389/fmats.2020.00241.

166 Chen, Q., Wu, J., Liu, Y. et al. (2019). Electrospun chitosan/PVA/bioglass nanofibrous membrane with spatially designed structure for accelerating chronic wound healing. *Materials Science and Engineering C* 105: 110083.

167 Zheng, K., Balasubramanian, P., Paterson, T.E. et al. (2019). Ag modified mesoporous bioactive glass nanoparticles for enhanced antibacterial activity in 3D infected skin model. *Materials Science and Engineering C* 103: 109764.

168 Zhu, J., Jiang, G., Song, G. et al. (2019). Incorporation of ZnO/bioactive glass nanoparticles into alginate/chitosan composite hydrogels for wound closure. *ACS Applied Bio Materials* 2: 5042–5052.

169 Paterson, T.E., Bari, A., Bullock, A.J. et al. (2020). Multifunctional copper-containing mesoporous glass nanoparticles as antibacterial and proangiogenic agents for chronic wounds. *Frontiers in Bioengineering and Biotechnology* 8: 246.

170 El-Kady, A.M., Ali, A.A., and El-Fiqi, A. (2020). Controlled delivery of therapeutic ions and antibiotic drug of novel alginate-agarose matrix incorporating selenium-modified borosilicate glass designed for chronic wound healing. *Journal of Non-Crystalline Solids* 534: 119889.

171 Kargozar, S., Mozafari, M., Hamzehlou, S., and Baino, F. (2019). Using bioactive glasses in the management of burns. *Frontiers in Bioengineering and Biotechnology* 7: 62.

172 Zhang, P., Jiang, Y., Liu, D. et al. (2020). A bioglass sustained-release scaffold with ECM-like structure for enhanced diabetic wound healing. *Future Medicine* 15: 2241–2253.

173 Gao, W., Jin, W., Li, Y. et al. (2017). A highly bioactive bone extracellular matrix-biomimetic nanofibrous system with rapid angiogenesis promotes diabetic wound healing. *Journal of Materials Chemistry B* 5: 7285–7296.

174 Wang, C., Wang, Q., Gao, W. et al. (2018). Highly efficient local delivery of endothelial progenitor cells significantly potentiates angiogenesis and full-thickness wound healing. *Acta Biomaterialia* 69: 156–169.

175 Miguez-Pacheco, V., Hench, L.L., and Boccaccini, A.R. (2015). Bioactive glasses beyond bone and teeth: emerging applications in contact with soft tissues. *Acta Biomaterialia* 13: 1–15.

176 Osmani, R.A.M., Singh, E., Jadhav, K. et al. (2021). Biopolymers and biocomposites: nature's tools for wound healing and tissue engineering. In: *Applications of Advanced Green Materials* (Chapter 23) (ed. S. Ahmed), 573–630. Woodhead Publishing.

177 Kang, M.S., Kim, J.-H., Singh, R.K. et al. (2015). Therapeutic-designed electrospun bone scaffolds: mesoporous bioactive nanocarriers in hollow fiber composites to sequentially deliver dual growth factors. *Acta Biomaterialia* 16: 103–116.

178 Nawaz, Q., Fuentes-Chandía, M., Tharmalingam, V. et al. (2020). Silibinin releasing mesoporous bioactive glass nanoparticles with potential for breast cancer therapy. *Ceramics International* 46: 29111–29119.

179 Das, M.P., Pandey, G., Neppolian, B., and Das, J. (2021). Design of poly-L-glutamic acid embedded mesoporous bioactive glass nanospheres for pH-stimulated chemotherapeutic drug delivery and antibacterial susceptibility. *Colloids and Surfaces B: Biointerfaces* 202: 111700.

180 Sui, B., Zhong, G., and Sun, J. (2016). Drug-loadable mesoporous bioactive glass nanospheres: biodistribution, clearance, BRL cellular location and systemic risk assessment via ^{45}Ca labelling and histological analysis. *Scientific Reports* 6: 33443.

181 Wang, Y., Pan, H., and Chen, X. (2019). The preparation of hollow mesoporous bioglass nanoparticles with excellent drug delivery capacity for bone tissue regeneration. *Frontiers in Chemistry* 7: 283.

182 Wu, J., Zheng, K., Huang, X. et al. (2019). Thermally triggered injectable chitosan/silk fibroin/bioactive glass nanoparticle hydrogels for in-situ bone formation in rat calvarial bone defects. *Acta Biomaterialia* 91: 60–71.

183 Valanezhad, A., Odatsu, T., Udoh, K. et al. (2015). Modification of resin modified glass ionomer cement by addition of bioactive glass nanoparticles. *Journal of Materials Science – Materials in Medicine* 27: 3.

184 Choi, Y., Sun, W., Kim, Y. et al. (2020). Effects of Zn-doped mesoporous bioactive glass nanoparticles in etch-and-rinse adhesive on the microtensile bond strength. *Nanomaterials (Basel)* 10: 1943.

185 Nam, H.-J., Kim, Y.-M., Kwon, Y.H. et al. (2019). Fluorinated bioactive glass nanoparticles: enamel demineralization prevention and antibacterial effect of orthodontic bonding resin. *Materials (Basel)* 12: 1813.

186 Park, S.Y., Yoo, K.-H., Yoon, S.-Y. et al. (2020). Synergetic effect of 2-methacryloyloxyethyl phosphorylcholine and mesoporous bioactive glass nanoparticles on antibacterial and anti-demineralisation properties in orthodontic bonding agents. *Nanomaterials (Basel)* 10: 1282.

187 Odermatt, R., Par, M., Mohn, D. et al. (2020). Bioactivity and physico-chemical properties of dental composites functionalized with nano- vs. micro-sized bioactive glass. *Journal of Clinical Medicine* 9: 772.

188 Bae, J., Son, W.-S., Yoo, K.-H. et al. (2019). Effects of poly(amidoamine) dendrimer-coated mesoporous bioactive glass nanoparticles on dentin remineralization. *Nanomaterials* 9: 591.

189 Corral Nuñez, C., Covarrubias, C., Fernandez, E., and Oliveira, O.B.D. Jr., (2017). Enhanced bioactive properties of Biodentine™ modified with bioactive glass nanoparticles. *Journal of Applied Oral Science* 25: 177–185.

190 Moonesi Rad, R., Pazarçeviren, E., Ece Akgün, E. et al. (2018). In vitro performance of a nanobiocomposite scaffold containing boron-modified bioactive glass nanoparticles for dentin regeneration. *Journal of Biomaterials Applications* 33: 834–853.

191 Son, S.-A., Kim, D.-H., Yoo, K.-H. et al. (2020). Mesoporous bioactive glass combined with graphene oxide quantum dot as a new material for a new treatment option for dentin hypersensitivity. *Nanomaterials (Basel)* 10: 621.

192 Camargos Lins, C.E., de Carvalho, S.M., de Oliveira, A.A.R., and de Magalhães Pereira, M. (2016). Application of fluorine containing bioactive glass nanoparticles in dentin hypersensitivity treatment. *Key Engineering Materials* 696: 103–107.

193 Choi, Y.-J., Bae, M.-K., Kim, Y.-I. et al. (2020). Effects of microsurface structure of bioactive nanoparticles on dentinal tubules as a dentin desensitizer. *PLoS One* 15: e0237726.

194 Song, H.-K., Yoo, K.-H., Yoon, S.-Y. et al. (2019). In vitro effect of gallium-doped bioactive glass on enamel anti-demineralization and bond strength of orthodontic resins. *Applied Sciences* 9: 4918.

195 Farooq, I., Majeed, A., Al Shwaimi, E., and Almas, K. (2019). Efficacy of a novel fluoride containing bioactive glass based dentifrice in remineralizing artificially induced demineralization in human enamel. *Fluoride* 52: 447–455.

196 Carvalho, S.M., Moreira, C.D.F., Oliveira, A.C.X. et al. (2019). Bioactive glass nanoparticles for periodontal regeneration and applications in dentistry. In: *Nanobiomaterials in Clinical Dentistry* (Chapter 15), 2e (ed. K. Subramani and W. Ahmed), 351–383. Elsevier.

197 Moonesi Rad, R., Atila, D., Evis, Z. et al. (2019). Development of a novel functionally graded membrane containing boron-modified bioactive glass nanoparticles for guided bone regeneration. *Journal of Tissue Engineering and Regenerative Medicine* 13: 1331–1345.

198 Mota, J., Yu, N., Caridade, S.G. et al. (2012). Chitosan/bioactive glass nanoparticle composite membranes for periodontal regeneration. *Acta Biomaterialia* 8: 4173–4180.

199 Chen, Y.-H., Rao, Z.-F., Liu, Y.-J. et al. (2021). Multifunctional injectable hydrogel loaded with cerium-containing bioactive glass nanoparticles for diabetic wound healing. *Biomolecules* 11: 702.

200 Dashnyam, K., El-Fiqi, A., Buitrago, J.O. et al. (2017). A mini review focused on the proangiogenic role of silicate ions released from silicon-containing biomaterials. *Journal of Tissue Engineering* 8: 2041731417707339.

10

Tailoring the Osteogenic Properties of Bioactive Glasses by Incorporation of Therapeutic Ions for Orthopedic Applications

Sebastian Wilkesmann and Fabian Westhauser

Orthopedic University Hospital, Heidelberg, Germany

10.1 Introduction

Biomaterials have gained an important role in bone tissue engineering (BTE). As well-coordinated interplay of multiple factors such as cells, growth factors, and remaining tissue is needed, bone tissue regeneration remains a demanding challenge. To successfully tackle this challenge biomaterials should ideally supply mechanical support, as well as they should exhibit osteoregenerative properties. These can be subdivided further into: osteoconduction, osteoinduction, and osteogenesis [1]. Osteogenic cells in general should be able to attach to the material, thus, the surface of the material must be biocompatible and allow the osteogenic precursor cells to grow and to differentiate and eventually to build new bone – this property is described as the "osteoconductivity" of the material [2]. Osteoinduction is provided if pluripotent undifferentiated precursor cells are driven into osteogenic differentiation in presence of the used graft [3]. New bone formation caused by differentiated cells originating from either graft or host is referred to as osteogenesis [4].

Biomaterials should ideally stimulate precursor cells toward differentiation, e.g. by the release of therapeutic ions. Starting in 2001 with the evaluation of the gene-profiles of human osteoblasts that have been treated with the ionic dissolution product of 45S5-bioactive glass (BG – composition in wt%: 45SiO_2, 24.5CaO, 24.5Na_2O, and 6.0P_2O_5) by Xynos et al., biodegradable bioactive glasses (BGs) have not only been proven to bond to bone or soft tissue due to their excellent bioactivity but also to effectively influence bone tissue regeneration by stimulating cells due to their supply of ionic dissolution products [5]. Therefore, they fulfill all mentioned requirements to be given the designation of being osteoregenerative. This inherent ability to guide surrounding cells into a "path of regeneration and self-repair," so-called by Hench [6], by modulating the differentiation of osteoblast precursor or other cells related to bone defect healing makes BGs unique, promising, and very attractive bone substitute materials. In the beginning, research focused on enhancing the inherent osteogenic properties to eventually improve bone tissue regeneration. Subsequently, angiogenic, anti-inflammatory, antibacterial, or even anticancerogenic properties were described adding further possible therapeutic options for the usage of BGs in various therapeutic scenarios [7].

Besides the initial 45S5-BG composition, multiple other BGs of varying compositions produced via different manufacturing processes (melt–quench or sol–gel method) were shown to exhibit

Bioactive Glasses and Glass-Ceramics: Fundamentals and Applications, First Edition.
Edited by Francesco Baino and Saeid Kargozar.

beneficial properties on bone healing [6, 8]. Moreover, BGs can act as vectors for the local application of various therapeutic agents adding further options for the applications of BGs. These agents can be delivered locally to guide bone tissue regeneration in the desired direction with minimized risk of adverse effects that might be caused if applied systemically [6]. Candidate substances are, for example antibiotics like gentamicine or other small molecules such as anti-inflammatory drugs like dexamethasone [9, 10]. Even proteins like vascular endothelial growth factor (VEGF) have been successfully loaded into the pores of mesoporous BGs produced by the sol–gel method [11]. Besides that, there is also the possibility of implementing therapeutically active ions directly in the amorphous BG-structure [12]. Especially, these therapeutic ions have gained growing interest of the BG-community lately as they are not only resistant to heat occurring during the BG fabrication process but also therapeutically and cost-effective [13]. Due to their rapid diffusion through cell membranes after being released from the glass network, metallic ions can influence multiple cellular processes. The so reached therapeutic effects can be of various types such as osteogenic, angiogenic, antibacterial, etc. (Figure 10.1). Furthermore, doping BGs with therapeutically active ions can be performed using all common BG fabrication methods such as the melt and quench, sol–gel, or ion-exchange technique and has therefore been performed and investigated extensively [14].

In this chapter, the biological effects of ions derived from dissolution products of various BG compositions are summarized in order to give an idea of how the biological and therefore therapeutic effects of BGs can be tailored by supplementing them with distinct ions.

Many of the below-mentioned therapeutically active ions can be cytotoxic when applied in high concentrations. Considering this fact, BGs offer themselves as attractive vector as the doping amount and ion release kinetics of the BGs can be modified by altering the BG fabrication process and type of application [14]. The aim is to supply ions locally and continuously in concentrations that show the most desired biological effect without being cytotoxic.

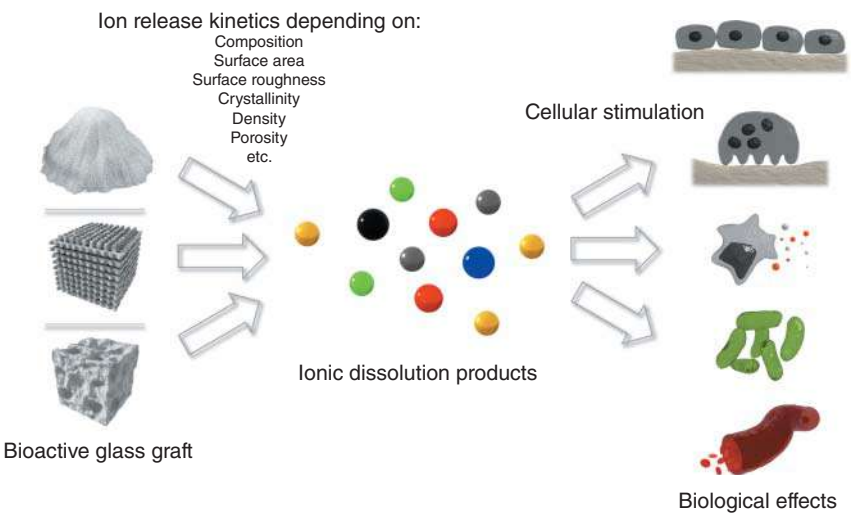

Figure 10.1 BG grafts release ionic dissolution products in a physiological environment. The concentration of the released ions depends on various factors that can be adjusted during the BG fabrication process, such as the graft's composition, surface area, porosity, crystallinity, or many more. Surrounding cells being involved in bone tissue regeneration are stimulated by the released ions. In this way, various biological effects, that can be tailored by altering the BGs release kinetics and composition are achieved.

However, practical implementation of this knowledge is still challenging. For example, there is evidence for better osteogenic or angiogenic properties for manganese (Mn) or cobalt (Co) doped BGs compared to undoped BGs. But the desired stimulating influences are still connected to cytotoxic effects of the dopant ion [15, 16]. This should be kept in mind when the published biological effects of a selection of common and promising candidate ions in the following are interpreted.

10.2 Ions Derived from Common Silicate-Based BGs

10.2.1 Calcium (Ca)

Starting with the ionic dissolution products of common silicate-based BG-compositions, calcium (Ca) ions show an enormous number of roles in many processes widely distributed in the human body – not only restricted to bone metabolism. Ca takes great part as second messenger in intracellular signaling in almost any human cell [17]. Processes like osteogenic differentiation and osteoclast cell function are included making it important to maintain balanced Ca homeostasis for bone tissue regeneration [18, 19]. However, most of the Ca in the human body is stored extracellular in the inorganic phase of bone providing structural stability in form of hydroxyapatite (HA), where it can be released and deposited if needed [20].

Keeping this major role in bone metabolism in mind, Ca also has cellular effects on osteoblast progenitor cells enhancing osteogenic differentiation. Moderate extracellular calcium levels are proposed to be most beneficial for bone tissue regeneration and different molecular mechanisms are postulated for the osteogenic impact of Ca. On the one hand, fluid shear mediated activation of extracellular signal-regulated kinases 1/2 (ERK1/2) and formation of nitric oxide, which is both essential to osteoblast function and proliferation was found to be dependent on the influx of extracellular Ca [19, 21]. There is further evidence that high extracellular calcium levels increase osteoblast survival via the calcium sensing receptor (CaSR) and downstream signaling cascades [22]. On the other hand, receptor activator of NF-κB ligand (RANKL)-induced increase of intracellular Ca impacts cell motility and bone-resorbing activity of mature osteoclasts [23]. It might even cause osteoclast apoptosis by activation of the CaSR, which is also expressed on osteoclasts [22].

Matching results were found when the osteogenic properties of Ca releasing biomaterials were evaluated. For example, MG-63, known as osteoblast like cell line, showed better adhesion, proliferation, and osteogenic differentiation on Ca supplemented TiO_2 nanotubes compared to untreated ones [24]. When 70S30C sol–gel derived BG scaffolds made of 70 mol% of silicon dioxide (SiO_2) and 30 mol% of calcium oxide (CaO), thus only releasing Ca an Si ions (biological properties discussed below), were exposed to human osteoblasts, formation of mineralized bone nodules was found without the supplementation of additional growth factors [25]. Also, *in vivo* projects investigating composite HA/tricalcium phosphate (TCP) scaffolds showed promising results, with more mature bone formed compared to HA-only scaffolds [26].

10.2.2 Silicon (Si)

Silicon (Si) being another fundamental component of silicate-BGs also takes part in bone metabolism and formation when released as BG dissolution product. Dietary supply of Si was found to be essential for skeleton development and beneficial for the bone mineral density of men and premenopausal women [27, 28].

However, the molecular mechanisms behind Si's osteogenic properties are not entirely understood. In general, Si is known to promote HA precipitation and is elevated during early bone calcification. In *in vitro* studies, multiple positive effects on osteoblasts and osteoblast precursor cells are published for Si. Si was found to stimulate collagen type 1 (COL1) synthesis in MG-63 and primary osteoblasts in the form of orthosilicate acid ($Si(OH)_4$) and shifts the osteoprotegerin (OPG)/RANKL balance toward OPG in Saos-2 cells [29, 30]. Also, *in vivo* studies showed promising effects with increased bone mineral density in rats under oral Si supplementation [31]. When the impact of dissolution products of β-TCP and β-calcium silicate/poly-D,L-lactide-glycolide (PDLGA) scaffolds, that mainly differ in their Si content, are compared, advantages in osteogenic and angiogenic properties are found in the Si-containing β-calcium silicate/PDLGA. More precisely, human umbilical vein endothelial cells showed higher proliferation and VEGF secretion, rat bone mesenchymal stromal cells (BMSCs) increased their expression of osteogenic marker genes like runt-related transcription factor 2 (RUNX2) or osteocalcin (OCN), and more new bone was formed in four weeks after scaffold implantation in critical size bone defects of rabbit femurs [32]. Additionally, Si shows negative effects on bone resorption *in vitro* by interfering in various important signaling pathways in osteoclast formation [33].

Besides the mentioned published data concerning the effect of Si alone, there is much more evidence on the osteogenic properties of the dissolution products of silicate-based BGs [34–36]. Here, Si cannot be made responsible for the BGs biological impact alone, as there are other ions released as well. But as one of the main released agents and seen in combination with the abovementioned findings, Si seems to exhibit promising osteogenic properties.

10.2.3 Phosphorus (P)

Phosphorus, usually found as phosphate (PO_4^{3-}; Pi) in body fluids, is another common mineral in the human body that participates in the amorphous glass structure of silicate-based BGs. As one of the most prevalent minerals in the human body, Pi takes part in many different processes such as cellular signaling, energy metabolism, or acid–base homeostasis [37]. Together with Ca, it forms HA in the inorganic phase of bone and is therefore a relevant part of extracellular matrix (ECM) mineralization. Additionally, extracellular Pi works as cellular signaling molecule affecting a variety of cells including osteoblasts, osteoblast precursor cells, and osteoclasts. Via the ERK1/2 and cyclic adenosine monophosphate (cAMP) protein kinase a pathways Pi is capable of increasing the bone morphogenic protein 2 (BMP 2) expression in dental pulp stem cells [38]. Due to negative feedback, Pi inhibits osteoclast activity and therefore bone resorption via the receptor activator of NF-κB (RANK)-RANKL pathway [39]. In hypophosphatemic dentin matrix acidic phosphoprotein 1 (DMP 1) null mice, reduced osteoclast numbers and impaired bone remodeling connected to an imbalance of RANKL to OPG was found [40]. Moreover, bisphosphonates, which represent structural analogs of the dimeric pyrophosphate (PPi), are commonly used in the therapy of osteoporosis as they cause apoptosis in osteoclasts and decrease bone resorption directly by inhibition of the HA breakdown. Furthermore, bisphosphonates inhibit calcification of HA [41]. This inhibition of HA-calcification is physiologically controlled by the tissue nonspecific alkaline phosphatase (ALP). Mediated by the hydrolyzation of PPi, this enzyme is responsible for the Pi to PPi ratio and is adjusted continuously [42].

Apart from the already mentioned publications in the introduction and the recent ones evaluating the influence of single ions, there is much more evidence of the biological effect of the dissolution products released by silicate-based BGs. 45S5-BG, S53P4-BG (composition in mol%: $53.85SiO_2$, $21.77CaO$, $1.72P_2O_5$, $22.66Na_2O$), 58S-BG (composition in mol%: $58SiO_2$, $36CaO$,

$6P_2O_5$), or 70S30C-BG (composition in mol%: 70SiO_2, 30CaO) are common examples [6, 43–45]. Here, no single ion can be identified as the main osteogenic agent, but the combination of Si, Ca, and Pi has been proven to be capable of enhancing osteogenic differentiation. This fact is important to be kept in mind if BGs are supplemented with other therapeutically active ions like the ones mentioned below that may alter the release kinetics of Si, Ca, and P. Possible effects on cells might either be caused by the presence of the supplemented ion or the modulated release kinetics of the dissolution products of the original BG-composition.

10.3 Ions Derived from BGs Supplemented with Further Therapeutically Active Ions

Besides enhancing the inherent osteogenic effects of the common BG dissolution products, there are more reasons to supplement BGs with therapeutic ions. Adding angiogenic, anti-inflammatory, antibacterial, or even anticancerogenic properties by supplementing specific ions is another promising way to reach the goal of successful bone tissue regeneration or – generally spoken – to tailor the properties of the BGs toward individual requirements. Among the available studies, usually essential or nonessential trace elements that are known to have an impact on bone metabolism are investigated. Strong hints on possible beneficial effects of a candidate ion to be applied as part of BGs would be if deficiency of the specific ion causes an impact on bone or skeleton formation or systemic application of the specific ion is already a therapeutic option for a bone metabolism-related disease. In the next step, an essential requirement for the usage of the distinct therapeutically active ion must be evaluated. The supplementation of the candidate ion must not affect the unique bioactive properties of BGs. The fundamental beneficial properties of BGs would be lost if bonding to bone and soft tissue by forming an HA layer upon contact with a physiological environment was impaired by the implementation of the dopant ion in the glass network. A selection of successfully supplemented ions that do not impair these important properties and their distinct therapeutic effect is presented in the following in alphabetical order.

10.3.1 Boron (B)

Like many of the selected ions, the nonmetallic dietary trace element boron (B) has various tasks in different compartments in the human body. Besides being involved in the metabolism of steroid hormones, it is known to influence calcium, magnesium, and vitamin D homeostasis [46]. Due to these facts and as dietary deficiency of B in rats caused impaired bone repair, trabecular thickness, and total bone volume, it is very likely to be essentially involved in bone metabolism [47]. Additionally, B also seems to influence the bodies' response on infection and injuries and might have an impact on brain function, at least in rats [48].

The *in vitro* application of B to MC3T3-E1 cells resulted in increased bone morphogenic protein (BMP) expression, pointing out its osteogenic potential [13]. As a component of BGs, boron has been investigated extensively. Compared to nonsupplemented BGs, B-doped BGs show faster formation of HA, which is linked to a rapid release of B to the local environment [49]. As high concentrations of above approximately 0.65 mM of B in cell culture medium limit cell proliferation, application of B is only reasonable in a rather small therapeutic window [48]. In this window, osteogenic and especially angiogenic effects of B have been discovered *in vitro* and *in vivo*. For example, B-containing mesoporous bioactive glass nanoparticle (MBGN) scaffolds were shown to enhance common osteogenic markers such as the α 1 type 1 collagen (COL1A1) or RUNX2 gene

expression in osteoblasts *in vitro* and borate glass discs composed of Na_2O, CaO, and B_2O_3 were found to induce ALP activity in human mesenchymal stromal cells (hMSCs) [10, 50].

In vivo, more bone tissue was formed after implantation of B-containing 45S5-BG in the medullary tibial compartment of Wistar rats compared to the conventional 45S5 composition [51]. Similar findings of higher bone formation were published when B-containing 13-93B3 BG was implanted in rat calvarial defects [52].

Concerning angiogenic properties, 0106-B1-BG (composition in wt%: $37.5SiO_2$, 22.6CaO, $5.9Na_2O$, $4.0P_2O_5$, $12.0K_2O$, 5.5MgO, and $12.5B_2O_3$) could enhance the VEGF expression of mesenchymal stromal cells (MSCs) *in vitro* [53]. This finding was confirmed further in *in vivo* studies, as 0106-B1-BG scaffolds also led to increased ectopic formation of mature bone 10 weeks after subcutaneous implantation in immunodeficient mice compared to 45S5-BG scaffolds [54]. With this not being an individual case, other B-containing BG compositions like 13-93B3 (composition in wt%: $53B_2O_3$, $6Na_2O$, 20CaO, 5MgO, $12K_2O$, and $4P_2O_5$) were shown to have similar effects [55, 56]. These effects were found to be so strong that 13-93B3 fibers were compressed into a cotton-like morphology and used as dressings for cutaneous wounds in rats. Upon degradation of the fibers, HA microspheres with vessels attached to them were discovered. Even better angiogenic properties were shown when Cu (biological properties discussed below) was supplemented to the 13-933B fibers additionally [56].

10.3.2 Cerium (Ce)

One factor counteracting successful bone defect healing can be prolonged inflammation. This complex process mediated by various players can result in tissue damage due to inactivation of enzymes and protein degradation. Reactive oxygen species (ROS) play a main role in this process and are usually fought by antioxidant enzymes such as superoxide dismutase and catalase to maintain physiological processes [57]. Cerium can support the body's anti-inflammatory response as it can switch its oxidation state between Ce^{4+} and Ce^{3+} during redox reactions in physiological fluids. In this way, it can neutralize radicals like ROS that would otherwise counteract successful osteo- or angiogenesis during bone tissue regeneration [58].

For example, cerium nanoconjugates showed to trigger endothelial cell proliferation, increased hypoxia-inducible factor 1α (HIF-1α) expression, and induced growth of blood vessels in chick embryos [59]. Additionally, applying Ce oxide nanoparticles on titanium surfaces led to better osseointegration depending on the Ce^{4+}/Ce^{3+} ratio [60].

As conventional BGs usually do not provide extensive antioxidant properties, efforts have been made to supplement BGs with Ce. Ce-doped MBGNs showed to significantly decrease interleukin-1β (IL-1β) and IL-6 expression of murine macrophages upon exposure in *in vitro* experiments compared to undoped MBGNs. The same Ce-containing MBGN composition also led to decreased RANKL expression in Saos-2 osteoblast-like cells, whereas undoped MBGNs caused a significant increase in this *pro-osteoclastic* gene. However, other osteogenic marker genes such as OPG, COL1A1, or ALP were not positively influenced by these Ce-MBGNs [58].

10.3.3 Cobalt (Co)

In contrast to many other ions, the supplementation of cobalt (Co) is not performed out of osteogenic but angiogenic rationales. In fact, it has shown to inhibit osteoblast proliferation and ALP gene expression and furthermore was found to enhance osteoclastic differentiation

and function [61]. Besides being an essential part of Vitamin B12, Co is capable of supporting vascularization in bone tissue due to its "hypoxia-mimicking" properties, which results in induction of HIF-1α [62].

This hypothesis is supported by data from Co releasing BGs as increased synthesis of VEGF and HIF-1α-expression were found upon exposure of Co-supplemented mesoporous bioactive glass scaffolds to BMSC [63]. Despite its lack of osteogenic properties, Co-supplemented BGs showed further promising results *in vitro* and *in vivo* studies. A melt-derived Sr-Co-BG (composition in mol%: 41.2SiO_2, 5.06P_2O_5, 29.64CaO, 6SrO, 7.17Na_2O, 3.26MgO, 7.17K_2O, and 0.5CoO) showed good cytocompatibility, osteogenic as well as angiogenic properties and highest bone formation 12 weeks after implantation in tibial or femoral critical size defects in rabbits compared to BGs that were not supplemented or only supplemented with a single ion [64]. Therefore, Co remains a promising therapeutic ion as its angiogenic effects outweigh its possibly negative osteogenic impact. Especially, a combined supplementation of Co and other ions with pronounced osteogenic properties may be beneficial for successful bone tissue regeneration. Co could provide the required angiogenic environment to enhance the inherent or by further supplementation reinforced osteogenic properties of the respective BG.

10.3.4 Copper (Cu)

Copper (Cu) is linked to many enzymatic reactions performing electron-transfers involved in many metabolic processes of the human body. While the majority of Cu is found in the liver, Cu also affects bone formation and integrity [65]. Cu-depletion results in brittle bone structure and impaired mechanical strength most probably due to reduced collagen crosslinking as Cu is an essential cofactor for lysyl oxidase [66]. Like Co, Cu is known to inherit hypoxia mimicking properties that result in increased activation of HIF-1α, expression of VEGF or fibroblast growth factor 2 and proliferation of endothelial cells.

These findings were confirmed when BGs with Cu-supplementation were examined *in vitro* and *in vivo*. Rat calvaria defects filled with Cu-BG showed improved angiogenesis and osteogenesis compared to non-Cu-doped BGs. Additionally, also *in vitro* osteogenic effects like increased ALP activity of Mouse MC3T3-E1 osteoblasts of Cu have been described [67]. Again, like Co, Cu is a promising candidate for combined supplementation of trace elements in BGs to achieve synergistic effects with Cu providing the angiogenic environment for successful bone healing driven by the osteogenic properties of a potential additional therapeutically active ion.

Besides that, Cu can generate ROS. On the one hand, these ROS damage the cytoderm and DNA of bacteria; on the other hand, they can also be toxic to human tissue. Therefore, antibacterial effects of Cu-doped BGs were found but high concentrations of Cu might also do harm, as seen in damaged liver and neuronal tissue caused by exceeding exposure of Cu [66, 67].

10.3.5 Fluoride (F)

Fluoride (F) is mainly known for preventing dental caries by substituting hydroxide-sites in dental apatite resulting in increased acid resistance. Thus, controlled local release of F can have beneficial effects on dental health by enhancing enamel remineralization [68]. Additionally, F is also capable of influencing bone mineralization and formation and F-containing BGs can form fluorapatite which is more stable than HA [61, 69]. These properties make F-supplemented BGs interesting for dental or oral applications in particular.

Depending on its applied concentration, F showed osteogenic properties with elevation of the common osteogenic markers such as ALP activity, collagen synthesis, or RUNX2 expression upon F exposure of *in vitro* cultivated osteoblasts [70]. Some of these effects are most probably mediated by an increase of intracellular Ca. However, with exceeding concentrations of F impaired bone mineralization and suppressed osteoblast activity have been found [71].

Also, cytotoxic effects of F released by F-doped BGs on MG-63 cells have been published. F-doped BGs showed to inhibit the pentose phosphate pathway indicating significant oxidative stress caused by F [72]. Apparently, this F-mediated impact might also hit microbial cells. Antibacterial properties of F-supplemented BGs have been described [73].

10.3.6 Gallium (Ga)

Doping of BGs with gallium has multiple effects on the BGs biological properties that are not thoroughly understood yet. For over 20 years, Ga is used for the therapy of cancer-related hypercalcemia as it inhibits osteoclast activity and was found to be effective in Paget's disease [74, 75]. Later, this anti-bone-resorbing effect has been confirmed in *in vitro* studies using different osteoclastic cell models. It is important to mention in this context, that Ga was shown to have no negative impact on osteoblast function [76].

Matching results were found when a Ga-doped mesoporous BG was exposed to osteoblastic MC3T3-cells leading to increased ALP activity after seven days of direct *in vitro* culture. When the same BG was exposed to osteoclastic RAW 2647 cells tartrate-resistant acid phosphatase expression, a marker gene for osteoclastic differentiation, was inhibited [77]. These findings make Ga-supplemented BGs an attractive therapeutic option for bone regeneration after osteoporotic fractures.

However, there are even more beneficial biological effects of Ga-doped BGs related to bone tissue regeneration. Like Ce, Ag, or Cu, Ga has antibacterial properties and inhibits the growth of various bacterial stems. It shares chemical properties with Fe and therefore interferes with essential bacterial enzymes using Fe as cofactor [78]. Furthermore, results on Ga-doped BGs hemostatic properties have been published. Ga-BG/chitosan composite scaffolds led to reinforced platelet aggregation, whole blood clotting, and thrombus formation compared to solely chitosan samples [79]. These diverse biological effects make Ga a valuable option for doping BGs and should be investigated further in the future.

10.3.7 Iron (Fe)

Bone loss or bone defects can occur in different situations such as trauma, infection, or surgical cancer treatment. Especially in the last setting, bone substitute materials with magnetic properties are promising new therapeutic options being developed. By applying a magnetic field, these materials can be used to create hyperthermia in a locally controlled manner directly at the defect site where it is needed. With temperatures of 42–45 °C being reached, tumorous cells with impaired blood vessel formation and their distinct microenvironment with low pH value are severely damaged. On the contrary, surrounding physiological cells are harmed significantly less as a physiological blood vessel system supplies sufficient heat transfer [80]. Magnetic BGs can combine bioactive properties with a strong bond to hard and soft tissue at the defect site with the possibility to apply hyperthermia without displacement of the magnetic agents [81].

Magnetite (Fe_3O_4), a magnetic iron oxide, is one common but not the only example of various dopants supplemented in BGs for this purpose. A biphasic glass–glass ceramic with 15 wt% of

sol–gel-derived S58-BG (composition in mol%: 58SiO_2, 6P_2O_5, 36CaO) and 85 wt% of melt-derived BG (composition in mol%: 40SiO_2, 40CaO, 20Fe_2O_3) was shown to induce hyperthermia mediated apoptosis and reduced proliferation Saos2 osteosarcoma cells [82]. Other examples of possible ferrimagnetic dopants are barium ferrite ($BaFe_{12}O_{19}$), zinc ferrite ($ZnFe_2O_4$), or hematite (Fe_2O_3) [83–85].

10.3.8 Lithium (Li)

The administration of lithium (Li) as a drug is usually performed to treat psychological disorders. Interestingly, adverse effects on the patient's calcium homeostasis such as hypercalcemia and hyperparathyroidism can occur upon lithium treatment stating its influence on bone metabolism [67].

There is evidence for positive effects of oral Li treatment on bone mineral density and decreased risk of bone fracture during Li treatment [66]. The molecular mechanism behind that might be connected to inhibitory effects on glycogen synthase kinase-3 (GSK-3). Li replaces Mg as enzyme cofactor resulting in impaired enzyme function which leads to decreased inhibition of the Wnt/β-catenin pathway. Activation of the Wnt/β-catenin pathway results in osteoblast proliferation and activation and is also crucial in cartilage formation and homeostasis [86, 87]; therefore, Li inherits promising osteogenic properties. *In vitro* and *in vivo* projects confirmed these findings with Li applied locally. Upon Li impact, MSC were shown to increase proliferation and Li_2CO_3 doped alginate scaffolds led to accelerated bone regeneration in 14 days after implantation in tibial defects of rats [67].

There is limited knowledge on the biological properties of Li-supplemented BGs. Li-doped glass ceramics were shown to have good cytocompatibility and induced mineralized matrix formation detected by the Alizarin Red assay [88]. Besides that, positive effects of SiO_2–Li_2O sol–gel derived glass dissolution products on the chondrogenic differentiation of murine chondrogenic ATDC5 cells were found emphasizing further therapeutic options of Li [86].

Again, high concentrations of Li might have adverse effects. If Li is applied for the therapy of psychological disorders frequent monitoring of Li serum levels are indicated to avoid damage to kidney or central nervous tissue [89].

10.3.9 Magnesium (Mg)

About half of the human body's magnesium (Mg) can be found in bone tissue. It is an essential cofactor to many enzymes connected to the synthesis of organic structures and energy metabolism [90]. Besides that, Mg was shown to be relevant in bone metabolism as well. Mg-deficiency in rats and humans led to impaired bone formation due to decreased activity of parathyroid hormone and calcitriol and enhanced bone resorption caused by increased levels of tumor necrosis factor α (TNF-α) and RANKL [91]. *In vitro* studies evaluating the impact of Mg on osteoblast-like cells showed good osteogenic properties. With a most favorable concentration of 50 ppm of Mg, MC3T3 cells' expression of osteogenic marker genes and ALP activity was found to be enhanced [92]. Also, increased ECM mineralization, higher expression of osteogenic marker genes, and enhanced synthesis of VEGF were discovered upon stimulation of human BMSCs with Mg [93]. Furthermore, the suppressing effects of Mg on bone resorbing mechanisms were proven *in vitro*. Due to decreased nuclear factor-κB (NF-κB) activity, reduced RANKL expression and a smaller number of osteoclasts were found [94].

Taking the next step, *in vivo* evaluation of Mg releasing biomaterials showed beneficial results. Better osseointegration and osteoconductivity was found for coated titanium implants [95, 96].

Matching results concerning good osteoconductive effects were also shown for Mg-supplemented HA scaffolds [97]. Integrin-Mediation or increased calcitonin gene-related peptide (CGRP) production by local neurons leading to stimulation of cAMP responsive element binding protein 1 (CREB1) in periosteum derived stem cells are interesting suggested explanations of the mechanisms behind the biological properties of Mg [98, 99].

When added to BGs, Mg influences the BG degradation significantly as Mg—O bonds tend to be less strong than Si—O bonds. Therefore, Mg supplemented BGs show a faster dissolution rate than nonsupplemented BGs [100]. There is little evidence on the biological properties of Mg-doped BGs where the release of Mg can securely be made responsible for osteogenic effects. For example, BG mixed with TCP supplemented with a combination of Sr and Mg stimulated mouse calvaria-derived pre-osteoblastic MC3T3-E1 cells toward increased ALP activity and ECM formation and mineralization [101]. Another study showed good biocompatibility and an increase in ALP activity of rat osteoblasts for BGs belonging to the $CaO–MgO–SiO_2$ system [102]. However, these results should be handled with care as there was no non-Mg-releasing BG investigated serving as control. Additionally, there were contradictory findings with decreased OCN expression of MC3T3-cells upon exposure to conditioned media of Mg-supplemented BGs [103]. In conclusion, Mg-doped BGs should be investigated further as the promising osteogenic and angiogenic properties of Mg are not yet proven when applied as part of BGs.

10.3.10 Manganese (Mn)

Another less extensively investigated ion in BGs is manganese (Mn). Dietary deprivation of Mn causes skeletal abnormalities in the early development of the skeletal system. If the deficiency occurs later it might be connected to osteoporosis [104]. Other roles of Mn in the human body are mainly connected to it being an essential cofactor for metalloenzymes which are needed for gluconeogenesis, the antioxidant stress system or glutamine synthesis in nervous system. However, high concentrations of Mn are known to be neurotoxic [105].

Upon addition of Mn to cell culture media, it showed to have a possible positive impact on osteoblastic MG-63 cells. Most probably caused by modulating integrin affinity and therefore cell adhesion to ECM. However, no pronounced osteogenic effects were found if all investigated osteogenic markers such as ALP activity, expression of osteogenic marker genes, or ECM formation were taken into account [106].

As part of sol–gel or melt and quench derived BGs, Mn was shown to induce osteogenic differentiation in MSC or osteoblast-like cell lines by stimulating ALP activity or enhancing osteopontin (OPN) expression. Though, especially in direct culture settings cytotoxic effects for high concentrations of Mn-supplemented BGs were found indicating a smaller therapeutic window for the application of Mn in bone tissue regeneration [15, 107]. As there are no results of *in vivo* projects evaluating solely Mn-doped BGs are published up to this point of time, knowledge concerning this issue could help specifying the therapeutic window of Mn supplementation in BGs significantly.

10.3.11 Niobium (Nb)

Niobium (Nb) is another therapeutic ion supplemented in BGs out of pro-osteogenic reasons. It first gained interest substituting the commonly used vanadium in metallic alloys leading to increased biocompatibility and corrosion resistance making it interesting for orthopedic applications, especially in implants [108, 109]. Mouse-derived MC3T3-E1 pre-osteoblast cells increased their ALP activity and calcium deposition when cultured in Nb-containing media [110].

In vitro studies with Nb-supplemented 45S5-BG showed good proliferating and osteogenic differentiating effects when 1 mol% of Si was replaced with Nb in the original composition. In the following *in vivo* experiments, the same composition was found to be osteoconductive and osteostimulative but did not offer advantages compared to the original 45S5-BG [111]. Comparable BG-compositions with higher Nb-content showed to be more advantageous when examined *in vitro* and *in vivo* tests by the same group. Further investigation is needed, *in vitro* as well as *in vivo*, to evaluate Nb-supplemented BG's full potential.

10.3.12 Silver (Ag)

Usually, silver (Ag) is added to biomaterials due to its well-established antimicrobial effects. It is known to counteract colonization and adherence of bacteria on the implant and is used to avoid impaired healing and severe infections [112]. Its antibacterial, antifungal, and antiviral properties have been known for a very long time and there are multiple mechanisms discussed for being responsible for these effects. Binding to DNA, interaction with cell components, increasing membrane permeability or interference with electron transfers are mentioned ways. Therefore, only very limited microbial resistance against silver is reported [113]. Apparently, dressings containing nanocrystalline Ag are successfully used for the therapy of infected wounds.

By providing a controlled release of 0.05–0.20 mg/ml of Ag, Ag-supplemented BG scaffolds were shown to inhibit the growth of clinically relevant Gram-negative and Gram-positive bacterial stems such as *Escherichia coli*, *Pseudomonas aeruginosa*, or *Staphylococcus aureus* [114]. Additionally, dental pulp cells showed a decrease in the expression of inflammatory-associated markers such as IL-1β, IL-6, IL-8, and TNF-α [115]. However, Ag has a distinct therapeutic window like almost all presented ions. Exceeding concentrations of Ag limit fibroblast and MG-63 proliferation and were shown to suppress ALP, COL1, and OCN expression [116].

10.3.13 Strontium (Sr)

As a nonessential trace element, strontium (Sr) appears to be a less common mineral in the human body. Sr deficiency does not seem to be connected to relevant clinical problems. However, due to its chemical and structural properties that are similar to those of Ca, the vast majority of Sr in the human body is found in bone tissue [66]. Also, due to this fact, Ca can be substituted with Sr in BG-compositions to a certain extent without losing bioactive properties [100]. With Sr-ranelate, a Sr-salt, being used for osteoporosis treatment of postmenopausal women in Europe, it offers itself as promising therapeutic ion in BTE [117].

Concerning its biological effects on bone-forming cells, Sr is known to influence osteoblasts and osteoclasts via various pathways. On the one hand, Sr was shown to induce RUNX2, OCN, and OPN expression, increased ALP Activity, and led to enhanced matrix mineralization, via the WNT/β-catenin or Ras/mitogen-activated-protein-kinase (MAPK) pathway thus having strengthening effects on bone formation [118]. On the other hand, it inhibits proliferation and formation of osteoclasts by activation of calcium-sensing receptors on osteoblasts. Here, it comes to increased expression of OPG combined with decreased expression of RANKL, shifting the OPG/RANKL balance resulting in impaired bone resorption by osteoclasts [117].

Due to promising beneficial effect of the local delivery of Sr to bone defect sites, Sr-substituted BGs have been investigated extensively. Various compositions have shown to possess the above-mentioned osteogenic effects increasing osteogenic markers of the investigated cells (e.g. ALP activity, RUNX2 expression) upon *in vitro* cultivation with Sr-substituted BGs [101, 119–122]. Strikingly

positive impact was found in an *in vivo* project evaluating BGs with a combined supplementation of Co and Sr. Increased bone formation was found due to synergism of Co's angiogenic and Sr's osteogenic properties as suggested above [64].

Adverse side effects such as cardiovascular events or venous thrombosis, as they occur in oral treatment with Sr-ranelate, could be reduced by local delivery of Sr via BGs without cutting its beneficial therapeutic effects [117]. Therefore, doping BGs with Sr represents a promising option for increasing BGs therapeutic options and should be investigated and pursued further.

10.3.14 Zinc (Zn)

As another essential trace element zinc is involved in many physiological processes throughout the human body being a cofactor in many enzymatic reactions. Related to bone metabolism, its role as cofactor for ALP is of great importance. ALP is essentially involved in maintaining an alkaline environment which is required for precipitation and mineralization of phosphates during bone maturation. Additionally, it cleaves PPi that otherwise would inhibit HA precipitation [123].

When applied to cells of osteoblast-like cell lines or osteoblast precursor cells, Zn has shown to have osteogenic properties with an elevated expression of osteogenic marker genes such as RUNX2, OPN, or OCN, increased matrix mineralization, and a decrease in osteoclast activity by inhibition of NF-κB activity. Zn-sulfate concentrations of 10–250 μM seemed to be most favorable for this purpose [124]. Zn-supplemented TCP showed promising osteogenic properties as well. Human MSCs increased their ALP activity on exposure with the supplemented TCP, and significantly more new bone was formed after 12 weeks in the paraspinal muscle of canines in the presence of Zn [125].

However, there are contradictory findings concerning the osteogenic properties of Zn-supplemented BGs. For example, the ALP activity of rat BMSCs stimulated with Zn-supplemented sol–gel-derived BG granules increased compared to nonsupplemented granules, the opposite effect was found when human adipose stem cells where exposed to Zn-containing BG-scaffolds [126, 127]. Combined Mg and Zn loading of HA coatings on 45S5 scaffolds showed more beneficial results than the supplementation of the respective single ion in terms of MG-63 cell proliferation [128]. On the contrary, cytotoxic effects of Zn-releasing BGs have been published. Here, evidence for increasing oxidative stress with increasing amount of Zn have been found [129]. *In vivo* evaluation of Zn-doped BGs resulted in improved mechanical properties of treated bone defects in female Wistar rats when Zn-doped BGs were used [130]. It is known that Zn leads to a decrease in the BG dissolution rate when incorporated in BG compositions and therefore slows down the HA formation of the BG upon contact with physiological fluids. This might lead to limited comparability when BGs from various studies investigating the biological effect of Zn in BGs are compared that differ in bioactivity due to different compositions and forms of application [126].

Apart from that, dissolution products of sol–gel-derived Zn-supplemented 58S-BG managed to decrease the inflammatory response of RAW 264.7 murine macrophage cells by inhibiting the TNF-α and IL-1 secretion upon stimulation with lipopolysaccharide [131]. These findings match others, where *in vitro* Zn application led to decreased inflammatory response of various none bone-related cell types [132]. Also, antibacterial effects of Zn-supplemented MBGNs or titanium dioxide (TiO_2) coatings have been described, as Zn generates oxidative stress that damages not only physiological cells but also microbial cells as well [78, 133–135].

Further studies on Zn-doped BGs should be conducted in order to clarify Zn's therapeutic potential as part of BGs. The previous contradictory findings do not to deliver sufficient and clear information to make definite conclusions.

10.4 Summary and Conclusions

In summary, doping BGs with therapeutically active ions is a cost-effective, broadly accessible, versatile, and potent way of enhancing BGs therapeutic implications for bone tissue regeneration. Yet some questions are still to be answered and some problems are still to be solved. Many of the molecular mechanisms behind the biological properties of specific ions are not definitely clarified. Figure 10.2 and Table 10.1 give a schematic overview about the roles of the mentioned selection of ions that are already known.

Furthermore, even though ions are applied locally if BGs are used as vector, there is no way known of how the ions can be directed to only affect the targeted cells. As the ions diffuse uncontrollably, there is always the possibility of (negative) ion impact on surrounding cells that are involved in bone defect healing. Even systemic side effects are possible but rather unlikely. Additional knowledge concerning these topics would further increase the therapeutic value of ion doped BGs significantly.

Besides continuous basic research involving BGs doped with various therapeutic ions, the aim of the research should be to eventually introduce these materials into the clinical medicine. Clinical trials will be the next essential step on the long journey toward the clinical use of ion-supplemented BGs [156].

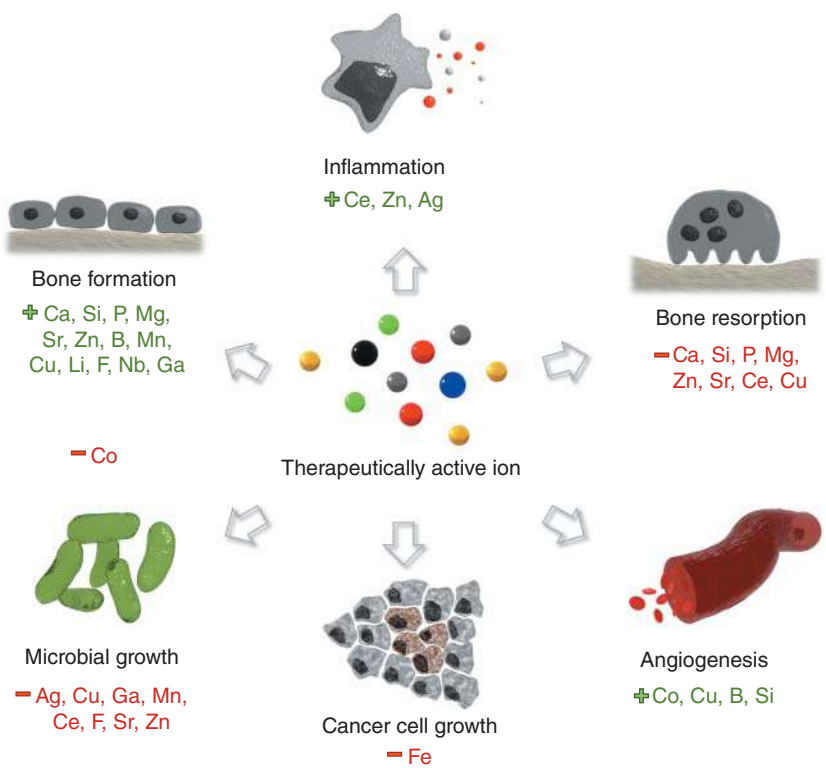

Figure 10.2 Schematic overview of the biological effects of the selected therapeutically active ions that can be released from BG grafts. Positive and negative effects on bone formation, bone resorption, angiogenesis, microbial growth, or growth of cancer cells can be achieved depending on the applied ion.

Table 10.1 Biological effects of candidate ions for doping of bioactive glasses (BGs).

	Biological effect as part of supplemented BGs					
Ion	**Osteogenic**	**Angiogenic**	**Anti-inflammatory**	**Antibacterial**	**Others**	**References**
Boron (B)	X	X				[10, 50–56]
Cerium (Ce)			X	X		[58, 136, 137]
Cobalt (Co)		X				[63, 64, 138]
Copper (Cu)	X	X		X		[139–141]
Fluoride (F)	X			X		[68, 73, 142]
Gallium (Ga)	X			X	Hemostatic	[77, 79, 143, 144]
Iron (Fe)					Anticancerogenic	[82–85]
Lithium (Li)	X					[86, 88, 145]
Magnesium (Mg)	X					[101, 102]
Manganese (Mn)	X			X		[15, 107, 146, 147]
Niobium (Nb)	X					[110, 111, 148, 149]
Silver (Ag)			X	X		[115, 150, 151]
Strontium (Sr)	X			X		[64, 120–122, 152–154]
Zinc (Zn)	X		X	X		[127, 130, 131, 134, 135, 155]

However, the limited interstudy comparability caused using different materials properties (e.g. shape, surface layout) and cells complicate the introduction of newly developed materials into clinical settings. For example it has recently been shown that broadly used "osteoblast-like" cell lines react significantly different upon exposure to the well-known 45S5-BG composition [157]. These differences that are not only limited to different cell types but also include cultivation methods or bone defect models complicate quantification and direct comparison of the biological effects of the respective ions.

References

1 Khan, S.N., Cammisa, F.P. Jr., Sandhu, H.S. et al. (2005). The biology of bone grafting. *Journal of the American Academy of Orthopaedic Surgeons* 13 (1): 77–86.

2 Weber, F.E. (2019). Reconsidering osteoconduction in the era of additive manufacturing. *Tissue Engineering Part B* 25 (5): 375–386.

3 Albrektsson, T. and Johansson, C. (2001). Osteoinduction, osteoconduction and osseointegration. *European Spine Journal* 10 (Suppl 2): S96–S101.

4 Roberts, T.T. and Rosenbaum, A.J. (2012). Bone grafts, bone substitutes and orthobiologics. *Organogenesis* 8 (4): 114–124.

5 Xynos, I.D., Edgar, A.J., Buttery, L.D. et al. (2001). Gene-expression profiling of human osteoblasts following treatment with the ionic products of Bioglass 45S5 dissolution. *Journal of Biomedical Materials Research* 55 (2): 151–157.

6 Hench, L.L. (2009). Genetic design of bioactive glass. *Journal of the European Ceramic Society* 29 (7): 1257–1265.

7 Baino, F., Hamzehlou, S., and Kargozar, S. (2018). Bioactive glasses: where are we and where are we going? *Journal of Functional Biomaterials* 9 (1): 75.

8 Vichery, C. and Nedelec, J.-M. (2016). Bioactive glass nanoparticles: from synthesis to materials design for biomedical applications. *Materials* 9 (4): 288.

9 Meseguer-Olmo, L., Ros-Nicolás, M., Vicente-Ortega, V. et al. (2006). A bioactive sol–gel glass implant for in vivo gentamicin release. Experimental model in Rabbit. *Journal of Orthopaedic Research* 24 (3): 454–460.

10 Wu, C., Miron, R., Sculean, A. et al. (2011). Proliferation, differentiation and gene expression of osteoblasts in boron-containing associated with dexamethasone deliver from mesoporous bioactive glass scaffolds. *Biomaterials* 32 (29): 7068–7078.

11 Wu, C., Fan, W., Chang, J., and Xiao, Y. (2013). Mesoporous bioactive glass scaffolds for efficient delivery of vascular endothelial growth factor. *Journal of Biomaterials Applications* 28 (3): 367–374.

12 Wu, C. and Chang, J. (2014). Multifunctional mesoporous bioactive glasses for effective delivery of therapeutic ions and drug/growth factors. *Journal of Controlled Release* 193: 282–295.

13 O'Neill, E., Awale, G., Daneshmandi, L. et al. (2018). The roles of ions on bone regeneration. *Drug Discovery Today* 23 (4): 879–890.

14 Hoppe, A. and Boccaccini, A.R. (2015). Biological impact of bioactive glasses and their dissolution products. *Frontiers of Oral Biology* 17: 22–32.

15 Westhauser, F., Wilkesmann, S., Nawaz, Q. et al. (2020). Osteogenic properties of manganese-doped mesoporous bioactive glass nanoparticles. *Journal of Biomedical Materials Research Part A* 108 (9): 1806–1815.

16 Kargozar, S., Lotfibakhshaiesh, N., Ai, J. et al. (2016). Synthesis, physico-chemical and biological characterization of strontium and cobalt substituted bioactive glasses for bone tissue engineering. *Journal of Non-Crystalline Solids* 449: 133–140.

17 Berridge, M.J., Lipp, P., and Bootman, M.D. (2000). The versatility and universality of calcium signalling. *Nature Reviews Molecular Cell Biology* 1 (1): 11–21.

18 Yaroslavskiy, B.B., Sharrow, A.C., Wells, A. et al. (2007). Necessity of inositol (1,4,5)-trisphosphate receptor 1 and μ-calpain in NO-induced osteoclast motility. *Journal of Cell Science* 120 (16): 2884.

19 Liu, D., Genetos, D.C., Shao, Y. et al. (2008). Activation of extracellular-signal regulated kinase (ERK1/2) by fluid shear is Ca^{2+}- and ATP-dependent in MC3T3-E1 osteoblasts. *Bone* 42 (4): 644–652.

20 Peacock, M. (2010). Calcium metabolism in health and disease. *Clinical Journal of the American Society of Nephrology* 5 (Suppl 1): S23–S30.

21 Foreman, M.A., Gu, Y., Howl, J.D. et al. (2005). Group III metabotropic glutamate receptor activation inhibits Ca^{2+} influx and nitric oxide synthase activity in bone marrow stromal cells. *Journal of Cellular Physiology* 204 (2): 704–713.

22 Marie, P.J. (2010). The calcium-sensing receptor in bone cells: a potential therapeutic target in osteoporosis. *Bone* 46 (3): 571–576.

23 Kajiya, H. (2012). Calcium signaling in osteoclast differentiation and bone resorption. *Advances in Experimental Medicine and Biology* 740: 917–932.

24 Lim, S.S., Chai, C.Y., and Loh, H.-S. (2017). In vitro evaluation of osteoblast adhesion, proliferation and differentiation on chitosan-TiO_2 nanotubes scaffolds with Ca^{2+} ions. *Materials Science and Engineering C* 76: 144–152.

25 Jones, J.R., Tsigkou, O., Coates, E.E. et al. (2007). Extracellular matrix formation and mineralization on a phosphate-free porous bioactive glass scaffold using primary human osteoblast (HOB) cells. *Biomaterials* 28 (9): 1653–1663.

26 Seol, Y.-J., Park, J.Y., Jung, J.W. et al. (2014). Improvement of bone regeneration capability of ceramic scaffolds by accelerated release of their calcium ions. *Tissue Engineering Part A* 20 (21–22): 2840–2849.

27 Jugdaohsingh, R., Tucker, K.L., Qiao, N. et al. (2004). Dietary silicon intake is positively associated with bone mineral density in men and premenopausal women of the Framingham Offspring cohort. *Journal of Bone and Mineral Research* 19 (2): 297–307.

28 Sripanyakorn, S., Jugdaohsingh, R., Thompson, R.P., and Powell, J.J. (2005). Dietary silicon and bone health. *Nutrition Bulletin* 30 (3): 222–230.

29 Wiens, M., Wang, X., Schröder, H.C. et al. (2010). The role of biosilica in the osteoprotegerin/RANKL ratio in human osteoblast-like cells. *Biomaterials* 31 (30): 7716–7725.

30 Reffitt, D.M., Ogston, N., Jugdaohsingh, R. et al. (2003). Orthosilicic acid stimulates collagen type 1 synthesis and osteoblastic differentiation in human osteoblast-like cells in vitro. *Bone* 32 (2): 127–135.

31 Kim, M.-H., Bae, Y.-J., Choi, M.-K., and Chung, Y.-S. (2008). Silicon supplementation improves the bone mineral density of calcium-deficient ovariectomized rats by reducing bone resorption. *Biological Trace Element Research* 128 (3): 239.

32 Wang, C., Lin, K., Chang, J., and Sun, J. (2013). Osteogenesis and angiogenesis induced by porous β-$CaSiO_3$/PDLGA composite scaffold via activation of AMPK/ERK1/2 and PI3K/Akt pathways. *Biomaterials* 34 (1): 64–77.

33 Mladenovic, Z., Johansson, A., Willman, B. et al. (2014). Soluble silica inhibits osteoclast formation and bone resorption in vitro. *Acta Biomaterialia* 10 (1): 406–418.

34 Modglin, V.C., Brown, R.F., Fu, Q. et al. (2012). In vitro performance of 13-93 bioactive glass fiber and trabecular scaffolds with MLO-A5 osteogenic cells. *Journal of Biomedical Materials Research Part A* 100A (10): 2593–2601.

35 Silver, I.A., Deas, J., and Erecińska, M. (2001). Interactions of bioactive glasses with osteoblasts in vitro: effects of 45S5 Bioglass, and 58S and 77S bioactive glasses on metabolism, intracellular ion concentrations and cell viability. *Biomaterials* 22 (2): 175–185.

36 Bielby, R.C., Christodoulou, I.S., Pryce, R.S. et al. (2004). Time- and concentration-dependent effects of dissolution products of 58S sol–gel bioactive glass on proliferation and differentiation of murine and human osteoblasts. *Tissue Engineering* 10 (7–8): 1018–1026.

37 Chande, S. and Bergwitz, C. (2018). Role of phosphate sensing in bone and mineral metabolism. *Nature Reviews Endocrinology* 14 (11): 637–655.

38 Tada, H., Nemoto, E., Foster, B.L. et al. (2011). Phosphate increases bone morphogenetic protein-2 expression through cAMP-dependent protein kinase and ERK1/2 pathways in human dental pulp cells. *Bone* 48 (6): 1409–1416.

39 Mozar, A., Haren, N., Chasseraud, M. et al. (2008). High extracellular inorganic phosphate concentration inhibits RANK–RANKL signaling in osteoclast-like cells. *Journal of Cellular Physiology* 215 (1): 47–54.

40 Zhang, R., Lu, Y., Ye, L. et al. (2011). Unique roles of phosphorus in endochondral bone formation and osteocyte maturation. *Journal of Bone and Mineral Research* 26 (5): 1047–1056.

41 Drake, M.T., Clarke, B.L., and Khosla, S. (2008). Bisphosphonates: mechanism of action and role in clinical practice. *Mayo Clinic Proceedings* 83 (9): 1032–1045.

42 Foster, B.L., Tompkins, K.A., Rutherford, R.B. et al. (2008). Phosphate: known and potential roles during development and regeneration of teeth and supporting structures. *Birth Defects Research Part C: Embryo Today: Reviews* 84 (4): 281–314.

43 Xynos, I.D., Hukkanen, M.V., Batten, J.J. et al. (2000). Bioglass 45S5 stimulates osteoblast turnover and enhances bone formation in vitro: implications and applications for bone tissue engineering. *Calcified Tissue International* 67 (4): 321–329.

44 Bielby, R.C., Pryce, R.S., Hench, L.L., and Polak, J.M. (2005). Enhanced derivation of osteogenic cells from murine embryonic stem cells after treatment with ionic dissolution products of 58S bioactive sol–gel glass. *Tissue Engineering* 11 (3–4): 479–488.

45 Ojansivu, M., Mishra, A., Vanhatupa, S. et al. (2018). The effect of S53P4-based borosilicate glasses and glass dissolution products on the osteogenic commitment of human adipose stem cells. *PLoS One* 13 (8): e0202740.

46 Devirian, T.A. and Volpe, S.L. (2003). The physiological effects of dietary boron. *Critical Reviews in Food Science and Nutrition* 43 (2): 219–231.

47 Nielsen, F.H. and Stoecker, B.J. (2009). Boron and fish oil have different beneficial effects on strength and trabecular microarchitecture of bone. *Journal of Trace Elements in Medicine and Biology* 23 (3): 195–203.

48 Balasubramanian, P., Büttner, T., Miguez Pacheco, V., and Boccaccini, A.R. (2018). Boron-containing bioactive glasses in bone and soft tissue engineering. *Journal of the European Ceramic Society* 38 (3): 855–869.

49 Huang, W., Day, D.E., Kittiratanapiboon, K., and Rahaman, M.N. (2006). Kinetics and mechanisms of the conversion of silicate (45S5), borate, and borosilicate glasses to hydroxyapatite in dilute phosphate solutions. *Journal of Materials Science – Materials in Medicine* 17 (7): 583–596.

50 Marion, N.W., Liang, W., Liang, W. et al. (2005). Borate glass supports the in vitro osteogenic differentiation of human mesenchymal stem cells. *Mechanics of Advanced Materials and Structures* 12 (3): 239–246.

51 Gorustovich, A., Guglielmotti, M., López, J., and Cabrini, R. (2005). Increased osteogenesis elicited by boron-modified bioactive glass particles in the SiO_2–CaO–P_2O_5–Na_2O system: a histomorphometric study in rats. *Key Engineering Materials* 284: 913–916.

52 Bi, L., Rahaman, M.N., Day, D.E. et al. (2013). Effect of bioactive borate glass microstructure on bone regeneration, angiogenesis, and hydroxyapatite conversion in a rat calvarial defect model. *Acta Biomaterialia* 9 (8): 8015–8026.

53 Balasubramanian, P., Hupa, L., Jokic, B. et al. (2017). Angiogenic potential of boron-containing bioactive glasses: in vitro study. *Journal of Materials Science* 52 (15): 8785–8792.

54 Westhauser, F., Widholz, B., Nawaz, Q. et al. (2019). Favorable angiogenic properties of the borosilicate bioactive glass 0106-B1 result in enhanced in vivo osteoid formation compared to 45S5 Bioglass. *Biomaterials Science* 7 (12): 5161–5176.

55 Haro Durand, L.A., Góngora, A., Porto López, J.M. et al. (2014). In vitro endothelial cell response to ionic dissolution products from boron-doped bioactive glass in the SiO_2–CaO–P_2O_5–Na_2O system. *Journal of Materials Chemistry B* 2 (43): 7620–7630.

56 Lin, Y., Brown, R.F., Jung, S.B., and Day, D.E. (2014). Angiogenic effects of borate glass microfibers in a rodent model. *Journal of Biomedical Materials Research Part A* 102 (12): 4491–4499.

57 Domazetovic, V., Marcucci, G., Iantomasi, T. et al. (2017). Oxidative stress in bone remodeling: role of antioxidants. *Clinical Cases in Mineral and Bone Metabolism* 14 (2): 209–216.

58 Zheng, K., Torre, E., Bari, A. et al. (2020). Antioxidant mesoporous Ce-doped bioactive glass nanoparticles with anti-inflammatory and pro-osteogenic activities. *Materials Today Bio* 5: 100041.

59 Nethi, S.K., Nanda, H.S., Steele, T.W., and Patra, C.R. (2017). Functionalized nanoceria exhibit improved angiogenic properties. *Journal of Materials Chemistry B* 5 (47): 9371–9383.

60 Li, J., Wen, J., Li, B. et al. (2018). Valence state manipulation of cerium oxide nanoparticles on a titanium surface for modulating cell fate and bone formation. *Advanced Science* 5 (2): 1700678.

61 Birgani, Z.T., Gharraee, N., Malhotra, A. et al. (2016). Combinatorial incorporation of fluoride and cobalt ions into calcium phosphates to stimulate osteogenesis and angiogenesis. *Biomedical Materials* 11 (1): 015020.

62 Muñoz-Sánchez, J. and Chánez-Cárdenas, M.E. (2019). The use of cobalt chloride as a chemical hypoxia model. *Journal of Applied Toxicology* 39 (4): 556–570.

63 Wu, C., Zhou, Y., Fan, W. et al. (2012). Hypoxia-mimicking mesoporous bioactive glass scaffolds with controllable cobalt ion release for bone tissue engineering. *Biomaterials* 33 (7): 2076–2085.

64 Kargozar, S., Lotfibakhshaiesh, N., Ai, J. et al. (2017). Strontium- and cobalt-substituted bioactive glasses seeded with human umbilical cord perivascular cells to promote bone regeneration via enhanced osteogenic and angiogenic activities. *Acta Biomaterialia* 41 (6): 7241–7251.

65 Arredondo, M. and Núñez, M.T. (2005). Iron and copper metabolism. *Molecular Aspects of Medicine* 26 (4): 313–327.

66 Wang, W. and Yeung, K.W.K. (2017). Bone grafts and biomaterials substitutes for bone defect repair: a review. *Bioactive Materials* 2 (4): 224–247.

67 Lin, S.H., Zhang, W.J., and Jiang, X.Q. (2019). Applications of bioactive ions in bone regeneration. *The Chinese Journal of Dental Research* 22 (2): 93–104.

68 Al-eesa, N.A., Wong, F.S.L., Johal, A., and Hill, R.G. (2017). Fluoride containing bioactive glass composite for orthodontic adhesives – ion release properties. *Dental Materials* 33 (11): 1324–1329.

69 Brauer, D.S., Karpukhina, N., O'Donnell, M.D. et al. (2010). Fluoride-containing bioactive glasses: effect of glass design and structure on degradation, pH and apatite formation in simulated body fluid. *Acta Biomaterialia* 6 (8): 3275–3282.

70 Lee, M., Arikawa, K., and Nagahama, F. (2017). Micromolar levels of sodium fluoride promote osteoblast differentiation through Runx2 signaling. *Biological Trace Element Research* 178 (2): 283–291.

71 Pak, C.Y.C., Zerwekh, J.E., and Antich, P. (1995). Anabolic effects of fluoride on bone. *Trends in Endocrinology and Metabolism* 6 (7): 229–234.

72 Bergandi, L., Aina, V., Garetto, S. et al. (2010). Fluoride-containing bioactive glasses inhibit pentose phosphate oxidative pathway and glucose 6-phosphate dehydrogenase activity in human osteoblasts. *Chemico-Biological Interactions* 183 (3): 405–415.

73 Liu, J., Rawlinson, S.C.F., Hill, R.G., and Fortune, F. (2016). Fluoride incorporation in high phosphate containing bioactive glasses and in vitro osteogenic, angiogenic and antibacterial effects. *Dental Materials* 32 (10): e221–e237.

74 Matkovic, V., Apseloff, G., Shepard, D.R., and Gerber, N. (1990). Use of gallium to treat Paget's disease of bone: a pilot study. *The Lancet* 335 (8681): 72–75.

75 Todd, P.A. and Fitton, A. (1991). Gallium nitrate. A review of its pharmacological properties and therapeutic potential in cancer related hypercalcaemia. *Drugs* 42 (2): 261–273.

76 Verron, E., Masson, M., Khoshniat, S. et al. (2010). Gallium modulates osteoclastic bone resorption in vitro without affecting osteoblasts. *British Journal of Pharmacology* 159 (8): 1681–1692.

77 Gómez-Cerezo, N., Verron, E., Montouillout, V. et al. (2018). The response of pre-osteoblasts and osteoclasts to gallium containing mesoporous bioactive glasses. *Acta Biomaterialia* 76: 333–343.

78 Kargozar, S., Montazerian, M., Hamzehlou, S. et al. (2018). Mesoporous bioactive glasses: promising platforms for antibacterial strategies. *Acta Biomaterialia* 81: 1–19.

79 Pourshahrestani, S., Zeimaran, E., Kadri, N.A. et al. (2017). Potency and cytotoxicity of a novel gallium-containing mesoporous bioactive glass/chitosan composite scaffold as hemostatic agents. *ACS Applied Materials & Interfaces* 9 (37): 31381–31392.

80 Kobayashi, T. (2011). Cancer hyperthermia using magnetic nanoparticles. *Biotechnology Journal* 6 (11): 1342–1347.

81 Miola, M., Pakzad, Y., Banijamali, S. et al. (2019). Glass-ceramics for cancer treatment: so close, or yet so far? *Acta Biomaterialia* 83: 55–70.

82 Alcaide, M., Ramírez-Santillán, C., Feito, M.J. et al. (2012). In vitro evaluation of glass–glass ceramic thermoseed-induced hyperthermia on human osteosarcoma cell line. *Journal of Biomedical Materials Research Part A* 100A (1): 64–71.

83 Leenakul, W., Ruangsuriya, J., Jantaratana, P., and Pengpat, K. (2013). Fabrication and characterization of ferrimagnetic bioactive glass-ceramic containing $BaFe_{12}O_{19}$. *Ceramics International* 39: S201–S205.

84 Shah, S.A., Hashmi, M.U., Alam, S., and Shamim, A. (2010). Magnetic and bioactivity evaluation of ferrimagnetic $ZnFe_2O_4$ containing glass ceramics for the hyperthermia treatment of cancer. *Journal of Magnetism and Magnetic Materials* 322 (3): 375–381.

85 Singh, R.K. and Srinivasan, A. (2010). Bioactivity of ferrimagnetic $MgO–CaO–SiO_2–P_2O_5–Fe_2O_3$ glass-ceramics. *Ceramics International* 36 (1): 283–290.

86 Li, S., Maçon, A.L.B., Jacquemin, M. et al. (2017). Sol–gel derived lithium-releasing glass for cartilage regeneration. *Journal of Biomaterials Applications* 32 (1): 104–113.

87 Hedgepeth, C.M., Conrad, L.J., Zhang, J. et al. (1997). Activation of the Wnt signaling pathway: a molecular mechanism for lithium action. *Developmental Biology* 185 (1): 82–91.

88 Daguano, J., Milesi, M.T.B., Rodas, A.C.D. et al. (2019). In vitro biocompatibility of new bioactive lithia-silica glass-ceramics. *Materials Science and Engineering C* 94: 117–125.

89 Frings, C.S. (1987). Lithium monitoring. *Clinics in Laboratory Medicine* 7 (3): 545–550.

90 Lakhkar, N.J., Lee, I.-H., Kim, H.-W. et al. (2013). Bone formation controlled by biologically relevant inorganic ions: role and controlled delivery from phosphate-based glasses. *Advanced Drug Delivery Reviews* 65 (4): 405–420.

91 Rude, R.K., Singer, F.R., and Gruber, H.E. (2009). Skeletal and hormonal effects of magnesium deficiency. *Journal of the American College of Nutrition* 28 (2): 131–141.

92 Wong, H.M., Wu, S., Chu, P.K. et al. (2013). Low-modulus Mg/PCL hybrid bone substitute for osteoporotic fracture fixation. *Biomaterials* 34 (29): 7016–7032.

93 Yoshizawa, S., Brown, A., Barchowsky, A., and Sfeir, C. (2014). Magnesium ion stimulation of bone marrow stromal cells enhances osteogenic activity, simulating the effect of magnesium alloy degradation. *Acta Biomaterialia* 10 (6): 2834–2842.

94 Zhai, Z., Qu, X., Li, H. et al. (2014). The effect of metallic magnesium degradation products on osteoclast-induced osteolysis and attenuation of NF-κB and NFATc1 signaling. *Biomaterials* 35 (24): 6299–6310.

95 Galli, S., Naito, Y., Karlsson, J. et al. (2014). Local release of magnesium from mesoporous TiO_2 coatings stimulates the peri-implant expression of osteogenic markers and improves osteoconductivity in vivo. *Acta Biomaterialia* 10 (12): 5193–5201.

96 Tao, Z.S., Zhou, W.S., He, X.W. et al. (2016). A comparative study of zinc, magnesium, strontium-incorporated hydroxyapatite-coated titanium implants for osseointegration of osteopenic rats. *Materials Science and Engineering C* 62: 226–232.

97 Landi, E., Logroscino, G., Proietti, L. et al. (2008). Biomimetic Mg-substituted hydroxyapatite: from synthesis to in vivo behaviour. *Journal of Materials Science – Materials in Medicine* 19 (1): 239–247.

98 Zhang, J., Ma, X., Lin, D. et al. (2015). Magnesium modification of a calcium phosphate cement alters bone marrow stromal cell behavior via an integrin-mediated mechanism. *Biomaterials* 53: 251–264.

99 Zhang, Y., Xu, J., Ruan, Y.C. et al. (2016). Implant-derived magnesium induces local neuronal production of CGRP to improve bone-fracture healing in rats. *Nature Medicine* 22 (10): 1160–1169.

100 Rabiee, S.M., Nazparvar, N., Azizian, M. et al. (2015). Effect of ion substitution on properties of bioactive glasses: a review. *Ceramics International* 58: 502–514.

101 Bellucci, D., Sola, A., Cacciotti, I. et al. (2014). Mg- and/or Sr-doped tricalcium phosphate/bioactive glass composites: synthesis, microstructure and biological responsiveness. *Materials Science and Engineering C* 42: 312–324.

102 Chen, X., Liao, X., Huang, Z. et al. (2010). Synthesis and characterization of novel multiphase bioactive glass-ceramics in the CaO–MgO–SiO_2 system. *Journal of Biomedical Materials Research Part B Applied Biomaterials* 93B (1): 194–202.

103 Saffarian Tousi, N., Velten, M.F., Bishop, T.J. et al. (2013). Combinatorial effect of Si^{4+}, Ca^{2+}, and Mg^{2+} released from bioactive glasses on osteoblast osteocalcin expression and biomineralization. *Materials Science and Engineering C* 33 (5): 2757–2765.

104 Beattie, J.H. and Avenell, A. (1992). Trace element nutrition and bone metabolism. *Nutrition Research Reviews* 5 (1): 167–188.

105 Peres, T.V., Schettinger, M.R.C., Chen, P. et al. (2016). Manganese-induced neurotoxicity: a review of its behavioral consequences and neuroprotective strategies. *BMC Pharmacology and Toxicology* 17 (1): 57.

106 Luthen, F., Bulnheim, U., Muller, P.D. et al. (2007). Influence of manganese ions on cellular behavior of human osteoblasts in vitro. *Biomolecular Engineering* 24 (5): 531–536.

107 Barrioni, B.R., Norris, E., Li, S. et al. (2019). Osteogenic potential of sol–gel bioactive glasses containing manganese. *Journal of Materials Science – Materials in Medicine* 30 (7): 86.

108 Antonini, L.M., Menezes, T.L., dos Santos, A.G. et al. (2019). Osteogenic differentiation of bone marrow-derived mesenchymal stem cells on anodized niobium surface. *Journal of Materials Science – Materials in Medicine* 30 (9): 104.

109 Metikoš-Huković, M., Kwokal, A., and Piljac, J. (2003). The influence of niobium and vanadium on passivity of titanium-based implants in physiological solution. *Biomaterials* 24 (21): 3765–3775.

110 Obata, A., Takahashi, Y., Miyajima, T. et al. (2012). Effects of niobium ions released from calcium phosphate invert glasses containing Nb_2O_5 on osteoblast-like cell functions. *ACS Applied Materials & Interfaces* 4 (10): 5684–5690.

111 Lopes, J.H., Souza, L.P., Domingues, J.A. et al. (2020). In vitro and in vivo osteogenic potential of niobium-doped 45S5 bioactive glass: a comparative study. *Journal of Biomedical Materials Research Part B Applied Biomaterials* 108 (4): 1372–1387.

112 Kuehl, R., Brunetto, P.S., Woischnig, A.-K. et al. (2016). Preventing implant-associated infections by silver coating. *Antimicrobial Agents and Chemotherapy* 60 (4): 2467–2475.

113 Khansa, I., Schoenbrunner, A.R., Kraft, C.T., and Janis, J.E. (2019). Silver in wound care-friend or foe?: a comprehensive review. *Plastic and Reconstructive Surgery - Global Open* 7 (8): e2390.

114 Hoppe, A., Guldal, N.S., and Boccaccini, A.R. (2011). A review of the biological response to ionic dissolution products from bioactive glasses and glass-ceramics. *Biomaterials* 32 (11): 2757–2774.

115 Zhu, N., Chatzistavrou, X., Ge, L. et al. (2019). Biological properties of modified bioactive glass on dental pulp cells. *Journal of Dentistry* 83: 18–26.

116 Xie, H., Wang, P., and Wu, J. (2019). Effect of exposure of osteoblast-like cells to low-dose silver nanoparticles: uptake, retention and osteogenic activity. *Artificial Cells, Nanomedicine, and Biotechnology* 47 (1): 260–267.

117 Pilmane, M., Salma-Ancane, K., Loca, D. et al. (2017). Strontium and strontium ranelate: historical review of some of their functions. *Materials Science and Engineering C* 78: 1222–1230.

118 Yang, F., Yang, D., Tu, J. et al. (2011). Strontium enhances osteogenic differentiation of mesenchymal stem cells and in vivo bone formation by activating Wnt/catenin signaling. *Stem Cells* 29 (6): 981–991.

119 Cui, X., Zhang, Y., Wang, J. et al. (2020). Strontium modulates osteogenic activity of bone cement composed of bioactive borosilicate glass particles by activating Wnt/β-catenin signaling pathway. *Bioactive Materials* 5 (2): 334–347.

120 Liu, J., Rawlinson, S.C., Hill, R.G., and Fortune, F. (2016). Strontium-substituted bioactive glasses in vitro osteogenic and antibacterial effects. *Dental Materials* 32 (3): 412–422.

121 Leite, Á.J., Gonçalves, A.I., Rodrigues, M.T. et al. (2018). Strontium-doped bioactive glass nanoparticles in osteogenic commitment. *ACS Applied Materials & Interfaces* 10 (27): 23311–23320.

122 Naruphontjirakul, P., Tsigkou, O., Li, S. et al. (2019). Human mesenchymal stem cells differentiate into an osteogenic lineage in presence of strontium containing bioactive glass nanoparticles. *Acta Biomaterialia* 90: 373–392.

123 Orimo, H. (2010). The mechanism of mineralization and the role of alkaline phosphatase in health and disease. *Journal of Nippon Medical School* 77 (1): 4–12.

124 Yamaguchi, M. and Weitzmann, M.N. (2011). Zinc stimulates osteoblastogenesis and suppresses osteoclastogenesis by antagonizing NF-κB activation. *Molecular and Cellular Biochemistry* 355 (1): 179.

125 Luo, X., Barbieri, D., Davison, N. et al. (2014). Zinc in calcium phosphate mediates bone induction: in vitro and in vivo model. *Acta Biomaterialia* 10 (1): 477–485.

126 Haimi, S., Gorianc, G., Moimas, L. et al. (2009). Characterization of zinc-releasing three-dimensional bioactive glass scaffolds and their effect on human adipose stem cell proliferation and osteogenic differentiation. *Acta Biomaterialia* 5 (8): 3122–3131.

127 Oh, S.-A., Kim, S.-H., Won, J.-E. et al. (2011). Effects on growth and osteogenic differentiation of mesenchymal stem cells by the zinc-added sol–gel bioactive glass granules. *Journal of Tissue Engineering* 2010: 475260.

128 Dittler, M.L., Unalan, I., Grünewald, A. et al. (2019). Bioactive glass (45S5)-based 3D scaffolds coated with magnesium and zinc-loaded hydroxyapatite nanoparticles for tissue engineering applications. *Colloids and Surfaces B: Biointerfaces* 182: 110346.

129 Aina, V., Perardi, A., Bergandi, L. et al. (2007). Cytotoxicity of zinc-containing bioactive glasses in contact with human osteoblasts. *Chemico-Biological Interactions* 167 (3): 207–218.

130 Samira, J., Saoudi, M., Abdelmajid, K. et al. (2015). Accelerated bone ingrowth by local delivery of zinc from bioactive glass: oxidative stress status, mechanical property, and microarchitectural characterization in an ovariectomized rat model. *Libyan Journal of Medicine* 10 (1): 28572.

131 Varmette, E., Nowalk, J., Flick, L., and Hall, M. (2009). Abrogation of the inflammatory response in LPS-stimulated RAW 264.7 murine macrophages by Zn- and Cu-doped bioactive sol–gel glasses. *Journal of Biomedical Materials Research Part A* 90: 317–325.

132 Prasad, A.S. (2014). Zinc is an antioxidant and anti-inflammatory agent: its role in human health. *Frontiers in Nutrition* 1: 14.

133 Hu, H., Zhang, W., Qiao, Y. et al. (2012). Antibacterial activity and increased bone marrow stem cell functions of Zn-incorporated TiO_2 coatings on titanium. *Acta Biomaterialia* 8 (2): 904–915.

134 Heras, C., Jiménez-Holguín, J., Doadrio, A.L. et al. (2020). Multifunctional antibiotic- and zinc-containing mesoporous bioactive glass scaffolds to fight bone infection. *Acta Biomaterialia* 114: 395–406.

135 Sergi, R., Bellucci, D., Salvatori, R. et al. (2019). Zinc containing bioactive glasses with ultra-high crystallization temperature, good biological performance and antibacterial effects. *Materials Science and Engineering C* 104: 109910.

136 Morais, D.S., Fernandes, S., Gomes, P.S. et al. (2015). Novel cerium doped glass-reinforced hydroxyapatite with antibacterial and osteoconductive properties for bone tissue regeneration. *Biomedical Materials* 10 (5): 055008.

137 Nicolini, V., Gambuzzi, E., Malavasi, G. et al. (2015). Evidence of catalase mimetic activity in Ce^{3+}/Ce^{4+} doped bioactive glasses. *Journal of Physical Chemistry B* 119 (10): 4009–4019.

138 Perez, R.A., Kim, J.-H., Buitrago, J.O. et al. (2015). Novel therapeutic core–shell hydrogel scaffolds with sequential delivery of cobalt and bone morphogenetic protein-2 for synergistic bone regeneration. *Acta Biomaterialia* 23: 295–308.

139 Wang, H., Zhao, S., Zhou, J. et al. (2014). Evaluation of borate bioactive glass scaffolds as a controlled delivery system for copper ions in stimulating osteogenesis and angiogenesis in bone healing. *Journal of Materials Chemistry B* 2 (48): 8547–8557.

140 Bari, A., Bloise, N., Fiorilli, S. et al. (2017). Copper-containing mesoporous bioactive glass nanoparticles as multifunctional agent for bone regeneration. *Acta Biomaterialia* 55: 493–504.

141 Wu, C., Zhou, Y., Xu, M. et al. (2013). Copper-containing mesoporous bioactive glass scaffolds with multifunctional properties of angiogenesis capacity, osteostimulation and antibacterial activity. *Biomaterials* 34 (2): 422–433.

142 Schmitz, S.I., Widholz, B., Essers, C. et al. (2020). Superior biocompatibility and comparable osteoinductive properties: sodium-reduced fluoride-containing bioactive glass belonging to the $CaO–MgO–SiO_2$ system as a promising alternative to 45S5 bioactive glass. *Bioactive Materials* 5 (1): 55–65.

143 Rahimnejad Yazdi, A., Torkan, L., Stone, W., and Towler, M.R. (2018). The impact of gallium content on degradation, bioactivity, and antibacterial potency of zinc borate bioactive glass. *Journal of Biomedical Materials Research Part B Applied Biomaterials* 106 (1): 367–376.

144 Keenan, T.J., Placek, L.M., Hall, M.M., and Wren, A.W. (2017). Antibacterial and antifungal potential of Ga-bioactive glass and Ga-bioactive glass/polymeric hydrogel composites. *Journal of Biomedical Materials Research Part B Applied Biomaterials* 105 (5): 1102–1113.

145 Ali, M., Okamoto, M., Komichi, S. et al. (2019). Lithium-containing surface pre-reacted glass fillers enhance hDPSC functions and induce reparative dentin formation in a rat pulp capping model through activation of Wnt/β-catenin signaling. *Acta Biomaterialia* 96: 594–604.

146 Miola, M., Brovarone, C.V., Maina, G. et al. (2014). In vitro study of manganese-doped bioactive glasses for bone regeneration. *Materials Science and Engineering C* 38: 107–118.

147 Nawaz, Q., Rehman, M.A.U., Burkovski, A. et al. (2018). Synthesis and characterization of manganese containing mesoporous bioactive glass nanoparticles for biomedical applications. *Journal of Materials Science – Materials in Medicine* 29 (5): 64.

148 Balbinot, G.S., Collares, F.M., Visioli, F. et al. (2018). Niobium addition to sol–gel derived bioactive glass powders and scaffolds: in vitro characterization and effect on pre-osteoblastic cell behavior. *Dental Materials* 34 (10): 1449–1458.

149 Souza, L., Lopes, J.H., Encarnação, D. et al. (2018). Comprehensive in vitro and in vivo studies of novel melt-derived Nb-substituted 45S5 bioglass reveal its enhanced bioactive properties for bone healing. *Scientific Reports* 8 (1): 12808.

150 Pajares-Chamorro, N., Shook, J., Hammer, N.D., and Chatzistavrou, X. (2019). Resurrection of antibiotics that methicillin-resistant *Staphylococcus aureus* resists by silver-doped bioactive glass-ceramic microparticles. *Acta Biomaterialia* 96: 537–546.

151 Ciraldo, F.E., Liverani, L., Gritsch, L. et al. (2018). Synthesis and characterization of silver-doped mesoporous bioactive glass and its applications in conjunction with electrospinning. *Materials (Basel, Switzerland)* 11 (5): 692.

152 Gentleman, E., Fredholm, Y.C., Jell, G. et al. (2010). The effects of strontium-substituted bioactive glasses on osteoblasts and osteoclasts in vitro. *Biomaterials* 31 (14): 3949–3956.

153 Gorustovich, A.A., Steimetz, T., Cabrini, R.L., and Porto López, J.M. (2010). Osteoconductivity of strontium-doped bioactive glass particles: a histomorphometric study in rats. *Journal of Biomedical Materials Research Part A* 92 (1): 232–237.

154 Isaac, J., Nohra, J., Lao, J. et al. (2011). Effects of strontium-doped bioactive glass on the differentiation of cultured osteogenic cells. *European Cells & Materials* 21: 130–143.

155 Nescakova, Z., Zheng, K., Liverani, L. et al. (2019). Multifunctional zinc ion doped sol–gel derived mesoporous bioactive glass nanoparticles for biomedical applications. *Bioactive Materials* 4: 312–321.

156 Hench, L.L. and Jones, J.R. (2015). Bioactive glasses: frontiers and challenges. *Frontiers in Bioengineering and Biotechnology* 3: 194.

157 Wilkesmann, S., Fellenberg, J., Nawaz, Q. et al. (2020). Primary osteoblasts, osteoblast precursor cells or osteoblast-like cell lines: which human cell types are (most) suitable for characterizing 45S5-bioactive glass? *Journal of Biomedical Materials Research Part A* 108 (3): 663–674.

11

Bioactive Glasses as Carriers for the Controlled Release of Therapeutic Species

Min Zhu[1] *and Yufang Zhu*[2]

[1] *School of Materials and Chemistry, University of Shanghai for Science and Technology, Shanghai, PR China*
[2] *State Key Laboratory of High Performance Ceramics and Superfine Microstructure, Shanghai Institute of Ceramics, Chinese Academy of Sciences, Shanghai, PR China*

11.1 Introduction: From BG Themselves to Platform Materials

Bioactive glasses (BGs) initialized the generation of bioactive materials instead of inert ceramics for the application of hard tissue engineering. The implanted BGs can bond to host tissues through a mineralization process and lead to new tissue growth while biodegrade over time themselves. Such ability to induce hydroxyapatite (HA) deposition at the host-glass interface is referred as "bioactivity" [1]. BGs are complex oxides with tunable constituents including different network-forming, network-modifying, and intermediate oxides. These constituents build a 3D extended network disorderly with other oxide participants together that determine final structure and properties of the glass materials.

Over the past few decades, BG family expanded from the first generation of well-known 45S5 Bioglass®, that was prepared by Prof. Hench's group in 1960s with a composition of $45SiO_2$–$24.5CaO$–$24.5Na_2O$–$6P_2O_5$ (wt%), to various BGs [2]. It is so far generally accepted that BGs are categorized into three types according to the network units: silicate glasses, borate glasses, and phosphate glasses. Early studies about BG materials focused on the constituent adjustment among these main oxides (SiO_2, CaO, P_2O_5, Na_2O, B_2O_3) to obtain optimal bioactivity, biocompatibility, and tissue regeneration performances [2]. However, encouraging successful tissue regeneration is a sophisticated procedure regarding complex interactions among cells, materials, biological growth factors (GFs), and host tissues. BGs themselves show limitations to fulfill further higher or more specific requirements during tissue regeneration. For example, the treatment of infected bone defects demands biomaterials with antimicrobial functions without loss of osteoconductivity/inductivity, and moreover, implants associated with bacterial infections must be prevented or treated afterward. Developing BGs integrated with antibacterial properties would be meaningful to promote healing and tissue regeneration. Studies show that one popular strategy is to load antibiotics into BGs that deliver and release the drugs to infected sites. To stimulate tissue growth simultaneously, BGs can serve as a platform to deliver functional species that produce enhanced performances. Therefore, BGs are destined to extend their use as carriers.

It is well-acknowledged that glass composition is readily to be designed as long as the additives do not undermine the network stability and integrity. Furthermore, a variety of studies demonstrated that bioactive inorganic ions contributed to improved pharmaceutic effects, such as angiogenesis, anti-inflammation, osteogenesis, and so on [3]. Naturally, BGs doped with bioactive ions is achieved

Bioactive Glasses and Glass-Ceramics: Fundamentals and Applications, First Edition.
Edited by Francesco Baino and Saeid Kargozar.

through the doping reactions during synthesis aiming to produce different biological effects, and the doped ions in the BG network could *in situ* release in a certain manner to the periphery environment and then influence the physiological processes. However, other species like therapeutic drugs or biomolecules are difficult to be doped into the BG network directly as ions, then porous structures of BG powders or BG-based implants are demanded for these bigger molecules.

Conventional fabrication methods of BGs include melt reactions and sol–gel processing. Unlike the melt-derived BGs, BGs fabricated by a sol–gel process have inherent meso-/nano-scaled pores, which enlarge the surface area of BGs and provide possibilities for drug loading and delivery. Nonetheless, ordered mesoporous bioactive glasses (MBGs) were discovered by Yan et al. in 2004 [4] and Vallet-Regi and coworkers in 2006 [5] via an evaporation-induced self-assembly route. The mesopores replicate the orderly packed surfactant micelle aggregates and exhibit regular pore morphology and narrowly distributed pore size. Compared with sol–gel-derived BGs, whose pores are randomly distributed and pore structure are hard to adjust, MBG carriers are of great potentials in controlled delivery of drug molecules. To date, increasing studies have reported various therapeutic drugs/molecules and bio-promotors that were encapsulated into mesoporous channels of MBGs, and in addition, the engineering of MBG porous architecture together with surface functionalities are performed to control the release kinetics of such moieties [6]. The spatiotemporal regulation of species delivery for achieving a safe and effective therapeutic result is then likely to be obtained. Another workable strategy of bigger molecule loading is constructing porous scaffolds with BG-based materials. The needed species can be either embedded in scaffold pores with suitable size or mixed into the scaffold body directly, in this way the release manner can be altered with scaffold pore structure or scaffold degradations.

On the other hand, the introduction of such pores as described above, from sol–gel-derived micropores, template-directed mesopores to macropores of scaffold/monolith, seeks not only to

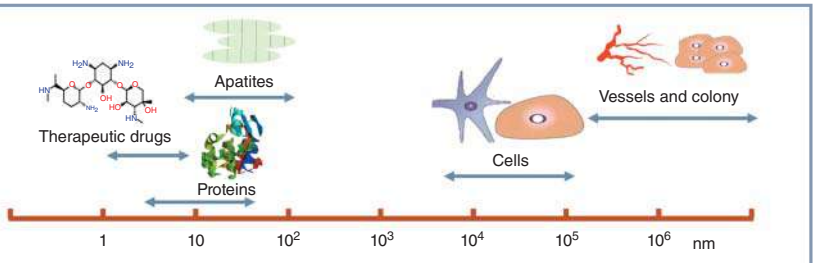

Scale	Function	Pore size
Micropores	• Larger surface area • Change the degradation rate and ion release kinetics	<2 nm
Apatite Drug molecules Growth factors	• Enhance apatite formation ability • Drug encapsulation • Nanoscaled patterns improve cell attachment	~10 nm
Cell	Cellular behaviors (adhesion, migration, differentiation, etc.)	10–100 μm
Scaffold pores	• Cell penetration and colonization • Nutrient supply • Blood vessel formation	>100 μm
Scaffold pores	Tissue in-growth	>500 μm

Figure 11.1 Hierarchical pores of implant materials provide mimetic dimension and structure for tissue engineering.

incorporate drugs but more importantly to mimic the hierarchical porosity of natural tissues. The pore size ranges are designed according to specific biological processes and the properties of key involved biocues (Figure 11.1). For example, synthetic scaffolds for bone tissue engineering are required to possess 3D interconnected porous architecture with pores similar in size and density to those existing in natural bone. It is well-acknowledged that submicro pores are suitable to interact with proteins, and the nanoscale micropores are responsible for accelerated apatite deposition when the surface area becomes larger. The pores with size in the range of several to several 10 μm play important roles in cell adhesion, spreading and orientation that influence cellular development. The last but not the least point, scaffold macropores larger than 100 μm are essential to facilitate tissue regeneration throughout the whole scaffold template.

This chapter intends to give a brief introduction of BG-based carriers for local release of different species for biomedical applications, especially for bone tissue engineering.

11.2 Therapeutic Ion Release

The bioactive effects of BG materials generally embodied in two fundamental ways both related to ion dissolution: (i) Ion dissolutions induce hydroxycarbonated bone-like apatite (HCA) deposition on the implanted BG surface that forms bone–material integrated bonding. In body fluid or simulated body fluid (SBF, similar ionic concentrations to body fluid), BGs can dissolve and release certain metallic cations resulting in changes of environmental pH and surface chemical groups, which then offer appropriate nucleation sites for apatite crystallites. Based on a great deal of experimental data, a typical process of HCA formation involves five sequential steps, that are cation dissolution and exchange with H^+, Si–OH, and SiO_2-rich layer formation, Ca^{2+} and PO_4^{3-} deposition, amorphous $CaO–P_2O_3$ formation, and finally reactions of OH^-/CO_3^{2-} ions with amorphous $CaO–P_2O_3$ to transform them into HCA crystals; (ii) a variety of ions in BGs are released and produce biological effects to stimulate cellular responses. Xynos's group firstly investigated the ionic products of 45S5 Bioglass and found its constitutive ions including Si^{4+}, Ca^{2+}, and PO_4^{3-} exerted stimulatory effects on osteoblast proliferation through insulin-like growth factor II (IGF-II) expression and mediation [7]. Several studies were succeeded to evaluate the ionic dissolution products of 45S5 Bioglass. Sun et al. revealed that these ions can reduce the human osteoblast growth cycle to pass through G1 and S phase and then enter G2 phase quickly [8]. Jell et al. suggested the leaching liquor of Bioglass increased expressions of alkaline phosphatase (ALP) and bone sialoprotein (BSP) promoting osteogenesis differentiation of fetal osteoblasts [9]. In addition, Day et al. demonstrated that ions extracted from 45S5 Bioglass stimulated the secretion of angiogenic GFs and promoted angiogenesis of tissue-engineered constructs [10]. Similarly, sol–gel-derived BGs with different compositions also presented positive biological effects for tissue regeneration owing to their particular released ions, such as Ca^{2+}, phosphate ions, boron and silicon ions. Table 11.1 gives a sum up of the constitutive ions of BGs which elicit favorable responses and manifest bioactivities.

Inspired by the positive biological effects of these therapeutic ions, more supplemental metallic ions are taken into consideration to be doped in glass network. These doped ions are usually added in terms of modifier oxides that do not participate in constructing glass network. Contrarily, the metallic cations bond to oxygen atoms leading to the Si–O breakage. As a result, the integrity of glass is destroyed and in turn, cation release kinetics are accelerated. Therefore, it is reasonable and expectable to control the fluctuation of local ion concentration around the lesion over time

Table 11.1 List of constitutive therapeutic ions of BGs and theirs main reported biological effects.

Ion	Biological effects	References
Silicon (Si)	Enhance bone mineralization and osteogenesis	[11, 12]
	Influence homeostasis of ECM proteins	
	Stimulate the secretion of pro-angiogenic growth factors	
	Improve skin strength and elasticity	
Calcium (Ca)	Major component of bone minerals	[13–15]
	Promote ECM mineralization Influence calcium signaling pathways which determine cellular functions	
	Play a key role in cell apoptosis in addition to the physiological processes of muscle contraction and generation of cardiac pulse creation	
Phosphate	Regulate bone mineralization, cellular signaling and metabolism, acid–base balance, and maintenance of cell membrane integrity	[16, 17]
	Induce apoptosis in osteoclasts and inhibits osteoclast differentiation and bone resorption activity	
Boron (B)	Promote osteogenic differentiation of BMSCs through enhanced ALP activity and increased expression of osteogenic gene markers (OCN, collagen I, and BMP-7)	[18–20]
	Upregulate ERK, FAK and increase vascularization	
	Stimulate keratinocytes migration and accelerate wound healing	

via controlling doping dosage, glass microstructures, and compositions. The *in vitro* and *in vivo* pharmacological effects of some typical therapeutic ions doped in BGs are briefly summarized in Table 11.2.

11.2.1 Bioactive Ion Delivery

11.2.1.1 Ionic Antibacterial Effects

Antibacterial metallic ions have been well accepted and reviewed in literatures [27, 42]. Hence, BGs can inherently inhibit the growth or viability of bacterial cells through the release of antibacterial cations incorporated in their glass network. The antibacterial ions used are briefly summarized in Table 11.2, including monovalent (Ag^+), divalent (Zn^{2+}, Cu^{2+}, and Mn^{2+}), and trivalent (Ce^{3+} and Ga^{3+}) ions with specific cellular and molecular antibacterial mechanisms.

Silver (Ag) gained popularity in the open wound healing, as largely due to the spread of methicillin-resistant *Staphylococcus aureus* (MRSA) and the reduction in first-line antibiotic prescribing [43]. Nowadays, silver ion is the most common metallic ion used in the antibacterial BGs as it exhibits a broad-spectrum bactericidal behavior at low concentrations without causing resistant bacteria, while keeping the bulk structure and main properties of the material mostly unaltered. The major mechanism toward antibacterial effect of Ag^+ ions is claimed by researches that lies in de-energizing of bacteria cell membrane and inactivation of relative enzymes resulting from Ag^+ interactions with disulfide (S–S) and sulfhydryl (–SH) groups. Hu et al. studied the potential of Ag-doped SiO_2–CaO–P_2O_5–Ag_2O nanoporous silicate BGs for wound healing [44]. The silicate BGs containing 0.02 wt% Ag reached 75% of antibacterial efficiency against *Escherichia coli* within 1 hour and the value increased to 99% in 12 hours. Moreover, they found that Ag-doped silicate glasses were in possession of an exceptional hemostatic performance due to the high

Table 11.2 List of additive therapeutic ions of BGs and theirs main reported biological effects.

Ion	Biological effects	References
Strontium (Sr)	Enhances proliferation and osteogenic differentiation of osteoblastic cells Inhibits osteoclast activity and upregulates osteoclast apoptosis Improve osseointegration and bone remodeling	[21, 22]
Magnesium (Mg)	Enhance matrix mineralization Stimulate BMSCs osteogenic gene expression, and protein expression of collagen and VEGF Decrease the secretion of proinflammatory cytokines	[23, 24]
Zinc (Zn)	Stimulate collagen synthesis, ALP activity, and matrix mineralization Induces proliferation, expression of type 1 collagen and OCN in human adipose-derived MSCs Show anti-inflammatory and antibacterial properties	[25–27]
Copper (Cu)	Upregulate HIF-1a to mimic hypoxia Increase VEGF secretion and promote angiogenesis Increase vascularization part of standard neural function, promotes neural differentiation	[28, 29]
Cobalt (Co)	Downregulate some osteogenic markers and reduce proliferation of osteoblasts Stimulate osteoclast activity Enhance blood vessel formation by mimicking hypoxia and stabilizing hypoxia inducible factor-1 alpha (HIF-1α)	[30, 31]
Manganese (Mn)	Improve bone mineralization, extracellular matrix remodeling and promotes osteoblastic-like cell adhesion Promote the expression of ALP and BMPs Antibacterial effect at a low concentration	[27, 32, 33]
Silver (Ag)	Show antimicrobial actions in cell culture Exhibit a marked bactericidal effect Exposure of MC3T3-E1 cells to silver-based nanoparticles resulted in upregulation of bone	[27, 34]
Gallium (Ga)	Block bone reabsorption by inhibiting osteoclast activity Inhibit *P. aeruginosa* growth and biofilm formation	[35, 36]
Cerium (Ce)	Show antibacterial effect Increase the proliferation and migration of fibroblasts, keratinocytes, and vascular endothelial cells Improve would healing by increase of collagen deposition	[37–39]
Lithium (Li)	Capable to treat arthritis and stimulate subchondral bone formation Stimulate chondrocyte proliferation	[40, 41]

surface area, and as such the glasses successfully promoted blood clotting and obtained hemorrhage control in the animal model. Pratten et al. prepared Ag-doped silicate BG coating on surgical sutures to prevent bacterial colonization. By comparison to the 45S5 Bioglass coated and the uncoated sutures, the *in vitro* investigations revealed that the Ag-doped BG coating limited the attachment of *Staphylococcus epidermidis* more significantly [45]. Similar studies of Ag ion incorporated BGs have been carried out by other groups. Catauro et al. demonstrated that

Ag ion release from $Na_2O–CaO–SiO_2$ glasses showed high antimicrobial effects against *E. coli* and *Streptococcus mutans* [46]. More importantly, the cytotoxicity of Ag ion was controlled in a reasonable level from impairing bone tissue engineering performances [47].

Biofilm-associated bacteria show a decreased susceptibility to antibiotics, disinfectants, and clearance by host defense system. Study has found that Ga^{3+} ions inhibit *Pseudomonas aeruginosa* growth and biofilm formation *in vitro* by decreasing bacterial Fe uptake and interfering with Fe signaling via the transcriptional regulator pvdS [48]. More importantly, a remarkable advantage of Ga^{3+} for practical clinical use is that Ga^{3+} is already approved by the US Food and Drug Administration (FDA) for intravenous administration, and the growing problem of antibacterial resistance makes Ga^{3+}-doped BGs a potentially highly promising new therapeutic agent against bacteria. For example, Knowles and coworkers synthesized Ga_2O_3-doped phosphate-based glasses (PBGs), which exhibit a potent antibacterial effect against planktonic bacteria including *P. aeruginosa*, MRSA, and *Clostridium difficile* due to the therapeutic effect of the released Ga^{3+}. However, the increase of Ga content in PBGs decreased the degradation rate and subsequent Ga^{3+} release, which need to improve the controlled delivery of Ga^{3+} for antimicrobial applications [36].

The application of antibacterial agents against infectious diseases needs not only excellent bacterial killing efficacy but also lower or even no toxicity to the human normal cells. However, the biosafety of most metallic ion doped BGs is not ideal.

Nowadays, cerium (Ce) has been verified to possess the potential to serve as an effective and long-lasting biocide for preventing bacterial infections, due to its higher safety to human cells and unique antibacterial mechanism compared with other metal ions. The reversible conversion of Ce^{3+} ions and Ce^{4+} ions could alter electron flow and respiration of bacteria and react with the thiol groups (–SH) [49]. Moreover, the conversion could also induce oxidative stress on the surface of bacterial membranes by the generation of reactive oxygen species (ROS) *in vivo* [50]. ROS can attack the nucleic acids, proteins, polysaccharides, lipids, and other biological molecules to cause the loss of their functions, eventually killing and decomposing bacteria. In a previous study, the antibacterial activity of BGs that doped with 1, 5, and 10 mol% Ce was investigated by the quantitative viable count method. As a result, the BGs containing 5 and 10 mol% Ce showed a significant antibacterial effect against *E. coli*, but there were no significant differences between the antibacterial property of BGs containing 5 and 10 mol% Ce [51]. Boccaccini and coworkers reported phosphate bioglasses (PGs) co-doped with gallium and cerium at different ratios [52]. The antibacterial character of Ga/Ce-doped PGs is confirmed by turbidity measurements against *E. coli* and *Staphylococcus carnosus*. PGs doped with Ga showed a high antibacterial effect, but became toxic for cells when the Ga content increased. PGs doped with cerium oxide stopped (Gram-negative) or inhibited (Gram-positive) the growth of bacteria and showed good cytocompatibility, especially glasses containing 7 mol% of CeO_2. Interestingly, PGs co-doped with Ga and Ce (3Ga2Ce) not only showed strong antibacterial properties for both Gram-negative and Gram-positive bacteria but also exhibited excellent cytocompatibility without being harmful to mammalian cells.

11.2.1.2 Ionic Pro-osteogenesis Effects

Besides ions toward microbials, several metallic cations (Sr^{2+}, Mg^{2+}, Mn^{2+}, Li^{+}, Fe^{3+}, Ce^{3+}, etc.) attracted concerns in the context of bone tissue engineering due to their therapeutic effects to improve osteogenesis.

Strontium (Sr) is well known as an essential component in bone minerals with chemical similarities to calcium. Given by this fact, strontium has already been used as medication for osteoporosis in the form of strontium ranelate (SrR, $C_{12}H_6N_2O_8SSr_2$) [53]. Studies demonstrated

that daily ingestion of SrR can decrease the risk of vertebral fractures by 41% for those postmenopausal women who were suffered from osteoporotic structural damage. The mechanism of Sr anti-osteoporosis effect comes from its role in reducing osteoclastic activity and even causing apoptosis of osteoblast cells, which suppress bone formation. In addition, Sr has the potential to stimulate bone formation via enhancing the expression of osteoblast-related genes, promoting osteogenic differentiation of mesenchymal stem cells, and upregulation of osteogenic genes such as ALP and osteocalcin (OCN) [54]. However, direct oral administration of SrR is associated with side effects, such as toxic epidermal necrolysis. BGs used as Sr^{2+} ion delivery systems can provide an alternative therapeutic strategy on bone tissue engineering. Several formulations of glasses have been developed, in which Ca is partially substituted by Sr. These formulations are presented as silicate-, phosphate-, and borosilicate-based glasses [55–57], which can be produced as fine powders, granules, fibers, and three-dimensional (3D) scaffolds. For example, Gentleman et al. have created a series of BGs (SiO_2–P_2O_5–Na_2O–CaO) with Sr-substituted for Ca on a molar percentage basis [22]. The released Sr^{2+} from BGs increased osteoblast proliferation and ALP activity and inhibits tartrate resistant acid phosphatase (TRAP) activity and osteoclast-mediated resorption of CaP films, in a similar manner to the osteoporosis drug SrR.

Magnesium (Mg) is distributed throughout human organs such as bone, dentin, enamel, muscle, soft tissues, and serum. This element is emerging as a key player in many physiological functions, for instance, promoting bone formation, adenosine triphosphate (ATP) metabolism, and activation of vitamin D. It has been reported that the presence of Mg in BGs can improve the expression of collagen I, ALP, OCN, and osteogenic markers to improve bone growth [58]. Precise analysis of sol–gel-derived SiO_2–P_2O_5–CaO–MgO BGs (MgO 5, 8, and 10 wt%) demonstrated that 8Mg-BG showed the optimal compositions offering optimum hydroxyapatite formation rates and thicker HCA layer on the surface after being immersed in SBF. Both cell viability and ALP activities of 8Mg-BG samples were higher than the control sample as well [59].

More to the point, lanthanide (Ln) ions also have close resemblances to Ca^{2+} including similar ion radius, donor atom preference, and almost the same protein binding site, thus Ln^{3+} are called "bone-seeking materials" and used as a functional simulant of Ca^{2+}. However, Ln^{3+}-release BGs applied in osteogenesis activation is still in its infancy and certainly needs more characterizations yet, the reported results could still provide references to future researches about lanthanide ion family. For example, Salinas et al. prepared mesoporous SiO_2–CaO–P_2O_5 BG with Ce_2O_3 partially substituted for SiO_2 by evaporation-induced self-assembly [60]. The mesopore size gradually decreased with the increase of Ce_2O_3 substitution concentration, keeping the mesoporous order and *in vitro* apatite-like formation ability and high biological activity *in vivo*. The Ce_2O_3-MBG scaffold prepared by Shruti et al. has interconnected super-large pores and is suitable for vascularization, nutrient supply, and normal cell growth [61].

11.2.1.3 Ionic Pro-angiogenesis Effects

Successful tissue engineering/regeneration requires sufficient neovascularization in an initial stage in order to ensure cells, GFs, and nutrient/waste transport to function properly at new tissue formation site. For instance, angiogenesis plays a crucial role in the scaffold-based bone tissue repair process for cell survival and for the maintenance of any cell populations that may be recruited during tissue formation. Angiogenesis, refers as generation of new blood vessels from host preexisting ones, is regulated by many conditions. While the development of biomaterials that promote angiogenesis by their own degradation products, e.g. delivery of bioactive stimulating ions, is very appealing. To date, a few literatures have demonstrated positive angiogenesis effect of Ca^{2+}, Co^{2+}, Cu^{2+}, Si^{4+}, and Eu^{3+} ions.

Cobalt (Co) ion supplementation has been seen toxicity to osteoblasts and reduction osteoblast proliferation, especially at high concentrations [62]. However, studies also showed that a suitable dosage of Co^{2+} could mimic hypoxia condition triggering the formation of new blood vessels by stabilizing the activator of angiogenesis-related genes, hypoxia inducible factor 1 subunit alpha (HIF-1α), and thereby upregulating the expression of vascular endothelial growth factor A (VEGFA). Wu et al. incorporated Co^{2+} into MBG scaffolds. *In vitro* evaluation confirmed enhanced expressions of genes encoding the proangiogenic proteins VEGF and HIF-1α, as well as pro-osteogenic protein OCN in bone marrow stromal cells [31]. Furthermore, another *in vivo* study also showed that Co-containing glasses stimulated VEGFA and HIF-1α expression in blood vessels and cell nuclei, respectively, in the deep dermis layer of the dorsal region of rats, featuring considerable local stimulation of the angiogenesis process due to Co^{2+} release [30]. Given that, carefully selected doses of Co^{2+} in engineered tissue treatment that minimize the cytotoxic effects and maximize angiogenic potential could prove to be beneficial overall.

Copper (II) ions recently also impressed us with the angiogenesis effect. Cu^{2+} can bind and interact to important vessel growth mediators, e.g. VEGF, and modulate relative gene and protein expressions. Wang's group has fabricated a series of borate BG powders doped with varying amounts of Cu (0–3.0 wt% CuO), and afterward the powders were prepared into 3D porous scaffolds using a polymer foam replication technique [29, 63]. As shown in Figure 11.2a, Cu^{2+} release from glasses was beneficial for blood vessel formation as well as new bone growth compared to the undoped formula. According to *in vivo* study in a rat calvarial defect model, 3.0 wt% Cu-doped borate silicate glass scaffolds confirmed higher number of blood vessels for bone tissue engineering. In 2015, the same group re-melt the Cu-borate BG particles and formed microfibers by injecting a high-pressure jet of gas (Figure 11.2b) [64]. Ionic products of the Cu-doped glass microfibers *in vitro* stimulated increased angiogenesis capacity in a manner of positive correlation to Cu^{2+} content. When the microfibers were used to treat full-thickness skin defects in rat, Cu-doped materials significantly induced more vessel formation at the defect site, while Cu^{2+} did not show marked improvement of collagen deposition, maturity, and orientation compared with the microfibers without doping at 14 days post-surgery.

11.2.1.4 Ionic Anticancer Effects

Magnetic hyperthermia therapy against tumors relies on the susceptibility of tumor cells to heat, which may cause irreversible damage to tumor cell membranes and initiates protein denaturation. The transition metallic ions are a category of photothermal agents for potential photothermal therapy which are also likely to exert toxicity to tumor cells by depressing cell metabolism and proliferation [65]. Therefore, several studies have proposed the incorporation of transition metallic ions into BG network for tumor inhibition.

Liu et al. reported the element (Cu, Fe, Mn, Co)-doped bioactive glass-ceramic (BGC) scaffolds fabricated by 3D printing technique [66]. All the doped-BGC scaffolds displayed good photothermal performances following the sequence: Cu-BGC > Fe-BGC > Mn-BGC > Co-BGC. The photothermal effect of the scaffolds was also dosage dependent and could be modulated through changing the doped ion type and amounts. On the other hand, compared to blank control, the Fe-BGC and Mn-BGC scaffolds promoted cell adhesion, proliferation, and osteoblast differentiation of rat bone mesenchymal stromal cells (rBMSCs) together with stimulated higher VEGF expression lever. It concluded that Fe-/Mn-doped BGC scaffolds offered a neat choice for bone tumor therapy and simultaneous bone regeneration.

Liu et al. also fabricated Mn-doped MBG scaffolds and further loaded chlorin e6 (Ce6) into Mn-MBG scaffolds. Such composite scaffolds showed a combined photothermal and photodynamic

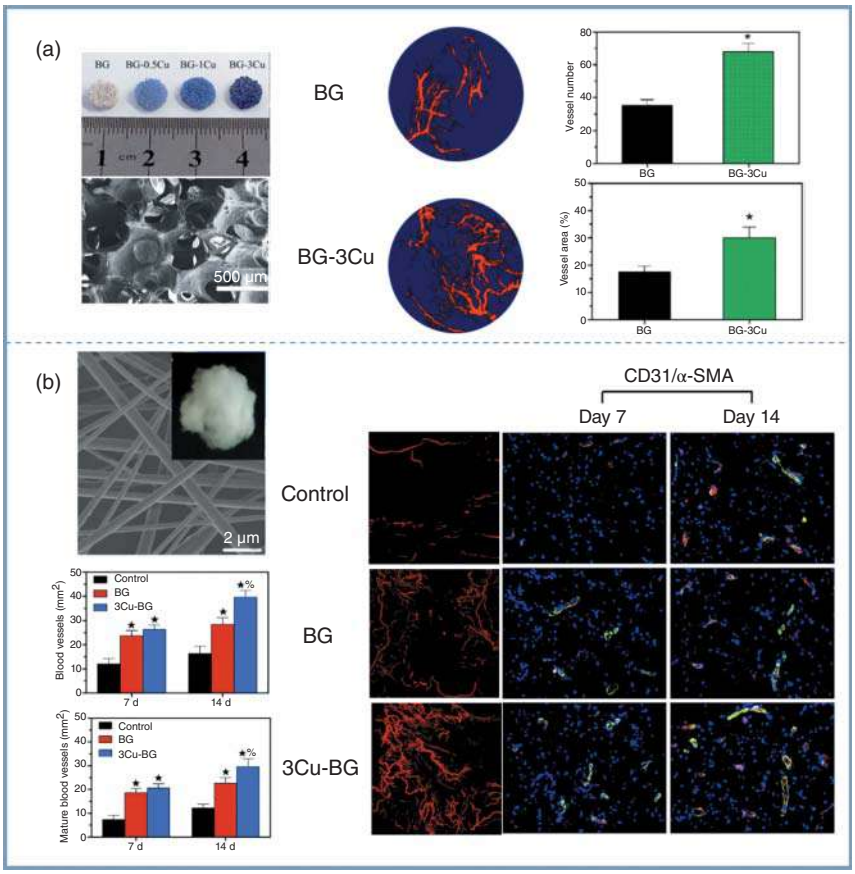

Figure 11.2 (a) Cu-doped borate bioactive glass scaffolds as a controlled delivery system for copper ions in stimulating osteogenesis and angiogenesis in bone healing. Borate glass scaffolds (pore size ~ 200–400 mm) doped with varying amounts of Cu (0–3.0 wt% CuO) were fabricated using a polymer foam replication technique. When implanted in rat calvarial defects for eight weeks, the scaffolds doped with 3 wt% CuO showed a significantly better capacity to stimulate angiogenesis and regenerate bone compared to the glass scaffolds without doping. (b) Cu-doped borate bioactive glass microfibers stimulate angiogenesis and full-thickness skin defect in a rodent model. The Cu-doped fibers (3.0 wt% CuO) promoted angiogenesis in the defect area and show great potential in wound or soft tissue regeneration. Source: (a) Wang et al. [29], Figure 01, 06, 10 [p. 196, 199, 201]/with permission from Elsevier; (b) Zhao et al. [64], Figure 01, 09, 12 [p. 382, 386, 389]/with permission from Elsevier.

effect caused by the doped Mn and the loaded Ce6, respectively [67], which achieved a synergistic enhanced therapeutic efficacy against tumors in comparison to photothermal therapy (PTT) or photodynamic therapy (PDT) treatment alone. More importantly, after a short term of PTT and PDT therapy, there was no loss of the biocompatibility and osteoinductivity with the Mn-MBG/Ce6 scaffolds. On the other hand, the Mn-MBG/Ce6 scaffolds promoted expression of several osteogenic genes of rBMSCs, indicating favorable bone regeneration with such scaffolds.

11.2.2 Control of the Ion Release Profiles

As discussed above, the pharmaceutic effects of functional ions are dosage dependent, and so do the possible toxicities. Therefore, BGs with ion delivery attempt to achieve an optimal balance among

particular issues regarding therapeutic effects and bio-safeties. It is undoubted that the ion release profile predominates the final performances of the ion-doped BGs. Normally, the ion release is accompanied with glass dissolution process which is determined cooperatively by the properties of both the ions themselves and BG matrix materials.

11.2.2.1 Ion Solubility

The ions themselves exist within the glass network in different forms. Some participate in network forming and are bonded with complete integrated network connectivity; however, some ions mainly take the role of glass network modifiers that have significantly changed and less-bonded chemical environment along with more nonbridged oxygen atoms. In this way, ions of higher degree of freedom are ready to release out. A more open and disrupted network of BGs allows water penetration easily to contact with the ions on the other hand. Molecular dynamics simulations confirmed that modifier cations and nonbridging oxygen (NBOs) atoms can act as Lewis acidic center allowing for strong interactions between BGs surface and H_2O [68]. To the contrast, bridging oxygen atoms are more hydrophobic, and no significant interaction with water has been observed.

In addition, the ion release behaviors controlled by diffusion are dependent to their own diffusion coefficient related to ionic radius, charges, and diffusion energy barriers. In many cases, the use of mixed alkali ions of different ionic radii is noted to decrease ion release from standard silicate glasses compared to structures with one loaded alkali oxide only [69]. And commonly an alkali ion with larger radius, for example, K for Na, can open the glass structure and enable faster ion exchange and ion release. Du and Xiang studied the Sr substitution effect on the structure, diffusion, and dynamic properties of 45S5 BGs via MD simulations [70]. The trajectories in Figure 11.3 provide direct visualization of different diffusion pathways for the three types of modifier ions (Na^+, Ca^{2+}, Sr^{2+}). Na^+ diffuses much faster than Ca^{2+} and Sr^{2+} and explores much larger area

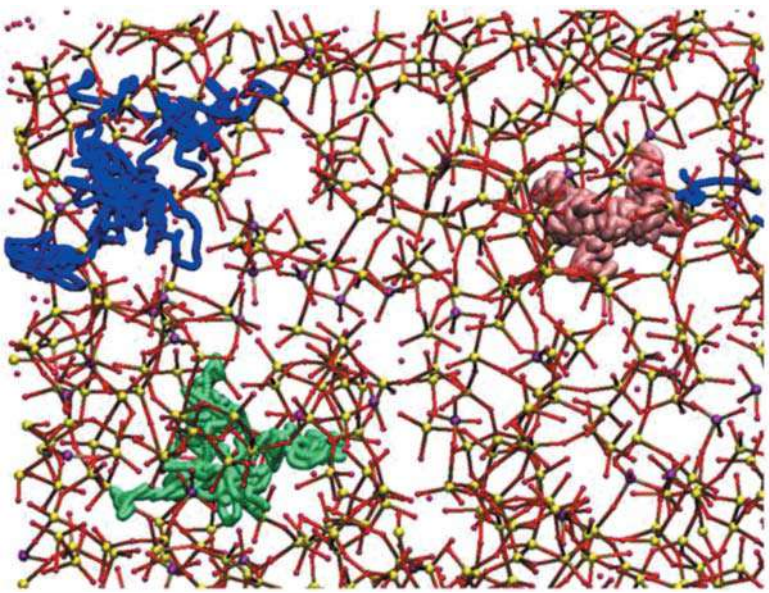

Figure 11.3 Diffusion pathways of three atoms: Na, Ca, and Sr. Trajectories from MD simulations for 45S5-5Sr at 2000 K in the duration of 20 ps. Pink ball: Sr; blue ball: Ca; green ball: Na; small yellow ball: Si; small purple ball: P; small red ball: O. Source: Reproduced with permission from Du and Xiang [70].

and configurational space, and diffuses longer distances. The diffusion pathway of Ca^{2+} and Sr^{2+} by contrast are much more localized indicating much less diffusion of two alkali earth ions.

11.2.2.2 Crystallinity

BGs have a tendency to crystallize when there is a high concentration of NBO atoms contributing to low network connectivity, either during the preparation process or further heat treatment. Therefore, it is reasonable to modulate the ion release rate by altering the glass crystallinity. Sintering is the most common approach to obtain different crystallinities, which has already been applied to produce glass-ceramics with partial crystallization of selected phases and partially remained glass phase [71]. Cacciotti et al. evaluated the dissolution rate of sol–gel derived BGs after heat treatment at different temperatures [72]. Crystalline phases were detected and very slow dissolution behavior was observed at 1100 °C as compared with BGs heated at 700 °C.

On the other hand, the compositions of BGs are able to change the devitrification tendency so as to obtain different heat processing temperature windows. For instance, Peitl et al. showed that silicate BGs can crystallize into either sodium calcium silicates (such as combeite, $Na_2O–2CaO–3SiO_2$) or wollastonite ($CaO–SiO_2$), with the latter showing a significantly increased processing window of 300 K compared to around 100 K for the former [73, 74]. Li et al. found that the substitution of Sr^{2+} for Na^+ induced an increase of the glass transition temperature (T_g) from 591 to 760 °C [75]. Brauer et al. reported that with partial substitution of MgO for CaO, the glass degradation rate decreased with the delay in HCA layer formation, which was ascribed to the effect of ionic field strength and diverse bonding configurations of glass [76].

11.2.2.3 Specific Surface Area

As mentioned before, the dissolution reaction starts from the interface between BG materials and the media after contacting with release medium. Hence, specific surface area is a critical parameter that can influence the degradation rate.

The best example to elucidate the importance of high surface area is a comparison among melt-quenching BGs, sol–gel derived BGs, and MBG materials. Due to the presence of micropores, sol–gel glasses show higher specific surface areas and accelerate dissolution rate compared to conventional melt-derived BGs. Likewise, mesoporous structure of MBGs greatly elevates the specific surface area of sol–gel BGs. The interconnected nanoscale-pores within MBGs favor solution penetration and circulation so as to improve the reactivity of BGs [4, 35].

On the other hand, the forms of BGs result differences in specific surface areas. For example, Maçon et al. compared 45S5 in two different particle size ranges (Bioglass, BG: particle size 45–90 μm; NovaBone, NB: 90–710 μm). The results clearly showed that BGs formed apatite slightly faster than NB, which is most likely caused by the smaller particle size and larger relative surface area of BGs, allowing for faster ion exchange kinetics than NB [77].

11.2.2.4 Medium Condition

Preliminary characterizations of BGs before *in vivo* tests are typically accomplished via immersion in acellular solutions, such as deionized water, SBF, different buffer solutions, and various cell culture medium formulations. Results proved that the dissolution rate of BGs can also be influenced by the surrounding medium conditions including medium temperature, pH, and medium composition [78]. For example, the dissolution rate of silicate BGs was enhanced with an increment in pH from 2 to 8.5 because of hydrolysis acceleration. The Si—O—Si bonds are destroyed due to the nucleophilic attack of OH^- in water-containing medium [78]. As the pH in the body can be acidic under inflammation or infected conditions, BGs immersion studies at low pH are also necessary.

A study by Bingel et al. investigated the ion release and apatite formation of fine 45S5 powder at an initial pH of 5 in sodium acetate buffer [79]. As expected, ion release was much higher comparing to that in a Tris-HCl buffer at a pH of 7.35 due to faster ion exchanges. Proteins in the release medium has an impact on the ion release as well. Sepulveda et al. performed a comparative assessment on the dissolution behavior of BGs in SBF or in cell culture medium [80]. Inductively coupled plasma (ICP) mass spectroscopy results demonstrated that positively charged serum proteins in culture medium can adsorbed on the surface of BGs and then suppress the glass dissolution.

In addition, BGs in many cases are not solely used but form composites with other materials in different terms of scaffolds, films, fibers, or hydrogels; hence, the ionic dissolution rate is influenced by other components as well. Those second phase of materials are commonly expected to prolong the ion release distance from BGs that are embedded. In this sense, the adjustment of therapeutic ion release from complex BG-containing delivery system need to consider more factors besides the BGs themselves.

11.3 Drug Release

As described previously, BGs can be reservoirs to release bioactive ions for specific purposes in tissue regeneration processes including the improvement of osteogenesis, angiogenesis, and new tissue growth. It is simply and straightforward to fabricate functional ion-doped BGs. However, constraints in effective local ion concentration and the potential ion toxicity make these ionic therapeutic agents not enough to achieve multifunctional properties of BGs. As a solution, BGs have been explored to behave as a bioactive platform to load therapeutic agents including drugs, biomolecules, and alternative small molecules of GFs. The drug loading aims at promoting tissue repair, providing support of treatment and decreasing postsurgical complications.

Current drug/molecule delivery strategies with BGs can be grouped into four types according to their loading mechanisms and the forms of carriers as well. A graphic illustration of four drug

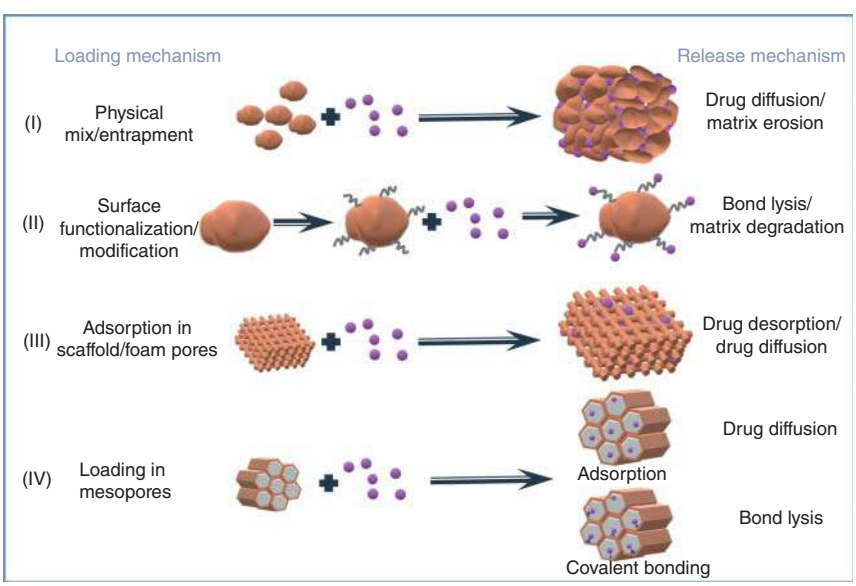

Figure 11.4 Illustrations of drug loading and release mechanisms from BG-based carriers.

delivery strategies is depicted in Figure 11.4. Interactions between drug species and BGs can be either physical or chemical in the final delivery systems:

(I) Drug and BGs powders are mixed together and directly compressed into a drug-loading monolith.
Once contacting to fluids, drugs diffuse out and the diffusion kinetics are determined comprehensively by the weight ratio of drug/BGs, release medium volume, and BGs degradation rate. For instance, Xie et al. firstly prepared melt-derived borate glass powders with the composition of $6Na_2O–8K_2O–8MgO–22CaO–54B_2O_3–2P_2O_5$ mol%, and then mixed it with vancomycin and phosphate-buffered saline (PBS) [81]. The paste was transferred into molds for self-hardening and forming cylindrical pellets (VBG). In comparison to commercially calcium sulfate (VCS), vancomycin in borate glasses showed longer antimicrobial effect due to slower resorption rate and gradually released at the concentration sufficient to inhibit bacterial growth during 18 days. *In vivo*, VBG pellets also presented the highest 81.25% negative rates of MRSA examination and osteomyelitis eradication for infected rabbits. However, the release kinetic is still unsatisfied and uncontrolled for achievement of long-term and effective drug concentrations at lesion sites. Therefore, additives including polymers, hydrogels, and microbeads are simultaneously entrapped in this system to establish diffusion hindrances and prolong drug release period [82]. The same group lately constructed similar borate BG pellets containing teicoplanin using chitosan/PBS solution instead of pure PBS, and they found that the release process sustained for around 30 days and still followed Fick's diffusion rules [83].

(II) Drugs are anchored on BGs particle surface through chemical bonding.
Size reduction of BG particles on some occasions brings beneficials because of higher surface area, enhanced bioactivity, and cell adhesion and other properties [84]. Bioactive glass nanoparticles (BGNs) recently have been developed for potential drug/gene delivery, bioimaging, and cancer therapy applications [85, 86]. In this regard, careful engineering of BGNs is a prerequisite for proper drug/molecule delivery, such as physiological stability, dispersity, improved immune responses, and so on.
The oxide network of BGs contains both bridging oxygens and nonbridging oxygens, and the surface chemical reactivity, namely the surface groups, of BGs is readily to be altered. Therefore, versatile functionalization/modification can be theoretically achieved, especially silicate BGs. By this means, initial burst release can be prevented and drugs grafted on the surface release along with bond lysis or BG matrix degradation. An interesting example is about that γ irradiation can play an equivalent role with chemical modification for the purpose of drug release modulation. Farag et al. prepared nano-bioactive 58S glasses particles which were treated with ^{60}Co γ irradiation at two different irradiation doses exposure times (25 and 50 kGy) [87]. The irradiation created more NBOs via breaking Si–O–Si network. These NBOs were susceptible to form more Si–OH groups on the surface of glass particles. As a result, negative-charged vancomycin drugs could present different states of interactions with the silanol groups so that to alter release kinetics.
Zarghami et al. synthesized amino-grafted BGNs via a post reaction with (3-aminopropyl) triethoxysilane (BGNs-APTES) [12]. Vancomycin was then immobilized via EDC/NHS cross-linking process onto the BGNs-APTES surface, and at the same time, the rest of drug entered pores in BGNs derived from sol–gel process. As a result, the release profile that had two stages include an initial burst release and subsequent constant-rate release, which did not fit any common models that have been explored to describe noncovalent bonding drug release. They raised a new mathematical model that the logarithm of cumulative released drug is a second-degree polynomial function of time logarithm.

Poor dispersion stability of BGNs in a physiological environment has limited their wide biomedical applications. Xue et al. proposed a novel idea to take advantage of Ca^{2+}-phosphate interaction to synthesize glycerolphosphate-functionalized bioactive glass nanoparticles (GP-BGNs) [85]. The GP-BGN particles exhibited monodispersity without aggregation, together with significantly enhanced particles stability in physiological environment, good hemocompatibility, and cellular biocompatibility, as well as high cellular uptake ability. It is worth noting that such modified particles can be further used to deliver other molecules by reactions with the surface terminal groups [88, 89].

(III) Drugs are adsorbed into the pores of BG scaffolds or foams.

The use of highly 3D porous structures instead of BG powder forms in tissue engineering is well accepted, such as macroporous scaffolds. The interconnected macropores facilitate cell, vascular, and nutrient penetration and transportation. Similarly, the drug/biomolecule species can also adsorb into such pores within scaffolds. Although physical adsorption of molecules to material surfaces is the simplest method of delivery, the loading and release of adsorbed functional molecules can be non-efficient. In such cases, surface functionalization again becomes important to avoid short-time drug retention, as Strategy (II) addressed above. For example, Wang et al. compared amino-modified MBG scaffolds with pure MBG scaffolds to deliver alendronate (AL) [90]. When amino groups were grafted covalently on the scaffold surface, the AL adsorption was increased almost twofold, with subsequent intensification of drug in the required area. It also revealed that the proliferation and osteogenic differentiation of rBMSCs-OVX were promoted by AL at a concentration of 10^{-8} M. Simultaneously, the osteoprotegerin (OPG) expression level was obviously upregulated by 10^{-8} M AL as well as the ratio of OPG/RANKL, an indicator of the anti-osteoclastogenic effect indicating that proper AL concentration can regulate osteoporotic bone regeneration by directly promoting osteogenic differentiation of bone mesenchymal stromal cells BMSCs as well as by promoting the osteoclastic inhibition effects of BMSCs to suppress osteoclast activity.

(IV) Drugs are loaded in mesopores of MBGs.

From melt-quenching BGs to sol–gel BGs, the presence of micropores plays important roles in improving bioactivity, degradation kinetic and biological properties. One step further, the highly ordered micropores are produced so as to increase the surface area, pore homogeneity, and pore volumes of BGs. These micropores are of nanoscale size falling in the range of 2–50 nm, thus such BGs are called MBGs. Likewise, similar to other mesoporous inorganics, MBGs also offer great opportunities for constructing delivery systems. Different terms of MBGs have been developed, e.g. powders, coatings, gels, nanoparticles, cements, and even 3D scaffolds [6]. The drugs, proteins, and GFs realize their loading into the mesopores generally through adsorption.

The adsorption process is driven by secondary forces between drug and surface including electrostatic force, van der Waals force, hydrogen bond, π–π packing, and capillary force. Chemical bonding is certainly another important stimulation for adsorption as that is called chemical adsorption. Adsorption is a superficial phenomenon; hence, either the physical or chemical interactions only occur on the pore surface. As such, the pore surface features (reactivity and specific surface area) clearly influence the drug loading capacity and release behavior, which is discussed in detail in Section 11.6. High specific surface area of MBGs represents an augment on the surface available for drug adsorption, and on the other hand allows the loading processes without the use of aggressive treatments, guaranteeing the stability of therapeutic molecules. In a word, drug delivery behaviors could be controlled by MBG porous

architectures. A variety of studies have demonstrated the achievements of optimal mesopore textures for MBG-based host-guest assembly and drug delivery, which aimed to treat different diseases or disorders.

11.3.1 Antibacterial Drugs

Prevention and treatment of bacterial infections is one of the greatest medical challenges in the field of cell/tissue transplantation as well as biomaterial implantation. Specifically, this problem occurs in various situations including trauma, reconstructive orthopedic procedures, and other local surgery. The bacterial infections could range from hard (e.g. bone) to soft (e.g. skin) structures with dangerous effects [91]. For example, chronic osteomyelitis is one of the major causes of morbidity and mortality worldwide. Oral or intravenous administration of large dosage antibiotics brings out the well-known issues related to antibiotic-resistance bacteria (PDR). The last frontier for the treatment of this disease requires the implantation of a controlled delivery system with the ability to locally release appropriate amounts of antibiotics or other antimicrobial agents for an extended period [92]. The delivery system can achieve *in situ* long-term and sustainable drug release all over the lesion area so as to reduce PDR risks and drug concentration change in plasma/organs of human body.

MBGs have been proved higher drug loading efficiency and prolonged release period compared to nonporous bioactive glasses (NBGs), thus attempts of delivering conventional antibiotics (gentamicin, vancomycin, tetracycline, ampicillin, etc.) were mostly focused on MBG-based carriers in recent decade. MBG carriers have been designed in various forms to achieve sufficient antibacterial inhibitory concentrations and effective prevention of biofilm deposition on implant surface.

To take gentamicin (GS) for an example, different MBG-based drug carriers were developed. As early as 2006, Xia and Chang synthesized ordered M58S and M77S MBGs with high specific surface area (277 and 400 m^2/g) by a two-step acid-catalyzed self-assembly process combined with hydrothermal treatment, while that of sol–gel 58S BGs was only 58 m^2/g [93]. As a result, three- to four-fold of gentamicin loading amounts were obtained in M58S compared with 58S, and the release curves crept slowly lasting for more than two weeks in SBF and in water. Moreover, the release profiles could be modulated by changing medium pH. In order to decelerate the drug release rate, Li et al. proposed to blend GS-preloaded MBG powders with poly-(lactide-*co*-glycolide) (PLGA) polymer matrix to form microparticles [94]. In both water and PBS, GS release from MBGs was very fast with more than 80 wt% released in two days. MBG/PLGA composite microspheres showed an initial release of about 33 wt% in the first day, and 48 wt% in two days, and a subsequent sustained release lasting for more than four weeks in PBS. Later on, Zhu and Kaskel fabricated MBG foams through sponge replication and also compared GS delivery behaviors with nonporous BG foams [95]. Due to abundant Si–OH and P–OH groups on the mesopore surfaces that linked to GS molecules by hydrogen bonds, MBG foams sustained GS release for more than seven days and varied along with medium pH values. In 2011, MBG precursor sols were dip-coated onto poly(L-lactic acid) (PLLA) porous scaffolds by Zhu et al. [96]. The mesopore directing agents were then removed by ethanol extraction instead of calcination so as to produce mesopores for GS loading. The drug-loading efficiency was increased simply by more dipping-dry cycles. In addition, the MBG coating significantly enhanced apatite deposition ability and bioactivity of PLLA scaffolds. Guo and coworkers in 2013 examined the antibacterial properties and biofilm formation on compacted MBG-GS disks [97]. The results confirmed that MBG-GS was able to significantly reduce bacterial adhesion and prevent biofilm formation of both ATCC25923 and ATCC35984. *In vitro* biocompatibility assays

Table 11.3 Some typical antibiotic delivery systems based on BG carriers.

Antibiotic	Drug carrier	Drug release	References
Gentamicin	• M58S/M77S powders • M80S-PLGA microspheres • Compacted MBG-GS disks	• Release curves crept slowly lasting for more than 2 wk • 80% of GS released from MBG in the first day while the percentage decreased to 44% from MBG/PLGA microspheres • Gent-MBG exhibits sustained drug release for more than 6 d	[93, 94, 97]
Vancomycin	• Borate bioglass powder mixture • Amino-functionalized BG nanoparticles (BGNs)	• Surrounding drug concentration retained above minimum inhibitory concentration (MIC) for 18 d • 1.5-fold increase of loading efficiency and half burst release compared to nonfunctionalized BGNs	[12, 81]
Tetracycline	MBG–*x*S95–*x*C–5P	CaO contents significantly influence the release kinetics because the chelation between the drug and the calcium species	[98]
Levofloxacin	• Zn-doped MBG scaffolds • ATP-capped MBGs	• Showed synergistic antibacterial effects against *S. aureus* and *E. coli* lasting for 18 and 8 d, respectively • ATP-capped MBGs showed equitoxic loading concentration of levofloxacin and more effective against bacteria than free drug	[99, 100]
Ampicillin	$CaO–SiO_2$ nanospheres	Gradually released in almost a week timeframe	[101]
Ceftriaxone	3D BG scaffolds with 60–65% porosity (bimodal distribution of macro- to micropore) with average pore size ~60 µm	*In vitro* and *in vivo* drug elution after 42 d showed drug release at least 10–15 times higher than minimum inhibitory concentration of ceftriaxone against *S. aureus* compared to parenteral treatment (two injections a day for 6 wk)	[102]
Curcumin	Ga-containing phospho-silicate glasses	25% within 72 h and prolonged release afterward	[103]

demonstrated that MBGs had better biocompatibility than NBGs, likely due to its mesoporous structure.

Table 11.3 summarized some typical BG-based antibiotic delivery systems, including commonly used first-line antibiotics and natural antibacterial products. A typical natural drug example is curcumin, which is highly expected to treat various diseases like inflammation, cancer, Alzheimer, and cardiovascular diseases. Malavasi et al. synthesized and characterized mesoporous Ga-containing phospho-silicate glasses loaded with curcumin as a new type of drug delivery systems (DDS) [103]. Their obtained results showed that Ga-containing glass loaded with curcumin is the most promising one as a DDS because it can be loaded with the largest amount of curcumin (4.7 mg/g) that is slowly released (25% within 72 hours), thereby allowing a prolonged therapeutic effect, and the presence of curcumin molecules in the SBF solution stabilizes Ga^{3+} ions, thereby preventing their precipitation. Besides, a few more herbal drugs (icariin, Yunnan Baiyao, polyphenols, etc.) have been loaded into BG carriers that gave out interesting preliminary results and diversify BG drug delivery systems [104, 105].

11.3.2 Small Therapeutic Drugs for Diseases

Implant biomaterials are commonly necessary for auxiliary use in defects after surgery removal of necrotic area or imperfects of other diseases. Local delivery of chemotherapeutic drugs by such implants is helpful to improve targeted and regional therapeutic effects, meanwhile reduce drug toxicity and side effects. It is well accepted in the fields of tissue engineering, would healing, prosthetic, and plastic medicine. Here, typical bone disorders as a representative treated with BG-based implantable drug livery systems are summarized in Table 11.4.

Bisphosphonates (BPs), containing a P–O–P linkage in a drug molecule, are one of the most used nonspecific synthesized chemo-drugs. The P–O–P linkage has an affinity to bone apatite, by that BPs can regulate bone mineralization and metabolism. Nowadays, BPs drugs have received widespread use toward bone disorders, such as osteoporosis, osseous imperfecta, osteosarcoma, and osseous metastasis from tumors. Therefore, BPs are frequently selected as drug model to test BG-based carrier performances to show potentials of BG–BPs complexes in clinic. Zhu et al. synthesized mesoporous silicate bioglass microspheres with different CaO contents for AL delivery [117]. It was found that increased CaO content can slow down AL release rate due to the combination reasons of less integrated mesopore structure and stronger Ca–AL interaction. Both of Ravanbakhsh's [114] and Wang's [90] groups attempted to functionalize MBG nanoparticles or scaffolds with amino groups, and then negatively charged AL were trapped/adsorbed into mesoporous channels. The amino groups certainly increased AL loading capacity and also prolonged the release time period. Another interesting study on controlling AL release manner was proposed by Diba et al. [110] who investigated the strong interaction between AL and 45S5 BG particles, and created hybrid biomaterials by immersing BG particles into AL solutions at different pH and AL/BG ratios. AL disrupted BG silicate network through substitution of phosphates in BG particles and thereby formed Ca cation-AL coordination complexes presenting tunable morphology, chemical composition, and structure. These hybrid particles showed *in vitro* controlled anti-osteoclastic effect and *in vivo* strong capacity to facilitate regeneration of bone defects in an osteoporotic rat model.

The third generation BPs including AL, zoledronate (ZOL) have attracted attentions to be delivered for bone tumor treatment, either primary or secondary. For example, ZOL was incorporated in metallic surgical implants via mesoporous glass coatings. Zhu et al. deposited HA particulate coating on stainless Kirschner wires by plasma spraying, and then loaded ZOL-containing mesoporous silica nanoparticles (MSN) onto the surface as well by acid etching [118]. In a result, the MSN-HA composite coating showed eightfold of ZOL loading efficiency compared to pure HA coating.

Besides those clinic medications, some interesting drug alternatives, which are not conventionally produced in industry for clinic use, have been encapsulated in BG-based carriers to create functional biomaterials for tissue engineering. The alternative chemicals are capable of sometimes simulating GFs without loss of activities or playing roles in regulating relative signaling pathways, such as inhibitors or activators [119]. The local delivery of these particular drugs is definitely worthy to investigate.

For example, phenamil, known as an irreversible inhibitor of sodium channel, has recently been highlighted as a potent small molecule bone morphogenic protein (BMP) signaling activator. Lee et al. co-delivered phenamil and Sr^{2+} with BG nanoparticles as carriers [120]. While Sr^{2+} constitutes "intrinsically" BG nanoparticle chemistry, phenamil is "extrinsically" loaded onto the mesopores of nanoparticles. These two molecules are internalized to cells to synergize the osteo/odontogenic stimulating BMP pathway.

Table 11.4 List of therapeutic drug delivery systems based on BGs for bone disease/disorder treatment.

Bone disorder	Drugs	Drug carriers	Drug release	References
Osteoarthritis	Acetaminophen	Cu-doped BG spherical clusters	Drug release profiles were influenced by Cu content, particle morphology, and porosity	[106]
	Dexamethasone	• Boron-containing MBG foams • 3D-printed Sr-MBG scaffolds	• The foams with a higher large-pore porosity (86% and 90%) have higher loading efficiency, but the large-pore porosity had no obvious effect on DEX release • Sr-MBG scaffolds exhibited similar sustained release behaviors. 75–85% of the loaded DEX was rapidly released in the first day, and then much more slowly	[107, 108]
	Ibuprofen	• Cu-doped BG spherical clusters • 3D-printed MBG/SA–SA scaffolds	• Drug release profiles were influenced by Cu content, particle morphology, and porosity • Exhibited a relatively rapid release rate in 12 h, and then 70% of ibuprofen released slowly within 168 h	[106, 109]
Osteoporosis/ osteogenic imperfecta	Alendronate Zoledronic acid	• Amino modified MBG scaffolds • Hybrid Ca_{BG}-AL complexes. • 45S5 Bioglass®/PLA coated scaffolds	• AL release from amino-modified MBGs is slower than that from unmodified scaffolds due to covalent bonding • pH controlled AL release from lysis of phosphate–Ca^{2+} interactions • PLA coating retarded ZOL release	[90, 110] [111]
Osteoporosis/ osteogenic imperfecta	Ibandronate	Mesoporous SiO_2–CaO–P_2O_5 and SiO_2–SrO–P_2O_5 bioglasses wrapped in PCL films	Not discussed	[112]
Osseous tuberculosis	Isoniazid/ rifampin	3D-printed macro/meso-porous BG composite scaffolds	COOH- and CH_3-grafted silicate mesoporous bioglasses enhanced the affinities specifically between drugs and mesopore walls	[113]
Osteosarcoma	Alendronate	MBG sub-micro particles	Si–OH and PO_4 groups in MBG particles achieved sustained release	[114]
	Camptothecin	MBG powders derived from rice husk (rMBG) and that grafted with folic acid (FA)	A rapid release of camptothecin (CPT) from rMBG and rMBG-FA occurred within 1 d and was sustained until day 7	[115]
	Doxorubicin	• MBG nanospheres • Eu-containing MBG nanospheres (60% SiO_2–(36 − x)% CaO–x% Eu_2O_3–4% P_2O_5)	• The loading amount and release kinetics of doxorubicin (DOX) can be controlled by adjusting the initial drug concentrations and the pH microenvironment • Eu content and pH of release medium controlled DOX release behaviors	[101, 116]

Wu's groups have developed MBG scaffolds for delivery of dimethyloxallyl glycine (DMOG) molecules, which is proved to be an effective reagent for enhancing HIF-1α stabilization [121]. The locally released DMOG in the periphery of bone defects, functioned similar to VEGF, stimulated better angiogenesis and osteogenesis performances simultaneously.

11.4 Biomolecule Release

Biomaterial-based tissue engineering is a comprehensive process involving cells, GFs and materials. In this context people have explored various physical cues and biochemical cues regarding to materials or cell activities for the purpose of optimal tissue healing. GFs are the most commonly used biomolecules to create favorable micro-environment to guide cellular behaviors and tissue growth by binding to cell surface receptors, which in turn activates signaling pathways. Local release of GFs from 3D porous scaffolds was proposed in early studies. However, GFs adsorption in scaffold reservoirs induced low drug retention and high burst release, which probably caused excessive dosages followed by proteolytic degradation, short half-life of GFs, and the gravest problem of immunological rejection. Similarly, other GFs carriers, such as hydrogels, sponges, bone cements, are also restricted owing to rapid release and loss of GFs bioactivity [122]. Recently, much effort has been made on MBG materials with feature of high surface areas that can obtain appropriate GFs release kinetics, so as to become an ideal GFs carrier candidate with lower effective dosages, low immunogenicity, and inherent pro-osteogenesis properties.

Wu et al., for the first time, investigated MBG scaffolds for the delivery of VEGF [123]. Here, the mesopores of MBG was 5.2 nm, which was believed to be able to load VEGF. After directly being impregnated into VEGF-PBS solutions at 20 or 80 ng/ml, about 95% of VEGF was loaded into MBG scaffolds. Although there was a slight burst release in the first day, the VEGF can still be detected even on day 14. To the contrast, nonporous BG scaffolds released all of GFs in the first day. Such sustain release of VEGF from MBG scaffolds was attributed to combined retardant effects of high surface area and fast apatite formation on the surface.

BMP family have acknowledged acceptance of substantial potential to accelerate bone regeneration. Two groups, Xia et al. [124] and Dai et al. [125], both developed mesoporous silicate bioglass scaffolds of $CaO–P_2O_5–SiO_2$ and $CaO–MgO–SiO_2$ formulations respectively for BMP-2 delivery. Berkmann et al. furthermore *in vivo* confirmed spray-dried MBG microspheres as prolonged local release system for BMP-2 to support bone repair [126]. Tang et al. proposed the concept of "size-matched mesoporous entrapment" for rhBMP-2 delivery [127], and to fulfill such proposition through the fabrication of a trimodal macro/micro/nano-porous BG scaffold. They tailored 7.5 nm of mesopores and 3D cubic (*Im*3*m*) mesoporous structure matching the dimension of rhBMP-2 molecule ($7 \times 3.5 \times 3\ nm^3$) to achieve a desirable immobilization, and further realized optimal bone regeneration by cooperation of multiscale structure and rhBMP-2 (Figure 11.5).

In consideration of inherent limitations about GFs, some other biomolecules have been concerned to replace GFs and offer a much safer solution when avoiding concomitant complications or even tissue regeneration failures, such as polypeptide, nucleic acid, small molecular GF alternatives.

Parathyroid hormone (PTH) is an 84-amino-acid polypeptide secreted from the parathyroid gland, that is essential for the maintenance of calcium homeostasis through, in part, its regulation of bone remodeling. Liang et al. modified PTH (1-34) sequences and designed a new PTH related protein named PTHrP-1, which was afterwards introduced into MBG scaffolds [128]. *In vivo* results revealed that the PTHrP-1-MBG scaffolds facilitated new bone formation and a higher

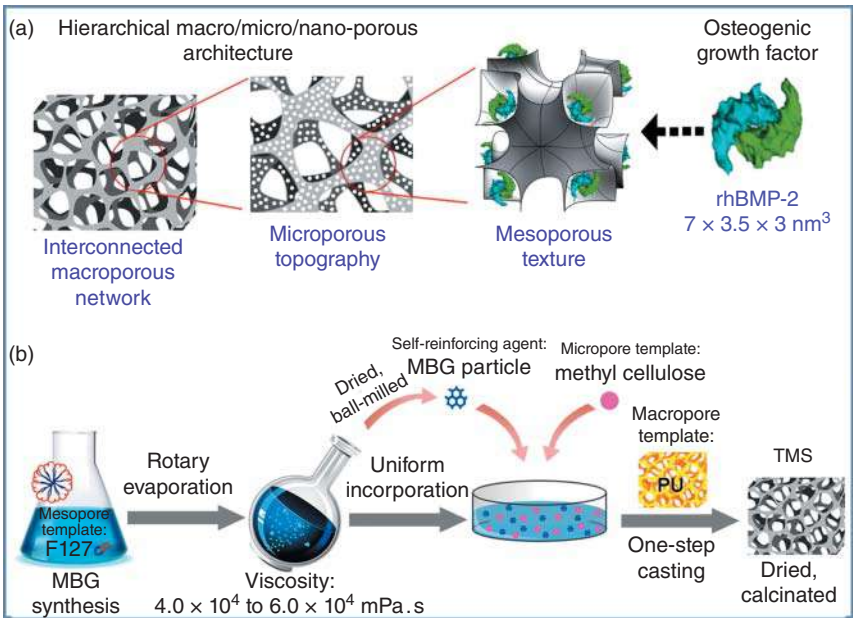

Figure 11.5 (a) Design of trimodal macro/micro/nano-porous scaffold loaded with rhBMP-2 for accelerated bone regeneration. (b) Schematic illustration of preparing trimodal MBG scaffold (TMS) by a modified multi-template method involving "viscosity controlling" and "homogeneous particle reinforcing" processes. Source: (b) Tang et al. [127], Figure 01 [p. 310]/with permission from Elsevier.

rate and quality of spinal fusion in a rat posterolateral spinal fusion model. Zhu et al. grafted one type of osteopontin sequenced polypeptide SVVYGLR onto mesopores of mesoporous $CaO–SiO_2$ bioglasses, which can mimic VEGF to specifically facilitate endothelialization and new vessel formation [129].

In recent years, increasing interests were raised to design BG nanoparticles for gene delivery due to their biocompatibility, biodegradability, and biological stability. Genetic modification of cells by proper delivery genes (siRNA, miRNA, and pDNA) toward cell cytoplasm or the nucleus has shown great promise for treating diseases and repairing damaged tissues. Kim et al. endeavored to synthesize nano-MBG vehicles for standard siRNA molecules [130]. They carefully selected different pore directing surfactant and reaction solvent to obtain tunable mesopores within BG nanoparticles. The results showed that larger mesopores (~6 nm) had a higher siRNA loading efficiency around 5–7%. The *in vitro* release was fairly sustainable, showing an almost linear pattern for up to three to four days, and the total siRNA quantity released was relatively high at ~70–75% of the initial loading quantity. This is not enough for continuous long-term release of genetic molecules, but it is believed to be acceptable for temporary target gene silencing in cells.

11.5 Dual/Multi-species Release

As summarized above, BG-based drug carriers in terms of nanoparticles, coatings, scaffolds, etc. are one of the most versatile, sophisticated and safe candidates for local species release including ion dopants, small drug molecules, large biomolecules or their alternatives. Basically, it is a natural direction to develop BG systems to simultaneous deliver two or even more species so that

multifunctional biomaterials are obtained. Those loaded species ready for local release can work independentaly providing inherent functions or coordinate with other species achieving synergistic performances. Loading sites within BG carrier matrices for larger drugs or biomolecules are limited to pores and surfaces, while the ions are doped in the BG framework without occupying surface areas, hence, diversities of multi-species delivery need to be considered among drug/bioactive molecules and functional ions. In this regard, drug–drug, GF–GF, or drug–GF combinations commonly require more than one carrier besides the BG-based materials to obtain particular separately controlled release profiles of each species. As a solution, BG-based carriers could instead develop composites with another cooperative delivery system.

Four typical types of loaded species combinations including (i) ion-therapeutic drug [104, 131]; (ii) ion–GF [116, 132, 133]; (iii) drug–drug [113, 134]; (iv) GF–GF [135] are briefly discussed here, and some examples were depicted in Figure 11.6, Figure 11.6a gives the schematic mechanism of Ag^+-doped BG nanoparticles, which evidenced good antibacterial performances in a bacteria infected tooth. Unlike microparticles or bulk materials [131], the Ag^+/tetracycline-BGNPs present unique intracellular delivery after bounding on bacterial membrane. On one hand, the internalization of tetracycline inhibited bacterial protein synthesis. On the other hand, the internalization of Ag^+ ions primarily ruptured bacterial membrane. Both of the *in situ* delivered species cooperatively obtain thorough bacteria killing. Similarly, epidermal growth factor (EGF) loaded Cu-BGn release EGF biomolecules and Cu^{2+} ions for synergistically enhancing angiogenesis before and after cell-internalization via micropinocytosis [132]. In addition to the role of Cu^{2+} ions in inhibiting bacterial infection, the released bioactive ions (calcium and silicate) could stimulate dental pulp mesenchymal stromal cells (MSC) differentiation to odontoblast and ultimately for pulp regeneration. However, ampicillin/gentamicin co-delivery system in Figure 11.6b employs modified surface for one drug grafting and inner mesopores for another one [134]. The results indicate that drugs inside the nano-assembled layer on particle surface release less sustainedly compared to that inside mesopores. Tang et al. (Figure 11.6c) developed a 2-*N*, 6-*O*-sulfated chitosan (26SCS) functionalized dual-modular scaffold composed of MBG with hierarchical porous structures (module I) and GelMA hydrogel columns (module II) *in situ* fixed in hollowed channels of module I, which is capable of realizing differentiated delivery modes for osteogenic rhBMP-2 and angiogenic VEGF [135]. A combinational release profile consisting of a high concentration of VEGF initially followed by a decreasing concentration over time, and a slower/sustainable release of rhBMP-2 was realized by immobilizing rhBMP-2 in module I and embedding VEGF in module II. Systematic *in vitro* and *in vivo* studies proved that the two coupled processes of osteogenesis and angiogenesis are well-orchestrated and both enhanced due to the specific GFs delivery modes.

11.6 Release Modulation on MBG-Based Carriers

MBGs show superiorities to construct delivery systems in comparison to conventional BGs due to the significant texture and bioactive features. The high specific surface area, tunable pore size and pore volume, controllable porous texture, and versatile surface activity of MBGs have been inspiring a surge of explorations on local species release.

The mesopores are supposed to serve as temporary species reservoirs till release occur upon implantation. Hence, regulation of mesoporous texture properties, such as pore size, pore inner-connectivity, pore surface charges, etc., are the most fundamental task for better species delivery performances. Here, how the crucial factors of mesoporous structures influence species delivery are briefly discussed for highlighting MBG potentials in drug/species delivery.

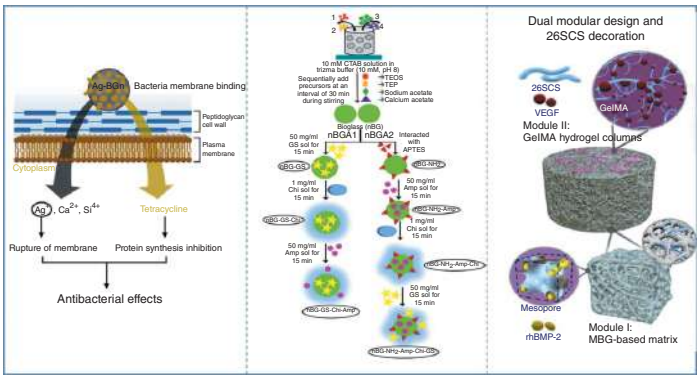

Figure 11.6 Example illustration of BG-based dual species delivery systems. (a) Design of the Ag ion and TC drug co-delivered BG NPs with enhanced antibacterial activities through internalizing Ag^+ and TC at the same time. (b) Schematic flowchart for the synthesis of dual drug loaded CTAB templated bioactive glass. TEOS, tetraethyl orthosilicate; TEP, triethyl phosphate; GS, gentamicin sulfate; Chi, chitosan; Amp, sodium ampicillin; APTES, 3-aminopropyl triethoxysilane. (c) Design of the 26SCS functionalized dual-modular scaffold for GFs delivery to enhance bone regeneration. The two modules include rhBMP-2/26SCS loaded amino-functionalized MBG with multilevel pores (MN/B/S, module I) and VEGF/26SCS loaded GelMA hydrogel columns (G/V/S, module II) *in situ* fixed in the hollowed channels of the module I. Source: (a, b) Reproduced with permission from Lee et al. [131], El-Fiqi et al. [132], and Gupta et al. [134]; (c) Tang et al. [135], Scheme 01 [p. 05]/with permission from Elsevier.

11.6.1 Pore Size

Species-pore size match is one essential premise for encapsulating guest species. Only when the guest molecules enter mesopores other than only adsorbing on the out surfaces, the loading efficiency can then achieve a high level and then the porous microstructure of MBGs is able to take responsible to adjust local release profile.

Pore size and size distribution are mainly determined by the synthesis process, namely the size of surfactant micelles. Previous studies have adopted different surfactant templates to direct mesopore formation. A classic experiment by Zhao et al. assessed two surfactants (P123 and F127) for preparing MBG powders. It was observed that P123-MBGs possess superior surface area and pore volume, and thereby induce much better drug loading efficiency (47.3%) with metoclopramide, as compared to F127-MBGs (16.6%) [136]. In another experiment, three surfactants (cetyltrimethylammonium bromide [CTAB], P123, and F127) were compared for their ability as drug (triclosan) delivery system. The loading efficiency of the MBGs were 10.7%, 9.1%, and 9.7% for CTAB, F127, and P123 respectively. Therefore, it can be speculated that the use of surfactant-CTAB is a better choice for improving drug loading efficiency of MBGs [137].

In recent years, large-mesopore structure of MBGs were achieved via some new methods. Miao et al. [138] reported a relatively simple W/O microemulsion method to synthesize MBG microspheres with loose and large-mesopore structure with an average pore diameter of 19.8 nm that is very suitable to load biomacromolecules, for example, serum albumin protein [139]. Tang et al. reported a novel biphasic delamination method to fabricate MBGs, and the average mesopore size was up to 21.87 nm for biomacromolecule encapsulation [140].

11.6.2 Pore Structure

Pore morphology, volume, and internal pore connections are important factors influencing mesoporous structure that concerns drug delivery. Recently, some delicate designed MBG carriers with novel pore structures offer more divergent ways to improve the guest storage as well as sustained drug release, for instance, hollow MBG nanostructures.

In comparison to solid nanospheres, hollow MBG nanospheres undoubtedly possess enlarged space for species storage. Several groups have successfully prepared hollow mesoporous bioactive glass (HMBG) nanoparticles with emulsion assisted sol–gel processing. Wang et al. firstly synthesized HMBG with tunable shell thickness and then regulated mesopore structure within the shell [141]. Corresponding to those different mesoporous structures, they achieved varied ibuprofen loading capacities and release rates. Thereinto, HMBG with orderly penetrative tunnels exhibited the best performance, which might transfer the drug molecules into the interior hollow cores and ensure IBU sustained release behavior.

Sun and coworkers have developed MBG nanospheres with hierarchical dendritic structure for cancer treatment, i.e. inner mesopores exhibit hexagonal channels and external mesopores show radial channels [142]. Based on the plasma concentration of Dox after intravenous administration with Dox-dendritic MBG nanospheres, the Dox-dendritic MBG group showed longer half-life, higher peak plasma concentration, and much slower release rate compared with regular mesoporous silica nanosphere. Such superior bioavailability of Dox delivered by dendritic MBG nanospheres is believed to be attributed to the unique mesopore structure that protects drugs from degradation under physiological conditions and allows slow drug release from inner mesopores in radial arrangements.

11.6.3 Compositions

Particular constituents in MBG show varying degree affinities with certain species. Yu et al. proposed a novel strategy of mesoporous BGN to deliver drugs and miRNA through interactions between Ca^{2+} and drug/miRNA groups without any cationic polymer modification (Figure 11.7) [143]. It is well known that Ca^{2+} ions have strong interactions with phosphate, carboxylate, or sulfate groups in nucleic acid or drugs. Based on this mechanism, hydrophilic diclofenac sodium was chosen as a drug model. After eliminating the specific surface area influences, BGN demonstrated an over 45-fold increase in drug loading (diclofenac sodium) and 7-fold enhancement in miRNA binding via Ca^{2+}–PO_4^{3-} interaction, over their corresponding MSN. BGN also showed

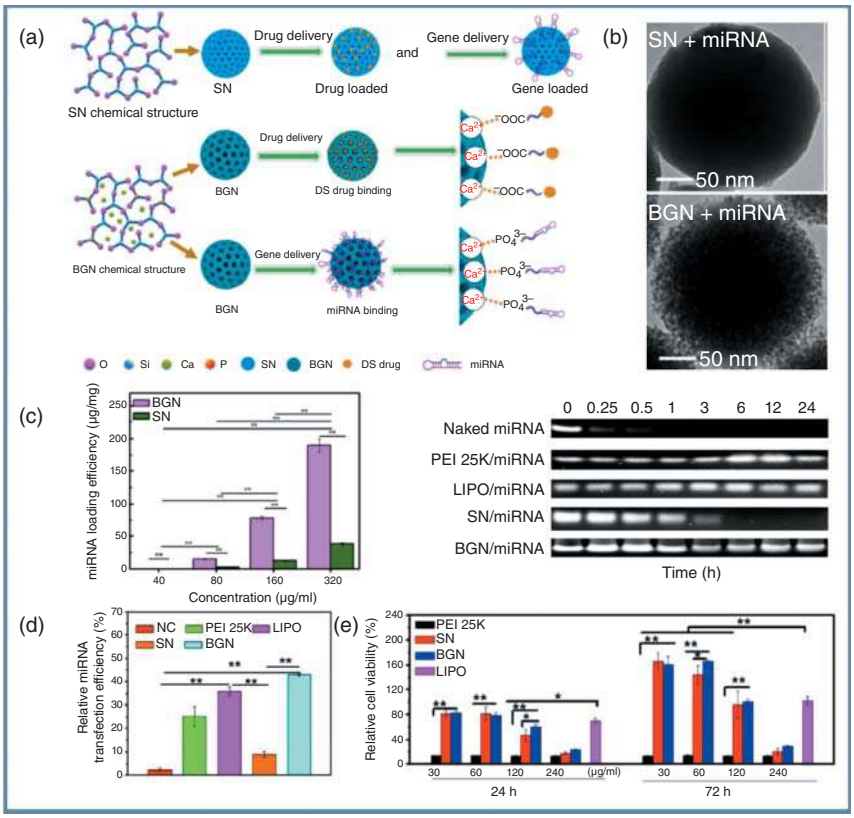

Figure 11.7 Investigation of the effects of BGN (mesoporous bioactive glass nanoparticles) and MSN (mesoporous silica nanoparticles) on the diclofenac sodium (drug) or miRNA-5106 (gene) binding (loading) ability, controlled release behavior, cytotoxicity, cellular uptake, and gene transfection. (a) Illustrations of drug/gene delivery process through BGN based on the calcium-organic group coordination mechanism. (b) TEM images and microstructure of BGN and SN after loading miRNA. (c) Quantification analysis of miRNA loading by BGN and SN with different concentrations (40–320 μg/ml) and the gel retardation images indicated inherent high miRNA binding ability and stability of BGN. (d) Quantitative positive BMSC cell expressions after miRNA transfection through various vectors, exhibiting the miRNA transfection efficiency. (e) Relative cellular viability of BMSCs after culture with different concentrations of various samples for 24 and 72 hours (relative to TCP). BGN shows significantly high cellular biocompatibility, as compared to commercial PEI 25K and LIPO. $^{*}P < 0.05$, $^{**}P < 0.01$. Source: (b, c) Yu et al. [143], Figure 05 [p. 30]/with permission from American Chemical Society.

significant low cytotoxicity, high cellular uptake, and miRNA transfection efficiency, as compared to commercial transfection reagents polyethylenimine (PEI, 25K) and lipofectamine 3000.

11.6.4 Surface Modification

Mesopore surface properties regarding to surface hydrophilicity, surface charges, surface functional groups, not only partially determine whether the drug can be loaded in but also influence bonding strength between the loaded species and the mesopores. For example, regular MBG inherently show good hydrophilicity so that hydrophobic oleo-soluble drugs have difficulties in entering the mesopores, and the situation is similar for those species charged the same to MBG surface owing to electrostatic repulsions. Heras et al. [99] evaluated the loading behaviors into MBG foams for four types of antibiotics (levofloxacin, vancomycin, rifampicin, and gentamicin). To predict drug loading efficiency and release kinetics through considering surface charges and superficial interactions, the electrostatic potential mapped density calculations of the MBG matrix materials and molecular modeling interaction studies between MBG receptor and drug ligands were utilized, respectively.

In such cases, the surface of MBG-based carriers needs modifications to adapt species for loading and release. So far, silanization is the most efficient and widely applied method for covalent modification of BG surface. Alkoxysilane molecules by hydrolysis can produce Si–OH moieties, which can condense with the BG surface groups to form chemical bonds. Moreover, the grafted coupling agents contain terminal functional groups, which alter the surface properties and facilitate drug/biomolecule attachment. Early in 2006, Vallet-Regi's group has already systematically investigated the host–guest interactions during drug adsorption and release processes with several organically modified mesoporous silica (chloropropyl, phenyl, benzyl, mercaptopropyl, cyanopropyl, and butyl) [144]. Ibuprofen as a model drug which contains a carboxylic group underwent higher interaction with polar groups than with nonpolar groups. Moreover, the ibuprofen release rate was considerably reduced from mesopores modified by mercapto- or amino- groups owing to hydrogen bond formation. Another typical example is to control the nonpolar drug release through functionalizing the mesopores with hydrophobic alkyl chains [145]. For this purpose, Doadrio et al. has modified SBA-15 using hydrocarbon moieties C8 and C18 for erythromycin delivery. As a result, the wettability of the surface by aqueous solution decreased, and then the release rate of erythromycin from C18-functionalized SBA-15 decreased by a factor of almost 1 order of magnitude as compared with that of non-modified SBA-15. However, it should be noted that grafting coupling agents by post-synthesis method will occupy quite a volume of mesopores. Thus, it is necessary to precisely control the balance between the surface group number and pore diameter/volume, and thereby optimize the species delivery profile.

11.7 Conclusions and Perspectives

More than bone and dental repair that BGs were initially invented for, BGs have broadened their applications in regenerative medicine fields of hard and soft tissue engineering. Compositional diversity gives birth of variable BGs, which thus specifically can be used against certain application. Among them, the particular sol–gel derived BGs have been fabricated into different forms to meet application requirements.

Basically, intrinsic bioactivity and therapeutic effects of BGs take their sources at ionic products upon implantation. The "*in situ*" delivery of pharmaceutic ions from BGs or BG-based materials

attracts tremendous interests; however, precise control of the release efficiency and manner remains challenges. Ion concentrations around local site are demanded to match biological processes at any time point. Although the beneficial ionic stimulations have been observed and affirmed *in vitro* as well as *in vivo*, the mechanisms are still asked for in-depth elucidation, especially the long-term release of ions *in vivo* needs comprehensive assessments with standardized test protocols. In addition, it is negligible to consider ion-doping influences to the BG matrix materials including physical, chemical, and biological properties of their own.

Being different from ion releases, delivery of drugs or biocues with BG systems is much more complicated. The loading strategies of those molecules majorly lie in surface adsorption/reaction to BG-based carriers. Inorganic local delivery systems composed of BGs possess high biocompatibility and biodegradability, however, which cause faster dissolution and less stability for species retention. In this regard, MBGs emerged to provide some solutions to achieve sustained release of species. Porous structures of this new generation BGs play pivotal roles in tailoring molecule type, encapsulation and also release. However, it remains a tricky issue for MBG carriers to balance the conflicts between loading efficiency and release rate with regular surface modifications, especially for large biomolecules. More smart carriers are in demand with gate keepers that are able to trigger cargo release responding to external stimuli, such as pH and temperature variations, light, redox processes, or enzymes. In this sense, the therapeutic species are protected by pore capping and a high local concentration of species release are targeted at the focus. For example, a decrease of environmental pH is usually observed after surgery, infection, or implant loosening. The pH-responsive BG carriers of certain species have been developed in the past. Yang et al. directly mineralized MBG drug vectors to form hydroxyapatite cap and restricted metformin hydrochloride release in a pH-sensitive controlled manner [146].

Furthermore, for multi-delivery of large biomolecules and tissue engineering purposes, BGs powders are inadequate while composite porous scaffolds show superiorities. Besides the basic requirements for scaffold use, the drug delivery properties influenced by every scaffold component are important as well. It is also a necessity to explore appropriate preparation methods to obtain better loading efficiency and controlled release.

Research and developments extended the use of BGs to a broader range of clinical applications rather than limiting to the hard tissue regenerations. The potentials of BGs for regeneration of spinal cord injuries, would healing, cardiac tissue engineering, muscle and ligament repair, and cancer treatment are extremely attractive. Several commercial BG-based products are now available concerning bone/tooth repair and would healing. However, BG-based drug carriers are far from commercialized or even being implanted in human patients. For one reason, *in vivo* testing assays about the released species, such as concentration, transportation pathways, and working principles, to date are not generally acknowledged and standardized. Additionally, the implantable devices loaded with species are totally different with pure implants. Long-term, comprehensive, and authentic investigations are in demand to achieve the clinic translation of BG-drug release systems. Therefore, future researches are motivated to develop refined and safe BG-drug release systems.

References

1 Hench, L.L. (2006). The story of Bioglass®. *Journal of Materials Science – Materials in Medicine* 17: 967–978.

2 Baino, F., Hamzehlou, S., and Kargozar, S. (2018). Bioactive glasses: where are we and where are we going? *Journal of Functional Biomaterials* 9: 25.

3 Mouriño, V., Vidotto, R., Cattalini, J.P., and Boccaccini, A.R. (2019). Enhancing biological activity of bioactive glass scaffolds by inorganic ion delivery for bone tissue engineering. *Current Opinion in Biomedical Engineering* 10: 23–34.

4 Yan, X.X., Yu, C.Z., Zhou, X.F. et al. (2004). Highly ordered mesoporous bioactive glasses with superior in vitro bone-forming bioactivities. *Angewandte Chemie International Edition* 43: 5980–5984.

5 Lopez-Noriega, A., Arcos, D., Izquierdo-Barba, I. et al. (2006). Ordered mesoporous bioactive glasses for bone tissue regeneration. *Chemistry of Materials* 18: 3137–3144.

6 Wu, C. and Chang, J. (2012). Mesoporous bioactive glasses: structure characteristics, drug/growth factor delivery and bone regeneration application. *Interface Focus* 2: 292–306.

7 Xynos, I.D., Edgar, A.J., Buttery, L.D.K. et al. (2000). Ionic products of bioactive glass dissolution increase proliferation of human osteoblasts and induce insulin-like growth factor II mRNA expression and protein synthesis. *Biochemical and Biophysical Research Communications* 276: 461–465.

8 Sun, J.Y., Yang, Y.S., Zhong, J.P., and Greenspan, D.C. (2007). The effect of the ionic products of Bioglass® dissolution on human osteoblasts growth cycle in vitro. *Journal of Tissue Engineering and Regenerative Medicine* 1: 281–286.

9 Jell, G., Notingher, I., Tsigkou, O. et al. (2008). Bioactive glass-induced osteoblast differentiation: a noninvasive spectroscopic study. *Journal of Biomedical Materials Research Part A* 86a: 31–40.

10 Day, R.M., Boccaccini, A.R., Shurey, S. et al. (2004). Assessment of polyglycolic acid mesh and bioactive glass for soft-tissue engineering scaffolds. *Biomaterials* 25: 5857–5866.

11 Dashnyam, K., El-Fiqi, A., Buitrago, J.O. et al. (2017). A mini review focused on the proangiogenic role of silicate ions released from silicon-containing biomaterials. *Journal of Tissue Engineering* 8: 1–13.

12 Zarghami, V., Ghorbani, M., Bagheri, K.P., and Shokrgozar, M.A. (2020). In vitro bactericidal and drug release properties of vancomycin-amino surface functionalized bioactive glass nanoparticles. *Materials Chemistry and Physics* 241: 122423.

13 Peacock, M. (2010). Calcium metabolism in health and disease. *Clinical Journal of the American Society of Nephrology* 5: S23–S30.

14 Seol, Y.J., Park, J.Y., Jung, J.W. et al. (2014). Improvement of bone regeneration capability of ceramic scaffolds by accelerated release of their calcium ions. *Tissue Engineering Part A* 20: 2840–2849.

15 Bohumila Rokosova, J.P.B. (1986). Effect of calcium on cell proliferation and ECM synthesis in arterial smooth muscle cells and dermal fibroblasts. *Experimental and Molecular Pathology* 44: 307–317.

16 Penido, M.G.M.G. and Alon, U.S. (2012). Phosphate homeostasis and its role in bone health. *Pediatric Nephrology* 27: 2039–2048.

17 Mozar, A., Haren, N., Chasseraud, M. et al. (2008). High extracellular inorganic phosphate concentration inhibits RANK-RANKL signaling in osteoclast-like cells. *Journal of Cellular Physiology* 215: 47–54.

18 Dogan, A., Demirci, S., Bayir, Y. et al. (2014). Boron containing poly(lactide-*co*-glycolide) (PLGA) scaffolds for bone tissue engineering. *Materials Science and Engineering C* 44: 246–253.

19 Chen, X.H., Zhao, Y.B., Geng, S.N. et al. (2015). In vivo experimental study on bone regeneration in critical bone defects using PIB nanogels/boron-containing mesoporous bioactive glass composite scaffold. *International Journal of Nanomedicine* 10: 839–846.

20 Chebassier, N., Ouijja, E.H., Viegas, I., and Dreno, B. (2004). Stimulatory effect of boron and manganese salts on keratinocyte migration. *Acta Dermato-Venereologica* 84: 191–194.

21 Bonnelye, E., Chabadel, A., Saltel, F., and Jurdic, P. (2008). Dual effect of strontium ranelate: stimulation of osteoblast differentiation and inhibition of osteoclast formation and resorption in vitro. *Bone* 42: 129–138.

22 Gentleman, E., Fredholm, Y.C., Jell, G. et al. (2010). The effects of strontium-substituted bioactive glasses on osteoblasts and osteoclasts in vitro. *Biomaterials* 31: 3949–3956.

23 Zreiqat, H., Howlett, C.R., Zannettino, A. et al. (2002). Mechanisms of magnesium-stimulated adhesion of osteoblastic cells to commonly used orthopaedic implants. *Journal of Biomedical Materials Research* 62: 175–184.

24 Kim, H.K., Han, H.S., Lee, K.S. et al. (2017). Comprehensive study on the roles of released ions from biodegradable Mg-5 wt% Ca-1 wt% Zn alloy in bone regeneration. *Journal of Tissue Engineering and Regenerative Medicine* 11: 2710–2724.

25 Courtheoux, L., Lao, J., Nedelec, J.M., and Jallot, E. (2008). Controlled bioactivity in zinc-doped sol–gel-derived binary bioactive glasses. *Journal of Physical Chemistry C* 112: 13663–13667.

26 Kwun, I.S., Cho, Y.E., Lomeda, R.A.R. et al. (2010). Zinc deficiency suppresses matrix mineralization and retards osteogenesis transiently with catch-up possibly through Runx 2 modulation. *Bone* 46: 732–741.

27 Lemire, J.A., Harrison, J.J., and Turner, R.J. (2013). Antimicrobial activity of metals: mechanisms, molecular targets and applications. *Nature Reviews Microbiology* 11: 371–384.

28 Jacobs, A., Renaudin, G., Forestier, C. et al. (2020). Biological properties of copper-doped biomaterials for orthopedic applications: a review of antibacterial, angiogenic and osteogenic aspects. *Acta Biomaterialia* 117: 21–39.

29 Wang, H., Zhao, S., Xiao, W. et al. (2016). Influence of Cu doping in borosilicate bioactive glass and the properties of its derived scaffolds. *Materials Science and Engineering C* 58: 194–203.

30 de Laia, A.G.S., Valverde, T.M., Barrioni, B.R. et al. (2020). Cobalt-containing bioactive glass mimics vascular endothelial growth factor A and hypoxia inducible factor 1 function. *Journal of Biomedical Materials Research Part A* 109: 1051–1064.

31 Wu, C.T., Zhou, Y.H., Fan, W. et al. (2012). Hypoxia-mimicking mesoporous bioactive glass scaffolds with controllable cobalt ion release for bone tissue engineering. *Biomaterials* 33: 2076–2085.

32 Nawaz, Q., Rehman, M.A.U., Burkovski, A. et al. (2018). Synthesis and characterization of manganese containing mesoporous bioactive glass nanoparticles for biomedical applications. *Journal of Materials Science – Materials in Medicine* 29: 64.

33 Miola, M., Brovarone, C.V., Maina, G. et al. (2014). In vitro study of manganese-doped bioactive glasses for bone regeneration. *Materials Science and Engineering C* 38: 107–118.

34 Verne, E., Di Nunzio, S., Bosetti, M. et al. (2005). Surface characterization of silver-doped bioactive glass. *Biomaterials* 26: 5111–5119.

35 Sanchez-Salcedo, S., Malavasi, G., Salinas, A.J. et al. (2018). Highly-bioreactive silica-based mesoporous bioactive glasses enriched with gallium(III). *Materials* 11: 367.

36 Valappil, S.P., Ready, D., Abou Neel, E.A. et al. (2009). Controlled delivery of antimicrobial gallium ions from phosphate-based glasses. *Acta Biomaterialia* 5: 1198–1210.

37 Chigurupati, S., Mughal, M.R., Okun, E. et al. (2013). Effects of cerium oxide nanoparticles on the growth of keratinocytes, fibroblasts and vascular endothelial cells in cutaneous wound healing. *Biomaterials* 34: 2194–2201.

38 Ma, X.M., Cheng, Y., Jian, H. et al. (2019). Hollow, rough, and nitric oxide-releasing cerium oxide nanoparticles for promoting multiple stages of wound healing. *Advanced Healthcare Materials* 8: 1900256.

39 Qi, M., Li, W., Zheng, X. et al. (2020). Cerium and its oxidant-based nanomaterials for antibacterial applications: a state-of-the-art review. *Frontiers in Materials* 7: 213.

40 Chen, L., Deng, C.J., Li, J.Y. et al. (2019). 3D printing of a lithium-calcium-silicate crystal bioscaffold with dual bioactivities for osteochondral interface reconstruction. *Biomaterials* 196: 138–150.

41 Wu, Y., Zhu, S.A., Wu, C.T. et al. (2014). A Bi-lineage conducive scaffold for osteochondral defect regeneration. *Advanced Functional Materials* 24: 4473–4483.

42 Kaya, S., Cresswell, M., and Boccaccini, A.R. (2018). Mesoporous silica-based bioactive glasses for antibiotic-free antibacterial applications. *Materials Science and Engineering C* 83: 99–107.

43 Chopra, I. (2007). The increasing use of silver-based products as antimicrobial agents: a useful development or a cause for concern? *Journal of Antimicrobial Chemotherapy* 59: 587–590.

44 Hu, G.F., Xiao, L.W., Tong, P.J. et al. (2012). Antibacterial hemostatic dressings with nanoporous bioglass containing silver. *International Journal of Nanomedicine* 7: 2613–2620.

45 Pratten, J., Nazhat, S.N., Blaker, J.J., and Boccaccini, A.R. (2004). In vitro attachment of *Staphylococcus epidermidis* to surgical sutures with and without Ag-containing bioactive glass coating. *Journal of Biomaterials Applications* 19: 47–57.

46 Catauro, M., Raucci, M.G., De Gaetano, F., and Marotta, A. (2004). Antibacterial and bioactive silver-containing $Na_2O{\cdot}CaO{\cdot}2SiO_2$ glass prepared by sol–gel method. *Journal of Materials Science – Materials in Medicine* 15: 831–837.

47 Jones, J.R., Ehrenfried, L.M., Saravanapavan, P., and Hench, L.L. (2006). Controlling ion release from bioactive glass foam scaffolds with antibacterial properties. *Journal of Materials Science – Materials in Medicine* 17: 989–996.

48 Chitambar, C.R. (2016). Gallium and its competing roles with iron in biological systems. *Biochimica et Biophysica Acta, Molecular Cell Research* 1863: 2044–2053.

49 Pelletier, D.A., Suresh, A.K., Holton, G.A. et al. (2010). Effects of engineered cerium oxide nanoparticles on bacterial growth and viability. *Applied and Environmental Microbiology* 76: 7981–7989.

50 Zhang, M.Z., Zhang, C., Zhai, X.Y. et al. (2019). Antibacterial mechanism and activity of cerium oxide nanoparticles. *Science China Materials* 62: 1727–1739.

51 Goh, Y.F., Alshemary, A.Z., Akram, M. et al. (2014). In vitro characterization of antibacterial bioactive glass containing ceria. *Ceramics International* 40: 729–737.

52 Łapa, A., Cresswell, M., Campbell, I. et al. (2020). Gallium- and cerium-doped phosphate glasses with antibacterial properties for medical applications. *Advanced Engineering Materials* 22: 1901577.

53 O'Donnell, S., Cranney, A., Wells, G.A. et al. (2006). Strontium ranelate for preventing and treating postmenopausal osteoporosis. *Cochrane Database of Systematic Reviews* 3: CD530026.

54 Kargozar, S., Montazerian, M., Fiume, E., and Baino, F. (2019). Multiple and promising applications of strontium (Sr)-containing bioactive glasses in bone tissue engineering. *Frontiers in Bioengineering and Biotechnology* 7: 161.

55 Lao, J., Jallot, E., and Nedelec, J.M. (2008). Strontium-delivering glasses with enhanced bioactivity: a new biomaterial for antiosteoporotic applications? *Chemistry of Materials* 20: 4969–4973.

56 Abou Neel, E.A., Chrzanowski, W., Pickup, D.M. et al. (2009). Structure and properties of strontium-doped phosphate-based glasses. *Journal of the Royal Society Interface* 6: 435–446.

57 Pan, H.B., Zhao, X.L., Zhang, X. et al. (2010). Strontium borate glass: potential biomaterial for bone regeneration. *Journal of the Royal Society Interface* 7: 1025–1031.

58 Kulanthaivel, S., Mishra, U., Agarwal, T. et al. (2015). Improving the osteogenic and angiogenic properties of synthetic hydroxyapatite by dual doping of bivalent cobalt and magnesium ion. *Ceramics International* 41: 11323–11333.

59 Sharifianjazi, F., Moradi, M., Abouchenari, A. et al. (2020). Effects of Sr and Mg dopants on biological and mechanical properties of SiO_2–CaO–P_2O_5 bioactive glass. *Ceramics International* 46: 22674–22682.

60 Salinas, A.J., Shruti, S., Malavasi, G. et al. (2011). Substitutions of cerium, gallium and zinc in ordered mesoporous bioactive glasses. *Acta Biomaterialia* 7: 3452–3458.

61 Shruti, S., Salinas, A.J., Lusvardi, G. et al. (2013). Mesoporous bioactive scaffolds prepared with cerium-, gallium- and zinc-containing glasses. *Acta Biomaterialia* 9: 4836–4844.

62 Birgani, Z.T., Gharraee, N., Malhotra, A. et al. (2016). Combinatorial incorporation of fluoride and cobalt ions into calcium phosphates to stimulate osteogenesis and angiogenesis. *Biomedical Materials* 11: 015020.

63 Wang, H., Zhao, S., Zhou, J. et al. (2014). Evaluation of borate bioactive glass scaffolds as a controlled delivery system for copper ions in stimulating osteogenesis and angiogenesis in bone healing. *Journal of Materials Chemistry B* 2: 8547–8557.

64 Zhao, S.C., Li, L., Wang, H. et al. (2015). Wound dressings composed of copper-doped borate bioactive glass microfibers stimulate angiogenesis and heal full-thickness skin defects in a rodent model. *Biomaterials* 53: 379–391.

65 Xu, S.J., Zheng, H.Z., Ma, R.L. et al. (2020). Vacancies on 2D transition metal dichalcogenides elicit ferroptotic cell death. *Nature Communications* 11: 3484.

66 Liu, Y.Q., Li, T., Ma, H.S. et al. (2018). 3D-printed scaffolds with bioactive elements-induced photothermal effect for bone tumor therapy. *Acta Biomaterialia* 73: 531–546.

67 Liu, Y.Q., Lin, R.C., Ma, L.L. et al. (2020). Mesoporous bioactive glass for synergistic therapy of tumor and regeneration of bone tissue. *Applied Materials Today* 19: 100578.

68 Brauer, D.S. (2015). Bioactive glasses – structure and properties. *Angewandte Chemie International Edition* 54: 4160–4181.

69 Bruckner, R., Tylkowski, M., Hupa, L., and Brauer, D.S. (2016). Controlling the ion release from mixed alkali bioactive glasses by varying modifier ionic radii and molar volume. *Journal of Materials Chemistry B* 4: 3121–3134.

70 Du, J.C. and Xiang, Y. (2012). Effect of strontium substitution on the structure, ionic diffusion and dynamic properties of 45S5 Bioactive glasses. *Journal of Non-Crystalline Solids* 358: 1059–1071.

71 Fernandes, H.R., Gaddam, A., Rebelo, A. et al. (2018). Bioactive glasses and glass-ceramics for healthcare applications in bone regeneration and tissue engineering. *Materials* 11: 2530.

72 Cacciotti, I., Lombardi, M., Bianco, A. et al. (2012). Sol–gel derived 45S5 bioglass: synthesis, microstructural evolution and thermal behaviour. *Journal of Materials Science – Materials in Medicine* 23: 1849–1866.

73 Peitl, O., Zanotto, E.D., and Hench, L.L. (2001). Highly bioactive P_2O_5–Na_2O–CaO–SiO_2 glass-ceramics. *Journal of Non-Crystalline Solids* 292: 115–126.

74 Peitl, O., Zanotto, E.D., Serbena, F.C., and Hench, L.L. (2012). Compositional and microstructural design of highly bioactive P_2O_5–Na_2O–CaO–SiO_2 glass-ceramics. *Acta Biomaterialia* 8: 321–332.

75 Li, Y., Placek, L.M., Coughlan, A. et al. (2015). Investigating the influence of Na^+ and Sr^{2+} on the structure and solubility of SiO_2–TiO_2–CaO–Na_2O/SrO bioactive glass. *Journal of Materials Science – Materials in Medicine* 26: 85.

76 Brauer, D.S., Wilson, R.M., and Kasuga, T. (2012). Multicomponent phosphate invert glasses with improved processing. *Journal of Non-Crystalline Solids* 358: 1720–1723.

77 Maçon, A.L.B., Kim, T.B., Valliant, E.M. et al. (2015). A unified in vitro evaluation for apatite-forming ability of bioactive glasses and their variants. *Journal of Materials Science – Materials in Medicine* 26: 115.

78 Paris, J.L., Colilla, M., Izquierdo-Barba, I. et al. (2017). Tuning mesoporous silica dissolution in physiological environments: a review. *Journal of Materials Science* 52: 8761–8771.

79 Bingel, L., Groh, D., Karpukhina, N., and Brauer, D.S. (2015). Influence of dissolution medium pH on ion release and apatite formation of Bioglass® 45S5. *Materials Letters* 143: 279–282.

80 Sepulveda, P., Jones, J.R., and Hench, L.L. (2002). In vitro dissolution of melt-derived 45S5 and sol–gel derived 58S bioactive glasses. *Journal of Biomedical Materials Research* 61: 301–311.

81 Xie, Z.P., Liu, X., Jia, W.T. et al. (2009). Treatment of osteomyelitis and repair of bone defect by degradable bioactive borate glass releasing vancomycin. *Journal of Controlled Release* 139: 118–126.

82 Min, J., Braatz, R.D., and Hammond, P.T. (2014). Tunable staged release of therapeutics from layer-by-layer coatings with clay interlayer barrier. *Biomaterials* 35: 2507–2517.

83 Zhang, X., Jia, W.-T., Gu, Y.-F. et al. (2010). Borate bioglass based drug delivery of teicoplanin for treating osteomyelitis. *Journal of Inorganic Materials* 25: 293–298.

84 Kong, C.H., Steffi, C., Shi, Z., and Wang, W. (2018). Development of mesoporous bioactive glass nanoparticles and its use in bone tissue engineering. *Journal of Biomedical Materials Research Part B Applied Biomaterials* 106: 2878–2887.

85 Xue, Y., Zhang, Z., Niu, W. et al. (2019). Enhanced physiological stability and long-term toxicity/biodegradation in vitro/in vivo of monodispersed glycerolphosphate-functionalized bioactive glass nanoparticles. *Particle and Particle Systems Characterization* 36: 1800507.

86 Sui, B., Zhong, G., and Sun, J. (2016). Drug-loadable mesoporous bioactive glass nanospheres: biodistribution, clearance, BRL cellular location and systemic risk assessment via ^{45}Ca labelling and histological analysis. *Scientific Reports* 6: 33443.

87 Farag, M.M., Abd-Allah, W.M., and Ibrahim, A.M. (2015). Effect of gamma irradiation on drug releasing from nano-bioactive glass. *Drug Delivery and Translational Research* 5: 63–73.

88 Mahapatra, C., Singh, R.K., Kim, J.J. et al. (2016). Osteopromoting reservoir of stem cells: bioactive mesoporous nanocarrier/collagen gel through slow-releasing FGF18 and the activated BMP signaling. *ACS Applied Materials & Interfaces* 8: 27573–27584.

89 Mohamadi, F., Ebrahimi-Barough, S., Nourani, M.R. et al. (2018). Use new poly(ε-caprolactone/collagen/NBG) nerve conduits along with NGF for promoting peripheral (sciatic) nerve regeneration in a rat. *Artificial Cells, Nanomedicine, and Biotechnology* 46: 34–45.

90 Wang, X., Zeng, D., Weng, W. et al. (2018). Alendronate delivery on amino modified mesoporous bioactive glass scaffolds to enhance bone regeneration in osteoporosis rats. *Artificial Cells, Nanomedicine, and Biotechnology* 46: 171–181.

91 Nathan, C. and Cars, O. (2014). Antibiotic resistance – problems, progress, and prospects. *New England Journal of Medicine* 371: 1761–1763.

92 Kluin, O.S., van der Mei, H.C., Busscher, H.J., and Neut, D. (2013). Biodegradable vs non-biodegradable antibiotic delivery devices in the treatment of osteomyelitis. *Expert Opinion on Drug Delivery* 10: 341–351.

93 Xia, W. and Chang, J. (2006). Well-ordered mesoporous bioactive glasses (MBG): a promising bioactive drug delivery system. *Journal of Controlled Release* 110: 522–530.

94 Li, X., Wang, X., Zhang, L. et al. (2009). MBG/PLGA composite microspheres with prolonged drug release. *Journal of Biomedical Materials Research Part B Applied Biomaterials* 89: 148–154.

95 Zhu, Y. and Kaskel, S. (2009). Comparison of the in vitro bioactivity and drug release property of mesoporous bioactive glasses (MBGs) and bioactive glasses (BGs) scaffolds. *Microporous and Mesoporous Materials* 118: 176–182.

96 Zhu, M., Zhang, L.X., He, Q.J. et al. (2011). Mesoporous bioactive glass-coated poly(L-lactic acid) scaffolds: a sustained antibiotic drug release system for bone repairing. *Journal of Materials Chemistry* 21: 1064–1072.

97 Li, Y., Liu, Y.Z., Long, T. et al. (2013). Mesoporous bioactive glass as a drug delivery system: fabrication, bactericidal properties and biocompatibility. *Journal of Materials Science – Materials in Medicine* 24: 1951–1961.

98 Zhao, L., Yan, X., Zhou, X. et al. (2008). Mesoporous bioactive glasses for controlled drug release. *Microporous and Mesoporous Materials* 109: 210–215.

99 Heras, C., Jimenez-Holguin, J., Doadrio, A.L. et al. (2020). Multifunctional antibiotic- and zinc-containing mesoporous bioactive glass scaffolds to fight bone infection. *Acta Biomaterialia* 114: 395–406.

100 Polo, L., Gomez-Cerezo, N., Aznar, E. et al. (2017). Molecular gates in mesoporous bioactive glasses for the treatment of bone tumors and infection. *Acta Biomaterialia* 50: 114–126.

101 Fan, W., Wu, C.T., Han, P.P. et al. (2012). Porous Ca–Si-based nanospheres: a potential intra-canal disinfectant-carrier for infected canal treatment. *Materials Letters* 81: 16–19.

102 Kundu, B., Nandi, S.K., Dasgupta, S. et al. (2011). Macro-to-micro porous special bioactive glass and ceftriaxone–sulbactam composite drug delivery system for treatment of chronic osteomyelitis: an investigation through in vitro and in vivo animal trial. *Journal of Materials Science – Materials in Medicine* 22: 705–720.

103 Malavasi, G., Ferrari, E., Lusvardi, G. et al. (2011). The role of coordination chemistry in the development of innovative gallium-based bioceramics: the case of curcumin. *Journal of Materials Chemistry* 21: 5027–5037.

104 Mosqueira, L., Barrioni, B.R., Martins, T. et al. (2020). In vitro effects of the co-release of icariin and strontium from bioactive glass submicron spheres on the reduced osteogenic potential of rat osteoporotic bone marrow mesenchymal stem cells. *Biomedical Materials* 15: 055023.

105 Kargozar, S., Montazerian, M., Hamzehlou, S. et al. (2018). Mesoporous bioactive glasses: promising platforms for antibacterial strategies. *Acta Biomaterialia* 81: 1–19.

106 Chitra, S., Bargavi, P., Balasubramaniam, M. et al. (2020). Impact of copper on in-vitro biomineralization, drug release efficacy and antimicrobial properties of bioactive glasses. *Materials Science and Engineering C* 109: 110598.

107 Wu, C., Miron, R., Sculean, A. et al. (2011). Proliferation, differentiation and gene expression of osteoblasts in boron-containing associated with dexamethasone deliver from mesoporous bioactive glass scaffolds. *Biomaterials* 32: 7068–7078.

108 Zhang, J., Zhao, S., Zhu, Y. et al. (2014). Three-dimensional printing of strontium-containing mesoporous bioactive glass scaffolds for bone regeneration. *Acta Biomaterialia* 10: 2269–2281.

109 Fu, S.Y., Du, X.Y., Zhu, M. et al. (2019). 3D printing of layered mesoporous bioactive glass/sodium alginate-sodium alginate scaffolds with controllable dual-drug release behaviors. *Biomedical Materials* 14: 065011.

110 Diba, M., Camargo, W.A., Zinkevich, T. et al. (2019). Hybrid particles derived from alendronate and bioactive glass for treatment of osteoporotic bone defects. *Journal of Materials Chemistry B* 7: 796–808.

111 Locs, J., Li, W., Sokolova, M. et al. (2015). Zoledronic acid impregnated and poly(L-lactic acid) coated 45S5 Bioglass®-based scaffolds. *Materials Letters* 156: 180–182.

112 Terzopoulou, Z., Baciu, D., Gounari, E. et al. (2019). Composite membranes of poly(ε-caprolactone) with bisphosphonate-loaded bioactive glasses for potential bone tissue engineering applications. *Molecules* 24: 3067.

113 Zhu, M., Li, K., Zhu, Y.F. et al. (2015). 3D-printed hierarchical scaffold for localized isoniazid/rifampin drug delivery and osteoarticular tuberculosis therapy. *Acta Biomaterialia* 16: 145–155.

114 Ravanbakhsh, M., Labbaf, S., Karimzadeh, F. et al. (2019). Mesoporous bioactive glasses for the combined application of osteosarcoma treatment and bone regeneration. *Materials Science and Engineering C* 104, 104: 109994.

115 Chen, S.Y., Chou, P.F., Chan, W.K., and Lin, H.M. (2017). Preparation and characterization of mesoporous bioactive glass from agricultural waste rice husk for targeted anticancer drug delivery. *Ceramics International* 43: 2239–2245.

116 Zhang, Y., Hu, M., Wang, X. et al. (2018). Design and evaluation of europium containing mesoporous bioactive glass nanospheres: doxorubicin release kinetics and inhibitory effect on osteosarcoma MG 63 cells. *Nanomaterials (Basel)* 8: 961.

117 Zhu, M., Shi, J., He, Q. et al. (2011). An emulsification–solvent evaporation route to mesoporous bioactive glass microspheres for bisphosphonate drug delivery. *Journal of Materials Science* 47: 2256–2263.

118 Zhu, M., Zhu, Y., Ni, B. et al. (2014). Mesoporous silica nanoparticles/hydroxyapatite composite coated implants to locally inhibit osteoclastic activity. *ACS Applied Materials & Interfaces* 6: 5456–5466.

119 Goonoo, N. and Bhaw-Luximon, A. (2019). Mimicking growth factors: role of small molecule scaffold additives in promoting tissue regeneration and repair. *RSC Advances* 9: 18124–18146.

120 Lee, J.H., Mandakhbayar, N., El-Fiqi, A., and Kim, H.W. (2017). Intracellular co-delivery of Sr ion and phenamil drug through mesoporous bioglass nanocarriers synergizes BMP signaling and tissue mineralization. *Acta Biomaterialia* 60: 93–108.

121 Wu, C.T., Zhou, Y.H., Chang, J., and Xiao, Y. (2013). Delivery of dimethyloxallyl glycine in mesoporous bioactive glass scaffolds to improve angiogenesis and osteogenesis of human bone marrow stromal cells. *Acta Biomaterialia* 9: 9159–9168.

122 Aravamudhan, A., Ramos, D.M., Nip, J. et al. (2013). Osteoinductive small molecules: growth factor alternatives for bone tissue engineering. *Current Pharmaceutical Design* 19: 3420–3428.

123 Wu, C., Fan, W., Chang, J., and Xiao, Y. (2013). Mesoporous bioactive glass scaffolds for efficient delivery of vascular endothelial growth factor. *Journal of Biomaterials Applications* 28: 367–374.

124 Xia, L.U., Zeng, D., Sun, X.J. et al. (2013). Engineering of bone using rhBMP-2-loaded mesoporous silica bioglass and bone marrow stromal cells for oromaxillofacial bone regeneration. *Microporous and Mesoporous Materials* 173: 155–165.

125 Dai, C.L., Guo, H., Lu, J.X. et al. (2011). Osteogenic evaluation of calcium/magnesium-doped mesoporous silica scaffold with incorporation of rhBMP-2 by synchrotron radiation-based μCT. *Biomaterials* 32: 8506–8517.

126 Berkmann, J.C., Herrera Martin, A.X., Pontremoli, C. et al. (2020). In vivo validation of spray-dried mesoporous bioactive glass microspheres acting as prolonged local release systems for BMP-2 to support bone regeneration. *Pharmaceutics* 12: 823.

127 Tang, W., Lin, D., Yu, Y. et al. (2016). Bioinspired trimodal macro/micro/nano-porous scaffolds loading rhBMP-2 for complete regeneration of critical size bone defect. *Acta Biomaterialia* 32: 309–323.

128 Liang, B., Huang, J., Xu, J. et al. (2018). Local delivery of a novel PTHrP via mesoporous bioactive glass scaffolds to improve bone regeneration in a rat posterolateral spinal fusion model. *RSC Advances* 8: 12484–12493.

129 Zhu, M., He, H., Meng, Q. et al. (2020). Osteopontin sequence modified mesoporous calcium silicate scaffolds to promote angiogenesis in bone tissue regeneration. *Journal of Materials Chemistry B* 8: 5849–5861.

130 Kim, T.H., Singh, R.K., Kang, M.S. et al. (2016). Inhibition of osteoclastogenesis through siRNA delivery with tunable mesoporous bioactive nanocarriers. *Acta Biomaterialia* 29: 352–364.

131 Lee, J.H., El-Fiqi, A., Mandakhbayar, N. et al. (2017). Drug/ion co-delivery multi-functional nanocarrier to regenerate infected tissue defect. *Biomaterials* 142: 62–76.

132 El-Fiqi, A., Mandakhbayar, N., Jo, S.B. et al. (2021). Nanotherapeutics for regeneration of degenerated tissue infected by bacteria through the multiple delivery of bioactive ions and growth factor with antibacterial/angiogenic and osteogenic/odontogenic capacity. *Bioactive Materials* 6: 123–136.

133 Biernat, M., Ciołek, L., Dzierżyńska, M. et al. (2020). Porous chitosan/ZnO-doped bioglass composites as carriers of bioactive peptides. *International Journal of Applied Ceramic Technology* 17: 2807–2816.

134 Gupta, N., Santhiya, D., and Aditya, A. (2016). Tailored smart bioactive glass nanoassembly for dual antibiotic in vitro sustained release against osteomyelitis. *Journal of Materials Chemistry B* 4: 7605–7619.

135 Tang, W., Yu, Y., Wang, J. et al. (2020). Enhancement and orchestration of osteogenesis and angiogenesis by a dual-modular design of growth factors delivery scaffolds and 26SCS decoration. *Biomaterials* 232: 119645.

136 Wu, C.T., Fan, W., and Chang, J. (2013). Functional mesoporous bioactive glass nanospheres: synthesis, high loading efficiency, controllable delivery of doxorubicin and inhibitory effect on bone cancer cells. *Journal of Materials Chemistry B* 1: 2710–2718.

137 Arcos, D., Lopez-Noriega, A., Ruiz-Hernandez, E. et al. (2009). Ordered mesoporous microspheres for bone grafting and drug delivery. *Chemistry of Materials* 21: 1000–1009.

138 Miao, G.H., Chen, X.F., Dong, H. et al. (2013). Investigation of emulsified, acid and acid-alkali catalyzed mesoporous bioactive glass microspheres for bone regeneration and drug delivery. *Materials Science and Engineering C* 33: 4236–4243.

139 Miao, G., Li, Z., Meng, Y. et al. (2019). Preparation, characterization, in vitro bioactivity and protein loading/release property of mesoporous bioactive glass microspheres with different compositions. *Advanced Powder Technology* 30: 1848–1857.

140 Tang, J.Y., Chen, X.F., Dong, Y.M. et al. (2017). Facile synthesis of mesoporous bioactive glass nanospheres with large mesopore via biphase delamination method. *Materials Letters* 209: 626–629.

141 Wang, Y., Pan, H., and Chen, X. (2019). The preparation of hollow mesoporous bioglass nanoparticles with excellent drug delivery capacity for bone tissue regeneration. *Frontiers in Chemistry* 7: 283.

142 Sui, B., Liu, X., and Sun, J. (2018). Dual-functional dendritic mesoporous bioactive glass nanospheres for calcium influx-mediated specific tumor suppression and controlled drug delivery in vivo. *ACS Applied Materials & Interfaces* 10: 23548–23559.

143 Yu, M., Xue, Y., Ma, P.X. et al. (2017). Intrinsic ultrahigh drug/miRNA loading capacity of biodegradable bioactive glass nanoparticles toward highly efficient pharmaceutical delivery. *ACS Applied Materials & Interfaces* 9: 8460–8470.

144 Horcajada, P., Ramila, A., Gerard, F., and Vallet-Regi, M. (2006). Influence of superficial organic modification of MCM-41 matrices on drug delivery rate. *Solid State Sciences* 8: 1243–1249.

145 Doadrio, J.C., Sousa, E.M.B., Izquierdo-Barba, I. et al. (2006). Functionalization of mesoporous materials with long alkyl chains as a strategy for controlling drug delivery pattern. *Journal of Materials Chemistry* 16: 462–466.

146 Yang, C.Y., Guo, W., Cui, L.R. et al. (2014). pH-responsive controlled-release system based on mesoporous bioglass materials capped with mineralized hydroxyapatite. *Materials Science and Engineering C* 36: 237–243.

12

Enhancing the Biological Performance of Bioactive Glasses by Combination with Phytotherapeutic Compounds

Kanwal Ilyas and Aldo R. Boccaccini

Department of Materials Science and Engineering, Institute of Biomaterials, University of Erlangen-Nuremberg, Erlangen, Germany

12.1 Introduction

The use of plant extracts to heal human disease and ailment can be traced back to the beginning of human history. Animals swallow leaves and chew bitter piths to protect themselves from parasitosis and other illnesses [1]. Interestingly, from history, it is evident that most of the plants utilized by local human populations for medicinal purposes have some links with those used by different animals [2]. According to the World Health Organization (WHO), nearly 4 billion people exploit plant species because of their remedial properties and rely on the effectiveness they have within their extracts [3, 4]. A worldwide survey assessed that 35 000–70 000 plant species are used in traditional medicine [5, 6]. However, in 1897 synthesis of the drug "aspirin" led to an era dominated by pharmaceutical synthetic drugs. Aspirin was synthesized from salicylic acid extracted from the willow bark, with the success of aspirin the concept of effectiveness of mono-drug therapeutics to cure complicated diseases emerged. As a consequence, the era of synthetic drug consumption dominated and conquered the use of natural products [5]. However, more recently, the nontoxic nature as well as the economical procurement of herbal drugs are driving research and innovative approaches for biomedical application, usually combined with engineered biomaterials [7].

Generally, secondary metabolites in plants that are considered pharmacologically active compounds comprise nitrogen-containing alkaloids, terpenoids, and phenolic compounds [8]. Phytotherapeutics are broad-spectrum phytochemicals which are extracted from medicinal plants and their active components have the capability to cure ailments [6]. It is significant to state that "medicinal plants" are neither phytomedicines nor phytotherapeutics. The WHO defined the ethical standards according to which a phytotherapeutic is processed [9]. The term phytotherapeutic drug is considered worthy after a cautious synthesis protocol from the interval of collection and preparation until the time of wrapping and distribution. Therefore, phytotherapeutic drugs are composed almost entirely of medicinal plants. However, on the other side, every medicinal plant cannot be considered a phytotherapeutic agent [6]. Phytotherapeutic drugs, typically flavonoidal drugs like quercetin (QT), rutin (RT), luteolin, diosmin, and curcumin (CUR), have the remarkable potential of antioxidant activity [10] with other potential biological effects reported, such as anti-inflammatory, anticancer, and anti-ulcer activities [7].

For the purpose of tissue engineering (TE), bioactive glasses (BGs) are being investigated for both soft and hard tissue regeneration. BGs of silicate, phosphate, and borate compositions are being used to develop suitable TE scaffolds [11, 12]. A recent approach being considered to enhance

Bioactive Glasses and Glass-Ceramics: Fundamentals and Applications, First Edition.
Edited by Francesco Baino and Saeid Kargozar.

the biological performance of BGs is doping BGs with biologically active agents such as metal ions, for example copper, strontium, zinc, cobalt, gallium, manganese, and silver [13, 14]. One weakness associated with this ion doping strategy is that a high concentration of metal ion accumulation can initiate inflammation and toxic effects after implantation in a living system. Moreover, enhanced metal ion concentration may decrease the dissolution rate of BGs while replacing calcium ions, they can reduce the mechanical property of BGs and can lead to possible cytotoxicity [11, 15]. Similarly, different kinds of growth factors, such as bone morphogenetic proteins (BMPs), transforming growth factor beta (TGF-β), insulin-like growth factors (IGFs), or platelet-derived growth factor (PDGF), can be incorporated to boost the therapeutic properties of BGs [16, 17]. However, because of the relatively high costs of growth factors, this type of combination is not always a favorable approach [18, 19]. To tackle these limitations, natural organic compounds such as phytotherapeutic drugs can be combined with BGs in an emerging strategy to enhance biological functionalities exploiting the several promising features provided by such combination [20]. Interaction of BGs with phytotherapeutic compounds modulates the biological performance in several different ways [21], adding to the natural process of ionic dissolution of BGs to stimulate the proliferation of cells, triggering specific gene expression to induce the required specific cellular responses (e.g. osteogenesis, angiogenesis) [22, 23]. The coupling of BGs with the biological activities of plant extracts is an advanced step toward improved bioactive scaffolds for TE and novel biomaterial combinations for a number of biomedical applications, e.g. antibacterial coatings and anticancer therapies [22]. Table 12.1 summarizes the several combinations of BGs with different herbal drugs and their loading techniques, including their biological activities and applications.

In this chapter, we cover comprehensively the emerging area of BG combinations with phytotherapeutic compounds to enhance the biological properties of BGs. The enhancement of the biological functions of BGs by surface modification with different organic groups and by tailoring surface topography as well as physical methods of drug loading onto mesoporous BGs are also discussed. Finally, therapeutic applications of presently developed phytotherapeutic-loaded BGs are summarized and areas for future research are highlighted. Figure 12.1 represents a schematic overview of this chapter. This chapter expands and updates a previous review paper on the same subject published in 2019 [21].

12.2 Phytotherapeutics: An Overview

Phytotherapeutic agents are natural organic compounds which are derived from medicinal plants and have the special ability to stimulate biological activities like antibacterial and anti-inflammatory responses [41]. The fusion of bio-friendly phytotherapeutic compounds or medicinal plant extracts into biomaterials, especially in BGs, signifies a novel paradigm leading to a new family of bioactive organic–inorganic biomaterials for TE and other biomedical applications. This herbal drug incorporation strategy has potential clinical advantages, including inhibiting surgical site inflammation, low risk for revision surgery, following better integration of implants, enhanced regenerative capacity (in case of TE scaffolds) and above all, it provides a cost-effective biomaterial approach to tackle healthcare challenges [29]. From a wide range of medicinal plants, some well-known examples and their phytotherapeutic significance are described in this section.

Curcuma longa (family name Zingiberaceae), a popular spice generally called turmeric, is a yellow colored spice that has been applied as an effective ointment for wound healing since ancient times [42]. It has been considered to have ingredients to cure a variety of skin infections

Table 12.1 Overview of systems that combine phytotherapeutic compounds with BGs, including biological properties and clinical applications, as reported in the literature.

Bioactive glass composition	Synthesis route	Phytotherapeutic compounds	Drug loading technique	Biological activity	Therapeutic application	References
$58SiO_2$–$33CaO$–$9P_2O_5$ wt% (silver doped BG)	Sol–gel	Neem	Mechanical mixing of neem leaf powder by ball milling with BG	Antibacterial and antiviral	Bone tissue engineering	[11]
45S5 ($45SiO_2$–$24.5Na_2O$–$24.5CaO$–$6P_2O_5$) wt%	Melt quench	Icariin	Coating of 45S5 BG scaffolds with icariin dissolved in crosslinked gelatin solution	Anti-inflammatory and angiogenic	Bone tissue engineering	[19]
45S5 ($45SiO_2$–$24.5Na_2O$–$24.5CaO$–$6P_2O_5$) wt%	Melt quench	Icariin	Immersion of BG scaffolds into the herbal drug solution	Anti-inflammatory	Bone tissue engineering	[24]
45S5 ($45SiO_2$–$24.5Na_2O$–$24.5CaO$–$6P_2O_5$) wt%	Melt quench	Curcumin	Coating of curcumin mixed into the solution of chitosan on poly-ether-ether- ketone PEEK/bioactive glass/ hexagonal Boron nitride by EPD	Antibacterial and anti-inflammatory	Implant protection therapy	[25]
$15CaO$–$5P_2O_5$–$80SiO_2$ and $14.5CaO$–$4.8P_2O_5$–$77.3SiO_2$–$3.4Ga_2O_3$ mol% (mesoporous glass)	Sol–gel	Curcumin	Immersion of BG into the ethanolic solution of curcumin	Antibacterial and anti-inflammatory activity	Drug delivery system for bone repair	[26]
$80SiO_2$–$15CaO$–$5P_2O_5$ mol% (microporous and mesoporous glass)	Sol–gel	Curcumin and synthetic curcuma derivates	Evaporation method	Antibacterial activity	Drug delivery system for bone repair	[27]
45S5 ($45SiO_2$–$24.5CaO$–$24.5Na_2O$–$6P_2O_5$) wt%	Melt-derived	Chrysanthemum rubellum (durian)	Incubation of immersed BG and Chrysanthemum rubellum mixture	Anti-inflammatory, antioxidant, and antimicrobial	Dental tissue regeneration	[28]
$56.5SiO_2$–$15CaO$–$11Na_2O$–$8.5MgO$–$6P_2O_5$–$3K_2O$ wt%	Melt-derived	*Curcuma longa* (turmeric)	Coating of BG mixed with *Curcuma longa* extract on polymethyl methacrylate (PMMA)-stainless steel	Osseointegration and antimicrobial effects	Implant protection therapy	[29]

$56.5SiO_2$–15CaO–$11Na_2O$–8.5MgO–$6P_2O_5$–$3K_2O$ wt%	Melt-derived	*Ocimum sanctum* (holy basil)	Coating of BG mixed with *Ocimum sanctum* extract on PMMA-stainless steel	Osseointegration and antimicrobial effects	Implant protection therapy	[29]
45S5 ($45SiO_2$–24.5CaO–$24.5Na_2O$–$6P_2O_5$) wt%	Melt-derived	Yunnan baiyao	Mixing of yunnan baiyao into vaseline containing BG	Hemostatic, anti-inflammatory, angiogenic	Diabetic wound healing	[30]
$46SiO_2$–24CaO–$24Na_2O$–$6P_2O_5$ wt%	Melt-derived	Curcumin	Curcumin is loaded into BG–chitosan films by swelling method	Antioxidative activities	Wound healing	[31]
16CaO–$4P_2O_5$–$80SiO_2$ wt%	Sol–gel	Propolis	Propolis is incorporated during sol–gel synthesis of BG	Antifungal, antibacterial, anti-inflammatory, antiviral	Drug delivery system for bone repair implants	[32]
33CaO–$9P_2O_5$–$58SiO_2$ wt% (mesoporous glass)	Sol–gel	Propolis and cranberry	Immersion of BG into solution containing propolis	Antifungal, antibacterial, anti-inflammatory, antiviral	Bone tissue engineering	[33]
$97.5SiO_2$–2.5CaO wt% (mesoporous glass)	Sol–gel	Coumarin	Coumarin loading on surface modified MBG and irradiated with different wavelength of UV light	Antimicrobial, anti-inflammatory	Intelligent drug delivery systems for tissue engineering applications	[34]
45S5 ($45SiO_2$–24.5CaO–$24.5Na_2O$–$6P_2O_5$) wt%	Melt-derived	Lawsone	Coating on stainless steel with PEEK/BG by EPD	Anti-inflammatory, antibacterial, antifungal, antiviral	Implant protection therapy	[35]
$40SiO_2$–45CaO–$6P_2O_5$ mol%	Sol–gel and melt-quenched BGs	Polyphenols extracted from sage	Extracted polyphenols are loaded on BG/PCL composite film during solvent casting method	Antioxidant, anti-inflammatory, anti-carcinogenic, and antibacterial	Anticancer	[22]
$40SiO_2$–45CaO–$6P_2O_5$ mol%	Sol–gel and melt-quenched BGs	Polyphenols extracted from sweet cherry	Extracted polyphenols are loaded on BG/PCL composite film during solvent casting method	Antimicrobial	Bone tissue regeneration	[36]
$57SiO_2$–34CaO–$6Na_2O$–$3Al_2O_3$ (SCNA) and $45SiO_2$–26CaO–$15Na_2O$–7MgO–$3P_2O_5$–$4K_2O$ (CEL2) mol%	Melt-quenched	Polyphenols extracted from grape skin	Grafted onto the surface of functionalized BG	Antiviral, antioxidant, antibacterial	Anticancer and cardioprotective	[37]

(Continued)

Table 12.1 (Continued)

Bioactive glass composition	Synthesis route	Phytotherapeutic compounds	Drug loading technique	Biological activity	Therapeutic application	References
$45SiO_2$–$26CaO$–$15Na_2O$–$7MgO$–$3P_2O_5$–$4K_2O$ (CEL2) mol%	Melt-quenched	Green tea leaves and red grapes skin polyphenols	Grafted onto the surface of functionalized BG	Antioxidant, anticancer, antibacterial, anti-inflammatory, vasoprotective and bone stimulating activities	Anticancer	[38]
$57SiO_2$–$34CaO$–$6Na_2O$–$3Al_2O_3$ (SCNA) and $45SiO_2$–$26CaO$–$15Na_2O$–$7MgO$–$3P_2O_5$–$4K_2O$ (CEL2) mol%	Melt-quenched	Gallic acid	Grafted onto the surface of functionalized BG	Antioxidant, anti-carcinogenic, and antibacterial	Anticancer	[39]
45S5 ($45SiO_2$–$24.5CaO$–$24.5Na_2O$–$6P_2O_5$) wt%	Melt-derived	Ferulic acid	Coating on stainless steel with chitosan/BG by EPD	Antioxidant, anti-inflammatory, antimicrobial, anti-allergic, hepatoprotective, anti-carcinogenic, anti-thrombotic, antiviral, and vasodilatory properties	Implant protection therapy	[40]

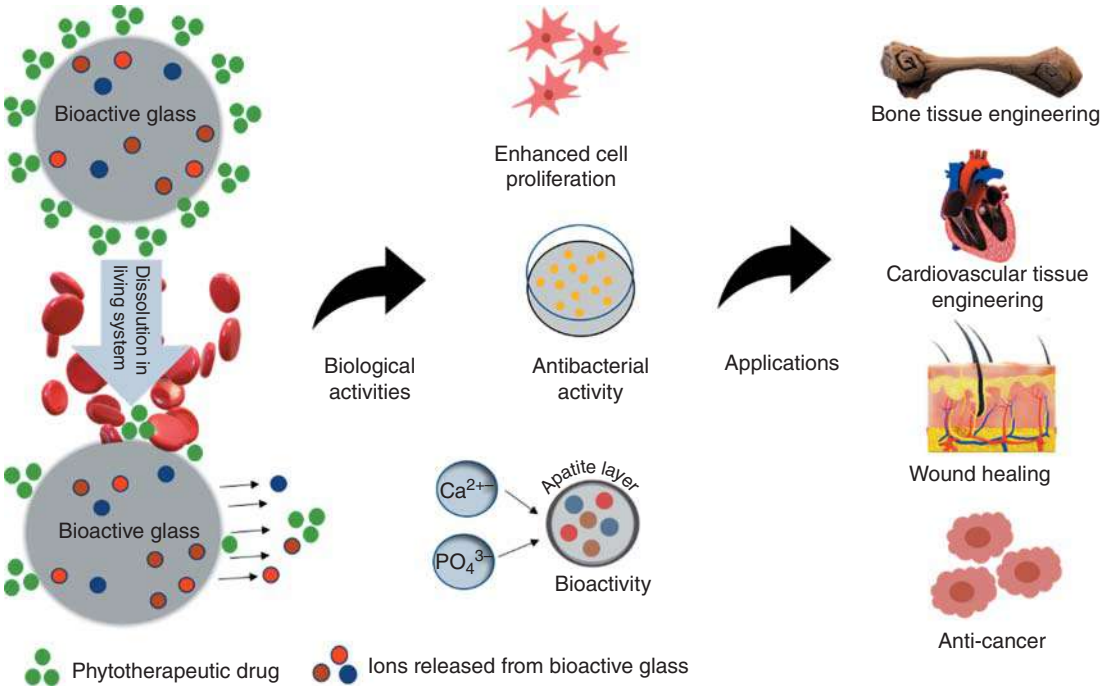

Figure 12.1 Schematic representation of dual release of ions and phytotherapeutic drugs from BGs with enhanced biological activities and therapeutic applications. (Illustration created with PowerPoint® software.)

as well as pulmonary, gastrointestinal, and hepatic disorders. In literature, several evidences show the efficacy of turmeric against cancer, microbial infections, and inflammation [43, 44]. Moreover, turmeric extract is popular because of its remarkable antibacterial property that significantly inhibits biofilm formation and therefore protects dental and bone implants from inflammation [45]. The chief phytochemical extracted from turmeric is "Curcumin." Being a polyphenol, it has a unique shielding property against bacteria and fungi. For example, its activity against periodontopathic bacteria is promising [46]. The compound is capable of modifying the architecture of developed multispecies biofilms; hence with this strategy, it is possible to decrease the biofilm metabolic activity [47]. These characteristics rank curcumin as a very effective antibacterial and antifungal agent [48]. Furthermore, curcumin has the potential to stimulate osteogenic mesenchymal stem cell differentiation [49], as a consequence, it can contribute to implant osseointegration [29].

Ocimum sanctum (family name Lamiaceae), in Hindi called as "tulsi" and "holy basil" in English, is famous for its medicinal compounds used to cure numerous ailments including infections [50, 51]. Not only its leaves have medicinal properties but also the other parts of the plant have shown influence against diseases. The most remarkable property of this plant is its capability to act as an antimicrobial, anti-inflammatory, analgesic, antipyretic, immunomodulatory, adaptogen, antidiabetic, antioxidant, and anticancer agent [50]. Moreover, the essential oil of tulsi is a potent botanical source of eugenol, which is a phenolic compound well known for its antimicrobial activity [52]. *O. sanctum* has also been reported to have bone fracture and wound healing properties [53, 54].

Neem (*Azadirachta indica*) has a significant history among medicinal herbs that have powerful anti-inflammatory, antibacterial, and antiviral properties [55]. The amalgam of organic/inorganic compounds present in it has encouraging physiological action on living organisms. Neem is considered a rich source of organic compounds used for the preparation of a variety of medicines to cure several life-threatening illnesses [11]. Being an antibacterial agent, antibacterial polymeric nanocomposite films with neem extracts have been applied for many years as food preservative [56].

Chrysanthemum rubellum (durian), a beautiful flowering plant, belongs to the broad family of species in genus *Chrysanthemum* and is renowned for its therapeutic properties [28]. It is widely employed for the development of conventional as well as advanced drugs. It is normally marketed as herbal drink, well-known for body cooling, soothing, and refreshing effects. In addition, its flowers contain several constituents, that are nontoxic and accountable to provide relief against various infectious diseases [28]. Moreover, several studies have shown the efficacy of its extract proving that it has activity against inflammation [57, 58], cancer [59], and osteoporosis [60]. Similarly, Chrysanthemum rubellum possess antioxidant [28] as well as antimicrobial activities [61]. The prominent therapeutic compounds of this perennial herb are undecane [62], 1,3-butanediol (6), benzene, eicosane 1,3-bis(1,1-dimethylethyl) (8), phenols, and 2,4-bis(1,1-dimethylethyl) [28].

Lawsonia inermis, is a well-known member to the family "Lythracae," commonly called Henna [63]. It is a widespread cosmetic agent being used to dye hair, paint skin, and stain nails [64]. Besides its cosmetic popularity, this herb contains a treasure of chemical constituents such as flavonoids, botulin, and coumarins. Additionally, approximately 0.4–1.5% of 2-hydroxy-1,4-naphthoquinone is present in the dried leaves [63]. All these components provide lowsonia with anti-inflammatory, antifungal, and antiviral properties [65]. Lowsonia has been used to treat burned skin of rats showing remarkable progress [64]. This herb can have the ability to heal wounds and burns [21].

Propolis, popular for its wax-like nature generally called "bee glue," Propolis is composed by worker-bees from different plants commonly including beech, conifer, and alder [66]. Further, it can be combined with pollen, bee wax, and several enzymes [67]. In antique civilizations, propolis has been used as a traditional medicine to treat the common cold; it has also wound healing capabilities and can cure ulcers [68]. Propolis consists of different polyphenols, aldehydes, and ketones. It has more than 300 chemical substances that mainly depend on the species of plants from where it is originated [68]. Propolis has encouraging properties toward hard and soft tissue regeneration, its potential as an antibacterial, antitumor, anti-inflammatory, antifungal, antioxidant, and antiviral agent has been reported [33, 69]. Hence, it is considered a potent herbal drug for TE purposes [70].

Cranberry fruit juice with up to 65% of proanthocyanidins (PACs) has been considered an anticancer and antibacterial agent. It has a long history of use against inflammations, and people used to drink it for the treatment of urinary tract infections [71]. Natural organic compounds in cranberry have been reported to be highly effective to control dental caries as well as periodontitis [72]. Moreover, Kim et al. [73] reported that PACs extracted from cranberry are capable to inhibit bacterial adhesion on the exopolysaccharide matrix and impart mechanical stability to the biofilm for microbial proliferation [73]. Several studies have also reported the antibiofilm potential of cranberry to treat bone-derived infections [33].

Natural polyphenols are secondary plant metabolites including coumarin (tonka bean), flavonoids, tannins, anthocyanin, phenolic acid, stilbenes, lignans, and lignin from plant extracts [21]. Coumarin represents a large group of polyphenols and is an essential constituent of many herbal extracts as well as microorganisms such as bacteria and fungi [74]. Coumarin

Table 12.2 Commonly used phytotherapeutic compounds that have been considered in combination with BGs.

Phytotherapeutic compounds	Classification	Herbal source	Chemical formula	Chemical structure	References
Curcumin	Diarylheptanoids	*Curcuma longa*	$C_{21}H_{20}O_6$	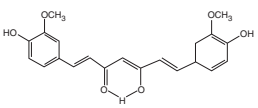	[21, 86]
Coumarin	Flavonoid	Tonka beans	$C_9H_6O_2$	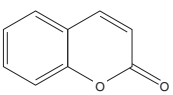	[87]
Quercetin	Flavonoid	Green tea, grapes skin, berries, red onion, apples	$C_{15}H_{10}O_7$	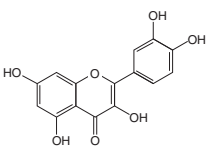	[88]
Daidzein	Flavonoid	Soya beans, nuts, and legumes	$C_{15}H_{10}O_4$	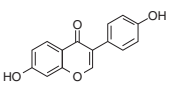	[21, 78]

Lawsone (hennotannic acid)	Naphthoquinone	*Lawsonia inermis* (Henna)	$C_{10}H_6O_3$	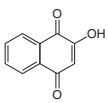	[89]
Icariin	Flavonoid	*Epimedium* L.	$C_{33}H_{40}O_{15}$	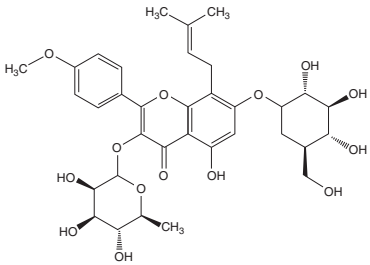	[21]
Gallic acid	Phenolic acid	Green tea, grapes skin, nuts	$C_7H_6O_5$	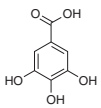	[90]
Ferulic acid	Phenolic acid	Whole grains, seeds, leaves, plant cell walls	$C_{10}H_{10}O_4$	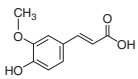	[40]

consists of many chemical compounds and their derivatives. However, two of them (pyrano- and furano-coumarins) are widely used in the pharmacological industry. A special class of coumarin having long-chain hydrocarbon provides a protective shield against microorganisms [75]. Furthermore, coumarins also provide defense against cancer and several inflammations. Moreover, according to several reports, coumarins comprise biocompatible natural compounds [76, 77] and have anticoagulant and antioxidant activities [75]. Another compound belonging to secondary plant metabolites is daidzein, an isoflavone. Soybeans, fruits, and nuts are an abundant source of daidzein. This compound has a remarkable effect as chemoprevention for heart disease and prostate cancer. Furthermore, it has been considered a potential drug for the treatment and prevention of osteoporosis [78, 79].

Flavonoids represent many biological advantages when used in combination with biomaterials. One such flavonoid is icariin that is extracted from the dried leaves of the medicinal herb *Epimedium* L. [80]. This phytotherapeutic substance has appealed several researchers in the past few years because of its biocompatibility nature, high melting point, and stable chemical structure. Above all, it is a cost-effective substance [81, 82]. Besides its anti-inflammatory activities and ability to improve neuronal viability, it is also recognized for its ability to heal disorders related to bone [80, 83, 84]. Similarly, sage and sweet cherry are enriched with polyphenolic compounds (PPhs) that include tannins, flavanols, hydroxycinnamates, and flavan-3-ols. All these flavonoids exhibit antioxidant properties. Besides, sweet cherry is also a rich source of ascorbic acid which can decrease the risk of cancer and cardiovascular diseases [85].

A large group of polyphenols consists of gallic acid and its derivatives, which can be extracted from different parts of medicinal plants. Several reports proved that gallic acid is a natural antioxidant that possess several medicinal and clinical advantages. It can destroy cancerous cells; moreover, it is widely employed as an antibacterial agent for drug development [21].

All in all, there is an endless list of botanical herbs treasured with phytotherapeutic compounds and the use of these phytotherapeutic agents in combination with engineered biomaterials is becoming more popular. Numerous studies have been conducted to evaluate the therapeutic effects of natural compounds after incorporation in combination with BGs. The summary of phytotherapeutic agents that have been used in combination with BGs, as reported in literature, is given in Table 12.2.

12.3 Bioactive Glasses and Drug Delivery

The origin of BGs goes back to 1969, when Prof. L. Hench (University of Florida, USA) synthesized the very first BG, which demonstrated a strong bonding to bone [91]. In the past years, numerous silicate, phosphate, and borate BGs have been synthesized and explored for several applications that include dental implants, bone substituting materials, antibacterial coatings, drug delivery carriers, and scaffolds to repair both bone and soft tissues [92, 93]. Osteostimulation activity and vascularization potential are special characteristics associated with borate and silicate BGs [94, 95]. Bioreactivity of BGs is also related to their partial dissolution after immersion in physiological solutions [92]. During this dissolution process, ions of biological significance are released from BGs. These ions depend on BG composition; for example, silicon (Si), phosphorous (P), calcium (Ca), magnesium (Mg), potassium (K) as well as many other biologically active ions in special BG compositions are released (e.g. Ag^{+}, Li^{+}, Mn^{2+}, Cu^{2+}, Zn^{2+}, etc.) [96]. Because of the surface reactivity, a hydroxyapatite (HA) layer forms on the surface of BGs, which is responsible for the bonding of BGs to bone [91]. Moreover, the ion release mechanism enables a direct interaction of

BGs with cellular pathways, and such BGs can be considered a class of cell instructive materials. BGs are produced traditionally by the melt quench method; however, more recently the sol–gel technique has been conquering the field. By using the sol–gel route, mesoporous BGs with large surface area can be synthesized that may improve bioactivity and enhance other properties desired for TE applications [95, 97, 98]. For example, it is possible to produce ordered mesoporous BGs by exploiting the supramolecular chemistry of surfactants during sol–gel synthesis [98, 99]. Ordered mesoporous glasses with well-defined surface area and symmetric porosity are suitable for drug delivery as they enable superior drug loading and release capability [100]. The fundamental reason for the controlled drug release is the high surface area, pore diameter, pore volume, and hence better functionalization of mesoporous BGs in comparison to melt derived counterparts [97, 98]. Several studies have been focused on enhancing the biological characteristics of BGs by incorporating synthetic or natural molecules, e.g. antibiotics [101], anticancer drugs [102] and/or phytotherapeutic compounds as well as growth factors [95]. In the past few years, the use of phytotherapeutics/herbal drugs to boost the biological functions of BGs has been the focus of an increasing number of studies [21].

BGs loaded with phytotherapeutic agents combine the therapeutic/biological activities of the loaded herbal extract with the specific properties of BGs, in particular their ability to release biologically active ions [21]. Therefore, many researchers are increasingly investigating BGs as carriers for phytotherapeutic drugs in order to improve the biological performance of BGs [103]. Interaction of BGs with phytochemicals gives rise to novel bioactive materials that exhibit efficacy to reduce the risk of inflammation, infection, and to prevent bacterial colonization on implant or scaffold surfaces. Before choosing a suitable material for the controlled release of a drug carrier, some general requirements such as biocompatibility and bioresorbability must be considered [91]. Moreover, the drug carrier should exhibit appropriate surface properties for enabling cell attachment, proliferation, and differentiation [104, 105]. It is not surprising that BGs fulfill all these requirements and hence, BGs are being increasingly considered appropriate phytotherapeutic drug delivery vehicles, specially mesoporous BGs [106].

12.4 Tailoring the Biological Response of Bioactive Glasses by the Interaction with Phytotherapeutics

12.4.1 Bioactivity and Antimicrobial Tuning

Bacterial proliferation during treatment or bacterial attachment to the surface of implants may cause the development of biofilms at the site of implantation [107]. An important approach to avoid implant-related infections is the use of antibiotics. The selection of suitable antibiotics, their application method, and administration time represent a common challenge in medicine [108–110]. The need of the hour is to develop appropriate drug doses that can be efficiently administered directly to the specific location in order to avoid toxic side effects [111]. The advantage of the direct and controlled release of drugs at the required site to achieve therapeutic effectiveness has been often highlighted [107].

The use of medicinal plants as antimicrobial agents is emerging because of the excellent activity of some phytochemicals against microbes as well as low risk of side effects [112]. Recently, Floroian et al. [29] reported a new composite material, derived by the combination of *C. longa* with BG (composition in wt%: 56.5SiO_2, 15CaO, 11Na_2O, 8.5MgO, 6P_2O_5, 3K_2O) blended with a polymer (poly(methyl methacrylate)) matrix. The composite was then deposited by matrix-assisted pulsed

laser evaporation as smooth thin films onto the surface of stainless steel substrates. The composite loaded with *C. longa* was reported to accelerate the osseointegration and to exert superior antimicrobial effects. Similarly, the authors described that combining the extract of tulsi with a BG (similar composition mentioned above) enhanced the osseointegration and antimicrobial activities in infected implants [29]. BG nanoparticles doped with neem have been synthesized and assessed for their improved *in vitro* bioactivity and cytotoxicity [11, 55]. It was observed that neem-based BG nanoparticles had excellent physical as well as chemical properties along with a broad spectrum of antimicrobial activity [11]. Similarly, Prabhu et al. [11] described that the powder of neem leaves incorporated into sol–gel derived nanoparticles (SiO_2–CaO–P_2O_5) containing 1 mol% of silver significantly magnifies the bioactivity and antimicrobial activity, reporting thus a synergistic effect of neem and Ag^+ ions.

Propolis and cranberry have potent antimicrobial properties [72]. Several research groups have studied their effect as anti-biofilm compounds [113]. In one study, propolis was incorporated in different ternary sol–gel derived BGs (composition: $(SiO_2)_x(P_2O_5)_y(CaO)_z$) with and without tetracycline and the release of the loaded components was studied [32]. Another group [33] prepared anti-biofilm compound by combining 58S mesoporous BG (composition in wt%: 58SiO_2, 33CaO, 9P_2O_5) with propolis and cranberry. The results showed the remarkable impact of these BG-phytotherapeutics combinations as anti-biofilm compounds. Besides, it was observed that the bioactivity of prepared samples was enhanced within 72 hours, which is suitable for clinical applications. Figure 12.2 shows field emission scanning electron microscope (FESEM) images of BG incorporated with propolis and cranberry [33], which shows that after 24 hours immersion in simulated body fluid (SBF) an increased hydroxyl-carbonate apatite (HCAp) formation took place on the surface of mesoporous bioactive glasses (MBG) particles loaded with 5 mg/ml cranberry PACs (Figure 12.2b). In addition, after 72 hours spherical apatite crystals were seen to form on the surface of the BG (Figure 12.2b). However, in case of 10 mg/ml cranberry PACs loaded MBG, a delayed HCAp formation was observed. The surface of the MBG was smooth even after 24 hours of immersion in SBF (Figure 12.2c). However, after 72 hours of immersion the presence of several rounded apatite structures was observed (Figure 12.2c). MBG particles loaded with both propolis concentrations (5 and 10 mg/ml) are shown in Figure 12.2d,e. Both samples showed the formation of an HCAp layer after 24 hours of immersion in SBF. The formation of HCAp, independently of the presence of the phytotherapeutic compound, is significant considering the application of such particles in bone TE.

Moreover, fruits and leaves of sweet cherry are a great source of PPhs. Dziadek et al. [36] introduced these PPhs into poly(ε-caprolactone) films synthesized by solvent casting method, which were modified with sol–gel and melt derived BG particles (composition: 40SiO_2–54CaO–6P_2O_5 mol% with particle size < 45 μm). The result showed 100% entrapment efficiency of polyphenols (extracted from leaves and fruits of sweet cherry) into the matrix. The *in vitro* bioactivity of both BGs loaded with PPh was studied. It was noticed that even though the leaf extracts had higher concentrations of PPh (72.63 mg of chlorogenic acid (CGA) 100 ml^{-1}) as compared to fruit extracts (58.82 mg CGA 100 ml^{-1}), higher concentration of PPh could be found on the surface of composite films combined with fruit extracts. Different composition of PPh in both extracts resulted in various PCL-PPh and BG-PPh intermolecular interactions [114]. Moreover, the fabrication method of the BG also induced different interactions between the BG component and the PPh. For example, sol–gel derived BGs containing large number of residual O–H groups on their surface can effectively bind PPh [115, 116]. It was concluded that the combination of polyphenols either extracted from leaf or fruit of sweet cherry with both types of BGs (synthesized by using sol–gel and melt quenching methods) represents a reliable approach to enhance the *in vitro* bioactivity of the biomaterials.

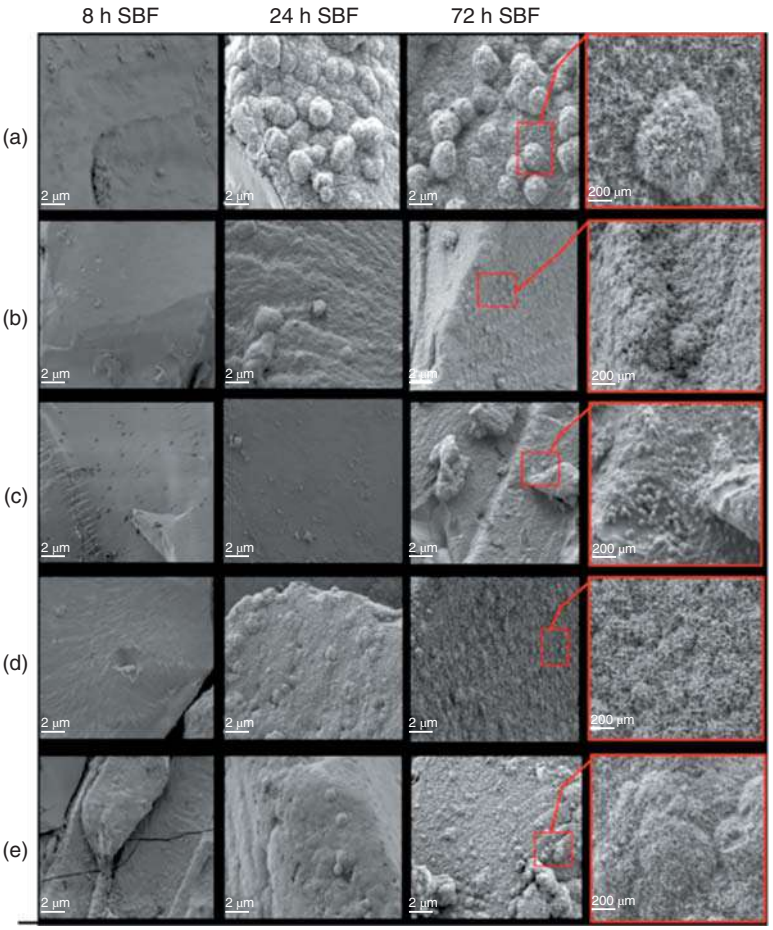

Figure 12.2 FESEM micrographs at magnification 10 000× recorded on 58S MBG particles after immersion in SBF for 8, 24, and 72 hours. (a) Pure MBG particles, (b) MBG particles containing 5 mg/ml cranberry PACs, (c) 10 mg/ml cranberry PACs, (d) 5 mg/ml propolis, and (e) 10 mg/ml propolis. Red squares exhibit corresponding micrographs at 50 000×. Source: Galarraga-Vinueza et al. [33], Figure 06 [p. 23]/with permission from John Wiley & Sons, Inc.

To prove the antibacterial efficiency as well as bioactivity of BGs loaded with herbal extracts, several techniques have been studied in the last few years. Ur Rehman et al. [35] used electrophoretic deposition (EPD) in order to investigate the antibacterial effects of a phytotherapeutic compound (lawsone) combined with 45S5 BG particles and chitosan. After mixing, the resulting material was deposited on top of stainless steel substrates by using EPD. Substrates previously coated with 45S5 BG and polyether ether ketone (PEEK) matrix were used. In addition to antibacterial effects, bioactivity analysis showed the formation of an apatite layer on the surface of coated samples, as well as a sustained release of the herbal drug from the composite coating (analyzed for a duration of six months) [35].

Recently, Akhtar et al. [40] used the same technique (EPD) to produce novel ferulic acid loaded BG (45S5) – chitosan composite coatings. It was observed that the presence of ferulic acid significantly increased the antibacterial effect of the coatings against *Staphylococcus aureus* and *Escherichia coli*. Moreover, it was observed that the antibacterial activity of the coatings was correlated with different concentrations of ferulic acid in the composite coatings. However, no

significant change in HA formation on the surface of the samples in SBF was observed with the presence of the phytotherapeutic agent.

Another attractive antimicrobial phytotherapeutic compounds is gallic acid, which is obtained from red grape skin and green tea leaves. Researchers have tried to co-functionalize two different BGs: SCN1 glass ($57SiO_2$, 34CaO, and $9Na_2O$, mol%) with larger reactivity and less reactive SCNA glass ($57SiO_2$, $6Na_2O$, 34CaO and $3Al_2O_3$, mol%) with extracted gallic acid from green tea and red grapes skin and combined them with silver nanoparticles [117]. The resulting smart multifunctional biomaterial exhibited enhanced antibacterial activities against *S. aureus*. The analyzed results therefore show that such phytotherapeutic compounds combined with BGs represent a novel biomaterial class with excellent antibacterial properties.

12.4.2 Biocompatibility and Cell Proliferation

Naturally occurring materials such as herbal extracts have inherent biochemical characteristics that can be exploited to induce cell proliferation [118]. In order to evaluate the effect of phytotherapeutic compounds, Zain et al. [28] reported the superior attachment and differentiation of dental pulp stem cells after loading 45S5 BG with "Chrysanthemum rubellum" extract. This novel biomaterial motivates the possibility to be applied as natural medicament for dental tissue regeneration [28]. Icariin is a well-known phytochemical for osteogenic differentiation of pre-osteoblastic cells and it has been shown to enhance osteogenic activity [82]. Further, it has been confirmed that icariin has the ability to encourage angiogenesis by inducing endothelial cell migration and attachment [82]. In this context, Jing et al. [24] reported *in vitro* experiments with rat adipose-derived stem cells and endothelial progenitor cells. They prepared 45S5 BG-based scaffolds by using the foam replica method, and then the surface of scaffolds was loaded with icariin. The results showed no considerable difference of *in vitro* cell proliferation on both loaded and unloaded scaffolds. Therefore, *in vivo* evaluation was performed by the same group, and it was found that icariin loaded scaffolds as compared to unloaded scaffolds showed not only better cell proliferation but also enhanced bone regeneration and neovascularization [24]. Chen et al. [78] synthesized polymer microspheres loaded with daidzein by using oil in water emulsion technique. 45S5 BG scaffolds were coated with this material and it was observed that multilayered coatings significantly enhanced the alkaline phosphatase (ALP) activity of MC3T3-E1 cells. Akhtar et al. [40] used EPD to develop composite coatings of 45S5 BG and chitosan with a phytotherapeutic compound (ferulic acid). It was observed that the viability of MG-63 cells increased due to the incorporation of ferulic acid in the composite coatings. By summarizing the above findings, there is emerging evidence that phytotherapeutic compounds may significantly improve the biological activity of BGs and synergistic effects of the phytotherapeutic agents and BG dissolution products are expected.

12.4.3 Sustained Release Kinetics of BGs Loaded with Phytotherapeutics

Biodegradability is a critical property of biomaterials in the context of regeneration of new tissues. During this process, some biomaterials need a few months to years to induce tissue regeneration [119]. Therefore, functionalization of materials and loading them with drugs, e.g. phytotherapeutic compounds, is a suitable option for the controlled release of non-covalently bonded phytochemicals, and hence to improve the time-dependant biological performance of the material [119, 120].

A new approach to drug delivery is the light-sensitive intelligent release of coumarin introduced by Lin et al. [34]. Coumarin was loaded into mesoporous binary BG (SiO_2–CaO) particles. The purpose of this combination was to design a photo-switched controlled release system. The strategy involved blocking the pores of the mesoporous BG and entrapping the drug coumarin into the

mesopores by irradiation with UV light (wavelength greater than 310 nm). After that, the same mesoporous BG particles with the entrapped drug were exposed to UV light (wavelength shorter than 250 nm). With this strategy, the induced photo-dimerization could be redeveloped, and the release of the entrapped drug could be initiated. This study has thus shown an interesting novel approach for controlled drug delivery from mesoporous BGs [34]. Moreover, microspheres incorporating daidzein synthesized by Chen et al. [78] depicted an alternative approach for the controlled release of the drug. Both metallic substrates and BG scaffolds were coated by microspheres loaded with daidzein. It was evident from this study that daidzein showed a tenable release by a diffusion-controlled mechanism.

In a related study, gelatin–icariin coatings on 45S5 BG-based scaffolds were prepared and crosslinked with *N*-(3-dimethylaminopropyl)-*N*′-ethylcarbodiimide hydrochloride/*N*-hydroxysuccinimide or caffeic acid [19]. Icariin release was studied by immersing the scaffolds in SBF solution. The results showed the sustained release of icariin from the scaffolds [19]. However, no study has investigated the controlled dual release of this phytotherapeutic agent and biologically active ions from BG scaffolds and long-term *in vivo* effects of such combination of icariin and ions remain unknown.

12.5 Loading Techniques of Phytotherapeutic Compounds on Bioactive Glasses

Several methods have been studied to incorporate or attach phytotherapeutic agents on the surface of BGs. Among them, the potentially most effective approach is to modify the surface chemistry of BGs with an organic functional group. Other strategies involve physical adsorption and the addition of herbal drugs during the room temperature synthesis process of BGs (by sol–gel method) [91].

12.5.1 Surface Modification of BGs

In order to develop active sites on the surface of BGs, numerous organic functional groups, for example, NH_2, SH, or COOH, have been considered [121]. The surface-active sites are advantageous for further molecular grafting to the surface of BGs or to insert specific properties. For the surface modification of BGs, use of coupling agents or changing the pH of the targeted surface are suitable strategies [122]. Generally, the introduction of the amino group (NH_2) onto the surface of BGs is performed by a silanization reaction with APTES [(3-aminopropyl) triethoxysilane, $C_9H_{23}NO_3Si$] [122]. Verné et al. [123] reported that APTES could attach BMPs, e.g. BMP-2, on the surface of BG CEL2 (composition: 45% SiO_2, 3% P_2O_5, 26% CaO, 7% MgO, 15% Na_2O, 4% K_2O mol%) via a proper covalent bond. APTES is a chemical agent considered to have silane groups in combination with amino groups, which could encourage the development of spherical HA agglomerates without reducing the bioactivity of the glasses [124]. The hydrolysis of APTES in an aqueous environment results in the development of silanol groups, which could then react with O–H groups exposed on the surfaces [121]. A typical surface modification could involve four steps, including hydrolysis, condensation reaction, hydrogen bonding, and finally bond formation [125]. Figure 12.3 is the graphical representation of these steps. Besides its use in silica-based BGs, APTES has been effectively grafted to borate and phosphate glasses as well [126, 127]. Therefore, this strategy introduces novel surface-functionalized materials for several biomedical purposes. In the domain of drug delivery, functionalized BGs can be effectively combined with the drug [121]. For example,

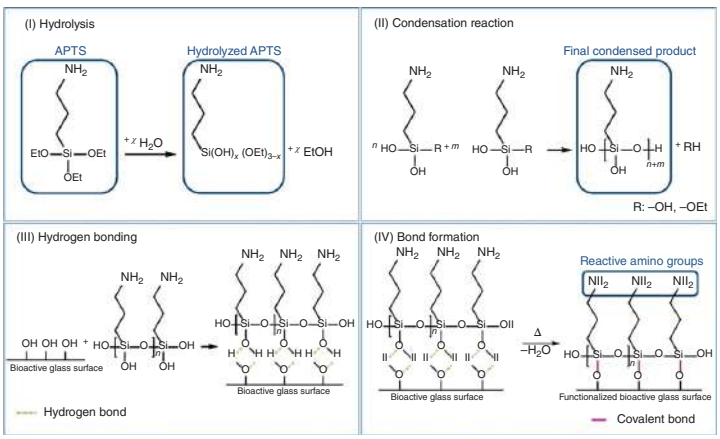

Figure 12.3 Schematic representation of different steps of surface functionalization of 45S5 BG-based scaffolds by using APTS. Source: Reproduced from Hum [125] from a MDPI journal under the Creative Common CC BY license.

in anticancer drug delivery approaches, functionalized BGs with surface grafted chemotherapeutic drugs in combination with specific targeting molecules are considered reliable systems [128]. Natural polyphenols extracted from grape skins and tea leaves grafted to the surface of BGs via gallic acid without using any coupling agent is another demonstrated approach for surface functionalization that was investigated to stimulate osteoblast cell attachment [37]. Moreover, these functionalized biomaterials are considered to have excellent antioxidant activities. The technique for grafting polyphenols onto the surface of functionalized BGs involved first the washing of BG samples with acetone solution which exposes OH groups, followed by functionalization with gallic acid [38]. It has been also shown that functionalization of BG of composition: $45SiO_2$, 26CaO, $3P_2O_5$, 7MgO, $15Na_2O$, $4K_2O$ (mol%) itself imparts certain antioxidant activity which could be further enhanced by grafting natural polyphenols to the surface [115]. Polyphenols extracted from grape skin were successfully grafted on two different BG surfaces namely SCNA (composition: $57SiO_2$, 34CaO, $6Na_2O$, $3Al_2O_3$, mol%) and CEL2 (composition: $45SiO_2$, $3P_2O_5$, 26CaO, 7MgO, $15Na_2O$, $4K_2O$, mol%) by Zhang et al. [37]. Initially, O–H groups on the surface of BGs were exposed and after that the BG was mixed with the phenolic solution. Furthermore, addition of citric acid was employed to evaluate the effect of pH on phenolic uptake by the BGs [37]. It was observed that CEL2 exhibited higher ability to bind with phenols which can be explained with its higher reactivity in comparison to SCNA. Summarizing, phytotherapeutic compound grafting to the functionalized surface of BGs is attracting increasing attention due to the advantage of achieving sustained release of herbal drugs [21]. Figure 12.4 shows a graphical representation of the technique for loading phytotherapeutic compounds onto surface-functionalized BGs.

12.5.2 Physicochemical Method

Physicochemical methods to combine phytotherapeutic agents with BGs include coating procedures, solvent casting, particle leaching, and immersion of samples into the solution of the phytotherapeutic drug [121]. Another approach is the addition of herbal drugs during the manufacturing process of BGs. However, this method does not qualify for the traditional BG melt quench process because of the high temperatures involved. On the contrary, the introduction of drugs, proteins, or other bioactive components into the sol–gel process preserves their functionality as the whole procedure is carried out at room temperature. Bonfim et al. [129] reported the introduction of Brazilian red and green propolis extract solution into BG (composition: SiO_2 80 wt%, P_2O_5 4 wt%, CaO 16 wt%) during the BG synthesis via sol–gel process. It was observed that the antimicrobial effect of the BG was significantly enhanced [129]. The simplest and commonly used loading technique is the immersion of BGs (in form of particles, coatings and scaffolds) into the solution containing the phytotherapeutic compound of interest. Immersion of MBG particles into solutions of herbal drugs can be used to entrap the organic components into the pores with or without chemical bonding, alternatively molecules can be simply adsorbed on the surface of

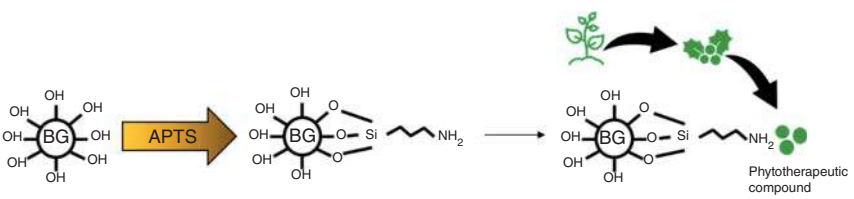

Figure 12.4 Loading of phytotherapeutic compound on amino functionalized BG surface. (Illustration created with PowerPoint® software.)

the MBG particles [91]. There are several studies reporting the loading of herbal compounds into BGs by the immersion method. For example, Galarraga-Vinueza et al. [33] successfully loaded the organic compound PACs extracted from green propolis and cranberry on mesoporous 58S BG by immersion of BG particles in the solution of the plant extract. Figure 12.5 shows a graphical representation of the immersion method for loading phytotherapeutic agents onto mesoporous BG. Similarly, icariin–gelatin coating onto 45S5 BG scaffolds were obtained by immersion technique was reported by Reiter et al. [19].

EPD was used by Virk et al. [25] in order to combine CUR with BG particles. EPD was employed first to produce poly-ether-ether-ketone/BG/hexagonal boron nitride layers on stainless steel substrate, and then chitosan/CUR layers were deposited on the previously deposited coating. The loading of CUR resulted in antibacterial effects [25]. In another study, polyphenols were introduced into polycaprolactone (PCL) and PCL/BG composite directly using a solvent containing the plant extract via the solvent-casting method [36]. This method is effective to combine BG particles with a wide variety of polyphenols to obtain multifunctional composites exhibiting several biological activities [36].

Despite the encouraging results reported by the investigations mentioned above, BGs incorporating phytotherapeutic compounds have not been extensively characterized *in vitro* or *in vivo*. Since BGs have the capability to combine with hydrophilic as well as hydrophobic groups, *in vivo* and *in vitro* studies involving plant-derived compounds combined with BGs (scaffolds, micro and nanoparticles) are expected to emerge. Future investigations (including relevant *in vivo* studies) should be performed to quantitatively assess the benefits and synergies achieved by the incorporation of organic plant derived compounds and BGs in a variety of applications, some of which are discussed in Section 12.6 [69].

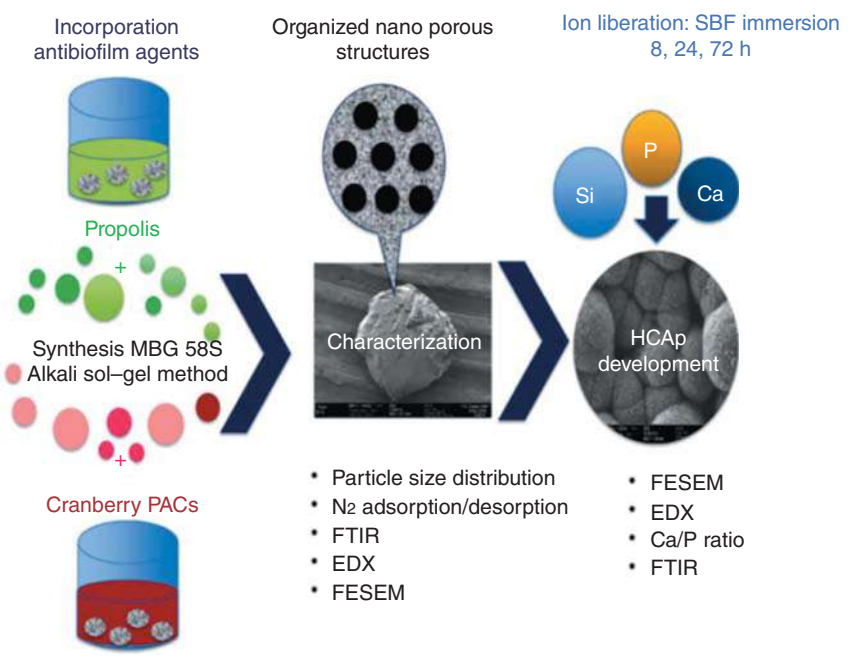

Figure 12.5 Schematic diagram showing the methodology proposed to prepare MBGs incorporating propolis and cranberry PACs. Source: Galarraga-Vinueza [33], Figure 01 [p. 18]/with permission from John Wiley & Sons, Inc.

12.6 Bioactive Glass with Phytotherapeutics: Toward Therapeutic Applications

12.6.1 Bone Tissue Engineering

Owing to the increasing aging population, there is a pressing demand for bone autografts; however, the procedure is limited primarily because of the surgical risk and the need for donor tissue [130]. Bone TE is an alternative approach, and the search for biomaterials with improved osteoconductivity and osteoinductive capability for bone TE is growing day by day [131]. Biomaterials based on BGs loaded with phytotherapeutic compounds are emerging candidates for bone TE. For example, the mechanical properties of BG (45S5) based scaffolds could be significantly reinforced by gelatin coatings [19]. Such natural polymer coatings were further exploited for loading the scaffolds with icariin to improve the bioactivity of scaffolds. The scaffolds thus showed a favorable combination of mechanical robustness, bioactivity, and drug delivery capability [19]. Similarly, ursolic acid (UA) is a pentacyclic triterpenoid compound existing in several medicinal plants that can effectively promote new *in vivo* bone formation. Recently, porous scaffolds of mesoporous BG/chitosan loaded with UA (MBG/CS/UA) were prepared in order to enhance bone regeneration [132]. UA had never been used in bone TE before; however, it was found that the MBG/CS/UA scaffolds exhibited excellent biocompatibility. The controlled release of UA from the scaffolds promoted stem cell osteogenic differentiation and *in vivo* new bone formation. The MBG/CS scaffolds were fabricated by a freeze-drying method and then loaded with UA. The hierarchical porous structure of the scaffolds resulted in a controllable UA drug release, which accelerated the expression of genes and proteins related to osteogenesis. *In vivo*, a critical-sized defect model indicated that the MBG/CS/UA scaffolds containing UA induced higher mineralization rate than the pure MBG/CS group, confirming that MBG/CS/UA scaffolds offer great potential for applications in bone repair and regeneration [132]. Moreover, for dental bone TE applications, Chrysanthemum rubellum (durian) yellow-colored petals freeze-dried extracts (CRE) combined with melt-derived 45S5 BG have been investigated [28]. It was observed that the presence of CRE in BG enhanced the dental pulp stem cells viability and proliferation. This BG-CRE combination showed potential for dental tissue regeneration [28].

Ur Rehman et al. [133] used EPD to deposit lawsone loaded BG/chitosan composite coatings. Authors found that the presence of lawsone induces an antibacterial effect. The novel coating approach combining a phytotherapeutic compound and BG particles was thus designed to protect implants against bacterial infections [133]. Similarly, the combination of BGs with plant extract blended with polymers (either natural or synthetic) to coat orthopedic implants, in order to protect the outer surface from bacterial infections has been reported [29].

12.6.2 Wound Healing

In the skin and mucosal wound healing process, inflammation is a huge barrier [31]. During healing, there is typically an initial inflammatory phase, then a proliferative phase and finally tissue remodeling. The progress of each of these phases not only depends on the features of the biomaterial used but also on the inflammation status sustained by oxidative stresses at the injury site. In this context, many natural antioxidants have been investigated, owing to the fact that many herbal compounds have been traditionally utilized as wound healing agents [119]. Increasing attention is being focused on natural compounds for wound healing [134], among which several reports distinguish CUR as phytotherapeutic agent presenting benefits such as antioxidative

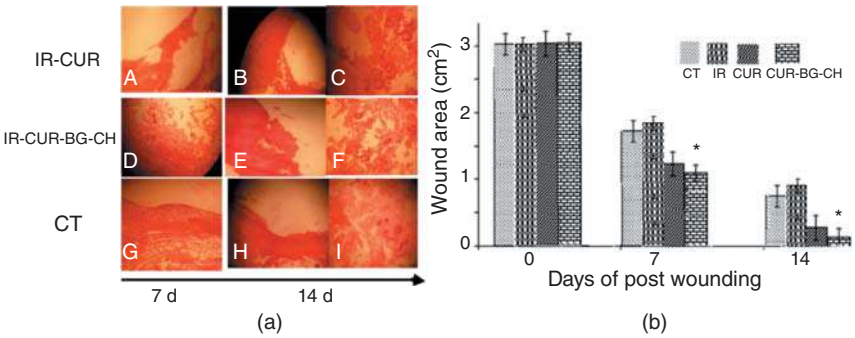

Figure 12.6 Skin histological observation: (a) hematoxylin and eosin staining of wounds treated with curcumin (CUR) and CUR–bioglass–chitosan (CUR–BG–CH) (×100) after 7 and 14 days of treatment, whereas IR represent the group of rats irradiated with γ rays. IR–CUR (irradiated and implanted with curcumin), IR–CUR–BG–CH (irradiated and implanted with curcumin–BG–chitosan), and (b) wound area in treated animals with curcumin (CUR) and curcumin–bioglass–chitosan (CUR–BG–CH) as compared with the control (control femoral condyle Wistar rats [CT]). The statistical significance of the wound area was evaluated on the 7th and 14th day of post-wounding. Source: (a) Jebahi et al. [31] Figure 05 [p. 157]/with permission from John Wiley & Sons, Inc.

activities. CUR has demonstrated safety; however, it has limitations because of its extremely rapid systemic elimination, inadequate tissue absorption, and degradation, which reduces its bioavailability. Therefore, the incorporation of CUR in polymer carriers is desirable to increase its availability for practical applications. Given its medicinal benefits, CUR has been introduced into BG–chitosan composites (BG composition: $46SiO_2$, 24CaO, $24Na_2O$, $6P_2O_5$, wt%) to investigate *in vitro* antioxidative and antimicrobial effects. *In vivo*, biomaterial potency in wound healing was investigated using a γ-irradiated model [31], and it was concluded that CUR–BG–chitosan composite might have promising potential applications for wound healing. Figure 12.6a represents the histological observation of the wound in rat skin, which shows the wound healing progress [31]. As described above, CUR exhibits several interesting properties to tackle microbial infections [29]. The results indicate that the application of unmodified CUR or curcumin–BG–chitosan (CUR–BG–CH) led to incomplete re-epithelialization of the epidermis after seven days. Interestingly, the complete re-epithelialization of the epidermis at the 14th day post-wounding was observed only in the irradiated curcumin–BG–chitosan (IR–CUR–BG–CH) group. Figure 12.6b shows the wound-healing area in the different groups. Similarly, Yunnan baiyao ointments have been investigated in combination with 45S5 BG. This combination was proven to be very effective in accelerating the recovery of diabetes-impaired skin wounds [30]. It can be concluded from the above discussion that BGs in combination with phytotherapeutic agents are attractive candidates for wound healing application, and more research in this promising field is expected.

12.6.3 Anticancer and Cardiovascular Tissue Engineering

Many researchers are considering natural plant compounds approved by the Food and Drug Administration (FDA) as anticancer agents. Such approaches are gaining attention due to their biocompatibility, biological activities, and superior physicochemical properties as well as safety profiles [135]. In this context, polyphenols extracted from different plant sources are at the center of interest. Several reports regarding the anticancer activity of polyphenols have confirmed their effectiveness when combined with BGs [21]. Polyphenols from sage, grape skin, and tea leaves are considered to have inhibitory effects against the abnormal growth of cancerous cells, having

also an effect to cure cardiovascular diseases [21]. For example, gallic acid grafted silica-based BG particles have been shown to damage tumor causing cells [38]. Cazzola et al. [38] studied the effect of CEL2 BG (composition: 45SiO_2, 3P_2O_5, 26CaO, 7MgO, 15Na_2O, 4K_2O, in mol%) functionalized with polyphenols on healthy and cancerous osteoblast cells. It was concluded that polyphenols, for example, gallic acid and green tea extracts, can effectively exert a selective cytotoxic effect against bone cancer cells upon grafting to the surface of a BG. Grapes are a great source of polyphenols which possess various biological activities and health benefits against cardiovascular diseases and certain types of cancer. Therefore, Zhang et al. [37] performed the surface functionalization of two BGs (SCNA and CEL2) with polyphenols that were extracted from grapes skin. Results demonstrated the possibility to prepare smart biomaterials by combining the inorganic activity of BGs with the specific biological properties of natural molecules to develop anticancer, antioxidant, and antibacterial activities. Similarly, to verify the positive effect of polyphenols extracted from sage against cancer cells, Dziadek et al. [22] used different BGs (composition: 40SiO_2, 54CaO, and 6P_2O_5, in mol%) produced by the melt-quenching technique and by sol–gel method, as discussed previously. During the fabrication process polyphenols extracted from sage were incorporated in order to enrich the composite films (PCL-BG). The composite showed remarkable hydrophilicity and *in vitro* bioactivity. Additionally, potential antioxidant effects and anticancer activities against cancerous cells (WM266-4) were observed.

12.7 Summary and Outlook

Owing to the broad spectrum of therapeutic properties and generally nontoxic nature of medicinal herbs, they are being increasingly considered in combination with engineered biomaterials for specific clinical applications. The complex combination of phytotherapeutic agents with BGs represents a good example of such novel approaches using natural compounds to tailor the biological properties of BGs and to intensify the positive effects of herbal drugs for medical applications. In this context, physical and chemical loading methods to incorporate natural organic compounds onto the surface of BGs with the aim to enhance biological properties for therapeutic applications are currently under extensive research. Moreover, the proper surface functionalization of BGs to attach natural compounds is at the center of research efforts for the fabrication of superior phytotherapeutic–BG combinations. Finally, further research (*in vitro* and *in vivo* studies) with deeper insights is needed to evaluate the complex interaction of herbal compounds and biologically active ions released from BGs. Generating knowledge on the positive (or non-desired cytotoxic) biological effects of the mentioned combinations will encourage the optimization of novel multifunctional and cost-effective phytotherapeutic–BG systems. These represent an alternative biomaterial technology for tackling multifactorial diseases combining the (synergistic) effects of ion releasing BGs and phytotherapeutic agents for a variety of biomedical applications.

References

1 Berger, M. (2006). Traditional medicine: a clear and present danger. *South African Journal of Science* 102 (5–6): 178–179. https://journals.co.za/doi/pdf/10.10520/EJC96553.

2 Huffman, M.A. (2003). Animal self-medication and ethno-medicine: exploration and exploitation of the medicinal properties of plants. *Proceedings of the Nutrition Society* 62 (2): 371–381. https://doi.org/10.1079/pns2003257.

3 Kadir, M.F., Bin Sayeed, M.S., Shams, T., and Mia, M.M.K. (2012). Ethnobotanical survey of medicinal plants used by Bangladeshi traditional health practitioners in the management of diabetes mellitus. *Journal of Ethnopharmacology* 144 (3): 605–611. https://doi.org/10.1016/j.jep.2012.09.050.

4 Rai, L., Prasad, P., and Sharma, E. (2000). Conservation threats to some important medicinal plants of the Sikkim Himalaya. *Biological Conservation* 93 (1): 27–33. https://doi.org/10.1016/S0006-3207(99)00116-0.

5 Ahmad, S., Zafar, M., Shinwari, S. et al. (2020). Ethno-medicinal plants and traditional knowledge linked to primary health care among the indigenous communities living in western hilly slopes of Dera Ghazi Khan, Pakistan. *Pakistan Journal of Botany* 52 (2): 519–530. https://doi.org/10.30848/PJB2020-2(19).

6 Kayani, S., Ahmad, M., Sultana, S. et al. (2015). Ethnobotany of medicinal plants among the communities of Alpine and Sub-alpine regions of Pakistan. *Journal of Ethnopharmacology* 164: 186–202. https://doi.org/10.1016/j.jep.2015.02.004.

7 Habbu, P., Hiremath, M., Madagundi, S. et al. (2018). Phytotherapeutics of polyphenolic-loaded drug delivery systems: a review. *Pharmacognosy Reviews* 12 (23): 7–19. https://doi.org/10.4103/phrev.phrev_33_17.

8 Efferth, T. and Koch, E. (2011). Complex interactions between phytochemicals. The multitarget therapeutic concept of phytotherapy. *Current Drug Targets* 12 (1): 122–132. https://doi.org/10.2174/138945011793591626.

9 Ferreira, T.S., Moreira, C.Z., Cária, N.Z. et al. (2014). Phytotherapy: an introduction to its history, use and application. *Revista Brasileira de Plantas Medicinais* 16 (2): 290–298. https://doi.org/10.1590/s1516-05722014000200019.

10 Dung, T.D., Day, C.H., Binh, T.V. et al. (2012). PP2A mediates diosmin p53 activation to block HA22T cell proliferation and tumor growth in xenografted nude mice through PI3K-Akt-MDM2 signaling suppression. *Food and Chemical Toxicology* 50 (5): 1802–1810. https://doi.org/10.1016/j.fct.2012.01.021.

11 Prabhu, M., Ruby Priscilla, S., Kavitha, K. et al. (2014). *In vitro* bioactivity and antimicrobial tuning of bioactive glass nanoparticles added with neem (*Azadirachta indica*) leaf powder. *BioMed Research International* 2014. https://doi.org/10.1155/2014/950691.

12 Prabhu, M., Kavitha, K., Manivasakan, P. et al. (2013). Synthesis, characterization and biological response of magnesium-substituted nanobioactive glass particles for biomedical applications. *Ceramics International* 39 (2): 1683–1694. https://doi.org/10.1016/j.ceramint.2012.08.011.

13 Hoppe, A., Mouriño, V., and Boccaccini, A.R. (2013). Therapeutic inorganic ions in bioactive glasses to enhance bone formation and beyond. *Biomaterials Science* 1 (3): 254–256. https://doi.org/10.1039/c2bm00116k.

14 Mouriño, V., Cattalini, J.P., and Boccaccini, A.R. (2012). Metallic ions as therapeutic agents in tissue engineering scaffolds: an overview of their biological applications and strategies for new developments. *Journal of the Royal Society Interface* 9 (68): 401–419. https://doi.org/10.1098/rsif.2011.0611.

15 El-Kady, A.M., Ali, A.F., Rizk, R.A., and Ahmed, M.M. (2012). Synthesis, characterization and microbiological response of silver doped bioactive glass nanoparticles. *Ceramics International* 38 (1): 177–188. https://doi.org/10.1016/j.ceramint.2011.05.158.

16 Liu, W.C., Robu, I.S., Patel, R. et al. (2014). The effects of 3D bioactive glass scaffolds and BMP-2 on bone formation in rat femoral critical size defects and adjacent bones. *Biomedical Materials (Bristol)* 9 (4): 45013. https://doi.org/10.1088/1748-6041/9/4/045013.

17 Liu, X., Rahaman, M.N., Liu, Y. et al. (2013). Enhanced bone regeneration in rat calvarial defects implanted with surface-modified and BMP-loaded bioactive glass (13-93) scaffolds. *Acta Biomaterialia* 9 (7): 7506–7517. https://doi.org/10.1016/j.actbio.2013.03.039.

18 Lee, K., Silva, E.A., and Mooney, D.J. (2011). Growth factor delivery-based tissue engineering: general approaches and a review of recent developments. *Journal of the Royal Society Interface* 8 (55): 153–170. https://doi.org/10.1098/rsif.2010.0223.

19 Reiter, T., Panick, T., Schuhladen, K. et al. (2019). Bioactive glass based scaffolds coated with gelatin for the sustained release of icariin. *Bioactive Materials* 4 (1): 1–7. https://doi.org/10.1016/j.bioactmat.2018.10.001.

20 Zhu, H., Zheng, K., and Boccaccini, A.R. (2021). Multi-functional silica-based mesoporous materials as co-delivery systems for biologically active ions and therapeutic biomolecules. *SSRN Electronic Journal*. https://doi.org/10.2139/ssrn.3770987.

21 Schuhladen, K., Roether, J.A., and Boccaccini, A.R. (2019). Bioactive glasses meet phytotherapeutics: the potential of natural herbal medicines to extend the functionality of bioactive glasses. *Biomaterials* 217 (June): 119288. https://doi.org/10.1016/j.biomaterials.2019.119288.

22 Dziadek, M., Dziadek, K., Zagrajczuk, B. et al. (2016). Poly(ε-caprolactone)/bioactive glass composites enriched with polyphenols extracted from sage (*Salvia officinalis* L.). *Materials Letters* 183: 386–390. https://doi.org/10.1016/j.matlet.2016.07.077.

23 Hench, L.L. (2009). Genetic design of bioactive glass. *Journal of the European Ceramic Society* 29 (7): 1257–1265. https://doi.org/10.1016/j.jeurceramsoc.2008.08.002.

24 Jing, X., Yin, W., Tian, H. et al. (2018). Icariin doped bioactive glasses seeded with rat adipose-derived stem cells to promote bone repair via enhanced osteogenic and angiogenic activities. *Life Sciences* 202: 52–60. https://doi.org/10.1016/j.lfs.2018.02.026.

25 Virk, R.S., Ur Rehman, M.A., Munawar, M.A. et al. (2019). Curcumin-containing orthopedic implant coatings deposited on poly-ether-ether-ketone/bioactive glass/hexagonal boron nitride layers by electrophoretic deposition. *Coatings* 9 (9): 572. https://doi.org/10.3390/coatings9090572.

26 Malavasi, G., Ferrari, E., Lusvardi, G. et al. (2011). The role of coordination chemistry in the development of innovative gallium-based bioceramics: the case of curcumin. *Journal of Materials Chemistry* 21: 5027–5037. https://doi.org/10.1039/c0jm03421e.

27 Nicolini, V., Caselli, M., Ferrari, E. et al. (2016). SiO_2–CaO–P_2O_5 bioactive glasses: a promising curcuminoids delivery system. *Materials* 9 (4). https://doi.org/10.3390/ma9040290.

28 Zain, N.S.M., Sharifulden, N.S.A.N., Noor, S.N.F.M. et al. (2019). Dental pulp stem cells response to chrysanthemum flower extract. *Malaysian Journal of Medicine and Health Sciences* 15 (109): 80–87. https://www.medic.upm.edu.my/upload/dokumen/2019121815245612_MJMHS_0353.pdf.

29 Floroian, L., Ristoscu, C., Candiani, G. et al. (2017). Antimicrobial thin films based on ayurvedic plants extracts embedded in a bioactive glass matrix. *Applied Surface Science* 417: 224–233. https://doi.org/10.1016/j.apsusc.2017.02.197.

30 Mao, C., Lin, C., and Chen, X. (2014). Enhanced healing of full-thickness diabetic wounds using bioactive glass and Yunnan baiyao ointments. *Journal Wuhan University of Technology, Materials Science Edition* 29 (5): 1063–1070. https://doi.org/10.1007/s11595-014-1044-y.

31 Jebahi, S., Saoudi, M., Farhat, L. et al. (2015). Effect of novel curcumin-encapsulated chitosan-bioglass drug on bone and skin repair after gamma radiation: experimental study on a Wistar rat model. *Cell Biochemistry and Function* 33 (3): 150–159. https://doi.org/10.1002/cbf.3098.

32 Andrade, Â.L., Manzi, D., and Domingues, R.Z. (2006). Tetracycline and propolis incorporation and release by bioactive glassy compounds. *Journal of Non-Crystalline Solids* 352 (32–35): 3502–3507. https://doi.org/10.1016/j.jnoncrysol.2006.03.083.

33 Galarraga-Vinueza, M.E., Mesquita-Guimarães, J., Magini, R.S. et al. (2018). Mesoporous bioactive glass embedding propolis and cranberry antibiofilm compounds. *Journal of Biomedical Materials Research Part A* 106 (6): 1614–1625. https://doi.org/10.1002/jbm.a.36352.

34 Lin, H.-M., Wang, W.-K., Hsiung, P.-A., and Shyu, S.-G. (2010). Light-sensitive intelligent drug delivery systems of coumarin-modified mesoporous bioactive glass. *Acta Biomaterialia* 6 (8): 3256–3263. https://doi.org/10.1016/j.actbio.2010.02.014.

35 Ur Rehman, M.A., Bastan, F.E., Nawaz, Q., and Boccaccini, A.R. (2018). Electrophoretic deposition of lawsone loaded nanoscale silicate glass/chitosan composite on PEEK/BG layers. *ECS Transactions* 82 (1): 45–50. https://doi.org/10.1149/08201.0045ecst.

36 Dziadek, M., Dziadek, K., Kopec, A. et al. (2017). Antioxidant activity of novel PCL/bioactive glass composites enriched with polyphenolic compounds extracted from fruits and leaves of sweet cherry (*Prunus avium* L.). *Materials Letters* 203: 28–31. https://doi.org/10.1016/j.matlet.2017.05.112.

37 Zhang, X., Ferraris, S., Prenesti, E., and Verné, E. (2013). Surface functionalization of bioactive glasses with natural molecules of biological significance, part II: grafting of polyphenols extracted from grape skin. *Applied Surface Science* 287: 341–348. https://doi.org/10.1016/j.apsusc.2013.09.152.

38 Cazzola, M., Vernè, E., Cochis, A. et al. (2017). Bioactive glasses functionalized with polyphenols: in vitro interactions with healthy and cancerous osteoblast cells. *Journal of Materials Science* 52 (15): 9211–9223. https://doi.org/10.1007/s10853-017-0872-5.

39 Zhang, X., Ferraris, S., Prenesti, E., and Verné, E. (2013). Surface functionalization of bioactive glasses with natural molecules of biological significance, part I: gallic acid as model molecule. *Applied Surface Science* 287: 329–340. https://doi.org/10.1016/j.apsusc.2013.09.151.

40 Akhtar, M.A., Mariotti, C.E., Conti, B., and Boccaccini, A.R. (2021). Electrophoretic deposition of ferulic acid loaded bioactive glass/chitosan as antibacterial and bioactive composite coatings. *Surface and Coatings Technology* 405: 126657. https://doi.org/10.1016/j.surfcoat.2020.126657.

41 Amin, E., El-Hawary, S., Fathy, M. et al. (2011). A phytochemical study of *Zygophyllum simplex* L. *Planta Medica* 77 (05): 40. https://doi.org/10.1055/s-0031-1273569.

42 Tanvir, E.M., Hossen, M.S., Hossain, M.F. et al. (2017). Antioxidant properties of popular turmeric (*Curcuma longa*) varieties from Bangladesh. *Journal of Food Quality* 2017. https://doi.org/10.1155/2017/8471785.

43 Aggarwal, B.B., Yuan, W., Li, S., and Gupta, S.C. (2013). Curcumin-free turmeric exhibits anti-inflammatory and anticancer activities: identification of novel components of turmeric. *Molecular Nutrition & Food Research* 57 (9): 1529–1542. https://doi.org/10.1002/mnfr.201200838.

44 Gupta, S.C., Patchva, S., and Aggarwal, B.B. (2013). Therapeutic roles of curcumin: lessons learned from clinical trials. *AAPS Journal* 15 (1): 195–218. https://doi.org/10.1208/s12248-012-9432-8.

45 Hayat, S. and Sabri, A.N. (2016). Screening for antibiofilm and antioxidant potential of turmeric (*Curcuma longa*) extracts. *Pakistan Journal of Pharmaceutical Sciences* 29 (4): 1163–1170. https://pubmed.ncbi.nlm.nih.gov/27393429/.

46 Izui, S., Sekine, S., Maeda, K. et al. (2016). Antibacterial activity of curcumin against periodontopathic bacteria. *Journal of Periodontology* 87 (1): 83–90. https://doi.org/10.1902/jop.2015.150260.

47 Shahzad, M., Millhouse, E., Culshaw, S. et al. (2015). Selected dietary (poly)phenols inhibit periodontal pathogen growth and biofilm formation. *Food & Function* 6 (3): 719–729. https://doi.org/10.1039/c4fo01087f.

48 Kali, A., Bhuvaneshwar, D., Charles, P.V., and Seetha, K. (2016). Antibacterial synergy of curcumin with antibiotics against biofilm producing clinical bacterial isolates. *Journal of Basic and Clinical Pharmacy* 7 (3): 93. https://doi.org/10.4103/0976-0105.183265.

49 Gu, Q., Cai, Y., Huang, C. et al. (2012). Curcumin increases rat mesenchymal stem cell osteoblast differentiation but inhibits adipocyte differentiation. *Pharmacognosy Magazine* 8 (31): 202–208. https://doi.org/10.4103/0973-1296.99285.

50 Cohen, M.M. (2014). Tulsi – *Ocimum sanctum*: a herb for all reasons. *Journal of Ayurveda and Integrative Medicine* 5 (4): 251–259. https://doi.org/10.4103/0975-9476.146554.

51 Singh, N. and Gilca, M. (2008). Tulsi ñ a potential protector against air travel health problems. *Indian Journal of Natural Products and Resources* 7 (1): 54–57. http://nopr.niscair.res.in/handle/123456789/5646.

52 Saharkhiz, M.J., Kamyab, A.A., Kazerani, N.K. et al. (2014). Chemical compositions and antimicrobial activities of *Ocimum sanctum* L. essential oils at different harvest stages. *Jundishapur Journal of Microbiology* 8 (1). https://doi.org/10.5812/jjm.13720.

53 Goel, A., Kumar, S., Singh, D.K., and Bhatia, A.K. (2010). Wound healing potential of *Ocimum sanctum* Linn. with induction of tumor necrosis-α. *Indian Journal of Experimental Biology* 48 (4): 402–406. http://nopr.niscair.res.in/handle/123456789/7652.

54 Mohammad, S., Pal, U., Pradhan, R., and Singh, N. (2014). Herbal remedies for mandibular fracture healing. *National Journal of Maxillofacial Surgery* 5 (1): 35. https://doi.org/10.4103/0975-5950.140167.

55 Sarmiento, W.C., Maramba, C.C., Liza, M., and Gonzales, M. (2011). An in-vitro study on the antibacterial effect of neem (*Azadirachta indica*) leaf extract on methicillin-sensitive and methicillin-resistant *Staphylococcus aureus*. *PIDSP Journal* 12 (1): 40–45. http://www.pidsphil.org/pdf/Journal_06302011/jo38_ja05.pdf.

56 Shanmuga Priya, D., Suriyaprabha, R., Yuvakkumar, R., and Rajendran, V. (2014). Chitosan-incorporated different nanocomposite HPMC films for food preservation. *Journal of Nanoparticle Research* 16 (2): 2248. https://doi.org/10.1007/s11051-014-2248-y.

57 Dong, M., Yu, D., Duraipandiyan, V., and Abdullah Al-Dhabi, N. (2017, 2017). The protective effect of *Chrysanthemum indicum* extract against ankylosing spondylitis in mouse models. *BioMed Research International*. https://doi.org/10.1155/2017/8206281.

58 Wu, X.L., Li, C.W., Chen, H.M. et al. (2013). Anti-inflammatory effect of supercritical-carbon dioxide fluid extract from flowers and buds of *Chrysanthemum indicum* Linnén. *Evidence-Based Complementary and Alternative Medicine* 2013. https://doi.org/10.1155/2013/413237.

59 Kim, C., Kim, M.C., Kim, S.M. et al. (2013). *Chrysanthemum indicum* L. extract induces apoptosis through suppression of constitutive STAT3 activation in human prostate cancer DU145 cells. *Phytotherapy Research* 27 (1): 30–38. https://doi.org/10.1002/ptr.4689.

60 Luyen, B.T.T., Tai, B.H., Thao, N.P. et al. (2015). The anti-osteoporosis and antioxidant activities of chemical constituents from *Chrysanthemum indicum* flowers. *Phytotherapy Research* 29 (4): 540–548. https://doi.org/10.1002/ptr.5281.

61 Arokiyaraj, S., Arasu, M.V., Vincent, S. et al. (2014). Rapid green synthesis of silver nanoparticles from *Chrysanthemum indicum* land its antibacterial and cytotoxic effects: an in vitro study. *International Journal of Nanomedicine* 9 (1): 379–388. https://doi.org/10.2147/IJN.S53546.

62 Krishnamoorthy, K. and Subramaniam, P. (2014). Phytochemical profiling of leaf, stem, and tuber parts of *Solena amplexicaulis* (Lam.) Gandhi using GC-MS. *International Scholarly Research Notices* 2014: 1–13. https://doi.org/10.1155/2014/567409.

63 Gozubuyuk, G.S., Aktas, E., and Yigit, N. (2014). An ancient plant *Lawsonia inermis* (henna): determination of in vitro antifungal activity against dermatophytes species. *Journal de Mycologie Medicale* 24 (4): 313–318. https://doi.org/10.1016/j.mycmed.2014.07.002.

64 Raja, W., Agrawal, R.C., and Ovais, M. (2009). Chemopreventive action of *Lawsonia inermis* leaf extract on DMBA-induced skin papilloma and B16F10 melanoma tumour. *Pharmacology-OnLine* 2: 1243–1249. https://pharmacologyonline.silae.it/files/archives/2009/vol2/122.Wasim.pdf.

65 Dinesh Babu, P. and Subhasree, R.S. (2009). Antimicrobial activities of *Lawsonia inermis* – a review. *Academic Journal of Plant Sciences* 2 (4): 231–232. https://www.idosi.org/ajps/ajps2(4).htm.

66 Fokt, H., Pereira, A., Ferreira, A.M. et al. (2010). How do bees prevent hive infections? The antimicrobial properties of propolis. *Applied Microbiology* 1: 481–493. https://www.researchgate.net/profile/Cristina_Almeida_Aguiar/publication/265978408_How_do_bees_prevent_hive_infections_The_antimicrobial_properties_of_propolis/links/54b96b610cf253b50e2a7aa9/How-do-bees-prevent-hive-infections-The-antimicrobial-properties-of-propolis.pdf.

67 Sforcin, J.M. (2016). Biological properties and therapeutic applications of propolis. *Phytotherapy Research* 30 (6): 894–905. https://doi.org/10.1002/ptr.5605.

68 Anjum, S.I., Ullah, A., Khan, K.A. et al. (2019). Composition and functional properties of propolis (bee glue): a review. *Saudi Journal of Biological Sciences* 26 (7): 1695–1703. https://doi.org/10.1016/j.sjbs.2018.08.013.

69 Galarraga-Vinueza, M.E., Mesquita-Guimarães, J., Magini, R.S. et al. (2017). Anti-biofilm properties of bioactive glasses embedding organic active compounds. *Journal of Biomedical Materials Research Part A* 105 (2): 672–679. https://doi.org/10.1002/jbm.a.35934.

70 Machado, B., Pulcino, T., Silva, A. et al. (2016). Propolis as an alternative in prevention and control of dental cavity. *Journal of Apitherapy* 1 (2): 47. https://doi.org/10.5455/ja.20160726115117.

71 Govers, C., Kasikci, M.B., van der Sluis, A.A., and Mes, J.J. (2018). Review of the health effects of berries and their phytochemicals on the digestive and immune systems. *Nutrition Reviews* 76 (1): 29–46. https://doi.org/10.1093/nutrit/nux039.

72 Alexander, B., & John, S. (2019). Oral health benefits of cranberry: a review. *IOSR Journal of Dental and Medical Sciences*, 18(1), 41–44https://doi.org/10.9790/0853-1801024144

73 Kim, D., Hwang, G., Liu, Y. et al. (2015). Cranberry flavonoids modulate cariogenic properties of mixed-species biofilm through exopolysaccharides-matrix disruption. *PLoS One* 10 (12): e0145844. https://doi.org/10.1371/journal.pone.0145844.

74 Wickenberg, J., Ingemansson, S.L., and Hlebowicz, J. (2010). Effects of *Curcuma longa* (turmeric) on postprandial plasma glucose and insulin in healthy subjects. *Nutrition Journal* 9 (1): 43. https://doi.org/10.1186/1475-2891-9-43.

75 Reen, F.J., Gutiérrez-Barranquero, J.A., Parages, M.L., and O'Gara, F. (2018). Coumarin: a novel player in microbial quorum sensing and biofilm formation inhibition. *Applied Microbiology and Biotechnology* 102 (5): 2063–2073. https://doi.org/10.1007/s00253-018-8787-x.

76 Gutiérrez-Barranquero, J.A., Reen, F.J., McCarthy, R.R. et al. (2015). Erratum to: Deciphering the role of coumarin as a novel quorum sensing inhibitor suppressing virulence phenotypes in bacterial pathogens [Applied Microbiology and Biotechnology, doi:10.1007/s00253-015-6436-1]. *Applied Microbiology and Biotechnology* 99 (6): 2923. https://doi.org/10.1007/s00253-015-6465-9.

77 Lee, J.H., Kim, Y.G., Cho, H.S. et al. (2014). Coumarins reduce biofilm formation and the virulence of *Escherichia coli* O157:H7. *Phytomedicine* 21 (8–9): 1037–1042. https://doi.org/10.1016/j.phymed.2014.04.008.

78 Chen, Q., Li, W., Yao, Q. et al. (2016). Multilayered drug delivery coatings composed of daidzein-loaded PHBV microspheres embedded in a biodegradable polymer matrix by electrophoretic deposition. *Journal of Materials Chemistry B* 4 (29): 5035–5045. https://doi.org/10.1039/c6tb00113k.

79 Macías-Andrés, V.I., Li, W., Aguilar-Reyes, E.A. et al. (2017). Preparation and characterization of 45S5 bioactive glass-based scaffolds loaded with PHBV microspheres with daidzein release function. *Journal of Biomedical Materials Research Part A* 105 (6): 1765–1774. https://doi.org/10.1002/jbm.a.36046.

80 Li, C., Li, Q., Mei, Q., and Lu, T. (2015). Pharmacological effects and pharmacokinetic properties of icariin, the major bioactive component in Herba Epimedii. *Life Sciences* 126: 57–68. https://doi.org/10.1016/j.lfs.2015.01.006.

81 Wu, T., Nan, K.H., Di Chen, J. et al. (2009). A new bone repair scaffold combined with chitosan/hydroxyapatite and sustained releasing icariin. *Chinese Science Bulletin* 54 (17): 2953–2961. https://doi.org/10.1007/s11434-009-0250-z.

82 Zhang, X., Liu, T., Huang, Y. et al. (2014). Icariin: does it have an osteoinductive potential for bone tissue engineering? *Phytotherapy Research* 28 (4): 498–509. https://doi.org/10.1002/ptr.5027.

83 Yang, C.R. and Chen, J.D. (2013). Preparation and biological evaluation of chitosan–collagen–icariin composite scaffolds for neuronal regeneration. *Neurological Sciences* 34 (6): 941–947. https://doi.org/10.1007/s10072-012-1165-z.

84 Zhao, J., Ohba, S., Komiyama, Y. et al. (2010). Icariin: a potential osteoinductive compound for bone tissue engineering. *Tissue Engineering Part A* 16 (1): 233–243. https://doi.org/10.1089/ten.tea.2009.0165.

85 Di Matteo, A., Russo, R., Graziani, G. et al. (2017). Characterization of autochthonous sweet cherry cultivars (*Prunus avium* L.) of southern Italy for fruit quality, bioactive compounds and antioxidant activity. *Journal of the Science of Food and Agriculture* 97 (9): 2782–2794. https://doi.org/10.1002/jsfa.8106.

86 Jiang, H., Timmermann, B.N., and Gang, D.R. (2006). Use of liquid chromatography-electrospray ionization tandem mass spectrometry to identify diarylheptanoids in turmeric (*Curcuma longa* L.) rhizome. *Journal of Chromatography A* 1111 (1): 21–31. https://doi.org/10.1016/j.chroma.2006.01.103.

87 Sarker, S.D. and Nahar, L. (2017). Progress in the chemistry of naturally occurring coumarins. *Progress in the Chemistry of Organic Natural Products* 106: 241–304. https://doi.org/10.1007/978-3-319-59542-9_3.

88 Materska, M. (2008). Quercetin and its derivatives: chemical structure and bioactivity – a review. *Polish Journal of Food and Nutrition Sciences* 58 (4): 407–413.

89 Monroy-Cárdenas, M., Méndez, D., Trostchansky, A. et al. (2020). Synthesis and biological evaluation of thio-derivatives of 2-hydroxy-1,4-naphthoquinone (lawsone) as novel antiplatelet agents. *Frontiers in Chemistry* 8: 533. https://doi.org/10.3389/fchem.2020.00533.

90 Mohammed, S., Asdaq, B., Nayeem, N. et al. (2016). Gallic acid: a promising lead molecule for drug development. *Journal of Applied Pharmacy* 8 (2). https://doi.org/10.4172/1920-4159.1000213.

91 Hum, J. and Boccaccini, A.R. (2012). Bioactive glasses as carriers for bioactive molecules and therapeutic drugs: a review. *Journal of Materials Science – Materials in Medicine* 23 (10): 2317–2333. https://doi.org/10.1007/s10856-012-4580-z.

92 Brauer, D.S. (2015). Bioactive glasses – structure and properties. *Angewandte Chemie International Edition* 54: 2–24. https://doi.org/10.1002/anie.201405310.

93 Jones, J.R. (2015). Reprint of: Review of bioactive glass: from Hench to hybrids. *Acta Biomaterialia* 23: S53–S82. https://doi.org/doi:10.1016/j.actbio.2015.07.019.

94 Gorustovich, A.a., Roether, J.a., and Boccaccini, A.R. (2010). Effect of bioactive glasses on angiogenesis: a review of *in vitro* and *in vivo* evidences. *Tissue Engineering Part B* 16 (2): 199–207. https://doi.org/10.1089/ten.TEB.2009.0416.

95 Wu, C. and Chang, J. (2012). Mesoporous bioactive glasses: structure characteristics, drug/growth factor delivery and bone regeneration application. *Interface Focus* 2 (3): 292–306. https://doi.org/10.1098/rsfs.2011.0121.

96 Hoppe, A., Güldal, N.S., and Boccaccini, A.R. (2011). A review of the biological response to ionic dissolution products from bioactive glasses and glass-ceramics. *Biomaterials* 32 (11): 2757–2774. https://doi.org/10.1016/j.biomaterials.2011.01.004.

97 Owens, G.J., Singh, R.K., Foroutan, F. et al. (2016). Sol–gel based materials for biomedical applications. *Progress in Materials Science* 77: 1–79. https://doi.org/10.1016/j.pmatsci.2015.12.001.

98 Wu, C. and Chang, J. (2014). Multifunctional mesoporous bioactive glasses for effective delivery of therapeutic ions and drug/growth factors. *Journal of Controlled Release* 193: 282–295. https://doi.org/10.1016/j.jconrel.2014.04.026.

99 Baino, F., Fiorilli, S., and Vitale-Brovarone, C. (2016). Bioactive glass-based materials with hierarchical porosity for medical applications: review of recent advances. *Acta Biomaterialia* 42: 18–32. https://doi.org/10.1016/j.actbio.2016.06.033.

100 Anand, A., Das, P., Nandi, S.K., and Kundu, B. (2020). Development of antibiotic loaded mesoporous bioactive glass and its drug release kinetics. *Ceramics International* 46 (4): 5477–5483. https://doi.org/10.1016/j.ceramint.2019.10.264.

101 Yao, Q., Nooeaid, P., Roether, J.A. et al. (2013). Bioglass®-based scaffolds incorporating polycaprolactone and chitosan coatings for controlled vancomycin delivery. *Ceramics International* 39 (7): 7517–7522. https://doi.org/10.1016/j.ceramint.2013.03.002.

102 Kargozar, S., Mozafari, M., Hamzehlou, S. et al. (2019). Mesoporous bioactive glasses (MBGs) in cancer therapy: full of hope and promise. *Materials Letters* 251: 241–246. https://doi.org/10.1016/j.matlet.2019.05.019.

103 Arcos, D. and Vallet-Regí, M. (2010). Sol–gel silica-based biomaterials and bone tissue regeneration. *Acta Biomaterialia* 6 (8): 2874–2888. https://doi.org/10.1016/j.actbio.2010.02.012.

104 Hutmacher, D.W. (2000). Scaffolds in tissue engineering bone and cartilage. In: *The Biomaterials: Silver Jubilee Compendium*, vol. 21 (ed. D. Williams), 175–189. Elsevier. https://doi.org/10.1016/B978-008045154-1.50021-6.

105 Tölli, H., Kujala, S., Levonen, K. et al. (2010). Bioglass as a carrier for reindeer bone protein extract in the healing of rat femur defect. *Journal of Materials Science – Materials in Medicine* 21 (5): 1677–1684. https://doi.org/10.1007/s10856-010-4017-5.

106 Sokolsky-Papkov, M., Agashi, K., Olaye, A. et al. (2007). Polymer carriers for drug delivery in tissue engineering. *Advanced Drug Delivery Reviews* 59 (4–5): 187–206. https://doi.org/10.1016/j.addr.2007.04.001.

107 Negut, I., Floroian, L., Ristoscu, C. et al. (2020). Functional bioglass – biopolymer double nanostructure for natural antimicrobial drug extracts delivery. *Nanomaterials* 10 (2): 385. https://doi.org/10.3390/nano10020385.

108 Jaeger, M., Maier, D., Kern, W.V., and Südkamp, N.P. (2006). Antibiotics in trauma and orthopedic surgery – a primer of evidence-based recommendations. *Injury* 37 (Suppl 2): S74–S80. https://doi.org/10.1016/j.injury.2006.04.012.

109 Krasny, M., Krasny, K., Zadurska, M., and Fiedor, P. (2016). Evaluation of treatment outcomes and clinical indications for antibiotic prophylaxis in patients undergoing implantation procedures. *Advances in Medical Sciences* 61 (1): 113–116. https://doi.org/10.1016/j.advms.2015.10.005.

110 Lindeboom, J.A., Frenken, J.W., Tuk, J.G., and Kroon, F.H. (2006). A randomized prospective controlled trial of antibiotic prophylaxis in intraoral bone-grafting procedures: preoperative single-dose penicillin versus preoperative single-dose clindamycin. *International Journal of Oral and Maxillofacial Surgery* 35 (5): 433–436. https://doi.org/10.1016/j.ijom.2006.01.003.

111 Floroian, L., Ristoscu, C., Mihailescu, N. et al. (2016). Functionalized antimicrobial composite thin films printing for stainless steel implant coatings. *Molecules* 21 (6): 740. https://doi.org/10.3390/molecules21060740.

112 Venkateshbabu, N., Anand, S., Abarajithan, M. et al. (2016). Natural therapeutic options in endodontics – a review. *The Open Dentistry Journal* 10 (1): 214–226. https://doi.org/10.2174/1874210601610010214.

113 Occhipinti, A., Germano, A., and Maffei, M.E. (2016). Prevention of urinary tract infection with Oximacro®, a cranberry extract with a high content of A-type proanthocyanidins: a pre-clinical double-blind controlled study. *Urology Journal* 13 (2): 2640–2649. https://doi.org/10.22037/uj.v13i2.3190.

114 Kim, Y.J., Park, M.R., Kim, M.S., and Kwon, O.H. (2012). Polyphenol-loaded polycaprolactone nanofibers for effective growth inhibition of human cancer cells. *Materials Chemistry and Physics* 133 (2–3): 674–680. https://doi.org/10.1016/j.matchemphys.2012.01.050.

115 Cazzola, M., Corazzari, I., Prenesti, E. et al. (2016). Bioactive glass coupling with natural polyphenols: surface modification, bioactivity and anti-oxidant ability. *Applied Surface Science* 367: 237–248. https://doi.org/10.1016/j.apsusc.2016.01.138.

116 Zhang, P., Zhou, T., He, L. et al. (2015). Dispersion of multi-walled carbon nanotubes modified by rosemary acid into poly(vinyl alcohol) and preparation of their composite fibers. *RSC Advances* 5 (68): 55492–55498. https://doi.org/10.1039/c5ra06804e.

117 Ferraris, S., Miola, M., Cochis, A. et al. (2017). In situ reduction of antibacterial silver ions to metallic silver nanoparticles on bioactive glasses functionalized with polyphenols. *Applied Surface Science* 396: 461–470. https://doi.org/10.1016/j.apsusc.2016.10.177.

118 Navarro, J., Calderon, G.A., Miller, J.S., and Fisher, J.P. (2019). Bioinks for three-dimensional printing in regenerative medicine. In: *Principles of Regenerative Medicine* (ed. A. Atala, R. Lanza, A.G. Mikos and R. Nerem), 805–830. Elsevier. https://doi.org/10.1016/b978-0-12-809880-6.00046-1.

119 Marrazzo, P. and O'leary, C. (2020). Repositioning natural antioxidants for therapeutic applications in tissue engineering. *Bioengineering* 7 (3): 1–35. https://doi.org/10.3390/bioengineering7030104.

120 Agarwal, R. and García, A.J. (2019). Chapter 37: Surface modification of biomaterials. In: *Principles of Regenerative Medicine* (Chapter 37) (ed. A. Atala, R. Lanza, A.G. Mikos and R. Nerem), 651–660. Academic Press https://doi.org/10.1016/B978-0-12-809880-6.00037-0.

121 Kargozar, S., Kermani, F., Mollazadeh Beidokhti, S. et al. (2019). Functionalization and surface modifications of bioactive glasses (BGs): tailoring of the biological response working on the outermost surface layer. *Materials* 12 (22): 3696. https://doi.org/10.3390/ma12223696.

122 Ferraris, S. and Vernè, E. (2017). Surface functionalization of bioactive glasses: reactive groups, biomolecules and drugs on bioactive surfaces for smart and functional biomaterials. In: *Bioactive Glasses: Fundamentals, Technology and Applications* (Chapter 9), RSC Smart Materials, vol. 2017 (ed. A.R. Boccaccini, D.S. Brauer and L. Hupa), 221–235. Royal Society of Chemistry. https://doi.org/10.1039/9781782622017-00221.

123 Verné, E., Vitale-Brovarone, C., Bui, E. et al. (2009). Surface functionalization of bioactive glasses. *Journal of Biomedical Materials Research Part A* 90 (4): 981–992. https://doi.org/10.1002/jbm.a.32153.

124 Sun, J., Li, Y., Li, L. et al. (2008). Functionalization and bioactivity in vitro of mesoporous bioactive glasses. *Journal of Non-Crystalline Solids* 354 (32): 3799–3805. https://doi.org/10.1016/j.jnoncrysol.2008.05.001.

125 Hum, J. and Boccaccini, A. (2018). Collagen as coating material for 45S5 bioactive glass-based scaffolds for bone tissue engineering. *International Journal of Molecular Sciences* 19 (6): 1807. https://doi.org/10.3390/ijms19061807.

126 Massera, J., Mishra, A., Guastella, S. et al. (2016). Surface functionalization of phosphate-based bioactive glasses with 3-aminopropyltriethoxysilane (APTS). *Biomedical Glasses* 2 (1): 51–62. https://doi.org/10.1515/bglass-2016-0007.

127 Stanić, V. (2017). Variation in properties of bioactive glasses after surface modification. In: *Clinical Applications of Biomaterials: State-of-the-Art Progress, Trends, and Novel Approaches* (ed. G. Kaur), 35–63. Springer. https://doi.org/10.1007/978-3-319-56059-5_2.

128 Schickle, K., Zurlinden, K., Bergmann, C. et al. (2011). Synthesis of novel tricalcium phosphate-bioactive glass composite and functionalization with rhBMP-2. *Journal of Materials Science – Materials in Medicine* 22 (4): 763–771. https://doi.org/10.1007/s10856-011-4252-4.

129 Bonfim, R., Chitarra, V., Gomes, R. et al. (2009). Antimicrobial activity of bioactive glass associated to Brazilian red and green propolis. *Planta Medica* 75 (09): PJ194. https://doi.org/10.1055/s-0029-1234999.

130 Gao, X., Qin, W., Wang, P. et al. (2019). Nano-structured demineralized human dentin matrix to enhance bone and dental repair and regeneration. *Applied Sciences (Switzerland)* 9 (5): 1013. https://doi.org/10.3390/app9051013.

131 Winkler, T., Sass, F.A., Duda, G.N., and Schmidt-Bleek, K. (2018). A review of biomaterials in bone defect healing, remaining shortcomings and future opportunities for bone tissue engineering: the unsolved challenge. *Bone & Joint Research* 7 (3): 232–243. https://doi.org/10.1302/2046-3758.73.BJR-2017-0270.R1.

132 Ge, Y.-W., Lu, J.-W., Sun, Z.-Y. et al. (2019). Ursolic acid loaded-mesoporous bioglass/chitosan porous scaffolds as drug delivery system for bone regeneration. *Nanomedicine: Nanotechnology, Biology and Medicine* 18: 336–346. https://doi.org/10.1016/j.nano.2018.10.010.

133 Ur Rehman, M.A., Bastan, F.E., Nawaz, Q. et al. (2018). Electrophoretic deposition of lawsone loaded bioactive glass (BG)/chitosan composite on polyetheretherketone (PEEK)/BG layers as antibacterial and bioactive coating. *Journal of Biomedical Materials Research Part A* 106 (12): 3111–3122. https://doi.org/10.1002/jbm.a.36506.

134 Jaques, J.A.d.S., Rezer, J.F.P., Gonçalves, J.F. et al. (2011). The effect of curcumin in the ectonucleotidases and acetylcholinesterase activities in synaptosomes from the cerebral cortex of cigarette smoke-exposed rats. *Cell Biochemistry and Function* 29 (8): 703–707. https://doi.org/10.1002/cbf.1804.

135 Alsayari, A., Muhsinah, A.B., Hassan, M.Z. et al. (2019). Aurone: a biologically attractive scaffold as anticancer agent. *European Journal of Medicinal Chemistry* 166: 417–431. https://doi.org/10.1016/j.ejmech.2019.01.078.

13

Bioactive Glass-Based Coatings: Concepts for Improving the Biocompatibility of Implantable Materials

Jessica Fletcher, William Alles, Timothy James Keenan, and Anthony William Wren

Kazuo Inamori School of Engineering, Alfred University, Alfred, NY, USA

13.1 Introduction

Implantable materials are utilized in nearly every facet of medicine, from drug-delivery systems to weight-bearing hip replacements and can greatly improve a person's quality of life. A wide and diverse array of implantable materials of varying compositions and architectures are currently being applied to the fields of orthopedics, dentistry, and cranio-maxillofacial reconstruction. However, nearly 10% of these implants will fail within the recipient's lifetime and are likely to fail within the first five years post-surgery. In order to combat this and improve the biocompatibility of medical materials *in situ*, coating technology has been developed for medical devices in order to improve some of the currently used materials' shortcomings. This includes enhancing a material's *bioactivity* (mineralization of material surfaces), *osseointegration* (bone bonding), *imparting antimicrobial properties* (antibacterial, antifungal), *enhance mechanical performance* (hardness, fatigue), in addition to being used as a *delivery mechanism* (drugs, therapeutics, ions). Applying a coating has the benefit in retaining the bulk properties and chemistry of the parent material, while tailoring the surface properties of the implant for the desired application.

Coatings on material surfaces can be applied using a variety of methods including *sol–gel processing*, *vapor deposition*, *sputtering*, *laser-assisted deposition*, *ultrasonic deposition*, and *spin and dip-coating* to name but a few. The selection of a particular coating method can rely on specific characteristics of the substrate material (e.g. temperature, solubility), the coating material itself, or the properties which need to be introduced. *Bioactive glasses (BGs)* have been shown to be promising candidates for coating applications, particularly in the fields of hard tissue repair (orthopedics and restorative dentistry) as they can induce mineralization *in vivo* and promote the process of new bone growth [1]. Additionally, BGs can be specifically designed to incorporate ions that have specific therapeutic functions, thereby facilitating greater design and tailoring of the implantable materials for a specific application. Some examples would be the inclusion of copper (Cu^{2+}) for enhancement of angiogenesis, silver (Ag^{+}) for antimicrobial effects, and strontium (Sr^{2+}) for promoting bone growth [2]. There are also numerous methods to process BGs (*sol–gel*, *melt quench*) and procedures to synthesize different glass morphologies (*glass fibers*, *microspheres*, *differing particle sizes*) depending on the desired application [3]. In relation to applying a coating to a material's surface, some of the more important characteristics include the thickness of the coating the microstructure of the coating post synthesis, the adhesive nature of the coating to the substrate, and the stability of the coating in its intended physiological environment [4].

Bioactive Glasses and Glass-Ceramics: Fundamentals and Applications, First Edition.
Edited by Francesco Baino and Saeid Kargozar.

The versatility of BGs permits a high degree of design and the ability to significantly enhance the biocompatibility of an implant material's surface.

13.1.1 Current Concepts in Coating Technology

Currently, there are a wide array of materials being modified by the coating process. Metallic materials are extensively investigated with coating technology as they are typically bioinert, and coating with *ceramics*, *bioactive particles*, *organic molecules*, or *functionalized polymers* can impart desired physical properties, in addition to encouraging biological responses such as osseo-induction and osseo-conduction [5]. Ceramic-based materials have been widely researched as coating materials for orthopedic and dental applications, as there exists a high degree of versatility available for modification of the metallic substrate.

It is well known that hydroxyapatite (HAp) coatings can be applied to metallic material surfaces to improve *biocompatibility*, *promote bone growth*, and *reduce toxic ions* leaching from the substrate metal [6]. However, there are additional effects on the mechanical properties of the substrate material as a result of the coating process. A reduction in surface stiffness can be attributed to HAp coatings, coupled with significant improvement in the metallic substrate's biocompatibility. Derivatives of HAp have also been extensively studied to further the diversity of desired properties. Arres et al. conducted tests on pure titanium (Ti) and citrate – hydroxyapatite (cHAp)-coated Ti. cHAp formed a coating that imparted nanorod-like HAp particles that resulted in nano-roughness and wettability, which ultimately improved the biological response. There were also mechanical benefits as the uncoated sample of Ti exhibited a larger area under stress than in the coated sample, suggesting the HAp coating reduces stress, and impacts stress distribution [7]. An additional study focused on modifying HAp as a coating was conducted by Horandghadim et al., and found that when Ta_2O_5 is added (10, 15, and 20 wt%) to a HAp coating on a NiTi substrate, several mechanical benefits were achieved. Increased wt% Ta_2O_5 decreased surface roughness, which resulted in improved tribology. Fewer Ni ions were leached from the substrate into a phosphate-buffered saline solution as Ta_2O_5 was added. Additional other positive attributes were also observed, which included a more stable attachment to the substrate, improved hardness, and increased elastic modulus, which were all attributed to the addition of Ta_2O_5 [8].

Other ceramics that have been applied to a variety of orthopedic implants include Zirconia (ZrO), Alumina (Al_2O), and Titanium nitride (TiN). As one of the more recent advancements, TiN coatings are of immense interest, as they have been shown to improve many properties useful to the implementation of biomedical materials, including hardness, toughness, biocorrosion resistance, antimicrobial efficacy, and elastic modulus [9]. Several studies on TiN have shown an increase in the overall biocompatibility of the implant substrate, as ceramics are ideal in that they rarely elicit any type of immune response. In implants that contact blood, especially in the cardiovascular system, the coating encourages tolerance and minimizes hemolysis [10]. Additionally, when applied to implants (including titanium alloys and cobalt alloys), this coating has exhibited the ability to influence the surface's mechanical properties (i.e. the friction and wear characteristics of the implant) [10]. The TiN coating itself has exceptional hardness and can withstand abrasion with bone where typical wearing of the implant would be found, thus minimizing the release of potentially harmful ions. A retroactive study conducted by van Hove et al. found that TiN coatings, analyzed between one and six years after implant, had success rates of over 90% in various clinical settings [10]. Additionally, Hussein et al. demonstrated that TiN deposited onto a Ti alloy (Ti-6Al-4V) in nanocrystalline form improved several properties of the material. The hardness values of the coated and uncoated alloys were observed to be 38.6 and 5.27 GPa, respectively. The coated sample exhibited a modulus of elasticity more than twice that of the uncoated sample

(358 and 151 GPa, respectively). Due to the increased hardness of the coated sample, the coefficient of friction was lower in the coated sample, which acts to improve the material's tribological properties and function as an articular implant. Furthermore, passivation tests in simulated body fluid (SBF) showed that there was no occurrence of pitting corrosion in the coated sample, and the calculated potential of pitting corrosion was reduced in the coated sample. Finally, the viability of bacteria (gram negative *Escherichia coli*) on the coated sample was reduced significantly after 48 hours [11].

Typically, inert ceramic coatings are used to modify the underlying metallic material's mechanical properties. Due to motion and fatigue that result in wear with joint surfaces, these coatings are required to endure extreme mechanical forces while existing in a corrosive and hydrated physiological environment. For example, diamond-like coatings (DLCs) are amorphous carbon-based coatings that mimic properties observed in diamonds due to a large concentration of sp^3 hybridized carbon bonds. These properties include exceptional *hardness*, *corrosion resistance*, *biocompatibility*, *hemocompatibility*, and a *low friction coefficient*. This makes DLC a promising coating especially for articular surfaces that require corrosion resistance and favorable tribological qualities. However, some of the limitations associated with DLCs include poor adhesion to metal surfaces due to high internal stress and low levels of bioactivity. As a result, work has commenced to modify these coatings in order to exhibit the beneficial properties, and mitigate the harmful properties, to allow for use in biomedical applications [12]. A study by Milan et al. investigated the effects of copper (Cu) within a DLC coating. The experimenters found that the coating's hardness increased as the [Cu] was increased until a saturation limit of ~37 wt%, at which point the addition of Cu reduced the hardness. An inverse trend was observed for Young's modulus. Cu was also found to reduce internal stresses within the coating, which increased adherence to the substrate. The samples coated with Cu-enriched DLC demonstrated improved *antibacterial*, *osteogenic*, and *angiogenic properties*, suggesting that both the mechanical and biological properties of the coatings can be optimized by modulating [Cu] within the coating [12].

Studies have also explored the use of polymeric materials for coating applications. Both *naturally derived polymers* (i.e. keratin and collagen) and *synthetic polymers* (polyurethane [PU], polyethylene glycol [PEG], etc.) have been extensively investigated for coating implantable metallic materials. Collagen is a natural polymer, which constitutes the protein component of bone matrix and has been widely investigated to improve the bioactivity and biocompatibility of inert metallic substrates. Bone matrix itself is comprised of two components: the calcified, inorganic portion (HAp) and the collagenous organic portion [13]. The calcified component imparts bone toughness and compressive strength, while the organic collagen matrix lends bone the ability to have flexibility and tensile resilience [14]. There have been many studies conducted on orthopedic implants that are coated with a HAp to promote integration of the implant into bone tissue. However, this is an imperfect process and bone-forming cells may be inhibited during integration [13]. Using collagen type-I as coatings has been investigated to address this issue and has been explored by Rammelt et al. [15]. In their study, Rammelt et al. investigated Ti rods which were coated with type-I collagen, and then inserted into rat tibia for observation over the course of 28 days. The first observation of the tissue surrounding the implant was taken after four days, where preliminary granulation tissue was forming at the interface between the implant and the bone tissue, and the presence of mononuclear/phagocytic cells was observed. This process marks the beginning of the bone remodeling process, which is necessary for proper integration into the bone tissue by the implant. After seven days, there was a significant increase in the active osteoblasts surrounding the collagen-coated rods in comparison to the uncoated rods. Osteoblasts are the cells responsible for laying the preliminary matrix for bone tissue, and an increase in their presence indicates a higher bone formation rate

near the implant. Finally, after 28 days, collagen-coated implants had roughly 75% of direct bone contact between the implant and the bone tissue, indicating a high-degree of integration as opposed to 62% direct bone contact observed for the uncoated implants. This study suggests type-I collagen coatings as an effective tool in stimulating bone remodeling on Ti, thereby significantly improving the implant's biocompatibility [15].

In addition to naturally derived polymers, *synthetic polymers* can also be utilized to coat Ti implants in a multifunctional way. Coatings of synthetic polymers can result in a variety of novel properties, ranging from altering the substrate's *hydrophilicity* and *electrical conductivity*, to *solubility*, *biocompatibility*, and *bioactivity*. Synthetic polymers can incorporate multiple particles and systems to facilitate specific properties within the coating itself. Studies by Szaraniec et al. investigated a dip-coating method to adhere a PU composite of varying composition (which included graphene and β-TCP [tricalcium phosphate]) to Ti metallic surfaces. This compositing resulted in a coating with adequate stability, where the biocompatibility of the implant relied heavily on the graphene component, while the bioactivity was attributed to the concentration of β-TCP [16]. Another key area of research in terms of changing the material properties of an implant using a coating is PEGylation of biologics to use for therapeutic purposes. In this process, the polymer PEG is employed, and PEG chains are synthesized and conjugated onto a substrate, which is often a drug or type of protein. The PEGylated structures possess the ability to circumvent the immune system, as the PEG markers essentially "mask" the macrostructure from T cells, B cells, and other host immune cells. Additionally, PEGylation inherently increases the size of the drug or protein, making it less likely to dissolve in solution where it can be excreted out of the body via the renal system. This enhances circulation time of the therapeutic and allows it to stay in the body for the necessary amount of time to be effective. PEGylation can also form surfaces that are non-conducive to bacterial colonization, limiting the chance of infection and limiting the formation of biofilms [17]. PEGylated peptides have also demonstrated a notable reduction in the ability of infection to spread in implants, particularly on Ti surfaces, as the spontaneous adsorption of the peptide onto the surface of the implant acts to create a non-fouling surface. Non-fouling surfaces repel adhesion by bacteria and other microorganisms, usually due to charge incompatibility, and prevent the buildup of a biofilm. Studies by Khoo et al. found a significant decrease in biofilm adherence, protein adsorption (nonspecific), inflammatory response, and subsequent loosening and failure in implants when the surfaces were PEGylated. This method displays tremendous promise in minimizing bacterial infection and can serve as both a nano-scale therapeutic, as well as a macro-scale coating [17].

Smart coatings involve the combination of the release of a biologic (i.e. antibiotic) with active "targeting" of a specific microbe which can potentially lead to implant failure. Antibiotics and other wound-care treatments have long been administered to the implant site, but are only accessible for a relatively short period of time. This means that the therapeutic properties of the biologic, whether applied topically or directly to the implant site, are only available for a few days following the operation and implant placement. This can be problematic, as it may mitigate the effects from acute infection, but not prevent against chronic infection, which can occur for longer periods of time post-implantation. A controlled-release coating can supply the implant site with an antibiotic for extended periods of time, and if the coating is a "*smart*" polymer, it can theoretically release antibiotics when challenged with bacteria based on specified triggers [18]. Studies by Stavrakis et al. developed a poly(ethylene glycol)-poly(propylene sulfide) (PEGS-PPS) polymer coating that can be applied to implant surfaces and act as a "*smart*" antibiotic delivery device. PEGS-PPS is nontoxic and biodegradable, meaning that as the polymer breaks down to release antibiotics to the body, it does not induce an immune response. This polymer is also "*smart*" as

the reactive oxygen cascade that is triggered by bacteria activates the release of the antibiotic, so it is only released where it is actually required. In a study conducted over the course of seven days in mouse models, PEGS-PPS filled with the antibiotic tigecycline demonstrated statistical significance in lowering the infection rate and bacterial colony formation in the area surrounding the implant (2.6×10^2 CFUs vs. 5.9×10^4 CFUs on the surrounding control tissue). It was particularly effective against *Staphylococcus aureus*, which accounts for half of all infection in implantation procedures. Combining with the antibiotic vancomycin also exhibited a decrease in colony formation. This experiment shows promise in developing devices that are able to slowly release antibiotic agents in response to an external trigger, in order to maximize the efficacy of the antibiotic when specific bacteria are locally present [19].

13.1.2 Bioactive Glasses – Therapeutic Value as a Coating Material

Bioceramic materials have been applied to the fields of hard tissue restoration due to their ability to (i) incorporate *therapeutic ions* which can stimulate specific responses within a physiological environment and (ii) tailor the material's chemistry to *control its solubility* and to facilitate enhanced biocompatibility with the surrounding tissues [20–22]. One key benefit of using a glass (amorphous) over a ceramic (crystalline) for applications within an aqueous environment is due to the material's solubility. The amorphous nature of glass generally permits greater solubility than crystalline ceramics, as glasses do not present long-range periodic atomic arrangement in contrast to their ceramic counterparts, which results in more reactive surface and bulk environments, leading to increased solubility within the aqueous environment present upon implantation [23, 24].

One class of materials that has taken advantage of their degradability in contact with the corrosive environment within a living physiological system are BGs. The most widely known of these being Bioglass® 45S5 (L. Hench 1969). This specific composition consists of 45% SiO_2–24.5% Na_2O–24.5% CaO–6% P_2O_5 and was found to form a direct bond to living bone tissue when tested in rat models, as cast glass implants were inserted into rat femurs, and exhibited a strong interfacial bond between implant and host tissue which formed over the course of six weeks, as opposed to the control samples which were easily removed [25, 26].

One of the key benefits associated with the use of BGs is the ability of these materials to partially degrade *in vivo* and initiate changes to the material's surface by forming a polycrystalline calcium phosphate (CaP) surface layer with respect to incubation time. This bioactive effect can be attributed to rapid release of soluble ionic species (Ca^{2+}, Na^+, PO_4^{3-}) from the glass resulting in the formation of a high surface area, hydrated *silica layer*. This eventually leads to precipitation of minerals on the surface and the formation of crystalline HAp. This effect is regarded as a highly positive attribute stemming from the BGs solubility and composition. The HAp phase that forms on bioactive BGs surface is chemically and structurally equivalent to the mineral phase of bone, and this similarity is key to the formation of interfacial bonding, and its presence is considered to be a precursor to bone bonding *in vivo* [1, 26].

Almost all BGs will experience dissolution in aqueous solutions; however, the rate of ion release and the tendency to form HAp surface layers vary, depending largely on the BGs composition. Upon immersion in an aqueous body fluid-like solution, BGs exhibit three general processes: *leaching*, *dissolution*, and *precipitation*. Leaching is characterized by release of alkali or alkaline earth elements such as Na^+ or Ca^{2+}, which is accelerated by cation exchange with H^+ or H_3O^+ ions. The release of network modifying ions is rapid and this ionic exchange process leads to an increase in pH. The dissolution stage occurs next and is initiated by the breaking of —Si—O—Si—O—Si— bonds through the action of hydroxyl (OH) ions [2, 27]. Degradation of the Si network occurs locally

and liberates Si^{4+} into solution in the form of silicic acid [$Si(OH)_4$]. The rate of Si^{4+} dissolution is highly dependent on the BGs composition and structure. Finally, in the precipitation stage, Ca^{2+} and PO_4^{3-} ions are released from the BGs as a result of dissolution, and with mineral ions already present in the solution migrate to the surface and precipitate to form a calcium-phosphate-rich (CaP) layer. This calcium phosphate phase that accumulates in the gel surface is initially amorphous, but will crystallize over time to an analogous form of natural HAp [2, 28].

13.2 Bioactive Glass Synthesis

BGs are typically used in the orthopedic and dental fields as bone grafts in non-load bearing applications, primarily due to the lack of mechanical suitability. Commercial products typically consist of glass particles of varying size, depending on the application, or glass monoliths [29]. However, extensive research has been conducted on developing complex shapes such as porous scaffold materials for tissue engineering applications [30–39], reinforcing and resorbable fibers in composite materials [40, 41], and glass microspheres for tumor treatment [42], to name but a few. A common characteristic associated with all the cited applications is the need to tailor the glass composition and solubility to suit the target applications.

BGs can be formed using high-temperature processing (i.e. *melt quench route*) or through *sol–gel processing*. Melt-derived BGs are melted and formed from mixed batches of high purity analytical grade reagents to minimize the concentration of trace impurities in the glasses. BGs are typically produced by melting batch components at temperatures ranging from 1350 to 1450 °C [3]. Melting times can be varying from 1 to 24 hours, and glasses can be re-melted in order to increase homogeneity or annealed post-quenching to control degradation of the glass particles in aqueous media [43]. Intricate shapes and morphologies can be produced by grinding, polishing, etching, casting into monoliths, spinning into fibers, flame forming into microspheres, or quenching into deionized water to produce glass granules [3].

Sol–gel processing of glasses offers an alternative to traditional melt-quenching. This process occurs at low temperatures and involves the synthesis of a solution (*sol*), typically composed of metal-organic and metal salt precursors followed by the formation of a *gel* by chemical reaction or aggregation. The final step in the process is thermal treatment for drying, organic removal, and for crystallization, if desired [44]. To produce sol–gel BGs, precursors used are typically tetraethyl orthosilicate, calcium nitrate, and triethylphosphate. When the hydrolysis and poly-condensation reactions are completed, a gel is formed which is subsequently calcinated (typically, between 600 and 700 °C) to form the glass. Some of the advantages to using this method are that sol–gel derived products (e.g. glasses particles, thin films, or fibers) can be highly porous, with a much higher specific surface area compared to the melt-quench analogs [45]. Sol–gel processes also make it possible to obtain highly homogeneous and chemically pure materials through lower processing temperatures than those involved in the traditional glass melting process. It has also been suggested that BGs produced through the sol–gel route retain superior compositional control are more easily synthesized with the required combination of biodegradability and bioactivity and routinely exhibit enhanced bioactivity compared to the melting-quenching method [46].

13.3 Principles of Coating Processing

With regard to metallic implants employed in the field of orthopedics, high mechanical strength and fracture toughness are some of the key attributes which make these materials suitable for

load-bearing applications. For the most part, metallic biomaterials can be classified as (i) Ti and its alloys (i.e. Ti6Al4V) (ii) stainless steels (i.e. 316L stainless steel), (iii) cobalt–chromium–molybdenum (Co–Cr–Mo) alloys, and (iv) precious metal alloys (i.e. gold, silver, or platinum-based alloys). To be suitable for implant applications, ideal metallic biomaterials should exhibit a Young's Modulus comparable to that of bone tissue to ensure a uniform distribution of stress through the implant [47]. Additionally, sufficient tensile, compressive, yield, and fatigue strength are all properties that are required to prevent brittle fracture under cyclical loading. However, aside from their mechanical benefits, metallic biomaterials can suffer with respect to bioactivity, osteointegration, and corrosion resistance when in contact with physiological fluids [48]. Limiting the corrosion of metallic implants is of the utmost importance, as this can negatively affect the mechanical integrity of the implant, as well as its biocompatibility by compromising cell metabolism and cell behavior. In particular, when motion is present, surface deterioration under high loads can cause elevated levels of metallic ions to release into the bloodstream [49], which can be extremely problematic, as some of these metallic degradation products have been linked to physiological issues such as metal sensitivity, genotoxicity, and carcinogenicity. To limit metallic ion release, encourage osseointegration, and improve overall biocompatibility, bioceramics of varying morphology and composition can be used to coat the implant surface [4, 50]. However, it is important to realize that the final characteristics of the coating are highly dependent on the deposition and coating technique: i.e. the physical and chemical properties can vary widely based on processing parameters. Physical characteristics which can vary include microstructure, thickness, surface roughness, porosity, and adhesion, whereas chemical characteristics such as long-term stability, dissolution/solubility, and cytocompatibility can be affected [3].

One of the more common and versatile methods to apply coatings to metallic substrates is sol–gel processing. The *sol–gel method* is widely employed and can be used to provide beneficial effects such as *improved bioactivity*, *antimicrobial efficacy*, and improved *mechanical characteristics* of the implant surface. Sol–gel coatings consist of a colloidal solution or suspension of monomers that exists within a liquid medium, which is hydrolyzed (typically by the Pechini process), and polymerized via condensation to form a gel, which is a suspension of a solid within a liquid and is completely resistant to flow. The gel itself can then be added to the desired substrate to create a thin film over the specimen. A variety of methods can be used to deposit sol–gel coatings on medical device surfaces, including *spin coating* and *dip-coating*. *Spin coating* involves spinning a small amount of the sol–gel (liquid form) onto a flat surface to create a uniform coating, which typically ranges between 40 nm and 10 μm [51]. The thickness of the resultant coating will depend on factors such as viscosity, rotation speed, and time (coating duration). *Dip-coating* usually involves the material being submerged in a solution for a short period of time, which allows for the deposition of particles onto the substrate surface, and the formation of a thin layer that forms when the substrate is removed from the solution. There are five steps associated with the dip-coating process, and these include:

(1.) immersion of the substrate into solution,
(2.) allowing the substrate to remain in solution,
(3.) deposition of the particles in the solution onto the substrate,
(4.) removal of the material from the solution at a constant speed, and finally,
(5.) allowing the remaining liquid to evaporate from of the substrate surface, leaving behind a thin film.

The addition of heat to the substrate prior to submersion may allow for better deposition and adherence of the particles in the solution to the material [52]. This method can be applied to coat materials with basic morphologies, all the way to three-dimensional materials such as those used

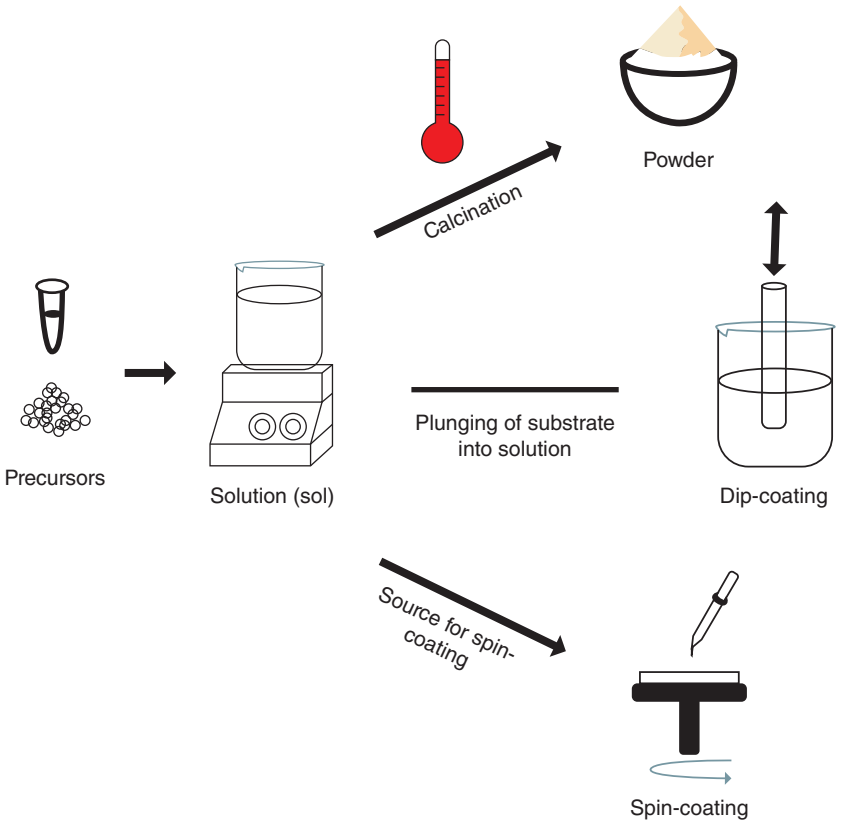

Figure 13.1 Author's schematic of sol–gel processing and associated coating methods. Source: Supporting references include Thiagarajan et al. [54] and Owens et al. [55].

in joint arthroplasty, in order to deposit bioceramic coatings which can aid in the promotion of bone bonding *in vivo* [53, 54] (Figure 13.1).

Electrophoretic deposition (EPD) is a method that requires the substrate to be electrically conductive in the suspension medium. With this process, substrates which act as electrodes are placed within the suspension medium, and an electric current is applied between the electrodes which creates an electric field between the particles contained within the suspension and the substrate (electrode), causing the particles to be attracted to the surface of the substrate [3]. The substrate in this case can have complex shapes, and the thickness of the coating can range between 1 and 100 μm. The thickness typically depends on the nature of the materials (solvent, dispersant, particle size) and physical parameters, including voltage and immersion time [6]. After deposition on the substrate surface, a heat treatment step is often required to densify the coating. This process is extremely flexible, allowing for colloidal suspensions of glass, ceramics, polymers, and metals to be processed via EPD [3]. Numerous studies have been conducted on composite coatings containing HAp and BGs. These materials are known to offer improvements in bioactivity, biocompatibility, and tissue adhesion, and their application as a coating avoids the weak mechanical properties and brittle nature typically associated with bioceramics [6]. A study by Khanmohammadi et al. on HAp/BG composite coatings on a pure Ti (99.9% purity) substrate employed isopropanol and triethanolamine (TEA) as the solvent and dispersant, respectively. This study utilized EPD to deposit the coating with sintering to follow at 800 °C for one hour. It was then determined that the resulting

coatings which performed best contained 50% HAp/50% BG, exhibiting sufficient bioactivity and bond strength, as well as a high surface area (80 m^2/g) [53].

The ability to coat glass employing mechanical methods such as *ultrasound* also exists. Depositing ionic nanoparticles (NaCl, $CuSO_4$, and KI) onto different substrates has been studied by Kiel et al. using the ultrasonic method. In this experiment, parylene-coated glass slides or silicon wafers were submerged in a 0.04–0.5 M solution of KI. A Ti horn was placed in the solution and tuned to a frequency of 20 kHz for a time ranging between 15 and 90 minutes, and ionic NPs were embedded in these substrates by a one-step, ultrasound-assisted procedure. Optimization of the coating process resulted in homogeneous distributions of nanocrystals (30 nm) on the surfaces of the substrates. Solubility studies demonstrated that nanoparticles were still adhered to the substrates after 24 hours, and it took over 96 hours for complete leaching to be achieved [56].

Another method used to form coatings is called *thermal spray processing*. Thermal spraying processes can be categorized on the basis of different energy sources used to heat the coating material to a softened/molten state (i.e. feedstock) during spraying, and include:

(1.) kinetic energy (cold spraying low/high pressure),
(2.) chemical energy (flame spraying [FS]),
(3.) high velocity oxygen fuel (HVOF),
(4.) high velocity air fuel (HVAF),
(5.) detonation gun (D-gun),
(6.) electric energy (plasma spraying such as atmospheric plasma spraying [APS]),
(7.) suspension plasma spraying (SPS), and
(8.) solution precursor plasma spraying (SPPS) [4].

Through the use of thermal spraying, molten particles (typically 10 μm to 2 mm) are formed and deposited onto a substrate in the form of drops that accumulate layer by layer. These particles are melted and accelerated toward the surface of the substrate. After the impact of the molten or semi-molten particles at a high speed, they spread and solidify to form "splats." The impact forms near-circular lamellae (10–100 μm) in diameter and >10 μm in thickness [3]. Over time, this results in a flattened and layered coating which can be deposited on a variety of different implant shapes [57]. The subsequent microstructure of the coating and its properties depend heavily on the feedstock and spray methods processing parameters. Thermal spraying employs a mixture of gases (i.e. argon/hydrogen) and high temperature (thousands of degrees Celsius). Spray methods that employ high temperatures are also one of the causes for concern when using this method for coating of metallic implants with BGs. At high temperatures, crystallization of BGs occurs, and this can lead to issues relating to the final density of the coating in addition to a reduction in bioactivity [4]. Some additional limitations have also been observed when spraying bioceramic particles on metallic surfaces. Coatings can experience cracking over time, which has been attributed to high dissolution rate, low mechanical strength, and low chemical stability of the BG coating [58]. The different types of deposition processes and the flexibility of this technique make it possible to deposit coatings from many different materials such as polymers and refractories to composite systems; however, much care must be taken in order to prevent against the development of negative properties post-implantation.

Enameling is a process that applies a glass-like coating that is fused on metallic substrates. It is a simple and relatively low-cost method. A powdered BG suspension is deposited on the metallic substrate and the glass powder is then glazed using a specific heat treatment profile. The BG particles are often dispersed in a liquid medium to obtain slurries which can be deposited on the surface using spraying or dipping to deposit the coating [4]. Post-drying, heat treatment of the BG coated

substrate is performed. The heat treatment temperature is usually between the glass transition temperature (T_g) and the crystallization temperature (T_c) to ensure softening and sintering of the BGs without inducing crystallization. Some glasses, such as Bioglass 45S5, experience crystallization at relatively low temperatures due to their relatively weak network structures, thus limiting their use in the enameling process. Altering the thermal profiles of the glass can be achieved by the addition of alkaline oxides [4]. This can increase the crystallization temperature and enhance the ability to retain an amorphous enamel coating [3]. The degree of adhesion between the BG coating and the metallic substrate depends on (i) glass composition and its structural characteristics, (ii) surface roughness, and (iii) the procedure used to apply coatings. One of the most pressing concerns is the requirement to match the substrate coefficient of thermal expansion (CTE) [3, 4]. If this characteristic is not considered, the development of thermal residual stresses can occur. This is likely due to the mismatch of the CTEs of the metallic substrate and the glass. Therefore, the difference between CTE of BGs and CTE of substrates should be as small as possible. To match the CTE of a BG to that of substrate, the glass composition can be modified by adding oxides such as MgO, K_2O, or SrO, to have similar coefficients to metallic substrates. Other options include applying a bond coat between the coating and the substrate to reduce the CTE mismatch [4]. Studies by Bharati et al. improved adhesion between a BG coating and the Ti–6Al–4V rod substrate by coating with a BG containing B_2O_3 and TiO_2. The B_2O_3 reduces both the CTE and the softening temperature of the glass, while the TiO_2 promotes the development of a controlled chemical bond, with a positive effect on the coating adhesion [59].

13.4 Characterization of Modified Surfaces

There are a number of technical tools used to characterize coatings. The most important characteristics to consider with a BG coating include adhesion, thickness, microstructure, roughness, porosity, and chemical phases. Another important aspect of coating a material's surface, regardless of the technique employed, is employing characterization tools to gain important information that can aid in experimental design and process optimization. Important characteristics such as the determination of CTE and thermal transition temperatures can be used to design the experimental process more accurately. There are several methods employed to perform thermal analysis on materials which can also include coated materials (particularly if the coated material involves a polymer). These methods include *thermogravimetric analysis (TGA)*, *differential scanning calorimetry (DSC)*, and *differential thermal analysis (DTA)*, as well as *dilatometry*. TGA is the primary method for determining how the overall weight of the material fluctuates when subjected to various temperatures, and is particularly useful when working with polymers, as evaporation of moisture or solvent leads to decomposition of the polymer, which helps to decipher the overall stability of the coating (polymer) that may be adhered onto an implant surface [60]. DSC/DTA is utilized to characterize thermal transitions such as the glass transition temperature (T_g), crystallization temperature (T_c), melting temperature (T_m), and vaporization within a material [60, 61]. If a material is encased within a polymer, it is imperative to know where this transition points exist to ensure that the polymer will not have an extensive property change that may compromise function. *Dilatometry* is a tool that can be employed to measure CTE. This tool is very important to analyze the CTE mismatch between bioceramics used in the coating process and the metallic substrates.

Light microscopy, also referred to as optical microscopy, is also a simple yet powerful tool in the initial characterization of coated materials. The mechanism behind this device is simple, as a specimen is placed on the stage of the microscope and illuminated above by a light source. The purpose

of using a light microscope is to make general observations on the surface of the coated material and note certain characteristics that may not be visible in a macroscopic setting [62]. Modern light microscopes can exhibit impressive magnifications, can visualize microstructures such as crystal structure, and can be used to observe physical characteristics such as coating stability and adherence [63]. A more advanced method for imaging a coating is *scanning electron microscopy (SEM)*. SEM utilizes the power of high-energy electrons in order to generate a beam that can "scan" over a coated material to give a detailed image that provides insight to the surface structure and topography (cracks, porosity, coating thickness) of the coating on a material [64]. X-rays can also be detected by the SEM and provide details on the elemental composition of the sample energy-dispersive X-ray spectroscopy (EDS). An X-ray detector can generate a spectrum that contains energy level peaks that corresponds to known elemental analysis. EDS can therefore be useful for confirming the presence of batched elements within a coating or identifying impurities. However, as with every method, SEM has its limitations, including the difficulty with charging, particularly on nonmetallic specimens [64]. *Transmission electron microscopy (TEM)* which differs from SEM from the perspective that it relies heavily on an electron beam that will pass through the surface of the specimen. This requires the sample to be extremely thin and often requires the specimen to be prepared in fine layers using ultramicrotome or focused ion beam microscopy (FIB). Th TEM can develop a high magnification image of the coating where the surface characteristics of the coated material can be elucidated [65]. TEM can also be equipped with EDS, in addition to providing insight into internal structures, including crystallinity by selected area electron diffraction (SAED). Crystallinity is an important characteristic to consider in the case of bioceramic coatings as it can significantly influence the physical properties (hardness), surface solubility, and bioactivity. While limited by a small area of surface being analyzed at one time and a flat, two-dimensional image, the detailed high resolution of the TEM lends itself to being an important device in characterizing coated materials [65].

Spectroscopy can be a very useful tool when composite coatings are being deposited on implant surfaces, particularly if a portion of the coating is comprised of organics. *Raman spectroscopy* is utilized for characterizing coated materials by analyzing vibrations of molecules to determine structural arrangement and molecular interactions [66]. The resultant peaks correspond to molecular bond vibrations which includes carbon double bonds, C–H groups, N–O groups, and other portions of the composition of the structure, like benzene rings for example. This can be used to not only infer the chemical identity of the coating but also the structural arrangement [66]. *Fourier-transform infrared spectroscopy (FTIR)* generates an infrared spectrum that provides similar information as Raman, including chemical composition of a coated material, as well as information related to the molecular interactions within the coating. FTIR can be used to map out the various components within the coating which correspond to known specific molecular linkages. This can help determine the presence of organic components such as polymer structure, cofactors, amino acid side groups, in addition to water molecules. These techniques are particularly useful for investigating composite coatings, i.e. bioceramic particles embedded in organic coatings/polymeric coatings [67].

Inductively coupled plasma mass spectroscopy (ICP-MS) is a technique that is employed to measure the release of ionic constituents from materials when in an aqueous medium. It is important to quantitatively determine the elemental release rates that may be exist in physiological fluids when the coated materials are present in the body. Coatings can contain various ions, or concentrations of ions, that can either provide positive therapeutic effects (osseointegration) or can have negative side effects (induce an immune response resulting in inflammation) [68]. ICP-MS analysis usually is done post-immersion after incubating coated samples in pseudo-physiological fluids such as SBF.

This technique can be used to determine the stability of the coating as a function of time in aqueous media, in addition to determining if the level of ion release remains within a therapeutic range or exceeds toxicity limits for the intended application [68].

Imaging the topography of the coated sample can also provide insight into characteristics such as defects within the coating, adhesion, coating thickness, porosity, and surface roughness. Techniques such as *atomic force microscopy (AFM)* and *profilometry* can be employed to provide 3D topographic information at different resolution. AFM is a high-resolution (nanoscale), noninvasive technique that can collect quantitative morphological measurements in real time [69]. There also exists the ability to measure physical properties (mechanical properties, surface roughness) at the nanometer level, in addition to performing experiments in both air and liquid environments [70]. Imaging and quantitative measurements of the surface roughness can also be achieved using profilometry. Profilometry operates by employing a mechanical (contact) or optical (non-contact) probe is passed across a surface. The probe follows the contours at each point on the surface, and the height of the probe at each point is recorded resulting in a 1D scan or a 2D map. A mechanical stylus captures the features over a large area (~100 mm), with a x–y resolution of 5 μm and a z-resolution of 0.01 μm. AFM scans a much smaller area (100 μm) but provides much higher resolutions (0.2 μm in x–y and 1.5 pm in z) [71].

13.5 Composite Coatings: Diversity of Inorganic–Organic Hybrids

Surface coating of metallic implants with bioceramics is one of the most widely adopted methods to improve the surface biocompatibility and bioactivity while retaining the properties of the bulk materials. As previously highlighted, BGs are highly biocompatible and are known to integrate with human tissues, which makes them an excellent candidate for initiating bond bonding between host tissue and metallic prosthesis. Additionally, BGs also have the ability to facilitate soft tissue regeneration and stimulate the deposition and crystallization of HAp when in contact with physiological fluids, which supports their role as a potential coating to initiate interfacial bonding between metallic implants and bone tissue or inhibit corrosions of the implant metals in biological environments [57]. The most widely investigated BG composition is 45S5 Bioglass ($46.1SiO_2$–$24.4Na_2O$–$26.9CaO$–$2.6P_2O_5$ [mol%]), but these glasses can accommodate a wide array of different dopants, while still maintaining the basic physical and chemical properties of an amorphous glass. Many new compositions have been proposed for several different biomedical applications, including improved dental materials, improved coatings on load-bearing metal implants, and tissue engineering scaffolds. In order to introduce additional functionality, various ions have been incorporated into these glass structures, such as Sr^{2+} and Mg^{2+} for enhanced bone formation, and Ag^{+}, Cu^{2+}, and Zn^{2+} for antimicrobial efficacy. However, while concepts like the introduction of ions with antimicrobial effects can be highly beneficial, cytocompatibility testing and solution characterization should be carefully conducted to ensure the rate of ion release does not exceed known toxicity limits [4].

Bioceramic materials also have the capability to be introduced into composite systems in order to maximize the properties of a coating. These hybrid systems can occur where bioceramics are processed with either *natural* or *synthetic polymers*. *Collagen* and *chitosan* polymers are examples of materials originating from tissue-based sources that can provide additional functionalities to surface coatings, such as enhanced biocompatibility. Chitosan, a *naturally occurring polymer* which is primarily sourced from the exoskeletons of crustaceans, has the ability to exhibit antimicrobial activity, biocompatibility, and biodegradability within the human body. To form a multifunctional

coating, studies have investigated the combination of chitosan with 45S5 Bioglass and observed enhanced adhesion of the implant to bone while garnering additional benefits from chitosan matrix [57, 72–75]. Studies by Montemor and coworkers also investigated the application of both collagen and chitosan on multilayered (silane TiO_2) coatings to improve corrosion-resistance of Mg alloys. The biopolymer layers were found to significantly influence the composition of the corrosion products produced, assisting in the trapping of H^+, and helping to prevent its release during the early stages of immersion. This mechanism resulted in enhanced corrosion-resistance of these Mg alloys, which is theorized to result in enhanced biointegration [76]. Another natural polymer source of interest is alginate, which has been investigated for applications in tissue regeneration and wound healing. Alginate is biodegradable and is known to break down due to reactions that occur between the crosslinking agents as monovalent ions are released and exchanged within body fluids. The degradation rate of alginate can be tailored and controlled by oxidation/reduction reactions within the molecular weight of the polymer, which suggests that this polymer could potentially be very useful in a wide range of applications [77].

Synthetic polymers, such as polycaprolactone (PCL), polymethylmethacrylate (PMMA), polylactic acid (PLA), poly(lactide-*co*-glycolic) acid (PLGA), polydopamine (PDA), and PU, have all been investigated as a component of hybrid coatings designed for the improvement of metallic implants [78]. However, coatings that consist solely of polymeric material inherently possess some drawbacks compared to composited coatings. This is because polymers are usually flexible and allow for adequate coating of even the most complex shapes, but often lack sufficient mechanical strength and chemical stability for long-term internal use [78]. As for inorganic materials as a solitary coating material, they generally exhibit weak adhesive strength on surfaces, poor film-forming ability, and tend to aggregate, rather than spread evenly. Therefore, inorganic-polymer composite coatings have been widely investigated, as inorganic components can reinforce the polymer, while polymers can work as matrices for the proper dispersion of inorganic fillers [78]. PCL is an important synthetic polymer that can be used to reduce the brittle nature of bioceramic coatings. PCL is known to be biocompatible, biodegradable, and presents qualities similar to collagen in natural bone where it can improve elasticity and cell adhesion. Since glass is brittle and can easily experience catastrophic failure, using a polymer (like PCL) to help counter these effects and increase overall elasticity makes the BG more stable in load-bearing or high fracture risk applications [57]. Studies on PMMA/BG coatings were conducted by Floroian et al. where frozen solutions of PMMA/BG were deposited by matrix assisted pulsed laser evaporation (MAPLE) deposition on Ti substrates. The corrosion behavior of the Ti was greatly reduced compared to the non-coated Ti control, in addition to the BG initiating the formation of a rapidly growing apatite layer on the coated Ti surface. This coupled result of reducing the effect of corrosion and imparting bioactivity of the metal's surface is significant, as it will likely result in osseointegration [79]. Complex hybrid coatings were synthesized by Caddeo et al. by incorporating the glass-ceramic (SiO_2–P_2O_5–CaO–MgO–Na_2O–K_2O) within a blend of a water-soluble mixture of PU and collagen. This study resulted in a strong interfacial covalent link between the blend and the substrate. Biological tests (human periosteal derived precursor cells) demonstrated that the polymer-coated material was a promising substrate for bone cell adhesion and growth, and a good candidate to mimic the composite nature of the bone extracellular matrix (ECM) [14].

The risk of infection in implants is a primary concern in the development of coatings, particularly for orthopedic usages. Up to 15% of all joint replacements result in infection, and the downstream effects include loosening, increased degradation of the implant which can result in heightened debris in the joint cavity, and ultimately, failure. Since over 7 million joint replacements are

performed in the United States annually, the cost and economic impact of infection and revision surgery is notable and can be upward of US $31 000 for each revision required. As a result, further research into improved antimicrobial coatings is necessary, as the drug regimen used to combat infection post-operation is not able to sustain an aseptic joint replacement on its own. Fortunately, there are plenty of options, ranging from passive finishing surfaces, to bioactive, integrative coatings [80]. Numerous studies have been conducted on incorporating antimicrobial ions and antibiotics onto material surfaces to eliminate opportunistic bacteria. Perhaps one of the most studied ions for implant purposes is silver (Ag^+). In a retrospective study by Wafa et al., it was found that the postoperative rate of infection in silver-coated orthopedic implants (total hip replacement [THR]) was reduced from 22.4% to 11.8%, compared to a non-silver coated control group [81]. This ion is of even greater interest, as metallic substrates plasma-sprayed with a glass coating doped with Ag^+ through ion-exchange have exhibited that the mechanical properties of the coating remain intact post-processing, while also introducing antimicrobial effects upon implantation, through Ag^+ leaching [82]. All of these prior studies suggest that not only are organic–inorganic composites worthy of further investigation for coatings on metallic implants, but that these materials could potentially provide a multitude of enormous effects, including reduced infection and revision rates, reduced anti-biotic/pharmaceutical use, and ultimately, reduced societal cost for restorative surgeries.

13.6 Conclusion

It is evident that the field of regenerative medicine can significantly expand and diversify through the use of coating technology. The ability to fabricate BGs with novel compositions and morphologies presents a significant benefit to improving the biocompatibility of implantable metallic materials, and to synthesize novel bioactive composite materials with polymers. The true benefit in employing BGs as a component of a coating lies in the ability of tailor the composition to a specific therapeutic application. Versatility exists in the processing methods, the particle morphology and solubility, and the ability to control the degradation rate under physiological conditions. BGs have proven their ability to induce mineralization *in vivo*, in addition to presenting positive biological responses in wound healing in soft tissues. It is likely in the near future that specific therapeutic products released from BG coatings will be linked to the biological responses responsible for full osseointegration of currently used implantable materials.

References

1 Jones, J.R. (2013). Review of bioactive glass: from Hench to hybrids. *Acta Biomaterialia* 9: 4457–4486.
2 Boccaccini, A.R., Brauer, D.S., and Hupa, L. (2016). *Bioactive Glasses: Fundamentals, Technology and Applications*. Royal Society of Chemistry.
3 Ylanen, H. (2018). *Bioactive Glasses: Materials, Properties and Applications*, 2e. Woodhead Publishing.
4 Sergi, R., Bellucci, D., and Cannillo, V. (2020). A comprehensive review of bioactive glass coatings: state of the art, challenges and future perspectives. *Coatings* 10: 757.
5 Heinz, S.A., Paliwal, S., and Ivanovski, S. (2015). Mechanisms of bone resorption in periodontitis. *Journal of Immunology Research* 2015: 1–10.

6 Khanmohammadi, S., Ojaghi-Ilkhchi, M., and Farrokhi-Rad, M. (2020). Evaluation of bioglass and hydroxyapatite based nanocomposite coatings obtained by electrophoretic deposition. *Ceramics International* 46: 26069–26077.

7 Arres, M., Salma, M., Rechena, D. et al. (2020). Surface and mechanical properties of a nanostructured citrate hydroxyapatite coating on pure titanium. *Journal of the Mechanical Behavior of Biomedical Materials* 108**:** 103794.

8 Horandghadim, N., Khalil-Allafi, J., and Urgen, M. (2019). Effect of Ta_2O_5 content on the osseointegration and cytotoxicity behaviors in hydroxyapatite-Ta_2O_5 coatings applied by EPD on superelastic NiTi alloys. *Materials Science and Engineering C* 102: 683–695.

9 Misra, D., Shariff, S.M., Mukhopadhyay, S., and Chatterjee, S. (2018). Analysis of instrumented scratch hardness and fracture toughness properties of laser surface alloyed tribological coatings. *Ceramics International* 44: 4248–4255.

10 van Hove, R.P., Sierevelt, I.N., van Royen, B.J., and Nolte, P.A. (2015). Titanium-nitride coating of orthopaedic implants: a review of the literature. *BioMed Research International* 2015: 485975.

11 Hussein, M.A., Adesina, A.Y., Madhan Kumar, A. et al. (2020). Mechanical, in-vitro corrosion, and tribological characteristics of TiN coating produced by cathodic arc physical vapor deposition on $Ti_{20}Nb_{13}Zr$ alloy for biomedical applications. *Thin Solid Films* 709**:** 138183.

12 Milan, P.B., Khamseh, S., Zarrintaj, P. et al. (2020). Copper-enriched diamond-like carbon coatings promote regeneration at the bone-implant interface. *Heliyon* 6 (4): e03798.

13 Viguet-Carrin, S., Garnero, P., and Delmas, P.D. (2006). The role of collagen in bone strength. *Osteoporosis International* 17 (3): 319–336.

14 Caddeo, S., Mattioli-Belmonte, M., Cassino, C. et al. (2019). Newly-designed collagen/polyurethane bioartificial blend as coating on bioactive glass-ceramics for bone tissue engineering applications. *Materials Science and Engineering C* 96: 218–233.

15 Rammelt, S., Schulze, E., Bernhardt, R. et al. (2004). Coating of titanium implants with type-I collagen. *Journal of Orthopaedic Research* 22 (5): 1025–1034.

16 Szaraniec, B., Pielichowska, K., Pac, E., and Menaszek, E. (2018). Multifunctional polymer coatings for titanium implants. *Materials Science and Engineering C* 93: 950–957.

17 Khoo, X., Hamilton, P., O'Toole, G.A. et al. (2009). Directed assembly of PEGylated-peptide coatings for infection-resistant titanium metal. *Journal of the American Chemical Society* 131 (31): 10992–10997.

18 Wang, Y., Papadimitrakopoulos, F., and Burgess, D.J. (2013). Polymeric "smart" coatings to prevent foreign body response to implantable biosensors. *Journal of Controlled Release* 169 (3): 341–347.

19 Stavrakis, A.I., Zhu, S., Hegde, V. et al. (2016). In vivo efficacy of a "smart" antimicrobial implant coating. *Journal of Bone and Joint Surgery* 98 (14): 1183–1189.

20 Jones, J.R., Ehrenfried, L.M., and Hench, L.L. (2006). Optimising bioactive glass scaffolds for bone tissue engineering. *Biomaterials* 27 (7): 964–973.

21 Hench, L.L. (2006). The story of Bioglass. *Journal of Materials Science – Materials in Medicine* 17: 967–978.

22 Hench, L.L. (2009). Genetic design of bioactive glass. *Journal of the European Ceramic Society* 29: 1257–1265.

23 Rahaman, M.N., Day, D.E., Bal, B.S. et al. (2011). Bioactive glass in tissue engineering. *Acta Biomaterialia* 7 (6): 2355–2373.

24 Hoppe, A., Guldal, N.S., and Boccaccini, A.R. (2011). A review of the biological response to ionic dissolution products from bioactive glasses and glass-ceramics. *Biomaterials* 32: 2757–2774.

25 Hench, L.L. (2016). Bioglass: 10 milestones from concept to commerce. *Journal of Non-Crystalline Solids* 432 Part A: 2–8.

26 Hench, L.L., Day, D.E., Holand, W., and Rheinberger, V.W. (2010). Glass and Medicine. *International Journal of Applied Glass Science* 1 (1): 104–117.

27 Gerhardt, L.-C. and Boccaccini, A. (2010). Bioactive glass and glass-ceramic scaffolds for bone tissue engineering. *Materials* 3: 3867–3910.

28 Kokubo, T. and Takadama, H. (2006). How useful is SBF in predicting in vivo bone bioactivity. *Biomaterials* 27: 2907–2915.

29 Kumar, A., Singh, S., Thumar, G., and Mengji, A. (2015). Bioactive glass nanoparticles (NovaMin®) for applications in dentistry. *IOSR Journal of Dental and Medical Sciences* 14 (8): 30–35.

30 Stábile, F.M., Stagnaro, S.Y.M., Ortiga, J., and Volzone, C. (2015). Production of porous scaffolds from Bioglass 45S5-derived glasses. *Procedia Materials Science* 9: 558–562.

31 Vitale-Brovarone, C., Verné, E., Robiglio, L. et al. (2007). Development of glass–ceramic scaffolds for bone tissue engineering: characterisation, proliferation of human osteoblasts and nodule formation. *Acta Biomaterialia* 3 (2): 199–208.

32 Vitale-Brovarone, C., Miola, M., Balagna, C., and Verné, E. (2008). 3D-glass–ceramic scaffolds with antibacterial properties for bone grafting. *Chemical Engineering Journal* 137 (1): 129–136.

33 Srinivasan, S., Jayasree, R., Chennazhi, K.P. et al. (2012). Biocompatible alginate/nano bioactive glass ceramic composite scaffolds for periodontal tissue regeneration. *Carbohydrate Polymers* 87 (1): 274–283.

34 Renghini, C., Giuliani, A., Mazzoni, S. et al. (2013). Microstructural characterization and in vitro bioactivity of porous glass-ceramic scaffolds for bone regeneration by synchrotron radiation X-ray microtomography. *Journal of the European Ceramic Society* 33 (9): 1553–1565.

35 López-Álvarez, M., Rodríguez-Valencia, C., Serra, J., and González, P. (2013). Bio-inspired ceramics: promising scaffolds for bone tissue engineering. *Procedia Engineering* 59: 51–58.

36 Gerhardt, L.-C., Widdows, K.L., Erol, M.M. et al. (2011). The pro-angiogenic properties of multi-functional bioactive glass composite scaffolds. *Biomaterials* 32 (17): 4096–4108.

37 Fu, Q., Saiz, E., Rahaman, M.N., and Tomsia, A.P. (2011). Bioactive glass scaffolds for bone tissue engineering: state of the art and future perspectives. *Materials Science and Engineering C* 31 (7): 1245–1256.

38 Chen, Q.Z., Thompson, I.D., and Boccaccini, A.R. (2006). 45S5 Bioglass®-derived glass-ceramic scaffolds for bone tissue engineering. *Biomaterials* 27 (11): 2414–2425.

39 Wren, A.W., Coughlan, A., Smale, K.E. et al. (2012). Fabrication of CaO–NaO–SiO_2/TiO_2 scaffolds for surgical applications. *Journal of Materials Science – Materials in Medicine* 23 (12): 2881–2891.

40 Yang, Q., Chen, S., Shi, H. et al. (2015). In vitro study of improved wound-healing effect of bioactive borate-based glass nano-/micro-fibers. *Materials Science and Engineering C* 55: 105–117.

41 Vallittu, P.K., Närhi, T.O., and Hupa, L. (2015). Fiber glass–bioactive glass composite for bone replacing and bone anchoring implants. *Dental Materials* 31 (4): 371–381.

42 Anderson, J.H., Goldberg, J.A., Bessent, R.G. et al. (1992). Glass yttrium-90 microspheres for patients with colorectal liver metastases. *Radiotherapy and Oncology* 25 (2): 137–139.

43 Nicholson, J.W. and Wilson, A.D. (1993). *Acid-Base Cements: Their Biomedical and Industrial Applications*, Chemistry of Solid State Materials, vol. 3. Cambridge: Cambridge University Press.

44 Li, R., Clark, A.E., and Hench, L.L. (1991). An investigation of bioactive glass powders by sol–gel processing. *Journal of Applied Biomaterials* 2 (4): 231–239.

45 Hong, Z., Liu, A., Chen, L. et al. (2009). Preparation of bioactive glass ceramic nanoparticles by combination of sol–gel and coprecipitation method. *Journal of Non-Crystalline Solids* 355 (6): 368–372.

46 Vafaa, I., Bazargan-Laria, R., and Bahrololoom, M.E. (2021). Synthesis of 45S5 bioactive glass-ceramic using the sol–gel method, catalyzed by low concentration acetic acid extracted from homemade vinegar. *Journal of Materials Research and Technology* 10: 1427–1436.

47 Liu, X., Chu, P.K., and Ding, C. (2005). Surface modification of titanium, titanium alloys, and related materials for biomedical applications. *Materials Science and Engineering C* 47: 49–121.

48 Pourhashem, S. and Afshar, A. (2014). Double layer bioglass-silica coatings on 316L stainless steel by sol–gel method. *Ceramics International* 4: 993–1000.

49 Hanawa, T. (2004). Metal ion release from metal implants. *Materials Science and Engineering C* 24: 745–752.

50 Fathi, M.H. and Doostmohammadi, A. (2009). Bioactive glass nanopowder and bioglass coating for biocompatibility improvement of metallic implant. *Journal of Materials Processing Technology* 209: 1385–1391.

51 Ben-Nissan, B. and Choi, A.H. (2006). Sol–gel production of bioactive nanocoatings for medical applications. Part 1: an introduction. *Nanomedicine (London)* 1 (3): 311–319.

52 Scriven, L. (1988). Physics and applications of DIP coating and spin coating. *MRS Symposium Proceedings* 121: 717.

53 Aksakal, B. and Hanyaloglu, C. (2008). Bioceramic dip-coating on Ti–6Al–4V and 316L SS implant materials. *Journal of Materials Science Materials in Medicine* 19 (5): 2097–2104.

54 Thiagarajan, S., Sanmugam, A., and Vikraman, D. (2017: https://doi.org/10.5772/intechopen.68708). Facile methodology of sol–gel synthesis for metal oxide nanostructures. In: *Recent Applications in Sol–Gel Synthesis* (ed. U. Chandra). IntechOpen.

55 Owens, G.J., Singh, R.K., Foroutan, F. et al. (2016). Sol–gel based materials for biomedical applications. *Progress in Materials Science* 77: 1–79.

56 Kiel, S., Grinberg, O., Perkas, N. et al. (2012). Forming nanoparticles of water-soluble ionic molecules and embedding them into polymer and glass substrates. *Beilstein Journal of Nanotechnology* 3: 267–276.

57 Oliver, J.N., Su, Y., Lu, X. et al. (2019). Bioactive glass coatings on metallic implants for biomedical applications. *Bioactive Materials* 4: 261–270.

58 Garcia, E., Miranzo, P., and Sainz, M.A. (2018). Thermally sprayed wollastonite and wollastonite-diopside compositions as new modulated bioactive coatings for metal implants. *Ceramics International* 44: 12896–12904.

59 Bharati, S., Soundrapandian, C., Basu, D., and Datta, S. (2009). Studies on a novel bioactive glass and composite coating with hydroxyapatite on titanium based alloys: effect of γ-sterilization on coating. *Journal of the European Ceramic Society* 29 (12): 2527–2535.

60 Feist, M. (2015). Thermal analysis: basics, applications, benefits. *ChemTexts* 1 (8): 1–12.

61 Huangfu, M.G., Zhang, Y., Zhang, X.L. et al. (2019). Preparation and thermal evaluation of novel polyimide protective coatings for quartz capillary chromatographic columns operated over 320 °C for high-temperature gas chromatography analysis. *Polymers (Basel)* 11: 6.

62 Thorn, K. (2016). A quick guide to light microscopy in cell biology. *Molecular Biology of the Cell* 27 (2): 219–222.

63 Masters, B. (2006). *Confocal Microscopy and Multiphoton Excitation Micrscopy: The Genesis of Live Cell Imaging*. Bellingham: Optical Engineering Press.

64 Fischer, E.R., Hansen, B.T., Nair, V. et al. (2012 . Chapter 2: Unit 2B 2.). Scanning electron microscopy. In: *Current Protocols in Microbiology*. Wiley.

65 Winey, M., Meehl, J.B., O'Toole, E.T., and Giddings, T.H. Jr., (2014). Convenional transmission electron microscopy. *Molecular Biology of the Cell* 25 (3): 319–323.

66 Ember, K.J.I., Hoeve, M.A., McAughtrie, S.L. et al. (2017). Raman spectroscopy and regenerative medicine: a review. *npj Regenerative Medicine* 2: 12.

67 Berthomieu, C. and Hienerwadel, R. (2009). Fourier transform infrared (FTIR) spectroscopy. *Photosynthesis Research* 101 (2–3): 157–170.

68 Wilschefski, S.C. and Baxter, M.R. (2019). Inductively coupled plasma mass spectrometry: introduction to analytical aspects. *Clinical Biochemist Reviews* 40 (3): 115–133.

69 Pompeo, G., Girasole, M., Cricenti, A. et al. (2005). AFM characterization of solid-supported lipid multilayers prepared by spin-coating. *Biochimica et Biophysica Acta (BBA) Biomembranes* 1712 (1): 29–36.

70 Roa, J.J., Oncins, G., Díaz, J. et al. (2011). Study of the friction, adhesion and mechanical properties of single crystals, ceramics and ceramic coatings by AFM. *Journal of the European Ceramic Society* 31 (4): 429–449.

71 Williams, R. (2011). *Surface Modification of Biomaterials: Methods, Analysis and Applications*. *Woodhead Publishing Limited*.

72 Akhtar, M.A., Mariotti, C.E., Conti, B., and Boccaccini, A.R. (2021). Electrophoretic deposition of ferulic acid loaded bioactive glass/chitosan as antibacterial and bioactive composite coatings. *Surface and Coatings Technology* 405**:** 126657.

73 Alaei, M., Atapour, M., and Labbaf, S. (2020). Electrophoretic deposition of chitosan-bioactive glass nanocomposite coatings on AZ91 Mg alloy for biomedical applications. *Progress in Organic Coatings* 147**:** 105803.

74 Vafa, E., Bazargan-Lari, R., and Bahrololoom, M.E. (2021). Electrophoretic deposition of polyvinyl alcohol/natural chitosan/bioactive glass composite coatings on 316L stainless steel for biomedical application. *Progress in Organic Coatings* 151**:** 106059.

75 Zarghami, V., Ghorbani, M., Pooshang Bagheri, K., and Shokrgozar, M.A. (2020). Prolongation of bactericidal efficiency of chitosan – bioactive glass coating by drug controlled release. *Progress in Organic Coatings* 139**:** 105440.

76 Córdoba, L.C., Marques, A., Taryba, M. et al. (2018). Hybrid coatings with collagen and chitosan for improved bioactivity of Mg alloys. *Surface and Coatings Technology* 341: 103–113.

77 Ahmad Raus, R., Wan Nawawi, W.M.F., and Nasaruddin, R.R. (2021). Alginate and alginate composites for biomedical applications. *Asian Journal of Pharmaceutical Sciences* 16 (3): 280–306.

78 Li, H.-y., Huang, D.-n., Ren, K.-f., and Ji, J. (2021). Inorganic-polymer composite coatings for biomedical devices. *Smart Materials in Medicine* 2: 1–14.

79 Floroian, L., Sima, F., Florescu, M. et al. (2010). Double layered nanostructured composite coatings with bioactive silicate glass and polymethylmethacrylate for biomimetic implant applications. *Journal of Electroanalytical Chemistry* 648 (2): 111–118.

80 Romano, C.L., Tsuchiya, H., Morelli, I. et al. (2019). Antibacterial coating of implants: are we missing something? *Bone & Joint Research* 8 (5): 199–206.

81 Wafa, H., Grimer, R.J., Reddy, K. et al. (2015). Retrospective evaluation of the incidence of early periprosthetic infection with silver-treated endoprostheses in high-risk patients: case-control study. *The Bone & Joint Journal* 97-B (2): 252–257.

82 Miola, M., Ferraris, S., Di Nunzio, S. et al. (2008). Surface silver-doping of biocompatible glasses to induce antibacterial properties. Part II: plasma sprayed glass-coatings. *Journal of Materials Science Materials in Medicine* 20 (3): 741.

14

Laser Cladding and Laser Direct Glass Deposition of Bioactive Glass and Glass-Ceramics

Rafael Comesaña[1,2], Jesús del Val[1,3], Félix Quintero[1,3], Antonio Riveiro[1,2], Felipe Arias-González[1,3], Mohamed Boutinguiza[1,3], Fernando Lusquiños[1,3], and Juan Pou[1,3]

[1] *LaserON Laser Applications Research Group, Research Center in Technologies, Energy and Industrial Processes, CINTECX, University of Vigo, Vigo, Spain*
[2] *Department of Materials Engineering, Applied Mechanics and Construction, EEI, University of Vigo, Vigo, Spain*
[3] *Applied Physics Department, EEI, University of Vigo, Vigo, Spain*

14.1 Laser Cladding and Laser Direct Glass Deposition

This chapter covers the production of bioactive glass (BG)-ceramic coatings by laser cladding (LC) and the additive fabrication of BG-ceramic by laser direct glass deposition (LDGD). The first technique is applied to produce bioactive glass (BG) coatings strongly bonded to metallic surfaces for metallic implant osseo-integration improvement (Figure 14.1a). The LDGD is able to generate BG three-dimensional parts by additive manufacturing from BG microparticles (Figure 14.1b) [1, 2].

14.1.1 The Laser Cladding (LC) Technique

LC is an integrative technology employing laser technology, computer-assisted design and fabrication, robotics, sensors and control, and materials. LC employs a laser energy source to deposit a layer of a desired material on a moving substrate. The precursor material can be conveyed to the laser–material interaction zone by several methods: powder injection, pre-placed powder on the substrate, or by wire feeding [3]. Figure 14.2 shows the LC principle with the different precursor material feeding. Between these, LC by powder injection is the most effective in general applications. In the LC process, the laser beam melts the powder particles to deposit a layer of the molten material on the substrate. Diverse materials can be deposited on a surface to create a layer with thicknesses and widths from millimeters to some microns [4–6].

The LC technique was introduced in the 1980s and is extensively applied as coating method in the metallurgical field [7]. In the biomedical field, LC with powder injection and Nd:YAG laser source started to be investigated two decades later to produce calcium phosphate (CaP) coatings on titanium alloys, as alternative to calcium phosphate coatings produced by plasma spray [8–11]. The obtained CaP coatings showed an improved bonding to the substrate and similar osteoblast proliferation activity (Figure 14.3) [11–13]. In addition, LC with calcium phosphate preplaced layers was tested using Nd:YAG laser [14–17] and CO_2 laser sources [18, 19]. The employment of LC to produce BG and glass-ceramic coatings was initiated some years later. Preplaced powder LC was tested to produce BG coatings on pure Ti with CO_2 laser [20, 21], and LC by blown BG powder was applied to coat Ti6Al4V alloy and Al_2O_3/ZrO_2 [1, 2, 22, 23].

Bioactive Glasses and Glass-Ceramics: Fundamentals and Applications, First Edition.
Edited by Francesco Baino and Saeid Kargozar.

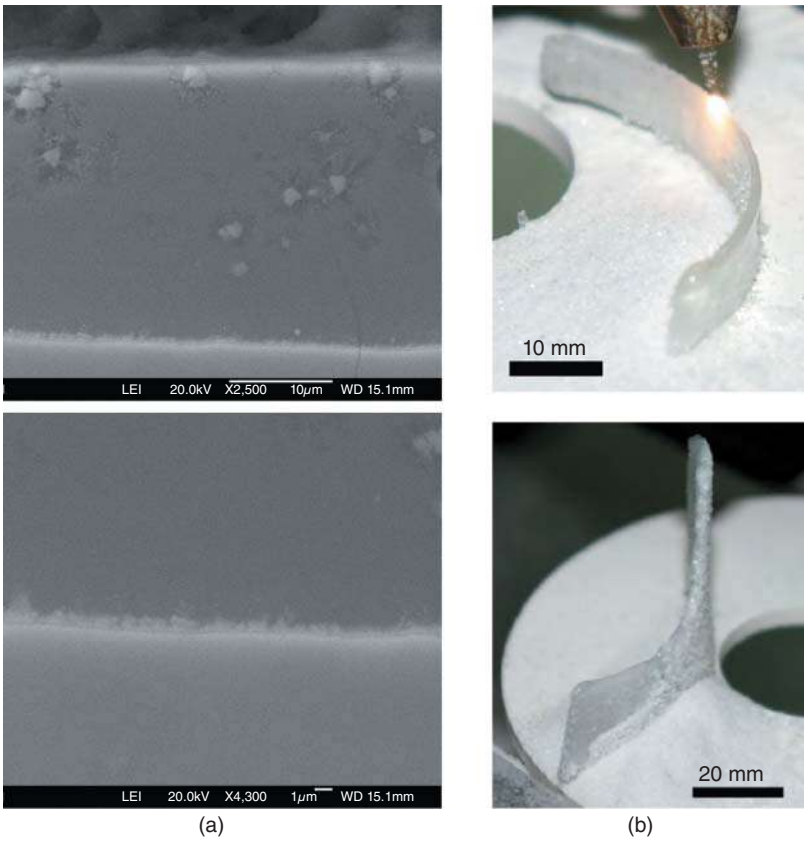

Figure 14.1 (a) Cross section of bioactive glass coating on Ti6Al4V titanium alloy produced by laser cladding [1]. (b) 3D bioactive glass parts produced by laser direct glass deposition. Source: (b) Comesaña et al. [2], Figure 05 [p. 3480]/with permission from Elsevier.

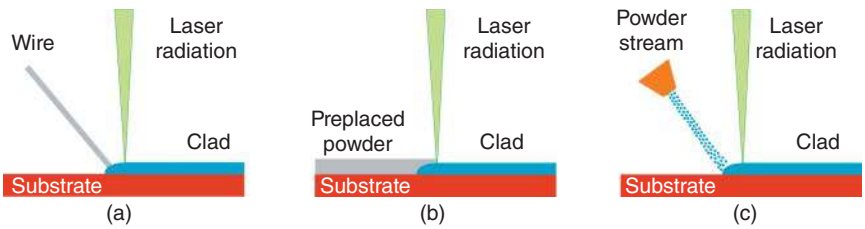

Figure 14.2 Laser cladding principle with different material feeding: (a) wire feeding, (b) preplaced powder layer, and (c) powder injection.

14.1.2 The Laser Direct Glass Deposition Technique (LDGD)

In the last decade, the additive fabrication has exponentially grown due to the development of affordable technology. The LDGD is an additive manufacturing technique based on LC (recently standardized in the metallurgical field as laser direct energy deposition, LDED, and early known as rapid prototyping based on LC), and it joined the group of revolutionary additive manufacturing techniques commonly identified as "3D printing." The capability to construct complex parts without intermediate processing stages is provided by the combination of the LC technology with a 3D

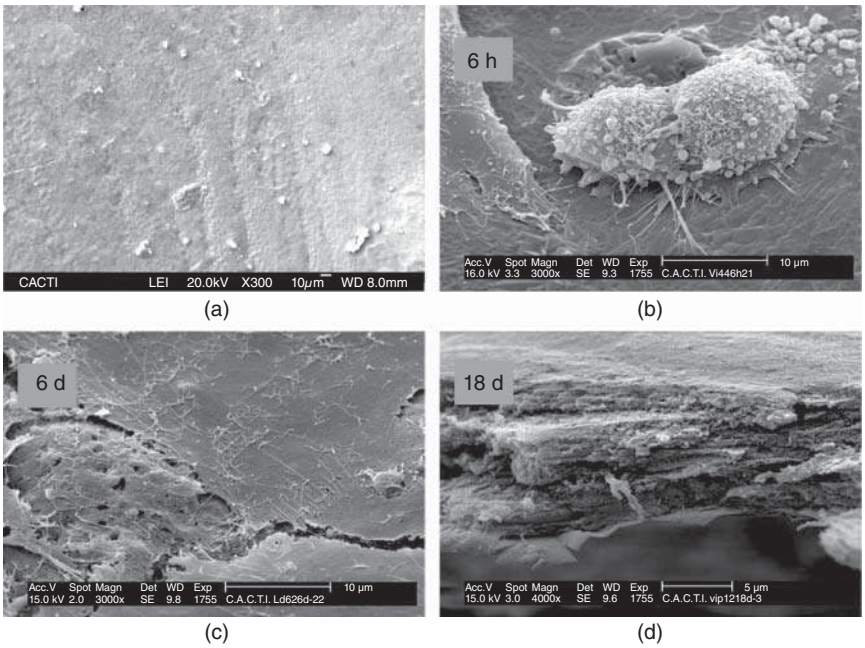

Figure 14.3 The first application of laser cladding in the biomaterials field was the production of calcium phosphate coatings on Ti6Al4V alloy. (a) Surface of laser cladded CaP; cell morphology after (b) 6 hours, (c) 6 days, and (d) 18 days of coating cell seeding. Source: De Carlos et al. [12], Figure 02 and 03 [p. 1157 and 1158]/with permission from Springer Nature.

computer model, which is divided in the required additive layers [24]. The outline of LDGD, with off-axis powder injection and with coaxial powder injection, respectively, is presented in Figure 14.4 [2, 25].

The development of the LC technology and LDGD technology has strongly depended on the enhancement and affordability of the involved equipment. Understanding the interconnections between the process quality and the involved technologies is a major step for the development of LC and LDGD. The large number of interrelations between the involved technologies not only increases the process complexity but also increments the process parameters. In the field of the glass and glass-ceramic materials, the main processing parameters are related to the laser beam, the processed material, the material feeding and injection system, the motion system, the environment, and the control and monitoring system. The processing parameters and the associated physical and chemical phenomena during processing determine the final part characteristics. Following, we describe how the main process parameters are related to the laser–material interaction. In addition, we analyze how the necessary parameters are substantiated in the LC and LDGD equipment.

14.1.3 Laser–Material Interaction

Laser assisted processes can be discriminated as a function of the laser–material interaction mechanism, which is mainly determined by the laser beam irradiance and the exposure time for a given material and laser wavelength. The beam irradiance is the average optical power that impinges in a unit surface area. At low irradiance, photochemical interaction occurs, leading to material chemical modifications. Increasing irradiances along to extended exposure times produce laser–material thermal interaction, normally accompanied by transformation or melting of the material. High

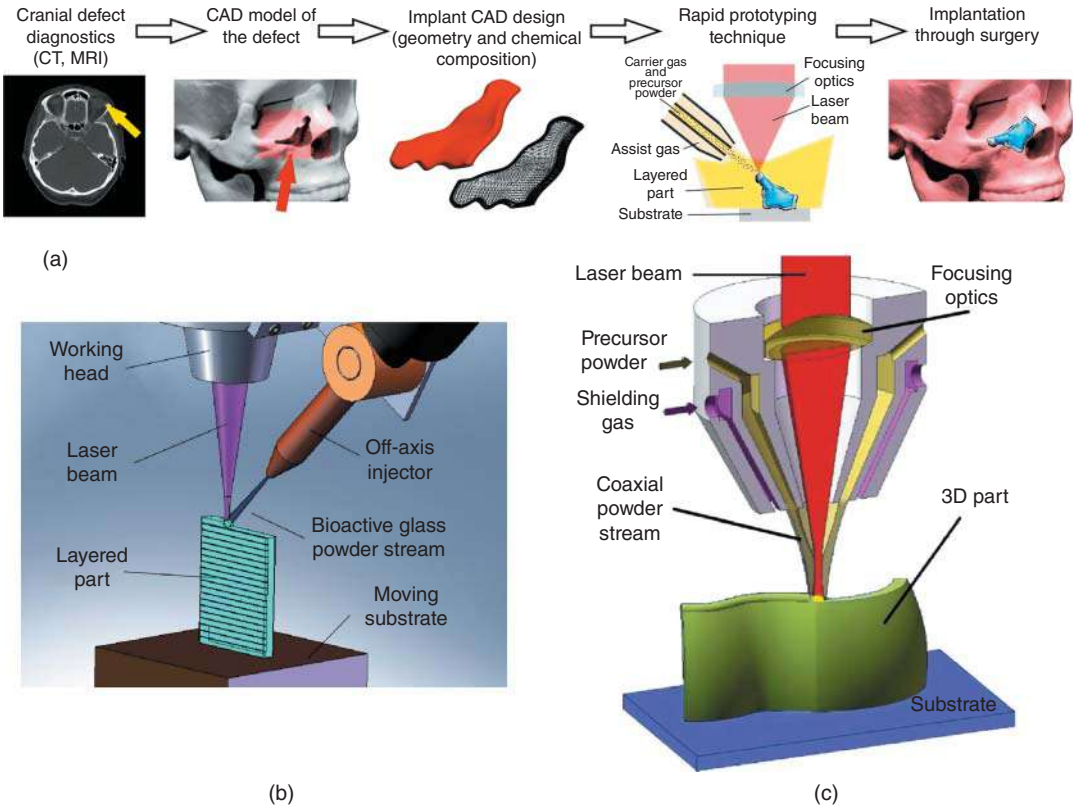

Figure 14.4 (a) The laser direct glass deposition allows to implement tailored additive manufacturing as an integral procedure from the diagnostics to the final surgical implantation. Source: Comesaña et al. [24], Figure 1 [p. 02]/Springer Nature/CC BY 4.0. Schematics of laser direct glass deposition with (b) off-axis powder injection and (c) coaxial powder injection. Source: Lusquiños et al. [2] and Comesaña et al. [24]. Reproduced with permission of Elsevier.

irradiances and moderate to reduced irradiance times allow to reach the vaporizing regime and material ablation is produced. Generally, LC and LDGD involve melting of the precursor glass material. Employed laser beam irradiances are comparatively low, and large interaction times allow to produce material heating, melting, and cooling (in addition to specific transformations such as phase transformation, crystallization, etc.). Figure 14.5a locates the LC technique within the different laser assisted processes. It has been experimentally observed that the BG particles injected in LC and LDGD processes require interaction times in the order of tens of milliseconds to integrate in the process molten pool (see Figure 14.5b).

14.1.4 The LC and LDGD Processing Station

The diagram in Figure 14.6 explains the systems basic function performed within the LC and LDGD working station. From one side, the powder feeding system and the carrier gas delivery systems must provide a homogeneous and consistent powder flow to the injection nozzle. Thus, the powder-carrier gas biphasic stream reaches the laser–material interaction area. From the other side, the laser radiation source provides the laser beam, which is guided and concentrated by the laser focusing system and irradiates the desired area of the molten pool. The motion system must

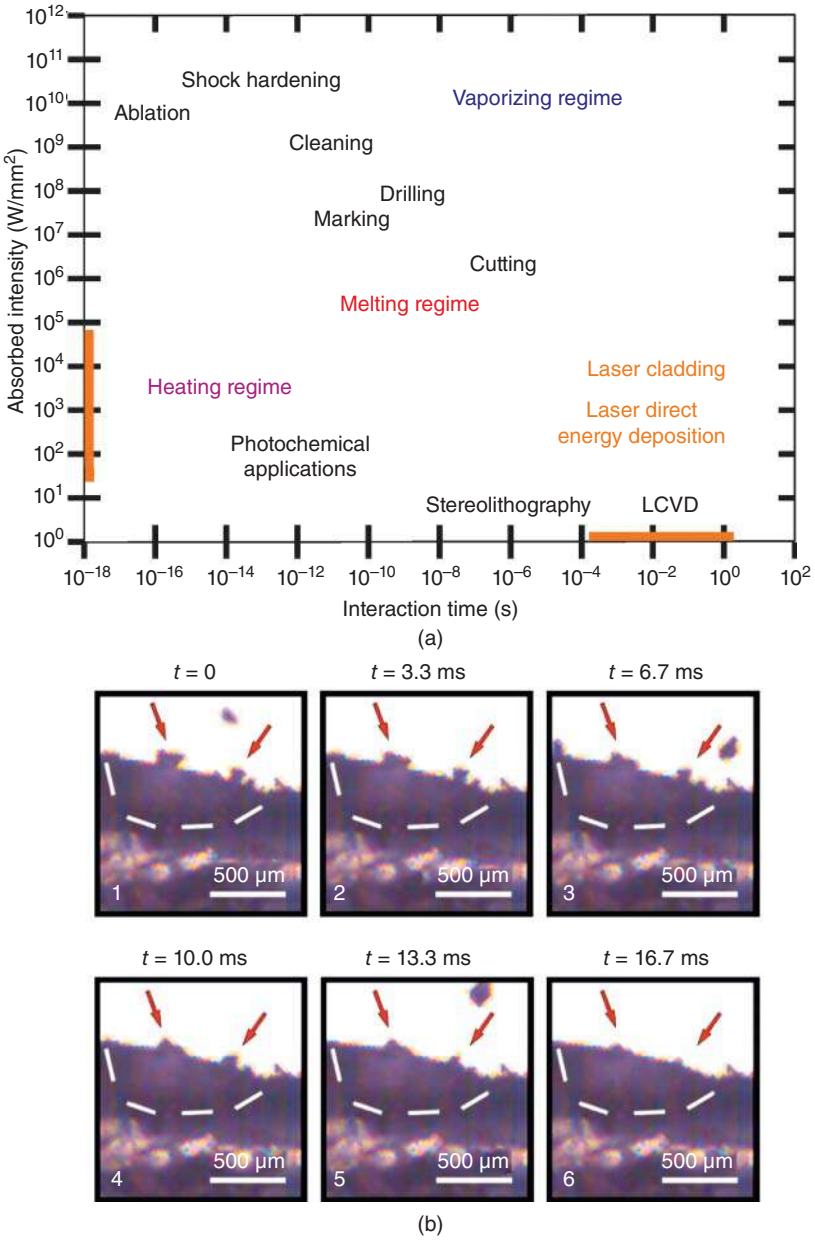

Figure 14.5 (a) Laser cladding and laser assisted processes as a function of the laser–material interaction time and irradiance. Source: Steen and Mazumder [3]. Reproduced with permission of Springer Nature. (b) High-speed video frames showing BG–laser interaction times in the order of tens of milliseconds to produce the incorporation of the particle to the molten pool. Source: Comesaña et al. [2], Figure 03 [p. 3479]/with permission from Elsevier.

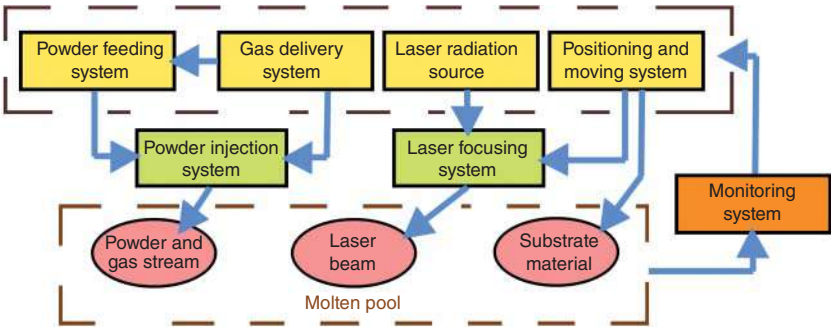

Figure 14.6 Diagram of subsystems of the working stations employed in laser cladding and in laser direct glass deposition.

locate very precisely the focusing and injection systems, and the relative displacement must be suitable for coating production by deposited material overlapping; or for additive part generation by deposited material overlying. In addition, the complex phenomena evolution during processing, such molten pool dynamics, dynamical environmental conditions, intensely urge the implementation of real-time monitoring and control systems. The specific properties of BGs and other bioceramic materials strongly determine the system requirements. Very specific solutions must be implemented and general purpose LC and LDED working stations are not always suitable for glass and ceramic processing.

14.1.4.1 Laser Energy Sources and Optical Guidance

In the field of laser materials processing, the group of most widespread laser sources include the CO_2 laser emitting at the fundamental wavelength of $\lambda = 10\,600$ nm (mid-infrared region of electromagnetic spectrum), and the Nd:YAG/Ytterbium-doped fiber lasers emitting at the fundamental wavelength of $\lambda = 1064/1070$ nm (near-infrared region of electromagnetic spectrum). Absorptivity of CO_2 laser by silicate glass is high; therefore, this laser source is an appropriate and versatile choice for LC coatings and LDGD three-dimensional processing. Low absorptivity of silicate glass in near infrared region prevents using a Nd:YAG/fiber laser as energy source in LDGD of BG. The reported value of silica absorptance at 1064 nm is as low as 0.04, in contrast to value 0.96 at 10 600 nm; but the 1064 nm wavelength shows analogous possibilities to CO_2 laser for some glass-ceramic combinations, such as CaP–BG combination processing [26]. In the use of 1064/1070 nm wavelength lasers for LC of BG, the substrate material plays the main role of laser energy absorption. The heat generated at the substrate transfers, by conduction predominantly, to the injected BG particles. On the contrary, in the LC process with 10 600 nm laser, both substrates surface and injected BG particles contribute to laser energy absorption. Therefore, feasible coating thicknesses and optimal processing conditions in LC of BG on metallic implant alloys are strongly reliant on the working station laser source.

In the LC and LDGD working stations, the laser source must be located at a certain distance due to integrity preservation and operational aspects. Thus, the laser beam must be guided from the laser source to the optical focusing system. The laser near-infrared wavelengths can be easily coupled to passive optical fibers at the laser source, and guided to the working station. The LC relative displacement between the laser working head and the substrate can be produced with a fixed working head, a fixed substrate, or intermediate solutions. Nevertheless, the CO_2 laser wavelength cannot be coupled to passive optical fibers, and must be guided using specific mirrors. In the case of this mid-infrared laser source, the working head displacement is usually limited to the laser beam

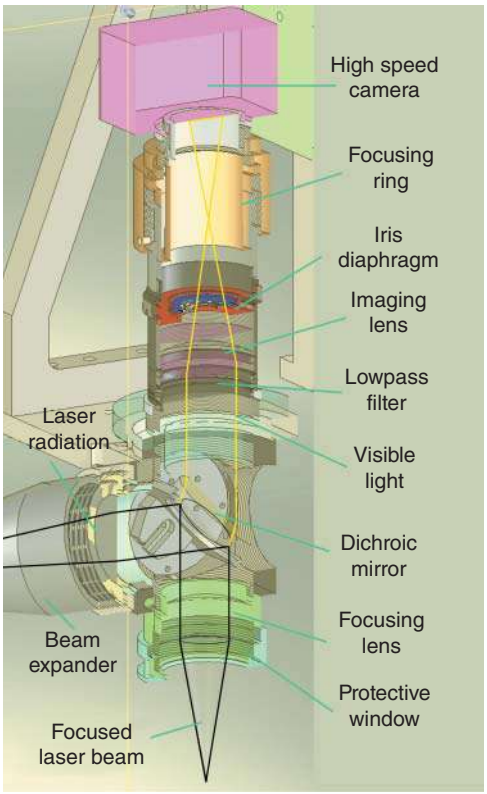

Figure 14.7 Laser cladding working heads can be equipped with molten pool temperature monitoring or coaxial image acquisition. The partial cut shows a focusing system equipped with a coaxial monitoring system in a laser cladding working head.

axis, although other options are available using adaptive optical system or with mobile CO_2 laser source configurations. At any case, the circular polarization of the laser beam is preferred to avoid directional heterogeneity during processing.

The optical systems to focus the laser beam on the laser–material area comprise of single optics or multi-lens systems, the common focal lengths are in the range 50–250 mm. Focusing systems employed in LC and LDGD processing accomplish the optical focusing function, but in addition allow the possibility of molten pool observation coaxially to the laser beam. An example of monitoring working head system is shown in Figure 14.7, where the laser radiation from a beam expander is reflected by a dichroic mirror. The dichroic mirror reflects only a narrow wavelength band centered in the near-infrared laser wavelength. Reflected laser radiation is focused by an achromatic cemented doublet; a flat protective window avoids damaging of the focusing optics by material projections from the processing zone. Visible light and near infrared radiation (except the band centered at the laser wavelength) emitted by the molten pool and surroundings is collected and nearly collimated by the laser focusing lens. Such radiation is transmitted through the dichroic mirror and is refracted by convergent imaging optics before reaching the camera sensor. With this observation system is also possible to perform temperature coaxial measurements, pyrometer specific optics are used and the imaging optics are substituted by corrective divergent optics.

14.1.4.2 Precursor Material Feeder and Powder Injectors

Precursor Material Feeder Powder feeders can rely on several operating principles. Widespread commercial systems are common to plasma spray coating technique and consist of a material particles vessel from which powder flows into a slot in a rotating disk. The material particles are fed to a

Table 14.1 Powder feed rate of different feeder configurations [2, 8, 11, 23, 27, 28].

	Powder feeder configuration		
Precursor material	**Rotating disk (mg/s)**	**Screw feeder (mg/s)**	**Piezoelectric microfeeder (mg/s)**
Bioactive glass	5–200	2–20	0.2–1.0
CaP hydroxyapatite	5–140	4–15	0.1–1.5

suction system from which it is conveyed by a gas stream to an injection nozzle. The volumetric powder feeding rate is governed by the slot dimensions of the disk rotation speed. High volumetric flows of carrier gas are required to obtain stable powder mass flows. This system is suitable to work with coaxial powder injection heads, especially at high laser power and elevated production regimes.

A different method for precursor material distribution is the employment of a pneumatic screw feeder. The powder is extracted from a vessel to the powder positive displacement pump and conveyed to the injection nozzle. The precursor material supply rate is determined by the rotational speed, and the screw dimensions, and presents a good stability regardless the carrier gas flow. An interesting property of this positive displacement system is the possibility of powder delivery without or with minimum carrier gas flow, which can be an advantage for ceramic materials processing or when off-axis powder injectors are used. Particle sizes suitable to rotating disk and screw feeders are roughly between 50 and 200 μm, depending on the precise particle morphology and material density. Other powder delivery systems were developed for more specific applications like nano-sized powder delivery for laser micro-cladding, where the aforementioned systems do not accomplish the required functions [27]. Table 14.1 provides useful feed rate ranges of different feeder configurations for glass and ceramic biomaterials.

The gas distribution system supplies the gas employed during processing. Although reactive gases can be used in bioceramic processing, argon gas is usually employed for LC and LDGD. Apart from auxiliary gases with optics cooling and protection functions, main gas flows involved in the process are the carrier gas and the assist gas. The carrier gas flow pneumatically transports the precursor material powder. Powder particles are dragged from the powder feeding system to the powder injection nozzle, and impinge directly to the molten pool. Inert gas must be used if oxidation reactions are not desired in the laser–material interaction area. Useful range of volumetric flow is preliminarily restricted by gravitational effects that take place at low flow values, while excessive mechanical effects into the molten pool penalize flow excessive values [7, 29, 30]. On the other side, the flow of assist gas, also called shield gas or protection gas, avoids or modifies chemical reactions during material laser irradiation. The initial function of this gas flow was to protect metallic alloys from oxidation in the area surrounding the molten pool. Volumetric flow values are limited by several secondary effects such as powder stream geometry modification or convection increase around processed material.

Transition between gravitational governed particle flow and the regime of gas dragging particle flow depends on the gas delivery system, the precursor powder system, and the powder injection system. Configurations including a screw feeder, in conjunction with an off-axis powder injector and properly selected processing parameters, can led to a minimum flow value around 1.5 l/min in normal conditions. Below the minimum flow limit, particle movement is defined by the particle–wall and gravitational interaction inside the feeding conducts. Parabolic powder stream

geometry and high sensitivity to acceleration are claimed weaknesses of gravitational feeding. Nevertheless, when protective gas is not required, processing without influence of carrier gas flow allows to reduce cooling rates. This benefit of gravitational feeding is of particular interest to reduce probability of ceramic material thermal shock.

Excessive values for the carrier gas or assist gas flows lead to shear stresses and distortion of the molten pool, resulting in deficient particle catchment from the powder stream. In LC of glass-ceramic coatings on metallic substrates, the argon assists gas flow around the laser–material interaction area, together with argon carrier gas flow, avoid rapid oxidation of substrate material. In addition to protective function, the assist gas stream can also be employed to modify the convection and related cooling rates in LDGD three-dimensional parts.

Powder Injection System Two different configurations of powder injection system are usually employed in LC and LDGD. One of them comprises of an off-axis injection nozzle (Figure 14.4a), while the other employs a nozzle placed coaxially with the laser beam (Figure 14.4b). In the off-axis injection system, or lateral injection system, the BG powder flows through the nozzle axis, is focused, and directed toward the laser–material interaction zone. If provided, the assist gas coaxially courses to the powder flow and enhances the stream focalization after the nozzle exit. The process is very sensitive to the position of the injection nozzle relative to the focusing system, and therefore relative to the laser beam spot. Therefore, the lateral injection LC and LDGD working heads are usually equipped with injector position and polar angle regulation.

The coaxial injection system is placed coaxially to the laser beam. The fluidized precursor powder arrives to LC working head peripherally from a multi-conduct homogenizer, flows through the conic coaxial conduct, and is injected toward a point located in the laser beam axis. The coaxial property between the powder stream and the laser beam is ensured by fabrication tolerances or *xy* regulation devices. The position of the injection point relative to the laser beam spot position is adjusted by axial displacement of the injection nozzle. Another coaxial conduct, located externally, is traversed by the assist gas flow. The coaxial injection systems are usually employed along with slotted disk feeders, as the effective flow cross section and flow rate capability are higher than those of the off-axis injection systems.

14.1.4.3 Moving Devices, Process Control, and Monitoring System

The moving devices and movement control play an important role in LC and LDGD processes. Motorized linear translation stages, CNC tables, or robotic arms are used to scan the laser–material interaction on the coated surface in LC or over the previous layer on additive LDGD. Although the precision of the paths is important, the speed stability and smoothness are key factor to obtain satisfactory results.

The thermal evolution experienced by the glass-ceramic during LC and LDGD processing depends on several factors such as processing speed, temperature of underlying material, precursor powder mass flow, or carrier and assist gas flows. An uncontrolled heterogeneous thermal cycle leads to undesired heterogeneous microstructure of the processed part and even failure due to thermal shock. Data acquisition in real time allows to study the phenomena occurred in the processed material, especially in the molten pool, and supply required information for process control. Thermal evolution of the molten pool can be monitored using pyrometer or camera coaxial observation as shown in Figure 14.7. In addition, molten pool behavior and thermal evolution of the deposited glass-ceramic can be measured following a lateral line of view (Figure 14.8). Laser power control is frequently implemented to keep a homogeneous molten pool temperature

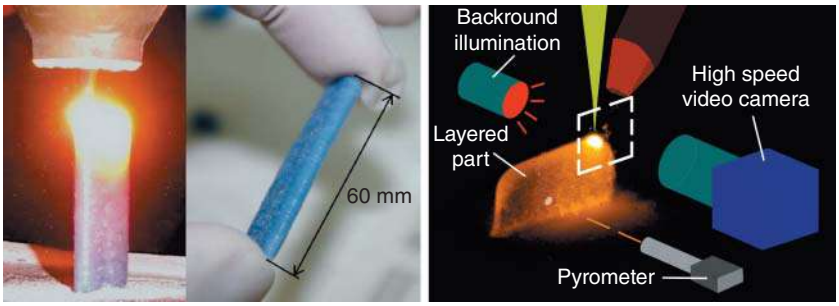

Figure 14.8 (a) Calcium phosphate glass-ceramic sample produced using a coaxial injection nozzle. Source: Comesaña et al. [25], Figure 4 [p. 33]/with permission from Elsevier. (b) Schematics of high-speed video and pyrometer lateral observation for molten pool and deposited BG. Source: Comesaña et al. [2], Figure 01 [p. 3477]/with permission from Elsevier.

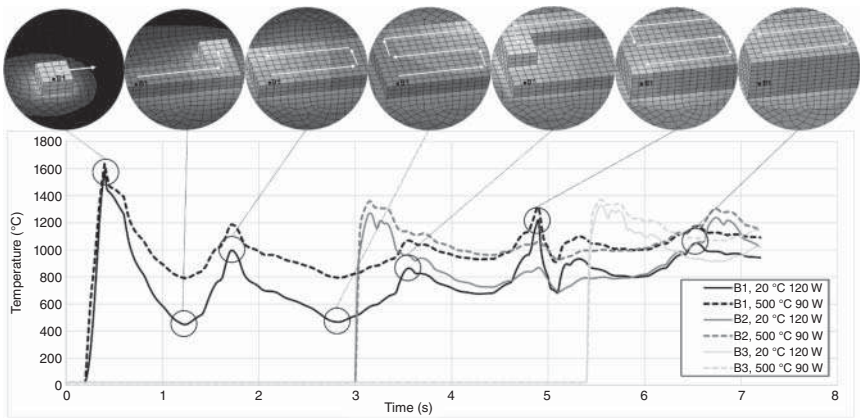

Figure 14.9 Temperature evolution of bioactive glass deposited on Ti6Al4V substrate. The numerical calculation was performed by finite element modeling of laser cladding with Nd:YAG laser irradiation at 90 and 120 W. Source: Krzyzanowski et al. [31]. Reproduced with permission of Elsevier.

or to correct the LDGD working head displacement during deposition of the initial layers of an additive manufacturing part. Krzyzanowski et al. showed the importance of substrate preheating and optimization of the working head scanning path when implementing LC of BG on Ti6Al4V. Figure 14.9 shows the temperature evolution of the deposited BG under an specific scanning path, the temperature prediction was performed by finite element modeling of the coating process with Nd:YAG laser irradiation [31].

14.2 Bioactive Glasses for Laser Cladding Processes

For a successful application of LC and LDGD to BG, the experimental system must comprise of determinate essential elements (Figure 14.6). As explained in Section 14.1.4, there are particular requirements for the powder feeding system, the laser radiation and positioning system. More of 90% of the commercially available laser sources do not fulfill these requirements, and, therefore, they are not suitable for LC and LDGD of BG. On the other side, an undefined feeding system

and precursor glass size combination can preclude the material injection, and a working head uneven movement can completely ruin the process outcome. The precursor BG composition and morphology are not an exception. The LC or LDGD with appropriate experimental system components can be a nightmare if inappropriate BG compositions or powder morphology are employed. Sections 14.2.1–14.2.3 present and discuss on the BG requirements for feasible application of these techniques.

14.2.1 Glass Working Range

The suitability of BGs is generally identified according their level of bioactivity [32]. The decreased network connectivity of silicate-based BGs, achieved by chemical modification, allowed to reach maximized osteoconductive and osteoinductive properties with high levels of resorbability. Nevertheless, when LC or LDGD processes are to be applied, other properties, such as rheological properties, have also to be considered. While cooling rates experienced by the material are still moderated, the conditions are quite different from glass casting, and nucleation and crystal growth can be produced. The BGs with high bioactivity are prone to phase-separation and devitrification due to the reduced network connectivity [33]. The crystallization makes more difficult the control of the deposited material part geometry due to abrupt viscosity–temperature relationship. Moreover, excessive crystallization deteriorates the mechanical properties of the obtained glass-ceramic parts. Thus, BG compositions with increased glass processing windows, i.e. higher temperature range between the glass softening point and the flow point, are employed in LC and LDGD processes. The glass bioactivity and the width of the processing window present opposite dependence on the silica network connectivity; therefore, the selected glass chemistry must provide a compromise between bioactivity and processing window. The Hruby *Hr* parameter has been proposed to quantify the processing window, this parameter relates the glass vitreous state stability with the crystallization tendency [34, 35]. Table 14.2 collects different BG compositions applied in LC and LDGD. Many of these alternative compositions to 45S5 BG were developed for fiber drawn processes and present a smooth viscosity–temperature evolution.

In the production of glass-ceramic coatings, the viscosity dependence on temperature determines the wetting angle on the metallic implant surface. It is observed a qualitative correlation between the BG-metal wetting angle evolution observed by hot stage microscopy and the wetting angle during LC processing. The wetting angle–temperature behavior of a BG powder pressed sample is analyzed at temperatures around the half ball formation. The BG compositions with smooth change of wetting angle with temperature are expected to behave better during LC processing.

Table 14.2 Composition (mol%) of bioactive glasses employed in laser cladding and laser direct glass deposition.

BG designation	SiO_2	CaO	Na_2O	P_2O_5	K_2O	B_2O_3	MgO	Al_2O_3	*Hr* [34]	References
45S5	46.1	26.9	24.4	2.6	—	—	—	—	0.28	[2, 28, 32, 36]
S520	52.0	18.0	20.9	2.0	7.1	—	—	—	0.39	[2, 24, 28, 36–38]
S50B2	50.0	35.0	7.0	6.0	—	2.0	—	—	0.37	[22, 23, 35]
1-98	53.0	22.0	6.0	2.0	11.0	1.0	—	—	0.48	[20, 21]
13-93	54.6	22.1	6.0	1.7	7.9	—	7.7	—	0.47	[33, 39]
S57A7 (inert interlayer)	57.0	30.0	6.0	—	—	—		7.0	0.55	[22, 23, 35]

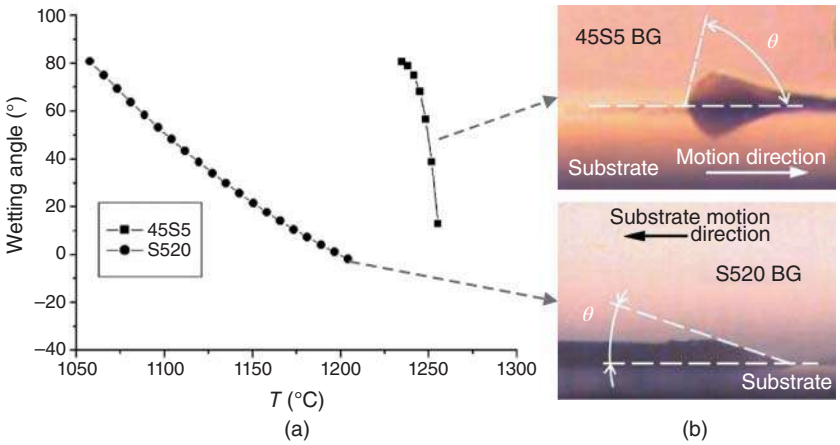

Figure 14.10 (a) Evolution of 45S5 BG and S520 BG wetting angle on Ti6Al4V alloy as a function of temperature measured by hot stage microscopy. (b) The high-speed video captions obtained during laser cladding processing shows enhanced molten pool wetting angles and homogeneity of deposited material. Source: Comesaña et al. [28], Figure 4 [p. 956]/with permission from Elsevier.

Figure 14.10a shows the wetting angle on Ti6Al4V alloy of two BGs with different glass processing windows. The S520 BG has a wide processing window and presents a gradual wetting angle decrease with temperature above the softening point. On the contrary, the 45S5 BG exhibits a narrow working window and a sharp wetting angle change at the flow point. Figure 14.10b shows the molten pool wetting angle during LC processing. High wetting angles and poor material deposition is produced with 45S5 BG powder, while good wettability of the melting pool and homogeneous deposition is produced with S520 BG powder. In addition, the ideal thermal expansion coefficient of the glass should be slightly lower than that of the metallic alloy. Thus, the glass-ceramic coating would be subjected to compressive stresses after cooling. This situation is difficult to attain due to the relatively high coefficient of thermal expansion of most of the BGs, several BG alternative compositions with lower coefficient of thermal expansion have been proposed [35, 40]. The S50B2 is a BG with a slightly narrower working window in comparison to S520 BG, but with a lower coefficient of thermal expansion due to the Na_2O and K_2O content and B_2O_3 addition [40]. This BG composition is very attractive for both metallic and ceramic coating production by LC.

14.2.2 Particle Size, Apparent Density, and Morphology

According the Geldart diagram, a precursor material in form of powder can be categorized as a function of fluidization behavior in ambient conditions [41]. In the specialized powder technology fields, the Geldart diagram classifies the material into different groups according to the difference between particle density and gas density and the particle size. For particle sizes below 20 μm and density differences around 3 g/cm^3 (values applicable to BG in powder form), the forces between the particles are comparable to the inertial forces. The precursor material particles cannot separate enough to be completely totally sustained by drag and buoyancy forces and, consequently it precludes the required fluidization [42]. Frequently, channels are produced by the gas throughout the material powder and only uneven conveying is reached (this situation corresponds to C region of Geldart diagram, see Figure 14.11). This kind of cohesive powder is not suitable for conventional powder feeders. Moreover, a stable gravity flow of this powder is practically impossible.

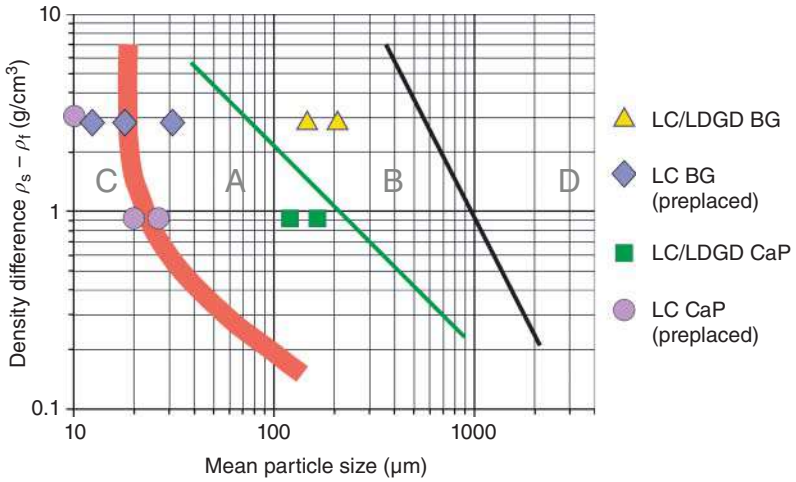

Figure 14.11 Geldart diagram for powder flow classification as a function of the particle size and density. Source: Adapted from Geldart [41].

In contrast, powders of higher particle size are classified by Geldart as aeratable, regions A, B, D in Figure 14.11. Therefore, a lower limit for particle size in precursor powder delivery with conventional feeders is established by interparticle forces. Precursor powder particle size has influence on several processing parameters, such as the LC layer width and thickness, the homogeneity of the produced microstructure, or the surface roughness. Gravity flow of powder is favored by increasing particle size. In addition to specifications of powder feeder, these features determine the upper limit of the particle size.

14.2.3 Preplaced BG Powder

As mentioned before, the precursor BG particles for LC with powder injection have to fulfill a number of requirements, particularly regarding to size distribution and working window. Specific BG powder preparation is frequently necessary, the available commercial BG powder do not fulfill the required size distribution for conventional powder feeding and injection systems. Powder preplacement can be applied as previous stage to laser irradiation. Thus, it is avoided the specific BG powder preparation and the integration of a powder system in the LC processing station. A BG particle size less than 45 μm, and much lower size, can be dissolved in liquid and dispersed on the substrate. BG emulsion preparation in ethanol or other organic solvents, and subsequent substrate dip-coating can be applied [28]. Nevertheless, this implementation of LC is limited to flat surfaces and does not allow selective modification of the coating composition. Moreover, the thin BG preplaced layer requires fine regulation of the laser irradiance to avoid coating contamination due to excessive substrate dilution. Kuo et al. coated Ti6Al4V substrates by spraying an emulsion of 45S5 BG in organic solvent. This preplaced layer was irradiated by a focused Nd:YAG laser, with optical power values between 400 and 800 W [43]. As a result, the coating lost the BG bioactivity due to Al migration from the substrate to the coating. Three key factors were responsible of such excessive substrate dilution: the thickness of the preplaced layer, the specific BG composition, and the laser energy density. Preplaced powder LC is only feasible with a thin preplaced layer, and the very low mass of BG per substrate surface cannot absorb much energy before melting. The 45S5 BG presents a narrow working window and requires a precise energy input for glass flow without overheating.

The operation range of high-power laser sources frequently lies above the 10% of the maximum output, what makes difficult the fine tuning of laser energy at low output, even at high processing speeds. As general rule to avoid excessive substrate dilution, high power laser sources can be only applied with elevated powder mass flows, such as in LC with coaxial BG injection.

14.3 Bioactive Glass and Glass-Ceramic Coatings by Laser Cladding

The LC of BG and glass-ceramic coatings is proposed as alternative to other coating methods proposed for metallic and ceramic bone prostheses. The conventional coating methods, such as enameling, plasma spray, or rapid immersion present problems related to porosity and cracks at the metal–glass interface [44]. The LC by powder injection can produce BG coatings (Figure 14.1a) with sound metal–glass interface. The obtained coatings show no significant substrate dilution and similar bioactivity to that of the precursor BGs [28]. The coating presents surface roughness *Ra* values in the range 5–16 μm. Such high roughness values are reported to enhance the cell adhesion and promote more rapid bone formation at the tissue-implant interfaces *in vivo* [45]. In addition, LC has been applied to produce BG coatings on ceramic acetabular cups by a multilayer strategy. The coatings show sound interface bonding and the behavior *in vitro*. Moreover, the coatings present intact BG apatite formation ability, and it is reported excellent biocompatibility in contact to mesenchymal stem and osteoblast-like cells [22, 23, 35].

14.3.1 Glass Structural Changes Induced by the Laser Cladding Process

The main structural changes produced in S520 BG coatings occur at the coatings surface. Devitrification in the coating surface has been observed by scanning electron microscope analysis (Figure 14.12). The degree of devitrification is dependent on the LC processing parameters, such as the laser beam power and the scanning speed. Surface of coatings obtained with high energy density values show dispersed crater-like features, see Figure 14.13a. This topography is attributed to crystals formation and associated shrinkage of the material. Nanometric sized bright crystals are found in the center and boundaries of crater-like features. The nanometric crystals present Na content as high as twice the precursor glass Na content, with an estimated composition close to $Na_4CaSi_3O_9$, or $N_2C_1S_3$ in simplified notation (see pseudo-binary diagram in Figure 14.14). The micro-Raman spectra show sodium calcium silicate characteristic spectrum at the center, along with vitreous material background signal (see Figure 14.13b). The silicate presence in the spectra increases from the boundary to the crater center.

On the contrary, Raman spectra from the zone surrounding the crater-like features are similar to this of S520 BG, without existence of crystalline phase characteristic peak. Presence of two different phases is suggested by scanning electron microscopy (SEM) micrographs of this zone, see Figure 14.13c. The elemental composition is similar to precursor BG composition, and the observed morphology and Raman spectra information suggest amorphous phase separation [47, 48].

The S520 BG coatings obtained at moderate and low laser energy density presents extensive surface crystallization (see Figure 14.12). Nevertheless, this fine silicate crystallite distribution reaches a limited penetration, and no detrimental effects are observed in the coating consistency or in the final bioactivity [25]. In such cases, elemental composition microanalysis of the aggregates, performed by energy dispersive X-ray spectroscopy, indicates a less Na increment, suggesting a composition close to stoichiometric $Na_2CaSi_2O_6$ or $N_1C_2S_2$. The Fourier transform infrared (FTIR) spectra of the coating surfaces reveal characteristic crystallization sharping of the bands corresponding to

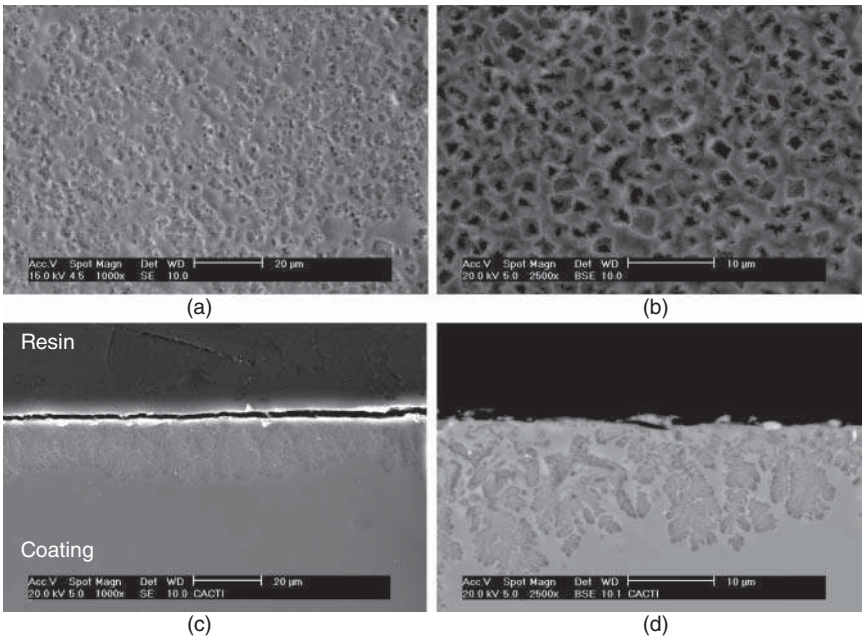

Figure 14.12 SEM micrographs of a S520 BG coating on Ti6Al4V alloy deposited by laser cladding. (a, b) Surface view. (c, d) Cross-sectional view. The BG coatings obtained at moderate and low laser energy density presents extensive surface crystallization. Source: Comesaña et al. [28], Figure 6 [p. 957]/with permission from Elsevier.

stretching vibration modes of Si–O and Si–O·2NBO (Si–O in SiO_4 groups with two non-bridging oxygen). The surface crystallization of the S520 BG coatings produced by LC is confirmed by X-ray diffraction (XRD), only sodium–calcium silicates are detected at surface [28]. This behavior is in agreement with BG reported crystallization. During crystallization of sodium calcium silicate, composition is continuously changing: crystals at very early stage of crystallization are sodium rich, deviates from parent glass composition, and only approach to the silicate stable phase at the end of crystallization [49]. Nucleated sodium rich crystallites are occasionally found on the brighter phase of amorphous phase separation zone. A higher phosphorous content of this domain agrees with reported separation in silica and phosphorous rich amorphous phases [48]. Phosphate-rich domains act as heterogeneous nucleation sites for crystallization, in addition to sharp boundaries of crater-like features.

Stoichiometric compound $Na_2CaSi_2O_6$ is not considered as a stable compound in the reported pseudo-binary diagram, but instead a solid solution of $Na_4CaSi_3O_9$ and $Na_2Ca_2Si_3O_9$. Crystalline phase derived from glasses with compositions similar to 45S5 BG is generally recognized as $Na_2Ca_2Si_3O_9$ [50, 51]. Nevertheless, some authors consider this phase as $Na_2CaSi_2O_6$, based on closer composition of the parent glass, the occurrence of almost fully crystallization and density variation [47, 48]. In short, although BG coating surface devitrification has been observed in any LC processing conditions, it can be stated that increasing the energy density leads to an earlier crystallization stage at coating surfaces.

The S50B2 BG coatings produced by LC are mainly amorphous, with minor occurrence of crystallization into $CaSiO_3$, as revealed by XRD and expected from the low Na_2O content [23]. The presence of wollastonite crystallites in the coating is not a concern as this ceramic phase

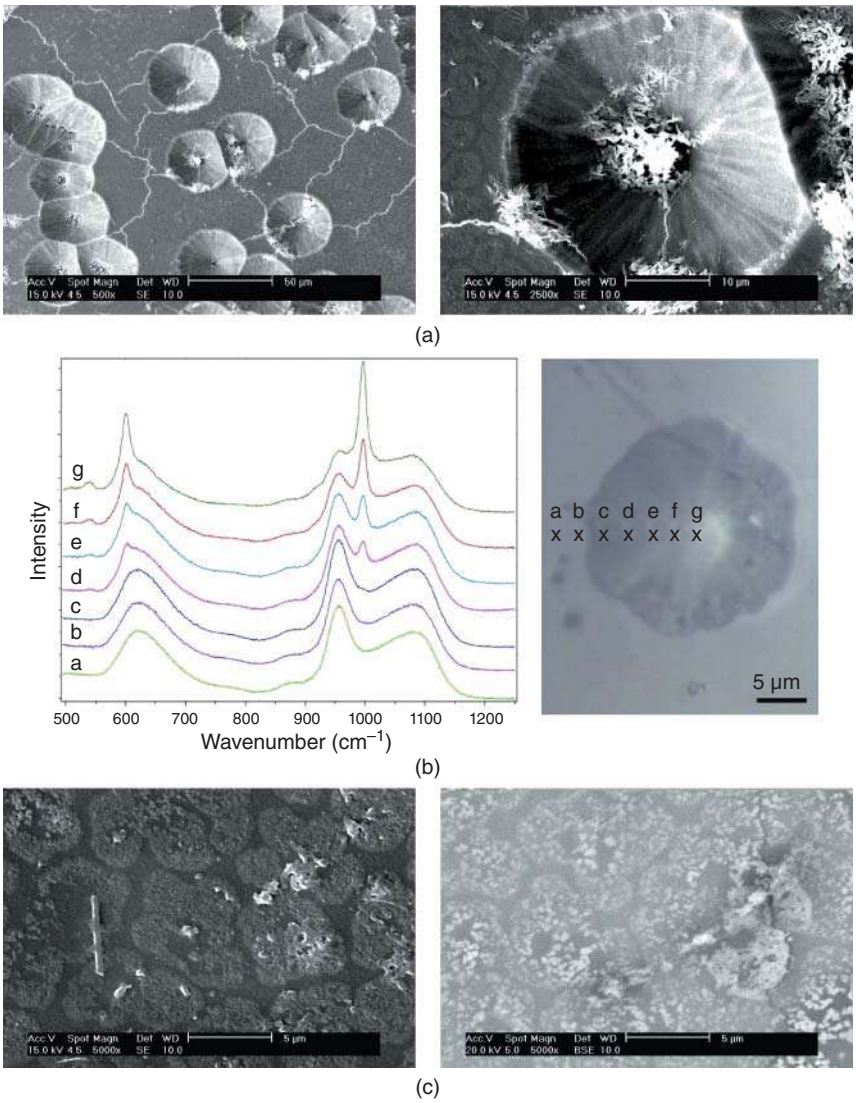

Figure 14.13 (a) Scanning electron micrograph of a S520 BG coating on Ti6Al4V alloy showing crater-like surface due to devitrification. The coating was deposited by laser cladding at elevated energy density values. (b) Micro-Raman spectra acquired from the border to the center of a crater produced due to crystallization. (c) Secondary electrons and backscattered electrons micrograph obtained from the crater surrounding areas.

is found in some biocompatible and BG-ceramic materials, it has been extensively investigated and reported as biocompatible, even single wollastonite bioceramic coatings have been proposed [52–54].

Regarding the coatings produced by LC with preplaced powder, Moritz et al. applied for first time the LC with preplaced powder for BG coatings on Ti substrate. The pure Ti surface was dip coated by a 1-98 BG glass suspension prepared in ethanol. These coatings are produced at comparatively low laser irradiances, therefore present micro-sized drop morphology and require several preplaced layers to produce a uniform coating. Nevertheless, the coating surface shows no

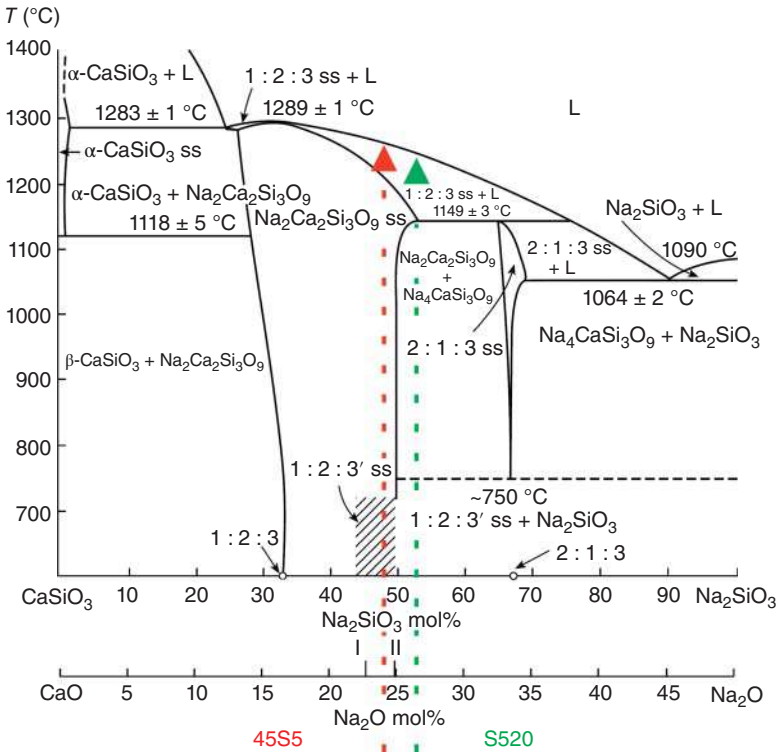

Figure 14.14 Phase diagram of the pseudo-binary section $CaO{\cdot}SiO_2$–$Na_2O{\cdot}SiO_2$ of the sodium calcium silicate system. Equivalent compositions of the S520 and 45S5 bioactive glasses are signaled by arrows. Source: Soboleva et al. [46]/Springer Nature.

evidence of surface crystallization and preserve the vitreous state of the precursor 1-98 BG [20, 21] (Table 14.3).

14.3.2 Substrate-Coating Bonding Mechanism

In the S520 BG coatings on Ti6Al4V, a TiP rich phase is formed at the glass–metal boundary, resulting in a continuous interface without voids or cracks. The titanium phosphide phase performs as adhesion enhancer at the interface. In addition to Ti incorporation from the metallic substrate to the BG coating, K content reduction is produced due to high temperature processing. In BG coatings produced by enameling, the high reactivity at the glass-implant interface is reported to produce excessive Si and P combination with Ti from the substrate, leading to liberation of oxygen and bubble formation [56]. In LC processing, the glass Marangoni flow in the molten pool helps to mitigate void formation due to trapped gas. Nevertheless, to prevent pore formation due this effect, reduced laser optical power and moderate scanning speeds are selected during BG coating production by LC.

Baino et al. demonstrated the feasibility of BG coating production by LC on ceramic acetabular cups for hip joint prosthesis. The coatings of BG on the Al_2O_3/ZrO_2 ceramic substrates are produced following a two-step LC procedure. An intermediate layer of S57A7 inert glass is deposited as previous stage to the S50B2 BG outer layer. The S57A7 glass layer works as bonding bridge between the BG coating and the substrate (see Figure 14.15a), with very promising results in terms of interfacial soundness.

Table 14.3 Laser wavelength, optical energy density, and structural changes in LC and LDGD of BG.

Coating precursor BG	BG particle size (μm)	Substrate	Laser wavelength (nm)	Laser energy density (J/mm^2)	Glass layer density (mg/mm^2)	Structural changes	References
45S5	100–250	Ti6Al4V	1 064	80	4.2	$Na_2Ca_2Si_3O_9$ volume crystallization	[2, 28, 38]
S520	100–250	Ti6Al4V	1 064	50	4.2	$Na_2Ca_2Si_3O_9$ and $Na_2CaSi_3O_8$ surface crystallization	[2, 28, 38]
S520	100–250	Ti6Al4V	1 064	83	3.3	Amorphous phase separation	[55]
S50B2	60–150	Al_2O_3/ZrO_2	10 600	35	4.2	Partial surface $CaSiO_3$ crystallization	[22, 23]
1-98 (preplaced)	<45	Ti	10 600	15	—	—	[21]
45S5 (preplaced)	<25	Ti6Al4V	1 070	2.0–4.0	0.11	Surface crystallization, excessive substrate dilution	[43]

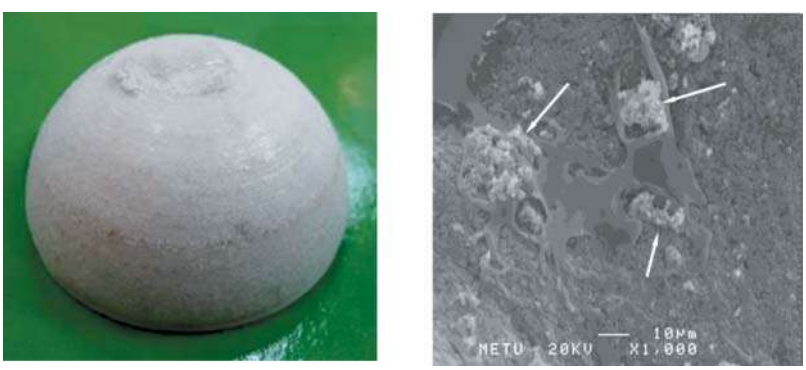

(a) (b)

Figure 14.15 (a) S57A7 glass interlayer coating by laser cladding on a ceramic acetabular cup. Source: Baino et al. [23], Figure 03 [p. 06]/with permission from Springer Nature. (b) SEM image of MSCs after 10 days of incubation on acetabular cup S50B2 BG coating. Source: Baino et al. [22], Figure 07 [p. 07]/MDPI/CC BY 4.0.

14.3.3 Bioactivity and Biocompatibility

The S520 BG coatings deposited by LC show comparable bioactivity to that of the precursor BG, see Figure 14.16. After one day of immersion in simulated body fluid (SBF), the characteristic silica rich layer is formed, as revealed by the Si–O·2NBO peaks absence from the surface FTIR spectrum.

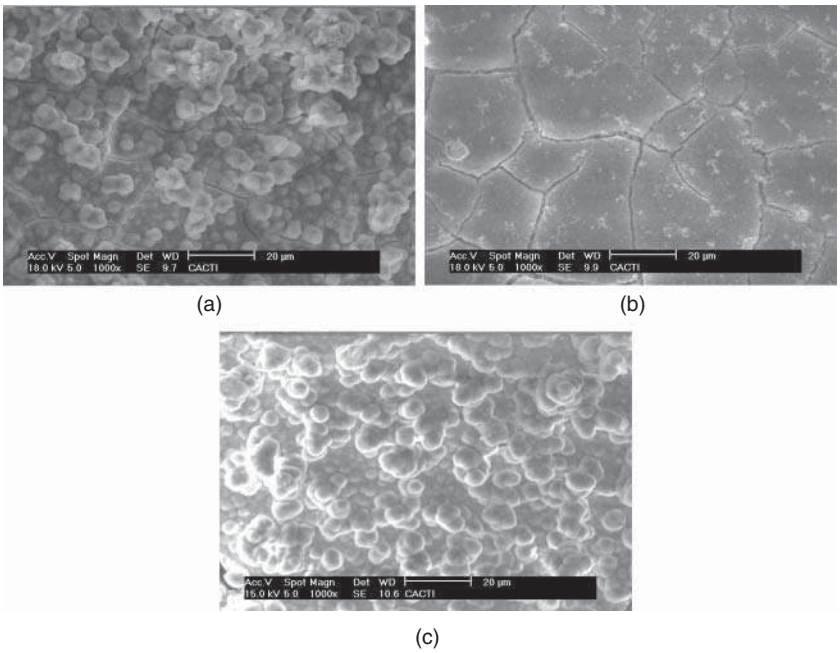

Figure 14.16 Scanning electron micrograph of the bioactive glass S520 coatings deposited by laser cladding after exposure in simulated body fluid: (a) two days exposure, (b) five days exposure, (c) nine days exposure. Source: Comesaña et al. [28], Figure 12 [p. 959]/with permission from Elsevier.

The apatite layer forms on the coating surface after two days of immersion SBF and has an average Ca/P ratio of 1.44 ± 0.1. By nine days of immersion, the biological-like carbonated apatite covers completely the coating surface.

The S50B2 BG coatings produced by LC on ceramic acetabular cups show good apatite formation ability *in vitro*, with characteristic average Ca/P ratios of calcium deficient apatite. Moreover, the biological testing with osteoblast-like cells and mesenchymal stem cells (MSCs) revealed a very good biocompatibility [22, 23]. Figure 14.15b shows flattened healthy morphology of MSCs, with numerous lamellipodia and filopodia, and presence of mineralized nodules.

The preplaced LC BG coatings developed by Moritz et al. show similar apatite forming ability in SBF than the precursor 1-98 BG [28]. These coatings on pure Ti cylindrical implants were *in vivo* tested in the femoral epicondyle of rabbits. The histological analysis after eight weeks shows that the 1-98 BG coated surfaces are covered by significantly more bone than bare metal and NaOH-treated Ti surfaces (see Figure 14.17). Moreover, the biomechanical tests reveal that the torsional load required to implant failure does not decrease due to BG coating [21].

14.4 Additive Manufacturing of Bioactive Glass by Laser Direct Deposition

In the well-known applications of additive manufacturing based on LC, LDED (according ISO/ASTM 52900 standard), metallic matrix materials are generally processed, the optical irradiance of the laser beam determines very precisely the spatial domain where the material is melted and deposited. The temperature field produced by a laser beam with Gaussian irradiance

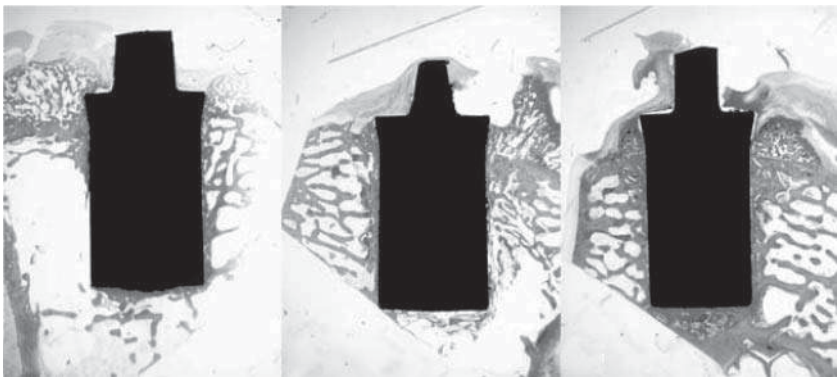

Figure 14.17 Histological slices of Ti implants after implantation in the femur of New Zealand white rabbit. (a) Bare Ti implant, (b) NaOH-treated implant, (c) implant coated by laser cladding with preplaced 1-98 bioactive glass. Source: Moritz et al. [20], Figure 8 [p. 800]/with permission from Springer Nature.

distribution, together with the well-defined melting point of metals, leads to a good control of the melting pool dimensions [4–6, 57]. Nevertheless, due to the rheological properties of glasses, in LDGD the geometrical properties of the deposited layers are also significantly dependent on other processing parameters such as glass powder mass flow, assist gas flow, or processing speed. The LDGD technique has been reported to produce minimum widths of approximately 1 mm and layer thickness down to 350 μm [38].

14.4.1 Influence of Processing Parameters in LDGD

When a layered three-dimensional part is produced by LDGD, the surface tension of the glass in the surroundings of the glass–laser interaction area is high and the layer exceeds the laser beam diameter dimensions. Moreover, the glass convection flow in the melting pool contributes to heat transmission outward the glass–laser interaction area. To increase the layer width, it requires higher laser irradiance. To increase the layer thickness, moderated laser irradiance is desired, as the increasing too much the melting pool temperature leads to glass side flow.

For a given laser irradiance and spot size, the glass deposition efficiency and consolidation are improved by setting the suitable powder injection rate. In LDGD, the total amount of injected glass particles can be incorporated to the molten pool, leading to glass deposition efficiencies up to the 100% when applying a high laser power to glass flow ratio. The layer cross section dimensions can be increased by injecting a higher amount of glass particles, keeping glass deposition efficiencies above 85%. Nevertheless, when the glass mass flow surpasses a certain threshold, the melting pool temperature decreases and the Marangoni flow is hindered, no more glass particles are molten and the single layer dimensions stop growing. In these conditions, similar layer cross-sectional area can be obtained over a wide range of glass flow, but the deposition efficiency dramatically deteriorates. Moreover, the glass particles experience low time–temperature conditions, toward the working range lower temperature, the particles only sinter, the aspect ratio (layer thickness to width ratio) increases, and full densification is not achieved.

14.4.2 Cooling Rates, Bioactive Glass Structural Changes, and Mechanical Properties

A key factor to produce sound glass and glass-ceramic part by LDGD is the control of the melting pool temperature and the glass cooling rate. The molten BG experiences exponential temperature decay from the melting point to the glass transition temperature, and the cooling rate is progressively reduced as the glass cools down. Cooling rates around nucleation and crystal growth temperatures determined by differential scanning calorimetry (DSC) determine the number and size of crystal aggregates. Cooling rates from 25 to 800 °C/min can be produced during additive fabrication of BG-derived LDGD parts. Fully glassy LDGD structures are formed by high cooling rates. Nevertheless, thermal shock at high cooling rate produces extensive cracking and the minimal required mechanical properties are not satisfied. On the other side, the occurrence of crystallization at low cooling rates can be a problem for layer dimension control and even for the part soundness, if the crystallization is extensive. As a result, the optimal cooling rate results from a compromise between mechanical integrity and crystallization. The assist gas flow, annular gas stream flowing coaxially to the BG injection stream, can change the heat convection around the processed part and allows to produce the desired deposited glass cooling rate.

Substrate preheating is frequently proposed in additive manufacturing to improve temperature related processes. When the substrate is preheated, better LDGD deposition efficiency is observed for low values of the combined parameter laser power/mass flow. Nevertheless, in optimized LDGD processing conditions, there is no clear evidence on the benefits of substrate preheating at temperatures below 250 °C. The influence of the substrate temperature is limited to the initial layers, due to the elevated glass temperature at the melting pool, the relative low glass thermal conductivity, and the use of insulating ceramic substrates. High temperature chambers or furnaces have been proposed to improve the cooling conditions of the whole BG part [58, 59].

Figure 14.18 shows the lateral surface and cross section of BG parts additively generated by LDGD. These optical and scanning electron micrographs correspond to LDGD processing conditions and BG compositions of the parts depicted in the Figure 14.1b. The parts produced by injection of 45S5 BG particles are extensively crystallized due to the reduced working range of this precursor BG. The crystallization of the surface is not a problem from the point of view of the material bioactivity as analyzed by immersion in SBF or Tris-HCl buffer. Moreover, the parts are non-cytotoxic in contact with pre-osteoblastic cells, and satisfactory results are observed in direct cell culture. Nevertheless, the feasibility of 45S5 BG processing decays as the LDGD part dimensions and geometrical complexity grows, and the narrow range or optimal cooling conditions are not satisfied in the whole part.

The additive generation of LDGD parts from BGs with enhanced working window has proven to be feasible over a wider range of processing conditions. The parts produced by injection of S520 BG particles, see Figure 14.18b–f, present only surface crystallization. The level of surface crystallization can be quantified from Raman spectra by comparison of the crystalline silicate characteristic band located at 988 cm^{-1} and the Si–O (NBO) stretching band at 944 cm^{-1}. A restrained surface crystallization is produced by keeping cooling rates above 200 °C/min. Volume crystallization in S520 BG parts produced by LDGD is inexistent and the X-ray diffractograms after pulverization are hardly distinguished from precursor BG powder [2].

The cooling rate of parts additively generated by LDGD below certain processing conditions can be too low to maintain the glassy nature of the precursor BGs. Crystal aggregate size and morphology of 45S5 BG LDGD devitrified samples are comparable to crystallization produced in bulk

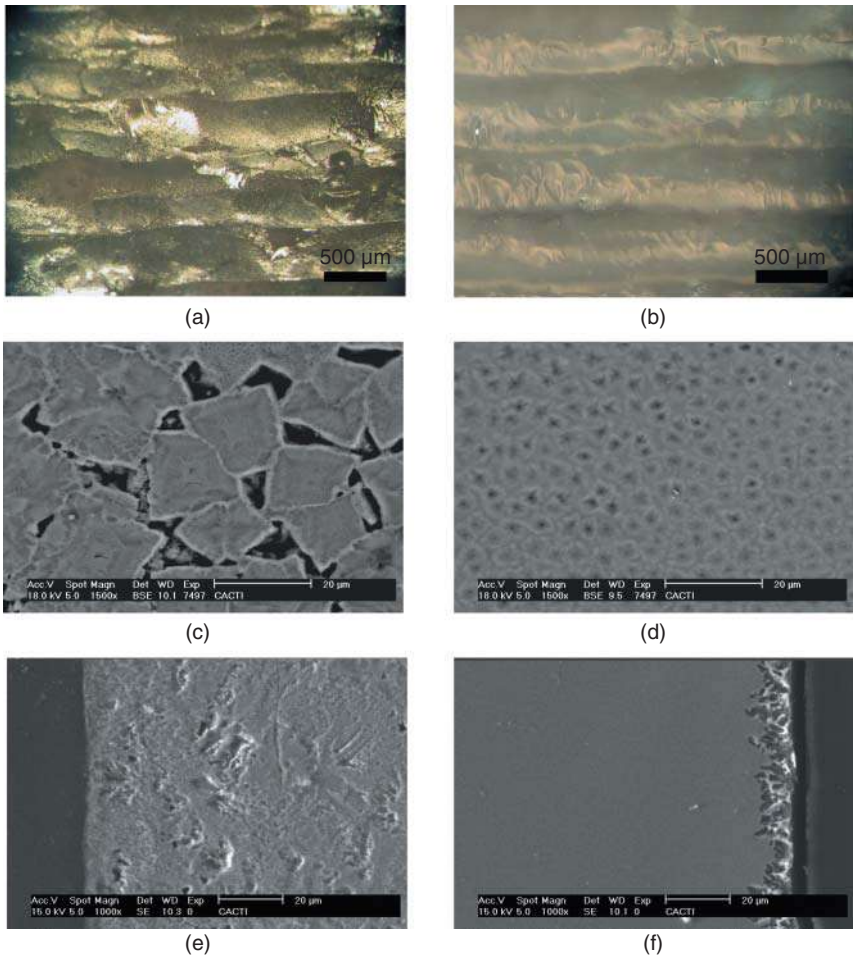

Figure 14.18 Surface and cross section of 3D bioactive glass parts produced by laser direct glass deposition from 45S5 BG (a, c, e) and S520 BG (b, d, f). Optical micrograph of the surface (a, b). SEM micrograph of the surface (c,d). SEM micrograph of the cross-section. Source: Comesaña et al. [2], Figure 06,09 [p. 3480,3482]/with permission from Elsevier.

45S5 glass after 30 minutes at 700 °C [47, 60]. As mentioned before, crystallization tendency or glass forming ability of a glass depends on nucleation rate and crystal growth rate. Thus, the glass viscosity at the temperature of maximum nucleation and maximum crystal growth, along with the thermal cycle, dominate the obtained crystal nucleation density and aggregate size [61, 62]. According to thermal analysis, reduced glass transition temperature calculated values for 45S5 and S520 precursor BGs are $T_{gr} = 0.55$ and 0.54, respectively ($T_{gr} = T_g/T_m$, T_m: melting temperature) [28]. Correlation developed by Fokin et al. [63] locates 45S5 BG and S520 BG respective temperature of maximum nucleation rate above the transition temperature and states that volume and surface crystallization is possible for both compositions. S520 BG LDGD parts present surface crystallization, while the unclear crystallite orientation at cross section suggests the combination of limited volume crystallization and intense surface crystallization in S45S5 BG LDGD parts.

Another factor used for crystallization tendency estimation is the already introduced Hruby coefficient, $Hr = (T_p - T_g)/(T_m - T_g)$. Calculated values $Hr = 0.28$ and $Hr = 0.39$ for 45S5 and S520,

respectively, indicate a lower crystallization tendency for the last one [34, 64]. Provided that similar temperature evolution is observed during LDGD processing, higher size of crystal aggregates suggests higher crystal growth rate in 45S5 BG derived parts. On the contrary, lower degree of crystallization along with higher nucleation density of S520 BG derived parts reflects crystal growth inhibition during processing. In order to correlate glass structure with crystallization tendency, nucleation rate dependence on similarity of the overall connectivity degree between the parent glass and nucleated crystal has been proposed [65]. Q^n species distribution (Q^n: silica tetrahedral containing n bridging Si—O—Si bonds) of 45S5 and S520 BGs are strongly dominated by Q^2 proportion, same species present in the structure of nucleated metasilicates. Distribution of Q^2 species calculated by Doweidar's method and corroborated by nuclear magnetic resonance (NMR) establishes a slightly higher density in 45S5 BG [65–67]. Hence, similar content of Q^2 species predict similar nucleation rates for both glasses. Presence of K_2O in S520 BG is related to inhibition of crystal growth during processing. Replacing Na_2O by K_2O is observed to decrease devitrification and increase the working range of glasses in the system Na_2O–K_2O–CaO–P_2O_5–SiO_2 [33].

The hardness and fracture toughness of the BG parts additively fabricated by LDGD is not significantly different from the hardness and fracture toughness observed for bulk precursor BGs. Figure 14.19 depicts the Weibull plot and the cumulative failure probability function for bulk 45S5 precursor BG and for S520 and 45S5 BG parts obtained by LDGD. The characteristic compressive strength for S520 BG parts produced by LDGD is about a 20% superior to the Weibull characteristic compressive strength shown by the 45S5 BG bulk reference. On the contrary, the extensive crystallization of 45S5 BG parts produced by LDGD lead to a 22% characteristic compressive strength reduction with respect to 45S5 bulk precursor BG, while still located in the upper values shown by cortical bone [32, 38].

14.4.3 Bioactivity and Biocompatibility

The bioactive properties of the BG parts produced by LDGD are similar to those of the precursor BGs. Analogous bioactivity to bulk BG is concluded from the unaltered behavior stated from different approaches: solubility in physiological solutions, apatite precipitation, non-cytotoxic behavior in contact to pre-osteoblastic cells, and cell morphology in LDGD BG parts direct cell seeding. The assessment of apatite precipitation in SBF of LDGD processed samples shows carbonated hydroxyapatite formation. Comparison with 45S5 BG bulk samples reveals only minor delay in calcium phosphate precipitation and allows to postulate that LDGD processed arts maintain the superior osteoconductive properties of precursor BG. This condition is valid even when considerable surface crystallization is produced.

The solubility of the BG parts generated by LDGD is similar to the precursor BG. When tested in Tris-HCl buffer solution, the Ca ion release profile of LDGD 45S5 BG parts up to 21 days do not present substantial differences from the 45S5 BG release profile, despite of the extensive crystallization shown by the additively manufactured parts. The reported Si and P ion release profiles of LDGD BG parts could suggest a slightly higher solubility than that of the precursor BG, in contrast to an expected solubility reduction due to surface crystallization. Nevertheless, if the apatite precipitation mechanism is carefully analyzed, it can be concluded that counterbalance between BG dissolution and layer precipitation explains the ion concentration differences.

Surface crystallization produces a slight delay in the silica layer precipitation that precedes calcium apatite precipitation, as already observed for BG coatings produced by LC. The delayed onsets of silica-rich and carbonated apatite layer precipitation produce less return of ions from the surrounding media, and can balance the lower solubility of silicate crystals. Between 2 and 10 days

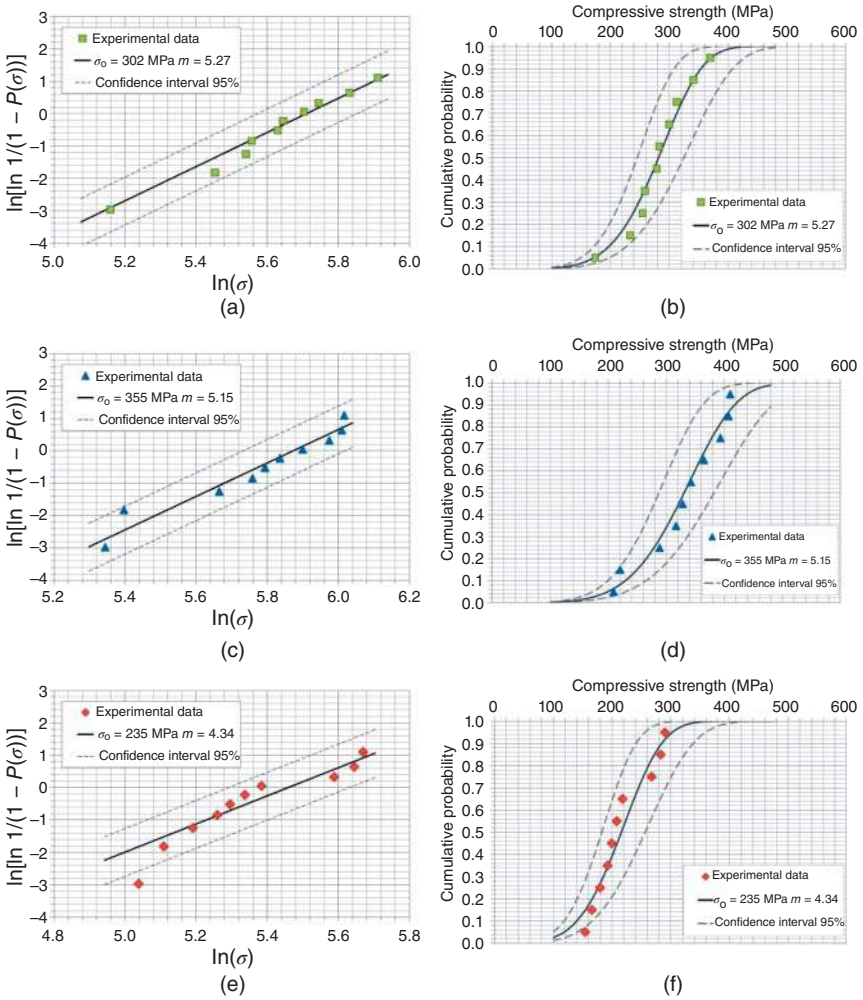

Figure 14.19 Compressive strength test: Weibull plot and cumulative failure probability plot for (a, b) 45S5 BG bulk control; (c, d) S520 BG LDGD; (e, f) 45S5 BG LDGD (realize different values in the horizontal axes of Weibull plots). Source: Del Vel et al. [38]. Reproduced with permission of Elsevier.

of immersion, LDGD 45S5 BG parts produce a higher Si and P concentration in Tris-HCl buffer than the 45S5 BG. These increased Si and P concentration is early observed in SBF, between 0.5 and 2 days, which is consistent with a faster apatite precipitation produced in SBF. Carbonate apatite layer covers the LDGD 45S5 BG parts after two days of immersion in SBF, while this time is decreased to one day for LDGD S520 BG parts. Figure 14.20 shows SEM micrographs of precipitated apatite after seven days of immersion in SBF. No differences are found between nanometric platelet apatite in LDGD glass and hot casted 45S5 BG.

The LDGD parts produced from 45S5 and S520 BGs present a non-cytotoxic behavior when non-direct contact tests are performed with pre-osteoblastic cell line MC3T3-E1. High cellular activity is reported by MTT quantification. The direct seeding cell culture on LDGD BG parts shows that pre-osteoblast attaches and spreads well, with abundant filopodia and healthy characteristic flattened morphology [2, 24]. Figure 14.21 shows quantified cell coverage, morphology, and

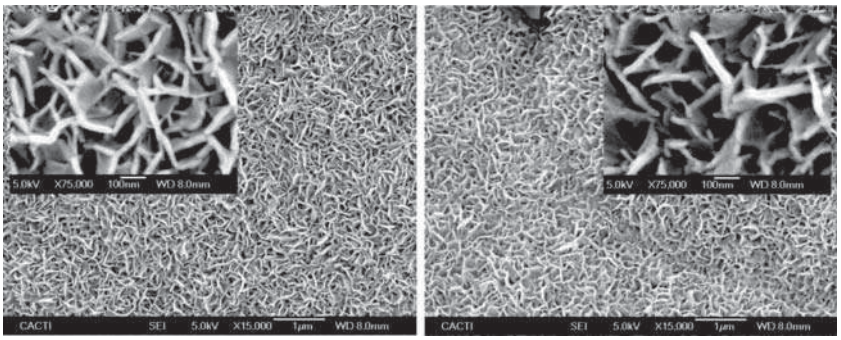

Figure 14.20 Precipitated apatite after seven days of immersion in simulated body fluid: (a) S520 BG part produced by laser direct glass deposition; (b) 45S5 BG produced by hot casting. Source: Del Vel et al. [38], Figure 9 [p. 13]/with permission from Elsevier.

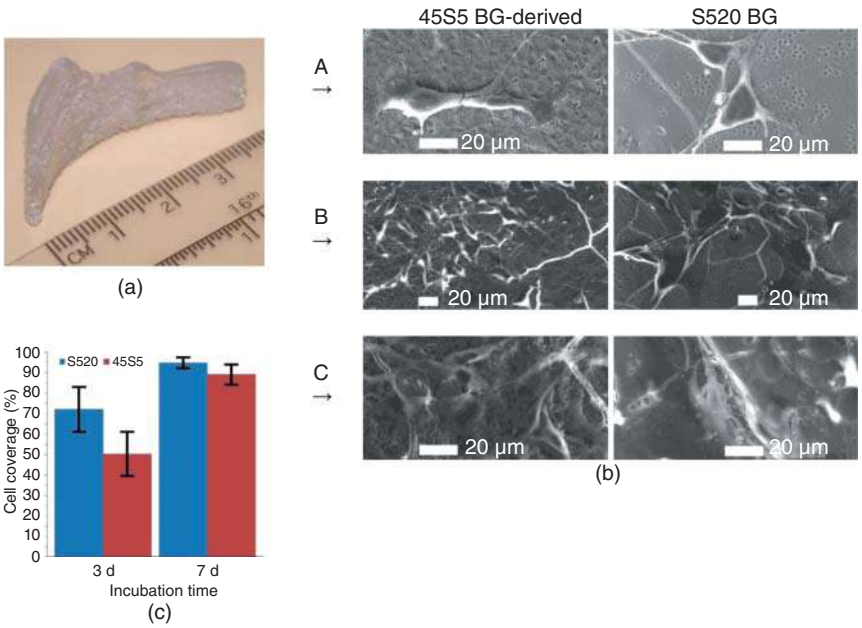

Figure 14.21 (a) S520 BG part produced by laser direct glass deposition from a three-dimensional CAD model of a left orbital rim implant. (b) SEM morphology and spreading of MC3T3-E1 cell line at one day, three days, and seven days on LDGD parts additively made from S520 and 45S5 BG. (c) Cell coverage of the sample surface after three and seven days of incubation time. Source: Comesaña et al. [24], Figure 6 [p. 06]/Springer Nature/CC BY 4.0.

spreading of MC3T3-E1 cell line on LDGD BG parts surface. The *in vitro* behavior of LDGD BG parts is very promising; however, no *in vivo* studies have been reported yet.

Recent reported applications of LDGD are directed toward additive smart implant synthesis. The LDGD technique has been applied to produce glass-ceramic parts with variable resorbability, with the purpose to match bone growth rates. Combination of LDGD CaP parts and LDGD BG parts allows to produce low-load-bearing bone repair parts with variable dissolution rates. These

BG-ceramic LDGD parts present tailor-made distribution with a low-resorbability multiphasic CaP nucleus and a high-resorbability BG external region [24].

14.5 Conclusions

LC is a feasible method to produce BG coatings on metallic alloy and ceramic substrates. The laser radiation must be precisely chosen to avoid BG contamination and preserve bioactivity. The processing of thermal coefficient expansion tailored BG compositions enhances the coating-substrate adhesion and opens the door to the application on a wide range of bioinert implant substrates. The LDGD is an additive manufacturing technique that can produce satisfactory three-dimensional additive parts if applied to BG compositions with enhanced working range. Processing parameters must be carefully selected to achieve suitable cooling rates, limited crystallization, and mechanically sound parts. Mechanical properties, dissolution rates, bioactivity, and osteoconductivity comparable to precursor BGs is concluded from reported behavior of the LDGD BG parts. Tailored dissolution rate parts can be produced by BG and CaP LDGD processing. These promising results appoint now to research on *in vivo* behavior and on gradual multi-material production challenges.

Acknowledgments

This work was partially supported by the EU research project Bluehuman (EAPA_151/2016 Interreg Atlantic Area), Government of Spain [RTI2018-095490-J-I00 (MCIU/AEI/FEDER, UE)], and by Xunta de Galicia (ED431C 2019/23, ED481D 2017/010, ED481B 2016/047-0). The technical staff from CACTI (University of Vigo) is gratefully acknowledged.

References

1 Lusquiños, F., Comesaña, R., and Quintero, F. et al. (2007). Bioceramic-glass coatings produced by laser cladding technique. *Proceedings of the International WLT-Conference on Lasers in Manufacturing*, Munich, Germany (18–22 June 2007). Stuttgart: AT-Verlag.

2 Comesaña, R., Lusquiños, F., Del Val, J. et al. (2011). Three-dimensional bioactive glass implants fabricated by rapid prototyping based on CO_2 laser cladding. *Acta Biomaterialia* 7 (9): 3476–3487. https://doi.org/10.1016/j.actbio.2011.05.023.

3 Steen, W.M. and Mazumder, J. (2010). Background to laser design and general applications. In: *Laser Material Processing*, 4th ed. (ed. W.M. Steen and J. Mazumder), 11–78. Springer.

4 Lusquiños, F., Comesaña, R., Riveiro, A. et al. (2009). Fibre laser micro-cladding of Co-based alloys on stainless steel. *Surface and Coatings Technology* 203 (14): 1933–1940. https://doi.org/10.1016/j.surfcoat.2009.01.020.

5 del Val, J., Comesaña, R., Lusquiños, F. et al. (2010). Laser cladding of Co-based superalloy coatings: comparative study between Nd:YAG laser and fibre laser. *Surface and Coatings Technology* 204 (12–13): 1957–1961. https://doi.org/10.1016/j.surfcoat.2009.11.036.

6 del Val, J., Comesaña, R., Riveiro, A. et al. (2018). Laser direct writing of Co-superalloy lines for micro-fabrication applications. *Surface and Coatings Technology* 345: 76–88. https://doi.org/10.1016/j.surfcoat.2018.03.089.

7 Weerasinghe, V.M. and Steen, W.M. (1983). Laser cladding with pneumatic powder delivery. In: *Proceedings of 4th International Conference on Lasers in Materials Processing* (ed. E.D. Metbowzer), 166–175. Metals Park, OH: ASM.

8 Lusquiños, F., Pou, J., Arias, J.L. et al. (2001). Production of calcium phosphate coatings on Ti6Al4V obtained by Nd:Yttrium-aluminum-garnet laser cladding. *Journal of Applied Physics* 90 (8): 4231–4236. https://doi.org/10.1063/1.1402975.

9 Lusquiños, F., De Carlos, A., Pou, J. et al. (2003). Calcium phosphate coatings obtained by Nd:YAG laser cladding: physicochemical and biologic properties. *Journal of Biomedical Materials Research Part A* 64 (4): 630–637. https://doi.org/10.1002/jbm.a.10440.

10 Lusquiños, F., Pou, J., Boutinguiza, M.Q. et al. (2005). Main characteristics of calcium phosphate coatings obtained by laser cladding. *Applied Surface Science* 247 (1–4): 486–492. https://doi.org/10.1016/j.apsusc.2005.01.134.

11 Roy, M., Vamsi Krishna, B., Bandyopadhyay, A. et al. (2008). Laser processing of bioactive tricalcium phosphate coating on titanium for load-bearing implants. *Acta Biomaterialia* 4 (2): 324–333. https://doi.org/10.1016/j.actbio.2007.09.008.

12 De Carlos, A., Lusquiños, F., Pou, J. et al. (2006). In vitro testing of Nd:YAG laser processed calcium phosphate coatings. *Journal of Materials Science – Materials in Medicine* 17 (11): 1153–1160. https://doi.org/10.1007/s10856-006-0543-6.

13 Pou, J., Lusquiños, F., Comesaña, R. et al. (2010). Production of biomaterial coatings by laser-assisted processes. In: *Advances in Laser Materials Processing: Technology, Research and Application* (ed. J. Pou, E. Toyserkani, J. Lawrence and D.K.Y. Low), 394–425. Woodhead Publishing.

14 Wang, Y., Li, Y., Yu, H. et al. (2005). In situ fabrication of bioceramic composite coatings by laser cladding. *Surface and Coatings Technology* 200 (7): 2080–2084. https://doi.org/10.1016/j.surfcoat.2005.07.076.

15 Kurella, A. and Dahotre, N.B. (2006). Laser induced hierarchical calcium phosphate structures. *Acta Biomaterialia* 2 (6): 677–683. https://doi.org/10.1016/j.actbio.2006.05.001.

16 Paital, S.R. and Dahotre, N.B. (2007). Laser surface treatment for porous and textured Ca–P bio-ceramic coating on Ti–6Al–4V. *Biomedical Materials* 2 (4): 274–281. https://doi.org/10.1088/1748-6041/2/4/011.

17 Kurella, A.K., Hu, M.Z., and Dahotre, N.B. (2008). Effect of microstructural evolution on wettability of laser coated calcium phosphate on titanium alloy. *Materials Science and Engineering C* 28 (8): 1560–1564. https://doi.org/10.1016/j.msec.2008.04.015.

18 Deng, C., Wang, Y., Zhang, Y. et al. (2007). In situ laser coating of calcium phosphate on TC4 surface for enhancing bioactivity. *Journal of Iron and Steel Research International* 14 (3): 74–79. https://doi.org/10.1016/S1006-706X(07)60047-8.

19 Zheng, M., Fan, D., Li, X. et al. (2008). Microstructure and osteoblast response of gradient bioceramic coating on titanium alloy fabricated by laser cladding. *Applied Surface Science* 255 (2): 426–428. https://doi.org/10.1016/j.apsusc.2008.06.078.

20 Moritz, N., Rossi, S., Vedel, E. et al. (2004). Implants coated with bioactive glass by CO_2-laser, an in vivo study. *Journal of Materials Science – Materials in Medicine* 15 (7): 795–802. https://doi.org/10.1023/B:JMSM.0000032820.50983.c1.

21 Moritz, N., Vedel, E., Ylänen, H. et al. (2004). Characterisation of bioactive glass coatings on titanium substrates produced using a CO_2 laser. *Journal of Materials Science – Materials in Medicine* 15 (7): 787–794. https://doi.org/10.1023/B:JMSM.0000032819.64994.42.

22 Baino, F., Minguella-Canela, J., Korkusuz, F. et al. (2019). In vitro assessment of bioactive glass coatings on alumina/zirconia composite implants for potential use in prosthetic applications. *International Journal of Molecular Sciences* 20: 722. https://doi.org/10.3390/ijms20030722.

23 Baino, F., Montealegre, M.A., Orlygsson, G. et al. (2017). Bioactive glass coatings fabricated by laser cladding on ceramic acetabular cups: a proof-of-concept study. *Journal of Materials Science* 52 (15): 9115–9128. https://doi.org/10.1007/s10853-017-0837-8.

24 Comesaña, R., Lusquiños, F., Del Val, J. et al. (2015). Toward smart implant synthesis: bonding bioceramics of different resorbability to match bone growth rates. *Scientific Reports* 5. https://doi.org/10.1038/srep10677.

25 Comesaña, R., Lusquiños, F., del Val, J. et al. (2011). Calcium phosphate grafts produced by rapid prototyping based on laser cladding. *Journal of the European Ceramic Society* 31 (1–2): 29–41. https://doi.org/10.1016/j.jeurceramsoc.2010.08.011.

26 Lu, L., Fuh, J., and Wong, Y.S. (2001). *Laser-Induced Materials and Processes for Rapid Prototyping*. Kluwer Academic.

27 del Val, J. (2008). Development of an automatic biphasic flow feeding system for nanometric particles in dilute phase. Master thesis. University of Vigo.

28 Comesaña, R., Quintero, F., Lusquiños, F. et al. (2010). Laser cladding of bioactive glass coatings. *Acta Biomaterialia* 6 (3): 953–961. https://doi.org/10.1016/j.actbio.2009.08.010.

29 Shuja, S.Z., Yuhas, B.S., and Budair, M.O. (1998). Modeling of laser heating of solid substance including assisting gas impingement. *Numerical Heat Transfer Part A: Applications* 33 (3): 315–339. https://doi.org/10.1080/10407789808913941.

30 Lusquiños, F. (2000). Biocompatible material processing with high power lasers. PhD thesis. University of Vigo.

31 Krzyzanowski, M., Bajda, S., Liu, Y. et al. (2016). 3D analysis of thermal and stress evolution during laser cladding of bioactive glass coatings. *Journal of the Mechanical Behavior of Biomedical Materials* 59: 404–417. https://doi.org/10.1016/j.jmbbm.2016.02.023.

32 Hench, L.L. (1998). Bioceramics. *Journal of the American Ceramic Society* 81 (7): 1705–1728.

33 Brink, M. (1997). The influence of alkali and alkaline earths on the working range for bioactive glasses. *Journal of Biomedical Materials Research* 36 (1): 109–117. https://doi.org/10.1002/(SICI)1097-4636(199707)36:1<109::AID-JBM13>3.0.CO;2-D.

34 Hruby, A. (1972). Evaluation of glass-forming tendency by means of DTA. *Czechoslovak Journal of Physics* 22: 1187–1193.

35 Baino, F., Marshall, M., Kirk, N. et al. (2016). Design, selection and characterization of novel glasses and glass-ceramics for use in prosthetic applications. *Ceramics International* 42 (1): 1482–1491. https://doi.org/10.1016/j.ceramint.2015.09.094.

36 Clapp, P.I. (2001). Development and testing of bioactive glass fibers drawn of minimally bioactive compositions using a continuous draw process. Master thesis. Alfred University.

37 Clupper, D.C., Gough, J.E., Hall, M.M. et al. (2003). In vitro bioactivity of S520 glass fibers and initial assessment of osteoblast attachment. *Journal of Biomedical Materials Research Part A* 67 (1): 285–294. https://doi.org/10.1002/jbm.a.10040.

38 Del Val, J., López-Cancelos, R., Riveiro, A. et al. (2016). On the fabrication of bioactive glass implants for bone regeneration by laser assisted rapid prototyping based on laser cladding. *Ceramics International* 42 (1): 2021–2035. https://doi.org/10.1016/j.ceramint.2015.10.009.

39 Fagerlund, S., Massera, J., Hupa, M. et al. (2012). T-T-T behaviour of bioactive glasses 1-98 and 13-93. *Journal of the European Ceramic Society* 32 (11): 2731–2738. https://doi.org/10.1016/j.jeurceramsoc.2011.10.040.

40 Bellucci, D., Cannillo, V., and Sola, A. (2011). Coefficient of thermal expansion of bioactive glasses: available literature data and analytical equation estimates. *Ceramics International* 37 (8): 2963–2972. https://doi.org/10.1016/j.ceramint.2011.05.048.

41 Geldart, D. (1973). Types of gas fluidization. *Powder Technology* 7 (5): 285–292. https://doi.org/10.1016/0032-5910(73)80037-3.

42 Klinzing, G.E., Marcus, R.D., Rizk, F. et al. (1997). *Pneumatic Conveying of Solids*. India: Chapman & Hall.

43 Kuo, P., Joshi, S.S., Lu, X. et al. (2019). Laser coating of bioactive glasses on bioimplant titanium alloys. *International Journal of Applied Glass Science* 10 (3): 307–320. https://doi.org/10.1111/ijag.12642.

44 Kitsugi, T., Nakamura, T., Oka, M. et al. (1996). Bone-bonding behavior of plasma-sprayed coatings of Bioglass®, AW-glass ceramic, and tricalcium phosphate on titanium alloy. *Journal of Biomedical Materials Research* 30 (2): 261–269. https://doi.org/10.1002/(SICI)1097-4636(199602)30:2<261::AID-JBM17>3.0.CO;2-P.

45 Gough, J.E., Notingher, I., and Hench, L.L. (2004). Osteoblast attachment and mineralized nodule formation on rough and smooth 45S5 bioactive glass monoliths. *Journal of Biomedical Materials Research Part A* 68 (4): 640–650. https://doi.org/10.1002/jbm.a.20075.

46 Soboleva, E.N., Yuritsyn, N.S., and Ugolkov, V.L. (2004, 2004). Kinetics of crystal nucleation of $Na_2O{\cdot}2CaO{\cdot}3SiO_2$-based solid solutions in glasses of the Na_2SiO_3–$CaSiO_3$ pseudobinary join. *Glass Physics and Chemistry* 30 (6): 481–486.

47 Huang, L., Lin, C., and Shen, P. (2007). Crystallization and stoichiometry of crystals in $Na_2CaSi_2O_6$–P_2O_5 based bioactive glasses. *Materials Science and Engineering A* 452–453: 326–333. https://doi.org/10.1016/j.msea.2006.10.136.

48 Lefebvre, L., Gremillard, L., Chevalier, J. et al. (2008). Sintering behaviour of 45S5 bioactive glass. *Acta Biomaterialia* 4 (6): 1894–1903. https://doi.org/10.1016/j.actbio.2008.05.019.

49 Fokin, V.M. and Zanotto, E.D. (2007). Continuous compositional changes of crystal and liquid during crystallization of a sodium calcium silicate glass. *Journal of Non-Crystalline Solids* 353 (24–25): 2459–2468. https://doi.org/10.1016/j.jnoncrysol.2007.04.014.

50 Filho, O.P., Latorre, G.P., and Hench, L.L. (1996). Effect of crystallization on apatite-layer formation of bioactive glass 45S5. *Journal of Biomedical Materials Research* 30 (4): 509–514. https://doi.org/10.1002/(SICI)1097-4636(199604)30:4<509::AID-JBM9>3.0.CO;2-T.

51 Peitl, O., Dutra Zanotto, E., and Hench, L.L. (2001). Highly bioactive P_2O_5–Na_2O–CaO–SiO_2 glass-ceramics. *Journal of Non-Crystalline Solids* 292 (1–3): 115–126. https://doi.org/10.1016/S0022-3093(01)00822-5.

52 Kokubo, T. (1991). Bioactive glass ceramics: properties and applications. *Biomaterials* 12 (2): 155–163. https://doi.org/10.1016/0142-9612(91)90194-F.

53 Wang, C., Lin, K., Chang, J. et al. (2013). Osteogenesis and angiogenesis induced by porous β-$CaSiO_3$/PDLGA composite scaffold via activation of AMPK/ERK1/2 and PI3K/Akt pathways. *Biomaterials* 34 (1): 64–77. https://doi.org/10.1016/j.biomaterials.2012.09.021.

54 Li, H., Wang, D., Chen, C. et al. (2015). Preparation and characterization of laser cladding wollastonite derived bioceramic coating on titanium alloy. *Biointerphases* 10 (3): 1–11. https://doi.org/10.1116/1.4929415.

55 Comesaña, R. (2010). Application of rapid prototyping based on laser cladding to the production of bone functional implants. PhD thesis. University of Vigo.

56 Gomez-Vega, J.M., Saiz, E., and Tomsia, A.P. (1999). Glass-based coatings for titanium implant alloys. *Journal of Biomedical Materials Research* 46 (4): 549–559. https://doi.org/10.1002/(SICI)1097-4636(19990915)46:4<549::AID-JBM13>3.0.CO;2-M.

57 Xue, L. and Islam, M.U. (2000). Free-form laser consolidation for producing metallurgically sound and functional components. *Journal of Laser Applications* 12 (4): 160–165. https://doi.org/10.2351/1.521927.

58 Comesaña, Lusquiños, F, Pou, J, et al. (2012). Method and apparatus form rapid prototyping of ceramic and glass functional parts. ES Patent 2368079, filed 24 October 2009 and issued 10 September 2012.

59 Díaz, P. (2020). Design of an additive manufacturing station for glass-ceramic materials. Master thesis. University of Vigo.

60 Arstila, H., Hupa, L., Karlsson, K.H. et al. (2008). Influence of heat treatment on crystallization of bioactive glasses. *Journal of Non-Crystalline Solids* 354 (2–9): 722–728. https://doi.org/10.1016/j.jnoncrysol.2007.06.092.

61 Kingery, W.D., Bowen, H.K., and Uhlmann, D.R. (ed.) (1976). *Introduction to Ceramics*. New York: Wiley-Interscience.

62 Scholze, H. (1991). *Glass: Nature, Structure and Properties*. New York: Springer-Verlag.

63 Fokin, V.M., Zanotto, E.D., and Schmelzer, J.W.P. (2003). Homogeneous nucleation versus glass transition temperature of silicate glasses. *Journal of Non-Crystalline Solids* 321 (1–2): 52–65. https://doi.org/10.1016/S0022-3093(03)00089-9.

64 Bretcanu, O., Chatzistavrou, X., Paraskevopoulos, K. et al. (2009). Sintering and crystallisation of 45S5 Bioglass® powder. *Journal of the European Ceramic Society* 29 (16): 3299–3306. https://doi.org/10.1016/j.jeurceramsoc.2009.06.035.

65 Schneider, J., Mastelaro, V.R., Panepucci, H. et al. (2000). ^{29}Si MAS-NMR studies of Q^n structural units in metasilicate glasses and their nucleating ability. *Journal of Non-Crystalline Solids* 273 (1–3): 8–18. https://doi.org/10.1016/S0022-3093(00)00139-3.

66 Doweidar, H. (1999). Density-structure correlations in silicate glasses. *Journal of Non-Crystalline Solids* 249 (2–3): 194–200. https://doi.org/10.1016/S0022-3093(99)00310-5.

67 Elgayar, I., Aliev, A.E., Boccaccini, A.R. et al. (2005). Structural analysis of bioactive glasses. *Journal of Non-Crystalline Solids* 351 (2): 173–183. https://doi.org/10.1016/j.jnoncrysol.2004.07.067.

15

Laser-Assisted Processing of $CaSiO_3$–$Ca_3(PO_4)_2$ Bioactive Eutectic Glasses and Glass-Ceramics for Functional Applications

Daniel J. Sola

Laboratorio de Óptica, Centro de Investigación en Óptica y Nanofísica (CIOyN), Campus Espinardo, Universidad de Murcia, Murcia, Spain
Aragonese Foundation for Research and Development (ARAID), Government of Aragon, Zaragoza, Spain

15.1 Introduction: Bioactive Glasses and Glass-Ceramics

Bioactive glasses and glass-ceramics are attractive materials to be employed in tissue engineering, as scaffolds in bone regeneration, for orthopedic and dental applications, and for *in situ* drug delivery [1–3]. Their utilization in biomedical applications has been a field of intense research since the discovery of the first bioactive glass, Bioglass®, by Hench et al. in 1969 [4] which belonged to the SiO_2–Na_2O–CaO–P_2O_5 system. Basically, a bioactive material is a material which undergoes a two-stage process when implanted in the living body or immersed in simulated body fluid (SBF). Firstly, the material undertakes specific surface reactions, giving rise, in the second stage, to a hydroxyapatite (HA)-like layer, which interacts with hard and soft tissues [5, 6]. The formation of this HA layer in an *in vitro* assessment, soaking the material into SBF, is mandatory prior to *in vivo* evaluation of the biological activity [6–8].

Concerning bone tissue engineering applications, materials with similar characteristics to the natural bone mineral phase are preferred, mainly bioceramics based on calcium phosphate ceramics [9–11]. For instance, biphasic calcium phosphate, BCP, β-tricalcium phosphate (TCP), $Ca_3(PO_4)_2$, and HA, $Ca_{10}(PO_4)_6(OH)_2$. It is worthy of highlight that an essential characteristic of bioactive glasses is that enhances osteoblast adhesion, revascularization, enzyme activity, and differentiation of mesenchymal stem cells [12–14].

Bioglasses design must consider an appropriate structural compatibility without inducing harmful impact on the living tissue [15]. Their properties are very versatile and can be conceived according to their initial composition and the processing conditions [6, 12, 13]. This design must also ponder the risk of toxicity in order to maintain the release of elements below the biological safe limits, hence providing negligible cytotoxicity. The fabrication of a glass is based on the rapid cooling of the departing molten composites avoiding crystallization to obtain a solid with an amorphous structure. The ability to glass formation depends on both glass transition and liquidus temperature, which are related to the melt composition, and the cooling rate. This rate must be high enough to avoid nucleation and crystal growth processes [3]. According to Lu and Liu [16], it is possible to estimate the minimum cooling rate by using the dimensionless parameter $\gamma = T_x/(T_g + T_l)$ as

Bioactive Glasses and Glass-Ceramics: Fundamentals and Applications, First Edition.
Edited by Francesco Baino and Saeid Kargozar.

Figure 15.1 Image of a Europium-doped $CaSiO_3$–$Ca_3(PO_4)_2$ bioactive eutectic glass manufactured by the casting technique.

an indicator of the glass-forming ability of the system, with T_x the crystallization temperature, T_g the glass transition temperature, and T_l the melting temperature. The relationship between this parameter and the critical cooling rate (R_c) for glass formation is, approximately, given by the following expression:

$$R_c = R_0 \exp[(-\ln R_0)\gamma/\gamma_0] \tag{15.1}$$

where the constants R_0 and γ_0 are, for inorganic glasses, 8×10^{27} K/s and 0.421, respectively [16]. The fabrication method limits, to some extent, the cooling rate. Among the techniques usually utilized to fabricate glasses worth mentioning are by casting, sol–gel, and directional solidification. As an example, Figure 15.1 shows an image of a Europium doped $CaSiO_3$–$Ca_3(PO_4)_2$ eutectic glass manufactured by the casting technique.

Glass-ceramics are materials obtained through the controlled nucleation and crystallization of a glass by means of thermal processes. These processes convert an amorphous material in a crystalline ceramic with fine grains, randomly oriented, without microcracks or voids, in which a broad variety of special microstructures can be developed [17]. In most cases, it is required a nucleating agent to induce the nucleation process. The control of the crystal growth by means of time and temperature, as processing variables, results generally in various types of crystals phases instead of only one. Glass-ceramics present major thermal, mechanical, and chemical properties compared to its parent glass. Nevertheless, the crystallization process affects the bioactivity, resulting in a decrease of the level of bioactivity [18, 19]. In addition to biocompatibility and the formation of a HA layer, it is needed for the bioglass/glass-ceramic to hold suitable mechanical properties, interconnected and three-dimensional porous structure to support vascularization, diffusion of nutrients and cell proliferation, and not to display any inflammatory response or cytotoxicity.

A novel approach to develop an *in situ* porous HA-like structure in a dense bioactive ceramic when implanted into a living body was proposed by de Aza et al. [20]. This material is constituted by two phases, $CaSiO_3$ (wollastonite, W), which is bioactive with osteostimulative properties,

Table 15.1 Calculated and measured eutectic composition and temperature in the $CaSiO_3$–$Ca_3(PO_4)_2$ system.

A	B	T^m_A (K)	T^m_B (K)	H^m_A (J/mol)	H^m_B (J/mol)	Calculated/ measured eutectic X_A–X_B (mol%)	Calculated/ measured T_{eut} (K)
$CaSiO_3$	$Ca_3(PO_4)_2$	1821	1943	36.844	156.057	80.25–20.61/80–20	1670/1675

and $Ca_3(PO_4)_2$ (TCP), which is osteoconductive and resorbable. This binary system presents an invariant point, a eutectic point, at 1402 °C with a composition of 80 mol% W and 20 mol% TCP. The estimation of the eutectic composition can be determined from the values of the melting temperature and the heat of fusion of the components according to the following expressions [21]:

$$RT \ln X^l_i = -\Delta H^m_i \left(1 - \frac{T}{T^m_i}\right) \quad i = 1,2,3,\ldots,k \tag{15.2}$$

$$\sum_{i=1}^{k} X^l_i = 1 \tag{15.3}$$

where X^l_i is the mole fraction of component i in the liquid, and T^m_i and H^m_i are the melting temperature and the molar heat of fusion of component i in the liquid, respectively. Both the calculated eutectic composition and the eutectic temperature estimated with expressions (15.2) and (15.3) are in good agreement with measured values, as shown in Table 15.1.

The mechanisms for the $CaSiO_3$–$Ca_3(PO_4)_2$ eutectic ceramic (Bioeutectic) to form a porous ceramic consists in the dissolution of the $CaSiO_3$ phase and the pseudomorphic transformation of $Ca_3(PO_4)_2$ into HA [20, 22, 23]. Both devitrification and crystallization processes of the $CaSiO_3$–$Ca_3(PO_4)_2$ eutectic glass were described by Magallanes-Perdomo et al. [24, 25]. The parent glass was manufactured by the casting technique and crystallization processes were carried out by means of controlled thermal treatments in high-temperature furnaces. They found that that the devitrification began at 870 °C with the crystallization of a Ca-deficient apatite phase, followed by wollastonite-2M ($CaSiO_3$) crystallization at around 1006 °C. At 1375 °C, the microstructure was found to be composed of quasi-rounded colonies formed by a homogeneous mixture of pseudowollastonite ($CaSiO_3$) and TCP ($Ca_3(PO_4)_2$), corresponding to irregular eutectic structures. Bioactivity, biocompatibility, *in vitro* and *in vivo* assessment of these ceramics and glass-ceramics have been widely studied [20, 22–27].

It is worthy of mention that these eutectic ceramics, glass-ceramics, and glasses have also been manufactured by directional solidification employing the Laser Floating Zone (LFZ) technique. *In vivo* evaluation of these directionally solidified ceramics has been carried out by means of implantation into tibia of adults New Zealand rabbits, concluding that this directionally solidified eutectic ceramic (DSEC) was also biocompatible, bioactive, and osteoconductive [28]. In addition, the spectroscopic properties of these glass-ceramics and glasses doped with rare-earth (RE) ions such as Nd^{3+}, Er^{3+}, and Eu^{3+}, resulted very suitable for luminescence applications [29–33]. As an example, Figure 15.2 shows Nd-doped (blue) and Er-doped (rose) $CaSiO_3$–$Ca_3(PO_4)_2$ bioactive eutectic glasses manufactured with the LFZ method.

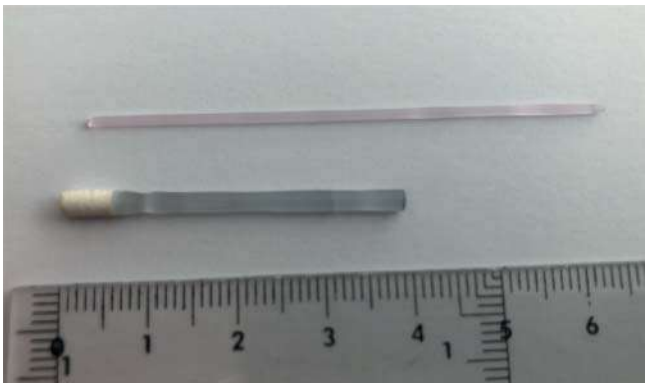

Figure 15.2 Image of $CaSiO_3$–$Ca_3(PO_4)_2$ bioactive eutectic glasses doped with Neodymium (blue) and Erbium (rose) ions manufactured by directional solidification with the laser floating zone technique.

15.2 Fundamentals of the Laser Floating Zone Technique

The LFZ fabrication method was first developed by Poplawsky and Tomas [34] and later improved by Feigelson [35] and Fejer et al. [36]. This directional solidification technique delivers high axial and radial thermal gradients, which provide a flat solid–liquid interface in the solidification front. This feature is an essential key point to obtain a regular homogeneous growth. These characteristics allow this technique to be used for the fabrication of fiber-shaped single crystals, DSECs, glass-ceramics, and glasses [32, 37–39]. This method is based on the formation of a small melt liquid zone between both seed and precursor rods, which is sustained by the liquid surface tension, as shown in Figure 15.3. A limit in the length of the molten zone is superimposed by capillary stable growth conditions as follows:

$$l_m = 2\pi R \tag{15.4}$$

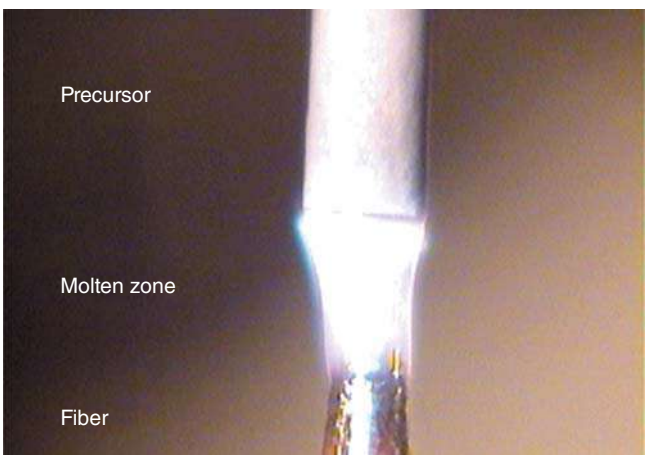

Figure 15.3 Image of the molten zone between precursor rod and fiber grown by the Laser Floating Zone technique. Source: Courtesy of Prof. J.I. Peña.

Figure 15.4 Image of the setup of the Laser Floating Zone. Reflaxicon (1), flat mirror (2), parabolic mirror (3), and translation and rotation axes (4).

where R is the radius of the grown fiber, which in turn, can be determined by the mass conservation law:

$$R^2 v = R_0^2 v_0 \tag{15.5}$$

where R_0, v_0, and R, v are the radius and rate of the feeding seed and grown fiber, respectively.

The LFZ system consists of a CO_2 or Nd:YAG laser as the heating source, and a sealed growth chamber to control the atmosphere in which the process is taking place. As shown in Figure 15.4, inside the chamber the focalization optics of the laser beam consists of a reflaxicon (i), a flat mirror (ii), and a parabolic mirror (iii). The reflaxicon turns the circular laser spot into a ring-shaped beam. The ring beam is deflected by the flat mirror at 45° and then is focused on the fiber precursor by means of a parabolic mirror, thus providing a homogeneous heating. The proper alignment of the optical system is carried out with the aid of a He–Ne laser whose optical path is coaxial to the heating laser beam. Two independent vertical axes control both rotation and translation rates (iv).

The fabrication process starts by placing the precursor rod in the upper axis and heating its lower end until a drop of molten material is formed, as shown in Figure 15.5a. Next, a small seed of the same material as the precursor, placed in the lower axis, is slowly brought into contact to the molten drop, establishing a bridge between the precursor and the seed, Figure 15.5b. Then, both precursor and seed are counter rotated to provide a homogeneous heat distribution to the molten material. Finally, the seed is withdrawn from the molten zone, whereas the precursor rod is moved toward it, keeping the volume of the liquid zone constant, as shown in the schematic representation of

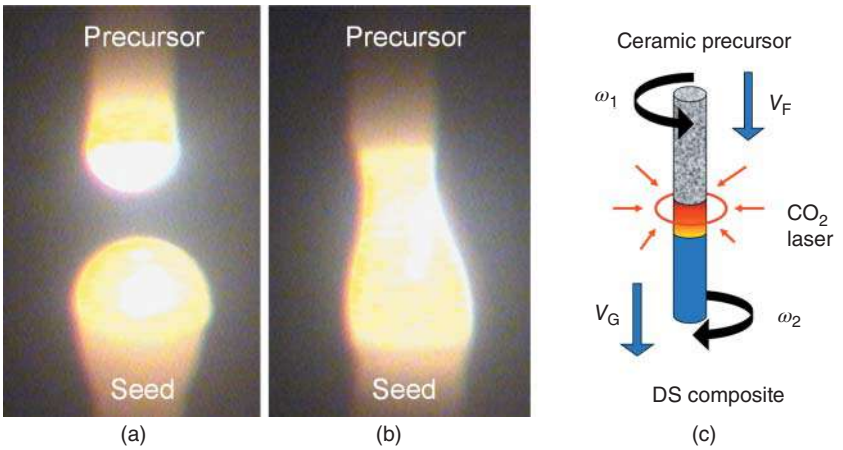

Figure 15.5 Images of the molten bridge formation as the previous stage to the growth process. The lower end of the precursor rod is melted (a). Next, the seed is approached to create the molten zone (b). Schematic representation of the growth process by the LFZ (c). Source: Courtesy of Prof. J.I. Peña.

Figure 15.5c. The feed and growth rates can be used to control the final diameter. Identical rates provide equal precursor and grown diameters. By increasing or decreasing the growth rate, the grown diameter is decreased or increased, respectively. In case the departing precursor is made up of sintered powder, the fabrication process is usually carried out in two steps: densification and growth, performing the latter downwards in order for the gas bubbles produced during the melting process not to be trapped within the grown fiber.

It is worthy of mention that whilst the maximum length of the grown fiber is only limited by the features of the movement system, the maximum crack-free diameter that can be attained depends on both the thermal properties of the material and the thermal transfer achieved during the growth process. The appearance of cracks during cooling is due to the high axial thermal gradients in the solidification interface, which are due to the stresses produced by the difference of temperature within the cylinder. Thermal gradients can be calculated using the simplified model of heat transfer from the cylinder proposed by Brice [40]:

$$T(r,z) = T_0 + (T_m - T_0)\frac{1 - \frac{hr^2}{2R}}{1 - \frac{1}{2}hR}\exp\left[-\left(\frac{2h}{R}\right)^{1/2} z\right] \tag{15.6}$$

where R is the radius of the cylinder, h is the cooling constant, T_m is the melting temperature, and T_0 is the room temperature. From this equation, axial and radial gradients are provided by:

$$G_z\big)_{r=R} = (T_m - T_0)\left(\frac{2h}{R}\right)^{1/2} \tag{15.7}$$

$$\frac{\partial T}{\partial r}\Big)_{z=0} \approx r\left(\frac{h}{2R}\right)^{1/2} G_z \tag{15.8}$$

The maximum axial gradient that the material can support without cracking is given by:

$$G_{crit} = \left.\frac{dT}{dz}\right|_{max} = \frac{2\varepsilon_b\sqrt{2}}{R\alpha}\left(\frac{hR}{2}\right)^{-1/2}\left(1 - \frac{hR}{2}\right) \tag{15.9}$$

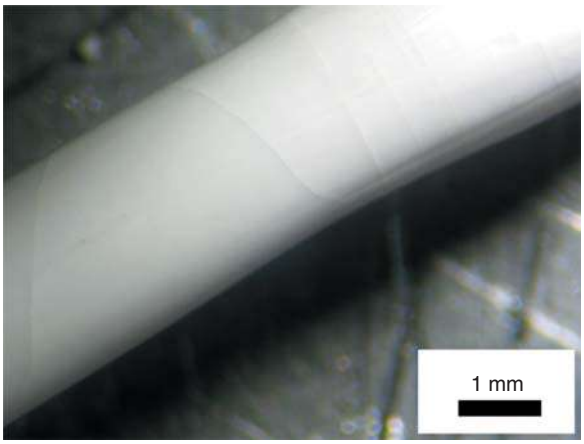

Figure 15.6 Stereoscopic image of cracks appeared in an Al_2O_3–$ZrO_2(Y_2O_3)$ rod during the directionally solidified growth.

where ε_b is the deformation limit and α is the thermal expansion coefficient. This equation allows the calculation of the maximum radius without the appearance of cracks. As an example, in Al_2O_3–$ZrO_2(Y_2O_3)$ and Al_2O_3–$Y_3Al_5O_{12}$ eutectic composites, the critical radii were estimated in 0.6 and 1.7 mm, respectively, corresponding with thermal gradients of 9.4×10^5 K/m and 4×10^5 K/m [41, 42]. Figure 15.6 shows the cracks appeared in an Al_2O_3–$ZrO_2(Y_2O_3)$ rod during the growth process.

Accounting that the origin of the thermal gradients is due to the heat dissipation by radiation and air convection from the surface of the cylinder, they would be reduced by the aid of additional heating sources such as lamp heaters, heat reservoirs, or by using a controlled atmosphere inside the growth chamber, using a gas with thermal conductivity higher that air, such as helium [43–45].

Besides the limit in the maximum radius that can be achieved, the quality of the resulting samples may also be affected by the vibrations of the displacement system caused by the movement of the stepper motors that control the axes, fluctuations in the laser power, non-uniformity heat distribution due to the misalignment of the heating laser source, or by poor alignment of both the rod precursor and the seed.

In addition to the LFZ technique, there are other unidirectional growth methods, the most important of which are the Bridgman and the Czochralski methods [46, 47]. The Bridgman method utilizes tungsten or iridium crucibles to perform the unidirectional solidification. The ceramic oxides are placed inside the crucible and melted by means of resistance or induction heaters. Then the crucible is slowly withdrawn from the hot region giving rise to the unidirectional solidified ingot. This method provides large samples which size is only limited by the size of the crucible. Conversely, both the growth rates and the thermal gradients achieved are low, below 100 mm/h and 10^2 K/m, respectively. Concerning the Czochralski method, the material is unidirectionally solidified by pulling the material from a melt pool in a crucible. Compared to these methods, the main advantages of the LFZ technique are the low amount of material required to explore new composites, the possibility to growth materials with high melting points, the control on the surrounding atmosphere, and the high thermal gradients attained, up to 2 orders of magnitude higher than in the Bridgman technique, which allow processing with high growth rates. In this way, it is easy to control the solidification characteristics to provide materials with very small phase size, or even glasses, managing the optical transmission, mechanical resistance, and thermal properties [48–60]. In addition, since this is a crucibleless technique, the resulting materials are with absence of contaminants coming from the melt container.

15.3 Fabrication and Characterization of Rare-Earth-Doped $CaSiO_3$–$Ca_3(PO_4)_2$ Biocompatible and Bioactive Eutectic Glasses and Glass-Ceramics

Directionally solidified $CaSiO_3$–$Ca_3(PO_4)_2$ eutectic glasses and glass-ceramics were fabricated by using the LFZ technique. With this technique, in addition to the advantage for growing samples at different rates, thus controlling the phase size, it is possible to incorporate small amounts of doping ions to the composite which can be used as a probe to control the crystallization stage. It is well-known that the spectroscopic properties of rare-earth (RE) ions depend on the chemical composition of the ceramic matrix so they can be used as a local ordering probe to study the local structure surrounding the rare-earth ion and the bonding at the ion site [54, 61, 62]. For this purpose, site-selective laser spectroscopy in the $^4I_{9/2} \rightarrow {}^4F_{3/2}/{}^4F_{5/2}$ and $^4I_{15/2} \rightarrow {}^4I_{13/2}$ transitions of Nd^{3+} and Er^{3+} ions, respectively, allow investigating the crystal field changes felt by these ions because of the sample crystallization stage. The changes in the spectral characteristics of the site-selective excitation and emission spectra of these ions enable to distinguish between crystalline and amorphous environment for the rare-earth ions [61, 63, 64]. In addition, Eu^{3+} ions, with a $4f^6$ electronic configuration, are highly sensitive to the local environment and have a relatively simple energy level structure, especially the $^5D_0 \rightarrow {}^7F_J$ manifold. Taking into account that $^5D_0$ state is non-degenerate under any symmetry, the structure of the $^5D_0 \rightarrow {}^7F_J$ emission is only determined by the splitting of the terminal levels caused by the local crystal field. Furthermore, the $^7F_0$ level is also non-degenerate, so that fluorescence line narrowing (FLN) spectroscopy in the $^7F_0 \rightarrow {}^5D_0$ absorption band provide information on the different local environments around the Eu^{3+} ions, making it an ideal experimental probe for crystalline as well as for glassy environments [65–67].

Bioactive glasses and glass-ceramics were prepared departing from a powder mixture of $CaSiO_3$ and $Ca_3(PO_4)_2$ in the eutectic composition, 80% and 20% mol% respectively. As optical probes, 1, and 2 wt% of Nd_2O_3, 1 wt% of Er_2O_3, and 0.5 wt% of Eu_2O_3 were added to the eutectic composite. Next, the mixture was isostatically pressed at 200 MPa for two minutes to obtain the precursor rods. Finally, the resulting powders were sintered a 1200 °C for 10 hours. Directionally solidified samples were grown by the LFZ technique at 50, 100, 250, and 500 mm/h maintaining the diameter constant at around 2.5 mm. Also, rod diameter was varied keeping the growth rate at 100 mm/h, modifying the feed rate to obtain samples with diameters between 2.5 and 4.5 mm. To relieve the inner stress induced during the growth process, the samples were annealed at 650 °C for five hours.

Figure 15.7 shows an example of the microstructure found in the glass-ceramic samples doped with 1 wt% of Nd_2O_3 grown at 100 and 500 mm/h, with a diameter of 2.5 mm, (a) and (b), respectively [32]. Details of the microstructure in the cross-section view is presented in the insets of each micrograph. It was found a strong dependence of the microstructure on the processing parameters, in accordance with the Hunt–Jackson law [68]. The microstructure was made up of fibers with irregular shape (clear contrast) embedded in a grayish matrix (dark and black contrast). The number of phases present in the sample and the parallel alignment to the growing direction were correlated to the flatness achieved in the solidification front. A growth rate increase or a diameter decrease led the microstructure to a parallel alignment and to a structural arrangement of from three to two phases.

A semi-quantitative chemical composition analysis of the samples carried out by energy-dispersive X-ray (EDX) microanalysis confirmed that the composition of the processed samples was around the theoretical composition, as shown in Table 15.2. Composition of the samples was close to the nominal value. The composition of the phases was also evaluated. In samples with

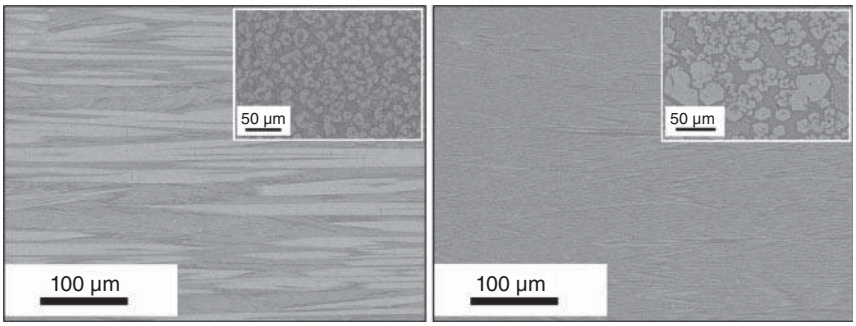

Figure 15.7 Micrograph of the longitudinal-section view of samples doped with 1 wt% of Nd_2O_3 with a diameter of 2.5 mm and grown at 100 mm/h (a) and 500 mm/h (b), respectively. The inset shows the details of the microstructure in a cross-section view. Source: Sola et al. [32], Figure 01 [p. 10706]/with permission from The Optical Society.

Table 15.2 Theoretical (T) and experimental composition of the glass-ceramic samples in wt%.

V (mm/h)	SiO_2	P_2O_5	CaO	Nd_2O_3	Er_2O_3	Eu_2O_3
T	31.00	18.30	50.70	(1.00–2.00)	(1.00)	(0.50)
50	29.50	18.92	51.57	0.91		
100	31.06	18.50	50.44	0.90		
250	31.31	18.30	50.38	1.02		
500	30.89	18.61	50.50	1.08		
100	31.17	18.51	50.32	1.83		
100	31.75	18.00	50.24	2.05		
50	32.23	21.10	46.67		1.20	
500	32.27	20.87	46.86		0.93	
50	30.28	18.95	50.77			0.63
500	30.40	18.95	50.65			0.70

three phases, the clear phase was rich in CaO and P_2O_5 with a low content of SiO_2, the dark phase was rich in SiO_2 and CaO with a very low content of P_2O_5, and in the black phase there was a high amount of CaO and SiO_2 and a low content of P_2O_5. Concerning the amount of rare-earth oxide, even though it was found in the three phases it was mainly placed in the black phase. In the case of samples with two phases, the composition of the clear and dark phases was like in the previous case. As an example, Table 15.3 shows the compositional analysis in wt% of samples grown at 50 and 500 mm/h with a diameter around 2.5 mm and doped with 1 wt% of Nd_2O_3. The same behavior was observed in the samples doped with Er_2O_3 and Eu_2O_3.

Electron backscatter diffraction analysis (EBSD) was performed in each sample to determine the crystalline nature of the phases. It was found that in the case of samples with three phases, the clear phase had apatite-like structure whereas the dark phase had a Ca_2SiO_4 structure and the black one was amorphous. It is highly remarkable that this crystalline phase had not been reported previously in these eutectic glass-ceramics. In the case of samples with two phases, the clear phase,

Table 15.3 Compositional analysis in wt% of the phases present in the eutectic glass-ceramic samples grown at 50 and 500 mm/h and doped with 1 wt% of Nd_2O_3.

	V (mm/h)	SiO_2	P_2O_5	CaO	Nd_2O_3
Clear phase	50	15.54	31.67	52.17	0.61
Dark phase	50	50.18	3.18	46.11	0.53
Black phase	50	42.02	18.17	38.21	1.60
Clear phase	500	15.38	32.82	51.1	0.69
Dark phase	500	46.2	11.57	41.56	0.68

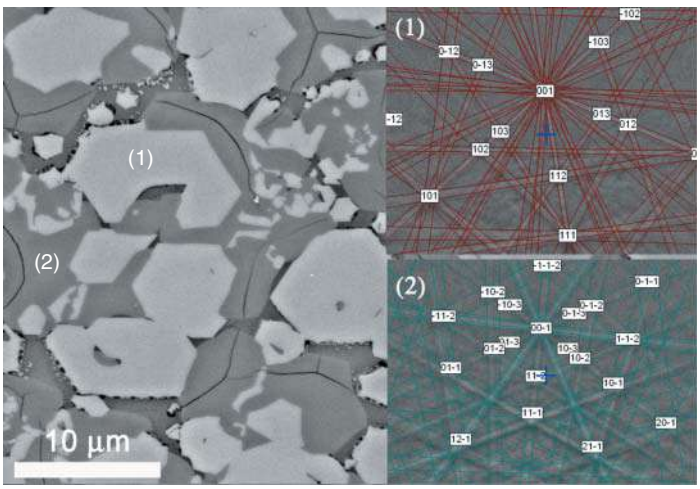

Figure 15.8 Cross section micrograph of a sample grown at 50 mm/h doped with 1 wt% of Nd_2O_3. The insets show the electron backscatter diffraction patterns corresponding to an oxyapatite structure, (1), and to the dicalcium silicate, (2). Source: Sola et al. [32], Figure 02 [p. 10707]/with permission from The Optical Society.

as in the previous case, had apatite-like structure and the dark was amorphous. As an example, Figure 15.8 shows the micrograph in cross-section view of a sample grown at 50 mm/h doped with 1 wt% of Nd_2O_3. The insets show the electron backscatter diffraction patterns corresponding to an oxyapatite structure found in the clear phase, (i), and to the dicalcium silicate found in the dark phase, (ii) [32].

The Ca_2SiO_4 structure observed in the glass-ceramic samples grown at low growth rate showed an excellent *in vitro* bioactivity [69]. The samples grown at 50 mm/h doped with 0.5 wt% of Eu_2O_3 were soaked into SBF for three months. Figure 15.9 shows a micrograph in longitudinal-section view of the sample after the immersion period [33]. It can be observed how the SBF dissolved the amorphous phase as well as the one with Ca_2SiO_4 structure, giving rise to a porous layer made up of fibers with a thickness of around 150 µm. EBSD analysis carried out in the sample confirmed that the apatite-like structure of the fibers was unaltered after the immersion period.

Site-selective excitation spectra in the $^4I_{9/2} \rightarrow {}^4F_{3/2,5/2}$ and $^4I_{15/2} \rightarrow {}^4I_{9/2}$ transitions were performed, respectively, by collecting the luminescence at different emission wavelengths along the $^4F_{3/2} \rightarrow {}^4I_{11/2}$ and $^4I_{13/2} \rightarrow {}^4I_{15/2}$ laser transitions for the Nd^{3+} and Er^{3+}, respectively. For the

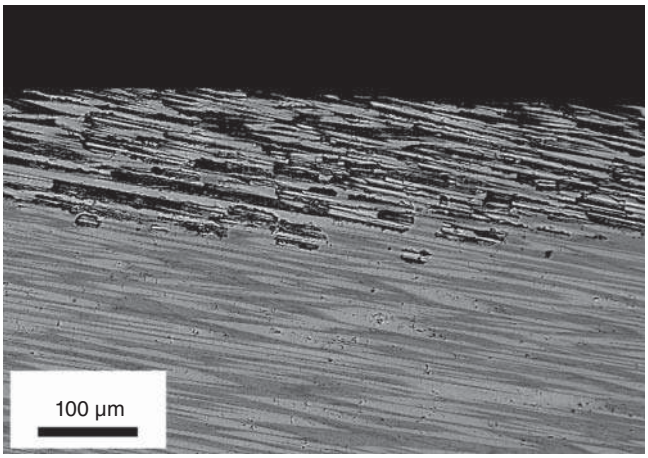

Figure 15.9 Micrograph in longitudinal section view of a glass-ceramic sample doped with 0.5 wt% of Eu_2O_3 grown at 50 mm/h after an immersion period of three months in simulated body fluid (SBF). Source: Sola et al. [33], Figure 03 [p. 6567]/with permission from The Optical Society.

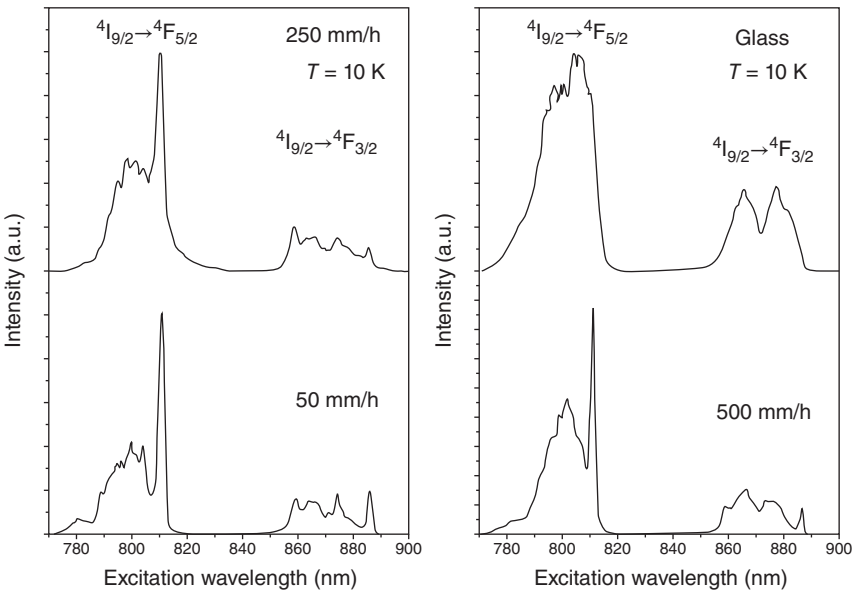

Figure 15.10 Excitation spectra of the $^4I_{9/2} \rightarrow {}^4F_{5/2,3/2}$ transitions obtained by collecting the luminescence at 1066 nm in the glass and glass-ceramic samples obtained at different growth rates and doped with 1 wt% of Nd_2O_3. Source: Adapted from Sola et al. [32].

case of Nd-doped glass-ceramics, Figure 15.10 shows the low temperature excitation spectra corresponding to the $^4I_{9/2} \rightarrow {}^4F_{3/2,5/2}$ transitions obtained at 1066 nm for the glass-ceramic samples doped with 1 wt% of Nd_2O_3 grown at 50, 250, and 500 mm/h [32]. The excitation spectrum of the glass sample is also presented for comparison purposes. The spectra corresponding to the $^4I_{9/2} \rightarrow {}^4F_{3/2}$ transition in the glass-ceramic samples presents four main bands instead of the two associated with the two Stark components of the $^4F_{3/2}$ doublet in a low crystal field symmetry, which indicated the presence of different environments for Nd^{3+} ions in these matrices.

By comparison with the excitation spectrum of the glass sample, the spectra of this transition showed two new peaks at around 859 and 886 nm, pointed out with arrows. The spectra corresponding to the $^4I_{9/2} \rightarrow {}^4F_{5/2}$ transition also showed a new sharp peak at around 810 nm, not observed in the excitation spectrum of the glass sample, which indicated that Nd^{3+} ions were in a crystalline environment. It is worthy of highlight that the position of these new peaks was almost independent of the growth rate and that as growth rate decreased the spectrum became more defined with narrower peaks, pointing out that the crystalline character of the sample increase at lower growth rate, confirming the results obtained by EDX analyses.

More precise information about the environments for Nd^{3+} ions was obtained by performing excitation spectra at 1050, 1066, and 1080 nm for the sample obtained grown at 50 mm/h and doped with 1 wt% of Nd_2O_3, Figure 15.11 [32]. Figure 15.11 depicts how the spectrum was very different depending on the emission wavelength which indicated that Nd^{3+} ions were in different crystal field sites. For the $^4I_{9/2} \rightarrow {}^4F_{5/2}$ transition, the spectrum obtained at 1050 nm showed sharp and well-resolved peaks with the most intense one located at around 802.2 nm which indicated a crystalline environment for Nd^{3+} ions. This intense peak disappeared, and the spectrum became an unstructured broad band for the samples grown at 500 mm/h, as shown in the left side of Figure 15.11. The low energy band corresponding to the $^4I_{9/2} \rightarrow {}^4F_{3/2}$ doublet narrowed into one single component as expected for one well defined crystal field site. Based on the previous microstructural analysis, these results suggested that this spectrum corresponded to Nd^{3+} ions in a crystalline phase, specifically in Ca_2SiO_4 structure which was only present for samples grown at low rates (50 and 100 mm/h). However, the spectrum obtained at 1080 nm showed broad bands similar to those found in the glass sample. The spectrum corresponding to the $^4I_{9/2} \rightarrow {}^4F_{3/2}$ transition showed at least two components in the low energy band. This behavior had also been observed in the glass sample being a consequence of contributions from Nd^{3+} ions in a multiplicity of environments, as shown in the right side of the Figure 15.11. In the case of the excitation spectrum collected at 1066 nm, sharp peaks appeared at around 810.8, 859, and 886 nm, which according to the EBSD analysis might correspond to the apatite-like crystalline phase which was present in all glass-ceramics samples.

Concerning the Er-doped glass-ceramics, Figure 15.12 shows the low temperature excitation spectra corresponding to the $^4I_{15/2} \rightarrow {}^4I_{9/2}$ transition obtained at 1526 nm for the glass-ceramic samples grown at 50 and 500 mm/h. The spectrum corresponding to the glass sample is also included for comparison purposes. Excitation spectra of glass-ceramic samples showed two narrow peaks around 787.0 and 789.5 nm, pointed out with arrows, which did not appear in the spectrum of the glass sample. These peaks, independent of the growth rate, indicated that Er^{3+} ions were in a crystalline environment, which according to EBSD characterization corresponded to the apatite-like crystalline phase. However, site-selective excitation spectra of Er^{3+} ions in these glass-ceramic did not allow obtaining information about the Er^{3+} ions incorporated in the Ca_2SiO_4 crystalline phase. Nevertheless, as in the Nd-doped glass-ceramic samples, the spectra obtained for the lower growth rate became more defined with narrower peaks.

Site-selective steady-state emission spectra in the Er-doped glass-ceramics confirmed the results provided by the excitation spectra. Figure 15.13 shows the emission spectra at 10 K obtained under excitation at 789.5 nm for the samples grown at 50 and 500 mm/h. Emission spectrum of glass sample is also included. Both glass-ceramic samples emission spectra showed sharp peaks which indicated that Er^{3+} ions were in crystalline environment. In particular, for the sample grown at low growth rate, a peak around 1519 nm appeared, pointed out with a black arrow, which was not present in the sample grown at 500 mm/h. Also, a narrow peak around 1526 nm was shown in the emission spectra of both glass-ceramic samples, pointed out with green arrows, which was not

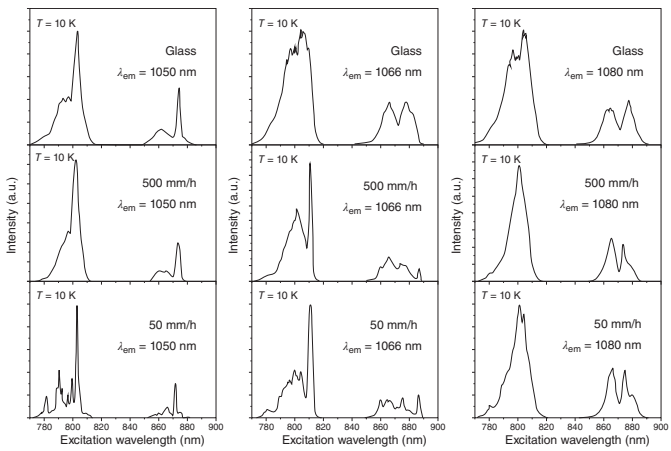

Figure 15.11 Excitation spectra obtained at 1050, 1066, and 1080 nm emission wavelengths for the Nd-doped glass-ceramic samples grown at 50, 500 mm/h and for the glass sample. Source: Adapted from Sola et al. [32].

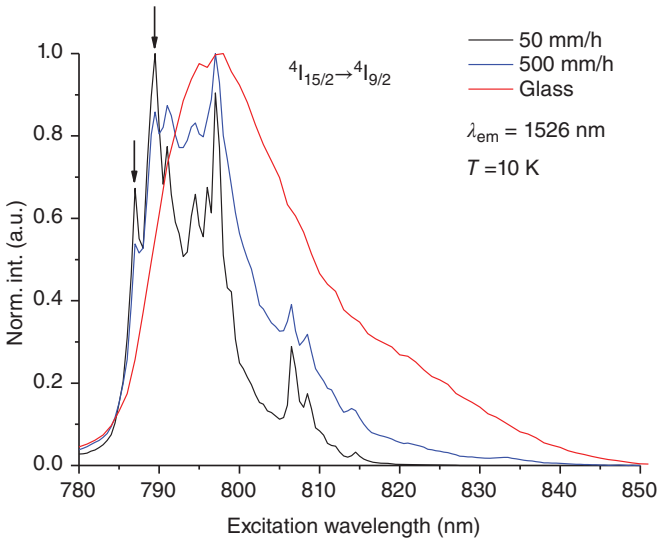

Figure 15.12 Excitation spectra obtained at different emission wavelengths for the Er-doped glass-ceramic samples grown at 50 and 500 mm/h. Excitation spectrum of the glass sample is also included.

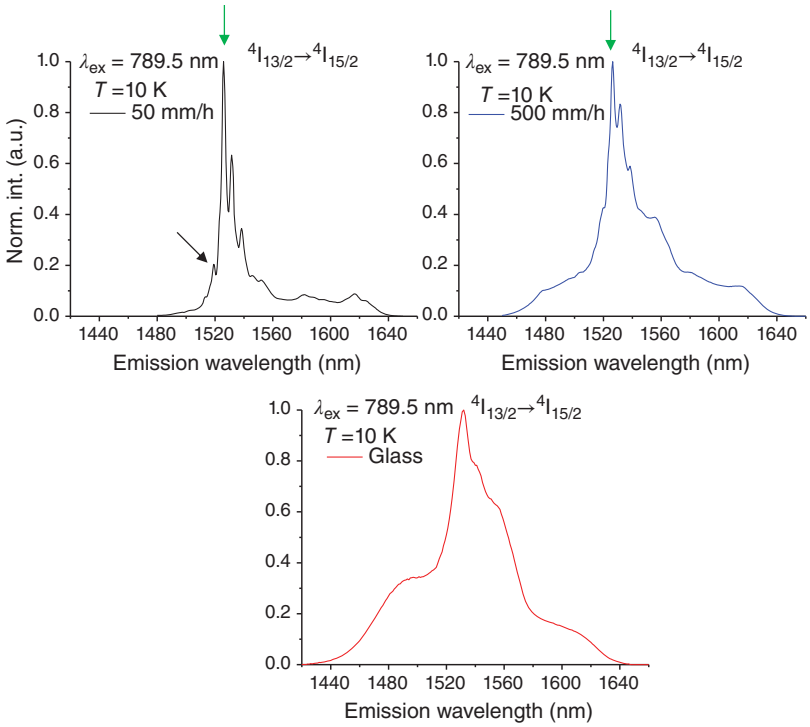

Figure 15.13 Steady-state emission spectra of the $^4I_{13/2} \rightarrow {}^4I_{15/2}$ transition obtained under excitation at 789.5 nm for the Er-doped glass-ceramic samples grown at 50 and 500 mm/h and for the glass sample.

present in the emission spectrum of the glass sample. These results indicated that at this excitation wavelength, Er^{3+} ions in the sample grown at low rate were excited in both crystalline environments, corresponding to dicalcium silicate structure at 1519 nm and also to the apatite-like structure at 1526 nm. The other components of the emission spectra might be associated to a mixture of both crystalline environments but also to the emission of Er^{3+} ions in the amorphous phase. For the samples grown at high rate, the sharp and narrow peak associated to dicalcium silicate disappeared and the spectrum became broader and unstructured. For this rare-earth, the complexity of its energy levels and the spectral overlapping of the emissions coming from the rare-earth ion in different amorphous and crystalline environments, made it impossible to isolate the emission corresponding to individual crystalline phases. Thus, Nd^{3+} ions showed better properties as optical probe for site-selective spectroscopy characterization in these glass-ceramics.

Time-resolved line-narrowed fluorescence spectra of the $^5D_0 \rightarrow {}^7F_{0-2}$ transitions of Eu^{3+} doped samples were obtained at 10 K by using different resonant excitation wavelengths into the $^7F_0 \rightarrow {}^5D_0$ transition with a time delay of 10 μs. The spectral features of the dicalcium silicate phase, which appeared only in the samples grown at low rate, 50 mm/h, can be clearly observed in Figure 15.14a, which shows the emission spectra obtained under excitation at 579.1 nm for the glass-ceramic samples grown at 50 and 500 mm/h and for the glass sample [33]. It can be observed that the emission spectrum of the sample grown at 500 mm/h was quite similar to the one obtained in the glass sample, which indicated that Eu^{3+} ions in this sample at this wavelength were excited in the amorphous phase. However, in the case of the glass-ceramic sample grown at 50 mm/h, the spectrum showed

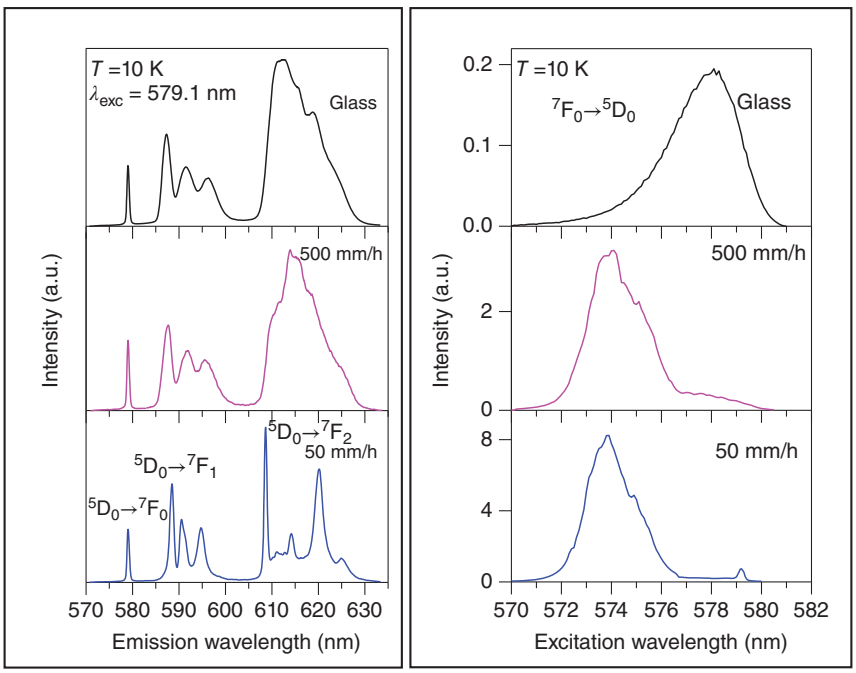

Figure 15.14 (a) $^5D_0 \rightarrow F_{0,1,2}$ emissions of Eu^{3+} for the glass-ceramic samples grown at 50 and 500 mm/h and for the glass sample obtained under excitation at 579.1 nm. (b) Excitation spectra of the $^7F_0 \rightarrow {}^5D_0$ transition for the glass-ceramic samples grown at 50 and 500 mm/h and for the glass sample obtained by collecting the luminescence at the $^5D_0 \rightarrow {}^7F_2$ emission. Data correspond to 10 K. Source: Figure reprinted with permission from Sola et al. [33] © The Optical Society.

sharp lines according to Eu^{3+} in the dicalcium silicate crystalline phase. This spectral feature is also clearly shown in the excitation spectra corresponding to the $^7F_0 \rightarrow {}^5D_0$ transition for the three samples, as shown in Figure 15.14b. As can be seen, the excitation spectrum of the sample grown at 50 mm/h showed a band centered around 574 nm which corresponded to the apatite-like crystalline phase, together with a narrow peak at around 579.1 nm, the excitation wavelength at which Eu^{3+} ions were excited in the dicalcium silicate crystalline phase. In the case of the sample grown at 500 mm/h, the spectrum showed the band around 574 nm and a shoulder at the long wavelength side of the spectrum that corresponded to the Eu^{3+} ions in the amorphous phase.

15.4 Laser-Induced Breakdown Spectroscopy (LIBS) as a Complementary Analytical Tool for Monitoring the Formation of Hydroxyapatite Porous Layers

Laser-induced breakdown spectroscopy (LIBS) is a powerful technique for analytical characterization. This technique is based on the generation of a micro-plasma and the subsequent assessment of the induced spectral emission [70]. For this purpose, a laser pulse of high energy which is used as the atomization and excitation source, is directly focused on the surface of the sample to be assessed and the formed plasma is analyzed to obtain the multi-elemental composition of the samples. LIBS is a single step, fast, robust, and a stable technique with high spatial resolution which can be carried out under atmospheric conditions [71, 72]. In addition, sample preparation is not required thus providing a wide range of advantages when compared to other analytical techniques [71–75].

Accounting the excellent features of the LIBS technique, it has been used to monitor and characterize the formation of the HA porous layer developed on $CaSiO_3$–$Ca_3(PO_4)_2$ biocompatible eutectic glasses after immersion in SBF [76]. The eutectic glasses were manufactured by the LFZ at a growth rate of 500 mm/h. After the fabrication process, samples were annealed at 650 °C for five hours to relieve the inner stresses. Next, to develop the HA layer on the surface of the sample, the glass was soaked in SBF and placed in a stove at human body temperature of 37 °C for a period of one month.

LIBS characterization was carried out by means of a Q-switched Nd:YAG laser emission at 1064 nm, emitting 7.7 ns laser pulses with a pulse energy of 50 mJ. Plasma emission was collected by using a bifurcated optical fiber adjusted at 45° to the sample surface and connected to a dual-channel spectrometer. To avoid the saturation of the detector, pulse energy and irradiance were set at 30 mJ and 73.5 MW/cm^2, respectively.

Figure 15.15a shows LIBS spectra recorded in the spectral range of 200–850 nm for both the $CaSiO_3$–$Ca_3(PO_4)_2$ eutectic glass and the layer developed on the sample surface after the immersion period in SBF. LIBS spectrum of HA is also presented for comparison purposes in Figure 15.15b [77]. The spectra show strong characteristic emission lines which were assigned according to the National Institute of Standards and Technology (NIST). The main atomic emission lines corresponding to Si (I), Ca (I), Ca (II), Mg (II), Na (I), and O (I) are pointed out in Figure 15.15b and the assigned wavelengths are listed in Table 15.4.

When the dense $CaSiO_3$–$Ca_3(PO_4)_2$ eutectic glass is immersed in SBF, the reaction of the material with the SBF gives rise to a porous layer of HA which finally covers the surface of the sample. It is well known that for a glass to be bioactive and hence to bond to bone, a calcium phosphate layer must form at its surface. The mechanisms of this reaction were proposed by Hench et al. [78, 79]

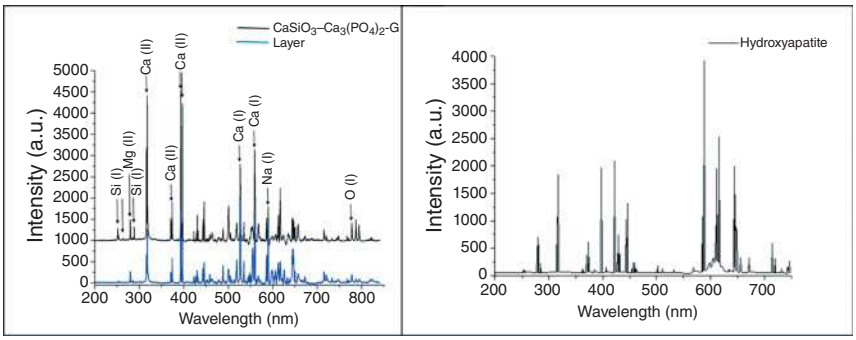

Figure 15.15 Comparative LIBS spectra between the $CaSiO_3$–$Ca_3(PO_4)_2$ eutectic glass and the layer produced on the surface of the sample (a). HA LIBS spectrum is also presented for comparison purposes (b). Source: Sola et al. [76]/MDPI/CC BY-4.0.

Table 15.4 List of main spectral lines observed in the samples.

Element	Sample	Wavelength (nm)
Si (I)	W-TCP	243.5, 250.69, 251.61, 252.41, 252.85, 263.1, 288.16
Ca (I)	W-TCP, HA	527.03, 559.45
Ca (II)	W-TCP, HA	317.93, 373.69, 393.37, 396.85
Mg (II)	W-TCP, HA	279.55
Na (I)	W-TCP, HA	589
O (I)	W-TCP, HA	777.5

and can be summarized in the following five stages: (i) rapid exchange of alkali or alkali-earth ions with H^+ or H_3O^+ from solution; (ii) loss of soluble silica in the form of $Si(OH)_4$ to the solution; (iii) condensation and repolymerization of SiO_2-rich layer on the surface depleted in alkalis and alkaline-earth cations; (iv) migration of Ca_2^+ and PO_4^{3-}groups to the surface through the SiO_2-rich layer forming a $CaO–P_2O_5$-rich film on top of the SiO_2-rich layer, followed by the growth of the amorphous $CaO–P_2O_5$-rich film by incorporation of soluble calcium and phosphorous from solution; and (v) crystallization of the amorphous $CaO–P_2O_5$ film by incorporation of OH^- anions from solution to form a HA layer. Figure 15.16 shows LIBS spectral emission lines of Si (I) at 243.5 (a), 250.69, 251.61, 252.41, 252.85 (b), 263.1 (c), and 288.16 (d) [76]. It is worthy of mention that none of these spectral emission signals appeared in the layer produced after immersion in SBF. Therefore, these results confirm the absence of Silicon in the layer developed on the surface of the sample.

Next, once the dissolution of the $CaSiO_3$ phase has been confirmed by LIBS, the pseudo-transformation of TCP, $Ca_3(PO_4)_2$, into HA was evaluated by micro-Raman spectroscopy. Figure 15.17 shows the Raman spectra obtained in the 50–1200 and 3500–3700 cm^{-1} wavenumber regions for the layer and for the TCP phase [76]. The Raman spectra collected from the layer were made up of sharp peaks and broad bands which can be assigned to the HA Raman spectra previously reported in the scientific literature as follows [20, 28]: a narrow intense peak placed at 962 cm^{-1} corresponding to symmetric stretching of PO_4^{3-} modes, broad bands at 400–500, 570–625, and 1020–1095 cm^{-1} attributed respectively to ν_2^-, ν_4^-, and ν_3^- type internal PO_4^{3-}

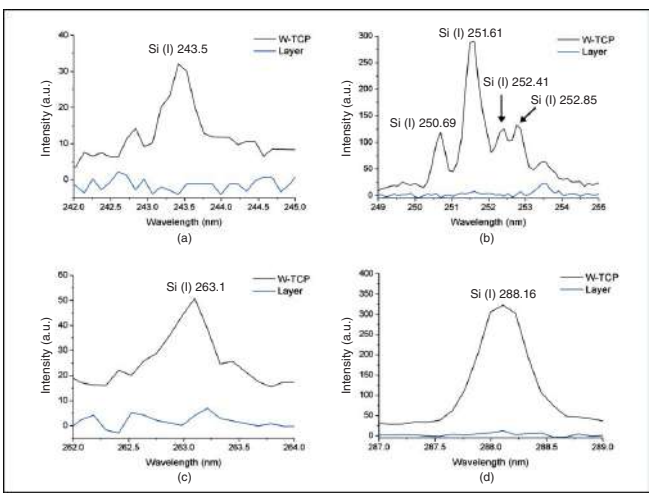

Figure 15.16 LIBS spectral signals of Si (I) in both $CaSiO_3-Ca_3(PO_4)_2$ eutectic glass and HA layer at 243.5 nm (a), 250.69, 251.61, 252.41, 252.85 nm (b), 263.1 nm (c), and 288.16 nm (d). Source: Sola et al. [76]/MDPI/CC BY-4.0.

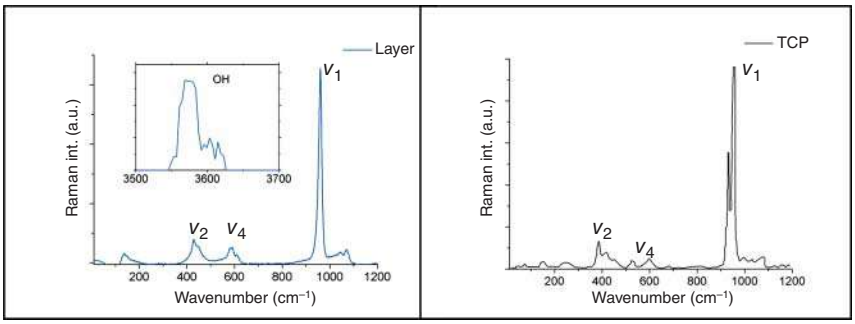

Figure 15.17 Micro-Raman spectra obtained on the surface of the sample after a soaking period in SBF of one month (a). Standard Raman spectrum of tricalcium phosphate (TCP) (b). Source: Sola et al. [76]/MDPI/CC BY-4.0.

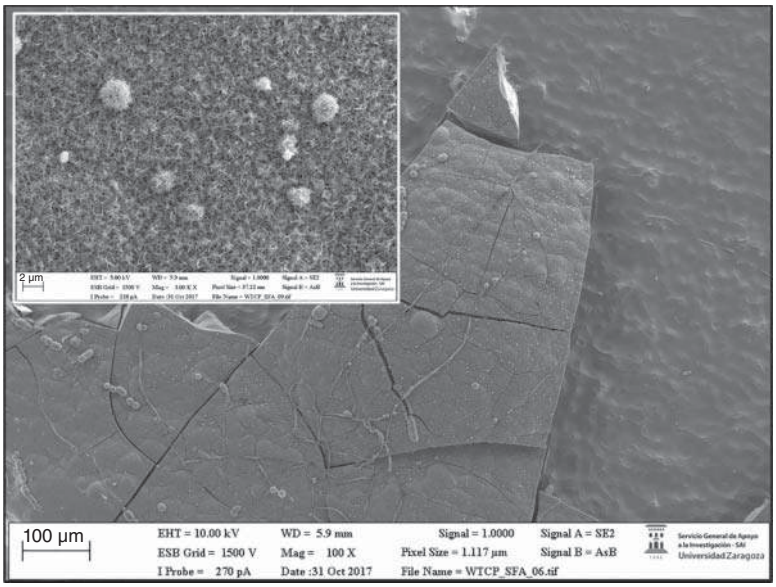

Figure 15.18 General view SEM micrograph of the $CaSiO_3$–$Ca_3(PO_4)_2$ eutectic sample after a 1-month immersion in SBF. The inset shows a detail of the layer developed on the surface.

modes, and a strong sharp peak located at 3576 cm^{-1} assigned to the O–H stretching mode. It is worthy of note that Raman spectra obtained from the layer showed significant variations when compared to TCP spectra, the most relevant of which is the absence of the O–H stretching at 3576 cm^{-1}. Consequently, micro-Raman analyses confirmed that the layer developed on the surface of the sample was HA.

Finally, the elements present in both the glass and the layer, and the Ca/P ratio on the layer were determined by SEM-EDX semi-quantitative chemical composition analysis. Figure 15.18 shows a micrograph of a general view of the sample soaked in SBF. The inset shows a detail of the layer developed on the surface. It can be observed that the layer formed on the surface of the samples consisted of HA nanocrystals, fibrils in shape and randomly oriented, thus providing porosity to the new surface. The cracks observed revealed that the coating formed had different properties

Table 15.5 EDX compositional analysis in at% of both $CaSiO_3$–$Ca_3(PO_4)_2$ glass and surface layer.

Sample	Si	P	Ca
Glass	12.73	6.27	18.86
Layer	—	16.56	21.70

than the parent glass, as cracks were not present on starting samples. The EDX spectrum showed in Table 15.5 indicated that the layer was rich in Ca and P, with a Ca/P ratio of about 1.3. Worth highlighting is that, according to these analyses, Si was not present in the layer. Therefore, during immersion, the bioactive glass surface was dissolved, and a new surface was formed by precipitation and transformation reactions leading to a crystallized, Ca-deficient apatite, similar to the bone mineral in its composition.

15.5 Laser Machining and *In Vitro* Assessment of $CaSiO_3$–$Ca_3(PO_4)_2$ Biocompatible and Bioactive Eutectic Glasses and Glass-Ceramics

In bioactive glasses and glass-ceramics used as scaffolds, a macroporous interconnected structure with controlled dimensions is essential. This structure may enhance bone ingrowth, vascularization, nutrient delivery, and cell proliferation [80, 81]. The optimal pore size in scaffolds is still subject to ongoing research and may range between 100 and 800 μm [82–87]. Laser machining is a suitable technique to create a controlled porous structure without causing an important detriment of its structural stability and mechanical properties. The interaction between pulsed laser radiation at 532 nm and both $CaSiO_3$–$Ca_3(PO_4)_2$ biocompatible eutectic glass and glass-ceramic samples has been studied, as a first approach, to generate a macroporous interconnected structure with controlled dimensions [88]. The samples were manufactured by the LFZ technique by controlling the solidification rate. Specifically, glass-ceramics were fabricated at a growth rate of 50 mm/h and the glass samples at 1000 mm/h. As usual, the stresses induced during the growth process were relieved by an annealing process at 650 °C for five hours. As the laser source, a Q-switched Nd:YVO_4 laser, coupled to a second harmonic generator, delivering laser pulses at 532 nm, with 5.5 ns pulse duration, and 15 kHz repetition rate was used to machine the samples. Laser radiation was focused by using an optical lens with 100 mm focal length. The samples were machined with 68 μJ pulse energy and 12.36 kW peak power. Craters 300 μm in diameter were machined in the glass and glass-ceramic samples to assess the interaction between the laser radiation at 532 nm in the nanosecond range and the samples, and to determine the ablation rates. For this purpose, samples were processed around the focal plane moving the surface of the samples upward and downward up to 3 mm out of focus. With these experimental conditions, the machining process was carried out processing the samples 20, 40, and 60 iterations.

Figure 15.19 shows the machined depth achieved around the focal plane for both samples and for the case of 60 iterations (a), and the profiles of the machined depth achieved in a 300 μm diameter crater for both the glass and the glass-ceramic samples for a reference position of −2 mm after iterating the laser processing 60 times (b). It can be observed that the maximal machined depth

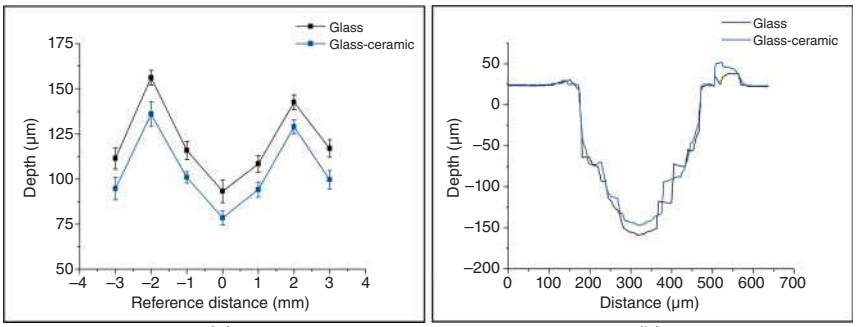

Figure 15.19 Machined depth achieved for the $CaSiO_3-Ca_3(PO_4)_2$ glass and glass-ceramic samples around the focal plane (cero position) for 60 iterations (a), and profile of the machined depth obtained in a 300 μm diameter laser ablated crater at a reference position of −2 mm out of focus (b). Source: Sola and Grima [88]/MDPI/CC BY-4.0.

was achieved by placing the sample out of focus, specifically at −2 mm. At this position, the maximal depths attained were 157.25 ± 4.21 and 134.99 ± 6.93 μm for the glass and the glass-ceramic, respectively. As previously reported, the machined depth and the removed volume depend on the laser machining method [39, 89–91]. When the samples are machined by using the percussion technique, i.e. delivering the whole laser pulses over the same area, the maximal machined depth and removed volume are achieved when the surface of the sample is placed at the focal plane. However, for machining large areas, it is required to deflect the laser beam over the sample or to move the sample by using a translation stage if the laser system is not equipped with a scanning head. It was shown that in this machining method the maximal machined depth and removed volume were achieved by placing the sample out of focus [89–91]. As shown in Figure 15.19a, this phenomenon also holds for the case of these eutectic glasses and glass-ceramic samples. It is worth mentioning that the machined depth for the glass-ceramic was slightly lower than for the glass which is related to the higher hardness of the glass-ceramic, 495 HV, vs. 458 HV for the glass. It was also demonstrated that there exists a close relation between the ablation yields and the material hardness so that the harder the material the lower the ablation yields [89, 91]. For the optimal conditions, the removed volume and the ablation yield were found to be 200 μm^3/pulse and 340 J/mm^3 for the glass and 183 μm^3/pulse and 371 J/mm^3 for the glass-ceramic sample.

Machined samples were characterized by means of SEM-EDX. Figure 15.20a and b show top-view micrographs of the craters machined in the glass and the glass-ceramic sample, respectively. In both cases, the surroundings of the machined areas presented a heat affected zone, HAZ, and deposition of the ejected material. The origin of the HAZ relies on the photothermal nature of the interaction between nanosecond laser pulses with matter [92]. Insets in Figure 15.20 show these areas in detail. The scale bar stands for 10 μm. It is worth noting that the glass-ceramic sample presented a higher amount of deposited material than the glass sample. EDX analyses were carried out on both machined samples to evaluate whether the composition of the departing sample was modified. Table 15.6 shows that composition of both glass and glass-ceramic samples was close to the theoretical eutectic composition. Additionally, these compositional analyses indicated that the HAZ's compositions were approximately the same as the departing materials.

Next, machined samples were immersed in SBF for two months to assess their bioactivity. Figure 15.21 shows top-view micrographs of the craters machined in the $CaSiO_3$–$Ca_3(PO_4)_2$ eutectic glass and glass-ceramic after this soaking period (a) and (c) respectively, and the

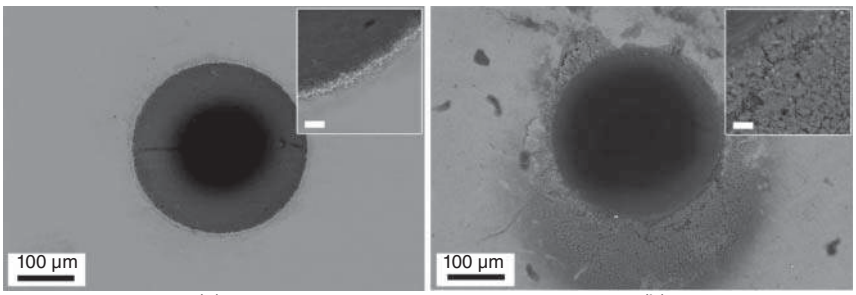

Figure 15.20 Top-view micrographs of the machined glass (a) and glass-ceramic (b). The insets show a detail of the heat affected zone, HAZ, produced in the surroundings of the processed area in the glass and glass-ceramic. The scale bar stands for 10 µm. Source: Sola and Grima [88], Figure 03 [p. 05]/MDPI/CC BY 4.0.

Table 15.6 EDX compositional analysis in at% of both $CaSiO_3$–$Ca_3(PO_4)_2$ glass and glass-ceramic sample.

Sample	Si	P	Ca
Glass (G)	11.00	6.48	18.96
Glass-ceramic (GC)	10.01	6.40	16.89
HAZ (G)	10.89	6.42	18.07
HAZ (GC)	10.71	6.33	16.44

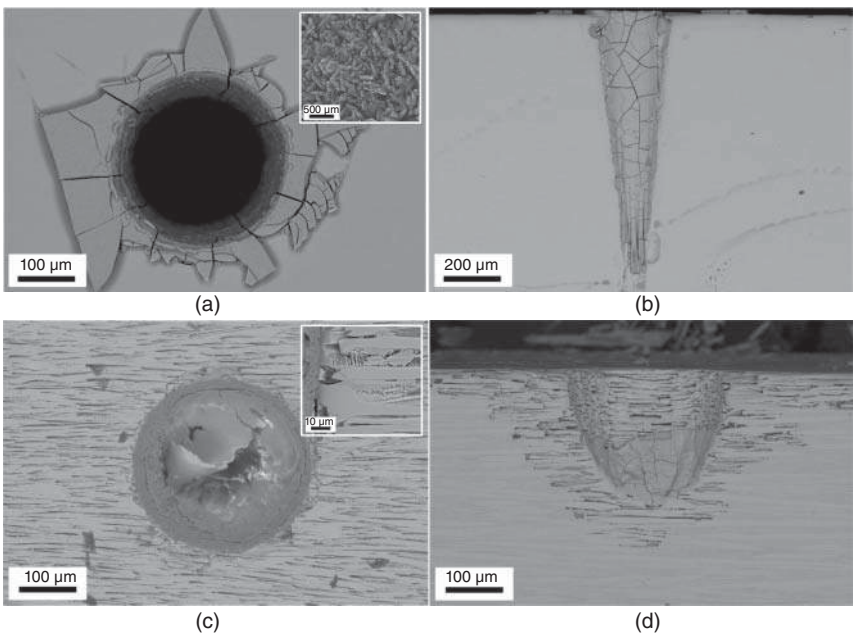

Figure 15.21 Top-view micrographs of the machined glass (a) and glass-ceramic (b) after two months immersed in SBF, and details of the microstructure in the surroundings of the processed area in the glass (c) and glass-ceramic (d). The scale bar in the inset of micrograph (c) is equal to 200 nm. Source: Sola and Grima [88], Figure 04 [p. 06]/MDPI/CC BY 4.0.

Table 15.7 EDX compositional analysis in at% of the microstructure found in the $CaSiO_3-Ca_3(PO_4)_2$ machined glass and glass-ceramic samples.

Sample	Stage	Site of interest	Si	P	Ca
Glass	Soaked	Layer, surface	—	13.92	19.48
Glass	Soaked	Layer, wall	—	12.88	17.45
Glass-ceramic	Non-soaked	Fiber (clear contrast)	5.82	9.74	19.50
Glass-ceramic	Non-soaked	Matrix (dark contrast)	18.20	0.47	15.70
Glass-ceramic	Soaked	Layer, wall	—	12.57	19.08
Glass-ceramic	Soaked	Fiber (clear contrast)	6.10	9.91	20.45

cross-section micrographs of the craters machined in the glass (b) and glass-ceramic (d). Details of the microstructure found in the surroundings of the machined area for the samples are presented in the insets. In the glass sample, a new layer was developed on the surface of the sample and on the walls of the machined hole, as shown in Figure 15.21a,b. This new layer was made up of fibrillar nanocrystals, randomly oriented, as shown in the inset of Figure 15.21a, hence providing porosity to the layer. This new layer showed cracks, not present in the starting glass, which were originated by the difference in the mechanical properties between the layer and the glass. The composition of this layer was characterized by EDX as on the surface as on the wall of the crater revealing that the layer did not contain Si and was rich in P and Ca, with Ca/P ratios of about 1.4 and 1.35 for the layer on the surface and the wall, respectively, Table 15.7.

Concerning the glass-ceramic samples, the microstructure was made up of fibers aligned to the growth direction embedded in matrix, as shown in Figure 15.21c,d. As shown in Table 15.7, the fibers, clear contrast, contained Si, P, and Ca, whereas the matrix, dark contrast, was rich in Si and Ca with low content of P. After the soaking period in SBF, the new layer was found only in the lower part of the walls of the machined hole, Figure 15.21c,d. The composition of this layer was similar to that found in the glass sample, with a Ca/P ratio of 1.5. It is worth of mention that the immersion of the glass-ceramic sample in SBF gave rise to the dissolution of the matrix, rich in Si, whereas the fibers remained unaltered. Likewise, it is also worth noting that although this glass-ceramic was obtained departing from a non-equilibrium state, the mechanisms of dissolution of the Si-rich phase proposed by de Aza et al. still seem to be applicable [22].

15.6 Fabrication of Buried Waveguides in $CaSiO_3-Ca_3(PO_4)_2$ Bioactive Eutectic Glasses by Femtosecond Direct Laser Writing

Femtosecond laser radiation has excellent properties to be used to produce 2D and 3D permanent structures inside transparent optical materials. This laser radiation, when focused through high numerical apertures, induce nonlinear processes in the focal volume, such as multi-photon absorption and avalanche ionization, which lead to localized micro- or sub-micrometric permanent changes [93, 94]. These unique features have allowed the fabrication of diffraction gratings, photonic crystals, beam splitters, waveguides, etc. [94]. In particular, since the first report on the fabrication of femtosecond laser written waveguides in a glass sample by Davis et al. [95], integrated optical waveguides have been produced in glasses, crystals, polycrystalline ceramics and

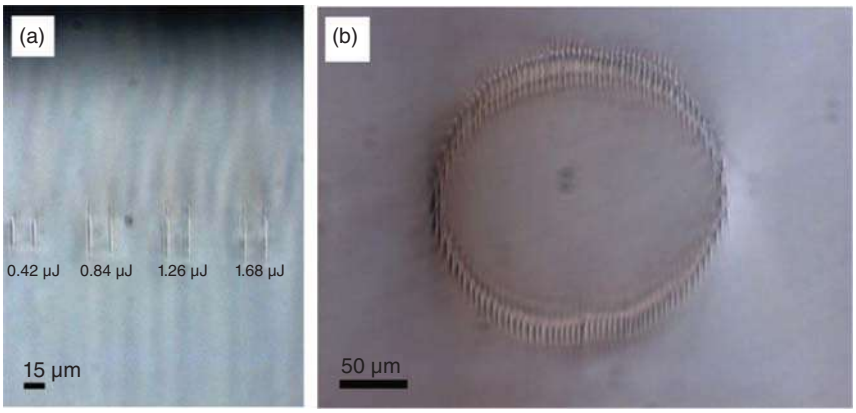

Figure 15.22 Double-line (a) and depressed cladding (b). Waveguides produced in the $CaSiO_3$–$Ca_3(PO_4)_2$ eutectic glass. Source: (a) Sola et al. [115], Figure 3 [p. 291]/with permission from Elsevier; (b) Martínez de Mendívil et al. [118], Figure 1 [p. 02]/with permission from AIP Publishing LLC.

polymers [96–124]. In femtosecond direct laser writing (f-DLW) the ultrashort laser radiation is tightly focused beneath the surface of the sample giving rise to a local refractive index change (Δn) in the focal volume forming the so-called *track* or *filament* [93]. This change can be either positive or negative, depending on the characteristics of the material and on the processing parameters. Optical waveguides are classified into four categories according to the structure generated by the laser radiation: single track, double-line, cladding, and ridge [102].

Double-line and cladding waveguides have been fabricated in Nd-doped $CaSiO_3$–$Ca_3(PO_4)_2$ eutectic glasses by f-DLW using a tunable Ti:Sapphire laser emitting at the central wavelength of 795 nm with 120 fs laser pulses and 1 kHz repetition rate [115, 118]. Double-line waveguides were structured at 150 and 250 μm beneath the surface of the sample, with pulse energy between 0.42 and 1.68 μJ, and scanning speed at 25 and 50 μm/s. The distance between filaments were set at 15 and 20 μm. The cladding waveguides, with a guiding core between 20 and 150 μm, were fabricated at 300 and 600 μm beneath the surface, with 1.44 μJ laser pulse energy. In this case, both the distance between filaments and the scanning speed were set constant at 3 μm and 500 μm/s.

Figure 15.22 shows an example of double-line and cladding waveguides obtained in this glass, (a) and (b) respectively. The dimensions of the laser-induced tracks depend on the laser pulse energy, with lengths from 16 up to 40 μm, as shown in Figure 15.22a. In the cladding structure, the close distance between tracks required lower pulse energy to avoid cracks in the irradiated area.

The near-field intensity distribution in the waveguides was evaluated by a continuous wave He–Ne laser with emission at 633 nm. All double-line waveguides were found to be monomode. The best light confinement conditions were achieved for the waveguides produced at a depth of 150 μm, with a track distance of 15 μm, and a scanning speed of 50 μm/s. In the case of the cladding waveguides, only the ones with the lower core diameter of 20 μm were monomode. Higher diameter gave rise to multimode waveguides. In addition, TE and TM propagation was presented in both types of waveguides. Figure 15.23 shows an example of the near-field distribution intensity of the TE mode in a double-filament waveguide inscribed 150 μm beneath the surface with 15 μm between tracks (a), and cladding waveguides (b) with core diameter of 20 μm (left) and 30 μm (right).

The spectroscopic properties of the waveguides were evaluated by luminescence characterization. It was found that these properties were well preserved in the volume of the waveguides and

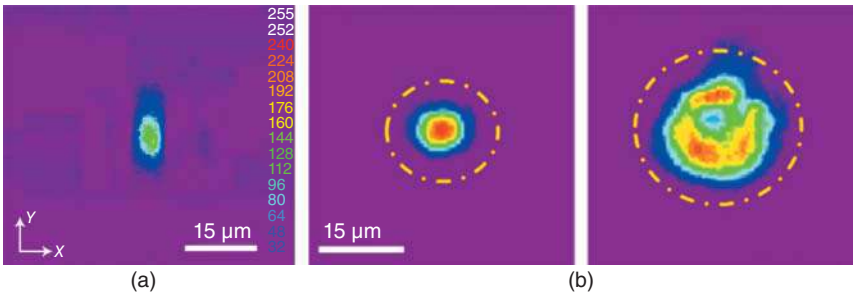

Figure 15.23 Near-field distribution intensity of the TE mode in a double-filament waveguide with 15 µm between tracks (a) and cladding waveguides (b) with core diameter of 20 µm (left) and 30 µm (right). Source: (a) Sola et al. [115], Figure 5 [p. 292]/with permission from Elsevier; (b) Martínez de Mendívil et al. [118], Figure 02 [p. 03]/with permission from AIP Publishing LLC.

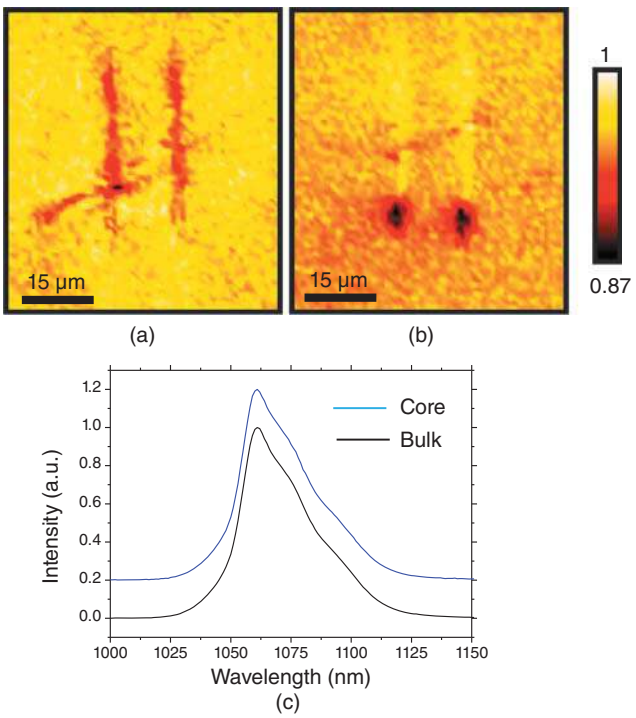

Figure 15.24 Spatial variation of the Nd^{3+} fluorescence intensity for a double-filament waveguide at room temperature (a) and at 550 °C (b), and emission of Nd^{3+} at 1060 nm under excitation at 808 nm for a 20 µm-diameter depressed cladding waveguide in the core of the waveguide and in the bulk (c). Source: (a) Sola et al. [115], Figure 8 [p. 293]/with permission from Elsevier.

that an annealing treatment at high temperature recombined the damaged produced in the irradiated areas, resulting in a worse light confinement. Fluorescence lifetimes were found to be around 240–250 µs. Luminescence spectra and µL map of the $^4F_{3/2} \rightarrow {}^4I_{11/2}$ transition in the bulk and in the waveguide's volume pointed out no significant modifications, as shown in Figure 15.24.

The refractive index modification was estimated accounting the refractive index distribution generated by femtosecond laser pulses in double-filament waveguides [125, 126], resulting in a

$\Delta n \sim 5 \times 10^{-3}$. This value was similar to those previously reported for other waveguides inscribed by femtosecond laser writing, such as Nd:YAG ceramics, Nd:YVO_4 and fused silica.

15.7 Conclusions and Outlook

Since the discovery of the first bioactive glass in the late 1960s by Hench et al., the development of bioactive glasses has been a field of intense research for biomedical applications. Among glass chemical compositions, the eutectic composite $CaSiO_3$–$Ca_3(PO_4)_2$ is particularly interesting because when implanted into a living body or soaked in SBF an *in situ* a porous HA-like structure is developed.

In this chapter, fabrication, characterization, and processing of $CaSiO_3$–$Ca_3(PO_4)_2$ eutectic glass-ceramics and glasses by using laser radiation have been revised. As the fabrication method, the fundamentals of the LFZ technique have been reviewed. This directional solidification technique delivers high axial and radial thermal gradients in the solidification front, providing control on the final microstructure so that it is possible to fabricate fiber-shaped single crystals, ceramics, glass-ceramics, and glasses, directly from ceramic precursors as well as incorporating doping ions.

Directionally solidified $CaSiO_3$–$Ca_3(PO_4)_2$ eutectic glass-ceramics and glasses doped with Nd_2O_3, Er_2O_3, and Eu_2O_3 were fabricated by the LFZ technique, obtaining novel microstructures nonreported in this system so far. Crystalline phases corresponded to Ca_2SiO_4 and apatite-like structures. In addition, the Ca_2SiO_4 phase showed high reactivity when soaked in SBF, so that the SBF dissolved this crystalline phase giving rise to a porous layer in which the apatite-like structure phase remained unaltered in the sample after the immersion period. Rare-earth ions were used as optical probes. It was shown that the differences among the spectral features allowed distinguishing between crystalline and amorphous environments for the rare-earth ions and to correlate the spectroscopic properties with the microstructure of these eutectics. These results show the potential applications of rare-earth as multicolor bioprobes and biosensors in biomedical applications.

LIBS was used as complementary analytical tool to monitor the formation of HA on the surface of a directionally solidified $CaSiO_3$–$Ca_3(PO_4)_2$ eutectic glass. The glass was soaked in SBF for a period of time of one month. LIBS spectra acquired on the sample surface showed that Si (I) emission lines were not present in the layer developed after the immersion period. Micro-Raman spectroscopy and SEM-EDX analyses confirmed that this layer corresponded to a HA crystalline phase.

Laser machining with short laser radiation, in the nanosecond range, was assessed as first approach to generate 3D interconnected porous structure in $CaSiO_3$–$Ca_3(PO_4)_2$ eutectic glasses and glass-ceramics manufactured by the LFZ method. The laser-structured samples were immersed in SBF for two months. In the glass samples, the HA layer was developed on the surface of the whole sample, including the laser-machined areas. In the glass-ceramic samples, the HA layer was found only in the surface of the walls of the machined hole. The soaking in SBF produced the dissolution of the Si-rich matrix giving rise to a porous fibrillar structure so that the laser machined holes enhanced the sample becoming a 3D porous structure.

Femtosecond Direct Writing was used for the fabrication of double-filament and depressed cladding waveguides in Nd-doped $CaSiO_3$–$Ca_3(PO_4)_2$ eutectic glasses. Both types of waveguides supported TE and TM polarization guiding under illumination of cw He–Ne laser radiation. All double-filament waveguides were found to be monomode whereas for cladding waveguides, only the one with the smallest core, 20 μm, presented monomode transmitted light. In addition, it was

shown that spectroscopic properties were well preserved in the volume of the waveguides. Finally, the refractive index modification, Δn, was estimated in 5×10^{-3}, in the same range of previously reported works by this technique.

As future scope, taking advantage of the exceptional characteristics of the LFZ technique to explore new composites, new multiphase bioactive ceramics have been recently developed in the $CaO–SiO_2–MgO–P_2O_5$ system. Microstructural features, bioactivity studies, and suitability as porous scaffold are currently under research.

Acknowledgments

D.J. Sola is indebted to Professor J.I. Peña from the Universidad de Zaragoza for the generous support that he has provided to him during his scientific career, sharing with him his extensive knowledge in materials science and materials laser processing. Likewise, he expresses his deep gratitude for the values that he has transmitted to him as a scientist and as a human being. D.J. Sola also gratefully acknowledge Professor G. Lifante from the Universidad Autónoma de Madrid for the long-standing inspiring and pleasant cooperation. Sincere thanks are also expressed to the Professors. P. Pena and A.H. de Aza from the Instituto de Cerámica y Vidrio and to Dr. J.R. Vazquez de Aldana from the Universidad de Salamanca for their significant contributions and helpful discussions. Financial support from BSH, JAEDOC086 fellowship, PIT2 program of the Universidad de Murcia and Fundación Séneca grant No 20647/JLI/18 are also acknowledged.

References

1 Miguez-Pacheco, V., Hench, L.L., and Boccaccini, A. (2015). Bioactive glasses beyond bone and teeth: emerging applications in contact with soft tissues. *Acta Biomaterialia* 13: 1–15.
2 Kaur, G., Pandey, O.P., Singh, K. et al. (2014). A review of bioactive glasses: their structure, properties, fabrication, and apatite formation. *Journal of Biomedical Materials Research Part A* 102: 254–274.
3 Boccaccini, A.R., Brauer, D.S., and Hupa, L. (2017). *Bioactive Glasses: Fundamentals, Technology and Applications*. Cambridge: The Royal Society of Chemistry.
4 Hench, L.L. (2006). The story of Bioglass. *Journal of Materials Science – Materials in Medicine* 17: 967–978.
5 Williams, D.F. (1987). *Definitions in Biomaterials*. Amsterdam: Elsevier.
6 Kokubo, T. and Takadama, H. (2006). How useful is SBF in predicting in vivo bone bioactivity? *Biomaterials* 27: 2907–2915.
7 Kokubo, T., Kushitani, H., Sakka, S. et al. (1990). Solutions able to reproduce in vivo surface-structure changes in bioactive glass-ceramic A-W. *Journal of Biomedical Materials Research* 24: 721–734.
8 Bohner, M. and Lemaitre, J. (2009). Can bioactivity be tested in vitro with SBF solution? *Biomaterials* 30: 2175–2179.
9 Witte, F., Kaese, V., Haferkamp, H. et al. (2005). In vivo corrosion of four magnesium alloys and the associated bone response. *Biomaterials* 26: 3557–3563.
10 Bandyopadhyay, A., Bernard, S., Xue, W., and Bose, S. (2006). Calcium phosphate-based resorbable ceramics: influence of MgO, ZnO, and SiO_2 dopants. *Journal of the American Ceramic Society* 89: 2675–2688.

11 Ohura, K., Bohner, M., Hardouin, P. et al. (1996). Resorption of and bone formation from, new β-tricalcium phosphate-monocalcium phosphate cements: an in vivo study. *Journal of Biomedical Materials Research* 30: 1993–2000.

12 Ohgushi, H., Dohi, Y., Yoshikawa, T. et al. (1996). Osteogenic differentiation of cultured marrow stromal stem cells on the surface of bioactive glass ceramics. *Journal of Biomedical Materials Research* 32: 341–348.

13 Lobel, K.D. and Hench, L.L. (1996). In-vitro protein interactions with a bioactive gel-glass. *Journal of Sol-Gel Science and Technology* 7: 69–76.

14 Kotani, S., Fujita, Y., Kitsugi, T. et al. (1991). Bone bonding mechanisms of β-tricalcium phosphate. *Journal of Biomedical Materials Research* 25: 1303–1315.

15 Chen, Q., Zhu, C., and Thouas, G.A. (2012). Progress and challenges in biomaterials used for bone tissue engineering: bioactive glasses and elastomeric composites. *Progress in Biomaterials* 1: 1–12.

16 Lu, Z.P. and Liu, C.T. (2004). A new approach to understanding and measuring glass formation in bulk amorphous materials. *Intermetallics* 12: 1035–1043.

17 Hölland, W. and Beall, G.H. (2012). *Glass-Ceramic Technology*. Hoboken, NJ: Wiley.

18 Filho, O.P., Latorre, G.P., and Hench, L.L. (1996). Effect of crystallization on apatite-layer formation of bioactive glass 45S5. *Journal of Biomedical Materials Research* 30: 509–514.

19 Li, P., Yang, Q., Zhang, F., and Kokubo, T. (1992). The effect of residual glassy phase in a bioactive glass-ceramic on the formation of its surface apatite layer in vitro. *Journal of Materials Science – Materials in Medicine* 3: 452–456.

20 de Aza, P.N., Guitian, F., and de Aza, S. (1997). Bioeutectic: a new ceramic material for human bone replacement. *Biomaterials* 18: 1285–1291.

21 Yong, D. and Zhonghon, J. (1991). Prediction of glass formation regions by calculation of eutectic using ideal-solution model. *Journal of the American Ceramic Society* 74: 2295–2298.

22 de Aza, P.N., Guitian, F., and de Aza, S. (1998). A new bioactive material which transforms in situ into hydroxyapatite. *Acta Materialia* 46: 2541–2549.

23 de Aza, P.N., de Aza, A.H., and de Aza, S. (2005). Crystalline bioceramic materials. *Boletin de la Sociedad Espanola de Ceramica y Vidrio* 44: 135–145.

24 Magallanes-Perdomo, M., Pena, P., de Aza, P.N. et al. (2009). Devitrification studies of wollastonite-tricalcium phosphate eutectic glass. *Acta Biomaterialia* 5: 3057–3066.

25 Magallanes-Perdomo, M., Luklinska, Z.B., de Aza, A.H. et al. (2011). Bone-like forming ability of apatite-wollastonite glass ceramic. *Journal of the European Ceramic Society* 31: 1549–1561.

26 Carrodeguas, R.G., de Aza, A.H., Jimenez, J. et al. (2008). Preparation and in vitro characterization of wollastonite doped tricalcium phosphate bioceramics. *Key Engineering Materials* 361–363: 237–240.

27 de Aza, A.H., Velasquez, P., Alemany, M.I. et al. (2007). In situ bone-like apatite formation from a Bioeutectic® ceramic in SBF dynamic flow. *Journal of the American Ceramic Society* 90: 1200–1207.

28 de Aza, P.N., Peña, J.I., Luklinska, Z.B., and Meseguer-Olmo, L. (2014). Bioeutectic® ceramics for biomedical application obtained by laser floating zone method. In vivo evaluation. *Materials* 7: 2395–2410.

29 Pardo, J.A., Peña, J.I., Merino, R.I. et al. (2002). Spectroscopic properties of Er^{3+} and Nd^{3+} doped glasses with $0.8CaSiO_3$–$0.2Ca_3(PO_4)_2$ eutectic composition. *Journal of Non-Crystalline Solids* 298: 23–31.

30 Balda, R., Fernández, J., Iparraguerri, I. et al. (2009). Broadband laser tunability of Nd^{3+} ions in $0.8CaSiO_3$–$0.2Ca_3(PO_4)_2$ eutectic glass. *Optics Express* 17: 4382.

31 Balda, R., Merino, R.I., Peña, J.I. et al. (2009). Laser spectroscopy of Nd^{3+} ions in glasses with the $0.8CaSiO_3$–$0.2Ca_3(PO_4)_2$ eutectic composition. *Optical Materials* 31: 1319–1322.

32 Sola, D., Balda, R., Peña, J.I., and Fernandez, J. (2012). Site-selective laser spectroscopy of Nd^{3+} ions in $0.8CaSiO_3$–$0.2Ca_3(PO_4)_2$ biocompatible eutectic glass-ceramics. *Optics Express* 20: 10701–10711.

33 Sola, D., Balda, R., Al-Saleh, M. et al. (2013). Time-resolved fluorescence line-narrowing of Eu^{3+} in biocompatible eutectic glass-ceramics. *Optics Express* 21: 6561–6571.

34 Poplawsky, R.P. and Tomas, J.E. (1960). Floating zone crystals using an arc image furnace. *Review of Scientific Instruments* 31: 1303–1309.

35 Feigelson, R.S. (1985). The laser-heated pedestal growth method: to powerful tool in the search for laser high performance crystals. *Springer Series in Optical Sciences* 47: 129–142.

36 Fejer, M.M., Nightingale, J.L., Magel, G.A., and Byer, R.L. (1984). Laser-heated miniature pedestal growth apparatus for single-crystal optical fibers. *Review of Scientific Instruments* 55: 1791–1796.

37 Llorca, J. and Orera, V.M. (2006). Directionally solidified eutectic ceramic oxides. *Progress in Materials Science* 51: 711–809.

38 Sola, D., Conejos, D., De Mendivil, J.M. et al. (2015). Directional solidification, thermo-mechanical and optical properties of $(Mg_xCa_{1-x})_3Al_2Si_3O_{12}$ glasses doped with Nd^{3+} ions. *Optics Express* 20: 26356–26358.

39 Sola, D. and Peña, J.I. (2012). Laser machining of Al_2O_3–ZrO_2 ($3\%Y_2O_3$) eutectic composite. *Journal of the European Ceramic Society* 32: 807–814.

40 Brice, J.C. (1968). Analysis of the temperature distribution in pulled crystals. *Journal of Crystal Growth* 2: 395–401.

41 Ester, F.J., Sola, D., and Peña, J.I. (2008). Thermal stresses in the Al_2O_3–$ZrO_2(Y_2O_3)$ eutectic composite during the growth by the laser floating zone technique. *Boletin de la Sociedad Espanola de Ceramica y Vidrio* 47: 352–357.

42 Sola, D., Ester, F.J., Oliete, P.B., and Peña, J.I. (2011). Study of the stability of the molten zone and the stresses induced during the growth of Al_2O_3–$Y_3Al_5O_{12}$ eutectic composite by the laser floating zone technique. *Journal of the European Ceramic Society* 31: 1211–1218.

43 Oliete, P.B. and Peña, J.I. (2007). Study of the gas inclusions in $Al_2O_3/Y_3Al_5O_{12}$ and $Al_2O_3/Y_3Al_5O_{12}/ZrO_2$ eutectic fibers grown by laser floating zone. *Journal of Crystal Growth* 304: 514–519.

44 Reyes Ardila, D., Barbosa, L.B., and Andreeta, J.P. (2001). Bifocal spherical mirror for laser processing. *Review of Scientific Instruments* 72: 4415–4418.

45 Tong, L. (2000). Growth of high-quality Y_2O_3–ZrO_2 single-crystal optical fibers for ultra-high-temperature fiber-optic sensors. *Journal of Crystal Growth* 217: 281–286.

46 Kennard, F.L., Bradt, R.C., and Stubican, V.S. (1973). Eutectic solidification of MgO–$MgAl_2O_4$. *Journal of the American Ceramic Society* 56: 566.

47 Rudolph, P. and Fukuda, T. (1999). Fiber crystal growth from the melt. *Crystal Research and Technology* 34: 3.

48 Llorca, J., Pastor, J.Y., Poza, P. et al. (2004). Influence of the Y_2O_3 content and temperature on the mechanical properties of melt-grown Al_2O_3–ZrO_2 eutectics. *Journal of the American Ceramic Society* 87: 633–639.

49 Larrea, A., Orera, V.M., Merino, R.I., and Peña, J.I. (2005). Microstructure and mechanical properties of Al_2O_3–YSZ and Al_2O_3–YAG directionally solidified eutectic plates. *Journal of the European Ceramic Society* 25: 1419–1429.

50 Oliete, P.B., Peña, J.I., Larrea, A. et al. (2007). Ultra-high-strength nanofibrillar Al_2O_3–YAG–YSZ eutectics. *Advanced Materials* 19: 2313–2318.

51 Mesa, M.C., Oliete, P.B., Orera, V.M. et al. (2011). Microstructure and mechanical properties of $Al_2O_3/Er_3Al_5O_{12}$ eutectic rods grown by the laser-heated floating zone method. *Journal of the European Ceramic Society* 31: 1241–1250.

52 Reyes-Coronado, A., Acosta, M.F., Merino, R.I. et al. (2012). Self-organization approach for THz polaritonic metamaterials. *Optics Express* 20: 14663–14682.

53 Mesa, M.C., Oliete, P.B., Merino, R.I., and Orera, V.M. (2013). Optical absorption and selective thermal emission in directionally solidified Al_2O_3–$Er_3Al_5O_{12}$ and Al_2O_3–$Er_3Al_5O_{12}$–ZrO_2 eutectics. *Journal of the European Ceramic Society* 33: 2587–2596.

54 Sola, D., Conejos, D., de Mendivil, J.M. et al. (2015). Directional solidification, thermo-mechanical and optical properties of $(Mg_xCa_{1-x})_3Al_2Si_3O_{12}$ glasses doped with Nd^{3+} ions. *Optics Express* 23: 26356–26368.

55 Arias-Egido, E., Sola, D., Pardo, J.A. et al. (2016). On the control of optical transmission of aluminosilicate glasses manufactured by the laser floating zone technique. *Optical Materials Express* 6: 2413–2421.

56 Sola, D., Oliete, P.B., Merino, R.I., and Peña, J.I. (2019). Directionally solidified Ni doped MgO–MgSZ eutectic composites for thermophotovoltaic devices. *Journal of the European Ceramic Society* 39: 1206–1213.

57 Moshtaghioun, B.M. and Peña, J.I. (2019). Non-Hall-Petch hardness dependence in ultrafine fibrous $MgAl_2O_4$–MgO eutectic ceramics fabricated by the laser-heated floating zone (LFZ) method. *Journal of the European Ceramic Society* 39: 3208–3212.

58 Moshtaghioun, B.M., Cumbrera, F.L., Gómez-García, D., and Peña, J.I. (2019). Elusive super-hard B_6C accessible through the laser-floating zone method. *Scientific Reports* 9: 13340.

59 Moshtaghioun, B.M., Peña, J.I., and Merino, R.I. (2020). Medium infrared transparency of MgO–$MgAl_2O_4$ directionally solidified eutectics. *Journal of the European Ceramic Society* 40: 1703–1708.

60 Sola, D., Miguel, A., Arias-Egido, E., and Peña, J.I. (2021). Spectroscopy and near-infrared to visible upconversion of Er^{3+} ions in aluminosilicate glasses manufactured with controlled optical transmission. *Applied Sciences* 11: 1–10.

61 Weber, M.J. (1990). Science and technology of laser glass. *Journal of Non-Crystalline Solids* 123: 208–222.

62 Jacobs, R.R. and Weber, M.J. (1975). Dependence of the $^4F_{3/2} \rightarrow {}^4I_{11/2}$ induced-emission cross section for Nd^{3+} on glass composition. *IEEE Journal of Quantum Electronics* 12: 102–111.

63 Uhlmann, E.V., Weinberg, M.C., Kreidl, N.J. et al. (1994). Spectroscopic properties of rare-earth-doped calcium-aluminate-based glasses. *Journal of Non-Crystalline Solids* 178: 15–22.

64 Baesso, M.L., Bento, A.C., Miranda, L.C.M. et al. (2000). Rare-earth doped low silica calcium aluminosilicate glasses for near and mid infrared applications. *Journal of Non-Crystalline Solids* 276: 8–18.

65 Cascales, C., Balda, R., Fernández, J. et al. (2006). Site selective spectroscopy of Eu^{3+} in heavy-metal oxide glasses. *Journal of Non-Crystalline Solids* 352: 2448–2451.

66 Cascales, C., Balda, R., Jubera, V. et al. (2008). Optical spectroscopic study of Eu^{3+} crystal field sites in $Na_3La_9O_3(BO_3)_8$ crystal. *Optics Express* 16: 2653–2661.

67 Cascales, C., Balda, R., Fernández, J. et al. (2009). Fluorescence line narrowing spectroscopy of Eu^{3+} in TeO_2–TiO_2–Nb_2O_5 glass. *Optical Materials* 31: 1092–1095.

68 Jackson, K.A. and Hunt, J.D. (1966). Lamellar and rod eutectic growth. *Transactions of the Metallurgical Society of AIME* 236: 1129–1142.

69 Gou, Z., Chang, J., and Zhai, W. (2005). Preparation and characterization of novel bioactive dicalcium silicate ceramics. *Journal of the European Ceramic Society* 25: 1507–1514.

70 Cremers, D.A. and Radziemski, L.J. (2013). *Handbook of Laser-Induced Breakdown Spectroscopy*. Oxford, UK: Wiley Blackwell.

71 Hahn, D.W. and Omenetto, N. (2010). Laser-induced breakdown spectroscopy (LIBS), Part I: review of basic diagnostics and plasma–particle interactions: still-challenging issues within the analytical plasma community. *Applied Spectroscopy* 64: 335A–366A.

72 Hahn, D.W. and Omenetto, N. (2012). Laser-induced breakdown spectroscopy (LIBS), Part II: review of instrumental and methodological approaches to material analysis and applications to different fields. *Applied Spectroscopy* 66: 347–419.

73 Miziolek, A.W., Palleschi, V., and Schechter, I. (2005). *Laser-Induced Breakdown Spectroscopy (LIBS). Fundamentals and Applications*. Cambridge, UK: Cambridge University Press.

74 Parigger, C.G. (2013). Atomic and molecular emissions in laser-induced breakdown spectroscopy. *Spectrochimica Acta Part B: Atomic Spectroscopy* 79–80: 4–16.

75 Paules, D., Hamida, S., Lasheras, R.J. et al. (2018). Characterization of natural and treated diatomite by laser-induced breakdown spectroscopy (LIBS). *Microchemical Journal* 137: 1–7.

76 Sola, D., Paulés, D., Grima, L., and Anzano, J. (2017). Laser-induced breakdown spectroscopy (LIBS) for monitoring the formation of hydroxyapatite porous layers. *Materials* 10: 1375.

77 Tariq, U., Haider, Z., Hussain, R. et al. (2017). LIBS analysis of hydroxyapatite extracted from bovine bone for Ca/P ratio measurements. *International Conference on Plasma Science and Applications* 1824: 030027-1–030027-7.

78 Hench, L.L., Splinter, R.J., Greenle, T.K., and Allen, W.C. (1971). Bonding mechanisms at the interface of ceramic prosthetic materials. *Journal of Biomedical Materials Research* 2: 171–141.

79 Hench, L.L. and Wilson, J. (2013). *An Introduction to Bioceramics*. London, UK: Imperial College Press.

80 Lu, J.X., Flautre, B., Anselme, K. et al. (1999). Role of interconnections in porous bioceramics on bone recolonization in vitro and in vivo. *Journal of Materials Science – Materials in Medicine* 10: 111–120.

81 LeGeros, R.Z., Parsons, J.R., Daculsi, G. et al. (1988). Significance of porosity and physical chemistry of calcium phosphate ceramics biodegradation-bioresorption. *Annals of the New York Academy of Sciences* 532: 268–271.

82 Von Doernberg, M.C., von Rechenberg, B., Bohner, M. et al. (2006). In vivo behaviour of calcium phosphate scaffolds with four different pore sizes. *Biomaterials* 27: 5186–5198.

83 Bungo, O., Mitsuru, T., Shunsuke, F. et al. (2006). Pore throat size and connectivity determine bone and tissue ingrowth into porous implants: three-dimensional micro-CT based structural analyses of porous bioactive titanium implants. *Biomaterials* 27: 5892–5900.

84 Zhu, Y. and Kaskel, S. (2009). Comparison of the in vitro bioactivity and drug release property of mesoporous bioactive glasses (MBGs) and bioactive glasses (BGs) scaffolds. *Microporous and Mesoporous Materials* 118: 176–182.

85 Cunningham, E., Dunne, N., Walker, G. et al. (2010). Hydroxyapatite bone substitutes developed via replication of natural marine sponges. *Journal of Materials Science – Materials in Medicine* 21: 2255–2261.

86 Minaberry, Y. and Jobbágy, M. (2011). Macroporous bioglass scaffolds prepared by coupling sol gel with freeze drying. *Chemistry of Materials* 23: 2327–2332.

87 Perez, R.A. and Mestres, G. (2016). Role of pore size and morphology in musculo-skeletal tissue regeneration. *Materials Science and Engineering C* 61: 922–939.

88 Sola, D. and Grima, L. (2018). Laser machining and in vitro assessment of wollastonite-tricalcium phosphate eutectic glasses and glass-ceramics. *Materials* 11: 125.

89 Sola, D., Escartín, A., Cases, R., and Peña, J.I. (2011). Laser ablation of advanced ceramics and glass-ceramic materials: reference position dependence. *Applied Surface Science* 257: 5413–5419.

90 Sola, D. and Peña, J.I. (2013). Laser machining and functional applications of glass-ceramic materials. *International Journal of Applied Ceramic Technology* 10: 484–491.

91 Sola, D. and Peña, J.I. (2013). Study of the wavelength dependence in laser ablation of advanced ceramics and glass-ceramic materials in the nanosecond range. *Materials* 6: 5302–5313.

92 Bäuerler, D. (2000). *Laser Processing and Chemistry*. Heidelberg, Germany: Springer-Verlag.

93 Misawa, H. and Juodkazis, S. (2006). *3D Laser Microfabrication: Principles and Applications*. Weinheim, Germany: Wiley-VCH.

94 Osellame, R., Cerullo, G., and Ramponi, R. (2012). *Femtosecond Laser Micromachining: Photonic and Microfluidic Devices in Transparent Materials*. Berlin, Germany: Springer.

95 Davis, K.M., Miura, K., Sugimoto, N., and Hirao, K. (1996). Writing waveguides in glass with a femtosecond laser. *Optics Letters* 21: 1729–1731.

96 Nolte, S., Will, M., Burghoff, J., and Tuennermann, A. (2003). Femtosecond waveguide writing: a new avenue to three-dimensional integrated optics. *Applied Physics A* 7: 109–111.

97 Zhou, G. and Gu, M. (2006). Direct optical fabrication of three-dimensional photonic crystals in a high refractive index $LiNbO_3$ crystal. *Optics Letters* 31: 2783–2785.

98 Psaila, N.D., Thomson, R.R., Bookey, H.T. et al. (2007). Er:Yb-doped oxyfluoride silicate glass waveguide amplifier fabricated using femtosecond laser inscription. *Applied Physics Letters* 90: 131102.

99 Silva, W.F., Jacinto, C., Benayas, A. et al. (2010). Femtosecond-laser-written, stress-induced Nd:YVO_4 waveguides preserving fluorescence and Raman gain. *Optics Letters* 35: 916–918.

100 Benayas, A., Silva, W.F., Rodenas, A. et al. (2011). Ultrafast laser writing of optical waveguides in ceramic Yb:YAG: a study of thermal and non-thermal regimes. *Applied Physics A* 104: 301–309.

101 Sola, D., Escartin, A., Cases, R., and Peña, J.I. (2011). Crystal growth induced by Nd:YAG laser irradiation in patterning glass ceramic substrates with dots. *Optical Materials* 33: 728–734.

102 Chen, F. and Vázquez de Aldana, J.R. (2014). Optical waveguides in crystalline dielectric materials produced by femtosecond-laser micromachining. *Laser & Photonics Reviews* 8: 251–275.

103 McMillen, B., Zhang, B., Chen, K.P. et al. (2012). Ultrafast laser fabrication of low-loss waveguides in chalcogenide glass with 0.65 dB/cm loss. *Optics Letters* 37: 1418–1420.

104 Morris, J.M., Mackenzie, M.D., Petersen, C.R. et al. (2018). $Ge_{22}As_{20}Se_{58}$ glass ultrafast laser inscribed waveguides for mid-IR integrated optics. *Optical Materials Express* 8: 1001–1011.

105 Lv, J., Cheng, Y., Lu, Q. et al. (2016). Femtosecond laser written optical waveguides in z-cut MgO:$LiNbO_3$ crystal: fabrication and optical damage investigation. *Optical Materials* 57: 169–173.

106 Morris, J., Stevenson, N.K., Bookey, H.T. et al. (2017). 1.9 μm waveguide laser fabricated by ultrafast laser inscription in Tm:Lu_2O_3 ceramic. *Optics Express* 25: 14910–14917.

107 Ren, Y., Zhang, L., Xing, H. et al. (2018). Cladding waveguide splitters fabricated by femtosecond laser inscription in Ti:Sapphire crystal. *Optics and Laser Technology* 103: 82–88.

108 Li, R., Nie, W., Lu, Q. et al. (2017). Femtosecond-laser-written superficial cladding waveguides in Nd:CaF_2 crystal. *Optics and Laser Technology* 92: 163–167.

109 Kifle, E., Mateos, X., Vázquez De Aldana, J.R. et al. (2017). Femtosecond-laser-written Tm:KLu(WO_4)$_2$ waveguide lasers. *Optics Letters* 42: 1169–1172.

110 Nguyen, H.-D., Ródenas, A., De Aldana, J.R.V. et al. (2016). Heuristic modelling of laser written mid-infrared $LiNbO_3$ stressed-cladding waveguides. *Optics Express* 24: 7777–7791.

111 Thorburn, F., Lancaster, A., McDaniel, S. et al. (2017). 5.9 GHz graphene based q-switched modelocked mid-infrared monolithic waveguide laser. *Optics Express* 25: 26166–26174.

112 Macdonald, J.R., Thomson, R.R., Beecher, S.J. et al. (2010). Ultrafast laser inscription of near-infrared waveguides in polycrystalline ZnSe. *Optics Letters* 35: 4036–4038.

113 Burghoff, J., Nolte, S., and Tunnermann, A. (2007). Origins of waveguiding in femtosecond laser-structured $LiNbO_3$. *Applied Physics A* 89: 127–132.

114 Zhang, C., Dong, N., Yang, J. et al. (2011). Channel waveguide lasers in Nd:GGG crystals fabricated by femtosecond laser inscription. *Optics Express* 19: 12503–12508.

115 Sola, D., de Mendibil, J.M., de Aldana, J.R.V. et al. (2013). Stress-induced buried waveguides in the 0.8$CaSiO_3$–0.2$Ca_3(PO_4)_2$ eutectic glass doped with Nd^{3+} ions. *Applied Surface Science* 278: 289–294.

116 Zhang, Y.J., Zhang, G.D., Bai, J. et al. (2017). Double line and tubular depressed cladding waveguides written by femtosecond laser irradiation in PTR glass. *Optical Materials Express* 7: 2626–2635.

117 Okhrimchuk, A.G., Shestakov, A.V., Khrushchev, I., and Mitchell, J. (2005). Depressed cladding, buried waveguide laser formed in a YAG:Nd^{3+} crystal by femtosecond laser writing. *Optics Letters* 30: 2248–2250.

118 Martínez de Mendívil, J., Sola, D., Vázquez de Aldana, J.R. et al. (2015). Ultrafast direct laser writing of cladding waveguides in the 0.8$CaSiO_3$–0.2$Ca_3(PO_4)_2$ eutectic glass doped with Nd^{3+} ions. *Journal of Applied Physics* 117: 4906963.

119 Okhrimchuk, A., Mezentsev, V., Shestakov, A., and Bennion, I. (2012). Low loss depressed cladding waveguide inscribed in YAG:Nd single crystal by femtosecond laser pulses. *Optics Express* 20: 3832–3843.

120 An, Q., Jia, Y., Liu, H. et al. (2014). Ultrafast laser inscribed cladding waveguides in Nd:YAG crystal for mid-infrared wavelength. *Optics and Laser Technology* 56: 382–386.

121 Li, L., Nie, W., Li, Z. et al. (2017). All-laser-micromachining of ridge waveguides in $LiNbO_3$ crystal for mid-infrared band applications. *Scientific Reports* 7: 7034.

122 Martínez De Mendívil, J., Hoyo, J., Solis, J. et al. (2015). Channel waveguide fabrication in $KY(WO_4)_2$ combining liquid-phase-epitaxy and beam-multiplexed femtosecond laser writing. *Optical Materials* 45: 304–309.

123 Sola, D. and Cases, R. (2020). High-repetition-rate femtosecond laser processing of acrylic intra-ocular lenses. *Polymers* 12: 242.

124 Sola, D., de Aldana, J.R.V., and Artal, P. (2020). The role of thermal accumulation on the fabrication of diffraction gratings in ophthalmic PHEMA by ultrashort laser direct writing. *Polymers* 12: 2965.

125 Ródenas, A., Torchia, G.A., Lifante, G. et al. Refractive index change mechanisms in femtosecond laser written ceramic Nd:YAG waveguides: micro-spectroscopy experiments and beam propagation calculations. *Applied Physics B* 95: 85–96.

126 Ródenas, A., Maestro, L.M., Ramírez, M.O. et al. (2009). Anisotropic lattice changes in femtosecond laser inscribed Nd^{3+}:MgO:$LiNbO_3$ optical waveguides. *Journal of Applied Physics* 106:013110.

16

Molecular Dynamics (MD) Simulations of Bioactive Glasses and Glass-Ceramics

Maziar Montazerian[1], Collin Wilkinson[2], and John C. Mauro[2]

[1]*Department of Materials Engineering, Northeastern Laboratory for Evaluation and Development of Biomaterials (CERTBIO), Federal University of Campina Grande, Campina Grande, Brazil*
[2]*Department of Materials Science and Engineering, The Pennsylvania State University, University Park, PA, USA*

16.1 Introduction

Theoretical and computational modeling is becoming ubiquitous in materials research. Modeling can enormously reduce the timescales required for the translation of basic research in advanced materials to manufacturing. Therefore, different governmental initiatives have been launched to improve current modeling capabilities and increase industrial competitiveness [1, 2]. Various programs have initiated collaboration between materials scientists with experimental and theoretical expertise and computer scientists in this framework. Therefore, the financial support, the improvement of codes, algorithms, methods, and the access to extensive computational facilities made possible by governmental actions and the research community's cooperation to tackle several modeling issues in materials science [1–3]. The appropriate choice of modeling technique depends on the nature of the property under investigation, the availability of high-quality data, and the level of physical understanding governing the materials' relevant structure–property relationships. Often, multiple modeling approaches at different levels can give a more comprehensive picture of the properties of interest. Model predictions must, of course, be confirmed through experimental validation. Models incorporating a greater level of physical understanding may offer a better ability to extrapolate into new composition spaces compared to purely empirical models [1–5].

In glass science, conventional experimental approaches to characterizing glass properties are quite time-consuming and expensive. Recently, modeling approaches have emerged as a significant research activity in glass science [1, 4, 5]. An extensive set of modeling techniques are available, from purely empirical to those incorporating detailed fundamental physics. Molecular dynamics (MD) simulations have proven to be especially helpful for understanding the atomic structure and properties of new glass compositions, for example, bioactive glasses (BGs) [4, 5]. These biomaterials, which were invented by Larry Hench [6] and are capable to selectively stimulate a favorable body response, exhibit unique properties including:

- Bone-bonding ability [7–9],
- Bone regeneration [10, 11],
- Regeneration of soft tissues [12–17],

Bioactive Glasses and Glass-Ceramics: Fundamentals and Applications, First Edition.
Edited by Francesco Baino and Saeid Kargozar.

- Bactericide [18],
- Therapeutic ion release [19],
- Drug delivery [20–23],
- Functionalizing resilient/tough bioactive implants (e.g. glass-ceramics) [24, 25], coatings [26], composites [27], and hybrids [28, 29].

MD simulation is the most studied method for atomistic simulation of BGs. The glass dissolution controlling biological activity of glasses happens at the typical size and timescales of a few angstroms. Elementary dynamical events lasting few picoseconds make atomistic computer simulation particularly suitable to study BGs. The MD simulation of BG was introduced in the early 2000s, and concerning other simulation methods, it directly yields an unbiased structural and dynamic picture of the system, regardless of whether experimental structural data are available. The precision of the simulation depends mainly on the ability to capture accurate interactions between atoms. The models can be either classical (such as with standard MD) or based on first-principles quantum mechanics (*ab initio*) [4–6].

In the interest of writing this chapter, we first tried to survey researches in which the modeling of the BGs has been addressed. Unfortunately, the range of modeling approaches or discussion on this topic was very narrow to mostly MD simulations. Then, we summarize all promising methods in modeling BGs by MD simulation. Finally, we offer a view to the future based on a review of current approaches and results in glass and biomaterials science and their successes and limitations.

16.2 Molecular Dynamics (MD) Simulations

Chronologically, classical MD modeling using empirical force fields, such as the BKS, Pedone, Stillinger, Rino-Vashista, or other potentials [30–33], is a versatile approach for calculating the structure and properties of simple glass-forming systems [33]. Other advanced approaches, such as the shell-model (SM) approach, where polarizability of atoms is incorporated into the model using core-shell dipoles, have also been utilized. The SM approach has been applied to study silicate glasses and calcium phosphates. Results showed the improvement mainly when studying the medium-range structures, e.g. Q^n distribution. *Ab initio* molecular dynamics (AIMD) is employed for a higher level of accuracy. The AIMD has much broader applicability than classical and SM simulations. However, due to the too demanding calculations, only relatively small systems (<1000 particles) can be modeled in a reasonable timescale. Therefore, the maximum reasonable size and timescales of AIMD simulations are usually too small to observe, e.g. sol–gel synthesis of nano-sized bio-glasses or their long-time reactivity [30–33].

In contrast, classical MD can simulate much larger sizes and longer timescales. However, most standard force fields are not adequate to describe the rapidly changing bonding configurations and charge distributions of reaction processes. Glass dissolution typically happens at a sub-nanometer length scale, with elementary kinetic events occurring over a few picoseconds. This is the relevant timescale for attempting to jump over an activation barrier. However, with so many unsuccessful jumps, the actual timescale of dissolution is much longer. Also, the dissolution process involves multiple chemical reactions, which may require different force fields. To address this issue, MD simulations of the silica polymerization, for example, have used "reactive" force fields capable of producing realistic changes (rupture and formation) in covalent chemical bonds during the reactions, such as dissociation silanol and of OH^- groups and in water, absorption of hydroxyls in the glass network and their condensation to Si–O–Si bridges, and so forth. The application of reactive force fields (such as ReaxFF) to glassy systems has been recently reviewed [34, 35].

Glass scientists often use classical MD with empirical potentials to obtain initial structures and then switch to *ab initio* methods using the classical structure as the "starting configuration." This method limits the study of short-range features or properties which have mainly local (short-range) character. On the other hand, a full *ab initio* approach could solve the latter two problems and view some structural features and dynamical properties of multicomponent BGs. The full *ab initio* procedure requires significantly more computational resources than the mixed *classical/ab initio* approach. At present, appropriate force fields are accessible, allowing one to investigate accurately relatively large system sizes of $\sim 10^9$ atoms for monoatomic systems and $\sim 10^6$ atoms for multicomponent. Models of these sizes, spanning lengths between two and a few tens of nanometer, are needed to extract structural properties relevant to glass dissolution with high statistical accuracy [30–37].

Here, we elaborate on all relevant findings related to this topic and discuss the remaining challenges. MD simulations have hitherto been applied to model **nano bio-glasses**, the **structure**, **ion migration in BGs**, to find descriptors of the **chemical degradation** and **crystallization** of BGs. In the following, we discuss those articles and point to relevant topics that warrant further research.

16.2.1 Structure of BGs

The structure of well-known 45S5 Bioglass® has been simulated by Tilocca [38–40]. The modeled structure (involving melt-quenched systems containing $\sim 10^3$ atoms at cooling rates of 5–10 K/ps) dominated by short silicate chains containing two to four monomers (tetrahedrons of silicon), confirming its low glass-forming ability and high solubility. The modeled structure essentially unaffected by the cooling rate, besides statistical fluctuations. The distributions of chain lengths also remained similar in a range of system sizes varied by a factor of 32; the only apparent effect of a smaller size is a somewhat higher fraction of the smallest (dimer and trimer) chain fragments [40, 41]. This finding conveyed that the medium-range structural order of BGs, obtained through models of silicate and phosphate glasses using standard MD simulations, are typically reliable. Therefore, the CPU-demanding to access more challenging conditions of larger size ($N > 10^5$ atoms) or slow cooling rate ($<10^{-2}$ K/ps) is usually unnecessary [39, 42] because it demands an arduous task even with powerful state-of-the-art computer resources. Then, Pedone et al. [43] combined classical MD simulations with nuclear magnetic resonance (NMR) for ^{17}O and ^{23}Na, ^{29}Si, ^{31}P, and ^{23}Na isotopes to study the 45S5 Bioglass with up to 248 atoms. Their results provided deep insights into fundamental open questions regarding the atomic-scale structural details of this glass. In particular, the host silica network, defined by the Q^n distribution, consists of both chains and rings of Q^2 (67.2%) SiO_4 tetrahedra, which are cross-linked with Q^3 (22.3%) species and terminated by a low quantity of Q^1 (10.1%) species. No Si–O–P bridges were detected by both ^{31}P NMR and ^{17}O NMR experiments, and therefore isolated orthophosphate units can form nano-domains that subtract sodium and calcium cations from their network modifying role into the silicate network. Finally, both the experimental and theoretical results showed a mixture of different cations of Na and Ca surrounding nonbridging oxygen (NBO) [43]. Stevensson et al. [44] also found through NMR experiments and MD simulations that the dispersion of phosphate ions is independent of the silicate network connectivity and almost independent of the P content of the glass in the space of 1–6 mol% P_2O_5 and silicate network connectivities up to 2.9. These results violated findings of Linati et al. that detected a small amount of Si–O–P link units in glasses with low P_2O_5-content, but at high P_2O_5 concentration, the percentage of Si–O–P bridges became important [45].

Lu et al. [46] have prepared a series of B_2O_3-substituted 45S5 BGs and performed *in vitro* biomineralization experiments. Hydroxyapatite (HAp) formation was observed on the glass surfaces of all compositions within three weeks of *in vitro* tests, but the glasses with higher boron oxide were slower and took longer to form HAp. MD simulations were used to complement the experimental efforts to understand the structural changes due to boron oxide to silica substitution by using newly developed partial charge composition-dependent potentials. Overall network connectivity obtained from MD simulations increased with increasing boron oxide content: from 2.06 for 45S5 to 2.45 for its pure borate glass. The increase of network connectivity with boron oxide concentration is partially responsible for the delayed HAp formation *in vitro* after inducing boron [46].

Mead and Mountjoy [47] have reported the first detailed models, obtained using MD simulations, of the local atomic structure in *bioactive gel-derived* SiO_2–CaO glasses, with the composition of $Ca_xSi_{1-x}O_{2-x-y}(OH)_{2y}$, which $0 \leq x \leq 0.5$ and $y = 0.2$. The models were in satisfactory agreement with experimental results and showed lower network connectivity of tetrahedral silica owing to the presence of Ca and hydroxyl groups. Ca coordination was ~6 for a Ca mole fraction of $x = 0.5$ and it was mostly located near NBOs, but with a small contribution from bridging oxygens. Hydroxyl groups bonded to Si form Si—O—H bonds, but there was a substantial contribution to Ca coordination with hydroxyl groups, reducing the number of NBO bonded to Si. The Ca distribution for $x = 0.5$ was comparable to that seen in $CaSiO_3$ melt-quenched glass models and neutron diffraction results. For $x \sim 0.1$, clustering of Ca greater than expected for a random distribution was observed. Hydroxyl group coordination to Ca was supposed to enhance the dissolution of Ca and hence bioactivity. Figure 16.1 shows the simulated structure of glass of composition $x = 0.3$ and $y = 0.2$, with SiO_4 tetrahedra, Ca (large spheres), and H (small spheres) [47].

Additionally, Malavasi et al. [48] derived a mathematical relationship that relates the Ca/P ratio in the Ca-phosphate micro-segregation zones to the P_2O_5 content in ternary SiO_2–CaO–P_2O_5 gel-glasses to fine-tuning the optimum amount of P in a glass for its very high *in vitro* bioactivity. They determined that the composition with optimal Ca/P ratio is $80SiO_2$–$14.8CaO$–$5.2P_2O_5$ (mol%), which has been confirmed by experimental bioactivity measurements [48]. More recently, Côté et al. [49] tried to understand through modeling how calcium interacts with silica sources during sol–gel processing of BGs and influences their polycondensation. For this purpose, the atomistic evolutions of a calcium-containing and Ca-free bioactive gel-glasses were compared using reactive MD simulations. The simulations highlighted that calcium accelerates the condensation rate significantly, leading to the formation of large and ramified silica clusters within 5 ns. Apparently, the calcium can induce nanosegregation in calcium-rich and silica-rich regions and promote the condensation reactions. Unveiling a possible mechanism behind incorporating calcium in the early stages of the sol–gel process could guide further studies to identify complementary experimental conditions to enhance initial calcium incorporation and thus produce sol–gel biomaterials with different properties [49].

In addition to Na, Ca, and P, whose structural roles in well-studied 45S5 and gel-derived SiO_2–CaO–P_2O_5 glasses have been unveiled by solid-state NMR and MD simulations [50, 51], the structure of silicate/phosphate BGs having other oxides and water [52] which lead to important biological or structural changes, have been thoroughly studied through MD simulations and compared with experimental data. These elements include cerium [53, 54], magnesium [55], chlorine [56], fluorine [57–63], zinc [64–66], boron in borosilicate BGs [67–70], strontium [71–73], gallium and aluminum [74], silver [75], copper and lithium [76, 77], and more [78–80]. In most cases, MD simulations could confirm the experimental observations of the structure revealed by NMR, neutron scattering, and other structural characterizations. For example, Figure 16.2 shows the local structure around cerium ions in cerium oxide doped bioactive phosphosilicate

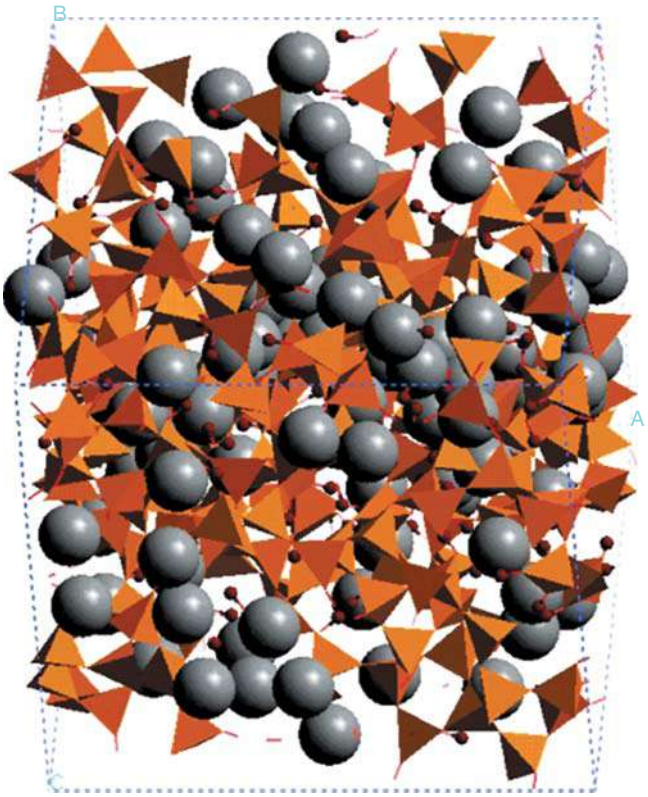

Figure 16.1 Structural model of a gel-derived bioactive glass of $Ca_{0.3}Si_{0.7}O_{1.5}(OH)_{0.4}$, showing SiO_4 tetrahedra, Ca (large spheres), and H (small spheres). Source: Reprinted with permission from Mead and Mountjoy [47]. Copyright 2006 American Chemical Society.

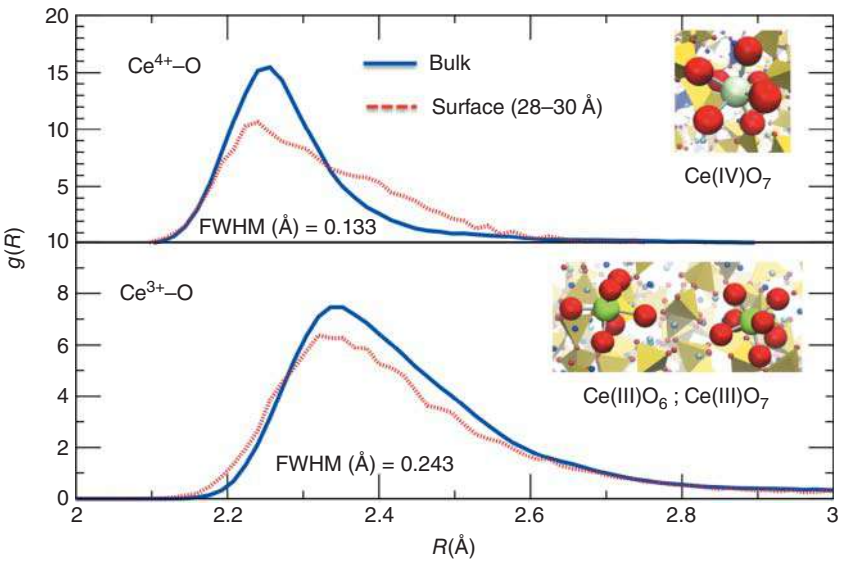

Figure 16.2 Pair radial distribution functions, $g(R)$, for the Ce–O pairs in the $3.6CeO_2-44.6SiO_2-23.4Na_2O-25.9CaO-2.5P_2O_5$ (mol%) glass. The data values of full width at half maximum (FWHM) and the typical oxygen arrangements around the Ce ions are shown. Source: Reproduced from Pedone et al. [53].

and silicate glasses determined using X-ray absorption fine structure (XAFS) at the Ce K-edge, in combination with classical MD simulations. Cerium ion (Ce^{3+} or Ce^{4+}) is an antibacterial and antioxidant that small quantities of it favor the depolymerization, dissolution, and antioxidant activity in silicate glass. However, the formation of cerium phosphate domains in phosphosilicate glasses is detrimental for both the solubility and the catalytic activity [53, 54].

In the memory of Larry Hench, the inventor of both bioactive melt and gel-derived glasses, Christie et al. [79] and Côté et al. [80] demonstrate the successful use of high-energy X-ray and neutron scattering/diffraction methods, NMR, and classical/*ab initio*/CPMD/reactive MD simulations as components of a powerful tactic for the study of BGs. Overall, combining experimental studies and MD simulations is very useful and promising to systematically investigate the impact of glass structure on bioactivity and understand the structural origin of other properties of interest, such as density and glass transition temperature, in complex glass compositions. This integrated approach can be precious in designing the next-generation of BGs. Finally, the structural roles of ions released from BGs revealed by MD simulations and experimental methods are summarized in Table 16.1.

16.2.2 Chemical Degradation of BGs

The key challenges in biodegradation related to the glass structure are the need to have experimental datasets covering the biodegradation of a wide range of suitable compositions (e.g. commercial ones), and the challenge of determining appropriate structural descriptors through MD simulations, such as network connectivity, ion clustering, nano-segregation, organization in chain and ring nanostructures or other new descriptors. For example, the initial dissolution stage following implantation of Bioglass in a physiological environment was modeled by Tilocca and Cormack [81, 82] using CPMD simulations of the interface between the 45S5 Bioglass and liquid water. The calculated CPMD trajectories highlighted the importance of Na^+/H^+ exchange during the initial stages of the bioactive mechanism [81, 82]. Then, Zeitler and Cormack [83] simulated the bulk structure of 45S5 glasses to shed light on the second reaction step in the bioactivity mechanism proposed by Hench, which is the dissolution of the network bonds between oxygen and the network formers silicon and phosphorus. The simulation results showed that the dissolution energy varies significantly depending on the environment around the Si—O—Si bonds which are broken. However, no correlation with bioactivity was found, suggesting that while network disruption is a necessary process, it is not rate-limiting [82, 83]. Then, Tilocca, Cormack, and De Leeuw [84] simulated the coordination environment changes, network connectivity, and ion aggregation with the silica content to support experimental data interpretation and provide new insight into the particular physicochemical behavior of these materials. The transition from highly bioactive to inert compositions was identified through the modeling by a marked increase in the silicate network connectivity and an increase in the fraction of phosphate groups involved in the network. Their results found a potential correlation between the loss of bioactivity and aggregation between Ca^{2+} and PO_4^{3-} ions, which leads to calcium-phosphate-rich regions for a bio-inactive composition containing 65% SiO_2 [84]. However, this phenomenon could be counterbalanced by a simultaneous increase in the number of free orthophosphate groups, which release fast and enhance the bioactivity. The strong affinity of the orthophosphates formation leads to a separation of silicate-rich and phosphate-rich regions for the high content of phosphorus (12 mol%) composition. Although this could reduce the bioactivity, in general, the favorable balance between the above should result in a beneficial effect of partial substitution of Si with P on the glass bioactivity [85].

Table 16.1 The structural roles of ions released from BGs, revealed by MD simulations and experimental techniques.

Ion	Structural roles revealed by MD simulations and experimental techniques
Si	45S5® Bioglass contains chains and rings of Q^2 (67.2%) SiO_4 tetrahedra cross-linked with Q^3 (22.3%) species and terminated by a smaller quantity of Q^1 (10.1%) species [43]
Ca	A modifier which surrounds NBOs [43]
P	Isolated orthophosphate units can form, when P_2O_5 content is ~1–6 mol%, building nano-domains with sodium and calcium cations. At higher concentrations, the Si–O–P bridges were observed [43–45]
B	Two species of boron (^{3}B and ^{4}B) have been observed. Increases the overall network connectivity in 45S5 Bioglass [46]. Changing pH value tends to release of boric acid into the solution. Also, the inability to form silica gel due to fast dissolution could be the main reason for the slower rate of HAp formation with higher boron oxide in the glass composition [67]
Zn	It plays an intermediate role. The majority of Zn ions (over 80%) are 4-coordinated and connect with the SiO_4 tetrahedra. Also, 5-coordinated Zn ions and oxygen were found in the glasses [64]
Mg	Mg in 45S5 Bioglass is coordinated by five NBOs of different PO_4 or SiO_4 tetrahedra leading to large rings in the structures. Mg is almost absent in Ca–Na-phosphate rich regions [55]
Sr	Have a slightly higher coordination number (CN) and longer cation–O bond distance than Ca. In 5 mol% SrO containing 45S5 Bioglass, CN ≈ 7.0 and the Sr—O bond length is ~2.56 Å. The diffusion energy barrier for Sr is ~0.80 eV [71–73]
Ce	Increase depolymerization, dissolution of silicate BGs. Conversely, the formation of cerium phosphate domains in phosphosilicate BGs is detrimental for both the solubility and ion activity [75, 79]
F	Is usually present as isolated fluoride ions in silicate BGs, which form strong ionic bonds to the network modifiers (CN ~ 4) rather than bonding to the silicate network (no Si—F bonds), causing structural nano-heterogeneities [57, 63]. In contrast, it induces re-polymerization in the phosphate BGs by stripping the network modifying cations from the glass network [58] and forming F—P bonds, without inducing inhomogeneities [59]
Cl	No Si—Cl and P—Cl bonds detected. Chlorine anions are present as Cl–Ca. In the mixed-fluoride/chloride-containing glasses, fluorine tends to surround phosphate, whereas chloride moves toward the silicate network [56]
Ga	Predominantly is in a fourfold coordination environment, small amounts of five- and sixfold coordinated atoms have been detected, suggesting its possible intermediate role in phosphosilicate BGs and it does not form segregated regions [74]
Ag	Bind to the phosphate chains and clustering happens at low concentrations of silver [75]
Cu	Cu^+ and Cu^{2+} ions form P–O · · · Cu linkages in phosphate glasses that could contribute to ion diffusion and release [76, 77]
Li	Fast moving modifier ion which should be released within the therapeutic range (<8.3 ppm). Each Q^3 unit is surrounded by approximately three lithium ions at an average distance of 320 pm, whereas the Q^4 units are much more remote from lithium [78–80]

The more detailed reaction of BGs with water has been simulated by Tilocca and Cormack [86, 87] to investigate the surface of a highly bioactive phosphosilicate glass, containing Na and Ca. They tried to identify active sites in interaction with water (Figure 16.3). Spontaneous water dissociation was observed on the surface, represented by three-coordinated Si atoms associated with a proton acceptor such as NBOs. Additional adsorption sites related to the Na/Ca cation modifiers, which

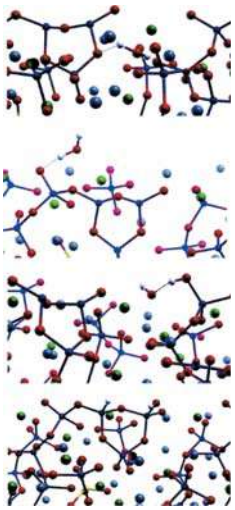

Figure 16.3 Water adsorption modes on the surface of BGs simulated by MD. A1: water has significantly penetrated within the surface, forming hydrogen bonds with a bridging oxygen belonging to the 3M-ring and with adjacent nonbridging oxygen. A2: water is coordinated near a Ca cation and donates a Hb to a surface NBO. A3: one of the two water O—H bonds is transferred to a surface NBO, leaving a metastable hydroxyl close to a Ca ion. A4: optimized structure after water adsorption and dissociation on the 3M-ring. Si, O, Na, Ca, and P atoms are represented as blue, red, gray, green, and yellow spheres, respectively. Source: Reprinted with permission from Tilocca and Cormack [86]. Copyright 2008 American Chemical Society.

involved in the glass dissolution and provided favorable paths allowing for water to penetrate the surface. Smaller silica rings, i.e. two- or three-membered (2M or 3M) rings, were the stable features of the surface, although there was a possible energetic configuration for opening the rings upon dissociation with water. The lowest energy barriers for the 2M ring-opening mechanisms, calculated using the String Method Car–Parrinello approach, revealed the energy barrier associated with the opening of small rings. The simulation showed that small rings not being open and hydroxylated after immersion in an aqueous environment assist nucleation of Ca and P ions on the surface, as previously proposed to understand the initial stages of the bioactive mechanism [86]. In another investigation, they modeled a bioactive surface ($46.1SiO_2$–$24.35Na_2O$–$26.9CaO$–$2.57P_2O_5$ in mol%) and a non-bioactive ($66.9SiO_2$–$14.47Na_2O$–$15.98CaO$–$2.63P_2O_5$ in mol%) glass composition in aqueous conditions. Their research highlighted the critical role of network fragmentation and sodium enrichment at the surface of the bio-glass in governing the rapid hydrolysis and release of silica fragments in solution, which is characteristic of highly bioactive compositions. In contrast, no correlation was found between the surface density of small (two- and three-membered) rings and bioactivity, suggesting that additional factors must be considered to fully understand the role of such sites in leading to calcium phosphate deposition on the glass surface [88].

In addition to phosphosilicate glasses which are the main representative of BGs, phosphate-based BGs have several unique biomedical applications due to the chemical reactions/degradations they experience with their surrounding environment, especially when implanted in the human body. The dissolution rate of such glasses in physiological conditions is an important consideration to ensure a desirable rate of drug delivery or therapeutic ions to the body. Christie et al. [89] provide, for the first time, an atomistic explanation of the well-known fact that the substitution of CaO with Na_2O in these glasses lowers the dissolution rate. Their MD simulations of ternary P_2O_5–CaO–Na_2O glasses showed the atomic structural properties could enhance chemical durability as more Ca is incorporated. Calcium binds to more fragments of the phosphate glass network compared to Na. Moreover, calcium links more PO_4 tetrahedra than Na and has a lower concentration of intra-tetrahedral phosphate bonding compared to Na. This behavior is because of the calcium ion's higher charge and field strength. These results could help to open the path to precise control and optimization of the degradation rate of phosphate BGs for specific applications [89].

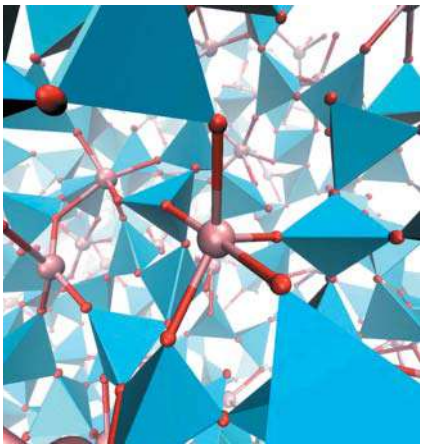

Figure 16.4 Structure of $67.09SiO_2-0.61P_2O_5-12.19Na_2O-12.19CaO-7.92Y_2O_3$ (mol%) glass. The tetrahedra forming the silicate backbone are shown in cyan, with the corner oxygen atoms highlighted as red spheres. Yttrium atoms are shown as pink spheres, and their Y–O links are also displayed as regular bonds. Na and Ca ions are not shown for clarity. Source: Reproduced with permission from Christie and Tilocca [91]/Royal Society of Chemistry.

Tilocca, Christie, and Malik [90–92] managed to identify new structural descriptors that influence the solubility and, therefore, the performances of yttrium-doped bioactive glasses (YBGs) used as radioisotope vectors for *in situ* radiotherapy, an application which also critically depends on the glass durability. MD simulation identified this structural descriptor as non-covalent cross-links between separate portions of the silicate network, bridged by a central modifier cation, which was yttrium in this case (Figure 16.4). They found that higher yttria compositions with a constant network connectivity are characterized by a less dense but stronger network of O···Y···O cross-linking and lower yttrium clustering. Thus, their results demonstrated that it should be possible to design YBGs with adequate bioactivity to ensure the growth of new tissues and deliver higher radiation doses through increased yttria concentration. The undesired dissolution of harmful quantities of radioactive yttrium is limited by the strong bonding of yttrium with NBO, which prevents a too rapid glass network degradation [90–92].

16.2.3 Diffusion in BGs

MD simulations have also been applied to study the kinetics of modifier ions in silicate and phosphate BGs. For example, it is known that the open structure of 45S5 Bioglasss leads to fast ions migration which does not happen in the denser network of conventional high silica-containing inert glasses [93]. It is known that the ion migration in BGs is very slow at room temperature which prohibitively needs long trajectories to gain a reasonably accurate sampling of the diffusion. One strategy to address this problem is to run the simulations at a high temperature, below the glass transition [93–95]. Results show that the modifier ions move within a static glass network similar to that at room temperature so that the description of the diffusive phenomenon at the higher temperature is still representative of realistic conditions [93–95]. Another difficulty is the possible inadequacy of force fields employed in classical MD runs. A potential that provides a good description of the glass structure does not necessarily perform equally well in reproducing dynamic processes. A safer solution would be represented by parameter-free AIMD approaches [96]. However, the higher computational demands of this approach limit the AIMD trajectory length to below the nanosecond range, with the consequence that a detailed investigation of the migration of slow-moving cations is complicated, even with the higher temperature strategy described above [96]. MD simulations have been employed to trace the ion migration in the structure of 45S5. Modifier ions migrate through transient vacancies created by interim displacements of another Na or a Ca cation (Figure 16.5) [93]. The formation of such transient sites would not be as favorable in a more rigid glass network, e.g.

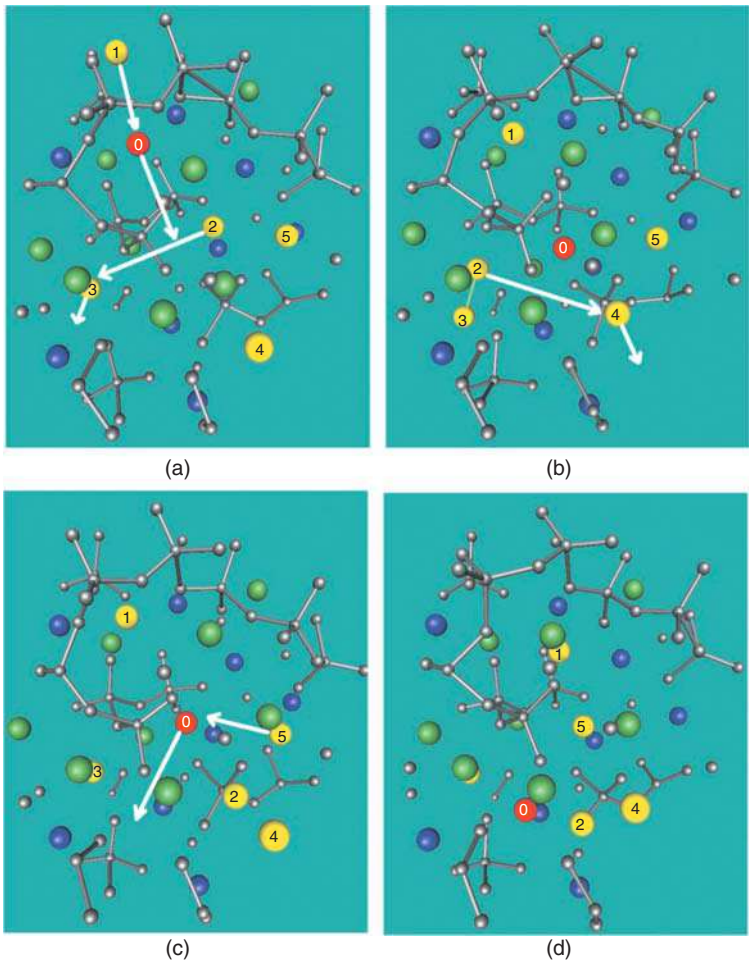

Figure 16.5 Four snapshots extracted from the CPMD trajectory simulation, illustrating the jumps of a Na ion (in red). Snapshots (a–d) are taken at $t = 69.6$, 72.7, 76.2, and 79.3 ps, respectively. The silicate network is represented as gray ball and stick, whereas spheres represent Na and Ca ions. Na ions involved in correlated jumps are highlighted in yellow, whereas Ca ions are colored blue. The arrows mark ionic displacements discussed in the text. Source: Reproduced with permission from Tilocca [93]/AIP Publishing LLC.

having higher silica content [97]. The AIMD has been employed to characterize sodium migration in 45S5 Bioglass, but not enough calcium migration events were observed during the simulation time to yield an equally clear picture of the (slower) diffusion of Ca [93]. Development of a more rigorous approach for addressing the timescale problem in MD simulations of migration in glasses, which experience more complex energy landscapes encountered by ions migrating in multicomponent BGs, is required to enable future advances [32]. An effort was made by Tilocca to model, through MD simulations, ion migration in two fluorine-containing BGs of significantly different durability [98]. Structural features alone could not explain the chemical degradation behavior of the BGs. Then, the ions' diffusion analysis helped to correlate glass durability determined experimentally and the activation barrier extracted by the simulations. This uncovered the source of the changing solubility and suggested appropriate "dynamical" properties of bioactivity to predict the degradation of a biomaterial, in some cases more effectively than with the current structural

descriptors [98]. This study also suggested the possibility of examining some additionally interesting compositions, the experimental ionic conductivities of the BGs could be used as an alternative or complementary tool to the customary ion-release experiments in simulated body fluid [98].

16.2.4 MD Simulation of Nano-BGs

MD simulations can also model crystalline and amorphous nanoparticles (NPs). In an isolated nanoparticle of a BG of 5–15 nm in size, 10^4–10^5 atoms exist, which is the simulable size for classical MD simulations [99, 100].

Tilocca [99] has stimulated a 45S5 Bioglass spherical nanoparticle of 6 nm in diameter by MD to study the impact of nanoparticle size on its structure, influencing the bioreactivity of the particles, in addition to altering the surface area to volume ratio. An appropriate computational method would involve quickly quenching a liquid within an isolated sphere of the specified size, thereby approximating the flame spray synthesis method used to prepare small BG NPs in the experiment [100]. MD simulations found that the most relevant impacts of the reduced nanoparticle size are a reduction in the network connectivity on the nanoparticle surfaces, together with an increase in the population of three-membered rings, as well as a higher Na^+/Ca^{2+} ratio at the surface [99]. Moreover, the mobility of modifier cations and the density of three-membered silicate rings – key features to support rapid dissolution and bone-bonding processes at the surface – are also enhanced at the nanoparticle surface compared to samples of larger size [99]. Furthermore, Pedone et al. [101] used MD simulations to study two glass nanoparticles with the composition of $25Na_2O$–$25CaO$–$50SiO_2$ (mol%) (Ce-K NP) and $46.1SiO_2$–$24.4Na_2O$–$26.9CaO$–$2.6P_2O_5$ (mol%) (Ce-BG NP) doped with 3.6 mol% of CeO_2. The MD results help to explain the effect of cerium on the enhanced antioxidant properties of the system. Their model structures (see Figure 16.6) showed that the different antioxidant activity of the two glasses is related to the ratio of Ce^{3+}/Ce^{4+} at the surface. The Ce^{3+}/Ce^{4+} ratio was ~3.5 and 13 in the bulk and at the surface of the Ce-BG NP, and 1.0 and 2.1 for the Ce-K NPs, respectively. A higher Ce^{3+}/Ce^{4+} ratio reduced the antioxidant properties. Moreover, the MD simulations identified reduced network connectivity and rapidly increased Na^+/Ca^{2+} ratio on the surface of the nanoparticle. The Na, Ca, and Ce sites near the surface are found to be under-coordinated, which accelerates the reaction with water in physiological environments, enhancing the kinetics of glass biodegradation [101–103].

The challenge in MD simulation of nanoparticles is to consider perturbations from fluids that contact the particle. Thus, modeling the specific interface between the nanoparticle and an aqueous medium and assessing the effects of this interaction on the properties is still tricky. It demands accurate force fields to model the other interactions at the biomaterial interface (the considerable size of the models prevents the straightforward application of AIMD approaches in this case) and a very long simulation time compared to the dry cases and largest NPs [32].

16.2.5 Crystallization of BGs

When studying glass-ceramics, the second most important parameter in the design is the control of crystallinity (after the compositional variables). Experimentally, this is often achieved by either temporally expensive mapping of nucleation/growth curves followed by carefully selecting times and temperatures based on these curves or by the costly cook-and-look method [1]. The ultimate promise of these computational approaches is to reduce the cost of developing new glass-ceramics by calculating the nucleation and growth rates (collectively called the crystallization rates), superseding the traditional expensive methods [4]. Computational studies of crystallization

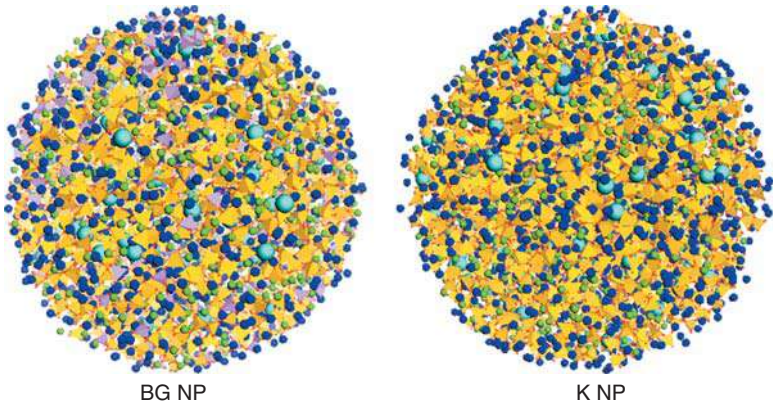

Figure 16.6 Pictures of the MD-calculated nanoparticle structures of Pedone et al. Yellow and purple tetrahedra are silicate and phosphate ions, blue spheres are Na, and Ce ions in cyan, and Ca in green spheres [101].

can then generally be split into two categories: direct calculation of crystallization rates [104, 105] and parameterization of models [106, 107]. For BG-ceramics, a direct calculation is not feasible since the rates are much slower for oxides than what is accessible in MD, instead, we are forced to rely on the parameterization of models.

Since parameterization is required, the models must be chosen carefully such that they can accurately reproduce nucleation curves with as few parameters as necessary. There is a common consensus that Wilson–Frenkel theory (WFT) of growth is able to capture the growth of crystalline phases when parameterized correctly [108]. WFT is given as a function of the free energy difference between the crystalline and liquid phase, ΔG, the average jump distance of the underlying atoms attaching to the crystal, d_0, and some key kinetic parameter, $D(U)$,

$$U = \frac{D(U)}{d_0}\left[1 - \exp\left(-\frac{\Delta G}{kT}\right)\right] \tag{16.1}$$

Sometimes an additional parameter relating to the dislocations is added that scales from 0 to 1 [109]. $D(U)$ is typically calculated through the Stokes/Eyring–Einstein relationship (SEE) but in literature, there are conflicting messages on whether this is reliable for all liquids due to a breakdown reported in very fragile systems [109]. Further analysis of the calculations of growth in glass-ceramics can be found in these locations.

Many possible nucleation models are available in the literature with the most common being classical nucleation theory (CNT). These nucleation theories are often fiercely fought over with each camp believing that their model is superior but the reality is that none of these models can be directly parameterized entirely from experiments (without fitting parameters) [108]. As such, they all fail to be truly useful for industrial applications. If the variables are not experimentally accessible, the next best option is a computational route.

All nucleation models generally follow a general form [107],

$$I = D(I)\exp\left[-\frac{W}{kT}\right] \tag{16.2}$$

where W is the work needed to form a nucleus. To enable industrial glass-ceramic design, there has been a large push to parameterize a nucleation model without any fitting parameters with an emphasis on CNT. CNT is an interesting model since the experimental methods can often lead to

an error in dozens of orders of magnitude (though some recent works have cast doubt on this experimental error [110]), and as such, it was widely considered a failure when looking for quantitative results. The advantages of CNT theory are that the calculation of nucleation only relies on three simple parameters, ΔG, $D(I)$, and the interfacial free energy (σ). The nucleation rate predicted by CNT is given by [108],

$$I = D(I) \exp\left[-\frac{16\pi\sigma^3}{3(\Delta G)^2}\right] \tag{16.3}$$

Since CNT is so divisive, much of the recent computational work is focused on testing the validity of this theory. There have been several recent attempts with a variety of methods being used for each CNT parameter to validate this theory [104–107]. These attempts have found that CNT can ***successfully approximate*** the nucleation rates experimentally found; however, only one of these systems was an oxide system: $BaO–2SiO_2$. The rest of these tests were done on extremely fast nucleating systems so that the nucleation rate could be directly observed in MD.

The driving force is the parameter that is common between growth and nucleation and is the variable describing the underlying thermodynamics. Due to its importance, a plethora of techniques has been developed to calculate the driving force ranging from simple approximations based on the enthalpy of melting (H_m) to full Monte–Carlo techniques. The simplest way to calculate the driving force from MD is to approximate the liquidus temperature (T_l) with different heating rates, followed by calculating the enthalpy difference at that temperature (H_m). Once those variables are known, they could be used in an approximation such as the Turnbull approximations [110, 111],

$$\Delta G = H_m\left(1 - \frac{T}{T_l}\right) \tag{16.4}$$

However, this method requires assumptions about the shape of the underlying free energy curve which is not guaranteed to work for all systems. An improved method that still only relies on MD comes from Lodesani et al., who was able to calculate the work function without even assuming CNT. In their work, Lodensani et al. [112] used liquid structures with different sizes of embedded crystalline phases to approximate the free energy with and without the crystals. Using this method, they calculated the work function as a function of the crystalline size, in good agreement with results expected from CNT, providing another check on the legitimacy of the theory.

The next two methods are slight departures from MD; however, they still rely on the same fundamental ideas, but with larger statistical constructs rather than relying on the Newtonian integration of time steps. These two methods come from McKenzie and Mauro [106] and from Wilkinson et al. [107]. McKenzie et al. uses an implicit solvated Monte–Carlo model to calculate the free energy of nucleation sites by placing and removing atoms based on Boltzmann statistics. This technique is compelling because the work function of the system is attainable without any assumptions about the system.

Wilkinson et al.'s model is also an extension of MD with the mapping of an energy landscape [4, 107, 108] corresponding to the system of interest then classifying the basins into either crystals or liquids based on their structure. This splitting of basins into liquids and crystals then allows not only the calculation of the thermodynamic driving force but also enables a standard transition rate to be found leaving only the interfacial free energy as an open parameter for CNT. This technique shows promise but has some limitations that the other methods are not constrained to, such as using the exact stoichiometric system for the crystal that is being calculated and much larger computational costs than other techniques considered.

The kinetics of nucleation is often calculated either through the SEE equation or through the mean diffusivity of MD [104, 105, 109]. The recent work from Wilkinson et al. has cast doubt on

the validity of SEE with the transition rate calculated from Wilkinson et al. being many orders of magnitude lower compared to that calculated from experimental data with SEE. Despite this, SEE will continue to be used because the SEE is the only experimental technique to enable the calculation of the kinetics without any fitting parameters and makes a prediction that can be compensated by fitting the surface energy (which is required when parameterizing from experiments, anyway). Using the diffusivities of the ions and fitting an Arrhenius expression to the diffusivities has appeared to work for simple systems; however, more work is needed to test its validity for complex oxide glasses.

The last missing parameter that is needed for CNT (but not for McKenzie and Mauro [106] or Lodesani et al. [112]) is the interfacial free energy. This parameter is often troublesome because it cannot be calculated directly from experiments and is always reliant on fitting. To directly calculate this, there have been two methods used in literature. The first comes from simulations where the nucleation rate is directly observable such as the work by Prado et al. [104]. When the rate is directly accessible, so is the lag time, which then allows for a calculation of the surface energy directly. This method for the surface energy, the kinetic term from ion diffusivities, and the approximation for the free energy difference have been used together on several occasions for simple systems and each time has shown remarkable agreement between CNT and the recorded nucleation rates. The other way that σ has been obtained is through the work done by Wilkinson et al. [107] in which they simulated a liquid structure and a crystalline structure, annealed it at a high temperature, and then quenched while measuring the total potential energy. The interfacial free energy, they proposed, was then the difference between the structure with the interface's potential energy and the two independent structures' potential energies. When this energy was then implemented with the free energy difference and kinetics calculated from the energy landscape, a good agreement with CNT was found. In Figure 16.7, we can see details that come from the study of Wilkinson et al. [107] as well as the comparison with experimental data for the barium disilicate system.

16.3 Conclusion

BG and glass-ceramics are posed to be necessary powerful tools as we enter a post-pandemic, more health-conscious world; however, despite this promise, the scientific backbone is still being developed and requires more work to reach its fruition. MD and computational methods are the most promising route to create science with the detail, accuracy, and speed needed for scientific and commercial development. The combination of MD simulations of structure with experimental data such as degradability, therapeutic ions release, and bone-bonding ability of BGs deepen the understanding of the bioactivity. The bulk structural features and the glass characteristics in biological applications have already been identified. However, more rigorous efforts are indispensable to shed more light on the properties of these materials. More simulation studies should be encouraged to further reveal the more complicated phenomena at the glass interface and body. For example, full *ab initio* models using reactive force fields are envisaged to yield valuable information on the surface properties of BGs. As the available computational power rapidly grows, it will become feasible to further extend the *ab initio* approaches to model the interface of BGs on a larger scale and thus fully understand the surface dissolution and interactions with biomolecules/cells. We believe with the growing acquired knowledge on the properties of glasses, experimental data, force field development, and computational power, the prospects for MD simulations of complex problems and predicting the surface interactions and biological responses are possible in the future.

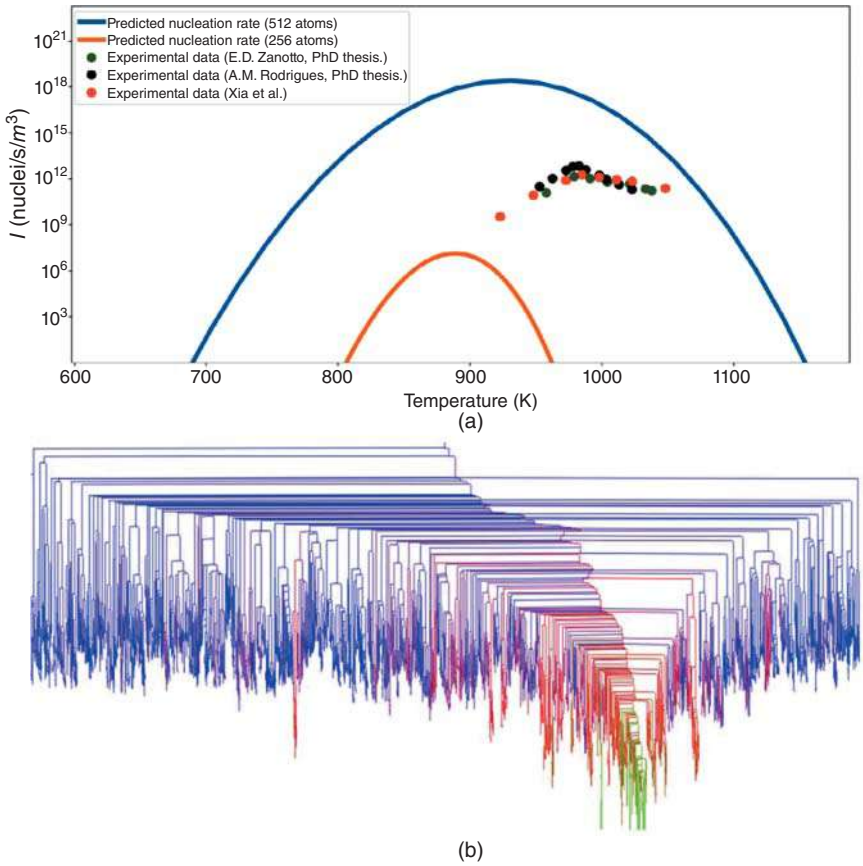

Figure 16.7 (a) The comparison between the computed nucleation curve for two different system sizes vs. experimental nucleation rates [113–115]. The error most likely originates in the fact that potentials were not trained for this system and we are considering a finite system and thus cannot capture all possible transition rates. (b) The first ever energy landscape reported for a glass-ceramic with the green showing the crystalline states, the blue showing glass states, and the red showing hybrid states. Source: (b) More information is available in the original work by Wilkinson et al. [107]/with permission of Elsevier.

Acknowledgment

We would like to thank Corning Incorporated for their ongoing support of our research.

References

1 Montazerian, M., Zanotto, E.D., and Mauro, J.C. (2020). Model-driven design of bioactive glasses: from molecular dynamics through machine learning. *International Materials Reviews* 65 (5): 297–321.
2 Editorial (2016). Boosting materials modeling. *Nature Materials* 15 (4): 365.
3 Editorial (2013). Fuelling discovery by sharing. *Nature Materials* 12 (3): 173.
4 Mauro, J.C., Tandia, A., Vargheese, K.D. et al. (2016). Accelerating the design of functional glasses through modeling. *Chemistry of Materials* 28 (12): 4267–4277.

5 Wondraczek, L. and Mauro, J.C. (2009). Advancing glasses through fundamental research. *Journal of the European Ceramic Society* 29 (7): 1227–1234.

6 Montazerian, M. and Zanotto, E.D. (2017). A guided walk through Larry Hench's monumental discoveries. *Journal of Materials Science* 52 (15): 8695–8732.

7 Hench, L.L. (2006). The story of Bioglass®. *Journal of Materials Science – Materials in Medicine* 17 (11): 967–978.

8 Montazerian, M. and Zanotto, E.D. (2016). Bioactive glass-ceramics: processing, properties and applications. In: *Bioactive Glasses: Fundamentals, Technology and Applications*, Smart Materials Series (ed. A.R. Boccaccini, D.S. Brauer and L. Hupa), 27–60. Cambridge: Royal Society of Chemistry.

9 Baino, F., Hamzehlou, S., and Kargozar, S. (2018). Bioactive glasses: where are we and where are we going? *Journal of Functional Biomaterials* 9 (1). Art. no.: 25.

10 El-Rashidy, A.A., Roether, J.A., Harhaus, L. et al. (2017). Regenerating bone with bioactive glass scaffolds: a review of in vivo studies in bone defect models. *Acta Biomaterialia* 62: 1–28.

11 Fu, Q., Saiz, E., Rahaman, M.N., and Tomsia, A.P. (2011). Bioactive glass scaffolds for bone tissue engineering: state of the art and future perspectives. *Materials Science and Engineering C* 31 (7): 1245–1256.

12 Rahaman, M.N., Day, D.E., Sonny Bal, B. et al. (2011). Bioactive glass in tissue engineering. *Acta Biomaterialia* 7 (6): 2355–2373.

13 Gorustovich, A.A., Roether, J.A., and Boccaccini, A.R. (2010). Effect of bioactive glasses on angiogenesis: a review of in vitro and in vivo evidences. *Tissue Engineering Part B* 16 (2): 199–207.

14 Miguez-Pacheco, V., Hench, L.L., and Boccaccini, A.R. (2015). Bioactive glasses beyond bone and teeth: emerging applications in contact with soft tissues. *Acta Biomaterialia* 13: 1–15.

15 Baino, F., Novajra, G., Miguez-Pacheco, V. et al. (2016). Bioactive glasses: special applications outside the skeletal system. *Journal of Non-Crystalline Solids* 432: 15–30.

16 Kargozar, S., Baino, F., Hamzehlou, S. et al. (2018). Bioactive glasses: sprouting angiogenesis in tissue engineering. *Trends in Biotechnology* 36 (4): 430–444.

17 Kargozar, S., Hamzehlou, S., and Baino, F. (2017). Potential of bioactive glasses for cardiac and pulmonary tissue engineering. *Materials* 10 (12). Art. no.: 1429.

18 Fernandes, J.S., Gentile, P., Pires, R.A. et al. (2017). Multifunctional bioactive glass and glass-ceramic biomaterials with antibacterial properties for repair and regeneration of bone tissue. *Acta Biomaterialia* 59: 2–11.

19 Hoppe, A., Güldal, N.S., and Boccaccini, A.R. (2011). A review of the biological response to ionic dissolution products from bioactive glasses and glass-ceramics. *Biomaterials* 32 (11): 2757–2774.

20 Wu, C. and Chang, J. (2012). Mesoporous bioactive glasses: structure characteristics, drug/growth factor delivery and bone regeneration application. *Interface Focus* 2 (3): 292–306.

21 Baino, F., Fiorilli, S., and Vitale-Brovarone, C. (2016). Bioactive glass-based materials with hierarchical porosity for medical applications: review of recent advances. *Acta Biomaterialia* 42: 18–32.

22 Kargozar, S., Montazerian, M., Hamzehlou, S. et al. (2018). Mesoporous bioactive glasses (MBGs): promising platforms for antibacterial strategies. *Acta Biomaterialia* 81: 1–19.

23 Ruskowitz, E.R. and Deforest, C.A. (2018). Photoresponsive biomaterials for targeted drug delivery and 4D cell culture. *Nature Reviews Materials* 3. Art. no.: 17087.

24 Montazerian, M. and Zanotto, E.D. (2017). Bioactive and inert dental glass-ceramics. *Journal of Biomedical Materials Research Part A* 105 (2): 619–639.

25 Montazerian, M. and Zanotto, E.D. (2016). History and trends of bioactive glass-ceramics. *Journal of Biomedical Materials Research Part A* 104 (5): 1231–1249.

26 Sola, A., Bellucci, D., Cannillo, V., and Cattini, A. (2011). Bioactive glass coatings: a review. *Surface Engineering* 27 (8): 560–572.

27 Bellucci, D., Sola, A., and Cannillo, V. (2016). Hydroxyapatite and tricalcium phosphate composites with bioactive glass as second phase: state of the art and current applications. *Journal of Biomedical Materials Research Part A* 104 (4): 1030–1056.

28 Sedighi, O., Alaghmandfard, A., Montazerian, M., and Baino, F. (2022). A critical review of bioceramics for magnetic hyperthermia. *Journal of the American Ceramic Society*. https://doi.org/10.1111/jace.17861 105: 1723–1747.

29 Kargozar, S., Baino, F., Hamzehlou, S. et al. (2018). Bioactive glasses entering the mainstream. *Drug Discovery Today* 23 (10): 1700–1704.

30 Tilocca, A. (2009). Structural models of bioactive glasses from molecular dynamics simulations. *Proceedings of the Royal Society of London Series A* 465: 1003–1027.

31 Tilocca, A. (2017). Molecular dynamics simulations of bioactive glass structure and in vitro reactivity. In: *BioactiveGlasses: Fundamentals, Technology and Applications*, RSC Smart Materials (Chapter 4), vol. 23 (ed. A.R. Boccaccini, D.S. Brauer and L. Hupa), 89–104. Royal Society of Chemistry.

32 Tilocca, A. (2014). Current challenges in atomistic simulations of glasses for biomedical applications. *Physical Chemistry Chemical Physics* 16 (9): 3874–3880.

33 Massobrio, C., Du, J., Bernasconi, M., and Salmon, P.S. (ed.) (2015). *Molecular Dynamics Simulations of Disordered Materials*. Switzerland: Springer Nature.

34 Senftle, T.P., Hong, S., Islam, M.M. et al. (2016). The ReaxFF reactive force-field: development, applications and future directions. *npj Computational Materials* 2: 15011.

35 Rimsza, J.M., Yeon, J., Van Duin, A.C.T., and Du, J. (2016). Water interactions with nanoporous silica: comparison of ReaxFF and ab initio based molecular dynamics simulations. *Journal of Physical Chemistry C* 120 (43): 24803–24816.

36 Christie, J.K., Ainsworth, R.I., Hernandez, S.E.R., and De Leeuw, N.H. (2017). Structures and properties of phosphate-based bioactive glasses from computer simulation: a review. *Journal of Materials Chemistry B* 5 (27): 5297–5306.

37 Pedone, A. and Menziani, M.C. (2016). What can we learn from atomistic simulations of bioactive glasses? *Advanced Structured Materials* 53: 119–145.

38 Tilocca, A. and De Leeuw, N.H. (2006). Ab initio molecular dynamics study of 45S5 bioactive silicate glass. *Journal of Physical Chemistry B* 110 (51): 25810–25816.

39 Tilocca, A. (2007). Structure and dynamics of bioactive phosphosilicate glasses and melts from ab initio molecular dynamics simulations. *Physical Review B: Condensed Matter and Materials Physics* 76 (22). Art. no.: 224202.

40 Tilocca, A. (2008). Short- and medium-range structure of multicomponent bioactive glasses and melts: an assessment of the performances of shell-model and rigid-ion potentials. *Journal of Chemical Physics* 129 (8). Art. no.: 084504.

41 Tilocca, A. (2013). Cooling rate and size effects on the medium-range structure of multicomponent oxide glasses simulated by molecular dynamics. *Journal of Chemical Physics* 139 (11). Art. no.: 114501.

42 Vollmayr, K., Kob, W., and Binder, K. (1996). Cooling-rate effects in amorphous silica: a computer-simulation study. *Physical Review B: Condensed Matter and Materials Physics* 54 (22): 15808–15827.

43 Pedone, A., Charpentier, T., Malavasi, G., and Menziani, M.C. (2010). New insights into the atomic structure of 45S5 bioglass by means of solid-state NMR spectroscopy and accurate first-principles simulations. *Chemistry of Materials* 22 (19): 5644–5652.

44 Stevensson, B., Mathew, R., and Edén, M. (2014). Assessing the phosphate distribution in bioactive phosphosilicate glasses by ^{31}P solid-state NMR and molecular dynamics simulations. *Journal of Physical Chemistry B* 118 (29): 8863–8876.

45 Linati, L., Lusvardi, G., Malavasi, G. et al. (2008). Medium-range order in phospho-silicate bioactive glasses: insights from MAS-NMR spectra, chemical durability experiments and molecular dynamics simulations. *Journal of Non-Crystalline Solids* 354 (2–9): 84–89.

46 Lu, X., Deng, L., Huntley, C. et al. (2018). Mixed network former effect on structure, physical properties, and bioactivity of 45S5 bioactive glasses: an integrated experimental and molecular dynamics simulation study. *Journal of Physical Chemistry B* 122 (9): 2564–2577.

47 Mead, R.N. and Mountjoy, G. (2006). Modeling the local atomic structure of bioactive sol–gel-derived calcium silicates. *Chemistry of Materials* 18 (17): 3956–3964.

48 Malavasi, G., Menabue, L., Menziani, M.C. et al. (2013). New insights into the bioactivity of SiO_2–CaO and SiO_2–CaO–P_2O_5 sol–gel glasses by molecular dynamics simulations. *Journal of Sol-Gel Science and Technology* 67 (1): 208–219.

49 Côté, A.S., Cormack, A.N., and Tilocca, A. (2016). Influence of calcium on the initial stages of the sol–gel synthesis of bioactive glasses. *Journal of Physical Chemistry B* 120 (45): 11773–11780.

50 Mathew, R., Stevensson, B., Tilocca, A., and Edén, M. (2014). Toward a rational design of bioactive glasses with optimal structural features: composition–structure correlations unveiled by solid-state NMR and MD simulations. *Journal of Physical Chemistry B* 118 (3): 833–844.

51 Mathew, R., Stevensson, B., and Edén, M. (2015). Na/Ca intermixing around silicate and phosphate groups in bioactive phosphosilicate glasses revealed by heteronuclear solid-state NMR and molecular dynamics simulations. *Journal of Physical Chemistry B* 119 (17): 5701–5715.

52 Berardo, E., Corno, M., Cormack, A.N. et al. (2014). Probing the fate of interstitial water in bulk bioactive glass by ab initio simulations. *RSC Advances* 4 (69): 36425–36436.

53 Pedone, A., Tavanti, F., Malavasi, G., and Menziani, M.C. (2018). An atomic-level look at the structure–property relationship of cerium-doped glasses using classical molecular dynamics. *Journal of Non-Crystalline Solids* 498: 331–337.

54 Benedetti, F., Luches, P., D'Addato, S. et al. (2017). Structure of active cerium sites within bioactive glasses. *Journal of the American Ceramic Society* 100 (11): 5086–5095.

55 Pedone, A., Malavasi, G., and Menziani, M.C. (2009). Computational insight into the effect of CaO/MgO substitution on the structural properties of phospho-silicate bioactive glasses. *Journal of Physical Chemistry C* 113 (35): 15723–15730.

56 Pedone, A., Chen, X., Hill, R.G., and Karpukhina, N. (2018). Molecular dynamics investigation of halide-containing phospho-silicate bioactive glasses. *Journal of Physical Chemistry B* 122 (11): 2940–2948.

57 Christie, J.K. and Brauer, D.S. (2017). The role of fluoride in the nanoheterogeneity of bioactive glasses. *Physics and Chemistry of Glasses – European Journal of Glass Science and Technology Part B* 58 (4): 180–186.

58 Shaharyar, Y., Wein, E., Kim, J.-J. et al. (2015). Structure–solubility relationships in fluoride-containing phosphate based bioactive glasses. *Journal of Materials Chemistry B* 3 (48): 9360–9373.

59 Christie, J.K., Ainsworth, R.I., and de Leeuw, N.H. (2014). Ab initio molecular dynamics simulations of structural changes associated with the incorporation of fluorine in bioactive phosphate glasses. *Biomaterials* 35 (24): 6164–6171.

60 Pedone, A., Charpentier, T., and Menziani, M.C. (2012). The structure of fluoride-containing bioactive glasses: new insights from first-principles calculations and solid state NMR spectroscopy. *Journal of Materials Chemistry* 22 (25): 12599–12608.

61 Christie, J.K., Pedone, A., Menziani, M.C., and Tilocca, A. (2011). Fluorine environment in bioactive glasses: ab initio molecular dynamics simulations. *Journal of Physical Chemistry B* 115 (9): 2038–2045.

62 Lusvardi, G., Malavasi, G., Tarsitano, F. et al. (2009). Quantitative structure–property relationships of potentially bioactive fluoro phospho-silicate glasses. *Journal of Physical Chemistry B* 113 (30): 10331–10338.

63 Lusvardi, G., Malavasi, G., Cortada, M. et al. (2008). Elucidation of the structural role of fluorine in potentially bioactive glasses by experimental and computational investigation. *Journal of Physical Chemistry B* 112 (40): 12730–12739.

64 Xiang, Y., Du, J., Skinner, L.B. et al. (2013). Structure and diffusion of $ZnO–SrO–CaO–Na_2O–SiO_2$ bioactive glasses: a combined high energy X-ray diffraction and molecular dynamics simulations study. *RSC Advances* 3 (17): 5966–5978.

65 Lusvardi, G., Malavasi, G., Menabue, L. et al. (2008). Properties of zinc releasing surfaces for clinical applications. *Journal of Biomaterials Applications* 22 (6): 505–526.

66 Malavasi, G., Lusvardi, G., Pedone, A. et al. (2007). Crystallization kinetics of bioactive glasses in the $ZnO–Na_2O–CaO–SiO_2$ system. *Journal of Physical Chemistry A* 111 (34): 8401–8408.

67 Ren, M., Lu, X., Deng, L. et al. (2018). B_2O_3/SiO_2 substitution effect on structure and properties of $Na_2O–CaO–SrO–P_2O_5–SiO_2$ bioactive glasses from molecular dynamics simulations. *Physical Chemistry Chemical Physics* 20 (20): 14090–14104.

68 Stevensson, B., Yu, Y., and Edén, M. (2018). Structure–composition trends in multicomponent borosilicate-based glasses deduced from molecular dynamics simulations with improved B–O and P–O force fields. *Physical Chemistry Chemical Physics* 20 (12): 8192–8209.

69 Lu, X., Deng, L., Kuo, P.-H. et al. (2017). Effects of boron oxide substitution on the structure and bioactivity of SrO-containing bioactive glasses. *Journal of Materials Science* 52 (15): 8793–8811.

70 Yu, Y., Stevensson, B., and Edén, M. (2017). Medium-range structural organization of phosphorus-bearing borosilicate glasses revealed by advanced solid-state NMR experiments and MD simulations: consequences of B/Si substitutions. *Journal of Physical Chemistry B* 121 (41): 9737–9752.

71 Du, J. and Xiang, Y. (2016). Investigating the structure–diffusion–bioactivity relationship of strontium containing bioactive glasses using molecular dynamics based computer simulations. *Journal of Non-Crystalline Solids* 432: 35–40.

72 Du, J. and Xiang, Y. (2012). Effect of strontium substitution on the structure, ionic diffusion and dynamic properties of 45S5 bioactive glasses. *Journal of Non-Crystalline Solids* 358 (8): 1059–1071.

73 Xiang, Y. and Du, J. (2011). Effect of strontium substitution on the structure of 45S5 bioglasses. *Chemistry of Materials* 23 (11): 2703–2717.

74 Malavasi, G., Pedone, A., and Menziani, M.C. (2013). Study of the structural role of gallium and aluminum in 45S5 bioactive glasses by molecular dynamics simulations. *Journal of Physical Chemistry B* 117 (15): 4142–4150.

75 Christie, J.K., Ainsworth, R.I., and De Leeuw, N.H. (2016). Investigating structural features which control the dissolution of bioactive phosphate glasses: beyond the network connectivity. *Journal of Non-Crystalline Solids* 432: 31–34.

76 Broglia, G., Mugoni, C., Siligardi, C., and Montorsi, M. (2018). Lithium and copper transport properties in phosphate glasses: a molecular dynamics study. *Journal of Non-Crystalline Solids* 481: 522–529.

77 Gross, T.M., Lahiri, J., Golas, A. et al. (2019). Copper-containing glass ceramic with high antimicrobial efficacy. *Nature Communications* 10 (1). Art. no.: 1979.

78 Voigt, U., Lammert, H., Eckert, H., and Heuer, A. (2005). Cation clustering in lithium silicate glasses: quantitative description by solid-state NMR and molecular dynamics simulations. *Physical Review B: Condensed Matter and Materials Physics* 72 (6). Art. no.: 064207.

79 Christie, J.K., Cormack, A.N., Hanna, J.V. et al. (2016). Bioactive sol–gel glasses at the atomic scale: the complementary use of advanced probe and computer modeling methods. *International Journal of Applied Glass Science* 7 (2): 147–153.

80 Côté, A.S., Cormack, A.N., and Tilocca, A. (2017). Reactive molecular dynamics: an effective tool for modelling the sol–gel synthesis of bioglasses. *Journal of Materials Science* 52 (15): 9006–9013.

81 Tilocca, A. and Cormack, A.N. (2011). The initial stages of bioglass dissolution: a Car–Parrinello molecular-dynamics study of the glass–water interface. *Proceedings of the Royal Society of London Series A* 467 (2131): 2102–2111.

82 Tilocca, A. (2015). Atomic-scale models of early-stage alkali depletion and SiO_2-rich gel formation in bioactive glasses. *Physical Chemistry Chemical Physics* 17 (4): 2696–2702.

83 Zeitler, T.R. and Cormack, A.N. (2006). Interaction of water with bioactive glass surfaces. *Journal of Crystal Growth* 294 (1): 96–102.

84 Tilocca, A., Cormack, A.N., and De Leeuw, N.H. (2007). The structure of bioactive silicate glasses: new insight from molecular dynamics simulations. *Chemistry of Materials* 19 (1): 95–103.

85 Tilocca, A. and Cormack, A.N. (2007). Structural effects of phosphorus inclusion in bioactive silicate glasses. *Journal of Physical Chemistry B* 111 (51): 14256–14264.

86 Tilocca, A. and Cormack, A.N. (2008). Exploring the surface of bioactive glasses: water adsorption and reactivity. *Journal of Physical Chemistry C* 112 (31): 11936–11945.

87 Tilocca, A. and Cormack, A.N. (2009). Modeling the water–bioglass interface by ab initio molecular dynamics simulations. *ACS Applied Materials and Interfaces* 1 (6): 1324–1333.

88 Tilocca, A. and Cormack, A.N. (2010). Surface signatures of bioactivity: MD simulations of 45S and 65S silicate glasses. *Langmuir* 26 (1): 545–551.

89 Christie, J.K., Ainsworth, R.I., Di Tommaso, D., and De Leeuw, N.H. (2013). Nanoscale chains control the solubility of phosphate glasses for biomedical applications. *Journal of Physical Chemistry B* 117 (36): 10652–10657.

90 Tilocca, A. (2015). Realistic models of bioactive glass radioisotope vectors in practical conditions: structural effects of ion exchange. *Journal of Physical Chemistry C* 119 (49): 27442–27448.

91 Christie, J.K. and Tilocca, A. (2012). Integrating biological activity into radioisotope vectors: molecular dynamics models of yttrium-doped bioactive glasses. *Journal of Materials Chemistry* 22 (24): 12023–12031.

92 Christie, J.K., Malik, J., and Tilocca, A. (2011). Bioactive glasses as potential radioisotope vectors for in situ cancer therapy: investigating the structural effects of yttrium. *Physical Chemistry Chemical Physics* 13 (39): 17749–17755.

93 Tilocca, A. (2010). Sodium migration pathways in multicomponent silicate glasses: Car–Parrinello molecular dynamics simulations. *Journal of Chemical Physics* 133 (1). Art. no.: 014701.

94 Smith, W., Forester, T.R., Greaves, G.N. et al. (1997). Molecular dynamics simulation of alkali-metal diffusion in alkali-metal disilicate glasses. *Journal of Materials Chemistry* 7 (2): 331–336.

95 Pedone, A., Malavasi, G., Cristina Menziani, M. et al. (2008). Role of magnesium in soda-lime glasses: insight into structural, transport, and mechanical properties through computer simulations. *Journal of Physical Chemistry C* 112 (29): 11034–11041.

96 Car, R. and Parrinello, M. (1985). Unified approach for molecular dynamics and density-functional theory. *Physical Review Letters* 55 (22): 2471–2474.

97 Cormack, A.N., Du, J., and Zeitler, T.R. (2002). Alkali ion migration mechanisms in silicate glasses probed by molecular dynamics simulations. *Physical Chemistry Chemical Physics* 4 (14): 3193–3197.

98 Tilocca, A. (2017). Dynamical descriptors of bioactivity: a correlation between chemical durability and ion migration in biodegradable glasses. *Physical Chemistry Chemical Physics* 19 (9): 6334–6337.

99 Tilocca, A. (2011). Molecular dynamics simulations of a bioactive glass nanoparticle. *Journal of Materials Chemistry* 21 (34): 12660–12667.

100 Brunner, T.J., Grass, R.N., and Stark, W.J. (2006). Glass and bioglass nanopowders by flame synthesis. *Chemical Communications* (13): 1384–1386.

101 Pedone, A., Muniz-Miranda, F., Tilocca, A., and Menziani, M.C. (2016). The antioxidant properties of Ce-containing bioactive glass nanoparticles explained by molecular dynamics simulations. *Biomedical Glasses* 2 (1): 19–28.

102 Nicolini, V., Varini, E., Malavasi, G. et al. (2016). The effect of composition on structural, thermal, redox and bioactive properties of Ce-containing glasses. *Materials and Design* 97: 73–85.

103 Nicolini, V., Gambuzzi, E., Malavasi, G. et al. (2015). Evidence of catalase mimetic activity in Ce^{3+}/Ce^{4+} doped bioactive glasses. *Journal of Physical Chemistry B* 119 (10): 4009–4019.

104 Prado, S.C.C., Rino, J.P., and Zanotto, E.D. (2019). Successful test of the classical nucleation theory by molecular dynamic simulations of BaS. *Computational Materials Science* 161: 99–106.

105 Tipeev, A.O. and Zanotto, E.D. (2019). Nucleation kinetics in supercooled $Ni_{50}Ti_{50}$: computer simulation data corroborate the validity of the classical nucleation theory. *Chemical Physics Letters* 735: 136749.

106 McKenzie, M.E. and Mauro, J.C. (2018). Hybrid Monte Carlo technique for modeling of crystal nucleation and application to lithium disilicate glass-ceramics. *Computational Materials Science* 149: 202–207.

107 Wilkinson, C.J., Cassar, D.R., DeCeanne, A.V. et al. (2021). Energy landscape modeling of crystal nucleation. *Acta Materialia* 217: 117163. https://doi.org/10.1016/j.actamat.2021.117163.

108 Varshneya, A. and Mauro, J.C. (2019). *Fundamentals of Inorganic Glass Science*, 3e. Elsevier.

109 Cassar, D.R., Rodrigues, A.M., Nascimento, M.L.F., and Zanotto, E.D. (2018). The diffusion coefficient controlling crystal growth in a silicate glass-former. *International Journal of Applied Glass Science* 9 (3): 373–382.

110 Cassar, D.R., Serra, A.H., Peitl, O., and Zanotto, E.D. (2020). Critical assessment of the alleged failure of the classical nucleation theory at low temperatures. *Journal of Non-Crystalline Solids* 547: 120297.

111 Cassar, D.R. (2016). Crystallization driving force of supercooled oxide liquids. *International Journal of Applied Glass Science* 7 (3): 262–269.

112 Lodesani, F., Menziani, M.C., Maeda, K. et al. (2020). Disclosing crystal nucleation mechanism in lithium disilicate glass through molecular dynamics simulations and free-energy calculations. *Scientific Reports* 10 (1): 1–14.

113 Zanotto, E.D. (1982). The effects of amorphous phase separation on crystal nucleation in baria-silica and lithia-silica glasses. PhD thesis. The University of Sheffield.

114 Rodrigues, A.M. (2014). Diffusion processes, crystallization and viscous flow in barium disilicate glass. PhD thesis. Federal University of Sao Carlos.

115 Xia, X., Dutta, I., Mauro, J.C. et al. (2017). Temperature dependence of crystal nucleation in $BaO{\cdot}2SiO_2$ and $5BaO{\cdot}8SiO_2$ glasses using differential thermal analysis. *Journal of Non-Crystalline Solids* 459: 45–50.

17

In Vitro and *In Vivo* Studies of Bioactive Glasses

Sadaf Batool, Zakir Hussain, and Usman Liaqat

School of Chemical and Materials Engineering (SCME), National University of Sciences and Technology (NUST), Islamabad, Pakistan

17.1 Introduction

Tissue regeneration is the most promising approach to regenerate lost and damaged tissues. At present, the number of incidents causing tissue or organ failure is increasing due to multiple reasons and their treatment is the major apprehension of health officials. To treat damaged or lost body tissues or parts, several treatments like surgical repairs, prostheses, transplantation, mechanical devices, and drug therapy have been used widely, but the results were not satisfactory enough to continue these practices at clinical levels. Living organisms have the potential to repair damaged tissues. Some organisms like lizards can regenerate whole lost body parts. In humans, the process of repairing and regeneration mainly occurs in bone and skin tissues. The healing process is efficient in the case of minor defects. However, it is slower and can lead to several complications for major tissue damages, musculoskeletal injuries, and lost body parts. To treat these defects, external support materials made up of metals, polymers, and ceramics are used. The earliest support materials were bioinert. Their primary function was to provide mechanical support to newly grown tissues. This process involves multiple surgeries which make the whole process not only painful but can also lead to several severe complications. Moreover, cytotoxicity and immune system rejections were the major drawbacks of these biomaterials. To avoid these complications and to make the tissue repairing system robust and biocompatible organ transplantation, allografts and autografts were introduced later. These practices have shown remarkable results, but the availability of the donor tissues in case of large defects and immune system rejections were the major limitations. Moreover, the repairing of damaged neuronal tissues was not possible using these traditional techniques because it was well established that neuronal tissues do not possess stem cells; therefore, they cannot regenerate themselves and need external assistance in the form of scaffold for regeneration. The traditional regeneration methods were suitable for bone tissue regeneration somehow but not for the repairing or regeneration of other body tissues. To repair other tissues, the tissue engineering field was developed. It is a combined engineering and basic sciences approach to solve the problem of tissue regeneration with minimal or no side effects. The term "tissue regeneration" was first defined by Joseph Vacanti and Robert Langer. It is defined as "An interdisciplinary field in which principles of engineering and life sciences are applied together for the synthesis of functional biological substitutes to maintain, restore, and improve biological tissue function" [1].

To fulfill the high demand for tissue regeneration, several new materials and methods were introduced. These materials have the potential to mimic the natural systems or to support the natural

Bioactive Glasses and Glass-Ceramics: Fundamentals and Applications, First Edition.
Edited by Francesco Baino and Saeid Kargozar.

healing process without eliciting any reaction in the body. Despite remarkable results and clinical applications of synthetic biomaterials, there are still several of limitations. In the past two decades, the work to develop ideal materials for tissue regeneration emerged dramatically and several biomaterials with different compositions have been developed. Practices have been done to regenerate bone, cartilage, skin, liver, and heart tissues using efficient materials.

Bioactive glasses were considered an ideal material for bone tissue engineering due to their osteogenic nature and the ability to promote angiogenesis [1, 2]. They are porous, biodegradable, and can be used for treating long-lasting bone defects due to their innate antiseptic ability [3]. They stimulate gene expression [4, 5]. The silica ions stimulate the osteoprogenitor cells at the genic level [5, 6] to induce osteoblast migration, adhesion, and proliferation at the defect site [7]. The exact mechanism by which bioactive glasses influence osteoblastic cells is uncertain; however, it is observed that the primary osteoblasts show higher phenotype expression and increase the mineralized collagen nodules formation ability in the presence of these glasses during *in vitro* experiments [8]. The byproducts elicit the overexpression of bone mitogenic growth factor (IGF-II) [9]. 45S5 Bioglass is the oldest known bioactive glass [10]. 45S5 monoliths were commercialized first and used as bone cement and substitutes [11]. However, the first bioglass particulates were commercialized with the name of PerioGlas. It was a 45S5 Bioglass with the size of the particulates in the range of 90–710 μm and used as bone grafts clinically. 45S5 Bioglass was also used in toothpaste and commercialized with the name of Nova Min. The clinical trials have shown that 45S5 can treat sensitivity and root canal issues along with mineralization of dentine defects [12]. Its particles along with autologous bone tissues provide good adherence and relive pain in dentine defects [13]. Another bioglass S53P4 was commercialized with the name of BonAlive in 2006 and used for grafting the maxilla bone. Bioactive glasses are Class-A biomaterials, i.e. these materials undergo rapid reactions on their surface and adapt to the surrounding environment quickly. The active ions are released which initiate intracellular responses at the interface of biomaterial. They have potential to regenerate tissue at the surface and along the interface in inward direction.

17.2 Bioactive Glass

Bioactive glasses were considered an ideal material for bone tissue engineering due to their excellent tissue regeneration and angiogenesis properties [1, 2]. It is bioactive, biodegradable, and can be used for treating long-lasting infectious defects due to its innate antiseptic ability [3]. It has the potential to initiate regeneration by stimulating gene expression [5].

The silica ions of bioactive glass stimulate the progenitor cells at the genetic level [6] to induce cell migration, adhesion, and proliferation at the defect site [7, 10]. Since its synthesis, it has been researched extensively at an academic and industrial scale which resulted in the formation of different compositions with improved biological and mechanical properties [14].

17.3 Chemical Composition of Bioactive Glass

The Hench Bioglass did not form fibrous tissues at the interface [15]. Hench developed a quaternary system which was later used to prepare different compositions of bioactive glass. The sole requirement for designing bioactive glass was not to include any element that is toxic to mammalian cells. The first bioglass, i.e. 45S5 BG ($45SiO_2$–$24.5CaO$–$24.5Na_2O$–$6P_2O_5$) has silica as a major component along with oxides of sodium and calcium [6]. It falls in the eutectic point but it is far from the

typical soda-lime glass compositions. The composition of bioglass depends upon the bioactivity index (I_B) which should be 50% at $t_{0.5}$ [16].

The bioactivity index can be measured by using the following formula.

$$I_B = \left[100/t_{0.5}\right] \text{ days}^{-1}$$

The bioactivity level of any material is measured by bioactivity index (I_B). It is a time taken by biomaterial to form half of interface bond with surrounding tissues ($t_{0.5}$). The bioactivity index helps to categorize material on the basis of binding properties. For example, a material having I_B greater than 8 will make interface with soft as well as hard tissues. Materials having I_B less than 8 but more than 0 will bind with hard tissues only. Bioactive glasses have I_B more than 8 while hydroxyapatite less than 8.

The typical composition of the bioglass and bioceramics is indicated in 45S5 BG and exists in the form of amorphous, semi-crystalline, and crystalline. The *in vitro*/*in vivo* activity of all three forms is the same; however, the crystallinity affects the mechanical properties [17]. Based on inorganic oxides, bioactive glasses are divided into three major categories [18], i.e.

(1) Network forming oxides (SiO_2, B_2O_3, P_2O_5)
(2) Network modifying oxides (Na_2O, CaO, MgO, K_2O)
(3) Intermediates oxides (Al_2O_3, ZnO, ZrO_2, TiO_2) [19]

The structure of bioactive glass is mandatory to understand the effect of composition on bioactivity. In 45S5 BG, the SiO_2 network is covalently bonded with P_2O_5. Both these components occupy a tetrahedron unit and are covalently bonded with oxygen atoms at the vertex. This structural bonding is called the network forming bond. Covalently linked silica gives structural stability and porosity to bioactive glasses [20]. Network modifiers form ionic interactions with the oxygen atoms as well as form nonbonding oxygen linkages. CaO is a network modifier. It provides the reactivity as it undergoes hydrolysis reaction to yield Ca^{2+} ions in the surrounding fluid and facilitates the incorporation of hydrogen ions into the bioactive glass. The role of P_2O_5 is more complicated because at the 10 mol% concentration, it can make bioactive glass non-bioactive [21]. This is because the P_2O_5 forms orthophosphate nanocrystals at the nucleation sites that limit the cation exchange reaction, i.e. calcium and hydrogen ion exchange between fluid and bioactive glass surface. This ion-exchange reaction is the base of carbonated hydroxyapatite (CHA) formation [22].

The network formers provide stability to the basic structural framework while network modifiers increase the bioreactivity [23]. Bioactive glasses have lower connectivity values "*Y*" as compared to pure glasses which have all the oxygen atoms bonded to silica and phosphate covalently. This bonding results in the formation of dense structures. Bioactive glasses have a low *Y* value, i.e. 45S5 BG has a connectivity value of 2.07. Network former and modifier species influence bioactivity [24].

17.4 Key Concepts Before Using Bioactive Glass for Tissue Regeneration

Following key points must be kept in mind before using bioactive glass-based scaffolds for tissue regeneration.

a. Bioactive glass is amorphous and mechanically weak. Traditionally glasses are made crystalline to improve their mechanical properties. Crystalline glasses are not fully crystalline rather the crystalline phase is embedded inside the amorphous glassy matrix. In the case of

bioactive glasses, mechanical strength and bioactivity are the two major considerations of researchers. The mechanical properties of 45S5 glass decrease with crystallization. Whereas 13-93 and borate 13-93B3 glass show higher elastic modulus and compressive strength after crystallization. Crystallization enhances fracture toughness and flexural strength. Crystallization in the case of bioactive glasses reduces their bioactivity and makes them inert. This competition between mechanical strength and bioactivity has been focused and it leads to the formation of bioactive glasses with different compositions. To date, the Na-containing 45S5 bioglass is crystalline glass with good bioactive and biodegradable properties. This glass is sintered to form crystalline phases in the glassy matrix. Its degradation reaction complements well with the healing rate of bone.

b. The bioactivity of BGs also depends upon microstructure along with the chemical composition. 13-93 BG scaffold with 60% porosity and 90–110 μm pore diameter showed good tissue infiltration in cortical bone than the same scaffold implanted to treat trabecular defect even with much less porosity, i.e. 85% and 100–150 μm pore diameter. The exact reason for this behavior is unknown; however, it is assumed that this could be due to improved mass transport and cell–cell interaction in anisotropic pores rather than randomly oriented microstructures.
c. 13-93 BG forms active hydroxyapatite layer in seven days *in vitro* in simulated body fluid (SBF) while 45S5 of same size forms CHA layer within eight hours. The lower biological activity of these glasses is because the active components have greater interconnected linkages with each other and higher content of silica which does not allow active ingredients to leave the surface easily.
d. Pore morphology also plays a critical role in tissue regeneration, i.e. the columnar pores show more biological activity. For example, the mechanical strength and biological potential of 13-93 BG scaffold possessing microstructure oriented columnar pores were evaluated *in vitro* against the rat calvarial defect model. Trabecular microstructure scaffolds were used as positive control prepared by using the polymer foam replication method, whereas empty defects were considered as a negative control. The columnar-oriented scaffolds have 50% porosity with a pore diameter of 50–100 mm, while trabecular scaffolds have 80% porosity with a pore size of 100–150 mm. The trabecular scaffolds induced bone growth into the periphery of implants with good tissue integration at 12 weeks. However, columnar-oriented scaffolds showed maximum growth on the Dural side and minimum into the periphery of the scaffold.
e. The surface roughness of bioactive glass cannot be neglected as it facilitates tissue infiltration [25].
f. During the fabrication of bioactive glass into scaffold, heat treatment is done which leads to nucleation of the crystalline phase. These crystalline phases must not induce toxicity in the living cells or the surrounding of the implant and must form a layer of hydroxyapatite on their surface when coming in contact with physiological fluids.
g. They should not elicit an inflammatory response and should not demonstrate immunogenicity.
h. They should undergo neogenesis and degrade into bioresorbable byproducts.
i. The surface and inner core of the bioactive glass scaffold should be designed in such a way that it can be sterilized easily.
j. The mechanical properties must be comparable with the tissue's mechanical strength which it is going to replace. It should be strong enough to support the vascularization and healing process.
k. It should have a controlled interconnect porous network to support adhesion and vascularization. A porosity of more than 90% and at least 100 μm pore size is desired for facilitating vascularization.

l. Procedure should be cost-effective and maintain all the required features [26, 27].

m. The chemical pretreatment of bioactive glass affects its CHA layer formation ability. For example, bioactive glass when immersed in K_2HPO_4 solution *in vitro* creates a rough layer of CHA on the bioactive glass surface. The thickness of the layer increases directly with immersion time. These implants show good tissue integration and $32 \pm 13\%$ bone growth in the form of islands with large interfacial gaps. Because the surface was made rough before implantation which provided better surface area to cells for growth and infiltration. The newly grown CHA layer has a mesoporous structure and supports the adsorption of endogenous proteins. This layer also plays important role in controlling the release of bone morphogenic protein-2 (BMP-2) from the scaffold [28].

17.5 Reactions of BGs in Physiological Fluids

Bioactive glass forms an active layer of CHA on its surface that facilitates its binding with the bone. This bonding mechanism was first proposed by Hench [14]. Eleven reaction steps occur to regenerate tissue while using Class-A biomaterial. The first five reactions occur within 2–24 hours post-implantation (Figure 17.1). The soluble ionic species are desorbed in these steps, and poly-crystalline CHA and hydrated silica layers form on the surface of bioactive glass. The rate of layer formation depends upon the localized concentration gradient.

a. Ion-exchange reaction

The first step after implantation is an exchange of active ions between the body's fluids and network modifying ions, i.e. Na^+, Ca^{2+}, Mg^{2+}, and K^+. The SiO_2 groups undergo hydrolysis reaction, and the interfacial pH is increased.

Following chemical reaction is involved in this step, i.e.

$$SiONa^+ + H_2O \longrightarrow SiOH + Na^+ + OH^-$$

The rate of this reaction is controlled by the diffusion of active ingredients. The pH is increased to 10.5 in the surroundings of the implant due to the consumption of hydrogen ions [29].

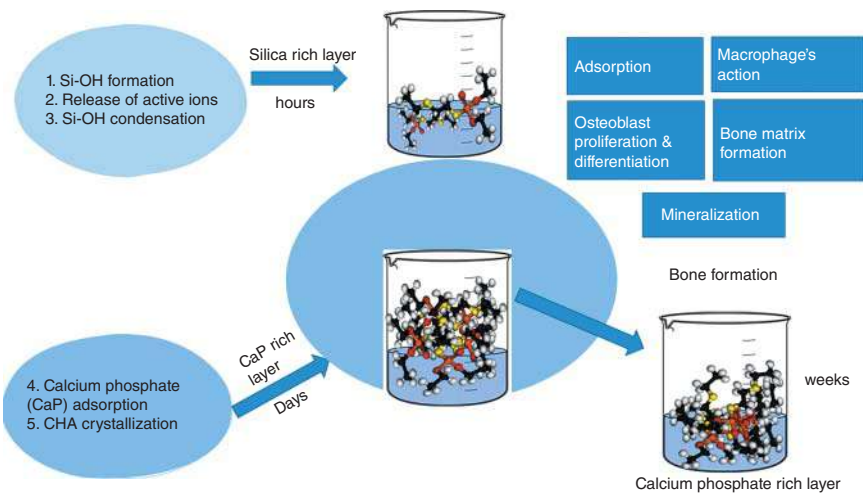

Figure 17.1 Schematics of bioactivity of BGs.

b. Dissolution of silica network
The increase in pH accelerates the dissolution of the basic silicon oxygen network. The layers of silicic acid keep on growing on the scaffold surface. Dissolution of silica is a crucial step to initiate reactions that lead to the formation of an amorphous hydroxyapatite layer [30].

$$-Si-O-Si- + H_2O \longrightarrow 2\left[SiOH^+\right]$$

c. Condensation reaction
The condensation reaction occurs in Na^+ and Ca^{2+} depleted region to induce polymerization of silanol groups and forms a SiO_2 rich layer on BGs surface.

d. Migration of calcium-phosphate ions
In this step, calcium and phosphate ions migrate to the surface to form a film of $CaO–P_2O_5$. The film grows with time due to the continuous migration of calcium and phosphate ions from the silica layer to the surface to form an amorphous apatite layer. This layer facilitates the bonding of the implant with surrounding tissues [31]. However, some researchers do not support the idea of migration of phosphate ions to the surface to facilitate tissue adhesion. The simpler hypothesis about the precipitation of calcium and phosphate ions is that the interfacial pH facilitates this step, not the amorphous silica layer as no amorphous silica layer was detected between CHA and biomaterial in later studies [32]. The interaction of BGs and surrounding tissues is governed by mechanochemical forces.

e. Formation of calcium phosphate (CaP) film
These silica layers adsorb OH^-, CO_3^{2-}, and F^- ions from physiological fluid and form a hydroxy-carbonate/hydroxyapatite layer. After that, the reaction sequence follows up to initiate the tissue bonding mechanism [33].

f. Cell bonding mechanisms
At stage 6, adsorption and desorption of growth factors occur, facilitated by the newly formed hydroxyapatite layer (Figure 17.2). The adsorption and desorption of bioactive growth factors influence the time required by macrophages to prepare the implant site for tissue repair. Macrophages secrete chemokines at stage 7 and attachment of stem cells occurs at stage 8, which leads to proliferation and differentiation of these cells during stage 9. The progenitor cells form colonies on the surface of bioglass during stage 10 which occur within two days. These

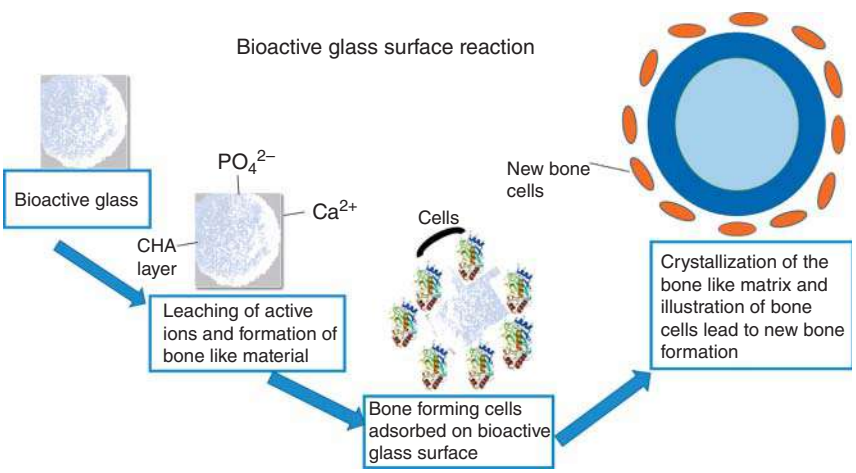

Figure 17.2 Bioactive glass surface reaction.

cells begin the production of growth factors that stimulate the biological repairing process, i.e. cell division, mitosis, and production of extracellular matrix proteins. Then mineralization of the matrix starts with the maturation of stem cells followed by encapsulation. Mineralization is the final product of *in vitro* and *in vivo* studies and is achieved with 6–12 days post-implantation. The formation of the hydroxyapatite layer is essential for the attachment and proliferation of stem cells and stages 8–10 are critical stages in tissue regeneration.

17.6 Interaction of Bioactive Glass with Proteins

The adsorption of proteins on the bioactive glass surface is a complex phenomenon. It is crucial step of the regeneration/repairing process and regulated by protein type, its environment, chemical, and surface properties of bioactive glass. The surface properties affect the confirmation and orientation of proteins which is necessary for the functioning of the protein. The exact phenomena and factors influencing the adsorption of protein on the bioactive surface have been studied extensively but it is not fully understood yet. The *in vitro* adsorption–desorption studies of proteins give an insight into protein interaction with bioactive glass surface, but these experiments usually involve a single type of proteins while in the natural system multiple proteins and parameters are simultaneously affecting the adsorption/desorption process. To combat these issues, more studies using serum proteins should be conducted along with advanced *in situ* characterization techniques. The protein interaction studies give a deep insight to improve the properties of bioactive glass and to reduce foreign body reactions. There are many driving forces like hydrogen bonding, van der Waal interactions, hydrogen bonding, electrostatic interactions, and hydrophobic and hydrophilic interactions that are responsible for the adsorption of proteins on the surface of bioactive glass. Proteins have carbon backbone, carboxylic acid and amine groups thus possess polar and nonpolar domains which bind with the surface groups of the bioactive glass to form chemical interactions. Proteins have complex structures therefore, almost all aforementioned forces are contributing in bioactive glass surface and protein interactions. However, the external environment, temperature, pH of surrounding media, chemistry, and topography of the scaffold surface affect the abovementioned driving forces. Protein size also plays a major role in adsorption, for example, larger proteins have more adsorption sites and they interact with a surface easily as compared to smaller proteins. Similarly, the surface properties of bioactive glass affect adsorption of proteins on surface. The surface properties of bioactive glasses change dramatically by changing the synthesis methods. For example, in the sol–gel synthesis method, material have a porous surface which facilitates protein adsorption while melt-derived bioactive glasses have a smooth surface. However, proteins have different types, i.e. some adsorb on the smooth surface while others adsorb efficiently on curved surfaces. Thus, it is a collective response of protein type and surface properties.

Porous materials have high surface reactivity which facilitates the formation of dynamic interactions with the biological fluids. The protein adsorption phenomenon starts immediately as soon as the bioactive glass scaffold comes in contact with physiological fluids. Other body reactions like the dissolution of active materials and formation of hydroxyapatite start immediately which change the surface properties of bioactive glass thus, affect the adsorption/desorption of proteins as it completely changes the surface chemistry of the bioactive glass. The surface reactions can be controlled by controlling the surface morphology and chemistry of bioactive glass. The difference in network former and network modifiers composition affects surface reactions significantly; however, detailed studies on these parameters will provide a deep insight to address these issues. To improve the mechanochemical and biological properties of bioactive glass, sometimes additional

metals are added which alter protein surface interactions completely. For example, in comparison to simple glasses, bioactive glass contains calcium which is charged in aqueous media and forms electrostatic bonds with charged domains of proteins. Moreover, calcium ions also alter textural properties of bioactive glasses for example hydrophobicity and surface reactions. The inclusion of calcium ions into bioactive glass reduces the interconnected network of bioactive glass, increases pore size which increases surface activity, and thus facilitates surface mineralization. The hydroxyapatite layer has a good affinity with the amine group and carboxylic group of proteins. However, some studies have shown that hydroxyapatite layer formation reduces silica ions concentration on the surface and increases cation activity which sometimes inhibits the adsorption of protein fibrinogen on the surface. But in the case of negatively charged proteins, the carboxy-glutamic acid residues chelate with calcium ions and improves adsorption of proteins. Similarly, the addition of other elements also affects the protein adsorption affinity. For example, silver ions facilitate the protein adsorption on the surface, and this may be due to the high binding affinity of bovine serum albumin (BSA) with silver. Similarly, iron oxide incorporation into the bioactive glass gives good surface coverage with BSA proteins. However, the bioactivity of foreign species depends upon their concentration. For example, iron oxide present up to 15–20% in the bioactive glass gives good surface coverage, while 10% concentration gives half surface coverage. These foreign species also change the secondary/tertiary conformation of the proteins. These conformal changes sometimes restrict the repairing of the damaged tissues. Thus, ionic content, surface reactions, interface, and surrounding environment affect the bioactivity of the proteins [34].

17.7 Cell Cycle Involved in Tissue Regeneration

In the natural repairing process, for bone cells to regenerate or repair themselves, osteoprogenitor cells must undergo mitosis. Older people have very few bone cells therefore, the repairing is slow in them which causes osteoporosis and musculoskeletal injuries quickly. The regrowth is slower and painful under extensive care. The local environment must send correct chemical stimuli to the osteoprogenitor to direct them to enter the cell cycle.

The resting cells are represented as G0 phase. A cell cycle begins after a cell completes foregoing mitosis. At step 1, the cell grows and carries out normal metabolism, called the G1 phase. Osteoblasts synthesize phenotype-specific cellular products that act as osteoblast differentiation markers. These cellular products can be an enzyme, protein, or alkaline phosphatase. This process occurs at stage 9 of the repairing cycle. The osteoblast differentiates and becomes functional to release tropocollagen macromolecules which self-assemble themselves to form type-I collagen. Type-I collagen is a predominant collagenous molecule that is present in the mineralizable extracellular bone matrix. The cell then enters in S phase if the local environment is favorably followed by the growth period in the G1 phase. In S phase, the synthesis of DNA begins and duplication of nucleus chromosomes occurs. After duplication, cell enters in G2 phase where it undergoes mitosis after critical assessment of DNA replication accuracy by using a DNA repair enzyme. In this phase, the synthesis of DNA and increase of mass are important. It is followed by the activation of various growth factors. Two daughter cells with a complete set of nuclei are produced at the end of the G2 phase. The checkpoints ensure the transfer of correct information to the next phase in the cell cycle. If the local chemical environment is not favorable, then the G1 or G2 phase is not completed and the cell proceeds toward apoptosis. The bioactive glass has the potential to produce a favorable local chemical environment that enables osteoprogenitor cells to grow and divide. Osteoprogenitor cells pass through cell cycle checkpoints to stimulate osteo-production *in vivo*. At an older age, there

is a fewer checkpoint through which progenitor cells can run the gauntlet to enter into M phase safely. The cells that cannot pass the checkpoints are not healthy. They do not fulfill the replication criteria and undergo apoptosis. The cumulative effect of damaged genes and the presence of fewer osteoprogenitor cells results in a progressive decrease in bone density at an older age. In the bioactive glass, rapid release of hydrated silica and calcium ions leads to nucleation and crystallization of amorphous calcium phosphate layers into polycrystalline CHA layers. The CHA provides a high surface area to cytokines of osteoprogenitor cells for binding. The osteoblasts grown on bioactive glass surface has more fiber and filopodia like processes. These morphologies are characteristic of cell activation. At S phase, the growth of osteoblasts on the surface of biomaterial is 100%. The *in vitro* studies have shown that the percentage of osteoblasts is more than 100% at the G2 phase in the case of bioactive glass scaffold than the other bioactive materials. The osteoblasts are more apoptotic in the case of bioactive glass and the only cells capable of differentiating, survive the first few days of growth on a bioactive glass substrate.

The rapid shift of the cell population in different phases is important as it leads to enhanced growth of bone. The cells that are not apoptotic form confluent sheets on the biomaterial surface. These cells cannot differentiate into mature osteoblasts. The confluent sheets form on the surface of bio-inert materials usually. These cells do not form bone nodules *in vitro* nor bone matrix *in vivo*. While in the case of bioactive glass, fiber-like processing is originated and cells become more apoptotic which leads to the development of healthy cells that differentiate and grow into mature bone osteocytes. However, the osteoblasts are mitotically active on the surface of bioactive glass and results in the expression of osteoblast phenotype and alkaline phosphatase activity. The *in vivo* and *in vitro* experiments show that bioactive glass takes control of the osteoblast cell cycle in six days. After six days the proportion of cells in the S phase and G2-M phase is larger than on the surface of bioactive glass. The bioactive stimulated expression of alkaline phosphate is greater than 700%, and the proportion of cells undergo apoptosis is large. At the same time, mature osteoblasts grown on the surface of bioactive materials start producing osteocalcin (OCN) which is a non-collagenous protein of the bone extracellular matrix. The formation of OCN is the onset of the mineralization process which is the critical step of bone regeneration. It is stage 11 of the tissue regeneration process by active biomaterials. The osteoblasts organize themselves into self-assembled 3-D structures of the mineralized extracellular matrix.

In the case of bioactive glass, the time of collagen formation on scaffold surface is similar *in vivo* and *in vitro*. The kinetics of bone nodule formed *in vitro* are also similar to bone formation *in vivo*. The self-assembled 3-D architecture is formed by osteoblasts when the soluble ionic constituents of bioactive glass reach a threshold concentration even if the substrate for supporting the osteoblast attachment is not present in the culture media. The ionic concentration is 17–20 ppm for silica and 88–100 ppm for calcium ions. The threshold concentration is achieved only by the controlled dissolution active ingredients of bioactive glass into the culture medium. From these observations, it is concluded that the role of bioactive glass is to release active ions in the culture media at the rate that complements well with the time and concentration required to initiate the growth of osteoblasts primarily. The bioactive glass stimulates the cell cycle on the 12th-day post-implantation. The cells present in S and G2-M phases are large in number and the process occurs so efficiently that the cells not capable of differentiating into the healthy osteoblast phenotypes undergo apoptosis at a higher rate than on the surface of class-B type biomaterials. The death of unhealthy cells and faster growth of healthy cells lead to the formation of healthy bone nodules at a significant rate. These nodules organize themselves into complex structures having a larger number of osteocytes (Figure 17.3).

The molecular biology studies of bone cell formation in the presence of bioactive glass suggest that bioactive glass stimulates the shift of the osteoblast cell cycle genetically. Within few

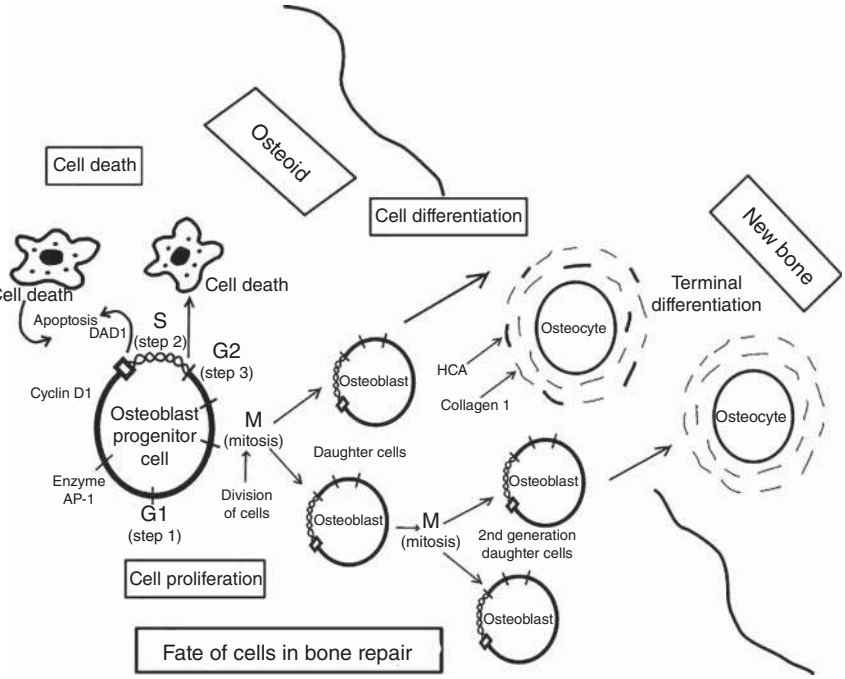

Figure 17.3 Cell cycle involved in bone tissue regeneration. Source: Image reproduced with permission from Hench [35].

hours of exposure, the bioactive glass ionic constituents stimulate human osteoblasts genes encoding nuclear transcription factors and growth factors. IGF-II, IGF-binding protein, and IGF-II proteinases are activated particularly. The expression of genes is increased from 200% to 500% in the case of bioactive glass. This quick gene activation along with the expression of several growth factors modulate the cell cycle of osteoblasts.

Thus, bioactive glass enhances bone tissue regeneration by controlling genes that are directly involved in induction and progression. The G0 to G1 transition of osteoblasts, following initiation of cell division, is controlled by a family of transcription factors. The transcription factors not only initiate the cell division as well as provide definite stimuli for the development of osteoblastic phenotype cells. These proteins must be present at the defect site for stem cells to differentiate into bone phenotype growing cells. The bioactive glass ionic dissolution byproducts can stimulate human osteoblast cell cultures to activate the expression of cell cycle regulators and transcription factors after 48 hours of implantation or exposure to culture media. The osteoblast transcription factors *c-Jun*, *fra-1*, and *c-myc* (*myc* proto-oncogene) are activated by the bioactive glass. The *c-Jun*, a heterodimeric complex, is formed with Fos protein. It interacts with the activator protein 1 (AP-1) binding site of DNA. The *Fos* (*FosssB*, *fra-1*, and *fra-2*) and *Jun* (*c-Jun*, *JunB*, *JunD*) genes together represent the AP-1 transcription factor. The AP-1 promotes osteoblast-specific genes like OCN, collagenase (matrix metalloproteinase-1 [MMP-1]), alkaline phosphatase, and α 1-collagen. This AP-1 transcription factor expression is crucial for osteogenesis *in vitro* and *in vivo*. It leads to osteogenic differentiation of cartilage and plays a critical role in the regulation of endochondral osteogenesis during earlier stages of bone formation as well as fracture healing *in vitro*. The transcription factor c-myc is important for controlling the growth of osteoblast. It is a member of the helix-loop-helix

transcription factor and a member of the myc family. It activates the growth-promoting genes like *rcl* (RNA terminal phosphate cyclase like 1). These genes stimulate cell proliferation. This effect is notably induced by ionic products of bioactive glass.

The post-fracture osteogenesis occurred by mediating parathyroid hormone-induced differentiation by c-myc expression *in vivo*. AP-1 expression is regulated by c-myc transcriptional factor Puf (Pumilio RNA-binding protein family) which binds with c-myc promoter *in vivo*. The osteoblast phenotype expression and proliferation are emulated by transcription factors like c-myc and AP-1. The successful progression of osteoblasts through the cell cycle is most important. It requires specific cyclin, i.e. D1 cyclin which is specific to move cells from the G1 phase to the S phase. This D1 cyclin phosphorylates the retinoblastoma gene product. The retinoblastoma gene releases transcription factors that stimulate the replication of DNA. In the presence of bioactive glass ionic products, the expression of cyclin D1 reaches 400% after 48 hours of exposure. It confirms that the bioactive glass not only increases the gene expression but also produces essential stimuli that are vital for the successful progression of a cell from the G1 to the S phase through checkpoints. It also activates the cyclin D1 and its binding partners CDK4 (CDKN14) and cyclin K cell cycle, regulators. These regulators are responsible for the supervision of the mitotic cycle at an earlier stage. The bioactive glass dissolution byproducts hyperactivate the genes involved in DNA synthesis, recombination, and repair up to 200%. These genes, i.e. DNA exclusion repair protein ERCC excision repair 1, endonuclease non-catalytic subunit (ERCC1), mutL protein homolog, high mobility group protein (HMG-1), and replication factor C 38-kDa subunit (RFC38) evaluate whether the daughter cells are damaged or healthy. They examine the extent of damage and correct it if possible so that the damaged cell cannot differentiate further. If the damage cannot be repaired, then the cell leaves the mitotic cycle and undergoes apoptosis. In this way, the cell faces an arsenal mechanism to prevent the creation of abnormal cells. Only healthy osteoblasts are differentiated. They grow and self-assemble into the complex 3-D architecture of extracellular matrix proteins and mucopolysaccharides. These proteins and polysaccharides are essential for the conversion of mature osteocytes into the mineralized matrix. The bioactive glass also activates the calpain and dolichyl-diphosphooligosaccharide—protein glycosyltransferase subunit DAD1 (DAD1) gene. DAD1 is a defender gene and the N-glycosylation-linked DAD1 regulator is essential for cell survival. The calpain gene activates the proteolytic mechanism which instigates apoptosis.

Bone covers a large number of phenotypes but the most prominent and dominant one is osteoblast. Bone has a central cellular population of osteocytes. Osteocytes are terminally differentiated osteoblasts that are not capable of cell division. They are postmitotic and maintain the mineralized extracellular matrix of the bone throughout life. They represent the cell population, responsible for the synthesis and maintaining of the bone mass. The bioactive glass increases the expression of CD44 phenotype up to 700%. It is an osteocyte marker that increases the number of cell transduction molecules. It also increases the expression of insulin-like growth factor II (IGF-II) to 300%. IGF-II is the strongest osteoblast mitogenic growth factor of bone which induces the proliferation of osteoblast *in vitro*. It creates paracrine effects. Bone cells produce it *in situ* and it is present in high quantity in developing bone periosteum growth plate. It also plays important role in healing fracture callus tissue and ectopic bone tissues. The bioactive glass has the potential to increase the concentration of unbound IGF-II protein by inducing transcription of growth factors and carrier proteins responsible for IGF-II production. The unbound IGF-II increases the cell proliferation of osteoblast. The most important and final step in bone development is collagen and CHA bonding. This bonding determines the mechanical strength of the bone [35].

17.8 *In Vitro/In Vivo* Evaluation of Bioactive Glass for Bone Tissue Regeneration

Some materials behave differently *in vivo* and *in vitro* like dicalcium phosphate di-hydrate forms the HA layer *in vitro* but not *in vivo*, and β-tricalcium phosphate (β-TCP) strongly bonds with bone *in vivo* but does not form the HA layer *in vitro* [36, 37]. There are two methods used for hard tissue engineering, i.e. *in vitro* and *ex vivo*. Multiple factors are affecting *in vivo* like the interaction of scaffold with blood, vascularization, clot formation, and requirements of stem cells. A variety of genes as well as cells, participating in regeneration, are interacting with the biomaterial. Despite all these, *in vitro* studies cannot be ignored as they provide future insight into possible *in vivo* results. Animal models are used for the assessment of scaffolds *in vivo* before clinical trials (Figure 17.4). In these studies, different loading conditions like time duration, age, and tissue qualities can be assessed. The animal selected as a model must show pathophysiological and physiological similarities to humans. The other important factors that must consider before selecting an animal are

- controllable operation
- observation on a variety of testing after surgery over the different period
- implant size
- number of animals
- number of implants per animal
- test duration must follow international standards.

Other selection parameters include animal availability, the cost for acquiring and care, the ability of the animal to withstand testing, social acceptability, and ease of housing. More specifically, an

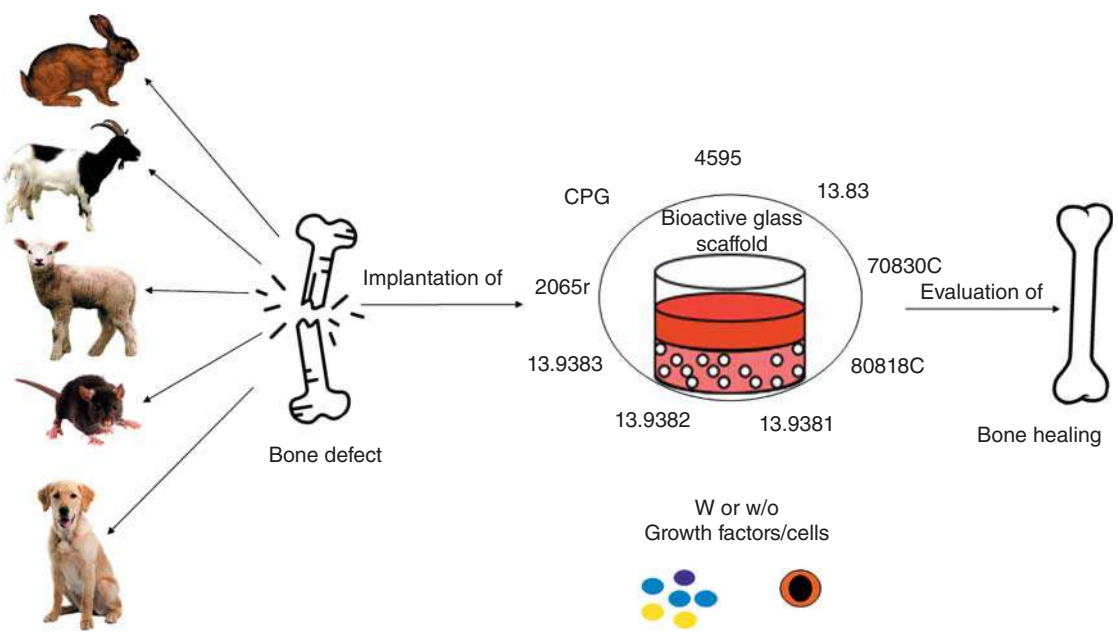

Figure 17.4 *In vivo* application of BGs for bone tissue regeneration (W = with, W/O = without). Source: El-Rashidy et al. [28]/with permission from Elsevier.

understanding of the species-specific bone characteristics, such as bone microstructure and composition, and bone remodeling characteristics is important for investigating bone-scaffold interactions, especially for later translating the results to the human situation. The possible bone defect models studied on animals are long bone, calvarial, and maxillofacial defects. The animal models can be classified into noncritical and critical-sized defects and used for testing osteogenesis and osteocompatibility. The calvarial defects are considered as a non-load bearing model for evaluating scaffolds with inferior mechanical properties to bone. The osteo-regenerative potential of scaffolds with similar properties to the bone is evaluated in the load-bearing defect model, e.g. femur, radius, humerus, and tibia.

An acellular scaffold is incorporated into the tissue injury site that initiates regeneration by attracting the osteoconductive mediators and stem cells *in situ* method. However, in *ex vivo*, the cells are seeded on the scaffold that orchestrates the bone formation by allowing them to divide and grow [38, 39]. Hench and his coworkers demonstrated the interaction of BGs with bone by performing a test on rats. The bioactive glass scaffold showed good tissue integration and new bone was formed within few days after implantations [40].

Silicon is present in the bone and extracellular matrix of the body in the range of 100–550 ppm. It exists at calcification sites and takes part in mineralization during bone growth [41]. 45S5 BG is a silicate-based bioglass. It has a 3-D network of Si–O–Si atoms coordinated in the fourfold axis. [42]. It forms a layer of CHA on its surface, similar to the bone inorganic phase, in contact with the physiological fluids. This layer forms a strong interfacial bond with surrounding tissues [43]. 45S5 BG undergoes chemical degradation reactions which release active ions from its matrix onto the surface to form the biological layer. Although silica is toxic to the cells, the silica released from the BGs is either eaten up by phagocytes within the body or excreted out through urine [44, 45]. The excretion mechanism for silica was studied *in vivo* against tibia defects in rabbits. The histopathological analysis of bone tissue and other organs confirmed that silica is excreted out of the body via urine without affecting any other body part. Although 45S5 BG has the importance of gold standard in bioactive materials. It has several limitations. It has poor mechanical strength, porosity, and is difficult to fabricate into 3-D scaffolds. Silicate-based glasses devitrify upon sintering to form a crystalline phase which improves their mechanical properties and density. Sintering does not affect the HA formation ability of 45S5 [46]. However, the hydroxyapatite layer forms, in this case, are highly crystalline whose degradation time does not complement tissue regeneration. Moreover, all silica present in the sintered 45S5 matrix is not released. It stays for a longer time in the body which can induce toxicity [47]. The limitation with amorphous, porous 45S5 BG is the sudden increase in pH in the surrounding environment. Because the ion exchange reaction occurs spontaneously, leading to fast degradation of the silica network. The active ions released quickly results in a sudden increase in the pH. It creates an ionic imbalance in the surrounding environment [36, 48]. This imbalance can be toxic to surrounding tissues especially during the initial stages of development. Another silicate-based glass 13-93 BG has been developed which is different from 45S5 BG based on a large concentration of silica. It contains an additional network of MgO and K_2O as modifiers. It has been approved to use clinically because it can be processed into 3-D scaffolds. The *in vitro* biological response of 13-93 and 45S5 for MC3T3-E1 and murine osteoblast cell line (MLO-A5) cells is similar but the degradation rate of amorphous 13-93 BG is much slower than the 45S5 [49].

The first studies on the evaluation of osteoinductive properties of 45S5 BG were conducted on dogs. The 45S5 porous foam was implanted in the thigh muscles of dogs for three months. Later another study was conducted on Fisher 344 rats to treat noncritical size load bearing femoral defect. As pH varies suddenly in these glasses, therefore, to minimize the pH variations in cell, culture media scaffolds were conditioned for seven days in (Tris base) with ions of Na^+, K^+, Ca^{2+}, Cl^-,

HCO_3^-, and HPO_4^{2-}. The minimal pH variation facilitates the formation of a CHA surface layer quickly on scaffold surface which improves the bone cell activity.

For the critical-sized defect (a "critically-sized" defect is regarded as one that would not heal spontaneously despite surgical stabilization and requires further surgical intervention) rabbit, femoral defects exhibited that 45S5/ZB4-500 scaffold osteoconductive potential was evaluated. It is a porous scaffold. 45S5 *in vivo* response was also studied to treat radius bone defects of Bengal goats. It shows faster vascularization. These scaffolds have fewer interfacial gaps between host and implant and more interfacial strength. Push out tests show that bioactive glass scaffold has a strong interface as they did not exhibit smooth fracture path along with the interface. The oral and maxillofacial defects vary from small alveolar gaps which result from mandibulectomy. 45S5 BG was first used commercially to prevent resorption of alveolar bone in jaws before dental surgery. The comparative analysis of bioactive glass with commercially available allogeneic and forsterite demineralized bone matrix was evaluated against lamellar and woven bone. The bioactive glass and commercially available scaffolds were implanted in jawbone defects in Persian male dogs. The forsterite showed the highest biological activity which could be attributed to its small size, i.e. in the nanometer range while bioactive glass and allogeneic are in the micrometer range. The nanosized materials have a large surface area which improves scaffold surface reactions and facilities good tissue integration [28]. 45S5 granules promote rapid bone growth as compared to HA when used to treat rabbit femurs defects [50]. The role of silica in inducing cell response is controversial as in recent studies, the biological activity of borate-based glasses has ruled out the role of silica in improving the biological response of BGs [39].

Borate-based bioactive glasses have lower chemical stability. They dissolve rapidly in physiological fluids to form a CHA layer [51, 52]. The mechanism of amorphous HA layer formation is the same as that of silicate-based glasses with one difference only, i.e. they do not form a SiO_2 rich layer [53]. They are osteogenic *in vitro* with good tissue integration *in vivo*. These bioglasses are highly porous and can be used as stimuli-responsive drug delivery systems [54]. Silicates required special conditions, i.e. pH, temperature to release from their crystalline matrix. However, with borate-based glasses it was assumed that borate ion will release from the matrix immediately after immersion and react with hydrogen ions present in physiological fluids to form boric acid which is cytotoxic. In-vitro results confirmed this theory. However, *in vivo* results showed good tissue integration and non-cytotoxicity in a rat model [55]. Similar studies conducted on the rabbit model confirmed the presence of borate ions in the blood. However, the concertation was far below the toxic level. Despite all controversies, these glasses are used clinically because of some good properties of borate ions. These glasses have a controlled degradation rate and other essential ions present in bones can be added to them without affecting biological activity and stability because of flexibility in their structure matrix [36, 56].

Cells like mesenchymal stem cells (MSCs) can be seeded *in vitro* on 13-93 glass scaffolds to improve their biological properties and tissue integration *in vivo*. *In vitro* study in the dorsum, rat model has shown tissue infiltration three times larger than the un-seeded control of the same material [37]. Borate-based glasses have shown promising results *in vivo*, but their *in vitro* toxicity cannot be ruled out. The amount of borate ions is far low than the threshold value of cytotoxicity for cells. It is assumed that maybe at some time the borate ions can cross this threshold value and can become toxic for the body and cells [38]. *In vivo* results with the dorsum of rats and calvaria of rats did not show any toxic results in histological evaluation after implantation [39]. These scaffolds also did not exhibit any toxicity to liver and kidney cells in the rat subcutaneous implantation model. Thus, borate-based BGs scaffolds are nontoxic in a dynamic body environment and have shown excellent

tissue infiltration along with good proliferation and differentiation of bone cells. *In vivo* studies also showed that borate glasses can be used to cure bone infectious diseases like osteomyelitis. A study was conducted on the osteomyelitis rabbit tibia model [53].

17.9 A Comparative Analysis of Silicate- and Borate-Based Glasses in Bone Tissue Regeneration

The silicate-based BGs (45S5 and 13-93) support proliferation and differentiation of MC3T3-E1 and MLO-A5 cells during *in vitro* cell culture experiments. On the other hand, borate-based glasses like 45S5B3 and 13-93B3 have shown very low cell proliferation and differentiation *in vitro* [57, 58].

45S5 BGs induce bone formation during *in vivo* studies. However, studies have shown that the chemical composition of BGs affects the *in vivo* activity and tissue ingrowth. 13-93 BG scaffolds facilitated the attachment and proliferation of MC3T3-E1 pre-osteoblastic cells on their surface as well as in the internal pores prepared by the polymer foam replication method [58]. Similarly, apatite-mullite glass-ceramic has shown bone ingrowth into the pores of scaffolds in the rabbit tibia model. The bonding between bone and scaffolds occurred quickly and bone ingrowth started after four weeks of implantation [59].

13-93B BGs which are rich in borate ions, the reaction is controlled by the bone-implant interface and follows the 3-D contracting sphere model. While in silicate glasses, the reaction is initially controlled by the interface and later it depends upon the diffusion of ionic species through the reaction interface to the surroundings, thus it follows the 3-D diffusion model. If the degradation reaction takes a long time, then the by-product obtained is crystallized HA. In general, the product obtained is amorphous hydroxyapatite with a Ca/P ratio of less than 1.67. The amorphous hydroxyapatite surface layer contains carbonate ions. The stoichiometry of HA formed change significantly from the surface to the interior of the BGs scaffold [47]. The formation of carbonated HA indicates the substitution of phosphate ions by carbonate ions and the formation of calcium carbonate on the bioactive glass surface along with hydroxyapatite. These carbonates can also substitute the hydroxyl ions of HA *in vitro* or nonaqueous but it is not possible in aqueous or biological systems. [60]. The by-products obtained are macroporous structures of HA. Depending upon the chemical composition of BGs, it can be fully converted to HA as in the case of highly reactive borate glasses or partially converted, i.e. the surface is made up of HA with unreacted core inside in case of slow reactive BGs like 45S5. However, the formation of the HA layer depends upon the concertation of Ca in the BG's chemical composition. As the reaction follows a pseudomorphic path, therefore, hollow products are obtained [61] which have in-homogenous, complex layered structure, i.e. outermost layer is compact, homogenous with the lowest porosity while the inner layers are porous and inhomogeneous [47]. The exact mechanism of the formation of the layered structure is unknown. However, it is assumed that the degradation reaction does not proceed continuously, and it starts and stops many times depending upon the concertation of ionic species taking part in the reaction.

A comparative analysis for borate and silica-based glass was done on dorsal rats, with the same microstructure. The borate-based BG scaffolds converted into HA-like material completely while silica-based glass showed partial conversion. The *in vivo* and *in vitro* results confirm that borate-based glasses are more bioactive when compared with silica-based glasses and are non-cytotoxic. 13-93 BG was also used to treat critical-size defects of the load-bearing femur bone in rats and the same results were obtained [62].

17.10 Bioactive Glass for Dentin Regeneration

Bioactive glass is used in dentistry to treat dentinal hypersensitivity. Hypersensitivity is a common dental disease that occurs due to periodontal disease, abrasive tooth brushing, and wear of enamel layer due to trauma. It leads to exposed dentinal tubules. Dental hypersensitivity is explained through hydrodynamic theory, i.e. the external stimuli in the form of hot, cold, or pressure affect fluid movement in the tubules. It results in pressure change which causes excitation of nerve endings in the pulp. Bioglass (NovaMin) has been used clinically to treat hypersensitivity. It mineralizes exposed dentinal tubules, reduces plaque growth and gingival bleeding up to 16.4–58.8%. A bioactive glass containing dentifrice shows superior occlusion of dentinal tubules as compared to regular dentifrice *in vitro*. The innate antimicrobial property of bioactive glass control bacterial counts kills *Streptococcus mutants*, *Actinomyces naeslundii*, and *Aggregatibacter actinomycetemcomitans*. These microbes cause enamel caries, periodontitis, and root caries. Bioactive glass is also coated on a metallic dental implant to improve its tissue integration properties. However, bioactive glass-based coating remove with time which results make metallic implant unstable in the physiological environment [63].

The apatite forming ability of bioactive glass *in vitro* was evaluated by using Kokubo SBF at 37 °C [64]. After immersing the bioactive glass base scaffold in SBF for 14–28 days, the X-ray diffraction (XRD) analysis was used for the cumulative analysis of calcium and silicon ions released from the bioactive glass surface. For cell culture, rDPSCs (rat dental pulp stem cells) were harvested from old male Sprague-Dawley rats' incisors. The rats were sacrificed and the rDPSCs were harvested from upper and lower incisors and added to phosphate-buffered saline (PBS) containing antibiotics like streptomycin, penicillin. Then, 0.08% collagenase type I and cells were incubated for 30 minutes The rDPSCs were collected after enzyme digestion through centrifugation. The cells were then cultured in α-MEM (minimum essential medium) containing 10% fetal bovine serum and antibiotics under a 5% CO_2 environment. The cells were cultured in an odontogenic supplemental medium to promote their differentiation into odontoblast. The culture medium also contains ascorbic acid, dexamethasone, and 10 mM β-glycerophosphate. The adenosine triphosphate (ATP)-dependent endocytosis pathway was locked by amiloride, amantadine, and genistein. It did not influence the endocytosis pathway. The mRNA expression of bone sialoprotein (BSP), collagen Type I alpha 1 chain (COL1A), and OCN genes was increased in the presence of bioactive glass. The mRNA level of dentin matrix acidic phosphoprotein 1 (DMP1), dentin sialophosphoprotein (DSPP), and OCN was also upregulated in the presence of bioactive glass. Alkaline phosphatase (ALP) activity also increased. BSP and COL1A are odontoblast differentiation markers. Their expression was upregulated. Other odontogenic markers like DMP1, DSPP, and OCN are expressed in the later stage of development. The ALP activity and alizarin red staining (ARS) have a relation with phosphate matrix formation in dentin before mineralization initiation. The higher the ALP activity, the high concentration of phosphate ions at the mineral site deposition. ARS is used to analyze the calcific deposition by cells and it is a crucial step in dentin formation. As bioactive glass biological properties are highly dependent upon concentration. The stem cells must rapidly differentiate into osteogenic lineage from stem cells. Endocytosis of bioactive glass and stem cells is initiated because of similar hard tissue regeneration potential of osteogenic [65].

In another study, the biological response was studied on dental pulp stem cells (DPSCs). DPSCs were collected from the crown and root of teeth by digesting in a collagenase type I (3 mg/ml), dispase (4 mg/ml) solution for one hour at 37 °C. Cell suspensions were seeded in the six well culture plates containing α DMEM (modified Eagle's medium) supplemented with 15% fetal bovine serum and antibiotics like penicillin, streptomycin. The culture plates were incubated under 5% CO_2 at

37 °C. 96 well culture plates were then used for seeding of DPSCs at the density of 5×10^3 cells/well. Cell viability and proliferation were measured using a cell counting kit 8 (CCK-8) assay. Flow cytometry was used to evaluate cell apoptosis by using the fluorescent detection of phosphatidylserine buffer (FITC) annexin V Apoptosis detection kit. Apoptotic cells were positive and healthy cells were negative under annexin V-FITC while the opposite was PI. To identify cell markers, the DPSCs were subcultured on 12 chamber slides and grown to 80% confluence. Then, cells were incubated for one hour. After growth DPSCs were fixed in 4% paraformaldehyde with no specific antigen. The cells were then incubated with diluted primary antibody CD73 (1 : 50), CD105, CD90 overnight at 4 C, washed, and incubated with fluorescein-conjugated secondary goat anti-mouse polyclonal antibody at room temperature.

To study the change in mesenchymal phenotype of DPSCs, flow cytometry analysis was done. Cells were trypsinized and incubated in PBS for one hour with conjugated fluorescein antibody CD73, CD90, and CD105. To study the cell differentiation of DPSC, a pulp-less tooth slice was incubated in a culture medium to stimulate odontogenic differentiation. The DPSCs showed good cell proliferation, viability, and higher growth of extra cellular matrix (ECM). The apoptosis rate was lower in the case of bioactive glass. Cell phenotype markers CD73, CD90, and CD105 showed positive expression and their phenotype characteristic remained unchanged. The DPSCs differentiated after 21 days post-incubation. Higher calcium deposition and gene expression were observed in the presence of bioactive glass. The expression of DMP1, Runx2, and ALP which are odontogenic differentiation markers was upregulated. Moreover, tooth slices showed significant expression of DSPP in the presence of bioactive glass. The pulp/dentin complex formation was induced eight weeks post-incubation. The newly grown tissues showed dentin-like morphology with a collagenous matrix which is deposited perpendicular to odontoblast-like layers on the surface of hydroxyapatite particles. The dentin-like matrix in dental mineralizing cells displayed protruding cytoplasmic processes in the matrix. They are positive immune-stained for DSP which is a main phenotypic marker of odontoblasts. This dentin-like matrix interfaces with pulp-like interstitial tissues containing blood vessels. The newly formed dentin-matrix complex expressed a negative response to anti-human nuclei antibody staining. Moreover, a higher number of odontoblast-like immune-positive cells for DSP were observed in the presence of bioactive glass [66].

17.11 Bioactive Glass for Cartilage Regeneration

It is difficult to regenerate cartilage as compared to bone. The engineered cartilage has limited ability to achieve mechanical and biochemical properties of native cartilage as full-thickness articular cartilage defects involve subchondral bone damage mostly. Moreover, the cartilage to bone interface integrates slower. Several studies have been conducted, but the role of subchondral support material on tissue integration and cell viability is still not clear.

The *in vitro* analysis of bioactive glass (13-93) has shown the formation of neocartilage when co-cultured with bovine chondrocytes. The bovine chondrocytes were cultured in transforming growth factor (TGFβ) 3 serum-free media for 28 days. The biological potential of bioactive glass-based agarose gel was evaluated after 7 and 14 days. The *in vivo* potential of bioactive glass as osteochondral graft has been evaluated by fabricating a polyethylene glycol (PEG)/13-93 based scaffold. New Zealand white adult rabbits MSCs allogenic bone marrows were suspended in scaffold before implantation into the rabbit knees. The 6- and 12-week post-implantation analysis showed good tissue integration and formation of viable cartilage cells at the articular layer [47].

Calcium ions play a critical role in cartilage regeneration and being an essential component of bioactive glass, it is assumed that maybe it is calcium that facilitates the repairing of cartilage. The foundation for cartilage reconstruction could be prepared by activating the Wnt signal pathways. These pathways assist the expression of the cartilage repair gene. Silicon ions of bioactive glass stimulate the differentiation of MSCs by activating the Wnt pathway. Moreover, silicon ions protect chondrocytes from osteoarthritis by suppressing their metabolic activity. Silicon ions of bioactive glass inhibit the hedgehog pathway and increase autophagy. Calcium along with silicon also activates the hypoxia-inducible factor (HIF) pathway which stimulates gene expression related to cartilage repair and suppresses osteoarthritis caused by the Wnt pathway by increasing autophagy and inhibiting the hedgehog pathway [67].

For *in vitro* analysis, bioactive glass composites were first placed in PBS solution and analyzed qualitatively as well as quantitively for the release of active ions. Mice chondrocytes were cultured in PBS solution containing ionic dissolution products of the bioactive glass. After 24 hours of incubation, the cultured cells were washed thrice with PBS solution. Then 4% paraformaldehyde was added for cell fixation at room temperature. The cultured samples were incubated in rhodamine-phalloidin for 30 minutes and in DAPI for 5 minutes before taking fluorescence microscopy images. qRT-PCR is used generally for evaluating chondrocyte gene expression, i.e. Cartilage-specific proteoglycan core protein (AGGRECAN), MMP13, SRY-box transcription factor 9 (SOX9), COL2. For this, the mice chondrocytes are seeded at the density of 2×10^4 cells/well and incubated for seven days. The cells are then harvested using TRIzoI reagent to extract RBA which is reversely transcribed into complementary DNA by using RevertAid First Strand cDNA Synthesis Kit. The qRT-PCR analysis is performed using ABI 7300 prism with the SYBR Green detection reagent. The fluorescence microscopic images confirm that the bioactive glass initiate regeneration of cartilage as prominent filopodia and unidirectional lamellipodia extensions have appeared. However, an increase in bioactive glass results in more proliferation and growth of chondrocytes. The gene's AGGRECAN expression increased in the presence of bioactive glass as well as the expression of biomarkers SOX9 and COL2 were also upregulated. The regeneration of cartilage leads to the formation of the extracellular matrix. The extracellular matrix is composed of collagen II and proteoglycans. MMP13 is a gene of metalloproteinase13 which has the potential to degrade the extracellular matrix. Bioactive glass downregulates the production of the MMP13 gene thus, supports cartilage regeneration and repair [67].

New Zealand white rabbit's articular cartilage was used to isolate chondrocytes by digestion using collagenase II. These chondrocytes were cultured in 10% fetal calf serum, 100 U/ml penicillin, and 100 μg/ml streptomycin in DMEM medium. The whole mixture was incubated at 37 °C in 5% CO_2 and the growth medium was changed every three days. Six well culture plates were used for inoculation. 5 ml of cell suspension was added to each well containing a bioactive glass-based scaffold. The specimen was harvested at 4, 8, and 12-weeks post-implantation. A green fluorescent protein labeled chondrocyte line was used to study cell migration. The cells were fixed using formaldehyde at room temperature and sectioned at 5 mm on a freezing microtome. For the cell adhesion study, the scaffolds were soaked in ethanol (75%) for 48 hours for sterilization under UV radiation. After sterilization, the scaffolds were washed using PBS and seeded with chondrocytes in 48 well plates at 70 cells/mm^2 density. The chondrocytes sued for this test were incubated for three hours before the addition of 1 ml fresh medium in cell culture well. For quantitative *in vivo* cartilage formation analysis, the total glycosaminoglycan and collagen were determined. The bioactive glass-based scaffold exhibited superior migration of cells toward the inner region of the scaffold with an increase *in vitro* culture time. The percentage of cell adhesion was also increased from 60% to 84% by adding bioactive glass as well as the DNA content measured *in vitro* before implantation was also higher

in a bioactive glass-containing group rather than control groups. Moreover, cells were proliferated better. The gross evaluation of *in vivo* constructs was monitored and the regeneration of cartilage was better in the presence of a bioactive glass-based scaffold. The mechanical properties of cartilage produced can be measured by glycosaminoglycan (GAG) content and collagen. The content of GAG and collagen was higher in the case of bioactive glass. The cartilage-like tissue formed in the control as well as bioactive glass scaffold group, but an obvious lacuna structure with strong expression of type II collagen was present in the case of bioactive glass. Cells migrated toward inner regions and formed thicker cartilage in the presence of bioactive glass. The neocartilage formed has better mechanical properties and ECM. The bioactive glass supported the cell activity, produced extracellular matrix, expressed phenotype, and played role in preserving characteristic spherical morphology associated with the synthesis of cartilage and proteoglycans. The thicker cartilage formed has a homogeneous structure. Bioactive glass has a direct effect on the lamellar bone repair of subchondral bone and restoration of the articular surface of primary hyaline-like cartilage in 12 weeks in rabbit femur osteochondral defects along with good integration with surrounding tissues [68, 69].

17.12 Evaluation of Bioactivity in Cartilage Regeneration

Bioactive glass reduces the gene expression of pro-inflammatory cytokines like IL-1β and tumour necrosis factor α (TNF-α). Transwell migration and scratch assays are used to evaluate the effect of bioactive glass on the migration of mouse aortic endothelial cells (MAEC) and L929 cells. MAEC and L929 are endothelial and fibroblast cells of mouse connective tissues. The *in vitro* studies on these cell lines have demonstrated that bioactive glass fastens the migration of these cells. Thus, it was hypothesized that bioactive glass can behave similarly *in vivo*, i.e. more migration, more differentiation, and proliferation. The *in vitro* studies on mouse cell lines also show that bioactive glass composites improve the protein and gene expression of collagen I, collagen III, fibronectin, and elastin. Similarly, the MAEC cell cultures have stimulated the gene expression of basic fibroblast growth factor (bFGF) and kinase insert domain receptor (KDR), while L929 upregulated the expression of vascular endothelial growth factor VEGF, KDR, and endothelial nitric oxide synthase (eNOS) in the presence of bioactive glass. These genes play role in angiogenesis.

The macrophage-depleted mouse model was used to study the functional aspects of macrophages *in vivo* in the presence of bioactive glass. C587 mice were used as model animals. Clodronate-liposome were injected in mice to reduce macrophage secretion. Clodronate-liposome is an artificially created hydrophilic vesicle. The shell of the vesicle has a lipid bilayer-like consistency. The liposomes are ingested by macrophages which result in the release of clodronate in the body's aqueous media. The clodronate accumulates in the body and when they reach a certain concentration, they stimulate the apoptosis of macrophages. The GFP fluorescence and immunohistochemistry staining images indicated the migration of L929 and MAEC cells at a higher rate in normal mice in the presence of bioactive glass. While in the macrophage depleted model, the migration of L929 and MAEC cells was depleted even in the presence of bioactive glass at the wound site. Based on these observations, it was concluded that bioactive glass affects the migration of macrophages at the wound site which results reduce the migration of L929 and MAEC cells.

The Hematoxylin and eosin stain results confirm that wound healing was faster in normal mice in the presence of bioactive glass composite than macrophage depleted mice. This implies that macrophages are important for wound healing. Moreover, in normal mice, the haemotoxylin and

eosin (H&E) stain confirms that more granulation occurs at the site treated with bioactive glass than in the control group. After seven days, the thick, intact nonepidermal layer formed at the bioactive glass treated site. While in macrophage-depleted mice, the bioactive glass treated site has a very thin new epidermis layer. However, after 14 days, all groups have formed a new epidermis layer but with different thicknesses. The bioactive glass treated site in normal mice has a thicker layer, while the macrophage depleted mice model has a thin layer but it was thicker than the control group.

CD68 immunohistochemistry test for total macrophages was performed which showed that macrophage depleted mice and normal mice have a higher number of macrophages at the bioactive glass treated site than that of the control site. However, the number of macrophages is a very low normal site in macrophage depleted mice which confirms the effect of clodronate liposome. The CD163 immunohistochemistry results showed the M2 macrophages are higher at the bioactive glass treated sites than the normal sites.

Masson staining confirms the deposition of collagen at the wound site in macrophage-depleted and normal mice. The collagen growth was enhanced at the bioactive glass site in normal and macrophage-depleted mice after 14 days. The collagen fibers arrangement was highly ordered in the presence of bioactive glass than at the control site. The CD-31 IH staining and CD-31/α-SMA IF staining were performed to study the angiogenesis at the wound site. The CD-31 positively stained cultures were present in a large amount at bioactive glass treated site in normal mice than macrophage depleted mice. The size of capillaries grown at the bioactive glass treated sites is larger as compared to the control site. After 14 days, the number of capillaries falls in normal mice at the bioactive glass treated site which confirmed the regeneration of skin while in macrophage depleted mice the number and thickness of capillaries increased after 14 days at the bioactive glass treated site which shows the role of macrophages in wound healing.

Bioactive glass can stimulate the M2 phenotype of macrophages *in vitro* as well as *in vivo*. Bioactive glass has a 3-D porous structure which facilitates the adhesion and ingrowth of cells as well as its polar nature help it to dissolve in body fluids quickly. The M2 phenotype activation results in the secretion of cytokines and chemokine which are pro-regenerant. It enhances the release of TGF-β, VEGF, and bFGF *in vitro* which attract endothelial and fibroblast cells at the wound site. While *in vivo* studies demonstrate that macrophages have an important role in wound healing. These results suggest that bioactive glass is only active in the release of M2 phenotype and other gene expression proteins in the presence of macrophages. The wound site showed good growth in the presence of bioactive glass in normal mice, while in macrophages depleted mice, no significant difference was observed between the control and bioactive glass site. This suggests that the repairing cells *in vivo* are recruited by macrophages which secrete chemokines and cytokines [70, 71].

17.13 Regeneration of Soft Connective Tissues

Bioactive glass can be used for the regeneration of soft tissues. *In vivo* and *in vitro* study using fibroblast model has suggested that bioactive glass increases the cell proliferation and produces VEGF. The increased neo-vascularization is due to the release of VEGF which is a highly pro-angiogenic factor as endothelial cells only [43, 72].

17.14 Bioactive Glass for Skin Tissue Regeneration

Bioactive glasses are used for skin regeneration in wound healing. A wound healing process is divided into three phases, i.e. inflammation, proliferation, and tissue remodeling. Tissue regeneration has been used to boost the natural wound healing process. When the biomaterial is implanted into the wound site the inflammatory responses by host cells occur which are undesirable and delay healing. The consensus is to use inert biomaterials to avoid inflammatory responses [70]. However, a detailed study of host reactions has revealed that immune system responses play critical roles in wound healing. These inflammatory responses can be tuned to achieve desired properties. Macrophages are released by immune cells during wound healing. At the same time, chemokines are secreted by neutrophils at the wound sites. Macrophages are neutrophils assemble and secrete different kind of molecules which enhance the growth of fibroblasts and endothelial cells at the defect site. Macrophages have a paracrine effect. They support the MSCs in bone healing and human dermal fibroblasts during skin regeneration thus enhance the deposition of fibroblast and angiogenesis. The effect of biomaterials on the macrophage's behavior has been studied *in vitro*.

It has been concluded that the physical, chemical, and structural characteristics of biomaterial influence the secretion and phenotypes of cytokines and chemokines by macrophages. Macrophages bond with all biomaterials, i.e. polymers, ceramics, and metals. The biomaterial and macrophage interaction involve adhesion, activation, and secretion of cytokines by macrophages at the implantation site. This collectively stimulates the chain of downstream biological reactions. Bioactive glass assists skin tissue regeneration by stimulating angiogenesis and extracellular matrix deposition. The ionic products of bioactive glass have the potential to activate the M2 phenotype and stimulate the secretion of anti-inflammatory growth factors by macrophages. There is one drawback to using pure bioactive glass for wound healing is that they incur pain at the defect site by increasing the pH. However, the fabrication of bioactive glass with polymers like sodium alginate can be done to reduce the pain. The polymeric composites also help in keeping the wound site moist which is necessary for wound healing [70].

17.15 Bioactive Glass for Angiogenesis

The bioactive glass increases cell proliferation and produces VEGF. The increased neovascularization is due to the release of VEGF which is a highly pro-angiogenic factor as endothelial cells only [43, 72].

For the *in vitro* analysis, the 45S5 bioactive glass with a composition (45% SiO_2, 24.5% Na_2O, 24.5% CaO, and 6% P_2O_5) was used. A slurry of 45S5 was made in deionized water and 594 µl of this slurry was added in 94 or 24 well plates. CCD-18Co cell lines (CRL-1459) were used for *in vitro* analysis. It is a human colon fibroblast cell line. The cells were obtained from passage 9, grown in Eagles minimal essential media with 2 mM/l glutamine and 1 mM sodium pyruvate, 1 non-essential amino acid, antibiotics (penicillin, 50 U/ml; streptomycin, 50 g/ml) supplemented with 10% fetal bovine serum. 45S5 BG was coated in triplicate on 96 well cell culture plates on which CCD-18Co cells were seeded. The plates were incubated for different intervals, i.e. 24, 48, and 72 hours at 37 °C in the 5% CO_2. After the incubation, the total number of cells was calculated

using Cell Titer 96 AQ_{ueous} non-radioactive cell proliferation assay. For the measurement of VEGF and bFGF secretion, CCD-Co cells were seeded on 24 well cell culture plates coated with 45S5 and incubated under 5% CO_2 for different intervals, i.e. 24, 48, and 72 hours. After incubation, the culture medium was immediately stored at −70 °C and the amount of VEGF and bFGF produced in the culture media was measured by a quantitative sandwich enzyme immunoassays. A commercial angiogenesis assay (angiogenesis assay kit; TCS Cell Works) was used to evaluate the effect of bioactive glass on fibroblast biological activity in the release of growth factors. The assay was prepared by the following method.

At first, the medium in culture plates was replaced by an optimized medium obtained from TCS Cell works. The plates were divided into positive control, negative control, and sample sections according to the amount of optimized medium used (alone [OM]; OM: conditioned medium [0 g/cm^2 or 0.3125 mg/cm^2 at 1 : 1 [v/v]]; OM containing VEGF at 2 ng/ml [positive control]; or OM containing 20 μM) suramin (negative control). The culture medium was removed on different days 4, 7, and 9 and replaced with a fresh preequilibrated (37 °C and 5% CO_2) optimized medium. The endothelial cells were stained for CD-31 after 11 days by using indirect immunocytochemistry and allowed to air dry. Photomicrographs of each were recorded using Nikon Eclipse TE 2000-S inverted photomicroscope fitted with a digital camera using an ×4 magnification lens. Image analysis software was used for the quantitative measurement of endothelial tubule development. The amount of VEGF mRNA produced was determined by Quantikine mRNA colorimetric mRNA quantitation assay.

Human CCD-18Co (0.031 25–6.25 mg/cm^2) was grown on cell culture wells coated with 45S5 BG. The fibroblasts grown on 45S5 secreted VEGF in a significant amount as compared to fibroblasts grown in control wells. The amount of bFGF and VEGF mRNA released was significant after 48 and 72 hours. The increase in VEGF mRNA and VEGF secretion in the presence of bioactive glass is attributed to *de novo* synthesis.

In another study to evaluate and confirm the potential of bioactive glass being angiogenic human dermal microvascular endothelial cells were culture in the endothelial basal medium in 1 : 1 conditioned with CCD-18Co cell lines. The growth of fibroblasts endothelial cells increased to 61.5% after 24 hours of conditioning media which confirms the angiogenic behavior of the bioactive glass. After 11 days of culture, the endothelial cells were stained for CD-31 expression, and the results were recorded in the form of digital micrographs to study *in vitro* model of angiogenesis. The endothelial cells grown on 45S5 produced an increased number of anastomosed endothelial tubules compared with control. The micrographs show that bioactive glass stimulated fibroblasts to secrete growth factors that increased angiogenesis.

The tubule branching increases, which results in the formation of a complex network in the presence of 45S5 BG. The endothelial tubules and junctions have increased significantly. The formation of tubules and complex networks mimics the angiogenesis stages, i.e. cell migration, cell proliferation, vessel branching, and anastomosis [73].

The effect of bioactive glass on angiogenesis was studied using the arteriovenous loop (AVL) model. The AVL model was created between the femoral artery and vein of a rat by injecting a venous graft from the contralateral side. The 45S4 BG with fibrin gel was embedded in a Teflon isolation chamber in which the loop was placed. The effect of bioactive glass on angiogenesis was studied three weeks post-implantation by using μ-CT tomography and histological analysis of the newly formed network of blood vessels. The μ-CT images showed that axial vascularization. For *in vivo* analysis, six male Lewis rats of 200–300 g weight were used. The incision from the groin to the knee in the medial thigh exposed the left femoral vessel. The contralateral leg was interposed between the femoral left vessel and 2 cm log femoral vein produced after separation of femoral

vein and artery to create AVL model. The microvascular anastomoses were performed using 11-0 sutures. A Teflon chamber is filled with a 45S5 BG-based granular matrix containing fibrinogen and thrombin in 10 mg/ml and 2 I.U/ml. Then, the AVL was placed in the Teflon chamber and it was covered with 45S5, fibrinogen, and thrombin mixture having the same concentration present below. After that, the chamber was closed and sutured to thigh musculature using 3-0 Prolene sutures. The isolation chamber was made up of Teflon having an internal diameter of 10 mm with a height of 10 mm. Four plastic tubes were placed inside the chamber to prevent the luxation of AVL. After three weeks post-implantation, the animals were perfused using Microfil. The aorta and Caval veins were exposed surgically under anesthesia. The aorta was flushed using 150 ml of heparin solution along with a 20 ml yellow Microfil containing a 5% MV curing agent. After that, the rats were placed at 4 C for 24 hours, and the specimen was transferred to nutrient media, macroscopically inspected, and fixed in a 3.5% formalin solution for histological analysis. After formalin fixation, the specimens were placed in ethylenediaminetetraacetic acid (EDTA) for decalcification for three weeks. Then, the μ-CT analysis was performed. After this, the tissues were dehydrated in graded ethanol and embedded in paraffin. The Leica microtome was used to obtain a cross section of two planes perpendicular to the AVL axis. The cross sections were stained using hematoxylin, eosin, and Masson's trichrome, and digital photographs were obtained. The Teflon chamber was surrounded by fibrous tissues, and fibrin gel was replaced by vascular connective tissues. The yellow filling of functional vessels with Microfil was visible which confirms the vascularization and patency of AVLs. Abundant connective tissue was formed and localized around the vascular pedicle without predominance in the venous and arterial parts of AVL.

The newly formed vessels penetrate the construct and are present in the form of connective tissues. The capillary sprouts were visible in μ-CT analysis that is penetrating the matrix. The blood vessel distribution was equal to 43–61 vessels/cross section and 43–23 vessels/cross section in the arterial and venous parts. The average vessel area formed as a result of exposure to bioactive glass was 658–195 mm^2. There was a significant increase in blood vessel length in the bioactive glass region [74].

17.16 Role of Other Metal-Based Network Modifiers in Tissue Regeneration (*In Vivo*/*In Vitro* Study)

To improve the biological properties of bioactive glasses, several new elements are incorporated as network modifiers in the bioactive glasses, i.e. boron, copper, cobalt, silver, zinc, cerium, gallium, strontium, etc. [75]. These ions have enhanced the cell proliferation and osteogenic response of BGs (Figure 17.5), but the relative toxicity of these ions must be considered before employing *in vivo* testing [76].

Strontium ions improve the cell adhesion, growth, proliferation, and mechanical property of BGs. These ions activate the fibroblast growth factor and calcium-sensing receptor simultaneously by using two different molecular pathways [77, 78]. It inhibits osteoclast activity and stimulates osteoblast differentiation and proliferation.

Lithium ions also facilitate osteoblast proliferation and differentiation. The *in vitro* cytotoxic study conducted using NIH3T3 mouse embryonic cells confirmed lithium and strontium presence in BG is non-cytotoxic. Similarly, the *in vivo* study conducted in rabbit femoral defect model following two to four months post-implantation showed bone growth for four months. However, microstructural studies of bone-implant interface, histological, radiological, μ-CT, and

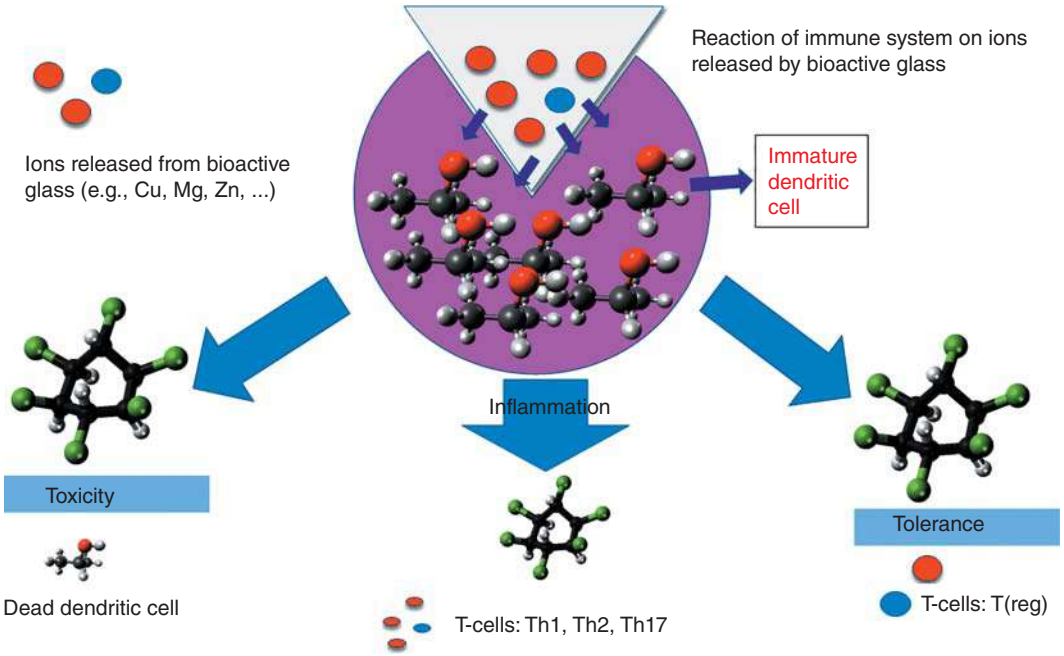

Figure 17.5 Immune system response to ionic species of bioactive glass.

fluorochrome labeling analysis showed that the Sr- and Li-based scaffolds accelerated early-stage bone formation [28].

Copper and cobalt ions improve the angiogenesis response of BGs *in vivo* as well as *in vitro* [79, 80].

Magnesium oxide slows down the hydroxyapatite formation reactions but improves the thickness of the CHA layer. It forms a whitlockite-like phase along with apatites on the surface of bioactive glass and thus reflects the significant role of network modifiers in apatite layer formation. The SiO_2–CaO–P_2O_5–MgO (Quaternary system) has an excellent ability to support the growth of human fetal osteoblastic cells *in vitro*. The *in vivo* studies in the goat model confirm, its nontoxicity [81].

Zinc ions provide high surface area and nucleation sites for apatite layer formation but decrease the rate of glassy network dissolution. It forms covalent interactions with network modifiers cations and plays a critical role to prevent inflammation by forming a direct linkage with key regulatory pathways for inflammatory responses [82].

Iron is also added in bioactive glasses to treat cancerous bones. These glasses prevent metastasis and grow new bone as a result of magnetic hyperthermia treatment [83]. Iron improves matrix metalloproteinase expression by executing the hypoxia conditions which results in stalk cell proliferation, migration, and faster degradation of extracellular matrix [84].

Bioactive glasses have innate antiseptic properties. The network modifier ions generate reactive oxygen species (ROS) in culture media which destroy the DNA/RNA of gram-positive and gram-negative bacteria. To further improve the antimicrobial property of BGs, cerium and silver ions are added [85, 86]. Cerium ions enhance the production of ROS which damage bacterial protein along with DNA and RNA [87]. They also protect the mammalian cells from ROS by emulating the superoxide dismutase activity [88] while silver forms strong bonds with di-sulfide

(S–S) and sulfhydryl (–SH) groups present on microbial cells wall proteins. It disrupts the oxidative mechanism and blocks the nutrient uptake which ultimately leads to the death of bacteria [89]. Silver and zinc ions improve the anti-inflammatory response of bioglass by inducing apoptosis of inflammatory cells and suppressing the production of α-tumor necrosis factor, TGF-β, and β-interleukin (IL). These ions also suppress MMP activity and improve the gene expression of peroxisome proliferator-activated receptors [90, 91].

58.60SiO_2, 9.32Na_2O, 23.66CaO, 3.38P_2O_5, 3.78, B_2O_3, and 1.26TiO_2, the biological potential was investigated *in vivo* by using radial segmental defect of Black Bengal goat's animal model. Porous scaffolds with a porosity range of 4–165 nm were prepared by using β-naphthalene and polyvinyl alcohol (PVA) as a combustible organic binder. Studies were done 90 days post-implantation which showed extensive bone growth as a result of Oxytetracycline labeling. Both groups showed vascularization and formation of well-organized blood vessels suggesting remarkable angiogenic properties.

Similarly, the Osseo-regenerative ability of 70S30C BG was studied *in vivo* using the rat tibial defect model. The 70S30C scaffold was used in the form of dry and wet foam. The μ-CT and isomorphic analysis showed defective bone healing by wet and dry foams which could be due to a sudden increase in pH of scaffold surroundings. However, the preconditioned samples showed osteointegration and differentiation up to 60% which prevent the burst release of calcium ions from scaffolds. The burst release of calcium ions is the main reason for the sudden increase in pH. These scaffolds degraded up to 80% at the 11th-week post-implantation. The degraded surface was replaced by healthy new bone.

60% SiO_2–36% CaO–4% P_2O_5 scaffold was implanted in a maxillary alveolar atrophic edge (a four-wall defect) of Mongrel dogs. The thickness of the alveolar ridge was measured with clinical observation of the defect region and taking a biopsy of the entire implanted region after 90 days post-implantation. Empty defect site was used as control. There was no difference in the defect areas in both groups and a normal-looking new bone is formed with the same color and texture. However, H&E-stained sections showed that mature and better organized new bone is formed at the region where the bioactive glass-based scaffold is used. The bone was grown in such a manner that it was difficult to distinguish the defect area from the surrounding bone. The new bone is grown from the edges to the center of the defect region which justifies the osteoconductive behavior of the bioactive glass-based scaffolds.

75 wt% SiO_2 and 25 wt% CaO BG were implanted for six weeks in sheep mandible and the osteogenic properties were evaluated. Scaffold has generated internal microchannels six weeks post-implantation which is the evidence of high surface activity of BG. The surface activity was because the initial SiO_2–CaO scaffold was completely changed into CaP after continuous and systematic surface reactions post six-week implantation. However, sometimes it is difficult to distinguish between the mineralized scaffold and surrounding bone. The calculated CaP ratio is 1.6 in the case of new bone formed while using bioactive glass. It falls in the range of 1.6–2.0 Ca/P ratio, which exists in natural bone. The amount of silicon was in the range of a few 100 ppm after six weeks and less than 100 ppm Si traces are present in the surrounding tissues which is a confirmation of successful elimination of silica from the scaffold surface. Trace amounts of Zn, Sr, and Mg were also present whose concentration gradually increases from the scaffold to surrounding bone but in biological systems, these atoms converted into calcium over time during apatite mineralization [28]. With time several new ions were added in BG to improve their properties as well as they were fabricated in different forms, i.e. from 2D scaffold to porous 3D scaffolds to BG fibers to improve their physical and biological properties. A 3-D bioactive glass fiber of 53.6% SiO_2, 13.2% CaO, 11.9% Na_2O, 15.1% K_2O, 3.2% MgO, 2.0% P_2O_5, and 1.0% B_2O_3 was pretreated in SBF and its osteogenic potential was evaluated *in vivo* using noncritical size rabbit calvarial bone

defect model. The comparative analysis was done using 45S5 Perioglass particles. The 3D fibers showed more bone deposition than commercially available fibers. The pilot animal study on New Zealand white rabbits was conducted for six months. Two morphologically different implants were investigated with different morphologies, i.e. cylindrical and morsels. Commercially available Perioglass particulate was used as positive control and empty bone cavity as a negative control. After six months, the animals were sacrificed and visual observation indicated the complete healing of the operative area. However, the glass fibers showed homogenous growth while commercially available Perioglass showed non-homogenous growth which could be attributed to its slower resorption rate. As it was a non-critical defect, therefore, negative control also showed complete physiological recovery. The noncritical defects heal spontaneously. Microbial infections are the major complications induced in internal prostheses and percutaneous implants. Therefore, antibiotic-loaded biomaterials were proposed more than 40 years ago. These materials are now part of standard medical practice. The main goals of these materials were to prevent infection in the implant area as well as to provide the correct quantity of drugs for sufficient time and to reduce the risk of systemic effects of drugs. These materials are used to treat infectious bones mostly. The *in vivo* studies of these biomaterials were conducted and divided into three groups. Group I was not given any CFS-loaded BG, group II was injected with CFS injection parenterally, and group III with impregnated bioactive glass scaffold. Scaffolds with higher porosity, i.e. from macro to micropores exhibit more efficient and prolonged drug release both *in vitro* and *in vivo*. CFS is used against *Staphylococcus aureus* normally. Group III has a constant drug concentration during the study which was 15 times higher than the minimum inhibitory concentration of CFS against *S. aureus*. This group showed prominent growth of periosteal bone. The parenteral treatment showed growth of bridging callus and fibrocartilaginous tissue but with the absence of mature bone. While the group I has decalcification of the bony matrix which is an indication of the osteolytic activity of *S. aureus*.

17.17 List of FDA Approved Bioactive Glass

Sr. #	Bioactive glass	Commercial name	Year	Application
1.		Ceravital®	1977	To replace the middle ear small bone
2.	Bioglass 45S5®	Bioglass 45S5	1978	Ocular implant
3.	Bioglass 45S5	Bioglass ossicular reconstruction prosthesis/middle ear prosthesis MEP®	1985	To replace small bone in the middle ear for treatment of conductive hearing loss
4.	Radioactive Bioglass 45S5		1987	Treatment of liver cancer
5.	45S5 Bioglass®	Endosseous ridge maintenance implant (ERMI®)	1988	In periodontal surgery (tooth root replacement and as support for dentures)
6.	45S5 Bioglass		1990	Temporal bone defects in deaf patients

Sr. #	Bioactive glass	Commercial name	Year	Application
7.	45S5 Bioglass particulate	PerioGlas® 45S5 Bioglass particulate	1993	Dental defects repairing (jawbone defects, regeneration of bone around the root tooth)
8.	Radioactive Bioglass	TheraSphere®	1999	Liver cancer treatment
9.	45S5 Bioglass particulate	NovaBone®	1999	Idiopathic scoliosis in posterior spinal fusions surgery
10.	45S5 Bioglass (300–360 μm)	Biogran®	1995	Maxillofacial and dental applications (repair of defects in the jawbone)
11.	S53P4 plates ($53SiO_2$–$20CaO$–$23Na_2O$–$4P_2O_5$)	BoneAlive®	2000	For the growth of orbital bone
12.	Ag containing 45S5 BG	Arglaes® (film, Powder)	2002	In wound healing and peripheral nerve regeneration
13.	BG-coated orbital implant	Medpor®-PlusTM (Porex Surgical, Newnan, GA, USA)	2002	In orbital implants and for fibro vascularization
14.	45S5 Bioglass particulate (mean size 18 μm)	NovaMin®	2004	To treat dental defects (tooth surface remineralization and occlusion of dentinal tubules)
15.	45S5 Bioglass	TheraGlass® 45S5 Bioglass	2007	Oral care
16.	($44.5SiO_2$–$4Na_2O$–$4K_2O$–$7.5MgO$–$17.8CaO$–$4.5P_2O_5$–$17.8SrO$) mol%	StronBone®	2010	Bone implants (to reduce bone resorption)
17.	13-93B3	Biodegradable tiny cotton-candy borate BG (Mo-Sci Corp., Rolla, MO, USA), DermaFuse™/Mirragen™ RediHeal	2011	Angiogenic function, wound healing, healing of venous stasis ulcers in diabetic

[92].

References

1 Leppäranta, O., Vaahtio, M., Peltola, T. et al. (2008). Antibacterial effect of bioactive glasses on clinically important anaerobic bacteria in vitro. *Journal of Materials Science – Materials in Medicine* 19 (2): 547–551. https://doi.org/10.1007/s10856-007-3018-5.

2 Aurégan, J.C. and Bégué, T. (2015). Bioactive glass for long bone infection: a systematic review. *Injury* 46: S3–S7. https://doi.org/10.1016/S0020-1383(15)30048-6.

3 Hench, L.L. (2006). The story of Bioglass®. *Journal of Materials Science – Materials in Medicine* 17 (11): 967–978. https://doi.org/10.1007/s10856-006-0432-z.

4 Xynos, I.D., Edgar, A.J., Buttery, L.D.K. et al. (2001). Gene-expression profiling of human osteoblasts following treatment with the ionic products of Bioglass® 45S5 dissolution. *Journal of Biomedical Materials Research* 55 (2): 151–157. https://doi.org/10.1002/1097-4636(200105)55:2<151::AID-JBM1001>3.0.CO;2-D.

5 Xynos, I.D., Hukkanen, M.V.J., Batten, J.J. et al. (2000). Bioglass® 45S5 stimulates osteoblast turnover and enhances bone formation in vitro: implications and applications for bone tissue engineering. *Calcified Tissue International* 67 (4): 321–329. https://doi.org/10.1007/s002230001134.

6 Hench, L.L., Splinter, R.J., Allen, W.C., and Greenlee, T.K. (1971). Bonding mechanisms at the interface of ceramic prosthetic materials. *Journal of Biomedical Materials Research* 5 (6): 117–141.

7 Williams, D.F. (2009). On the nature of biomaterials. *Biomaterials* 30 (30): 5897–5909.

8 Christodoulou, I., Buttery, L.D.K., Saravanapavan, P. et al. (2005). Dose- and time-dependent effect of bioactive gel-glass ionic-dissolution products on human fetal osteoblast-specific gene expression. *Journal of Biomedical Materials Research Part B Applied Biomaterials* 74 (1): 529–537. https://doi.org/10.1002/jbm.b.30249.

9 Xynos, I.D., Edgar, A.J., Buttery, L.D.K. et al. (2000). Ionic products of bioactive glass dissolution increase proliferation of human osteoblasts and induce insulin-like growth factor II mRNA expression and protein synthesis. *Biochemical and Biophysical Research Communications* 276 (2): 461–465. https://doi.org/10.1006/bbrc.2000.3503.

10 Jones, J.R. (2013). Review of bioactive glass: from Hench to hybrids. *Acta Biomaterialia* 9 (1): 4457–4486.

11 Bossard, C., Granel, H., Wittrant, Y. et al. (2018). Polycaprolactone/bioactive glass hybrid scaffolds for bone regeneration. *Biomedical Glasses* 4 (1): 108–122. https://doi.org/10.1515/bglass-2018-0010.

12 AboElsaad, N.S., Soory, M., Gadalla, L.M.A. et al. (2009). Effect of soft laser and bioactive glass on bone regeneration in the treatment of bone defects (an experimental study). *Lasers in Medical Science* 24 (4): 527–533.

13 Turunen, T., Peltola, J., Yli-Urpo, A., and Happonen, R. (2004). Bioactive glass granules as a bone adjunctive material in maxillary sinus floor augmentation. *Clinical Oral Implants Research* 15 (2): 135–141.

14 Hench, L.L. (1991). Bioceramics: from concept to clinic. *Journal of the American Ceramic Society* 74 (7): 1487–1510.

15 Montazerian, M. and Zanotto, E.D. (2017). A guided walk through Larry Hench's monumental discoveries. *Journal of Materials Science* 52 (15): 8695–8732.

16 El-Ghannam, A. and Ducheyne, P. (2017). Bioactive ceramics. In: *Comprehensive Biomaterials II* (ed. P. Ducheyne), 204–234. Oxford: Elsevier https://doi.org/10.1016/B978-0-12-803581-8.10169-9.

17 Greenlee, T.K. Jr., Beckham, C.A., Crebo, A.R., and Malmborg, J.C. (1972). Tissue responses at the interface of a ceramic. *Biomedical Materials Research* 6: 244.

18 Baino, F., Novajra, G., Miguez-Pacheco, V. et al. (2016). Bioactive glasses: special applications outside the skeletal system. *Journal of Non-Crystalline Solids* 432: 15–30. https://doi.org/10.1016/j.jnoncrysol.2015.02.015.

19 Baino, F., Ferraris, M., Bretcanu, O. et al. (2013). Optimization of composition, structure and mechanical strength of bioactive 3-D glass-ceramic scaffolds for bone substitution. *Journal of Biomaterials Applications* 27 (7): 872–890.

20 Arcos, D., Greenspan, D.C., and Vallet-Regí, M. (2002). Influence of the stabilization temperature on textural and structural features and ion release in SiO_2–CaO–P_2O_5 sol–gel glasses. *Chemistry of Materials* 14 (4): 1515–1522. https://doi.org/10.1021/cm011119p.

21 Yamasue, H., Shimizu, K., and Nagata, K. (2015). Direct measurement of standard generated Gibbs energy of $4CaO \cdot P_2O_5$ and $3CaO \cdot P_2O_5$ by steam transport method. *J-Stage-Iron and Steel* 101 (3): 169–176.

22 Leonova, E., Barba, A.A., Arcos, D. et al. (2008). Multinuclear solid-state NMR studies of ordered mesoporous bioactive glasses. *Journal of Physical Chemistry C* 112 (14): 5552–5562. https://doi.org/10.1021/jp7107973.

23 Arcos, D., Greenspan, D.C., and Vallet-Regí, M. (2003). A new quantitative method to evaluate the in vitro bioactivity of melt and sol–gel-derived silicate glasses. *Journal of Biomedical Materials Research Part A* 65 (3): 344–351. https://doi.org/10.1002/jbm.a.10503.

24 Gross, U. and Strunz, V. (1985). The interface of various glasses and glass ceramics with a bony implantation bed. *Journal of Biomedical Materials Research* 19 (3): 251–271. https://doi.org/10.1002/jbm.820190308.

25 Ma, P.X. and Zhang, R. (2001). Microtubular architecture of biodegradable polymer scaffolds. *Journal of Biomedical Materials Research* 56 (4): 469–477. https://doi.org/10.1002/1097-4636(20010915)56:4<469::AID-JBM1118>3.0.CO;2-H.

26 Chaikof, E.L., Matthew, H., Kohn, J. et al. (2002). Biomaterials and scaffolds in reparative medicine. *Annals of the New York Academy of Sciences* 961: 96–105. https://doi.org/10.1111/j.1749-6632.2002.tb03057.x.

27 Karageorgiou, V. and Kaplan, D. (2005). Porosity of 3D biomaterial scaffolds and osteogenesis. *Biomaterials* 26 (27): 5474–5491. https://doi.org/10.1016/j.biomaterials.2005.02.002.

28 El-Rashidy, A.A., Roether, J.A., Harhaus, L. et al. (2017). Regenerating bone with bioactive glass scaffolds: a review of in vivo studies in bone defect models. *Acta Biomaterialia* 62: 1–28. https://doi.org/10.1016/j.actbio.2017.08.030.

29 De Aza, P.N., Guitian, F., Merlos, A. et al. (1996). Bioceramics – simulated body fluid interfaces: pH and its influence of hydroxyapatite formation. *Journal of Materials Science – Materials in Medicine* 7 (7): 399–402.

30 Rohanová, D., Boccaccini, A.R., Yunos, D.M. et al. (2011). TRIS buffer in simulated body fluid distorts the assessment of glass-ceramic scaffold bioactivity. *Acta Biomaterialia* 7 (6): 2623–2630. https://doi.org/10.1016/j.actbio.2011.02.028.

31 De Aza, P.N., Luklinska, Z.B., Anseau, M.R. et al. (2001). Transmission electron microscopy of the interface between bone and pseudowollastonite implant. *Journal of Microscopy* 201 (1): 33–43. https://doi.org/10.1046/j.1365-2818.2001.00779.x.

32 Kokubo, T., Ito, S., Sakka, S., and Yamamuro, T. (1986). Formation of a high-strength bioactive glass-ceramic in the system MgO–CaO–SiO_2–P_2O_5. *Journal of Materials Science* 21 (2): 536–540.

33 Hench, L.L., Boccaccini, A.R., Day, R.M., and Gabe, S.M. (2003). Third-generation gene-activating biomaterials. In: *Materials Science Forum*, vol. 426 (ed. T. Candra, J.M. Torralba and T. Sakai), 179–184. Switzerland: Trans Tech Publications Limited.

34 Zheng, K., Kapp, M., and Boccaccini, A.R. (2019). Protein interactions with bioactive glass surfaces: a review. *Applied Materials Today* 15: 350–371. https://doi.org/10.1016/j.apmt.2019.02.003.

35 Hench, L.L. (2009). Genetic design of bioactive glass. *Journal of the European Ceramic Society* 29 (7): 1257–1265. https://doi.org/10.1016/j.jeurceramsoc.2008.08.002.

36 Fu, Q., Rahaman, M.N., Fu, H., and Liu, X. (2010). Silicate, borosilicate, and borate bioactive glass scaffolds with controllable degradation rate for bone tissue engineering applications. I. Preparation and in vitro degradation. *Journal of Biomedical Materials Research Part A* 95 (1): 164–171. https://doi.org/10.1002/jbm.a.32824.

37 Stokols, S. and Tuszynski, M.H. (2006). Freeze-dried agarose scaffolds with uniaxial channels stimulate and guide linear axonal growth following spinal cord injury. *Biomaterials* 27 (3): 443–451. https://doi.org/10.1016/j.biomaterials.2005.06.039.

38 Fu, Q., Huang, W., Jia, W. et al. (2011). Three-dimensional visualization of bioactive glass-bone integration in a rabbit tibia model using synchrotron X-ray microcomputed tomography. *Tissue Engineering Part A* 17 (23–24): 3077–3084.

39 Bi, L., Jung, S., Day, D. et al. (2012). Evaluation of bone regeneration, angiogenesis, and hydroxyapatite conversion in critical-sized rat calvarial defects implanted with bioactive glass scaffolds. *Journal of Biomedical Materials Research Part A* 100 (12): 3267–3275.

40 Bielby, R.C., Christodoulou, I.S., Pryce, R.S. et al. (2004). Time- and concentration-dependent effects of dissolution products of 58S sol–gel bioactive glass on proliferation and differentiation of murine and human osteoblasts. *Tissue Engineering* 10 (7–8): 1018–1026. https://doi.org/10.1089/ten.2004.10.1018.

41 Wu, C. and Chang, J. (2013). A review of bioactive silicate ceramics. *Biomedical Materials* 8 (3): 032001. https://doi.org/10.1088/1748-6041/8/3/032001.

42 Huang, W., Rahaman, M.N., Day, D.E., and Li, Y. (2006). Mechanisms for converting bioactive silicate, borate, and borosilicate glasses to hydroxyapatite in dilute phosphate solution. *Physics and Chemistry of Glasses – European Journal of Glass Science and Technology Part B* 47 (6): 647–658.

43 Hench, L.L., Xynos, I.D., and Polak, J.M. (2004). Bioactive glasses for in situ tissue regeneration. *Journal of Biomaterials Science Polymer Edition* 15 (4): 543–562.

44 Wilson, J., Pigott, G.H., Schoen, F.J., and Hench, L.L. (1981). Toxicology and biocompatibility of bioglasses. *Journal of Biomedical Materials Research* 15 (6): 805–817.

45 Lai, W., Garino, J., and Ducheyne, P. (2002). Silicon excretion from bioactive glass implanted in rabbit bone. *Biomaterials* 23 (1): 213–217.

46 Filho, O.P., Latorre, G.P., and Hench, L.L. (1996). Effect of crystallization on apatite-layer formation of bioactive glass 45S5. *Journal of Biomedical Materials Research* 30 (4): 509–514. https://doi.org/10.1002/(SICI)1097-4636(199604)30:4<509::AID-JBM9>3.0.CO;2-T.

47 Rahaman, M.N. et al. (2011). Bioactive glass in tissue engineering. *Acta Biomaterialia* 7 (6): 2355–2373. https://doi.org/10.1016/j.actbio.2011.03.016.

48 Yao, A., Wang, D., Huang, W. et al. (2007). In vitro bioactive characteristics of borate-based glasses with controllable degradation behavior. *Journal of the American Ceramic Society* 90 (1): 303–306. https://doi.org/10.1111/j.1551-2916.2006.01358.x.

49 Brown, R.F., Day, D.E., Day, T.E. et al. (2008). Growth and differentiation of osteoblastic cells on 13-93 bioactive glass fibers and scaffolds. *Acta Biomaterialia* 4 (2): 387–396. https://doi.org/10.1016/j.actbio.2007.07.006.

50 Oonishi, H., Hench, L.L., Wilson, J. et al. (1999). Comparative bone growth behavior in granules of bioceramic materials of various sizes. *Journal of Biomedical Materials Research* 44 (1): 31–43. https://doi.org/10.1002/(SICI)1097-4636(199901)44:1<31::AID-JBM4>3.0.CO;2-9.

51 Day, D.E., White, J.E., Brown, R.F., and McMenamin, K.D. (2003). Transformation of borate glasses into biologically useful materials. *Glass Technology* 44 (2): 75–81.

52 Han, X. and Day, D.E. (2007). Reaction of sodium calcium borate glasses to form hydroxyapatite. *Journal of Materials Science – Materials in Medicine* 18 (9): 1837–1847. https://doi.org/10.1007/s10856-007-3053-2.

53 Zhang, X., Jia, W., Gu, Y. et al. (2010). Teicoplanin-loaded borate bioactive glass implants for treating chronic bone infection in a rabbit tibia osteomyelitis model. *Biomaterials* 31 (22): 5865–5874. https://doi.org/10.1016/j.biomaterials.2010.04.005.

54 Liu, X., Xie, Z., Zhang, C. et al. (2010). Bioactive borate glass scaffolds: in vitro and in vivo evaluation for use as a drug delivery system in the treatment of bone infection. *Journal of Materials Science – Materials in Medicine* 21 (2): 575–582. https://doi.org/10.1007/s10856-009-3897-8.

55 Brown, R.F., Rahaman, M.N., Dwilewicz, A.B. et al. (2009). Effect of borate glass composition on its conversion to hydroxyapatite and on the proliferation of MC3T3-E1 cells. *Journal of Biomedical Materials Research Part A* 88 (2): 392–400. https://doi.org/10.1002/jbm.a.31679.

56 Jung, S.B., Day, D.E., Brown, R.F., and Bonewald, L.F. (2013). Potential toxicity of bioactive borate glasses in-vitro and in-vivo. In: *Advances in Bioceramics and Porous Ceramics V-36th International Conference on Advanced Ceramics and Composites, ICACC 2012*, Ceramic Engineering and Science Proceedings, vol. 33, no. 6, 65–74. Wiley-Blackwell.

57 Gerhardt, L.C. and Boccaccini, A.R. (2010). Bioactive glass and glass-ceramic scaffolds for bone tissue engineering. *Materials (Basel)* 3 (7): 3867–3910. https://doi.org/10.3390/ma3073867.

58 Fu, Q., Rahaman, M.N., Sonny Bal, B. et al. (2008). Mechanical and in vitro performance of 13-93 bioactive glass scaffolds prepared by a polymer foam replication technique. *Acta Biomaterialia* 4 (6): 1854–1864. https://doi.org/10.1016/j.actbio.2008.04.019.

59 Goodridge, R.D., Wood, D.J., Ohtsuki, C., and Dalgarno, K.W. (2007). Biological evaluation of an apatite-mullite glass-ceramic produced via selective laser sintering. *Acta Biomaterialia* 3 (2): 221–231. https://doi.org/10.1016/j.actbio.2006.10.005.

60 LeGeros, R.Z. and Legeros, J.P. (1984). Phosphate minerals in human tissues. In: *Phosphate Minerals* (ed. J.O. Nriagu and P.B. Moore), 351–385. Springer.

61 Conzone, S.D. and Day, D.E. (2009). Preparation and properties of porous microspheres made from borate glass. *Journal of Biomedical Materials Research Part A* 88 (2): 531–542. https://doi.org/10.1002/jbm.a.31883.

62 Kokubo, T., Kushitani, H., Sakka, S. et al. (1990). Solutions able to reproduce in vivo surface-structure changes in bioactive glass-ceramic A-W3. *Journal of Biomedical Materials Research* 24 (6): 721–734.

63 Sawant, K. and Pawar, A. (2020). Bioactive glass in dentistry: a systematic review. *Saudi Journal of Oral Sciences* 7 (1): 3. https://doi.org/10.4103/sjos.sjoralsci_56_19.

64 Kokubo, T. and Takadama, H. (2006). How useful is SBF in predicting in vivo bone bioactivity? *Biomaterials* 27 (15): 2907–2915. https://doi.org/10.1016/j.biomaterials.2006.01.017.

65 Lee, J.H., Kang, M.S., Mahapatra, C., and Kim, H.W. (2016). Effect of aminated mesoporous bioactive glass nanoparticles on the differentiation of dental pulp stem cells. *PLoS One* 11 (3): 1–22. https://doi.org/10.1371/journal.pone.0150727.

66 Wang, Y.Y., Chatzistavrou, x., Faulk, D. et al. (2015). Biological and bactericidal properties of Ag-doped bioactive glass in a natural extracellular matrix hydrogel with potential application in dentistry. *European Cells & Materials* 29: 342–355. https://doi.org/10.22203/eCM.v029a26.

67 Lin, B., Hongxing, H., Zhengwei, D. et al. (2020). Novel bioactive glass cross-linked PVA hydrogel with enhanced chondrogenesis properties and application in mice chondrocytes for cartilage repair. *Journal of Non-Crystalline Solids* 529: 119594. https://doi.org/10.1016/j.jnoncrysol.2019.119594.

68 Wu, J., Xue, K., Li, H. et al. (2013). Improvement of PHBV scaffolds with bioglass for cartilage tissue engineering. *PLoS One* 8 (8): https://doi.org/10.1371/journal.pone.0071563.

69 Souza, M.T., Tansaz, S., Zanotto, E.D., and Boccaccini, A.R. (2017). Bioactive glass fiber-reinforced PGS matrix composites for cartilage regeneration. *Materials (Basel)* 10 (1): 1–14. https://doi.org/10.3390/ma10010083.

70 Zhu, Y., Ma, Z., Kong, L. et al. (2020). Modulation of macrophages by bioactive glass/sodium alginate hydrogel is crucial in skin regeneration enhancement. *Biomaterials* 256 (March): 120216: https://doi.org/10.1016/j.biomaterials.2020.120216.

71 Dong, X., Chang, J., and Li, H. (2017). Bioglass promotes wound healing through modulating the paracrine effects between macrophages and repairing cells. *Journal of Materials Chemistry B* 5 (26): 5240–5250. https://doi.org/10.1039/C7TB01211J.

72 Jell, G. and Stevens, M.M. (2006). Gene activation by bioactive glasses. *Journal of Materials Science – Materials in Medicine* 17 (11): 997–1002. https://doi.org/10.1007/s10856-006-0435-9.

73 Day, R.M. (2005). Bioactive glass stimulates the secretion of angiogenic growth factors and angiogenesis in vitro. *Tissue Engineering* 11 (5–6): 768–777. https://doi.org/10.1089/ten.2005.11.768.

74 Arkudas, A., Balzer, A., Buehrer, G. et al. (2013). Evaluation of angiogenesis of bioactive glass in the arteriovenous loop model. *Tissue Engineering Part C* 19 (6): 479–486. https://doi.org/10.1089/ten.tec.2012.0572.

75 Kargozar, S., Baino, F., Hamzehlou, S. et al. (2018). Bioactive glasses entering the mainstream. *Drug Discovery Today* 23 (10): 1700–1704. https://doi.org/10.1016/j.drudis.2018.05.027.

76 Mouriño, V., Cattalini, J.P., and Boccaccini, A.R. (2012). Metallic ions as therapeutic agents in tissue engineering scaffolds: an overview of their biological applications and strategies for new developments. *Journal of the Royal Society Interface* 9 (68): 401–419. https://doi.org/10.1098/rsif.2011.0611.

77 Caverzasio, J. and Thouverey, C. (2011). Activation of FGF receptors is a new mechanism by which strontium ranelate induces osteoblastic cell growth. *Cellular Physiology and Biochemistry* 27 (3–4): 243–250. https://doi.org/10.1159/000327950.

78 Lao, J., Jallot, E., and Nedelec, J.M. (2008). Strontium-delivering glasses with enhanced bioactivity: a new biomaterial for antiosteoporotic applications? *Chemistry of Materials* 20 (15): 4969–4973. https://doi.org/10.1021/cm800993s.

79 Giacomelli, C., Trincavelli, M.L., Satrian, C. et al. (2015). Copper (II) ions modulate Angiogenin activity in human endothelial cells. *International Journal of Biochemistry & Cell Biology* 60: 185–196. https://doi.org/10.1016/j.biocel.2015.01.005.

80 Tanaka, T., Kojima, I., Ohse, T. et al. (2005). Cobalt promotes angiogenesis via hypoxia-inducible factor and protects tubulointerstitium in the remnant kidney model. *Laboratory Investigation* 85 (10): 1292–1307. https://doi.org/10.1038/labinvest.3700328.

81 Saboori, A., Rabiee, M., Moztarzadeh, F. et al. (2009). Synthesis, characterization and in vitro bioactivity of sol–gel-derived SiO_2–CaO–P_2O_5–MgO bioglass. *Materials Science and Engineering C* 29 (1): 335–340. https://doi.org/10.1016/j.msec.2008.07.004.

82 Varmette, E.A., Nowalk, J.R., Flick, L.M., and Hall, M.M. (2009). Abrogation of the inflammatory response in LPS-stimulated RAW 264.7 murine macrophages by Zn- and Cu-doped bioactive sol–gel glasses. *Journal of Biomedical Materials Research Part A* 90 (2): 317–325. https://doi.org/10.1002/jbm.a.32098.

83 Serrano, M.C., Portoles, M.T., Pagani, R. et al. (2008). In vitro positive biocompatibility evaluation of glass–glass ceramic thermoseeds for hyperthermic treatment of bone tumors. *Tissue Engineering Part A* 14 (5): 617–627. https://doi.org/10.1089/tea.2007.0205.

84 Kargozar, S., Baino, F., Hamzehlou, S. et al. (2018). Bioactive glasses: sprouting angiogenesis in tissue engineering. *Trends in Biotechnology* 36 (4): 430–444. https://doi.org/10.1016/j.tibtech.2017.12.003.

85 Raghupathi, K.R., Koodali, R.T., and Manna, A.C. (2011). Size-dependent bacterial growth inhibition and mechanism of antibacterial activity of zinc oxide nanoparticles. *Langmuir* 27 (7): 4020–4028. https://doi.org/10.1021/la104825u.

86 Catauro, M., Raucci, M.G., De Gaetano, F., and Marotta, A. (2004). Antibacterial and bioactive silver-containing $Na_2O{\cdot}CaO{\cdot}2SiO_2$ glass prepared by sol–gel method. *Journal of Materials Science – Materials in Medicine* 15 (7): 831–837. https://doi.org/10.1023/B:JMSM.0000032825.51052.00.

87 Alpaslan, E., Geilich, B.M., Yazici, H., and Webster, T.J. (2017). pH-controlled cerium oxide nanoparticle inhibition of both gram-positive and gram-negative bacteria growth. *Scientific Reports* 7 (April): 1–12. https://doi.org/10.1038/srep45859.

88 Nicolini, V., Malavasi, G., Menabue, L. et al. (2017). Cerium-doped bioactive 45S5 glasses: spectroscopic, redox, bioactivity and biocatalytic properties. *Journal of Materials Science* 52 (15): 8845–8857. https://doi.org/10.1007/s10853-017-0867-2.

89 Silvestry-Rodriguez, N., Sicairos-Ruelas, E.E., Gerba, C.P., and Bright, K.R. (2007). Silver as a disinfectant. *Reviews of Environmental Contamination and Toxicology* 191: 23–45. https://doi.org/10.1007/978-0-387-69163-3_2.

90 Jarosz, M., Olbert, M., Wyszogrodzka, G. et al. (2017). Antioxidant and anti-inflammatory effects of zinc. Zinc-dependent NF-κB signaling. *Inflammopharmacology* 25 (1): 11–24. https://doi.org/10.1007/s10787-017-0309-4.

91 Shruti, S., Salinas, A.J., Lusvardi, G. et al. (2013). Mesoporous bioactive scaffolds prepared with cerium-, gallium- and zinc-containing glasses. *Acta Biomaterialia* 9 (1): 4836–4844. https://doi.org/10.1016/j.actbio.2012.09.024.

92 Baino, F. (2018). Bioactive glasses: where are we and where are we going? *Journal of Functional Biomaterials* 9 (1): 25. https://doi.org/10.3390/jfb9010025.

18

Production of Bioactive Glass-Ceramics for Dental Application Through Devitrification of Glasses in the $Na_2O/K_2O-CaO-MgO-SiO_2-P_2O_5-CaF_2$ System

Konstantinos Dimitriadis[1,2], Dilshat U. Tulyaganov[3], and Simeon Agathopoulos[1]

[1] *Department of Materials Science and Engineering, University of Ioannina, Ioannina, Greece*
[2] *Division of Dental Technology, Department of Biomedical Sciences, University of West Attica, Athens, Greece*
[3] *Department of Natural–Mathematical Sciences, Turin Polytechnic University in Tashkent, Tashkent, Uzbekistan*

18.1 Introduction

Glass-ceramics (GCs) are polycrystalline materials, derived from controlled crystallization of a parent glass. They were discovered by Stookey at Corning Inc., USA, in 1953, and are considered as a combination of a glass with ceramic crystallized phases [1–4]. The discovery of GCs itself reveals the direct relationship between the resultant GCs and the parent glasses. This relationship immediately reveals the importance of the chemical composition of the parent glass as well as of the heat-treatment, which was actually the way that the GCs were discovered, i.e. through heat treatment [1, 3–5].

Nowadays, GCs are widely used in a variety of technological applications, including biomedical ones, such as dental materials, which is the focus of this chapter. More specifically, glasses and GCs attract a great interest in repairing and replacing natural bone and dental hard tissues, owing to their biocompatibility [1, 3, 6–9]. Also, various glasses and GCs exhibit, apart from biocompatibility, bioactivity that is the ability to develop chemical bond to bones and soft tissues [1, 3, 10].

Various systems of GCs have been studied by many research groups and are proposed as potential materials for biomedical applications (Table 18.1). The first and probably the best-known bioactive glass is the famous 45S5 Bioglass, which was invented by Larry Hench and his coworkers in Florida, USA, at the end of 1960s [10, 11]. The strong chemical bond between the bioactive glasses or bioactive GCs and living bone is due to the formation of a biologically active layer of hydroxyapatite (HA), which is spontaneously developed on the surface of the glasses/GCs, when they are in biological environment [11]. Nevertheless, it was soon realized that bioactive glasses cannot be used in load-bearing applications (e.g. in orthopedics or dentistry) due to their poor mechanical properties [6], as the bioactive glasses have a bending strength of ~70 MPa and fracture toughness of ~0.5 $MPa{\cdot}m^{0.5}$ [12].

Therefore, the scientific interest was shifted to bioactive GCs, starting with Ceravital® (invented by Bromer in 1973), because they can combine the characteristics of the bioactive glass (i.e. high bioactivity) with the properties of the ceramic of the same composition (i.e. high mechanical properties) [1, 3, 4, 13]. Nowadays, there are bioactive GCs which exhibit significantly better mechanical properties compared to bioactive glasses [14–17]. Nevertheless, they still demonstrate lower values of fracture toughness than that of human jaw bone (which is K_{IC} = 2–12 $MPa{\cdot}m^{0.5}$) [14].

Bioactive Glasses and Glass-Ceramics: Fundamentals and Applications, First Edition.
Edited by Francesco Baino and Saeid Kargozar.

Table 18.1 Various systems of GCs proposed as potential materials for biomedical applications.

Glass composition/GC system		Crystalline phases
Alkaline and alkaline earth silicates	SiO_2–Li_2O	Lithium disilicate
Aluminosilicates	SiO_2–Al_2O_3–CaO	Wollastonite
	SiO_2–Al_2O_3–K_2O	Leucite
Fluorosilicates	SiO_2–Al_2O_3–MgO–CaO–ZrO_2–F	Mica, zirconia
Silicophosphates	SiO_2–CaO–Na_2O–P_2O_5	Apatite
	SiO_2–MgO–CaO–P_2O_5–F	Apatite, wollastonite
	SiO_2–MgO–Na_2O/K_2O–CaO–P_2O_5	Mica, apatite
Phosphates	P_2O_5–Al_2O_3–CaO	Apatite

Source: Höland and Beall [4]/The American Ceramic Society/CCBY 4.0.

Dental implants are a reliable solution to restore lost teeth [12, 18]. The disadvantages of commercially pure titanium (cpTi) and Ti6Al4V dental implants, such as patients' allergic reactions and poor aesthetic performance in the case of replacing anterior teeth, have been overcome by the introduction of zirconia dental implants. Nonetheless, the mismatch of the mechanical properties, in particular the modulus of elasticity and fracture toughness, between the human jaw bone and these dental implant materials is still a serious problem. The mismatch of the above properties can cause the *stress shielding* phenomenon (which is discussed in detail in Section 18.6) [12]. Zirconia presents other problems, as well, which are related to the intrinsic nature of this material, such as accelerated aging in the presence of moisture, leading to surface degradation and propagation of microcracks that can eventually result in catastrophic failure. In the case of dental implants, the expression of bioactivity, beyond the fact that it improves osseointegration by suppressing the formation of fibrous tissue around the dental implant (which prevents osteogenesis), should also be related to the improvement of the load distribution between the dental implant and the jaw bone, by means of interfacial bonding, resulting in suppressing the *stress shielding* phenomenon.

This work reports on the design and the development of novel bioactive GC materials in the Na_2O/K_2O–CaO–MgO–SiO_2–P_2O_5–CaF_2 system. The GCs produced are suggested for dental applications as dental implants because their mechanical properties are a good match to those of the human jaw bone and dentine.

18.2 State-of-the-Art

The discovery of the bioactive glass 45S5 by Prof. Larry Hench, 50 years ago, inaugurated the field of modern bioactive glasses and ceramics [13]. However, the relatively poor mechanical properties of the bioactive glasses limit their application in many areas of biomedical applications. This fact triggered the research toward GCs [12, 19–26]. Bioactive GCs, produced by controlled crystallization of glasses with a specific composition, attract increasing interest in biomedicine, either in bulk form or as coatings [4], because they can optimally combine the characteristics of the bioactive glass and the high mechanical strength of the ceramic of the same composition [3, 27].

A fundamental presupposition for a successful hard tissue implantation is a continuation at the interface between the implant and the living part. The HA layer formed onto the surface of bioactive glasses or ceramics serves a dual aim, where the optimum combination of these two functions

is the key to the success of an implantation [26]. First, the chemical resemblance of the newly formed HA on the surface of the bioactive material with the biological HA of the living bone assures the development of a strong chemical bonding with the living tissue at the interface and favors osteointegration. Additionally (i.e. the second aim), this HA layer facilitates the distribution of the stress between the biomaterial and the surrounding bone and thereby reduces stress shielding [28].

The success of a material intended for use as a dental material is based on its ability to work in balance with the surrounding tissues without causing injury to them. Thus, according to the ISO 6872 standard, a dental material, should exhibit good chemical, mechanical, and optical properties, comparable to those of natural teeth [29]. Hence, in the case of dental implant materials, in the stage of the design of the compositions, it would be useful to take into account (i) where (i.e. anatomically, at which point) a dental implant will be placed, and which hard dental tissue a dental implant is called on to replace, (ii) what requirements a dental implant should meet (i.e. which properties must reach specific values in order to be similar to the adjacent physiological tissues), and (iii) the materials which are used nowadays, in order to highlight how much they satisfy the above requirements and consequently to emerge the challenges that the future research has to face, as the present work does.

A dental implant is a prosthetic device of alloplastic materials that is surgically placed on the jaw bone to replace one or more missing teeth, and, specifically, is called on to replace the root of the tooth. Macroscopically, the human jaw bone, like most human bones, is divided, based on porosity, into an external dense cortical bone, whose structure and microstructure provide the principal mechanical strength of the jaw bone, and its thickness and the inside cross-sectional areas are strong indicators of gross bone strength and fracture resistance [30], and an internal trabecular bone (spongy or cancellous), the structure of which is less in density and has a greater degree of macro-porosity than the cortical bone [31]. Microscopically, the human jaw bone is made up of an extracellular matrix, bone cells (osteoblasts, osteocytes, and osteoclasts), blood vessels, and nerves. In the case of dental implants, cells are inevitably involved in the formation of the strong bond between the jaw bone and an implanted material. This process was discovered by Brånemark in the 1950s and it is called osseointegration [32, 33]. In Section 18.6, the importance of cells in osteointegration is discussed in more detail and emphasis.

A dental implant aims at restoring the root of natural teeth that comes in contact with the jaw bone, which, in contrast to a crown (which protrudes into the oral cavity), is mostly composed of dentine, which is covered by a thin layer of cementum (it is the smallest dental hard tissue, with 10–200 μm thickness). Cementum has a structure similar to that of bone tissue but has a lower hardness than dentine (<0.6 GPa). Thus, it has no contribution to the mechanical strength of the natural tooth, but its role is limited to lining the root and to maintain the tooth in the alveolar [34, 35]. Hence, an ideal dental implant material should exhibit mechanical properties that are close to those of the natural teeth without (far) exceeding those of the jaw bone.

The mechanical properties of both the natural tissue (jaw bone and dentine) and the materials used for the production of a dental implant play a crucially important role in the longevity of a dental implant in the oral cavity [36]. More specifically, the mechanical properties of the natural tissue (jaw bone and dentine), listed in Table 18.2, are of the utmost importance in cases where the bones come in contact with biomaterials (due to either loss or destruction of a natural hard/soft tissue). Ideally, in most clinical cases and even more in the case of dental implants (which are in an intensely continuous changing dynamic environment), the mechanical properties of the implanted biomaterial should be a good match for the mechanical properties of the natural human tissue (jaw bone and dentine). Otherwise, a mismatch of the above properties may cause injury to the human tissue or fracture of the restoration.

Table 18.2 Mechanical properties of the natural tissues [6, 10, 17, 18] and dental implant materials of zirconia and Ti-alloys [9, 10, 12, 30].

	Flexural strength (MPa)	Modulus of elasticity (GPa)	Micro-hardness (GPa)	Fracture toughness ($MPa \cdot m^{0.5}$)	References
Dentine	230–305	15–30	<0.6	3	[6]
Cortical bone	50–150	7–30	0.06–0.075	2–12	[6, 10, 17, 18]
Trabecular bone	10–20	0.05–0.5	0.5–1	0.7–1.1	[17, 18]
Zirconia	>500	210	12	6–10	[9, 10, 12, 30]
Ti alloys	>1200	105–110	2.2–4	—	[9, 10]

In dental implant applications, the most popular materials used, such as titanium (Ti) or zirconia, are non-bioactive or bioinert. Like any other dental material, Ti has some minor drawbacks. For instance, according to Simonis et al., who conducted a long-term clinical study with Ti dental implants, frequent occurrences of biological (such as peri-implant mucositis and peri-implantitis) and technical complications were observed [37]. In addition, a disadvantage of Ti dental implants is the poor aesthetics in the gingival area, especially in the case of anterior teeth, because of the dark grayish color of titanium [12, 38]. These disadvantages of Ti dental implants motivated the researchers to develop novel implant materials, such as ceramic materials [39–41].

Thus, in recent years, the material of choice, among other ceramic materials (e.g. ceria-stabilized tetragonal zirconia polycrystals, Ce-TZP), is yttria-stabilized tetragonal zirconia polycrystals (Y-TZP). Y-TZP exhibits very good aesthetics (i.e. tooth-like color), excellent mechanical properties (bending strength 1200 MPa, modulus of elasticity 200 GPa, and fracture toughness of 6–10 $MPa \cdot m^{0.5}$), and attractive biological properties [12, 41]. Nonetheless, early clinical findings showed that there is a main drawback for zirconia related to an inherent accelerated aging, which is intensified in the presence of moisture, known as "low-temperature degradation (LTD)." This problem is due to spontaneous phase transformation of the zirconia crystals from the tetragonal phase to the weaker monoclinic phase. The above problem negatively influences the fracture toughness of zirconia dental implants, resulting in surface degradation and microcracks propagation [12, 42]. The process of chemical degradation of zirconia ceramic implants results in formation of a space between the dental implant and the bone, which is getting bigger over implantation time. There is a debate if this phenomenon creates the necessary space for newly formed bone growth between the implant and the bone (i.e. it may favor osseointegration process, also known as biointegration), or it leads to formation of fibrous tissue or collagen. The above mechanism is not completely known, yet [43].

Besides the mismatch of mechanical properties of the abovementioned dental implant materials (Ti and zirconia) with those of human jaw bone and dentine, since the mechanical properties of Ti and Y-TZP (Table 18.2) are higher than those of the human jaw bone and dentine (Table 18.2), these materials are also non-bioactive or bioinert. The surface of such bioinert materials can obtain bioactive properties through bioactive coatings, for instance with plasma-sprayed HA. Nevertheless, this configuration has the drawback of not displaying a uniform degradation, giving rise to weak points at the bone-coating interface [12, 44–46].

Thus, the development of novel bioactive dental implant materials, which can develop a strong chemical bond between the dental implant and the jaw bone, as well as to accelerate implant anchorage by inducing the formation of an HA layer on the implant surface [12, 44, 45],

is vitally important in these applications. The HA layer will not only speed up the process of osteoconduction, but the formation of such an HA surface layer adjacent to the bone will prevent the formation of fibrous tissue around the dental implant, favor osteointegration, and suppress stress shielding [28, 46].

Bearing the above in mind and being aware of the problems arising from the mismatch of the mechanical properties between the natural tissues (i.e. jaw bone and dentine) and dental implant materials, it is important to develop new materials, such as GC materials, capable of producing dental implants. Several research teams around the world have been involved in the development of GC materials for dental implant applications [12, 19, 28, 34, 44, 47]. Although the materials resulted from these studies (which will be discussed in more detail in Section 18.6) meet the desired chemical and biological properties, the values of their mechanical properties (whenever reported) are higher than the desired ones, and actually they are far beyond those of the human jaw bone.

18.3 Design of Novel Compositions in the CaO–MgO–SiO_2 System

The selection of glass composition and of the heat treatment schedule are key factors for GC-production process. In order to obtain the desired final properties, the components of the glass and their proportions should promote the precipitation of specific crystalline phase (or phases) and avoid long heat treatment. The addition of an oxide (network former, modifier, or intermediate oxide) in a glass composition influences the chemical, physical, and mechanical properties of the final material. Therefore, in the stage of designing a glass composition, it is important to know the influence of each oxide/fluoride on the final material (glass or GC).

GCs in the ternary CaO–MgO–SiO_2 system have attracted considerable technological interest in biomedical applications because of their good mechanical and chemical properties [3, 48]. As far as the crystalline phases are concerned, the GCs used in biomedical applications consist of wollastonite $CaSiO_3$, fluorapatite $Ca_5(PO_4)_3F$, and diopside $CaMgSi_2O_6$ [4]. Fluorapatite (FA)-based GCs are potential candidates in various medical and dental applications due to the antibacterial effect of F^- ions [49]. Moreover, fluorapatite and wollastonite are bioactive materials that form a surface layer of HA upon their exposure to SBF (simulated body fluid) solution, which is a key requirement for an artificial material to be used as a bioactive bone substitute [3, 50]. Diopside plays an important role in producing a durable GC material. It provides mechanical strength to GCs, needed in dynamically changing environments [4, 9, 51–54]. Accordingly, a combination of the crystalline phases of diopside, fluorapatite, and wollastonite is expected to result in GCs with high mechanical strength and excellent bioactivity. Despite the above very interesting prospects, literature survey reveals that GCs of diopside–fluorapatite–wollastonite has received little attention and are poorly documented [9].

The physicomechanical properties and the *in vitro* and *in vivo* performance of bioactive glasses and GCs in the ternary CaO–MgO–SiO_2 system can be modified and improved with the addition of oxides (and fluorides), such as K_2O/Na_2O, P_2O_5, CaF_2, B_2O_3, Li_2O, Ti_2O, and ZrO_2. However, this has to be done carefully, since the addition of an oxide may improve one property, but it may eventually jeopardize another desired property in the final material [1, 4, 48, 55].

The effect of incorporation of various oxides on bioactivity has been well investigated [1, 55, 56]. For example, the presence of MgO promotes the formation of apatite layer, and, according to *in vitro* studies, Mg increases cell adhesion, proliferation, and differentiation of osteoblast cells [1, 57]. Thus, the presence of Mg in compositions, which aim to be used in biomedical applications, such as in jaw bone environment, is essential.

In the course of the design of a glass composition, it is necessary to understand the influence of each oxide on various parameters that are equally important to biological performance, such as melting point, glass transition, and crystallization temperatures. For instance, the oxides of K_2O/Na_2O and MgO favor the increase of glass transition and crystallization temperatures and hence the sintering window. A wide sintering window means that there is enough time to complete the sintering before the crystallization of the glass begins. A striking example is the Bioglass 45S5, since the early crystallization, which occurs just above T_g [58], results in GCs with undesirable crystalline structure and microstructure. Consequently, a wide sintering window is very welcome in GC technology.

In the light of the above general aspects, the next lines in this section describe the evolution of the design of the novel compositions in the above system, as performed by our research team. The early efforts of our research team for producing GCs in the $CaO–MgO–SiO_2$ system for use in biomedical applications (dentistry and orthopedics) began in 2006. According to Tulyaganov et al. [7], the produced GCs in the $CaO–MgO–SiO_2$ system with B_2O_3, P_2O_5, Na_2O, and CaF_2 additives, displayed satisfactory physicomechanical properties, such as modulus of elasticity and hardness, for applications in dentistry. Agathopoulos et al. [54], who studied these compositions with focus on their ability in HA formation, used "composition 1" (Table 18.3), which was modified by increasing the percentage of P_2O_5 (from 3.26 to 4.81, and finally 6.32 wt%). Thus, after full characterization, they concluded that the increase in the amount of P_2O_5 favored the formation of A-type HA. This composition was named as "composition 1b".

Table 18.3 Glass compositions (in wt%) of the previous works, which led to the bioactive parent glasses 1d and 1e.

Glass	SiO_2	B_2O_3	CaO	MgO	P_2O_5	Na_2O	CaF_2
1	41.39	5.33	30.05	9.25	3.26	4.74	5.98
2	42.23	4.89	31.54	8.50	2.99	4.36	5.49
3	42.95	4.52	32.80	7.86	2.77	4.03	5.07

Source: Tulyaganov et al. [7]/Elsevier.

Glass	SiO_2	B_2O_3	CaO	MgO	P_2O_5	Na_2O	CaF_2
1	41.39	5.33	30.05	9.25	3.26	4.74	5.98
1a	40.73	5.24	29.57	9.10	4.81	4.67	5.88
1b	40.08	5.16	29.10	8.96	6.32	4.59	5.79

Source: Agathopoulos et al. [54]/Elsevier.

Glass	SiO_2	B_2O_3	CaO	MgO	P_2O_5	Na_2O	CaF_2
1b	40.08	5.16	29.10	8.96	6.32	4.59	5.79
1d	46.06	—	28.66	8.83	6.22	4.53	5.70
1e	43.48	—	30.44	8.75	7.19	4.49	5.65

Source: Data from Tulyaganov et al. [48].

Table 18.4 The modified compositions (in wt%).

Composition	SiO_2	CaO	MgO	P_2O_5	Na_2O	K_2O	CaF_2
			Base compositions [48]				
1d	45.45	30.30	12.99	2.60	4.33	0	4.33
1e	43.10	32.33	12.93	3.02	4.31	0	4.31
			Complete substitution of K_2O for Na_2O				
1d-k	45.45	30.30	12.99	2.59	0	4.33	4.33
1e-k	43.10	32.32	12.93	3.02	0	4.31	4.31
			Partial substitution of MgO for CaO				
1d-m	45.45	25.97	17.31	2.59	4.33	0	4.33
1e-m	43.10	28.01	17.24	3.02	4.31	0	4.31

Further, B_2O_3 was omitted from the "composition 1b" [48] resulting in the boron-free "composition 1d" and "composition 1e" (Table 18.3). It is briefly stated that the compositions 1d and 1e refer to two glasses which differ by about 2 mol% in the content of both SiO_2 and CaO [6]. Furthermore, 1e has a higher amount of P_2O_5 than 1d (3.02 and 2.60 mol%, respectively). The glasses 1d and 1e were considered as promising materials for biomedical applications, since they were biocompatible, bioactive, and nontoxic. *In vivo* animal studies showed that the glass 1d was fully compatible with the surrounding tissue without showing any significant adverse reactions [20]. Further preliminary clinical trials demonstrated that 1d glass particulates would be particularly interesting in conventional treatment of bone defects [20]. Bearing the above in mind, the compositions 1d and 1e were qualified and selected as the parent compositions.

Importantly, that no attempt was undertaken earlier to produce and characterize GCs based on compositions 1d and 1e. Therefore, in this work, GCs with compositions 1d and 1e were prepared through sintering and crystallization of corresponding fine glass powder compacts.

The GCs 1d and 1e were also modified aiming at producing GC materials which are suitable for dental implant applications. Two series of novel modified compositions were designed. In the first series, complete substitution of K_2O for Na_2O was carried out in both 1d and 1e. These new compositions (Table 18.4) are denoted as "1d-k" and "1e-k," (where the letter k is after K_2O). In the second series of compositions, partial substitution of MgO for CaO took place in 1d and 1e, and these new compositions (Table 18.4) are denoted as "1d-m" and "1e-m," (where the letter m is after MgO).

The properties of the produced GCs, such as sintering behavior, crystallization, mechanical properties, aesthetics, and bioactivity, were evaluated with regard to their suitability for dental implant applications.

18.4 Synthesis of the Novel Glass-Ceramics and Characterization Methods

The process for fabricating the above GCs (Figure 18.1) included the preparation of a homogeneous parent glass, either in bulk form or in a glass-frit form, followed by its sintering and crystallization through a controlled heat treatment [1, 4].

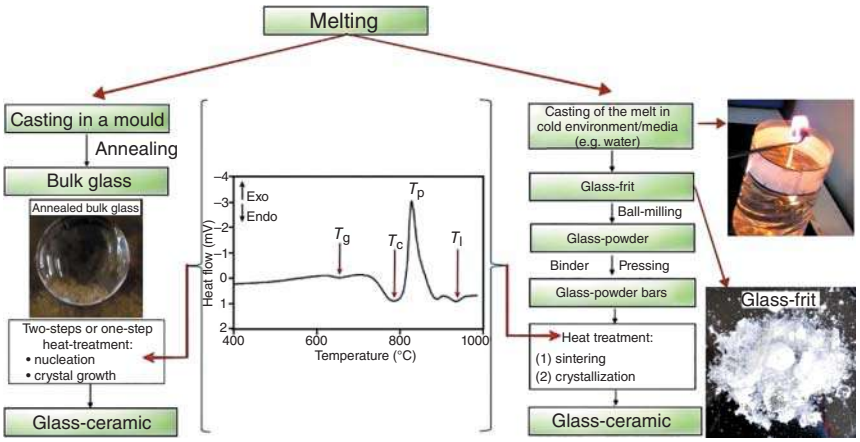

Figure 18.1 Outline of the production process of the GCs by the glass-melting method.

18.4.1 Glass Synthesis and Thermal Analysis

Fine powders of SiO_2 (Sigma Aldrich; 99.8%), $CaCO_3$ (Fluka; ≥99.0%), $Mg(NO_3)_2{\cdot}6H_2O$ (Sigma Aldrich; ≥99.0%), $(NH_4)_2HPO_4$ (Merck; ≥99.0%), Na_2CO_3 (Lachner; 99.6%), K_2CO_3 (Sigma Aldrich; 99.99%), and CaF_2 (Alfa Aesar; 99%) were used as raw materials. For each composition, batches of 100 g were prepared by weighing the raw powders, which were homogenized through ball-milling. Next, each mixture was preheated at 900 °C for one hour in air (Controller S5, Nabertherm®, Germany) in an Al_2O_3 crucible, at a heating rate of 1.5 K/min. Then, for each composition, the obtained oxide powder mixture was melted (Fornos Electricos, Termolab, Portugal) in a platinum crucible (Alfa Aesar, Germany) at 1400–1450 °C for one hour, in air.

Bulk glasses with no crystalline inclusions (confirmed by X-ray diffraction [XRD] analysis, afterwards) were produced by casting the molten glass into preheated bronze molds, which were then immediately subjected to annealing at 650 °C (that is close to the glass transition temperature) for one hour, in air, and then let to slow cooling inside the furnace. Glass frit was also produced by rapid pouring of the molten glass into cold water. The glass frit was dried, ground in a planetary ball-mill (Pulverisette, Fritisch, Germany; at 400 rpm, for 45 minutes) resulting in a fine glass powder and then sieved through a sieve of 32 μm. This allowed to exclude relatively course particles and to get fine glass powder with a final particle size <32 μm.

In order to decide on the crystallization process via controlled heat treatment, which had to be followed in order to produce the GCs, full characterization of the thermal properties of the produced glasses was performed. Differential scanning calorimetry (DSC, STA 449 C, Netzsch, Selb Germany), in the temperature range of 25–1000 °C in air, was conducted, where ~15 mg of glass powder was placed into an Al_2O_3 crucible in the DSC equipment. The recorded thermographs allowed the determination of the temperatures of glass transition (T_g), of the onset crystallization (T_c), of the peak of crystallization (T_p), and of the liquids (T_l) for each investigated composition (Figure 18.1) (these temperatures are calculated automatically by the software of the equipment, according to the geometric determination method on the thermographs, as shown in Section 18.5).

From the thermographs, two important thermodynamic magnitudes were also calculated: the activation energy (E_a) of glass crystallization, and the Avrami exponent (n_A or m), which is an index of the growth dimensionality. In order to determine these two thermodynamic parameters, DSC experiments were performed at five different heating rates (φ), between 5 and 25

(i.e. 5, 10, 15, 20, and 25) K/min. For each heating rate, three independent runs ($n = 3$) were performed. The n_A refers to the growth dimensionality, where three-dimensional growth of crystal occurs for $n_A \geq 3$, $n_A \geq 2$ signifies a two-dimensional crystallization, and for $n_A \geq 1.0$ it corresponds to one-dimensional growth of crystal [59–62]. The calculation of them was done from the thermographs as follows.

The E_a (in kJ/mol), was evaluated by the Kissinger equation [63, 64]:

$$\frac{E_a}{RT_p{}^2} = \ln\frac{T_p}{\varphi} + \text{constant} \tag{18.1}$$

where T_p is the temperature of the crystallization exothermal peak, R is the universal gas constant (8.314 J/mol·K), and φ is the heating rate. The plot of $\ln((T_p{}^2)/\varphi)$ vs. $1000/T_p$ yields a straight line, whose slope can be used to calculate the value of E_a.

The n_A (it is also designed often with the letter m) was estimated by using the Augis–Bennett equation [65]:

$$n_A = \frac{2.5}{\Delta T}\cdot\frac{RT_p{}^2}{E_a} \tag{18.2}$$

where ΔT is the full width at the half maximum of the exothermic crystallization peak, T_p is the temperature of the crystallization exothermal peak, E_a is the activation energy of crystallization, and R is the universal gas constant (8.314 J/mol·K).

18.4.2 Glass-Ceramics Production and Characterization

Fine glass powders were granulated by mixing with a 2.5 vol% polyvinyl alcohol (PVA) solution (glass powder/PVA = 97.5/2.5, in wt%). Parallelepiped bars ($5 \times 4 \times 40$ mm^3) were prepared by uniaxial pressing (150–200 bar). The bars of the glass powder compacts were heat-treated at 450 °C for two hours in air, for debinding, and then at various temperatures, according to the results from thermal analysis, for one hour, in air.

The crystalline phases developed in the produced GCs were identified by XRD analysis (XRD, D8 Advance, Bruker AXS, Billerica, Massachusetts, USA; Cu K_α radiation [$\lambda = 1.5406$ Å], produced at 30 kV and 25 mA, was used), in the range of diffraction angles (2θ) between 20° and 60° with a 2θ step of 0.02°/s. The diffractograms were compared to standards complied by the International Center for Diffraction Data (ICDD).

The microstructure of the GCs was observed in a scanning electron microscope (SEM, 6510 LV, JEOL, Freising, Germany, using an acceleration voltage of 20 kV) equipped with an energy dispersive spectroscopy (EDS) device for elemental analysis. The sample preparation was as follows. The GC specimens were embedded in an acrylic resin (Resine Phenolique, Presi, France) and ground using SiC papers (from 200 to 1400 grid) in a polishing machine (RotoPol-25, Struers, Denmark) under continuous water cooling. Then, they were polished with diamond pastes (Diamant Mecaprex Spray, Presi, France), using a diamond paste of 1 μm as a final polishing step, i.e. mirror finishing. The polished surfaces, after being cleaned in an ultrasonic bath with distilled water and dried, were chemically etched by immersion in 2 vol% HF solution for 30 seconds. Immediately after this period of time, they were washed with tap water in order to stop the etching process and avoid the formation of fluorides on the GCs surface, and finally cleaned with distilled water. To obtain a conductive surface, the samples were sputtered with a Au–Pd thin film (4–8 nm) in a sputtering machine.

The linear shrinkage during sintering was calculated from the difference of the dimensions between the green and the sintered bars. The Archimedes immersion method (in water) was used

to measure the density of the sintered GC specimens (which were fully dense with no porosity). For comparison purposes, the density of the bulk-glass samples was also measured.

In order to determine the mechanical properties of the produced GCs, the bars were rectified by grinding with SiC papers (from 200 to 1400 grid) to obtain the dimensions, according to the ISO 6872 "Dentistry – Ceramic materials" [29]. More specifically, the dimensions of the specimens were width 4.0 (±0.2) mm, thickness 3.0 (±0.2) mm, and length 35.0 (±0.2) mm, (according to this standard, the samples must be at least 2 mm longer than the span between the supporting rods, and the ratio of thickness to length (b/L) must be ≤0.1).

The flexural strength (σ, MPa) and the modulus of elasticity (E, GPa) were calculated according to the ISO 6872 [29] by using the results of three-point bending strength tests (conducted in an Autograph AGS-H equipment, Shimadzu, Japan), carried out with a head speed of 1.0 mm/min and a span of 25 mm between the supporting rods. The values of σ and E were calculated by using the following equations, respectively

$$\sigma = \frac{3FL}{2wh^2} \tag{18.3}$$

and

$$E = \frac{L^3 m}{4wh^3} \tag{18.4}$$

where F is the fracture load, L is the span between the supporting rods (25 mm), w is the specimen width (4 mm), h is the specimen thickness (3 mm), and m is the slope of the straight line in the plot of load vs. displacement.

Vickers microhardness (HV) measurements were performed on polished surfaces (prepared as reported above for the preparation of the samples for SEM, up to the mirror finishing stage) with the use of a Digital Microhardness Tester (Time Instrument, Indonesia), by applying a load of 500 g (or 4.9 N) for 30 seconds. From the length (l) of the cracks propagated from the corners of the pyramid indentation, the value of fracture toughness (K_{IC}, in MPa·m$^{0.5}$) was also calculated by using the Niihara equation [66]:

$$\frac{\varphi K_{IC}}{H\alpha^{1/2}}\left(\frac{H}{\varphi E}\right)^{2/5} = 0.035\left(\frac{1}{\alpha}\right)^{-1/2} \tag{18.5}$$

where φ is a constraint factor (~3), E is the modulus of elasticity (in GPa), H is the hardness (in GPa), and α is the indent half-diagonal.

The presenting results (shown in the Sections 18.5.1.2 and 18.5.2.2) for the above properties of the GCs are the average (and their standard deviation) from 10 independent measurements made on different GC specimens (i.e. $n = 10$, for each GC).

Brittleness is a measure of the relative susceptibility of a material to deformation and fracture. It is related with hardness (H), which quantifies the resistance to deformation, and toughness (K_{IC}), which quantifies the resistance to fracture. Accordingly, the ratio of hardness to fracture toughness (H/K_{IC}) has been proposed as a simple index of brittleness (BI) [67].

Finally, the *in vitro* bioactivity of the produced GCs was evaluated by their ability for inducing HA formation on their surface, after immersion in SBF (which has an ionic concentration (in mM) of Na^+ 142.0, K^+ 5.0, Ca^{2+} 2.5, Mg^{2+} 1.5, Cl^- 147.8, HCO_3^- 4.2, HPO_4^{2-} 1.0, and SO_4^{2-} 0.5, and buffered at pH = 7.25 by tris-hydroxymethyl-aminomethane and hydrochloric acid) at 37 °C for several periods of time [48, 68] (i.e. 7, 14, and 21 days). Polished bars and fine powders (0.2 g, which exposed an area of ~1 cm^2) of the investigated GCs were immersed (separately) in 25 ml SBF (SBF had passed through a filter of 0.2 μm, aiming at sterilizing the SBF, since the small pore size of

the filters is generally smaller than the average size of bacteria), sealed in sterilized plastic flasks, and stored at 37 °C. At the aforementioned periods of time, measurements of the pH of the liquid, XRD analysis of the powders, and SEM/EDS analysis of the surface of the bars were conducted (the conditions of the XRD and SEM analyses have been reported above).

18.5 Properties of the Glass-Ceramic Materials

This section presents the properties of the novel GCs, which are (i) the densification and crystallization, as estimated by the thermal properties of the glasses (i.e. T_g, T_c, T_p, and T_l for each investigated composition), the crystallization mechanism (E_a and n_A), sintering, and aesthetics, crystalline structure and microstructure, (ii) the mechanical properties (flexural strength, modulus of elasticity, hardness, fracture toughness, and brittleness index [BI]), and (iii) the bioactivity performance. Before their presentation, it should be reminded in brief that these GCs were obtained through controlled crystallization of the parent glasses, which occurs via heat treatment, whereby the crystalline phases are precipitated from the reservoir of the parent glasses. As far as the parent glasses are concerned, they were produced by melting in a Pt crucible at 1400 °C for one hour, in air, and subsequently by quenching (in cold water). The schedule of the heat treatment is based on the results of the thermal analysis of the glass and is crucially important for the successful sintering and crystallization process of the resultant GCs.

According to the design of the compositions, presented in Section 18.3, the section is subdivided into two subsections. The first one presents the experimental results related to the qualification of the parent compositions 1d and 1e, with regard to the production of bioactive GCs which are suitable for fabricating dental implants. The second subsection presents the results of the modifications made to the parent glasses 1d and 1e, i.e. complete substitution of K_2O for Na_2O (1d-k and 1e-k) and partial substitution of MgO for CaO (1d-m and 1e-m), in order to obtain GCs with mechanical properties as close as possible to those of dentine and human jaw bone.

18.5.1 Parent Glass-Ceramic Compositions

18.5.1.1 Densification and Crystallization

Thermal Analysis of the Parent Glasses and Crystallization Mechanism The DSC thermographs of the parent glasses 1d and 1e are shown in Figure 18.2a (these plots correspond to a heating rate of 15 K/min). The first endothermic peak (marked with the downwards arrow) corresponds to T_g and the second indicates the onset of crystallization, T_c, followed by a strong and sharp exothermic peak at T_p, attributed to glass crystallization. The endothermic peak at T_l reveals the liquidus temperature, which resulted from the decomposition and the dissolution of the crystalline phases. The values of T_g, T_c, T_p, and T_l (calculated by three independent experiments) are summarized in Table 18.5.

DSC was also performed at five different heating rates. The results (not shown) showed that the temperatures of T_g, T_c, T_p, and T_l was increased as the heating rate was increased. Besides choosing the heat treatment processing of the glasses in order to prepare the corresponding GCs, the plots of $\ln((T_p^2)/\varphi)$ vs. $1000/T_p$ were made, using the results of the DSC analyses. It should be stressed that in these calculations, temperature should be expressed in K. A good linear fitting was obtained for the five tested heating rates in both glasses, 1d and 1e, as shown in Figure 18.2c.

The calculated E_a of crystallization for each glass is shown in Table 18.5. The values of E_a for the glasses 1d and 1e were 430 ± 30 and 384 ± 18 kJ/mol, respectively. Furthermore, from the analysis

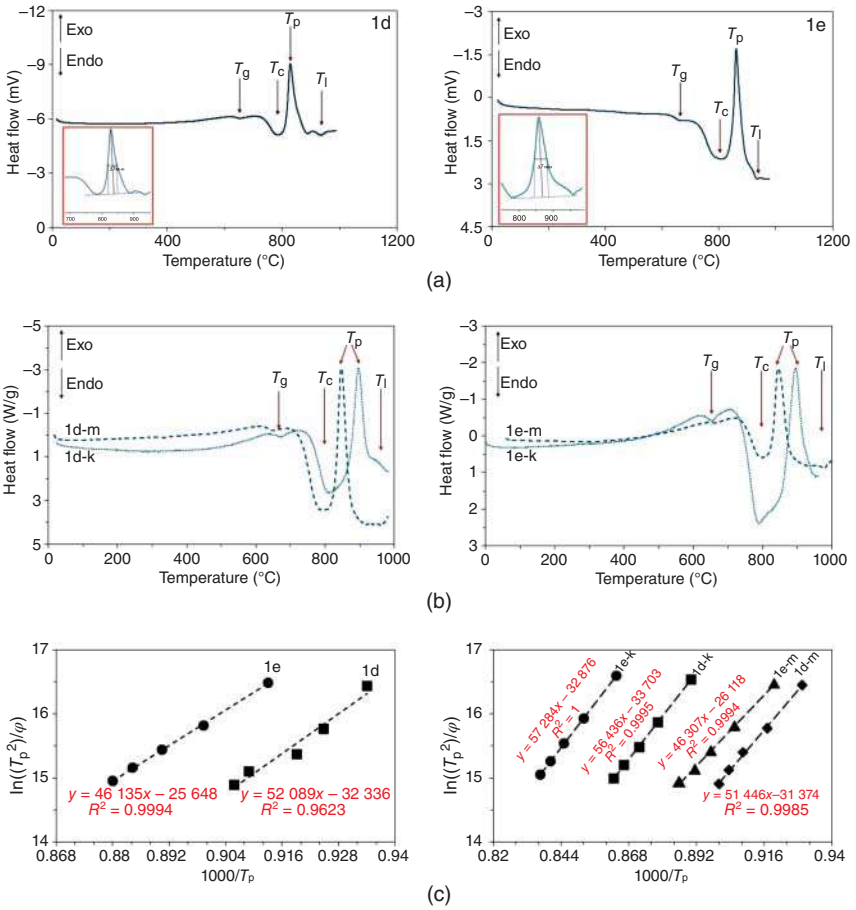

Figure 18.2 Thermographs of (a) the parent and (b) the modified glasses recorded with a heating rate of 15 K/min. The insets in (a) show the measurement of the full width at the half maximum of the crystallization peak. The graphical estimation of T_g, T_c, T_p, and T_l is shown (the software of the equipment used in this work automatically estimates these temperatures through this method). The plot of $\ln((T_p^2)/\varphi)$ vs. $1000/T_p$ for these glasses is presented in (c).

Table 18.5 Mean values (and standard deviation; $n = 3$) of glass transition temperature (T_g), onset crystallization temperature (T_c), crystallization temperature (T_p), liquidus temperature (T_l), activation energy (E_a) of crystallization, and Avrami exponent (n_A) (determined by the DSC measurements) of the glasses 1d and 1e.

Glass	T_g (°C)	T_c (°C)	$T_c - T_g$ (°C)	T_p (°C)	T_l (°C)	E_a (kJ/mol)	n_A
1d	649 ± 9	783 ± 2	134	815 ± 13	936 ± 9	430 ± 30	3.8 ± 0.2
1e	653 ± 8	788 ± 8	135	847 ± 16	952 ± 5	384 ± 18	3.0 ± 0.2

The sintering window ($T_c - T_g$) is also presented.

of the exothermic peaks (i.e. from the measurements of the full width at the half maximum at T_p, as shown in the insets of Figure 18.2a), the n_A for each glass was calculated. The results are listed in Table 18.5 and suggest that the glasses 1d and 1e are prone to three-dimensional growth of crystals, since $n_A \geq 3$ in all cases.

Sintering and Aesthetics The parallelepiped bars of the glass-powder compacts were heat-treated at temperatures which were suggested from the results of the thermal analysis of the glasses. Thus, the heat treatment of the parallelepiped bars of the glass-powder compacts was carried out at the temperatures of 800, 850, and 900 °C.

Well-sintered dense GC bars of white color (as shown in the insets of Figure 18.3a,b) were produced from the glass powder compacts. Their densities along with the density of the corresponding bulk parent glass (which was always smaller than that of the corresponding GC, suggesting that crystallization occurred in the glass powder compacts at these temperatures) are presented in Table 18.6. The linear shrinkage of the GCs ranged between 9.6% and 11.6% (Table 18.6).

Crystalline Structure and Microstructure In the GCs 1d and 1e, diopside $CaMgSi_2O_6$, fluorapatite $Ca_{10}(PO_4)_6F_2$, and wollastonite ($CaSiO_3$) were predominantly crystallized (Figure 18.3a,b). There is no evidence of formation of other secondary or minor phases, according to the assignment of the peeks in the diffractograms.

Figure 18.4a,c shows typical SEM images of the microstructure of the produced GCs 1d and 1e, heat-treated at 850 °C (observed after chemical etching with HF). Three different types of crystals were observed, whose identification was made with the aid of EDS spot analysis, in conjunction with the results of the XRD analysis (Figure 18.3a,b). More specifically, in the EDS spectra, Mg was registered only in the bigger crystals, where the Mg/Ca/Si/O molar ratio was found approximately as 1/1/2/6, respectively; thus, these crystals were assigned to diopside (D). Flour was detected in the coralloid-like small crystals marked with FA, assigned, therefore, to fluorapatite. In the crystals marked with the letter W, the Ca/Si molar ratio was 1/1; hence, these crystals were assigned to wollastonite. Consequently, SEM/EDS (Figure 18.4a,c) and XRD (Figure 18.3a,b) analyses suggest that the microstructure of the produced GCs 1d and 1e is composed of a glass matrix with embedded prismatic diopside (D) and smaller acicular wollastonite (W) crystals, along with small crystals of fluorapatite (FA).

Table 18.6 Mean values (and standard deviation, $n = 5$) of linear shrinkage and density of the parent annealed glasses and the prepared GCs 1d and 1e heat-treated at various temperatures for one hour.

		Heat treatment temperature (°C)		
GCs	**Annealed glass**	**800**	**850**	**900**
		Linear shrinkage (%)		
1d	—	11.6 ± 1.14	10.2 ± 1.13	9.6 ± 0.07
1e	—	10.4 ± 0.95	10.2 ± 0.46	9.7 ± 0.32
		Density (ρ, g/cm^3)		
1d	2.57 ± 0.12	3.03 ± 0.33	2.85 ± 0.31	2.70 ± 0.09
1e	2.53 ± 0.61	3.07 ± 0.51	3.01 ± 0.15	2.99 ± 0.29

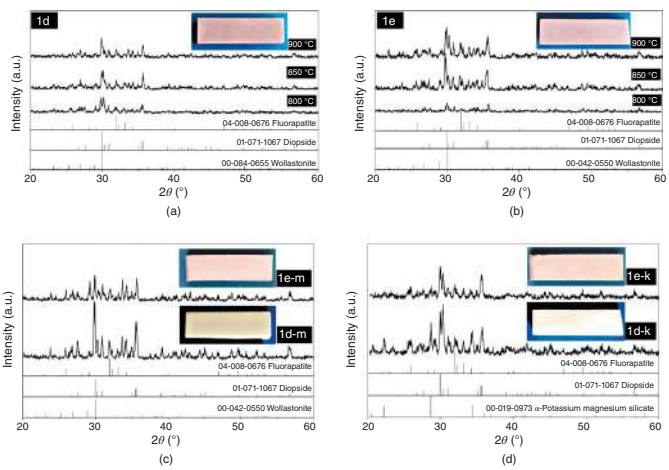

Figure 18.3 X-ray diffractograms of the glass-powder compacts of the parent compositions (a) 1d and (b) 1e heat-treated at various temperatures for one hour, and of the modified GCs (c) 1d-k and 1e-k heat-treated at 900 °C and (d) 1d-m and 1e-m at 850 °C for one hour. The standard patterns of diopside ($CaMgSiO_6$, 01-071-1067), fluorapatite ($Ca(PO_4)_3F$, 04-008-0676), wollastonite ($CaSiO_3$, 00-042-0550), and α-potassium magnesium silicate ($K_2MgSi_3O_8$, 00-019-0973) are plotted at the bottom of the diagrams. The insets present the resultant well-sintered dense GC bars with white color.

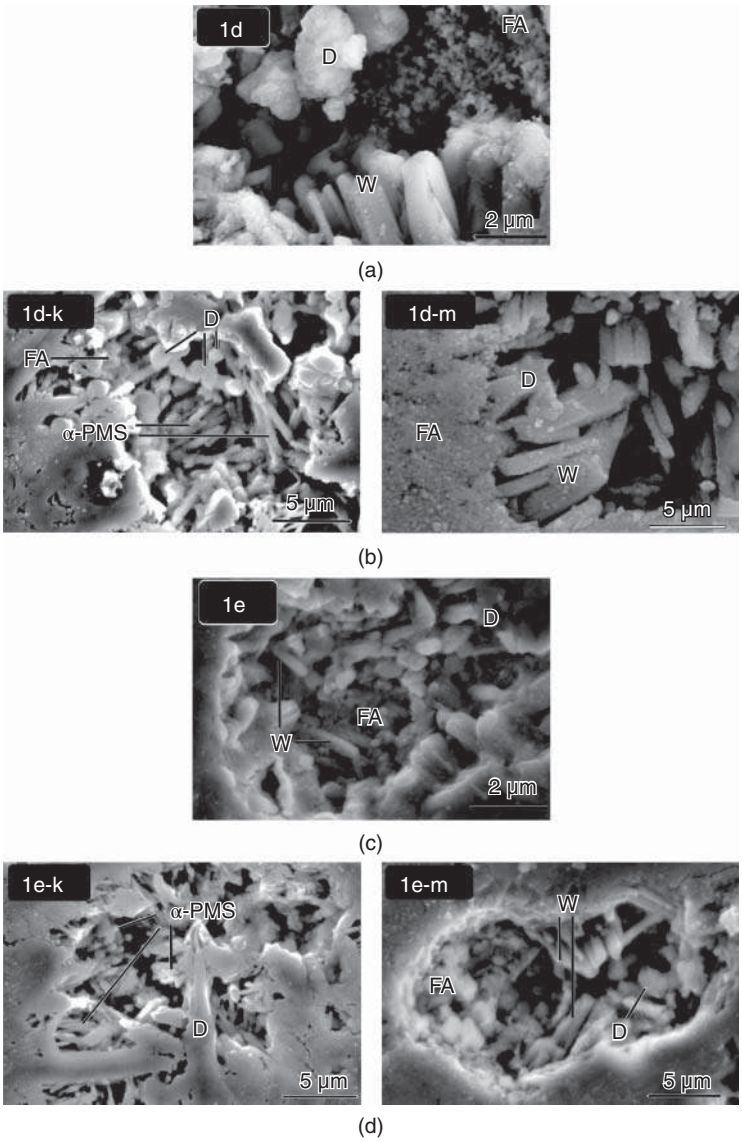

Figure 18.4 Typical microstructure of the GCs (a) 1d, and (b) 1d-m and 1d-k, produced after heat-treatment at 850 °C, and (c) 1e, and (d) 1e-m and 1e-k produced after heat-treatment at 900 °C, revealed after chemical etching of polished surfaces with 2% HF solution (D, diopside; FA, fluorapatite; W, wollastonite; α-PMS, α-potassium magnesium silicate).

18.5.1.2 Mechanical Properties

The influence of heat treatment temperature on the mechanical properties of the produced GCs 1d and 1e is presented in Table 18.7. At 800 °C, crystallization in glass powder compacts 1d and in 1e was seemingly just initiated (Figure 18.3a,b). Owing to the fact that crystallization causes an improvement in mechanical properties, the highest values of mechanical properties, such as flexural strength, modulus of elasticity, hardness, and fracture toughness, were recorded in the GCs heat-treated at temperatures near their corresponding T_p (Table 18.5).

Table 18.7 Mean values (and standard deviation, $n = 10$) of mechanical properties of the investigated GCs 1d and 1e, heat-treated at various temperatures for one hour.

	Heat treatment temperature (°C)	Flexural strength (σ, MPa)	Modulus of elasticity (E, GPa)	Vickers microhardness (HV, GPa)	Fracture toughness ($K_{IC,}$ MPa·m$^{0.5}$)
GC 1d	800	119 ± 10	24 ± 6	6.0 ± 0.4	1.6 ± 0.1
	850	171 ± 11	27 ± 5	6.1 ± 0.5	1.7 ± 0.1
	900	141 ± 6	22 ± 4	5.2 ± 0.7	1.4 ± 0.1
GC 1e	800	86 ± 19	24 ± 5	5.9 ± 0.5	1.8 ± 0.3
	850	141 ± 9	30 ± 1	6.0 ± 0.5	1.9 ± 0.3
	900	122 ± 9	25 ± 1	5.8 ± 0.1	1.7 ± 0.2
Cortical jaw bone	—	50–150	7–30	0.06–0.075	2–12
Dentine	—	230–305	15–30	<0.6	3

For comparison purposes, the mechanical properties of cortical jaw bone and dentine are also presented.
The significance for bold formatting of 850 °C is made to emphasize that the highest values of mechanical properties were recorded in the GCs heat-treated at temperatures near their corresponding T_p.

From the values of Vickers microhardness and fracture toughness, the BI of the produced GCs was calculated and was found in the range of 3.6–3.7 μm$^{-0.5}$ for the GCs 1d and 3.3–3.5 μm$^{-0.5}$ for the GCs 1e.

18.5.1.3 Bioactivity

The excellent mechanical properties of the produced GCs 1d and 1e, motivated to assess their bioactivity by SBF tests. The results of the SBF testing showed a clear evidence of bioactivity. More specifically, the pH of the solution (Figure 18.5a,c) was rapidly increased in the first week (from 7.25 to ~9.5), and then there was a slight tendency for a slow increase, suggesting an ion exchange between the surface of the GC and the SBF.

The formation of HA layer on the surface of the produced GCs was verified by SEM observations and EDS analyses (characteristic images for each composition are presented in Figure 18.5a,c), which showed that the Ca/P molar ratio on the surface of the 1d and 1e GC samples, after 21 days, was 1.67 and 1.68, respectively. It was also observed that the EDS spectra (not shown), recorded from samples immersed in SBF at different times, showed an increase in the intensity of the peaks attributed to Ca and P (which are ascribed to HA formed on the surface of the GCs) and a decline or disappearance of the Si, Na, and Mg peaks (with are witnesses of the elements in the bulk of the GC). Consequently, the GCs 1d and 1e induce the formation of HA on their surface from the very first time of their immersion in SBF at 37 °C.

18.5.1.4 General Evaluation of the Parent GCs 1d and 1e

The above experimental results show that the produced GCs 1d and 1e display bioactivity, reflected in their ability to spontaneously form HA on their surface after immersion in SBF at 37 °C. Besides bioactivity, the assemblage of the crystalline phases formed leads to well-sintered and well-crystallized GCs with a dense microstructure, which affects their mechanical properties. These features, in conjunction with the attractive aesthetics (white color), qualify the produced GCs 1d and 1e for further consideration and experimentation as potential dental implant materials. More specifically, heat treatment at 850 °C resulted in GCs with mechanical properties close

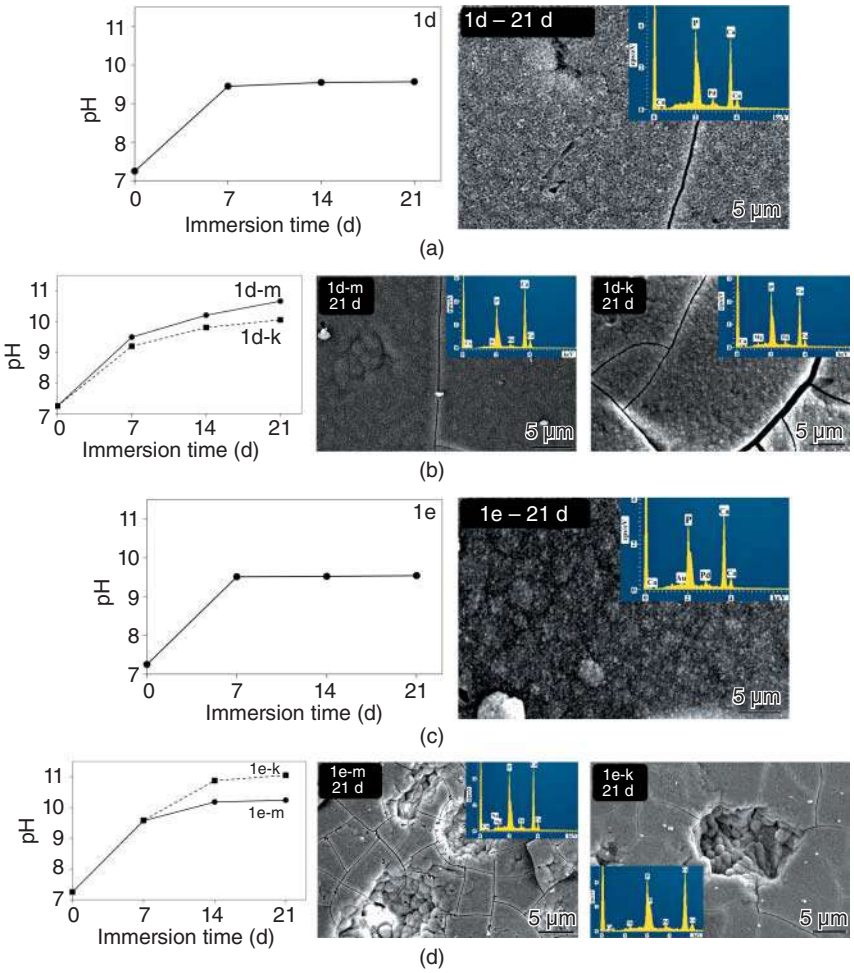

Figure 18.5 Evolution of pH in the solution over immersion time of powder of the GCs in SBF (at 37 °C) and SEM images and the corresponding EDS spectra (in the inset) of the surface of bulk samples after immersion in SBF for 21 days for (a) 1d, (b) 1d-m and 1d-k, (c) 1e, and (d) 1e-m and 1e-k GCs.

enough to those of dentine (which is the biological tissue that a dental implant is called on to replace) and jaw bone (that is the biological tissue with which the material of an implant comes into contact) (Table 18.7).

18.5.2 Modified Glass-Ceramic Compositions

18.5.2.1 Densification and Crystallization

Thermal Analysis of Glasses and Crystallization Mechanism The DSC thermographs of the parent glasses 1d-k, 1d-m, 1e-k, and 1e-m are plotted in Figure 18.2b. The values of T_g, T_c, T_p, and T_l (calculated by three independent experiments) are summarized in Table 18.8. The K-free glasses (1d-m and 1e-m) have a T_g between 650 and 660 °C and a T_p close to 850 °C. K-substitution (in the glasses 1d-k and 1e-k) causes an increase in both temperatures, i.e. T_g is 670–677 °C and T_p is ~900 °C. The experimental results (not shown) showed that the temperatures of T_g, T_c, T_p, and T_l were increased as the heating rate was increased.

Table 18.8 Mean values (and standard deviation; $n = 3$) of glass transition temperature (T_g), onset crystallization temperature (T_c), crystallization temperature (T_p), liquidus temperature T_l, activation energy (E_a) of crystallization, and Avrami exponent (n_A) (determined by the DSC measurements) of the modified glasses.

Glass	T_g (°C)	T_c (°C)	$T_c - T_g$ (°C)	T_p (°C)	T_l (°C)	E_a (kJ/mol)	n_A
1d-k	670 ± 8	816 ± 7	146	872 ± 14	>988	469 ± 9	3.3 ± 0.4
1d-m	652 ± 8	785 ± 3	133	824 ± 14	973 ± 3	428 ± 15	3.7 ± 0.2
1e-k	677 ± 9	820 ± 11	143	907 ± 15	>992	476 ± 29	2.6 ± 0.2
1e-m	660 ± 7	788 ± 9	128	838 ± 16	960 ± 8	385 ± 31	3.3 ± 0.1

The sintering window ($T_c - T_g$) is also presented.

The E_a of crystallization for each glass was calculated using the plots of $\ln((T_p^2)/\varphi)$ vs. $1000/T_p$ (Figure 18.2c) and the results are listed in Table 18.8. The n_A value for each glass (Table 18.8) was calculated from the analysis of the exothermic peaks through the measurement of the full width at the half maximum at T_p. The results, listed in Table 18.8, suggest that the modified glasses are generally prone to three-dimensional growth of crystals since $n_A \geq 3$, while the glass 1e-k is prone to two-dimensional crystallization ($n_A \geq 2$).

Sintering and Aesthetics The parallelepiped bars of the glass-powder compacts of these four compositions were heat-treated at temperatures, whose choice was based on the findings of the thermal analysis of the glasses, i.e. the temperatures T_g, T_s, and T_p (Table 18.8). Here, it is necessary to notice that the highest values of mechanical properties of the GCs 1d and 1e were recorded in the GCs heat-treated at temperatures near to their corresponding T_p. Accordingly, after a plateau at 450 °C for two hours (to complete the de-binding), the K-free glasses were heat-treated at 850 °C and the K-containing glasses at 900 °C.

Well-sintered GCs were produced at 850 °C in the case of the 1d-m, and 1e-m GCs, and at 900 °C in the case of the 1d-k and 1e-k GCs. The density values of the produced GCs at these temperatures, along with the density of the corresponding parent bulk glass (which was always smaller than that of the corresponding GC, suggesting that crystallization occurred in the glass powder compacts at these temperatures) are presented in Table 18.9. The linear shrinkage of the GCs ranged between

Table 18.9 Mean values (and standard deviation, $n = 5$) of linear shrinkage and density of the modified GCs.

	Density (g/cm^3)		Linear shrinkage (%)
Composition	Glass	GC	GC
1d-k	2.49	2.61	9.4 ± 0.3
1d-m	2.58	2.77	10.6 ± 0.3
1e-k	2.48	2.80	9.1 ± 0.3
1e-m	2.55	2.68	9.3 ± 0.8

For comparison purposes, the density values of the bulk glasses are also presented (The SD of density values was <5%).

9.1% and 10.6% (Table 18.9). As far as the aesthetics is concerned, the produced GCs had a white color, but K-substitution favored this effect markedly (as shown in the insets of Figure 18.3c,d).

Crystalline Structure and Microstructure Similar to the GCs 1d and 1e, the GCs 1d-m and 1e-m were comprised of diopside ($CaMgSi_2O_6$), wollastonite ($CaSiO_3$), and fluorapatite ($Ca_{10}(PO_4)_6F_2$) (Figure 18.3c), while diopside ($CaMgSi_2O_6$), fluorapatite ($Ca_{10}(PO_4)_6F_2$), and α-potassium magnesium silicate (α-PMS, $K_2MgSi_3O_8$) were formed in the GCs 1d-k and 1e-k (Figure 18.3d). There is no evidence of formation of other secondary or minor phases, according to the assignment of the peaks in the diffractograms.

The microstructure of these GCs (Figure 18.4b,d), according to elemental EDS analysis, is composed of well-defined big prismatic crystals assigned to diopside (D, where the Mg/Ca/Si/O molar ratio was found approximately as 1/1/2/6, respectively), and smaller acicular crystals assigned to wollastonite (W, where the Ca/Si molar ratio was 1/1), or to α-PMS, in the case of the potassium-substituted GCs (since potassium was recorded by EDS on these crystals), whose thickness was smaller than those of wollastonite, embedded in a glassy phase. Flour was detected in the coralloid-like small crystals marked with FA, assigned, therefore, to fluorapatite. The microstructure observations are consistent with the results of the XRD analysis (Figure 18.3c,d).

18.5.2.2 Mechanical Properties

The mechanical properties of these modified GCs are summarized in Table 18.10 and are a direct result of both the crystalline assemblage and the microstructure. The flexural strength varied from 107 to 129 and the modulus of elasticity ranged between 23 and 31 GPa. The microhardness and fracture toughness values of these GCs ranged between 5.4 and 5.6 GPa, and 1.7–1.9 $MPa{\cdot}m^{0.5}$, respectively. Additionally, the BI values for the GCs 1d-k, 1d-m, 1e-k, and 1e-m were 3.0 ± 0.6, 3.3 ± 0.5, 3.0 ± 0.4, and $3.0 \pm 0.4\ \mu m^{-0.5}$, respectively. Because of their excellent mechanical properties, the produced 1d-k, 1d-m, 1e-k, and 1e-m GCs were subjected to further studies to assess their bioactivity in SBF.

18.5.2.3 Bioactivity

The results of the SBF testing showed clear evidence of bioactivity of all the modified GCs. The pH of the SBF solution (Figure 18.5b,d) was rapidly increased in the first week (from 7.25 to ~9.5 and ~9.7), and over the immersion time there was a tendency for a slow increase, suggesting that ion exchange occurs between the surface of these GCs and the SBF at 37 °C.

The bioactivity performance of these GCs was confirmed by SEM/EDS analysis on their surface after immersion in SBF. Characteristic images for each GC are presented in Figure 18.5b,d. The

Table 18.10 Mean values (and standard deviation, $n = 10$) of the mechanical properties of the modified GCs, heat-treated at 850 °C (for 1d-m and 1e-m) and 900 °C (for 1d-k and 1e-k) for one hour.

	GC			
Mechanical properties	**1d-k**	**1d-m**	**1e-k**	**1e-m**
Flexural strength (σ, MPa)	129 ± 5	128 ± 10	117 ± 5	107 ± 16
Modulus of elasticity (E, GPa)	26 ± 1	23 ± 1	26 ± 1	31 ± 2
Vickers microhardness (HV, GPa)	5.6 ± 0.4	5.6 ± 0.4	5.4 ± 0.4	5.6 ± 0.3
Fracture toughness($K_{IC,}$ $MPa{\cdot}m^{0.5}$)	1.9 ± 0.5	1.7 ± 0.2	1.8 ± 0.2	1.9 ± 0.2

EDS analyses showed that the Ca/P molar ratio, after 21 days immersion in SBF, was in the range of 1.67–1.69 (note that the Ca/P molar ratio of stoichiometric HA is 1.67). Similar to 1d and 1e GCs, the EDS spectra showed that the peaks attributed to Ca and P (on account of HA formed on the surface of the GCs) increase over immersion time, while a decline or disappearance of the Si, Na, and Mg peaks (which are witnesses of elements in the bulk substrate of the GCs) is observed.

18.5.2.4 General Evaluation of the Modified Glass-Ceramics

The results showed that the modified GCs 1d-k, 1d-m, 1e-k, and 1e-m exhibit the ability to spontaneously form HA on their surface after immersion in SBF at 37 °C. Besides bioactivity, the results show that both substitutions (i.e. K for Na, and Mg for Ca) in group 1d resulted in lowering of the modulus of elasticity from 27 to 26 and 23 GPa and in increasing of the fracture toughness, from 1.7 to 1.9 MPa·m$^{0.5}$. In group 1e, K-substitution led to a reduction of the modulus of elasticity from 30 to 26 GPa, but there is a negligible effect of this substitution on the value of fracture toughness, which remained almost stable (1.9–1.8 MPa·m$^{0.5}$). In all cases, the attempted substitutions caused a reduction in the microhardness of the produced GCs (Figure 18.6). It is important to note that the proposed modifications resulted in GCs with mechanical properties even more close (than those of the non-modified 1d and 1e GCs) to those of dentine (which is the biological tissue that the dental implant is called on to replace) and jaw bone (that is the biological tissue with which the material of the implant comes into contact) (Figure 18.6).

Consequently, the most important issue is that the above modifications have a positive effect as far as the adaptation of the mechanical properties of produced GCs (1d, 1d-k, 1d-m, 1e, 1e-k, and 1e-m) to those of human jaw bone and dentine, suggesting these materials as promising ones for dental implant applications (Figure 18.6). The Section 18.6 focuses on this important aspect.

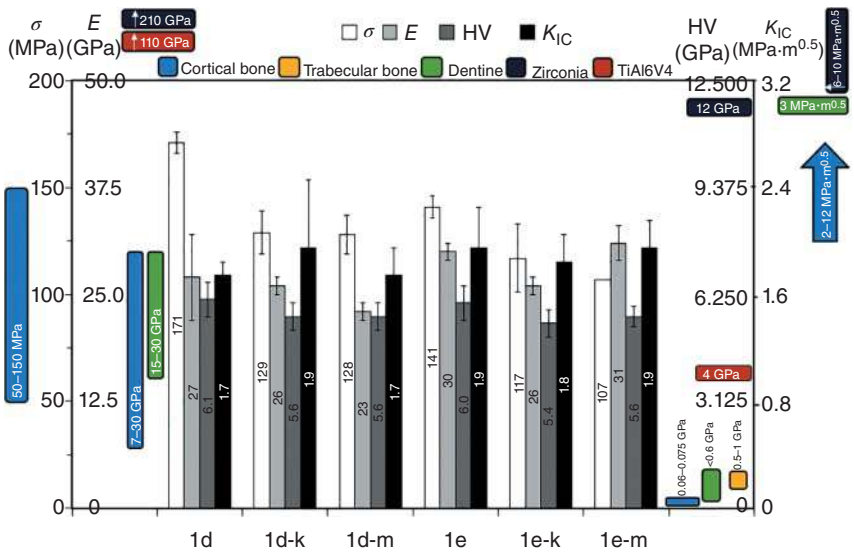

Figure 18.6 Influence of substitutions of K for Na and of Mg for Ca in the compositions 1d and 1e on the mechanical properties (flexural strength, σ; modulus of elasticity, E; Vickers microhardness, HV; and fracture toughness, K_{IC}) of the produced GCs, 1d-k, 1d-m, 1e-k, and 1e-m. For comparison purposes, the values of the mechanical properties of natural tissues (cortical bone, trabecular bone, and dentine) are also shown in the diagram.

18.6 Feasibility of the Application of the Novel Glass-Ceramics in Dental Implantology

In the field of dental implantology, it is important to stress the biological importance of the mechanical properties of natural tissues (jaw bone and dental hard tissue). In the case of dental implants, bone cells (osteoblasts, osteocytes, and osteoclasts) are directly involved in the process of forming a strong bond between the jaw bone and the implant material. This is called osteointegration and was discovered by Branemark in the 1950s. Osteointegration is not an isolated phenomenon, but it depends on previous osteoinduction (the process by which osteogenesis is induced, because it implies the recruitment of immature cells and the stimulation of these cells to be developed into preosteoblasts) and osteoconduction, which is associated to the formation of HA (i.e. an osteoconductive surface permits bone growth on it, or down into pores, channels, or pipes) [1, 33]. Once the bone's organic matrix production is successfully completed by the osteoblasts, the majority of the osteoblasts undergo programmed cell death, while a small portion of osteoblasts that had been embedded in the organic matrix transforms into osteocytes. Osteocytes contribute to conservation of the extracellular matrix, by responding to local strains resulted from external loads applied on bone. In the case of the human jaw bone, these external loads come mainly from the forces of the repeated chewing cycles. Osteoclasts are responsible for bone resorption. It is important to note that, in order to sustain skeletal remodeling and to maintain bone mass, there is a continuous balanced interaction between osteoblasts and osteoclasts.

The knowledge of the rules of biomechanics in living jaw tissues is crucially important because these rules are related to the longevity of a dental implant in the oral cavity. Obviously, the evaluation of the influence of the factors that play an important role in the ultimate success of dental implant restorations is necessary. The above factors, among others, are related to the mechanical properties of both the human jaw bone and the materials used for the production of a dental implant [36]. After the placement of a dental-implant prosthetic restoration, the dental implant receives the loads from the occlusal forces. If the value of the modulus of elasticity and the fracture toughness of the dental-implant material is close to the corresponding values of the jaw bone, then the dental implant distributes the load from the occlusal forces to the adjacent bone (jaw-bone) and thereby its density is maintained (actually, this is the main aim of the majority of research teams). On the other hand, if the values of the above properties are far from the corresponding values of the jaw bone, then the dental implant is the only one that is charged by the occlusal forces; as a result, the implant does not transfer the occlusal forces to the jaw bone. This phenomenon is called stress shielding. Thus, the osteocytes lose their main role (i.e. the conservation of the extracellular matrix), resulting in a reduction of the bone density of the jaw bone. This eventually leads to the failure of the dental implant restoration.

As mentioned in Section 18.2, a dental material must have notably good chemical, mechanical, and optical properties, comparable to those of the dental hard tissues (i.e. enamel, dentine) and bone, depending on the application [34]. In the case of dental implants, the knowledge of the mechanical properties of cortical bone, trabecular bone, and dentine will help in designing of new dental materials [27, 34, 69–72]. The values of the modulus of elasticity of the popular (in dentistry) implant materials used, i.e. titanium and zirconia (110 and 220 GPa, respectively) [12, 44], are markedly higher than that of the jaw bone (7–30 GPa) and dentine (15–30 GPa) [34, 44]. The values of the mechanical properties of the novel GCs produced in the present study are at desired levels. Actually, through the substitutions, the values of the natural tissues were satisfactorily approached. To stress this issue, in the light of the fact that the produced bioactive GCs are still not in use as dental implant materials in the daily dental clinical practice, it is important to compare the properties

of the novel GCs both with the properties of materials used in dental clinical practice (titanium and zirconia) and of the natural tissues (jaw bone and dentine). This is comprehensively presented in Figure 18.6.

Starting from the fracture toughness value and knowing that after the placement of a prosthetic restoration, the occlusal forces are mostly received by the body of the dental implant, unlike the natural teeth, where jaw bone plays this role, it would be ideal for this property to range from 2 to 12 $MPa \cdot m^{0.5}$ [34]. The experimental results showed that the substitutions of K and Mg in the initial compositions 1d and 1e affected the mechanical properties of the resultant GCs, since the fracture toughness was increased. The fracture toughness of the produced GCs, after the substitutions of K and Mg (1.7–1.9 $MPa \cdot m^{0.5}$) was clearly lower than that of zirconia implants (6–10 $MPa \cdot m^{0.5}$) [12], which are used in the daily clinical dental practice, but very close to that of compact bone (2–12 $MPa \cdot m^{0.5}$) [14, 34].

In order to increase the fracture-toughness value and maintain (as much as possible) the modulus of elasticity value, it was proposed a complete substitution of K_2O for Na_2O and a partial substitution of MgO for CaO. The experimental results showed that these substitutions affected the mechanical properties of the resultant GCs, since the modulus of elasticity was reduced while the fracture toughness was increased. The produced GCs have a considerably smaller modulus of elasticity, for instance 26 and 23 GPa for the series 1d, which almost fits to the maximum value of the jaw bone. This anticipates an efficient suppression of stress shielding.

As far as microhardness is concerned, the substitutions resulted in a slight reduction. Nevertheless, these values (5.4–5.6 GPa) are higher than those of the spongy bone (0.5–1 GPa) [73, 74], with which a dental implant comes in contact, but they are still lower than that of zirconia implants and rather close to that of titanium implants (12 and 4 GPa, respectively) [74–76].

The BI, which is a measure of machinability, is 3.0–3.7 $\mu m^{-0.5}$ for the produced GCs. In glasses and ceramics, BI values in the range of 3–9 $\mu m^{-0.5}$ anticipate good machinability [67, 77]. In the light of the rapid development of additive manufacturing, Baino and Verné [47] have suggested interesting ideas, such as the production of bi-layered prototype implants for total tooth replacement. The above idea is very promising, especially nowadays, on account of the introduction of digital technology, such as the computer aided design (CAD) and the CAD/chorioallantoic membrane (CAM) technology, in dentistry, for fabricating dental prosthetic restorations [78–80]. Ideally, the combination of bioactive [46] (in order to fabricate the root of the tooth) and bio-inert (in order to fabricate the crown of the tooth) GCs in a CAD/CAM plate, which will then undergo mechanical cutting, might be possible to occur, provided that a strong interface between the bioactive and the bio-inert GC materials can be achieved. Selective laser melting (SLM), or, for ceramics, selective laser sintering (SLS) technique is a modern solution of the later problem (i.e. development of strong interface), since sintering takes place layer by layer, in a single mass [81, 82]. Indeed, Fateri et al. [83] successfully fabricated the first GC tooth, with a size similar to the human tooth by SLM. Accordingly, the SLM technique is a very promising technique in the construction of dental restorations and the produced GCs display properties that satisfy the requirements of this modern fabricating technique.

18.7 Concluding Remarks

The results of this study demonstrated that the produced novel GCs were well-sintered and dense materials. This is greatly attributed to the fact that sintering was not impeded by crystallization. As far as the substitutions are concerned, the partial substitution of Mg for Ca and the complete

substitution of K for Na were attempted in the two parent glasses, 1d and 1e, whose bioactivity is well documented in literature. In the case of K for Na substitution, the glass transition (T_g) and the crystallization temperatures (T_p) were shifted to higher temperatures, while there were no significant alterations in T_g and T_p in the glasses with Mg for Ca substitution. The GCs were produced through sintering-crystallization of fine glass-powder compacts in the temperature interval of 800–900 °C, and comprised of an assemblage of diopside, wollastonite, and fluorapatite, or diopside, fluorapatite, and α-PMS, depending on the type of substitution. The GC materials showed ability to spontaneously form HA on their surface *in vitro* that might be attributed to the formation of wollastonite or α-PMS crystalline phases.

Compared to the parent GCs, the modified GC compositions featured lower modulus of elasticity and microhardness, and higher fracture toughness. Consequently, the substitutions attempted in the parent GCs offer the possibility to suitably tune the mechanical properties of the novel bioactive GCs in order to be a good match to the properties of the natural hard tissues, such as bone and dentine.

References

1 Fernandes, H.R., Gaddam, A., Rebelo, A. et al. (2018). Bioactive glasses and glass-ceramics for healthcare applications in bone regeneration and tissue engineering. *Materials (Basel)* 11 (12): E2530.

2 Shelby, J. (2005). *Introduction to Glass Science and Technology*. Cambridge: The Royal Society of Chemistry.

3 Jones, J.R. and Clare, A.G. (2012). *Bio-glasses: An Introduction*. New York: Wiley.

4 Höland, W. and Beall, G. (2002). *Glass-Ceramic Technology*. Ohio: The American Ceramic Society.

5 Zheng, Q., Zhang, Y., Montazerian, M. et al. (2019). Understanding glass through differential scanning calorimetry. *Chemical Reviews* 119: 7848–7939.

6 Agathopoulos, S. and Tulyaganov, D.U. (2019). Bioglasses and glass-ceramics in the Na_2O–CaO–MgO–SiO_2–P_2O_5–CaF_2 system. In: *Bioceramics and Biocomposites: From Research to Clinical Practice* (ed. I. Antoniac), 123–148. New York: Wiley.

7 Tulyaganov, D.U., Agathopoulos, S., Ventura, J.M. et al. (2006). Synthesis of glass-ceramics in the CaO–MgO–SiO_2 system with B_2O_3, P_2O_5, Na_2O and CaF_2 additives. *Journal of the European Ceramic Society* 26: 1463–1471.

8 Agathopoulos, S., Tulyaganov, D.U., Ventura, J.M.G. et al. (2006). Structural analysis and devitrification of glasses based on the CaO–MgO–SiO_2 system with B_2O_3, Na_2O, CaF_2 and P_2O_5 additives. *Journal of Non-Crystalline Solids* 352: 322–328.

9 Kansal, I., Tulyaganov, D.U., Goel, A. et al. (2010). Structural analysis and thermal behavior of diopside-fluorapatite-wollastonite-based glasses and glass-ceramics. *Acta Biomaterialia* 6: 4380–4388.

10 Baino, F., Marshall, M., Kirk, N., and Vitale-Brovarone, C. (2016). Design, selection and characterization of novel glasses and glass-ceramics for use in prosthetic applications. *Ceramics International* 42: 1482–1491.

11 Hench, L.L. (2006). The story of Bioglass. *Journal of Materials Science – Materials in Medicine* 17: 967–978.

12 Saadaldin, S.A., Dixonb, S.J., Costad, D.O., and Rizkalla, A.S. (2013). Synthesis of bioactive and machinable miserite glass-ceramics for dental implant applications. *Dental Materials* 29: 645–655.

13 Hench, L.L. (1991). Bioceramics: from concept to clinic. *Journal of the American Ceramic Society* 74: 1487–1510.

14 Montazerian, M. and Zanotto, E.D. (2016). History and trends of bioactive glass-ceramics. *Journal of Biomedical Materials Research Part A* 104: 1231–1249.

15 Kokubo, T. (1991). Bioactive glass-ceramics: properties and applications. *Biomaterials* 12: 155–163.

16 Kokubo, T., Ito, S., Shigematsu, M. et al. (1985). Mechanical properties of a new type of apatite-containing glass-ceramic for prosthetic application. *Journal of Materials Science* 20: 2001–2004.

17 Höland, W., Vogel, W., Naumann, K., and Gummel, J. (1985). Interface reactions between machinable bioactive glass-ceramics and bone. *Journal of Biomedical Materials Research* 19: 303–312.

18 Li, J., Jansen, J.A., Walboomers, X.F., and van den Beucken, J.J. (2020). Mechanical aspects of dental implants and osseointegration: a narrative review. *Journal of the Mechanical Behavior of Biomedical Materials* 103: 103574.

19 Chen, X., Liao, X., Huang, Z. et al. (2010). Synthesis and characterization of novel multiphase bioactive glass-ceramics in the $CaO–MgO–SiO_2$ system. *Journal of Biomedical Materials Research Part B Applied Biomaterials* 93 (1): 194–202.

20 Tulyaganov, D.U., Makhkamov, M.E., Urazbaev, A. et al. (2013). Synthesis, processing and characterization of a bioactive glass composition for bone regeneration. *Ceramics International* 39: 2519–2526.

21 Daguano, J.K.M.B., Milesi, M.T.B., Rodas, A.C.D. et al. (2019). In vitro biocompatibility of new bioactive lithia-silica glass-ceramics. *Materials Science and Engineering C* 94 (1): 117–125.

22 Islam, M.T., Felfel, R.M., Abou Neel, E.A. et al. (2017). Bioactive calcium phosphate-based glasses and ceramics and their biomedical applications: a review. *Journal of Tissue Engineering* 21 (8): 1–16.

23 Jmal, N. and Bouaziz, J. (2017). Synthesis, characterization and bioactivity of a calcium-phosphate glass-ceramics obtained by the sol–gel processing method. *Materials Science and Engineering C* 71 (1): 279–288.

24 Bibby, J.K., Bubb, N.L., Wood, D.J., and Mummery, P.M. (2005). Fluorapatite-mullite glass sputter coated Ti6Al4V for biomedical applications. *Journal of Materials Science – Materials in Medicine* 16 (5): 379–385.

25 Agathopoulos, S., Tulyaganov, D.U., Valerio, P., and Ferreira, J.M.F. (2005). A new model formulation of the $SiO_2–Al_2O_3–B_2O_3–MgO–CaO–Na_2O–F$ glass-ceramics. *Biomaterials* 26 (15): 2255–2264.

26 Chen, Q.Z., Thompson, I.D., and Boccaccini, A.R. (2006). 45S5 Bioglass-derived glass-ceramic scaffolds for bone tissue engineering. *Biomaterials* 27: 2414–2425.

27 Gerhardt, L.C. and Boccaccini, A.R. (2010). Bioactive glass and glass-ceramic scaffolds for bone tissue engineering. *Materials* 3: 3867–3910.

28 Saadaldin, S., Dixon, J., and Rizkalla, A. (2014). Bioactivity and biocompatibility of a novel wollastonite glass-ceramic biomaterial. *Journal of Biomaterials and Tissue Engineering* 4: 939–946.

29 ISO 6872 (2008). *Dentistry – Ceramic Materials*, 3e. Geneva: International Organization for Standardization.

30 Augat, P. and Schorlemmer, S. (2006). The role of cortical bone and its microstructure in bone strength. *Age and Ageing* 35: 27–31.

31 Lakatos, E., Magyar, L., and Bojtár, I. (2014). Material properties of the mandibular trabecular bone. *Journal of Medical Engineering* 2014: 470539.

32 Fanghänel, J., Gedrange, T., and Proff, P. (2008). Bone quality, quantity and metabolism in terms of dental implantation. *Biomedizinische Technik* 53 (5): 215–219.

33 Albrektsson, T. and Johansson, C. (2001). Osteoinduction, osteoconduction and osseointegration. *European Spine Journal* 10: S96–S101.

34 Montazerian, M. and Zanotto, E.D. (2017). Bioactive and inert dental glass-ceramics. *Journal of Biomedical Materials Research Part A* 105 (2): 619–639.

35 Zhang, Y.R., Du, W., Zhou, X.D., and Yu, H.Y. (2014). Review of research on the mechanical properties of the human tooth. *International Journal of Oral Science* 6 (2): 61–69.

36 Natali, A.N. (2003). *Dental Biomechanics*. London: CRC Press.

37 Simonis, P., Dufour, T., and Tenenbaum, H. (2010). Long-term implant survival and success: a 10–16-year follow-up of non-submerged dental implants. *Clinical Oral Implants Research* 21 (7): 772–777.

38 Ozkut, Z. and Kazazoglu, E. (2011). Zirconia dental implants: a literature review. *Journal of Oral Implantology* 37 (3): 367–376.

39 Guess, P.C., Att, W., and Strub, J.R. (2012). Zirconia in fixed implant prosthodontics. *Clinical Implant Dentistry and Related Research* 14 (5): 633–645.

40 Kohal, R.J. and Klaus, G. (2004). A zirconia implant-crown system: a case report. *International Journal of Periodontics and Restorative Dentistry* 24: 147–153.

41 Andreiotelli, M., Wenz, H.J., and Kohal, R.J. (2009). Are ceramic implants a viable alternative to titanium implants? A systematic literature review. *Clinical Oral Implants Research* 20 (S4): 32–47.

42 Al-Amleh, B., Lyons, K., and Swain, M. (2010). Clinical trials in zirconia: a systematic review. *Journal of Oral Rehabilitation* 37 (8): 641–652.

43 Yazdani, J., Ahmadian, E., Sharifi, S. et al. (2018). A short view on nanohydroxyapatite as coating of dental implants. *Biomedicine & Pharmacotherapy* 105: 553–557.

44 Saadaldin, S.A. and Rizkallaa, A.S. (2014). Synthesis and characterization of wollastonite glass-ceramics for dental implant applications. *Dental Materials* 30: 364–371.

45 Palmquist, A., Omar, O.M., Esposito, M. et al. (2010). Titanium oral implants: surface characteristics, interface biology and clinical outcome. *Journal of the Royal Society Interface* 7: S515–S527.

46 Dimitriadis, D., Moschovas, D., Tulyaganov, D.U., and Agathopoulos, S. (2020). Development of novel bioactive glass-ceramics in the $Na_2O/K_2O–CaO–MgO–SiO_2–P_2O_5–CaF_2$ system. *Journal of Non-Crystalline Solids* 533: 119936.

47 Baino, F. and Verné, E. (2017). Production and characterization of glass-ceramic materials for potential use in dental applications: thermal and mechanical properties, microstructure, and in vitro bioactivity. *Applied Sciences* 7: 1–16.

48 Tulyaganov, D.U., Agathopoulos, S., Valerio, P. et al. (2011). Synthesis, bioactivity and preliminary biocompability studies of glasses in the system $CaO–MgO–SiO_2–Na_2O–P_2O_5–CaF_2$. *Journal of Materials Science – Materials in Medicine* 22 (2): 217–227.

49 Hill, R.G., Stamboulis, A., Law, R.V. et al. (2004). The influence of strontium substitution in fluorapatite glasses and glass-ceramics. *Journal of Non-Crystalline Solids* 336 (3): 223–229.

50 Liu, X., Ding, C., and Chu, P.K. (2004). Mechanism of apatite formation on wollastonite coatings in simulated body fluids. *Biomaterials* 25 (10): 1755–1761.

51 Kansal, I., Goel, A., Tulyaganov, D.U. et al. (2011). Diopside ($CaO·MgO_2·SiO_2$)–fluorapatite ($9CaO_3·P_2O_5·CaF_2$) glass-ceramics: potential materials for bone tissue engineering. *Journal of Materials Chemistry* 21 (40): 16247–16256.

52 Toya, T., Kameshima, Y., Yasumori, A., and Okada, K. (2004). Preparation and properties of glass-ceramics from wastes (Kira) of silica sand and kaolin clay refining. *Journal of the European Ceramic Society* 24 (8): 2367–2372.

53 Nonami, T. and Tsutsumi, S. (1999). Study of diopside ceramics for biomaterials. *Journal of Materials Science – Materials in Medicine* 10 (8): 475–479.

54 Agathopoulos, S., Tulyaganov, D.U., Ventura, J.M. et al. (2006). Formation of hydroxyapatite onto glasses of the CaO–MgO–SiO_2 system with B_2O_3, Na_2O, CaF_2, P_2O_5 additives. *Biomaterials* 27: 1832–1840.

55 Rabiee, S.M., Nazparvar, N., Azizian, M. et al. (2015). Effect of ion substitution on properties of bioactive glasses: a review. *Ceramics International* 41: 7241–7251.

56 Rabiee, S.M., Ravarian, R., Mehmanchi, M. et al. (2013). Effect of alumina on microstructure and compressive strength of a porous silicated hydroxyapatite. *Journal of Applied Biomaterials & Functional Materials* 12 (2): 102–106.

57 Prabhu, M., Kavitha, K., Manivasakan, P. et al. (2013). Synthesis, characterization and biological response of magnesium-substituted nanobioactive glass particles for biomedical applications. *Ceramics International* 39: 1683–1694.

58 Bretcanu, O., Chatzistavrou, X., Paraskevopoulos, K. et al. (2009). Sintering and crystallization of 45S5 Bioglass powder. *Journal of the European Ceramic Society* 29 (16): 3299–3306.

59 Mastai, Y. (2012). Advances in crystallization processes. In: *Crystallization Kinetics of Amorphous Materials* (ed. M. Çelikbilek, A.E. Ersundu and S. Aydın), 127–157. Rijeka: InTechOpen.

60 Araújo, E.B. and Idalgo, E. (2009). Non-isothermal studies on crystallization kinetics of tellurite $20Li_2O$–$80TeO_2$ glass. *Journal of Thermal Analysis and Calorimetry* 95: 37–42.

61 Erol, M., Küçükbayrak, S., and Ersoy-Meriçboyu, A. (2009). The application of differential thermal analysis to the study of isothermal and non-isothermal crystallization kinetics of coal fly ash based glasses. *Journal of Non-Crystalline Solids* 355 (9): 569–576.

62 Matusita, K. and Sakka, S. (1981). Kinetic study on non-isothermal crystallization of glass by thermal analysis. *Bulletin of the Institute for Chemical Research* 59 (3): 159–171.

63 Karamanov, A., Avramov, I., Arrizza, L. et al. (2012). Variation of Avrami parameter during non-isothermal surface crystallization of glass powders with different sizes. *Journal of Non-Crystalline Solids* 358: 1486–1490.

64 Kissinger, H. (1956). Variation of peak temperature with heating rate in differential thermal analysis. *Journal of Research of the National Bureau of Standards* 57 (4): 217–321.

65 Augis, J. and Bennett, J. (1978). Calculation of the Avrami parameters for heterogeneous solid state reactions using a modification of the Kissinger method. *Journal of Thermal Analysis and Calorimetry* 13 (2): 283–292.

66 Niihara, K., Morena, R., and Hasselman, D.P.H. (1982). Evaluation of K_{IC} of brittle solids by the indentation method with low crack-to-indent ratios. *Journal of Materials Science Letters* 1: 13–16.

67 Boccaccini, A.R. (1997). Machinability and brittleness of glass-ceramics. *Journal of Materials Processing Technology* 65: 302–304.

68 Kamitakahara, M. and Ohtsuki, C. (2006). Apatite formation on CaO, SiO_2-based glass-ceramics in a simulated body fluid. *Phosphorus Research Bulletin* 20: 101–110.

69 Rezwan, K., Chen, Q.Z., Blaker, J.J., and Boccaccini, A.R. (2006). Biodegradable and bioactive porous polymer/inorganic composite scaffolds for bone tissue engineering. *Biomaterials* 27: 3413–3431.

70 Kaur, G., Kumar, V., Baino, F. et al. (2019). Mechanical properties of bioactive glasses, ceramics, glass-ceramics and composites: state-of-the-art review and future challenges. *Materials Science and Engineering C* 104: 109895.

71 Dimitriadis, K., Tulyaganov, D.U., and Agathopoulos, S. (2021). Development of novel alumina-containing bioactive glass-ceramics in the $CaO–MgO–SiO_2$ system as possible candidates for dental implant applications. *Journal of the European Ceramic Society* 41: 929–940.

72 Dimitriadis, K., Vasilopoulos, K.C., Vaimakis, T.C. et al. (2020). Synthesis of glass-ceramics in the $Na_2O/K_2O–CaO–MgO–SiO_2–P_2O_5–CaF_2$ system as candidate materials for dental applications. *International Journal of Applied Ceramic Technology* 17: 2025–2035.

73 Agathopoulos, S., Nikolopoulos, P., Salomoni, A. et al. (1996). Preparation and properties of binary oxide bioceramics. *Journal of Materials Science – Materials in Medicine* M7: 629–636.

74 Seong, W.J., Kim, U.K., Swift, J.Q. et al. (2009). Elastic properties and apparent density of human edentulous maxilla and mandible. *International Journal of Oral and Maxillofacial Surgery* 38: 1088–1093.

75 Bankoglu Gungor, M., Aydin, C., Yilmaz, H., and Gul, E.B. (2014). An overview of zirconia dental application implants: basic properties and clinical application of three cases. *Journal of Oral Implantology* 40: 485–494.

76 Niinomi, M. (1998). Mechanical properties of biomedical titanium alloys. *Materials Science and Engineering A* 243: 231–236.

77 Tsitrou, E.A., Northeast, S.E., and van Noort, R. (2007). Brittleness index of machinable dental materials and its relation to the marginal chipping factor. *Journal of Dentistry* 35: 897–902.

78 Spagnuolo, G. and Sorrentino, R. (2020). The role of digital devices in dentistry: clinical trends and scientific evidence. *Journal of Clinical Medicine* 9 (6): 1692.

79 Revilla-León, M., Sadeghpour, M., and Özcan, M. (2020). An update on applications of 3D printing technologies used for processing polymers used in implant dentistry. *Odontology* 108 (3): 331–338.

80 Fung, L. and Brisebois, P. (2020). Implementing digital dentistry into your esthetic dental practice. *Dental Clinics of North America* 64 (4): 645–657.

81 Razavykia, A., Brusa, E., Delprete, C., and Yavari, R. (2020). An overview of additive manufacturing technologies – a review to technical synthesis in numerical study of selective laser melting. *Materials (Basel)* 13 (17): 3895.

82 Dimitriadis, K., Papadopoulos, T., and Agathopoulos, S. (2019). Effect of bonding agent on metalceramic bond strength between Co–Cr, fabricated with selective laser melting and dental feldspathic porcelain. *Journal of Prosthodontics* 28 (9): 1029–1036.

83 Fateri, M., Gebhardt, A., Thuemmler, S., and Thurn, L. (2014). Experimental investigation on selective laser melting of glass. *Physics Procedia* 56: 357–364.

19

Applications of Bioactive Glasses for Implants in the Ear

Mario Milazzo[1,2,5], Glauco Cristofaro[3,4], Stefano Berrettini[2,4], and Serena Danti[1,2,4,5]

[1] *Laboratory for Atomistic and Molecular Mechanics (LAMM), Massachusetts Institute of Technology, Cambridge, MA, USA*
[2] *University of Pisa Research Unit, National Interuniversity Consortium of Materials Science and Technology (INSTM), Florence, Italy*
[3] *Division of Otorhinolaryngology (ORL), Arcispedale di "Santa Maria Nuova", Florence, Italy*
[4] *Laboratory of Temporal Bone Dissection and Otologic Tissue Engineering (OtoLab), Department of Surgical, Medical, Molecular Pathology and Emergency Medicine, University of Pisa, Pisa, Italy*
[5] *Department of Civil and Industrial Engineering, University of Pisa, Pisa, Italy*

19.1 Introduction

From a biomaterials point of view, the path of middle ear reconstruction has somehow retraced that of orthopedic implants, searching for stiff, permanent biocompatible materials with osteointegration capacity [1]. Even if ear and limb bones deal with very different mechanical forces, the peculiar constraints of biocompatibility after reconstructive surgery have rendered the long-term survival of any replacements extremely difficult in the ear [1, 2]. Biocompatibility relies on the ability of a biomaterial to perform with a suitable host response, so it is strongly dependent on the specific tissue/organ and pathologic state [3]. Anatomically, ossicular bone is special type compact bone tissue, quite similar to femoral compact bone [4]. Other important bones in the auditory compartment include the mastoid bone, a porous bone made up by mastoid cells, either filled with air or bone marrow, and external auditory canal, which is an osseocartilaginous structure extending from the auricle to the tympanic membrane. Overall, ear tissues can be affected by congenital, infectious, inflammatory, traumatic, and neoplastic diseases, thus reconstructive materials are required [5]. Along with non-toxicity and effective sterilization, mechanical forces and cell–material interactions have been highlighted among the most important key factors affecting biocompatibility. Middle ear biocompatibility is a very special case, which has deserved specificity. Indeed, the failure of biomaterial-based devices (i.e. passive implants) in the ear has deeply been studied, and was found to rely on anatomic modifications due to reconstructive surgery, such as inefficient aeration, perpetration of inflammation sustained by residual infections, and continuous vibration of the involved tissues, which overall render this environment very aggressive toward any biomaterials [6]. To face these issues, mostly bioinert stiff materials, including alloplastic materials, metals and later on bioinert ceramics were applied, using a thin slice of cartilage as an interface between the ossicular prosthesis and the eardrum [2, 7]. The presence of an interposed autologous material concurs to reduce the device extrusion, which is a consequence of poor biocompatibility, as defined above. Differently, biological tissue grafts tend to be resorbed as a consequence of inflammatory processes [8–10]. Several surgical techniques have also been explored to stably connect the ossicular replacement prosthesis (ORP) to the tympanic membrane softer tissue at one end, and

Bioactive Glasses and Glass-Ceramics: Fundamentals and Applications, First Edition.
Edited by Francesco Baino and Saeid Kargozar.

to the harder bony tissue on the opposite end, including drilling grooves to allow fibrous tissue to grow in [11].

In the search for better biocompatible materials for orthopedic applications than metal alloys, about 60 years ago, silicate-based glasses and glass-ceramics containing high amounts of Ca and P ions appeared as very intriguing options [12]. Bioactive materials are intermediate between resorbable and bioinert, meaning that they dissolve at a small rate sufficient to trigger chemical and biochemical reactions. In fact, bioactive glasses (BAGs) are surface reactive glasses. There are three main compositional characteristics that enable the surface to be highly reactive in a water solution, thus making them different from traditional glasses: (i) less than 60 mol% SiO_2; (ii) high Na_2O and CaO content; and (iii) a high CaO/P_2O_5 ratio, namely, low P_2O_5 [13]. As intermediate between bio-inertness and bio-resorption, the actual behavior of BAGs is greatly affected by composition. Their peculiarity is to elicit a specific biological response at the material/tissue interface as a consequence of chemical changes occurring in wet environment [13]. Once in contact with biofluids, the ions released from the BAG surfaces can locally induce biological reactions leading to new bone formation. This phenomenon was discovered in the late 1960s by Larry Hench and colleagues at the University of Florida (USA). After implanting a low content (45 wt%) SiO_2 glass containing (24.5 wt%) Na_2O and (24.5 wt%) CaO and (6 wt%) P_2O_5 (namely, 45S5; also known with the tradename Bioglass®), it was found that the material was chemically bound to bone tissue, becoming inseparable [14]. The interfacial adhesion strength of BAGs to biological tissues may even be higher than the cohesive strength of the implant, leading to difficult revision surgery [15]. In addition to the BAG family, BAG-ceramics and dense hydroxyapatite are also able to form an interfacial bond with neighboring tissues. A key advantage of a BAG is the ability to bond to both hard and soft tissues. The mechanism leading to chemical bond formation with tissues is a multistep process, which in turn prevents the formation of a fibrotic capsule, typical of bioinert materials. BAGs attach to human tissues through the formation of hydrated silica, further covered by a carbonate hydroxyapatite surface layer, the latter being responsible for interfacial bonding [16]. After, cell adhesion and consequent collagen deposition occur, which entail the strong connection to tissues. Moreover, BAGs can stimulate osteogenesis by locally exerting a control over gene expression in the bone lineage induced by the microenvironment. As such, they naturally possess not only osteoinductive (i.e. osteoblast spreading) but also desirable osteoconductive (i.e. osteo-differentiative) properties.

Since 1979, ceramics have been used in tympanoplasty, in particular to reconstruct the ossicular chain (i.e. ossiculoplasty) or the posterior canal wall [17]. Hench's Bioglass was in fact modified by Brömer et al., who marketed another BAG-ceramic under the tradename of Ceravital® [18]. In 1983, the first histologic and clinical experience with the BAG-ceramic Ceravital showed that, unlike other types of ceramics, it could be applied without the need of cartilage for protection, thus behaving similarly to the homologous bone ossicles [19]. Importantly, the use of interposed material with BAGs is controversial, as it would prevent implant-to-tissue fixation, desirable for stability [11]. In a similar fashion, Ceravital showed good outcomes for external auditory canal; the reconstructed wall displayed no extrusion, but re-epithelization [19]. In general, bioactive ceramics have demonstrated an excellent rate of integration with the surrounding osseous tissue: 8–10 days after the implant, osteoblasts initiate proliferation, leading to a stable connection with bone in 2 months. After such initial intriguing results, BAGs and glass-ceramics started to became popular among otologic surgeons, and still represent a possible option [20, 21]. The optimal biomaterial for middle ear reconstruction, in terms of long-term functional outcomes – and therefore, biocompatibility – is still an ambitious challenge. Recently, emerging disciplines, such as tissue engineering, have disclosed new option for otology, which could also boost novel applications of BAGs in this field [1].

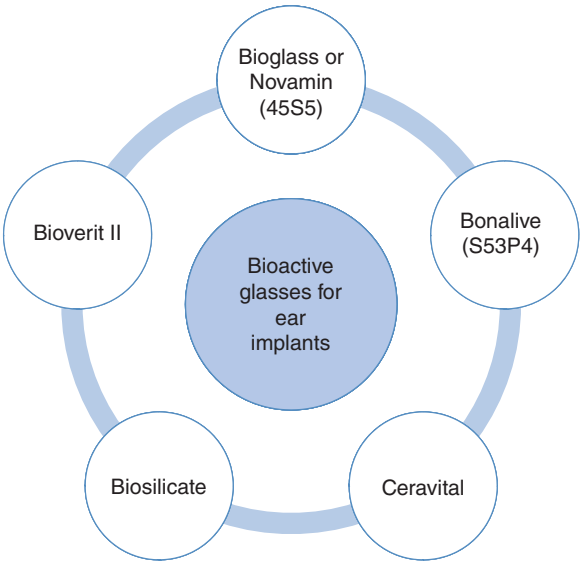

Figure 19.1 Bioactive glasses (BAGs) for ear implants.

This chapter overviews the available results using BAGs in the ear and surrounding compartments (Figure 19.1), including nose–throat and craniofacial, to finally approach new options for reconstruction and regeneration of these tissues.

19.2 Bioactive Glasses in Otorhinolaryngology: Biological Properties

19.2.1 Bioactive Glasses in Otorhinolaryngology

In this section, we provide a brief description of the BAGs used in the ear–nose–throat, head–neck, and maxillofacial surgery.

Bioglass 45S5 (SiO_2–CaO–P_2O_5), also called Novamin, has been the first bioglass introduced in surgery in 1970s, thanks to its ability to form direct chemical bonds with both hard and soft tissues through surface chemistry more rapidly than other materials of the same class [22]. As the Si^{4+} and Ca^{2+} ions remarkably influence cell differentiation and regulation [23–25] earlier works have shown osteogenic properties *in vitro* [26]. Due to its intrinsic brittleness, BAG is less suitable for load-bearing devices, making it preferred as a composite with polymers [27]. For instance, Qu and Liu, proposed a scaffold made of gelatin and BAG for odontoiatric applications [28].

Bonalive (S53P4) is a BAG that is composed of silicon dioxide, sodium oxide, calcium oxide, and phosphorous pentoxide. This BAG has shown remarkable osteoconductive and antibacterial properties [29, 30], and has been successfully used as a material for micro-prostheses [31] and structural obliteration [32–35]. Ceravital was introduced by Reck in 1980s and after a decade had been used in 1300 cases [11]. To activate the biogenic reaction of Ceravital with the eardrum side, bone paste or powder were used also in combination with fibrin glue, leading to better anatomical results than alloplastic material Plasti-Pore. The long-term outcomes have highlighted material degradation in case of persistent inflammation sustained by an infected mucosa [36].

Biosilicate is a bioactive vitroceramic that is able to bind to bone or soft tissues because of the hydroxy-carbonateapatatie that are formed as a coating on its surface when in contact with body

fluids [37]. It has been extensively used to reconstruct the ossicular chain in several animal models, showing no ototoxicity or vestibular toxicity [38–42].

Bioverit is a glass ceramic that exists in four different types based on a glass of composition SiO_2–Al_2O_3–MgO–Na_2O–K_2O–F + CaO + P_2O_5 [43]. Bioverit II is the one that has been largely employed in dentistry, otorhinolaryngology, and orthopedic surgery because of its machinability and stability [44–46]. It has shown a high level of biocompatibility, observed with implants in mice and rabbits [44, 45, 47–50], and can be implanted even in infected sites since it possesses antifouling properties [51].

19.2.2 Antimicrobial Activity

One of the most important challenges for an implant is undoubtedly the capability of preventing infections. The antimicrobial and antifouling properties are key features that a biomedical device must possess in order to ensure a biological stability in the host tissues [52]. A remarkable example is given by cochlear implants that can be infected by bacteria following pathologies like otitis media [53–57]. BAGs have been successfully employed in the clinics because of their ability to positively react with biological fluids and, through a progressive release of ions, increase the osmotic pressure and pH [58], thus making the environment unsuitable for a bacterial colonization [59–61]. A large number of studies have been carried out using S53P4 granules, which have been employed both *in vitro* and *in vivo* also as coatings for structural replacements [59–62]. Positive effects have been observed in applications for filling bone cavities [63], orthopedic surgery [64], or sinus and mastoid obliterations [32, 34, 65] using granules with diameters below 3.5 mm. A recent study has also observed how the dimensions of the granules can have a remarkable effect on the antimicrobial property of the material, highlighting how granules with diameters below 45 μm can reduce recurrent infections from *Staphylococcus aureus* in both planktonic and biofilm states [66].

Another work observed a pronounced reduction of the biofilm formation when using S53P4 granules as a coating for middle-ear prostheses or fracture fixtures. Remarkable results were observed either in normoxic or hypoxic conditions, this latter used to mimic the oxygen conditions in bone and bone cavities [67]. Although this study was carried out *in vitro*, the achieved results make BAGs good candidates for reducing post-operative infections against clinically important bacteria [22, 26, 68–70].

S53P4 has been also tested on the components of cochlear implants: evidences from two different works showed, with an observation via Scanning Electronic Microscope, a significant reduction of the biofilm against *S. aureus* and *Pseudomonas aeruginosa* [71, 72].

Other studies involved Bioverit II, a material that has shown a high level of biocompatibility and whose antimicrobial properties were demonstrated as improved when posing a layer of Ciprofloxacin on a BAG-coated ossicular prosthesis [73].

19.2.3 Tissue Induction and Integration

Kwon et al. studied a composite made of BAG-embedded methacrylated gelatin-based cryogel and observed the bioactivity of the nanobioglass for bone regeneration. Results showed that a small amount of BAG is able to trigger the formation of hydroxyapatite, which is dependent on the Ca^{2+} and P^{3+} ions [74]. This outcome also confirmed the findings achieved by Hench et al. in an earlier work [60].

Vallittu et al. investigated the differences on implant-induced ossification when using either 45S5 or S53P4 as coatings for a fiber-reinforced composite implant to replace cranial bone structures

both *in vitro* and *in vivo*. The authors observed that while in both cases collagen subunits and pro-osteogenic genes were enhanced, 45S5 dissolved faster than S53P4 due to a higher induced pH in the site. In contrast, 45S5 was able to inhibit mesenchymal stem cell (MSC) proliferation and differentiation due to the environmental basicity, an effect that was not observed for S53P4 [75].

Vogt et al. investigated the stability of a middle-ear structural replacement made of Bioverit II without or in the presence of nanostructured silica coating. Aggregates of material were detected after 84 days in both cases [49]. Using this cylinder-like structure as a total ossicular replacement prosthesis (TORP) between the manubrium and the stapes footplate, they also observed proliferation of the epithelium that was more pronounced for the coated implants. Moreover, implants after 6 and 12 weeks showed augmented bone formation in case of nanocoated structures. These outcomes supported the hypothesis that a nanostructured coating may enhance cell growth and bone formation [44].

19.3 Clinical Applications

19.3.1 Mastoid Obliteration and Posterior Meatal Wall Reconstruction

Cholesteatoma surgery aims at eradicating the disease and at preventing of its recurrence. This can be achieved through two main techniques, namely canal wall up (CWU) and canal wall down (CWD) mastoidectomy. In CWU, the posterior canal wall is preserved to some extent. This surgery results in a normal-sized outer ear, thus avoiding ear discharge and the need for recurrent cavity cleaning by surgeons. In contrast, it is associated with a high recurrence rate (~36% in adults and ~67% in children) [76, 77]. The CWD technique, instead, is associated with quite a low recurrence rate but the resulting open tympano-mastoid cavity leads to several drawbacks, including ear discharge that is reluctant to antimicrobial administration, vertigo on exposure to water and even to wind, debris accumulation within the cavity requiring frequent surgical removal, and inability to wear traditional hearing aids since they do not fit the enlarged ear canal [76].

Such issues can be avoided by mastoid obliteration, a procedure in which the mastoid cavity is filled by one or more materials, thus separating the mastoid cavity from a normal-sized outer ear canal. Two types of materials are used for mastoid obliteration: biological (autologous grafts, allografts, and xenografts) and synthetic [78]. In the ear, biological materials possess undoubtable biocompatibility but tend to resorb over time, they are difficult to shape, and require to be morbidly harvested. Previous surgical operations or local spread of ear infection can limit the availability of such materials or use make their use disadvantageous, due to increased donor site morbidity [79, 80]. In contrast, synthetic materials are handy, free from exogenous contamination, and available in large amounts [81], and the increased costs associated with their use can be compensated by the shorter surgical time [82].

In a recent review on 15 case series, the most widely applied materials for mastoid obliteration (i.e. 9 studies out of 15) were BAGs, mostly S53P4 and 45S5 [83]. Sorour et al. presented the results of a rather peculiar technique on a group of 20 patients operated for the first time in absence of intracranial complications [84]. Here, only the posterior meatal wall was reconstructed by means of a small amount (~0.5 g) of BAG mixed with the patient's blood held in place with foil and cotton, while the void mastoid cavity was obliterated with a superiorly based musculoperiosteal flap (i.e. Palva flap) (Figure 19.2).

Tympanic membrane reconstruction was achieved by means of temporalis muscle fascia graft placed over and beyond the newly reconstructed posterior meatal wall, and eventually covered by

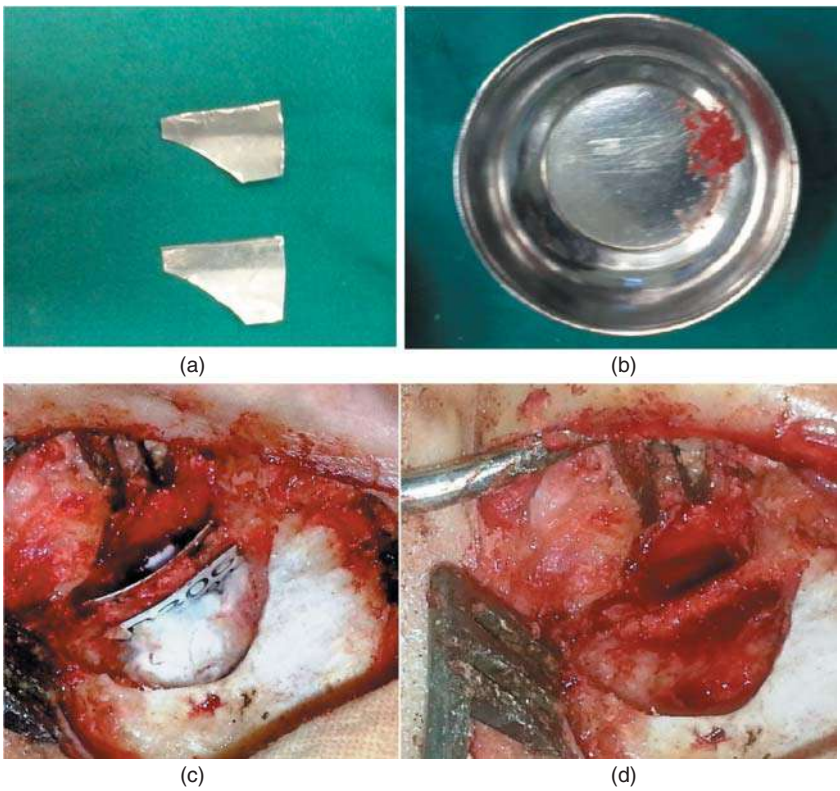

Figure 19.2 Obliteration of the mastoid using foil templates (a), bioactive glass (BAG) mixed with patient's venous blood (b). Placement in the implant site (c) and removal of the foils after BAG has hardened (d). Source: Sorour et al. [84], Figure 01 (p. 017)/reproduced with permission from Elsevier.

the tympano-meatal flap held in place of Gelfoam®. The reported surgical results were satisfactory, with neither intraoperative complications nor technical difficulties. During follow-up periods up to 36 months, the postoperative appearance of the external auditory canal contour was found smooth without hidden pouches, irregularities, and stenosis in all cases. None registered granulation, foreign body reaction, extrusion, resorption, nor displacement of the BAG were observed. Audiological results were also quite satisfactory, as all patients gained more than 10 dB hearing gain. No worsening of bone conduction thresholds occurred in any operated ear, thus supporting the fact that there is no toxic effect by BAG on the cochlea. Therefore, BAGs appeared to be a reliable, safe, and effective solution for surgical reconstruction of the posterior meatal wall. de Veij Mestdagh et al. presented a single-center retrospective follow-up study on 67 patients, in which the technique was quite clear-cut [85]. Patients underwent either CWU or CWD tympano-mastoidectomy. In both cases, the mastoid cavity was filled with 2.5 ml S53P4 granules and fibrin glue, while subcutaneous tissue was used to cover the BAG and close the mastoid. Postoperative wound infections did not occur in any patients. During follow-up period (mean 22 months), diffusion-weighted magnetic resonance imaging (MRI) and clinical otoscopy were performed for detection of recurrent cholesteatoma, occurring in four patients, mainly young (6% of cases) localized in the tympanic sinus or epitympanum. No residual disease in the obliterated mastoid was encountered. A revision of the CWD procedure was required by drilling out granule samples, showing that an acceptably dry ear was obtained in 96% of cases. A persistently wet ear after surgery (defined as Merchant

grade 3) was not observed in any patients. General audiometric performance was determined by preoperative and postoperative pure tone audiometry in 66 patients. Overall, both air conduction (AC) thresholds and air bone gap (ABG) did not change significantly. S53P4 mastoid obliteration did not worsen hearing capacity and there were no signs of inner ear damage. In contrast to the use of hydroxyapatite outlined by Yung and Bennett [86], there was no need to cover the S53P4 granules with a vascularized pedicle flap to prevent exposure and leakage of the filler materials into the ear canal [85].

In 2017, a retrospective follow-up study reported on 94 patients (i.e. 96 ears) to evaluate the efficacy and safety of BAG S53P4 as a filler material in mastoid obliteration surgery (both CWU and CWD) performed on non-cholesteatomatous chronic otitis media patients with chronically discharging ears despite conservative therapy. Specifically, 23 patients (23 ears) were treated with additional mastoid obliteration with S53P4, whereas the remaining 71 patients (73 ears) were considered as controls. The mean follow-up length was 2.4 years for the S53P4 group. The number of previous mastoid surgeries was significantly higher in the S53P4 group when compared to the control group. Sixteen patients (70%) in the S53P4 obliteration group received empirical intravenous wound infection antibiotic prophylaxis intravenously vs. three patients (4%) in the control group. A complete control of infection and a dry, safe ear at the last postoperative clinic visit (defined as Merchant grade 0) could be obtained only in the S53P4 obliterated group, specifically in 17 out of 23 (74%) patients. Of note, all seven patients who did not receive intraoperative antibiotics in the S53P4 obliteration group yet achieved Merchant grade 0 outcome. Mastoid obliteration using S53P4 granules increased the odds of achieving a completely dry and safe ear by 3.6-folds. None of the patients in the S53P4 obliteration were graded 3 on Merchant's scale. This positive effect of S53P4 was prominent when considering only revision procedures. A number of 14 out of 18 (78%) ears in the S53P4 obliteration group vs. 10 out of 25 (40%) in the control group, previously operated, achieved complete control of infection. Both groups showed no significant difference between preoperative and postoperative hearing status. Patients with Merchant grade 0 or 1 outcomes were able to use their hearing aids. No postoperative complications, such as wound infections, facial nerve paralysis, and cochlear or vestibular damage, were encountered in each group [87].

In 2017, Bernardeschi et al. published a prospective observational uncontrolled study aimed to analyze the anatomical, functional, radiological, and quality-of-life results of mastoid and epitympanic obliteration using the BAGs in primary and revision CWD and CWU mastoidectomy. They reported that out of 41 cases (39 patients, 2 operated bilaterally), 88% required revision surgery, while in 17% perioperative complications occurred. Anatomical results were overall defined satisfactory. Three months after surgery, 34 cases (83%) presented a well-healed external auditory canal with an intact tympanic membrane; two cases (5%) presented a narrow but functional external auditory canal with an intact eardrum. Only one patient (2%) presented uncovered granules in the external auditory canal and underwent revision surgery five months after being implanted, under local anesthesia, to cover the granules with cartilage. At one year, the patient had a well-healed external auditory canal and tympanic drum, with unchanged results in the second follow-up. No cases of recurrent cholesteatoma and/or retraction pocket were observed. No residual disease was found one year after surgery and the mean ABG closure was 7.7 ± 1.84 dB. No statistically significant differences were found in the ABG closure when comparing the different types of tympanoplasty, primary vs. revision surgery, CWU vs. CWD procedures, and the presence vs. absence of cholesteatoma [88].

In a retrospective observational study conducted along four years (2008–2013), Ezzat and Eid evaluated the effectiveness of obliteration with 45S5 Bioglass in overcoming the open cavity problems in a cohort of 40 patients who underwent CWD tympanoplasty for eradication of

cholesteatoma. The surgery included removal of the cholesteatoma sac, pathologic mucosa, incus, malleus head, and tensor fold. In a vast majority of cases, the result of the procedure was a Merchant grade 1 (47.5%) or grade 0 (30%). Postoperative hearing assessment showed that an average gain in air conduction of 29.1 dB. Serviceable hearing (i.e. threshold 40 dB or less) was obtained after surgery in the totality of cases. No patient developed facial palsy without a previously exposed facial nerve. Hence, according to the authors, there is no relation between the obliteration materials or techniques and facial nerve palsy. Albeit little is known about the length of the follow-up in this case series, information on the incidence and type of complications is provided. Ear discharge was found in 36 patients (90%) preoperative and only in 6 (15%) postoperative. Cholesteatoma recidivism or recurrence was present in four patients (10%). One case (2.5%) developed inflammatory reaction from biomaterial with aural polyp managed by repeated packing, free at secondary look. A second case (2.5%) developed inflammatory reaction from biomaterial with frequent discharge, healed after performing fascia interposition between the skin and bioactive material. Second look operation was performed in six patients (15%) in case of persistent discharge or computer tomography (CT) suspicion of cholesteatoma recurrence. One of them had cholesterol granuloma and other three patients had cholesteatoma in the oval window and at the under surface of the tympanic membrane. No otoscopic incidence of retraction pockets is reported. Altogether in this study, the authors claimed that the observed complications of an open cavity with obliteration of the mastoid are less than those given by the CWU technique [89].

A former case series is reported by Shokry in 2012 on 20 cases: 6 operated with CWU mastoidectomy followed by obliteration with particulate BAG and a large anteriorly based Palva flap to cover the filled cavity; 9 cases with CWD mastoidectomy and reconstruction of the posterior meatal wall with BAG held in place by foil templates where conchal cartilage has been used to fit the defect in the posterior canal wall reinforced by the same temporalis fascia graft applied below the remaining eardrum; and 5 cases with CWD mastoidectomy, followed by closure of the defect in the posterior meatal wall with conchal cartilage reinforced by temporalis fascia graft in the same fashion, and obliteration of the whole mastoidectomy cavity by particulate form BAG. Complications mentioned in this series were infection of the surgical wound, occurring in two cases and controlled by application of topic antibiotics daily for one week, and extrusion of the conchal cartilage, occurring in a case from the latter group one month postoperatively. The authors believed that obliteration using a BAG is a technique that facilitates exposure of the middle ear and ensures complete removal of cholesteatoma, thus providing biocompatibility, resistance to infection, favoring healing and new bone formation, while a reconstruction of the posterior canal wall with conchal cartilage and BAG recreates the normal external canal anatomy [90].

In a single-institution case series, Sarin et al. reported on 26 consecutive patients operated between 1996 and 2011. Twenty patients had undergone previous surgery because of chronic otitis media, and the number of previous operations varied between 1 and 5. Eight patients had an active middle ear and/or mastoid cavity cholesteatoma at the time of surgery, and eight patients had previous cholesteatoma in the operated ear. Three patients also had a bony dehiscence at the middle cranial fossa with intact dura resulting in a loss of dural support toward the mastoid cavity, and three patients had a dural fistula at the middle cranial fossa region resulting in cerebrospinal fluid leakage. All operations in this series were performed under general anesthesia via retroauricular approach. Previously operated patients underwent through revision surgery, while two patients in the naive group received CWD mastoidectomy. The mastoidectomy cavity was filled with BAG granules, moistened with 0.9% saline solution, along with bone pate when applicable and fibrin glue. The temporalis muscle fascia served as a cover for the granules to avoid contact with the posterior meatal skin flap and a Palva musculoperiosteal flap was accordingly

applied for the retroauricular area. Lyoplant (B. Braun, Melsungen, Germany) was used in many patients in addition to fascia to ensure complete coverage of all BAG granules. Dural protrusion was treated with a BAG plate, designed for blowout fractures of the orbital floor, thus giving support to the dural plane. Two patients with dural fistulas and cerebrospinal fluid leakage were treated via a CWU mastoidectomy by occluding the fistula with a suitable fascia or Lyoplant with fibrin glue in addition to mastoid cavity obliteration via BAG [65].

In this early case series by Stoor et al., seven patients received a CWD mastoidectomy via retroauricular incision with a superiorly based musculoperiosteal flap according to Palva. The cavity resulting from the effacement of all mastoid cells was then filled with S53P4 granules, mixed with saline to obtain a malleable mass. Closure of the BAG filled cavity occurred through proper distension of the Palva flap, positioning of temporalis muscle fascia under the ear canal skin sometimes reinforced with Lyoplant. After the operation, antibiotics were administered for 10 days and Merocel wicks were removed from the outer ear canal 1 week after surgery. Cleaning and topical administration of boric acid was applied when indicated. In all the patients, the cavities were reduced in size, in two patients totally eliminated and the obtained posterior meatal wall resembled a normal one. In five patients, a small cavity remained. A transient fistula with granulation, along with growth of *S. aureus* in microbiological examinations, was seen in one patient over several months. However, no bioactive extrusion occurred. The infection responded to conservative treatment without the use of antibiotics, showing no association with the filling material. The study concluded that BAG is a well-tolerated and easy-to-use filler material, sparing the morbidity of autologous materials by offering a low susceptibility to infection despite a potentially infected environment and a gradual dissolution which maintains the obliteration of the cavity while the tissue growth slowly proceeds from the surrounding cells [91].

Król et al. in 2020 reported a study enrolling 11 adult patients who received obliteration of the postoperative cavity with S53P4 after a CWD mastoidectomy for eradication of cholesteatoma. The posterior meatal wall was hence reconstructed with periosteum and cartilage harvested from tragus or temporal bone, and the cavity was filled with S53P4 granules. Preoperative swabs resulted negative in seven patients, *S. aureus* in two patients, *P. aeruginosa* in one subject, and concurrent fungi in another subject [92].

Al Tamami et al. in 2020 published the results of a retrospective study conducted between November 2017 and January 2019 to evaluate the tolerance of both the external and middle ear along with the safety of the inner ear after using 45S5 Bioglass as a synthetic bone graft filler on patients operated for primary cholesteatoma, revision surgery, or rehabilitation of a previous CWD mastoidectomy. Preoperative and postoperative pure tone audiometric data were collected and analyzed, comparing the preoperative and one-year postoperative bone conduction thresholds averages [93].

19.3.2 Replacements for the Ossicular Chain

Conductive hearing loss is a condition that affects more than 300 million people worldwide and mainly the ossicular chain in the middle ear. The employment of ORPs has been the most largely used approach to recover the hearing sense in this setting. These piston-like structures connect the tympanic membrane with the stapes (i.e. partial ORP; PORP) or the stapes footplate (i.e. total ORP; TORP), thus enabling the material continuity that is gone due to surgery or missing following pathologies or traumas [10]. Even though the initially preferred material in this field was alumina because of its inertness, Ceravital has been successfully used in animal models by exploiting the inherent bioactivity for forming osseous junctions [94]. Later, another similar study was carried

out by Zikk et al. who employed Ceravital granules in guinea pigs [40]. Applications of Ceravital in humans was documented with reasonable results after eight years post-implant [19, 95]. Another approach consists in using 45S5 Bioglass since, in contrast to Ceravital, it is able to bond also with soft tissues, and in this specific scenario, to the eardrum. Prostheses made of 45S5 Bioglass have been used in several *in vivo* studies, and the results compared with a control group composed of alumina implants [96–99]. The main outcome concerns the good adhesion of the BAG on the soft tissues on one hand, and on the stapes footplate on the other hand, while alumina-based implants eroded the tympanic membrane, thus inducing the extrusion in few years [100]. As also reported by Rust et al., sound conduction with 45S5-based devices is generally acceptable without any appreciable migration of the prostheses [101]. More recently, other studies observed a fragmentation of 45S5-based implants after 14 years from the implant, raising concerns about the durability of this material [102]. A valuable alternative to 45S5 is biosilicate that was tolerated by guinea pigs with no signs of toxicity after 90 days from the implant [38]. In 2013, Hesse et al., manufactured a TORP made of Bioverit II composed of a plate with a diameter of 3 mm and a 2.5-mm long cylinder with a diameter of 1 mm. The prosthesis, having a weight of 8 mg, was treated to embed a layer of tested in synergy with a layer of ciprofloxacin to prevent the formation of a biofilm. This study did not aim at evaluating the acoustic properties of the prosthesis, but rather its biocompatibility and bacterial colonization [73]. Turck et al. employed Bioverit II as the constitutive material for TORPs in rabbits (Figure 19.3). The authors investigated the differences in using a nanoporous silica layer, eventually achieving no significant differences with the plain Bioverit II prosthesis [49].

19.3.3 Cochlear Implants

Cochlear implants are complex electronic devices devoted to recover sensorineural hearing loss, a condition that affects the mechano-electric transduction function in the cochlea. 45S5 Bioglass was

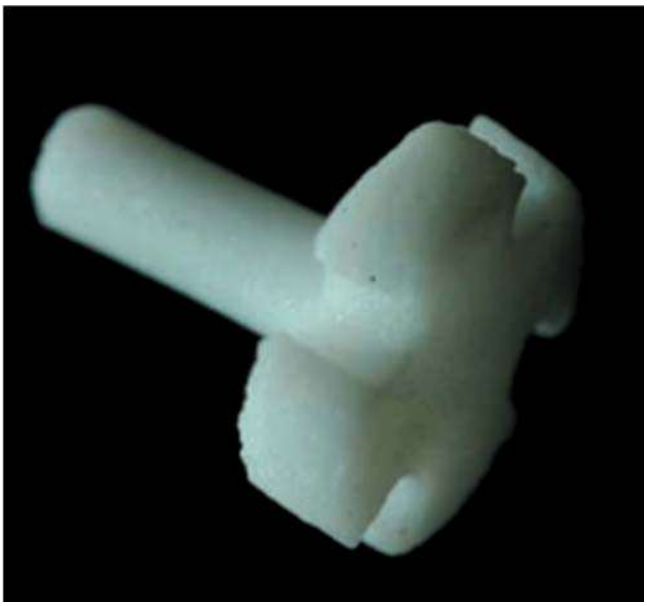

Figure 19.3 TORP made of Bioverit II. Source: Turck et al. [49], Figure 01, (p. 03)/reproduced with permission from 2007 Taylor & Francis.

employed in a few studies to anchor the implants to the temporal bone thanks to its ability to form strong connections with hard and soft tissues. Bioglass has resulted as a good sealing material to protect the electronic components [103], but it was replaced by titanium in the late 1990s because of several concerns about its stability in the long term [104].

19.3.4 Other Uses in the Craniofacial Area

19.3.4.1 Cranial Defect Repair

S53P4 has been largely applied to coat fiber-reinforced composites in order to reconstruct cranial defects. Outcomes from a large number of studies have shown a significant osteoconduction induced by the BAG, which enables the proliferation and differentiation of the cells on the implant site. Moreover, the increase of the local pH due to the implant bioactivity activates an antimicrobial effect that prevents inflammations and infections [105, 106]. The ossification process, fully activated from 10 months after implantation [107], can be considered completed after 6 years [105].

19.3.4.2 Sinonasal Obliteration

Obliteration is a major surgical procedure reserved for those chronically infected sinuses that have failed to respond to other means of treatment [108, 109]. Sinuses are filled with suitable material after complete removal of the mucosal surface. The benefits of synthetic materials are the avoidance of donor-site morbidity and scars, the reduction of the operatory time and complexity of surgical technique [110]. Also, the risks related to the use of heterologous materials, such as biohazard infections, for example human immunodeficiency (HIV) and hepatic viruses, are limited [111].

Peltola et al. carried out a study on 45 male rabbits to investigate the clinical usefulness of bioactive glass 9 (BAG1), bioactive glass 13 (BAG2), and hydroxyapatite, in terms of new bone formation by means of Fourier transform infrared spectroscopy (FTIR) and scanning electron microscopy (SEM) studies. A coronal U-shaped incision was made over the frontal bone, and the upper walls of paired frontal sinuses were drilled with four 5-mm separate holes. Sinuses were filled with BAG1 and BAG2 on one side, and with hydroxyapatite on the other side (Figure 19.4). Two parallel openings in the posterior part of the frontal sinuses were covered with a pedicled flap, and the other two anterior openings with a free periosteum flap. In the histologic evaluation after six months postoperatively, all the implants were found in their original places without signs of infection or inflammatory reactions. Moreover, there were no postoperative mortality and complications.

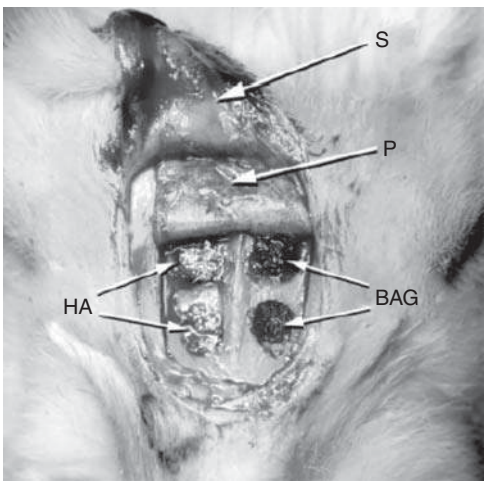

Figure 19.4 Sinonasal obliteration on a rabbit model. The periosteum (P) was separated from the skin (S). A number of four 5-mm holes were drilled and filled with bioactive glass (BAG) on the right and hydroxyapatite (HA) on the left. Source: Peltola et al. [112], Figure 02, (p. 366)/reproduced with permission from John Wiley and Sons.

SEM and FTIR analyses supported each other in the estimation of the composition of new bone formation, including the reaction layers both at the interface with the used materials and within the new bone formation front. The latter started from the periphery of the defects and progressed toward the center. New bone deposition was stronger in defects covered by a pedicled than a free periosteum flap with all the biomaterials used. In general, bone formation and healing process were faster with BAG1 than BAG2 and hydroxyapatite in both conditions of periosteum vascularization. An influence of the periosteum vascularization on the healing process was documented: the earlier sufficient vascularization occurred, the faster new bone formation and resorption of materials were seen in the filled sinuses [112].

The same authors in 2006 reported on the long-term usefulness of the frontal sinuses obliterations performed on 42 patients performed via bicoronal or eyebrow access. The nasofrontal duct was obliterated using a dense three-layer containing occlusion plug and fibrin glue. The results of the clinical examinations and patient symptoms were recorded at 1 week, 1–3–6 months, and thereafter annually. CT scans were obtained at each observation point. The stability and preservation of BAG obliteration were estimated by the variation in Hounsfield units (HU). The cortical calvarial bone was used as a reference in the clinical evaluation. All the patients reported a relief from their intense frontal pain and had a satisfactory cosmetic result at 12 months postoperatively. Two patients had discomfort related to the miniplates used for fixation of the osteoplastic flap and, thus, they were removed. One patient had severe basal cell carcinoma in the frontal skin area and a residual excision was performed. In addition, two patients underwent re-obliteration because of mucocele formation. Histologic and microbiologic samples were harvested from the abovementioned five patients. These samples were harvested from different patients at 6, 12, 60, 104, and 120 months after the primary BAG obliteration. In the obliterated frontal sinuses, the dense fibrous tissue revealed by histopathologic studies, between the BAG granules and the reaction layers formed on the granule surface at 6 and 12 months. The histologic studies revealed more new bone formation with less scattered fibrous tissue formation between the BAG granules in frontal sinuses at 104 and 120 months vs. at 60 months. FTIR spectroscopy studies showed that the natural anterior frontal bone was very similar to the bone produced by the BAG in the frontal sinus obliteration. Microbiologic cultures from the BAG obliterations showed no growth of bacteria. In CT studies, the variation in HU showed reliable preservation of BAG obliteration in frontal sinuses [34].

The same research group published in 2008 more detailed data on one case complicated by postoperative mucocele formation. At reoperation, SEM analysis and histologic examination demonstrated normal bone without connective tissue in direct contact with the biomaterial particles. No inflammatory changes or foreign body reactions were observed. A three-year follow-up examination after reoperation revealed a progressive healing process with diminishing postoperative clinical symptoms and normally progressing skin wound healing. CT studies demonstrated accurate frontal sinus obliteration with no loss of volume. Microbiologic cultures showed no growth of bacteria, and blood chemistry results revealed to be in basic blood parameters. SEM studies demonstrated new bone formation with BAG granule remnants covered by a calcium phosphate layer 12 years after the original frontal sinus obliteration. The energy-dispersive X-ray (EDX) spectroscopy profile revealed continuous traces of P, Si, and Ca across the interface of host bone and the surface layer induced by BAG [113].

19.3.4.3 Septal Cartilage Repair

Nasal septal cartilage repair represents a surgical challenge due to the poor tendency to proliferation of cartilaginous tissue. BAG was hypothesized to exert stimulatory effects on chondrogenesis.

Hence, implantation of autologous chondrocytes in combination with this biomaterial was considered a promising strategy to support cartilage repair.

In a clinical study in 2001, Stoor et al. reported on 11 patients who underwent surgery for septal perforation. The mucosal damage was repaired by means of anteriorly based inferior turbinate mucoperiosteal flap either performed on both sides or combined with an advancement flap on the other side. The perforation was grafted with one or two discs of the BAG S53P4 and when available, also with crushed autosomal cartilage or bone from the operation area. In one patient with a nearly total septum perforation after hypophysis surgery, the perforation could not be closed. Ten patients with successful primary closure of the septum perforation were followed up for 2–37 months. No extrusions of the BAG implants or BAG-associated infections of the nasal cavity were seen. In eight patients, the recovery was uneventful. In two patients, a small recurrent perforation was closed in a second operation. No re-perforation was seen in these patients during the follow-up. *In vitro* studies showed anti-microbial properties of S53P4 in adhesion tests and growth inhibition experiments as evaluated by electron microscopy and adsorption percentage results [114].

In a subsequent publication from the same research group, the results of the abovementioned surgical technique were analyzed, though partly combined with BAG interposition graft, and partly without. The authors drew the conclusion that S53P4 was a good interpositional graft in the repair of nasal septal perforations and was especially suitable in medium and large perforations, which are difficult to close without an interpositional implant material. Turbinate flaps are reliable and often sufficient alone in the closure of small perforations no larger than 10 mm in diameter or in oval-shaped perforations up to 20 mm in which sufficient cartilage and bone can be harvested and used as an interpositional graft [115].

In a molecular study on rat nasal chondrocyte cultures exposed to 45S5, Asselin et al. demonstrated a significant ability of the biomaterial to support the growth of chondrocytes, as shown in contrast-phase and SEM, and to stimulate osteo-chondrogenic markers, such as alkaline phosphatase, collagen X, transcription factors Sox-9, Runx-2, and Indian hedgehog [116].

Another molecular study investigated the functionalization of poly(L-lactic acid) (PLLA) foams with BAG 1393 using human nasoseptal chondrocytes from healthy donors. PLLA scaffolds allowed the maintenance of chondrogenic phenotype, as indicated by mRNA analysis, in addition to immunohistochemistry and Alcian blue staining. Thus, unlike the findings reported for 45S5, which was associated with the osteoblastic marker Runx-2 and the hypertrophic cartilage marker collagen type X, BAG 139/PLLA promoted the expression of chondrogenic markers, like collagen type II and aggrecan [117].

19.3.4.4 Orbital Floor Repair

Orbital floor repair is another interesting application of BAGs. This structural target comes from the need to repair the eye socket after eye evisceration [118, 119], in order to later place a prosthesis into the orbital cavity [120]. Glasses have been used in this field since 1880s in the form of spheres [121], and later replaced by silicone and poly(methyl methacrylate) (PMMA). However, the complications in using such materials spanning from inflammations, traumas, and rejections have pushed the need to develop new and better biocompatible materials able to adapt to the host tissues [120, 122–124].

Since 1969, BAGs have been considered a valuable alternative to the traditional materials used in this field. Recent applications in animal models observed the ability of such materials to be integrated in the body. Brandão et al. highlighted the differences between 45S5 Bioglass and two types of biosilicate (single-1P and double-2P crystalline phase). The results confirmed that with all

the samples, infections did not occur, being the best results achieved with 45S5 and biosilicate-P, less inflammatory and more efficiently integrated with the host tissue [125].

19.4 Conclusions and Future Directions

The application of BAGs has led to innovative reconstruction of bone structures in the craniofacial area with remarkable clinical outcomes. Spanning from replacing the orbital floor after eye surgery to the replacement of spare parts of the skull, the BAG capability of providing a reliable reconstruction or replacement with adequate mechanical and biological properties, has deeply been appreciated in surgery over the years. In the specific case of otorhinolaryngology, BAGs have become an actual alternative to other biomaterials, mainly because of their tight binding to soft and hard tissues, which prevents fibrotic encapsulation, antimicrobial activity in such contaminated tissues and biostability within chemically aggressive environments, overall enabling a proper adaptation and strong connection to the host tissues.

As such, BAGs have been successfully employed in a large number of otologic applications. Among the others, structural obliterations and ossicular replacements are definitely the most interesting ones, as supported by the successful results achieved in clinics. Otologic surgeons have used different types of BAGs, either as granular components to reconstruct the structural integrity of the mastoid bone after invasive surgeries or as constitutive materials of PORPs and TORPs to recover from conductive hearing loss.

Among the different classes of BAGs described in this chapter, 45S5 and Bonalive (S53P4) have demonstrated the most promising results by showing both remarkable long-term mechanical and antimicrobial properties that still encourage their employment in clinical settings. In contrast, the use of other classes of BAGs has been progressively reduced due to a number of long-term follow-ups reporting disputable results. Instead of using such materials, surgical approaches have thus moved toward other biomaterials with similar mechanical properties, which can be better tolerated by the host tissues even if they are not entitled with the bioactivity proper of these glasses.

To date, the increasingly wide use of additive manufacturing approaches, such as the three-dimensional (3D) printing, suggest new promises for BAG applications, since they could be used as reinforcement for polymeric inks to create functionalized composites for fabricating personalized replacements [126]. These composites could successfully synergize the mechanical, bioactive, and antimicrobial properties of BAGs with the flexibility and moldability of polymeric matrices. Such a new generation of prosthetic devices would enable the development of patient-specific structures with a high level of customization in terms of shape and behavioral functionalization, leading to a reduction of extrusion phenomena in the medium and long term. As an example, a 3D printed BAG auricle has been recently fabricated, assuming that this material could promote the regeneration of the cartilaginous structure [127]. Having bioactive, antimicrobial, mechanically strong yet middle ear biocompatible and finally customizable replacements could drastically reduce failures and suboptimal outcomes in otologic surgery.

Acknowledgments

This study was supported by 4NanoEARDRM project (EuroNanoMed III co-funded action by the Italian Ministry of University and Research – MIUR, grant number B56H18000140001).

References

1 Danti, S., D'Alessandro, D., Pietrabissa, A. et al. (2010). *Journal of Biomedical Materials Research Part A* 92 (4): 1343–1356.
2 Sellari-Franceschini, S., Piragine, F., Bruschini, P., and Berrettini, S. (1987). *The American Journal of Otology* 8: 551.
3 Williams, D.F. (2008). *Biomaterials* 29: 2941.
4 D'Alessandro, D., Danti, S., De Vito, A. et al. (2012). *Otology & Neurotology* 33: 1458.
5 Danti, S., Stefanini, C., D'Alessandro, D. et al. (2009). *Biomedical Microdevices* 11 (4): 783–793.
6 Beutner, D. and Hüttenbrink, K.-B. (2009). *GMS Current Topics in Otorhinolaryngology, Head and Neck Surgery* 8: 1–19.
7 Milazzo, M., Muyshondt, P.G.G., Carstensen, J. et al. (2020). *Journal of the Mechanical Behavior of Biomedical Materials* 103: 103541.
8 Berrettini, S., Bruschini, L., Stefanini, C. et al. (2011). *Annals of Otology, Rhinology and Laryngology* 120 (1): 9–16.
9 Berrettini, S., Danti, S., De Vito, A. et al. (2012). *Clinical Otolaryngology* 37: 415.
10 Milazzo, M., Danti, S., Inglese, F. et al. (2017). *Journal of Biomedical Materials Research Part B Applied Biomaterials* 105: 2495.
11 Tos, M. (1993). *Manual of Middle Ear Surgery*. Stuttgart: Georg Thieme.
12 Hench, L.L. (1991). *Journal of the American Ceramic Society* 74: 1487.
13 Hench, L.L. and Best, S.M. (2013). Ceramics, glasses, and glass-ceramics: basic principles. In: *Biomaterials Science* (ed. B.D. Ratner, A.S. Hoffman, F.J. Schoen and J.E. Lemons), 128–151. Academic Press.
14 Clark, A.E., Hench, L.L., and Paschall, H.A. (1976). *Journal of Biomedical Materials Research* 10: 161.
15 Piotrowski, G., Hench, L.L., Allen, W.C., and Miller, G.J. (1975). *Journal of Biomedical Materials Research* 9: 47.
16 Cerruti, M., Greenspan, D., and Powers, K. (2005). *Biomaterials* 26: 1665.
17 Emmett, J.R. (1989). *The American Journal of Otology* 10: 215.
18 Brömer, H., Käs, H., and Pfeil, E. (1976). Glaskeramisches Material mit Apatit-Kristallphase, insbesondere zur Verwendung für prothetische Zwecke, sowie Verfahren zu seiner Herstellung. Patentschrift. DE2326100A1, filed 23 May 1973, issued 15 January 1976.
19 Reck, R. and Helms, J. (1985). *The American Journal of Otology* 6: 280.
20 Niparko, J.K., Kemink, J.L., Graham, M.D., and Kartush, J.M. (1988). *Laryngoscope* 98: 822.
21 Della Santina, C.C. and Lee, S.C. (2006). *Archives of Otolaryngology – Head & Neck Surgery* 132: 617.
22 Hench, L.L. and Paschall, H.A. (1973). *Journal of Biomedical Materials Research* 7: 25.
23 Ros-Tárraga, P., Rabadan-Ros, R., Murciano, A. et al. (2016). *Materials (Basel)* 9: 969.
24 Barradas, A.M.C., Fernandes, H.A.M., Groen, N. et al. (2012). *Biomaterials* 33: 3205.
25 Kendrick, J. and Chonchol, M. (2011). *American Journal of Kidney Diseases* 58: 826.
26 Jones, J.R. (2013). *Acta Biomaterialia* 9: 4457.
27 Gomez-Vega, J.M., Saiz, E., Tomsia, A.P. et al. (2000). *Biomaterials* 21: 105.
28 Qu, T. and Liu, X. (2013). *Journal of Materials Chemistry B* 1: 4764.
29 Andersson, Ö.H. and Kangasniemi, I. (1991). *Journal of Biomedical Materials Research* 25: 1019.
30 Drago, L., Vassena, C., Fenu, S. et al. (2014). *Future Microbiology* 9: 593.

31 Perez-Tanoira, R., Garcia-Pedrazuela, M., Hyyrynen, T. et al. (2015). *Journal of Materials Science – Materials in Medicine* 26: 239.
32 Silvola, J.T. (2012). *Otolaryngology – Head & Neck Surgery* 147: 119.
33 Stoor, P., Söderling, E., and Grenman, R. (1999). *Journal of Biomedical Materials Research* 48: 869.
34 Peltola, M., Aitasalo, K., Suonpää, J. et al. (2006). *Head & Neck* 28: 834.
35 Cui, X., Zhao, C., Gu, Y. et al. (2014). *Journal of Materials Science – Materials in Medicine* 25: 733.
36 Gersdorff, M. and André, M. (1986). *Archives of Oto-Rhino-Laryngology* 243: 20.
37 Moura, J., Teixeira, L.N., Ravagnani, C. et al. (2007). *Journal of Biomedical Materials Research* 82: 545.
38 Massuda, E.T., Maldonado, L.L., de Lima Júnior, J.T. et al. (2009). *Brazilian Journal of Otorhinolaryngology* 75: 665.
39 Mischke, R.E., Hyams, V., Shea, J.J., and Gross, C.W. (1977). *Archives of Otolaryngology* 103: 489.
40 Zikk, D., Rapoport, Y., Bloom, J., and Himelfarb, M.Z. (1990). *European Archives of Oto-Rhino-Laryngology* 248: 102.
41 Kawanabe, K., Yamamuro, T., Nakamura, T., and Kotani, S. (1991). *Journal of Biomedical Materials Research* 25: 117.
42 Pinilla, M., Ramírez-Camacho, R., Jorge, E. et al. (2001). *Otolaryngology–Head and Neck Surgery* 124: 515.
43 Geyer, G. (1992). *European Archives of Oto-Rhino-Laryngology Supplement* 1: 185.
44 Vogt, J.C., Brandes, G., Krüger, I. et al. (2008). *Journal of Materials Science – Materials in Medicine* 19: 2629.
45 Vogt, J.C., Brandes, G., Ehlert, N. et al. (2009). *Journal of Biomaterials Applications* 24: 175.
46 Siedek, V., Nehls, K., Zur Nieden, K. et al. (2014). *Lasers in Medical Science* 29: 965.
47 Jutte, M., Klein, S., Katenkamp, D. et al. (1992). *Klinische Monatsblätter für Augenheilkunde* 200: 674.
48 Siebert, H., Schleier, P., Beinemann, J. et al. (2006). *Mund-, Kiefer- und Gesichtschirurgie (MKG)* 10: 185.
49 Turck, C., Brandes, G., Krueger, I. et al. (2007). *Acta Oto-Laryngologica* 127: 801.
50 Schneider, G., Blechschmidt, K., Linde, D. et al. (2010). *Journal of Materials Science – Materials in Medicine* 21: 2853.
51 Koscielny, S. and Beleites, E. (2001). *HNO* 49: 367.
52 Milazzo, M., Gallone, G., Marcello, E. et al. (2020). *Journal of Functional Biomaterials* 11 (3): 60.
53 Lampikoski, H., Aarnisalo, A.A., Jero, J., and Kinnari, T.J. (2012). *Otology & Neurotology* 33: 785.
54 Farinetti, A., Ben Gharbia, D., Mancini, J. et al. (2014). *European Annals of Otorhinolaryngology, Head and Neck Diseases* 131: 177.
55 McAllister, K., Linkhorn, H., Gruber, M. et al. (2017). *Otology & Neurotology* 38: 694.
56 Pawlowski, K.S., Wawro, D., and Roland, P.S. (2005). *Otology & Neurotology* 26: 972.
57 Mühlhofer, H.M.L., Deiss, L., Mayer-Kuckuk, P. et al. (2017). *In Vivo (Brooklyn)* 31: 673.
58 Stoor, P., Söderling, E., and Salonen, J.I. (1998). *Acta Odontologica Scandinavica* 56: 161.
59 Drago, L., Toscano, M., and Bottagisio, M. (2018). *Materials (Basel)* 11: 326.
60 Hench, L.L. and Paschall, H.A. (1973). Direct chemical bond of bioactive glass-ceramic materials to bone and muscle. *Journal of Biomedical Materials Research* 7: 25–42.

61 van Gestel, N.A.P., Geurts, J., Hulsen, D.J.W. et al. (2015). *BioMed Research International* 2015: 1–12.

62 Baino, F., Hamzehlou, S., and Kargozar, S. (2018). *Journal of Functional Biomaterials* 9: 25.

63 Kluge, A., Neudert, M., Kunert-Keil, C. et al. (2019). *Otology & Neurotology* 40: e415.

64 Lindfors, N.C., Hyvönen, P., Nyyssönen, M. et al. (2010). *Bone* 47: 212.

65 Sarin, J., Grénman, R., Aitasalo, K., and Pulkkinen, J. (2012). *Annals of Otology, Rhinology, and Laryngology* 121: 563.

66 Grønseth, T., Vestby, L.K., Nesse, L.L. et al. (2020). *Upsala Journal of Medical Sciences* 125: 217.

67 Perez-Tanoira, R., Kinnari, T.J., Hyyrynen, T. et al. (2015). *Journal of Materials Science – Materials in Medicine* 26: 246.

68 Pérez-Tanoira, R., García-Pedrazuela, M., Hyyrynen, T. et al. (2015). *Journal of Materials Science – Materials in Medicine* 26: 1.

69 Yung, M., Tassone, P., Moumoulidis, I., and Vivekanandan, S. (2011). *The Journal of Laryngology & Otology* 125: 221.

70 Drago, L., Romanò, D., De Vecchi, E. et al. (2013). *BMC Infectious Diseases* 13: 1.

71 Höing, B., Kirchhoff, L., Arnolds, J. et al. (2018). *Otology & Neurotology* 39: e985.

72 Kirchhoff, L., Arweiler-Harbeck, D., Arnolds, J. et al. (2020). *PLoS One* 15: e0229198.

73 Hesse, D., Ehlert, N., Lüenhop, T. et al. (2013). *Otology & Neurotology* 34: 1138.

74 Kwon, S., Lee, S.S., Sivashanmugam, A. et al. (2018). *Polymers (Basel)* 10: 914.

75 Vallittu, P.K., Posti, J.P., Piitulainen, J.M. et al. (2020). *Journal of Tissue Engineering and Regenerative Medicine* 14: 1157.

76 Mehta, R.P. and Harris, J.P. (2006). *Otolaryngologic Clinics of North America* 39: 1129.

77 Shohet, J.A. and de Jong, A.L. (2002). *Otolaryngologic Clinics of North America* 35: 841.

78 Chan, C.Y. and Chan, Y.M. (2012). *Proceedings of Singapore Healthcare* 21: 23.

79 Alves, R.D., Cabral Junior, F., de. Fonseca, A.C., O., and Bento, R.F. (2016). *International Archives of Otorhinolaryngology* 20: 76.

80 Leatherman, B.D. and Dornhoffer, J.L. (2004). *Otology & Neurotology* 25: 22.

81 Jang, C.H., Cho, Y.B., and Bae, C.S. (2007). *In Vivo (Brooklyn)* 21: 651.

82 El-Seifi, A. and Fouad, B. (1998). *ORL* 60: 198.

83 Skoulakis, C., Koltsidopoulos, P., Iyer, A., and Kontorinis, G. (2019). *The Journal of International Advanced Otology* 15: 400.

84 Sorour, S.S., Mohamed, N.N., Fattah, M.M.A. et al. (2018). *American Journal of Otolaryngology* 39: 282.

85 de Veij Mestdagh, P.D., Colnot, D.R., Borggreven, P.A. et al. (2017). *Acta Oto-Laryngologica* 137: 690.

86 Yung, M. and Bennett, A. (2013). *Current Opinion in Otolaryngology & Head and Neck Surgery* 21: 455.

87 Vos, J., de Vey Mestdagh, P., Colnot, D. et al. (2017). *European Archives of Oto-Rhino-Laryngology* 274: 4121.

88 Bernardeschi, D., Pyatigorskaya, N., Russo, F.Y. et al. (2017). *Clinical Otolaryngology* 42: 387.

89 Ezzat, A.E.M. and Eid, M.I. (2014). *Current Science International* 3: 87.

90 Shokry, S., Hafez, A.A., Abdulsalam, H.M. et al. (2012). *Egyptian Journal of Hospital Medicine* 47: 321.

91 Stoor, P., Pulkkinen, J., and Grénman, R. (2010). *Annals of Otology, Rhinology, and Laryngology* 119: 377.

92 Król, B., Porowski, M., Cywka, K.B. et al. (2020). *American Journal of Case Reports* 21: e925914.
93 Al Tamami, N., Bawazeer, N., Fieux, M. et al. (2020). *American Journal of Otolaryngology* 41 (6): 102542.
94 Blayney, A.W., Bebear, J.-P., Williams, K.R., and Portmann, M. (1986). *The Journal of Laryngology & Otology* 100: 1359.
95 Brewis, C., Orrell, J., and Yung, M.W. (2003). *Otology & Neurotology* 24: 20.
96 Merwin, G.E. (1986). *Annals of Otology, Rhinology, and Laryngology* 95: 78.
97 Merwin, G.E. (1990). Bioactive glasses and glass-ceramics. In: *Handbook of Bioactive Ceramics*, vol. 1 (ed. T. Yamamuro, L.L. Hench and J. Wilson), 323. CRC Press.
98 Wilson, J., Douek, E., Rust, K. et al. (1995). *Bioceramics* 8: 239.
99 Hench, L.L. (1998). *American Ceramic Society Bulletin* 77: 67.
100 Hench, L.L. and Wilson, J. (1996). *Clinical Performance of Skeletal Prostheses*. Springer.
101 Rust, K.R., Singleton, G.T., Wilson, J., and Antonelli, P.J. (1996). *The American Journal of Otology* 17: 371.
102 Bahmad, F. Jr., and Merchant, S.N. (2007). *Annals of Otology, Rhinology, and Laryngology* 116: 181.
103 Walliker, J., Carson, H., Douek, E. et al. (1987). *Proceedings of the Cochlear Implant Symposium*, Düren, Germany, 7–12.
104 Downing, M., Johansson, U., Carlsson, L. et al. (1997). *Ear, Nose & Throat Journal* 76: 328.
105 Piitulainen, J.M., Kauko, T., Aitasalo, K.M.J. et al. (2015). *World Neurosurgery* 83: 708.
106 Piitulainen, J.M., Posti, J.P., Aitasalo, K.M.J. et al. (2015). *Acta Neurochirurgica* 157: 681.
107 Posti, J.P., Piitulainen, J.M., Hupa, L. et al. (2016). *Journal of the Mechanical Behavior of Biomedical Materials* 55: 191.
108 Amble, F.R., Kern, E.B., Neel, H.B. III, et al. (1996). *Laryngoscope* 106: 809.
109 Metson, R. and Gliklich, R.E. (1998). *Archives of Otolaryngology-Head and Neck Surgery* 124: 1090.
110 Hardy, J.M. and Montgomery, W.W. (1976). *Annals of Otology, Rhinology, and Laryngology* 85: 523.
111 Har-El, G. and Lucente, F.E. (1995). *Laryngoscope* 105: 440.
112 Peltola, M.J., Aitasalo, K.M.J., Suonpää, J.T.K. et al. (2003). *Journal of Biomedical Materials Research* 66: 364.
113 Peltola, M.J., Aitasalo, K.M.J., Aho, A.J. et al. (2008). *Journal of Oral and Maxillofacial Surgery* 66: 1699.
114 Stoor, P., Söderling, E., and Grénman, R. (2001). *Journal of Biomedical Materials Research* 58: 113.
115 Stoor, P. and Grénman, R. (2004). *Annals of Otology, Rhinology, and Laryngology* 113: 655.
116 Asselin, A., Hattar, S., Oboeuf, M. et al. (2004). *Biomaterials* 25: 5621.
117 Conoscenti, G., Carfì Pavia, F., Ongaro, A. et al. (2019). *Connective Tissue Research* 60: 344.
118 Migliori, M.E. (2002). *Current Opinion in Ophthalmology* 13: 298.
119 Perry, J.D., Lewis, C.D., and Levine, M. (2009). *Archives of Ophthalmology (Chicago, Ill. 1960)* 127: 1227.
120 Su, G.W. and Yen, M.T. (2004). *Ophthalmic Plastic & Reconstructive Surgery* 20: 274.
121 Tonkelaar, J., Henkes, H.E., and Leersun, G.K. (1991). *Documenta Ophthalmologica* 77: 349.
122 Rodrigues, A.C., Schellini, S.A., Moraes-Silva, M.R.B., and Padovani, C.R. (1997). *Revista Brasileira de Oftalmologia* 56: 259.

123 Brito, M.M. (2008). Estud. Comp. com polietileno poroso. Dissertação. Botucatu Fac. Med. Botucatu da Univ. Estadual Paul. p. 94.

124 França, V.P., Figueiredo, A.R., Vasconcelos, A.C., and Oréfice, R.L. (2005). *Arquivos Brasileiros de Oftalmologia* 68: 425.

125 Brandão, S.M., Schellini, S.A., Moraes, A.D. et al. (2012). *Orbit* 31: 143.

126 Milazzo, M., Contessi Negrini, N., Scialla, S. et al. (2019). *Advanced Functional Materials* 29: 1903055.

127 3DNextech (2016). Medical 3D printing: bio-glass replaces cartilage. https://www.3dnextech.com/en/medical-3d-printing-bio-glass-replaces-cartilage/ (accessed 28 February 2021).

20

Bioactive Glass: Soft Tissue Reparative and Regenerative Applications

Shreyasi Majumdar, Smriti Gupta, and Sairam Krishnamurthy

Neurotherapeutics Laboratory, Department of Pharmaceutical Engineering and Technology, Indian Institute of Technology (Banaras Hindu University), Varanasi, India

20.1 Introduction

The discovery of Bioglass® in 1971 has led to numerous developments in the tissue engineering applications of skeletal tissues like bone and teeth. Bioglass owing to its bioactivity and osteogenic properties (i.e. osteoconduction and osteostimulation) lead to its clinical use for the first time as middle-ear prosthetics (MEP®) in 1985 to treat the otomastoiditis-induced hearing loss [1]. It was reported that the ability of the Bioglass to bind with the soft tissue of the eardrum eliminated the need for the interposition of cartilage in between the prosthetics and the eardrum. Furthermore, these prosthetics were improvised and marketed as DOUEK MED™ (US Biomaterials, Alachua, FL) with the advantage of being shaped at the time of surgery as per the anatomical variations of the middle ear of the patients.

Bioglass was further commercially molded as cones to fill up the tooth extraction sites to secure the dentures and launched as Endosseous Ridge Maintenance Implant (ERMI®) in 1988 [2]. Later on, with the escalating clinical demand of cutting the grafts as per the requirement, Bioglass was synthesized in the form of granules to be pressed into the defects that lead to the development of NovaBone® (NovaBone, Florida) in 1993 for periodontal diseases. Following the success of NovaBone, the Food and Drug Administration (FDA) approval was granted in 2005 for orthopedic use, mainly for adolescent idiopathic scoliosis. Bioglass was later explored to restore the jaw defect, and thus Biogran® (Biomet 3i, Palm Beach Gardens, FL) came into existence [3]. Similarly, Unigraft® (Unicare Biomedical, Laguna Hills, CA) and GlassBone® (Noraker, Lyon-Villeurbanne, France), the particulate form of Bioglass, were marketed for orthopedic and cranio-maxilo-facial surgeries. With the success of Bioglass, another bioactive glass (BAG), i.e. S53P4, received FDA approval in 2008 and was marketed as BonAlive® (BonAlive Biomaterials Ltd., Turku, Finland) for bone filling purposes [4], currently available in more than 50 countries.

BAGs also have an immense impact on the healthcare sector, and the most extensive commercial use of BAGs is toothpaste. The dentine and enamel of the teeth are homologous due to carbonated hydroxyapatite (HCA). In 2004, Bioglass particulate-incorporated toothpaste was marketed as NovaMin® (GlaxoSmithKline) for treating dentinal hypersensitivity. Currently, available as Sensodyne Repair and Protect® toothpaste formulation (GlaxoSmithKline), and clinical data reported that NovaMin significantly alleviated the pain compared to the dentifrice containing

Shreyasi Majumdar and Smriti Gupta are contributed equally.

Bioactive Glasses and Glass-Ceramics: Fundamentals and Applications, First Edition.
Edited by Francesco Baino and Saeid Kargozar.

anesthetic potassium nitrate [5]. After the discovery of soft connective tissue bonding to Bioglass in 1981 [6], in recent years, numerous studies have reported the beneficial interaction of BAGs with the nonosseous and soft tissues [7–13]. Despite this, limited BAG-based products have received FDA clearance for clinical use. For instance, ophthalmic porous polyethylene orbital implants (Medpor®), commercially available since 1985, suffered from poor tissue anchorage. A modified version of this added melt-derived Bioglass particles in a 30 : 70 volume ratio and received the FDA clearance in 2002. It has since been commercialized worldwide as Medpor Plus™ Sphere (Porex Surgical Products Group) for achieving a higher fibrovascularization rate and good tissue anchorage [14]. Furthermore, yttrium-90 microspheres (TheraSphere®; MDS Nordion, Ottawa, Canada) received humanitarian device exemption (HDE) FDA approval in December 1999. TheraSphere delivered high levels of yttrium-90 β radiations in patients with unresectable hepatocellular carcinoma [15]. Recently, a borate-based bioactive glass (BBG) matrix was FDA approved for dressing acute and chronic deep wounds (MIRRAGEN™, ETS Wound Care LLC, USA) [16].

Despite the myriad of scientific evidence available so far, a limited number of FDA-approved products are commercially available for nonosseous and soft tissue applications. In the domain of tissue regeneration and repair, much has already been known for the role of BAGs in osseous tissues. However, for a faster pace of developing clinically valuable products for the nonosseous and soft tissues, a detailed understanding of the experimental, preclinical, and clinical evidence is available so far, with the limitations hindering clinical translation biological activities observed under laboratory settings, is required. The nonosseous applications, including the regenerative and reparative potential of BAGs in noncalcified soft tissues, have been reviewed and critically comprehended in separate subsections.

20.2 BAGs in Contact with Soft Tissues

BAG is a well-established, clinically adopted inorganic biomaterial for the restorative and reconstructive procedures of the hard calcified tissues such as bone [17, 18] and teeth [19, 20]. In recent years, BAGs have found their way for regenerating and repairing nonosseous and noncalcified tissues, including the epithelial tissue [13, 21], fibrous connective tissues including ligaments [22], and tendons [23, 24], nervous tissue [25–27], voluntary skeletal muscles [28–30], and involuntary organ systems including pulmonary [7–11], cardiac [31–33], gastrointestinal [34–36], and urinary system [37]. Further, BAGs have also been explored for the repair and restoration of the defects of eyes [14, 38–44], ears [45–54], nose [55–60], larynx [61, 62], and mouth [63–69].

20.2.1 Wound Healing

Wound healing is the dynamic and well-orchestrated physiological process involving the overlapping of four different mechanisms: hemostasis, inflammation, proliferation, and tissue remodeling. It requires an optimal environment to heal, but the extreme loss of blood increases the chance of hypothermia, acidosis, infections, and causes multiple organ failure [70]. The existing treatment strategies mainly involve palliative wound dressings, which otherwise are incompetent; thus, there is a need for safe and biocompatible biomaterials to stop arterial and venous bleeding. Current research has paved the way for BAGs as an effective hemostatic agent (Table 20.1) due to the release of ions simulating various processes involved in different stages of wound healing [75]. A study has investigated the silver exchanged mesoporous silica sphere (AgMSS) for its antibacterial properties

Table 20.1 Overview of the studies performed highlighting the application of BAGs in wound healing.

Bioactive glasses (BAGs)	Composition	Formulation	Proposed mechanism of action	References
SiO_2–CaO sol–gel system	$100-xSiO_2$–$xCaO$ system (mol%), (coded as $100-xSx$) 70S30C, 80S20C	3D BAG fiber by electrospinning	– Significant increase in VEGF production in cells exposed to the BAG samples compared to control	[71]
Borosilicate BAG0106-B1	$37.5SiO_2$–$22.6CaO$–$5.9Na_2O$–$4.0P_2O_5$–$12.0K_2O$–$5.5MgO$–$12.5B_2O_3$ wt%	Scaffold prepared using the foam replica technique	– Enhanced expression of the VEGF-A	[72]
Borosilicate BAG (BBG)	—	Borosilicate BAG incorporated sodium alginate composite dressing (SA-BBG)	– Increased collagen deposition – The SA-BBG group exhibited a faster wound healing than other groups, suggesting accelerated wound healing in full-thickness skin defects in rats – The incorporation of BBG stimulated cell proliferation of fibroblasts (L929) and human umbilical vein endothelial cells (HUVECs)	[73]
Sol–gel derived mesoporous BAG particles	$70SiO_2$–30CaO mol%	Absorbable nanocomposites	– The composites had the lowest blood loss in the hepatic hemorrhage model in rabbits, which was reportedly due to the negatively charged surface of mesoporous BAG particles that activated the intrinsic cascade of blood clotting – The nanocomposite was cytocompatible to MC3T3-L1 fibroblasts with increased viability	[74]

for uncontrollable hemorrhage control [12]. The thromboelastographic analysis reported the thrombotic property of AgMSS. The time for the fibrin formation in the silver-doped mesoporous silica sphere (2.9 ± 0.2 minutes) was significantly lower than the control (9.1 ± 2.5 minutes). The prothrombin (PT) and activated partial thromboplastin time (aPTT) are critical parameters for predicting the hemostatic properties of a biomaterial. AgMSS treatment reduced PT, and aPTT, supporting the fascinating role of BAG in hemostasis. Similarly, silver-doped nanoporous BAG (n-BGS) prepared using the sol–gel process possessed significantly greater hemostatic and antibacterial properties compared to the BAG without nanopores (BGS) [76]. Further, due to the

high surface area of the nonporous n-BGS, complete *in vivo* hemostasis in substantially less time, i.e. 27 ± 2.0 seconds, than BGS and control (86 ± 3 and 193 ± 8 seconds, respectively) was observed.

More recently, BAGs were explored in diseases like diabetes, where the wound healing ability is primarily compromised and hence causes a greater risk of infection. Diabetic foot ulcer (DFU), one of the severe complications of diabetes mellitus, was treated using the rubidium-doped bioactive glass nanospheres (Rb-BGNs) [21]. The *in vitro* study reported that the ionic dissolution products (IDPs) of Rb-BGMs induced the proliferation of fibroblasts (FBs) and human immortal keratinocytes (HaCaTs) along with cell migration in the scratch assay, gold standard for repair of the injured tissues. The consolidated findings support the role of Rb-BGMs in wound healing as FBs and HaCaTs are primarily associated with the re-epithelialization and collagen deposition, vital steps of wound healing. Besides, Rb-BGMs increased the expression of various growth factors essential for wound healing (i.e. vascular endothelial growth factor [VEGF], epidermal growth factor [EGF], and platelet-derived growth factor [PDGF]). Based on the effectiveness of growth factor on wound closure, EF was loaded into Rb-BGM and produced a synergistic effect with improved hemostasis and collagen deposition compared to unloaded Rb-BGMs. A further study by Mao et al. [13] established the potential of BAGs in accelerating the healing of full-thickness diabetes wounds in rodents. Bioglass ointment significantly improved the fibroblast proliferation and formation of the granulation tissue compared to the saline-treated diabetic rats. Hence, BAGs can heal wounds by incorporating various other ions to elicit several different cellular responses.

BAGs also possess angiogenic properties, a pivotal phase of wound healing as it forms the granulation tissue that acts as a matrix for the proliferating blood vessels [72]. In a study, extracts of 58S-NBG ($60SiO_2$–$36CaO$–$4P_2O_5$ wt%) and 80S-NBG ($80SiO_2$–$15CaO$–$5P_2O_5$ wt%) have been reported to enhance the expression of VEGF, basic fibroblast growth factor (bFGF), and their receptors along with the downstream mediator, endothelial nitric oxide synthase (eNOS), suggesting that the angiogenic activity of BAG is nitric oxide (NO) dependent. The ability of 58S-NBG and 80S-NBG to stimulate angiogenesis at multiple physiological downstream cascades *in vitro* also further suggests its potential as an angiogenesis promoting material in tissue engineering constructs [77]. Studies have reported that six hours postinjury, the chemotaxis of the neutrophils occur at the site of tissue insult, leading to debridement of the damaged tissues and phagocytosis of foreign bodies [78]. Following this, the inflammatory cytokines and chemokines are released, which are the critical parts of the complex wound healing process. Dong et al. [79] demonstrated that incubating the RAW 264.7 cells with Bioglass alleviated the expression of pro-inflammatory cytokines (tumor necrosis factor alpha [TNF-α] and IL-1β) and increased the anti-inflammatory interleukin-10 (IL-10) compared to the control group. A recent study also reported the anti-inflammatory potential of the barium-doped bioactive glass (BaBG) [80]. BAGs having a profound effect on the immune response affect the extracellular matrix (ECM) remodeling and hence wound healing.

The US-FDA has approved a melt-derived borate-based Bioglass matrix as a wound dressing (MIRRAGEN, ETS Wound Care LLC, USA) to treat acute and chronic deep wounds [16]. The preclinical study data reported MIRRAGEN® advanced wound matrix to exhibit the slightest inflammation and healed deep wounds in less time. There was significantly more granulation tissue than synthetic polymer fiber and silver-doped collagen fiber [16]. Following these seminal results, BAGs can serve as an advanced material system for faster wound healing. However, more preclinical and clinical research is required to translate BAGs efficiently.

20.2.2 Skeletal Muscle, Ligament, and Tendon Regeneration

Skeletal muscles, accounting for approximately 50% of the total body mass, have regenerative capacity after response to appropriate stimuli and activate the muscle resident stem cells, namely, satellite

cells (SCs) [81]. Muscle loss could be due to acute conditions such as sports injury or trauma or progressive diseases such as muscular dystrophy, diabetes mellitus, and amyotrophic lateral sclerosis. Posttrauma, muscle SCs form new myotubes within 1 week, and within 28 days, almost the entire muscle regenerates [81]. However, up to the threshold of 20%, the muscle fibers can renew and restore, and beyond 20% of severe loss at the myofiber level leads to muscular disability and affects locomotion. This putative wastage of skeletal muscles leads to chronic functional deficiency, termed "volumetric muscle loss" (VML). Therefore, to restore the typical architecture and functionality, therapeutic reconstructive procedures are required. The clinically prevalent gold standard for muscle repair includes "autologous muscle graft" and supportive therapies such as acupuncture and physiotherapy, which otherwise have their limitations [82]. Cell-based tissue engineering strategies coupled with the delivery of growth factors using biopolymers have certainly been promising in overcoming the limitations associated with current therapies. For smaller tissue loss, biological scaffolds of decellularized extracellular matrix (dECM) incorporating xenogeneic ECM have been under research for muscle reconstruction [83]. However, limitations such as poor biomechanical properties, lack of degradation, poor biocompatibility, immunogenicity, infection transmission, and absence of SCs migration into the decellularized scaffold have limited their widespread clinical use [82, 84]. Hence, for the safer and efficient repair and regeneration of sizeable skeletal muscle tissue, there is a need to look for new regenerative strategies. BAGs offer a tremendous opportunity to be used in skeletal muscle engineering to provide initial support and specific biophysical cues for regeneration by being bioactive and biodegradable at the same time (see Figure 20.1).

Ideally, the degradation rate of the scaffolds used for cell transplantation applications should be predictable and match the pace of tissue regeneration. More than a decade back, phosphate BAG-based scaffolds were studied for skeletal muscle regeneration by several research groups [29, 30, 85, 86]. A key challenge has been to identify the composition and concentration of the BAG, including the structure and substrate coating of the scaffold, which could promote both the unidirectional myocyte alignment and myofiber maturation *in vitro* and degrade at a predictable rate, *in vivo*. The initially synthesized phosphate-based BAG fibers ($CaO–Na_2O–P_2O_5$) doped with a low concentration of iron (1–5 mol%) were chemically durable due to the formation of durable cross-links between the phosphate chains and the Fe^{3+} ions [29]. Enhanced glass durability endowed scaffolds with predictable degradation rate imparting improved biocompatibility, *in vitro* myocyte attachment, and myotube formation along the axis of the fibers. In preceding studies, the role of scaffold configuration, macrotopography, and substrate coating on cell behavior and *in vitro* myogenesis was reported. A 3D soluble scaffold material coated with gelatin or Matrigel (a cocktail of entactin, heparan sulfate proteoglycan, collagen type IV, and laminin) arranged into a bundle, spread, or mesh for craniofacial skeletal muscle regeneration based on phosphate-based BAG ($62.9P_2O_5–21.9Al_2O_3–15.2ZnO$) (diameter 6.5 μm and solubility rate 0.16 mg/g/d) was synthesized. The mesh scaffolds coated with Matrigel supported better myocyte attachment, migration, and differentiation into myotubes over the bundle and spread. However, the mesh arrangement of the BAG fibers could not support *in vitro* cell alignment [86].

Phosphate-based BAG fibers encased within the collagen matrix mimic the skeletal muscle architecture and provide mechanical compliance to the stiffer glass fiber constructs, thus preventing breakage during *in vivo* myofiber contraction. The 3D fiber scaffolds of phosphate BAG containing 5 mol% Fe_2O_3 and coated with collagen supported better *in vitro* human masseter cell attachment, unidirectional alignment, maturation, and formation myotube-like structures along the axis of the glass fibers over the 2D disks [85]. Furthermore, iron-phosphate BAG fibers (with 5 mol% Fe_2O_3) encased within reinforced collagen gel showed mechanical compliance. They could support unidirectional orientation and "end-to-end" alignment, cell retention, myofiber

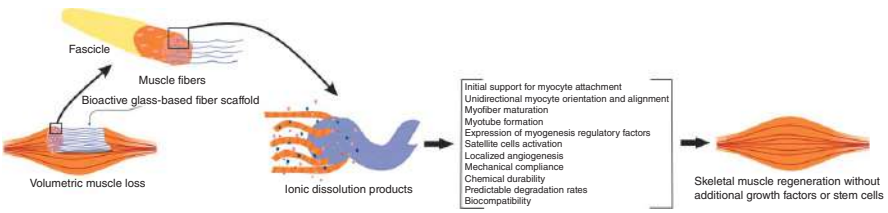

Figure 20.1 Illustrative representation of the BAG-based scaffold for the skeletal muscle regeneration in volumetric muscle loss.

formation, and maturation. The use of reinforced collagen-supported myofiber formation and growth by maintaining a sustained and enhanced expression of myogenin regulatory factors, including the developmental (*MYH8*) and adult (*MYH1*, *MYH2*, *MYH6*, *MYH7*) genes for myosin heavy chain isoforms [30]. These studies suggested that iron-phosphate BAG fibers could serve as a biomimetic scaffold for cell transplantation applications. The myotubes grown on these phosphate-iron BAG fibers could afterward be implanted *in vivo* after the degradation of the glass during skeletal muscle regeneration.

In a recent comparative study, silicate (Bioglass), borate (13-93B3: $56.7B_2O_3$–$5.5Na_2O$–$11.1K_2O$–$4.6MgO$–$18.4CaO$–$3.4P_2O_5$ wt%), and aluminoborate (8A3B: $50.7B_2O_3$–$10.8Al_2O_3$–$4.9Na_2O$–$9.9K_2O$–$4.1MgO$–$16.4CaO$–$3.2P_2O_5$ wt%) glasses could regenerate muscles in VML without resorting to additional growth factors or stem cells [28]. The formation of aluminum polyhedra and subsequent reduction of nonbonding oxygen atoms in the BAG network improved glass durability. It showed better degradation and a stable pH profile of 8A3B over 13-93B3 and Bioglass. Moderate *in vitro* degradation rate was suggested to be a crucial factor affecting cell behavior. The optimum release of ions such as B^{3+} and Ca^{2+} from the aluminoborate 8A3B supported better *in vitro* endothelial cell migration, tube formation, and VEGF secretion, indicating their ability to stimulate angiogenesis without being cytotoxic due to a lower level of B^{3+} release. The IDPs of the BAGs also enhanced *in vitro* gene expression of muscle-defect-related growth factors (CX43 and insulin-like growth factor-1 [IGF-1]) from mouse muscle myoblast cells (C2C12s), required for the growth, differentiation, and increased contractility of skeletal muscle tissues. Moreover, *in vivo* activation of SCs and formation of laminin and muscle fibers along with the mature blood vessels after implantation in a rat VML model suggested the potential of these BAGs for vascularized regeneration of skeletal muscles. 8A3B being relatively better than either Bioglass or 13-93B3. The 3D fibers of iron-phosphate-based BAG (CaO–Na_2O–P_2O_5) with 3 mol% Fe_2O_3 for the tissue engineering of the hard–soft tissue interface had the slowest degradation rate and good biocompatibility [87]. These BAG fibers supported higher viability, proliferation, and functional differentiation of human craniofacial osteoblasts and oral fibroblasts and the expression of osteogenesis-related genes (Cbfa1, osteonectin, collagen 1). In contrast, the more soluble BAG fibers with 1 mol% Fe_2O_3 failed to support the survival of cells beyond seven days in culture. The study also suggested that the glass dissolution rate is a decisive factor in determining the nature of cell–composition interaction.

Regeneration of another soft tissue component of the musculoskeletal system, ligaments such as anterior cruciate ligament (ACL) and/or posterior cruciate ligament (PCL) reconstruction is required after knee injury due to accidents and trauma when these cannot heal on their own and have to be surgically replaced. The first attempt for ACL reconstruction using an artificial ligament was made at the beginning of the twentieth century using silk sutures hammered into the bone and stitched to the infrapatellar tendon, which failed within the three months of implantation [88]. Currently available options for ACL reconstruction include the gold standard autograft of four-strand hamstring tendons or bone-patellar tendon-bone and have their limitations. By the end of the twentieth century, a synthetic graft, Ligament Advanced Reinforcement System (LARS) (Surgical Implants and Devices, Arc-sur-Tille, France), made of polyethylene terephthalate (PET), was introduced and is still preferred clinically for reconstructing human knee ligaments in conjunct with autograft and allograft [89]. PET grafts suffer from poor osseointegration due to their hydrophobicity and chemical inertia. This delays healing and leads to the formation of the fibrous scar tissue between the artificial ligament graft and the bone tunnel and subsequent ligament loosening and graft failure [90–92]. PET sheets coated with 58S ($58SiO_2$–$33CaO$–$9P_2O_5$ wt%) show enhanced osseointegration [93]. After implantation into the proximal tibia metaphysis of New

Zealand rabbits, 58S-coated PET sheets formed a dense vascularized trabecular network of new bone at the graft-bone interface with less scar tissue formation. Higher secretion of VEGF and BMP-2 growth factors induced by 58S BAG coating around the implanted graft was beneficial for vascularized new bone formation at the interface between the graft and host bone tunnel [93]. In the following study, PET grafts coated with 5 mol% CuO-doped BAG (CuBG/PET) for ACL reconstruction enhanced *in vitro* osteogenic and angiogenic differentiation of rat BMSCs. Expression of osteogenesis-related genes (S100A10, BMP-2, OCN) and angiogenesis-related genes (HIF-1α, VEGF) was upregulated, thereby activating the HIF-1α/S100A10/Ca^{2+} signal pathway. Therefore, Cu^{2+} doping coupled angiogenesis and osteogenesis. Additionally, after implanting CuBG coated grafts in a goat model, the IDPs provided soluble signals promoting *in vivo* bone and blood vessel formation and ligament healing in the bone tunnel [22].

Tendons (similar to ligaments) are a tough band of fibrous connective tissue (made of collagen) that connects muscle to bone and can withstand tension. Traumatic injury to the tendon, such as rotator cuff tear, causes shoulder pain and dysfunction and requires surgical attachment of the tendon to its bony insertion, which, however, suffers higher retear rates following surgical repair [94]. The mechanisms and processes of tendon–bone repair are considered highly complex. The implant material required is a functionally graded material that exhibits a gradual transition from soft tissue to hard tissue through a fibrocartilaginous transition region. In a study, the semitendinosus healing of an interfacial gap between a bone and a tendon or ligament in an *in vivo* model of ACL reconstruction in adult male New Zealand white rabbits was enhanced after being filled with a paste of BAG [23]. Formation of new bone and the Sharpey's fiber adjacent to the grafted tendon surface was observed. BAG has also been implicated in tendon tissue engineering as a synergistic mixture with platelet-rich plasma (PRP) [24]. BAG upregulated the *in vivo* expression of osteogenesis-related genes, improved angiogenesis, strength, and maturity of the remodeled tendon-to-bone junction [24]. While, PRP (preparation of autologous plasma contains a higher concentration of autologous growth factors) released relevant growth factors such as PDGF, transforming growth factor-beta (TGF-β), IGF, and EGF [95], thus enhancing the remodeling and healing process in tendon-bone healing. A mixture of 58S BAG (0.02 mg) and PRP (2 ml) sprayed onto the sutured conjunction at the rotator cuff tear in male New Zealand white rabbits accelerated the tendon–bone healing process [24]. PRP + BAG caused an initial acute inflammatory reaction, which resolved spontaneously within 12 weeks of implantation. Enhanced healing was reported with no implant migration or gross infection. Histologically, hyperchromatic cells and capillary blood vessels were observed. The interface between the tendon–bone integration was much sturdier with re-established collagen-fiber, orderly arranged tendon fibers with aligned chondrocytes and osteocytes, and higher ECMs were observed in the PRP + BAG group after 12 weeks of operative implantation. Enhanced mRNA expression of BMP-2 was also reported, suggestive of bone formation. However, load failure at the tendon-bone joint was a limitation and concern.

20.2.3 Gastrointestinal Tissue Regeneration

The gastrointestinal epithelium has an immense potential for rapid self-renewal and regeneration that continues throughout life [96]. The progenitor cells of the stomach and intestine give rise to almost all kinds of epithelial-lineage cells. Despite such enormous regenerative potential, in pathological conditions like peptic ulcer disease (PUD), dysfunction of stem cell machinery is proposed to be causative of poor quality of ulcer healing leading to relapses, recurrences, and refractoriness. The regenerated epithelium is aberrant, scarred, with histologic and structural abnormalities, including poor differentiation and degenerative changes in glandular cells, increased connective tissue,

and disorganized microvascular arrays, increasing susceptibility of the regenerated epithelium to damage and other diseases [97]. PUD is a group of pathologies that include crater-like excavations lying at the interphase of the distal side of the glandular borderline (mucosal rule) and line of distortion of movement (muscular rule) [98]. Depending upon the extent and dimension of ulceration, healing can take days or months. Moreover, considering the interplay of *Helicobacter pylori* infection and infective ulcer, the chronic inflammation, as induced by infection, also adversely affects differentiation and promotes stem cell metaplasias [99]. In these cases, an optimal approach for complete regeneration of damaged gastrointestinal epithelia is desirable. Current treatment approaches include medications that reduce gastric acid secretion (proton pump inhibitors, H_2 receptor antagonists), enhance gastric pH (nonsystemic antacids), form a protective layer over ulcerated epithelium (colloidal bismuth subcitrate), heal ulcer (Carbenoxolone sodium), and abate *H. pylori* infection (Anti-*H. pylori* antibiotics) [100]. None of the clinically available treatments focuses on enhancing the regenerative potential of the ulcerated zones. It is where tissue engineering and regenerative approaches come into play.

The first study reporting the possible application of BAGs in gastrointestinal regeneration was almost 10 years ago [34]. BAG conditioned media could promote the process of epithelial restitution in the injured superficial intestinal mucosal wound (simulated by using the coculture model of wounded intestinal epithelial cell monolayers and subepithelial myofibroblasts). Bioglass at a low concentration (0.1%) promoted the migration of epithelial cells across the wound margin along with the secretion of bFGF from myofibroblasts. However, a high concentration (1%) was reported to be cytotoxic and adversely affect cell viability, migration, and wound healing due to the raised pH of the culture medium [34]. The beneficial role of Bioglass on paracrine mucosal signaling by enhancing cell migration and bFGF secretion in a dose-dependent manner would promote rapid epithelial repair modulating intestinal epithelial cell growth and migration without causing cell proliferation. Based on these preliminary findings, the researchers suggested the possible application of Bioglass in tissue regeneration and repair via a process of epithelial restitution in superficial mucosal ulceration.

In the following study, the anti-gastric ulcer activity of Bioglass was evaluated in rodent models [35]. Single and multiple oral gavages of Bioglass in acute and chronic experimental animal models of ulcer protected against gastric ulceration and recurrence in a dose-dependent manner. Moreover, the IDPs of Bioglass could restore *in vitro* cell proliferation after injury of mucosal cells (GES-1) with ethanol in a concentration-dependent way. Additionally, the apparent absence of systemic absorption after multiple oral dosages suggested that the anti-ulcer activity is local. Thus, there is a minimum possibility of adverse effects associated with the systemic absorption, which otherwise is frequent with the proton pump inhibitor, omeprazole, and an anionic clay antacid, hydrotalcite, making it a suitable alternative to the currently available drugs of choice for the treatment of gastric ulcer. However, an appropriate mechanism for the observed effect was still elusive. Hence, to further assess the anti-gastroduodenal activity and its probable pharmacological mechanism, *in vivo* experiments in rats using BAG containing 1.3 mol% of BaO (BaBG) were performed [36]. The researchers reported a higher pH in simulated body fluid (SBF) for BaBG over Bioglass, maintained for a more extended period, hence chosen for *in vivo* evaluation. The mechanistic findings included the gastric pH incrementing behavior, termed as an "antacid-like" activity, without altering the gastric volume. BaBG treatment in experimental models of gastroduodenal ulcers in rats enhanced gastric mucosal cell proliferation and differentiation. Electron microscopy showed the adhesion of BaBG particles to the gastric and duodenal mucosa, acting as a local protective barrier, protecting the damaged epithelium from further damage. The layer of BaBG and probable apatite was suggested to provide local binding sites for proteins and cells, conferring a

suitable milieu to the ulcerated wounds against a holistic gastric environment for rapid healing. Figure 20.2 gives a consolidated schematic representation of the probable mechanisms of gastroprotection in gastroduodenal ulcers elucidated so far for the IDPs of the BAGs.

The gastrointestinal environment is dynamic and highly motile. A suitable tissue engineering scaffold for the regeneration at these sites must offer sufficient mechanical strength and maintain the integrity of the construct in these conditions. A BAG-polymeric scaffold has been designed as a scaffold material for the engineering of tissues with a tubular shape such as the trachea, esophagus, and small intestine [101]. The tubular foams of polylactide-*co*-glycolide (PLGA) and 1% Bioglass synthesized via a thermally induced phase separation process had radially aligned and highly interconnected pores with a wall thickness in the range 1.5–3 mm. The tube geometry and pore morphology of the synthesized composite foams would allow rapid cell infiltration while maintaining the sufficient mechanical strength and structural integrity required for successful tissue regeneration. A hybrid nanoglue of Bioglass (15 wt%) and ceria nanoparticles (85 wt%) has been formulated through a method of liquid feed flame spray pyrolysis for tissue gluing in pathological anastomotic leakages and impaired wound healing [102]. The addition of Bioglass enhanced the hemostatic activity, small intestine adhesion, and cytocompatibility of the metal oxide-based nanoglue. However, high concentrations of BAG caused hemolysis and impaired cell membrane integrity.

In infancy, these studies have suggested the ocean of opportunities that lie ahead for the interested researchers in exploring BAG applications in gastrointestinal tissue regeneration in pathological conditions where failed regenerative machinery becomes causal for more worst relapses and subsequent other following diseases [103]. Even the surgical treatment options in conditions such as perforated and bleeding peptic ulcers and Crohn's disease demand rapid wound healing and faster tissue regeneration [104, 105]. A BAG-based tissue engineering scaffold should, however, assist these processes. Nevertheless, one consideration should involve the multilayered, complex architectural design of the gastrointestinal system, including the gut neuronal and vascular system. The aim is to regenerate the tissue structurally and restore the maximum functionality and intrinsic anatomy with the vascular and neuronal connections.

20.2.4 Lung Tissue Engineering

Adult lung tissue fails to regenerate itself beyond the local level spontaneously. Localized progenitor cells (e.g. type II alveolar pneumocyte) have shown to be capable of epithelial repair; however, these progenitor cells lose their regenerative potential in multiple lung diseases. Lung regeneration offers an attractive opportunity to replace the injured or the failed parts of the lungs. Cell-based tissue engineering scaffolds, for repairing the tracheal and large airways, have been reported to have some success. However, among the scientific community, regenerating the distal part of lung tissue has been most challenging. Major issues, including poor host tissue integration, immunogenicity, and scaling up the *in vitro* miniaturized cell aggregate to a whole human-sized lung while maintaining a higher degree of anatomic organization for the physiological function, prevent clinical translations [106]. A suitable matrix for supporting cell adhesion, growth, and differentiation while helping propagate the essential rhythm of the spatial and temporal patterns of cellular signals between the progenitor cells is crucial. Based on the available scientific evidence, BAGs have been looked upon to certainly address some of these issues for developing a genuinely applicable scaffold for lung tissue regeneration. About 20 years back, a group of researchers reported that murine lung epithelial (MLE-2) cells could grow favorably into the macropores of the sol–gel derived 58S BAG-based foams. The foams were functionalized with amine and

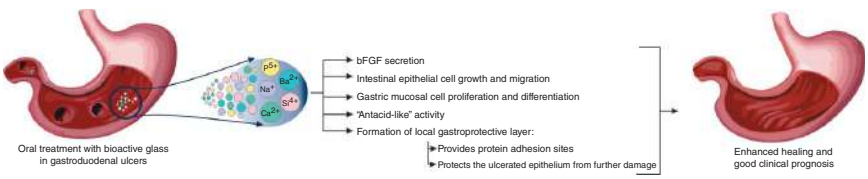

Figure 20.2 Illustrative representation of the mechanisms involved in the gastroprotection by the IDPs of the BAGs in gastroduodenal ulcers.

coated with laminin, a noncollagenous extra-cellular matrix protein present in the basement membrane of lung epithelial cells [8]. Laminin coating was reported beneficial for the *in vitro* growth, attachment, and migration of cells into the amine-functionalized foams over mercaptan functionalization, the mechanism for which was not evaluated.

Considering the need for mechanical strength, structural integrity, and a suitable microenvironment for attachment, growth, and proliferation of human lung cells, polymeric composite porous foams of poly-D,L-lactic acid (PDLLA) with Bioglass were evaluated as a lung tissue engineering construct [7]. The *in vitro* analysis revealed that the human lung adenocarcinoma epithelial cells (A549) could attach and proliferate inside the mesopores of the scaffold, based upon the concentration of Bioglass used for synthesis. The scaffold containing 5% Bioglass provided favorable microenvironment changes and alkalization of the medium, supporting optimum cell behavior over the scaffold containing 40% Bioglass and pure PDLLA foams. Similarly, the addition of polymer (PLGA) enhanced the overall mechanical competence of 1% Bioglass based tubular composite foams [101]. The addition of polymer enhanced the general mechanical competence. The compound walls could sustain axial and diametrical compressive loads without collapsing while maintaining the porous structure, supporting the regeneration of tubular tissues such as the trachea. These studies demonstrated the critical role of concentration, microstructural, and topographical features on cell behavior and the chemistry of cell–biomaterial interaction.

In another study, the effect of BAG composition on A549 cells adhesion and proliferation was explored [9, 10]. The presence of phosphate in the BAG system, 58S ($60SiO_2$–$36CaO$–$4P_2O_5$ mol%), has been beneficial for *in vitro* A549 cell adhesion and proliferation over binary S70C30 ($70SiO_2$–30CaO mol%) substrates. The discrepancy was attributable to the rapid dissolution and the nucleation of amorphous calcium phosphate occurring at the surface of the ternary gel BAG over the binary system [9]. Despite the slower pace of proliferation on the binary BAG system, both the glass system were nontoxic, supporting cellular viability, and proliferation even after four weeks of cell seeding. Similarly, 2 mol% silver-doped sol–gel-derived 58S BAG evaluated for its anti-*Leishmania* activity was also reported to be noncytotoxic toward A549 cells under *in vitro* setting [10]. Interestingly, in another research, a sol–gel-derived magnetic BAG based on the quaternary composition (SiO_2–CaO–Na_2O–P_2O_5) doped with iron was developed for hyperthermia therapy to treat lung carcinoma [11]. The magnetic BAG was reported to be noncytotoxic toward normal human lung fibroblasts (HFL1) (<20 mg/ml). The magnetic BAG reduced the cell viability of A549 cells when exposed to the alternating magnetic field based upon the concentration of Fe^{3+} used for doping [11]. The study suggested a possible prospect for the magnetic BAGs in magnetic hyperthermia therapy of lung cancer and subsequent regeneration of lung tissues.

The failing lung conditions such as emphysema, cystic fibrosis, sarcoidosis, and cancers demand a whole new lung or a segment for replacement when the existing disease is incurable with the conventional therapies. While lung transplantation has its limitations, tissue engineering approaches for segmental or complete lung regeneration are still far from being applicable clinically [106]. There are particular challenges associated with the currently available approaches; hence, we are in a dire need to explore beyond. Amongst the biomaterial, BAGs have been a promising tool for soft tissue engineering applications after a successful establishment in orthopedic and dentistry. The amalgam of existing resources and techniques for regenerating lung tissue with BAG would address some current limitations. Limited scientific evidence has helped understand the beneficial role of concentration, microstructural, and topographical characteristics of BAGs in supporting *in vitro* pneumocyte adhesion, growth, and proliferation. The mechanism behind these has been insufficient. For a contractile organ like the lung, the apatite mineralization may prove hazardous. Thus, the inherent stretching capability of alveoli could be affected, hampering fast and efficient air

exchange despite supporting tissue regeneration. These issues need consideration when applying the principles of material science to physiology.

20.2.5 Cardiac Tissue Engineering

Myocardial infarction (MI) is one of the leading causes of death worldwide, leading to irreversible tissue necrosis [107]. The current treatment strategies mainly involve invasive surgery and cardiac catheterization. These are expensive and cannot regenerate the cardiomyocytes at the infracted site [108]. Based on these shortcomings, BAGs have been investigated for cardiac tissue engineering either as injectable hydrogels or as cardiac patches (see Figure 20.3). Mechanical support is an essential criterion for cardiac patches. Heart beating generates higher filling pressure that prevents the cells supplied during cell therapy from adhering and leads to negative remodeling of the affected region. In a study, incorporation of the microsized Bioglass particles improved the mechanical properties of the elastomeric poly(glycerol sebacate) (PGS) with enhanced Young's modulus (from 0.38 to 1.62 MPa). It maintained this trend even in the physiological fluid and eliminated cytotoxicity associated with the acidic degradation by-product of PGS [31]. The addition of Bioglass prevented the composites from hardening when implanted *in vivo* and enhanced the stability over a more extended period, desired characteristics for soft tissue engineering. Following this, the same researcher group designed another Bioglass nanocomposite to address post-MI pathological conditions, i.e. irreversible cellular loss and ventricular dilation [32]. The elastomer-Bioglass nanocomposites could serve as a cell-delivery vehicle to supply viable, functional cells to the infarct zone and provide mechanical support. The addition of Bioglass (5 wt%) counteracted the acidic degradation of the PGS and hence improved the durability of the patch postimplantation. Moreover, the nanocomposites did not affect the viability of the human endometrial stromal cell (ESC)-derived cardiomyocytes (hESC-CM). Thus, establishing that nanocomposites can be used both as cell-therapy vehicle as well as catch patch.

In another study, injectable hydrogels of gelatin and collagen (Gel/Col) incorporated with Bioglass were designed [109]. The endometrial stromal stem cells (EnScs) cultured on the hydrogel differentiated into cardiomyocytes, as evident from the presence of the cardiac-specific proteins like α-Actinin, Desmin, and Con43. Further, in a recent study, Bioglass-loaded sodium alginate (BG-SA) hydrogel was investigated for their cytocompatibility for the cardiomyoblasts cells (H9C2) and was reported not to influence the proliferation of the cells [33]. Besides, in a rodent model of MI (ligation of the left anterior descending coronary artery), the intramyocardial injection of the BG-SA hydrogel showed a significant improvement in the cardiac functions, as evident from the echocardiography studies. Surprisingly, the histological analysis of the left ventricular tissue of the heart postinjection showed significant increase in the relative scar thickness with attenuated infarct expansion index in the BG-SA treated group compared to the SA group. The currently available literature highlights the ability of the Bioglass to induce positive tissue remodeling post-MI. Moreover, the Bioglass loaded hydrogel also suppressed the apoptosis of the cardiomyocytes and hence can be a potential treatment for MI. However, more preclinical research is required to establish the BAGs for cardiac tissue engineering.

20.2.6 Ophthalmology

BAGs have been explored in the field of ophthalmology for the osseous and nonosseous applications. The osseous applications include repair of orbital floor fractures [110–112] while nonosseous purposes comprises of orbital implants for promoting fibrovascularization [38–40], wound

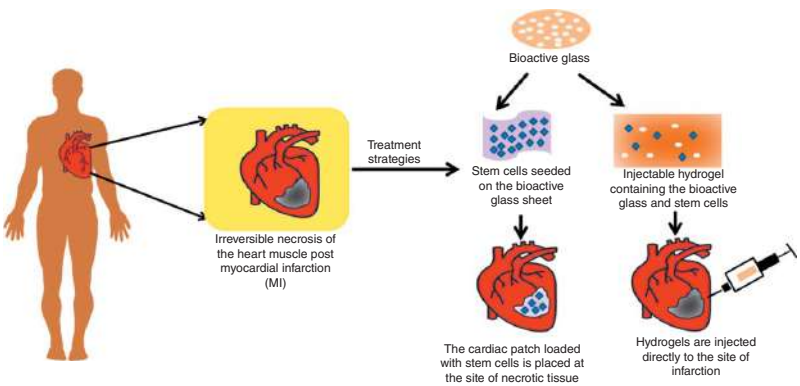

Figure 20.3 Schematic representation of the treatment strategies of MI using BAGs. Stem cells seeded onto the BAG sheet are placed at the site of the necrosis, post-MI. Injectable hydrogels encapsulating the BAG and differentiated stem cells are injected directly into the infraction area.

healing [41], anchorage [42], and preventing their infection [43], and postenucleation/evisceration after anophthalmic surgery and replacing the opacified portion of cornea in patients unresponsive to corneal donor transplant as keratoprostheses (artificial cornea) [113, 114]. The early work describing the use of a bioactive glass-ceramic (BGC) as an orbital implant dates back to the end of the twentieth century [115]. After six months of BGC implantation in the eviscerated rabbits, fibrovascular tissues filled the 90% gaps of the implant. The porosity of the BAG implants support fibrovascular colonization, tissue ingrowth, and anchorage, thereby improving the clinical success rate and implant life. The satisfactory clinical outcomes of these, including the cosmetic appearance and motility, laid down the foundation for future researches [116].

The formation of the surface hydroxyapatite (HA) layer is not a goal in orbital implants. However, neovascularization for anchoring the implant to orbital tissues and supporting nutrient, growth factor, and oxygen delivery along with immune surveillance and chemotaxis of the stem cells to the injured site for healing is needed [117]. Medpor Plus Sphere received FDA clearance in 2002 for use as orbital implants for achieving a higher fibrovascular ingrowth and tissue integration [14]. Despite this, a study showed that the implantation of Medpor Plus Sphere postenucleation or evisceration in rabbits did not significantly influence vascular connective tissue ingrowth. However, one week after surgery, a statistically significant increase in fibrovascular ingrowth of the Medpor Plus group indicated faster fibrovascularization in the early phase [118]. Contrarily, postenucleation implantation in human patients, a statistically significant higher fibrovascularization rate was reported for Medpor Plus over Medpor implants [38, 39]. Postoperative follow up of 170 human patients showed new bone formation, biocompatibility, absence of immunogenicity, and an increased fibrovascularization rate, rendering it less susceptible to contraction, fistulization, infection, inflammation, migration, and a lower extrusion rate, suggesting the suitability of Medpor Plus for orbital reconstruction after primary enucleation or as a secondary implant [39]. In another preclinical study, implantation of orbital cones of Bioglass and Biosilicate® ($48.5SiO_2$–$23.75Na_2O$–$23.75CaO$–$4P_2O_5$ wt%) with a single crystalline phase (Biosilicate 1P) into the eviscerated sockets of rabbit lead to an initial inflow of fibroblasts and inflammatory cells, neovascularization, and formation of a pseudocapsule around the implant followed by chronic healing and reduction in edema and inflammatory cell count supporting wound healing with the replacement of injured intraocular tissues by connective tissue [41]. A superior biological response was obtained for Bioglass and Biosilicate 1P over Biosilicate with double crystalline phase (Biosilicate 2P). Additionally, all the implants bonded with soft tissue, thereby preventing extrusion. Recently, the clinical implantation of cone-shaped Biosilicate orbital implant has also been reported to increase the orbital volume of anophthalmic sockets with few inflammatory signs and no systemic adverse effects [42].

The presence of interconnected and large macropores (~250 μm) favors fibrovascularization and tissue ingrowth. Foam-like wollastonite-containing implants ($57SiO_2$–$30CaO$–$6Na_2O$–$7Al_2O_3$ mol%) having high porosity (55 vol%), pore size (240 μm), chemical stability, and mechanical strength have been fabricated as an economical alternative to existing polymeric or ceramic bioinert orbital implants [44]. In another study, two types of macroporous glass-ceramic orbital implants (type A and B) based on different silicate glass compositions were synthesized, characterized, and the morphological and surface topographical parameters (such as porosity, roughness) were compared with the commonly used commercial devices (bioceramic implant, Medpor, acrylic, and silicone ball) for ocular tissue engineering [117]. Type A implant ($57SiO_2$–$34CaO$–$6Na_2O$–$3Al_2O_3$ mol%) had 53 vol% porosity, an average pore size of 230 μm, and compressive strength of 18.5 MPa. In contrast, type B ($45SiO_2$–$26CaO$–$15Na_2O$–$7MgO$–$4K_2O$–$3P_2O_5$ mol%) had 60.5% porosity, an average pore size of 520 μm, and compressive strength of 4.2 MPa, suggesting the morphological features to be

potentially suitable for ocular tissue engineering. Additionally, type A glass was bioinert with excellent stability in an aqueous solution which is a crucial feature for preventing *in situ* degradation and resorption of the orbital implants. In contrast, type B glass was bioactive, facilitating angiogenesis required for implant stability and anchorage.

To prevent infection of the orbital implants, systemic or local delivery of antibiotics is needed. The systemic approach is mostly inefficient for nonporous implants due to insufficient vascularization and subsequent drug concentrations at the infection site below the minimum inhibitory concentration (MIC), leading to multidrug-resistant strains. Additionally, adverse effects associated with systemic exposure to drugs and ions are also a concern. With porous implants, it is possible to achieve local delivery of antibacterial drugs and biocide ions in the same cargo. Porous HA orbital implants coated with sol–gel-derived copper (Cu^{2+})-doped mesoporous bioactive glass (MBG) and loaded with ofloxacin have been developed [43]. The sustained release of Cu^{2+} ions from the Cu-MBG coated implant with 2, and 5 mol% of CuO provided *in vitro* antibacterial activity against Gram-positive (*Staphylococcus aureus*) and Gram-negative (*Escherichia coli*) bacteria. The same scaffold implanted in the rabbit panniculus carnosus muscle supported early-stage vascularization attributable to its porous architecture, suggesting that Cu-MBG modification would provide favorable functionality to the porous HA orbital implants for future orbit reconstructive procedures [40].

Keratoprostheses include implantable composite devices that typically comprise a transparent part capable of transmitting light from the eye's exterior to the retina. The central optical part surrounded by a supporting skirt keeps the keratoprostheses anchored within the cornea. In the early clinical attempts, implantation of Ceravital® anchorage skirt around experimental osteo-odonto-keratoprosthesis (OOKP) was deemed unsuitable due to its resorption [119–121]. Later on, it was reported that the porous skirt of Bioverit® I and II could successfully integrate into the corneal tissue of rabbits without irritation [122]. To prevent the infections and extrusion of the prosthesis associated with ingrowth of corneal or conjunctival epithelium into the anterior chamber, glass-ceramic coated titanium prostheses were designed and implanted in the rabbit eyes giving successful outcomes [123]. However, paradoxical findings were reported [124]. Experimental Bioglass ceramic disk implants (diameter 8 mm, thickness 0.5 mm, pore diameter 20–70 μm, and porosity 37–62 vol%) were deemed unsuitable keratoprosthetic material due to their rough, brittle, and hard nature. After seven months of implantation in 11 New Zealand albino rabbits, five implants with higher porosity (51–62 vol%) were all broken and extruded within one month of operation along with other complications such as corneal edema, the opacity of the corneal lamella, lipid deposits, and severe degrees of corneal neovascularization. However, the authors suggested that structural modifications such as porosity and implant thickness may lead to more satisfactory results.

To date, finding an ideal synthetic replacement for the dental laminate of the OOKP remains a cause of concern. Glass-reinforced hydroxyapatite (GRHA), a porous composite of phosphate-based BAG ($65P_2O_5$–15CaO–$10CaF_2$–$10Na_2O$ mol%) in a proportion of 2.5 wt% with HA, was synthesized as a synthetic skirt material for the artificial cornea. Poly(vinyl alcohol) (PVA), as a porogen agent (10–50 vol%) mixed to the physical powder blend of HA and phosphate-based glass, was pressed and sintered at 1300 °C for one hour to obtain small porous disks of GRHA. GRHA with 30% and 50% PVA porogen with a mean pore size of 110 μm promoted *in vitro* human dermal fibroblasts invasion, growth, and proliferation compared with those of the dense GRHA (control), suggesting the suitability to support cellular implant colonization [125].

Ideally, the skirt materials must be flexible, must not loosen or leak at their interface, form a permanent, firm anchorage with the optic and the host tissue, and be biocolonizable [126]. Since BAGs

have a rough surface, are brittle, and suffer from inferior mechanical strength, composite formation with polymeric substances helps address some of these limitations. Composites of PMMA and BAGs, namely Bioglass, S53P4, and 1-98 ($53SiO_2$–$22CaO$–$6Na_2O$–$11K_2O$–$5MgO$–$1B_2O_3$–$2P_2O_5$ mol%) and a slowly resorbing glass, FL107 ($64SiO_2$–$16CaO$–$10Na_2O$–$6MgO$–$2B_2O_3$–$2P_2O_5$ mol%), were fabricated as a synthetic OOKP keratoprosthesis skirt [114]. Their comparative morphological parameters, mechanical properties, and dissolution behavior were studied. FL107 had the slowest dissolution in aqueous humor (2.4% of the initial glass content in three weeks) with limited pore formation. On the other hand, composites of PMMA and BAGs had higher dissolution rates (12–17%) with porosity on the outermost surfaces of the composite. Composite with BAG1-98 showed moderate bioactivity and could be worked into different shapes (i.e. fibers, particles, and sintered blocks), while the composite with BAGs, Bioglass, and S53P4 showed higher bioactivity. The study suggested that all the composites had sufficient mechanical strength and could withstand the intra-ocular pressure. In another study, porous BBG, namely, 1-98 and 28-04 ($60.1SiO_2$–$16.2CaO$–$4.9Na_2O$–$7.2K_2O$–$9.0MgO$–$2.6B_2O_3$ mol%), were investigated as a potential synthetic OOKP skirt material. BAG 1-98 showed a faster dissolution over 28-04 with a proportionate increase in the pH of the simulated aqueous humor. The porous BAGs supported keratocytes adhesion and spreading onto the surface, with the highest adhesion for 1-98 BAG with particle size in the range 250–315 μm limited inflammatory potential based upon *in vitro* pro-inflammatory interleukins (IL-8 and IL-6) production [113].

Retinal pigment epithelium (RPE) transplantation is required to restrict visual deterioration in patients with age-related macular degeneration (AMD). An appropriate substrate material is desired to support the RPE monolayer and protect it from the diseased Bruch's membrane (separates the RPE and the choroid layer), which otherwise prevents cell adhesion and proliferation [127]. In this regard, the electrospun poly(ε-caprolactone) nanofibers loaded with sol–gel-derived BAG nanoparticles ($60SiO_2$–$36CaO$–$4P_2O_5$ wt%) have been synthesized and suggested as a substrate for attachment and proliferation for RPE cells transplantation in RPE dysfunction [128]. Incorporation of BAG nanoparticles into PCL nanofibers supported *in vitro* nonimmortalized human ARPE-19 and Müller cells (MIO-M1 cells; specialized glial cells that support the functioning and metabolism of retinal neurons) attachment, viability, and proliferation with good biocompatibility and absence of toxicity, vascular injury, or coagulation in hen's egg test-chorioallantoic membrane (HET-CAM) assay.

Reviewing the recently available literature, it is clear that the potential of BAGs in ophthalmology is not fully explored, and the limited understanding of the biomolecular mechanisms hinders the clinical applicability. Additionally, the development of compositions or composites with tailorable biological behavior in the ocular environment is yet to be exploited to its full potential. For instance, resorption is beneficial in repairing orbital floor fractures, while it is a cause of concern when used as an OOKP keratoprosthetic skirt material or for corneal healing.

20.2.7 Stomatology

The term "stomatology" derived from the Latin word *Stoma-* (mouth) and *-ology* (the study of) is also called oral medicine. Stomatology is a dental specialty that deals with studying the structure and function of the oral cavity, including its disorders and diseases [129]. BAGs play an essential role in the repair and regeneration of oral tissues and oral health maintenance. Damaged dental pulp requires endodontic treatment for both preventing and curing apical periodontitis. Vital pulp therapy (VPT) protects the injured pulp, reduces inflammation, and promotes reparative hard tissue formation that shields the pulp tissue from harmful agents [130]. Re-infection of the tooth can

occur due to a poorly obturated root canal, causing periapical periodontitis; hence, a treated root canal is obturated with a biocompatible filling material. BAG-based root canal sealer has been suggested as a next-generation direct pulp capping material in clinical endodontic treatment. S53P4 studied as a filler material postpulpotomy in a preclinical study showed an initial acute inflammatory response at two weeks, which resolved spontaneously at four weeks of pulpotomy without producing localized necrosis and fibrosis [131]. Direct pulp capping preserves pulp viability and induces wound healing, including reparative dentin formation on the exposed dental pulp caused by deep caries or tooth fracture. Ideally, pulp-capping material should adhere to the tooth substrate and maintain a sufficient seal. It should be dimensionally stable, nonresorbable, nontoxic, noncarcinogenic, nongenotoxic, radiopaque, and exhibit biocompatibility, bioactivity, bactericidal, and anti-inflammatory properties [63, 130]. No material currently available satisfies all the desirable properties for direct pulp capping [132]. Commercially available root canal sealers containing BAG include GuttaFlow Bioseal (GFB) (Colte'ne/Whaledent, Altstätten, Switzerland) and Nishika Canal Sealer bioactive glass (NBG) (Nippon ShikaYakuhin, Yamaguchi, Japan) [63, 64]. GFB comprises gutta-percha powder, polydimethylsiloxane, a platinum catalyst, zirconium dioxide, silver (preservative), and BAG ceramic [133]. It has alkalinizing activity, low porosity, low solubility, shows bioactivity, and forms HA [133], shows dentin penetration [134], and possesses cytocompatibility [135]. However, evidence concerning the mechanism of hardening or its ability to seal the canal and be removed for retreatment is limited [64]. NBG, initially intended for both dental pulp and bone regeneration, is available as a two-phased paste in a double syringe. Upon pushing the plunger, the two-phase paste is dispensed at a 1 : 1 ratio and hardens upon exposure to heat or moisture [64]. Silica dioxide, bismuth subcarbonate, and fatty acids constitute phase A paste. Phase B paste consists of calcium silicate glass, magnesium oxide, silica dioxide, and purified water [65]. It is stored in the syringes in a resealable aluminum foil bag and then placed in a cold storage location (1–10 °C) without freezing to prevent in-bag hardening. Biologically, NBG hardens in SBF and shows HA formation [136], promotes cell viability and migration of human periodontal ligament cells and osteoblast-like cells [137]. NBG offers excellent sealing ability with the root canal dentinal wall required to avoid reinfection postroot canal obturation [138]. Additionally, it can be removed entirely, allowing reopening of dentin cavities, suggesting NBG allows subsequent endodontic retreatment when reinfection at the periapical tissue of a treated tooth occurs [137]. NBG-treated human periodontal ligament stem cells (hPDLCs) and human umbilical vein endothelial cells (HUVECs) showed enhanced *in vitro* alkaline phosphatase (ALP) activity and osteogenic differentiation along with endothelial cell tubulogenesis and expression of angiogenic genes (VEGF, PDGF-BB, bFGF) without increasing the expression of inflammatory genes (IL-6, TNF-α, IL-17) suggesting the potential of NBG to give vascularized healing of apical periodontitis and bone formation without inflammation [65]. NSY-222-S (a modified form of NBG) promoted reparative dentin formation without inflammation in rats [63]. Moreover, root canal obturation with NBG supported periapical clinical wound healing and bone formation of the periapical tissues after one year of obturation with or without a semisolid core material [64, 66]. For better wound healing and the regeneration of complex tissues such as dental pulp (soft tissue) and dentin (hard tissue), gelatin hydrogel sponges with BAG capable of the controlled release of FGF-2 have been recently devised [63].

Dental caries is a biofilm-mediated, dietomicrobial multifactorial dynamic disease resulting in the phasic demineralization and remineralization of dental hard tissues. It is classified among the most common chronic diseases worldwide [139, 140]. Treatment involves using materials with regenerative and antibacterial properties, and controlling inflammation is critical for successful endodontic regeneration. The incorporation of BAGs could impart antibacterial and

anti-inflammatory properties to the dental pulp-capping material for future clinical applications. Treatment of lipopolysaccharide (LPS)-induced inflammatory-reacted dental pulp cells (DPCs) with a sol–gel-derived silver-doped BAG (AgBG) ($60SiO_2$–$6CaO$–$3P_2O_5$–$14Al_2O_3$–$5Na_2O$–$5K_2O$–$7Ag_2O$ wt%) in chitosan (CS) hydrogel at a 1 : 1 weight ratio (AgBG/CS) downregulated the *in vitro* mRNA expressional levels of inflammatory cytokines (IL-1β, IL-6, TNF-α, IL-8) and reduced nuclear translocation of p65 significantly, suggesting the inactivation of NF-κB pathway in the inflamed DPCs [67]. The ALP activity decreased when DPCs became inflamed but significantly recovered after being treated with AgBG/CS, even higher values than noninflamed DPCs. AgBG/CS promoted adherence and *in vitro* odontogenic differentiation potential of DPCs to AgBG/CS without negatively affecting the cell proliferation. Furthermore, the addition of CS (thermogelling, biocompatible, and bacteriostatic) enhanced the operability of AGBG dental pulp capping agents. Ag-BG/CS strongly inhibited the growth of Gram-positive bacteria, *Streptococcus mutans*, and *Lactobacillus casei*.

High mechanical strength with elastic modulus matching that of the natural bone is a prerequisite for tooth-periodontal implants [141]. Poor mechanical properties, such as high brittleness and low-tensile strength of BAGs, limit their applicability in dental tissue engineering. Composite formation of polymer PCL with submicron BAG through solvent casting technique and the thermal pressing method improved mechanical properties required for long-term performance in tooth engineering [142]. Additionally, the hybrid significantly promoted human DPCs proliferation, odontogenic differentiation, and generation of mineralized nodules compared to the pure BAG or PCL scaffolds.

Zirconia has been a preferred dental implant material over titanium owing to its superior esthetic and biocompatibility features. However, poor tissue integration and bond formation at the interfaces between zirconia and peri-implant soft tissues are associated concerns. Additionally, to hasten the healing process of the wounded marginal gingiva following implant surgery, the migration, attachment, and proliferation of gingival fibroblasts are required for underlying collagen matrix production and soft-tissue regeneration. To promote the formation of a stable bond and efficient seal between the Zirconia abutment dental implant and the surrounding soft tissue at the abutment surface and/or transmucosal portion of the implants, and to slow the marginal bone loss following implantation, thermal coating with Biosilicate (Vitrovita, Sao Carlos, SP, Brazil) has been investigated [143]. Biosilicate promoted proliferation, viability, migration, and collagen synthesis by L929 fibroblast cells, suggesting *in vitro* wound healing with superior biocompatibility.

Wound healing of any kind is delayed in diabetes mellitus. Complications associated with delayed wound healing in the oral cavity lead to inflammatory soft tissue pathologies, including gingivitis and irreversible periodontitis. Reduced salivation and persistent high plasma glucose concentration leading to reduced cell proliferation and migration, obstructive vascular sclerosis, and prolonged hypoxia impair the process of wound healing. Electrospun sol–gel-derived borate-based bioactive glass nanofibers (BGnfs) with (1–2) mol% of B_2O_3, (68–69) mol% of SiO_2, and (29–30) mol% of CaO have been synthesized for enhancing oral mucosal wound regeneration in diabetes mellitus [144]. Bilateral elliptical oral mucosal defects in type I diabetic New Zealand male rabbits grafted with borate-based BGnfs promoted normal epithelialization with mature connective tissue matrix formation without inflammation. BGnfs also promoted cell migration from the surrounding epithelium toward the center of the wounding area and *in vivo* VEGF expression suggestive of vascularized wound healing, starting from one-week postoperation.

Oral bisphosphonates (such as zoledronic acid), primarily prescribed for the treatment of osteoporosis, have an antiangiogenic activity and produce direct soft tissue toxicity in the oral cavity. Long-term treatment leads to a high turnover of alveolar bone. It exposes the jaw to the

outside environment through the teeth and periodontal ligament, leading to a well-known clinical condition called bisphosphonate-related osteonecrosis of the jaw (BRONJ) [145]. Treatment with a BBG ($53.8B_2O_3$–20CaO–$12.1K_2O$–$4.6Na_2O$–4.6MgO–$3.8P_2O_5$ wt%) has promoted *in vivo* soft tissue regeneration and restoration of vascularization in the bisphosphonate-associated jaw lesions [69]. Treatment with zoledronic acid prevented *in vitro* BMSC proliferation and ALP activity which was reversed by BBG treatment. BBG upregulated expression of osteogenesis-related genes (Runx2, OPN, OCN, BMP-2, and ALP). Similarly, zoledronic acid-induced apoptosis of HUVECs and reduced migration and tubulogenesis were restored post-BBG treatment. Additionally, treatment with BBG in rats with BRONJ lesions promoted *in vivo* soft tissue recovery and a decrease in necrotic bone area and empty osteocyte lacunae in the extraction sockets and neovascularization.

With or without cleft palate, a cleft lip is a congenital craniofacial defect caused by disturbed embryonic development of soft and hard tissues around the oral cavity and face area [146]. Reconstructive procedures promoting vascularized tissue regeneration in highly vascularized bones have been a critical challenge [147]. A clinical study has reported the transoral mucosal repair of cleft alveolar bone with Z-plasty and Bioglass use in unilateral alveolar cleft patients. Implantation of Bioglass mixed with blood into the pocket after the closure of the nasal floor, post-Z-plasty improved wound healing and bony bridge formation up to the level of the typical alveolar crest (type 1 Bergland's scale) after one year of clinical follow-up [68]. BAGs have been reviewed as a suitable material for the reconstruction of soft and hard tissues of the cleft lip/palate based on their favorable biological (osteoconduction, biocompatibility), and physiological (facilitation of proliferation and osteoblast differentiation) properties [148].

20.2.8 Otorhinolaryngology

20.2.8.1 Otology

Conditions of the middle ear such as chronic inflammation, tumors, congenital disorders, infection, or prior surgeries can damage the ossicular chain and tympanic membrane and lead to conductive hearing loss [149]. Treatment involves reconstructive ossiculoplasty and tympanoplasty, respectively. The first attempt to repair the perforated tympanum dates back to 1640 when the first tympanoplasty was performed using a pig's bladder [150]. In the early 1950s, basic techniques for tympanoplasties using alloplastic graft materials were starting to be explored, and since then, multiple strategies and materials have been investigated [151, 152]. Based upon the ability to establish a firm bond with both hard and soft tissues, regenerative applications of BGCs in otology have been sought for middle-ear reconstruction and as cochlear implants. BAGs are well-known to promote bone regeneration; however, few studies have been discussed here highlighting the applicability of BAGs to bond to soft and connective tissues for repair and regeneration after ear surgery. Considering the limitations of the current reconstructive strategies, the early preclinical and clinical investigation using Ceravital has been for posterior auditory canal wall reconstruction and tympanum transplantation [45]. Fibroblasts and macrophages surge at the implant site within the first week of operative implantation, favoring tissue regeneration without inducing inflammatory reactions and resorption [45]. Clinical investigations have also shown good tissue compatibility and hearing gains with Ceravital for tympanoplastic reconstruction [46, 47]. BAG implants formed a stable bond with the collagen of the tympanum and are not extruded, suggesting good stability [48, 49].

External auditory canal wall reconstruction is performed post-canal-wall-down (CWD) mastoidectomy in patients with persistent infections in the mastoid cavities, desiring freedom from frequent mastoid bowl debridement. Post-CWD-mastoidectomy, mastoid cavities can be

obliterated with BAG. Ceravital implant in external auditory canal wall reconstruction formed a firm bond with the bone and did not disintegrate with time owing to the thickness of the implant [153]. Incidences of postoperative otorrhea and cholesteatomas were observed in a few of the patients. The researchers suggested that canal wall reconstruction shall be avoided in patients suffering from conditions that impair healing like diabetes and hypothyroidism and due to retraction of the soft tissue part of the graft (i.e. either the homograft tympanic membrane or temporalis fascia graft), respectively. In another study, BGC particulate, NovaBone produced mastoid cavity obliteration in Mongolian gerbils in addition to angiogenesis and wound healing within nine weeks of implantation. The implant remained biocompatible, with no signs of inflammatory reactions and ototoxicity along with trabecular bone formation and minimal resorption, suggesting NovaBone as a suitable graft material for mastoid obliteration procedures [154]. Successful clinical obliteration, preventing postoperative infections, and ceasing regular outpatient cleaning with S53P4 (BonAlive) have also been reported [155].

Studies have also suggested BAGs to be a safe and promising prosthetic material for clinical ossiculoplasty. In 1985, the FDA cleared Bioglass-based implant (Bioglass Ossicular Reconstruction Prosthesis) (MEP) for middle-ear ossicle replacement. Despite good short-term and mid-term performance results, long-term clinical studies (10 years of clinical follow-up) showed that Bioglass was prone to progressive dissolution and fragmentation in the physiological milieu of the middle ear [54]. Therefore, MEP implants were taken off the US market a few years later. A modified version of the original MEP implant (Douek-MEDTM; Bioglass cones of three different sizes) is still commercialized in a few European countries since 1985 [156]. Similarly, BAG-based ossicular grafts in the chronic otitis media break down into small fragments and get partially resorbed by a host response within the middle ear despite being were enveloped by a lining of connective tissue and mucosal epithelium [157]. Thus, warranting caution in the use of ear prostheses made of BAGs.

Clinical studies have reported stable hearing outcomes of Ceravital middle-ear implant with minimal resorption over an eight-year implantation follow-up [50]. A pseudarthrotic connection develops between the Ceravital implant and the stapedial footplate in the rabbit's middle ear [158]. However, in another study, Ceravital granules after the middle-ear implantation in guinea pigs have shown to produce a temporary postoperative conductive hearing loss due to the surgical manipulation of the middle ear and the biochemical reactions between the Ceravital granules and the middle ear wall due to the silica-rich layer and collagen bed formation which resolved spontaneously after 20 days of operation without altering the cochlear function [159]. Another study reported a lack of oto- or vestibular toxicity of Biosilicate ($23.75Na_2O–23.75CaO–48.5SiO_2–4P_2O_5$ wt%) after middle-ear implantation in guinea pigs [160]. In another clinical study, BAG UF45S5 ($45SiO–24.5CaO–24.5Na_2O–6.0P_2O_5$ wt%) maintained the biomechanical motion between malleus and stapes with minor inflammation and fibrous tissue encapsulation compared to the control prosthetic material, Silastic [161].

The combined bioceramic stapedial implant (Bioverit I and Bioverit II) has been studied for reconstructing sound-conducting ossicular chains. In the middle ear of guinea pigs, the implant bonds to the bony walls of the tympanic cavity irrespective of the differences in their bioactivity. However, the enormous potential for bone regeneration in the middle-ear ossicular chain makes this species unsuitable for exploring human middle-ear reconstruction [162]. A thin epithelium layer covered the Bioverit II implanted in the middle ear of rabbits and establishes a direct connection between bone and implant. Additionally, strategies to prevent bacterial growth on middle ear prostheses are highly desirable. It has been found that Bioverit II middle-ear prostheses functionalized with silver-containing dense and nanoporous silica films stopped bacterial growth in the middle ear of rabbits and hastened healing by reducing fibrosis [163]. Similarly, when used

in the mastoid and epitympanic obliteration for clinical chronic otitis surgery, S53P4 provided a bone-conduction hearing threshold [53, 54]. Antibacterial activity [164] and absence of labyrinth complications [54] were the added advantages.

Severe hearing loss due to cochlear sensory hair damage requires cochlear implants comprising a microphone, a speech processor, a transmitter, and a receiver sending signals to the cochlear nerve through thin wire electrodes. Bioglass anchored the cochlear implants with four platinum electrodes insulated by Al_2O_3 [52]. This device was commercialized as Bioglass-EPI (extracochlear percutaneous implant) about 30 years ago. Bioglass connector sleeve binds to the temporal bone and collagenous soft tissues as it protrudes through the skin and acts as a percutaneous and stable seal, protecting the interior electronics. However, due to temporal glass dissolution and structural integrity (similar to MEP), Bioglass-EPI was taken off the market in the late 1990s. However, to address the shortcoming of the Bioglass sleeve, a titanium peg was installed in the next-generation design by the University College London [165].

20.2.8.2 Rhinology

One of the essential aspects and a formidable challenge of oral and maxillofacial surgery is the nasal reconstruction considering the complex 3D structure, varying degrees of thickness of the skin covering, associated support structures ranging from rigid bone to flexible cartilage, and the sensitive inner nasal epithelium [166]. The purpose of nasal reconstruction is to restore the normal anatomy and function of the nose by replacing the damaged tissue or augmenting the existing undamaged tissue associated with trauma, animal bite, toxins (cocaine, sulfuric acid, mercury, phosphorus, nasal decongestants), inflammatory conditions (lupus erythematosus, vasculitis, sinonasal sarcoidosis), infections (nasal tuberculosis, fungal rhinosinusitis, leprosy, and syphilis), or cancers. Significant aspects of nasal reconstruction to be taken into consideration include the lining, support, skin coverage, local nasal flaps, nasolabial flap, and paramedian forehead flap. BAGs play a crucial role in the field of facial plastic surgery, including nose reconstruction.

Atrophic rhinitis (also called "ozena") is a debilitating nasal mucosal disease characterized by progressive nasal mucosal atrophy, nasal crusting, fetor, and enlargement of the nasal space with paradoxical nasal congestion [167]. Implant materials (such as glass beads, acrylics, plastic gauzes, Teflon, Dacron, Proplast, Silastic, glycerine, paraffin) for the surgical treatment of atrophic rhinitis suffer limitations without long-lasting success [168]. Moreover, postimplantation, the development of biomaterial-associated infections due to direct contact of implant material with the atrophic rhinitis-associated microorganisms is a concern. S53P4 has been implicated in the treatment of infected paranasal sinuses. A study demonstrated the inhibitory effect of S53P4 plates and granules on the atrophic rhinitis-associated Gram-negative bacterium, *Klebsiella ozaenae*, both experimentally and clinically after implantation in the sub-perichondrial/periosteal space, along the septum, the floor of the nose, and lateral wall of the patients suffering from severe atrophic rhinitis [55]. S53P4 prevented *in vitro* adhesion and surface colonization/biofilm formation of *K. ozaenae*, due to the high pH and the nonphysiological concentration of ions caused by the presence of the glass while preserving bioactivity and Si-rich layer formation. The clinical follow-up of 19–74 months showed an absence of implant extrusion and BAG-associated infections or reinfections of the nasal cavity. The study suggested S53P4 without serum precoating to be a suitable filling material of greatly enlarged internal nasal cavities in patients suffering from atrophic rhinitis. Another research group investigated the electrospun fibrous composite membranes of PCL coated with a 5 mol% zinc-doped sol–gel-derived BAG ($40SiO_2$–$49CaO$–$6P_2O_5$–5ZnO mol%) as an implant layering material of the scaffold for the reconstruction of the upper layer of the nasal septum [56].

Incorporation of Zn^{2+} ions into nasal implants could potentially provide antibacterial properties to decrease or eliminate bacterial infections on the implant surface and subsequent surgical complications and favor osteogenic differentiation at the same time.

Nasal septal perforation is another complication requiring surgical reconstruction. It includes a full-thickness defect of the nasal septum consisting of necrosis of the septal cartilage and soft tissues associated with trauma, autoimmune (such as granulomatosis with polyangiitis), infections, cancer, intranasal drug abuse, steroid, or vasoconstrictor nasal spray, or even as an occupational hazard. Prolonged atrophic rhinitis also often results in septal perforation [169]. To minimize discomfort, crusting, and epistaxis; surgical repair techniques such as external, intranasal, endoscopic, midfacial degloving, or sublabial approach, with the use of various grafts (synthetic or autograft) and combined flaps (unilateral or bilateral), are recommended when other conventional methods are unsuccessful; each with their advantages and disadvantages. A substitute graft material that is biocompatible, nontissue toxic, integrates with the bone and soft tissue, and is osteoconductive is desirable. Surgically, for effective closure and resolution of symptoms associated with the repair of nasal septal perforations, the interposition of grafts between the repaired mucoperichondrial flaps is required [170]. S53P4 disc implants as an interpositional graft successfully obliterates the clinical nasal septal perforations without being extruded and causing BAG-associated infections [57, 58]. S53P4 interpositional graft favored cartilage and soft tissue formation in medium and large perforations, which otherwise are difficult to close without interpositional implant material. Experimentally, the S53P4 discs without serum precoating showed low adhesion for respiratory infection-associated Gram-negative (*Haemophilus influenzae*) and Gram-positive (*Streptococcus pneumoniae*) bacteria [58].

Osteoplastic flap frontal sinus obliteration has been traditionally recommended in trauma (frontal sinus fractures), frontal sinus diseases such as chronic frontal rhinosinusitis, or tumor [59, 60]. After removing the mucosal lining of the frontal sinus and the intersinus septum, the frontonasal duct is occluded using the pedicled pericranial flap rest of the sinus is packed with autologous or alloplastic material. Several autogenous (such as autogenous fat, muscle, bone) and alloplastic (such as HA, calcium phosphate, glass ionomer cement) materials have been advocated for this purpose, each having its strengths and limitations [171]. S53P4 has been investigated for human frontal sinus obliteration [172, 173]. S53P4 granules and blocks moistened in sterile physiologic saline implanted in the frontal sinus cavity of the patients suffering from chronic frontal sinusitis produced absolute obliteration of sinusal recesses and excavations without any inflammation or foreign-body reactions over a mean follow-up period of five years. The obliteration was maintained due to the implant material stability, circumventing the need for a second operation to harvest autogenous material [173]. BAGs have also been implicated in sinus augmentations such as elevating the human sinus floor in edentulous patients with severely resorbed maxillae suffering from inferior dental implants and prostheses retention [174–176]. Sinus floor augmentation followed by the consecutive installation of implant fixtures in the reconstructed bone is required to stabilize these implants [177]. Bioglass-based product, Biogran (Biomet 3i, Palm Beach Gardens, Florida, USA) [178], and S53P4 granules [174] mixed with autologous bone chips showed mineralized tissue formation and healing in clinical sinus floor augmentation.

Analyzing and consolidating findings these far, the antimicrobial activity of BAG against nasal pathogens along with the ability to promote tissue formation without producing inflammatory responses would successfully provide benign conditions for wound healing, postnasal reconstructive procedures.

20.2.8.3 Laryngeal Repair

The need to repair larynx is required in postoperative vocal cord paralysis in laryngeal cancer, laryngeal lesions in Wegner's granulomatosis, laryngeal sarcoidosis, adductor laryngeal dystonia, or viral infection. The laryngeal lesion is manifested as vocal fatigue, dysphagia, dyspnea, and tracheal stenosis caused by reduced vocal cord mobility. The goal is to provide a safe and stable breathing airway and repair the voice box. Approaches employed by phono-surgeons include metal alloy plates, vocal cord injections of bovine gelatin products, injectable polytetrafluoroethylene (PTFE), HA, or silicone rubber insertion for vocal cord medialization. Nonresorbable implants, Teflon, and silicone rubber (to a lesser extent) produce an infiltration of lymphocytes, eosinophils, and histiocytes [179]. While HA supports soft tissue regeneration and cartilage formation in the fenestra region, between the implant and thyroid lamina, implant extrusion and airway obstruction secondary to edema is a concern [179, 180].

Aqueous suspensions of photopolymerizable derivatives of bioactive and biocompatible glasses viz 45SS Bioglass, 52S4.6 ($46.1SiO_2$–$24.4Na_2O$–$26.9CaO$–$2.6P_2O_5$ mol%), SSS43 ($52.1SiO_2$–$21.5Na_2O$–$23.8CaO$–$2.6P_2O_5$ mol%), 6OS3.8 ($60.1SiO_2$–$17.7Na_2O$–$19.6CaO$–$2.6P_2O$ mol%) in carrier dextran have been prepared and patented for injection through a needle into the tissue of the vocal fold on the affected side for several otolaryngologic conditions [61]. The spherical BAG particles (with carrier) after injection as a viscous liquid polymerize *in situ*, forming a solid to establishing the functional aspect of the affected vocal cord. The degradation rate of dextran can be tailored to match the regeneration of new tissue. A study has shown that implantation of Bioglass-based particulate in a functional canine model improved bark characteristics over the paralyzed control suggesting an increased laryngeal valving during phonation caused by collagen-BAG bonding [62]. The Bioglass particulate lodged between the vocal cord and thyroid cartilage supported bony metaplasia, conducive to the physiological cartilage repair. The Bioglass particulate implant could provide vocal cord medialization caused by an immobilized implant along with hard and soft tissue regeneration (Table 20.2).

20.2.9 Urinary Tract Infection

Urinary tract infections (UTIs) are the most common ambiguous bacterial infections caused by the uropathogens that colonize and invade the urinary bladder [184]. It is primarily a hospital or community-acquired infection leading to dysuria, pyuria, and irritation in the urinary tract, and even pyelonephritis that may cause irreversible damage to the bladder. Studies have reported that catheter-associated UTI is one of the most common device-associated infections in healthcare facilities and 30 days of continuous catheterization leads to deposition of biofilms [185]. To overcome these complications, zinc-doped phosphate-based bioactive glass (Zn-PBG) was devised, and its antimicrobial activity was reported [186]. Zn-PBG exhibited a significantly higher antimicrobial effect against Gram-negative *E. coli* (the commonly associated pathogen with UTI) within two hours of incubation, unlike Gram-positive bacteria *S. aureus* where the outcome was observed after four hours incubation. This discrepancy in the activity was attributable to the thick layer of peptidoglycan that restricts the penetration of released ions.

Furthermore, the BAGs have even been explored as a coating over the silicone catheters used for peritoneal dialysis [187]. Typically, the catheterization leads to the development of a fibrous layer around it, and the space between them acts as a passage for the pathogens that cause UTI. Thus, catheters need cuff to anchor them properly and also act as a barrier for the microbes. The coating of Bioglass binds to the host tissue due to HA formation, thus eliminating a cuff. BAGs have shown

Table 20.2 Nonosseous application of BAGs in ophthalmology, stomatology, and otorhinolaryngology.

Field of application	BAG	Composition	Application	Remarks	References
Ophthalmology	Silico-phosphate	$60SiO_2$–$36CaO$–$4P_2O_5$ wt%	RPE cell transplantation for the regeneration of diseased retina in AMD	Incorporation of BAG nanoparticles into PCL nanofibers supported *in vitro* human ARPE-19 and Müller cells (MIO-M1 cells) attachment, proliferation with good biocompatibility, and absence of toxicity, vascular injury, or coagulation in HET-CAM assay	[128]
	Silico-phosphate	$80SiO_2$–$10CaO$–$5P_2O_5$–$5CuO$ mol%	Prevention of implant-site infection of the artificial implants in anophthalmic orbit restoration	The sustained release of antibacterial ion (Cu^{2+}) and drug (ofloxacin) from the 5 mol% CuO-containing MBG (Cu-MBG)-modified porous HA scaffolds provided *in vitro* antibacterial activity against *S. aureus* and *E. coli*	[43]
	Silico-phosphate	$53SiO_2$–$23Na_2O$–$20CaO$–$4P_2O_5$ wt%	Maintenance of the retrobulbar orbital volume postorbital floor reconstruction	Clinically, a drop-shaped S53P4 implant restored the shape of the distorted orbital floor and the original volume of the orbit without negative soft tissue changes, scar formation, diplopia, implant-related infection, or sinus dysfunction after 32 months follow-up of orbital implantation	[181]
Stomatology	Borate	$60SiO_2$–$6CaO$–$3P_2O_5$–$14Al_2O_3$–$5Na_2O$–$5K_2O$–$7Ag_2O$ wt%	Dental caries	Antibacterial activity against *S. mutans* and *L. casei*, reduced *in vitro* mRNA expressional levels of inflammatory cytokines IL-1β, IL-6, TNF-α, IL-8, and inactivation of NF-κB pathway in inflamed DPCs along with enhanced *in vitro* odontogenic differentiation potential of DPCs after treatment with sol–gel-derived AgBG in a chitosan hydrogel in a 1 : 1 weight ratio	[67]
	Borate	$(68–69)SiO_2$–$(1–2)B_2O_3$–$(29–30)CaO$ mol%	Diabetic oral wound	*In vivo* regeneration of epithelial cell layers, dense collagen fibers with regular vascular distribution leading to complete wound closure with the absence of inflammation signs starting from one week postoperative in type 1 diabetic New Zealand rabbits with bilateral elliptical oral mucosal defects	[144]

(Continued)

Table 20.2 (Continued)

Field of application	BAG	Composition	Application	Remarks	References
	Borate	$53.8B_2O_3$–20CaO–$12.1K_2O$–$4.6Na_2O$–4.6MgO–$3.8P_2O_5$ wt%	Bisphosphonate-induced osteonecrosis of the jaw	Restoration of *in vitro* proliferation of BMSCs and HUVECs, upregulation of osteogenesis (Runx2, OPN, OCN, BMP-2, and ALP)- and angiogenesis (CD31, HIF-α, KDR, and VEGF mRNA)- related genes, enhanced *in vitro* tubulogenesis, and *in vivo* soft tissue recovery and neovascularization along with a reduced necrotic bone area and empty osteocyte lacunae in the extraction sockets	[69]
Otology	Bioverit® II	Nonresorbable glass-ceramic based on SiO_2–Al_2O_3–MgO–Na_2O–K_2O–F composition with crystal phase (approx. 60%) mainly phlogopite embedded in an aluminosilicate BAG matrix (approx. 40%)	Prevention of bacterial growth on middle ear prostheses	Bioverit II middle ear prostheses functionalized with silver-containing dense and nanoporous silica films prevented bacterial growth in the middle ear of rabbits along with supporting healing by reducing fibrosis after 21 days of implantation	[163, 182]
	Silico-phosphate (S53P4)	$53SiO_2$–$3Na_2O$–20CaO–$4P_2O_5$ wt%	Mastoidectomy cavity obliteration	Successful clinical obliteration, preventing postoperative infections, and ceasing of the regular outpatient cleaning	[155]
	Ceravital®	(40–50)SiO_2–(5–10)Na_2O–(30–35)CaO–(2.5–5)MgO–(10–15)P_2O_5 wt%	Tympanoplasty	Tissue regeneration and epithelialization at the implant site without inducing inflammatory reactions, perforation of the eardrum over the implants, resorption, and extrusion post 1.5 years of clinical follow-up	[45, 183]

Rhinology	Silico-phosphate (S53P4)	$53SiO_2$–$23Na_2O$–$20CaO$–$4P_2O_5$ wt%	Prevention of implant-related infection of paranasal sinuses in atrophic rhinitis	Prevention of *in vitro* adhesion, growth, and colonization, and *in vivo* implant-related infection or reinfection of *K. ozaenae*	[55]
	Silico-phosphate s20(S53P4)	$53SiO_2$–$23Na_2O$–$20CaO$–$4P_2O_5$ wt%	Nasal septal perforation	The interpositional S53P4 graft promoted cartilage and soft tissue formation and closure of medium and large perforations, clinically, without extrusion	[57]
	Silico-phosphate (S53P4)	$53SiO_2$–$23Na_2O$–$20CaO$–$4P_2O_5$ wt%	Prevention of infection of implants used for repairing the nasal septal perforation	*In vitro* growth inhibition and low adhesion for respiratory infection-associated Gram-negative (*H. influenza*) and Gram-positive (*S. pneumonia*) bacteria	[58]
Laryngology	Bioglass®	$45SiO_2$–$24.5Na_2O$–$24.5CaO$–$6P_2O_5$ wt%	Vocal cord medialization	Hard and soft tissue regeneration and cartilage repair causing improved *in vivo* bark characteristics due to increased laryngeal valving during phonation caused by collagen-BAG bonding after implantation of Bioglass particulates between the vocal cord and thyroid cartilage in a functional canine model	[62]

the potential to be used in the UTI based on their antimicrobial properties and a supportive coating over the catheters. However, further research is required involving the detailed *in vivo* preclinical studies to assess the efficacy of BAG in the treatment of UTI.

20.3 Conclusion

It has been more than 50 years since the first BAG, 45S5 Bioglass, was invented by Prof. Larry Hench to regenerate fractured bones. BAGs have been established as a new field in bioceramic and have been well known for restoring and repairing hard calcified tissue (bones and teeth). With further research, BAGs could have immense potential in biomedical tissue engineering of nonmineralized soft tissues. On a gross level, out of 11 systems present in the human body, the reparative and regenerative potential of BAGs, more or less, has been explored in 9 systems: namely, skeletal, integumentary, muscular, cardiovascular, respiratory, nervous, digestive, and urinary; reports concerning the endocrine and reproductive systems are unknown.

BAGs have been referred to as versatile bioceramic because of the freedom in synthetic (compositional, structural, and topographical) and postsynthesis processing (electrospun fiber, polyphasic composite, substrate coating, or obtained as powder) it provides to the material scientist and wide spectrum of biological activity it would offer to a clinician. The IDPs of BAGs regenerate, repair, or restore the diseased or missing tissue. The fundamental biochemical processes such as adsorption of protein, chemotaxis of macrophages, stem cell migration, proliferation, and differentiation form the basis of osteoconduction, osteoinduction, and osteostimulation required for regenerating hard calcified tissues, are also crucial for nonmineralized soft tissue regeneration and growth.

The successful integration of BAGs with the soft tissues bases upon the temporal pattern of ion dissolution and bonding at the interface of host tissue and BAG upon contact with physiological fluids. The extent of regeneration and repair is also a function of the series of interfacial spatial reactions governing protein adsorption and cell attachment. The nature of subsequent cell surface-specific receptor-ligand interaction and downstream signaling pathways determine the scientifically reported physiological significant activity. Understanding the biochemical pathways at the interplay behind the *in vitro* and *in vivo* effects has been in their formative years. Elucidation of the specific molecular biological mechanism involved in regulating these processes due to the ionic products that result from the dissolution of BAGs when implanted into soft tissue is the next step challenge required for translating the findings of material science and biomedical engineering to the clinics.

References

1 Wilson, J., Clark, A., Douek, E. et al. (1994). Clinical applications of bioglass implants. In: *Bioceramics*, Proceedings of the 7th International Symposium on Ceramics in Medicine. Turku, Finland, vol. 7 (ed. Ö.H. Andersson and A. Yli-Urpo), 415–422. Elsevier.

2 Stanley, H.R., Hall, M.B., Clark, A.E. et al. (1997). Using 45S5 bioglass cones as endosseous ridge maintenance implants to prevent alveolar ridge resorption: a 5-year evaluation. *The International Journal of Oral & Maxillofacial Implants* 12 (1): 1–19.

3 Schepers, E.J., Ducheyne, P., Barbier, L., and Schepers, S. (1993). Bioactive glass particles of narrow size range: a new material for the repair of bone defects. *Implant Dentistry* 2 (3): 151–157.

4 Jones, J.R., Brauer, D.S., Hupa, L., and Greenspan, D.C. (2016). Bioglass and bioactive glasses and their impact on healthcare. *International Journal of Applied Glass Science* 7 (4): 423–434.

5 Pradeep, A. and Sharma, A. (2010). Comparison of clinical efficacy of a dentifrice containing calcium sodium phosphosilicate to a dentifrice containing potassium nitrate and to a placebo on dentinal hypersensitivity: a randomized clinical trial. *Journal of Periodontology* 81 (8): 1167–1173.

6 Hench, L.L. (2013). Chronology of bioactive glass development and clinical applications. *New Journal of Glass and Ceramics* 3 (2): 67–73.

7 Verrier, S., Blaker, J.J., Maquet, V. et al. (2004). PDLLA/Bioglass® composites for soft-tissue and hard-tissue engineering: an in vitro cell biology assessment. *Biomaterials* 25 (15): 3013–3021.

8 Tan, A., Romanska, H., Lenza, R. et al. (ed.) (2003). The effect of 58S bioactive sol–gel derived foams on the growth of murine lung epithelial cells. In: *Key Engineering Materials*, vol. 240, 719–724. Trans Tech Publications Ltd.

9 Saravanapavan, P., Verrier, S., and Hench, L.L. (ed.) (2004). A549 lung carcinoma cells: binary vs. ternary bioactive gel-glasses. In: *Key Engineering Materials*, vol. 254, 781–784. Trans Tech Publications Ltd.

10 Pires, E.G., Bonan, R.F., Rocha, Í.M. et al. (2018). Silver-doped 58S bioactive glass as an anti-Leishmania agent. *International Journal of Applied Glass Science* 9 (1): 52–61.

11 Wang, T.W., Wu, H.C., Wang, W.R. et al. (2007). The development of magnetic degradable DP-Bioglass for hyperthermia cancer therapy. *Journal of Biomedical Materials Research Part A* 83 (3): 828–837.

12 Dai, C., Yuan, Y., Liu, C. et al. (2009). Degradable, antibacterial silver exchanged mesoporous silica spheres for hemorrhage control. *Biomaterials* 30 (29): 5364–5375.

13 Mao, C., Lin, C., and Chen, X. (2014). Enhanced healing of full-thickness diabetic wounds using bioactive glass and Yunnan baiyao ointments. *Journal of Wuhan University of Technology Materials Science Edition* 29 (5): 1063–1070.

14 Später, T., Menger, M.D., and Laschke, M.W. (2020). Vascularization strategies for porous polyethylene implants. *Tissue Engineering* 27 (1): 29–38.

15 Westcott, M.A., Coldwell, D.M., Liu, D.M., and Zikria, J.F. (2016). The development, commercialization, and clinical context of yttrium-90 radiolabeled resin and glass microspheres. *Advances in Radiation Oncology* 1 (4): 351–364.

16 MIRRAGEN® (2017). MIRRAGEN® Advanced Wound Matrix. http://www.etswoundcare.com/clinical-case-studies1.htw./ (accessed 28 May 2021).

17 Heikkilä, J.T., Kukkonen, J., Aho, A.J. et al. (2011). Bioactive glass granules: a suitable bone substitute material in the operative treatment of depressed lateral tibial plateau fractures: a prospective, randomized 1 year follow-up study. *Journal of Materials Science. Materials in Medicine* 22 (4): 1073–1080.

18 Pernaa, K., Koski, I., Mattila, K. et al. (2011). Bioactive glass S53P4 and autograft bone in treatment of depressed tibial plateau fractures – a prospective randomized 11-year follow-up. *Journal of Long-Term Effects of Medical Implants* 21 (2): 139–148.

19 Froum, S.J., Weinberg, M.A., and Tarnow, D. (1998). Comparison of bioactive glass synthetic bone graft particles and open debridement in the treatment of human periodontal defects. A clinical study. *Journal of Periodontology* 69: 698–709.

20 Gatti, A.M., Simonetti, L.A., Monari, E. et al. (2006). Bone augmentation with bioactive glass in three cases of dental implant placement. *Journal of Biomaterials Applications* 20 (4): 325–339.

21 He, X., Ding, Y., Duan, S. et al. (2019). Wound dressings based on rubidium-doped bioactive glass nanospheres promote diabetic wound healing. *Journal of Biomedical Nanotechnology* 15 (10): 2059–2071.

22 Li, H., Li, J., Jiang, J. et al. (2017). An osteogenesis/angiogenesis-stimulation artificial ligament for anterior cruciate ligament reconstruction. *Acta Biomaterialia* 54: 399–410.

23 Tien, Y.-C., Lin, J.-H., and Ju, C.-P. (2003). Method of enhancing healing of interfacial gap between bone and tendon or ligament. Google Patents, US 20030216777 A1, filed 16 May 2002 and issued 20 November 2003.

24 Wu, Y., Dong, Y., Chen, S., and Li, Y. (2014). Effect of platelet-rich plasma and bioactive glass powder for the improvement of rotator cuff tendon-to-bone healing in a rabbit model. *International Journal of Molecular Sciences* 15 (12): 21980–21991.

25 Lin, B., Dun, G., Jin, D., and Du, Y. (2019). Development of polypyrrole/collagen/nano-strontium substituted bioactive glass composite for boost sciatic nerve rejuvenation in vivo. *Artificial Cells, Nanomedicine, and Biotechnology* 47 (1): 3423–3430.

26 Souza, M.T., Peitl, O., Zanotto, E.D., and Boccaccini, A.R. (2016). Novel double-layered conduit containing highly bioactive glass fibers for potential nerve guide application. *International Journal of Applied Glass Science* 7 (2): 183–194.

27 Marquardt, L.M., Day, D., Sakiyama-Elbert, S.E., and Harkins, A.B. (2014). Effects of borate-based bioactive glass on neuron viability and neurite extension. *Journal of Biomedical Materials Research Part A* 102 (8): 2767–2775.

28 Jia, W., Hu, H., Li, A. et al. (2020). Glass-activated regeneration of volumetric muscle loss. *Acta Biomaterialia* 103: 306–317.

29 Ahmed, I., Collins, C., Lewis, M. et al. (2004). Processing, characterisation and biocompatibility of iron-phosphate glass fibres for tissue engineering. *Biomaterials* 25 (16): 3223–3232.

30 Shah, R., Knowles, J.C., Hunt, N.P., and Lewis, M.P. (2016). Development of a novel smart scaffold for human skeletal muscle regeneration. *Journal of Tissue Engineering and Regenerative Medicine* 10 (2): 162–171.

31 Liang, S.-L., Cook, W.D., Thouas, G.A., and Chen, Q.-Z. (2010). The mechanical characteristics and in vitro biocompatibility of poly(glycerol sebacate)-Bioglass® elastomeric composites. *Biomaterials* 31 (33): 8516–8529.

32 Chen, Q., Jin, L., Cook, W.D. et al. (2010). Elastomeric nanocomposites as cell delivery vehicles and cardiac support devices. *Soft Matter* 6 (19): 4715–4726.

33 Qi, Q., Zhu, Y., Liu, G. et al. (2020). Local intramyocardial delivery of bioglass with alginate hydrogels for post-infarct myocardial regeneration. *Biomedicine & Pharmacotherapy* 129: 110382.

34 Moosvi, S.R. and Day, R.M. (2009). Bioactive glass modulation of intestinal epithelial cell restitution. *Acta Biomaterialia* 5 (1): 76–83.

35 Ma, A.-n., Gong, N., Lu, J.-m. et al. (2013). Local protective effects of oral 45S5 bioactive glass on gastric ulcers in experimental animals. *Journal of Materials Science. Materials in Medicine* 24 (3): 803–809.

36 Paliwal, P., Kumar, A.S., Tripathi, H. et al. (2018). Pharmacological application of barium containing bioactive glass in gastro-duodenal ulcers. *Materials Science and Engineering C* 92: 424–434.

37 Raja, F.N., Worthington, T., Isaacs, M.A. et al. (2018). The antimicrobial efficacy of hypoxia mimicking cobalt oxide doped phosphate-based glasses against clinically relevant Gram positive, Gram negative bacteria and a fungal strain. *ACS Biomaterials Science & Engineering* 5 (1): 283–293.

38 Naik, M.N., Murthy, R.K., and Honavar, S.G. (2007). Comparison of vascularization of Medpor and Medpor-Plus orbital implants: a prospective, randomized study. *Ophthalmic Plastic & Reconstructive Surgery* 23 (6): 463–467.

39 Ma, X., Schou, K.R., Maloney-Schou, M. et al. (2011). The porous polyethylene/bioglass spherical orbital implant: a retrospective study of 170 cases. *Ophthalmic Plastic & Reconstructive Surgery* 27 (1): 21–27.

40 Wang, C., Jin, K., He, J. et al. (2018). Synergistic effect of copper-containing mesoporous bioactive glass coating on stimulating vascularization of porous hydroxyapatite orbital implants in rabbits. *Journal of Biomedical Nanotechnology* 14 (4): 688–697.

41 Brandão, S.M., Schellini, S.A., Moraes, A.D. et al. (2012). Biocompatibility analysis of Bioglass® 45S5 and Biosilicate® implants in the rabbit eviscerated socket. *Orbit* 31 (3): 143–149.

42 Brandão, S.M., Schellini, R.A., Peitl, O. et al. (2020). Conical biosilicate implant for volume augmentation in anophthalmic sockets. *The Journal of Craniofacial Surgery* 31 (6): 1838–1840.

43 Ye, J., He, J., Wang, C. et al. (2014). Copper-containing mesoporous bioactive glass coatings on orbital implants for improving drug delivery capacity and antibacterial activity. *Biotechnology Letters* 36 (5): 961–968.

44 Baino, F. (2018). Porous glass-ceramic orbital implants: a feasibility study. *Materials Letters* 212: 12–15.

45 Reck, R. (1984). Bioactive glass-ceramics in ear surgery: animal studies and clinical results. *The Laryngoscope* 94 (S33): 1–54.

46 Niparko, J.K., Kemink, J.L., Graham, M.D., and Kartush, J.M. (1988). Bioactive glass ceramic in ossicular reconstruction: a preliminary report. *The Laryngoscope* 98 (8): 822–825.

47 Babighian, G. (1984). Our experience with Ceravital® implants in middle ear surgery. (A middle term evaluation). In: *Biomaterials in Otology* (ed. J.J. Grote), 242–247. Springer.

48 Van Blitterswijk, C., Grote, J., De Groot, K. et al. (1986). The biological performance of calcium phosphate ceramics in an infected implantation site: I. Biological performance of hydroxyapatite during *Staphylococcus aureus* infection. *Journal of Biomedical Materials Research* 20 (7): 989–1002.

49 Rust, K.R., Singleton, G.T., Wilson, J., and Antonelli, P.J. (1996). Bioglass middle ear prosthesis: long-term results. *The American Journal of Otology* 17 (3): 371–374.

50 Reck, R., Störkel, S., and Meyer, A. (1988). Bioactive glass-ceramics in middle ear surgery. An 8-year review. *Annals of the New York Academy of Sciences* 523: 100–106.

51 Gunhan, K., Bariskan, S., Uz, U. et al. (2018). 13-93B3 bioactive glass: a new scaffold for transplantation of stem cell-derived chondrocytes. *The Journal of Craniofacial Surgery* 29 (1): 233–236.

52 Walliker, J., Carson, H., Douek, E. et al. (1987). An extracochlear auditory prosthesis. In: *Proceedings of the Cochlear Implant Symposium*, Düren, Germany (7–12 September), vol. 265 (ed. P. Banfai), 7–12. New York, NY: Springer.

53 Stoor, P., Pulkkinen, J., and Grénman, R. (2010). Bioactive glass S53P4 in the filling of cavities in the mastoid cell area in surgery for chronic otitis media. *Annals of Otology, Rhinology and Laryngology* 119 (6): 377–382.

54 Bernardeschi, D., Nguyen, Y., Russo, F.Y. et al. (2015). Cutaneous and labyrinthine tolerance of bioactive glass S53P4 in mastoid and epitympanic obliteration surgery: prospective clinical study. *BioMed Research International* 2015: 1–6.

55 Stoor, P., Söderling, E., and Grenman, R. (1999). Interactions between the bioactive glass S53P4 and the atrophic rhinitis-associated microorganism *Klebsiella ozaenae*. *Journal of Biomedical Materials Research* 48 (6): 869–874.

56 Rajzer, I., Dziadek, M., Kurowska, A. et al. (2019). Electrospun polycaprolactone membranes with Zn-doped bioglass for nasal tissues treatment. *Journal of Materials Science. Materials in Medicine* 30 (7): 80.

57 Stoor, P. and Grénman, R. (2004). Bioactive glass and turbinate flaps in the repair of nasal septal perforations. *Annals of Otology, Rhinology and Laryngology* 113 (8): 655–661.

58 Stoor, P., Söderling, E., and Grénman, R. (2001). Bioactive glass S53P4 in repair of septal perforations and its interactions with the respiratory infection-associated microorganisms *Heamophilus influenzae* and *Streptococcus pneumoniae*. *Journal of Biomedical Materials Research* 58 (1): 113–120.

59 Silverman, J.B., Gray, S.T., and Busaba, N.Y. (2012). Role of osteoplastic frontal sinus obliteration in the era of endoscopic sinus surgery. *International Journal of Otolaryngology* 2012: 1–5.

60 Rohrich, R.J. and Mickel, T.J. (1995). Frontal sinus obliteration: in search of the ideal autogenous material. *Plastic and Reconstructive Surgery* 95 (3): 580–585.

61 Hench, L.L., West, J.K., LaTorre, G., et al. (2001). Injectable bio-active glass in a dextran suspension. Google Patents, US 6,190,684 B1, filed 23 November 1998 and issued 20 February 2001.

62 Hench, L.L. and Greenspan, D. (2013). Interactions between bioactive glass and collagen: a review and new perspectives. *Journal of the Australian Ceramic Society* 49 (2): 1–40.

63 Hanada, K., Morotomi, T., Washio, A. et al. (2019). In vitro and in vivo effects of a novel bioactive glass-based cement used as a direct pulp capping agent. *Journal of Biomedical Materials Research Part B Applied Biomaterials* 107 (1): 161–168.

64 Washio, A., Morotomi, T., Yoshii, S., and Kitamura, C. (2019). Bioactive glass-based endodontic sealer as a promising root canal filling material without semisolid core materials. *Materials* 12 (23): 3967.

65 Jo, S.B., Kim, H.K., Lee, H.N. et al. (2020). Physical properties and biofunctionalities of bioactive root canal sealers in vitro. *Nanomaterials* 10 (9): 1750.

66 Washio, A., Oda, M., Morimoto, Y., and Kitamura, T. (2020). One-year follow-up of the first and second molars on the right side of the upper jaw sealed with single-point root canal filling using a sealer for root canals containing bio-active glass. *Japanese Journal of Dental Preservation* 63 (1): 90–95.

67 Zhu, N., Chatzistavrou, X., Ge, L. et al. (2019). Biological properties of modified bioactive glass on dental pulp cells. *Journal of Dentistry* 83: 18–26.

68 Ezzat, A.E. and El-Shenawy, H.M. (2015). Repair of cleft alveolar bone with bioactive glass material using Z-plasty flap. *International Journal of Applied & Basic Medical Research* 5 (3): 211.

69 Su, Z., Li, J., Bai, X. et al. (2020). Borate bioactive glass prevents zoledronate-induced osteonecrosis of the jaw by restoring osteogenesis and angiogenesis. *Oral Diseases* 26 (8): 1706–1717.

70 Heckbert, S.R., Vedder, N.B., Hoffman, W. et al. (1998). Outcome after hemorrhagic shock in trauma patients. *Journal of Trauma and Acute Care Surgery* 45 (3): 545–549.

71 Norris, E., Ramos-Rivera, C., Poologasundarampillai, G. et al. (2020). Electrospinning 3D bioactive glasses for wound healing. *Biomedical Materials* 15 (1): 015014.

72 Westhauser, F., Widholz, B., Nawaz, Q. et al. (2019). Favorable angiogenic properties of the borosilicate bioactive glass 0106-B1 result in enhanced in vivo osteoid formation compared to 45S5 Bioglass. *Biomaterials Science* 7 (12): 5161–5176.

73 Wu, C., Zhang, Z., Zhou, K. et al. (2020). Preparation and characterization of borosilicate bioglass incorporated sodium alginate composite wound dressing for accelerated full-thickness skin wound healing. *Biomedical Materials* 15 (5): 055009.

74 Chen, X., Li, S., Yan, Y. et al. (2020). Absorbable nanocomposites composed of mesoporous bioglass nanoparticles and polyelectrolyte complexes for surgical hemorrhage control. *Materials Science and Engineering C* 109: 110556.

75 Naseri, S., Lepry, W.C., and Nazhat, S.N. (2017). Bioactive glasses in wound healing: hope or hype? *Journal of Materials Chemistry B* 5 (31): 6167–6174.

76 Hu, G., Xiao, L., Tong, P. et al. (2012). Antibacterial hemostatic dressings with nanoporous bioglass containing silver. *International Journal of Nanomedicine* 7: 2613.

77 Mao, C., Chen, X., Miao, G., and Lin, C. (2015). Angiogenesis stimulated by novel nanoscale bioactive glasses. *Biomedical Materials* 10 (2): 025005–025016.

78 Nwomeh, B.C., Yager, D.R., and Cohen, I.K. (1998). Physiology of the chronic wound. *Clinics in Plastic Surgery* 25 (3): 341–356.

79 Dong, X., Chang, J., and Li, H. (2017). Bioglass promotes wound healing through modulating the paracrine effects between macrophages and repairing cells. *Journal of Materials Chemistry B* 5 (26): 5240–5250.

80 Majumdar, S., Hira, S.K., Tripathi, H. et al. (2020). Synthesis and characterization of barium-doped bioactive glass with potential anti-inflammatory activity. *Ceramics International* 47 (5): 7143–7158.

81 Zouraq, F.A., Stölting, M., and Eberli, D. (2013). Skeletal muscle regeneration for clinical application. In: *Regenerative Medicine and Tissue Engineering* (ed. J.A. Andrades). IntechOpen.

82 Liu, J., Saul, D., Böker, K.O. et al. (2018). Current methods for skeletal muscle tissue repair and regeneration. *BioMed Research International* 2018: 1–11.

83 Porzionato, A., Sfriso, M.M., Pontini, A. et al. (2015). Decellularized human skeletal muscle as biologic scaffold for reconstructive surgery. *International Journal of Molecular Sciences* 16 (7): 14808–14831.

84 Patel, K.H., Dunn, A.J., Talovic, M. et al. (2019). Aligned nanofibers of decellularized muscle ECM support myogenic activity in primary satellite cells in vitro. *Biomedical Materials* 14 (3): 035010.

85 Shah, R., Ready, D., Knowles, J.C. et al. (2014). Sequential identification of a degradable phosphate glass scaffold for skeletal muscle regeneration. *Journal of Tissue Engineering and Regenerative Medicine* 8 (10): 801–810.

86 Shah, R., Sinanan, A., Knowles, J. et al. (2005). Craniofacial muscle engineering using a 3-dimensional phosphate glass fibre construct. *Biomaterials* 26 (13): 1497–1505.

87 Bitar, M., Knowles, J., Lewis, M., and Salih, V. (2005). Soluble phosphate glass fibres for repair of bone-ligament interface. *Journal of Materials Science. Materials in Medicine* 16 (12): 1131–1136.

88 Smith, S.A. (1918). The diagnosis and treatment of injuries to the crucial ligaments. *British Journal of Surgery* 6 (22): 176–189.

89 Parchi, P.D., Ciapini, G., Paglialunga, C. et al. (2018). Anterior cruciate ligament reconstruction with LARS artificial ligament – clinical results after a long-term follow-up. *Joints* 6 (2): 75.

90 Donelli, I., Taddei, P., Smet, P.F. et al. (2009). Enzymatic surface modification and functionalization of PET: a water contact angle, FTIR, and fluorescence spectroscopy study. *Biotechnology and Bioengineering* 103 (5): 845–856.

91 Huang, Z., Bi, L., Zhang, Z., and Han, Y. (2012). Effects of dimethylolpropionic acid modification on the characteristics of polyethylene terephthalate fibers. *Molecular Medicine Reports* 6 (4): 709–715.

92 Pu, F., Williams, R., Markkula, T., and Hunt, J. (2002). Effects of plasma treated PET and PTFE on expression of adhesion molecules by human endothelial cells in vitro. *Biomaterials* 23 (11): 2411–2428.

93 Kehoe, S., Langman, M., Werner-Zwanziger, U. et al. (2012). Mixture designs to assess composition–structure–property relationships in SiO_2–CaO–ZnO–La_2O_3–TiO_2–MgO–SrO–Na_2O glasses: potential materials for embolization. *Journal of Biomaterials Applications* 28 (3): 416–433.

94 Miller, B.S., Downie, B.K., Kohen, R.B. et al. (2011). When do rotator cuff repairs fail? Serial ultrasound examination after arthroscopic repair of large and massive rotator cuff tears. *American Journal of Sports Medicine* 39 (10): 2064–2070.

95 Wen, Y.-H., Lin, W.-Y., Lin, C.-J. et al. (2018). Sustained or higher levels of growth factors in platelet-rich plasma during 7-day storage. *Clinica Chimica Acta* 483: 89–93.

96 Andersson-Rolf, A., Zilbauer, M., Koo, B.-K., and Clevers, H. (2017). Stem cells in repair of gastrointestinal epithelia. *Physiology* 32 (4): 278–289.

97 Aihara, E., Matthis, A.L., Karns, R.A. et al. (2016). Epithelial regeneration after gastric ulceration causes prolonged cell-type alterations. *Cellular and Molecular Gastroenterology and Hepatology* 2 (5): 625–647.

98 Arakawa, T., Watanabe, T., Tanigawa, T. et al. (2012). Quality of ulcer healing in gastrointestinal tract: its pathophysiology and clinical relevance. *World Journal of Gastroenterology* 18 (35): 4811.

99 Mills, J.C. and Shivdasani, R.A. (2011). Gastric epithelial stem cells. *Gastroenterology* 140 (2): 412–424.

100 Sanders, S.W. (1996). Pathogenesis and treatment of acid peptic disorders: comparison of proton pump inhibitors with other antiulcer agents. *Clinical Therapeutics* 18 (1): 2–34.

101 Boccaccini, A.R., Blaker, J.J., Maquet, V. et al. (2005). Preparation and characterisation of poly(lactide-*co*-glycolide) (PLGA) and PLGA/Bioglass® composite tubular foam scaffolds for tissue engineering applications. *Materials Science and Engineering C* 25 (1): 23–31.

102 Matter, M.T., Starsich, F., Galli, M. et al. (2017). Developing a tissue glue by engineering the adhesive and hemostatic properties of metal oxide nanoparticles. *Nanoscale* 9 (24): 8418–8426.

103 Okamoto, R. and Watanabe, M. (2004). Molecular and clinical basis for the regeneration of human gastrointestinal epithelia. *Journal of Gastroenterology* 39 (1): 1–6.

104 Zittel, T., Jehle, E., and Becker, H. (2000). Surgical management of peptic ulcer disease today – indication, technique and outcome. *Langenbeck's Archives of Surgery* 385 (2): 84–96.

105 Yamamoto, T. (2005). Factors affecting recurrence after surgery for Crohn's disease. *World Journal of Gastroenterology* 11 (26): 3971.

106 Petersen, T.H., Calle, E.A., and Niklason, L.E. (2011). Strategies for lung regeneration. *Materials Today* 14 (5): 196–201.

107 Wu, Z., Huang, Z., Wu, Y. et al. (2019). Sedentary time, metabolic abnormalities, and all-cause mortality after myocardial infarction: a mediation analysis. *European Journal of Preventive Cardiology* 26 (1): 96–104.

108 Matteucci, M., Fina, D., Jiritano, F. et al. (2019). Treatment strategies for post-infarction left ventricular free-wall rupture. *European Heart Journal Acute Cardiovascular Care* 8 (4): 379–387.

109 Barabadi, Z., Azami, M., Sharifi, E. et al. (2016). Fabrication of hydrogel based nanocomposite scaffold containing bioactive glass nanoparticles for myocardial tissue engineering. *Materials Science and Engineering C* 69: 1137–1146.

110 Aitasalo, K., Kinnunen, I., Palmgren, J., and Varpula, M. (2001). Repair of orbital floor fractures with bioactive glass implants. *Journal of Oral and Maxillofacial Surgery* 59 (12): 1390–1395.

111 Kinnunen, I., Aitasalo, K., Pöllönen, M., and Varpula, M. (2000). Reconstruction of orbital floor fractures using bioactive glass. *Journal of Cranio-Maxillofacial Surgery* 28 (4): 229–234.

112 Peltola, M., Kinnunen, I., and Aitasalo, K. (2008). Reconstruction of orbital wall defects with bioactive glass plates. *Journal of Oral and Maxillofacial Surgery* 66 (4): 639–646.

113 Huhtinen, R., Sandeman, S., Rose, S. et al. (2013). Examining porous bio-active glass as a potential osteo-odonto-keratoprosthetic skirt material. *Journal of Materials Science. Materials in Medicine* 24 (5): 1217–1227.

114 Laattala, K., Huhtinen, R., Puska, M. et al. (2011). Bioactive composite for keratoprosthesis skirt. *Journal of the Mechanical Behavior of Biomedical Materials* 4 (8): 1700–1708.

115 Xu, X., Wang, C., Huang, T. et al. (1997). An experimental study of bioactive glass ceramics as orbital implants. *Hunan yi ke da xue xue bao = Hunan yike daxue xuebao = Bulletin of Hunan Medical University* 22 (1): 25.

116 Xu, X., Huang, Z., and Wang, C. (1997). Clinical study of bioactive glass ceramics as orbital implants. *Hunan yi ke da xue xue bao = Hunan yike daxue xuebao = Bulletin of Hunan Medical University* 22 (5): 440–442.

117 Baino, F., di Confiengo, G.G., and Faga, M.G. (2018). Fabrication and morphological characterization of glass-ceramic orbital implants. *International Journal of Applied Ceramic Technology* 15 (4): 884–891.

118 Choi, H.Y., Lee, J.-E., Park, H.J., and Oum, B.S. (2006). Effect of synthetic bone glass particulate on the fibrovascularization of porous polyethylene orbital implants. *Ophthalmic Plastic & Reconstructive Surgery* 22 (2): 121–125.

119 Bigar, F., Krähenmann, A., Landolt, E., and Witmer, R. (1978). Biocompatibility of bioactive glass-ceramic in cornea and conjunctiva. *Bericht über die Versammlung der Deutschen Ophthalmologische Gesellschaft* 75: 192–196.

120 Strunz, V., Bunte, M., Gross, U. et al. (1978). Glass-ceramic keratoprosthesis. *Bericht über die Versammlung der Deutschen Ophthalmologische Gesellschaft* 75: 197–200.

121 Blencke, B.-A., Hagen, P., Brömer, H., and Deutscher, K. (1978). Studies on the usability of glass ceramics to osteo-odonto-keratoplasty. *Ophthalmologica* 176 (2): 105–112.

122 Krause, A. (1992). Intracorneal biocompatibility of glass ceramics. *Eye & Contact Lens* 18 (3): 212.

123 Linnola, R., Happonen, R.-P., Andersson, Ö. et al. (1996). Titanium and bioactive glass-ceramic coated titanium as materials for keratoprosthesis. *Experimental Eye Research* 63 (4): 471–478.

124 Liang, D., Chen, J., Li, Y. et al. (2001). Tissue interaction with bioglass ceramic implanted in the rabbit cornea. *Yan ke xue bao = Eye science* 17 (4): 198–201.

125 Santos, L., Ferraz, M.P., Shirosaki, Y. et al. (2011). Degradation studies and biological behavior on an artificial cornea material. *Investigative Ophthalmology & Visual Science* 52 (7): 4274–4281.

126 Hicks, C.R., Fitton, J.H., Chirila, T.V. et al. (1997). Keratoprostheses: advancing toward a true artificial cornea. *Survey of Ophthalmology* 42 (2): 175–189.

127 Lu, L., Yaszemski, M.J., and Mikos, A.G. (2001). Retinal pigment epithelium engineering using synthetic biodegradable polymers. *Biomaterials* 22 (24): 3345–3355.

128 Henrique Lima, T., Fernandes-Cunha, G.M., Jensen, C.E.M. et al. (2016). Bioactive glass nanoparticles-loaded poly(ε-caprolactone) nanofiber as substrate for ARPE-19 cells. *Journal of Nanomaterials* 2016: 1–12.

129 Scully, C., Miller, C.S., Urizar, J.-M.A. et al. (2016). Oral medicine (stomatology) across the globe: birth, growth, and future. *Oral Surgery, Oral Medicine, Oral Pathology, and Oral Radiology* 121 (2): 149–157.e5.

130 Qureshi, A., Soujanya, E., and Nandakumar, P. (2014). Recent advances in pulp capping materials: an overview. *Journal of Clinical and Diagnostic Research* 8 (1): 316.

131 Salako, N., Joseph, B., Ritwik, P. et al. (2003). Comparison of bioactive glass, mineral trioxide aggregate, ferric sulfate, and formocresol as pulpotomy agents in rat molar. *Dental Traumatology* 19 (6): 314–320.

132 Roberts, H.W., Toth, J.M., Berzins, D.W., and Charlton, D.G. (2008). Mineral trioxide aggregate material use in endodontic treatment: a review of the literature. *Dental Materials* 24 (2): 149–164.

133 Gandolfi, M., Siboni, F., and Prati, C. (2016). Properties of a novel polysiloxane-guttapercha calcium silicate-bioglass-containing root canal sealer. *Dental Materials* 32 (5): e113–e126.

134 Akcay, M., Arslan, H., Durmus, N. et al. (2016). Dentinal tubule penetration of AH Plus, iRoot SP, MTA fillapex, and guttaflow bioseal root canal sealers after different final irrigation procedures: a confocal microscopic study. *Lasers in Surgery and Medicine* 48 (1): 70–76.

135 Collado-González, M., Tomás-Catalá, C.J., Oñate-Sánchez, R.E. et al. (2017). Cytotoxicity of GuttaFlow Bioseal, GuttaFlow2, MTA Fillapex, and AH Plus on human periodontal ligament stem cells. *Journal of Endodontics* 43 (5): 816–822.

136 Washio, A., Nakagawa, A., Nishihara, T. et al. (2015). Physicochemical properties of newly developed bioactive glass cement and its effects on various cells. *Journal of Biomedical Materials Research Part B Applied Biomaterials* 103 (2): 373–380.

137 Washio, A., Yoshii, S., Morotomi, T. et al. (2017). Effects of bioactive glass based sealer on cell migration ability and viability of periodontal ligament cells and osteoblast-like cells. *The Japanese Journal of Conservative Dentistry* 60: 96–104.

138 Yoshii, S., Washio, A., Morotomi, T., and Kitamura, C. (2016). Root canal sealing ability of bioactive glass-based sealer and its effects on dentin. *The Japanese Journal of Conservative Dentistry* 59: 463–471.

139 Zero, D.T., Fontana, M., Martínez-Mier, E.A. et al. (2009). The biology, prevention, diagnosis and treatment of dental caries: scientific advances in the United States. *The Journal of the American Dental Association* 140: 25S–34S.

140 Selwitz, R.H., Ismail, A.I., and Pitts, N.B. (2007). Dental caries. *The Lancet* 369 (9555): 51–59.

141 Traini, T., Mangano, C., Sammons, R. et al. (2008). Direct laser metal sintering as a new approach to fabrication of an isoelastic functionally graded material for manufacture of porous titanium dental implants. *Dental Materials* 24 (11): 1525–1533.

142 Wang, S., Hu, Q., Gao, X., and Dong, Y. (2016). Characteristics and effects on dental pulp cells of a polycaprolactone/submicron bioactive glass composite scaffold. *Journal of Endodontics* 42 (7): 1070–1075.

143 Barros, S.A.L., Soares, D.G., Leite, M.L. et al. (2019). Influence of zirconia-coated bioactive glass on gingival fibroblast behavior. *Brazilian Dental Journal* 30 (4): 333–341.

144 Elshazly, N., Khalil, A., Saad, M. et al. (2020). Efficacy of bioactive glass nanofibers tested for oral mucosal regeneration in rabbits with induced diabetes. *Materials* 13 (11): 2603.

145 Coskun Benlidayi, I. and Guzel, R. (2013). Oral bisphosphonate related osteonecrosis of the jaw: a challenging adverse effect. *ISRN Rheumatology* 2013: 1–6.

146 Gatti, G.L., Freda, N., Giacomina, A. et al. (2017). Cleft lip and palate repair. *The Journal of Craniofacial Surgery* 28 (8): 1918–1924.

147 Santos, M.I. and Reis, R.L. (2010). Vascularization in bone tissue engineering: physiology, current strategies, major hurdles and future challenges. *Macromolecular Bioscience* 10 (1): 12–27.

148 Martín-del-Campo, M., Rosales-Ibañez, R., and Rojo, L. (2019). Biomaterials for cleft lip and palate regeneration. *International Journal of Molecular Sciences* 20 (9): 2176.

149 Trojanowska, A., Drop, A., Trojanowski, P. et al. (2012). External and middle ear diseases: radiological diagnosis based on clinical signs and symptoms. *Insights Into Imaging* 3 (1): 33–48.

150 Sarkar, S. (2013). A review on the history of tympanoplasty. *Indian Journal of Otolaryngology and Head & Neck Surgery* 65 (3): 455–460.

151 Wullstein, H. (1953). Functional operations in the middle ear with split-thickness skin graft. *Archives of Otorhinolaryngology* 161: 422–435.

152 Zöllner, F. (1955). The principles of plastic surgery of the sound-conducting apparatus. *Journal of Laryngology & Otology* 69 (10): 637–652.

153 Della Santina, C.C. and Lee, S.C. (2006). Ceravital reconstruction of canal wall down mastoidectomy: long-term results. *Archives of Otolaryngology – Head & Neck Surgery* 132 (6): 617–623.

154 Leatherman, B.D. and Dornhoffer, J.L. (2002). Bioactive glass ceramic particles as an alternative for mastoid obliteration: results in an animal model. *Otology & Neurotology* 23 (5): 657–660.

155 Silvola, J.T. (2012). Mastoidectomy cavity obliteration with bioactive glass: a pilot study. *Otolaryngology–Head and Neck Surgery* 147 (1): 119–126.

156 Ylänen, H. (2017). *Bioactive Glasses: Materials, Properties and Applications*. Woodhead Publishing.

157 Bahmad, F. Jr., and Merchant, S.N. (2007). Histopathology of ossicular grafts and implants in chronic otitis media. *Annals of Otology, Rhinology and Laryngology* 116 (3): 181–191.

158 Schmid, S., Felix, H., and Böhmer, A. (1988). Histological study of the binding of Polycel and Ceravital implants to the stapes footplate in rabbits. *HNO* 36 (6): 221–225.

159 Zikk, D., Rapoport, Y., Bloom, J., and Himelfarb, M. (1990). Auditory brain-stem responses in guinea pigs following middle ear implantation of Ceravital. *European Archives of Oto-Rhino-Laryngology* 248 (2): 102–104.

160 Massuda, E.T., Maldonado, L.L., de Lima Júnior, J.T. et al. (2009). Biosilicate® ototoxicity and vestibulotoxicity evaluation in guinea-pigs. *Brazilian Journal of Otorhinolaryngology* 75 (5): 665–668.

161 Merwin, G.E., Atkins, J.S., Wilson, J., and Hench, L.L. (1982). Comparison of ossicular replacement materials in a mouse ear model. *Otolaryngology–Head and Neck Surgery* 90 (4): 461–469.

162 Dost, P., Ellermann, S., Missfeldt, N.N. et al. (2002). Reconstruction of the stapes superstructure with a combined glass-ceramic (Bioverit®) implant in guinea pigs. *ORL* 64 (6): 429–432.

163 Duda, F., Bradel, S., Bleich, A. et al. (2015). Biocompatibility of silver containing silica films on Bioverit® II middle ear prostheses in rabbits. *Journal of Biomaterials Applications* 30 (1): 17–29.

164 Lindfors, N., Geurts, J., Drago, L. et al. (2016). Antibacterial bioactive glass, S53P4, for chronic bone infections – a multinational study. In: *Adv Exp Med Biol - Advances in Microbiology, Infectious Diseases and Public Health*, 81–92. Springer International Publishing Switzerland.

165 Downing, M., Johansson, U., Carlsson, L. et al. (1997). A bone-anchored percutaneous connector system for neural prosthetic applications. *Ear, Nose, and Throat Journal* 76 (5): 328–332.

166 Fischer, H. and Gubisch, W. (2008). Nasal reconstruction: a challenge for plastic surgery. *Deutsches Ärzteblatt International* 105 (43): 741.

167 Moore, E.J. and Kern, E.B. (2001). Atrophic rhinitis: a review of 242 cases. *American Journal of Rhinology* 15 (6): 355–361.

168 Dutt, S.N. and Kameswaran, M. (2005). The aetiology and management of atrophic rhinitis. *Journal of Laryngology & Otology* 119 (11): 843–852.

169 Downs, B.W. and Sauder, H.M. (2020). *Septal Perforation*. StatPearls Publishing.

170 Kridel, R.W., Foda, H., and Lunde, K.C. (1998). Septal perforation repair with acellular human dermal allograft. *Archives of Otolaryngology – Head & Neck Surgery* 124 (1): 73–78.

171 Bell, R.B. (2009). Management of frontal sinus fractures. *Oral and Maxillofacial Surgery Clinics of North America* 21 (2): 227–242.

172 Aitasalo, K., Suonpää, J., Peltola, M., and Yli-Urpo, A. (1997). Behaviour of bioactive glass (S53P4) in human frontal sinus obliteration. *Bioceramics* 10: 429–432.

173 Peltola, M., Suonpää, J., Aitasalo, K. et al. (1998). Obliteration of the frontal sinus cavity with bioactive glass. *Head & Neck: Journal of the Sciences and Specialties of the Head and Neck* 20 (4): 315–319.

174 Turunen, T., Peltola, J., Yli-Urpo, A., and Happonen, R.P. (2004). Bioactive glass granules as a bone adjunctive material in maxillary sinus floor augmentation. *Clinical Oral Implants Research* 15 (2): 135–141.

175 Stavropoulos, A., Sima, C., Sima, A. et al. (2012). Histological evaluation of healing after transalveolar maxillary sinus augmentation with bioglass and autogenous bone. *Clinical Oral Implants Research* 23 (1): 125–131.

176 Tadjoedin, E.S., De Lange, G.L., Lyaruu, D. et al. (2002). High concentrations of bioactive glass material (BioGran®) vs. autogenous bone for sinus floor elevation: histomorphometrical observations on three split mouth clinical cases. *Clinical Oral Implants Research* 13 (4): 428–436.

177 Kirker-Head, C.A., Nevins, M., Palmer, R. et al. (1997). A new animal model for maxillary sinus floor augmentation: evaluation parameters. *International Journal of Oral and Maxillofacial Implants* 12 (3): 1–17.

178 Tadjoedin, E.S., De Lange, G.L., Holzmann, P.J. et al. (2000). Histological observations on biopsies harvested following sinus floor elevation using a bioactive glass material of narrow size range. *Clinical Oral Implants Research* 11 (4): 334–344.

179 Flint, P.W., Corio, R.L., and Cummings, C.W. (1997). Comparison of soft tissue response in rabbits following laryngeal implantation with hydroxylapatite, silicone rubber, and Teflon. *Annals of Otology, Rhinology and Laryngology* 106 (5): 399–407.

180 Cummings, C.W., Purcell, L.L., and Flint, P.W. (1993). Hydroxylapatite laryngeal implants for medialization: preliminary report. *Annals of Otology, Rhinology and Laryngology* 102 (11): 843–851.

181 Stoor, P., Mesimäki, K., Lindqvist, C., and Kontio, R. (2015). The use of anatomically drop-shaped bioactive glass S53P4 implants in the reconstruction of orbital floor fractures – a prospective long-term follow-up study. *Journal of Cranio-Maxillofacial Surgery* 43 (6): 969–975.

182 Yokoi, T., Miyazaki, T., Kawashita, M., and Ohtsuki, C. (2017). Bioactive glass-ceramics. In: *Nanobioceramics for Healthcare Applications* (ed. E.S. Thian, J. Huang and M. Aizawa), 213–237. World Scientific.

183 Reck, R. (1983). Bioactive glass ceramic: a new material in tympanoplasty. *The Laryngoscope* 93 (2): 196–199.

184 Gupta, K., Grigoryan, L., and Trautner, B. (2017). Urinary tract infection. *Annals of Internal Medicine* 167 (7): ITC49–ITC64.

185 Trautner, B.W. and Darouiche, R.O. (2004). Role of biofilm in catheter-associated urinary tract infection. *American Journal of Infection Control* 32 (3): 177–183.

186 Raja, F.N., Worthington, T., Isaacs, M.A. et al. (2019). The antimicrobial efficacy of zinc doped phosphate-based glass for treating catheter associated urinary tract infections. *Materials Science and Engineering C* 103: 109868.

187 Ross, E.A., Batich, C.D., Clapp, W.L. et al. (2003). Tissue adhesion to bioactive glass-coated silicone tubing in a rat model of peritoneal dialysis catheters and catheter tunnels. *Kidney International* 63 (2): 702–708.

21

Bioactive Glasses as Biologically Active Materials for Healing of Skin Wounds

Tina Mehrabi, Abdorreza S. Mesgar, and Zahra Mohammadi

Biomaterials Laboratory, Division of Biomedical Engineering, Department of Life Science Engineering, Faculty of New Sciences and Technologies, University of Tehran, Tehran, Iran

Abbreviations

bFGF	Basic fibroblast growth factor
ECM	Extracellular matrix
HCA	Hydroxycarbonate apatite
HDF	Human dermal fibroblast
HUVEC	Human umbilical vein endothelial cell
IL-6	Interleukin 6
NMR	Nuclear magnetic resonance
PDGF	Platelet-derived growth factor
TNF-α	Tumor necrosis factor-alpha
VEGF	Vascular endothelial growth factor

21.1 Introduction

Since the invention of 45S5 bioactive glass ($45.0SiO_2$–$24.5Na_2O$–$24.5CaO$–$6.0P_2O_5$ [wt%]) as the first generation of materials with the ability to bond to living tissues, bioactive glasses have opened the gates for developing bioceramics with the aim of hard tissue repair and regeneration [1, 2]. The mechanism of bone-bonding relies on the bioactivity of glasses, and the concept of bioactivity arises from the formation of hydroxycarbonate apatite (HCA) at the surface of glasses in contact with physiological fluids [1, 2]. Over the years, the possible potential of bioactive glasses for the regeneration of cardiac tissue [3], peripheral nerve [4] and spinal cord injuries [5], cancer treatment [6], gastrointestinal applications [7], and wound healing [8] have been investigated more intensively, which has extended the concept of bioactivity.

All over the world, wound healing is still one of the main challenges in healthcare systems since the healing process may be more complicated by the presence of underlying diseases, diversity of wound types, and aging population [9, 10]. In some cases, the wounds fail to progress over the natural healing phases, and the conventional therapeutic approach may be ineffective in treating these

Bioactive Glasses and Glass-Ceramics: Fundamentals and Applications, First Edition.
Edited by Francesco Baino and Saeid Kargozar.

nonhealing wounds [9]. Thus, advanced therapeutic approaches should be undertaken to fulfill the unmet requirements of the healing process [9]. The ongoing improvement of wound dressings and skin substitutes composed of natural and synthetic materials (e.g. polymers), biomolecules, and drugs associated with growth factors and cells is bringing hope to successfully restore the missing skin tissue [11, 12].

Until now, various compositions and forms (e.g. nano/microparticles, fibers, and scaffolds) of melt-derived or sol–gel-derived bioactive glasses have been applied alone or in combination with polymeric materials [13]. Furthermore, different biologically active elements including silver (Ag) [14], gold (Au) [15], copper (Cu) [16], cobalt (Co) [17], gallium (Ga) [18], selenium (Se) [19], and zinc (Zn) [14] can be incorporated in the glass composition, and the gradual release of them in physiological environments may stimulate multiple cell functions and elicit angiogenesis, anti-inflammatory, and antibacterial effects. As a result, the multifunctionality and tunability of bioactive glasses have motivated researchers to use their beneficial effects for accelerating the wound healing process. Additionally, the development of mesoporous bioactive glasses by Yan et al. [20] has led to utilizing these nanostructured materials as delivery systems of drugs and biomolecules besides the local release of therapeutic ions [21]. This approach has further improved the functionality of bioactive glasses in tissue regeneration due to the synergistic effect of ions and biomolecules/drugs in biological responses, for example, angiogenesis and antibacterial activity [21].

This chapter aims to present an overview of the possible mechanisms of bioactive glasses containing biologically active elements in the wound healing process. To this end, the biological effects of bioactive glasses and the role of their ionic products in the wound environment and healing stages are discussed, and the investigations on the specific role of bioactive glasses incorporated into the wound dressings and skin tissue engineering scaffolds are summarized.

21.2 The Healing Process of Skin Wounds and Wound Care Approaches

Skin is an active immune organ in the human body, which serves as a protective barrier against ultraviolet radiation, micro-organisms, harmful chemical substances, and physical damages [22]. The disruption of normal structure and functionality of the skin may lead to the formation of skin wounds [23]. These injuries can arise from accidents, burns, or surgeries. Based on the severity of the damage, skin layers comprised of epidermis, dermis, and hypodermis, and even muscles or bones may be affected [11, 12].

Wound healing is a physiological process that immediately initiates after the injury to restore the native structure and functions of the skin. This process is regulated by different cell types and chemical mediators and includes four distinct but overlapping phases of hemostasis, inflammation, proliferation, and remodeling [24]. Unlike the acute wounds that heal in a reasonable time, the healing of chronic wounds is prolonged and stuck in one of the phases of healing [25]. The normal healing process may be impaired or delayed due to several local and systemic factors such as infection, malnutrition, ischemia, aging, and diseases [26, 27].

Different wound care approaches have been emerged owing to the diversity of the nature and characteristics of wounds. Generally, skin grafts may be a preferable choice for surgeons and clinicians in severe burn injuries and chronic wounds, relying on their clinical experience [28]. However, the limitations of the grafting method have attracted considerable attention for developing tissue engineering products and skin substitutes for the treatment of severe skin injuries [29].

Additionally, according to the wound type, biomaterial-based temporary wound dressings may be selected to shield the wounds and provide a better environment to facilitate the healing process [30].

The first generation of dressings was developed to protect the wound against external contamination and trauma [25, 31]. Gauze dressings are a known example of these traditional coverings, and they are still available in the market. However, their drawbacks, including being unable to provide a moist environment and absorb excess wound exudate, have limited their application [32]. Although these dressings met the basic requirements of wound healing, they were mainly based on passive materials that did not play an active role in the healing process. Understanding the importance of a moist wound environment for cell metabolism and functions of growth factors and optimal wound healing requirements revolutionized the traditional wound care approaches [32]. Over time, modern dressings such as polyurethane films, hydrocolloids, hydrogels, foams, and fibers appeared in the market to compensate for the ineffectiveness of traditional dressings [24].

Furthermore, wound dressings with different physical forms (e.g. fiber, film, hydrogel, and sponge) based on natural and synthetic polymers containing antimicrobial agents, drugs, and biomolecules were investigated to promote the healing process more effectively [33, 34]. Interestingly, bioceramics were also identified as potential materials for soft tissue repair and regeneration [35]. Bioactive glasses are among the widely discussed types of bioceramics in regenerative medicine of soft tissues, including wound healing [36–38].

21.3 Overview of Bioactive Glass Structure

Bioactive glasses are amorphous materials with the atomic arrangement of short-range order in which this specific atomic organization is related to their composition [39]. Generally, the components of bioactive glasses are divided into three main oxide groups, including network forming oxides, intermediate oxides, and network modifying oxides [40]. As the main constituent of bioactive glasses, network-forming oxides are able to form the glass backbone. The most common network forming oxides in bioactive glasses are SiO_2, B_2O_3, and P_2O_5 [40]. Intermediate oxides such as ZnO, MgO, TiO_2, and Al_2O_3 may behave as a network former or network modifier depending on the glass composition [40]. Network modifiers are the oxides of alkali or alkaline earth metals such as CaO, Na_2O, and K_2O that disrupt the glass network by altering the bridging oxygen between network forming elements to nonbridging oxygen [40].

According to the type of network former in the glass composition, bioactive glasses are classified into the silicate, borate, or phosphate-based ones. In silicate glasses, the basic structural unit is SiO_4 tetrahedron, which can be linked to other silica tetrahedra by (Si—O—Si) covalent bonds [41]. The incorporation of modifier cations (M^+) into the glass network can disrupt the Si—O—Si bonds by altering the bridging oxygen atom to a nonbridging oxygen atom that leads to the formation of Si—O—M^+ bonds [42]. When the number of modifier cations increases in the glass structure, the average number of bridging oxygen per network forming atom decrease, that leads to the decrease in network polymerization or connectivity and chemical stability of the obtained glass [43].

In borate glasses, BO_3 trigonal groups are present as basic structural units. When modifier cations are added to these glasses, the trigonal groups transform into the BO_4 tetrahedral units, which increase the network connectivity of glass. The addition of higher amounts of modifying oxides can lead to the conversion of BO_4 to BO_3 groups and an increase in the number of nonbridging oxygen [41, 44]. This behavior, called “boron anomaly,” can be used to tune the glass properties

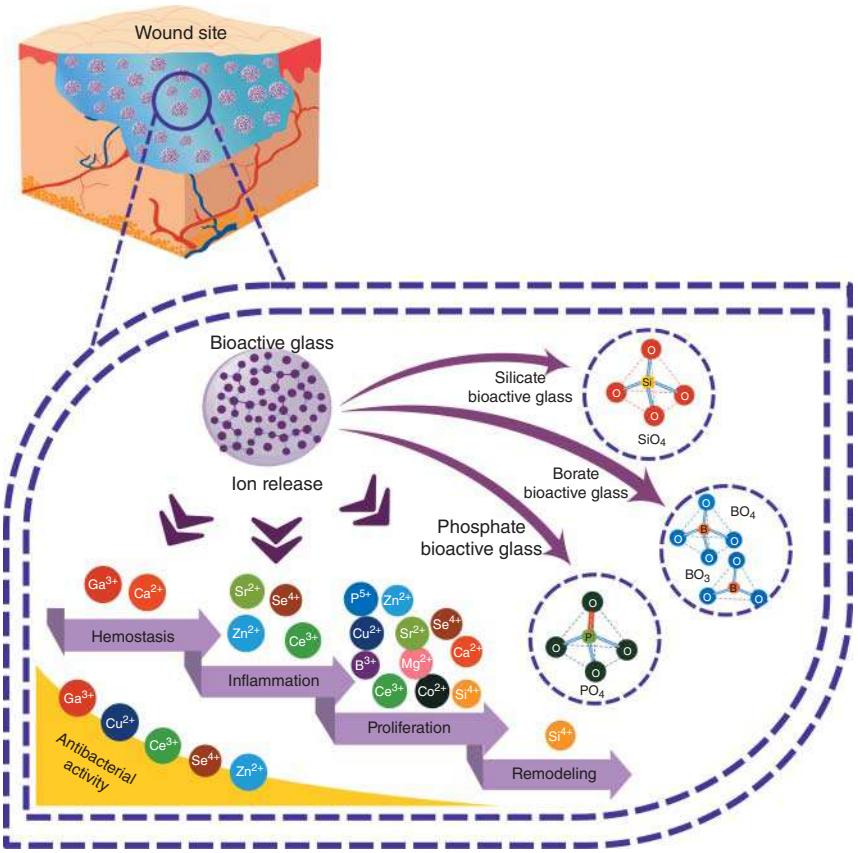

Figure 21.1 Schematic representation of silicate-, borate-, and phosphate-based bioactive glasses structural units and the biological effects of their dissolution products in different stages of the wound healing process. Source: Tina Mehrabi.

such as stability [45]. For example, it is reported that the addition of copper as a modifier cation to the borosilicate glass has led to the BO_3 to BO_4 transformation and more stable glass. The obtained Cu-doped glass showed a slower degradation rate and sustained release of copper ions with the potential application in wound healing [46].

The structural unit of phosphate glasses is the orthophosphate tetrahedron (PO_4^{3-}) in which the phosphorous atom is connected to three oxygen atoms by single bonds and one oxygen atom by a double bond [47]. Thus, the phosphate tetrahedron is able to connect to a maximum of three other phosphate tetrahedra with its three single-bonded oxygen atoms [47]. The basic structural units of silicate, borate, and phosphate-based bioactive glasses are presented in Figure 21.1. The structural building units of bioactive glasses are denoted as Q^n species, where Q defines network-forming polyhedron and n is the number of bridging oxygen atoms [47]. The structural changes and distribution of Q^n species in the glass network upon changing the composition of glasses can be determined by nuclear magnetic resonance (NMR) spectroscopy [44]. This structural assessment may provide insight into the dissolution rate of glasses, which are correlated with the glass composition [46]. Investigating the glass dissolution behavior is necessary due to the importance of the controlled release of therapeutic ions for targeting specific disease conditions, including different types of wounds.

21.4 Metallic, Metalloid, and Nonmetallic Elements: The Main Role Players of Biological Effects of Bioactive Glasses in Human Body

Several metallic, metalloid, and nonmetallic elements of the periodic table can be incorporated into the glass network to obtain glass composition with specific properties [13]. According to the literature, ionic dissolution products of bioactive glasses are key players for inducing different biological responses in the target tissue, including wound site [13], which is illustrated in Figure 21.1. Generally, several chemical elements are present in the human body to maintain a healthy state by regulating body fluids and acid–base balance and by involving in cell functions and enzymatic reactions [48]. On the other hand, some of these elements have specific biological roles in the human body, making them a potential candidate for biomaterial-based therapeutic purposes. Although the biological effects of the elements are in a dose-dependent manner, and there is an optimal concentration range for the following ionic products to be effective in the human body [49, 50]. Table 21.1 presents a brief overview of the most investigated elements found in the composition of bioactive glasses, emphasizing their biological effects in wound healing.

Table 21.1 A summary of the reported biological roles relevant to chemical elements that can affect skin wound healing.

Element	Biological effects
Boron (B)	– Involving in the inflammatory response, cell membrane maintenance [51], and synthesis of ECM [52] – Stimulating the release of TNF-α in fibroblasts [53] – Stimulatory effect on migration of fibroblasts [54] and keratinocytes [55] – Enhancing angiogenesis [54]
Calcium (Ca)	– Modulating cell proliferation and differentiation in the epidermis [56] – Regulating the proliferation of fibroblasts and collagen synthesis [57, 58] – Hemostatic effects as clotting factor [56]
Cerium (Ce)	– Antioxidant and anti-inflammatory activity [59] – Antibacterial activity [60] – Increasing the proliferation and migration of keratinocytes, fibroblasts and vascular endothelial cells [61] – Increasing the deposition of collagen and wound strength [62]
Cobalt (Co)	– Promoting angiogenesis [63]
Copper (Cu)	– Antibacterial activity [64] – Involving in the activity of angiogenin, PDGF, and VEGF [65] – Stimulating the angiogenesis [65]
Gallium (Ga)	– Antibacterial activity [66] – Possible effects in accelerating blood clot formation [67]
Magnesium (Mg)	– Regulating epidermal proliferation, differentiation, and barrier functions of skin [68, 69]
Phosphorus (P)	– Stimulating the angiogenesis [63]
Selenium (Se)	– Increasing angiogenesis and reducing oxidative stress [70] – Antifungal [71], antibacterial [72], and antibiofilm activity [73]
Silicon (Si)	– Stimulating the secretion of pro-angiogenic growth factors [74] – Improving the strength and elasticity of skin [75] – Involving in the synthesis of glycosaminoglycans [75] – Important for optimal synthesis of collagen and formation of collagen network [75]

(Continued)

Table 21.1 (Continued)

Element	Biological effects
Strontium (Sr)	– Promoting the proliferation of fibroblasts and enhancing the expression of VEGF and bFGF from fibroblasts [76] – Promoting angiogenesis [77] – Inhibitory effect on the expression of pro-inflammatory factors including IL-6 and TNF-α [78, 79]
Zinc (Zn)	– Antioxidant, anti-inflammatory, and antibacterial activity [80] – Involving in the proliferation of melanocytes and keratinocytes [36] – Involving in hemostasis of Langerhans cells and maturation of dendritic cells [36]

ECM, extracellular matrix; PDGF, platelet-derived growth factor; IL-6, interleukin 6.

21.5 The Applications of Bioactive Glasses in Skin Wound Healing

Over the last decade, the potential therapeutic effects of bioactive glasses in soft tissue healing have received much attention [81]. In this regard, a number of *in vitro* and *in vivo* studies have been conducted on silicate; borate- and phosphate-based bioactive glasses in which glasses have been used alone (in the form of microfibers) or as additives (in the form of nano/microparticles) embedded in a polymeric matrix to take advantage of their unique features for accelerating skin wound healing [36]. A list of bioactive glass compositions, which have been investigated in this field, is provided in Table 21.2.

Table 21.2 Overview of the type of bioactive glasses used for wound healing applications.

Form	Glass composition (mol%)	Synthesis method	Type of study	References
Particle	$46.1SiO_2$–26.9CaO–$2.6P_2O_5$–$24.4NaO_2$	Melt-quenching	*In vitro* (fibroblast and endothelial cell)/*in vivo* (rabbit ischemic chronic wound)	[82]
	$50SiO_2$–40CaO–$5P_2O_5$–$2.5Ag_2O$–2.5CoO	Sol–gel	Characterization of physicochemical and mechanical properties required for wound healing applications	[83]
	$54.6SiO_2$–22.1CaO–$1.7P_2O_5$–$6NaO_2$–$7.7MgO$–$7.9K_2O$	Flame-spray	*In vitro* (fibroblast)	[84]
	$56SiO_2$–17CaO–$1.8P_2O_5$–$6.1NaO_2$–$7.9MgO$–$8.1K_2O$–3.1SrO	Flame-spray	*In vitro* (fibroblast)	
	$60SiO_2$–36CaO–$4P_2O_5$	Sol–gel	*In vitro* (endothelial cell)/*in vivo* (rat diabetic full-thickness wound)	[85]
	$70SiO_2$–$(20-x)$ CaO–$10P_2O_5$–xCuO ($x = 0, 3, 5$)	Sol–gel	*In vitro* (fibroblast)	[86]

Table 21.2 (Continued)

Form	Glass composition (mol%)	Synthesis method	Type of study	References
	$34.7SiO_2$–$10.9B_2O_3$–$25.3CaO$–$2.7P_2O_5$–$24.9Na_2O$–$1.5ZnO$	Sol–gel	*In vivo* (rat second-degree scald)	[87]
	$80SiO_2$–$18B_2O_3$–$2Se_2O$	Sol–gel	*In vitro* (fibroblast)	[19]
Fiber	$46.1SiO_2$–$26.9CaO$–$2.6P_2O_5$–$24.4Na_2O$	Melt-quenching	*In vitro* (endothelial cell)/ *in vivo* (rat full-thickness dermal wound)	[88]
	$49.7B_2O_3$–$24CaO$–$1.9P_2O_5$–$6.5Na_2O$–$8.3MgO$–$8.5K_2O$–$0.3CuO$–$0.8ZnO$	Melt-quenching	*In vitro* (fibroblast)	[89]
	$16.6SiO_2$–$33.2B_2O_3$–$20.1CaO$–$1.8P_2O_5$–$5.5Na_2O$–$7.4MgO$–$7.3K_2O$–$5.5SrO$–$2.6CuO$	Melt-quenching	*In vitro* (fibroblast and endothelial cell)/*in vivo* (rat full-thickness wound)	[90]
	$45P_2O_5$–$10CaO$–$24Na_2O$–$18MgO$–$3CeO_2$	Melt-quenching	*In vitro* (keratinocyte and fibroblast)	[91]
	$45P_2O_5$–$10CaO$–$24Na_2O$–$18MgO$–$3Ga_2O_3$	Melt-quenching	*In vitro* (keratinocyte and fibroblast)	
	$46P_2O_5$–$17CaO$–$11Na_2O$–$22MgO$–$4Fe_2O_3$	Melt-quenching	*In vitro* (keratinocyte)	[92]

21.5.1 Can Bioactive Glasses Meet the Requirements of a Hard to Heal Wound to Be Successfully Healed?

Considering the inherent characteristics of soft tissues, the fact is that polymeric materials are more suitable candidates for mimicking the natural structure of the skin. However, a wide range of additives can improve the biological and physicochemical properties of polymeric constructs to get close to natural skin in terms of functionality [35]. The combination of bioactive glasses as an additive with polymers represents a promising approach to integrate the advantages of both materials while minimizing the disadvantages of each phase [93]. In this regard, biocomposite wound dressings and skin tissue engineering scaffolds containing bioactive glass particles have been fabricated using freeze-drying, solvent casting, and electrospinning methods in different forms of sponges, hydrogels, films, and fibers [36]. To date, many attempts have been made in order to elucidate the mechanisms of the bioactive glasses in the wound healing process, which are mainly related to the composition and ionic dissolution products of bioactive glasses in the wound environment [36]. The possible biological mechanisms of bioactive glasses and the approaches of using them in wound healing are depicted in Figure 21.2.

In recent years, some studies have proposed bioactive glasses for hemostatic applications. In a study by Ostomel et al. [94], the glass morphology, porosity, surface area, pore volume, Si/Ca ratio, and the presence of Ca^{2+} (coagulation factor IV) in the composition of glass have been reported as

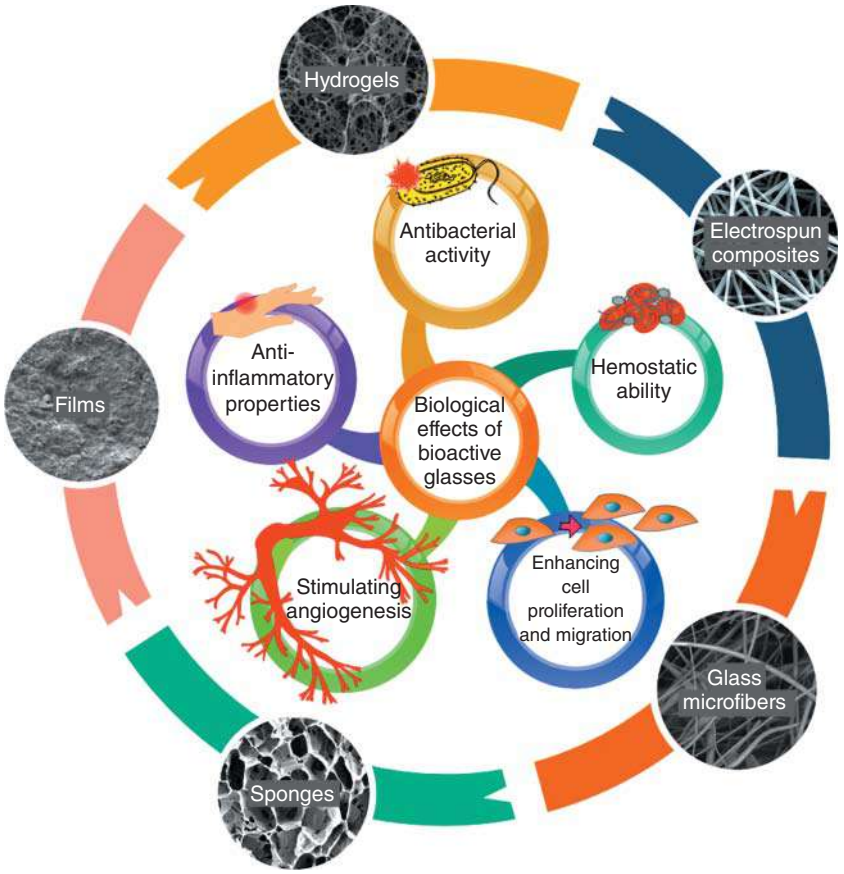

Figure 21.2 The possible biological mechanisms of bioactive glasses in wound healing and different approaches of incorporating bioactive glasses in the polymeric matrix to be used in wound treatment. Source: Tina Mehrabi (author).

major effective factors for the hemostatic ability of silicate-based bioactive glass [94]. Furthermore, it is suggested that the formation of $Si–O^-$ negatively charged functional groups following the surface reactions of glass in contact with physiological body fluid may trigger the intrinsic pathway of blood coagulation by contact activation of factor XII [18, 95]. The hemostatic potential of bioactive glasses is desirable for controlling hemorrhage at the early stages of healing.

It should be noted that the regulation of anti-inflammatory response by bioactive glasses has also been addressed in a number of investigations. For instance, in the case of 45S5 bioactive glass, the released ions have shown anti-inflammatory properties by activating the macrophages toward the M2 phenotype and upregulating the expression of anti-inflammatory factors in macrophages [96]. Moreover, the results of *in vivo* studies on full-thickness wounds of rats treated with bioactive glasses have also clarified the reduction of inflammatory response due to the presence of fewer neutrophils and more M2 macrophages in the wound site [96]. On the other hand, introducing the metallic ions with inherent anti-inflammatory activity such as zinc [97] and cerium [98] into the glass formulation is another approach to increase the efficacy of glasses for accelerating the healing process of nonhealing wounds.

The ionic dissolution products of bioactive glasses have also elicited biological effects on cell functions, which favor the new tissue formation of healing process. For example, the ions released from the Cu-doped borate glass microfibers increased the proliferation of human umbilical vein endothelial cells (HUVECs) and fibroblasts [99] and in another study, the proliferation rate of keratinocytes enhanced by $SiO_2–CaO–P_2O_5$ glasses doped with gold nanoparticles [100].

The importance of new blood vessel formation in the healing process is to provide the oxygen, nutrients, and also immune cells in the wound bed for the regeneration of damaged skin [101]. Moreover, considering the fact that in chronic wounds, the angiogenesis may be impaired because of a decrease in expression of pro-angiogenic and overexpression of anti-angiogenic cytokines [101], the stimulating effect of angiogenesis can further increase by using angiogenic agents along with bioactive glasses. The angiogenic potential of bioactive glasses, which arise from the potential of inorganic ions in stimulating the secretion of pro-angiogenic growth factors such as basic fibroblast growth factor (bFGF) and vascular endothelial growth factor (VEGF) and proliferation of endothelial cells, has sparked an interest to use them is soft tissue engineering [63, 102]. One example is the synergistic effect of bioactive glass and deferoxamine drug embedded into an alginate-based injectable hydrogel on tube formation and migration of HUVEC and healing of the diabetic chronic wound of rat [103]. On the other hand, this approach can be regarded as an effective inorganic ion delivery method that may overcome the limitations of growth factor-based therapeutic strategies.

Wound infections, especially those caused by antibiotic-resistant micro-organisms, are among the main issues for caregivers, which lead to serious and challenging complications in the normal healing process [104]. Accordingly, alternative antimicrobial agents are necessary to reduce the bacterial colonization in the wound site and deal with life-threatening wound infections [105]. Interestingly, bioactive glasses have possessed antibacterial activity against Gram-positive and Gram-negative bacteria [106]. In general, the main factors influencing the antibacterial activity of bioactive glasses are composition, particle size, and concentration of glass and also bacterial species [106]. According to the previous studies, the antibacterial activity of bioactive glasses can be explained by the following mechanisms. First, the dissolution of bioactive glasses in contact with physiological fluids, which results in the release of alkali and alkaline earth ions, can increase the pH and osmotic pressure of the local environment [106, 107]. Second, it is suggested that the sharp glass debris may induce damage to the bacterial cell wall, which can facilitate the penetration of antibacterial agents into the bacterial cytoplasm [107]. Finally, several metallic elements with antibacterial properties such as copper, zinc, silver, cerium, and gallium can also be incorporated into the glass network [18], and bioactive glasses with porous structure (e.g. mesoporous glasses) have the potential to serve as carriers for controlled release of antibiotic drugs through their pores, which can further inhibit the growth of bacteria [108].

Owing to the antimicrobial potential of bioactive glasses, wound dressings that contain these materials may be appropriate candidates for shielding the wound from contamination. In a recent investigation, neat alginate–agarose membranes which were designed for chronic wound healing showed no antibacterial effect against *Staphylococcus aureus* bacteria and also *Candida albicans* fungi, while nanocomposites containing 5 and 10 wt% of $80SiO_2$–$18B_2O_3$–$2SeO_2$ (mol%) nano bioactive glasses exhibited significant microbial reduction and the antifungal activity of composite enhanced with the increase of glass content [19].

It is expected that a product, which aims to use for accelerating the healing, would be able to fill the irregularly shaped wound sites. To this end, *in situ*-forming hydrogels containing bioactive glasses have been investigated to address the needs of the wounds mentioned above. In a study, an injectable hydrogel composed of agarose, alginate, and 45S5 Bioglass has developed by Zeng et al. [82]. The findings confirmed the role of ionic products of glasses in promoting the healing of chronic wounds. This composite hydrogel was able to provide a moist environment and significantly increases the migration of human dermal fibroblast (HDF) and human umbilical endothelial cells [82]. Furthermore, the stimulatory effect of this hydrogel on angiogenesis was assessed *in vitro* and *in vivo*, which showed the up-regulation of VEGF gene expression in HDF and HUVEC and formation of more new blood vessels in ischemic wounds of rabbit ear [82]. It is worth mentioning that bioactive glass fibers in the form of flexible dressings were also able to fill the voids and fit the shape of chronic wounds of patients in clinical trials.

Table 21.3 Commercially available bioactive glass-based products for wound healing applications.

Product name/glass system	Form and use	Producer
Arglaes®/phosphate	Film and powder Human use	Medline Industries (USA)
Dermfactor®/silicate	Powder Human use	UEG Medical Group (China)
MIRRAGEN®/borate	Fiber Human use	ETS Wound Care (USA)
RediHeal™/borate	Fiber and ointment Animal use	Avalon Medical (USA)
TendaHeal™/borate	Fiber, spray, and hydrogel Animal use	Tenda Horse Products (USA)

21.5.2 Clinical Studies and Commercial Products

The first advanced glass-based wound dressing is MIRRAGEN® (also known as DermaFuse™), which has received Food and Drug Administration (FDA) clearance in 2016. The dressing comprises of 13-93B3 borate glass fibers with the formulation of $53B_2O_3$–$20CaO$–$2K_2O$–$6Na_2O$–$5MgO$–$4P_2O_5$ (wt%) and a fibrous morphology that resembles the natural microstructure of fibrin clot [38, 109]. Besides, this wound dressing has been shown its effectiveness in increasing angiogenesis and migration of epidermal cells [109]. The dressing is also easy to apply in different wound geometry and can be used to treat acute and chronic wounds, including traumatic ones, first- and second-degree burns, diabetic ulcers, pressure ulcers, and venous ulcers [36, 110]. A recent case study has evaluated the efficacy of MIRRAGEN borate-based bioactive glass fibers to treat four patients with chronic wounds that their previous therapeutic interventions using negative-pressure therapy, skin grafts, and synthetic/biological based wound care products have been failed for about a year [110]. MIRRAGEN dressing has significantly reduced the cost of treatment and duration of wound closure compared to previous interventions in all patients and their wounds completely healed in an average of 55 days after the initial application of dressing [110]. Borate-based bioactive glasses have also been formulated in the form of fiber, ointment hydrogel, and spray for treating various types of wounds in animals [36].

Dermfactor® and Arglaes® are other bioactive glass-based commercial products for wound healing applications composed of silicate glass powder and Ag-doped phosphate glass, respectively [36, 111]. Dermfactor has been used in form of powder for burn wounds, diabetic foot ulcers, and bedsores; meanwhile, Arglaes is designed to control the infection of partial and full-thickness wounds by sustained release of Ag ions [36, 112]. An overview of available bioactive glass-based commercial products for animal and human use are summarized in Table 21.3.

21.6 Conclusions and Outlook

Despite the ongoing development of biomaterials for wound healing purposes, there is still a need for seeking more effective biomaterial-based wound care approaches to successfully restore the full

anatomy and functions of the skin tissue after an injury. In the light of recent investigations, there is now considerable interest in using bioactive glasses in wound repair and regeneration. Bioactive glasses can be used as delivery systems of therapeutic ions for accelerating wound healing by hemostatic ability, antibacterial activity, anti-inflammatory properties, promoting angiogenesis, and regulating cell functions in the wound bed. Even though the aim of using bioactive glasses in soft tissue applications is controlled release of ions instead of HCA formation, most of the bioactive glass compositions that have been used in this field are prone to mineralize in contact with physiological fluids and possible risk of calcification in soft tissues due to the potential of HCA formation at the surface of bioactive glasses, remains unclear. However, HCA's durability that formed on the surface of bioactive glasses may be affected by the local condition of the surrounding tissue, including pH. For healthy skin tissue, the pH is between 4 and 6, unlike the alkaline pH of chronic wounds. Hence, it would be expected that as the wound progresses toward successful healing, the acidic pH of the skin will be restored, and the hydroxyapatite dissolves under the acidic condition.

Taken together, further studies are needed to formulate the composition of bioactive glasses and optimize the biological and physicochemical properties of bioactive glass-based therapeutic approaches according to the requirements of wounds. More importantly, future research should focus on the explanation of HCA's role in wound healing applications.

References

1 Hench, L.L., Splinter, R.J., Allen, W.C., and Greenlee, T.K. (1971). Bonding mechanisms at the interface of ceramic prosthetic materials. *Journal of Biomedical Materials Research* 5 (6): 117–141. http://doi.wiley.com/10.1002/jbm.820050611.

2 Hench, L.L. (1998). Biomaterials: a forecast for the future. *Biomaterials* 19 (16): 1419–1423. https://linkinghub.elsevier.com/retrieve/pii/S0142961298001331.

3 Chen, Q., Jin, L., Cook, W.D. et al. (2010). Elastomeric nanocomposites as cell delivery vehicles and cardiac support devices. *Soft Matter* 6 (19): 4715–4726.

4 Kim, Y.P., Lee, G.S., Kim, J.W. et al. (2015). Phosphate glass fibres promote neurite outgrowth and early regeneration in a peripheral nerve injury model. *Journal of Tissue Engineering and Regenerative Medicine* 9 (3): 236–246. http://doi.wiley.com/10.1002/term.1626.

5 Joo, N.Y., Knowles, J.C., Lee, G.S. et al. (2012). Effects of phosphate glass fiber-collagen scaffolds on functional recovery of completely transected rat spinal cords. *Acta Biomaterialia* 8 (5): 1802–1812. http://dx.doi.org/10.1016/j.actbio.2012.01.026.

6 Miola, M., Pakzad, Y., Banijamali, S. et al. (2019). Glass-ceramics for cancer treatment: so close, or yet so far? *Acta Biomaterialia* 83: 55–70. https://linkinghub.elsevier.com/retrieve/pii/S1742706118306676.

7 Boccaccini, A.R., Blaker, J.J., Maquet, V. et al. (2005). Preparation and characterisation of poly(lactide-*co*-grycolide) (PLGA) and PLGA/Bioglass® composite tubular foam scaffolds for tissue engineering applications. *Materials Science and Engineering C* 25 (1): 23–31.

8 Gillette, R.L., Swaim, S.F., Sartin, E.A. et al. (2001). Effects of a bioactive glass on healing of closed skin wounds in dogs. *American Journal of Veterinary Research* 62 (7): 1149–1153. http://avmajournals.avma.org/doi/abs/10.2460/ajvr.2001.62.1149.

9 Frykberg, R.G. and Banks, J. (2015). Challenges in the treatment of chronic wounds. *Advances in Wound Care* 4: 560–582.

10 Mahmoudi, M. and Gould, L. (2020). Opportunities and challenges of the management of chronic wounds: a multidisciplinary viewpoint. *Chronic Wound Care Management and Research* 7: 27–36.

11 Paul, W. and Sharma, C.P. (2015). Classification of wound dressing products. In: *Advances in Wound Healing Materials: Science and Skin Engineering*, vol. 1, 49–59. Shropshire, UK: Smithers Rapra Technology.

12 Boateng, J.S., Matthews, K.H., Stevens, H.N.E., and Eccleston, G.M. (2008). Wound healing dressings and drug delivery systems: a review. *Journal of Pharmaceutical Sciences* 97 (8): 2892–2923. http://dx.doi.org/10.1002/jps.21210.

13 Hoppe, A., Güldal, N.S., and Boccaccini, A.R. (2011). A review of the biological response to ionic dissolution products from bioactive glasses and glass-ceramics. *Biomaterials* 32 (11): 2757–2774. https://www.sciencedirect.com/science/article/pii/S0142961211000056.

14 Shahrbabak, M.S.N., Sharifianjazi, F., Rahban, D., and Salimi, A. (2019). A comparative investigation on bioactivity and antibacterial properties of sol–gel derived 58S bioactive glass substituted by Ag and Zn. *Silicon* 11 (6): 2741–2751. http://link.springer.com/10.1007/s12633-018-0063-2.

15 Aina, V., Cerrato, G., Martra, G. et al. (2013). Gold-containing bioactive glasses: a solid-state synthesis to produce alternative biomaterials for bone implantations. *Journal of the Royal Society Interface* 10 (82): 1–10. https://royalsocietypublishing.org/doi/10.1098/rsif.2012.1040.

16 Zheng, K., Wu, J., Li, W. et al. (2018). Incorporation of Cu-containing bioactive glass nanoparticles in gelatin-coated scaffolds enhances bioactivity and osteogenic activity. *ACS Biomaterials Science & Engineering* 4 (5): 1546–1557. https://pubs.acs.org/doi/10.1021/acsbiomaterials.8b00051.

17 Barrioni, B.R., de Laia, A.G.S., Valverde, T.M. et al. (2018). Evaluation of *in vitro* and *in vivo* biocompatibility and structure of cobalt-releasing sol–gel bioactive glass. *Ceramics International* 44 (16): 20337–20347. https://doi.org/10.1016/j.ceramint.2018.08.022.

18 Pourshahrestani, S., Zeimaran, E., Adib Kadri, N. et al. (2016). Gallium-containing mesoporous bioactive glass with potent hemostatic activity and antibacterial efficacy. *Journal of Materials Chemistry B* 4 (1): 71–86. http://dx.doi.org/10.1039/C5TB02062J.

19 El-Kady, A.M., Ali, A.A., and El-Fiqi, A. (2020). Controlled delivery of therapeutic ions and antibiotic drug of novel alginate-agarose matrix incorporating selenium-modified borosilicate glass designed for chronic wound healing. *Journal of Non-Crystalline Solids* 534: 119889. http://xlink.rsc.org/?DOI=C9TB00820A.

20 Yan, X., Yu, C., Zhou, X. et al. (2004). Highly ordered mesoporous bioactive glasses with superior in vitro bone-forming bioactivities. *Angewandte Chemie International Edition* 43 (44): 5980–5984. http://doi.wiley.com/10.1002/anie.200460598.

21 Wu, C. and Chang, J. (2014). Multifunctional mesoporous bioactive glasses for effective delivery of therapeutic ions and drug/growth factors. *Journal of Controlled Release* 193: 282–295. http://dx.doi.org/10.1016/j.jconrel.2014.04.026.

22 Chaudhari, A., Vig, K., Baganizi, D. et al. (2016). Future prospects for scaffolding methods and biomaterials in skin tissue engineering: a review. *International Journal of Molecular Sciences* 17 (12): 1974. http://www.ncbi.nlm.nih.gov/pubmed/27898014.

23 Sorg, H., Tilkorn, D.J., Hager, S. et al. (2017). Skin wound healing: an update on the current knowledge and concepts. *European Surgical Research* 58: 81–94. https://www.karger.com/Article/FullText/454919.

24 Writers, A.M. (2014). Select appropriate wound dressings by matching the properties of the dressing to the type of wound. *Drugs & Therapy Perspectives* 30 (6): 213–217. http://link.springer.com/10.1007/s40267-014-0125-5.

25 Dhivya, S., Padma, V.V., and Santhini, E. (2015). Wound dressings – a review. *Biomedicine* 5 (4): 24–28. http://biomedicine.cmu.edu.tw/.

26 Harding, K.G. (2002). Science, medicine, and the future: healing chronic wounds. *BMJ* 324 (7330): 160–163. http://www.bmj.com/cgi/doi/10.1136/bmj.324.7330.160.

27 Han, S. (2016). Basics of wound healing. In: *Innovations and Advances in Wound Healing*, 1–37. Berlin, Heidelberg: Springer Berlin Heidelberg. http://link.springer.com/10.1007/978-3-662-46587-5.

28 Jeschke, M.G., Finnerty, C.C., Shahrokhi, S. et al. (2013). Wound coverage technologies in burn care: novel techniques. *Journal of Burn Care & Research* 34: 612–620.

29 Haddad, A.G., Giatsidis, G., Orgill, D.P., and Halvorson, E.G. (2017). Skin substitutes and bioscaffolds. *Clinics in Plastic Surgery* 44 (3): 627–634. http://dx.doi.org/10.1016/j.cps.2017.02.019.

30 Saghazadeh, S., Rinoldi, C., Schot, M. et al. (2018). Drug delivery systems and materials for wound healing applications. *Advanced Drug Delivery Reviews* 127: 138–166. http://linkinghub.elsevier.com/retrieve/pii/S0169409X18300607.

31 Morin, R.J. and Tomaselli, N.L. (2007). Interactive dressings and topical agents. *Clinics in Plastic Surgery* 34 (4): 643–658. https://linkinghub.elsevier.com/retrieve/pii/S0094129807001046.

32 Maibach, H.I. (2005). Therapeutic approach to cutaneous ulcers according to appearance. In: *Wound Healing and Ulcers of the Skin* (ed. M. Philipp), 241–253. http://link.springer.com/10.1007/b138035. Berlin/Heidelberg: Springer-Verlag.

33 Pereira, R.F. and Bártolo, P.J. (2016). Traditional therapies for skin wound healing. *Advances in Wound Care* 5 (5): 208–229. http://www.liebertpub.com/doi/10.1089/wound.2013.0506.

34 Vig, K., Chaudhari, A., Tripathi, S. et al. (2017). Advances in skin regeneration using tissue engineering. *International Journal of Molecular Sciences* 18 (4): 789. http://www.mdpi.com/1422-0067/18/4/789.

35 Kargozar, S., Singh, R.K., Kim, H., and Baino, F. (2020). "Hard" ceramics for "soft" tissue engineering: paradox or opportunity? *Acta Biomaterialia* 115: 1–28. https://linkinghub.elsevier.com/retrieve/pii/S1742706120304748.

36 Mehrabi, T., Mesgar, A.S., and Mohammadi, Z. (2020). Bioactive glasses: a promising therapeutic ion release strategy for enhancing wound healing. *ACS Biomaterials Science & Engineering* 6 (10): 5399–5430. https://pubs.acs.org/doi/10.1021/acsbiomaterials.0c00528.

37 Kargozar, S., Mozafari, M., Hamzehlou, S., and Baino, F. (2019). Using bioactive glasses in the management of burns. *Frontiers in Bioengineering and Biotechnology* 28 (7): 1–12. https://www.frontiersin.org/article/10.3389/fbioe.2019.00062/full.

38 Naseri, S., Lepry, W.C., and Nazhat, S.N. (2017). Bioactive glasses in wound healing: hope or hype? *Journal of Materials Chemistry B* 5 (31): 6167–6174. http://pubs.rsc.org/en/Content/ArticleLanding/2017/TB/C7TB01221G.

39 Shelby, J.E. (2007). Structures of glasses. In: *Introduction to Glass Science and Technology* (ed. J.E. Shelby), 72–110. Cambridge: Royal Society of Chemistry. http://ebook.rsc.org/?DOI=10.1039/9781847551160.

40 da Silva, A.C. (2016). Structure and percolation of bioglasses. In: *Biocompatible Glasses from Bone Regeneration to Cancer Treatment* (ed. J. Marchi), 49–84. Switzerland: Springer. http://link.springer.com/10.1007/978-3-319-44249-5.

41 Brauer, D.S. and Möncke, D. (2017). Introduction to the structure of silicate, phosphate and borate glasses. In: *Bioactive Glasses: Fundamentals, Technology and Applications* (ed. A.R. Boccaccini, D.S. Brauer and L. Hupa), 61–88. Cambridge, UK: The Royal Society of Chemistry. http://ebook.rsc.org/?DOI=10.1039/9781782622017-FP005.

42 Granel, H., Bossard, C., Nucke, L. et al. (2019). Optimized bioactive glass: the quest for the bony graft. *Advanced Healthcare Materials* 8 (11): 1801542. https://onlinelibrary.wiley.com/doi/abs/10.1002/adhm.201801542.

43 Huang, C. and Cormack, A.N. (1990). The structure of sodium silicate glass. *Journal of Chemical Physics* 93 (11): 8180–8186. http://aip.scitation.org/doi/10.1063/1.459296.

44 Fernandes, H.R., Gaddam, A., Rebelo, A. et al. (2018). Bioactive glasses and glass-ceramics for healthcare applications in bone regeneration and tissue engineering. *Materials* 11 (12): 2530. http://www.mdpi.com/1996-1944/11/12/2530.

45 Schuhladen, K., Wang, X., Hupa, L., and Boccaccini, A.R. (2018). Dissolution of borate and borosilicate bioactive glasses and the influence of ion (Zn, Cu) doping in different solutions. *Journal of Non-Crystalline Solids* 502: 22–34. https://linkinghub.elsevier.com/retrieve/pii/S0022309318305003.

46 Wang, H., Zhao, S., Xiao, W. et al. (2016). Influence of Cu doping in borosilicate bioactive glass and the properties of its derived scaffolds. *Materials Science and Engineering C* 58: 194–203. http://dx.doi.org/10.1016/j.msec.2015.08.027.

47 Julian Jones, A.C. (ed.) (2012). *Bio-glasses: An Introduction*. Wiley. 320 pp.

48 Kaur, G., Pandey, O.P.O.P., Singh, K. et al. (2014). A review of bioactive glasses: their structure, properties, fabrication and apatite formation. *Journal of Biomedical Materials Research Part A* 102 (1): 254–274. http://doi.wiley.com/10.1002/jbm.a.34690.

49 Skalnaya, M.G., Skalny, A.V., and Radysh, I.V. (2018). General introduction. In: *Essential Trace Elements in Human Health: A Physician's View*. Reviewers: Philippe Collery and Ivan V. Radysh, 6–16. Tomsk, Russia: Publishing House of Tomsk State University.

50 Zoroddu, M.A., Aaseth, J., Crisponi, G. et al. (2019). The essential metals for humans: a brief overview. *Journal of Inorganic Biochemistry* 195: 120–129. https://doi.org/10.1016/j.jinorgbio.2019.03.013.

51 Uluisik, I., Karakaya, H.C., and Koc, A. (2018). The importance of boron in biological systems. *Journal of Trace Elements in Medicine and Biology* 45: 156–162. http://dx.doi.org/10.1016/j.jtemb.2017.10.008.

52 Nzietchueng, R.M., Dousset, B., Franck, P.P. et al. (2002). Mechanisms implicated in the effects of boron on wound healing. *Journal of Trace Elements in Medicine and Biology* 16 (4): 239–244. https://linkinghub.elsevier.com/retrieve/pii/S0946672X02800517.

53 Dzondo-Gadet, M., Mayap-Nzietchueng, R., Hess, K. et al. (2002). Action of boron at the molecular level effects on transcription and translation in an acellular system. *Biological Trace Element Research* 85 (1): 23–33. https://pubmed.ncbi.nlm.nih.gov/11881796/.

54 Demirci, S., Doğan, A., Karakuş, E. et al. (2015). Boron and poloxamer (F68 and F127) containing hydrogel formulation for burn wound healing. *Biological Trace Element Research* 168 (1): 169–180. http://link.springer.com/10.1007/s12011-015-0338-z.

55 Chebassier, N., Ouijja, E.H., Viegas, I., and Dreno, B. (2004). Stimulatory effect of boron and manganese salts on keratinocyte migration. *Acta Dermato-Venereologica* 84 (3): 191–194. https://medicaljournals.se/acta/content/abstract/10.1080/00015550410025273.

56 Lansdown, A.B.G.G. (2002). Calcium: a potential central regulator in wound healing in the skin. *Wound Repair and Regeneration* 10 (5): 271–285. https://onlinelibrary.wiley.com/doi/abs/10.1046/j.1524-475X.2002.10502.x.

57 Wang, T., Gu, Q., Zhao, J. et al. (2015). Calcium alginate enhances wound healing by up-regulating the ratio of collagen types I/III in diabetic rats. *International Journal of Clinical and Experimental Pathology* 8 (6): 6636–6645. http://www.ncbi.nlm.nih.gov/pubmed/26261545.

58 Navarro-Requena, C., Pérez-Amodio, S., Castaño, O. et al. (2018). Wound healing-promoting effects stimulated by extracellular calcium and calcium-releasing nanoparticles on dermal fibroblasts. *Nanotechnology* 29 (39): 395102. http://stacks.iop.org/0957-4484/29/i=39/a=395102?key=crossref.c6c3aabb1c7b66b841d112066cd0eb19.

59 Xu, C. and Qu, X. (2014). Cerium oxide nanoparticle: a remarkably versatile rare earth nanomaterial for biological applications. *NPG Asia Materials* 6 (3): e90. http://www.nature.com/articles/am201388.

60 Kaygusuz, H., Torlak, E., Akın-Evingür, G. et al. (2017). Antimicrobial cerium ion-chitosan crosslinked alginate biopolymer films: a novel and potential wound dressing. *International Journal of Biological Macromolecules* 105: 1161–1165. https://linkinghub.elsevier.com/retrieve/pii/S0141813017310073.

61 Chigurupati, S., Mughal, M.R., Okun, E. et al. (2013). Effects of cerium oxide nanoparticles on the growth of keratinocytes, fibroblasts and vascular endothelial cells in cutaneous wound healing. *Biomaterials* 34 (9): 2194–2201. https://linkinghub.elsevier.com/retrieve/pii/S0142961212013336.

62 Davan, R., Prasad, R.G.S.V., Jakka, V.S. et al. (2012). Cerium oxide nanoparticles promotes wound healing activity in in-vivo animal model. *Journal of Bionanoscience* 6 (2): 78–83. http://openurl.ingenta.com/content/xref?genre=article&issn=1557-7910&volume=6&issue=2&spage=78.

63 Kargozar, S., Baino, F., Hamzehlou, S. et al. (2018). Bioactive glasses: sprouting angiogenesis in tissue engineering. *Trends in Biotechnology* 36 (4): 430–444. http://www.cell.com/trends/biotechnology/pdf/S0167-7799(17)30324-4.pdf.

64 Mahmoodi, S., Elmi, A., and Hallaj Nezhadi, S. (2018). Copper nanoparticles as antibacterial agents. *Journal of Molecular Pharmaceutics & Organic Process Research* 6 (1).

65 Kornblatt, A.P., Nicoletti, V.G., and Travaglia, A. (2016). The neglected role of copper ions in wound healing. *Journal of Inorganic Biochemistry* 161 (2): 1–8. https://linkinghub.elsevier.com/retrieve/pii/S0162013416300381.

66 Minandri, F., Bonchi, C., Frangipani, E. et al. (2014). Promises and failures of gallium as an antibacterial agent. *Future Microbiology* 9 (3): 379–397. http://www.ncbi.nlm.nih.gov/pubmed/23567940.

67 Goodley, P.H. and Rogosnitzky, M. (2011). The effect of gallium nitrate on arresting blood flow from a wound. *Case Reports in Medicine* 2011 (4): 1–3. http://www.mdpi.com/1996-1944/9/4/288.

68 Denda, M., Katagiri, C., Hirao, T. et al. (1999). Some magnesium salts and a mixture of magnesium and calcium salts accelerate skin barrier recovery. *Archives of Dermatological Research* 291 (10): 560–563. http://link.springer.com/10.1007/s004030050454.

69 Proksch, E., Nissen, H.-P., Bremgartner, M., and Urquhart, C. (2005). Bathing in a magnesium-rich Dead Sea salt solution improves skin barrier function, enhances skin hydration, and reduces inflammation in atopic dry skin. *International Journal of Dermatology* 44 (2): 151–157. http://doi.wiley.com/10.1111/j.1365-4632.2005.02079.x.

70 Bajpai, S., Mishra, M., Kumar, H. et al. (2011). Effect of selenium on connexin expression, angiogenesis, and antioxidant status in diabetic wound healing. *Biological Trace Element Research* 144 (1–3): 327–338. http://link.springer.com/10.1007/s12011-011-9097-7.

71 Shakibaie, M., Salari Mohazab, N., and Ayatollahi Mousavi, S.A. (2015). Antifungal activity of selenium nanoparticles synthesized by *Bacillus* species Msh-1 against *Aspergillus fumigatus* and *Candida albicans*. *Jundishapur Journal of Microbiology* 8 (9): e26381. https://www.ncbi.nlm.nih.gov/pmc/articles/PMC4609177/.

72 Tran, P.A. and Webster, T.J. (2013). Antimicrobial selenium nanoparticle coatings on polymeric medical devices. *Nanotechnology* 24 (15): 155101. http://stacks.iop.org/0957-4484/24/i=15/a=155101?key=crossref.9f4b96d736a259e691856e5d29076860.

73 Shakibaie, M., Forootanfar, H., Golkari, Y. et al. (2015). Anti-biofilm activity of biogenic selenium nanoparticles and selenium dioxide against clinical isolates of *Staphylococcus aureus*, *Pseudomonas aeruginosa*, and *Proteus mirabilis*. *Journal of Trace Elements in Medicine and Biology* 29: 235–241. https://linkinghub.elsevier.com/retrieve/pii/S0946672X14001515.

74 Dashnyam, K., El-Fiqi, A., Buitrago, J.O. et al. (2017). A mini review focused on the proangiogenic role of silicate ions released from silicon-containing biomaterials. *Journal of Tissue Engineering* 8: 1–13. http://journals.sagepub.com/doi/10.1177/2041731417707339.

75 de Araújo, L.A., Addor, F., and Campos, P.M.B.G.M. (2016). Use of silicon for skin and hair care: an approach of chemical forms available and efficacy. *Anais Brasileiros de Dermatologia* 91 (3): 331–335. http://www.scielo.br/scielo.php?script=sci_arttext&pid=S0365-05962016000300331&lng=en&tlng=en.

76 Li, S., Li, L., Guo, C. et al. (2017). A promising wound dressing material with excellent cytocompatibility and proangiogenesis action for wound healing: strontium loaded silk fibroin/sodium alginate (SF/SA) blend films. *International Journal of Biological Macromolecules* 104: 969–978. https://linkinghub.elsevier.com/retrieve/pii/S0141813017314356.

77 Zhao, F., Lei, B., Li, X. et al. (2018). Promoting in vivo early angiogenesis with sub-micrometer strontium-contained bioactive microspheres through modulating macrophage phenotypes. *Biomaterials* 178: 36–47. https://doi.org/10.1016/j.biomaterials.2018.06.004.

78 Lee, C.-H., Kim, Y.-J., Jang, J.-H., and Park, J.-W. (2016). Modulating macrophage polarization with divalent cations in nanostructured titanium implant surfaces. *Nanotechnology* 27 (8): 085101. http://dx.doi.org/10.1088/0957-4484/27/8/085101.

79 Buache, E., Velard, F., Bauden, E. et al. (2012). Effect of strontium-substituted biphasic calcium phosphate on inflammatory mediators production by human monocytes. *Acta Biomaterialia* 8 (8): 3113–3119. http://dx.doi.org/10.1016/j.actbio.2012.04.045.

80 Lang, C., Murgia, C., Leong, M. et al. (2007). Anti-inflammatory effects of zinc and alterations in zinc transporter mRNA in mouse models of allergic inflammation. *American Journal of Physiology-Lung Cellular and Molecular Physiology* 292 (2): L577–L584. https://www.physiology.org/doi/10.1152/ajplung.00280.2006.

81 Kargozar, S., Hamzehlou, S., and Baino, F. (2019). Can bioactive glasses be useful to accelerate the healing of epithelial tissues? *Materials Science and Engineering C* 97: 1009–1020. https://doi.org/10.1016/j.msec.2019.01.028.

82 Zeng, Q., Han, Y., Li, H., and Chang, J. (2015). Design of a thermosensitive bioglass/agarose–alginate composite hydrogel for chronic wound healing. *Journal of Materials Chemistry B* 3 (45): 8856–8864. http://xlink.rsc.org/?DOI=C5TB01758K.

83 Moura, D., Souza, M.T.T., Liverani, L. et al. (2017). Development of a bioactive glass-polymer composite for wound healing applications. *Materials Science and Engineering C* 76: 224–232. http://dx.doi.org/10.1016/j.msec.2015.05.049.

84 Tansaz, S., Schulte, M., Kneser, U. et al. (2018). Soy protein isolate/bioactive glass composite membranes: processing and properties. *European Polymer Journal* 106: 232–241. https://doi.org/10.1016/j.eurpolymj.2018.07.003.

85 Gao, W., Jin, W., Li, Y. et al. (2017). A highly bioactive bone extracellular matrix-biomimetic nanofibrous system with rapid angiogenesis promotes diabetic wound healing. *Journal of Materials Chemistry B* 5 (35): 7285–7296. http://xlink.rsc.org/?DOI=C7TB01484H.

86 Ahmed, M.M., Abd-Allah, W.M., Omar, A.E., and Soliman, A.A.F. (2020). The dual effect of copper and gamma irradiation on chronic wound healing of nanobioactive glass. *Journal of Inorganic and Organometallic Polymers and Materials* 30: 3646–3657. http://link.springer.com/10.1007/s10904-020-01501-0.

87 Gu, W., Li, Y., Yang, X. et al. (2018). Systematic investigation of a new nanoscale bioactive glass on wound healing in vivo in comparison with the clinically applied 45S5 Bioglass. *International Journal of Regenerative Medicine* 1 (1): 1–8.

88 Zhou, J., Wang, H., Zhao, S. et al. (2016). In vivo and in vitro studies of borate based glass micro-fibers for dermal repairing. *Materials Science and Engineering C* 60: 437–445. https://linkinghub.elsevier.com/retrieve/pii/S0928493115305993.

89 Yang, Q., Chen, S., Shi, H. et al. (2015). In vitro study of improved wound-healing effect of bioactive borate-based glass nano-/micro-fibers. *Materials Science and Engineering C* 55: 105–117. http://dx.doi.org/10.1016/j.msec.2015.05.049.

90 Hu, H., Tang, Y., Pang, L. et al. (2018). Angiogenesis and full-thickness wound healing efficiency of a copper-doped borate bioactive glass/poly(lactic-*co*-glycolic acid) dressing loaded with vitamin E in vivo and in vitro. *ACS Applied Materials & Interfaces* 10 (27): 22939–22950. https://pubs.acs.org/doi/10.1021/acsami.8b04903.

91 Łapa, A., Cresswell, M., Campbell, I. et al. (2019). Ga and Ce ion-doped phosphate glass fibres with antibacterial properties and their composite for wound healing applications. *Journal of Materials Chemistry B* 7 (44): 6981–6993. http://xlink.rsc.org/?DOI=C9TB00820A.

92 Sghayyar, H.N.M., Lim, S.S., Ahmed, I. et al. (2020). Fish biowaste gelatin coated phosphate-glass fibres for wound-healing application. *European Polymer Journal* 122: 109386. https://linkinghub.elsevier.com/retrieve/pii/S0014305719320142.

93 Ding, Y., Souza, M.T., Li, W. et al. (2014). Bioactive glass–biopolymer composites for applications in tissue engineering. In: *Handbook of Bioceramics and Biocomposites* (ed. I.V. Antoniac), 1–26. Cham: Springer.

94 Ostomel, T.A., Shi, Q., Tsung, C.-K.K. et al. (2006). Spherical bioactive glass with enhanced rates of hydroxyapatite deposition and hemostatic activity. *Small* 2 (11): 1261–1265. http://doi.wiley.com/10.1002/smll.200600177.

95 Pourshahrestani, S., Kadri, N.A., Zeimaran, E., and Towler, M.R. (2019). Well-ordered mesoporous silica and bioactive glasses: promise for improved hemostasis. *Biomaterials Science* 7 (1): 31–50. http://xlink.rsc.org/?DOI=C8BM01041B.

96 Dong, X., Chang, J., Li, H. et al. (2017). Bioglass promotes wound healing through modulating the paracrine effects between macrophages and repairing cells. *Journal of Materials Chemistry B* 5 (26): 5240–5250. http://xlink.rsc.org/?DOI=C7TB01211J.

97 Agarwal, H. and Shanmugam, V. (2020). A review on anti-inflammatory activity of green synthesized zinc oxide nanoparticle: mechanism-based approach. *Bioorganic Chemistry* 94: 103423. https://linkinghub.elsevier.com/retrieve/pii/S0045206819315020.

98 Zheng, K., Torre, E., Bari, A. et al. (2020). Antioxidant mesoporous Ce-doped bioactive glass nanoparticles with anti-inflammatory and pro-osteogenic activities. *Materials Today Bio* 5: 100041. https://doi.org/10.1016/j.mtbio.2020.100041.

99 Zhao, S., Li, L., Wang, H. et al. (2015). Wound dressings composed of copper-doped borate bioactive glass microfibers stimulate angiogenesis and heal full-thickness skin defects in a

rodent model. *Biomaterials* 53: 379–391. https://www.sciencedirect.com/science/article/pii/S0142961215002501.

100 Mârza, S.M., Magyari, K., Bogdan, S. et al. (2019). Skin wound regeneration with bioactive glass-gold nanoparticles ointment. *Biomedical Materials* 14 (2): 025011. https://iopscience.iop.org/article/10.1088/1748-605X/aafd7d.

101 Bodnar, R.J. (2015). Chemokine regulation of angiogenesis during wound healing. *Advances in Wound Care* 4 (11): 641–650. http://www.liebertpub.com/doi/10.1089/wound.2014.0594.

102 Gorustovich, A.A., Roether, J.A., and Boccaccini, A.R. (2010). Effect of bioactive glasses on angiogenesis: a review of in vitro and in vivo evidences. *Tissue Engineering Part B* 16 (2): 199–207. https://www.liebertpub.com/doi/10.1089/ten.teb.2009.0416.

103 Kong, L., Wu, Z., Zhao, H. et al. (2018). Bioactive injectable hydrogels containing desferrioxamine and bioglass for diabetic wound healing. *ACS Applied Materials & Interfaces* 10 (36): 30103–30114. https://pubs.acs.org/doi/10.1021/acsami.8b09191.

104 Bowler, P.G. (2018). Antibiotic resistance and biofilm tolerance: a combined threat in the treatment of chronic infections. *Journal of Wound Care* 27 (5): 273–277.

105 Negut, I., Grumezescu, V., and Grumezescu, A. (2018). Treatment strategies for infected wounds. *Molecules* 23 (9): 2392. http://www.mdpi.com/1420-3049/23/9/2392.

106 Zhang, D., Leppäranta, O., Munukka, E. et al. (2009). Antibacterial effects and dissolution behavior of six bioactive glasses. *Journal of Biomedical Materials Research Part A* 93A (2): 475–483. http://doi.wiley.com/10.1002/jbm.a.32564.

107 Drago, L., Toscano, M., and Bottagisio, M. (2018). Recent evidence on bioactive glass antimicrobial and antibiofilm activity: a mini-review. *Materials* 11 (2): 326. http://www.mdpi.com/1996-1944/11/2/326.

108 Kargozar, S., Montazerian, M., Hamzehlou, S. et al. (2018). Mesoporous bioactive glasses: promising platforms for antibacterial strategies. *Acta Biomaterialia* 81: 1–19. https://linkinghub.elsevier.com/retrieve/pii/S1742706118305816.

109 Taylor, P. (2010). "Cotton candy" that heals? *American Ceramic Society Bulletin* 90 (4): 25–29.

110 Buck, D.W. (2020). Innovative bioactive glass fiber technology accelerates wound healing and minimizes costs: a case series. *Advances in Skin & Wound Care* 33 (8): 1–6. https://journals.lww.com/10.1097/01.ASW.0000672504.15532.21.

111 Chen, S., Huan, Z., Zhang, L., and Chang, J. (2018). The clinical application of a silicate-based wound dressing (DermFactor®) for wound healing after anal surgery: a randomized study. *International Journal of Surgery* 52: 229–232. https://www.sciencedirect.com/science/article/pii/S1743919118305661.

112 Baino, F., Hamzehlou, S., and Kargozar, S. (2018). Bioactive glasses: where are we and where are we going? *Journal of Functional Biomaterials* 9 (1): 25. http://www.mdpi.com/2079-4983/9/1/25.

22

Biocompatible Glasses Applied in Cancer Treatment: Magnetic Hyperthermia and Brachytherapy

Roger Borges[1], Ana Carolina S. Souza[1], Luis A. Genova[2], Joel Machado Jr.[3], Giselle Z. Justo[4], and Juliana Marchi[1]

[1] *Centro de Ciências Naturais e Humanas, Universidade Federal do ABC, Santo André, Brazil*
[2] *Centro de Ciência e Tecnologia dos Materiais, Instituto de Pesquisas Energéticas e Nucleares, São Paulo, Brazil*
[3] *Departamento de Ciências Biológicas, Universidade Federal de São Paulo, Diadema, Brazil*
[4] *Departamento de Bioquímica, Universidade Federal de São Paulo, São Paulo, Brazil*

22.1 General Aspects of Cancer Molecular Biology

Cancer is a complex disease with many faces behind a name. It is caused by a series of successive changes in normal cell and tissue physiology, breaking down the evolved and balanced tumor-suppressive mechanisms that avoid uncontrolled cell proliferation. For a somatic cell to disrupt such equilibrium, it must acquire adaptive solutions from internal controls and constraints from tissue microenvironment forces. Throughout a sequence of genetic and epigenetic alterations accumulated over time, selected clones may adopt different identities, evolve, and expand into more adapted subclones exhibiting signatures of positive selection with unlimited proliferative capacities and increased potential to disseminate and colonize other tissues [1, 2].

Hanahan and Weinberg have originally proposed six essential hallmarks involved in the progression of benign tumors of proliferating cells (hyperplasia) to malignant tumors with acquired metastatic properties: (i) sustained proliferative signaling, (ii) loss of sensitivity to growth suppressors, (iii) resistance to cell death, (iv) uncontrolled proliferation, (v) new blood vessels formation (angiogenesis), (vi) increased capacity to invade tissues and become metastatic [3]. Based on the development of new critical concepts in the cancer biology field over the past two-decade, additional hallmarks have been proposed, including (vii) development of genomic instability, yielding random mutations including chromosomal rearrangements; (viii) evasion of immune surveillance, and (ix) reprogramming energetic cellular metabolism to support unlimited proliferation [4]. Furthermore, epigenetic changes have been proposed as another hallmark of cancer as evidence showing that deregulated epigenetic mechanisms also contribute to every single hallmark in the tumorigenic process. Therefore, to acquire a malignant phenotype, a cell must be exposed to a complex interplay of genetic and epigenetic disorders that act cooperatively with extracellular microenvironmental signals to yield a favorable context for tumor development.

Genetic changes in cancer result from inherited and environmental factors [5]. Replication errors or deoxyribonucleic acid (DNA) damage is the leading causes of mutations. These abnormalities can be induced either by extrinsic (e.g. ionizing radiation, ultraviolet light, chemicals) or intrinsic

Bioactive Glasses and Glass-Ceramics: Fundamentals and Applications, First Edition.
Edited by Francesco Baino and Saeid Kargozar.

(e.g. reactive oxygen species, DNA repair enzymes, mistakes during mitosis) factors [6]. Some viral integration may also promote tumorigenesis by expressing cellular oncogenes [7]. Although most mutations are neutral and do not contribute to cancer development, multiple gain-of-function modifications in proto-oncogenes and loss-of-function in tumor suppressor genes are critical to driving tumor development and progression and metastasis [8]. Different types of mutations can be observed in the genome during the development of cancer (e.g. gene amplification, point mutation, truncation, insertion activation, deletion, and translocation), which can result in inappropriate expression or activation/inactivation of genes and their protein products [9].

Epigenetic silencing such as DNA methylation also alters gene expression but independent of changes in the DNA sequence. Methylation in DNA is catalyzed by a group of DNA methyltransferases (DNMT) that add a methyl group to the 5′ carbon of cytosine residues present in regions of the genome known as CpG Island, which is typically found within the promoter of many human genes. In this way, CpG methylation regulates gene expression by controlling transcription factors' interaction to promoter regions of genes preventing or allowing their transcription. Moreover, DNA methylation is heritable during cell division through well-known propagation mechanisms [10]. Hence, it is not surprising that proto-oncogenes are commonly hypomethylated in several cancers, while tumor suppressor genes are hypermethylated [11].

Histones acetylation is another epigenetic mechanism that affects gene expression by altering chromatin structure [12], although the heritability of this modification is less known. Histones comprise a group of positively charged proteins associated with DNA forming a nucleosome structure, which is the basic element of chromatin [13]. Acetylation of lysine residues on histone tails neutralizes the positive charge of histones and control chromatin compaction. This chemical modification diminishes DNA interaction in the nucleosome, making the chromatin less compact and accessible to proteins and transcription factors to target genes [14]. Therefore, transcriptional activation is associated with acetylation of histones, whereas transcription repression is linked with deacetylation. The oscillation between these two states is regulated by a family of enzymes known as histone acetyltransferases (HATs) and histone deacetylases (HDACs) [15, 16]. Both HAT and HDACs must function in equilibrium to properly control gene expression (STRUHL, 1998). However, abnormal histone acetylation patterns have been common in cancer [17, 18]. It has been demonstrated that HDACs are overexpressed in cancer, causing aberrant loss of histone acetylation and silencing of tumor suppressor genes [19]. Accordingly, HDAC inhibitors have been extensively developed and are in many clinical trials for tumor therapy [20].

Aberrant changes in genetic and epigenetic events can accumulate throughout the tumorigenic process, which dramatically alter the function of proteins that participate in biochemical and signaling networks, therefore, providing cells with solid pressure to acquire cancer hallmarks.

22.1.1 Cancer Treatment in the Clinical Practice

Current standard treatments for most cancers include surgical resection, chemotherapy, and radiotherapy [21], among which chemotherapy has remained the backbone of cancer treatment [22]. Traditional cancer chemotherapeutics were the first line of antitumor drugs established to effectively kill the fast proliferating tumor cells and avoid mitotic division by inhibiting the replication machinery involved in DNA synthesis. Prominent traditional chemotherapeutic agents include alkylating agents (e.g. cyclophosphamide, dacarbazine, and platinum compounds), antimetabolites (e.g. methotrexate, 6-mercaptopurine, and 5-fluorouracil), antimitotics of natural origin (e.g. vinblastine, vincristine, vinorelbine, vindesine, teniposide, etoposide, topotecan, irinotecan, paclitaxel, docetaxel, and cabazitaxel), cytotoxic antibiotics and related substances

(e.g. daunorubicin, doxorubicin actinomycin-D, and bleomycin), polyamine inhibitors (e.g. α-difluoro methyl ornithine), and iron-modulating drugs (e.g. desferrioxamine, di-2-pyridyl ketone-4,4,-dimethyl-3-thiosemicarbazone, ciclopirox, and triapine) [23].

Despite the existence of numerous adversities related to severe side effects, rapid drug metabolism, and drug resistance, traditional chemotherapeutics are still actively used either isolated or in combination with surgical resection and/or radiotherapy. Although these strategies can overcome early diagnosed tumors and impact patient survival and even cure some types of tumors, the overall outcome of these approaches is disappointing, as statistics have shown that cancer incidence and mortality are growing.

The scientific community's understanding of cancer's molecular biology has significantly improved over the past decades, revealing that malignant cells dynamically evolve during tumor development, generating random heterogeneous populations with distinct molecular phenotypes resulting from genetic, and epigenetic abnormalities (intratumor heterogeneity) [21]. Moreover, it has been recognized that intratumor heterogeneity is the basis for the expansion of resistant cells due to selective pressures triggered by chemotherapy, which is one of the causes of therapeutic failure. Also, intratumor heterogeneity is distinct between different patients holding the same histological type of tumor (intertumor heterogeneity) [21]. Besides the complexity of this chaotic molecular milieu, more than 100 types of cancer are originated from different cell types and tissues, which may contain specific molecular subtypes or express distinct marks depending on the location or stage of the tumor [24]. Hence, a comprehensive understanding of all these multifactorial variables is essential to paving new and better therapeutic strategies that contemplate novel personalized or targeted approaches. In fact, in the last two decades, we have witnessed the development of a collection of new techniques for treating cancer based on identifying potential molecular biomarkers for designing targeted drugs in contrast with the nonselective conventional chemotherapeutic method. Besides, emerging therapies have been proposed such as magnetic hyperthermia, brachytherapy, and even improved technologies for chemotherapies' drug delivery approaches. Nevertheless, glass technologies are related to the crucial development of these therapies, mainly in treating bone cancer.

22.2 Bioactive Glasses Applied in Hyperthermia

22.2.1 Magnetic Hyperthermia: Introduction and Physics Aspects

Hyperthermia derives from two Greeks words, *hyper* and *therme*, which mean high and temperature. Therefore, hyperthermia can be any medical procedure that increases body temperature to bring any medicinal effect, regardless of being a whole body or local hyperthermia. Probably, hyperthermia may stand as one of the most ancient modalities of cancer treatment. The first historical report of hyperthermia dates back to 2655–2600 BC in ancient Egyptian society, where Egyptians were used to kill tumors using fire drills, according to Edwin Smith's papyrus [25]. Like the Greeks, Chinese, Indians, and Romans, other ancient societies also used heat sources to treat diseases [26]. Hippocrates used to say: "That which drugs fail to cure, the scalpel can cure. That which the scalpel fails to cure, heat can cure. If heat cannot cure, it must be deemed incurable."

In modern history, the first evidence of whole-body hyperthermia as a possible cancer treatment was pointed out by Carl D.W. Busch (1826–1881) who reported the regression of an advanced sarcoma in the face of a 43-years-old woman after she had a fever due to bacterial infection, erysipelas. This fact encourages Dr. Busch to carry out clinical trials in which he infected

patients with pathogenic agents – like malaria-contaminated blood – on open wounds of cancer patients [25]. Some years later, the American surgeon William B. Coley (1862–1936) developed Coley's toxins based on streptococcal, which was used to treat more than 1000 patients with bone or soft-tissue sarcoma by whole-body hyperthermia [27].

Later in the 19' sec, whole-body hyperthermia derived from infectious agents was eclipsed by modern methods that caused an increase in temperature by external stimuli like magnetic fields and microwaves. In 1891, Jacques-Arsene d'Arsonval built a human-sized induction coil device, which allowed the passage of a 3 A current to induce eddy current effect in water molecules due to the high magnetic field frequencies (>10 MHz). Later, Dr. d'Arsonval also developed other devices that also allowed him to perform localized hyperthermia treatments. This kind of cancer treatment was later called diathermia in clinical practice. Using a similar device, Nils Westermark observed that cancer cells were likely to be killed at temperatures spam between 40 and 45 °C, bringing therapeutic effects with fewer side effects to healthy cells [28].

Because diathermia was based on water molecules' heat, side effects related to increased blood flow were uncontrollable, thereby interfering with venous return, leading to necrosis [29]. Therefore, at that time, there was a need for devices that could allow the local increase in temperature without affecting blood flow and healthy cells. In 1957, R.K. Gilchrist et al. [30] reported the infusion of a suspension of fine magnetic ferrite particles into lymph node tumors (Figure 22.1). Upon applying a low-frequency (5 kHz to 1.2 MHz) external alternating magnetic field, the magnetic particles heated up due to the dispersion of magnetic energy as heat, causing a localized increase in temperature to kill cancer cells selectively and minimally affecting healthy ones. This work was the first report of magnetic hyperthermia as it is currently known, that is, a treatment of cancer based on magnetic micro or nanoparticles heated up by an external magnetic field.

In the experiment of Gilchrist et al. [30], magnetic energy dissipation as heat happens due to hysteresis loss. This phenomenon is typical of ferromagnetic and ferrimagnetic materials like those used by Gilchrist, which consisted of maghemite microparticles. These materials show a hysteresis cycle when the magnetization is measured as an external magnetic field function. The hysteresis cycle is a consequence of domain wall movement in the magnetic domain boundaries. These movements are responsible for absorbing magnetic energy and its later release as heat [26]. Therefore, the power loss (P_1) associated with this physical process can be defined according to Eq. (22.1):

$$P_1 = \mu \cdot f \cdot \int H \, dM \tag{22.1}$$

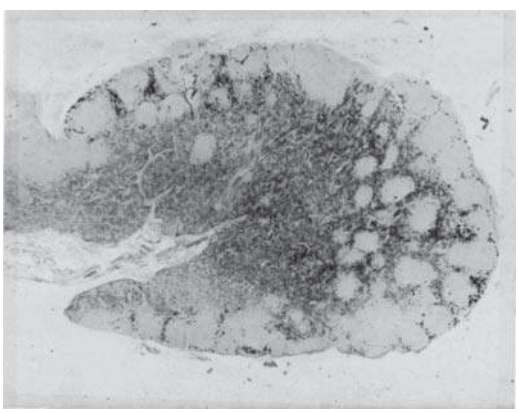

Figure 22.1 Photomicrograph of a lymph node after administration of colloidal maghemite. The photomicrograph was stained with Prussian blue; therefore, the darkest regions contain the submicron particles. Source: Gilchrist et al. [29], Figure xv (p. 09)/Wolters Kluwer Health, Inc.

H is the field strength, M is the magnetization, f is the magnetic field frequency, and μ is a constant hysteresis. It is worth noting to mention that $\int H\,dM$ is equivalent to the area of the hysteresis cycle. In this sense, the ferrimagnetic materials' delivery of heat depends on the hysteresis loop area [26].

The advent of nanotechnology in the 1990s allowed the synthesis of materials to control their size [31]. In this sense, instead of using microparticles of magnetic materials as Gilchrist did, the advances in magnetic hyperthermia shifted toward superparamagnetic nanoparticles. The main reason for using superparamagnetic materials was the possibility of generating heat under lower magnetic field strength, minimizing eddy current events that could compromise the surrounding tissue as diathermia did in the past.

Superparamagnetism is a property found only in nanometric materials that were supposed to be ferrimagnetic or ferromagnetic. Because the particle size is smaller than the magnetic domain, the whole particle behaves like a single magnetic domain, and domain wall effects are negligible [32]. Therefore, these materials do not display hysteresis, which means that the saturation magnetization can be reached at lower frequencies (Figure 22.2). Besides, the power loss (P_2, Eq. (22.2)) does not depend on the hysteresis area, but it is somewhat influenced by other parameters like Néel relaxation (τ_N), Brownian relaxation (τ_B), particle volume (V), saturation magnetization (M_s), and temperature (T).

$$P_2 = \pi\mu_0\chi'' H_0^2 f = \pi\mu_0\left(\chi_0 \frac{2\pi f\tau_{eff}}{1+(2\pi f\tau_{eff})^2}\right) H_0^2 f = \pi\mu_0\left(\frac{\mu_0 M_s^2 V}{K_B T}\right)\left(\frac{2\pi f\tau_{eff}}{1+(2\pi f\tau_{eff})^2}\right) H_0^2 f \tag{22.2}$$

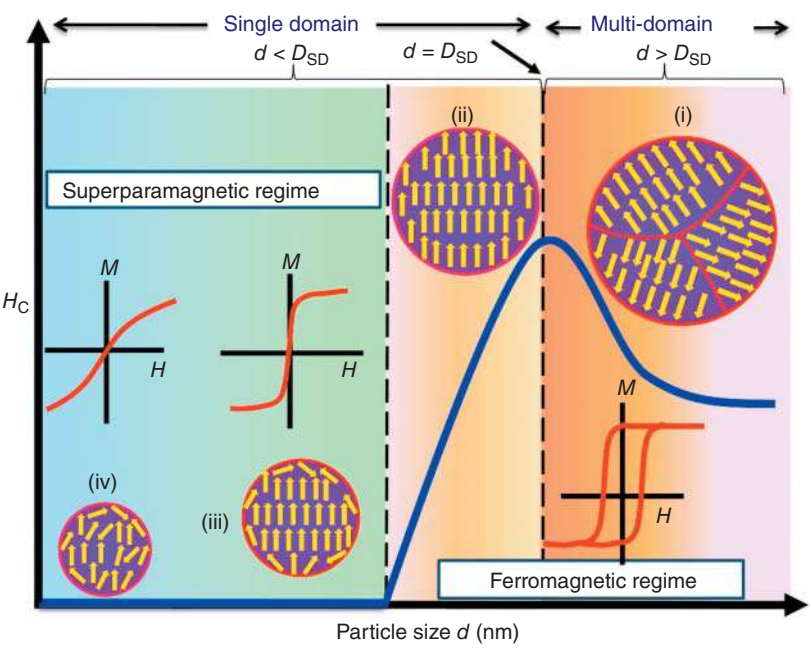

Figure 22.2 Magnetic behavior under the influence of a magnetic field. Ferromagnetic regime occurs in multidomain materials – the particle or crystal size (d) is bigger (i) than or equal (ii) to the magnetic domain size (D_{SD}) – where domain walls effect is tangible, and there is the presence of coercivity. Superparamagnetic regime occurs in single-domain particles or crystals, in which the particle or crystal size is smaller than the magnetic domain ($d < D_{SD}$), thereby do not display coercivity ($H_c = 0$). (iii) When the particle size is much smaller than the magnetic domain (iv), the effect of glass spins on the surface is more pronounced. Source: Mohapatra et al. [32]/MDPI/CCBY 4.0.

where μ_0 is the permeability in the free space, H_0 is the maximum field strength, f is the frequency of the magnetic field, χ'' is the imaginary part of the susceptibility ($\chi = \chi' + i\chi''$), χ_0 is the initial susceptibility, M_s is the saturation magnetization, V is the particle volume, K_B is Boltzmann constant, T is the temperature, and τ_{eff} is the effective relaxation time (τ_{eff}), which is given by Eq. (22.3):

$$\frac{1}{\tau_{eff}} = \frac{1}{\tau_N} + \frac{1}{\tau_B} \tag{22.3}$$

where τ_N is the Néel relaxation time, and τ_B is the Brownian relaxation time. The Néel relaxation is associated with the time and energy required for a spin fluctuation and its relationship with temperature. Below a given temperature (T_b), the spins do not have thermal energy needed for spin fluctuation between up and down orientation. However, above a given temperature (T_b), the spins have enough energy to overcome an energy barrier (ΔE) that allows spin fluctuations. Then, T_b is known as blocking temperature. This relationship is given by Eq. (22.4). Note that ΔE is equivalent to KV, which implies that the energy barrier is related to particle volume; thereby, the bigger the particle, the higher the energy [33]

$$\tau = \tau_0 \exp\left(\frac{KV}{K_B T_b}\right) = \tau_0 \exp\left(\frac{\Delta E}{K_B T_b}\right) \tag{22.4}$$

where τ_0 typically is a value between 10^{-12} and 10^{-9} seconds, K_B is the Boltzmann constant, T_b is the blocking temperature in Kelvin, K is the effective magnetic anisotropy constant, and V is particle volume. KV also represents the anisotropy barrier energy (ΔE).

On the other hand, the Brownian relaxation time is the relationship between the time for a spin fluctuation, considering that the nanoparticle will mechanically rotate in a fluid with viscosity γ to align their spins with the applied magnetic field (Eq. (22.5)).

$$\tau_B = \frac{3V_H \eta}{K_B T} \tag{22.5}$$

where V_H is the hydrodynamic volume of the particle, and η is the viscosity of the fluid. Note that the Brownian relaxation is dependent on the fluid viscosity as well as the hydrodynamic particle volume. Furthermore, V_H is different from the V of Néel relaxation because it also includes the attached layers of water surrounding the nanoparticles, which are considered due to the particle's rotation in the fluid [34].

One may infer that determining the power loss through the variable from Eqs. (22.2–22.5) may be time-consuming and propagate some uncertainties. In this sense, the specific absorption rate (SAR) of superparamagnetic materials and ferromagnetic materials can be experimentally obtained from Eq. (22.6). The SAR is also equivalent to the power loss divided by the density of the superparamagnetic material. Briefly, to get the data needed for Eq. (22.6), the material is placed in a container in nonadiabatic conditions, and an external alternating magnetic field is applied from a coil. A thermometer is then used to measure the increase in temperature (dT) in the function of time (dt).

$$\text{SAR (W/g)} = \frac{C_w m_w + C_{MNP} m_{MNP}}{m_{MNP}} \frac{dT}{dt} \tag{22.6}$$

C_w is the water heat capacity, C_{MNP} is the nanoparticle heat capacity, m_w is the water mass, and m_{MNP} is the nanoparticle mass.

The most used magnetic nanoparticles for hyperthermia applications are magnetite and maghemite; once these nanoparticles display high saturation magnetization, covering a high power loss that, in turn, increases the efficiency of the cancer treatment [35]. Indeed, in Europe,

the treatment of glioblastoma by magnetite nanoparticle-induced hyperthermia is already approved [36], and as more clinical trials are being conducted, other tumors' treatment modalities may be approved as well.

Despite its efficiency in inducing tumor cell death, in the clinical practice, some technical and physiological limitations make the use of hyperthermia as a single anticancer therapy only partially satisfactory. Thus, hyperthermia is currently used in multimodal tumor therapy approaches, combined with other antitumor treatments, mainly with surgery, immunotherapy, radiotherapy, and chemotherapy. In this way, hyperthermia promotes thermal chemosensitization and thermal radiosensitization of tumor cells, amplifying the therapeutic effects of radiation and anticancer drugs by increasing vascular permeability, blood flow, and tumor oxygenation. As a result, hyperthermia improves disease-free survival and local tumor control without increasing toxicity for the combined treatments [37, 38].

Besides its use in multimodal cancer treatment, an increasing number of works demonstrates the potential use of hyperthermia in heat-controlled gene therapy or heat-enhanced immunotherapy or vaccination. In these studies, the increase in temperature induced by hyperthermia acts as an enhancer of cellular functions or a switch that can turn on or turn off cellular mechanisms such as those associated with gene expression, cell cycle progression, DNA repair, and regulated cell death. However, to explore these opportunities for clinical purposes, it is essential that sophisticated control of temperature, both spatially and temporally, must be improved in deep body regions.

To understand the limitation of using hyperthermia as the only cancer treatment strategy as well as the advantages of its use combined with radiotherapy and chemotherapy, we first need to understand the systemic and cellular effects of hyperthermia and how such effects can sensitize the cells to radiation and chemotherapeutic drugs or synergize with them. As we will see in the following topics, hyperthermia displays direct cytotoxicity, systemic effects, chemosensitization, radiosensitization, and immune modulation, which fosters apoptotic and immunogenic death of tumor cells leading to local and, in exceptional cases, to systemic tumor control.

22.2.2 Biological Effects of Hyperthermia

Understanding the direct cytotoxicity of hyperthermia is linked to the preclinical research developed since the 1970s. Such studies demonstrated that temperatures ranging from 41 to 47 °C exhibited an immediate cell-killing effect *in vitro* and *in vivo* hyperthermic experiments [39, 40]. However, when analyzing the growth curve of the cells subjected to these experiments, it was clear that there were two distinct stages in this process: at the beginning of exposure to heat, a linear growth arrest was observed, followed by exponential cell death. Interestingly, the researchers observed a correlation between the thermal energy dose necessary to induce exponential cell death and cellular proteins' denaturation. Therefore, from these studies, it was possible to conclude that hyperthermia treatment's direct cytotoxicity was based on the denaturation and aggregation of cytoplasmic, nuclear, or membrane proteins [41].

Today, hyperthermia presents multiple effects and induces many changes in cells, including disruption of the cytoskeleton, fragmentation of the Golgi system and endoplasmic reticulum, changes in nuclear processes and cell membrane, and decrease in the number of mitochondria and lysosomes [42]. More than modifying the cellular structure, the alteration of these molecules, many of which are signaling proteins, induced by the increase in temperature can affect cell signaling pathways responsible for the control of cellular processes such as growth capacity, proliferation, adhesion, migration, death, among others [43, 44]. Importantly, hyperthermia has been shown to induce apoptosis in cancer cells by activating the intrinsic pathway and inducing the activity of

death receptors and activation of the extrinsic pathway. Furthermore, hyperthermia activates the apoptotic machinery due to the endoplasmic reticulum stress induced by unfolded or misfolded proteins. The signaling pathways associated with the induction of apoptosis in cancer cells will depend on the duration and intensity of heat stress in addition to the cell type [42, 45].

Over time, it became increasingly clear that thermal stress induced by hyperthermia promoted cell death through apoptosis and was also associated with the induction of systemic immunomodulatory effects, which are essential for controlling recurrent tumors and metastases [41]. Interestingly, the immune response triggered by hyperthermia is a direct result of its ability to induce cell death, which, in this way, can be described as immunogenic cell death. Several types of cell death differ in biochemical mechanisms and morphological characteristics. Also, some types of cell death can be considered immunogenic, while others can be known for their inability to induce an immune response. Apoptosis is an example of cell death that can be regarded as nonimmunogenic and noninflammatory most of the time. However, currently, the new concept of immunogenic cell death has challenged this traditional view and has granted apoptosis with immunogenic abilities [46]. Unlike apoptosis, necrosis is recognized for being an extraordinarily inflammatory and immunogenic cell death. Necrotic cells are affected by the loss of plasma membrane integrity, swelling, and release of cytoplasmic content in the medium. Present in the released cytoplastic content is danger signals or damage-associated molecular patterns (DAMPs). Danger signals can be recognized by innate immune cells or dendritic cells inducing innate immune responses or adaptive immune responses, respectively. Among the potent danger signals released by cells undergoing hyperthermia are high-mobility group box 1 (HMGB1) protein, adenosine triphosphate (ATP), and heat-shock proteins like Hsp70 [41, 47].

Molecular chaperones, such as the stress proteins Hsp70 and Hsp90, facilitate the folding of numerous oncogenic proteins, maintain proliferative potential, and inhibit apoptosis in cancer cells contributing to the malignant phenotype's maintenance [48]. These proteins undergo increased expression when stimuli induce intracellular stress, such as increased temperature caused by hyperthermia, and help in protein folding, the resolution of protein aggregates, and intracellular protein transport to prevent heat-induced stress and cell death. Interestingly, when HSPs, especially Hsp70, are exposed to the cell membrane or stay free in the extracellular environment, it will act as a messenger communicating the cells' interior protein composition to the immune system to initiate immune responses against intracellular proteins from the cancer cells [49]. Such events can induce both innate immune responses through the activation of natural killer (NK) cells as adaptive immune responses through maturation and activation of dendritic cells [50].

During the innate immune response stimulation, Hsp70 is exposed to the cancer cell surface and can be recognized and lysate by NK cells [51]. The induction of an adaptive immune response showed a different role for Hsp70, which acts as a carrier of tumor antigens peptides recognized and processed by dendritic cells stimulated to mature and secrete cytokine by heat shock proteins like Hsp70. Once acquired by the tumor cells' antigenic profile, dendritic cells induce antigen-specific T cell recognition and activation via major histocompatibility complex (MHC) class I molecules, a cross-presentation mechanism [49, 52, 53].

It is known that generating a cancer cell is formed by multiple stages and to become a complete cancer cell, premalignant cells must learn to avoid the so-called "immunosurveillance" and promote immune subversion, actively suppressing immune responses [4, 54]. Thus, efficient anticancer therapies must, among other characteristics, be able to restore the ability of the immune system to detect cancer cells inducing immune responses. This fact is the case of hyperthermia that, mainly through Hsp70, can trigger an immune response that fights cancer at the local and systemic

levels preventing the local tumor recurrence and the appearance of distant metastasis [55]. Studies have also shown heat-dependent immunological reactions of human leucocytes and specific effects on NK cells and cytokine depletion in response to hyperthermia, demonstrating that this therapy's actions are not restricted to the consequences of the Hsp70 expression [50, 56].

The biological effects of hyperthermia also include changes in the cellular and tissue structures of the tumor and repression of cellular programs associated with gene expression, DNA repair, proliferation, macromolecules synthesis, cell cycle progression, among others [42]. Results from preclinical studies have been demonstrated that in temperatures of 40–41 °C, most human tumors have increased blood flow under hyperthermia and hours later. In agreement, clinical data and experiments *in vivo* show increased perfusion in the tumor and the surrounding microenvironment, leading to a higher oxygen concentration (pO_2) [57, 58]. Such effects can be associated with hyperthermia's ability to increase the vascularization of the tumor mass and, at the same time, enhance the vessel's permeability.

From a biochemical point of view, all these effects can be seen as consequences of the structural alteration of biomolecules and, consequently, loss or changes in their functions, promoted by increased temperature. The biological effects of hyperthermia are not yet fully understood and are still under investigation. However, it is known that these effects comprise direct cytotoxicity, systemic effects, and immune modulation [41].

22.2.3 Bioactive Glass-Ceramics Applied in Magnetic Hyperthermia

In the 1970s and 1980s, magnetic hyperthermia from magnetic materials flourished as a counterpoint to magnetic induction hyperthermia derived from eddy current. Therefore, the search for materials able to perform magnetic hyperthermia and allow high selectivity and safety was at the center of researches in this field. Then, in 1983, Albert A. Luderer proposed the first ferrimagnetic glass-ceramic suggested for hyperthermia applications. According to Dr. Luderer, *The reason for using a glass-ceramic material as opposed to a pure ferrimagnetic ceramic material was that much greater control could be exercised over the physical, chemical, biochemical, and magnetic properties of the glass-ceramic by virtue of glass composition, glass-forming technique, and thermal history*. The glass-ceramic was based on the $60.5Fe_2O_3$–$23.7P_2O_5$–$11.6Li_2O$–$3.4SiO_2$–$0.4Al_2O_3$ system and was tested in subcutaneous cancer in mice, and the results evidenced significant tumor regression or complete cure [59].

Simultaneously, in the 1970s and 1980s, Dr. Larry L. Hench published his first works about bioactive glasses for bone regeneration applications [60], which encourages other researchers to develop other glass-ceramics for the same purpose [61]. Some years later, by putting together the valuable ideas from Luderer and Hench, Ebisawa et al. [62] proposed the first magnetic bioactive glass-ceramic (MBGC), which was able to display (i) ferrimagnetic properties for applications in magnetic hyperthermia and (ii) bioactivity properties able to bond to the host tissue through an apatite-like layer grown on its surface through a bioactivity process.

Since the work from Ebisawa et al. [62], many other researchers developed glass-ceramic and composites aiming for better magnetic properties – which is required for high efficient hyperthermia – or better bioactivity properties, considering that the growth of crystalline phases during the thermal treatment to produce glass-ceramics sometimes jeopardize the bioactive ability of the final material. These scientific breakthroughs were mainly driven by the development of new synthesis routes like the sol–gel synthesis. In Sections 22.2.3.1–22.2.3.3, we will cover the advances of MBGCs from the perspective of glass processing technologies, including melt-derived glass-ceramics, biphasic glass-ceramics, and sol–gel-derived glass-ceramics.

22.2.3.1 Melt-Derived Glass-Ceramics

The first bioactive glass-ceramics were produced by melt-quenching, followed by thermal treatment, which is the most traditional method to make glass-ceramics. That was the first approach used by Ebisawa et al. [62]. The first generation is divided into two subcategories: (i) glass-ceramics containing magnetite crystals; (ii) glass-ceramics containing zinc ferrite crystals.

Glass-ceramics containing magnetite crystals were the first studied glass-ceramics aiming at hyperthermia applications in bone cancer. Ebisawa et al. [62] produced a glass based on the Fe_2O_3–$CaO{\cdot}SiO_2$ system. Later, to nucleate magnetite (Fe_3O_4) crystals, the glass was submitted to different thermal treatments between 600 and 1100 °C. Their results evidenced that thermal treatment between 700 and 950 °C leads to the crystallization of magnetite crystals, but above 950 °C, there is thermal oxidation of magnetite converted into hematite, besides the formation of wollastonite.

Moreover, the magnetic characterization of these glass-ceramics showed that ferrimagnetic properties were related to the fraction of magnetite crystals. Therefore, these results raised awareness about precise temperature control to enhance magnetic properties suitable for the hyperthermia effect. Furthermore, the authors also showed in *in vivo* studies that these glass-ceramics were able to generate heat under safe frequencies and magnetic field strength and bond to the bone tissue, which is evidence of proper bioactivity [63].

Once Ebisawa observed that thermal treatments could lead to magnetite thermal oxidation, other researchers evaluated other variables related to loss of magnetic properties, such as the fraction of iron oxide in the glass structure. In this sense, two works were complementary to one another: (i) the work from Singh et al. [64] that evaluated the influence of low content of iron oxide in the glass-ceramic structure, (ii) and the work from Leventouri et al. [65] that studied the influence of more extensive contents.

Singh et al. [64] showed that glass-ceramics based on the system $41CaO–(52-x)SiO_2–4P_2O_5–xFe_2O_3–3Na_2O$ ($x = 0$, 2, 4, 6, 8, and 10 mol%) treated at 1050 °C yields ferrimagnetic properties proportional to the iron oxide content in the glass composition, mainly regarding saturation magnetization and hysteresis loop area, which suggests that thermal oxidation is less intense at lower iron oxide fractions. However, in the work of Leventouri et al. [65], it was shown that at high fractions of iron content, thermal oxidation is more prominent and limits ferrimagnetic properties. It was studied the influence of heat treatment between 600 and 1100 °C on the crystallization and magnetic behavior of glasses based on the system $[45(CaO, P_2O_5)(52-x)SiO_2–xFe_2O_3–3Na_2O]$, $x = 5$, 10, 15, 20 wt%. The results evidenced that iron oxide content up to 15 wt% and thermal treatment until 950 °C favors magnetite crystallization. On the other hand, either higher iron oxide fractions or higher temperatures favor the formation of hematite in the thermal treatment. Consequently, the magnetic properties are favored in the same conditions that favor the crystallization of magnetite. Despite hematite formation, the glass-ceramics from Leventouri et al. still display better magnetic properties than those produced by Singh et al. For example, Leventouri et al. reached $M_s \sim 26$ emu/g, while Singh et al. obtained $M_s \sim 7.95$ emu/g.

Another significant contribution to the field of MBGC was brought by Bretcanu et al. [66], who showed that the magnetic phase's crystal size plays an essential role in maximizing power loss in ferrimagnetic glass-ceramics. Glass-ceramics based on the $Na_2O–CaO–SiO_2–P_2O_5–FeO–Fe_2O_3$ system containing 20 and 45 wt% of magnetite phase, named as S35 and S45, respectively, were produced without the formation of undesired phases. Although the glass-ceramic S35 had fewer magnetite crystals and displayed lower saturation magnetization (Figure 22.3a), a more significant coercive force was addressed to this glass-ceramic due to smaller magnetite crystals responsible for creating more magnetic domains per unit of volume. Consequently, under low magnetic field

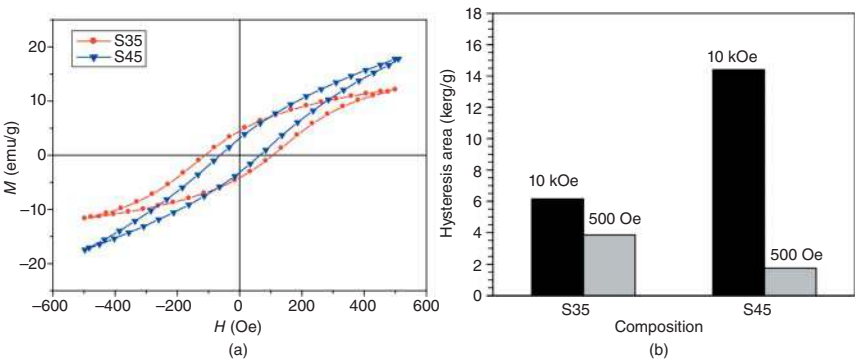

Figure 22.3 Magnetic characterization performed by Bretcanu et al.: (a) magnetization vs. magnetic field strength of the S35 and S45 glass-ceramic; (b) hysteresis loop area of glass-ceramics at 10 kOe and at 500 Oe that is the magnetic field strength used in clinical practice. Source: Bretcanu et al. [66]/with permission of Elsevier.

strength of 500 Oe, which is commonly used in the clinical practice, the glass-ceramic S35 showed higher hysteresis area (Figure 22.3b), once coercive force displays a more substantial influence on the hysteresis area under external magnetic fields lower than the M_s. In this sense, a crystal engineering approach can be used to tune magnetic properties.

Zinc ferrite's magnetic crystal is another strategy to enhance magnetic properties, thus making the glass-ceramic better transductor of magnetic energy into heat. Zinc ferrite is an oxide of spinel crystalline structure and paramagnetic. However, when Zn^{2+} and Fe^{2+} assume aleatory distribution in the tetrahedral A sites or octahedral B sites, their spins are coupled by superexchange interactions, turning zinc ferrite into a ferrimagnetic material [67]. Besides, zinc ferrite displays higher saturation magnetization than magnetite, which favors a more significant hysteresis area and a consequent higher power loss.

The superior magnetic properties of glass-ceramics containing zinc ferrite were showed by Shah et al. [67], who studied the influence of different ZnO content on the magnetic properties of glass-ceramics based on the system xZnO–25Fe_2O_3–(40 – x)SiO_2–25CaO–7P_2O_5–3Na_2O (x = 4, 6, 8, and 10 wt%). An increase of saturation magnetization as in the function of ZnO in the glass-ceramic composition was reported. Also, Shah et al. [68] showed that if an external magnetic field (1 T) is applied during the cooling of the thermal treatment used to grow zinc ferrite, the magnetic domains become trapped and more stable preferential directions. Consequently, these materials' coercive force becomes much higher, which increases the hysteresis area and their power loss, as shown in Figure 22.4.

Although the melt-derived MBGC had significant advances in magnetic properties, bioactivity and glass dissolution were still concerned about melt-derived glass-ceramics, once crystallization of undesired phases could negatively affect bone regeneration in the long term. Besides, the advent of sol–gel synthesis enabled bioactive glass and glass-ceramics with tuned bioactivity [69, 70], and many researchers tried to figure out how to produce MBGC by this method to enhance bioactivity and bone regeneration properties. Altogether, these points lead us to the next topic, which is the biphasic MBGC.

22.2.3.2 Biphasic Glass-Ceramics

The period between 1950s and 1990s was crucial for the establishment of sol–gel synthesis based on alkoxides. One of the first materials studied for such a purpose was silica particles derived from

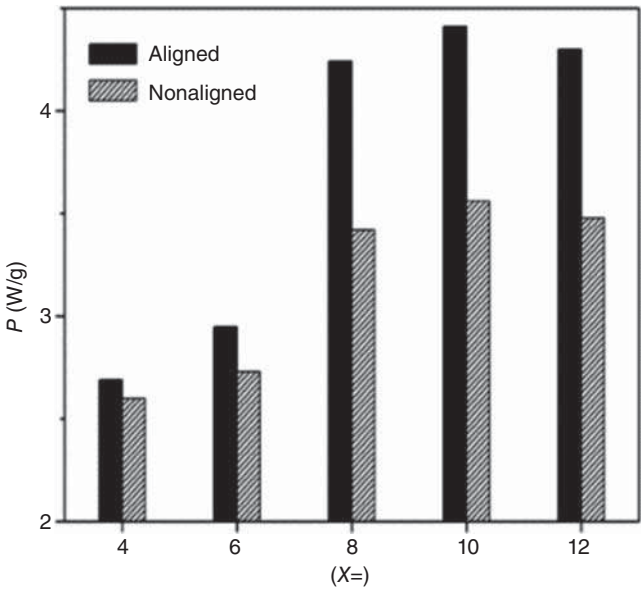

Figure 22.4 Comparison of zinc ferrite glass-ceramics power loss after heat treatment performed in an aligned or nonaligned magnetic field. Source: Shah et al. [68]/with permission of Elsevier.

alkoxides like tetraethyl orthosilicate (TEOS) or tetramethyl orthosilicate (TMOS). The advance of sol–gel synthesis had a tremendous impact not only in electronics and biomedicine but also in glass science [71–73]. The main advantage of sol–gel synthesis was the control of particle size and shape, which is not easily controlled by traditional techniques like frit glasses. Concerning bioactive glasses and glass-ceramics, the advance of sol–gel synthesis meant controlling the effective surface area and chemical reactivity of glass powders; thus, these glasses display better apatite forming-ability in simulated body fluid (SBF) solution than their melt-derived counterparts [70, 74].

To overcome the bioactive limitations of MBGC produced by the melt-derived method, Arcos and Real [75] introduced the concept of biphasic glass-ceramics, which is a mixture of sol–gel glass with other phases that show magnetic properties. In this sense, there are two types of biphasic glass-ceramics: (i) mixture of sol–gel glass with melt-derived magnetic glass-ceramic, and (ii) mixture of sol–gel glass with magnetic crystals. In the following paragraphs, we shall cover both types of biphasic glass-ceramics.

In 2003, Arcos and Real [75] introduced the concept of biphasic glass-ceramics, which were made of a mixture of sol–gel-derived highly bioactive glasses and melt-derived ferrimagnetic glass-ceramics. Then, these biphasic glass-ceramics were able to take advantage of the best of each phase, that is: (i) the high bioactivity of sol–gel bioactive glasses; (ii) the ferrimagnetic properties of melt-derived glass-ceramics.

The first biphasic glass-ceramic was based on different ratios (5 : 1, 2 : 1, and 1 : 1) of a 58S sol–gel glass ($58SiO_2$–$33CaO$–$9P_2O_5$) and glass-ceramic based on the $45SiO_2$–$45CaO$–$10Fe_2O_3$ system. The powders were homogenized, uniaxially pressured, and heat-treated at 750 °C for three hours at the N_2 atmosphere. This last step allowed the growth of crystalline phases of ferroan wollastonite ($CaSiO_3 \cdot FeSiO_3$) and ε-(Fe, Ca)SiO_3 in the melt-derived phase, where the ferroan wollastonite was the ferrimagnetic phase. Although these biphasic ceramics were highly bioactive due to the sol–gel glass content, they still displayed low saturation magnetization, ranging from 0.09 to 0.75 emu/g.

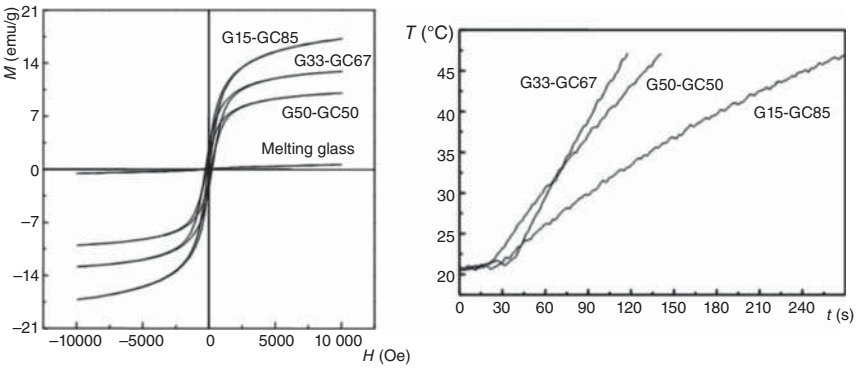

Figure 22.5 Magnetic characterization of biphasic composite: (a) magnetic hysteresis of the samples G15-GC85, G33-GC67, G50-GC50, and melting glass, where G refers to the wt% fraction of the sol–gel glass and GC to the melt-derived glass-ceramic; (b) calorimetric test of the biphasic composites in an aqueous medium. Note that the temperature rise's rate was higher in those composites that displayed higher coercivity at a low magnetic field (500 Oe). Source: Ruiz-Hernandez et al. [76]/with permission of John Wiley & Sons.

To overcome this limitation, Ruiz-Hernandez et al. [76] increased the iron oxide content in the melt-derived phase, yielding a system based on the system $40SiO_2$–$40CaO$–$20Fe_2O_3$. The 58S glass was maintained as the sol–gel phase. The increase in iron oxide content led to saturation magnetization between 10 and 17.2 emu/g, much higher than the previous biphasic glass-ceramic. However, the power loss was dependent on the crystal size. The composition containing intermediate iron oxide content (G33-GC67 in Figure 22.5) showed more refined magnetic crystals; thus, this composition had a more effective interface area between the crystals and the glassy phase, which increased the coercive field strength, increasing the area in the hysteresis loop. Consequently, this composition showed higher power loss than the composition of G150GC85 that had higher saturation magnetization.

In 2010, Li and coworkers [77] proposed a similar method to obtain MBGCs, but the authors replaced the glass-ceramic with ferrite crystals. Therefore, instead of using a glass-ceramic and a sol–gel glass as precursors of the biphasic composite, the author used magnetic crystals and sol–gel glasses. Two interesting examples are biphasic glass-ceramics based on magnesium ferrite (Fe_2MgO_4) [77] and manganese ferrite ($MnFe_2O_4$) [78]. In both cases, the ferrimagnetic crystals were mixed with sol–gel glasses based on the CaO–SiO_2–P_2O_5–MgO–CaF_2–Fe_2O_3 system, sintered at 1200 °C/2 h at air atmosphere. The author employed a ferrite to sol–gel glass ratio of 1 : 10. In both cases, the authors evidenced that part of the ferrites was consumed during sintering, affecting the saturation magnetization. For example, before sintering, mixtures showed M_s values between 16 and 25 emu/g, which was decreased to values between 6 and 8 emu/g after sintering. Moreover, the bioactivity was delayed in the biphasic glass-ceramics when compared with the pure sol–gel glass.

From processing and chemical structure, the biphasic glass-ceramics are different from the glass-ceramic that belongs to the first generation because the biphasic ones are made of two different materials, besides being partially derived from sol–gel glasses. However, some limitations of crystalline glass-ceramics were still persistent, such as the formation of undesired phases or delayed bioactivity. The different phases also showed different thermal coefficients, yielding thermal coefficient mismatch, which could favor crack propagation during thermal treatment. Taking these points into account, one may infer that the melt-derived and biphasic glass-ceramics still had room for improvements, which drive us to the sol–gel-derived MBGC.

22.2.3.3 Sol–Gel-Derived Glass-Ceramic

Melt-derived and sol–gel MBGC could not overcome either limitation in magnetic properties or bioactivity. However, the advance of sol–gel synthesis enabled the production of glass-ceramics entirely by the sol–gel method, making these glasses different from the glass-ceramics from the other classification, and deserves a new one. These glass-ceramics belonging to the third generation of MBGC were able to improve these ceramics' bioactivity. It is worth noting that bioactive glasses produced by the sol–gel method usually exhibit better bioactive properties due to the higher surface area and reactivity than their melt-derived counterparts [79]. The glass-ceramics from the third generation can be grouped into three categories: (i) MBGC powers; (ii) mesoporous MBGC; (iii) MBGC scaffolds. In the next paragraphs, we shall describe the advances and the properties of each subcategory of MBGC from the third generation.

If Li et al. [69] were the first group to report bioactive glasses' development using the sol–gel method, then Wang et al. [80] was the first research group to produce MBGC by the sol–gel method. Their glass-ceramics were based on the system $(100-x)(40CaO–39.6SiO_2–12P_2O_5–8.4Na_2O)–xFe_2O_3$ (where x = 16.6, 33.3, 42.2, and 50) and were produced by an acidic route proposed by Brinker and Scherer [73]. In this method, the glass precursors are dissolved in an acidic medium, and the sol–gel reaction occurs during aging at mild temperatures (60–70 °C). Also, along with aging, the precipitation of iron oxide crystals concomitant to the glass precursors' gelling caused the incorporation of magnetic crystals in the glass network. Finally, after heat treatments at 220 °C/20 h and 800 °C/2 h, the final glass-ceramic showed ferrimagnetic properties with saturation magnetization between 4 and 5 emu/g with different coercive field strength. This method evidences the lack of control of the magnetic phase's growth once these crystals are grown during aging.

Nevertheless, these glasses showed the ability to selectively kill tumor cells in *in vitro* experiments under an external alternating magnetic field, which evidences their potential application in hyperthermia. Figure 22.6 shows the effect of hyperthermia of these glass-ceramics on healthy fibroblast cells (HFL 1) and human lung cancer cells (A549). Note that cancer cells were much more affected by glass-ceramics under AC magnetic field than the healthy cells, evidencing the selectively hyperthermic effect displayed by the glass-ceramics.

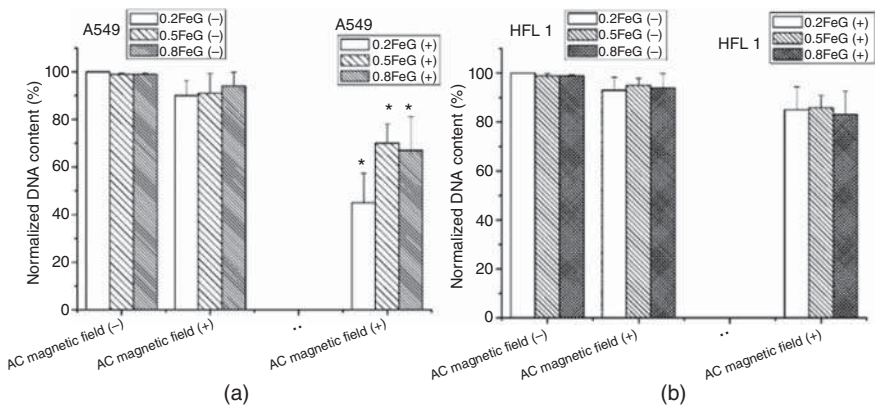

Figure 22.6 Magnetic and biological characterization of sol–gel derived magnetic glass-ceramic: (a) cytotoxicity test in human lung cancer cell linage (A549); (b) cytotoxicity test in fibroblast cell linage (HFL 1). In both cytotoxicity tests, signals positive or negative in the labels refer to the variable's presence or absence. Source: Wang et al. [80]/with permission of John Wiley & Sons.

The method proposed by Wang et al. [80] demonstrated that the control of magnetic crystal growth was not possible due to their precipitation along with glass precursors' aging. Almost 10 years later, Shankhwar and Srinivasan [74] further showed that the concentration of iron precursors used in the sol–gel synthesis also plays a significant role in the growth of magnetic phases. Shankhwar et al. proposed a sol–gel synthesis to produce glass-ceramics based on the 45S5 bioactive glass ($45SiO_2{\cdot}24.5CaO{\cdot}24.5Na_2O{\cdot}6P_2O_5$) containing fractions of iron oxide of 2 and 3 wt%, named BG_Fe_2 and BG_Fe_3, respectively. They showed that the BG_Fe_2 glass did not have any crystalline phase, while the BG_Fe_3 glass-ceramic had sodium calcium silicate and maghemite. This fact evidenced that a lower fraction of iron precursor in the synthesis could not promote the precipitation of iron oxide phases. Further thermal treatment was needed to induce the nucleation of magnetic crystals in the BG_Fe_2 glass, yielding a glass-ceramic, named BC_Fe_2, containing magnetite. However, this method yields glass ceramic with low saturation magnetization (<1.5 emu/g), which can be considered as a limitation of this "co-precipitation" sol–gel synthesis.

Besides the fraction of iron oxide precursors used in the sol–gel synthesis to produce MBGC, the calcination atmosphere is another crucial variable. Baino et al. [81] showed that glass-ceramics based on the system $60SiO_2–(40-x)CaO–xFe_2O_3$ ($x = 2$ and 10 wt%) and calcined either at air or argon atmosphere lead to different crystallization paths. After performing the calcination at 800 °C, Baino et al. observed that low fractions of iron oxide (2 wt%) do not lead to glass devitrification during calcination, regardless of the employed atmosphere, similar to the results reported by Shankhwar and Srinivasan [74]. On the other hand, at high iron contents (10 wt%), calcination performed at the air atmosphere yields the formation of hematite, while the calcination performed at argon atmosphere yields the formation of magnetite and maghemite crystals. Undesired crystalline phases were also grown in high iron content synthesis. Once magnetite and maghemite are inherent ferrimagnetic materials, those glass-ceramics calcined at argon atmosphere showed much better magnetic properties (2.17 emu/g) when compared with the other compositions (<0.2 emu/g). Therefore, calcination or thermal treatment atmosphere can be used to tune magnetic properties.

The advances in the sol–gel synthesis allowed the development of mesoporous structures, including mesoporous bioactive glasses [82, 83]. In summary, these mesoporous structures are obtained by adding self-assembled micelles and the synthesis, which are responsible for forming highly ordered structures. When the gels are calcined, the ordered micelles are degraded, leaving empty mesopores.

The production of mesoporous MBGC can be performed in two different ways: (i) a mesoporous glass can be synthesized, and magnetic crystals can be grown within the mesopores [84]; (ii) magnetic nanoparticles can be added to the synthesis of the mesoporous glasses [85]. Note that the different approaches yield different structures, as evidenced in Figure 22.7. It is worth noting to mention that in the first case, the magnetic crystals are confined in the mesopores, enabling the control of crystal growth. In contrast, in the second approach, the magnetic nanoparticles are previously synthesized and dispersed within a mesoporous structure.

The production of mesoporous MBGC through the growth of magnetite crystals confined in the mesopores was proposed by Yan et al. [84], which produced an amorphous mesoporous structure through the ELISA method, and based on the system $80SiO_2–(15-x)Fe_2O_3–5P_2O_5–xCaO$ ($x = 0$, 5, and 10 mol%). After obtaining the powders, after calcination, the glasses were submitted to a heat treatment at 380 °C in an H_2 atmosphere. It caused the reduction of Fe_2O_3 into Fe_3O_4. The pores were exposed to the hydrogen atmosphere, favoring the nucleation of crystals within the mesopores, although crystals were also grown on particle surfaces. Also, because the grown crystals

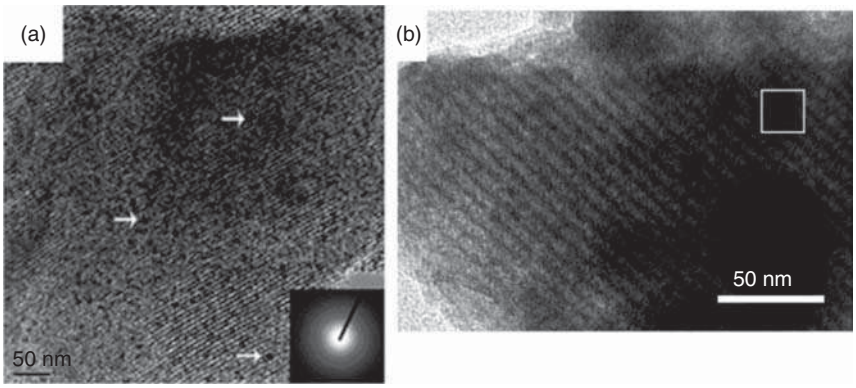

Figure 22.7 Transmission electron microscopy of mesoporous MBGC obtained by different methods. (a) Growth of nanocrystals confined in the mesopores (the white arrows are pointing these crystals). The inset shows the diffraction pattern of the samples, which show that the MBG is fully amorphous. Source: Li et al. [86], Fig 02a (p. 3262)/Elsevier. (b) Magnetite nanoparticles added in the ELISA process. Source: Liu et al. [85], Fig 3c (p. 200)/Elsevier.

were nanometric, they display superparamagnetic properties that, in turn, were dependent on the iron content in the glass structure (M_s from 0.21 to 3.57).

The production of mesoporous MBGC by incorporating nanoparticles in the ELISA method was proposed by Liu et al. [85], yielding nanocomposites based on the system $75SiO_2$–$15CaO$–$5P_2O_5$:$5Fe_3O_4$. In this case, there is no need for additional thermal treatment besides calcination. However, the ELISA method does not allow the incorporation of large quantities of nanoparticles, limiting the magnetic properties ($M_s \sim 1.5$ emu/g).

The mesoporous structure can also be used to load drugs to be delivered into the cancer site, thus combining hyperthermia to drug delivery approaches. Both mesoporous MBGC proposed by Li et al. or Liu et al. were incorporated with ibuprofen and gentamicin, respectively (Figure 22.8). Both studies showed that the magnetic crystals affected drug loading and accessibility, which disturb the pores' permeability over a concentration-dependent manner. As more crystals are in the final material, less drug or less accessible becomes the mesopores.

Besides drugs, therapeutic ions can also be incorporated into the glass structure and cause a specific desired biological response. Koohkan et al. [87] produced glass-ceramics through the EISA process, based on the system SiO_2–CaO–Fe_2O_3–P_2O_5 with the addition of copper oxide (CuO). However, the authors did not report any thermal treatment to induce crystals' formation in the mesopores once the crystals were grown along with the EISA process. In this case, the copper was intended to display an angiogenic effect, favoring bone regeneration. In this case, the authors not only showed that the HUVEC (human umbilical vein endothelial cells/C554) had an enhanced proliferation under indirect contact with dissolution products from the Fe–Cu-containing MBGC but also showed that the addition of copper caused tuned magnetic properties (M_s from 0.2 emu/g in the Fe-MBG to 1.0 emu/g in the Fe–Cu-MBG).

The development of scaffolds allowed osteoconductive 3D structure production and gives mechanical support for cell growth and bone regeneration. The production of powders by the sol–gel method also favored scaffold production by foam-replication process, one of the most widely employed methods to produce bioactive glass scaffolds.

Baikousi et al. [88] were the pioneers in producing MBGC scaffolds. In their work, scaffolds based on the system $70SiO_2$–$25CaO$–$5P_2O_5$ (CSP, mol%) were produced and subsequently submitted to a chemical treatment sequence to grow maghemite crystals in the pores. First, the scaffolds were immersed in an iron III nitrate solution, dried, and treated under vapor of acetic acid

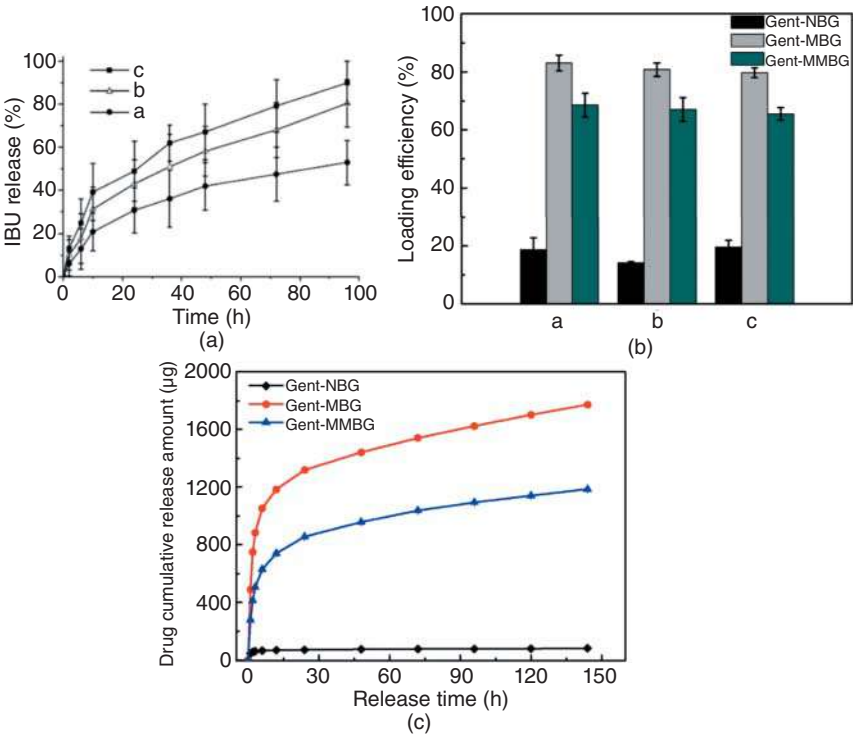

Figure 22.8 Drug release results of mesoporous MBGC obtained from different methods. (a) Growth of nanocrystals confined in the mesopores. Source: Li et al. [86]/with permission of Elsevier. (b, c) Magnetite nanoparticles added in the ELISA process. Source: Liu et al. [85]/with permission of Elsevier.

(99.5%). Then, the scaffolds were submitted to two thermal treatments, which favored the growth of maghemite: 15 minutes in argon (Ar) flowing atmosphere at 400 °C (CSP400@mag-17) or 800 °C (CSP800@mag-17). In this work, it was evidenced that the thermal treatment played an essential role in magnetic crystal growth: the higher the thermal treatment, the higher the saturation magnetization values. Besides, the grown crystal did not jeopardize the scaffold bioactivity, even though undesired crystalline phases were also formed.

Wu et al. [89] showed that the polymer foam replication method could be coupled with the EISA method to produce scaffolds with mesoporous structures. The authors then immersed a polyurethane sponge (25 ppi) in a sol phase of the EISA method. After calcination at 700 °C to eliminate the polymer template, a trabecular-like scaffold containing a mesoporous structure was obtained (Figure 22.9). The authors were able to produce glasses similar to that from Li et al. [86] (Aforementioned in the Section 22.2.3.3), with the addition of 5 and 10 mol% of magnetite. The final scaffolds showed ferrimagnetic properties, besides being bioactive and stimulating the gene expression of osteocalcin and alkaline phosphatase activity. However, the final scaffolds' saturation magnetization was still low, ranging from 0.2 to 1.0 emu/g, a limitation of mesoporous MBGC when the crystals are grown in the mesopores.

22.2.4 Future Perspectives, Open Questions, and Challenges

Based on the three generations of MBGC showed so far, it is clear that allying magnetic properties with bioactivity is still a challenge. None of them could make highly magnetic and highly bioactive

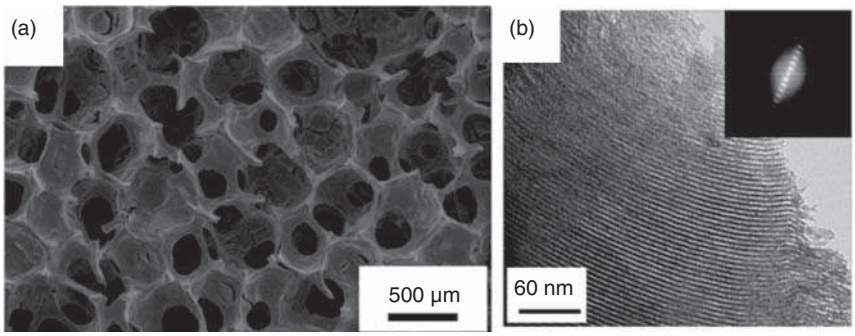

Figure 22.9 Magnetic scaffolds produced by the sol–gel method. (a) SEM micrograph of the trabecular-like structure of the scaffold. Source: Wu et al. [89], Figure 02 (p. 04)/Elsevier. (b) TEM micrograph showing the mesoporous structure of the walls of the scaffold. The inset figure shows the diffraction pattern of the mesopores. Source: Wu et al. [89], Figure 03 (p. 05)/Elsevier.

materials, and the fourth generation of MBGC may be the one to overcome this challenge. It is worth noting that the only material approved for clinical applications is superparamagnetic iron oxide nanoparticles (SPIONs) intended for applications in neuroblastoma. It means that magnetic hyperthermia, as a whole, needs more advances to make this treatment widely available for different cancer treatments. However, the comparison between scientific knowledge about SPIONs and MBGC can bring interesting questions about physical and biological studies.

When MBGCs are compared with SPIONs, it is noted that magnetic interactions between SPIONs and how to make them more effective transducers in clinical applications have been exhaustively studied [90, 91]. There is limited knowledge about the magnetic interactions between magnetic crystals embedded in a bioactive glass matrix. Maybe, suppose more studies were performed by magnetic susceptibility or zero-field cooling, field cooling (ZFC–FC), measurements are performed. In that case, we could understand how magnetic crystals interact with one another, bringing more new ideas about glass-ceramic structure engineering [90]. For example, it is already known that SPIONs coated with SiO_2 are likely to display magnetic coupling if the coating is too thin to enable interparticle interactions [92], which leads to lower power loss. Ideas like that can be interesting to enhance the magnetic properties of MBGC without changing glass composition.

Regarding biological properties, there is a considerable lack of *in vivo* studies about the effectiveness of MBGC. Ironically, the first study of MBGC was maybe the only one to perform *in vivo* studies. There is a need for more evidence about these glasses' ability to treat the bone tumor and regenerate the tumor's bone defect. So far, studies have been focused on evaluating the effectiveness of these glasses through *in vitro* cell culture. Of course, these *in vitro* studies are needed, but the lack of *in vivo* studies establishes a gap between technological innovation and clinical practice in the long term. Nonetheless, *in vitro* studies still lacks an understanding of the molecular biology interplay happening during MBGC-derived hyperthermia. This kind of approach could help to understand the success or failure of these materials in treating cancer.

22.3 Bioactive Glasses Applied in Brachytherapy

22.3.1 Brachytherapy: Classification and Physical Aspects

The name brachytherapy is derived from ancient Greek words for "short distance" (brachios) and "treatment" (therapy) and has been developed for more than 100 years, merging with the evolution

of oncology and nuclear medicine [93]. Thus, it is considered a generic term used to treat different cancer types when a sealed ionizing radiation source is positioned near the diseased tissue. It is also known as internal radiation therapy.

Compared to external therapy, the main advantage of brachytherapy is the radiation concentrated only in the region of interest, i.e. in a tumor, significantly reducing the harmful side effects of radiation on healthy tissues [94, 95]. Ionizing radiation comes from the decay of radioisotopes, α or β particles, or γ rays. These radioisotopes react with cells by direct or indirect mechanisms. Through the direct mechanism, they interact with the atoms of biomolecules, such as DNA. On the other hand, they can break down water molecules by the indirect mechanism, resulting in highly reactive oxidizing agents, which affect other vital cells, leading to cell death [96].

Some therapies use nonsealed radioactive sources, such as radiopharmaceuticals. Once injected into the patient's body, these bioactive are chemically attracted to the damaged tissue to be diagnosed or treated. On the other hand, in brachytherapy procedures, the radiation source is located at short distances from the tissue to be irradiated, up to 12 mm. It is surrounded by a capsule, thread, needle, or microsphere to keep radionucleotides immobilized without migrating to other body regions. It is successfully applied in treating several types of cancer, including prostate, breast, uterus, skin, rectum, head and neck, esophagus and stomach, eyeball, and liver. In addition to the direct therapeutic approach, this technique can be used together with other conventional techniques, such as external radiotherapy and chemotherapy, or even as a complementary treatment after tumor extraction [97].

Brachytherapy can be classified as interstitial, intracavitary, intraluminal, superficial, and intravascular, according to the radioactive source's implantation technique [98, 99]. Interstitial brachytherapy occurs when the source is placed directly on the tissue to be irradiated, as in the case of head and neck, prostate, among others. Intracavitary brachytherapy is used to treat gynecological diseases, in which the radioactive source is introduced in the vagina or uterus. In intraluminal brachytherapy, the source is placed inside the lumen, such as the esophagus and trachea. On the other hand, skin and eyeball can be treated by superficial brachytherapy, in which molds or plate sources are positioned on the surface of damaged tissue. Finally, considering intravascular brachytherapy procedures, the radioactive source, as microspheres containing the radioisotope, achieve the damaged tissue through the blood vessels, being suitable for liver cancer treatment.

Another classification of brachytherapy can be related to the applied radiation rate. In the high dose rates (HDRs), the radioactive source is implanted temporarily, reaching up to 12 Gy/h at 1 cm from the source. The middle dose rate (MDR) is considered between 2 and 12 Gy/h, rarely clinically used. The low dose rates (LDR) are procedures with doses between 0.4 and 2 Gy/h. The very low dose rates (vLDR) are applied considering dose rates below 0.4 Gy/h. For the last ones, radioactive sources can be permanently implanted [100].

The treatment can also be performed with a pulsed dose rate (PDR), where the high-intensity radiation dose is applied periodically (typically at every hour) for short periods, aiming to simulate the LDR treatment [93].

The type, site, and stage of cancer, together with the patient's health conditions, are essential variables to be considered to choose the most appropriate dose rate to be applied. High-dose brachytherapy is commonly used once the treatment period is reduced, diminishing possible associated side effects. LDRs are typically used to reduce the patient's pain [93].

Finally, brachytherapy can be classified as permanent or temporary, depending on the patient's interaction with the radiation source. Examples of brachytherapy with permanent implants are prostate, liver, head and neck, lung cancer, and sarcoma treatments. The sources permanently used

must have low energy and a short half-life so that the patient is not excessively exposed to radiation. On the other hand, the temporary procedures consider a limited radiation source action, thus being removed after an established treatment period. This treatment can be from a few minutes, considering HDR, to a few days, for LDR [101].

Among the several factors that should be taken into account in brachytherapy procedures, the source of ionizing radiation, called radioisotope, deserves significant attention. The choice of the most suitable radioisotope for a specific brachytherapy treatment must consider the type of radiation emitted (α, β, or γ radiation), the radiation energy, the radioisotope half-life, their specific activity, safety radiology procedures, and the involved cost of production [102].

Radioisotopes can be produced from the bombardment either by natural nonradioactive isotopes, neutrons in nuclear reactors or by protons and other ions (deuterons, α particles, etc.) particle accelerators, such as cyclotrons. During this bombardment, the atomic nucleus is modified due to the difference between the number of protons and neutrons, becoming unstable and with excessive energy. Therefore, radioisotopes produced in reactors are neutron-rich, such as Mo-99, while those produced in cyclotrons contain more protons in their nuclei, such as F-18. Through radioactivity, the unstable isotope reduces its nucleus's excessive energy to achieve a more stable configuration. This energy reduction process, called radioactive decay or disintegration, occurs through the emission of α or β particles, or γ radiation, in a spontaneous and stochastic process. However, through the probabilistic approach, it is possible to estimate the proportion of atoms as a function of the total number of radioactive N atoms, which will decay in a certain period, known as decay rate [99]. Such a decay rate (Eq. (22.7)) also indicates the radioactive source activity (A).

$$A = \frac{dN}{dt} = -\lambda N \tag{22.7}$$

where λ is the decay constant, the negative sign indicates that, over time, the number of remaining radioactive atoms is continuously decreasing. The number of remaining radioactive atoms can also be predicted as a function of time ($N(t)$, Eq. (22.8)). The radioactive source activity can be estimated ($A(t)$, Eq. (22.9)). At time $t = 0$, the total number of radioactive atoms is N_0, and the respective activity is A_0:

$$N(t) = N_0 \cdot e^{-\lambda t} \tag{22.8}$$

$$A(t) = A_0 \cdot e^{-\lambda t} \tag{22.9}$$

Another critical characteristic of radioisotopes is the corresponding half-life ($t^{1/2}$), i.e. the estimated time for half of the initial atoms to decay. Replacing t by $t^{1/2}$ in Eq. (22.8), it is possible to predict $N(t^{1/2})$ (Eq. (22.10)) and the radioisotope half-life ($t^{1/2}$), according to Eq. (22.11) [100]. Each radioisotope has its decay rate related to the instability of its nucleus. Therefore, half-life varies from milliseconds (like 20.2 ms for ^{12}B) to billions of years (4.47×10^9 years for ^{238}U).

$$N(t^{1/2}) = N_0/2 = N_0 \times e^{-\lambda t^{1/2}} \tag{22.10}$$

$$t^{1/2} = \frac{\ln 2}{\lambda} \tag{22.11}$$

Knowing the radioisotope half-life is essential for any area where these radionuclides are applied. It gives information about how long a radioisotope can remain active. For brachytherapy, the half-life is necessary for choosing the radioactive source and the most suitable treatment.

Table 22.1 β-Emitters useful in particulate radiopharmaceuticals.

Radioisotope	Half-life	Average/maximum β energy (keV)	Maximum range in tissue (mm)	γ-Lines
^{3}H	12.3 yr	5.7/18.0	None	
^{14}C	5730 yr	49.5/156.0	None	
^{32}P	14.3 d	694.9/1710.2	8.7	None
^{90}Y	64.1 h	933.6/2280.0	12.0	None
^{131}I	8.0 d	181.7/806.9	2.4	^{131}Te (β−)^{131}I
^{153}Sm	46.5 h	224.2/808.2	3.0	103.2 keV (29.8%)
^{165}Dy	2.3 h	440.2/1286.7	6.4	94.7 keV (3.6%)
^{166}Ho	26.8 h	665.1/1853.9	10.2	80.6 keV (6.7%)
^{169}Er	9.4 d	99.6/350.9	1.0	$^{168}Er(n,\gamma)^{169}Er$
^{177}Lu	6.7 d	133.3/497.8	1.7	$^{176}Lu(n,\gamma)^{177}Lu$
^{186}Re	89.2 h	346.7/1069.5	5.0	137.2 keV (9.42%)
^{188}Re	17.0 h	764.3/2120.4	11.0	155.0 keV (15.1%)
^{198}Au	2.7 d	311.5/960.7	4.4	411.8 keV (95.5%)

Source: Burrill et al. [103]/with permission of Springer Nature.

Considering the characteristics of radiation emitted by the radioisotope, the α particles' penetration ability in living tissue does not exceed 90 μm. On the other hand, β particles have a maximum penetration of 12 mm, while γ radiation can penetrate deep several centimeters. Thus, the most appropriate radioisotope for cancer treatment must consider, in addition to the characteristics mentioned above, the type and energy of emitted radiation [103].

In general, the radioisotope used in brachytherapy must have a radiation spectrum that allows the treatment of tumors with different dimensions. In this sense, a radioisotope emitting β radiation with high-energy, high-activity, and a short half-life is preferable. This radioisotope must not emit α particles but γ radiation once this last one is used for imaging diagnostics and follow-up. Thereby, it is possible to identify the radioactive source site in the body and monitor its biodistribution. However, this γ radiation must be of low energy to avoid unnecessary radiation dose to the patient [104].

Several radioisotopes have characteristics that allow their application in brachytherapy to treat tumors: ^{32}P, ^{90}Y, ^{109}Pd, ^{140}La, ^{153}Sm, ^{165}Dy, ^{166}Ho, ^{169}Er, ^{186}Re, ^{188}Re, ^{198}Au. Table 22.1 shows the main characteristics of these radioisotopes. ^{188}Re, ^{90}Y, ^{166}Ho are close to ideal conditions. It is also possible to combine radioisotopes with different traits, considering the type of emission, radiation dose, and the half-life, aiming to promote the most appropriate conditions for a specific treatment [105, 106].

22.3.2 Radiobiology of Brachytherapy for Cancer Treatment

The biological effects of antitumor therapies based on ionizing radiation are related to inducing damage to biological molecules such as DNA, proteins, and lipids. Ionizing radiation can interact directly or indirectly with these molecules. The direct interaction of ionizing radiation occurs when an incident photon or an electron released into the medium by ionization interacts directly with the molecules causing structural and functional changes. In indirect interaction, the photon

or free-electron interacts with some molecule in the environment, usually water, leading to the formation of reactive oxygen species such as the hydroxyl radical (·OH) that interacts and causes damage to the other molecules in the environment [96].

The main target of radiotherapy, including brachytherapy, is the DNA chain that can undergo single or double-strand break in addition to chromosomal rearrangements, translocations, and inversions. For dose rates used in brachytherapy (ranging from 0.3 Gy/h to 1 Gy/min), DNA repair is the preeminent parameter of cell lethality, and the ability to repair sublethal damages was a significant factor of the radiobiological effect [95]. At the time of cell replication, DNA's structural integrity is assessed before the cell replicates this molecule to pass copies to daughter cells. Checking systems inhibit cell cycle progression and cell replication when DNA single or double-strand breaks and other damage types are detected while DNA repair mechanisms are activated. These mechanisms involve many proteins capable of identifying the type of injury that has occurred and initiating processes that aim to eliminate the damage and correct the error. Once the error is restored, the cell progresses through the cell cycle phases until it can finish its replication phase. However, if the damage cannot be corrected, the cell is often induced to death by apoptosis or is eliminated in the next proliferative cycle. According to lethality, damage caused by ionizing radiation can be classified as lethal DNA damage, which is irreversible and irreparable, potentially fatal damage, which becomes lethal if not repaired (mainly double-strand DNA break), and sublethal damage, which become lethal when accumulating during a fractionated irradiation, resulting in a cumulative dose effect [95, 107].

Cells' ability to repair the damages caused by ionizing radiation to DNA is associated with several factors, such as the type of damage and its extent. DNA single-strand breaks and double breaks are induced by ionizing radiation, the latter being more lethal because it has less ability to be corrected by cell repair systems. When high doses of ionizing radiation are applied to a cell, DNA damage accumulates, especially the DNA double-strand breaks, leading to cell death. In this way, DNA double-strand breaks have been associated with lethal and potentially lethal damage from ionizing radiation. In contrast, single breaks are generally seen as sublethal damage that can only cause cell death when accumulated after irradiation sessions [108].

Understanding radiobiology, that is, the effects of ionizing radiation on cells and tissues, goes far beyond knowing the types and extent of damage caused by radiation to DNA molecules. Indeed, after a cell is exposed to irradiation, its ability to survive or commitment to death will be determined not only by the type of DNA damage that has occurred and the ability of the cell to repair it but also by its proliferation rate, brachytherapy specificities, and radiosensitivity of cancer and normal cells. The last one is related to cancer cells' interaction and the tumor microenvironment, immune responses, the radiation dose, dose rate, and the treatment duration [108].

The "4R" concept has been used to understand the radiobiology of treatments using external beam radiotherapy (EBRT) to describe the cellular response to ionizing radiation concerning DNA repair, redistribution in the cell cycle, repopulation, and reoxygenation. However, it can also be used to understand BT's biological effects, although some considerations are needed [108].

22.3.2.1 DNA Repair

As mentioned earlier, cells rely on DNA repair systems, and sublethal and potentially lethal damage, especially DNA single-strand breaks, can be repaired. Radiotherapies like BT exploit the differences in normal and tumor cells' capabilities to detect and repair DNA damage as a strategy for treating cancer. Normal cells have a higher DNA repair capacity than tumor cells. Tumor cells generally have defects in the G1 and G2 cell cycle checkpoint systems, often allowing DNA duplication or distribution among daughter cells even in the presence of damage to these molecules.

The p53 transcription factor is considered a tumor suppressor protein whose activity is associated with the modulation of molecular mechanisms responsible for detecting DNA damages and DNA repair machinery. In the presence of structural damage in the DNA molecule, p53 accumulates in the nucleus, where it transactivates the target gene leading to the expression of proteins responsible for inhibiting the cell cycle's progression and repairing the detected damage. If the damage cannot be corrected, p53 induces the expression of proteins associated with the activation and execution of programmed cell death programs, such as apoptosis. The *p53* gene (TP53) is the most frequently mutated tumor suppressor across all cancers, and the loss of its normal function justifying these cells' high sensitivity to the effects of ionizing radiation [108]. Malignant cell transformation, a process that leads a normal cell to become neoplastic, involves the loss of function in various components of DNA repair systems, allowing the future tumor cell to acquire genetic instability. Genetic instability is still fundamental in developing many of a neoplastic cell's characteristics and its progression to more aggressive and resistant phenotypes [4]. In this way, the tumor cells can be seen as defective cells in repair mechanisms and are continually undergoing DNA changes and accumulating genetic alterations. Therefore, in radiotherapy treatments including BT, if the ionizing radiation dose is fractionated and the fractions administered six to eight hours apart (time required to allow the repair in normal tissues), normal cells can repair the DNA damages. Under the same conditions, the tumor cells accumulate potentially lethal and sublethal damage causing them to turn into lethal damage leading to cell death.

22.3.2.2 Redistribution in the Cell Cycle

From the moment a cell is induced to proliferate, a series of molecular events responsible for cell growth will begin, including the synthesis of macromolecules and the duplication of genetic material, and the division of the synthesized material between the daughter cells. These steps characterize the cell cycle that can be divided into two major phases: interphase and mitosis. The interphase can be subdivided into three phases called G1 (gap1), S (synthesis), and G2 (gap 2). In the S phase, DNA is duplicated, while the G1 and G2 phases are those that precede and succeed, respectively, this event. Mitosis is known as the M phase of the cell cycle, and together with the G2 phase, and they are recognized as the phases of the cell cycle most sensitive to the effects of ionizing radiation. The highly compacted state of the genetic material in phase M contributes to a more significant accumulation of damage in the cells submitted to irradiation at this phase. At the same time, in this more compacted state of the genetic material, proteins from DNA repair systems have more difficulty accessing DNA.

In contrast, the S phase presents a lower sensitivity to irradiation, most likely due to the duplicity and decompression of DNA and the increase of the DNA-PKc enzyme involved in repairing DNA double-strand breaks [109, 110]. Thus, tissues with a higher proliferative rate generally have greater sensitivity to radiotherapy and brachytherapy since more cells will be progressing through the cell cycle and reaching the M phase. Tumor cells have a high proliferative rate, while cells from normal nontumor tissues are more differentiated and have a less replicative capacity, which partially explains the greater sensitivity of tumor cells to the effects of ionizing radiation. Each time a tumor tissue is exposed to radiotherapy or brachytherapy, tumor cells in the M phase are eliminated or accumulate sublethal or potentially lethal damage. Tumor cells in the remaining phases of the cycle that have survived continue to progress through the cell cycle and are redistributed in each phase, including phase M. Then, if the tumor tissue is irradiated again, more tumor cells are eliminated. Therefore, the continuous redistribution of tumor cells throughout the cell cycle and treatment with fractional doses of ionizing radiation contributes to more efficient radiotherapy and brachytherapy.

22.3.2.3 Repopulation

The irradiation of nontumor cells during treatments with ionizing radiation is responsible for the usual late side effects associated with the use of this type of therapy. Over the years, imaging techniques and equipment improvement have enabled the development of precision EBRTs, such as stereotactic irradiation and intensity-modulated radiotherapy (IMRT). However, even with these improvements and even in brachytherapy, considered highly accurate, it is still necessary that the protocols aim to minimize the effects on healthy cells and increase the impact on tumor cells. The principle of repopulation is based on the fact that normal cells have a greater capacity to repair the damage caused by ionizing radiation. In this way, as long as there is an appropriate time interval between the fractions of the applied radiation dose, normal tissue cells can repair the sublethal and potentially lethal damage caused by the first radiation exposure and regrow, repopulating the tissue. In contrast, the tumor cells tend to accumulate the lesions culminating in the induction of death.

22.3.2.4 Reoxygenation

The presence of oxygen in the irradiated tissue is essential in radiotherapy treatments because oxygen "fixes" the damage caused to the DNA by radiation. In this way, cells located in environments with low oxygen availability are less affected by ionizing radiation. It is the case, for example, of cells found in the innermost parts of the tumors that constitute markedly hypoxic regions. In general, the tumor environment is marked by an O_2 pressure gradient from the most peripheral cells (more oxygenated) to the most internal and most hypoxic cells in the tumor mass. Unlike healthy tissues, where blood vessels ensure adequate distribution of oxygen and nutrients to all cells, blood vessel networks often present with irregular and chaotic distribution in tumor tissues.

In contrast, blood vessels can be structurally altered, impairing adequate oxygen perfusion in the tissue [111]. The situation becomes even worse for the tumor mass's innermost cells, considering that in the trajectory of the blood vessels, the most peripheral cells are the first to come into contact with the blood, managing to capture oxygen and nutrients in an adequate amount. In contrast, the innermost cells end up in contact with blood vessels where the amount of oxygen and blood nutrients is already quite limited. In the cancer treatment performed by radiotherapy or brachytherapy, there is the more apparent death of peripheral cells, which are more prone to suffer the effect of ionizing radiation. With the loss of the most peripheral cells, the innermost cells have increased oxygen availability, are reoxygenated, and become more sensitive to exposure to a new fraction of radiation.

The "4R" theory is of great importance for fractional radiotherapy treatments that aim to expose tumors to higher total radiation doses while ensuring less toxicity to neighboring healthy tissues. In these treatments, the total dose administered, dose per fraction, number of fractions, and whole treatment time are also carefully defined to increase treatment efficiency and reduce side effects. Importantly, in the last decades, the progress in tumor biology understanding and further studies on the impact of radiotherapy in cancer treatment have brought new components to the study of radiobiology and those already described by the "4R" theory. The amount of radiation tolerated by each patient, intrinsic sensitivity to radiation, radiation interaction with the tumor microenvironment, and the induction of an immune response are among the main biological factors to be considered together with the 4R.

Different types of tumors may differ markedly in their intrinsic radiosensitivity. Radioresistance may be related to tumor cells' inability to activate death mechanisms in the face of lethal damage, among other factors [112]. In these cases, the planning of radiotherapy treatments may involve high doses of radiation to achieve better results. Then, radioresistance has been considered another

radiobiological factor to be considered when planning brachytherapy and radiotherapy in general, therefore, being considered the fifth R to be added to the 4R theory [113].

Although for a long time, tumor characteristics have been associated only with the features and abilities of the tumor cells, today we know that the behavior of the tumor cells and the characteristics of the tumor result from the interaction between the tumor cells and their surrounding environment, the tumor microenvironment. Understanding cancer is understanding the intricate relationships established between tumor cells and fibroblasts, cells of the immune system, blood vessels, and signaling molecules distributed by the extracellular matrix. It is through interaction with the tumor microenvironment that preneoplastic cells acquire, among other characteristics, the immune system's evasion and subversion capabilities, as already described in Section 22.2 of this chapter [4, 54]. Currently, immunotherapies are being introduced as adjuvants to treat metastatic cancers to restore antitumor immunity allowing the target of such cells that fail to be eliminated by the traditional antitumor therapies [114].

Remarkably, radiotherapy is an efficient immune-modulatory therapy. Indeed, radiotherapy's immune-stimulatory effects, referred to as the "abscopal effect," emerged as a hypothesis to explain the rare clinical observations of tumor response in metastases outside the radiation field. According to preclinical models, the abscopal effect is largely immune-mediated, involving the priming of tumor antigen-specific T cells, immune cell infiltration into the tumor tissue, changes in the immunosuppressive tumor microenvironment, and immunogenic modulation of the tumor cell phenotype, leading to an increased sensitivity of irradiated tumor cells to lymphocyte-mediated lysis [115, 116].

The association of BT to immunotherapy is a promising strategy for cancer treatment, including cases where the disease reached the metastatic stage. The higher radiation doses of BT may induce a massive release of tumor-associated antigens, triggering distant abscopal responses. In addition, the heterogeneity of the radiation dose delivered to the tumor may minimize antagonistic effects on peripheral immune cells by avoiding irradiation of draining lymph nodes at the same time allowing multiple immunogenic mechanisms corresponding to each distinct dose range [117, 118]. Indeed, it has been shown that close to the radiation source, the exposure of the cells to hyperdoses results in a high rate of immunogenic tumor cell death followed by the release of tumor-specific antigens needed for the priming of T cells [115]. Along the dose gradient, survivor tumor cells exposed to high-to-intermediate doses per fraction (5–12 Gy) may suffer phenotype modifications that can undergo immunogenic modulation [119]. Tumor regions exposed to moderate doses per fraction (2–5 Gy) may induce leukocyte infiltration in the tumor tissue enhanced by immune-stimulatory cytokines [120, 121]. Even regions exposed to low doses per fraction (1–2 Gy) could benefit from BT promoting the local depletion of suppressive immune cell lineages, highly sensitive to radiation [122, 123]. Besides the potential improvement that can be reached by combining brachytherapy with immunotherapy, only a few preclinical studies have been reported. The results have shown that coupling irradiation of colorectal carcinoma, lung, and pancreatic adenocarcinoma with immunotherapy increase the occurrence of abscopal effects in mice models [121, 124, 125], reinforcing the need for more studies to be carried out in this area.

The effects of brachytherapy on the tumor microenvironment depend on the type of treatment used, the radiation sources, and how they are implanted in patients. As already mentioned, the sensitivity to ionizing radiation's effects is hugely dependent on the availability of oxygen in the irradiated environment, and the higher the oxygenation, the greater the treatment's ability to induce lethal effects. Although brachytherapy effects on tumor vascularization are poorly known, some studies have shown an increase in partial oxygen pressure (pO_2) in murine tumor models treated with ^{125}I seeds [126]. Besides, experiments using mammalian cell cultures irradiated with HDR-BT

(66 Gy/h) and LDR-BT (0.32 Gy/h) showed that the oxygen enhancement ratio for HDR-BT was approximately 2.4 vs. 1.5 for LDR-BT, suggesting a more significant oxygen effect with HDR-BT in contrast to LDR-BT [127, 128]. Finally, data from preclinical studies indicate that BT's implantation technique can determine the level of perfusion and oxygenation in the irradiated tissue, potentially affecting treatment outcomes. In a preclinical mouse model, a significant decrease in perfusion and oxygenation was observed after implantation of interstitial catheters suggesting that this procedure could lead to local hypoxemia with a substantial reduction in the radiation effect of an HDR-BT treatment [129].

In the past and even nowadays, studies of brachytherapy's radiobiology seem to be scarce and limited only to evaluate the dose-rate effects of the radiation. Indeed, most available data have been obtained in the 1980s from studies focusing on the dose-rate effect. Little data are known concerning the cell cycle distribution, repopulation, or reoxygenation, which are significant therapeutic index parameters. As in the case of immunotherapy, BT could be an excellent adjuvant with other therapies reinforcing the need to develop more studies of the radiobiological effects of BT in isolated and combinatory ways.

22.3.3 Biocompatible Glasses Applied in Brachytherapy

This section of this chapter deserves special attention regarding definitions. The authors of this chapter define "biocompatible glasses" as any vitreous material used in biomedical applications, regardless of any bioactivity property. In contrast, we define "bioactive glasses" as glasses that show bioactivity. Therefore, bioactive glasses are a subgroup of biocompatible glasses; once the last one is a more broad definition because it includes bioinert, resorbable, and bioactive glasses. This section was named "Biocompatible Glasses Applied in Brachytherapy" because we will discuss the applications of bioinert aluminosilicate glasses in radioembolization, as well as bioactive glasses containing rare-earth elements aiming treatment of bone cancer. Considering that most of the literature concerning glasses in brachytherapy applications is focused on radioembolization, we shall introduce radioembolization principles and later discuss aspects related to glass technologies.

22.3.3.1 Introduction to Radioembolization: Materials and Applications

Radioembolization, also known as selective internal radiation therapy (SIRT), is intra-arterial brachytherapy, in which the radioactive source comes from ceramic or polymeric microspheres containing the radioisotope in their structure [103]. The microspheres are injected into the patient artery, and the microspheres are accumulated in the tumor site due to the tumor's high vascularization. The world's brachytherapy market could reach US $2.4 billion in 2030, with a growth rate of 8% per year, driven mainly by the development of microspheres and electronic devices used in brachytherapy [130].

The success of radioembolization procedures relies on the properties of the microspheres, which should fulfill some characteristics, such as [131, 132]: be easily labeled and resistant to elution of the radioactive label, macrophage removal, or radiolysis; and present uniform microsphere size (i.e. greater than microcapillary diameter of around 8 μm and small enough to lodge as distal as possible) and density comparable to that of blood is necessary to prevent settling and ensure uniform distribution. The radionuclide label must be a high-energy β-emitter with an acceptable range and an intermediate half-life of a few days for suitable efficacy. Finally, the microspheres should be visible by PET (positron emission), SPECT (γ-emission), CT (sufficient density), or MRI (paramagnetic properties) to assess distribution [103, 133].

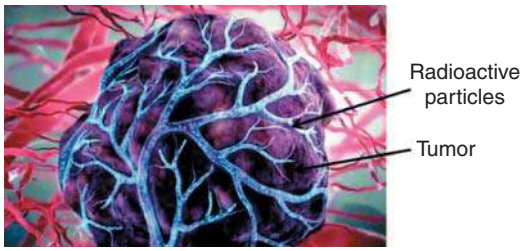

Figure 22.10 Illustration of a highly vascularized tumor and microspheres distribution throughout the tumor. Source: Bretcanu and Evans [134], Fig 03 (p. 270)/Elsevier.

Currently, there are three different kinds of microspheres commercially available: (i) TheraSphere® (BTG International Medicine, USA): glass microspheres containing ^{90}Y as a radioisotope; (ii) SIR-Spheres® (SIRTEX Medical Limited, USA): resin microspheres containing ^{90}Y radioisotope; (iii) QuiremSpheres® (Quirem Medical, Deventer, The Netherlands): PLLA microspheres, with ^{166}Ho radioisotope [133–136]. Figure 22.10 shows glass microspheres containing ^{90}Y (TheraSphere) used in radioembolization. The most used microsphere in clinical practice is the TheraSphere and the SIR-Spheres. A systematic review [137] that evaluated the adverse event profile of TheraSphere and SIR-Spheres in the treatment of hepatocarcinoma suggested using a glass microsphere as a vector of ^{90}Y is more suitable than resin ones. For example, patients treated with SIR-Sphere had a more hepatobiliary adverse event of grade 3 or higher. The review concluded that glass microspheres were safer than resin microspheres due to fewer gastrointestinal and pulmonary adverse effects in the treatment of hepatocarcinoma. These outcomes evidence that technological advances are more likely to be performed in the glass microsphere once they are more promising for cancer treatment than the other materials available.

Although microspheres for radioembolization can be made of different materials, glassy microspheres have been researched once they display two critical properties that make them suitable for brachytherapy applications: lack of periodical structure and tailored chemical durability. Because of the lack of periodical structure, glasses can successfully incorporate different radioisotopes into their glassy structure even at different concentrations. Furthermore, by controlling their chemical durability and dissolution kinetics, the release of radioactive ions into the body can be successfully avoided [138, 139]. When the glasses are produced as microspheres, precise control of microsphere size is required to ensure that the microsphere can circulate in an arteria until it reaches the tumor.

The initial concepts of radioembolization were first published in 1960 [102, 134], significantly improving since then. This therapy is currently widely used to treat renal tumors [140], primary hepatocellular carcinoma (HCC) [135], or metastasis, such as colorectal, neuroendocrine, breast, and uveal melanomas [103].

For example, when surgical removal is no longer desired in the advanced stage of renal cancer due to the risk of spreading cancer cells to other tissues, treatment with radioactive microspheres can be considered a promising alternative. After initial treatment, in which microspheres are applied through the renal artery, tumor reduction is expected because of cancer cells' death caused by ionizing radiation. Consequently, surgery removal can be performed with more success. Hamoui et al. [140] reported the successful treatment of an advanced renal cancer stage using glass microspheres containing ^{90}Y. *In vivo* studies have also shown exciting results about radioactive glass microsphere usage in renal cancer radioembolization. Ehrhardt and Day [141] used glass microspheres based on $52SiO_2$–$21Al_2O_3$–$20MgO$–$7Sm_2O_3$ composition (in wt%) in *in vitro* rabbit experiments that varied the radiation dose and showed a reduction in irradiated kidney size (25–35%) and no side effects to the other tissues.

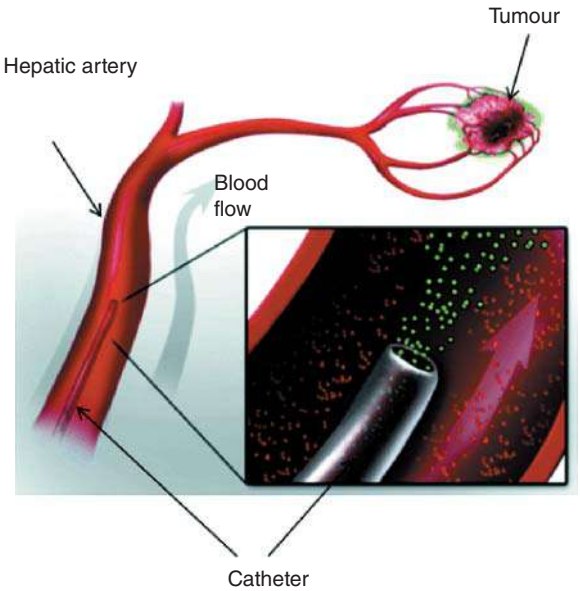

Figure 22.11 Delivery of microsphere through a catheter in the hepatic artery. Source: Bretcanu and Evans [134]/with permission of Springer Nature.

Brachytherapy can be successfully used by the particular feature of the liver's vascular irrigation concerning liver cancer. The liver tumors are almost entirely irrigated by the hepatic artery, while the blood supply to healthy tissue occurs through vein access (Figure 22.11). Thus, by introducing radioactive microspheres through the hepatic artery, they will be located into the small arterioles inside and on the tumor's periphery through a microcatheter (Figure 22.11). The cancer cells' death occurs by high-energy β-particles irradiation, with almost no damage to healthy cells. Besides cell death induced by ionizing radiation, microspheres are lodged within arterioles that irrigate the tumor, obstructing the blood circulation due to their diameter (between 20 and 30 μm).

22.3.3.2 Advances in Glass Microspheres for Radioembolization

The glasses used in brachytherapy are first proposed in the early 1980s. The microspheres of these glasses were first proposed for the treatment of rheumatoid arthritis and intracavitary tumor. Since 2005, they have offered radioembolization or intra-arterial brachytherapy to treat liver cancer [103, 134]. The radioactive microspheres for cancer treatment by radioembolization were first reported by Debert E. Day and colleagues in 1987 [139, 141, 142]. These microspheres were glasses based on the system Y_2O_3–Al_2O_3–SiO_2 (YAS), with a diameter size between 20 and 30 μm, being the basis for the commercial ^{90}Y TheraSpheres. However, the YAS composition of the glass microspheres has some limitations, such as melting and spheroidization temperatures are too high; the dissolution rate is very low, considering the half-life of ^{90}Y. Thus, the possible long-side effects of these microspheres were not yet evaluated. Finally, it is challenging to monitor its biodistribution due to the radioactive characteristics of the ^{90}Y.

The success of glass microspheres for brachytherapy applications relies on three well-known variables: (i) biocompatibility, (ii) chemical durability (dissolution kinetics), (iii) radioactive properties. Concerning the different materials, glass materials are among the scarce ones that combine all these variables. Of course, their chemical structure plays a crucial role in explaining how all these features can be found together. Therefore, let us first understand the glass structure of glasses used in biomedical applications.

The prominent glasses for biomedical applications can be classified according to their network formers oxides: silicates (SiO_2), phosphates (P_2O_5), and borates (B_2O_3) [143]. Besides the network formers oxides, the glasses are also made of network modifiers, including Li_2O, Na_2O, K_2O, CaO, and MgO; other elements from the periodic table either behave like network formers or modifiers and are so-called "intermediate oxides" (such as Al_2O_3, ZnO, TiO_2, CuO, Ag_2O_3). The network formers are linked to one another through covalent oxygen-bridging bonds, such as Si—O—Si, P—O—P, and B—O—B, leading to a tridimensional connected network. The network modifiers form covalent and ionic nonbridging oxygen bonds, such as Si—O—X, P—O—X, and B—O—X, where X is an alkaline, alkaline-earth, or a transition metal. In contrast to bridging oxygens that yield a connected network, the nonbridging oxygens are responsible for disrupting the tridimensional network, thereby decreasing the glass network connectivity. The intermediate oxides are responsible for a complex modification of the glass network once their inclination to a more former or modifier role depends on their concentration and all the other elements that are part of the glass composition [144–146].

It is worth noting to mention that since the glass network is free of periodicity, it is also free of crystalline defects that, in turn, allows the inclusion of almost all the elements from the periodic table in a glass structure [147]. Consequently, elements with suitable properties for brachytherapy applications can be included in the glass composition, such as ^{90}Y, $^{186}Re/^{188}Re$, ^{32}P, ^{156}Sm, ^{142}Pr, and ^{166}Ho. A note of caution is due here; these chemical elements are added in the glass structure as stable isotopes and are later submitted to neutron activation when the microspheres are already done.

The glass formers oxides play a significant role in glass reactivity and stability. In this sense, understanding the behavior of glass formers on glass reactivity helps design new compositions of glasses aimed at brachytherapy applications. Phosphates glasses are formed by orthophosphate (PO_4^{3-}) tetrahedron units [148]. However, one oxygen atom is double-bonded with phosphorus, remaining the other three oxygen atoms available to be shared with another tetrahedron, forming bridging oxygen bonds. This particularity reduces its connectivity network but allows more options about glass composition. In contrast to silicate glasses, in which the increase in SiO_2 content increases their chemical reactivity, pure phosphate glasses are very reactive and hygroscopic. Thus, network modifier oxides increase the chemical stability of phosphate glasses by breaking the P—O—P bonds and forming nonbridging oxygen. The nonbridging oxygen bonds of phosphate glasses are stronger than bridging oxygen ones. The strength of P—O—X bonds increases as the valence of modifier ion increases or ionic radius decreases, leading to an overall increase in the chemical stability of the phosphate glass structure [149, 150]. Like phosphate glasses, borates glasses are also very reactive, with low chemical stability leading to faster dissolution. These glasses have been developed as borosilicate, varying the SiO_2/B_2O_3 ratio to control their dissolution properties and chemical stability [145].

Once known as glass formers influence the strength of chemical bonds in the glass structure, one can infer how the glass composition is responsible for the glass chemical durability, the glass dissolution in an aqueous medium. Moreover, their chemical durability must be enough to resist the elution of radioactive ions and compatible with the radioisotope's half-life. Ideally, they should have high chemical stability in the medium during the high activity of radioisotope, maintaining activity only in the specific tumor site. However, after eight half-lives, when the radioisotope activity reaches less than 0.4% of the initial activity, the dissolution process is desired. It is worth noting that the ^{90}Y TheraSphere does not meet the dissolution criteria for the ideal glass microsphere for radioembolization once it shows very high chemical durability.

Taking all these points into account, special attention should be given to aluminosilicate glasses once these glasses show high chemical durability due to their well-connected glass network and high bond strengths between silicate and alumina species. Over the past few years, several studies have focused on overcoming the limitations of the ^{90}Y TheraSphere, mainly its high chemical durability. Then, these proposed alternatives rely on glass compositions based on the system RE_2O_3–Al_2O_3–SiO_2, known as rare earth aluminosilicate (REAS) glasses. The REAS glasses aim at replacing ^{90}Y with other rare earth like ^{186}Re/^{188}Re, ^{32}P, ^{156}Sm, ^{142}Pr, and ^{166}Ho. In addition to β emitters, they also are γ-emitters, having suitable radioactive characteristics (Table 22.1) [102].

Despite the remarkable properties of REAS glasses, other systems have also been researched and deserve some mention, such as glasses based on phosphates ($^{32}P_2O_5$–MgO–Al_2O_3–SiO_2) and borates ($^{186/188}Re_2O_3$–B_2O_3–MgO–Al_2O_3–SiO_2). Note that the glasses are also aluminosilicate glasses, but they also contain other glass formers like phosphorus and boron oxides. Because of the high chemical reactivity of phosphorous and boron in the glass structure, the chemical durability of these glasses is lower than in REAS and the ^{90}Y TheraSphere. Although these glasses are noncommercial compositions, there are intended to overcome the too high chemical durability of the ^{90}Y TheraSphere, allowing the glass to be dissolved after the cancer treatment [134].

Special attention must be given to the fact that all the aluminosilicate glasses developed for radioembolization, so far, are classified as bioinert materials; that is, they neither chemically interact nor trigger any biological response in living tissues that could be related to dissolution products from glass dissolution. The bioinert properties of these microspheres are addressed to their high chemical durability, which impedes ion-exchange reactions or the break of network formers bonds that are considered the initial mechanisms needed to trigger a bioactive response [102, 138].

Considering the radioisotope that is commonly applied in radioembolization, some characteristics should be considered [105]: (i) to have a radiation spectrum that allows the treatment of tumors of different sizes, which means having an emission of β-energy that allows the particle's penetration through the entire tumor tissue; (ii) to ally HDR with a shorter half-life, which provides a more effective treatment; (iii) to emit low-energy γ-radiation, just enough to determine the radioisotope's biodistribution by mammography, thereby avoiding the patient's exposure to unnecessary doses; (iv) the incorporation of the radioisotope must be focused, without dispersing it through the matrix; (v) to have a high shock session for thermal neutrons, guaranteeing a high specific activity with a shorter activation period inside the reactor. Currently, ^{166}Ho radioisotope has been showing the most promising results, considering all these requirements mentioned above.

22.3.3.3 Manufacturing Methods of Glass Microspheres

Glass microspheres can be produced by different methods, considering specificities related to raw materials, size and porosity distribution, and cost. They can be classified into sol–gel or thermal processes (Figure 22.12). The sol–gel methodology includes many variations, such as hydrothermal process, emulsification, internal gelation, solvent extraction, spray-pyrolysis, and spray drying [152–154]. Thermal methods, on the other hand, require melting with flame spheroidization, dripping, or plasma.

The melting and spheroidization process is the most traditional method to produce glass microspheres in size range between 20 and 40 μm is through [138, 155–157]. The process can be summarized into four steps: (i) the oxides components are manually mixed and melted in a platinum crucible, at specific conditions defined for each composition; (ii) the fused material is fast cooled to avoid possible crystallization. The powder is grounded and classified to have the desired particles

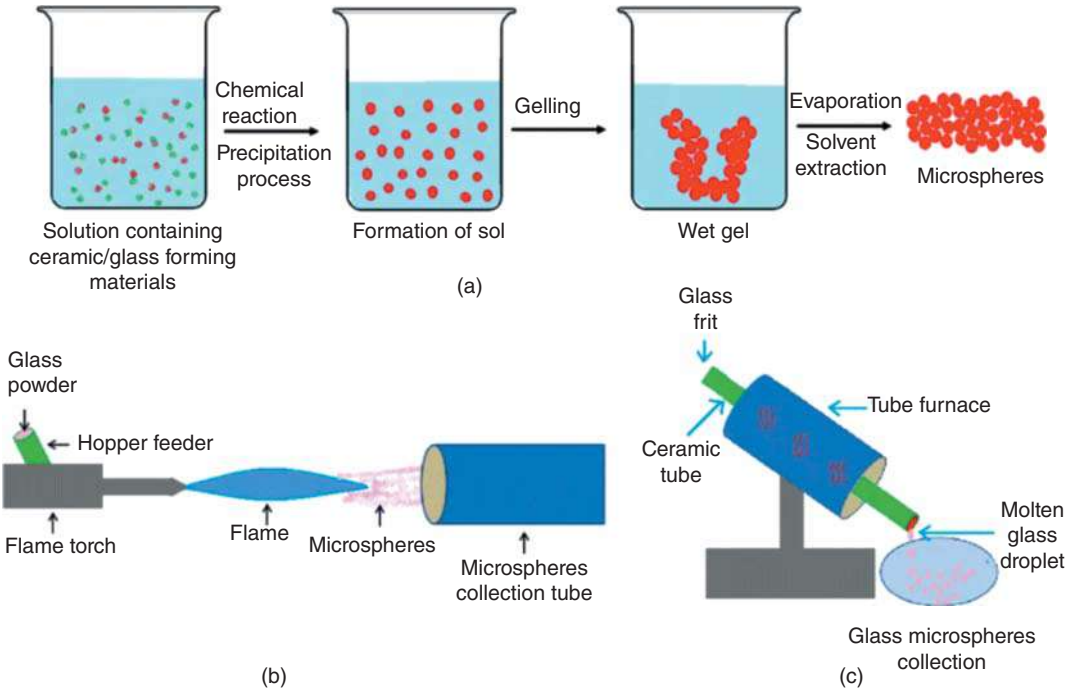

Figure 22.12 Illustration of glass microsphere production by the (a) sol–gel, (b) flame spheroidization, and (c) furnace methods. Source: Hossain et al. [151]/with permission of Springer Nature.

size range; (iii) spheroidization process, which consists of using a gas flame at high temperature that softens the particles, making them spherical due to the superficial tension effect; (iv) the obtained spheres are submitted to a size classification.

The melting and particle spheronization conditions depend directly on the glass composition, as exemplified for REAS compositions in Figure 22.13 that show the region in which REAS glasses can be spheroid at an acetylene/oxygen flame temperature in a short period. Different rare earth displays additional compositional features due to the different chemical bond strengths displayed by them. The phase diagram in Figure 22.13 is also interesting to design glass composition with final density suitable to allow microspheres to be transported throughout the blood flux in arteries.

After the microsphere production, they are neutron-irradiated in a nuclear reactor to produce the intended radioisotopes. Although the radioisotope is not sealed or encapsulated, as in other seeds, it remains immobilized into the matrix, which allows its positioning at short distances from the irradiated tissue without being spread to other body regions. They must fulfill the glass specification, as discussed above.

22.3.3.4 Bioactive Glasses for Treatment of Bone Cancer by Brachytherapy

Because aluminosilicate glasses display high chemical durability and very low dissolution kinetics in the body fluid, they do not chemically interact with the living cell from the human body and are classified as bioinert glasses. However, other glass compositions have been proposed aiming at bioactive glasses with radioactive properties. The development of Bioglass® ($24.35Na_2O–26.9CaO–2.57P_2O_5–46.1SiO_2$, in mol%) by Larry Hench et al. in 1971 [158] was a milestone of glass and vitroceramics applications in the biomedical field, mainly in bone tissue,

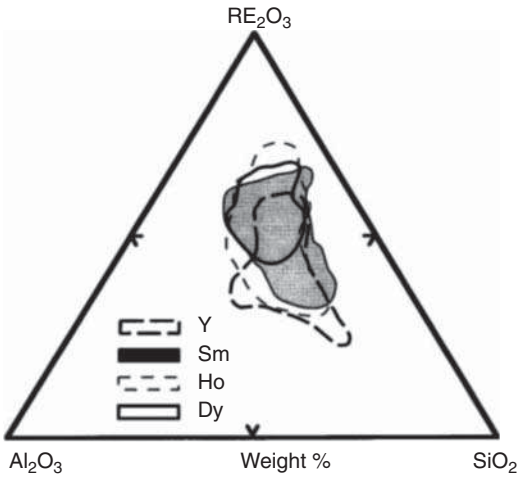

Figure 22.13 Compositional diagram showing the glass formation range for rare earth aluminosilicate (REAS) compositions that melt below 1600 °C. Source: Day [102]/with permission of John Wiley & Sons.

due to its biocompatible properties and strong chemical bond interface with hard and soft tissues [60]. Since then, advances have been made aiming at new compositions for other specific applications beyond bone regeneration, which led to the development of bioactive and resorbable glass compositions with radioactive properties for cancer treatment [101, 144, 159, 160].

In 2003, the first report of resorbable glass as a radioisotope vector was published by a Brazilian research group [159]. This glass was based on the SiO_2–CaO system containing between 4.5 and 11.5 wt% of Sm_2O_3 as a precursor of ^{153}Sm radioisotope. Although glasses based on the SiO_2–CaO system are known to be bioactive, the glasses developed by Roberto and Magalhães showed a high dissolution rate, yielding a resorbable glass. Moreover, these glasses were intended to replace ^{125}I seeds used in the brachytherapy of prostate cancer, being the reason why ^{153}Sm was chosen as a radioisotope. While ^{125}I has a half-life of 54.9 days, ^{153}Sm has a half-life of 46.27 hours, making ^{153}Sm more suitable for resorbable seeds for brachytherapy. *In vivo* studies of these resorbable glasses in the rabbit's liver model showed that the glasses completely dissolve in living tissues after seven months.

After the work of Roberto et al. [159], other research groups also developed studies focusing on prostate cancer treatment by brachytherapy. Most of these works consist of Monte Carlo simulation to study the dose calculation of different resorbable glasses containing other radioisotopes such as ^{153}Sm, ^{32}P, $^{90}Sr/^{90}Y$, ^{166}Ho, ^{142}Pr, and ^{188}Re. These studies focused on finding which radioisotope can combine a high initial dose rate with a short distance of β-particle emission. So far, these studies have suggested ^{166}Ho, ^{188}Re, and ^{153}Sm as the best radioisotopes for applications in prostate cancer. It is essential to highlight that these Monte Carlo simulations are performed using the AAPM TG-60 (American Association of Physicist in Medicine, Task Group-60) formalist, which recommends a dosimetry protocol for interstitial brachytherapy, considering parameters such as source of β emitters, dose rate, radial dose function, and material's anisotropy [101].

Besides resorbable glasses, bioactive glasses have also been proposed for brachytherapy applications, but their focus relies on bone cancer treatment. Fascinatingly, the first studies of bioactive glass matrix as a vector of a radioactive isotope came from dynamic molecular studies carried out by Christie et al. [144] that proposed a ^{90}Y-bioactive glass (^{90}Y–BG, SiO_2–Na_2O–CaO–P_2O_5–Y_2O_5). The computational simulation carried out by Christie showed that yttrium plays an exciting role in the glass network. While yttrium addition fragments in the silicate network favor glass dissolution, the high bond strength of yttrium-mediated cross-linked silicates bonds disfavor glass dissolution.

Therefore, the counterbalance between bond strength and network fragmentation is responsible for not changing the glass chemical durability, thereby keeping their bioactivity [161].

A series of experimental studies performed with rare-earth-containing bioactive glasses (RE-BG) helped to understand the role of rare earth on the glass structure, dissolution, and bioactivity, encouraging more studies of radioactive bioactive glasses, besides confirming the theoretical results from computational simulations. Borges et al. experimentally showed that the rare-earth majority plays a modifier role in the glass structure of bioactive silicate glasses, being responsible for a decrease in network connectivity [162]. Despite the less-connected network, experimental results confirmed that RE-BG dissolves slower than nondoped glasses because of the strong chemical strength of Si—O—RE bonds [163]. On the other hand, the slower dissolution rate does not seems to affect the bioactivity of RE-BG, which shows the formation of hydroxyapatite on their surface in bioactivity studies using SBF.

Recently, Delpino et al. [164] showed that sol–gel-derived bioactive glasses based on the system SiO_2–CaO–P_2O_5–Ho_2O_3 are prominent compositions for the treatment of bone cancer by brachytherapy. This study showed that a less-connected glass network caused by the holmium addition is responsible for favoring glass dissolution in an early stage. However, in the long-term, Si—O—Ho bonds' strength takes place, diminishing the glass dissolution rate. Those finds were essential to understanding how RE-BG can be bioactive despite the addition of rare earth elements. It was confirmed that the initial faster dissolution kinetics is responsible for releasing calcium and phosphate ions toward the body fluid, favoring bioactivity. In contrast, the slower dissolution kinetics retains holmium ions attached to the glass structure in the long term. Considering bone cancer treatment, these glasses would bond to the bone tissue through osteointegration and treat the bone cancer without releasing ^{166}Ho in the body fluid over pathological concentration. In other words, these bioactive glasses are safe materials for brachytherapy applications.

22.3.4 Challenges and Future Perspective

Despite the advantages of brachytherapy, there is a decline in its usage over the last years, which has raised awareness in the scientific community, which was exhaustively reported by the "Nature Outline: Prostate Cancer," an editorially independent supplement from the journal *Nature*. In the United States, brachytherapy has been eclipsed by sophisticatedly specialized treatment like robot-assisted surgery and proton therapy, caused by facilitated reimbursement policies that favor new approaches in private healthcare facilities [165, 166]. However, brachytherapy is a safe, effective, and cheaper procedure than other current interventions like robot-assisted surgery and beam therapy [167]. Therefore, in countries that offer universal healthcare afforded by public funds, brachytherapy is one of the most cost-effective options for treating some types of cancers [93]. In this sense, brachytherapy still deserves special attention and new technological advances to keep this treatment affordable, effective, and less invasive [98].

The advances in glasses for brachytherapy applications rely mainly on rare-earth development containing silicate glasses, once rare-earth isotopes such as ^{166}Ho, ^{188}Re, and ^{152}Sm among those with the most suitable properties for application in radioembolization or interstitial brachytherapy. Currently, there is much more understanding about the influence of these rare earth on the glass structure, enabling the better design of glass compositions aiming at the desired properties for brachytherapy. However, there is a considerable gap between glass characterization and biological properties, which impedes this technology from reaching the market soon. Of course, the need for nuclear facilities is a limitation of these studies, but those interested in stepping forward

in this field need to understand how brachytherapy from biocompatible glasses affects the tumor microenvironment and immune responses.

Also, the combination of brachytherapy with immunotherapy can be the key to successful treatments in the future. Brachytherapy is therapy with spatial resolution, able to treat tumors locally. However, brachytherapy also causes an abscopal effect that affects cancer cells in areas that radiotherapy has not been performed through immune-mediated anti-tumor effect. This biological effect favors the treatment of metastatic cancers, making the treatment more effective. Nonetheless, if immunotherapy is combined with brachytherapy, a synergy between local and whole-body therapy would treat the tumor and avoid metastasis events. This strategy may be advantageous to treat bone cancer, which is metastatic cancer. Considering that bioactive glasses can regenerate bones, the advances in radioactive bioactive glasses combined with immunotherapy may be an effective alternative to treat bone cancer and regenerate bones by using the same material. Again, the need for biological experiments remains the limitation of studies of brachytherapy combined with immunotherapy once immune responses can be better understood in integrated biological systems. However, efforts in these studies are needed to bring more advances in this area.

Acknowledgments

The authors acknowledge the financial support from Fundação de Amparo à Pesquisa do Estado de São Paulo (FAPESP, # 2016/16521-9); Conselho Nacional de Desenvolvimento Científico e Tecnológico (CNPq, #130637/2016-5) and Coordenação de Aperfeiçoamento de Pessoalde Nível Superior, Brasil (CAPES, Finance Code 001).

References

1 Casás-Selves, M. and Degregori, J. (2011). How cancer shapes evolution, and how evolution shapes cancer. *Evolution (NY)* 4 (4): 624–634.
2 Greaves, M. and Maley, C.C. (2012). Clonal evolution in cancer. *Nature* 481 (7381): 306–313.
3 Hanahan, D. and Weinberg, R.A. (2000). The hallmarks of cancer. *Cell* 100 (1): 57–70.
4 Hanahan, D. and Weinberg, R.A. (2011). Hallmarks of cancer: the next generation. *Cell* 144 (5): 646–674.
5 Gillies, R.J., Verduzco, D., and Gatenby, R.A. (2012). Evolutionary dynamics of carcinogenesis and why targeted therapy does not work. *Nature Reviews Cancer* 12 (7): 487–493.
6 Martincorena, I. and Campbell, P.J. (2015). Somatic mutation in cancer and normal cells. *Science* 349 (6255): 1483–1489.
7 Luo, G.G. and Ou, J.J. (2015). Oncogenic viruses and cancer. *Virologica Sinica* 30 (2): 83–84.
8 Stratton, M.R., Campbell, P.J., and Futreal, P.A. (2009). The cancer genome. *Nature* 458 (7239): 719–724.
9 Paul, P., Malakar, A.K., and Chakraborty, S. (2019). The significance of gene mutations across eight major cancer types. *Mutation Research, Reviews in Mutation Research* 781: 88–99.
10 Speicher, P.J., Ganapathi, A.M., Englum, B.R. et al. (2014). Survival in the elderly after pneumonectomy for early-stage non-small cell lung cancer: a comparison with nonoperative management. *Journal of the American College of Surgeons* 218 (3): 439–449.
11 Blair, L.P. and Yan, Q. (2012). Epigenetic mechanisms in commonly occurring cancers. *DNA and Cell Biology* 31 (Suppl 1): S49–S61.

12 Feinberg, A.P. (2007). Phenotypic plasticity and the epigenetics of human disease. *Nature* 447 (7143): 433–440.
13 Ramakrishnan, V. (1997). Histone structure and the organization of the nucleosome. *Annual Review of Biophysics and Biomolecular Structure* 26 (1): 83–112.
14 Wolffe, A.P. and Hayes, J.J. (1999). Chromatin disruption and modification. *Nucleic Acids Research* 27 (3): 711–720.
15 Khochbin, S., Verdel, A., Lemercier, C., and Seigneurin-Berny, D. (2001). Functional significance of histone deacetylase diversity. *Current Opinion in Genetics & Development* 11 (2): 162–166.
16 Nakatani, Y. (2001). Histone acetylases-versatile players. *Genes to Cells* 6 (2): 79–86.
17 Audia, J.E. and Campbell, R.M. (2016). Histone modifications and cancer. *Cold Spring Harbor Perspectives in Biology* 8 (4): a019521.
18 Fraga, M.F., Ballestar, E., Villar-Garea, A. et al. (2005). Loss of acetylation at Lys16 and trimethylation at Lys20 of histone H_4 is a common hallmark of human cancer. *Nature Genetics* 37 (4): 391–400.
19 Timmermann, S., Lehrmann, H., Polesskaya, A., and Harel-Bellan, A. (2001). Histone acetylation and disease. *Cellular and Molecular Life Sciences* 58 (5): 728–736.
20 Li, Y. and Seto, E. (2016). HDACs and HDAC inhibitors in cancer development and therapy. *Cold Spring Harbor Perspectives in Medicine* 6 (10): a026831.
21 Dagogo-Jack, I. and Shaw, A.T. (2017). Tumour heterogeneity and resistance to cancer therapies. *Nature Reviews Clinical Oncology* 15 (2): 81–94.
22 Alfarouk, K.O., Stock, C.-M., Taylor, S. et al. (2015). Resistance to cancer chemotherapy: failure in drug response from ADME to P-gp. *Cancer Cell International* 15: 71.
23 Mills, C.C., Kolb, E.A., and Sampson, V.B. (2018). Development of chemotherapy with cell-cycle inhibitors for adult and pediatric cancer therapy. *Cancer Research* 78 (2): 320–325.
24 Krzyszczyk, P., Acevedo, A., Davidoff, E.J. et al. (2018). The growing role of precision and personalized medicine for cancer treatment. *Technology* 6 (3–4): 79–100.
25 Watmough, D.J. and Ross, W.M. (1986). *Hyperthermia: Clinical and Scientific Aspects*. Glasgow: Blackie and Son.
26 Gas, P. (2011). Essential facts on the history of hyperthermia and their connections with electromedicine. *Przegląd Elektrotechniczny* 87 (12b): 37–40.
27 McCarthy, E. (2006). The toxins of William B. Coley and the treatment of bone and soft-tissues sarcomas. *Iowa Orthopaedic Journal* 26: 154–158.
28 Guy, A.W. (1984). History of biological effects and medical applications of microwave energy. *IEEE Transactions on Microwave Theory and Techniques* 32: 1182–1200.
29 Gilchrist, R.K., Medal, R., Shorey, W.D. et al. (1957). Selective inductive heating of lymph nodes. *Annals of Surgery* 146 (4): 596–606.
30 Gilchrist, R.K., Medal, R., Shorey, W.D. et al. (1957). Selective inductive heating of lymphonodes. *Annals of Surgery* 146: 596–606.
31 Toumey, C. (2009). Plenty of room, plenty of history. *Nature Nanotechnology* 4 (12): 783–784.
32 Mohapatra, J., Xing, M., and Liu, J.P. (2019). Inductive thermal effect of ferrite magnetic nanoparticles. *Materials (Basel)* 12 (19): 26–29.
33 Bihlmayer, G. (2007). *Handbook of Magnetism*. Wiley.
34 Nikiforov, V.N. (2007). Magnetic induction hyperthermia. *Russian Physics Journal* 50 (9): 913–924.
35 Sohail, A., Ahmad, Z., Bég, O.A. et al. (2017). A review on hyperthermia via nanoparticle-mediated therapy. *Bulletin du Cancer* 104 (5): 452–461.

36 Mahmoudi, K., Bouras, A., Bozec, D. et al. (2018). Magnetic hyperthermia therapy for the treatment of glioblastoma: a review of the therapy's history, efficacy and application in humans. *International Journal of Hyperthermia* 34 (8): 1316–1328.

37 Schilsky, R.L. (2010). Personalized medicine in oncology: the future is now. *Nature Reviews Drug Discovery* 9 (May): 363–366.

38 Kang, J.K., Kim, J.C., Shin, Y. et al. (2020). Principles and applications of nanomaterial-based hyperthermia in cancer therapy. *Archives of Pharmacal Research* 43 (1): 46–57.

39 Dewey, W.C. (1994). Arrhenius relationships from the molecule and cell to the clinic. *International Journal of Hyperthermia* 10 (4): 457–483.

40 Urano, M. (1999). Invited review: for the clinical application of thermochemotherapy given at mild temperatures. *International Journal of Hyperthermia* 15 (2): 79–107.

41 Schildkopf, P., Ott, O.J., Frey, B. et al. (2010). Biological rationales and clinical applications of temperature controlled hyperthermia – implications for multimodal cancer treatments. *Current Medicinal Chemistry* 17 (27): 3045–3057.

42 Ahmed, K., Tabuchi, Y., and Kondo, T. (2015). Hyperthermia: an effective strategy to induce apoptosis in cancer cells. *Apoptosis* 20 (11): 1411–1419.

43 Fajardo, L.F., Schreiber, A.B., Kelly, N.I., and Hahn, G.M. (1985). Thermal sensitivity of endothelial cells. *Radiation Research* 103 (2): 276.

44 Ma, D., Huang, C., Zheng, J. et al. (2019). Azoreductase-responsive nanoprobe for hypoxia-induced mitophagy imaging. *Analytical Chemistry* 91 (2): 1360–1367.

45 Han, J., Back, S.H., Hur, J. et al. (2013). ER-stress-induced transcriptional regulation increases protein synthesis leading to cell death. *Nature Cell Biology* 15 (5): 481–490.

46 Serrano Del Valle, A., Anel, A., Naval, J., and Marzo, I. (2019). Response: commentary: immunogenic cell death and immunotherapy of multiple myeloma. *Frontiers in Cell and Developmental Biology* 7: 306.

47 Toraya-Brown, S. and Fiering, S. (2014). Local tumour hyperthermia as immunotherapy for metastatic cancer. *International Journal of Hyperthermia* 30 (8): 531–539.

48 Martinková, V., Trčka, F., Vojtěšek, B., and Müller, P. (2018). The role of HSP70 in cancer and its exploitation as a therapeutic target. *Klinická Onkologie* 31 (Suppl 2): 46–54.

49 Jolesch, A., Elmer, K., Bendz, H. et al. (2012). HSP70, a messenger from hyperthermia for the immune system. *European Journal of Cell Biology* 91 (1): 48–52.

50 Hurwitz, M.D. (2019). Hyperthermia and immunotherapy: clinical opportunities. *International Journal of Hyperthermia* 36 (sup1): 4–9.

51 Multhoff, G. (2007). Heat shock protein 70 (Hsp70): membrane location, export and immunological relevance. *Methods* 43 (3): 229–237.

52 Noessner, E., Gastpar, R., Milani, V. et al. (2002). Tumor-derived heat shock protein 70 peptide complexes are cross-presented by human dendritic cells. *Journal of Immunology* 169 (10): 5424–5432.

53 Castelli, C., Rivoltini, L., Rini, F. et al. (2004). Heat shock proteins: biological functions and clinical application as personalized vaccines for human cancer. *Cancer Immunology, Immunotherapy* 53 (3): 227–233.

54 Zitvogel, L., Tesniere, A., and Kroemer, G. (2006). Cancer despite immunosurveillance: immunoselection and immunosubversion. *Nature Reviews Immunology* 6 (10): 715–727.

55 Issels, R.D., Lindner, L.H., Verweij, J. et al., European Organisation for Research and Treatment of Cancer Soft Tissue and Bone Sarcoma Group (EORTC-STBSG); European Society for Hyperthermic Oncology (ESHO)(2010). Neo-adjuvant chemotherapy alone or with regional

hyperthermia for localised high-risk soft-tissue sarcoma: a randomised phase 3 multicentre study. *Lancet Oncology* 11 (6): 561–570.

56 Shen, R.-N., Lu, L., Young, P. et al. (1994). Influence of elevated temperature on natural killer cell activity, lymphokine-activated killer cell activity and lectin-dependent cytotoxicity of human umbilical cord blood and adult blood cells. *International Journal of Radiation Oncology Biology Physics* 29 (4): 821–826.

57 Meyer, R.E., Braun, R.D., Rosner, G.L., and Dewhirst, M.W. (2000). Local 42 °C hyperthermia improves vascular conductance of the R3230Ac rat mammary adenocarcinoma during sodium nitroprusside infusion. *Radiation Research* 154 (2): 196–201.

58 Hua, H., Kong, Q., Zhang, H. et al. (2019). Targeting mTOR for cancer therapy. *Journal of Hematology & Oncology* 12 (1): 71.

59 Luderer, A.A., Borrelli, N.F., Panzarino, J.N. et al. (1983). Glass-ceramic-mediated, magnetic-field-induced localized hyperthermia: response of a murine mammary carcinoma. *Radiation Research* 94 (1): 190–198.

60 Hench, L.L. (2006). The story of Bioglass®. *Journal of Materials Science: Materials in Medicine* 17: 967–978. https://doi.org/10.1007/s10856-006-0432-z.

61 Marchi, J. (2016). *Biocompatible Glasses: From Bone Regeneration to Cancer Treatment*. Cham, Switzerland: Springer International Publishing.

62 Ebisawa, Y., Sugimoto, Y., Hayashi, T. et al. (1991). Crystallization of (FeO, Fe_2O_3)–CaO–SiO_2 glasses and magnetic properties of their crystallized products. *Nippon Seramikkusu Kyokai Gakujutsu Ronbunshi* 99 (1): 7–13.

63 Ohura, K., Ikenaga, M., Nakamura, T., and Yamamuro, T. (1991). A heat-generating bioactive glass-ceramic for hyperthermia. *Journal of Applied Biomaterials* 2: 153–159.

64 Singh, R.K., Srinivasan, A., and Kothiyal, G.P. (2009). Evaluation of $CaO–SiO_2–P_2O_5–Na_2O–Fe_2O_3$ bioglass-ceramics for hyperthermia application. *Journal of Materials Science: Materials in Medicine* 20: 147–151.

65 Leventouri, T., Kis, A.C., Thompson, J.R., and Anderson, I.M. (2005). Structure, microstructure, and magnetism in ferrimagnetic bioceramics. *Biomaterials* 26: 4924–4931.

66 Bretcanu, O., Spriano, S., Verne, E. et al. (2005). The influence of crystallised Fe_3O_4 on the magnetic properties of coprecipitation-derived ferrimagnetic glass-ceramics. *Acta Biomaterialia* 1: 421–429.

67 Shah, S.A., Hashmi, M.U., Alam, S., and Shamim, A. (2010). Materials magnetic and bioactivity evaluation of ferrimagnetic $ZnFe_2O_4$ containing glass ceramics for the hyperthermia treatment of cancer. *Journal of Magnetism and Magnetic Materials* 322 (3): 375–381.

68 Shah, S.A., Hashmi, M.U., and Alam, S. (2011). Effect of aligning magnetic field on the magnetic and calorimetric properties of ferrimagnetic bioactive glass ceramics for the hyperthermia treatment of cancer. *Materials Science and Engineering C* 31 (5): 1010–1016.

69 Li, R., Clark, A.E., and Hench, L.L. (1991). An investigation of bioactive glass powders by sol–gel processing. *Journal of Applied Biomaterials* 2: 231–239.

70 Sepulveda, P., Jones, J.R., and Hench, L.L. (2001). Characterization of melt-derived 45S5 and sol–gel-derived 58S bioactive glasses. *Journal of Biomedical Materials Research* 58 (6): 734–740.

71 Sinclair, D. and La Mer, V.K. (1948). Light scattering as a measure of particle size in aerosols. *Chemical Reviews* 44 (2): 245–267.

72 Brinker, C.J., Scherer, G.W., and Roth, E.P. (1985). Sol → gel → glass: II. Physical and structural evolution during constant heating rate experiments. *Journal of Non-Crystalline Solids* 72 (2–3): 345–368.

73 Brinker, C. and Scherer, W. (1990). *Sol-Gel Science, the Physics and Chemistry of Sol-Gel Processing* (eds C. J. Brinker and G.W. Scherer), xiv, 908 pp. Boston: Academic Press.

74 Shankhwar, N. and Srinivasan, A. (2016). Evaluation of sol–gel based magnetic 45S5 bioglass and bioglass-ceramics containing iron oxide. *Materials Science and Engineering C* 62: 190–196.

75 Arcos, D. and Real, R.P. (2003). Biphasic materials for bone grafting and hyperthermia treatment of cancer. *Journal of Biomedical Materials Research Part A* 65 (1): 71–78.

76 Ruiz-Hernandez, E., Serrano, M.C., Arcos, D., and Vallet-Regí, M. (2006). Glass–glass ceramic thermoseeds for hyperthermic treatment of bone tumors. *Journal of Biomedical Materials Research Part A* 79 (3): 533–543.

77 Da, G., Li, D., Lin, Y. et al. (2010). Synthesis and characterization of magnetic bioactive glass-ceramics containing Mg ferrite for hyperthermia. *Materials Science and Engineering C* 30 (1): 148–153.

78 Li, G., Feng, S., and Zhou, D. (2011). Magnetic bioactive glass ceramic in the system $CaO–P_2O_5–SiO_2–MgO–CaF_2–MnO_2–Fe_2O_3$ for hyperthermia treatment of bone tumor. *Journal of Materials Science: Materials in Medicine* 22: 2197–2206.

79 Saravanapavan, P., Jones, J.R., Pryce, R.S., and Hench, L.L. (2003). Bioactivity of gel-glass powders in the $CaO–SiO_2$ system: a comparison with ternary ($CaO–P_2O_5–SiO_2$) and quaternary glasses ($SiO_2–CaO–P_2O_5–Na_2O$). *Journal of Biomedical Materials Research Part A* 66 (1): 110–119.

80 Wang, T., Wu, H., Wang, W. et al. (2007). The development of magnetic degradable DP-Bioglass for hyperthermia cancer therapy. *Journal of Biomedical Materials Research Part A* 83 (3): 828–837.

81 Baino, F., Fiume, E., Miola, M. et al. (2018). Fe-doped sol–gel glasses and glass-ceramics for magnetic hyperthermia. *Materials (Basel)* 11 (173): 1–15.

82 Izquierdo-Barba, I. and Vallet-Regi, M. (2015). Mesoporous bioactive glasses: relevance of their porous structure compared to that of classical bioglasses. *Biomedical Glasses* 1 (1): 140–150.

83 Yang, T., Shen, C., Li, Z. et al. (2005). Highly ordered self-assembly with large area of Fe_3O_4 nanoparticles and the magnetic properties. *Journal of Physical Chemistry B* 109: 23233–23236.

84 Yan, X., Yu, C., Zhou, X. et al. (2004). Highly ordered mesoporous bioactive glasses with superior in vitro bone-forming bioactivities. *Angewandte Chemie International Edition* 43 (44): 5980–5984.

85 Liu, Y.Z., Li, Y., Yu, X.B. et al. (2014). Drug delivery property, bactericidal property and cytocompatibility of magnetic mesoporous bioactive glass. *Materials Science and Engineering C* 41: 196–205.

86 Li, X., Wang, X., Hua, Z., and Shi, J. (2008). One-pot synthesis of magnetic and mesoporous bioactive glass composites and their sustained drug release property. *Acta Materialia* 56: 3260–3265.

87 Koohkan, R., Hooshmand, T., Tahriri, M., and Marefati, M.T. (2018). Synthesis, characterization, and in vitro biological evaluation of copper-containing magnetic bioactive glasses for hyperthermia in bone defect treatment. *ACS Biomaterials Science & Engineering* 4 (5): 1797–1811.

88 Baikousi, M., Agasthopoulos, S., Panagliotopoulos, I. et al. (2008). Synthesis and characterization of sol–gel derived bioactive $CaO–SiO_2–P_2O_5$ glasses containing magnetic nanoparticles. *Journal of Sol–Gel Science and Technology* 47: 95–101.

89 Wu, C., Fan, W., Zhu, Y. et al. (2011). Multifunctional magnetic mesoporous bioactive glass scaffolds with a hierarchical pore structure. *Acta Biomaterialia* 7 (10): 3563–3572.

90 Mamiya, H., Ohnuma, M., Nakatani, I., and Furubayashim, T. (2005). Extraction of blocking temperature distribution from zero-field-cooled and field-cooled magnetization curves. *IEEE Transactions on Magnetics* 41 (10): 3394–3396.

91 Mikhaylova, M., Kim, D.K., Bobrysheva, N. et al. (2004). Superparamagnetism of magnetite nanoparticles: dependence on surface modification. *Langmuir* 17: 2472–2477.

92 Cannas, C., Concas, G., Gatteschi, D. et al. (2001). Superparamagnetic behaviour of Fe_2O_3 nanoparticles dispersed in a silica matrix. *Physical Chemistry Chemical Physics* 3: 832–838.

93 Skowronek, J. (2017). Current status of brachytherapy in cancer treatment – short overview. *Journal of Contemporary Brachytherapy* 9 (6): 581–589.

94 Cunha, J.A.M., Flynn, R., Bélanger, C. et al. (2020). Brachytherapy future directions. *Seminars in Radiation Oncology* 30 (1): 94–106.

95 Chargari, C., Deutsch, E., Blanchard, P. et al. (2019). Brachytherapy: an overview for clinicians. *CA: A Cancer Journal for Clinicians* 69 (5): 386–401.

96 Pouget, J.-P., Lozza, C., Deshayes, E. et al. (2015). Introduction to radiobiology of targeted radionuclide therapy. *Frontiers in Medicine* 2: 12.

97 Zhao, D., Huang, W., Rahaman, M.N. et al. (2012). Preparation and characterization of composite microspheres for brachytherapy and hyperthermia treatment of cancer. *Materials Science and Engineering C* 32 (2): 276–281.

98 Dahiya, M. (2016). Brachytherapy: a review. *Journal of Critical Reviews* 3 (2): 6–10.

99 Schubert, L.K. and Miften, M. (2016). The physics of brachytherapy. In: *Brachytherapy. Medical Radiology* (eds P. Montemaggi, M. Trombetta, and L. Brady). Cham: Springer.

100 Li, Z. (2006). Physics and clinical aspects of brachytherapy. In: *Technical Basis of Radiation Therapy. Medical Radiology* (eds S.H. Levitt and J.A. Purdy). Berlin, Heidelberg: Springer.

101 Aspasio, R.D., Borges, R., and Marchi, J. (2016). Biocompatible glasses for cancer treatment. In: *Biocompatible Glasses: From Bone Regeneration to Cancer Treatment* (ed. J. Marchi), vol. 53, 249–265. Switzerland: Springer International.

102 Day, D.E. (2012). Glasses for radiotherapy. In: *Bio-glasses: An Introduction* (ed. J.R. Jones and A.G. Clare), 203–228.

103 Burrill, J., Hafeli, U., and Liu, D.M. (2011). Advances in radioembolization – embolics and isotopes. *Journal of Nuclear Medicine and Radiation Therapy* 2: 107.

104 Arruebo, M., Vilaboa, N., Sáez-Gutierrez, B. et al. (2011). Assessment of the evolution of cancer treatment therapies. *Cancers (Basel)* 3 (3): 3279–3330.

105 Atroshchenko, G.N. and Sigaev, V.N. (2016). Glassy microspheres and their applications in nuclear medicine (review). *Glass and Ceramics* 72 (11–12): 397–404.

106 Haeli, U. (2001). Radioactive microspheres for medical applications. In: *Physics and Chemistry Basis of Biotechnology. Focus on Biotechnology* (eds M. De Cuyper and J.W.M. Bulte), vol 7. Dordrecht: Springer.

107 Dewey, W.C., Miller, H.H., and Leeper, D.B. (1971). Chromosomal aberrations and mortality of X-irradiated mammalian cells: emphasis on repair. *Proceedings of the National Academy of Sciences of the United States of America* 68 (3): 667–671.

108 Marcus, J.M., Burke, R.T., Doak, A.E. et al. (2018). Loss of p53 expression in cancer cells alters cell cycle response after inhibition of exportin-1 but does not prevent cell death. *Cell Cycle* 17 (11): 1329–1344.

109 Joiner, M.C., and van der Kogel, A. (2009) *Basic Clinical Radiobiology*. Taylor & Francis Ltd.

110 Pacelli, R. and Mansi, L. (2007). Eric Hall and Amato J. Giaccia: radiobiology for the radiologist, 6th edn. *European Journal of Nuclear Medicine and Molecular Imaging* 34 (6): 965–966.

111 Ollauri-Ibáñez, C., Núñez-Gómez, E., Egido-Turrión, C. et al. (2020). Continuous endoglin (CD105) overexpression disrupts angiogenesis and facilitates tumor cell metastasis. *Angiogenesis* 23 (2): 231–247.

112 Harrington, K., Jankowska, P., and Hingorani, M. (2007). Molecular biology for the radiation oncologist: the 5Rs of radiobiology meet the hallmarks of cancer. *Clinical Oncology* 19 (8): 561–571.

113 Steel, G.G., McMillan, T.J., and Peacock, J.H. (1989). The 5Rs of radiobiology. *International Journal of Radiation Biology* 56 (6): 1045–1048.

114 Sambi, M., Bagheri, L., and Szewczuk, M.R. (2019). Current challenges in cancer immunotherapy: multimodal approaches to improve efficacy and patient response rates. *Journal of Oncology* 2019: 4508794.

115 Demaria, S., Ng, B., Devitt, M.L. et al. (2004). Ionizing radiation inhibition of distant untreated tumors (abscopal effect) is immune mediated. *International Journal of Radiation Oncology Biology Physics* 58 (3): 862–870.

116 Walle, T., Martinez Monge, R., Cerwenka, A. et al. (2018). Radiation effects on antitumor immune responses: current perspectives and challenges. *Therapeutic Advances in Medical Oncology* 10: 1758834017742575.

117 Wild, A.T., Herman, J.M., Dholakia, A.S. et al. (2016). Lymphocyte-sparing effect of stereotactic body radiation therapy in patients with unresectable pancreatic cancer. *International Journal of Radiation Oncology Biology Physics* 94 (3): 571–579.

118 Patel, R.B., Baniel, C.C., Sriramaneni, R.N. et al. (2018). Combining brachytherapy and immunotherapy to achieve in situ tumor vaccination: a review of cooperative mechanisms and clinical opportunities. *Brachytherapy* 17 (6): 995–1003.

119 Vanpouille-Box, C., Alard, A., Aryankalayil, M.J. et al. (2017). DNA exonuclease Trex1 regulates radiotherapy-induced tumour immunogenicity. *Nature Communications* 8: 15618.

120 Liu, S.-Z. (2003). Nonlinear dose–response relationship in the immune system following exposure to ionizing radiation: mechanisms and implications. *Nonlinearity in Biology, Toxicology and Medicine* 1 (1): 71–92.

121 Rodriguez-Ruiz, M.E., Rodriguez, I., Barbes, B. et al. (2017). Brachytherapy attains abscopal effects when combined with immunostimulatory monoclonal antibodies. *Brachytherapy* 16 (6): 1246–1251.

122 Nakamura, N., Kusunoki, Y., and Akiyama, M. (1990). Radiosensitivity of CD4 or CD8 positive human T-lymphocytes by an in vitro colony formation assay. *Radiation Research* 123 (2): 224.

123 Balogh, A., Persa, E., Bogdándi, E.N. et al. (2012). The effect of ionizing radiation on the homeostasis and functional integrity of murine splenic regulatory T cells. *Inflammation Research* 62 (2): 201–212.

124 Hodge, J.W., Sharp, H.J., and Gameiro, S.R. (2012). Abscopal regression of antigen disparate tumors by antigen cascade after systemic tumor vaccination in combination with local tumor radiation. *Cancer Biotherapy and Radiopharmaceuticals* 27 (1): 12–22.

125 Xia, N., Haopeng, P., Gong, J.U. et al. (2019). Robo1-specific CAR-NK immunotherapy enhances efficacy of 125I seed brachytherapy in an orthotopic mouse model of human pancreatic carcinoma. *Anticancer Research* 39 (11): 5919–5925.

126 Cron, G.O., Beghein, N., Crokart, N. et al. (2005). Changes in the tumor microenvironment during low-dose-rate permanent seed implantation iodine-125 brachytherapy. *International Journal of Radiation Oncology Biology Physics* 63 (4): 1245–1251.

127 Bedford, J.S. and Hall, E.J. (1966). Threshold hypoxia: its effect on the survival of mammalian cells irradiated at high and low dose-rates. *The British Journal of Radiology* 39 (468): 896–900.

128 Hall, E.J., Bedford, J.S., and Oliver, R. (1966). Extreme hypoxia; its effect on the survival of mammalian cells irradiated at high and low dose-rates. *The British Journal of Radiology* 39 (460): 302–307.

129 van den Berg, A.P., van Geel, C.A.J.F., van Hooije, C.M.C. et al. (2000). Tumor hypoxia – a confounding or exploitable factor in interstitial brachytherapy? Effects of tissue trauma in an experimental rat tumor model. *International Journal of Radiation Oncology Biology Physics* 48 (1): 233–240.

130 MEDraysintell (2014). Brachytherapy market recovery to reach US$ 2.4 billion. Press Release Distribution.

131 Wunderlich, G., Pinkert, J., Stintz, M., and Kotzerke, J. (2005). Labeling and biodistribution of different particle materials for radioembolization therapy with ^{188}Re. *Applied Radiation and Isotopes* 62 (5): 745–750.

132 Wunderlich, G., Drews, A., and Kotzerke, J. (2005). A kit for labeling of [^{188}Re] human serum albumin microspheres for therapeutic use in nuclear medicine. *Applied Radiation and Isotopes* 62 (6): 915–918.

133 Benson, A.B., Geschwind, J.-F., Mulcahy, M.F. et al. (2013). Radioembolisation for liver metastases: results from a prospective 151 patient multi-institutional phase II study. *European Journal of Cancer* 49 (15): 3122–3130.

134 Bretcanu, O. and Evans, I. (2016). Glasses for treatment of liver cancer by radioembolization. In: *Biocompatible Glasses: From Bone Regeneration to Cancer Treatment* (ed. J. Marchi), 267–283. Switzerland: Springer International Publishing.

135 Wang, E.A., Broadwell, S.R., Bellavia, R.J., and Stein, J.P. (2017). Selective internal radiation therapy with SIR-Spheres in hepatocellular carcinoma and cholangiocarcinoma. *Journal of Gastrointestinal Oncology* 8 (2): 266–278.

136 Reinders, M.T.M., Smits, M.L.J., van Roekel, C., and Braat, A.J.A.T. (2019). Holmium-166 microsphere radioembolization of hepatic malignancies. *Seminars in Nuclear Medicine* 49 (3): 237–243.

137 Kallini, J.R., Gabr, A., Thorlund, K. et al. (2017). Comparison of the adverse event profile of TheraSphere® with SIR-Spheres® for the treatment of unresectable hepatocellular carcinoma: a systematic review. *CardioVascular and Interventional Radiology* 40 (7): 1033–1043.

138 Kawashita, M., Shineha, R., Kim, H., and Kokubo, T. (2003). Preparation of ceramic microspheres for in situ radiotherapy of deep-seated cancer. *Biomaterials* 24: 2955–2963.

139 Erbe, E.M. and Day, D.E. (1993). Chemical durability of Y_2O_3–Al_2O_3–SiO_2 glasses for the in vivo delivery of beta radiation. *Journal of Biomedical Materials Research* 27 (10): 1301–1308.

140 Hamoui, N., Gates, V.L., Gonzalez, J. et al. (2013). Radioembolization of renal cell carcinoma using yttrium-90 microspheres. *Journal of Vascular and Interventional Radiology* 24 (2): 298–300.

141 Ehrhardt, G.J. and Day, D.E. (1987). Therapeutic use of 90Y microspheres. *International Journal of Radiation Applications and Instrumentation. Part B. Nuclear Medicine and Biology* 14 (3): 233–242.

142 Hyatt, M.J. and Day, D.E. (1987). Glass properties in the yttria-alumina-silica system. *Journal of the American Ceramic Society* 70 (10): C-283–C-287.

143 Kaur, G., Pandey, O.P., Singh, K. et al. (2013). A review of bioactive glasses: their structure, properties, fabrication and apatite formation. *Journal of Biomedical Materials Research Part A* 102 (1): 254–274.

144 Christie, J.K., Malik, J., and Tilocca, A. (2011). Bioactive glasses as potential radioisotope vectors for in situ cancer therapy: investigating the structural effects of yttrium. *Physical Chemistry Chemical Physics* 13 (39): 17749–17755.

145 Jung, S.B. (2012). Bioactive borate glasses. In: *Bio-glasses* (eds J.R. Jones and A.G. Clare), 75–95. Wiley.

146 Fu, Y. and Christie, J.K. (2017). Atomic structure and dissolution properties of yttrium-containing phosphate glasses. *International Journal of Applied Glass Science* 8 (4): 412–417.

147 Zanotto, E.D. and Coutinho, F.A.B. (2004). How many non-crystalline solids can be made from all the elements of the periodic table? *Journal of Non-Crystalline Solids* 347 (1–3): 285–288.

148 Brow, R.K. (2000). Review: the structure of simple phosphate glasses. *Journal of Non-Crystalline Solids* 264: 1–28.

149 Bunker, B.C., Arnold, G.W., and Wilder, J.A. (1984). Phosphate glass dissolution in aqueous solutions. *Journal of Non-Crystalline Solids* 64 (3): 291–316.

150 Christie, J.K., Ainsworth, R.I., and De Leeuw, N.H. (2016). Investigating structural features which control the dissolution of bioactive phosphate glasses: beyond the network connectivity. *Journal of Non-Crystalline Solids* 432: 31–34.

151 Hossain, K.M.Z., Patel, U., and Ahmed, I. (2015). Development of microspheres for biomedical applications: a review. *Progress in Biomaterials* 4 (1): 1–19.

152 Poorbaygi, H., Reza Aghamiri, S.M., Sheibani, S. et al. (2011). Production of glass microspheres comprising ^{90}Y and ^{177}Lu for treating of hepatic tumors with SPECT imaging capabilities. *Applied Radiation and Isotopes* 69 (10): 1407–1414.

153 Nosrati, Z., Khanchi, A.R., and Sheybani, S. (2014). Preparation of low-density ^{90}Y microspheres consisting of mesoporous silica core/yttria shell: a potential therapeutic agent for hepatic tumors. *Journal of Radioanalytical and Nuclear Chemistry* 301 (2): 373–382.

154 Ghahramani, M.R., Garibov, A.A., and Agayev, T.N. (2014). Production and quality control of radioactive yttrium microspheres for medical applications. *Applied Radiation and Isotopes* 85: 87–91.

155 Sreekumar, K.P., Saxena, S.K., Kumar, Y. et al. (2010). Studies on the preparation and plasma spherodization of yttrium aluminosilicate glass microspheres for their potential application in liver brachytherapy. *Journal of Physics: Conference Series* 208: 12117.

156 Kawashita, M. (2002). Ceramic microspheres for in situ radiotherapy of cancer. *Materials Science and Engineering C* 22 (1): 3–8.

157 Sene, F.F., Martinelli, J.R., and Okuno, E. (2008). Synthesis and characterization of phosphate glass microspheres for radiotherapy applications. *Journal of Non-Crystalline Solids* 354 (42–44): 4887–4893.

158 Hench, L.L., Splinter, R.J., Allen, W.C., and Greenlee, T.K. (1971). Bonding mechanisms at the interface of ceramic prosthetic materials. *Journal of Biomedical Materials Research* 5 (6): 117–141.

159 Roberto, W.d.S., Pereira, M.M., and de Campos, T.P.R. (2003). Analysis of bioactive glasses obtained by sol–gel processing for radioactive implants. *Materials Research* 6 (2): 123–127.

160 Hadush Tesfay, A., Chou, Y.-J., Tan, C.-Y. et al. (2019). Control of dopant distribution in yttrium-doped bioactive glass for selective internal radiotherapy applications using spray pyrolysis. *Materials (Basel, Switzerland)* 12 (6): 986.

161 Christie, J.K. and Tilocca, A. (2012). Integrating biological activity into radioisotope vectors: molecular dynamics models of yttrium-doped bioactive glasses. *Journal of Materials Chemistry* 22: 12023–12031.

162 Borges, R., Schneider, J.F., and Marchi, J. (2019). Structural characterization of bioactive glasses containing rare earth elements (Gd and/or Yb). *Journal of Materials Science* 54 (17): 11390–11399.

163 Zambanini, T., Borges, R., Faria, P.C. et al. (2019). Dissolution, bioactivity behavior, and cytotoxicity of rare earth-containing bioactive glasses (RE = Gd, Yb). *International Journal of Applied Ceramic Technology* 16 (5): 2028–2039.

164 Delpino, G.P., Borges, R., Zambanini, T. et al. (2021). Sol–gel-derived 58S bioactive glass containing holmium aiming brachytherapy applications: a dissolution, bioactivity, and cytotoxicity study. *Materials Science and Engineering C* 119: 111595.

165 Eisenstein, M. (2019). Prostate cancer: a declining art. *Nature* 574: S81.

166 Eisenstein, M. and Reading-Ikkanda, L. (2019). Keeping treatment options open. *Nature* 574: S82–S83.

167 Dutta, S.W., Bauer-Nilsen, K., Sanders, J.C. et al. (2018). Time-driven activity-based cost comparison of prostate cancer brachytherapy and intensity-modulated radiation therapy. *Brachytherapy* 17 (3): 1–8.

23

Bioactive Glasses with Antibacterial Properties: Mechanisms, Compositions, and Applications

Mostafa Awaid and Ilaria Cacciotti

Department of Engineering, University of Rome "Niccolò Cusano", INSTM RU, Rome, Italy

23.1 Introduction

Bioglasses (BGs) were discovered in 1969 by Hench with the first composition (45S5, SiO_2 45%, Na_2O 24.5%, CaO 24.5%, P_2O_5 6%, all in wt%), and provided for the first time an alternative interfacial bonding of an implant with host tissues [1–4]. A series of biophysical and biochemical reactions occur at the tissue interface once the bioactive material is implanted in the human body, leading to mechanically strong chemical interfacial bonding called "bioactive fixation" [5]. Third-generation BGs are being designed to activate genes that stimulate regeneration of living tissues [2, 6, 7]. Various studies have been done on BG and glass-ceramic materials for more than 50 years and hundreds of different formulations have been developed [8].

BGs have been successfully used in many medical applications such as repairing or replacing damaged tissues, bone grafting scaffolds, and as coating for implants [9–13], due to their unique ability to bond with the bone tissue through ion exchange in biological fluids (e.g. simulated body fluid [SBF]) when implanted into the human body [14].

A lot of efforts have been recently devoted to the BGs chemical modifications in order to provide additional properties, such as antimicrobial activity, as well as improved osteogenic behavior [8], taking into account the development of infections in the case of joint and bone implants, whose need and request are progressively increasing due to population aging [15].

Indeed, the occurrence of bacterial infections and inflammations due to the contamination of implanted medical devices is a critical complication that often leads to the implant failure with significant impact concerning public health in developed countries [16–18]. Moreover, for the management of medical-device associated infections (MDAIs), surgical intervention or/and prolonged usage of intravenous or oral antibiotic therapies are necessary with consequent possible bone loss, significant morbidity, and, thus, severe limitations to the patient's normal life and well-being [19, 20], as well as the development of bacteria resistance to antibiotics. For example, chronic osteomyelitis is considered as one of the main causes of morbidity and mortality worldwide, as a consequence of reconstructive orthopedic procedures, trauma, and other local surgery [21].

In particular, for the infectious diseases treatment, several antibiotics have been developed, and they are commonly intaked through oral administration and injection [22, 23], to accomplish and maintain minimum inhibitory concentrations (MICs) in the target tissues. The situation

Bioactive Glasses and Glass-Ceramics: Fundamentals and Applications, First Edition.
Edited by Francesco Baino and Saeid Kargozar.

is more complicated in the case of bone, due to its reduced blood supply, and, thus, the use of very high systemic antibiotics concentrations is strongly requested to reach the MIC in this tissue. Additionally, antibiotic levels below the MIC favor the development of antibiotic-resistant species [24].

For all these reasons, a lot of efforts have to be devoted to the development of local controlled delivery systems aimed at releasing proper amounts of antibiotics or other antimicrobial agents (e.g. ionic dissolution products) for an extended period [21], to avoid/decrease the bacterial attachment and growth, and biofilm formation [25].

In this context, the proper design of antimicrobial BGs could allow to overcome these criticisms, fighting the bacterial colonization of implant sites which usually leads to the implant failure [9].

Different approaches can be followed in order to provide antimicrobial features to BGs, including the incorporation of biocidal metals within their network, the addition of antibiotics, and the combination with antimicrobial agents, compounds, and materials.

The present chapter is aimed at providing a complete overview about the strategies employed to obtain BGs with improved antimicrobial behavior, starting from the underlying mechanisms, associated to the antimicrobial action, to the most widely investigated compositions, on the basis of specific biocide metal ions and antibiotics, and potential biomedical and clinical applications. Finally, some concluding remarks and future perspectives are reported.

23.2 Mechanisms of Antimicrobial Activities

BGs antibacterial effects depend on several aspects, such as the bacterial type, the glass composition and concentration [26–28].

However, the exact mechanisms associated to the BGs antibacterial behavior have not been completely comprehended yet and are still under investigation.

It has been suggested that BG exerts antibacterial activity by increasing pH, osmotic effects, and calcium ion concentrations [29, 30]. Indeed, BGs are able to diminish pathogens' biofilm production [15] and to kill microbes, owing to the induction of enhanced pH caused by high alkali cations release during dissolution [31].

Recently, several involved mechanisms have been summarized according to their mode of action, such as the change in the environmental pH (alkaline) and osmotic pressure, and the ability of BG debris to damage the bacterial cell walls [15] (Figure 23.1).

In particular, the most accredited mechanism is related to the calcium and alkalis release from the BG surface within the medium. Zhang et al. [28] assumed that the BGs fast dissolution, leading to an increase in the pH value (on the basis of the BG alkali oxide/silica ratio), and the alkali ions concentration (controlled by the total BG composition) at the powder interface strongly influence the antibacterial behavior [28].

Similarly, Drago et al. [15] supposed that the BGs antibacterial properties are due to the increase in local pH and the *in vivo* and *in vitro* sodium ions exchange with protons in body fluids. Due to the interaction with biological fluids, the ions are released from the granules' surface with consequent increase in the osmolarity and pH. In detail, the high calcium and alkalis concentrations within the medium lead to a high increase in the environment pH due to the rapid ion exchange between the alkaline ions (Na^+, Ca^{2+}) from the glass surface and the hydrogen ions from the solution [33, 34], as well as to the bacteria membrane potential perturbation [27]. Thus, the surrounding environment resulted hostile for the microbial growth without affecting the host tissues [15].

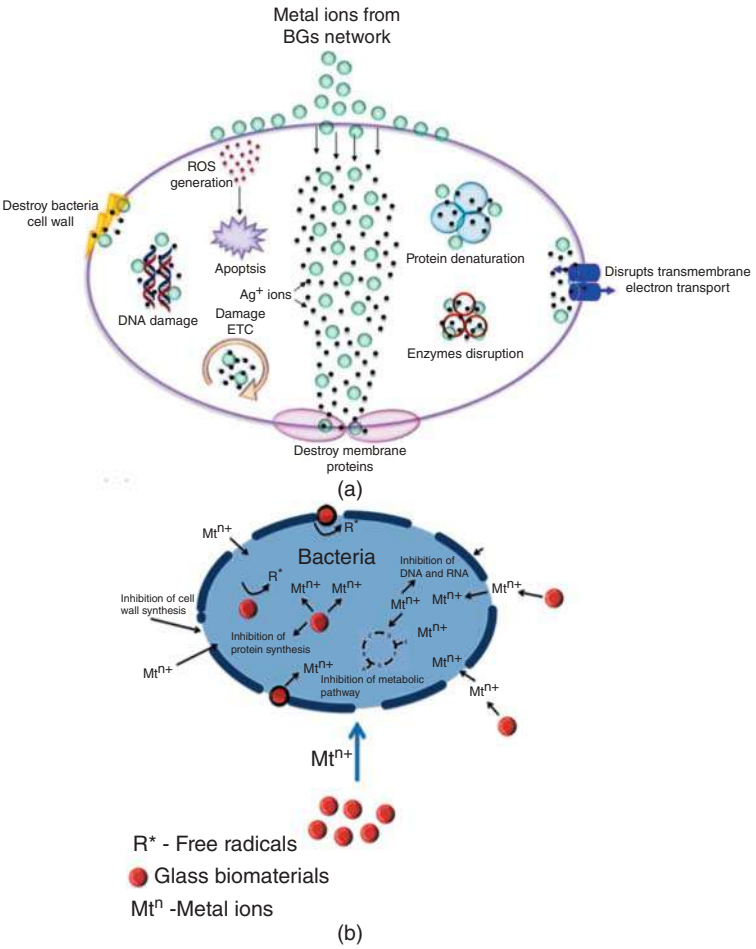

Figure 23.1 (a) Potential and main mechanism of metal ions antimicrobial activity. Source: Singh et al. [32]/MDPI/Licensed under CC BY 4.0. (b) Hypothesized mechanisms ascribed to the metal ions antibacterial activity. Source: Reproduced with permission from Fernandes et al. [8].

Zehnder et al. [34] proposed another mechanism based on the silica release from BGs, Hu et al. [26] reported that the "needle-like" sharp glass debris are able to damage the bacterial cell walls, leading to their inactivation [15].

The same considerations were reported and confirmed by Echezarreta-López and Landin [35], who created an artificial intelligence tool (neurofuzzy logic technology), using a machine learning, from a wide literature database on the BGs compositions, antibacterial properties, and microbiological experiments. They concluded that the antibacterial activity is mainly defined by the release of alkaline ions (Ca^{2+} ions) to the medium and pH increasing. These mechanisms of action unbalanced the bacterial intracellular Ca^{2+}, leading to cell membrane depolarization and subsequent death [35].

Moreover, the particles size plays a pivotal role in determining the BGs antimicrobial activity. Waltimo et al. [36] reported that nanometric BGs show stronger antimicrobial effect than micron-sized ones, due to the release of more alkaline species because of the large surface area.

23.3 Intrinsic Antibacterial Properties of Bioactive Glass Compositions Without Any Specific Bactericidal Ion

BGs and BG-ceramics compositions, also without any specific bactericidal ions, are intrinsically effective against bacteria sessile communities, due to several well-known chronic infections [8]. Indeed, they show strong antibacterial effects against numerous bacteria species, even if at a high sample concentration (100 mg/ml) [28]. Their antimicrobial activity depends on the bacteria species, BGs composition and concentration [28], and is effective against a wide range of aerobic and anaerobic bacteria, in forms of either planktonic or sessile. The BGs intrinsic antimicrobial activity depends on the network degradation and on the species leaching to the surrounding environment [8].

Stoor et al. [30] demonstrated the *in vitro* antibacterial properties of S53P4 BG composition, based on sodium, silicate, calcium, and phosphate, against oral bacteria, for the first time.

Successively, many authors reported the *in vitro* antibacterial action of several BG formulations, including both sol–gel- and melt-quenching-derived particles, such as in the case of 45S5 [26, 36–38].

Similarly, different formulations of S53P4 showed the ability to reduce the methicillin resistant *Staphylococcus aureus* (MRSA) and multi-drug-resistant *Pseudomonas aeruginosa* (MDRPA), avoiding the bacterial biofilm production on prosthetic material [39], as well as the potentiality to be used in the chronic osteomyelitis treatment [40, 41].

Allan et al. [29] demonstrated the Bioglass® supernatants antibacterial activity against certain supragingival and subgingival bacteria in all media after three hours exposure. The same experimental evidences were reported by Hu et al. [26], highlighting that 45S5 Bioglass showed a higher antibacterial effect (against Gram+ and Gram− bacteria) in the case of suspensions with 45S5 Bioglass particles with respect to the supernatants without particles, due to the aqueous pH value increment [26].

Munukka et al. [27] reported the sol–gel-derived glass $CaPSiO_2$ antibacterial action against 29 bacterial species. The $CaPSiO_2$ antibacterial features were comparable to BG S53P4 ones, even if the detected pH increase was lower. Zhang et al. [28] found that the BGs antibacterial effects enhanced with the BG concentration, and with increasing the ratio of BG surface area to suspension volume (SA/V). Moya et al. [42] proved that soda-lime glasses based SiO_2–Na_2O–CaO–B_2O_3 system, enriched with a high concentration of calcium oxide ("Ca-rich glass") (15–20 wt%), are efficient biocides against Gram+ and Gram− bacteria and yeast, and considered as "green" antimicrobials.

It has been also evidenced that BG fillers are able to provide antibacterial features to natural or synthetic polymers. For example, Misra et al. [38] showed that poly(3-hydroxybutyrate) (P(3HB)) based biocomposites, loaded with 45S5 BG nanoparticles (10 wt%), were able to inhibit the *Streptococcus aureus* NCTC6571 growth, ascribing this experimental evidence to the pH increase of the culture medium during the incubation period. Rivadeneira et al. [33] evidenced the capability of 45S5 coating on agar–gelatin films to provide *in vitro* antistaphylococcal activity, owing to the medium alkalinization.

23.4 Strategies to Provide Antimicrobial Properties

Several strategies can be applied and followed in order to provide improved antimicrobial properties to BGs compositions, such as the doping with biocidal metals and the functionalization with antibiotics (Figure 23.2), as described in detail in the following paragraphs.

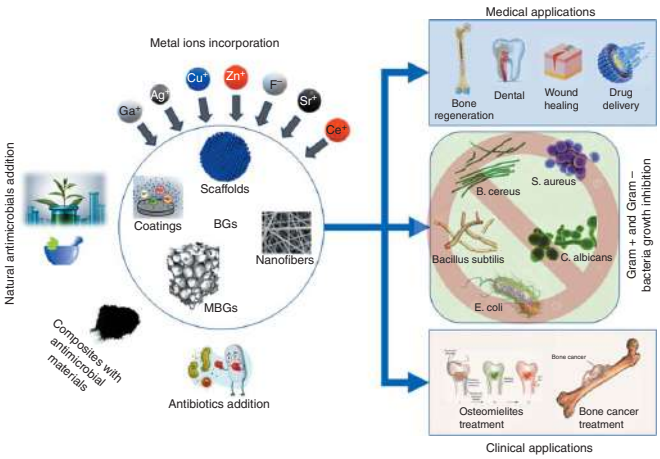

Figure 23.2 Main strategies aimed at improving the BGs antimicrobial features and leading applications of antimicrobial BGs formulations.

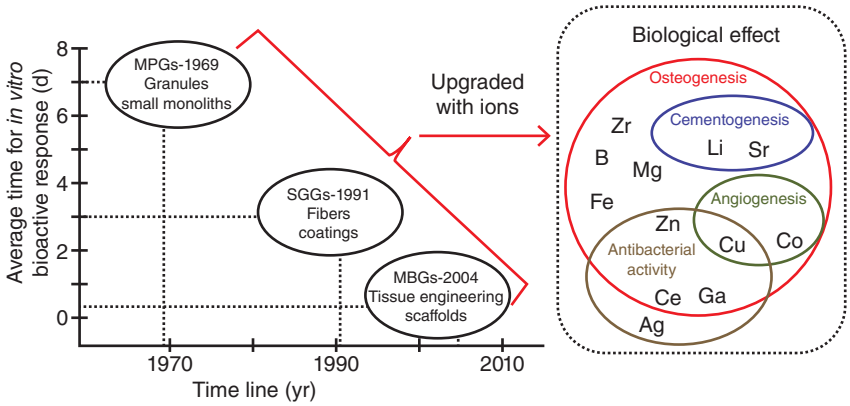

Figure 23.3 Timeline in the discovering of bioactive glasses and the average time required for *in vitro* bioactive responsiveness (surface deposition of an apatite layer during soaking in a simulated body fluid) (left side); biological actions of some ions commonly added to BGs compositions (right side). Source: Reproduced from Salinas and Vallet-Regí [43] with permission.

23.4.1 Addition of Biocidal Metals in the Formulated Compositions

The incorporation of antimicrobial metallic ions into BGs is considered as one of the most promising strategies for inhibiting bacterial growth and reproduction, due to their controlled and gradual release during BGs dissolution in aqueous media [24], as well as for enhancing their bioactivity and promoting the osteogenesis and angiogenesis (Figure 23.3). They could be added as pure metal, colloids, metal or oxide nanoparticles, and coordinative bound metal ions [44]. The doped BGs antimicrobial behavior depends on the bacteria type and the incorporated biocide metal ion [45]: for instance, the integration of bivalent cations as copper (Cu^{2+}), zinc (Zn^{2+}), strontium (Sr^{2+}), etc. within the bio-glass structure has been proposed to improve the antimicrobial effect, promoting the tissue formation, and, simultaneously, inhibiting its resorption by osteoclasts [15].

Therefore, the use of specific biocide metal ions as antimicrobial agents in different medical applications is paying much attention [24], because of their well-known antibacterial properties [46]. The biocide ions incorporation within BGs does not only improve their antibacterial properties but also strongly influences their physical, chemical, and biological properties [47, 48]. Indeed, it leads to a decrease of the glass transition temperature, of the density and the local symmetry of the network, of the material viscosity, and to an increment of the glass solubility in the physiological medium, as well as to an improved therapeutic behavior, due to the release of antibacterial (Ag, Cu, Au, Mg, Ti, Ga), osteogenic, and/or pro-angiogenic (B, Cu, Co, Sr, Li) ions [49, 50].

Several BGs compositions, including silicates, phosphates, and borates, have been doped with selected metals [51], making them carriers of specific antibacterial agents, since they are able to exchange ions within their networks with those present in the biological fluids. Many researchers have developed bio-glasses substituted with additive biocidal metals such as monovalent (Ag^{+}, Cu^{+}, and B^{+}), divalent (Zn^{2+}, Sr^{2+}, Mg^{2+}, and Cu^{2+}) [52], and trivalent (Ce^{3+}, Ga^{3+}, and Ti^{3+}) [53] ions, to fabricate glassy biomaterials with efficient antimicrobial properties and enhanced bioactivity and functionality (Table 23.1). Different approaches can be followed in order to obtain biocidal metals doped BGs: (i) by their addition during the glass-melting process, (ii) by their addition during the sol–gel synthesis, (iii) by their incorporation within the glass network via an ion-exchange route, and (iv) by coating the glass structure with ionic metals or dispersing the metal compound within the glass matrices [89].

Table 23.1 Compositions, synthesis methods, and antimicrobial action related to antimicrobial metals doped BGs.

Agent(s)	Composition(s)	Method(s)	Antimicrobial action	References
Ag^+	**Ag-BG** Bioglass® 45S5 $AgNO_3$ solution (concentration: 0.01 M or 0.1 M)	Tape casting and heat treatment+dipping	Inhibition of the bacterial growth	[54]
	Ag-BG $(1-y)(58SiO_2–33P_2O_5–9CaO)–yAg_2O$ (mol%) $y = 1$ and 2 (mol%)	Sol–gel	Effective antimicrobial action against bla_{DMP} gene-positive *P. aeruginosa* strains, *Klebsiella pneumonia*, *S. aureus*, and *E. coli*	[55]
	Ag-BG $(76SiO_2–2P_2O_5–19CaO)–3Ag_2O$ (wt%)	Sol–gel	Inhibition of the *E. coli*, *P. aeruginosa*, and *S. aureus* growth	[56]
	Ag-BG $(70SiO_2–30CaO)–xAg_2O$ (mol%) $0.08 \leq x \leq 0.27$	Sol–gel	Effective antimicrobial action against *S. aureus*	[57]
	Ag-SM58S $(58SiO_2–9P_2O_5–33CaO)$ (wt%) $AgNO_3$ solution (concentration: 0.1002 mol/l)	Sol–gel (surfactant: P123)+dipping	Effective antimicrobial action against *E. coli* and *S. aureus*	[58]
	Ag-BG $(64SiO_2–26CaO–5P_2O_5)–5Ag_2O$ (mol%)	Sol–gel	Inhibition of the *E. coli* growth	[59]
	Ag-BG $(70.1SiO_2–15.2CaO–4.7P_2O_5)–10Ag_2O$ (wt%)	Sol–gel	Effective antimicrobial action against *E. coli* DH5α ampicillin-resistant and *S. mutans*	[45]
	Ag-BG Bioglass® 45S5 $AgNO_3$ solution (concentration: 2 %wt)	Transition metal ion dopants via bio-inspired route	Effective antimicrobial action against *E. coli* NCIMB-1 and *S. aureus* NCIMB-17	[60]
	Ag-BG $(76SiO_2–19CaO–2P_2O_5)–3Ag_2O$ (wt%)	Sol–gel	Effective antimicrobial action against *E. coli* (MG1655)	[61]
	Ag-MBGN $(86SiO_2–14CaO)$ (mol%) $AgNO_3$ solution (concentration: 0.05 M)	Microemulsion-assisted sol–gel+impregnation	Effective antimicrobial action against *P. aeruginosa* and *S. aureus*	[62]
	Ag-BG/Ag-BG-ceramic Bioglass® 45S5 $(45SiO_2–24.5Na_2O–24.5CaO–6P_2O_5)–xAgNO_3$ (wt%) $x = 0.5$ and 1 (wt%)	Melt-quenching	Inhibition of the *E. coli* and *B. subtilis* growth	[31]

(Continued)

Table 23.1 (Continued)

Agent(s)	Composition(s)	Method(s)	Antimicrobial action	References
Cu^{+}/Cu^{2+}	**Cu-MBG** ($75SiO_2$–$15CaO$–$5P_2O_5$)–$5CuO$ (mol%)	Evaporation Induced Self-Assembly (EISA) (surfactant: F108)	Inhibition of the *E. coli* growth	[63]
	Cu-MBG ($80SiO_2$–$10CaO$–$5P_2O_5$)–$5CuO$ (mol%)	Polymer sponge method (surfactant: P123)	Inhibition of the *E. coli* growth	[64]
	Cu-PGF ($10Na_2O$–$30CaO$–$50P_2O_5$)–$10CuO$ (mol%)	Fiber drawing method (fiber-rig)	Effective antimicrobial action against *S. epidermidis*	[65]
	Cu-PBG/Cu-BG ($68SiO_2$–$23CaO$–$4P_2O_5$)–$5CuO$ (mol%)	Sol–gel (surfactant: P123)	Inhibition of the *E. coli* growth	[66]
	Cu-BG ($67.7SiO_2$–$18.9CaO$–$5P_2O_5$)–$8.4CuO$ (wt%)	Sol–gel	Effective antimicrobial action against *E. coli* DH5α ampicillin-resistant and *S. mutans*	[45]
	Cu-BG Bioglass® 45S5 $CuCl_2$ (concentration: 2 %wt)	Transition metal ion dopants via bio-inspired route	Effective antimicrobial action against *E. coli* NCIMB-1 and *S. aureus* NCIMB-17	[60]
	Cu-MBG NPs ($85SiO_2$–$13CaO$–$2CuO$) (mol%)	One-pot ultrasound-assisted sol–gel	Effective antimicrobial action against *E. coli*, *S. aureus*, and *S. epidermidis*	[67]
Zn^{2+}	**Zn-BG** ($70SiO_2$–$(26-x)CaO$–$4P_2O_5$)–$xZnO$ (mol%) $x = 0$, 3, and 5 (mol%)	Sol–gel (surfactant: P123)	Inhibition of the *B. subtilis* and *P. aeruginosa* growth	[9]
	Zn-MBG (($(80-x)SiO_2$–$15CaO$–$5P_2O_5$)–$xZnO$ (mol%) $x = 4$ and 7 (mol%)	Sol–gel	Inhibition of the *S. aureus* growth	[68]
	Zn-BG ($38.73SiO_2$–$49.96CaO$–$6.53P_2O_5$–$4.35Na_2O$–$0.43CaF_2$)–$xZnO$ (mol%) $x = 0$, 0.76, 3.96, 7.78, 15.53 (mol%)	Melt-quenching	Inhibition of the *S. epidermidis*, *K. pneumoniae*, *S. aureus*, and *B. subtilis* growth	[69]
	Zn-BG ($57.00SiO_2$–$29.45CaO$–$3.80P_2O_5$–$4.75MgO$)–$5ZnO$ (mol%)	Sol–gel	Effective antimicrobial action against *P. aeruginosa*	[70]

	Zn-BG ceramic ($45B_2O_3$–$29.4SiO_2$–$8.2Na_2O$–$4.6Al_2O_3$)–12.8ZnO (mol%) ($35.3B_2O_3$–$23.1SiO_2$–$6.4Na_2O$–$3.6Al_2O_3$)–31.6ZnO (mol%)	Melt-quenching	Effective antimicrobial action against *E. coli*	[71]
	Zn-BG (Glass A) ($42SiO_2$–5CaO)–53ZnO (mol%) **Zn-BG (Glass B)** ($42SiO_2$–5SrO)–53ZnO (mol%)	Melt-quenching	Inhibition of the *S. mutans* and *Actinomyces viscosus* growth	[72]
	Zn-BG/Zn-BG-ceramic Bioglass® 45S5 ($45SiO_2$–$24.5Na_2O$–24.5CaO–$6P_2O_5$)–xZnO (wt%) $x = 0.5$ and 1 (wt%)	Melt-quenching	Inhibition of the *E. coli*, and *Bacillus subtilis* growth	[31]
Sr^{2+}	**Sr-BG** ($47.32SiO_2$–(10.41–x)CaO–(11.04-y) CaF_2–31.23MgO)–xSrO–ySrF_2 (mol%) $x = 0$, 0.26, 1.04, and 5.21 (mol%); $y = 0$, 0.28, 1.10, and 5.52 (mol%)	Melt-quenching	Effective antimicrobial action against *S. aureus* and *Streptococcus faecalis*	[73]
Ga^{3+}	**Ga-MBGNPs** ($60SiO_2$–(40–x)CaO)–xGa_2O_3 (mol%) $x = 1$, 3, 5 (mol%)	Microemulsion assisted sol–gel	Effective antimicrobial action against *E.* coli and *S.* aureus	[86]
	Ga-(13-93B3)BG ($56.6B_2O_3$–18.5CaO–$5.5Na_2O$–$11.1K_2O$–4.6MgO –$3.7P_2O_5$)–xGa_2O_3 (wt%) $x = 1$, 5 (wt%)	Melting-cast technique	No antibacterial response against *E. coli* and *S. aureus*	[87]
	Ga-MBG ((80 – x)SiO_2–15CaO–$5P_2O_5$)–xGa_2O_3 (mol%) $x = 0$, 1, 2, and 3 (mol%)	Evaporation-Induced Self-Assembly (EISA) (surfactant: P123)	Effective antimicrobial action against *E. coli* and *S. aureus*	[74]
	Ga-PBG (16CaO–$45P_2O_5$–yNa_2O)–xGa_2O_3 (mol%) $y = 34$, 36, 38, and 39 (mol%) $x = 1$, 3, and 5 (mol%)	Melt-quenching	Effective antimicrobial action against *E. coli*, *P. aeruginosa*, *S. aureus*, methicillin-resistant *S. aureus* and *Clostridium difficile*	[75]
	Ga-PBG (xCaO–$45P_2O_5$–(52 – x)Na_2O)–$3Ga_2O_3$ (mol%) $x = 14$, 15, and 16 (mol%)	Melt-quenching	Effective antimicrobial action against *P. aeruginosa*	[76]

(Continued)

Table 23.1 (Continued)

Agent(s)	Composition(s)	Method(s)	Antimicrobial action	References
	Ga-BG Bioglass® 45S5 $Ga(NO_3)_3$ solution (concentration: 200, 400, and 600 mM)	Commercially available powder (by melt-quenching)/foam replication technique+coating with sodium alginate crosslinked with Ga^{3+}	Inhibition of the *S. aureus* growth	[77]
	Ga-PBGs $(14CaO–45P_2O_5–38Na_2O)–3Ga_2O_3$ (mol%)	Melt-quenching	Inhibition of the *S. mutans* growth	[78]
	Ga-(13-93 BGs) $((53–x)SiO_2–4P_2O_5–20CaO–6Na_2O–12K_2O–5MgO)–xGa_2O_3$ (wt%) $x = 0$, 1, 3, and 5 (wt%)	Sol–gel	Inhibition of the *S. aureus* and *E. coli* growth	[79]
F^-	**F-BG** Bioglass® 45S5 NaF solution (concentration: ~0.59 mg/ml)	Commercially available powder+dipping	Effective antimicrobial action against *Streptococcus mutans*	[80]
	F-CPG $(37.7CaO–59.7P_2O_5–1.3Na_2O–1.3MgO–0.5NaF)$ (wt%)	Melt-quenching	Effective antimicrobial action against *S. mutans*	[52]
	F-BG $(1 – x)(58SiO_2–33P_2O_5–9CaO)–xCaF_2$ (mol%) $x = 0$, 5, 10, 20 (mol%)	Sol–gel	Inhibition of the *E. coli*, *S. aureus*, and *P. aeruginosa* growth	[81]
Ce^{3+}	**Ce-BG** $(50SiO_2–(45 – x)CaO–5P_2O_5)–xCeO_2$ $x = 0$, 1, 5, 10 (mol%)	Sol–gel	Effective antimicrobial action against *E. coli*	[82]
	GR-HAp_Ce $(10CaF_2–10Na_2CO_3–15CaO–60P_2O_5)–5CeO_2$ (mol%)	Melt-quenching	Effective antimicrobial action against *S. aureus* and *S. epidermidis*	[83]
	Ce-BG $(20Na_2O–14CaO–(66 – x)P_2O_5)–xCeO_2$ (wt%) $x = 0.1$, 0.3, 0.7, 1.0 (wt%)	Melt-quenching	– Effective antimicrobial action against *E. coli* and *S. aureus* – No effective antimicrobial action against *B. cereus*, *B. subtilis*, and *C. albicans*	[84]

	Ce-BG $(46.1SiO_2–2.6P_2O_5–16.9CaO–10.0MgO–19.4Na_2O)–5.0CeO_2$ (mol%)	Sol–gel	Effective antimicrobial action against *E. coli*	[85]
	Ce-MBGNPs $(60SiO_2–(40 – x)CaO)–xCe_2O_3$ (mol%) $x = 1, 3, 5$ (mol%)	Microemulsion assisted sol–gel	Effective antimicrobial action against *E. coli* and *S. aureus*	[86]
	Ce-BG $(50SiO_2–(45 – x)CaO–5P_2O_5)–xCeO_2$ $x = 0, 1, 5,$ and 10 (mol%)	Sol–gel	No effective antimicrobial action against *E. coli*	[53]
	Ce-(13-93) BGs $((53 – x)SiO_2–4P_2O_5–20CaO–6Na_2O–12K_2O–5MgO)–xCe_2O_3$ (wt%) $x = 0, 1, 3,$ and 5 (wt%)	Sol–gel	No effective antimicrobial action against *S. aureus* and *E. coli*	[79]
	Ce-(13-93B3)BG $(56.6B_2O_3–18.5CaO–5.5Na_2O–11.1K_2O–4.6MgO–3.7P_2O_5)–xCe_2O_3$ (wt%) $x = 1, 3, 5$ (wt%)	Melting-cast technique	No antibacterial response against *E. coli and S. aureus*	[87]
Ag^+ and Sr^{2+}	**AgSr-BG** $(55SiO_2–40CaO–(5 – x)SrO–xAg_2O)$ (mol%) $x = 0, 2, 4$ (mol%)	Sol–gel	Effective antimicrobial action against *E. coli* and *S. aureus*	[14]
Ga^{3+} and Ag^+	**GaAg-PBGs** $(xCaO–45P_2O_5–(47 – x)Na_2O)–5Ag_2O–3Ga_2O_3$ (mol%) $x = 10, 11, 12$ (mol%)	Melt-quenching	Inhibition of the *P. aeruginosa* growth	[88]

BG, bioactive glass; MBG, mesoporous bioactive glass; MBGNPs, mesoporous bioactive glass nanoparticles; SM58S bioactive glass, surface modification of mesoporous 58S bioactive glass; PGF, phosphate-based glass fibers; PBG, phosphate-based glasses; CPG, calcium phosphate glass; GR-HAp, glass-reinforced hydroxyapatite.

The main biocidal metals and the related doped BG compositions are described in details in the following paragraphs.

23.4.1.1 Bioactive Glasses Doped with Silver

Silver (Ag) is characterized by high thermal stability and, mainly, by a broad antimicrobial action spectrum, which is relevant in the case of polymicrobial colonization associated with infections [61]. Ag^+ ions antimicrobial properties have been exploited since ancient times by Mediterranean and Asiatic cultures [90]. Historical use of silver in surgical treatment of wounds and bone regeneration is documented [61]. Moreover Ag^+ ions have limited toxicity toward the human cells [14] and their bacteriostatic and bactericidal action impacts against *Escherichia coli* and Gram+ and Gram− bacteria without human cells damage [2].

Different mechanisms have been reported for Ag antimicrobial behavior: (i) interference with electron transport, (ii) binding to DNA, and (iii) interaction with the cell components [91]. The unelucidated antibacterial mechanism of the silver ions might be related to its complexation with membranes, enzymes, and other cellular components, mainly with thiols (electron donors) groups [61, 91].

Owing to the showed antimicrobial properties, in major of the studies aimed at providing antimicrobial properties to BG compositions, silver was used as main dopant. Furthermore, the dissolution rate of silver ions from the prepared BGs resulted slower compared with other materials, aspect which makes them even more interesting, taking into account that the slow dissolution is required for applications based on sustained antibacterial action [61].

The antibacterial effects of Ag-containing BGs against *Streptococcus mutans* [45], *S. aureus* [55–58, 60, 62], *E. coli* [55, 56, 59–61], *Klebsiella pneumoniae* [55], *P. aeruginosa* [55, 56, 62] have been reported (Table 23.1).

Bellantone et al. [61] investigated a BG system, i.e. $76SiO_2$–$19CaO$–$2P_2O_5$–$3Ag_2O$ (wt%), with controllable degradation properties, demonstrating its ability to minimize the risk of microbial infections through the Ag^+ ions leaching from the glass matrix. An efficient antibacterial action against *E. coli* was revealed with a very low concentration (0.2 mg/ml).

Clupper and Hench [54] reported that the release of silver ion was above the minimum concentrations (0.1 μg/ml) required to inhibit bacterial growth, and thus Ag-containing BGs can be considered promising for the use in clinical applications and have been tested in bone replacement and wastewater treatment.

Similarly, Catauro et al. [92] highlighted the high antimicrobial activities against *E. coli* and *S. mutans* in the case of Ag containing Na_2O–CaO–SiO_2 glass system.

El-Batal et al. [31] reported the antibacterial and antifungal effects of BG and BG-ceramics based on Hench's 45S5 Bioglass doped with 1 wt% Ag ($AgNO_3$) in comparison with free-Ag against several microorganisms. The collected findings demonstrated an antibacterial activity against Gram positive (*Bacillus subtilis*) and Gram negative (*E. coli*) bacteria, as well as a moderate inhibitory effect against yeast (*Candida tropicalis*) and fungi (*Aspergillus niger*), without presenting any cell damage [31].

23.4.1.2 Bioactive Glasses Doped with Copper

Copper (Cu) has shown to act as an efficient antimicrobial agent against some Gram-negative and Gram-positive bacteria [93], as well as a promoting agent for the bone growth and healing [94]. Thus, Cu-doped BG have been employed for bone regeneration and wound healing applications [94, 95], due to their antimicrobial activity against *E. coli* [45, 60, 63, 64, 66, 67], *Staphylococcus epidermidis* [65, 67], *S. aureus* [60, 67], and *S. mutans* [45, 96] (Table 23.1).

Similar to Ag-BGs, the Cu-BGs antibacterial behavior has been completely ascribed to the Cu^{2+} ions release from the glass matrix [65, 82], increasing with the Cu amount [65, 82, 94]. However, as known, Cu-BGs provide weaker antibacterial features than Ag-BGs, due to the much lower Cu ions release during the first 24 hours with respect to the burn Ag ions release [82], as well as to more effective Ag ions action in inhibiting the bacteria growth [45]. Indeed, Ag-doped BGs presented a minimum bactericidal concentration around 30 times and 8 times lower than Cu-BGs, against *E. coli* and *S. mutans*, respectively [45].

El-Batal et al. [31] showed a remarkable increase of the antibacterial and antifungal effects of BGs and BG-ceramics based on Hench's 45S5 Bioglass substituted with 0.5 and 1 wt% Cu (CuO) in comparison with free-Cu against Gram-positive, Gram-negative bacteria, fungi, and yeast. The results showed better antifungal activity against fungi (*A. niger*) than yeast (*C. tropicalis*) [31]. Moreover, they reported that the glass-ceramic derivatives have more antimicrobial effects than the parent glasses [31].

23.4.1.3 Bioactive Glasses Doped with Zinc

Among other doping ions, zinc (Zn^{2+}) has gained a special interest due to its characteristics and benefits, showing an antimicrobial action against many bacterial strains through direct contact with cell walls [97].

Zn is able not only to provide antibacterial activity but also to improve the mechanical strength of the bio-glasses [9], to play an important role in bone cell attachment, growth, development, and differentiation [98], and to maintain the biological fluids pH within the physiological limits [99]. Indeed, it is a cofactor for many enzymes, promoting the protein synthesis, which is essential in DNA replication, bone cell growth, development, and differentiation [9].

ZnO antibacterial mechanism is ascribed to the induction of oxidative stress and to the Zn ability to damage the cell membrane and interact with intracellular contents [71, 100].

The antibacterial effects of Zn doped glasses against *S. mutans* [52], *S. aureus* [68, 69], *S. epidermidis* and *K. pneumoniae* [69], *P. aeruginosa and B. subtilis* [9, 69], and *S. mutans* and *Actinomyces viscosus* [72] have been reported (Table 23.1).

In particular, Baghbani et al. [70] demonstrated the antimicrobial features of the sol–gel derived SiO_2–CaO–P_2O_5–MgO–ZnO (ZnO 5 mol%) composition against *P. aeruginosa*, by means of the halo zone test. Similarly, Esteban-Tejeda et al. [71] revealed the antimicrobial action against *E. coli* in the case of B_2O_3–SiO_2–Na_2O–ZnO based coatings applied on different biometallic substrates.

Atkinson et al. [9] highlighted the good biocompatibility and antibacterial activity against *P. aeruginosa* and *B. subtilis* strains of the mesoporous bio-glasses substituted with 3 and 5 mol% ZnO by a sol–gel technique, using surfactant (Pluronic P123) as structure directing agent. Non-ionic block polymer P123 (EO_{20}–PO_{70}–EO_{20}) is commonly used to produce mesoporous (several nanometers) structures [64]. Moreover, this surfactant is able to improve the homogeneity of mesoporous structures and biological characteristics of BGs [66]. The revealed decrease of the infections associated with implant materials was ascribed to the Zn ions release.

Similarly, El-Batal et al. [31] reported a significant increase of the antibacterial and antifungal effects against Gram positive bacteria, Gram negative bacteria, fungi, and yeast, in the case of 45S5 composition doped with 0.5 and 1 wt% Zn (ZnO) in comparison with free-Zn samples.

In agreement with the Ag-doped or Cu-doped BGs behavior, the Zn-doped BGs antimicrobial efficiency also increases with Zn concentration [9, 69, 71], as well as the bioactivity. However, the cytotoxicity tends to enhance with Zn amount [101].

On the basis of the collected data, Zn-doped BGs antibacterial activity has not been properly and deeply investigated yet and further studies are requested.

23.4.1.4 Bioactive Glasses Doped with Strontium

Among various metal ions, strontium (Sr^{2+}) is a promising bactericidal one, widely employed in the bone tissue engineering field, due to its capacity to induce an enhancement of bone stability, diminish/inhibit the bone resorption, promote bone recovery processes, stimulate bone formation, provide antioxidant properties [14], and increase the BGs degradation [73]. Due to the ionic radius similarities of Ca and Sr, they can be substituted for each other without significantly changing the silicate network.

Sr^{2+} ions antimicrobial activity allows to inhibit the bacterial growth and reproduction, avoiding the cytoplasmic membrane permeability, the cell wall synthesis, the replication of bacterial chromosomes, and cell metabolism [73]. This behavior has to be ascribed to Sr^{2+} ions release that relies on BG composition and increases with strontium concentration, resulting in higher concentrations in the culture medium over time [73]. In this regard, Brauer et al. [73] demonstrated the antibacterial activity of melt-derived Sr-doped BGs against *S. aureus* and *Streptococcus faecalis* for the treatment of osteoporosis-related vertebral compression fractures [73].

23.4.1.5 Bioactive Glasses Doped with Gallium

Gallium (Ga^{3+}) has emerged among the new generation of antimicrobial and anticancer elements [102], resulted effective in the treatment of some disorders (including autoimmune and infectious diseases) [24], and may serve as a promising new therapeutic agent [76].

Many studies have found that gallium ion (Ga^{3+}) (approved by Food and Drug Administration [FDA]) is able to treat hypercalcemia, to prevent localized infections [75], and to inhibit *P. aeruginosa*, MRSA, and *Clostridium difficile* [77]. Other studies have reported that gallium ions have antibacterial effect against the organisms involved in the development of tuberculosis, malaria, and in pneumonia due to *Rhodococcus equi* in foals [76].

Concerning the action mechanism, bacterial cells (which require iron for their survival and growth) are unable to distinguish Ga^{3+} from Fe^{3+} [103], due to their similar oxidation state and atomic radius, thereby leading to the microorganism death [24, 75].

Thus, Ga is very interesting as antimicrobial agent, since it is able to target the bacterial Fe^{3+} metabolism, vital for the most microbes survival, and it is not sensible to antibiotics induced resistance mechanisms [104].

For all aforementioned reasons, gallium-doped, melt-quenched, and sol–gel phosphate BGs [75, 76, 78, 105–107], borate BGs [87, 108], and silicate BGs [79, 109, 110] have been prepared and tested at Ga_2O_3 concentrations in the range 1–8 mol%, investigating several bacterial strains, mainly those involved in biomaterial-associated infections (e.g. MRSA, *S. aureus*, *S. epidermidis*, *E. coli*, *P. aeruginosa*) and human oral pathogens associated to oral infections (e.g. *Streptococcus gordonii*, *Porphyromonas gingivalis*, and *S. mutants*) (Table 23.1).

In details, Ga-doped phosphate-based glasses (PBGs) revealed good antibacterial behavior against several planktonic bacterial pathogens and some biofilms [78, 88], due to the controlled gallium ions release [78]. Thus, the antibacterial activity strictly depends on the BGs degradation rate, that can be monitored properly tailoring the glass composition [75], and is also influenced by both Ga and Ca amount. Indeed, Valappil et al. [76] evidenced that the degradation rate and the related Ga ions release decrease with the concentrations of both Ga (1–5 mol%) and Ca (14–16 mol%). Consequently, Valappil et al. [75] reported that BGs containing a Ga concentration of 1 mol% were able to induce an inhibition zone larger than those related to higher Ga concentrations (i.e. 3 or 5 mol% Ga).

Finally, it has to be taken into account that, even if increasing the gallium concentration can improve the antimicrobial behavior, high Ga concentrations could be toxic and may cause side effects to nonbacterial healthy cells [24].

23.4.1.6 Bioactive Glasses Doped with Fluoride

Fluoride (F^-) is a well-known agent which can prevent dental cavities by inhibiting enamel and dentine demineralization. Moreover, fluoride-implants releasing might be of interest for osteoporosis patients [111].

F^-- and Zn-doped calcium phosphate glasses (CPGs) were prepared by Liu et al. [52], evidencing the F ability to improve the antibacterial action against *S. mutans*, even if less efficiently than Zn. Indeed, fluoride shows biocidal activity at certain concentration. For example, Xu et al. [80] synthesized fluoride-doped 45S5 samples and they showed their antibacterial activity on *S. mutans* biofilm at concentrations of 75 (~0.59 mg/ml) [80].

Rostami et al. [81] produced sol–gel-derived BG particles doped with different amounts of F (i.e. 5–20 mol%), demonstrating their ability to inhibit the *E. coli*, *S. aureus*, and *P. aeruginosa* growth with a concentration depending on trend, whereas F-free BG samples did not show any antibacterial activity. Moreover, all the produced compositions resulted cytobiocompatible both *in vitro* and *in vivo*.

23.4.1.7 Bioactive Glasses Doped with Cerium

Cerium is able to promote the osteoblast growth and bone formation, improve bone mechanical properties, provide antibacterial and antioxidant properties, and it owns multi-enzyme mimetic properties, being able to resemble enzymes such as superoxide dismutase, oxidase, and catalase [112–114]. Furthermore, Ce can change its oxidation states (Ce^{4+} and Ce^{3+}) in physiological fluids, and, in this manner, it can lead to a reactive oxygen species (ROS) reduction, pivotal for healthy biological functions [115].

For all these reasons, Ce-doped BGs have been widely synthesized [82–86, 113, 115–117] (Table 23.1).

Ce-BGs present antibacterial and microbicidal actions against *E. coli* [82, 84–86] and *S. aureus* [83, 86]. However, in other works, the lack of Ce-doped BGs antibacterial properties was evidenced [118–121].

Concerning the Ce antibacterial action, several mechanisms have been reported, mainly associated to the direct contact between Ce and the bacterial membrane [122]: (i) impaired transport exchange through the bacterial membrane followed by decreased growth [84, 123]; (ii) Ce reaction with proteins or transporters within the cell [124]; and (iii) oxidative stress induction [24, 125].

Recently, it has been suggested that Ce antibacterial activity depends on glass composition, glass morphology, and Ce concentration [126]. In particular, it has been reported that the cerium concentration increase enhanced the antibacterial activity against *E. coli* and *S. aureus*, but not against *Bacillus cereus*, *B. subtilis*, and *Candida albicans*, in the case of Ce-doped phosphate glasses [84]. For example, Goh et al. [82] highlighted that Ce-BGs presented higher antibacterial activity for cerium oxide concentration between 5 and 10 mol% range than for 1 mol%.

Moreover, the oxidation inhibition and assimilation of glucose and of endogenous respiration have been also proposed as possible mechanisms responsible of Ce antibacterial activity [127].

23.4.2 Bio-glasses Loaded with Antibiotics

Another strategy aimed at providing antibacterial features to BGs is the loading with antibiotics. It has been highlighted that the simultaneous incorporation of therapeutic metallic ions and antibiotics can further promote the antibacterial action [128]. Generally, the synergistic effects of incorporated antibacterial ions and loaded antibacterial drugs lead to an acceleration of tissue repair and regeneration. This approach has been mainly applied in the case of mesoporous bioactive glasses (MBGs), with the final aim to improve and monitor their antibacterial activity in the long term,

taking into account the slower drug release from MBGs than that from conventional BGs, with a consequent more prolonged effect.

For example, tetracycline hydrochloride (THC) was added to BG particles synthesized by sol–gel process [129–132], evidencing that the drug-loading capacity is strongly affected by the particles surface area and porosity [130] and the release profile controlled by diffusion through the porosities [132].

Teicoplanin [133, 134], vancomycin [135], and gentamicin [136] were added to pellets produced starting from melt-derived borate BGs microparticles. However, a limited drug loading was achieved due to the pellets tendency to fracture after immersion for several days in SBF, as well as to the pellet's high density [132].

Miola et al. [137] loaded BGs with carbenicillin by dipping them in SBF. Some samples were submitted to a pre-treatment in SBF, in order to promote the development of a silica gel layer before the surface exposition to the antibiotic. They demonstrated the ability of all the produced systems to incorporate a significant antibiotic amount and to tailor the drug release by modifying the SBF pre-treatment.

Despite all their limits, melt-derived BGs scaffolds have been employed as drug delivery systems, loading them with the antibiotic by means of the vacuum infiltration method which consists in dipping them in a drug solution, applying a negative pressure [138].

This approach was employed in the case of gatifloxacin and cefuroxime axetil [138, 139], revealing a Fickian diffusion mechanism for their release, as well as an influence of the initial drug concentration on the loading efficiency and/or release kinetics. On the other hand, their release is not affected by the BG scaffolds composition.

However, MBGs resulted more promising and a wide plethora of antibiotics has been added to MBGs, such as the gentamicin sulfate (GS) for its local delivery to bone defects for the orthopedic peri-implant infections treatment [140]. In this case, high antibiotic loading (79–83%) was achieved, due to the MBGs structure high surface area, ensuring a GS sustained release for more than six days and, thus, the inhibition of *Scleropages aureus* and *S. epidermidis* bacterial adhesion and biofilm formation [140].

Ultrathin MBG hollow fibers, obtained by electrospinning technique associated to a phase-separation-induced polymer, i.e. poly(ethylene oxide) (PEO), were also proposed as a gentamicin carrier. Antibiotic loading was strongly affected by the fiber length: fibers with length >50 μm could be considered good drug delivery carriers, whereas reduced finer lengths could decrease the drug loading and promote the drug release [141].

Moreover, in order to guarantee a prolonged drug release, GS-loaded MBGs particles were embedded within poly(D,L-lactide-*co*-glycolide) (PLGA) matrix [142]. As expected, the GS release, in both distilled water and phosphate-buffered saline (PBS) for more than 30 days, was faster from MBG (60 and 80 wt% after 24 and 48 hours, respectively) with respect to MBG/PLGA composite (33 and 48 wt% after 24 and 48 hours, respectively).

23.5 Applications of Antimicrobial Bio-glasses

Antimicrobial BGs have been used for several applications, such as for the production of scaffolds for bone tissue engineering [60, 68, 143], for wound healing [63, 65], as implant [9] and coating [144–147] materials (Table 23.2, Figure 23.2).

Table 23.2 Main outputs and applications for antimicrobial BGs.

Agent(s)	BGs	Main outputs	Application sector(s)	References
Cu^{+}/Cu^{2+}	**Cu-BG**	No influence on the cytotoxicity for CuO amount up to 0.8 wt%	Bone regeneration and angiogenesis in osseous defects	[94]
	Cu-MBG	– Control of the moisture over the wounds – Angiogenic effect – Enhancement of the Vegfa, Vegfc, Pdgfb, and Fgf2 (bFgf) genes expression	Chronic wound healing	[63]
	Cu-MBG	– Improved angiogenesis capacity – Osteostimulation - Drug delivery – Antibacterial properties	Large bone defects treatment	[64]
	Cu-PGF	– Prevention of the implant or biomaterial-related infections	Wound healing	[65]
	Cu-PBG/Cu-BG	– Low risk toxic bioactive glasses – Improved drug delivery and biological behavior	Bone defects treatment in tissue engineering	[66]
	Cu-BG	– Inactivation of both *E. coli* and *S. mutans* bacteria growth at higher concentrations – Influence of the metal ions release into solution on the antimicrobial behavior	Medical applications	[45]
	Cu-BG	Enhanced biocompatibility	Bone tissue engineering	[60]
	Cu-MBGNPs	Inhibition of the biofilm formation by *S. epidermidis*	Bone regeneration	[67]
Zn^{2+}	**Zn-BG**	Enhanced *in vitro* bioactivity by formation of both calcite and apatite layers	Implant material	[9]
	Zn-MBG	– Enhanced HOS cell development in the case of lower ZnO amount – Antibacterial properties against *S. aureus*	Bone regeneration	[68]
Ag^{+}	**Ag-BG**	– Enhanced bioactive response – Fast surface hydroxyapatite layer formation	Bone treatment	[54]
	Ag-BG	– Infection prevention – Pain reduction – Removal of excessive exudates	Wound healing	[55]
	Ag-BG	—	Orthopedic, dental graft material and tissue engineering	[56]

(Continued)

Table 23.2 (Continued)

Agent(s)	BGs	Main outputs	Application sector(s)	References
	Ag-BG	High bioactivity and biocompatibility	Dental implants	[57]
	Ag-SM58S (58S bioactive glass)	– Sustained release of Ag^{+} – Good bioactivity and osteoblast biocompatibility	Treatment of bone infection	[58]
	Ag-BG	Controlled sustained delivery of the antibacterial agent	Dental sector	[59]
	Ag-BG	– Inhibition of both *E. coli* and *S. mutans* bacteria at higher concentrations – Influence of the metal ions release into solution on the antimicrobial behavior	Medical applications	[45]
	Ag-BG	Enhanced biocompatibility	Bone tissue engineering	[60]
	Ag-BG	– Enhanced tissue integration – Direct inhibition of the bacterial adhesion	Medical applications	[61]
	Ag-MBGN	– Non-cytotoxicity toward fibroblasts – Drug delivery carriers	Tissue regeneration	[62]
Ag^{+} and Sr^{2+}	**AgSr-BG**	Enhanced cell proliferation	Orthopedic coating and osteoporosis treatment	[14]
Sr^{2+}	**Sr-BG**	Enhanced bone formation	Bone enhancing cements	[73]
Ga^{3+}	**Ga-MBG**	Controlled hemorrhage	Wound infection	[74]
	Ga-PBG	Promising new therapeutic agent for bacterial pathogens and hypercalcemia treatment	Bone tissue engineering	[75]
	Ga-PBG	Employment as coating either subcutaneously or transcutaneously on fracture fixation pins	Treatment of bone infection	[76]
	Ga-(45S5 Biactive glass)	Improved mechanical properties without decrease of the high bioactivity level	Bone tissue engineering	[77]
	Ga-PBGs	Helping to maintain the integrity of the enamel	Dental sector	[78]
	Ga-(13-93 BGs)	Control on microbial toxicity	Soft tissue repair and regeneration	[79]
Ga^{3+} and Ag^{+}	**GaAg-PBGs**	Catheters coating to avoid bloodstream infections	Antibiotics treatments or supplement current therapies	[88]
F^{-}	**F-BG (45S5)**	Higher effectiveness for microorganism inactivation	Dental sector	[80]
	F-BG	Preventing of post-surgery infections, especially hydatidosis	Surgery	[81]

Ce^{3+}	**Ce-BG**	Good *in vitro* bioactivity	Bone regeneration	[82]
	GR-HAp_Ce	Enhanced osteoblastic cell response and cell adhesion and proliferation	Bone tissue regeneration	[83]
	Ce-BG	Promoted bone metabolism	Tissue engineering	[84]
	Ce-BG	Improved bioactivity and biocompatibility	Orthopedic implants	[85]
	Ce-MBGNPs	– No cytotoxicity toward MG-63 osteoblast-like cells – Improved cell viability (>10 w/v%)	– Drug delivery carriers – Bioactive fillers for bone tissue engineering	[86]

BG, bioactive glass; MBG, mesoporous bioactive glass; MBGNPs, mesoporous bioactive glass nanoparticles; SM58S bioactive glass, surface modification of mesoporous 58S bioactive glass; PGF, phosphate-based glass fibers; PBG, phosphate based glasses; CPG, calcium phosphate glass; GR-HAp, glass-reinforced hydroxyapatite.

For tissue engineering applications, the improved antibacterial, bone regeneration capability and/or angiogenesis activity of BGs doped with therapeutic and antibacterial metal ions (e.g. Ag, Sr, Cu, Zn, Co, and Ga) could guarantee a bacteria-free environment in implanted sites during the soft and hard tissue healing and regeneration [148].

For instance, Ni et al. [149] produced a scaffold by the sol–gel dip coating of porous anodic alumina (PAA) with $CaO–SiO_2–Ag_2O$ formulation, then submitted to a specific thermal treatment. They demonstrated the efficacy of the obtained $CaO–SiO_2–Ag_2O$/PAA system in decreasing/avoiding the *E. coli* and *S. aureus* bacteria growth, due to Ag ions release with consequent enhanced medium pH values.

Yazdimamaghani et al. [150] fabricated gelatin/bioactive-glass/silver nanoparticles macroporous scaffolds, characterized by a macro-scale 3D interconnected porosity with pore size between 350 and 635 μm, increasing the pore size and the porosity with the Ag nanoparticles (NPs) concentration. They highlighted a remarkable decrease of *S. aureus* and *E. coli* growth and reduction of the biofilm formation on the scaffolds.

Alginate/60S BG (containing zinc and magnesium) scaffolds (porosity of 80%) were produced by Zamani et al. [151], significantly improving the mechanical behavior and antibacterial activity against *E. coli* and *S. aureus* bacteria, as well as MG-63 cells responsiveness in terms of adhesion, viability, attachment and proliferation, and osteoblast differentiation.

Mouriño et al. [77] developed multifunctional composite scaffolds for bone tissue engineering with prophylaxis effect against *S. aureus* by coating the 45S5 based scaffold surface with sodium alginate films crosslinked with Ga^{3+}, without changing the pore structure, and improving mechanical properties and antibacterial effects to prevent any possible bacterial colonization of the biomaterial after surgery [77].

A good antibacterial action against *E. coli* (antibacterial rate of 75% in 1 hour and 99% in 12 hours) was demonstrated in the case of sol–gel derived $SiO_2–CaO–P_2O_5–Ag_2O$ silicate BG (Ag 0.02 wt%) scaffolds (pore size ~6 nm, specific surface area of 467 m^2/g) by Hu et al. [152], for wound healing applications.

MBGs were also used to produce pH-sensitive 3D hierarchical meso-macroporous 3D scaffolds, loaded with levofloxacin (Levo) as an antibacterial agent for the treatment and prevention of bone infection [153]. The obtained systems were able to simultaneously inhibit the *S. aureus* growth and promote the bone regeneration. The shown controlled Levo release was pH-dependent: it was sustained with time at physiological pH (7.4) and remarkably increased at infection pH (6.7 and 5.5), due to the different Levo species/silica matrix interaction rate.

Co-doped MBG scaffolds with large interconnective pores (300–500 μm) and well-ordered mesopore channels (~5 nm) were produced to promote the hypoxia-inducible factor (HIF)-1α and vascular endothelial growth factor (VEGF) expression in human bone marrow stromal cells (hBMSCs), as well as their osteogenic differentiation [64] (Table 23.1). The antimicrobial properties were further enhanced by the addition and consequent sustained release of ibuprofen. On the basis of the collected outcomes, Cu^{2+} ions incorporation within MBGs structure is able to remarkably increase the hypoxia-like tissue reaction, promoting both angiogenesis and osteogenesis.

Macroporous poly(L-lactic acid) (PLLA) scaffolds coated with GS-loaded MBGs by dip-coating method were proposed to improve the cell adhesion/growth, due to the higher surface hydrophilicity, and to provide significant antibacterial behavior for an extended period (more than seven days), as well as enhanced bioactivity and promoted attachment to the host tissue [154]. Preliminary tests performed on coatings obtained by the laser ablation method and enriched with Ce-BGs suggested high antibacterial activity due to the presence of partially crystallized layers with cerium cations embedded in a glassy matrix, which was more prone to degradation [85].

The employment of antimicrobial BGs as drug delivery systems has been also reported. Valappil et al. [75] investigated a novel drug delivery system based on gallium-doped PBGs (1 mol% Ga_2O_3) against both Gram-negative and Gram-positive bacterial pathogens. The proposed approach may offer advantages over conventional therapeutic agents as antibiotic-resistant organisms. This system presented controlled and long-term release profile of Ga^{3+} ions [75].

In another study, Valappil et al. [76] prepared Ga_2O_3-doped PBGs as a novel drug delivery system against bacteria associated with hospital-acquired infections (HAIs), and their results showed a controlled delivery of gallium ion and demonstrated a relevant antimicrobial activity against both planktonic cells and *P. aeruginosa* biofilms.

Another possible application of antimicrobial BGs consists in the coating of metallic or polymeric substrates and implantable systems.

For instance, Ti–6Al–4V substrates were coated with Ga- and Zn-doped $80SiO_2$–$15CaO$–$5P_2O_5$ (mol%) MBG in combination with polycaprolactone (PCL) to provide enhanced *in vitro* bioactive responsiveness, adequate mechanical strength, and antibacterial properties [147]. Pratten et al. [146] coated Mersilk sutures with undoped and Ag doped 45S5, using an "in house" slurry-dipping process, demonstrating that Ag-doped 45S5 was able to prevent *in vitro* bacterial colonization on surgical sutures, by reducing the bacterial attachment. *In vitro* tests were performed against *S. epidermidis* under both batch and flow conditions, to evaluate the number of viable cells adhered to the surface and to study the cell attachment and detachment over time, respectively. Comparable results were reported by Blaker et al. [144, 145].

For wound healing applications, fibers based on Cu doped BGs were proposed as wound dressing meshes for severe burns and leg ulcers treatments [65]. Similarly, Ga-containing BGs could be promising for wound healing applications [74].

Another interesting application of metal ions doped BGs is related to photothermal therapy of bone tumor, associated to its regeneration, taking into account the laser-induced photothermal properties of Cu-, Fe-, Mn-, or Co-doped bioactive scaffolds prepared by the 3D printing technique, as well as their osteogenic differentiation activity [155]. The potential antimicrobial activity of these systems could enhance their photothermal activity.

Moreover, in some cases, applications different from bone healing have been evidenced and reported, such as the use of Cu-containing MBG for coating the orbital implants for ocular surgery [156], characterised by the *S. aureus* and *E. coli* growth inhibition due to the simultaneous release of Cu^{2+} and ofloxacin antibiotic sustained release.

Intrinsically antimicrobial BGs have been also used in clinical applications. For example, S53P4 formulation, commercially available and known as BonAlive®, has been clinically employed for over 25 years for several applications, such as mastoid and benign bone tumor, frontal sinus, trauma, and spine surgery, with success and without relevant toxic reactions [157].

Moreover, it has been exploited for the treatment of chronic osteomyelitis, due to the *S. aureus* that is commonly involved in orthopedic infections, and, after an initial colonization, leads to the production of a biofilm difficult to eliminate [158–160].

Lindfors et al. [40] treated the spine of 11 patients with diagnosed chronic osteomyelitis in the lower extremity, filling the cavitary bone defect and the spinal implant surroundings with S53P4. They highlighted that nine patients healed without complications.

Similarly, Romanò et al. [41] compared the employment of S53P4 and antibiotic-loaded calcium-based bone substitutes (antibiotic-loaded hydroxyapatite and calcium sulfate compound and a mixture of tricalcium phosphate and an antibiotic loaded demineralized bone matrix) in the treatment of chronic osteomyelitis. They evidenced the obtainment of a comparable infection eradication (up 85%) and less drainage for S53P4 with respect to the different antibiotic-loaded calcium-based bone substitutes.

23.6 Concluding Remarks and Future Perspectives

Actually, for the treatment of bone infections, few effective antimicrobial molecules have been identified and the development of multidrug-resistant (MDR) bacteria is causing the failure of the antibiotic therapy with consequent remarkable morbidity and mortality increase [15]. For these reasons, the use of specific BGs formulations is gaining a lot of attention, taking into account that they are characterized by strong antibacterial action against several aerobic and anaerobic bacteria, due to the pH and osmolarity increase in the surrounding environment, and, mainly, by the absence of resistance selection [15]. Indeed, bacteria are not able to adapt to the hostile BG induced environment. Furthermore, BGS can reduce the biofilm mass, improve the diagnostic process and patient compliance, and, thus, can be considered ideal bone substitutes for the osteoarticular and prosthetic joint infections treatment [15]. However, their action mechanism has not been completely comprehended yet, and many mechanisms have been proposed to explain the antimicrobial properties of specific BG compositions. Generally, the antibacterial properties are due to the release of ions into the reaction media and their effect in the surrounding physiological environment such as pH and osmotic pressure [8]. Indeed, BGs can provide antimicrobial action easily raising the pH of an aqueous environment [29]. In particular, they could inhibit the bacterial colonization at the surgical site [37] by increasing the pH and calcium levels [29], if implanted in areas of periodontal defects.

The strategies commonly followed in order to obtain BGs formulations with enhanced antimicrobial behavior consist in the incorporation of biocidal ions and the addition of specific antibiotics.

However, recently, further approaches have been proposed, such as the addition of natural antimicrobials and/or antimicrobial particles to BGs formulations (Figure 23.2) [80, 161], the co-doping with more than one metallic ion [162–164], and the co-loading of different drugs [165, 166].

For example, concerning the use of natural antimicrobials, Prabhu et al. [161] reported sol–gel derived silicate and phosphate BGs loaded with neem (*Azadirachta indica*) leaf powder and silver nanoparticles, ascribing the good antimicrobial behavior against *S. aureus* and *E. coli* to neem leaf powder, and evidencing their less bioactivity with respect to Ag NPs. Similarly, 58S sol–gel MBGs were loaded with green propolis dry extracts from *Baccharis dracunculifolia* and cranberry proanthocyanidins (PACS) dry extracts from *Vaccinium macrocarpon*, due to their well-known antibiofilm properties, even if no any antibacterial activity was detected [167]. In another study, mesoporous Ga-doped MBGs were loaded with curcumin [168], evidencing a curcumin slow release (25% within 72 hours), which would ensure a prolonged therapeutic effect, as well as a stabilization of Ga^{3+} ions, in the SBF solution, avoiding their precipitation.

Regarding the production of composites based on antimicrobial particles and BGs, BGs loaded with graphene-oxide (GO), reduced graphene-oxide (rGO), and nitrate acid treated-graphene-oxide (N-GO) (5 wt%) were characterized by improved antibacterial activity with respect to neat BG powder (reduction of 1.6%) [169]. In details, the highest antibacterial activity (82.7% reduction) against *E. coli* was revealed in the case of N-GO/MBGs with respect to the other composites (3.8% and 1.2% for GO/MBG and rGO/MBG, respectively).

For the BGs co-doping strategy, Valappil and Higham [88] produced Ga–Ag–PBGs, able to ensure a Ga and Ag controlled release, with a consequent synergic antibacterial action against planktonic and biofilm growth of *P. aeruginosa* [88] and biofilm of oral human pathogens [107].

Similarly, Ranga et al. [14] investigated a new sol–gel BG composition (SiO_2–CaO–SrO–Ag_2O) doped with strontium and silver as antibacterial agents. The results demonstrated a significant effect on *E. coli* and *S. aureus* bacteria (Table 23.1).

A new proposed approach consists in the combination and simultaneous release of different drugs. For instance, Kaur et al. [165] loaded $(25 - x)$CaO–xCuO–10P_2O_5–5B_2O_3–60SiO_2 ($x = 2.5$, 5, 7.5, and 10 mol%) with both doxorubicin (anticancer drug) and vancomycin (antibacterial drug). Similarly, Polo et al. [166] loaded MBGs with doxorubicin (anticancer) and levofloxacin (antibacterial drug), but they proposed a molecular gated approach, modifying some MBGs with triamine and adenosine triphosphate (ATP) and other ones with isocyanates and ε-poly(L-lysine), as functionalizing and capping agents, respectively. Both molecular gates (ATP and ε-poly(L-lysine)) usually open when exposed to related enzymes (alkaline phosphatase [ALP] and pronase, respectively), promoting the doxorubicin (DOX) and levofloxacin release, respectively, and, thus, allowing a finer controlled drug delivery.

Furthermore, contradictory data are available about the antimicrobial properties of some BGs formulations tested both in *in vitro* and *in vivo* experiments. Even if the 45S5 Bioglass antibacterial action has been widely demonstrated in *in vitro* studies [26, 29], very interestingly, Xie et al. [170] evidenced a completely different behavior in *in vivo* experiments. They highlighted the 45S5 particles inability in inhibiting/decreasing the *S. aureus* infection rate after the fixation of open tibial fractures in rabbits. Their findings were ascribed to the unaltered local body fluid pH also after BG release, due to the buffering fluids capacity. However, the study by Xie et al. [170] was limited, taking into account that only a single strain of *S. aureus* was exploited, and a single body site was considered. Thus, the incapacity of BGs to induce the bacteria growth inhibition *in vivo* has to be further confirmed and investigated, carrying out deeper studies with other strains or species of bacteria and other body sites.

Similarly, the antibacterial activity of Ga-doped phosphate-based BGs was also studied in *in vivo* tests, with contradictory results. Sahdev et al. [106] demonstrated, in *in vivo* studies in rats, their antibacterial action against *P. gingivalis*, whereas, in another studies Ga-doped 13-93-based BG electrospun fibers [79] and borate 13-93 BG scaffolds [87] did not show antibacterial properties, probably due to the used Ga concentration and its slow release, as well as to the considered BGs shape and architecture. Comparable experimental evidences were highlighted in the case of Ce doped 13-93 electrospun fibers [79] and scaffolds [87], in the same works. The same behavior was observed for Ce-doped BGs coated electrospun poly(lactic acid) (PLA)/chitosan nanofibers, and this lack of antibacterial activity was ascribed to the very low amount of adsorbed BG on the fibers surface, as well as to the ions slow release [53].

Taking into account all the collected data and results in the present chapter, it is evident that there is an urgent need to carry out further and deeper studies about specific antibacterial and antibiofilm activities, to better comprehend the underlying mechanisms and optimize and finalize the employment of BGs in eradicating bone and joint infections [15]. Moreover, it is necessary to perform *in vivo* studies using antimicrobial BGs, in order to develop optimized BG-based biomaterials for regenerative medicine applications.

References

1 Cacciotti, I., Lombardi, M., Bianco, A. et al. (2012). Sol–gel derived 45S5 bioglass: synthesis, microstructural evolution and thermal behaviour. *Journal of Materials Science: Materials in Medicine* 23 (8): 1849–1866.

2 Hench, L.L. (2006). The story of Bioglass®. *Journal of Materials Science: Materials in Medicine* 17 (11): 967–978. https://doi.org/10.1007/s10856-006-0432-z.

3 Hench, L.L. and Jones, J.R. (2015). Bioactive glasses: frontiers and challenges. *Frontiers in Bioengineering and Biotechnology* 3: 1–12. https://doi.org/10.3389/fbioe.2015.00194.

4 Lombardi, M., Gremillard, L., Chevalier, J. et al. (2013). A comparative study between melt-derived and sol–gel synthesized 45S5 bioactive glasses. In: *Key Engineering Materials*, vol. 541 (ed. A. Bianco, I. Cacciotti and I. Cappelloni), 15–30. Trans Tech Publications Ltd.

5 Cao, W. and Hench, L.L. (1996). Bioactive materials. *Ceramics International* 22 (6): 493–507. https://doi.org/10.1016/0272-8842(95)00126-3.

6 Cacciotti, I., Lehmann, G., Camaioni, A., and Bianco, A. (2013). AP40 bioactive glass ceramic by sol–gel synthesis: in vitro dissolution and cell-mediated bioresorption. In: *Key Engineering Materials*, vol. 541 (ed. A. Bianco, I. Cacciotti and I. Cappelloni), 41–50. Trans Tech Publications Ltd.

7 Lombardi, M., Cacciotti, I., Bianco, A., and Montanaro, L. (2015). RKKP bioactive glass-ceramic material through an aqueous sol–gel process. *Ceramics International* 41 (3): 3371–3380.

8 Fernandes, J.S., Gentile, P., Pires, R.A. et al. (2017). Multifunctional bioactive glass and glass-ceramic biomaterials with antibacterial properties for repair and regeneration of bone tissue. *Acta Biomaterialia* 59: 2–11. https://doi.org/10.1016/j.actbio.2017.06.046.

9 Atkinson, I., Anghel, E.M., Predoana, L. et al. (2016). Influence of ZnO addition on the structural, in vitro behavior and antimicrobial activity of sol–gel derived $CaO–P_2O_5–SiO_2$ bioactive glasses. *Ceramics International* 42 (2): 3033–3045. https://doi.org/10.1016/j.ceramint.2015.10.090.

10 Bellucci, D., Sola, A., Cacciotti, I. et al. (2014). Mg and/or Sr-doped tricalcium phosphate/bioactive glass composites: synthesis, microstructure and biological responsiveness. *Materials Science and Engineering C* 42: 312–324. https://doi.org/10.1016/j.msec.2014.05.047.

11 De Bonis, A., Curcio, M., Fosca, M. et al. (2016). RBP1 bioactive glass-ceramic films obtained by pulsed laser deposition. *Materials Letters* 175: 195–198.

12 Ledda, M., De Bonis, A., Bertani, F.R. et al. (2015). Interdisciplinary approach to cell–biomaterial interactions: biocompatibility and cell friendly characteristics of RKKP glass–ceramic coatings on titanium. *Biomedical Materials* 10 (3): 035005.

13 Rau, J.V., Teghil, R., Fosca, M. et al. (2012). Bioactive glass–ceramic coatings prepared by pulsed laser deposition from RKKP targets (sol–gel vs melt-processing route). *Materials Research Bulletin* 47 (5): 1130–1137.

14 Ranga, N., Poonia, E., Jakhar, S. et al. (2019). Enhanced antimicrobial properties of bioactive glass using strontium and silver oxide nanocomposites. *Journal of Asian Ceramic Societies* 7 (1): 75–81. https://doi.org/10.1080/21870764.2018.1564477.

15 Drago, L., Toscano, M., and Bottagisio, M. (2018). Recent evidence on bioactive glass antimicrobial and antibiofilm activity: a mini-review. *Materials* 11 (2): 1–11. https://doi.org/10.3390/ma11020326.

16 Axford, J.S. (2010). Joint and bone infections. *Medicine* 38 (4): 194–201.

17 Bistolfi, A., Massazza, G., Verné, E. et al. (2011). Antibiotic-loaded cement in orthopedic surgery: a review. *International Scholarly Research Notices* 2011: https://doi.org/10.5402/2011/290851.

18 De Santis, M. and Cacciotti, I. (2020). Wireless implantable and biodegradable sensors for postsurgery monitoring: current status and future perspectives. *Nanotechnology* 31 (25): 252001.

19 Darouiche, R.O. (2004). Treatment of infections associated with surgical implants. *New England Journal of Medicine* 350 (14): 1422–1429.

20 Sia, I.G., Berbari, E.F., and Karchmer, A.W. (2005). Prosthetic joint infections. *Infectious Disease Clinics* 19 (4): 885–914.

21 Kluin, O.S., Van der Mei, H.C., Busscher, H.J., and Neut, D. (2013). Biodegradable vs non-biodegradable antibiotic delivery devices in the treatment of osteomyelitis. *Expert Opinion on Drug Delivery* 10 (3): 341–351.

22 Jin, J.F., Zhu, L.L., Chen, M. et al. (2015). The optimal choice of medication administration route regarding intravenous, intramuscular, and subcutaneous injection. *Patient Preference and Adherence* 9: 923.

23 Bhusal, P., Harrison, J., Sharma, M. et al. (2016). Controlled release drug delivery systems to improve post-operative pharmacotherapy. *Drug Delivery and Translational Research* 6: 441–451. https://doi.org/10.1007/s13346-016-0305-z.

24 Kargozar, S., Montazerian, M., Hamzehlou, S. et al. (2018). Mesoporous bioactive glasses: promising platforms for antibacterial strategies. *Acta Biomaterialia* 81: 1–19. https://doi.org/10.1016/j.actbio.2018.09.052.

25 Bazaka, K., Jacob, M.V., Chrzanowski, W., and Ostrikov, K. (2015). Anti-bacterial surfaces: natural agents, mechanisms of action, and plasma surface modification. *RSC Advances* 5 (60): 48739–48759.

26 Hu, S., Chang, J., Liu, M., and Ning, C. (2009). Study on antibacterial effect of 45S5 Bioglass®. *Journal of Materials Science: Materials in Medicine* 20 (1): 281–286. https://doi.org/10.1007/s10856-008-3564-5.

27 Munukka, E., Leppäranta, O., Korkeamäki, M. et al. (2008). Bactericidal effects of bioactive glasses on clinically important aerobic bacteria. *Journal of Materials Science: Materials in Medicine* 19 (1): 27–32.

28 Zhang, D., Leppäranta, O., Munukka, E. et al. (2010). Antibacterial effects and dissolution behavior of six bioactive glasses. *Journal of Biomedical Materials Research Part A* 93 (2): 475–483. https://doi.org/10.1002/jbm.a.32564.

29 Allan, I., Newman, H., and Wilson, M. (2001). Antibacterial activity of particulate Bioglass® against supra- and subgingival bacteria. *Biomaterials* 22 (12): 1683–1687. https://doi.org/10.1016/S0142-9612(00)00330-6.

30 Stoor, P., Söderling, E., and Salonen, J.I. (1998). Antibacterial effects of a bioactive glass paste on oral microorganisms. *Acta Odontologica Scandinavica* 56 (3): 161–165.

31 El-Batal, F.H., El-Kheshen, A.A., Abd El Aty, A.A., and El-Bassyouni, G.T. (2018). Studies of bone-bonding ability and antibacterial properties of Ag^{+}, Cu^{2+} or Zn^{2+} ions doping within Hench's bioglass and glass-ceramic derivatives. *Silicon* 10 (4): 1231–1241. https://doi.org/10.1007/s12633-017-9580-7.

32 Singh, P., Garg, A., Pandit, S. et al. (2018). Antimicrobial effects of biogenic nanoparticles. *Nanomaterials* 8 (12): 1009.

33 Rivadeneira, J., Carina Audisio, M., Boccaccini, A.R., and Gorustovich, A.A. (2013). In vitro antistaphylococcal effects of a novel 45S5 bioglass/agar–gelatin biocomposite films. *Journal of Applied Microbiology* 115 (2): 604–612.

34 Zehnder, M., Waltimo, T., Sener, B., and Söderling, E. (2006). Dentin enhances the effectiveness of bioactive glass S53P4 against a strain of *Enterococcus faecalis*. *Oral Surgery, Oral Medicine, Oral Pathology, Oral Radiology, and Endodontology* 101 (4): 530–535.

35 Echezarreta-López, M.M. and Landin, M. (2013). Using machine learning for improving knowledge on antibacterial effect of bioactive glass. *International Journal of Pharmaceutics* 453 (2): 641–647. https://doi.org/10.1016/j.ijpharm.2013.06.036.

36 Waltimo, T., Mohn, D., Paqué, F. et al. (2009). Fine-tuning of bioactive glass for root canal disinfection. *Journal of Dental Research* 88 (3): 235–238.

37 Allan, I., Wilson, M., and Newman, H. (2002). Particulate Bioglass® reduces the viability of bacterial biofilms formed on its surface in an in vitro model. *Clinical Oral Implants Research* 13 (1): 53–58.

38 Misra, S.K., Ansari, T.I., Valappil, S.P. et al. (2010). Poly(3-hydroxybutyrate) multifunctional composite scaffolds for tissue engineering applications. *Biomaterials* 31 (10): 2806–2815.

39 Drago, L., Vassena, C., Fenu, S. et al. (2014). In vitro antibiofilm activity of bioactive glass S53P4. *Future Microbiology* 9 (5): 593–601.

40 Lindfors, N.C., Hyvönen, P., Nyyssönen, M. et al. (2010). Bioactive glass S53P4 as bone graft substitute in treatment of osteomyelitis. *Bone* 47 (2): 212–218.

41 Romanò, C.L., Logoluso, N., Meani, E. et al. (2014). A comparative study of the use of bioactive glass S53P4 and antibiotic-loaded calcium-based bone substitutes in the treatment of chronic osteomyelitis: a retrospective comparative study. *The Bone & Joint Journal* 96 (6): 845–850.

42 Moya, J.S., Esteban-Tejeda, L., Pecharromán, C. et al. (2011). Glass powders with a high content of calcium oxide: a step towards a "green" universal biocide. *Advanced Engineering Materials* 13 (6): 256–260. https://doi.org/10.1002/adem.201080133.

43 Salinas, A.J. and Vallet-Regí, M. (2016). Glasses in bone regeneration: a multiscale issue. *Journal of Non-Crystalline Solids* 432: 9–14.

44 Choy, K.L., Schnabelrauch, M., and Wyrwa, R. (2017). Bioactive coatings. In: *Biomaterials in Clinical Practice: Advances in Clinical Research and Medical Devices* (ed. F. Zivic, S. Affatato, M. Trajanovic, et al.), 361–406. Springer International Publishing https://doi.org/10.1007/978-3-319-68025-5_13.

45 Palza, H., Escobar, B., Bejarano, J. et al. (2013). Designing antimicrobial bioactive glass materials with embedded metal ions synthesized by the sol–gel method. *Materials Science and Engineering C* 33 (7): 3795–3801. https://doi.org/10.1016/j.msec.2013.05.012.

46 Palza, H. (2015). Antimicrobial polymers with metal nanoparticles. *International Journal of Molecular Sciences* 16 (1): 2099–2116.

47 Brauer, D.S. (2015). Bioactive glasses – structure and properties. *Angewandte Chemi International Edition* 54 (14): 4160–4181.

48 Kaur, G., Pickrell, G., Sriranganathan, N. et al. (2016). Review and the state of the art: sol–gel and melt quenched bioactive glasses for tissue engineering. *Journal of Biomedical Materials Research Part B: Applied Biomaterials* 104 (6): 1248–1275.

49 Gorustovich, A.A., Roether, J.A., and Boccaccini, A.R. (2010). Effect of bioactive glasses on angiogenesis: a review of in vitro and in vivo evidences. *Tissue Engineering Part B* 16 (2): 199–207.

50 Hoppe, A., Güldal, N.S., and Boccaccini, A.R. (2011). A review of the biological response to ionic dissolution products from bioactive glasses and glass-ceramics. *Biomaterials* 32 (11): 2757–2774.

51 Rivadeneira, J. and Gorustovich, A. (2017). Bioactive glasses as delivery systems for antimicrobial agents. *Journal of Applied Microbiology* 122 (6): 1424–1437.

52 Liu, L., Pushalkar, S., Saxena, D. et al. (2014). Antibacterial property expressed by a novel calcium phosphate glass. *Journal of Biomedical Materials Research Part B: Applied Biomaterials* 102 (3): 423–429.

53 Goh, Y.F., Akram, M., Alshemary, A., and Hussain, R. (2016). Antibacterial polylactic acid/chitosan nanofibers decorated with bioactive glass. *Applied Surface Science* 387: 1–7.

54 Clupper, D.C. and Hench, L.L. (2001). Bioactive response of Ag-doped tape cast Bioglass® 45S5 following heat treatment. *Journal of Materials Science: Materials in Medicine* 12 (10–12): 917–921. https://doi.org/10.1023/A:1012836426866.

55 Gholipourmalekabadi, M., Sameni, M., Hashemi, A. et al. (2016). Silver- and fluoride-containing mesoporous bioactive glasses versus commonly used antibiotics: activity against multidrug-resistant bacterial strains isolated from patients with burns. *Burns* 42 (1): 131–140. https://doi.org/10.1016/j.burns.2015.09.010.

56 Bellantone, M., Williams, H.D., and Hench, L.L. (2002). Broad-spectrum bactericidal activity of Ag_2O-doped bioactive glass. *Antimicrobial Agents and Chemotherapy* 46 (6): 1940–1945. https://doi.org/10.1128/AAC.46.6.1940-1945.2002.

57 Catauro, M., Bollino, F., Papale, F., and Vecchio Ciprioti, S. (2015). Investigation on bioactivity, biocompatibility, thermal behavior and antibacterial properties of calcium silicate glass coatings containing Ag. *Journal of Non-Crystalline Solids* 422: 16–22. https://doi.org/10.1016/j.jnoncrysol.2015.04.037.

58 Zhu, H., Hu, C., Zhang, F. et al. (2014). Preparation and antibacterial property of silver-containing mesoporous 58S bioactive glass. *Materials Science and Engineering C* 42: 22–30. https://doi.org/10.1016/j.msec.2014.05.004.

59 Balamurugan, A., Balossier, G., Laurent-Maquin, D. et al. (2008). An in vitro biological and anti-bacterial study on a sol–gel derived silver-incorporated bioglass system. *Dental Materials* 24 (10): 1343–1351. https://doi.org/10.1016/j.dental.2008.02.015.

60 Gupta, N., Santhiya, D., Murugavel, S. et al. (2018). Effects of transition metal ion dopants (Ag, Cu and Fe) on the structural, mechanical and antibacterial properties of bioactive glass. *Colloids and Surfaces A: Physicochemical and Engineering Aspects* 538: 393–403. https://doi.org/10.1016/j.colsurfa.2017.11.023.

61 Bellantone, M., Coleman, N.J., and Hench, L.L. (2000). Bacteriostatic action of a novel four-component bioactive glass. *Journal of Biomedical Materials Research* 51 (3): 484–490. https://doi.org/10.1002/1097-4636(20000905)51:3%3C484::AID-JBM24%3E3.0.CO;2-4.

62 Zheng, K., Balasubramanian, P., Paterson, T.E. et al. (2019). Ag modified mesoporous bioactive glass nanoparticles for enhanced antibacterial activity in 3D infected skin model. *Materials Science and Engineering C* 103 (January): 109764. https://doi.org/10.1016/j.msec.2019.109764.

63 Wang, X., Cheng, F., Liu, J. et al. (2016). Biocomposites of copper-containing mesoporous bioactive glass and nanofibrillated cellulose: biocompatibility and angiogenic promotion in chronic wound healing application. *Acta Biomaterialia* 46: 286–298. https://doi.org/10.1016/j.actbio.2016.09.021.

64 Wu, C., Zhou, Y., Xu, M. et al. (2013). Copper-containing mesoporous bioactive glass scaffolds with multifunctional properties of angiogenesis capacity, osteostimulation and antibacterial activity. *Biomaterials* 34 (2): 422–433. https://doi.org/10.1016/j.biomaterials.2012.09.066.

65 Abou Neel, E.A., Ahmed, I., Pratten, J. et al. (2005). Characterisation of antibacterial copper releasing degradable phosphate glass fibres. *Biomaterials* 26 (15): 2247–2254. https://doi.org/10.1016/j.biomaterials.2004.07.024.

66 Koohkan, R., Hooshmand, T., Tahriri, M., and Mohebbi-Kalhori, D. (2018). Synthesis, characterization and in vitro bioactivity of mesoporous copper silicate bioactive glasses. *Ceramics International* 44 (2): 2390–2399. https://doi.org/10.1016/j.ceramint.2017.10.208.

67 Bari, A., Bloise, N., Fiorilli, S. et al. (2017). Copper-containing mesoporous bioactive glass nanoparticles as multifunctional agent for bone regeneration. *Acta Biomaterialia* 55: 493–504. https://doi.org/10.1016/j.actbio.2017.04.012.

68 Sánchez-Salcedo, S., Shruti, S., Salinas, A.J. et al. (2014). In vitro antibacterial capacity and cytocompatibility of SiO_2–CaO–P_2O_5 meso-macroporous glass scaffolds enriched with ZnO. *Journal of Materials Chemistry B* 2 (30): 4836–4847.

69 Riaz, M., Zia, R., Saleemi, F. et al. (2015). In vitro antimicrobial activity of ZnO based glass–ceramics against pathogenic bacteria. *Journal of Materials Science: Materials in Medicine* 26 (12): 1–12.

70 Baghbani, F., Moztarzadeh, F., Hajibaki, L., and Mozafari, M. (2014). Synthesis, characterization, antibacterial activity and bioactivity evaluation of quinary glass system SiO_2–CaO–P_2O_5–MgO–ZnO: an in vitro study. *Bulletin of Materials Science* 36: 1339–1346. https://doi.org/10.1007/s12034-013-0593-6.

71 Esteban-Tejeda, L., Díaz, L.A., Prado, C. et al. (2014). Calcium and zinc containing bactericidal glass coatings for biomedical metallic substrates. *International Journal of Molecular Sciences* 15 (7): 13030–13044.

72 Boyd, D., Li, H., Tanner, D.A. et al. (2006). The antibacterial effects of zinc ion migration from zinc-based glass polyalkenoate cements. *Journal of Materials Science: Materials in Medicine* 17 (6): 489–494.

73 Brauer, D.S., Karpukhina, N., Kedia, G. et al. (2013). Bactericidal strontium-releasing injectable bone cements based on bioactive glasses. *Journal of the Royal Society Interface* 10 (78): 1–8. https://doi.org/10.1098/rsif.2012.0647.

74 Pourshahrestani, S., Zeimaran, E., Kadri, N.A. et al. (2016). Gallium-containing mesoporous bioactive glass with potent hemostatic activity and antibacterial efficacy. *Journal of Materials Chemistry B* 4 (1): 71–86.

75 Valappil, S.P., Ready, D., Abou Neel, E.A. et al. (2008). Antimicrobial gallium-doped phosphate-based glasses. *Advanced Functional Materials* 18 (5): 732–741. https://doi.org/10.1002/adfm.200700931.

76 Valappil, S.P., Ready, D., Abou Neel, E.A. et al. (2009). Controlled delivery of antimicrobial gallium ions from phosphate-based glasses. *Acta Biomaterialia* 5 (4): 1198–1210. https://doi.org/10.1016/j.actbio.2008.09.019.

77 Mouriño, V., Newby, P., and Boccaccini, A.R. (2010). Preparation and characterization of gallium releasing 3-D alginate coated 45S5 Bioglass® based scaffolds for bone tissue engineering. *Advanced Engineering Materials* 12 (7): 283–291. https://doi.org/10.1002/adem.200980078.

78 Valappil, S.P., Owens, G.J., Miles, E.J. et al. (2014). Effect of gallium on growth of *Streptococcus mutans* NCTC 10449 and dental tissues. *Caries Research* 48 (2): 137–146.

79 Deliormanlı, A.M. (2016). Electrospun cerium and gallium-containing silicate based 13-93 bioactive glass fibers for biomedical applications. *Ceramics International* 42 (1): 897–906. https://doi.org/10.1016/j.ceramint.2015.09.016.

80 Xu, Y.T., Wu, Q., Chen, Y.M. et al. (2015). Antimicrobial effects of a bioactive glass combined with fluoride or triclosan on *Streptococcus mutans* biofilm. *Archives of Oral Biology* 60 (7): 1059–1065.

81 Rostami, A., Mozafari, M., Gholipourmalekabadi, M. et al. (2015). Optimization of fluoride-containing bioactive glasses as a novel scolicidal agent adjunct to hydatid surgery. *Acta Tropica* 148: 105–114.

82 Goh, Y.F., Alshemary, A.Z., Akram, M. et al. (2014). In-vitro characterization of antibacterial bioactive glass containing ceria. *Ceramics International* 40 (1 PART A): 729–737. https://doi.org/10.1016/j.ceramint.2013.06.062.

83 Morais, D.S., Fernandes, S., Gomes, P.S. et al. (2015). Novel cerium doped glass-reinforced hydroxyapatite with antibacterial and osteoconductive properties for bone tissue regeneration. *Biomedical Materials* 10 (5): 055008.

84 Youness, R.A., Taha, M.A., El-Kheshen, A.A. et al. (2019). In vitro bioactivity evaluation, antimicrobial behavior and mechanical properties of cerium-containing phosphate glasses. *Materials Research Express* 6 (7): 075212.

85 Prefac, G.A., Milea, M.L., Vadureanu, A.M. et al. (2020). CeO_2 containing thin films as bioactive coatings for orthopaedic implants. *Coatings* 10 (7): 642.

86 Kurtuldu, F., Mutlu, N., Michálek, M. et al. (2021). Cerium and gallium containing mesoporous bioactive glass nanoparticles for bone regeneration: bioactivity, biocompatibility and antibacterial activity. *Materials Science and Engineering C* 124: 112050.

87 Deliormanlı, A.M., Vatansever, H.S., Yesil, H., and Özdal-Kurt, F. (2016). In vivo evaluation of cerium, gallium and vanadium-doped borate-based bioactive glass scaffolds using rat subcutaneous implantation model. *Ceramics International* 42 (10): 11574–11583.

88 Valappil, S.P. and Higham, S.M. (2014). Antibacterial effect of gallium and silver on *Pseudomonas aeruginosa* treated with gallium–silver–phosphate-based glasses. *Bio-Medical Materials and Engineering* 24 (3): 1589–1594.

89 Diba, M. and Boccaccini, A.R. (2014). Silver-containing bioactive glasses for tissue engineering applications. In: *Precious Metals for Biomedical Applications* (ed. N. Baltzer and T. Copponnex), 177–211. Woodhead Publishing.

90 Block, S.S. (ed.) (2001). *Disinfection, Sterilization, and Preservation*. Lippincott Williams & Wilkins.

91 Liau, S.Y., Read, D.C., Pugh, W.J. et al. (1997). Interaction of silver nitrate with readily identifiable groups: relationship to the antibacterial action of silver ions. *Letters in Applied Microbiology* 25 (4): 279–283. https://doi.org/10.1046/j.1472-765X.1997.00219.x.

92 Catauro, M., Raucci, M.G., de Gaetano, F., and Marotta, A. (2004). Antibacterial and bioactive silver-containing $Na_2O{\cdot}CaO{\cdot}2SiO_2$ glass prepared by sol–gel method. *Journal of Materials Science: Materials in Medicine* 15 (7): 831–837.

93 Chatterjee, A.K., Chakraborty, R., and Basu, T. (2014). Mechanism of antibacterial activity of copper nanoparticles. *Nanotechnology* 25 (13): 135101.

94 Lin, Y., Xiao, W., Bal, B.S., and Rahaman, M.N. (2016). Effect of copper-doped silicate 13-93 bioactive glass scaffolds on the response of MC3T3-E1 cells in vitro and on bone regeneration and angiogenesis in rat calvarial defects in vivo. *Materials Science and Engineering C* 67: 440–452.

95 Zhao, S., Li, L., Wang, H. et al. (2015). Wound dressings composed of copper-doped borate bioactive glass microfibers stimulate angiogenesis and heal full-thickness skin defects in a rodent model. *Biomaterials* 53: 379–391.

96 Cordero, P., Humberto, R.C.C., Dosque, M.D. et al. (2021). Li-doped Bioglass® 45S5 for potential treatment of prevalent oral diseases. *Journal of Dentistry* 105 (December 2020): https://doi.org/10.1016/j.jdent.2020.103575.

97 Gul, H., Nayyer, M., Gilani, M. et al. (2020). Comparative fluoride release and antimicrobial analysis of commercial and experimental bioactive glass/nano-oxide-based dentifrices. *European Journal of Dentistry* 14 (1): 38–44. https://doi.org/10.1055/s-0040-1701292.

98 Rabiee, S.M., Nazparvar, N., Azizian, M. et al. (2015). Effect of ion substitution on properties of bioactive glasses: a review. *Ceramics International* 41 (6): 7241–7251. https://doi.org/10.1016/j.ceramint.2015.02.140.

99 Balamurugan, A., Balossier, G., Kannan, S. et al. (2007). Development and in vitro characterization of sol–gel derived $CaO–P_2O_5–SiO_2–ZnO$ bioglass. *Acta Biomaterialia* 3 (2): 255–262. https://doi.org/10.1016/j.actbio.2006.09.005.

100 Yousef, J.M. and Danial, E.N. (2012). In vitro antibacterial activity and minimum inhibitory concentration of zinc oxide and nano-particle zinc oxide against pathogenic strains. *Journal of Health Science* 2 (4): 38–42.

101 Bini, M., Grandi, S., Capsoni, D. et al. (2009). $SiO_2–P_2O_5–CaO$ glasses and glass-ceramics with and without ZnO: relationships among composition, microstructure, and bioactivity. *Journal of Physical Chemistry C* 113 (20): 8821–8828. https://doi.org/10.1021/jp810977w.

102 Lessa, J.A., Parrilha, G.L., and Beraldo, H. (2012). Gallium complexes as new promising metallodrug candidates. *Inorganica Chimica Acta* 393: 53–63. https://doi.org/10.1016/j.ica.2012.06.003.

103 Chitambar, C.R. (2016). Gallium and its competing roles with iron in biological systems. *Biochimica et Biophysica Acta (BBA) – Molecular Cell Research* 1863 (8): 2044–2053.

104 Kelson, A.B., Carnevali, M., and Truong-Le, V. (2013). Gallium-based anti-infectives: targeting microbial iron-uptake mechanisms. *Current Opinion in Pharmacology* 13 (5): 707–716.

105 Pickup, D.M., Moss, R.M., Qiu, D. et al. (2009). Structural characterization by X-ray methods of novel antimicrobial gallium-doped phosphate-based glasses. *Journal of Chemical Physics* 130 (6): 064708.

106 Sahdev, R., Ansari, T.I., Higham, S.M., and Valappil, S.P. (2015). Potential use of gallium-doped phosphate-based glass material for periodontitis treatment. *Journal of Biomaterials Applications* 30 (1): 85–92.

107 Valappil, S.P., Coombes, M., Wright, L. et al. (2012). Role of gallium and silver from phosphate-based glasses on in vitro dual species oral biofilm models of *Porphyromonas gingivalis* and *Streptococcus gordonii*. *Acta Biomaterialia* 8 (5): 1957–1965.

108 Deliormanlı, A.M. (2015). Synthesis and characterization of cerium- and gallium-containing borate bioactive glass scaffolds for bone tissue engineering. *Journal of Materials Science: Materials in Medicine* 26 (2): 67.

109 Franchini, M., Lusvardi, G., Malavasi, G., and Menabue, L. (2012). Gallium-containing phospho-silicate glasses: synthesis and in vitro bioactivity. *Materials Science and Engineering C* 32 (6): 1401–1406.

110 Zeimaran, E., Pourshahrestani, S., Djordjevic, I. et al. (2016). Antibacterial properties of poly(octanediol citrate)/gallium-containing bioglass composite scaffolds. *Journal of Materials Science: Materials in Medicine* 27 (1): 1–11.

111 Brauer, D.S., Anjum, M.N., Mneimne, M. et al. (2012). Fluoride-containing bioactive glass-ceramics. *Journal of Non-Crystalline Solids* 358 (12–13): 1438–1442. https://doi.org/10.1016/j.jnoncrysol.2012.03.014.

112 Nicolini, V., Malavasi, G., Menabue, L. et al. (2017). Cerium-doped bioactive 45S5 glasses: spectroscopic, redox, bioactivity and biocatalytic properties. *Journal of Materials Science* 52 (15): 8845–8857.

113 Varini, E., Sánchez-Salcedo, S., Malavasi, G. et al. (2019). Cerium (III) and (IV) containing mesoporous glasses/alginate beads for bone regeneration: bioactivity, biocompatibility and reactive oxygen species activity. *Materials Science and Engineering C* 105: 109971.

114 Zhou, G., Gu, G., Li, Y. et al. (2013). Effects of cerium oxide nanoparticles on the proliferation, differentiation, and mineralization function of primary osteoblasts in vitro. *Biological Trace Element Research* 153 (1): 411–418.

115 Zheng, K., Torre, E., Bari, A. et al. (2020). Antioxidant mesoporous Ce-doped bioactive glass nanoparticles with anti-inflammatory and pro-osteogenic activities. *Materials Today Bio* 5: 100041.

116 Farag, M.M., Al-Rashidy, Z.M., and Ahmed, M.M. (2019). In vitro drug release behavior of Ce-doped nano-bioactive glass carriers under oxidative stress. *Journal of Materials Science: Materials in Medicine* 30 (2): 18.

117 Salinas, A.J., Shruti, S., Malavasi, G. et al. (2011). Substitutions of cerium, gallium and zinc in ordered mesoporous bioactive glasses. *Acta Biomaterialia* 7 (9): 3452–3458.

118 Ershad, M., Ali, A., Mehta, N.S. et al. (2020). Mechanical and biological response of $(CeO_2+La_2O_3)$-substituted 45S5 bioactive glasses for biomedical application. *Journal of the Australian Ceramic Society* 56: 1243–1252.

119 Mehrabi, T., Mesgar, A.S., and Mohammadi, Z. (2020). Bioactive glasses: a promising therapeutic ion release strategy for enhancing wound healing. *ACS Biomaterials Science & Engineering* 6 (10): 5399–5430.

120 Nicolini, V., Varini, E., Malavasi, G. et al. (2016). The effect of composition on structural, thermal, redox and bioactive properties of Ce-containing glasses. *Materials & Design* 97: 73–85.

121 Shruti, S., Salinas, A.J., Lusvardi, G. et al. (2013). Mesoporous bioactive scaffolds prepared with cerium-, gallium- and zinc-containing glasses. *Acta Biomaterialia* 9 (1): 4836–4844.

122 Thill, A., Zeyons, O., Spalla, O. et al. (2006). Cytotoxicity of CeO_2 nanoparticles for *Escherichia coli*. Physico-chemical insight of the cytotoxicity mechanism. *Environmental Science & Technology* 40 (19): 6151–6156.

123 Zhang, M., Zhang, C., Zhai, X. et al. (2019). Antibacterial mechanism and activity of cerium oxide nanoparticles. *Science China Materials* 62 (11): 1727–1739.

124 Begum, S., Johnson, W.E., Worthington, T., and Martin, R.A. (2016). The influence of pH and fluid dynamics on the antibacterial efficacy of 45S5 Bioglass. *Biomedical Materials* 11 (1): 015006.

125 Rahimi, R., Nikfar, S., Larijani, B., and Abdollahi, M. (2005). A review on the role of antioxidants in the management of diabetes and its complications. *Biomedicine & Pharmacotherapy* 59 (7): 365–373.

126 Zambon, A., Malavasi, G., Pallini, A. et al. (2021). Cerium containing bioactive glasses: a review. *ACS Biomaterials Science & Engineering* 7: 4388–4401.

127 Qi, M., Li, W., Zheng, X. et al. (2020). Cerium and its oxidant-based nanomaterials for antibacterial applications: a state-of-the-art review. *Frontiers in Materials* 7: 213.

128 Wu, C. and Chang, J. (2014). Multifunctional mesoporous bioactive glasses for effective delivery of therapeutic ions and drug/growth factors. *Journal of Controlled Release* 193: 282–295.

129 Andrade, A.L., Souza, D.M., Vasconcellos, W.A. et al. (2009). Tetracycline and/or hydrocortisone incorporation and release by bioactive glasses compounds. *Journal of Non-Crystalline Solids* 355 (13): 811–816.

130 Cavalu, S., Banica, F., Gruian, C. et al. (2013). Microscopic and spectroscopic investigation of bioactive glasses for antibiotic controlled release. *Journal of Molecular Structure* 1040: 47–52.

131 Domingues, Z.R., Cortés, M.E., Gomes, T.A. et al. (2004). Bioactive glass as a drug delivery system of tetracycline and tetracycline associated with β-cyclodextrin. *Biomaterials* 25 (2): 327–333.

132 Zheng, K., Bortuzzo, J.A., Liu, Y. et al. (2015). Bio-templated bioactive glass particles with hierarchical macro–nano porous structure and drug delivery capability. *Colloids and Surfaces B: Biointerfaces* 135: 825–832.

133 Jia, W.T., Zhang, X., Luo, S.H. et al. (2010). Novel borate glass/chitosan composite as a delivery vehicle for teicoplanin in the treatment of chronic osteomyelitis. *Acta Biomaterialia* 6 (3): 812–819.

134 Zhang, X., Jia, W., Gu, Y. et al. (2010). Teicoplanin-loaded borate bioactive glass implants for treating chronic bone infection in a rabbit tibia osteomyelitis model. *Biomaterials* 31 (22): 5865–5874.

135 Xie, Z., Liu, X., Jia, W. et al. (2009). Treatment of osteomyelitis and repair of bone defect by degradable bioactive borate glass releasing vancomycin. *Journal of Controlled Release* 139 (2): 118–126.

136 Xie, Z., Cui, X., Zhao, C. et al. (2013). Gentamicin-loaded borate bioactive glass eradicates osteomyelitis due to *Escherichia coli* in a rabbit model. *Antimicrobial Agents and Chemotherapy* 57 (7): 3293–3298.

137 Miola, M., Vitale-Brovarone, C., Mattu, C., and Verné, E. (2013). Antibiotic loading on bioactive glasses and glass-ceramics: an approach to surface modification. *Journal of Biomaterials Applications* 28 (2): 308–319. https://doi.org/10.1177/0885328212447665.

138 Soundrapandian, C., Mahato, A., Kundu, B. et al. (2014). Development and effect of different bioactive silicate glass scaffolds: in vitro evaluation for use as a bone drug delivery system. *Journal of the Mechanical Behavior of Biomedical Materials* 40: 1–12.

139 Nandi, S.K., Mukherjee, P., Roy, S. et al. (2009). Local antibiotic delivery systems for the treatment of osteomyelitis – a review. *Materials Science and Engineering C* 29 (8): 2478–2485.

140 Li, Y., Liu, Y.Z., Long, T. et al. (2013). Mesoporous bioactive glass as a drug delivery system: fabrication, bactericidal properties and biocompatibility. *Journal of Materials Science: Materials in Medicine* 24 (8): 1951–1961.

141 Hong, Y., Chen, X., Jing, X. et al. (2010). Fabrication and drug delivery of ultrathin mesoporous bioactive glass hollow fibers. *Advanced Functional Materials* 20 (9): 1503–1510.

142 Li, X., Wang, X., Zhang, L. et al. (2009). MBG/PLGA composite microspheres with prolonged drug release. *Journal of Biomedical Materials Research Part B Applied Biomaterials* 89 (1): 148–154.

143 Jones, J.R., Ehrenfried, L.M., Saravanapavan, P., and Hench, L.L. (2006). Controlling ion release from bioactive glass foam scaffolds with antibacterial properties. *Journal of Materials Science: Materials in Medicine* 17 (11): 989–996.

144 Blaker, J.J., Nazhat, S.N., and Boccaccini, A.R. (2004). Development and characterisation of silver-doped bioactive glass-coated sutures for tissue engineering and wound healing applications. *Biomaterials* 25 (7–8): 1319–1329.

145 Blaker, J.J., Boccaccini, A.R., and Nazhat, S.N. (2005). Thermal characterizations of silver-containing bioactive glass-coated sutures. *Journal of Biomaterials Applications* 20 (1): 81–98.

146 Pratten, J., Nazhat, S.N., Blaker, J.J., and Boccaccini, A.R. (2004). In vitro attachment of *Staphylococcus epidermidis* to surgical sutures with and without Ag-containing bioactive glass coating. *Journal of Biomaterials Applications* 19 (1): 47–57.

147 Shruti, S., Andreatta, F., Furlani, E. et al. (2016). Cerium, gallium and zinc containing mesoporous bioactive glass coating deposited on titanium alloy. *Applied Surface Science* 378: 216–223.

148 Deshmukh, K., Kovářík, T., Křenek, T. et al. (2020). Recent advances and future perspectives of sol-gel derived porous bioactive glasses: a review. *RSC Advances* 10 (56): 33782–33835. https://doi.org/10.1039/d0ra04287k.

149 Ni, S., Li, X., Yang, P. et al. (2016). Enhanced apatite-forming ability and antibacterial activity of porous anodic alumina embedded with $CaO–SiO_2–Ag_2O$ bioactive materials. *Materials Science and Engineering C* 58: 700–708.

150 Yazdimamaghani, M., Vashaee, D., Assefa, S. et al. (2014). Hybrid macroporous gelatin/bioactive-glass/nanosilver scaffolds with controlled degradation behavior and antimicrobial activity for bone tissue engineering. *Journal of Biomedical Nanotechnology* 10 (6): 911–931.

151 Zamani, D., Moztarzadeh, F., and Bizari, D. (2019). Alginate-bioactive glass containing Zn and Mg composite scaffolds for bone tissue engineering. *International Journal of Biological Macromolecules* 137: 1256–1267.

152 Hu, G., Xiao, L., Tong, P. et al. (2012). Antibacterial hemostatic dressings with nanoporous bioglass containing silver. *International Journal of Nanomedicine* 7: 2613.

153 Cicuéndez, M., Doadrio, J.C., Hernández, A. et al. (2018). Multifunctional pH sensitive 3D scaffolds for treatment and prevention of bone infection. *Acta Biomaterialia* 65: 450–461.

154 Zhu, M., Zhang, L., He, Q. et al. (2011). Mesoporous bioactive glass-coated poly(L-lactic acid) scaffolds: a sustained antibiotic drug release system for bone repairing. *Journal of Materials Chemistry* 21 (4): 1064–1072.

155 Liu, Y., Li, T., Ma, H. et al. (2018). 3D-printed scaffolds with bioactive elements-induced photothermal effect for bone tumor therapy. *Acta Biomaterialia* 73: 531–546.

156 Ye, J., He, J., Wang, C. et al. (2014). Copper-containing mesoporous bioactive glass coatings on orbital implants for improving drug delivery capacity and antibacterial activity. *Biotechnology Letters* 36 (5): 961–968.

157 Rahaman, M.N., Bal, B.S., and Huang, W. (2014). Emerging developments in the use of bioactive glasses for treating infected prosthetic joints. *Materials Science and Engineering C* 41: 224–231.

158 Arciola, C.R., Campoccia, D., Ehrlich, G.D., and Montanaro, L. (2015). Biofilm-based implant infections in orthopaedics. In: *Biofilm-Based Healthcare-Associated Infections*, vol. 830 (ed. G. Donelli), 29–46. New York: Springer.

159 Inzana, J.A., Schwarz, E.M., Kates, S.L., and Awad, H.A. (2016). Biomaterials approaches to treating implant-associated osteomyelitis. *Biomaterials* 81: 58–71.

160 ter Boo, G.J.A., Grijpma, D.W., Moriarty, T.F. et al. (2015). Antimicrobial delivery systems for local infection prophylaxis in orthopedic- and trauma surgery. *Biomaterials* 52: 113–125.

161 Prabhu, M., Ruby Priscilla, S., Kavitha, K. et al. (2014). *In vitro* bioactivity and antimicrobial tuning of bioactive glass nanoparticles added with neem (*Azadirachta indica*) leaf powder. *BioMed Research International* 2014: 10.

162 Cacciotti, I. (2017). Bivalent cationic ions doped bioactive glasses: the influence of magnesium, zinc, strontium and copper on the physical and biological properties. *Journal of Materials Science* 52 (15): 8812–8831.

163 Cacciotti, I. (2019). Multisubstituted hydroxyapatite powders and coatings: the influence of the codoping on the hydroxyapatite performances. *International Journal of Applied Ceramic Technology* 16 (5): 1864–1884.

164 Camaioni, A., Cacciotti, I., Campagnolo, L., and Bianco, A. (2015). Silicon-substituted hydroxyapatite for biomedical applications. In: *Hydroxyapatite (HAp) for Biomedical Applications* (ed. M. Mucalo), 343–373. Woodhead Publishing.

165 Kaur, G., Pandey, O.P., Singh, K. et al. (2016). Combined and individual doxorubicin/vancomycin drug loading, release kinetics and apatite formation for the $CaO–CuO–P_2O_5–SiO_2–B_2O_3$ mesoporous glasses. *RSC Advances* 6 (56): 51046–51056.

166 Polo, L., Gómez-Cerezo, N., Aznar, E. et al. (2017). Molecular gates in mesoporous bioactive glasses for the treatment of bone tumors and infection. *Acta Biomaterialia* 50: 114–126.

167 Galarraga-Vinueza, M.E., Mesquita-Guimarães, J., Magini, R.S. et al. (2018). Mesoporous bioactive glass embedding propolis and cranberry antibiofilm compounds. *Journal of Biomedical Materials Research Part A* 106 (6): 1614–1625.

168 Malavasi, G., Ferrari, E., Lusvardi, G. et al. (2011). The role of coordination chemistry in the development of innovative gallium-based bioceramics: the case of curcumin. *Journal of Materials Chemistry* 21 (13): 5027–5037.

169 Shih, S.J., Chen, C.Y., Lin, Y.C. et al. (2016). Investigation of bioactive and antibacterial effects of graphene oxide-doped bioactive glass. *Advanced Powder Technology* 27 (3): 1013–1020.

170 Xie, Z.P., Zhang, C.Q., Yi, C.Q. et al. (2008). Failure of particulate bioglass to prevent experimental staphylococcal infection of open tibial fractures. *Journal of Antimicrobial Chemotherapy* 62 (5): 1162–1163.

Index

Bioactive Glasses and Glass-Ceramics: Fundamentals and Applications, First Edition.
Edited by Francesco Baino and Saeid Kargozar.

C

d

e

h

i

n

q

r